JAERI-Review
2003-019

JP0350405

研究炉利用における研究成果集（平成13年度）

2003年7月

（編） 研究炉利用課

日本原子力研究所
Japan Atomic Energy Research Institute

本レポートは、日本原子力研究所が不定期に公刊している研究報告書です。
入手の問合わせは、日本原子力研究所研究情報部研究情報課（〒319-1195 茨城県那珂郡東海村）あて、お申し越し下さい。なお、このほかに財団法人原子力弘済会資料センター（〒319-1195 茨城県那珂郡東海村日本原子力研究所内）で複写による実費頒布を行っております。

This report is issued irregularly.
Inquiries about availability of the reports should be addressed to Research Information Division, Department of Intellectual Resources, Japan Atomic Energy Research Institute, Tokai-mura, Naka-gun, Ibaraki-ken 〒319-1195, Japan.

© Japan Atomic Energy Research Institute, 2003

編集兼発行　日本原子力研究所

JAERI－Review 2003-019

研究炉利用における研究成果集（平成１３年度）

日本原子力研究所東海研究所研究炉部
（編）研究炉利用課

（2003年5月12日受理）

平成13年度、研究炉においてはJRR-3の7サイクルとJRR-4の41サイクルの共同利用運転が行われ、中性子散乱実験や放射化分析のための照射等様々な目的に利用された。

本報告書は、実験あるいは照射利用を行った利用者（原研外を含む）から成果の提出を受け、これを分野別に取りまとめたものである。

東海研究所：〒319-1195　茨城県那珂郡東海村白方白根2-4

JAERI－Review 2003-019

Activity Report on the Utilization of Research Reactors (Japanese Fiscal Year, 2001)

(Ed.) Research Reactor Utilization Division

Department of Research Reactor
Tokai Research Establishment
Japan Atomic Energy Research Institute
Tokai-mura, Naka-gun, Ibaraki-ken

(Received May 12, 2003)

This is the fourth issue of the activity report on the utilization of research reactors in the fields of neutron beam experiments, neutron activation analysis, radioisotope production, etc., performed during Japanese Fiscal Year 2001(April 1, 2001- March 31, 2002).

All reports in this volume were described by users in JAERI and also users in the other organizations, i.e., universities, national research institutes and private companies, who had utilized our research reactor utilization facilities for the purpose of the above studies.

Keywords: JRR-3, JRR-4, Research Reactor, Neutron Scattering, Neutron Radiography, Neutron Activation Analysis, Neutron Beam, Irradiation

目　　次

はじめに …… 1
研究成果一覧 …… 3
1. 中性子散乱 …… 25
1) 構造・励磁 …… 25
2) 磁　性 …… 87
3) 超伝導現象 …… 187
4) 非晶質・液体 …… 209
5) 高分子 …… 233
6) 生物学 …… 271
7) 基礎物理学・中性子光学 …… 285
8) 装　置 …… 301
9) その他 …… 319
2. 中性子ラジオグラフィ …… 341
3. 放射化分析 …… 375
4. ＲＩの製造 …… 435
5. 原子炉材料照射試験 …… 439
6. 即発ガンマ線分析 …… 445
7. その他 …… 451
謝 辞 …… 480
付 録 …… 481

Contents

Preface 1
Research Reports 3
1. Neutron Scattering 25
1) Structure・Excitation 25
2) Magnetism 87
3) Superconductivity 187
4) Amorphous・Liquid 209
5) Polymer 233
6) Biology 271
7) Fundamental Physics・Neutron Optics 285
8) Instrument 301
9) Others 319
2. Neutron Radiography 341
3. Neutron Activition Analysis 375
4. Produciton of Radioisotopes 435
5. Irradiation Test of Reactor Materials 439
6. Prompt Gamma-ray Analysis 445
7. Others 451
Acknowledgments 480
Appendix 481

はじめに

平成１３年度には、ＪＲＲ－３において７サイクルの共同利用運転、ＪＲＲ－４において４１サイクルの共同利用運転が行なわれ、これに伴いさまざまな利用が行われた。

本報告書は、利用者（原研外利用者を含む）から当該利用の成果の提出を受け、取りまとめたものである。

提出して頂いた成果の件数は、中性子散乱２１１件、中性子ラジオグラフィ８件、放射化分析１６件、ＲＩの製造１件、原子炉材料２件、即発ガンマー線２件、その他１２件で合計２５２件であった。なお、本報告書では下記の報告書の中から一部を転載させて頂いた。

最後に、原稿を提出して頂いた利用者の皆様のご協力に感謝するとともに、今後も研究炉が有効に利用され、種々の研究がさらに進展されることを期待します。

研究炉利用課長
佐川　尚司

---

1) レポート番号：Vol.9（第９巻）
標　　題：ACTIVITY REPORT ON NEUTRON SCATTERING RESEARCH issued by ISSP-NSL,University of Tokyo
（東京大学物性研究所発行）
編　　者：Y.Oohara and M.Shibayama （藤井保彦,中島健次,大原泰明,）
発 行 年：２００２年

2) レポート番号：UTRCN-G-31
標　　題：原研施設利用共同研究成果報告書（平成１３年度）
編　　者：東京大学原子力研究総合センター
発 行 年：２００３年

This is a blank page.

研 究 成 果 一 覧

Research Reports

This is a blank page.

No.	「 Title 」	Page
	Neutron Scattering - Structure・Excitation -	
1-1-1	**Hydrothermal Synthesis of Iron Phosphate Cathode Materials** S. Tajima, H. Okawa, K. Uematsu, K. Toda, M. Sato	27
1-1-2	**High-temperature neutron Powder Diffraction study of Structural Change in Tricalcium Phosphate** A.Sakai, M.Yashima, R.Ali, M.Mori, K.Nakamura, K.Ohoyama, Y.Yamaguchi	29
1-1-3	**Phonon Anomaly in the Spin-Peierls System $CuGeO_3$** M.Nishi,H.Kadowaki,S.Katano,Y.Fujii,K.Kakurai,J.Akimitsu	31
1-1-4	**Structural Change of B_4C at High Temperatures** M.Yashima,K.Nakamura,R.Ali,K.Ohoyama,Y.Yamaguchi	32
1-1-5	**In Situ Study of Structural Change of $YTaO_4$ at High Temperatures** M.Yashima,T.Nogami,K.Ohoyama,Y.Yamaguchi	33
1-1-6	**Structures and Phase Transitions in Rb_2MoO_4 and Rb_2WO_4** H.Shigematsu,T.Matsui,K.Ohoyama	34
1-1-7	**Phonon Dispersions of the Normal Phase in Rb_2CoCl_4** H.Shigematsu,T.Matsui	35
1-1-8	**Crystal Structure in the Martensitic Phase of $Ni_{2.18}Mn_{0.82}Ga$ Alloy** K.Inoue,Y.Yamaguchi,K.Ohoyama,R.Note	36
1-1-9	**Structure Analysis of MeHPLN in Low Temperature Phase** R.Kiyanagi,H.Kimura,M.Watanabe,Y.Noda,A.Kojima,T.Mochida,T.Sugawara	38
1-1-10	**Zero Point Distribution of Protons in Ammonium Hexachloroplatinate by Single Crystal Neutron Diffraction II** T.Matsuo,N.Onoda,O.Yamamuro,Y.Fukuda,H.Kimura,S.Maesaki,Y.Noda	39
1-1-11	**Phonon Measurement on the Antiferroquadrupolar Order Compound $Ho^{11}B_2C_2$** A.Tobo,K.Ohoyama,K.Hirota,T.Ohmori,H.Onodera,Y.Yamaguchi	41
1-1-12	**Crystalline-State Photoisomerization of α , β -Unsaturated Thioamide Analyzed By X-Ray and Neutron Diffractions** T.Hosoya,T.Ohhara,H.Uekusa,Y.Ohashi	42
1-1-13	**Orbital Ordering in Highly Doped Single-Layered Manganite $Nd_{1-X}Sr_{1+X}MnO_4$** R.Kajimoto,H.Mochizuki,H.Yoshizawa,T.kimura,Y.Tokura	43
1-1-14	**Stripe-type Charge Ordering in the A-type Antiferromagnet $Pr_{0.5}Sr_{0.5}MnO_3$** R.Kajimoto, H.Yoshizawa,Y.Tomioka,Y. Tokura	45
1-1-15	**Spontaneous Rearrangement of the Checkerboard Charge Order to Stripe Order in $La_{1.5}Sr_{0.5}NiO_4$** R.Kajimoto,K.Ishizaka,H.Yoshizawa,Y.Tokura	47
1-1-16	**Phonon Density of States for Filled Skutterudite, $Ba_{0.1}CoSb_3$** T.Kajitani,Y.Ono,Y.Miyazaki,T.Goto	49
1-1-17	**Electron Doping Effects in Conducting Sr_2FeMoO_6** Y.Moritomo, Sh.Xu, K.Ohoyama	50

1-1-18	**Phase Separation and Ferromagnetic Transition in B-site Substituted Mangnaites** A.Machida,Y.Moritomo,K.Ohoyama	51
1-1-19	**Neutron Structural Analysis of $Tb_{1-x}Ca_xMnO_3$** A.Machida,Y.Moritomo,K.Ohoyama	52
1-1-20	**Modulated Structure of the Composite Crystal $[(Ca_{1-x}Sr_x)_2CoO_3]_{0.62}CoO_2$** Y.Miyazaki,T.Miura,M.Onoda,T.Kajitani	53
1-1-21	**Phase Transitions and Structures of $CH_3NH_3PbCl_3$** H.Mashiyama,Y.Kawamura,K.Ohoyama	54
1-1-22	**Relation between Crystal Structure, Thermodynamic Stability, and Electrode Characteristics of $LiMn_{2-x}M_xO_4$ (M=Ni,Zn) as a Cathode Active Material for the 4V, 5V Class Lithium Secondary Battery** Y.Idemoto,Y.Ito,H.Narai,Y.Tsunoda,N.Koura	55
1-1-23	**Martensitic Transformation of $Ni_{2.18}Mn_{0.82}Ga$ Single Crystal** K.Inoue,Y.Noda,H.Kimura,Y.Yamaguchi	57
1-1-24	**Crystal structure of Trivalent Ion Conductive Perovskite: $Y_x(Ta_{3x}W_{1-3X})O_3$** K.Toda,Y.Aoyama,M.Sato	59
1-1-25	**Shear-Induced Transformations in the Lamellar Phase Formed in Nonionic Surfactant-Water System** K.Minewaki,T.Kato,M.Imai,Y.Takahashi	61
1-1-26	**Jahn-Teller Induced Structural Phase Transition in $TbVO_4$** M.Hidaka,M.Fujii,S.Watanabe, S.R.P.Smith,K.Ohoyama,Y.Yamaguchi	62
1-1-27	**Crystal Structure and the Structural Phase Transition in an Itinerant 5*f* Antiferromagnet UCr_2Si_2** T.D.Matsuda,N.Metoki,Y.Haga,S.Ikeda,K.Kaneko,Y.Onuki	64
1-1-28	**Modulated Structure of the Composite Crystal $[Ca_2CoO_3]_{0.62}CoO_2$** Y.Miyazaki,M.Onoda,T.Oku,Y.Ishii,Y.Morii,T. Kajitani	66
1-1-29	**Diffuse Neutron Scattering from AgBr** A.Thazin,M.Arai,T.Sakuma,H.Takahashi,Y.Ishii	68
1-1-30	**Neutron Diffraction Study of $Sr_2YCu_2CoO_7$** T.Mochiku,Y.Hata,Y.Mihara,Y.Nakano,J.Suzuki,K.Kadowaki,K.Hirata	69
1-1-31	**Crystal Structure Study on Defective Silicalite by Neutron Diffraction** T.Suzuki,K.Sugita,Y.Ishii	70
1-1-32	**Magnetic Properties of $CaMn_{1-x}Ru_xO_3$** K.Yoshii,A.Nakamura,H.Abe,Y.Ishii,Y.Shimojo,Y.Morii	71

1-1-33	**Jahn-Teller Distortion and Orbital Ordering in $La_{0.875}Ca_{0.125}MnO_3$** Y.Ono,S.Begum,Y.Ishii,Y.Morii,T.Kajitani	72
1-1-34	**Static Structure Factor and Self-diffusion Coefficient of Molten Tin in the Wide Temperature Range** T.Masaki,H.Aoki,S.Munejiri,Y.Ishii,T.Itami	73
1-1-35	**Lattice Dynamics of Tetragonal $PbTiO_3$** I.Tomeno,Y.Tsunoda,Y.Ishii,K.Oka,H.Unoki	75
1-1-36	**Structural Transition in $LiErO_2$** Y.Hashimoto,M.Wakeshima,K.Matsuhira,Y. Hinatsu,Y.Ishii	76
1-1-37	**Measurement of Internal Strain in Si Single Crystal by Neutron Diffraction Method** T.Saito,N.Minakawa,Y.Morii,T.Sasaki,Y.Hirose	77
1-1-38	**Stress Measurement in Thin Steel Plate by Means of Neutron Image Plate** T.Sasaki, N.Niimura, Y.Morii , N.Minakawa, Y.Hirose	78
1-1-39	**Neutron Diffraction Study for Locating Proton in Cryptomelane-Type MnO_2 Crystal** M.Tsuji,K.Kawasaki,Y.Tanaka,Y.Ishii	80
1-1-40	**Neutron Powder Diffraction Study on BaF_2 at High Temperature** T.K.Datta,Y.Ishii	81
1-1-41	**Neutron Diffraction Study on Metane-Ethane Hydrate** Y. Ishii,C.J.Rawn,A.J.Rondinone,L.A.Sten,S.Circone, S.H. Kirby, B.C. Chakomakos	82
1-1-42	**Neutron Diffraction Study on Trimethlene Oxide Deuterate** Y.Ishii,A.J.Rondinone,C.J. Rawn,B.C.Chakomakos	84
1-1-43	**The Use of Rigid Body Constraints in Rietveld Refinements of Neutron Diffraction Data of Clathrate Hydrate** B.C.Chakoumakos,C.J.Rawn,A.J.Rondinone,S.L.Marshall,L.A.Stern,S.Circone S.H.Kirby,C.Y.Jones,B.H.Toby,Y. Ishii	85
1-1-44	**Structure Study on Tetrahydrofuran Deuterate by Neutron Powder Diffraction** Y.Ishii,C.Y.Jones,S.L.Marshall,C.J.Rawn,B.C.Chakomakos	86

No.	「 Title 」	Page
	Neutron Scattering - Magnetism -	
1-2-1	**Spin-Wave Excitations in the Metallic Ferromagnetic State of the CMR Manganite $Sm_{0.55}Sr_{0.45}MnO_3$** H. Hiraka, K. Hirota, Y. Endoh, Y. Tomioka, Y. Tokura	89
1-2-2	**Inelastic Neutron Scattering of NaV_2O_5 Under High Pressure** M. Nishi, T. Yosihama, K. Kakurai, K. Nakajima, Y. Fujii, M. Isobe, Y. Ueda M. Yethiraj, J. A. Fernandez-Baca, W. Montfrooij, S. Nagler	90
1-2-3	**Crystal and Magnetic Structures of $Ba_3TbRu_2O_9$** Y. Doi, M. Wakeshima, Y. Hinatsu, A. Tobo, K. Ohoyama, Y. Yamaguchi	92
1-2-4	**Neutron Scattering of $BaVS_3$ Oriented Crystals** M. Shiga , H. Nakamura, T. Yamasaki, M. Nishi, K. Kakurai	93
1-2-5	**Atomic and Magnetic Order in $RbCo_{1-x}Mg_xF_3$ System** K. Motoya, R. Masaoka, J. Kikuchi, S. Itoh	94
1-2-6	**Ferromagnetic and Antiferromagnetic Correlations in Concentrated Alloy System $Fe_{65}(Ni_{1-x}Mn_x)_{35}$** K. Motoya, K. Hioki	95
1-2-7	**Spin density distribution in CeB_6** M. Saitoh, N. Okada, E. Nishibori, H. Takagiwa, T. Yokoo, M. Nishi, K. Kakurai S. Kunii, M. Takata, M. Sakata, J. Akimitsu	96
1-2-8	**Orbital Ordering in $La_{0.5}Sr_{1.5}MnO_4$** M. Togasaki, L. Kano, M. Saitoh, M. Takeda, M. Nishi, K. Hirota, J. Akimitsu	98
1-2-9	**Neutron Diffraction Study of Magnetic Structure in $Ca_3Co_2O_6$** S. Niitaka, K. Yoshimura , M. Nishi, K. Kakurai	99
1-2-10	**The Magnetic Structure of Pt3Fe** Y.Higashiyama, Y.Tsunoda	100
1-2-11	**Spin-dynamics in PdMn Spin-glass Alloy** H. Hama, Y.Tsunoda	102
1-2-12	**Sample Dependence of Frustration System in Mn_3Pt Alloy** T. Ikeda,Y. Tsunoda	104
1-2-13	**Neutron Powder Diffraction for Frustrated $^{110}CdFe_2O_4$** K. Kamazawa, S. Hashiguchi, Y.Tsunoda	105
1-2-14	**Magnetic Neutron Scattering Measurements in Frustrated $ZnFe_2O_4$ Single Crystal** K. Kamazawa, Y, Tsunoda, H. Kadowaki, K. Kohn	106
1-2-15	**Neutron Diffraction Study on Single Crystal HoB_2C_2** A. Tobo, T. Ohmori, T. Matusumura, N. Oumi, K. Hirota, K. Ohoyama H. Yamauchi, H. Onodera, Y. Yamaguchi	107
1-2-16	**Magnetic Form Factor of $U_3Pd_{20}Si_6$** H. Sagayama, K. Kuwahara, M. Kohgi, M. Nishi, K. Nakajima, N. Aso,Y. Koike N. Metoki, N. Tateiwa, N. Kimura, H. Aoki	108
1-2-17	**Anisotropy of Magnetic Form Factor in UGe_2** H. Sagayama, K. Kuwahara, K. Iwasa, M. Kohgi, M. Nishi, K. Nakajima N. Aso K. Kakurai, Y. Haga, Y. Onuki	110
1-2-18	**Neutron Scattering of Ferroelectric-antiferromagnetic YMn_2O_5 Single Crystal** I. Kagomiya, Y. Fukuda, H. Kimura, Y. Noda, K.Kohn	112

1-2-19	**Metamagnetism of $TbRu_2Ge_2$ with a Two-Dimensional Modulated Magnetic Structure** T. Shigeoka, S. Kawano, M. Takahashi, M. Nishi	113
1-2-20	**Unusual Magnetism in the Strongly Correlated 5f-Electron System URu_2Si_2** H. Amitsuka, M. Yokoyama, J. Nozaki, S. Itoh, K. Watanabe, S. Kawarazaki H. Yoshizawa, J.A. Mydosh	114
1-2-21	**Non-Magnetic Impurity Effect on Domain Growth Kinetics in Isosceles Triangular Antiferromagnet $CoNb_2O_6$** H.Okano, S. Mitsuda, M. Kumagai, S. Kobayashi	115
1-2-22	**Neutron Diffraction Study on Mn_2RuGa Alloy** T. Hori, K. Ohoyama, Y. Yamaguchi	116
1-2-23	**Magnetic and Neutron Diffraction Study on $(Mn_{1-x}Pd_x)_2Ga$** H. Shiraishi, T. Hori, K. Ohoyama, Y. Yamaguchi	117
1-2-24	**Neutron Diffraction Study on the Magnetic Structure of GdB_2C_2** Y. Yamaguchi, K. Ohoyama, H. Yamauchi, K. Indoh, H. Onodera	118
1-2-25	**Magnetic Structure of β-$Na_{0.33}V_2O_5$ at Low Temperature(I)** S. Nagai, M. Nishi, K. Nakajima, Y. Fujii, K. Kakurai, T. Yamauchi, J. Yamaura M. Isobe, Y. Ueda	120
1-2-26	**Magnetic Structure of β-$Na_{0.33}V_2O_5$ at Low Temperature(II)** S. Nagai, M. Nishi, Y. Fujii, K. Kakurai, T. Yamauchi, J. Yamaura, M. Isobe Y. Ueda, H. Kimura, Y. Noda	121
1-2-27	**Powder Neutron Diffraction Measurements of TbPdSn** Y. Andoh, G. Nakamoto, M. kurisu, T. Tsutaoka, S. Kawano	122
1-2-28	**Phonon Dispersion in the Heavy-Electron Compound URn_2Si_2** K. Kuwahara, K. Iwasa, M. Kohgi, M. Yokoyama, H. Amistuka	123
1-2-29	**Lattice Distortion and Magnetic Moment in CoO** K. Tomiyasu, Y. Tsunoda	124
1-2-30	**Magnetic Excitations in the Quantum Spin System NH_4CuCl_3** A. Oosawa, T. Ono, K. Kakurai, H. Tanaka	125
1-2-31	**Inelastic Neutron Scattering Study on Quasi-Two-Dimensional Distorted Triangular Antiferromagnet Cs_2CuBr_4** T. Ono, H. Tanaka, K. Nakajima, K. Kakurai	126
1-2-32	**Neutron Diffraction Studies of Tow-Dimensional Magnetic Modulation in $TbRu_2Ge_2$** S. Kawano, M. Toda, M. Takahashi, T. Shigeoka, N. Iwata	127
1-2-33	**Electronic Structures of $Sr_{1-x}La_xRuO_3$** H. Nakatsugawa, Y. Oohara	128
1-2-34	**Neutron Diffraction Studies on Ho_7Rh_3 Single Crystal** T. Tsutaoka, T. Tokunaga, Y. Andoh, S. Kawano, G. Nakamoto, M.Kurisu	129
1-2-35	**Magnetic Correlations and Crystal Field Excitations in Ce_2PdSi_3** A.Donni, Y. Nemoto, H. Mitsunobu, T. Goto, H. Kitazawa, N. Aso, S.R.Saha	130
1-2-36	**Magnetic Properties of Hexagonal $LuMnO_3$ and Their Doping Effect** T. Katsufuji, Y. Masaki, Y. Moritomo, K. Ohoyama, K.Kitazawa, H.Takagi	132
1-2-37	**Field Cooling Effect in Magnetic Neutron Scattering of $ZnCr_2O_4$ Crystal II** I. Kagomiya, Y. Hata, M. Toki, E. Kita, K. Kohn, K. Siratori, K. Nakajima, K. Kakurai	133

1-2-38	**Cold Neutron Scattering Study of $La_{1-x}Ca_xMnO_3$ With x=0.05-0.20** S. Begum, Y. Ono, Y. Miyazaki, Y. Tomioka, Y. Tokura, T. Kajitani	134
1-2-39	**Magnetic Structure and the Anomalous Hall Effect of $SrFe_{1-x}Co_xO_3$** Y. Yasui, T. Ido, S. Iikubo, M. Ito, M.Sato, K.Kakurai	135
1-2-40	**Magnetic Structure and the Anomalous Hall Effect of $Nd_2Mo_2O_7$** Y. Yasui, S. Iikubo, H. Harashina, T. Kageyama, M. Ito, M.Sato, K.Kakurai	137
1-2-41	**Crystal Electric Field in Tetragonal $Nb^{11}B_2C_2$** K. Ohyama, A. Tobo, K. Hirota, H. Onodera, Y. Yamaguchi	139
1-2-42	**La-Dope Effect on the Magnetic Structure in Tetragonal TmB_2C_2** K. Ohoyama, K. Indoh, A. Tobo, H. Onodera, Y.Yamaguchi	140
1-2-43	**Antiferro-Quadrupolar Ordering of Pr-Ion 4f-Electron State in $PrFe_4P_{12}$** K. Iwasa, L. Hao, M. Nakajima, M. Kohgi, H. Sugawara, Y. Aoki T. D. Matsuda, H. Sato	141
1-2-44	**Neutron Diffraction Study on TbPtSn** M. Kurisu, G. Nagamoto, T. Himi, Y. Andoh, T. Tsutaoka, Y. Makihara S. Kawano	143
1-2-45	**Paramagnetic Scattering from Nio** Y. Todate, K. Nakajima, K. Kohn	144
1-2-46	**Magnetic Structure in Ordered Pt-14.4 at.%Mn** M. Takahashi, T. Sembiling, K. Ohshima, Y. Noda	145
1-2-47	**Evidence of the Anisotropically Developed Antiferromagneticspin Fluctuation in $CeFe_2$ Under High Pressures** T. Fujiwara, H. Fujii, Y. Ishii, S. Koiwai, M. Kosaka, Y. Uwatoko, M. Nishi K. Kakurai	146
1-2-48	**Antiferromagnetic Phase Transition in $KMnF_3$ by means of Neutron Diffraction Camera** M. Hidaka, S. Takahashi, S. Watanabe, Y. Kawamura	147
1-2-49	**Correlation Between the Structural and Antiferromagnetic Phase Transitions in $ZnCr_2Se_4$** M. Hidaka, N. Tokiwa, M. Fujii, S. Watanabe, J. Akimitu	149
1-2-50	**Magnetic Excitation in Pt-Mn Spin Glass Alloy** M. Takahashi, T. Sembiling, K. Ohshima	151
1-2-51	**Magnetic Structure Analysis of $KCuF_3$** M. Takahashi	152
1-2-52	**Antiferromagnetic Phase Transition in Substituted Spinel of $Zn_{1-x}Cu_xCr_2Se_4$; x=0.50 and 0.60** M. Hidaka, N. Tokiwa, H. Fujii, K. Ohoyama	153
1-2-53	**Magnetic Structure and *H-T* Phase Diagram in a Localized 5*f* System $U_3Pd_{20}Si_6$** N. Metoki, Y. Koike, Y. Haga, K. A.McEwen, M. Kohgi, N. Aso, N. Tateiwa T. Komatsubara, N. Kimura, H. Aoki	155
1-2-54	**Magnetic Structure in an Itinerant 5*f* Antiferromagnet UCr_2Si_2** T. D. Matsuda, N. Metoki, Y. Haga, S. Ikeda, Y. Ohnuki	157

1-2-55	**Magnetic Excitations in an Itinerant 5*f* Antiferromagnet UPt_2Si_2** N. Metoki, Y. Koike, N. Bernhoeft, G. H. Lander, Y. Tokiwa, Y. Haga, Y. Ohnuki	159
1-2-56	**Neutron Scattering Study of the Magnetic and Crystal Structures in Itinerant-5*f* Antiferromagnets $UNiGa_5$ and $UPtGa_5$** Y. Tokiwa, Y. Haga, N. Metoki, Y. Ishii, Y. Ohnuki	161
1-2-57	**Magnetic Structure of the Coupled Edge-Sharing CuO_2 Chains in $Ca_2Y_2Cu_5O_{10}$** M. Matsuda, K. Kakurai, H. Yamaguchi, T. Ito, C. H. Lee, K. Oka	163
1-2-58	**SANS Study of Slow Dynamics in Concentrated Spin Glasses** K. Motoya, K. Hioki, J. Suzuki	165
1-2-59	**Relationship Between the Magnetic Structure and the Anomalous Hall Effect of $Cu_{1-x}Zn_xCr_2Se_4$** S. Iikubo, Y. Ohno, Y. Yasui, T. Fukamachi, K. Oda, M. Sato, K. Kakurai	167
1-2-60	**Neutron Diffraction Study of Antiferromagnetic Order in UGa_3 Under Pressure** M.Nakamura, Y.Koike, N.Metoki, K.Kakurai, Y.Haga, G.H.Lander, Y.Ohnuki	169
1-2-61	**Neutron Scattering Study on the Antiferroquadrupolar Order of DyB_2C_2 Under Magnetic Fields** H. Yamauchi, K. Ohoyama, S. Katano, M. Matsuda, H. Onodera, Y. Yamaguchi	171
1-2-62	**Determination of the Magnetic Structures of Exotic Spin-Density Waves in Cr(001)/Sn Epitaxial Films** M. Takeda, K. Mibu, J. Suzuki, M. Nakamura, M. Matsuda, K. Kakurai, Y. Endoh	173
1-2-63	**Investigation of the Magnetic Structure of a TbB_{50}-type B_{12} Cluster Compound** T. Mori, F. Izumi, Y. Ishii	175
1-2-64	**Magnetic *P-T* Phase Diagrams of CeSb and CeBi** T. Osakabe, A. Hannan, D. Kawana, K. Kohgi, H. Kitazawa	177
1-2-65	**Crystal and Magnetic Structure of the Antiferromagnetic Iron Sulfide $Bapr_2FeS_5$** M. Wakeshima, K. Ino, Y. Hinatsu, Y. Ishii, Y. Shimojo, Y. Morii	179
1-2-66	**Neutron Diffraction Study on Ordered Perovskites Ba_2LnRuO_6 (Ln=Tm,Yb) and Sr_2YbRuO_6** Y. Doi, Y. Hinatsu, Y. Shimojo, Y. Ishii	180
1-2-67	**Spin fluctuations in $Pr_{0.5}Ca_{0.5}Mn_{1-y}Cr_yO_3$ (y=0, 0.03)** J. Suzuki, M. Watahiki, T. Katsufuji	181
1-2-68	**Crystalline Electric Field Excitations in *f* Electron Compound $PrCu_6$** Y. Morii, Y. Koike, N. Metoki, Y. Onuki	182
1-2-69	**Field-Induced Antiferroquadrupolar Ordering in The Tetragonal TbB_2C_2 Compound** K. Kaneko, S. Katano, M. Matsuda, K. Ohoyama, H. Onodera, Y. Yamaguchi	183
1-2-70	**Spin Dynamics of Hole Doped Haldane System $Nd_{2-x}Ca_xBaNiO_5$** T. Sasaki, T. Yokoo, S. Katano, K. Kakurai, J. Akimitsu	185

No.	「 Title 」	Page
	Neutron Scattering - Superconductivity -	
1-3-1	**Phonon Density of States of β -ZrNBr** S.Shamoto, S.Takeda, T.Kajitani	189
1-3-2	**Relation Among Crystal Structure, Stripe Order and Superconductivity in$(La,Ba,Sr)_2CuO_4$** M.Fujita, H.Goka, M.Matsuda, K.Yamada	190
1-3-3	**Magnetic Excitation Spectra of $La_{1.48}Nd_{0.4}Sr_{0.12}CuO_4$** M.Ito, Y.Yasui, S.Iikubo, M.Soda, M.Sato, K.Kakurai, M.Nishi	191
1-3-4	**Neutron Scattering Study on In-Plane Phonon Modes of $YBCO_{6+x}$** M.Ito, Y.Yasui, M.Kanada, S.Iikubo, H.Harashima, M.Sato, K.Kakurai, M.Nishi	193
1-3-5	**Observation of a Gapped Excitation in the Overdoped $La_{2-x}Sr_xCuO_4$** H.Hiraka, C.R.V.Rao, C.H.Lee, Y.Endoh, K.Yamada	195
1-3-6	**Magnetic Field Effect in Lightly Doped $La_{2-x}Sr_xCuO_4$** M.Matsuda, M.Fujita, K.Yamada, R.J.Birgeneau, Y.Endoh, G.Shirane	196
1-3-7	**Magnetic Field Effect on the Static Magnetic Order in the Electron-Doped superconductor $Nd_{1.86}Ce_{0.14}CuO_4$** M.Matsuda, S.Katano, T.Uefuji, M.Fujita, K.Yamada	198
1-3-8	**Measurements of the In Plane Longitudinal Phonons of $La_{1.48}Nd_{0.4}Sr_{0.12}CuO_4$** M.Ito, Y.Yasui, S.Iikubo, M.Sato, K.Kakurai, M.Nishi	199
1-3-9	**Low Temperature Scattering in $La_2Cu_{1-x}Li_xO_4$** P.K.Mang, N.Kaneko, M.Greven, K.Kakurai, M.Matsuda	201
1-3-10	**Search for Antiferromagnetic Fluctuations in Bismuth-Based Superconductors** N.Kaneko, P.K.Mag, K.Kakurai, M.Matsuda, H.Hiraka, Y.Endoh, K.Nakajima M.Greven	203
1-3-11	**Relationship Between Spin Fluctuations and Superconductivity in the Electron-Doped Superconductor $Pr_{1-x}LaCe_xCuO_{4+y}$** M.Fujira, S.Kuroshima, T.Uefuji, M.Matsuda, K.Kakurai, K.Yamada	205
1-3-12	**Charge-Spin Self-Organization in Superconducting Cuprate** T.Egami, J.-H.Chung, Y.Endoh, S.Tajima, K.Kakurai	206
1-3-13	**Low-Energy Spin Fluctuations in the Ni-substituted $La_{2-x}Sr_xCuO_4$** H.Hiraka, T.Chuurei, M.Matsuda, Y.Endoh, M.Fujita, K.Yamada	208

No.	「 Title 」	Page
	Neutron Scattering -Amorphous・Liquid-	
1-4-1	**NSE and SANS Studies on the Temperature and Pressure Dependencies of the Curvature Elasticity of Amphiphilic Membranes** Y.Kawabata, M.Nagao, H.Seto, T.Takeda, S.Komura	211
1-4-2	**Dynamic Anomalies Accompanied by the Semiconductor-Metal Transition in Liquid Chalcogen** M.Yao, Y.Ohmasa, H.Kohno, Y.Kawabata	213
1-4-3	**Neutron Spin Echo Investigations on Dynamics of Lipid Bilayers in the DPPC/D_2O/$CaCl_2$ System** T.Takeda, N.Yamada, Y.Kawabata, H.Seto, M.Nagao	214
1-4-4	**Fast Relaxation in Glass-forming Electrolyte Aqueous Solutions** O.Yamamuro, Y.Madokoro, H.Ymasaki, T.Matsuo	216
1-4-5	**Medium-Range Order in Electrolyte Aqueous Solution Glasses** O.Yamamuro, Y.Madokoro, H.Yamasaki, T.Matsuo	217
1-4-6	**Neutron Scattering Study on Dynamics of Methanol Molecules in MCM-41** S.Kittaka, S.Takahara, Y.Kuroda, T.Mori, T.Yamaguchi	219
1-4-7	**Doppler Shift Neutron Spin Echo at Bragg Reflection of Magnetite Particle in Ferrofluid** N.Achiwa, H.Nishioka, T.Ebisawa, K.Kakurai, T.Yagi	220
1-4-8	**Rheo-SANS Behavior of an Aqueous Suspension of Poly (Methyl Methacrylate-co-Stytene) Particles** H.Watanabe, Y.Matsumiya, T.Kanaya, Y.Takahashi	222
1-4-9	**Structure Factors of Liquid Ge at High Temperatures and Electron-Ion Correlation** S.Takeda, Y.Kawakita, T.Enosaki, K.Oshima, H.Aoki, T.Masaki	223
1-4-10	**Slow Dynamics of *n* -Butoxyethanol-Water Mixture by Neutron Spin Echo Technique** K.Yoshida, T.Yamaguchi, M.Nagao, H.Seto	225
1-4-11	**Hydrogen-Bonded Structure in Concentrated Aqueous DL- and L-Alanine Solutions** Y.Kameda, M.Yaegashi, M.Imano, H.Naganuma, K.Mochiduki, T.Usuki O.Uemura	227
1-4-12	**Diffusion Dynamics of Water and Aqueous Solutions at Hydrothermal Conditions** N.Matubayasi, Y.Nagai, H.Munemura, M.Misawa, M.Nakahara	229
1-4-13	**Small Angle Scattering of Liquid As-Te Mixtures around Semiconductor-Metal Transition** K.Maruyama, T.Miyanaga	230
1-4-14	**Structural Changes in Liquid As-Te Mixtures around Semiconductor-Metal Transition** K.Maruyama, T.Shibuya, Y.Kawakita	231
1-4-15	**The Origin of FSDP in AgI-Ag_2O-V_2O_5 Glasses** H.Takahashi, N.Rikitake, T.Sakuma, Y.Ishii	232

No.	「 TItle 」	Page
	Neutron Scattering - Polymer -	
1-5-1	**Polysaccharides Induced Crystallization of TMV Particles** M. Imai, N.Uralami, K. Nakaya	235
1-5-2	**Structural Analysis of Metastable Phases of Triacylglycerols** F. Kaneko, T. Kawaguchi	236
1-5-3	**Analysis of Aggregation Structure of Natural Aluminum Silicate Nanofiber Gel and Its Polymer Hybrids** A. Takahara, K. Yamamoto, K. Hara, M. Sugiyama, M. Annaka, M. Nagao, M.Shibayama	237
1-5-4	**Dynamics of a Glass-forming Polymer near T_gAs Revealed by Thermal Neutron Spin Echo Technique** T. Kanaya, I.Tsukushi, K.Kakurai, M.Nishi, K.Nakajima	238
1-5-5	**Role of Local Dynamics in the Gas Permeability of Glassy Substituted Polyacetylenes. A Quasielastic Neutron Scattering Study** T. Kanaya, I.Tsukushi, K.Kaji, T. Sakaguchi, G. Kwak, T. Masuda	239
1-5-6	**Neutron Incoherent Quasi-elastic Scattering and Raman Scattering of Oriented Oleic Acid in alpha-phase** N.Achiwa, T. Yokoyama, K.Kumagai, M. Suzuki, M. Kasahara, T.Yagi	240
1-5-7	**Viscoelastic effects on the Dynamics of Concentration Fluctuations in Dynamics Asymmetric polymer blend** M.Takenaka, H. Hasegawa, S. Saito, H.Takeno, T. Hashimoto, M.Nagao	241
1-5-8	**Neutron and X-ray Structure Analyses of Poly(Pyridobisimidazole) PIPD** Y. Takahashi	242
1-5-9	**SANS Study on Melting Process of Poly(vinyl alchol) Gels** N. Takahashi, T. Kanaya, K. Nishida, K.Kaji	243
1-5-10	**Structural Analysis of Weakly-Charged Polymer Gels Including Local Hydrophobic Micro-Aggregations in Mixed Solvents** F. Ikkai, N. Masui, T. Karino, S. Naito, K. Kurita, M. Furusaka, M. Shibayama	245
1-5-11	**Small Angle Neutron Scattering Studies on Structural Inhomogeneities in Temperature Sensitive Polymer Gels: Irradiation Cross-linked Gels VS Chemically Cross-linked Gels** N. Masui, S. Takata, T.Norisuye, M. Shibayama	247
1-5-12	**Association Behavior of Fluorine-Containing Amphiphilic Block Copolymer in Aqueous Media** K. Matsumoto, H. Mazaki, H. Matsuoka	249
1-5-13	**Neutron Spin Echo Study of the Dynamics of Tethered Polyelectrolyte Chains on Solid Substrate in Aqueous Media** H. Matsuoka, P. Kaewsaiha, T. Ikeda, K. Matsumoto	251
1-5-14	**Molecular Weight Dependence of Interfacial Broadening at (Polystyrene/ Deuterated Polystyrene) Bilayers Below Bulk Glass Transition Temperature by Neutron Reflectivity** T. Kajiyama, D. Kawaguchi, K. Tanaka, S. Tasaki, A. Takahara	252

1-5-15	**Chain End Distribution near the Surface in polymer Films by Neutron Reflectivity** A. Takahara, D. Kawaguchi, K. Tanaka, S. Tasaki, T. Kajiyama	253
1-5-16	**Complex Microphase Transitions in an ABC Triblock Terpolymer** K. Yamauchi, H.Hasegawa, T. Hashimoto, M. Nagao	254
1-5-17	**Small-Angle Neutron Scattering Study on Droplet Density Dependence of Static Structure in a Ternary Microemulsion System** M.Nagao, H. Seto, N. Yamada	255
1-5-18	**Temperature and Pressure-Induced Phase Transition in Aerosol-OT, Water, n-Hexane Microemulsion System** M. Nagao, H. Seto, Y. Kawabata, N. Yamada, T.Takeda	257
1-5-19	**Small-angle Neutron Scattering Study on Thermal Phase Behavior of NIPA-PEG Diblock Copolymer** R. Motokawa, M. Annaka, S. Koizumi	259
1-5-20	**Phase Diagram for Polystyrene/Poly(vinyl methylether) Blend and Dynamical Symmetry-Asymmetry Crossover Line** S. Koizumi, H. Takeno	261
1-5-21	**Elastic Incoherent Structure Factors for Poly(styrene) and Poly(vinyl methyl ether) Mixtures** H. Takeno, S. Koizumi	263
1-5-22	**Small-Angle Neutron Scattering and Dielectric Studies on Poly(styrene) and Poly(vinyl methyl ether) Mixtures** H. Takeno, M. Kobayashi, M. Naoki, S. Koizumi	264
1-5-23	**Small-Angle Neutron Scattering Study of Long-Chain Branched Polyethylenes** T. Kasahara, T. Sakurai, T. Fujii, S. Koizumi	266
1-5-24	**Pressure-Induced Interdigitation of DPPC Aqueous Solution with Small Amount of Ethanol** H. Seto, H. Nobutou, N. Yamada, M. Nagao, D. Ihara, T.Takeda	268

No.	「 Title 」	Page
	Neutron Scattering - Biology -	
1-6-1	**Oligomeric Forms of the Light-harvesting Complexes from Photosynthetic Bacteria** Z.-Y. Wang, Y. Muraoka, M. Shimonaga, T. Nozawa	273
1-6-2	**Small-Angle Neutron Scattering of Lipophorin** C. Katagiri, M. Nagao, M. Sato, Y. Ito	274
1-6-3	**Structure Analysis of Ganglioside/Dipalmitoyl Phosphatidylcholine Vesicle Using Inverse Contrast Variation** M. Hirai, T. Hayakawa, K. Koisumi, R. Kan, H. Iwase	275
1-6-4	**The Origin of Non-Gaussianity in q Dependence of Incoherent Elastic Neutron Scattering** H. Nakagawa, H. Kamikubo, I. Tukushi, T. Kanaya, M. Kataoka	276
1-6-5	**Structure of Short and Long Chain Phosphatidylcholine Mixtures in Trehalose Solution** H. Takahashi	277
1-6-6	**Neutron Scattering Study on Self-Assembly of Keratin Molecules in Water** S. Naito, F. Ikkai, T. Karino, M. Furusaka, S. Fujiwara, N. Niimura	278
1-6-7	**Small-Angle Neutron Scattering Measurements of TroponinC on the Thin Filament** F. Matsumoto, K. Makino, K. Maeda, H. Patzelt, Y. Maeda, S. Fujiwara	279
1-6-8	**Analysis of the Muscle Structure from Neutron Fiber Diffraction Measurements Using the Contrast Variation Method** S. Fujiwara, Y. Takezawa, Y. Sugimoto, K. Wakabayashi	280
1-6-9	**Neutron Diffraction of a Single Crystal of a Complex of Hen Egg-White Lysozyme and Substrate-Analogue** S. Fujiwara,	281
1-6-10	**Neutron Diffraction Experiments of Fully Deuterated B-DNA Crystal** T. Chatake, S. Arai, T. Ohara, K. Kurihara, I. Tanaka, N. Niimura	282
1-6-11	**Neutron Crystallography of Human Lysozyme** K. Chiba-Kamoshida, T. Matsui, A. Ostermann, T. Chatake, T. Ohhara, I. Tanaka, K. Yutani, N. Niimura	283

No.	「 Title 」	Page
	Neutron Scattering - Fundamental Physics · Neutron Optics -	
1-7-1	**Echo Condition in Time Beat Neutron Spin Interferometry** N. Achiwa, G. Shirozu, T. Ebisawa, D. Yamazaki, M. Hino, S. Tasaki, T. Kawai	287
1-7-2	**Mieze Spin Echo Method Using RF Flippers** T. Ebisawa, S. Tasaki, R. Maruyama, N. Achiwa, D. Yamazaki, T. Kanaya N. Torikai, M. Hino	289
1-7-3	**Jamin-type Interferometer for Cold Neutron Using Etalon Plates** M. Kitaguchi, H. Funahashi, M. Hino, T. Nakura, H.M. Shimizu	290
1-7-4	**Neutron Diffraction Measurement of Residual Strain of Partial Penetration Welds for ITER Vacuum Vessel** M. Nakahira, A. Moriai, N. Minakawa	291
1-7-5	**Strain Measurment in Laser Peened Stainless Steel** Y. Akiniwa, K. Tanaka, H. Kimura, N. Minakawa, Y. Morii	292
1-7-6	**Residual Stress Measurement and Verification of Quenched Steel Based on Neutron Diffraction Method and Numerical Analysis** D.Y. Ju, R. Mukai, N. Minakawa	293
1-7-7	**Evaluation of Fatigue Damage in SiC Particulate Reinforced Aluminum Alloy by Neutron Diffraction** Y. Akiniwa, K. Tanaka, H. Kimura, N. Minakawa, Y. Morii	295
1-7-8	**Feasibility Study on Nondesutructive Measurement of Residual Stress Profile in Carburized Bearing Rings Using Neutron Diffraction Method** Y. Matsumoto, A. Moriai, N. Minakawa	296
1-7-9	**Residual Strain of W/Ta Joint Material for Spallation Neutron Source** K. Kikuchi, N. Minakawa, A. Moriai, Y. Morii, M. Kawai, M. Furusaka J.F. Li, H. Kurishita	297
1-7-10	**Internal Stress Analysis of Tungsten Fiber Reinfoeced Copper Composite** T. Hanabusa, M. Nishida	299

No.	「 Title 」	Page
	Neutron Scattering - Instrument -	
1-8-1	**Characteristics of Deuterated Diamond-like Carbon as Neutron Mirror** Y. Kawabata, T. Horie, M. Hino, S. Tasaki, K. Yoshida, I. Kanno, M. Nakayama	303
1-8-2	**Development of a New Spin Echo Spectrometer Using Multilayer Spin Splitters II** S.Tasaki, T. Ebisawa, M. Hino, R. Maruyama, N.Achiwa, D.Yamazaki, T.Kawai	304
1-8-3	**Characteristics of Photostimulable Phosphor $SrBPO_5:Eu^{2+}$ for Neutron Imaging** K. Sakasai, M. Katagiri, K. Toh, H. Takahashi, M. Nakazawa, Y. Kondo	305
1-8-4	**Comparison Between Symmetric Diffraction Geometry And Fully Asymmetric Diffraction Geometry (FADG) of Bent Perfect Silicon Monochromator** M.R. Muslih, I. Tanaka, P. Mikula, N. Niimura	306
1-8-5	**Improvement of the Polarized Neutron Beam Flux in TAS-1 Spectrometer by Doubly Focusing Heusler Monochromator** M. Nakamura, M. Takeda, K. Kakurai	307
1-8-6	**Beam Enhancement by a Pre-Crystal in the Precise Neutron Optics** H. Tomimitsu, Y. Hasegawa, K. Aizawa	309
1-8-7	**Development of Electrostatic Levitation Furnace for Neutron Diffraction** H. Aoki, P.-F. Paradis, T. Aoyama, T. Ishikawa, T. Masaki, Y. Ishii, T. Itami	311
1-8-8	**Development of Neutron Reflectometer for Air/Water Interface with Imaging Plate** H.Matsuoka, M. Matsutani, E. Mouri, A.Moriai, K. Soyama	313
1-8-9	**Off-Specular Reflection From Ni/Ti Multilayers** K. Soyama, C. Bin	314
1-8-10	**The Characteristic of the very Small-Angle Neutron Scattering Instrument Using thin Type ch-cut Si** K. Aizawa, H. Tomimitsu	315
1-8-11	**A new Single Crystal Diffractometer for Biological Macromolecules (BIX-3M)** K. Kurihara, I. Tanaka, T.Chatake, A. Ostermann, N. Niimura	316

No.	「 Title 」	Page
	Neutron Scattering - Others -	
1-9-1	**Structural Phase Transition in Pyroclore Compound $Cd_2Re_2O_7$** M. Toda, Y. Wakabayashi, R. Tazaki, H. Sawa, H. Kimura, Y. Noda, Z. Hiroi	321
1-9-2	**Structure and Battery Properties of $LiCoPO_4$ and Li_2CoPO_4F** S. Okada, M. Ueno, Y. Uebo, J. Yamaki	322
1-9-3	**Structure and Battery Properties of Calcite-Type MBO_3(M:V,Fe)** S. Okada, Y. Uebo, J. Yamaki	324
1-9-4	**Residual Strain Measurement of the Three Layers Material ,[WC-10mass%Ni]-[SUS304]-[WC-10mass%Ni]** K.Inoue, T. Tsujikami, M. Ohyanagi, M. Sugimoto, N. Minakawa, A. Moriai	326
1-9-5	**Deformation Behavior of Ferrite-Cementite Steels Examined by Neutron Diffraction** A. Kanie, Y. Tomota, T. Suzuki, A. Moriai, N. Minakawa, Y. Morii	328
1-9-6	**In Situ Neutron Diffraction Experiment During Tensile Defformation for a TRIP Type Multi-Phase Steel** Y. Tomota, H. Tokuda, N. Minakawa, A. Moriai, Y. Morii, Y. Adachi M. Wakita	330
1-9-7	**In Situ Obseravation of Deformation and Recovery Behavior by Neutron Diffraction in an Fe-Mn-Si Shape Memory Alloy** A.Onizawa, Y. Tomota, S. Torii, T. Suzuki, A. Moriai, N. Minakawa, Y. Morii	331
1-9-8	**Texture Measurement by Neutron Diffraction for Pearlite Steel Wires** T. Suzuki, Y. Tomota, A. Kanie, Y. Moriai, N. Minakawa, Y. Morii	332
1-9-9	**Development of Optical Devices for Cold Neutrons** H.M. Shimizu, T. Adachi, T. Oku, K. Ikeda, H. Sato, Y. Takizawa, K. Morimoto S. Morita, H. Ohmori, K. Sakai, F. Tokanai, K. Sasaki, Y. Kiyanagi, J. Suzuki	334
1-9-10	**Residual Strain Measurement of S45C Round Bar Hardened by Induction** K. Inoue, T. Horikawa, T. Tsujikami, M. Sugimoto, N. Minakawa, A. Moriai F. Ikuta	336
1-9-11	**Masurment of Residual Steress in the Neutron Cold Moderator Cell for High Intensity Proton Accelators II** A. Moriai, H. Kogawa, M. Kaminaga, N. Minakawa, Y. Horiguchi	338
1-9-12	**Masurment of Residual Stress in Distrbution Vicinity of the Crack on Peened Surface of Type 304 Stainless Steel by Neutron Diffraction Method** S. Okida, K. Enomoto, T. Machida, M. Hayashi, Y. Morii, N. Minakawa	339
1-9-13	**The Possibility of Internal Stress Measurement of the King-size Sample** N. Minakawa, A. Moriai, Y. Morii	340

No.	「 Title 」	Page
	Neutron Radiography	
2-1	**Development of Electronic Imaging System for Pulsed Neutron Radiography** M.Matsubayashi, K. mochiki, Y. Murata, M. Kuwako, T. Nakagawa, Y. Ikeno D. Masiko, S. Itoh	343
2-2	**Study on Stroboscopic Imaging Technique Using Neutron Radiography** M. Matsubayashi, T. Hibiki, K. Mishima, H. Unezaki	344
2-3	**Imaging of Spatial Development in Concentration Instability of Recursive two Liquid Phase Separative Aqueous Solution** M. Matsubayashi, M. Misawa	345
2-4	**Measurement of Point of Vapor Generation by Neutron Radiography** M. Kureta, H. Akimoto	346
2-5	**Development of Advanced Neutron Radiography Techniques Using Thermal and Cold Neutron from JRR-3 Part III** K. Mishima, Y. Saito, K. Kambe	347
2-6	**Neutron Radiography of Thick Hydrogenous Materials with use of an Imaging Plate Neutron Detector** K. Kato, G. Matsumoto, N. Niimura, Y. Haga, M. Matsubayashi, Y. Ikeda	354
2-7	**Development of Advanced Neutron Radiography Using Imaging Plates at JRR-3 TNRF and CNRF** M. Tamaki, Y. Masunaga, S. Taguchi, K. Iida, M. Okada	359
2-8	**Neutron - γ - ray Radiography Using Multi-Color Scintillator** K. Mochiki, Y. Murata, M. Kuwako, Y. Kimoto, T. Sato, T. Nakagawa, Y. Ikeno D. Masuko	365

No.	「 Title 」	Page
	Neutron Activation Analysis	
3-1	**Detection of the Particles Containing Natural Uranium by Fission-Track Method** K. Takai, F. Esaka, T. Onodera, S. Sakurai, S. Usuda, K. Watanabe	377
3-2	**Development of the Measuring Method Using Bromine Isotope Ratio in Order to Soil Water** N. Kihou, H. Fjiwara	378
3-3	**Distribution and Migration of Iodine in the Soil Water System of the Field** N. Kihou, K. Yuita	379
3-4	**Determination of Sodium and Copper in Saltwater Clam Shell by Activation Analysis** H. Kamioki	380
3-5	**Labeling of Heavy Metals in Soil Organic matter With Stable Isotopes** Y. Sakurai, N. Kihou, T. Makino, K. Sugahara	381
3-6	**Minor and Trace Elements Determination of Environmental Samples(2)** Y. Miyamoto, Y. Saito, S. Sakurai, K. Usuda	382
3-7	**Application of high Sensitive Determination by Using Multiparameter Coincidence Method - Analysis for an Ancient Chinese Bronze Vessel -** Y. Hatsukawa, N. Shinohara, Y. Toh, M. Oshima	384
3-8	**Neutron Activation Analysis of the Extraterrestrialmaterials** M. Ebihara, H. Nakahara, Y. Oura, G.W. Kallemeyn, S.K. Latif, H. Minowa K. Hirayama, T. Nagamine, M. Setoguchi, J. Chai, T. Nakamoto, T. Nishino R. Yamaguchi, X. Li, S. Yoneda	386
3-9	**INAA and FTD for Sedimentary Rocks from the Shimanto Terrane of South Kyushu , Japan** T. Suzuki	391
3-10	**Biological Monitoring of Pollution on Armadillidium Vulgare(Latreille) by Instrumental Neutron Activation Analysis** S. Kawanishi, N. Nogawa, H. Sawahata, M. Mori	398
3-11	**Basic Study for Using Lichen as an Environmental Index** R. Seki, Y. Saito	401
3-12	**Influence of Arbuscular Mycorrhizal Colonization on Uptake of Various Element by Host Plant** H. Suzuki, H. Kumagai, N. Nogawa, H. Sawahata, M. Kawate, K. Oohashi	405
3-13	**Neutron Activation Analysis of Aeolian Sediment Samples in China** K. Toyoda, Y. Shinozuka, A. Watanabe, K. Hasebe	415
3-14	**Extractable Organohalogens (EOX) in Brown Booby(Sula Leucogaster)** M. Kawano, M. Matsuda, T. Wakimoto	418
3-15	**Mobility of Lanthanides Accompanying Rock Alteration and Formation of Secondary Minerals in Acidic Environment** T. Oi, Y. Kikawada, R. Ohira, T. Honda	422
3-16	**Study on Neutron Activation Analysis** C. Yonezawa, H. Matsue, Sri. Wardani	432

No.	「 Title 」	Page
	Production of Radio Isotopes	
4-1	**Reactor Irradiation Experiment for Yttria Microspheres** K. Kobayashi, T. Sorita, T. Obata, Y. Shimizu, Y. Sawada, M. Saito, Y. Asada H. Saeki, M. Nemoto, S. Iwamoto	437

No.	「 Title 」	Page
	Irradiation Test of Reactor Materials	
5-1	**Irradiation Test of the Small Sized Motor with JRR-4** E. Ishitsuka, M. Nakamiti, S. Kan	441
5-2	**Tritium Release from Neutron-Irradiated Li_2O Sintered Pellets:Fluence Dependence** T. Tanifuji, D. Yamaki, S. Jitsukawa	442

No.	「 Title 」	Page
	Prompt Gamma-ray Analysis	
6-1	**Study on Neutron Induced Prompt Gamma-Ray Analysis** H. Matsue,C. Yonezawa	447
6-2	**Studies on Chemical Behaviors of High-Energy Charged Particles using Neutron-Beam Guide in JRR-3M** Y. Sakai, K. Kubo, Y. Kobayashi, Y. Yamada, H. Shoji, T. Saito C.Yonezawa, H. Matsue	449

No.	「 Title 」	Page
	Others	
7-1	**Comparison of Dosimetry by the Realistic Patient Head Phantom and by the Patient's Brain, and the JCDS Calculation - A Clinical Dosimetry Study** K. Endo, A. Matsumura, T. Yamamoto, T. Nose, K. Yamamoto, H. Kumada, T. Kishi, Y. Torii, T. Kashimura, S. Ohtake	453
7-2	**Radiobiological Characterization of JRR-4 Neutron Beams** T. Yamamoto, A. Matsumura, K. Yamamoto, H. Kumada, N. Hori, Y. Torii, K. Endo, A. Matsushita, F. Yoshida, Y. Shibata, T. Nose	455
7-3	**Comparative Study of the JCDS Calculation and Patient Brain Dose Measurements** T. Yamamoto, A. Matsumura, K. Yamamoto, H. Kumada, Y. Torii, K. Endo A. Matsushita, Y. Shibata, T. Nose	457
7-4	**Influence of Superfluidity on Recombination Reactions of H+T→ HT and T+T →T_2 in ^{3}He-^{4}He Quantum Media Under Saturated Vapor Pressure at 1.6K** Y. Aratono	459
7-5	**Characteristics of Dap Plastic Detector and its Application to Fission Track Dating** H. Iwano, T. Yoshioka, T. Danhara, T. Tsuruta	460
7-6	**Measurements of Neutron Capture Cross Section on $^{nat.}$Re** T. Shizuma, T. Hayakawa	461
7-7	**Basic and Clinical Research of Epithermal Neutron Capture Therapy for Malignant Brain Tumors Department of Neurosurgery and Anesthesiology Institute of Clinical Medicine** T. Nose, A. Matsumura, T. Yamamoto, F. Yoshida, Z.Tian, S. Takano, H. Toyooka T. Mizutani, H. Takahashi	462
7-8	**A Study of Exchange Interactions Between Localized Moments by Low Temperature Nuclear Orientation** K. Nishimura, S. Ohya, T. Ohtsubo T. Izumikawa, S. Muto, Y. Kawamura M. Sasaki	465
7-9	**Paramagnetic Lattice Defects in Quartz Created Internal Alpha and Alpha Recoil Particles** S. Toyoda	471
7-10	**Characteristic Measurements of the Multi-Leaf Collimator for Boron Neutron Capture Therapy at JRR-4** H. Kumada, T. Kishi, N. Hori, K. Yamamoto, Y. Torii	476
7-11	**Residual Strain of W/Ta Joint Material for Spallation Neutron Source** K.kikuchi, N. Minakawa, A. Moriai, M. Kawai, M. Furusaka, Y. Chul.Park Y. kurishita	478
7-12	**Intraoperative Boron Neutron Capture Therapy using Thermal/Epithermal Mixed Beam** A. Matsumura, T. Yamamoto, Y. Shibata, K. Nakai, Z. Tiang, A. Matsushita S. Takano, K. Endo, K. Yamamoto, H. Kumada, Y. Torii, T. Mizutani, H. Takahash H. Toyooka, T. Nose	479

This is a blank page.

1. 中性子散乱 1)構造・励磁

1. Neutron Scattering 1)Structure・Excitation

This is a blank page.

研究テーマ：新規合成法による全固体電池用正極材料と固体電解質の開発
表題：水熱法によるりん酸鉄系正極材料の合成

HYDROTHERMAL SYNTHESIS OF IRON PHOSPHATE CATHODE MATERIALS

1-1-1

Shigehisa Tajimi, Hirokazu Okawa, Kazuyoshi Uematsu, Kenji Toda and Mineo Sato

Department of Chemistry and Chemical Engineering, Faculty of Engineering, Niigata University, Ikarashi 2 no-cho 8050, Niigata, Niigata 950-2181, Japan

ABSTRACT

Well crystalline $Li_3Fe_2(PO_4)_3$ with an orthorhombic $Fe_2(SO_4)_3$-type structure was able to be synthesized by using two synthetic routs where hydrothermal reaction and successive heat treatment with low temperatures were employed. The sample prepared was found to show orthorhombic symmetry, contrary to the fact that a conventional solid state syntheses with high temperatures more than 1000°C gives monoclinic symmetry [1]. The sample showed two plateau potentials, 2.8 and 2.7 V vs. Li/Li^+, upon discharge, and the total discharge capacity of the sample exhibited more than 80 $mAhg^{-1}$ under 0.5 $mAcm^{-2}$.

INTRODUCTION

Intensive research is recently focused on $LiCoO_2$, $LiNiO_2$ and $LiMn_2O_4$ as currently practical materials for a positive electrode material in rechargeable lithium batteries. Natural resources and environment considerations as well as material efficiency and performance are also very important for developing cathode materials. This makes us prompt a research on alternative cathode systems of iron compounds, which are quite attractive in viewpoint of natural abundance and environment issue.

$Li_3Fe_2(PO_4)_3$ has been reported to exhibit relatively high potentials, 2.7-2.8 V vs. Li/Li^+, and good performance for a rechargeable lithium battery [2]. Usually, high temperatures are required in order to obtain well crystalline $Li_3Fe_2(PO_4)_3$ samples. We report here a new synthetic method for $Li_3Fe_2(PO_4)_3$ by using hydrothermal reaction and successive low temperature heat treatment.

EXPERIMENTAL

The starting materials for the hydrothermal reaction were LiOH, FeO(OH) and H_3PO_4. A mixture of these compounds in a molar ratio of 2 : 1 : 2 was placed in a Teflon vessel which was filled to a degree of 15% with water and enclosed in a stainless steel bomb. The mixture was heated at 220°C under autogenous pressure for 24h. The product was filtrated and dried in air, and then heated in an alumina crucible at various temperatures of 450-700°C for 24h in air. The crystal structure of sample was refined by the Rietveld method by neutron diffraction. Powder neutron diffraction pattern for the refinement was recorded using the PKD (HERMES) diffractometer installed at JRR-3M Guide Hall in the Japan Atomic Energy Research Institute (TAERI). An incident neutron wavelength λ = 1.8196 Å was obtained from a Ge(311) monochromater. The powder sample was enclosed in the cylindrical vanadium vessel and mounted on a double-axis diffractometer. The data were collected on thoroughly ground powders by a multi-scanning mode in the 2θ range from 5° to 155° with a step width of 0.05° and a monitoring time of 16 min. The powder patterns obtained were analyzed using the RIETAN2000 profile refinement program [3].

RESULTS AND DISCUSSION

After the hydrothermal reaction, the main crystalline product was identified to be $LiFe(PO_4)(OH)$ by powder X-ray diffraction. The product also contained a small amount of some unidentified crystalline materials. In the next heat treatment, $Li_3Fe_2(PO_4)_3$ began to crystallize from 450°C, and a single phase of $Li_3Fe_2(PO_4)_3$ could be obtained over 525°C. Rietveld analysis for the neutron diffraction pattern was carried out on the data sets measured at room temperature for the sample fired at 700℃ (Fig. 1). The fitting pattern shows well crystalline $Li_3Fe_2(PO_4)_3$ prepared by a two-step route of a hydrothermal reaction and a solid state reaction. DTA analysis showed no phase transition for the sample prepared by this method. In general, materials with the $Fe_2(SO_4)_3$-type structure such as $Li_3Sc_2(PO_4)_3$, $Li_3In_2(PO_4)_3$ and $Li_3V_2(PO_4)_3$ usually

使用施設：JRR-3M, 装置：HERMES(T1-3), 分野：1. Structures & Excitations

have three kinds of structural modifications, monoclinic low-temperature form, monoclinic middle-temperature form and orthorhombic high-temperature form, where all transitions are reversible. In fact, the sample prepared by a conventional solid-state reaction at 1100°C showed two reversible transition points at 240 and 260°C. From these facts, the sample prepared by the new method may be a high-temperature modification with orthorhombic symmetry [4].

Figure shows the discharge/charge curves obtained at 0.5 $mAhg^{-1}$ for the sample heat-treated at 525°C. The insertion of lithium into the material actually occurs in two separate intercalation plateaus, at 2.8 and 2.7 V. The similar behavior are found for $Li_3V_2(PO_4)_3$ in our previous study. The $Fe_2(SO_4)_3$-type structure has three kinds of sites for lithium atoms. In the orthorhombic high-temperature, one site is fully occupied and the other two sites are partially occupied with 1/4 occupancy. Probably, the existence of such partially occupied sites, which inserted lithium ions can occupy, is responsible for the two separate potential plateaus. The sample showed a good cycle performance, about 85% capacity efficiency after 10 cycles (Fig. 2). Contrary to this, the sample prepared by the solid-state reaction exhibited a quite poor cycle performance, only 30% capacity efficiency after 3 cycles. The good cycle performance of the sample prepared by the new method could be attributed to high surface area given by the low temperature synthesis.

REFERENCES

[1] K. S. Nanjundaswamy, A. K. Padhi, J. B. Goodenough, S. Okada, H. Ohtsuka, H. Arai, J. Yamaki, Solid State Ionics., 92, 1 (1996)

[2] A. K. Padhi, K. S. Nanjundaswamy, C. Masquelier, S. Okada, J. B. Goodenough, J. Electrochem. Soc., 144,5,1609(1997)

[3] F. Izumi, in R. A. Youg (ed.), The Rietveld Method, Oxford University Press, Oxford, 1993, Chp 13.

[4] A. B. Bykov, A. P. Chirkin, et al, Solid State Ionics., 38, 31 (1990)

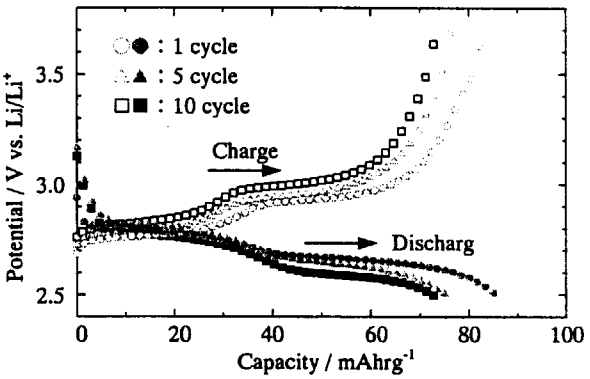


Figure 2. Charge and Discharge curves of $Li_3Fe_2(PO_4)_3$

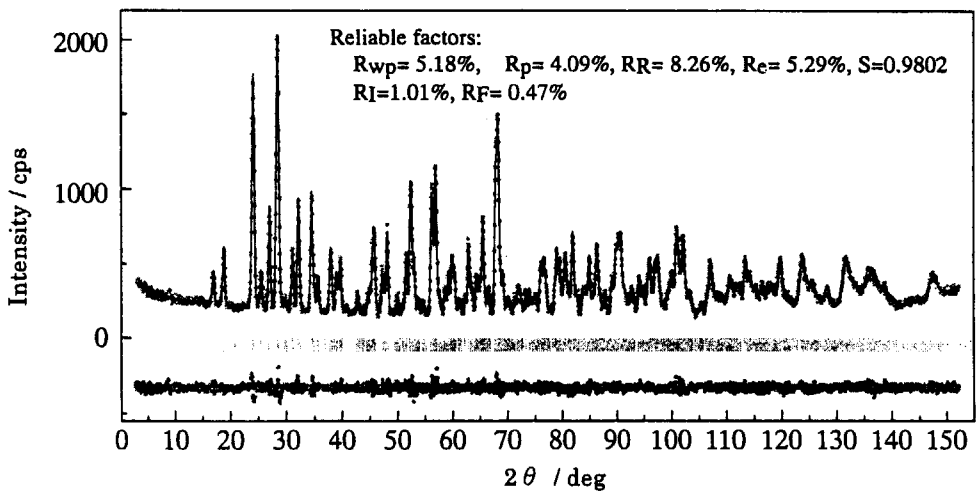


Figure 1. Neutron diffraction pattern fitting of Rietveld refinement for $Li_3Fe_2(PO_4)_3$ prepared by hydrothermal and solid state reactions

研究テーマ：蛍石関連固溶体の構造変化
表題：高温粉末中性子回折によるリン酸三カルシウムの構造変化の研究

1-1-2

High-temperature neutron powder diffraction study of structural change in tricalcium phosphate

Atsushi Sakai, Masatomo Yashima, Roushown Ali, Mizuki Mori, Kazumasa Nakamura, Kenji Ohoyama[1] and Yasuo Yamaguchi[1]

Department of Materials Science and Engineering Interdisciplinary Graduate School and Engineering, Tokyo Institute of Technology, 4259, Nagatsuta-cho, Midori, Yokohama, 226-8502, JAPAN
[1]Institute for Materials Research, Tohoku University, Katahira, Aoba, Sendai, 980-8577, JAPAN

Apatites and calcium phosphates are increasingly used as biocompatible materials for bone replacement and for the coating of bone prostheses. According to the literature, β-$Ca_3(PO_4)_2$ (β-TCP) transforms to α-$Ca_3(PO_4)_2$ (α-TCP) around 1125 °C [1], and α-TCP transforms to a high-temperature phase, α'-$Ca_3(PO_4)_2$ (α'-TCP) around 1430°C [2]. The crystal structures of β- and α-TCPs were determined, while the structure of α'-TCP has not been known yet. The purpose of this work is to study the α-α' phase transition of TCP, and to determine the crystal structure of α'-TCP.

High-purity α-TCP was prepared by solid-state reactions from $CaHPO_4$ and $CaCO_3$. The neutron-diffraction measurements were performed in air with a 150-detector system, HERMES, installed at the JRR-3M reactor in JAERI [3]. Diffraction data were collected in the 2θ range from 20° to 150° in step interval of 0.1°, in the temperature range from 24°C to 1524°C. A furnace with $MoSi_2$ heater was placed on the sample table [4], and used for neutron-diffraction measurements at high temperatures. The temperature was kept constant within ±1.5°C during each data collection. The neutron-diffraction data were analyzed by Rietveld analysis using a computer program RIETAN-2000 [5].

Figure 1 shows the temperature dependence of neutron-diffraction pattern for TCP. All the neutron-diffraction peaks were indexed by $h\ k\ l$ of α-TCP, indicating the single phase of α phase between 24°C and 1449°C. At 1474°C, the pattern exhibited both peaks of α (●) and α' (○) phases. Therefore α and α' phases coexisted at this temperature. The characteristic peaks of α phase (●) disappeared between 1474°C and 1499°C. The single phase of α'-TCP existed at 1499°C and 1524°C. During cooling, $\alpha' \rightarrow \alpha$ phase transition was observed also between 1499°C and 1449°C. These results indicate that the α-α' phase transition occurred reversibly between 1449°C and 1499°C.

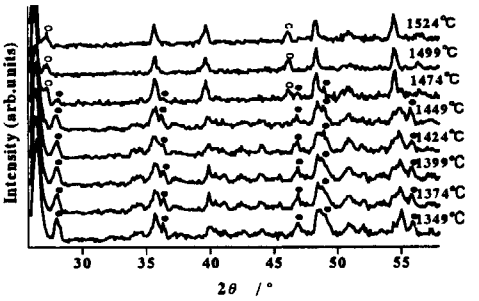


Fig.1 Neutron powder diffraction patterns of TCP obtained at different temperatures. Each diffraction patern was measured keeping the sample temperature constant after heating.

Structural refinements of α phase were successfully done using a monoclinic structure (space group $P2_1/a$) for the neutron-diffraction data between 24°C and 1449°C. For the data obtained at 1499°C and 1524°C, structural refinements of α' phase

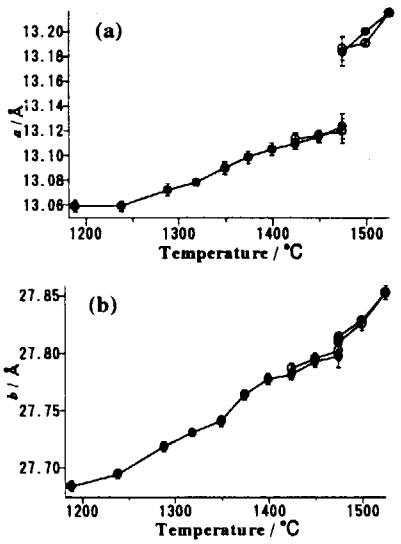
使用施設：JRR-3M，装置：(HERMES)，分野：1. Structures & Excitations

研究テーマ：蛍石関連固溶体の構造変化
表題：高温粉末中性子回折よるリン酸三カルシウムの構造変化の研究

were successfully performed using a new monoclinic structure (space group *C*2/*c*). The data measured at 1474°C was successfully analyzed by the mixture of α- and α'-TCP.

Figure 2 shows the temperature dependence of unit-cell parameters (a) *a*-axis, (b) *b*-axis, (c) *c*-axis, (d) β angle and (e) unit-cell volume *V*. The unit-cell parameters and unit-cell volume of α phase increased continuously with an increase of temperature between 1188 °C and 1474 °C. At 1474°C, the α and α' phases coexisted. The *a*-axis length and unit-cell volume *V* of α' phase were larger than those of α phase, while the *c*-axis length and β angle of α' phase were smaller than those of α phase. The *b*-axis length of α' phase was almost equal to that of α phase. The unit-cell parameters and unit-cell volume of α' phase increased between 1474°C and 1524°C. The unit-cell parameters and unit-cell volume obtained on heating exhibited fairly good agreements with those on cooling.

The α-α' phase transition of TCP is of first order, because (1) the α and α' phases coexisted at 1474°C, (2) the *a*- and *c*-axis lengths, β angle and unit-cell volume *V* changed discontinuously at the α-α' phase transition point.



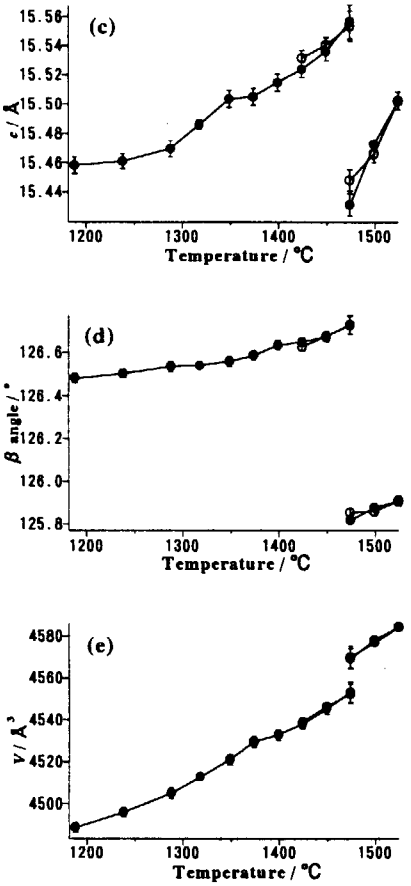


Fig.2 Temperature dependence of unit-cell parameters (a) *a*-axis, (b) *b*-axis, (c) *c*-axis, (d) β angle and (e) unit-cell volume *V*. Filled and open circles denote the data obtained on heating and cooling, respectively.

References

[1] Welch J. H, Gutt W: J. Chem. Soc. 1961, 4442-4444.
[2] Nurse R. W, Welch JH, Gutt W: J. Chem. Soc. 1959, 1077-1083.
[3] Ohoyama K, Kanouchi T, Nemoto K, Ohashi M, Kajitani T, Yamaguchi Y: Jpn. J. Appl. Phys. 1998, 37, 3319-3326.
[4] Yashima M: J. Cryst. Soc. Jpn. 2002, 44, 121-126.
[5] Izumi F, Ikeda T: Materia. Sci. Forum. 2000, 321-324, 198-204.

使用施設：JRR-3M，装置：(HERMES)，分野：1. Structures & Excitations

研究テーマ：CuGeO3の中性子非弾性散乱
表題：スピン・パイエルス系 $CuGeO_3$ におけるフォノン異常

1-1-3 Phonon Anomaly in the Spin-Peierls System $CuGeO_3$

M. Nishi[1], H. Kadowaki[2], S. Katano[3], Y. Fujii[1], K. Kakurai[3] and J. Akimitsu[4]
[1] *Neutron Scattering Laboratory, ISSP, University of Tokyo, 106-1, Shirakata, Tokai, Ibaraki*
[2] *Dept. of Physics, Tokyo Metropolitan University, Hachiohji, Tokyo*
[3] *Advanced Science Research Center, JAERI, Tokai, Ibaraki*
[4] *Dept. of Physics, Aoyama-Gakuin University, Chitosedai Setagayaku, Tokyo*

Magnetic energy of the dimerized singlet pair is lower than that of homogeneous antiferromagnetic system theoretically. Spin-Peierls (SP) transition is the magnetically induced transition from the paramagnetic state to the singlet ground state in an one-dimensional S=1/2 spin system with the lattice dimerization simultaneously. With the discovery of the first inorganic SP compound $CuGeO_3$ by Hase *et al.* in 1993 [1]. many efforts to clarify the SP mechanism were performed theoretically and experimentally. The soft phonon mode which is expected in the standard SP transition by Cross and Fisher [2] has not been observed yet. In the case of organic SP compound $MEM(TCNQ)_2$ (T_{SP}=19 K), a soft phonon mode with the energy of 1.05 meV was observed by Raman scattering [3]. In the TTF-CuBDT (T_{SP}= 11 K) the energy of soft mode was also obtained to 1.4 meV by the analysis of X-ray diffuse scattering [4]. Then we expect to find the soft mode of $CuGeO_3$ with the energy of about 1 meV in considering the SP transition temperature of 14 K. Recently, the longitudinal optical phonon dispersion along the b*-axis was determined [5], which mode behaves like the acoustic phonon branch with small energy difference. Inelastic neutron scattering experiments were performed to measure the low-lying phonon of $CuGeO_3$. ISSP-HER triple axis spectrometer was used for the experiment at C1-1 port of the guide hall at JRR-3M of JAERI in Tokai. The experimental condition with the horizontal and vertical focusing analyzer was used. The temperature dependence of the phonon spectrum at (0, 3, 0) was measured below 250 K. The full width at half maximum (FWHM) (~0.2 meV) and the central energy (~1 meV) of the phonon peak does not depend the temperature. Usually the temperature dependence of phonon intensity is described by the Bose factor, and the intensity decrease from 300 K to 175 K is consistent to the formula. However, below 150 K the integral intensity of phonon spectrum decreases significantly in discrepancy from the Bose factor curve as shown in Fig. 1. From the mode analysis the anomalous decrease of phonon intensity is speculated to stem from the structural fluctuation with lattice dimerization along the c-axis. The SP transition of $CuGeO_3$ is not displacive type which shows the soft phonon behavior but order-disorder.

References

[1] M. Hase, I. Terasaki and K. Uchinokura, Phys. Rev. Lett. **70** (1993) 3651.
[2] M. Cross and D. S. Fisher, Phys. Rev. **19** (1979) 402.
[3] Y. Tanaka, N. Satoh, K. Nagasaka, J. Phys. Soc. Jpn. **59** (1990) 319.
[4] D.E. Moncton, R.J. Birgeneau, L.V. Interrante and F. Wudl, Phys. Rev. Lett **39** (1977) 507.
[5] M. Nishi, K. Kakurai, Y Fujii, S Katano, J Akimitsu, M Yethiraj and JA Fernandez-Baca, J. Phys. Chem. Solids **60** (1999) 1109.

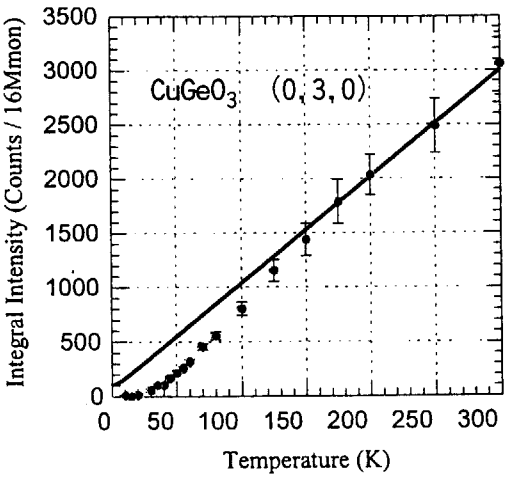


Fig. 1. Temperature dependence of the integral intensity of the optical phonon at (0, 3, 0). Calculated Bose factor curve with a phonon energy of 1meV is shown by solid line fitted to the data between 175 K and 300 K.

使用施設：JRR-3M, 装置：HER(C1-1), 分野：1

研究テーマ：窒化物、炭化物の構造変化
表題： B_4Cの高温での構造変化

1-1-4

Structural Change of B_4C at High Temperatures

M. Yashima, K. Nakamura, R. Ali, K. Ohoyama[1], and Y. Yamaguchi[1]

Department of Materials Science and Engineering, Interdisciplinary Graduate School of Science and Engineering, Tokyo Institute of Technology, Nagatsuta, Midori, Yokohama, 226-8502, Japan.
[1]Institute for Materials Research, Tohoku University, Katahira, Aoba, Sendai, 980-8577, Japan.

Boron carbide B_4C is an important high-temperature material with excellent mechanical properties. But, the structural change at high temperatures has not been known yet. Furthermore, there is an inconsistency in the temperature dependence of unit-cell parameters in the literature. Here we report the results of high-temperature neutron-diffraction measurements of B_4C.

Neutron-diffraction measurements at high temperatures from 23° to 993°C were performed using the Kinken neutron diffractometer HERMES (T1-3) of JRR-3M research reactor of Japan Atomic Energy Research Institute, using a high-temperature furnace (λ=1.8196Å). We used an isotope-substituted boron carbide specimen with the composition of $B_{0.807}C_{0.193}$ (99.68 % ^{11}B in boron), to prevent from the absorption by the ^{10}B. Neutron-diffraction data were analyzed using a Rietveld program RIETAN.

We have successfully refined the unit-cell and structural parameters by the Rieveld analysis, assuming the B_{12}+(C1-B3-C1 chain) model with the space group of $R\bar{3}m$ (Fig. 1). The reliability factors were R_{wp}=9.22% and R_I=2.12% for the neutron-diffraction data analysis for the data measured at 23°C, and R_{wp}=8.83% and R_I=2.91% at 993°C. The unit-cell parameters were a=5.6262(1) and c=12.1337(2)Å, and atomic coordinates were x(B1)=-y(B1)=-0.1627(2), z(B1)=0.5386(1), x(B2) =-y(B2)=-0.1074(2), z(B2)= 0.1142(2), x(C1)=y(C1)=0.0 and z(C1)=0.3816(3), x(B3) =y(B3)=0.0 and z(B3)=0.5 at 993°C. All the thermal parameters increased with an increase of temperature. The thermal parameters of B3 atoms were higher than those of others (Fig. 2). This would be ascribed to the void around the B3 site (Fig. 1). Probably due to the C1-B3-C1 chain structure, B3 has higher thermal parameter values. The U_{11}(B3) was higher than the U_{33}(B3) probably because the void exists in the x direction from the B3 site (Fig. 1).

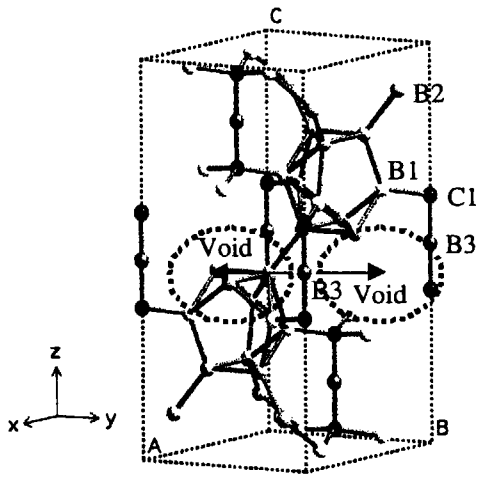


Fig. 1 Crystal structure of boron carbide drawn based on the refined crystal parameters.

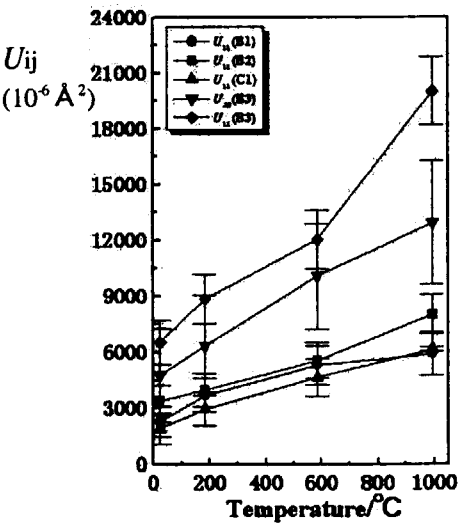


Fig. 2 Temperature dependence of anisotropic thermal parameters of boron carbide.

使用施設: JRR-3M, 装置: (KSD, HERMES), 分野: 1. Structures & Excitations

研究テーマ：螢石関連固溶体の構造変化
表題： $YTaO_4$の構造変化の高温でのその場研究

1-1-5

In Situ Study of Structural Change of $YTaO_4$ at High Temperatures

M. Yashima, T. Nogami, K. Ohoyama[1], and Y. Yamaguchi[1]

Department of Materials Science and Engineering, Interdisciplinary Graduate School of Science and Engineering, Tokyo Institute of Technology, Nagatsuta, Midori, Yokohama, 226-8502, Japan.
[1]*Institute for Materials Research, Tohoku University, Katahira, Aoba, Sendai, 980-8577, Japan.*

Stable phase of yttrium orthotantalate $YTaO_4$ at room temperature might be the monoclinic (M') form with a fergusonite structure that could be a fluorite-related structure. There are three polymorphisms for $YTaO_4$: two monoclinic forms of M'- and M-$YTaO_4$ and one tetragonal T- $YTaO_4$. However, the structural change of this material has not been known in detail yet. Here we report *in situ* neutron-powder-diffraction study of structural change and of $YTaO_4$ at high temperatures up to 1500°C.

Neutron-diffraction measurements were done using the Kinken neutron diffractometers HERMES (T1-3) and KSD (T1-2) of JRR-3M research reactor of Japan Atomic Energy Research Institute, using a high-temperature furnace (λ=1.8196Å for HERMES and λ=1.53Å for KSD). M single phase of the $YTaO_4$ was prepared by solid-state reactions. Each neutron-diffraction measurement was done keeping the sample temperature constant. The average heating and cooling rate including the measurements was 3.3°C/min and 0.19°C/min for HERMES and KSD measurements, respectively. Neutron-diffraction data were analyzed using a Rietveld program RIETAN.

Figure 1 shows temperature dependence of β angle refined through the Rietveld analyses where the average heating rate for the neutron-diffraction measurements was about 0.19°C/min. The β angle of M phase decreased with an increase of temperature up to 1200°C. The metastable M form transformed to more stable M' phase between 1200°C and 1300°C, leading to a discontinuous change in β angle. The stable M' phase changed into the high-temperature T form between 1500°C and 1550°C during heating. The discontinuous change in the β angle indicates that the M-to-M' and M'-to-T transformations are reconstructive.

In case of the higher heating rate we have succeeded in the observation of the reversible M-T transformation. As shown in Fig. 2, the β angle of M phase decreased with an increase of temperature up to 1400°C and became 90 deg., indicating the M-to-T phase transformation. The continuous behavior strongly suggests that the M-T transformation has a 2nd-order nature. In fact, the critical exponent was estimated to be about 0.5 when we apply the Landau's theory.

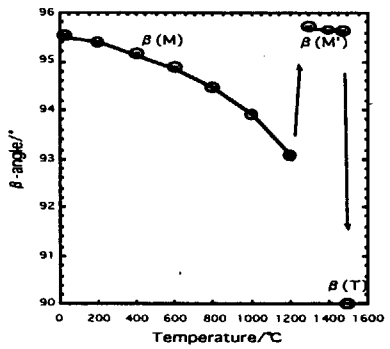


Fig.1: Temperature dependence of β angle. Heating rate was about 0.19 K/min.

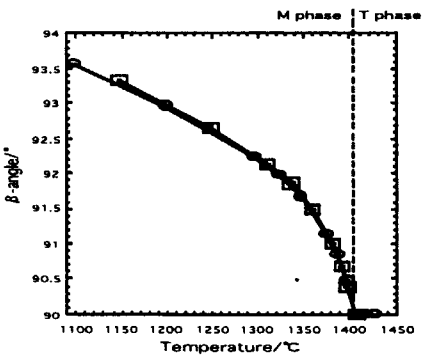


Fig.2: Temperature dependence of β angle. Heating rate was about 3.3 K/min.

使用施設: JRR-3M, 装置: (KSD, HERMES), 分野: 1. Structures & Excitations

研究テーマ：A_2BO_4の高温不整合転移とフォノン分散
表題：Rb_2MoO_4とRb_2WO_4の構造と構造相転移

1-1-6 Structures and Phase Transitions in Rb_2MoO_4 and Rb_2WO_4

H. Shigematsu*, T. Matsui and K Ohoyama[1]

Department of Quantum Engineering, Nagoya University, Nagoya 464-8603, Japan
[1]*Institute for Materials Research, Tohoku University, Sendai 980-8577, Japan*

Many of the A_2BO_4-type ferroelectrics, for example, A_2CrO_4, A_2SO_4, Rb_2SeO_4, Cs_2SeO_4, Rb_2MoO_4 and Cs_2MoO_4 (A=K, Rb and Cs), undergo the same succession of phase transition: these transform from the parent high-symmetry phase (phase I, space group $P6_3/mmc$) to the orthorhombic phase (phase II, *Pmcn*) at high temperatures (T ~600 – 800 K) and retain the orthorhombic structure down to 2 K. On the other hand, in Rb_2WO_4, K_2WO_4 and K_2MoO_4, there is another intermediate incommensurate phase between phases I and II. In K_2SeO_4, as temperature decreases the crystal transforms from phase I to phase II and to a incommensurate phase (phase III), which is followed by a ferroelectric phase (phase IV). Among the A_2BO_4-type ferroelectrics, the low-temperature incommensurate phase was observed only in K_2SeO_4. However, we found new transition points at 200, 691 and 784 K in Rb_2MoO_4 with a differential scanning calorimeter and there were expected as a displacive-type normal-incommensurate phase transition such as K_2SeO_4 and as a high-temperature incommensurate one. In Rb_2WO_4, crystal structures still remains unclear.

In order to clarify the structures in Rb_2MoO_4 and Rb_2WO_4, we performed neutron powder diffraction experiments using the Kinken powder diffractometer for high efficiency and high resolution measurements, HERMES, of Institute for Materials Research (IMR), Tohoku University, installed at JRR-3M of JASRI.

Figure 1 shows neutron powder diffraction patterns for Rb_2MoO_4 at 20 and 290 K. The pattern was obtained at 290 K in the normal phase (space group *Pmcn*). The lattice parameters are a = 8.0955(7), b = 6.3758(6) and c = 11.1031(9) Å. The superlattice reflections were observed below 200 K and the structure is incommensurate with the wave vector $q \sim c_0^*/3$. However, we could not check for the presence of high-temperature incommensurate phase between phases I and II.

On the other hand, the crystal structure at 290 K of Rb_2WO_4 is not orthorhombic but monoclinic one (space group $C2/m$). And Rb_2WO_4 retains this structure down to 8 K.

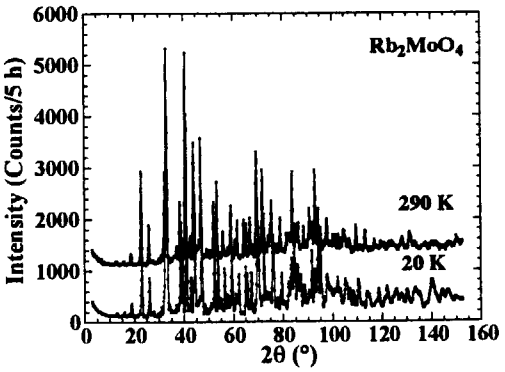


Fig. 1 Neutron powder diffraction patterns of Rb_2MoO_4 at 20 and 290 K.

* Present address: Faculty of Education, Shimane University, Matsue 690-8504, Japan.

使用施設：JRR-3M, 装置：HERMES(T1-3), 分野：1. Structures & Excitations

研究テーマ：Rb_2CoCl_4の常誘電相のフォノン分散
表題：Rb_2CoCl_4の常誘電相のフォノン分散

1-1-7

Phonon Dispersions of the Normal Phase in Rb_2CoCl_4

H. Shigematsu* and T. Matsui

Department of Quantum Engineering, Nagoya University, Nagoya 464-8603, Japan

Rubidium tetrachlorocobaltate, Rb_2CoCl_4, belongs to a family of A_2BX_4 type with the β-K_2SO_4 type structure such as Rb_2ZnCl_4. Three phase transitions are observed at temperatures T_i = 294 K, T_C = 194 K and T_3 = 66 K.

Samara pointed out an empirical law between the pressure coefficient dT/dp of the transition temperature and the mechanisms of the ferroelectric phase transition: a displacive type transition temperature has a positive coefficient with soft zone-boundary optic phonons, while an order-disorder type transition temperature has a negative coefficient. In Rb_2ZnBr_4, Rb_2ZnCl_4 and K_2ZnCl_4, the coefficients are positive, and soft modes have not been observed in the normal phase (above T_i). On the other hand, although the absolute value of the pressure coefficient is small in Rb_2CoCl_4, the coefficient is negative. Therefore, we expected that the underdamped soft modes will be observable in the normal and low-temperature phases.

In the previous report, we reported the observation of soft mode in the low-temperature phases by neutron scattering [1]. The existence of the mode is indeed quite certain. As the second step, in order to clarify the behavior of the mode in the normal phase, we performed inelastic neutron scattering experiments by using the triple-axis spectrometers (4G and C1-1) at JRR-3M of JASRI. Single crystals were grown from melt by the Bridgman method. Energy scans were done with the fixed incident neutron momentum k_i = 2.57 Å at 4G and k_i = 1.55 Å at C1-1. The data collections were carried out in the (a^*, c^*) scattering planes.

Figure 1 shows the phonon dispersion curves along the (0 0 ξ) direction in the normal phase.

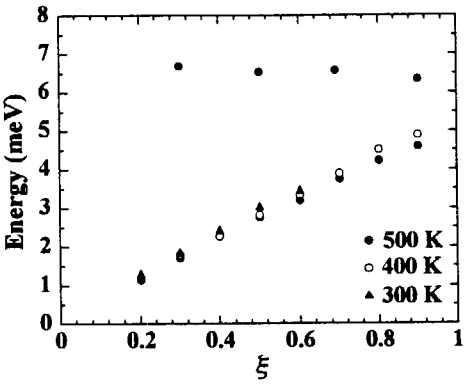


Fig. 1 phonon dispersion curves along the (0 0 ξ) direction in the normal phase.

Although the behavior of the phonon dispersion was clearly observed, no softening of the branch was observed around ξ = 2/3. Furthermore, the anticrossing of the acoustic branch with an optic one was not observed. Although the pressure coefficient dT/dp in Rb_2CoCl_4 is negative, the order-disorder nature remained remarkably because the absolute value of the coefficient is small.

We arrived at the new conclusion that the transition mechanism is related to the ratio between the ionic radius of A^+ and the average bond length B-X in the tetrahedral BX_4^{2-} ion, and the lattice distortive parameters.

References

[1] H. Shigematsu *et al.* : Activity Report on NER **Vol. 7** (2000) 76.

* Present address: Faculty of Education, Shimane University, Matsue 690-8504, Japan.

使用施設：JRR-3M, 装置：GPTAS(4G) and HER(C1-1), 分野：1. Structures & Excitations

研究テーマ：形状記憶合金の中性子回折
表題：$Ni_{2.18}Mn_{0.8}2Ga$ 合金のマルテンサイト相の結晶構造

1-1-8 Crystal Structure in the Martensitic Phase of $Ni_{2.18}Mn_{0.82}Ga$ Alloy

Kazuko INOUE[1], Yasuo YAMAGUCHI[2], Kenji OHOYAMA[2] and Ryunosuke NOTE[2]
[1]*Fac. of Sci. and Tech., Ryukoku University, Seta, Otsu 520-2194*
[2]*IMR, Tohoku University, Aoba-ku, Sendai 980-8577*

We have made the powder neutron diffraction of an off-stoichiometric Heusler-type $Ni_{2.18}Mn_{0.82}Ga$ alloy. It has a thermo-elastic martensitic transformation temperature of about 340K, coincident with the Curie temperature. A single crystal of this alloy shows a shape memory effect at 339 K. [1]

The diffractometer, HERMES, installed on T1-3 port of JRR-3M reactor was used. The wave length was 1.8196 Å. The measurements were made with increasing and decreasing temperature. We re-analyzed the crystal structure in the martensitic phase, using the computer program, RIETAN-2000. [2]

The results of the Rietveld analysis at 405K, at 324K and at 279K are shown in Figs. 1 (a) to (c). They were measured with decreasing temperature. We found that two structures coexist in the martensitic phase. One is an orthorhombic structure distorted from the cubic Heusler structure, and the other is a tetragonal one made from the shuffling of the 220 plane of the orthorhombic structure. This tetragonal structure coincides with the monoclinic one with 6 layers shuffling in the [110] direction of the orthorhombic structure, which we suggested formerly. [1,3]

The mutual relation of the cubic Heusler structure, the orthorhombic one and the tetragonal one is shown in Fig. 2. We see that the lattice constant, a(ortho.), of the orthorhombic structure is slightly longer than a(cubic) of the cubic structure. The lattice constant, b(ortho.), is equal to a(cubic), and c(ortho.) is slightly shorter than a(cubic). We also see that the lattice constants, a(tetra.) and b(tetra.), of the tetragonal structure are equal to c(ortho.) of the orthorhombic structure. The value of c(tetra.) is longer than that of a(ortho.). The volumes of unit cell for these three structures are the same. The lattice spacing along [111] of each structure is also the same. In Fig. 2, we also see that the (220) plane of the orthorhombic structure is the same as the (202) plane of the tetragonal structure. These many common lattice spacing and planes will be the background of easy marten-

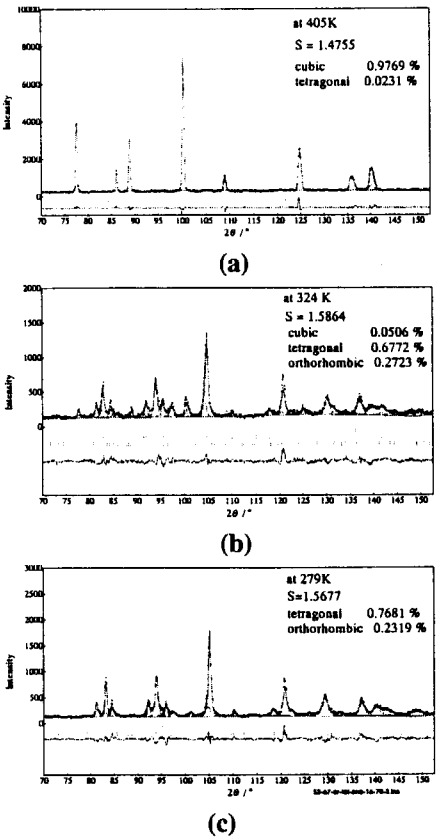


Fig. 1. Results of Rietveld analysis, (a) at 405 K, (b) at 324 K and (c) at 279 K.

使用施設：JRR-3M, 装置：HERMES(T1-3), 分野：1.Structures & Excitations

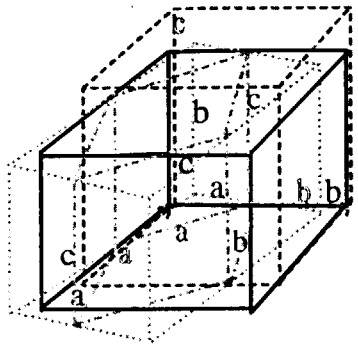
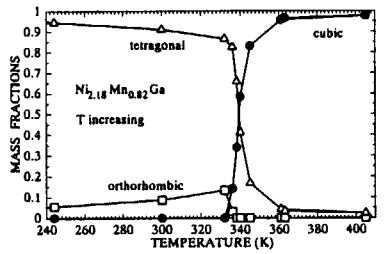
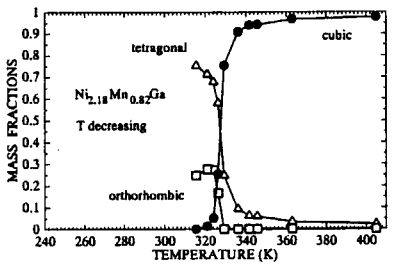


Fig. 2. Relation of three structures, the cubic structure, the orthorhombic structure and the tetragonal structure.



(a)



(b)

Fig. 3. Temperature dependence of the mass fraction of each structure (a) with increasing temperature and (b) with decreasing temperature.

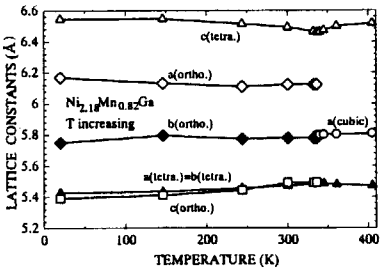


Fig. 4. Temperature dependence of each lattice constant with increasing temperature.

sitic transformation and of coexistence of three different structures. The temperature dependence of the mass fraction of each structure determined with increasing temperature and with decreasing temperature are shown in Figs. 3 (a) and (b). We see that there is a small hysteresis of the martensitic transformation temperature. We also see that the mass fraction of tetragonal structure in the martensitic phase is much larger than that of orthorhombic structure. This fact indicates that the tetragonal structure is more stable than the orthorhombic structure.

The temperature dependence of lattice constants of each structure measured with increasing temperature is shown in Fig. 4. We see the mutual relations of lattice constants, which we described above.

References

[1] K. Inoue, Y. Yamaguchi, K. Ohoyama, K. Enami and K. Inoue: *Proc. Fourth Pacific Rim Int. Conf. on Advanced Materials and Processing* (PRICM4), Vol.II (2001) 1689.

[2] F. Izumi: *The Rietveld method*, ed. R. A. Young (Oxford Univ. Press, Oxford, 1993) Chap. 13.

[3]] K. Inoue, K. Enami, M. Igawa, K. Inoue, Y. Yamaguchi and K. Ohoyama: *Proc. of the Int. Conf. on Solid-Solid Phase Transformation '99* (1999) 1120.

研究テーマ：MeHPLN (C14O2H10) の水素の原子核分布と電子分布の比較
表題：低温相における MeHPLN の構造解析

1-1-9 Structure Analysis of MeHPLN in Low Temperature Phase

R. Kiyanagi[1], H. Kimura[1], M. Watanabe[1], Y. Noda[1],
A, Kojima[2], T. Mochida[3] and T. Sugawara[4]
[1]*IMRAM, Tohoku University.*
[2]*Graduate School of Science and Technology, Faculty of Science, Chiba University.*
[3]*Department of Chemistry, Faculty of Science, Toho University.*
[4]*Department of Basic Science, Graduate School of Arts and Science, The University of Tokyo*

5-R-9-hydoroxyphenalenon(R=I, Br, Methyl) is one of the ferroelectric groups containig hydrogen-bonds. These compounds are unique because they are classified in an isolated hydorogen-bond system that has only intramolecular hydrogen-bonds. Preliminary structure analysis of 5-Methyl-9-hydoroxyphenalenon(MeHPLN) by X-ray and neutron at room temperature reveals that there is a local electrical dipolemoment in the hydorogen-bond region.

X-ray structure analysis of MeHPLN in low temperature phease has already been carried out and the electron distribution in low temperature phase has been obtained. In order to compare this electron distribution and reveal the phase transition scheme of MeHPLN, structure analysis of MeHPLN by neutron diffraction in the low temperature phase was carried out.

Experiments were performed at JRR-3M in JAERI, utilizing the four circle diffractmeter FONDER installed at T2-2 beam port. Neutron beam of which wave length is 1.5696Å monochromized by Si monochrometer was used. The total number of collected Bragg reflections at 10K were 1536, including 681 superlattice reflections. After absorption correction, the parameters of positions, thermal factors and so on were determined by means of a least square method. The final reliable factor was R=3.96%. Secondly the nuclear density was calculated by means of Maxmum Entropy Method(MEM) and the final reliable factor was R=4.06%.

Taking note of the hydrogen atom in the hydrogen-bond region, it is revealed that there are two types of distributions of electrons and nuclei(Fig.1). One of the independent molecule clearly shows ordering of the electron and nuclear distribution, whereas the hydrogen atom in the other molecule has almost the same electron and nuclear distribution as at room temperature. There is obvious descrepancy between electron and nuclear ditribution in the ordered hydrogen atom (not shown here), indicating the static dipolemoments with antiferroelectric order in the low temperature phase.

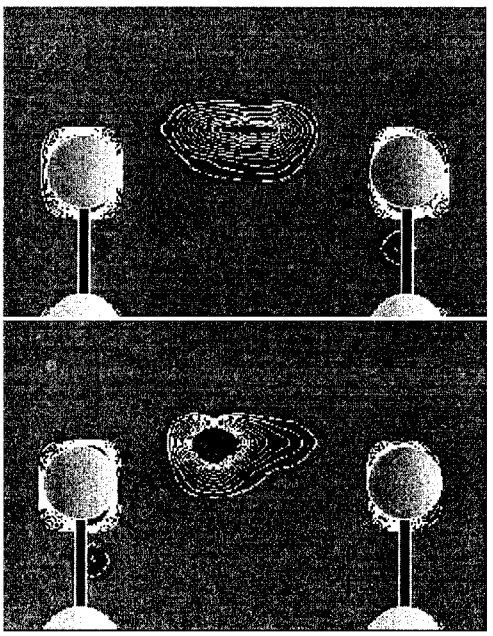


Fig. 1. The nuclear distribution of the disordered hydrogen atom(upper) and ordered one(lower) in Hydrogen-Bond region

使用施設：JRR-3M，装置：FONDER(T2-2)，分野：1. Structures

研究テーマ：アンモニウム塩におけるプロトンゼロ点分布の単結晶に中性子回折法による研究
表題：ヘキサクロロ白金酸アンモニウムにおけるプロトンゼロ点分布の単結晶中性子回折による研究 II

1-1-10 Zero Point Distribution of Protons in Ammonium Hexachloroplatinate by Single Crystal Neutron Diffraction II

T. Matsuo[1], N. Onoda-Yamamuro[2], O. Yamamuro[1],
Y. Fukuda[3], H. Kimura[3], S. Maesaki[3] and Y. Noda[3]

1) Department of Chemistry, Graduate School of Science, Osaka University, Toyonaka, Osaka

2) Department of Natural Sciences, College of Science and Engineering, Tokyo Denki University, Saitama

3) Institute of Multidisciplinary Research for Advanced Materials, Tohoku University, Katahira, Sendai

Introduction

Ammonium-d4 hexachloroplatinate undergoes an order-disorder phase transition at 27 K whereas the un-deuterated crystal is cubic down to the lowest temperature examined (4K). The transition entropy of the deuterated crystal is larger than R (= 8.3145 J / K mol). This suggests an interesting possibility that each of the protons and deuterons belonging to the ammonium ions are distributed over a set of positions dictated by the cubic symmetry. Multiple positions for a deuterium atom are a consequence of orientational disorder. For the hydrogenous ammonium compounds, the crystal symmetry is cubic even at the lowest temperature. Therefore, a multi-maximum proton distribution, if actually found, should be a characteristic of the ground state of the crystal. The low temperature heat capacity shows that the rotational motion of the ammonium ion is essentially in the ground state at 7 K (where the neutron experiment was performed) both for the hydrogenous and deuterated crystals. We have performed a low temperature neutron diffraction on ammonium hexachloroplatinate single crystals, using the diffractometer FONDER at JRR-3M

Experiment

The sample ($(NH_4)_2PtCl_6$) was prepared from ammonium chloride and hexachloroplatinic acid dissolved in water by slow evaporation of the solvent. Single crystals of an appropriate size (ca. 3.5mm) was chosen and fixed to the cold finger of a closed-cycle refrigerator mounted on the diffractometer. Diffraction data were collected at T = 7 and 35 K. The neutron wavelength was 1.5696 Å in the experiment at 7 K and 1.5683 A at 35 K. In total 70 and 69 (*hkl*) independent peak intensities were determined at T = 7 and 35 K, respectively. Because of the high symmetry of the crystal, several equivalent Bragg peaks occurred within the available ranges (2θ<=150 deg.) of the diffraction angle for many of the indices. The number of the peak intensities determined was ca. 400 before averaging the equivalent ones.

Result

All the peaks observed were consistent with the $Fm3m$ symmetry. The cubic lattice constant was 9.7466 A and 9.7472 Å at 7 and 35 K, respectively. The lattice constant from high-resolution neutron powder diffraction is 9.7429 Å at 6 K in good agreement with the present values.

First the diffraction data were analyzed using the least squares program RADIEL. The least squares calculation converged smoothly, resulting in the following structural parameters.

T = 7 K RADIEL R-factor=4.51% Rw=4.93%, Scale=20.48(34). Number of Reflections 70

	x	y	z
N	1/4	1/4	1/4
H	0.3175(34)	0.3175(34)	0.2870(35)
Pt	0	0	0
Cl	0.2390(2)	0	0

原子炉：JRR-3M　装置：FONDER (T2-2)　分野：中性子散乱 (構造)

Uij x10^3

	U11	U22	U33	U12	U13	U23
N	7(2)	7(2)	7(2)	0	0	0
H	71(10)	71(10)	49(15)	-31(6)	-16(12)	-16(12)
Pt	2(1)	2(1)	2(1)	0	0	0
Cl	2(1)	5(1)	5(1)	0	0	0

N-H distance 0.99(4) A
Pt-Cl distance 2.329(4) A

T=35 K RADIEL R-factor=4.32% Rw=4.79%, Scale=20.56(38). Number of Reflections 69

	x	y	z
N	1/4	1/4	1/4
H	0.3183(20)	0.3183(20)	0.2830(21)
Pt	0	0	0
Cl	0.2396(2)	0	0

Uij x10^3

	U11	U22	U33	U12	U13	U23
N	5(2)	5(2)	5(2)	0	0	0
H	66(8)	66(8)	52(12)	-30(5)	-10(11)	-10(11)
Pt	3(1)	3(1)	3(1)	0	0	0
Cl	2(0)	5(1)	5(1)	0	0	0

N-H distance 1.00(5) A
Pt-Cl distance 2.332(5) A

MEM Calculation

Next we transformed the intensity data to the scatterer density in the unit cell by the Maximum Entropy Method (MEM). We divided the unit cell into 256x256x256 pixels and optimized the scatterer distribution in each pixel using the maximum of the information entropy compatible with the intensity data as the criterion for the most likely distribution. The negative scattering length of protons was taken into account by calculating their contribution separately from the scattering by other atoms. The results of the MEM calculation are shown in Fig. 1 and Fig. 2. Fig. 1 presents an ammonium ion with the nitrogen atom at the center and four hydrogen atoms surrounding it tetrahedrally. Interestingly, each of the four hydrogen atoms is distributed on a torus about 0.7 A in diameter. The torus is very close uniform. As shown in Fig. 2, The representation could be a disk perpendicular to the three-fold axis. It could also be discreet three elongated maxima, depending on the threshold value used in the preparation of the image. This is in clear contrast to the delta function like distribution of the N, Cl and Pt. nuclei.

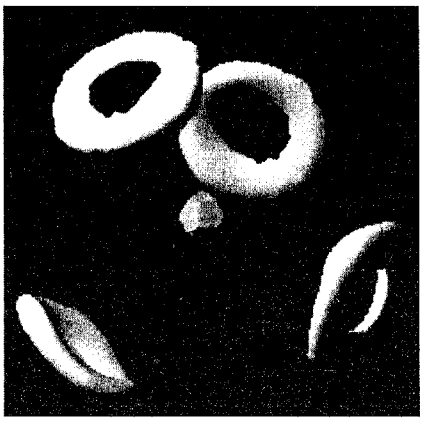


Fig.1 3D-map of nuclear density for N and H atoms obtained by MEM at 7K.

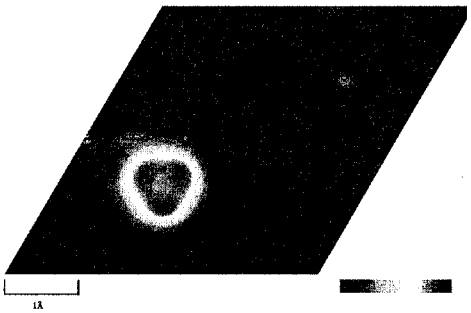


Fig. 2 Contour map of Nuclear density for H atoms projected along <111> axis at 7K.

研究テーマ： 正方晶四極子秩序化合物 $R^{11}B_2C_2$ のスピン格子ダイナミクス
表題： 正方晶四極子秩序化合物 $Ho^{11}B_2C_2$ のフォノン測定

Phonon measurement on the antiferroquadrupolar Order compound $Ho^{11}B_2C_2$

1-1-11

A. Tobo[1], K. Ohoyama[1], K. Hirota[2], T. Ohmori[1], H. Onodera[1] and Y. Yamaguchi[1]
[1] *Institute for Materials Research, Tohoku University, Sendai, 980-8577 Japan*
[2] *Department of Physics, Tohoku University, Sendai, 980-8578 Japan*

RB_2C_2 (R=rare earth) compounds, which have the tetragonal LaB_2C_2-type crystal structure, have been attracting many interests, because some of them shows strong antiferroquadrupolar (AFQ) interactions. DyB_2C_2 shows both of an AFQ ordering and an antiferromagnetic (AFM) ordering. The AFQ ordering temperature and the Néel temperature are T_Q = 24.7 K and T_N = 15.3 K, respectively, which is almost 10 times as high as those of the other system reported so far [1]. HoB_2C_2 also shows both of an AFQ ordering and an AFM ordering, but it is observed that an AFM transition occurs at T_N = 5.9 K and an AFQ ordering transition at T_Q = 4.5 K [2, 3]. T_Q is lower than T_N in HoB_2C_2, which is unusual for quadrupolar ordering compounds. TbB_2C_2 shows an AFM transition at T_N = 21.7 K but no AFQ transition at zero field. However it is confirmed by neutron diffraction that an AFQ ordered phase is induced by magnetic fields. These system which have both of an AFQ ordering and an AFM ordering shows complicated magnetic behavior.

In order to clarify the dynamical properties of RB_2C_2, we performed inelastic neutron scattering measurements on the single crystal $Ho^{11}B_2C_2$. Here B was replaced with enriched ^{11}B isotope, because natural B is a strong neutron absorber. The measurements were made at room temperature by using TOPAN (6G) spectrometer installed at JRR-3M, JAERI. From the measurements, we investigated the phonon dispersion relations of $Ho^{11}B_2C_2$. Fig. 1 shows the phonon dispersion curves of $Ho^{11}B_2C_2$ at room temperature for the [0 0 k] direction. We obtained the dispersion relations for both LA and TA modes, and a possible TO mode. The phonon dispersions for the [h 0 0] direction were also examined, and the dispersion curves for transverse phonons were obtained. However, the signals for the longitudinal phonons are unclear and we cannot determine the dispersion relations for a LA mode, although it seems that there exists a low-energy LO phonon. Further measurements are needed to understand the nature of these longitudinal phonons.

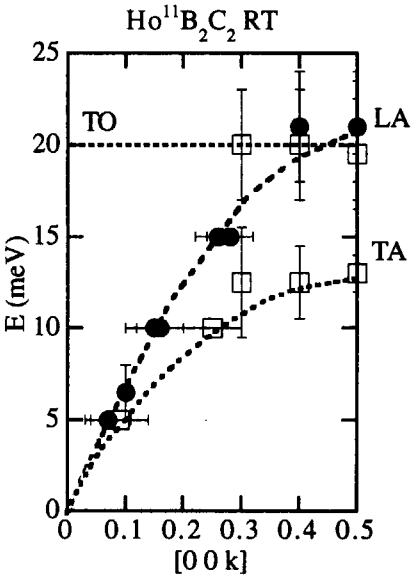


Fig. 1. The phonon dispersion curves of $Ho^{11}B_2C_2$ at room temperature.

References

[1] H. Yamauchi *et al.*, J. Phys. Soc. Jpn. 68 (1999) 2057.
[2] H. Onoderaet *al.*, J. Phys. Soc. Jpn. 68 (1999) 2426.
[3] H. Shimada *et al.*, J. Phys. Soc. Jpn. 70 (2001) 1705.
[4] K. Ohoyama *et al.*, J. Phys. Soc. Jpn. 69 (2000) 3401.

使用施設： JRR-3M, 装置： TOPAN (6G), 分野： 1 Structures & Excitations

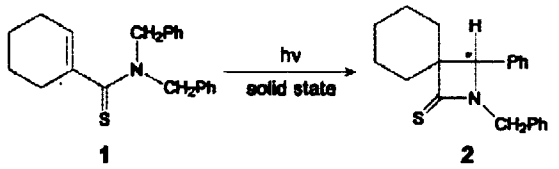
1-1-12

Crystalline-State Photoisomerization of α, β-Unsaturated Thioamide Analyzed by X-Ray and Neutron Diffractions

Takaaki Hosoya[1], Takashi Ohhara[2], Hidehiro Uekusa[1], and Yuji Ohashi[1]

[1] Department of Chemistry and Materials Science, Tokyo Institute of Technology, O-okayama, Meguro-ku, Tokyo 152-8551, Japan
[2] Institute of Materials Structure Science, High Energy Accelerator Research Organization, Oho, Tsukuba, Ibaraki 305-0801, Japan

The absolute asymmetric synthesis in the solid state has been extensively studied, in which the chiral product is produced from the achiral reactant in a chiral crystal environment. Among them, *N, N*-dibenzyl-1-cyclohexene-carbothioamide, **1**, was photoisomerized to optically active β-thiolactam, 1-benzyl-4-phenyl- 2- thioxoazetidine- 2- thione- 3-spiro-cyclohexane, **2**, as shown in Scheme 1.



1 2

Scheme 1

When a crystal of **1** was exposed to UV light at 263 K, the cell dimensions were gradually changed with retention of the single crystal form. Since the crystal gradually decomposed after 330 h, the irradiation was stopped and the structure was analyzed by X-rays. The thioamide, **1**, was converted by 65.0 % to the thiolactam, **2**. The thioamide and thiolactam molecules were observed as a disordered structure in the crystal as shown in Fig. 1. The disordered structure clearly indicates that the hydrogen atom of one of the benzyl groups is extracted by one of the olefin carbon atoms of the cyclohexenyl group and that the benzyl carbon atom makes a bond with another olefin carbon to form a thiolactam ring. The mechanism of the ring formation and the chirality of the produced thiolactam are well explained from the reaction cavity.

An important question still remains; which hydrogen atom is extracted by C3 when the crystal was exposed to UV light. Since the C–C bond is made between C2 and C8, H8A or H8B should be extracted by C2 within a molecule or in the neighboring molecules. The intramolecular H8A atom is probably extracted by C3, since the interatomic distance is the shortest. This indicates that the extracted H and original H3 atoms, H3A' and H3B', should occupy the positions upside and downside the cyclohexane ring. Recently a new compound with deuterium atoms atoms at the positions of H8A and H8B were prepared, Large crystals suitable for neutron analysis were obtained. The crystal structures before and after photoirradiation were analyzed by neutron diffraction with FONDER. The structure after irradiation gave a definitive answer to the question, that is, the intramolecular hydrogen is transferred in the process of the four- membered ring formation.

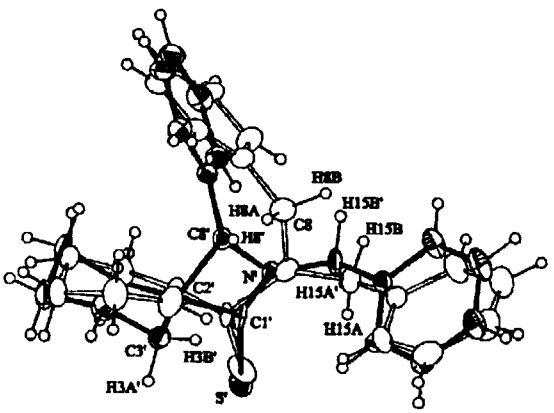


Fig. 1 Disordered structure after photo-irradiation

使用施設：JRR-3M、装置：FONDER(T2-2)、分野：1.Structures & Excitations

1-1-13

研究テーマ：$Nd_{1-x}Sr_{1+x}MnO_4$ の高ホール濃度領域における軌道秩序

表題：層状 Mn 酸化物 $Nd_{1-x}Sr_{1+x}MnO_4$ の高ホール濃度領域における軌道秩序

Orbital ordering in highly doped single-layered manganite $Nd_{1-x}Sr_{1+x}MnO_4$

R. Kajimoto[1], H. Mochizuki[2], H. Yoshizawa[2], T. Kimura[3] and Y. Tokura[3]

[1]*Department of Physics, Ochanomizu University, Bunkyo-ku, Tokyo 112-8610, Japan*

[2]*Neutron Scattering Laboratory, ISSP, University of Tokyo, Tokai, Ibaraki, 319-1106, Japan*

[3]*Department of Applied Physics, University of Tokyo, Bunkyo-ku, Tokyo 113-8656, Japan*

The ordering of the e_g electrons and e_g orbitals of manganese ions play essential roles in determining the physical properties in the hole-doped perovskite manganites. The charge ordering and orbital ordering are strongly coupled to or compete with the ferromagnetic (FM) metallic interactions mediated by the double exchange mechanism. As a result, the manganites exhibit a great variety of the charge/orbital ordered states depending on the hole concentration and the one-electron band width.

One of the important aspects of the charge/orbital ordering is the introduction of the low dimensionality in the physical properties through the strong anisotropy of the e_g orbitals. It would be interesting to examine whether the dimensionality of the crystal structure influences the character of the charge/orbital ordering. Previous studies on the charge and orbital ordering, however, are performed mainly against the cubic or bi-layered manganites.

Accordingly, we studied the charge and orbital ordering in single-layered manganites $Nd_{1-x}Sr_{1+x}MnO_4$ with x = 0.75 and 0.78, which have the lowest dimensionality of crystal structure among perovskite-derived manganites, using a neutron diffraction technique. The samples are single crystals grown by the floating zone method. The neutron diffraction measurements were performed using a triple-axis spectrometer GPTAS with k_i = 2.57 Å^{-1} and 3.81 Å^{-1}.

The x = 0.75 sample has a tetragonal $I4/mmm$ structure through all temperature range measured. Width decreasing temperature, superlattice peaks due to lattice modulations appear below T_{OO} ~ 270 K where the inplane resistivity ρ_{ab} exhibits a steep rise [1]. Figures 1(a) and 1(b) show profiles of the superlattice reflections measured along the [110] and [1$\bar{1}$0] directions at T = 10 K. Superlattice reflections

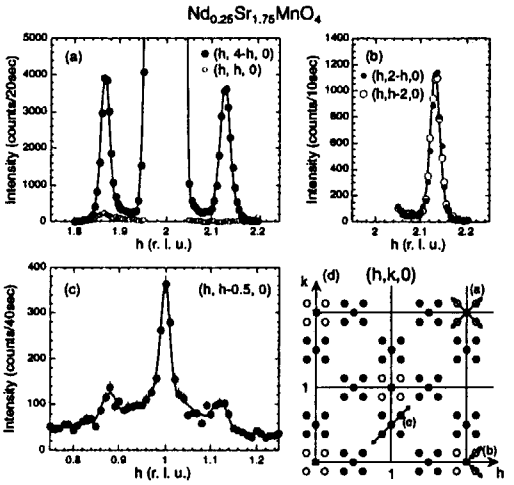


Fig. 1. Profiles of the superlattice reflections of orbital ordering (a),(b) and spin ordering (c) in the x = 0.75 sample along the [110] and [1$\bar{1}$0] directions at 10 K. The positions of the superlattice reflections and the scan directions in the (hk0) scattering plane are indicated in (d).

appear at $\boldsymbol{Q} = (h, k, 0) \pm (\frac{1}{8}, \pm\frac{1}{8}, 0)$ with $h + k$ = even. The $\boldsymbol{Q}$ dependence of the intensities indicates that the related lattice modulations consist chiefly of a transverse component. These nuclear superlattice reflections can be interpreted as arising from the stripe charge/orbital order within the MnO_2 planes as presented in Fig. 3(a). This charge/orbital order consist of $d(3x^2 - r^2)$ and $d(3y^2 - r^2)$ orbitals, and resembles that observed in a highly doped region in cubic manganites like $La_{1/3}Ca_{2/3}MnO_3$ [2]. The charge/orbital order also produces magnetic superlattice peaks. Figure 1(c) shows a profile of the magnetic peaks along the [110] directions. Strong magnetic peaks are observed at $\boldsymbol{Q}$ = $(h/2, k, 0)$ and $(h, k/2, 0)$ with h, k = integer, while weak magnetic peaks appear at $\boldsymbol{Q}$ = $(h/2, k, 0) \pm (\frac{1}{8}, \pm\frac{1}{8}, 0)$ and $(h, k/2, 0) \pm (\frac{1}{8}, \pm\frac{1}{8}, 0)$. These magnetic peaks are consistent with a spin structure shown in Fig. 3(a), where zig-zag FM chains run along the $d(3x^2 - r^2)/d(3y^2 - r^2)$ or-

使用施設：JRR-3M，装置：GPTAS(4G)，分野：1. Structures & Excitations

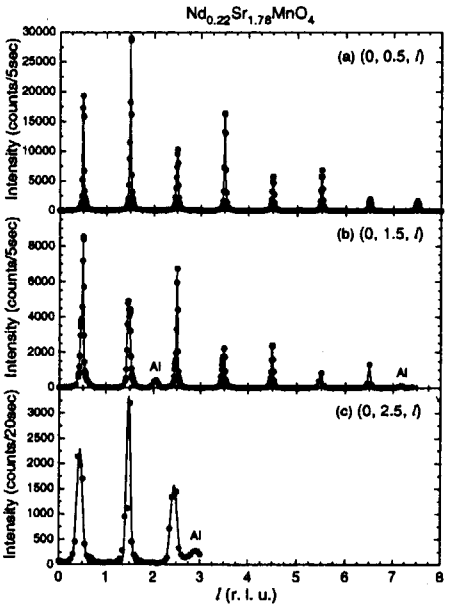


Fig. 2. Profiles of the magnetic Bragg reflections in the $x = 0.78$ sample along the [001] direction for (a) $k = 0.5$, (b) $k = 1.5$ and (c) $k = 2.5$ at 10 K.

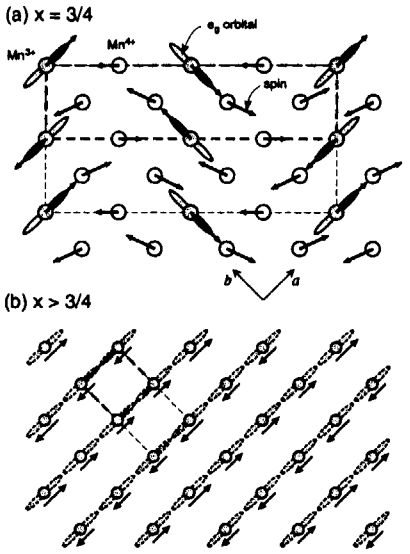


Fig. 3. Proposed models of the orbital orderings and spin orderings for (a) $x = 3/4$ and (b) $x > 3/4$. Thick and thin broken squares indicate unit cells of the orbital and spin orders, respectively.

bitals, though there is still an ambiguity in the spin directions.

The $x = 0.78$ sample has a tetragonal $I4/mmm$ structure at room temperature, while it shows a transition to an orthorhombic $Immm$ structure with $a > b$ below $T_N = 150$ K. We observed antiferromagnetic (AFM) Bragg reflections below this transition temperature (Fig. 1). The magnetic peaks appear at $(h, k/2, l/2)$ with k, l = integer. The magnetic structure that satisfies the observed peak positions is so-called C-type AFM structure. It contains FM chains within the MnO_2 planes as depected in Fig. 3(b) [3].

The C-type AFM structure has been observed in cubic and bi-layered manganites in similar doping region [4, 5], and it has been proposed that this AFM structure is induced by a one-dimensional ordering of the $d(3z^2 - r^2)$ orbitals. In the present single-layered crystal, the FM chains of the C-type AFM structure are parallel to the a-axis, which is longer than the b-axis. This relation between the magnetic and the crystal structure implies that the C-type AFM structure in the $x = 0.78$ sample has its origin in an ordering of the $d(3x^2 - r^2)$ orbitals extending along the a-axis (Fig. 3(b)). The orbital and magnetic order also affects the transport properties. ρ_{ab} shows a sudden drop below T_N [1]. This anomaly in the resistivity can be interpreted as that the electron transfer is enhanced within the FM chains due to the double exchange interactions.

The present results indicate that the type of charge/orbital order in single-layered manganites shows an interesting switching within the MnO_2 layers around $x = 3/4$: a stripe-type charge/orbital order for $x \leq 3/4$ and a rod-type orbital order for $x > 3/4$. Because same types of orbital orders are observed in cubic and bi-layered manganites in similar doped regions, the orbital order is not much affected by the dimensionality of crystal structure, but strongly depends on the hole concentration.

References

[1] T. Kimura *et al.*, Phys. Rev. B **65** (2001) 020407(R).
[2] P. G. Radaelli *et al.*, Phys. Rev. B **59** (1999) 14440.
[3] R. Kajimoto *et al.*, Physica B **312-313** (2002) 760.
[4] R. Kajimoto *et al.*, Phys. Rev. B **60** (1999) 9506.
[5] C. D. Ling *et al.*, Phys. Rev. B **62** (2000) 15096.

1-1-14

研究テーマ：$Pr_{1-x}Sr_xMnO_3$ のA型反強磁性相における電荷秩序

表題：$Pr_{0.5}Sr_{0.5}MnO_3$ におけるストライプ的電荷秩序

Stripe-type charge ordering in the A-type antiferromagnet $Pr_{0.5}Sr_{0.5}MnO_3$

R. Kajimoto[1], H. Yoshizawa[2], Y. Tomioka[3] and Y. Tokura[3,4]

[1]*Department of Physics, Ochanomizu University, Bunkyo-ku, Tokyo 112-8610, Japan*

[2]*Neutron Scattering Laboratory, ISSP, University of Tokyo, Tokai, Ibaraki, 319-1106, Japan*

[3]*Joint Research Center for Atom Technology (JRCAT), Tsukuba, Ibaraki 305-8562, Japan*

[4]*Department of Applied Physics, University of Tokyo, Bunkyo-ku, Tokyo 113-8656, Japan*

A drastic increase of the conductivity accompanied by a ferromagnetic (FM) transition, or a colossal magnetoresistance (CMR) effect, in perovskite manganites has attracted enormous interests. Recent studies have revealed that the checkerboard-type (CE-type) charge ordering which appears at $x \sim 1/2$ is essential to this dramatic change of the transport property. The CE-type charge ordering is stabilized in systems with a narrow one-electron band width W such as $Pr_{1-x}Ca_xMnO_3$ and $La_{1-x}Ca_xMnO_3$. On the other hand, the CMR phenomenon is not limited to the narrow W manganites, and is indeed observed in systems with wider W such as $Pr_{1-x}Sr_xMnO_3$, $Nd_{1-x}Sr_xMnO_3$, and $La_{2-2x}Sr_{1+2x}Mn_2O_7$ with $x \sim 0.5$. An important characteristics of these compounds is they show a *highly conductive* A-type antiferromagnetic (AFM) state around $x = 1/2$, where a planar ordering of the $d(x^2 - y^2)$ orbitals is established. This orbital ordering mediates the FM coupling and fairly large mobility of carriers within the orbital-ordered planes [1, 2]. The scenario for the CMR phenomenon based on the CE-type charge ordering is clearly irrelevant in this case, and another microscopic mechanism ought to be invoked.

To find what causes a drastic change in the transport property in wide W manganites with the A-type AFM state, we have performed a neutron diffraction study on a single crystal of a cubic A-type antiferromagnet $Pr_{0.5}Sr_{0.5}MnO_3$. This material exhibits a first-order phase transition from a FM metal to an A-type AFM less-conductive state at $T_N \sim 140$ K (Fig. 1(c)), and it exhibits a significant MR below T_N [3]. The neutron diffraction measurement was performed using the triple axis spectrometer GPTAS installed at the JRR-3M reactor in JAERI with an incident neutron momentum $k_i = 3.83$ Å^{-1}. The crystal has a distorted cubic structure with $a \sim 3.8$ Å, and we employ the cubic notation in indexing with the FM layers of the A-type AFM structure perpendicular to the [010] direction.

First, we surveyed the $(h, 0, l)$ scattering plane. Figure 1(a) presents a map of the scattering intensities around (002) at 7 K. Apart from an intense fundamental nuclear Bragg re-

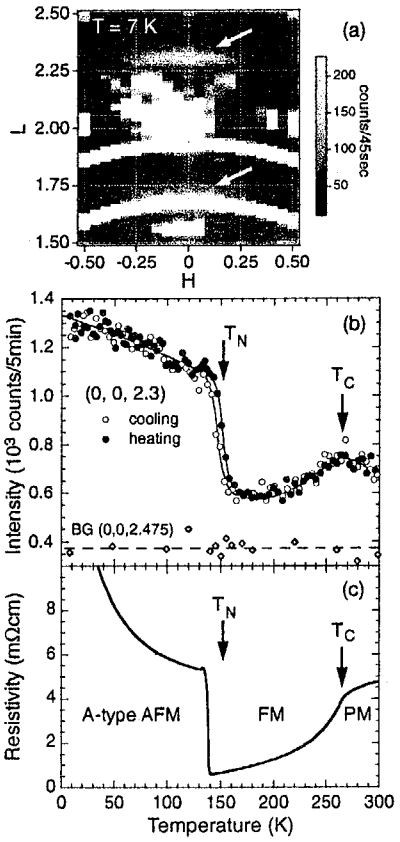


Fig. 1. (a) Intensity maps around $(0, 0, 2)$ at $T = 7$ K. Two ring-shaped scatterings are due to the Al sample cell. (b) Temperature dependence of the intensity at $(0, 0, 2.3)$. The background (BG) intensity measured at $(0, 0, 2.475)$ is also shown. Open symbols and closed symbols denote the data for cooling and for heating, respectively. (c) Temperature dependence of the resistivity.

使用施設：JRR-3M，装置：GPTAS(4G)，分野：1. Structures & Excitations

flection at (002) and A-type AFM Bragg reflections at $(\pm 0.5, 0, 2)$ and $(0, 0, 1.6)$, anisotropic diffuse scatterings are clearly observed around $(0, 0, 2 \pm 0.3)$ (white arrows). The profiles are elongated towards the [100] direction, indicating the correlation length along the modulation vector $q = (0, 0, \pm 0.3)$ is much longer than that perpendicular to q. By examining the Q dependence of the similar scatterings, we can conclude that these are attributable to longitudinal lattice modulations. A similar feature was also observed in the stripe-like charge ordering in a two-dimensional (2D) A-type AFM manganite $La_{2-2x}Sr_{1+2x}Mn_2O_7$ [4, 5].

In order to investigate the influence of newly found diffuse scattering on the transport property, we measured the temperature (T) dependences of the intensity at $(0, 0, 2.3)$ (Fig. 1(b)). There is a strong correlation between the intensity and the resistivity (Fig. 1(c)), which establishes that the observed diffuse scattering arises from the charge ordering. Especially, the diffuse peak has large intensity in the A-type AFM state. In addition, we found that the correlation length of the charge ordering is well-developed below T_N. These observations verify that the charge ordering is intrinsic to the A-type AFM state. Since a similar charge ordering was observed in the 2D A-type AFM manganites, the existence of such charge ordering must be specific to the wide W manganites independent of the spatial dimensionality.

The observed features of the charge ordering can be well explained by a model of the stripe-like charge ordering depicted in Fig. 2 for $q = 1/3$ r.l.u. In this model, Mn^{4+} ions segregate within the metallic matrix of Mn^{3+}-like sites with $d(x^2 - y^2)$ orbitals, and form stripe-

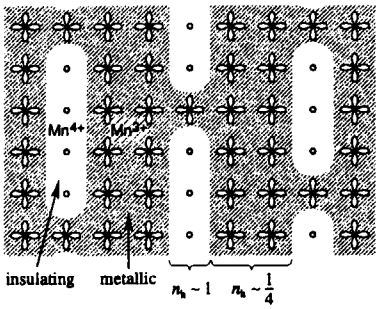


Fig. 2. Schematic illustration of the charge order and orbital order for $q = 1/3$ r.l.u. Cloverleaf symbols represent the $d(x^2 - y^2)$ orbitals. n_h denotes the hole concentration within the Mn^{4+} stripe or the Mn^{3+}-like matrix.

stripe-like objects along the Mn-O-Mn bond direction. The insulating Mn^{4+} stripes block the hopping of the e_g electrons, whereas the Mn^{3+}-like matrix retains the mobility of carriers, producing the high conductivity in the AFM state. In Fig. 2, the hole concentration of the Mn^{4+} stripe is fixed to 1, while that of two Mn^{3+} lines be 1/4, resulting in the overall concentration $x = 1/2$. In reality, some e_g electrons may enter the line of Mn^{4+} ions as depicted in Fig. 2 to disturb the correlation along the stripes resulting in the observed anisotropy in the correlation lengths.

References

[1] H. Kuwahara *et al.*, Phys. Rev. Lett. **82** (1999) 4316.

[2] H. Kawano *et al.*, Phys. Rev. Lett. **78** (1997) 4253.

[3] Y. Tomioka *et al.*, Phys. Rev. Lett. **74** (1995) 5108.

[4] M. Kubota *et al.*, J. Phys. Soc. Jpn. **69** (2000) 1986.

[5] L. Vasiliu-Doloc *et al.*, Phys. Rev. Lett. **83** (1999) 4393.

1-1-15

研究テーマ：高ホール濃度 $Nd_{2-x}Sr_xNiO_4$ 系のスピン揺動と電荷秩序

表題：$La_{1.5}Sr_{0.5}NiO_4$ が示す市松模様型電荷秩序からストライプ型電荷秩序への自発的変化

Spontaneous rearrangement of the checkerboard charge order to stripe order in $La_{1.5}Sr_{0.5}NiO_4$

R. Kajimoto[1], K. Ishizaka[2], H. Yoshizawa[3], and Y. Tokura[2]

[1]*Department of Physics, Ochanomizu University, Bunkyo-ku, Tokyo 112-8610, Japan*

[2]*Department of Applied Physics, University of Tokyo, Bunkyo-ku, Tokyo 113-8656, Japan*

[3]*Neutron Scattering Laboratory, ISSP, University of Tokyo, Tokai, Ibaraki, 319-1106, Japan*

One of the most fascinating examples of charge ordering may be a so-called stripe order discovered in the high-T_c superconducting cuprates [1]. In hole-doped nickelates $La_{2-x}Sr_xNiO_{4+\delta}$, the static stripe order is observed for a wide hole concentration region $0.15 \lesssim n_h \leq 1/2$ [2, 3], where $n_h = x + 2\delta$. The incommensurability ϵ of the stripe order is approximately proportional to the hole concentration, but the stripe order is most stabilized at the *commensurate hole concentration* $n_h = 1/3$ with $\epsilon = 1/3$. Considering the commensurability effect, one can expect that another stable commensurate charge order may exist at $n_h = 1/2$. An early electron diffraction study, indeed, indicated the existence of a checkerboard-type charge order at $n_h = 1/2$ [4]. From our recent study on the highly Sr-doped nickelate system, however, we observed an *incommensurate spin* order with the incommensurability $\epsilon \sim 0.44$ [3]. This result gives rise to a question whether the ground state of nickelates at $n_h = 1/2$ is the checkerboard-type charge ordering or stripe-type. In this study, we solve such a mystery of the charge ordering in the 50% doped nickelate by a neutron diffraction technique. We will demonstrate that the charge ordering shows an interesting rearrangement from checkerboard-type to stripe-type in the 50% Sr-doped nickelate.

A large single crystal sample was grown by the floating zone method, and pre-characterized by a resistivity measurement. The in-plane resistivity ($j \perp c$) is almost metallic at high temperature ($\rho_{ab}(600\,\mathrm{K}) \sim 2.5 \times 10^{-3}\ \Omega$cm), but it increases monotonically as temperature (T) is lowered. The T derivative of the resistivity $d\log\rho/dT$ suggests that the T dependence of the resistivity changes its slope twice at $T_{CO}^{C} \sim 480$ K and $T_{CO}^{IC} \sim 180$ K. These anomalies in the resistivity may indicate that two different types of charge ordering are formed below the temperatures of two respective anomalies. The neutron diffraction experiments were performed using the triple axis spectrometer GPTAS with a fixed incident neutron momentum of $k_i = 3.81\ \mathrm{Å}^{-1}$ and a combination of horizontal collimators of 40′-40′-40′-80′. The sample has a pseudo-tetragonal structure, and we employ an orthorhombic setting.

In order to find the signals due to possible charge orderings inferred by the anomalies of the resistivity, we surveyed reciprocal lattice positions around $(h, k, 0)$ with $h + k$ = odd, where a superlattice peak due to the checkerboard-type charge order is expected. Figures 1(a) and (b) show the scan profiles along the [100] direction around $(5, 0, 0)$ and $(4, 3, 0)$ at several T's. In Fig. 1 (c) is also shown the profile of the magnetic peak at $(1, \epsilon, 0)$ measured along the [010] direction at 10 K. In Figs. 1(a) and (b), quite sharp peaks appear at commensurate positions at $(5, 0, 0)$ and $(4, 3, 0)$ below T_{CO}^{C}. These profiles clearly demonstrate that the checkerboard-type charge ordering is formed in our $x = 1/2$ sample below T_{CO}^{C}, being consistent with the early electron diffraction experiment [4].

More importantly, with further lowering T, another pair of satellite peaks emerges below T_{CO}^{IC} at the both sides of the commensurate superlattice peaks for the checkerboard-type charge order, as indicated by arrows in Figs. 1(a) and 1(b) ($h \sim 5 \pm 0.13$ and $h \sim 4 \pm 0.13$, respectively). With use of the incommensurability of the magnetic reflections $\epsilon \sim 0.44$, the satellite peaks are indexed as $(h \pm 2\epsilon, k, 0)$ with $h + k$ = even. Thereby, we identify them as the charge and spin superlattice peaks from the stripe-type charge order with $\epsilon \sim 0.44$. These observations lead us to conclude that the two types of charge order coexist at low tempera-

使用施設：JRR-3M，装置：GPTAS(4G)，分野：1. Structures & Excitations

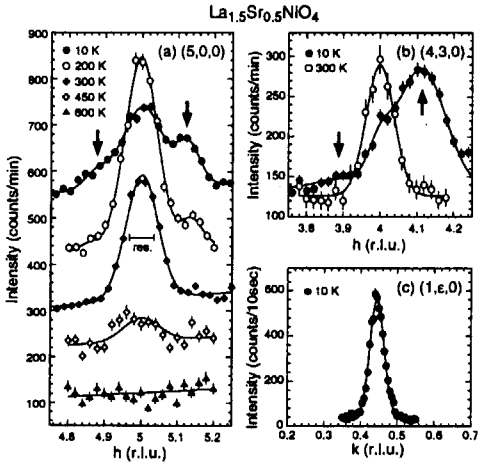


Fig. 1. Temperature dependences of the profiles of charge order peaks: panel (a) at and around (5, 0, 0), panel (b) (4, 3, 0), and panel (c) that of a spin order peak (1, 0.44, 0). In the panel (a), the y axis is sifted by 100 counts for each data.

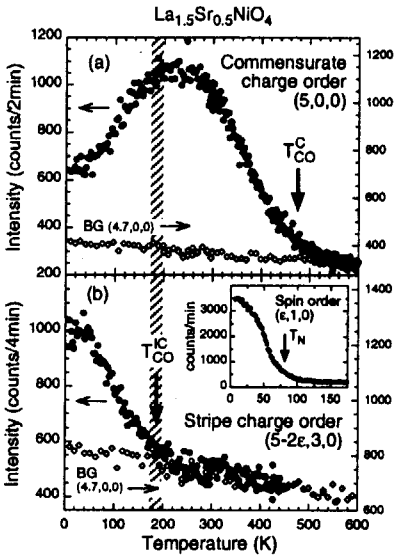


Fig. 2. Temperature dependencies of the peak intensities of the commensurate charge order peak (5, 0, 0) (a), stripe charge order peak (4.13, 3, 0) (b). The background intensities measured at (4.7, 0, 0) are also depicted. The inset in (b) is the temperature dependence of the peak intensity of the stripe spin order peak at (0.44, 1, 0).

tures in the Sr-doped nickelate with $n_h = 1/2$.

In order to show an ordering process of these two charge orders, the T dependencies of the intensity of the commensurate peak at (5, 0, 0) and the satellite peak at $(4.13, 3, 0) = (5 - 2\epsilon, 3, 0)$ are depicted in Fig. 2. With decreasing T, the intensity at (5, 0, 0) starts to grow around $T_{CO}^{C} \sim 480$ K. Further decreasing T, the intensity reaches a maximum around $T_{CO}^{IC} \sim 180$ K, and then turns to decrease below T_{CO}^{IC}. The maximum of the commensurate component is well correlated with the onset of the satellite (incommensurate) components. The intensity of the satellite peak gradually develops below T_{CO}^{IC}. In addition, the stripe-type spin order sets in at much lower temperature $T_N \sim 80$ K (see the inset of Fig. 2(b)). These T-dependent behaviors of the stripe-type charge and spin order manifest the marvelous stability of the stripe-type ordering at the very high hole concentration for $n_h \sim 1/2$ in the Sr-doped nickelate.

The incommensurate charge ordering in $x = 1/2$ can be understood in terms of a discommensuration picture of the stripe ordering introduced in our previous study [3]. An important result of the discommensuration is the energy gain by the spin exchange interactions. For the checkerboard-type charge ordered state, the exchange interaction between the nearest neighbor sites is unique, and there is only the one between Ni^{2+} and Ni^{3+} ions, which is expected to be quite small [5]. By contrast, when the charge order becomes incommensurate, Ni^{2+}–Ni^{2+} bond and/or Ni^{2+}–hole–Ni^{2+} bond may be introduced in the discommensuration region, depending on whether the holes enter the metal site or the oxygen site. Because the exchange interaction for these bonds is much stronger than that between Ni^{2+} and Ni^{3+}, the energy gain due to the spin exchange interactions is larger in the stripe state, and favors the stripe ordering. The present observation suggests the importance of the role of the spin exchange interactions in the charge ordering in the Sr-doped nickelate system.

References

[1] J.M. Tranquada *et al.*, Nature (London) **375**, 561 (1995).

[2] J.M. Tranquada *et al.*, Phys. Rev. B **54**, 12318 (1996).

[3] H. Yoshizawa *et al.*, Phys. Rev. B **61**, R854 (2000).

[4] C.H. Chen *et al.*, Phys. Rev. Lett. **71**, 2461 (1993).

[5] J. Zaanen and P.B. Littlewood, Phys. Rev. B **50**, 7222 (1994).

研究テーマ：冷中性子分光器 C3-1-1 AGNES (IMT)
表題：filled Skutterudite $Ba_{0.1}CoSb_3$ のフォノン状態密度

1-1-16

Phonon density of states for filled Skutterudite, $Ba_{0.1}CoSb_3$

T.Kajitani, Y.Ono, Y.Miyazaki, T.Goto[1]
Department of Applied Physics, Graduate School of Engineering, and IMR[1], Tohoku Univ.,
Sendai 980-8579,Japan

The Skutterudite is a name of a group of $\square MX_3$ –type unique minerals in which □, M and X refer to the vacancy , metals, Co, Rh and Ir, and anions, P, As and Sb, respectively. The crystal structure of this mineral is regarded as formed from the cubic perovskite structure as shown in figure 1. By the partial filling of the vacancy site with relatively heavy cations, i.e., Ba, La, Ce or Th, these crystals become promising thermo-electric materials suitable to generate electric power by the Seebeck effect in the temperature range from 500K to 700K[1].

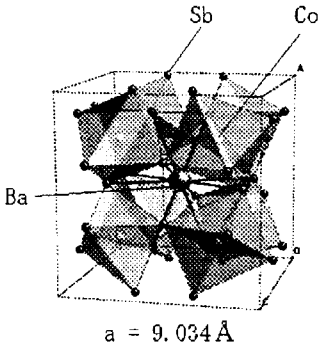


Fig.1 Crystal structure of Ba_xCoSb_3 ,Skutterudite, being cubic, Im-3(#204).

The ever reported figure of merit, Z, times temperature, ZT, of these crystals exceeded the value of 1.0 in above temperature range[2]. One of the characteristic physical phenomena is a dramatic decrease of the thermal conductivity in the range from 1/2 to 1/4 less than the matrix by the partial site filling. That is mainly responsible for the extra-large ZT values. Dramatic decrease of the thermal conductivity has been explained in terms of the "rattling" of the "filled" heavy cation, which sits in a roomy 2a(000) site as shown in Fig.1. Twelve Sb atoms coordinate to a heavy atom. Metallic transport property of these crystals is also a characteristic feature. $CoSb_6$ octahedrons are slightly squeezed in [111] and its equivalent directions. The Co-Sb-Co distance and the bond angle are 2.595 Å-2.595 Å and 121 degree, respectively, being suitable for the metallic transport and weak magnetic coupling between the 3d electrons due to the Kanamori-rule. The "rattling" of the filled heavy cations corresponds to the local and low energy vibration mode in the Skutterudites. It has been accepted that the "rattling" mode causes significant decrease either of the mean free path of phonons and of the thermal conductivity. Present work was motivated to ensure this prediction experimentally.

Unfilled and filled Skutterudite powder samples were synthesized. The phonon density of states are measured by JRR-3M AGNES at temperatures from 12K to the ambient. Figure 2 shows parts of the DOS curves. Some new modes are seen at about 15 and 18meV in the filled Skutterudite, being consistent with the prediction[3].

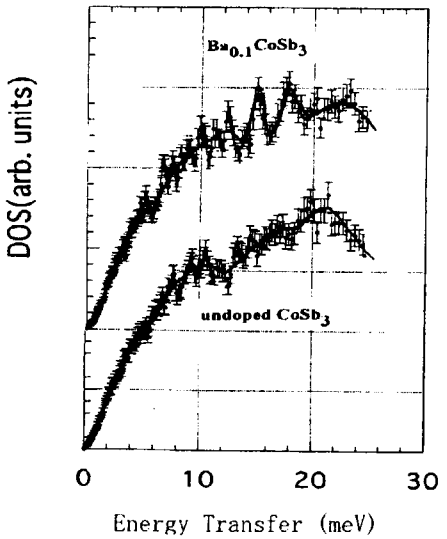


Fig.2 Observed DOS of Skutterudites at room temperature by AGNES. New peaks, hopefully the "rattleing mode" at E=15 and 18meV appeared in the filled Skutterudite.

References

[1] J.W.Sharp et al.:J.Appl.Phys. 78(1995) 1013.
[2] J.P.Feurial et al.:Proc.15th ICT meating(1996) pp.91.
[3] D.Mandrus et al.:Mat.Res.Soc.Symp.Proc. 478(1997) pp.199.

使用施設：JRR3M, 装置：AGNES(C3-1-1) ：分野 1.Structure & Excitations

1-1-17
研究テーマ：モリブデン子固溶体の格子・磁気構造
表題：Sr_2FeMo0_6の電子ドープ効果

Electron doping effects in conducting Sr_2FeMoO_6

Y. Moritomo[1], Sh. Xu[2] and K. Ohoyama[3]
[1]*Department of Applied Physics, Nagoya University, Nagoya 464-8601, Japan*
[2]*Department of Crystalline Materials Science, Nagoya University, Nagoya 464-8603, Japan*
[3]*Institute for Materials Research, Tohoku University, Sendai 980-8577, Japan*

The carrier doping by chemical substitution is a powerful tool for investigation of strongly correlated electron systems, especially the perovskite-like 3d and 4d transition metal oxides. Most of the 3d transition metal oxides with integer filling, e.g., $LaMnO_3$ and $LaCoO_3$, are insulating due to the strong on-site Coulomb repulsion U. With substitution of the divalent Sr^{2+} ions for the trivalent La^{3+} ion, however, these compounds become ferromagnetic metal due to the double-exchange mechanism.

Recently, ordered double-perovskite molybdenum oxides A_2MMoO_6 (A is a rare-earth metal and M is a 3d transition metal) begin to attract current interest of material scientists in the applicational point of view. Among the double-perovskite molybdenum oxides, Sr_2FeMoO_6 is most extensively studied, because high-quality single crystals can be obtained by the floating-zone method. Sr_2FeMoO_6 is ferrimagnetic and metallic with critical temperature T_C =400 K. On the basis of a LDA band calculation, the conduction band is dominated by the Mo4d level, while Fe3d-electrons behave as local spins. We have investigated the electron-doping effects on the properties in the conducting double-perovskite $(Sr_{2-x}La_x)FeMoO_6$.

A stoichiometric mixture of commercial $SrCO_3$, La_2O_3, Fe_2O_3, Mo and MoO_3 was well ground, and pressed into a rod and sintered at 1200 C for 2 h in a flow of Ar gas. The crystal is grown at a feeding speed of 20 mm in an Ar atmosphere. Black and shiny crystals, typically 4 - 5 mm in diameter and 20 mm in length, were obtained. The actual chemical composition of the melt-grown $(Sr_{1.7}La_{0.3})FeMoO_6$ crystal was determined by the inductively coupled plasma (ICP) method, and is almost the same as the ideal values; Sr : La : Fe : Mo = 1.692 (1.7: prepared value) : 0.316 (0.3) : 1.024 (1.0) : 0.972 (1.0). The crystal symmetry at room temperature (< T_C) is tetragonal (I4/mmm; Z = 2).

We have measured neutron powder diffraction patterns of Sr_2FeMoO_6 and $(Sr_{1.7}La_{0.3})FeMoO_6$ with the Kinken powder diffractometer for high efficiency and high resolution measurements, HERMES, installed at the JRR-3M reactor in Japan Atomic Energy Research Institute, Tokai, Japan. Neutrons with wavelength 1.819 A were obtained by the (331) reflection of Ge monochromater, and 12'-B-Sample-18' collimation. Melt-grown crystal ingots (5 g) were crushed into a fine powder and were sealed in a vanadium capsule with helium gas, and mounted at the cold head of the closed-cycle He-gas refrigerator.

Magnitudes of the respective moments are determined by the Rietveld fitting (RIETAN-97B), in which we assume a collinear magnetic structure with spin direction along c..Several impurity peaks, which are inevitably introduced from the skin region of the crystal ingot, were observed and were removed from the pattern.The obtained moments are μ_{Fe} = 4.2(2) μ_B and μ_{Mo} = – 0.5(2) μ_B at x = 0.0, and μ_{Fe} = 3.8(2) μ_B and μ_{Mo} = – 0.8(2) μ_B at x = 0.3. At x =0.0, both the moments are suppressed as compared with the ideal values (5.0 μ_B and - 1.0 μ_B for the Fe^{3+} and Mo^{5+} ions, respectively).This is partly due to the disorder of the B-site ions.With increase of x, absolute magnitude of μ_{Mo} increases from -0.5(2) μ_B at x =0.0 to -0.8(2) μ_B at x = 0.3. This enhancement of μ_{Mo} indicates that the doped electrons occupy mainly the Mo4d down-spin band, consistently with the LDA band calculation.

使用施設：JRR－3M、装置：HERMES、分野：1 Structure&Excitation、2 magnetism

1-1-18

研究テーマ：Bサイト置換されたマンガン酸化物のミクロ相分離構造
表題：Bサイト置換されたマンガン酸化物の相分離と強磁性

Phase separation and ferromagnetic transition in B-site substituted Mangnaites

A. Machida[1]„ Y. Moritomo[2], and K. Ohoyama[3]
[1]*Department of Crystalline Materials Science, Nagoya University, Nagoya 464-8603, Japan*
[2]*Department of Applied Physics, Nagoya University, Nagoya 464-8601, Japan*
[3]*Institute for Materials Research, Tohoku University, Sendai 980-8577, Japan*

The charge-ordered insulating (COI) phase, which is frequently observed in half-doped manganites (e.g., $R_{1/2}Ca_{1/2}MnO_3$: R = Nd. Pr, Sm and Tb), is amenable to the external perturbations, such as, magnetic field, external pressure and chemical pressure. This amenability of the COI state reflects a strong competition of the COI state with the ferromagnetic metallic state due to the double-exchange mechanism

By contrast, Raveau *et al.* have found that 3% substitution of the perovskite B-site of $Pr_{1/2}Ca_{1/2}MnO_3$ by another transition metals, *e.g.*, Cr and Co, induces a ferromagnetic transition at low temperature. This B-site substitution effect on the COI phase is rather complicated, since the B-site impurity is usually considered to be disadvantageous to the metallic state. Here, we should take into account the phase separation phenomena, that is, coexistence of the COI and ferromagnetic metallic phases, in addition to these microscopic effects between the dopant and Mn. For example, $Nd_{1/2}Ca_{1/2}Mn_{1-y}Cr_yO_3$ consists of ferromagnetic and charge-ordered microregions of the order of 10 nm, as was confirmed by dark field image of the superlattice reflection from the COI region.

We have systematically investigated the B-site substitution effects on the structural and magnetic properties in $Nd_{1/2}Ca_{1/2}(Mn_{0.97}M_{0.03})O_3$ (M = Al, Zn, Sc, Fe, Ni, Co and Cr).The ground state of the non-doped $Nd_{1/2}Ca_{1/2}MnO_3$ is charge-ordered insulator with CE-type antiferromagnetic spin ordering. We found that all the compounds transform into two-phase state with decreases of temperature below 200 K. With further decreases of temperature below 100 K, the Cr-, Co- and Ni-doped compounds show the ferromagnetic transition, while the other compounds show only the CE-type component. We have discussed interrelation between the phase separation and the ferromagnetic transition in these B-site substituted manganites.

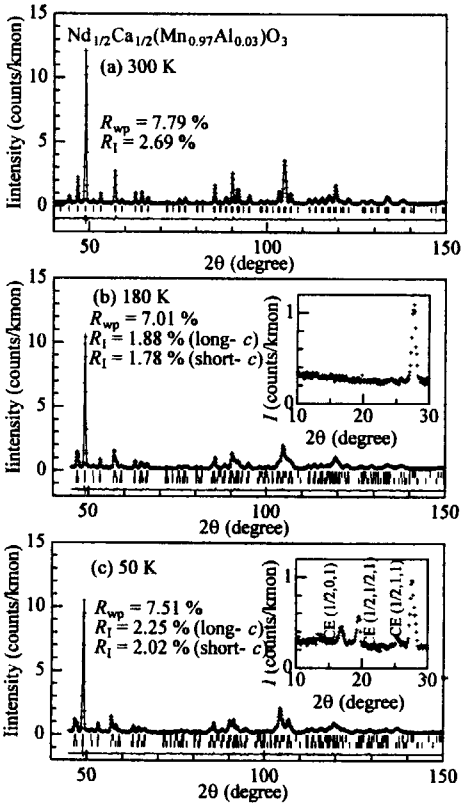


Fig.1: Prototypical examples of neutron powder pattern (cross) of $Nd_{1/2}Ca_{1/2}(Mn_{0.97}Al_{0.03})O_3$ at (a) 300 K, (b) 180 K and (c) 50 K. Solid curves are the results of Rietveld refinement with one [(a)] or two [(b) and (c)] distorted perovskites. Inset of (b) and (c) shows the powder pattern in the low angle region..

使用施設：JRR-3M、装置：HERMES、分野：1 Structure&Excitation、2 magnetism

研究テーマ：マンガン酸化物の軌道安定性と磁気相転移
表題：中性子回折による $Tb_{1-x}Ca_xMnO_3$ の研究
1-1-19

Neutron Structural Analysis of $Tb_{1-x}Ca_xMnO_3$

A. Machida[1], Y. Moritomo[2], and K. Ohoyama[3]
[1]*Department of Crystalline Materials Science, Nagoya University, Nagoya 464-8603, Japan*
[2]*Department of Applied Physics, Nagoya University, Nagoya 464-8601, Japan*
[3]*Institute for Materials Research, Tohoku University, Sendai 980-8577, Japan*

Perovskite-type doped manganites, $R_{1-x}A_xMnO_3$, where R and A are trivalent rare-earth and divalent alkaline-earth ions, respectively, have three dimensional networks of the MnO_6 octahedra. In this structure, variation of the averaged ionic radius r_A of the perovskite A-site modifies the one-electron bandwidth W of the eg band through the variation of the Mn-O-Mn bond angle (*chemical pressure*). Actually, Radaelli *et al.* have experimentally confirmed this trend at a fixed-x (= 0.3). Thus, the insulator-metal crossover at the fixed-x has been understood in terms of W-control by the chemical pressure. A similar chemical pressure effect is expected even in the hole-doping procedure, i.e. substitute of the A^{2+} ions for the R^{3+} ions.

So far, many and theoretical studies have been carried out on such phase separation problem to clarify the origin of the colossal magnetoresistance (CMR). For example, Mori *et al.* performed an electron diffraction measurement on $La_{0.5}Ca_{0.5}MnO_3$ and found a coexistence of the FM metallic and charge-ordered insulating (COI) microdomains of the order of 10 nm. The coexistence of the different phase has been confirmed also by the synchrotron radiation (SR) x-ray diffraction as well as the NMR measurements. Recently, Machida *et al.* have investigated the lattice and magnetic structures of the phase separated state of $Nd_{0.55}(Sr_{0.17}Ca_{083})_{0.45}MnO_3$, and argued possible mechanism for the phase separation. Their scenario, the lattice structural change at the charge-ordering transition (CE-type orbital-ordering) causes the internal stress into the domain, and induces the secondary phase in the surrounding area. Similarly, the C-type orbital-ordering can couple with the Jahn-Teller-type lattice distortion, and may cause the phase separation.

We have investigated the structural and magnetic properties of $Tb_{1-x}Ca_xMnO_3$ by means of neutron powder diffraction experiments. We chose Tb compound in order to perform the neutron diffraction experiments and reveal the magnetic property of the narrow band system. First, we derived a magnetic phase diagram against hole concentration x and temperature. We observed the magnetically phase separated states around the phase boundaries between the CE-type and C-type and between the C-type and G-type antiferromagnetic (AFM) phase. Secondly, we observed the metal-insulator behavior in the wide x region above T_N We rather found that the chemical pressure effects well explain the observed metal-insulator behavior. Lastly, we compared the present magnetic phase diagram with that of the layered system.

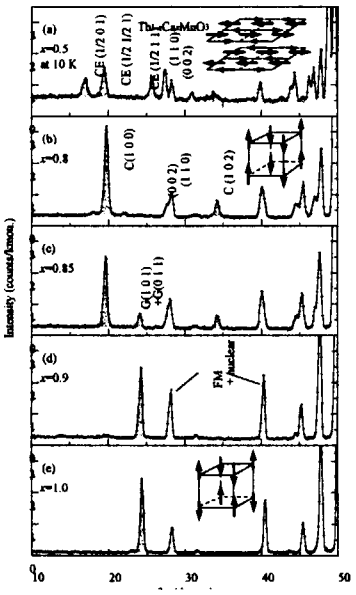


Fig.1: Neutron diffraction patterns of $Tb_{1-x}Ca_xMnO_3$ at 10-K. Hatched reflections indicate the magnetic Bragg reflections. Inset shows the schematic illustration of the CE-, C-, and G-type spin structure.

使用施設：JRR-3M、装置：HERMES、分野：1 Structure&Excitation、2 magnetism

研究テーマ：Ca-Co-O 系熱電酸化物の中性子回折
表題：複合結晶 $[(Ca_{1-x}Sr_x)_2CoO_3]_{0.62}CoO_2$ の変調構造

1-1-20

Modulated Structure of the Composite Crystal $[(Ca_{1-x}Sr_x)_2CoO_3]_{0.62}CoO_2$

Y. Miyazaki[1], T. Miura[1], M. Onoda[2] and T. Kajitani[1]

1 Department of Applied Physics, Graduate School of Engineering, Tohoku University, Aramaki Aoba, Aoba-ku, Sendai 980-8579, JAPAN
2 Advanced Materials Laboratory, National Institute for Materials Science, 1-1 Namiki, Tsukuba, Ibaraki 305-0044, JAPAN

Layered composite crystal cobaltite $[Ca_2CoO_3]_{0.62}CoO_2$ has recently attracted much interest owing to its superb thermoelectric properties. Partial substitution of the Sr ions for the Ca ions was found to further enhance the thermoelectric power-factor due to a substantial decrease in electric resistivity. In order to elucidate the origin of such a change from a structure point of view, we have performed the structure analysis by means of a four-dimensional superspace group approach.

Polycrystalline samples of $[(Ca_{1-x}Sr_x)_2CoO_3]_{0.62}CoO_2$ were prepared by the standard solid-state reaction method. Neutron powder diffraction (ND) data were collected at room temperature using HERMES diffractometer, installed at the JRR-3M reactor in JAERI. The ND data were analyzed using a Rietveld refinement program PREMOS 91 [1] designed for modulated structure analyses.

As shown in Fig. 1, the non-doped compound consists of a CdI_2-type CoO_2 sheet (subsystem 1) and a triplicated rock salt-type Ca_2CoO_3 block (subsystem 2) alternatively stacked parallel to the c-axis [2]. Both the subsystems have common monoclinic a- and c- axes but mutually incommensurate b-axes (b_1 and b_2). With increasing the Sr content x, the a-, b_2- and c- axis lengths continuously increased while the b_1-axis length gradually decreased from 2.8201(3) Å (x = 0) to 2.8170(3) Å (x = 0.20).

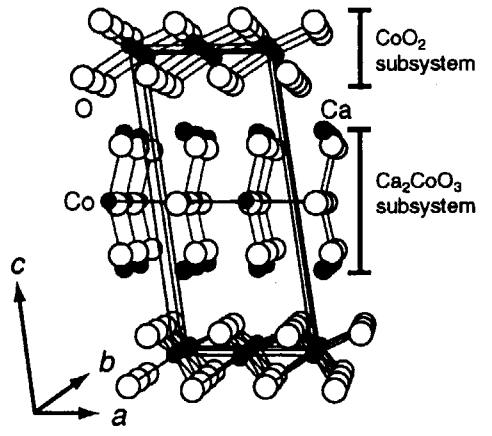


Fig. 1 Fundamental structure of $[Ca_2CoO_3]_{0.62}CoO_2$.

Figure 2 shows the modulation of the Co-O distances in the CoO_2 subsystem plotted against a complementary coordinate t'. As is clearly recognized, the modulation amplitudes are significantly reduced with x. The decrease of resistivity can be thus understood in terms of the reduction of the displacive modulations in the conducting paths.

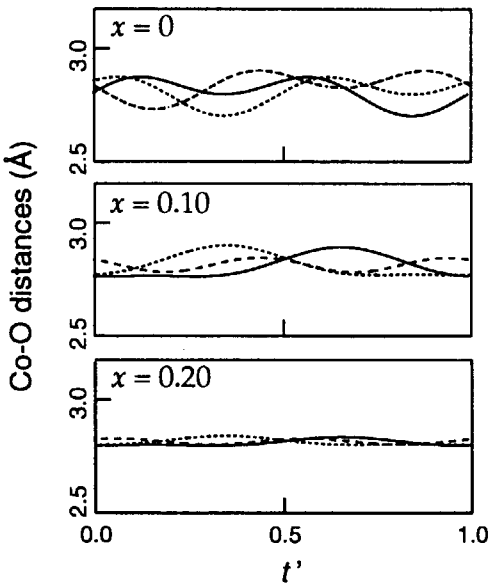


Fig. 2 The Co-O distances in the CoO_2 subsystem plotted against a complementary coordinate t'.

References

[1] A. Yamamoto, *Acta Cryst. A* **49** (1993) 831.
[2] Y. Miyazaki et al., *J. Phys. Soc. Jpn*, **71** (2002) 491.

使用施設：JRR-3M、装置：HERMES (T1-3)、分野：1. Structures & Excitations

研究テーマ：メチルアンモニウム基をもつペロブスカイト型誘電体の構造と相転移機構
表題：$CH_3NH_3PbCl_3$の相転移と構造

1-1-21

Phase Transitions and Structures of $CH_3NH_3PbCl_3$

H. Mashiyama[1], Y. Kawamura[1] and K. Ohoyama[2]

[1] *Faculty of Science, Yamaguchi University, Yamaguchi 753-8512*

[2] *Institute for Materials Research, Tohoku University, Sendai 980-8577*

A Methylammonium compound, $CH_3NH_3PbCl_3$, performs a cubic-orthorhombic transition around 170K[1,2]. In the perovskite cubic phase, a methyl-ammonium (MA) ion occupies disordered orientations to satisfy the O_h symmetry. In the intermediate phase, satellite reflections have been observed[3], however, no further structural study has been reported.

In order to clarify the ordering mechanism of MA ions, we have been investigating the compound by neutron powder-diffraction methods. The crystal was milled and dried before canning in a vanadium cell, which was set on a goniometer. The measurements were carried out with using HERMES of IMR in JRR-3M. The wave length of neutron was 1.8196A. The scattered intensity was obtained for 1500 points with a 0.1° step, each 50min. A profile fitting program RIETAN-94[4] was used to determine the crystal structure.

The cubic structure at 180K (phase I: *Pm3m*, Z=1) has been successfully analyzed; Rp=2.64%, Rf=8.56%, S=1.172, d=1.725, although the back-ground was very high because of protons of MA.

The temperature dependence of the diffraction intensity is demonstrated in Fig. 1, where indexes are referred to the cubic phase. Super-lattice reflections (h/2 k/2 l) or (h/2 k l) appear below 170K, and increase their intensity with lowering the temperature. This suggests that the phase III is orthorhombic. The structure analysis was almost successful with *Pnma*, Z=4; Rp=5.05%, S=2.13, d = 0.713, Rf=7.52%. The atomic parameters for protons are not fully refined as yet.

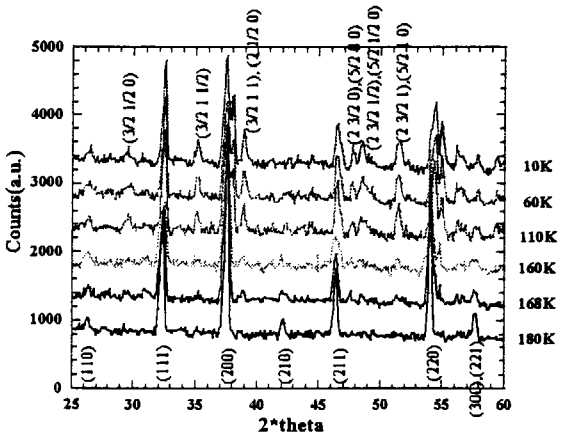


Fig. 1 Diffraction intensity at 6 temperatures.

The lattice parameters are plotted in Fig.2, where a/1.414, b/2 and c/1.414 are compared with the cubic a. The intermediate phase was difficult to be recognized. The rotation and the tilting of $PbCl_3$ octahedron take place through the phase transition. The orthorhombic structure is a modification from *Cmcm*. In order to analyze the mechanism of the ordering process of MA ions, more detailed investigation is desirable.

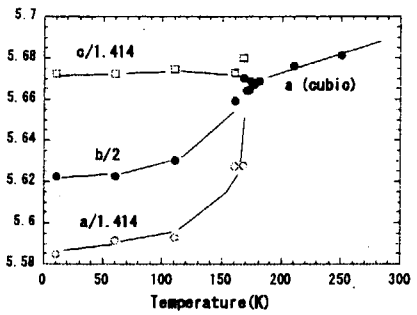


Fig. 2 Lattice constants.

References

[1] A. Poglitsch & D. Weber: J. Chem. Phys. **87** (1987) 6373.

[2] N. Onoda- Yamamuro, T. Matsuo & H. Suga: J. Phys. Chem. Solids **51** (1990) 1383.

[3] H. Mashiyama, Y. Kurihara & T. Azetsu: J. Korea Phys. Soc. **32** (1998) S156.

[4] F. Iizumi: *The Rietveld Method*, ed. by R. A. Young, (Oxford Univ. Press, 1993) Chap.13.

使用施設：JRR-3M, 装置：HERMES(T1-3), 分野：1. Structures & Excitations

1-1-22

研究テーマ：4V, 5V 級リチウム二次電池正極材料 $LiMn_{2-x}M_xO_{4-\delta}$ の結晶構造,熱力学的安定性と電池特性

表題：4V, 5V 級リチウム二次電池正極活物質 $LiMn_{2-x}M_xO_{4-\delta}$ (M=Ni, Zn)の結晶構造,熱力学的安定性と電極特性の関係

Relation between Crystal Structure, Thermodynamic Stability, and Electrode Characteristics of $LiMn_{2-x}M_xO_4$ (M = Ni, Zn) as a Cathode Active Material for the 4V, 5V Class Lithium Secondary Battery

Y. Idemoto, Y. Ito, H. Narai, Y.Tsunoda and N. Koura

Faculty of Science and Technology, Tokyo University of Science

2641 Yamazaki, Noda-shi, Chiba 278-8510, JAPAN

The relation between crystal structure, thermodynamic stability and electrode characteristics of the spinel $LiMn_{2-x}M_xO_{4-\delta}$ (M=Ni, x=0, 0.1, 0,3, 0.5 Zn; x=0, 0.05, 0.10) was investigated.

1. $LiMn_{1.5}Ni_{0.5}O_4$ as a Cathode Active Material for 5V Class Li Secondary Battery

$LiMn_{1.5}Ni_{0.5}O_4$ as a 5V class cathode material were prepared by changing synthesized method and heat treatment. We investigated the dependence of their properties, crystal structure and cathode performance on oxygen content.

Oxygen content of the samples (sol-gel method and annealed at high Po_2) increased in comparison with the sample (solid-state method).

The charge-discharge curves of the samples (solid-state method) appeared at 4.1V and 4.7-5.0V plateaus. On the other hand, the 4.1V plateau is disappeared (sol-gel method or annealed at high Po_2). The discharge capacity with respect to cycle number of the 5V region in $LiMn_{1.5}Ni_{0.5}O_4$ (sol-gel method) electrodes shows especially good cycle performance.

The neutron-diffraction intensity profiles of $LiMn_{1.5}Ni_{0.5}O_4$ using HERMES were analyzed by Rietan 2000. From the results, the samples are assigned to the ordered form (space group $P4_332$). The amount of impurity phase decreases by annealing at high Po_2 or sol-gel method. Furthermore, the distortion of Mn,Ni(12d)-O octahedral site was restrained with increasing oxygen content.

2. $LiMn_{2-x}M_xO_4$(M=Ni, Zn) as a Cathode Active Material for 4V Class Li Secondary Battery

We investigated the relation between electrode performance and electronic state of $LiMn_{2-x}M_xO_4$(M= Ni, Zn) as cathode active materials for 4V class lithium secondary battery.

The cycle performance is improved by substitution of Mn with Ni or Zn. The neutron-diffraction intensity profiles of $LiMn_{2-x}M_xO_4$ (M=Ni: x=0, 0.1, 0.3; M=Zn: x=0, 0.05, 0.1) were analyzed over a wide range at room temperature and 200K sing HERMES. A refinement was carried out by assuming a cubic unit cell(space group: Fd-3m) by Rietan2000. From the results of room temperature and 200K, the phase transition (cubic to orthorhombic) were restrained by substitution of Zn, Ni for Mn. The bond lengths of Li-O, (Mn, M)-O [M=Ni, Zn] and Madelung energy decrease with increasing M content. The bond lengths of (Mn, M)–O dependence of temperature is decreased with

increasing M content, x(M=Zn, Ni). Hence, the crystal structure is more stable by the substitution of Zn, Ni for Mn.

We obtained the electron density distribution by XRD using *MEM/Rietveld* method.

Moreover, we investigated the electronic states of $LiMn_{1.75}M_{0.25}O_4$ (M=Mn, Ni, Zn) using First-principles calculation by DV-Xa method. The net charges of each atom, the bond overlap populations of Li-O, Mn-O, Ni-O and Zn-O were calculated. From the results, Li is high ionicity and the covalent bonding of Mn-O of $LiMn_{1.75}M_{0.25}O_4$ (M= Ni, Zn) is stronger than that of $LiMn_2O_4$. As a results of the DOS, the oxygen 2p orbital and Mn 3d orbital gives the overlap and the overlap of $LiMn_{1.75}M_{0.25}O_4$ is larger than that of $LiMn_2O_4$.

Furthermore, the standard enthalpies of formation, $\Delta_f H^0$, and the enthalpy change of reaction, ΔH, were calculated form the heat of dissolution. Thermodynamic stability was examined by these parameters. These thermodynamic data was compared with the calculated one of samples to partially replace Mn by Ni or Zn. When $\Delta_f H^0$ and ΔH decreased, it brought to a good cycle performance.

Accordingly, it is suggested that the stability of the host structure brought to improvement for the cycle performance.

研究テーマ：ホイスラー型 Ni_2MnGa 系合金単結晶のマルテンサイト変態
表題：$Ni_{2.18}Mn_{0.82}Ga$ 単結晶のマルテンサイト変態

1-1-23 Martensitic Transformation of $Ni_{2.18}Mn_{0.82}Ga$ Single Crystal

Kazuko INOUE[1], Yukio NODA[2], Hiroyuki KIMURA[2] and Yasuo YAMAGUCHI[3]
[1]*Fac. of Sci. and Tech., Ryukoku University, Seta, Otsu 520-2194*
[2] *IMRAM, Tohoku University, Aoba-ku, Sendai 980-8577*
[3]*IMR, Tohoku University, Aoba-ku, Sendai 980-8577*

We have made the neutron diffraction of an off-stoichiometric Heusler-type $Ni_{2.18}Mn_{0.82}Ga$ single crystal. It has a thermo-elastic martensitic transformation temperature of about 340K, coincident with the Curie temperature. The diffractometer, FONDER, installed on T2-2 port of JRR-3M reactor was used. The Q-scan at 416 K, 344 K and 302 K was made with decreasing temperature. The intensity map in Q-space was measured at 297 K, after cooling down from 400 K to room temperature under magnetic field of 1.5 T.

We determined previously the crystal structure of the martensitic phase using the Rietveld analysis of the powder diffraction patterns obtained by HERMES. Two structures coexist in the martensitic phase. One is an orthorhombic structure distorted from the cubic Heusler structure, and the other is a tetragonal one made from the shuffling of the 220 plane of the orthorhombic structure. This tetragonal structure is equal to the monoclinic one with 6 layers shuffling, which we suggested formerly. [1,2] The temperature dependence of mass fractions of three structures and the mutual relation of the lattice constants determined with increasing temperature are shown in Figs. 1 and 2. We see that there are several coincidences in the lattice constants of three structures.

The single crystal on the sample holder is shown in Fig. 3. The length of the crystal is about 6 mm. From the measurements by FONDER, we found that the single crystal at 416K has a cubic Heusler structure of single domain, where the direction of the crystal growth is [001]. As the examples, Q-scans along (1.8 0 0) to (2.2 0 0) around 200 peaks of

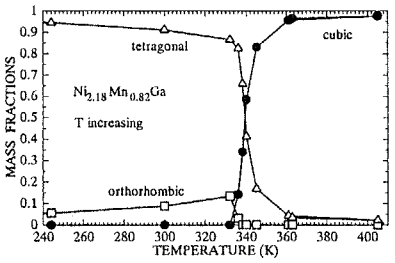


Fig. 1. Temperature dependence of the mass fraction of each structure with increasing temperature.

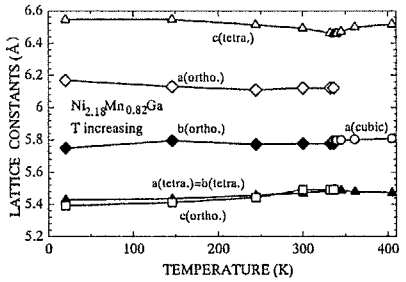


Fig. 2. Temperature dependence of each lattice constant with increasing temperature.

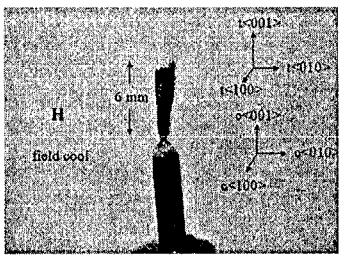


Fig. 3. Single crystal of $Ni_{2.18}Mn_{0.82}Ga$.

cubic Heusler structure are shown in Figs.4 (a) to (c) for three temperatures. We see that 200 peak at 416 K becomes to have two satellites near (1.9 0 0) and (2.1 0 0) at 344 K. At 302 K, the (2.1 0 0) satellite grows up and the other two

使用施設：JRR-3M, 装置：FONDER, 分野：Structures & Excitations

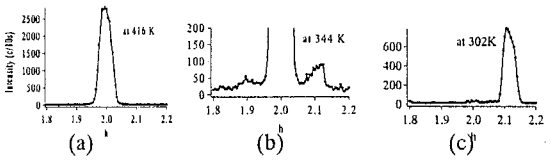


Fig. 4. Q-scan of cubic Heusler 200 peak, (a) at 416 K, (b) at 344 K and (c) at 302 K.

peaks disappear. The (1.9 0 0) peak corresponds to the lattice constant, a(ortho.) of the orthorhombic structure. The (2.1 0 0) peak corresponds to c(ortho.) of orthorhombic structure or a(tetra.) of tetragonal structure. Figure 4 indicates that at 344K near the martensitic transformation temperature, both of the orthorhombic structure and the tetragonal one begin to appear in addition to the cubic Heusler structure. However, at 302 K sufficiently lower than the martensitic transformation temperature, only the tetragonal structure remains. This fact is consistent with the result of powder neutron diffraction, that the mass fraction of tetragonal structure in the martensitic phase exceeds 90 % at low temperatures. The fact indicates that the tetragonal structure is more stable than the orthorhombic structure.

The magnetic field of field cooling was applied along the direction of crystal growth. By searching the crystal direction using FONDER, we found that the direction of the crystal growth in martensitic phase is tetragonal [001] direction. The intensity maps around the tetragonal (200) peak and the tetragonal (002) peak at 297 K are shown in Figs. 5 (a) to (c). In the (h0l) reciprocal plane around tetragonal (002) peak shown in Fig. 5 (c), we see three tetragonal (002) peaks and a weak orthorhombic (020) peak. In the (hk0) reciprocal plane around tetragonal (200) peak shown in Fig. 5 (a), we also see two tetragonal (200) peaks and nearby three tetragonal (202) peaks, which are equal to orthorhombic (220) peaks. From these three pictures, we conclude that field cooling under the magnetic field of 1.5 T could not produce a martensitic phase of single domain.

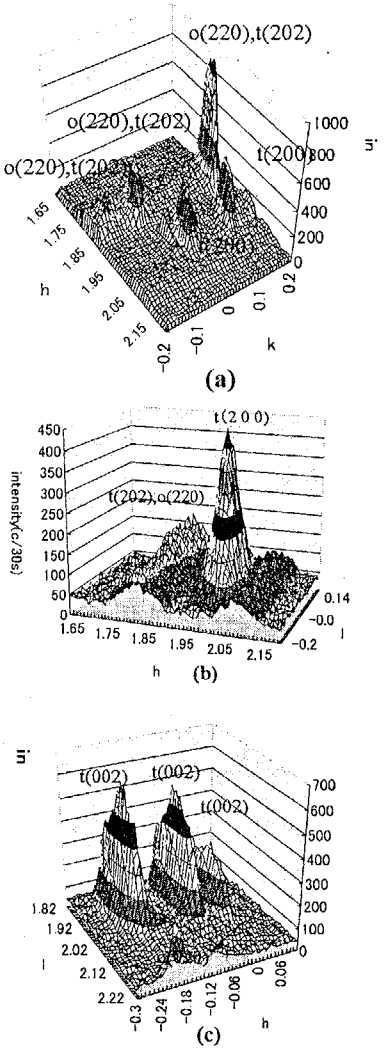


Fig. 5. Intensity maps in Q-space of single crystal, (a) (hk0) reciprocal plane around tetragonal (200), (b) (h0l) one around tetragonal (200) and (c) (h0l) one around tetragonal (002).

The plural number of tetragonal domains and the small amount of orthorhombic structure exist.

References

[1] K. Inoue, K. Enami, M. Igawa, K. Inoue, Y. Yamaguchi and K. Ohoyama: *Proc. of the Int. Conf. on Solid-Solid Phase Transformation '99* (1999) 1120.

[2] K. Inoue, Y. Yamaguchi, K. Ohoyama, K. Enami and K. Inoue: *Proc. Fourth Pacific Rim Int. Conf. on Advanced Materials and Processing* (PRICM4), Vol.II (2001) 1689.

研究テーマ：タングステンを骨格とする高速イオン伝導体の構造解析
表題：三価イオン伝導性ペロブスカイト $Y_x(Ta_{3x}W_{1-3x})O_3$ の結晶構造

Crystal structure of Trivalent Ion Conductive Perovskite: $Y_x(Ta_{3x}W_{1-3x})O_3$

1-1-24

Kenji Toda[1], Yoshio Aoyama[1], Mineo Sato[2]
[1]Graduate School of Science and Technology, Niigata University, Niigata 950-2181, Japan
[2]Department of Chemistry and Chemical Engineering, Niigata University, Niigata 950-2181, Japan

Introduction

It has recently been shown that non-stoichiometry and ordering of A-site cation in the perovskite-based oxides can influence the electronic conduction and structural phase transition of materials such as lithium conducting A-site deficient perovskites [1]. Quite recently, we have reported some possibilities of high trivalent ion conduction in $Y_x(Ta_{3x}W_{1-3x})O_3$ (YTWO), which possesses an highly A-site cation-deficient perovskite structure [2]. The higher trivalent ionic conductivity for YTWO may be attributed to the larger number of A-site vacancies in the solid. However, there are a number of unclarified points regarding crystal chemistry of highly A-site cation-deficient perovskite, YTWO. The present report therefore aims at presenting basic crystallographic data on YTWO by the powder neutron diffraction pattern analysis.

Experimental

The perovskite, $Y_{0.06}Ta_{0.18}W_{0.82}O_3$, was prepared by a conventional solid state reaction. Starting materials were a stoichiometric mixture of Y_2O_3, Ta_2O_5 and WO_3. The mixture was pressed into a pellet and heated in a platinum boat at 1200℃ for 30 min in air. The completion of the reaction and the phase purity of samples were confirmed by the powder X-ray diffraction and fluorescence X-ray method. Thermo gravimetric analysis and differential thermal analysis were used to check the absence of the phase transition. We performed neutron powder diffraction experiments on the Kinken powder diffractometer for high efficiency and high resolution measurements, HERMES [3], of Institute for Materials Research(IMR), Tohoku University, installed at the JRR-3M reactor in Japan Atomic Energy Research Institute (JAERI), Tokai. The fine powder sample was sealed in a vanadium cylinder. Rietveld structure refinement was carried out with the program RIETAN2000 [4]

Result and Discussion

The synthesis of the A-site deficient perovskites, $Y_x(Ta_{3x}W_{1-3x})O_3$, was first reported by Studer, Montfort and Raveau [5]. They refined the structure of orthorhombic $Y_{0.06}Ta_{0.18}W_{0.82}O_3$ in the space group Cmmm (a = 0.5298, b = 0.5377 and c = 0.3774 nm) without a tilting of (Ta, W)O_6 octahedra. However, it is unreasonable if we take account of the fact the (Ta, W)O_6 octahedra have d0-type character regarding the electronic configuration. From the XRD analysis, the reasons for different lattice parameter of the $Y_{0.06}Ta_{0.18}W_{0.82}O_3$ are not difficult to see. It is likely this compound may actually have a lower symmetry. To investigate the occupancy at the A-site and possible tilting of BO_6 octahedra, the powder neutron diffraction data were collected from the single phase x = 0.06 samples. Preliminary Rietveld analysis indicated that the superstructure peaks could not be indexed on the basis of the space group Cmmm. Figure 1 shows the powder neutron diffraction pattern fiting for the solid solution system, $Y_{0.06}Ta_{0.18}W_{0.82}O_3$. All of the patterns matched with that of orthorhombic space group Pnma and the calculated profile show good agreement with observed pattern. A monoclinic distortion model (Space group $P2_1/n$; R_{wp} = 9.45%) with a long-range ordering of the B-site cations and same tilt system was rejected by the Rietveld analysis. The refined crystallographic data obtained from Rietveld refinement listed in Table 1. The orthorhombic Pnma structure is a distorted form of ideal cubic perovskite. The distortion mechanism is a tilting of essentially rigid (Ta, W)O_6 octahedra. It occurs when the A-site cation is too small for its 12 coordinate cavity in the cubic perovskite structure. This distortion is the predominant for perovskites with tolerance factors smaller than 0.98. In the

使用施設：JRR-3M, 装置：HERMES(T1-3), 分野：1.Structures & Excitations

A-site deficient perovskites $Y_x(Ta_{3x}W_{1-3x})O_3$, the tolerance factor is 0.91 and the coordination number of the yttrium ion is effectively lowered from 12 to 8. In addition, neutron diffraction pattern analysis confirmed the disorder arrangement of A-site cations. The yttrium ions are statistically distributed only over 6 % of a single 4c site with 94 % vacancy in the space group Pnma. In this structure, trivalent yttrium ions can move easily through many A-site vacancies. Therefore, $Y_{0.06}Ta_{0.18}W_{0.82}O_3$ with the average structure showed the 800 times higher ion conductivity than an isostructural $La_{0.33}TaO_3$ with the order structure [2].

References

[1] Y. Inaguma, C. Liquan, M. Itoh, T. Nakamura, T. Uchida, H. Ikuta, M. Wakihara, K. Mizumoto and S. Hayashi, *Solid State commun.*, 86 (1993), 689-693

[2] N. Sakai, K Toda and M. Sato, *Electrochemistry*, 6 (2000), 504-506

[3] K. Ohoyama, T. Kanouchi, K. Nemoto, M. Ohashi, T. Kajitani, Y. Yamaguchi, *Jpn. J. Appl. Phys.*, 37 (1998), 3319-3326

[4] F. Izumi and T. Ikeda, *J. Crystallogr. Soc. Jpn.*, 42 (2000), 516-521

[5] F. Studer, Y. Montfort and B. Raveau, *J. Solid State Chem.*, 7 (1973), 269-276

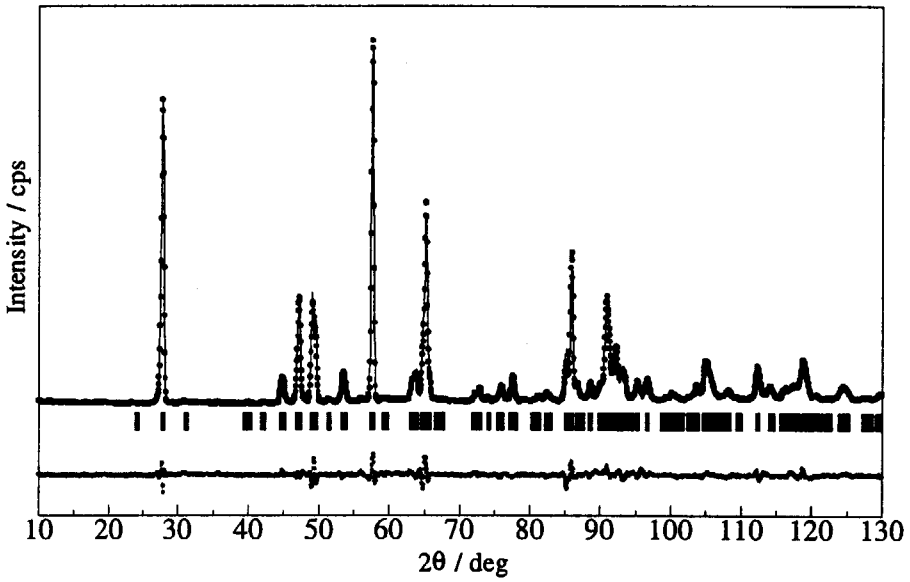


Fig.1 The powder neutron diffraction pattern fitting for the solid solution system, $Y_{0.06}Ta_{0.18}W_{0.82}O_3$.

Table 1. Structural parameters and reliable factors of the $Y_{0.06}(Ta_{0.18}W_{0.82})O_3$

Atom	Site	x	y	z	$B_{eq}(\times 10^{-2}\,nm^2)$
Y	4c	0.060(4)	1 / 4	-0.006(4)	1.34(4)
Ta	4b	0	0	1 / 2	2.36(5)
W	4b	0	0	1 / 2	2.36(5)
O(1)	4c	0.492(4)	1 / 4	0.064(3)	1.07(4)
O(2)	8d	0.281(2)	0.031(1)	0.717(2)	0.98(3)

Space group : Pnma (No. 62)
Lattice parameters (nm) : a = 0.5373(3), b = 0.7547(5), c = 0.5297(3)
Reliable factors : R_{wp} = 6.51 %, R_p = 5.08 %, R_I = 2.50 %, R_F = 1.52 %

研究テーマ：界面活性剤が形成するラメラ相の構造に対するずり流動場の効果
表題：非イオン界面活性剤－水系が形成するラメラ相におけるずり流動場誘起転移
1-1-25

Shear-Induced Transformations in the Lamellar Phase Formed in Nonionic Surfactant-Water System

K. Minewaki, T. Kato, M. Imai[1], and Yoshiaki Takahashi[2]

Department of Chemistry, Tokyo Metropolitan University
[1] Department of Physics, Ochanomizu University
[2] Department of Molecular and Material Sciences, Kyushu University

In recent years, much attention has been paid to the effects of shear flow on the structure of a lamellar phase by using various scattering techniques. In the previous studies[1)2)], we have measured small-angle neutron scattering (SANS) on a nonionic surfactant $C_{16}H_{33}(OC_2H_4)_7OH$ ($C_{16}E_7$)-water system at 48 and 55wt% of $C_{16}E_7$ at 55 and 70°C under shear flow for the shear rates $\dot{\gamma}$ = 10^{-3}-10^{2} s^{-1} much lower than those for other studies reported so far. We have found specific shear rate dependences in both the position and the intensity of the first reflection. In the present study, measurements have been made at 40 wt% of $C_{16}E_7$ at 70°C which is close to the low concentration limit of the lamellar phase.

Measurements of SANS were carried out at the instrument SANS-U of Institute for Solid State Physics of University of Tokyo in JRR-3M at Tokai with a Couette shear cell.

Figure 1 shows examples of the observed diffraction patters for different shear rates. At the shear rates 0.1- 0.3 s^{-1}, the diffraction peak is shifted to the higher scattering angle. With the further increase in the shear rate, the peak position is moved to the lower scattering angle. These results indicate that the repeat distance (d) takes a minimum at the shear rates 0.1- 0.3 s^{-1}. Similar results have been obtained in our previous studies. However, the decrese of d in the present study is much more pronounced than in the previous study. Moreover, the shear rate giving a minimum of d (d_{min}) is slightly lower than the previous one (0.3- $1s^{-1}$). In Figure 2, d_{min} is plotted against the concentration together with the d value and the film thickness at rest obtained from the analysis of SAXS. This figure demonstrates that d_{min} depends on concentration only slightly, suggesting phase separation induced by shear flow.

1) K. Minewaki, T. Kato, and M. Imai, *Studies in Surface Science and Catalysis*, **132**, 185-188 (2001).
2) K. Minewaki, T. Kato, M. Imai, and Y. Takahashi, *Activity Report on Neutron Scattering Research*, **8**, 208 (2001).

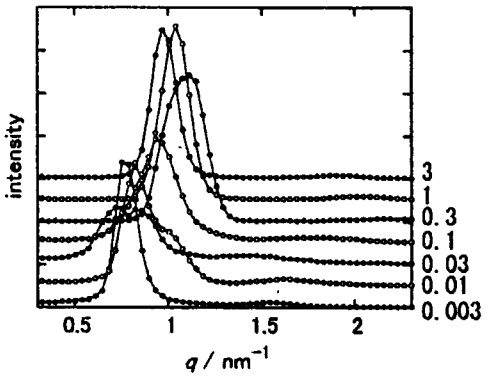


Figure 1 Examples of diffraction patterns at 48 wt% and 70°C for gradient direction for different shear rates (indicated in the figure in s^{-1}).

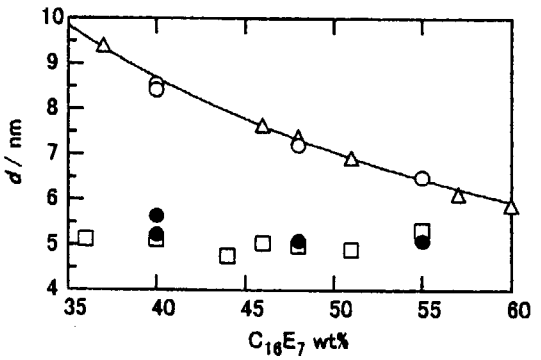


Figure 2 Concentration dependence of the repeat distance (d) at 70°C for the shear rate of 0.003 (○) and 0.1～1 s^{-1} (●) compared with d (△) and the film thickness (□) at rest obtained from SAXS.

研究テーマ：希土類化合物のヤーン・テラー効果による構造相転移
表題：$TbVO_4$におけるヤーン・テラー効果の誘導構造相転移

1-1-26
Jahn-Teller induced structural phase transition in $TbVO_4$

M.Hidaka[1], M.Fujii[2], S.Watanabe[1,3], S.R.P.Smith[4], K.Ohoyama[5] andY.Yamaguchi[5]

1.Department of Physics, Faculty of Science, Kyushu University, Fukuoka 812-0053, Japan.
2.Department of Physics, Faculty of Education, Oita University, Oita 870-1192, Japan
3.Neutron scattering Laboratory, I.S.S.P., University of Tokyo, Tokai, Ibaraki 319-1106,Japan
4.Clarendon Laboratory, University of Oxford, Oxford OX 3PU, U.K.
5.Insitite of Materials Research, Tohoku University, Sendai 980-8577, Japan

The rare earth vanadates have proved ideal systems for study of structural phase transition involving lattice strains arising from the cooperative Jahn-Teller effect. The transition are driving by a coupling between the low-lying electronic energy levels of the rare earth ions and the lattice phonon. $TbVO_4$ has a tetragonal symmetry D_{4h}^{19}-$I4_1/amd$ of zircon structure at room temperature. The structural phase transition occurs at about 34K(Tc). It is known that the structure is an orthorhombic symmetry D_{2h}^{24}-Fddd in the low-temperature phase. However, the structural property has been not adequately analyzed by appearance of multi-domains below Tc. Thus, we carried out neutron diffraction to re-study the structural modulation in the vicinity of tetragonal symmetry. The measurements were done at KSD in JRR-3. At the present experiments, a specimen was made by fixing 9 small crystals with adhesive, whose size is about 1 x 1 x 5mm^3.

Fig.1 shows peak profiles of (4,0,0) and (0,4,0) fundamental reflections, taken at about 8K and 50K in $TbVO_4$. Since the structure is tetragonal at 50K, their intensities are approximately same. However, below Tc, the peak profiles of reflections are largely modified by the structural phase transition. It was found from Fig.1 that there are two kinds of orthorhombic domains in the used specimen and an angle γ between [100] and [010] of is not 90°. Because the peak profiles at 8K are refined by two Gaussian curves. This suggests that a structural distortion mode is a B_{2g} mode, not B_{1g} mode. Will et al.[1] argued from X-ray powder diffraction that there was no evidence for any discontinuous change in the cell volume at 32K(Tc) and the structural phase transition was of

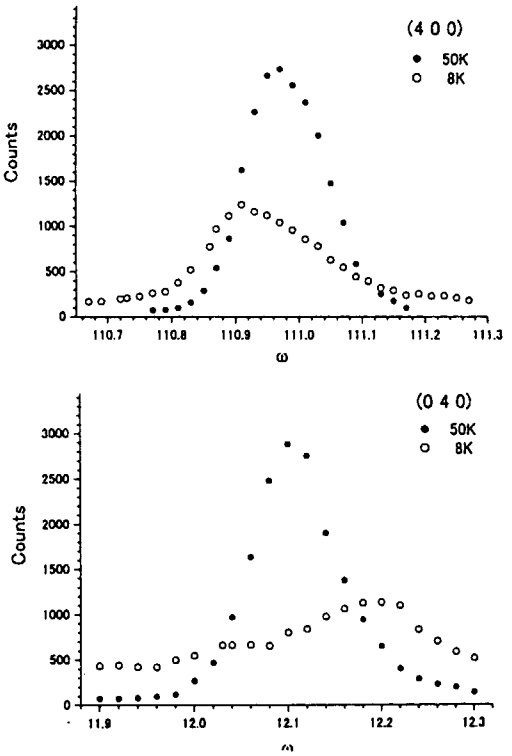


Fig.1. Peak prifiles of the (4,0,0) and (0,4,0) retlections in $TbVO_4$, taken at 8K and 50K by a ω-scan

second order. In order to study the transitional order, we carried out measurements of the integrated intensity of (0,4,0) reflection, as shown in Fig.1. Fig.2 shows the peak profiles of the (0,4,0) reflection taken by the ω-scan at the respective temperature in the vicsinity of the phase transition. It was interested in the peak profile taken at 31K, around which the phase transition occurs. This suggests that there is probably an semi-stable intermediate state related to the first-order structural modulation around Tc. Since the peak position in the low temperature

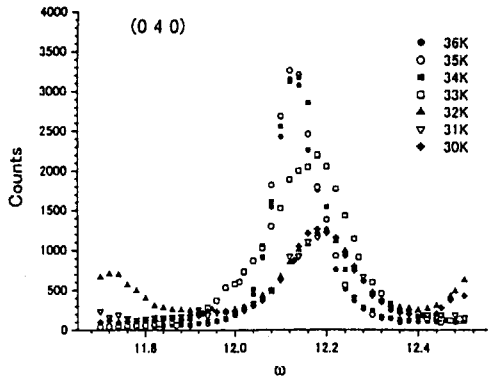


Fig.2.Temperature dependence of the peak profiles of (0,4,0) reflection in the vicinity of the phase transition.

phase is not cleared by the peak splitting, we first fixed the neutron detector at a maximum peak position of the (0,4,0) reflection at 50K. Second, we cooled the specimen till 8K. After that, we continuously measured the intensity, on heating. The results are shown in Fig.3. It was found that the structural phase transition occurs at 33K and should be of first order, not second one. On the other hand, we first fixed the detector at a maximum peak position of the (0,4,0) reflection at 8K. Secondly, we continuously measured the intensity, on heating. The results are shown in Fig.4. The phase transition was confirmed at 31K.

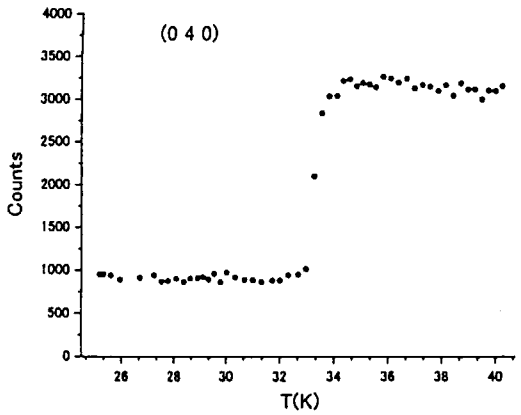


Fig.3.Temperature dependence of the maximum peak intensity of (0,4,0) reflection taken at 50K in Fig.2.

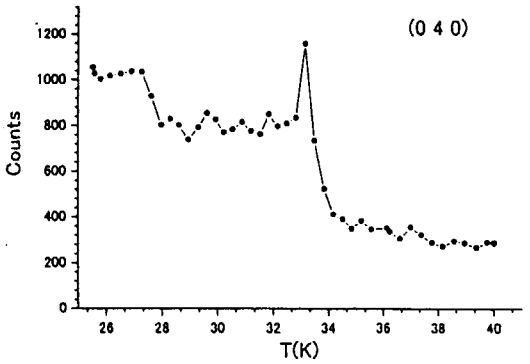


Fig.4.Temperature dependence of the maximum peak intensity of (0,4,0) reflection taken at 8K in Fig.2.

However, its (I-T) curve is characterized around Tc by a critical dispersion. In order to study the critical scattering, we carried out measurements of the intensity of (0,4,0) reflection observed in the intermediate phase, which is at ω= 11.7 0° in Fig.2. Fig.5 suggests that the intermediate phase occurs in a region from about 30.5K to 33K. The structural phase transition occurs at 33K, as shown in Figs.3 and 4.Therfore, we considered that the large elastic strain induced at the phase transition by the Jahn-Teller effect is quickly transformed to a construction of the semi-stable intermediate phase in such narrow temperature region below Tc.

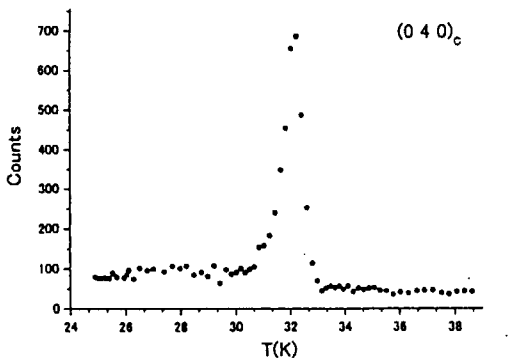


Fig.5.Temperature dependence of the peak intensity of (0,4,0) reflection in the intermediate phase, which is observed at ω= 11.7 0° in Fig.2.

[1].G.Will, H.Gobel, C.F.Sampson and J.B.Forsyth, Phys.Let.38A(1972)297.

研究テーマ：多重極限環境下における中性子散乱実験法の研究
表　題：UCr_2Si_2 の結晶構造と構造相転移

1-1-27

Crystal structure and the structural phase transition in an itinerant 5*f* antiferromagnet UCr_2Si_2

T. D. Matsuda[1], N. Metoki[1], Y. Haga[1], S. Ikeda[1,2], K. Kaneko[1] and Y. Ōnuki[1,2]

[1]ASRC-JAERI, Tokai, Naka, Ibaraki 319-1195
[2]Graduate School of Science, Osaka University, Toyonaka, Osaka 560-0043

UT_2X_2[1] is one of the traditional 5*f* electron systems that the unusual magnetic and transport properties have been studied systematically for various compounds with different transition metal T and X=Si, Ge. In UCr_2Si_2 the small number of *d*-electrons and small distance between U atoms give rise to rather enhanced itinerant character of the 5*f*-electrons. Very recently, we have succeeded in growing single crystals of UCr_2Si_2 for the first time. The purpose of this study is to reveal the structural properties of UCr_2Si_2 by means of neutron scattering.[2]

Polycrystalline samples were grown by arc-melting of stoichiometric amount of the starting materials. Single crystals were grown by the Czochralski-pulling method in a tetra-arc furnace under argon gas atmosphere. Powder diffraction patterns were measured by using HRPD (λ=1.8242 Å). The structural phase transition was studied in detail with a single crystal sample using triple axis spectrometers LTAS and TAS-2, respectively.

Figure 1 shows the neutron powder diffraction pattern of UCr_2Si_2. At 300 K the data were satisfactorily explained by the $ThCr_2Si_2$-type structure with the space group $I4/mmm$. At 100 K we observed clear splitting of the peaks, indicating the structural phase transition below T_a = 210 K. We found that the observed diffraction pattern was well explained by the model calculation with space group $P\bar{1}$ (A-2). The obtained structural parameters after Rietvelt refinement are listed in Table 1. The distortions due to the structural transition are very small.

Figure 3 shows the contour plot of the scattering intensities around the (2,0,0), (0,2,0),

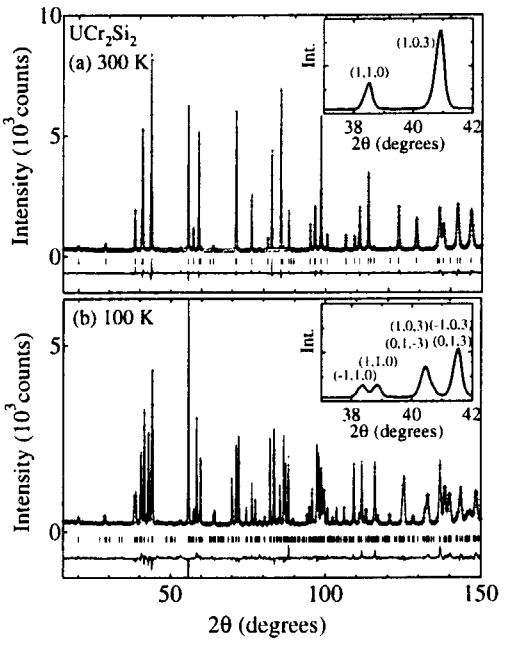


Figure 1: The high resolution neutron powder diffraction pattern of UCr_2Si_2 at (a) 300 K and (b) 100 K. The solid line is the calculated diffraction intensity after Rietvelt refinement.

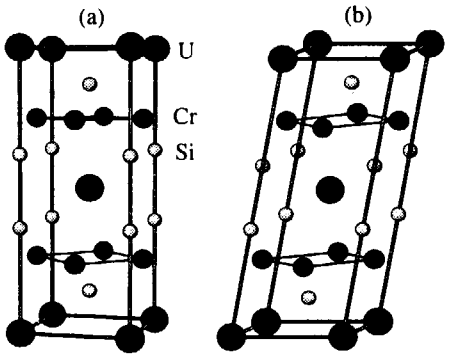


Figure 2: The crystal structure of UCr_2Si_2 for (a) high-temperature tetragonal phase and (b) low temperature triclinic phase.

原子炉：JRR-3M　　装置：HRPD(1G)　　分野：中性子散乱（構造）

Table 1: Structural parameters of UCr_2Si_2. Numbers in parentheses following refined parameters represent the estimated standard deviations of the last significant digit(s)

Space group	lattice parameter	atom (site)	position			B
T(K)	(nm, degrees)		x	y	z	
$I4/mmm$	a=b= 0.3913(1)	U (2a)				0.271886
300 K	c= 1.0507(5)	Cr(4d)				0.646982
	α=β=γ= 90	Si (4e)			0.38631(5)	0.505441
	R_{wp}= 5.21	R_p= 3.97	R_e= 4.61	S=1.1299		
$P\bar{1}$	a= 0.3906(5)	U (1a)				0.2
	b= 0.3903(6)	U (1h)				0.2
	c= 1.0506(2)	Cr(2i)	0.52134(0)	0.24977(2)	0.0308(1)	0.2
100 K	α= 91.49(6)	Cr(2i)	-0.0320(3)	0.24993(7)	0.47201(3)	0.3
	β= 88.51(3)	Si (2i)	0.21823(5)	0.38567(5)	-0.0176(0)	0.3
	γ= 90.74(1)	Si (2i)	0.51053(9)	0.88644(4)	0.48675(1)	0.3
	R_{wp}= 6.43	R_p= 4.95	R_e= 4.81	S=1.3351		

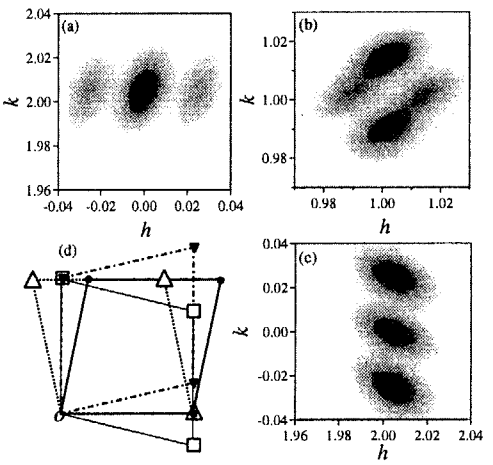


Figure 3: The contour plot of the scattering intensity around (a) (2,0,0), (b), (0,2,0), and (c) (1,1,0) nuclear reflections. The panel (d) is the schematic view of the domain structure.

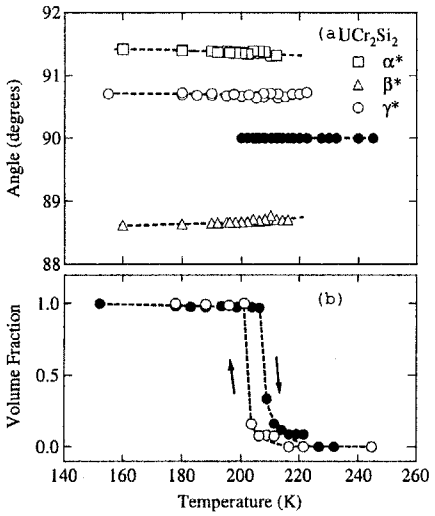


Figure 4: The temperature dependence of (a) the angles α^*, β^* and γ^* and (b) the volume fraction of the triclinic phase.

and (1,1,0) peak. The splitting of the peaks can be explained in terms of four domains as schematically shown in Fig. 3(d). On the other hand, the (0,0,2) reflection showed no change throughout the structural transition, namely all domains have a common c^*-axis.

The angles α^*, β^*, and γ^* are plotted as a function of temperature in Fig. 4 (a). The angles exhibit a clear jump with a hysteresis of 5 K and a two phase coexistence in the temperature range of 20 K. Figure 4 (b) indicates the volume fraction of the triclinic phase.

The volume fraction showed a very sharp jump with a hysteresis of 5 K. These behaviors are clear nature for the first-order transition.

References

1) T. Endstra, G. J. Nieuwenhuys and J. A. Mydosh, Phys. Rev. B **48** (1993) 9595.
2) T. D. Matsuda, N. Metoki, Y. Haga, S. Ikeda, T. Okubo, K. Sugiyama, N. Nakamura, K. Kaneko and Y. Ōnuki, J. Phys. Soc. Jpn., to be published.

研究テーマ：半磁性電気伝導体の磁性と化学構造
表　題：複合結晶 $[Ca_2CoO_3]_{0.62}CoO_2$ の変調構造

1-1-28

Modulated Structure of the Composite Crystal $[Ca_2CoO_3]_{0.62}CoO_2$

Y. MIYAZAKI, M. ONODA[1], T. OKU[2], Y. ISHII[3], Y. MORII[3] and T. KAJITANI

Department of Applied Physics, Tohoku University, Sendai 980-8579
[1]Advanced Materials Laboratory, NIMS, Tsukuba, Ibaraki 305-0044
[2]Institute of Scientific and Industrial Research, Osaka University, Osaka 567-0047
[3]Advanced Science Research Center, JAERI, Tokai, Ibaraki 319-1195

The compound known as $Ca_3Co_4O_9$ [1, 2, 3] has recently attracted much attention as a potential candidate for a thermoelectric material. However, the precise composition and the crystal structure have not yet been fully studied due to its incommensurate strucure. We have revealed that the compound is classified as a composite crystal and its structure formula should be expressed as $[Ca_2CoO_3]_{0.62}CoO_2$. In this report, we present the structure parameters of the compound on the basis of a four-dimensional superspace group approach using powder neutron diffraction data.

Neutron powder diffraction (ND) data were collected at 293 K by means of HRPD diffractometer ($\lambda = 1.8226$ Å) installed at the JRR-3M reactor in JAERI. The ND data were analyzed using a Rietveld refinement program PREMOS 91 [4] designed for modulated structure analyses. The observed electron diffraction patterns demonstrated that the compound consists of two bace-centered monoclinic subsystems with different b-axis lengths. The superspace group of $Cm(0\ 1\text{-}p\ 0)$ was then adopted on the basis of the observed systematic absences.

Figure 1 shows the observed, calculated and difference profiles for the ND data. Short vertical lines below the patterns indicate the peak positions of main (upper) and satellite (lower) reflections for the two subsystems. A satisfactorily good fit was achieved and the final R_{WP} factor was 10.6 %.

Figure 2 shows the fundamental structure (atomic site modulations are not shown for clarity) viewed in perspective from the b-axis. The closed circles represent the Co atoms, and the shaded and open circles are the Ca and O atoms. The fundamental structure consists of a CoO_2 sheet (subsystem 1) and an ordered tripled NaCl-type Ca_2CoO_3 block (subsystem

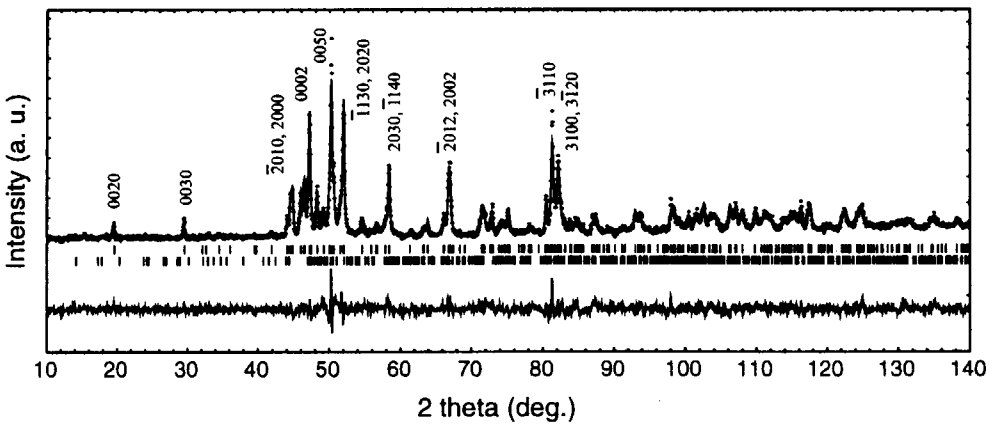


Figure 1: Observed, calculated and difference patterns of the powder neutron diffraction data for $[Ca_2CoO_3]_{0.62}CoO_2$ measured at 293 K.

原子炉：JRR-3M　　装置：HRPD(1G)　　分野：中性子散乱（構造）

2), stacked parallel to the c-axis. The CoO_2 sheet is composed of edge-shared CoO_6 octahedra forming a triangular lattice as seen in the CdI_2-type structure. No substitution of the Ca sites with Co in the $[Ca_2CoO_3]$ subsystem was noticed. The most interesting finding is a buckled atomic arrangement in the Ca_2CoO_3 subsystem. That is due to the x coordinates of the Co2 and O3 atoms in the middle-layer of Ca_2CoO_3 subsystem being slightly shifted toward -x direction from the center of the regular NaCl-type sites. Lattice parameters were refined to be a = 4.8339(3) Å, b_1 = 2.8238(2) Å, b_2 = 4.5582(2) Å, c = 10.8436(7) Å and β = 98.14(1)°. The resulting b_1/b_2 ratio of 0.6195(1) corresponds to the stoichiometry of the sample, $[Ca_2CoO_3]_{0.6195}CoO_2$.

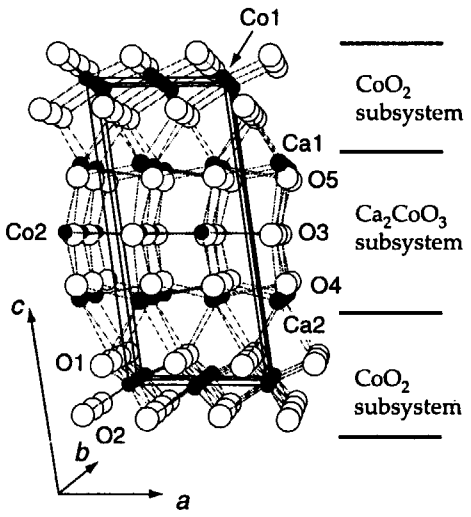


Figure 2: The refined fundamental structure of $[Ca_2CoO_3]_{0.62}CoO_2$ projected in perspective from the b-axis.

In the real structure, however, periodic difference between the subsystems causes atomic displacive modulations. Figure 3 exemplifies the modulation of the Co1-O distance (d_{Co1-O}) plotted against t' (= -(b_1/b_2)x_2 + x_4= -0.6195x_2 + x_4), a complementary (four-dimensional) coordinate in the superspace. [4] Any section with different t' value corresponds to a different phase of the modulation wave in the structure. The Co1-O bond lengths have periodical alteration with the interval of t' = 1.0 because these atoms belong to the $[CoO_2]$ subsystem. Despite their large difference in modulation amplitudes, the mean bond distances are in the range of 1.87-2.02 Å.

Both the Co1 and Co2 atoms and their oxygen networks could be responsible for electric conduction. However, strong modulation and long bond distances observed in the Co2-O networks would prevent carrier transfer. A recent band calculation made on γ-Na_xCoO_2 demonstrated that electric conduction occurs between the Co sites directly in the CdI_2-type CoO_2 layers. [5] Judging from the similarity between γ-Na_xCoO_2 and $[Ca_2CoO_3]_{0.62}CoO_2$, the electric conduction would mainly occur within the CoO_2 sheet in the present compound. The $[Ca_2CoO_3]$ block can be thus regarded as a charge reservoir which supplies carriers into the CoO_2 sheet.

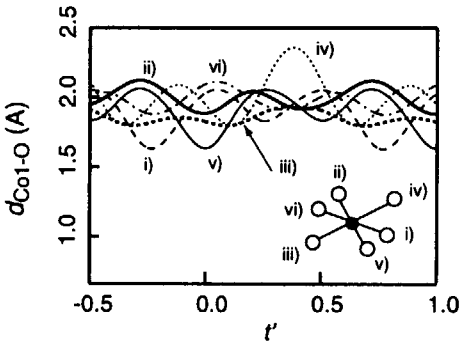


Figure 3: Co1-O distances, d_{Co1-O} plotted against a complementary coordinate, t' (= -(b_1/b_2)x_2 + x_4 = -0.6195x_2 + x_4) in the superspace.

References

1) S. Li *et al.*: J. Mater. Chem. **9** (1999) 1659.
2) Y. Miyazaki *et al.*: Jpn. J. Appl. Phys. **39** (1997) L531.
3) A. C. Masset *et al.*: Phys. Rev. B **62** (2000) 166.
4) A. Yamamoto: Acta Crystallogr. A **49** (1993) 831.
5) D. J. Singh: Phys. Rev. B **61** (2000) 13397.

研究テーマ：超イオン導電体における構造不規則性と動的性質
表　題：AgBrの中性子散漫散乱

1-1-29

Diffuse Neutron Scattering from AgBr

A. THAZIN, M. ARAI, T. SAKUMA, H. TAKAHASHI[1] and Y. ISHII[2]

Faculty of Science, Ibaraki University, Mito 310-8512, Japan
[1]Faculty of Engineering, Ibaraki University, Hitachi 316-8511, Japan
[2]Japan Atomic Energy Research Institute, Tokai 319-1195, Japan

Correlation effects between the thermal displacements of atoms play an important role to explain the oscillatory diffuse scattering in solid electrolytes, AgI and CuI. The correlation effect is specific in solid electrolytes which have large thermal vibrations. In order to obtain the dynamical correlation among atoms in AgBr, diffuse neutron background intensity of AgBr has been measured from 8 K to 450 K using a neutron diffractometer HRPD installed at JRR-3 in JAERI. A powder sample of AgBr in a vanadium container with 10 mm in diameter was used. The incident neutron wave length of 1.823 Å was used. Neutron diffraction data were collected for 1 d over the 2θ range of 20° to 150°. Fig. 1 shows the powder diffraction intensities of AgBr at 8 K and 450 K. Several sharp Bragg lines and a large diffuse scattering were observed at 450 K. The peaks of the oscillatory diffuse scattering appear at 2θ~40°, 53° and 98° in Fig. 1. The oscillatory characteristic in the diffuse scattering at 8 K is not clear. The values of thermal parameter B_{Ag} and B_{Br} at 450 K are 4.739 $Å^2$ and 3.959 $Å^2$, respectively. The values of B at 8 K are about 1/100 of those at 450 K. The temperature dependence of the oscillatory diffuse scattering from AgBr, which was predicted with the correlation effect, was confirmed by the measurement.

Crystal of AgBr is assumed to belong to the rock-salt structure with a space group Fm3m. Silver and bromine atoms occupy 4(a) and 4(b) sites, respectively. The peak positions at 2θ~53° and 98° in diffuse scattering at 450 K in Fig. 1 are related to the reciprocal of the distance between first nearest neighbor atoms. The distance in AgBr is 2.899 Å at 450 K. The main contribution to the oscillatory diffuse scattering of superionic conductors was from the correlation among the displacements of cation and anion atoms. It is suggested that the main contribution of AgBr would be from the correlation among the displacements of silver and bromine atoms. The estimated value of the thermal correlation among Ag-Br is 0.742. However the peak at 2θ~40° dose not appear from the correlation between first nearest neighbor atoms. The peak could be explained by the correlation between second nearest neighbor atoms. The distance between second nearest neighbor atoms (Ag-Ag and Br-Br) is 4.101 Å. The estimated value of the thermal correlation among Ag-Ag and Br-Br is 0.471. The peak at 2θ~40° is almost in agreement with the calculated value. Most influences on diffuse scattering above third nearest neighbor atoms could be disregarded. The value of thermal correlation depends on interatomic distance and crystal structure.

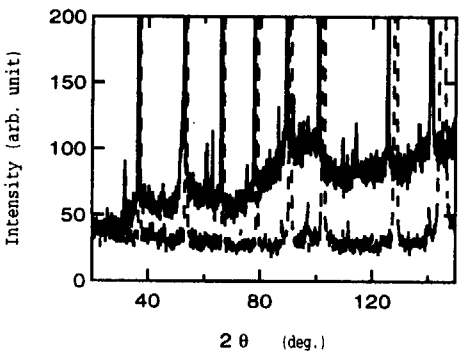


Figure 1: Observed neutron powder diffraction intensity for AgBr at 8 K (broken line) and 450 K (solid line).

原子炉：JRR-3M　　装置：HRPD(1G)　　分野：中性子散乱（構造）

研究テーマ：中性子散乱による高温超伝導体の研究
表　題：$Sr_2YCu_2CoO_7$の中性子回折による研究

1-1-30

Neutron Diffraction Study of $Sr_2YCu_2CoO_7$

T. Mochiku, Y. Hata[1], Y. Mihara[2], Y. Nakano[2], J. Suzuki[1], K. Kadowaki[2] and K. Hirata

Superconducting Materials Center, National Institute for Materials Science,
1-2-1 Sengen, Tsukuba, Ibaraki 305-0047
[1]Advanced Science Research Center, Japan Atomic Energy Research Institute,
2-4 Shirakata-Shirane, Tokai, Ibaraki 319-1195
[2]Institute of Materials Science, University of Tsukuba,
1-1-1 Tennoudai, Tsukuba, Ibaraki 305-8573

Crystal structure of $Sr_2YCu_2CoO_{6+\delta}$ has been analyzed using neutron powder diffraction to compare with that of $Sr_2YCu_2FeO_{6+\delta}$[1]. These compounds consist of nanometer-scale sequence of alternating double CuO_2 sheets as those in high-T_c superconductors, and $(Fe,Co)O_\delta$ sheet similar to that in the $Sr(Fe,Co)O_{2+\delta}$ magnetic compound with brownmillerite-type structure. $Sr_2YCu_2FeO_{6+\delta}$ exhibits superconductivity around 50 K when it is annealed under N_2 atmosphere and subsequently under O_2 atmosphere, while $Sr_2YCu_2CoO_{6+\delta}$ with the same annealing process does not exhibit superconductivity. Neutron diffraction can distinguish between Cu and Co because the scattering length of Cu differs from that of Co, while X-ray diffraction can hardly do so. Then, we can analyze the mutual substitution of Cu and Co.

Samples were prepared by the solid state reaction of stoichiometric amount of $SrCO_3$, Y_2O_3, CuO and Co_3O_4 powders. We prepared three kinds of samples: as-synthesized sample, and the samples which were N_2-annealed and oxidized under high oxygen pressure. Neutron powder diffraction experiments were carried out using a high-resolution powder diffractometer, HRPD, installed in JRR-3M. Intensity data were collected at room temperature and then were analyzed using the Rietveld refinement program RIETAN[2] on the basis of the orthorhombic $Sr_2YCu_2GaO_7$-type structure model[3].

Neutron diffraction study indicates that Cu is hardly substituted for Co in $Sr_2YCu_2CoO_{6+\delta}$, while it is easy to substitute Cu for Fe in $Sr_2YCu_2FeO_{6+\delta}$ and the N_2-annealing suppresses this substitution. $Sr_2YCu_2CoO_{6+\delta}$ without N_2-annealing already has the ordered distribution of the Cu and Co atoms, and this distribution does not change by N_2-annealing and oxidization under high oxygen pressure. The δ value does not deviate substantially from unity by the annealing process in all $Sr_2YCu_2CoO_{6+\delta}$ samples, although the annealing process is very effective on the control of oxygen content, $6+\delta$, in $Sr_2YCu_2FeO_{6+\delta}$. These results show that enough amount of oxygen can not be supplied onto the CoO_δ sheet to exhibit superconductivity in $Sr_2YCu_2CoO_{6+\delta}$.

The Co and oxygen atoms on the CoO_δ sheet have large thermal vibration in all $Sr_2YCu_2CoO_{6+\delta}$ samples. This indicates that the arrangement of the CoO_4 tetrahedra is disordered although the four coordination of the Co atom is stable. The disorder of the arrangement is not also influenced by the annealing process.

References

1) T. Mochiku, Y. Mihara, Y. Hata, S. Kamisawa, M. Furuyama, J. Suzuki, K. Kadowaki, H. Fujii and K. Hirata, J. Phys. Soc. Jpn. **71** (2002) 790.
2) F. Izumi and T. Ikeda, Mater. Sci. Forum **321-324** (2000) 198.
3) Q. Huang, R. J. Cava, A. Santoro, J. J. Krajewski and W. F. Peck, Physica C **193** (1992) 196.

原子炉：JRR-3M　　装置：HRPD(1G)　　分野：中性子散乱（構造）

研究テーマ：ゼオライトの結晶構造研究
表　題：シリカライトの中性子回折
1-1-31

Crystal Structure Study on Defective Silicalite by Neutron Diffraction

T. Suzuki, K. Sugita and Y. Ishii[1]

Basic Chemicals Research Lab., Sumitomo Chemical Co., Ltd., Sobiraki, Niihama, 792-5821
[1]ASRC, Japan Atomic Energy Research Institute, Tokai, Ibaraki 319-1195

Zeolites are used in the industry as catalysts. Performance of catalysts is strongly related to the crystal structure and the concentration of point defects in the zeolite crystal, because the point defects in the crystal often behave as active sites for reaction. Artioli *et al.*[1)] determined the crystal structure of silicalite by neutron diffraction experiments. However, information for concentration of the defect is insufficient. Therefore we study the crystal structure and defect concentration of silicalite with neutron diffraction measurements.

Silicalite powder samples were stirred in D_2O water at 353 K for H-D exchange. IR measurement of this sample was carried out for checking the H-D exchange. After this checking the fully deuterated sample was dehydrated at 673 K under He-gas flow. The sample was sealed in a special quartz tube without air exposure. The neutron powder diffraction pattern of the deuterated silicalite sample was observed with the High-Resolution Powder Diffractometer (HRPD) installed at the JRR-3M in JAERI.

Measurements were carried out at low temperature of 15 K in order to minimize the diffraction effect due to thermal vibration of atoms. Data were collected between 5 deg. and 150 deg. in diffraction angle with an equal step of 0.05 degree. Diffraction intensities of deuterated silicalite were obtained by subtracting the diffraction data of the blank quartz-tube(empty) from that of the sample.

A typical diffraction pattern of deuterated silicalite is shown in Fig. 1. We refined the observed data with a Rietveld method by using a RIETAN-2000 program package. Obtained results of the refinement are rather good. More detailed analysis of the diffraction data is being conducted in the current studies.

References

1) G. Artioli, C. Lamberti and G. L. Marra, Acta Cryst. (2000) **B56**, 2-10.

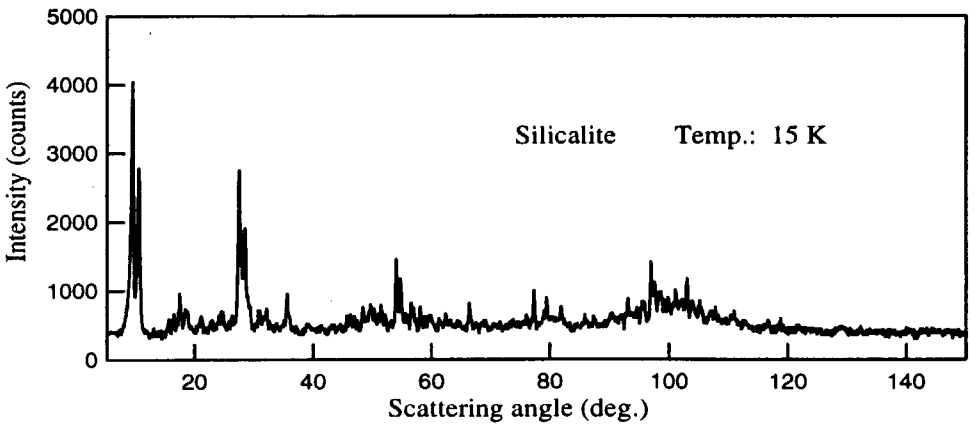


Figure 1: A typical diffraction pattern of deuterated silicalite measured at 15 K.

原子炉：JRR-3M　　装置：HRPD(1G)　　分野：中性子散乱（構造）

研究テーマ：アクチノイド、ランタノイド複合化合物系の構造、磁気的性質の研究
表　題：$CaMn_{1-x}Ru_xO_3$ の磁性
1-1-32

Magnetic Properties of $CaMn_{1-x}Ru_xO_3$

K. YOSHII, A. NAKAMURA[1], H. ABE[2], Y. ISHII[3], Y. SHIMOJO[3] and Y. MORII[3]

Synchrotron Radiation Research Center, Japan Atomic Energy Research Institute (JAERI), Mikazuki, Hyogo 679-5148
[1]Department of Materials Science, JAERI, Tokai, Ibaraki 319-1195
[2]National Institute for Materials Science, Tsukuba, Ibaraki 305-0047
[3]Advanced Science Research Center, JAERI, Tokai, Ibaraki 319-1195

Numerous studies have been reported in recent years for perovskite manganites because of their interesting properties such as the CMR (colossal magnetoresistance) effect. One of the compounds, $CaMnO_3$, have an orthorhombic crystal structure (space group *Pnma*) and is an insulating antiferromagnet below a Néel temperature (T_N) of about 130 K. Recently, it was found that ferromagnetism and metallicity are developed for $CaMn_{1-x}Ru_xO_3$ where the Mn ion is substituted by Ru in $CaMnO_3$.[1)] $CaRuO_3$ (x=1) has the same *Pnma* structure and exhibits metallic conductivity with a tendency toward magnetic order at low temperatures. The Curie temperature reaches a maximum value of 210 K for $CaMn_{0.6}Ru_{0.4}O_3$ (x=0.4). In this work, magnetic properties of this compound have been investigated.

The sample was prepared by the solid-state reaction in air.[1)] Magnetization measurements revealed a ferromagnetic transition at around 210 K. Figure 1(a) shows powder neutron diffraction patterns at room temperature measured with a high resolution powder diffractometer (HRPD). Though the previous X-ray diffraction measurements[1)] led to an orthorhombic *Pnma* (No.62) structure, the present Rietveld analysis using the program RIETAN-2000 provided a better result for a monoclinic structure of $P2_1/n$ (No.14) with the lattice parameters of a=5.3168(2), b=5.3974(2), c=7.5548(3)Å, and β=89.977(9)°.

Figure 1(b) shows an experimental result at 4 K. It is seen that some magnetic peaks, such as that pointed by the arrow, are developed at low temperatures. From a preliminary analysis, this pattern could be fitted assuming ferrimagnetic spin alignment of the Mn and Ru moments with 1-3 μ_B. In the previous work,[1)] coexistence of ferromagnetic and antiferromagnetic phases was observed in the same sample. A further detailed analysis for the present data is in progress.

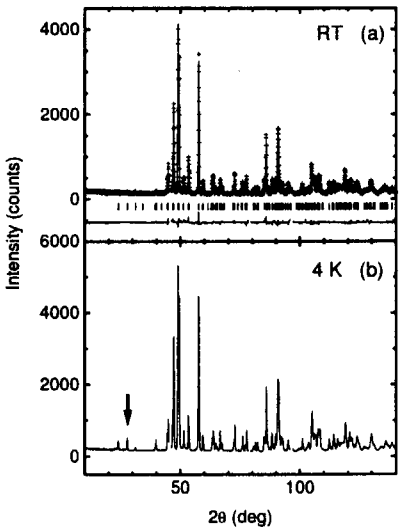


Figure 1: Neutron powder diffraction patterns of $CaMn_{0.6}Ru_{0.4}O_3$ at (a) room temperature and (b) 4 K. The arrow shows a representative magnetic Bragg peak.

References

1) A. Maignan et al: Solid State Commun. **117** (2001) 377.

原子炉：JRR-3M　　装置：HRPD(1G)　　分野：中性子散乱（構造）（磁性）

研究テーマ：半磁性電気伝導体の磁性と化学構造
表　題：　$La_{0.875}Ca_{0.125}MnO_3$ におけるヤーンテラー歪みと軌道秩序

1-1-33

Jahn-Teller distortion and orbital ordering in $La_{0.875}Ca_{0.125}MnO_3$

Y. ONO, S.BEGUM, Y.ISHII[1], Y.MORII[1] and T.KAJITANI

Department of Applied Physics, Tohoku University, Sendai 980-8579
[1]Advanced Science Research Center, JAERI, Tokai, Ibaraki 319-1195

Much attention has been paid to the rich phase diagram of $La_{1-x}A_xMnO_3$ (A=Ca and Sr) system[1,2]. There is the interplay between the super exchange and the double exchange interactions controlled by the orbital degree of freedom[3]. We have studied the Ca-doped manganites in the ferromagnetic insulating region ($0.08 \leq x \leq 0.18$) to identify the low temperature phase detected by the ultrasonic measurements[4]. In this study, we report the temperature variation of Mn-O bond lengths of $La_{0.875}Ca_{0.125}MnO_3$.

Polycrystalline samples of $La_{0.875}Ca_{0.125}MnO_3$ were prepared by a solid state reaction. Stoichiometric mixture of La_2O_3 (99.9%), $CaCO_3$(99.9%) and Mn_2O_3(99.9%) powders was pressed into pellets and calcined in air at 1273 K for 48 h and 1773 K for 36 h with an intermediate grinding. The Curie temperature T_c was determined to be 170 K by the magnetization measurement under magnetic field of 50 Oe[5]. Neutron diffraction measurements were carried out at several temperatures between 10 K and 293 K using HRPD (λ =1.8196 Å). The measured intensities were analyzed by a program RIETAN[6], assuming the space symmetry Pnma (No.62) and collinear spins at Mn sites below T_c. The longest unit cell edge was assigned to the b-axis.

There is good agreement between the observed and calculated intensities in all data sets. As an example, the observed, calculated and difference profiles at 10 K were shown in Fig.1. Figure 2 shows the temperature variation of the Mn-O bond lengths. Mn-O(1) monotonically decreases with decreasing temperature, while small elongation and contraction were observed for Mn-O(2) and Mn-O(2′) below 100 K, respectively. Such changes lead to the breathing type Jahn-Teller distortion of MnO_6 octahedra in the a-c plane, suggesting partial ordering of $3x^2$-r^2/$3z^2$-r^2 orbitals of Mn[3]. This distortion occurs well below T_c.

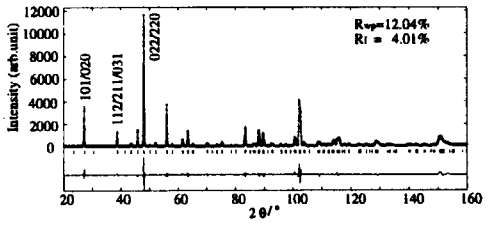


Figure 1: Observed, calculated and difference neutron diffraction profiles of $La_{0.875}Ca_{0.125}MnO_3$ at 10 K.

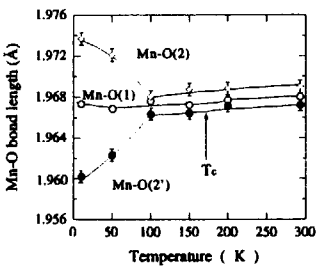


Figure 2: Temperature variation of Mn-O bond lengths in $La_{0.875}Ca_{0.125}MnO_3$.

References

1) A.J.Millis : Nature **392** (1998) 147.
2) Y.Yamada, O.Hino, S.Nohdo and R.Kawano: Phys. Rev.Lett **77** (1996) 904.
3) R.Maezono, S.Ishihara and N.Nagaosa: Phys.Rev. B **57** (1998) R13993.
4) H.Fujishiro, T.Fukase, M.Ikebe and T.Kikuchi: J.Phys.Soc.Jpn. **68**(1999) 1469.
5) S.Begum, Y.Ono, Y.Tomioka, Y.Tokura, Y.Ishii, Y.Morii and T.Kajitani: J.Phys.Chem Solids in press.
6) F.Izumi : *The Rietveld Method* (Oxford University press, Oxford, 1993) .

原子炉：JRR-3M　　装置：HRPD(1G)　　分野：中性子散乱（構造）

研究テーマ：拡散現象のモデル化および高精度拡散係数測定
表　題：液体スズの静的構造因子と拡散係数

1-1-34

Static Structure Factor and Self-diffusion Coefficient of Molten Tin in the Wide Temperature Range

T. MASAKI, H. AOKI, S. MUNEJIRI[1], Y. ISHII[2] and T. ITAMI[1,3]

[1]National Space Development Agency of Japan, 2-1-1 Sengen, Ibaraki, Tsukuba, 305-8505, Japan
[2]Advanced Science Research Center, JAERI, Tokai, Ibaraki 319-1195
[3]Graduate School of Science, Hokkaido University, N10W8, Sapporo, Hokkaido, 060, Japan

The understanding of diffusion phenomena and its temperature dependence in liquids both in microscopic and macroscopic point of views is one of the most difficult problem of condensed matter physics because the temperature dependence of many body interaction should be take into account. Especially, in the case of group IVB elements such as Pb, Sn, Ge and Si, the electron-ion interaction induces the complicated interatomic interaction and liquid structures.

Recently, the evaluation scheme of effective pair interatomic potential directly from the static structure factors is proposed by Reatto *et.al*[1]. This method solves the inverse problem by the predictor-corrector method with the application of molecular dynamics simulation. Munejiri *et.al*[2] reported that the effective pair interatomic potential can be obtained from static structure factors with a high accuracy in combination with the large scale molecular dynamics simulation and the accurate experimental *S(Q)*. In this study, the effective pair potential of liquid tin was calculated by the inverse problem scheme and the diffusion coefficient was evaluated from the molecular dynamics simulation in which the obtained effective pair potential is applied. The calculated self-diffusion coefficient was compared with the experimental one measured under low gravity condition.

The static structure of liquid tin was measured with the use of neutron scattering and small angle X-ray scattering. The low Q region (0.4 A^{-1} - 2.0 A^{-1}) of *S(Q)* was measured carefully by the small angle X-ray scattering at the temperature of 573 K, 773 K and 1073 K. The *S(Q)* in the high Q range (1.5 A^{-1} - 10.4 A^{-1}) was measured by the neutron scattering at the temperatures of 573 K, 773 K, 1073 K 1473 K 1673 K and 1873 K respectively. The neutron scattering experiment was performed with the use of triple axis spectrometer (TAS-1). The fused silica ampoule was used for the experiments at temperatures lower than 1073 K. For the experiments at the temperature higher than 1073 K, the glassy carbon ampoule was developed. The sample was placed in a high temperature radiation furnace with Nb foil heating element (at the highest 2100 K). The counting time at each temperature was typically 8-12 hours. Neutron and X-ray scattering data were treated using a standard procedure, which includes subtraction of cell intensities and correction for absorption.

The effective pair interatomic potential of liquid tin was evaluated with the use of solution scheme of inverse problem from the static structure factor which was measured by the small angle X-ray and the neutron scattering. In this scheme, the predictor-corrector method is applied to solve the effective pair potential, which is the combination of the integral equation theory and the computer simulation. The effective pair interatomic potentials were calculated by the inverse problem scheme at 573K,773K and 1073K respectively at which the structure factors of liquid tin in the low Q range were measured. The convergence of evaluation procedure was quite well and the molecular dynamics simulation applying the obtained interatomic potential well reproduces the experimental static structure

原子炉：JRR-3M　　装置：TAS-1(2G)　　分野：中性子散乱（構造）

factor at each temperature, as shown in Fig.1. The obtained interatomic potential at 1073K is applied also to the molecular dynamics simulation at higher temperature than 1073K. Good agreements were found between molecular dynamics simulations and experiments.

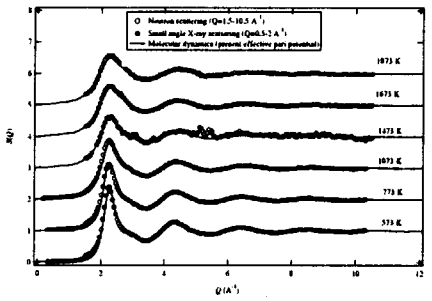


Figure 1: The static structure factor of liquid tin.

The self-diffusion coefficient was evaluated from the molecular dynamics simulation, in which the obtained interatomic potential was applied, from the slope of mean square displacement. In the case of liquid tin, the self-diffusion coefficient was measured with high accuracy with the use of low gravity in space in the wide temperature range [3,4]. The self-diffusion coefficients calculated from the molecular dynamics simulation are shown in Fig.2 together with the experimental data which were measured both under normal gravity (1g) [5,6] and low gravity [3,4]. The low gravity circumstances have been known to be ideal for the measurements of diffusion coefficient of melts with high melting temperatures due to the absence of convection. As a result, an agreement between low gravity data is rather excellent [3,4]. On the other hand, duffusion data on the ground differs each other considerably depending on data sources probably due to the convection, though data of Bruson *et.al*[6] is rather close to the low gravity data.

The obtained self-diffusion coefficients from the present molecular dynamics simulations are extremely in good agreement with the self-diffusion data under low gravity in the wide temperature range. The quantitatively good agreement between the present diffusion coefficient and the microgravity data indicates that this scheme is valid for the quantitative prediction of the self-diffusion coefficient in liquids with shoulders, such as liquid tin, by using the pair potential derived from the *S(Q)* of liquids.

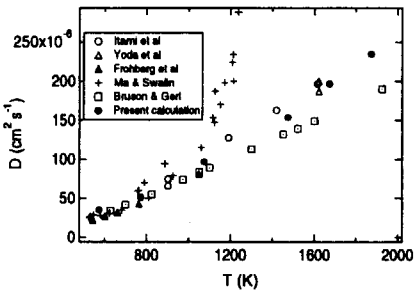


Figure 2: Self-diffusion coefficient of liquid tin.

References

1) L.Reatto, D.Levesque and J. J. Weis, Phys. Rev. **A33** (1986) 3451.
2) S. Munejiri, F. Shimojo, K. Hoshino and M. Watabe, J. Phys. Soc. Japan, **64** (1995) 344.
3) G. Frohberg, K.H. Kraatz and H. Weber, Proc 6th europ. symp. on material sciences under microgravity conditions, Bordeaux, 2-5 Dec. 1986.
4) T. Itami, NASA/CP-1998-208868, Proc. MSL-1 sci. rev. meeting, Huntsville, 25-26 Aug 1998.
5) C.H. Ma and R.A. Swallin, J. Chem. Phys., **46** (1962) 3014.
6) A. Bruson and M. Gerl, Phys. Rev. B, **21** (1980) 5447.

研究テーマ：$PbTiO_3$のフォノン分散関係
表　題：正方晶$PbTiO_3$の格子力学

1-1-35

Lattice dynamics of tetragonal $PbTiO_3$

I.Tomeno, Y.Tsunoda[1], Y. Ishii[2], K.Oka[3] and H. Unoki[3]

Faculty of Education and Human Studies, Akita University, Akita 010-8502
[1]School of Science and Engineering, Waseda University, Shinjuku-ku, Tokyo 169-8555
[2]Advanced Science Research Center, JAERI, Tokai, Ibaraki 319-1195
[3]Nanoelectronics Research Institute, AIST, Tsukuba, Ibaraki 305-8568

$PbTiO_3$ occupies an important position in ferroelectric perovskites. First, $PbTiO_3$ undergoes a single phase-transition from a cubic to tetragonal ferroelectric phase at T_C=763 K. Cohen[1)] pointed out that the covalent nature of Pb 6s and O 2p states is responsible for the stability of the tetragonal phase. Second, $PbTiO_3$ is the end member of relaxor ferroelectrics $(1\text{-}x)Pb(Zn_{1/3}Nb_{2/3})O_3$-$xPbTiO_3$ (PZN-PT) system. The introduction of x=0.1 $PbTiO_3$ enhances piezoelectric and dielectric constants. Recent neutron scattering studies for PZN show that the low-lying TO phonon branch drops sharply near the Brillouin-zone center.[2, 3)] The limited data for $PbTiO_3$[4)], however, does not permit a detailed comparison of the lattice dynamics of $PbTiO_3$ and PZN. In this report, we present the phonon dispersion relations for the tetragonal $PbTiO_3$ measured at room temperature.

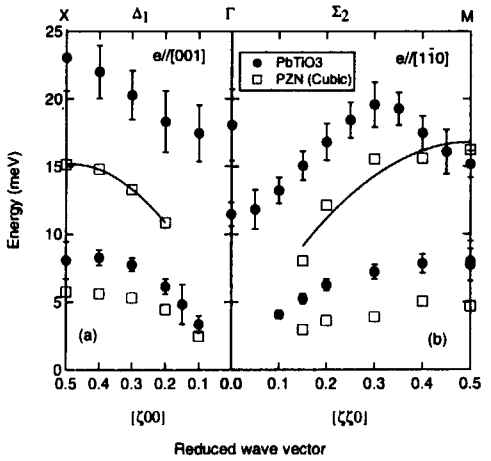


Figure 1: Phonon dispersion curves for $PbTiO_3$ and PZN. The data for PZN are taken from Ref.1.

Figure 1 demonstrates the difference of phonon dispersion relations between $PbTiO_3$ and PZN. A large splitting between the zone-center TO phonon modes in $PbTiO_3$ is consistent with Raman scattering[5)] and dielectric constant measurements.[6)] The Σ_2 TO phonon frequency exhibits the maximum at [0.3 0.3 0], whereas the Δ_1 TO phonon frequency increases toward [1 0 0]. The low-frequency TO mode at the M point corresponds to an oxygen octahedron rotation along the z axis. On the other hand, the isotropic TO phonon dispersion relations in PZN are mainly due to the compositional disorder at the B site. $PbTiO_3$ and PZN have the isotropic dispersion relations for the TA phonon branches. The TA phonon frequencies for $PbTiO_3$ are higher than the values for PZN in the entire zone.

In PZN the well-defined TO peak is absent around the zone center. For $PbTiO_3$ the low-lying TO phonon mode are expected to be temperature dependent. High-temperature neutron scattering experiments are now progressing.

References

1) R.E. Cohen : Nature **358** (1992) 136.
2) I.Tomeno, S. Shimanuki, Y. Tsunoda and Y. Ishii : J. Phys. Soc. Jpn. **70** (2001) 1444.
3) P. M. Gehring, S. -E. Park and G. Shirane : Phys. Rev. B **63** (2001) 224109.
4) G. Shirane, J. D. Axe, J. Harada and J. P. Remeika : Phys. Rev. B **2** (1970) 155.
5) C.M.Foster, Z. Li, M. Grimsdtch, S.-K. Chan and D. J. Lam : Phys. Rev. B **48** (1993) 10160.
6) Z. Li, M. Grimsdtch, X. Xu and S.-K. Chan : Ferroelectrics **141** (1993) 313.

原子炉：JRR-3M　　装置：TAS-1(2G)　　分野：中性子散乱（構造）

研究テーマ：ランタノイド-白金族元素を含む複合酸化物の磁気構造
表　題：$LiErO_2$における構造相転移

1-1-36

Structural Transition in $LiErO_2$

Y. Hashimoto, M. Wakeshima, K. Matsuhira, Y. Hinatsu, Y. Ishii[1]

Division of Chemistry, Graduate School of Science, Hokkaido University, Sapporo 060-0810
[1]Japan Atomic Energy Research Institute, Tokai-mura, Ibaraki 319-1195

The crystal structure of ternary lithium oxides, $LiRO_2$ (R = rare earths), are grouped into four type structures ($\alpha, \beta, \gamma, \delta$-type). A ternary lithium oxide, $LiErO_2$, has a tetragonal α-type structure (space group : $I4_1/amd$) at room temperature. Its magnetic susceptibility and specific heat showed that a first-order phase transition and an antiferromagnetic transition occurred at *ca.* 200 K and 4.2 K, respectively [1].

In order to determine the crystal structures at low temperatures, powder neutron diffraction patterns of $LiErO_2$ were measured at 150 and 250 K using a High Resolution Powder Diffractometer (HRPD) in the JRR-3M reactor with a neutron incident wave length (λ = 1.82268 Å). The Rietveld analyses were performed with the neutron diffraction data.

Figure 1 shows the observed and calculated diffraction patterns. The crystal structure at 250 K was determined to be the tetragonal α-type structure with the space group, $I4_1/amd$ (a = 4.4291(2) Å and c = 10.2210(5) Å; z = 4). Data collected at 150 K indicates that the crystal structure at this temperature transforms from α-type to β-type structure. The Rietveld analysis of the crystal structure at 150 K using a monoclinic β-type structure with the space group, $P2_1/c$ (No. 14), gives a good agreement with experimental data (a = 6.0761(6) Å, b = 6.1617(4) Å, c = 6.1546(6) Å, and β = 118.479(4)°; z = 2). The crystal structure at 250 K and 150 K are illustrated in Fig. 2.

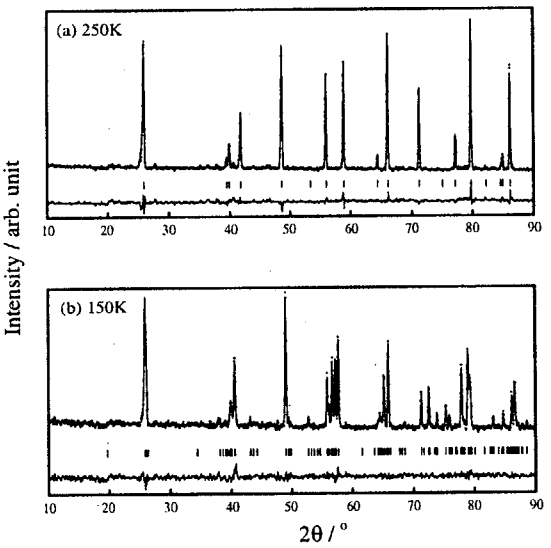


Figure 1: Powder neutron diffraction patterns of $LiErO_2$ at (a)250 K and (b)150 K.

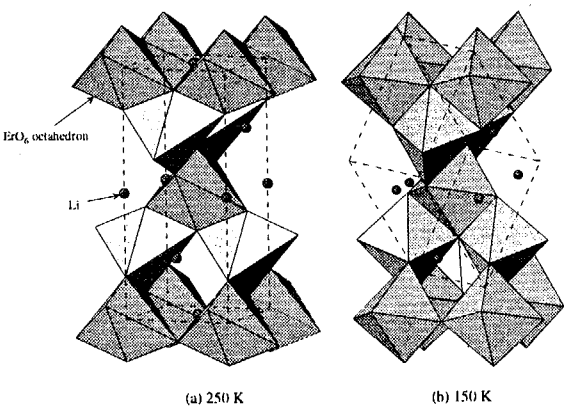


Figure 2: The crystal structure of $LiErO_2$ at (a)250 K and (b)150 K.

References

1) Y. Hashimoto, M. Wakeshima, K. Matsuhira, Y. Hinatsu, and Y. Ishii, Chem. Mater. (2002), in press.

原子炉：JRR-3M　　装置：HRPD(1G)　　分野：中性子散乱（構造）

研究テーマ：多重極限環境下における中性子散乱実験法の研究
表　題：中性子回折法によるSi単結晶内部のひずみ測定

1-1-37

Measurement of internal strain in Si single crystal by neutron diffraction method

T. SAITO, N. MINAKAWA[1], Y. MORII[1], T. SASAKI, Y. HIROSE

Kanaza University, Kanazawa, Ishikawa 920-1192
[1]Advanced Science Research Center, JAERI, Tokai, Ibaraki 319-1195

The monochromator of RESA in JRR-3M of Japan Atomic Energy Research Institute is Si(311) single crystal. This monochromator has been bending with the piano wire. The intensity of neutron is increased with this bend mechanism. However, the internal strain of monochromator bent with this mechanism has not been examined in detail untill now.

Then, we gave the bend load to the Si(311) single crystal with a piano wire, and examined the distribution of internal strain. This single crystal is 200mm in length, 20mm in height, and 5mm in thickness. This shape was processed by the wire electrical discharge machine.

Fig.1 shows the measurement method of bend mechanism. The slit used by this experiment is 10mm in length, and 0.3mm in width. The wave length is 0.209613nm. Four kinds of the applied strain (200,300,400 and 500 μ strain) were added to the sample. Figure 2 shows the relationship between intensity and applied strain. As the intensity increases, the applied strain increases. However, the change of intensity between 400 and 500 μ strain is little. Figure 3 shows the relationship between distribution of internal strain and applied strain. Like Fig.2, the change of internal strain between 400 and 500 μ strain is little. The internal strain varies a little for the applied strain of 200 and 300 μ strain. However, the applied strain of 400 and 500 μ strain is constant. This phenomenon influences the change of intensity in Fig.2. In other words, the intensity keeps increasing until the internal strain becomes uniform. Moreover, the intensity steadies when the internal strain becomes uniform, and the single crystal causes destruction afterwards.

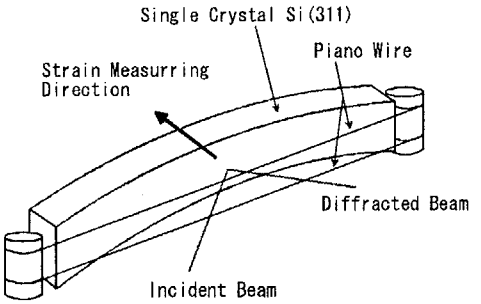


Figure 1: Bend mechanism and measurement method

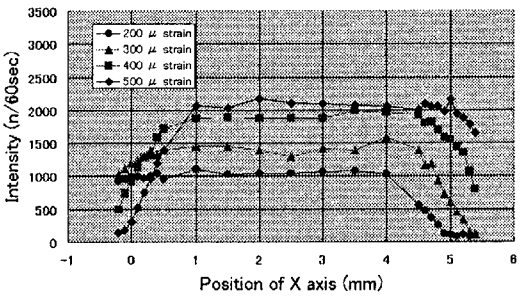


Figure 2: The relationship between intensity and applied strain.

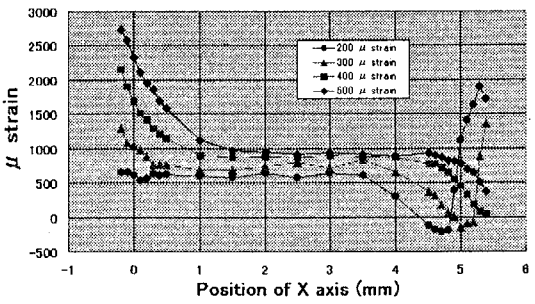


Figure 3: The relationship between distribution of internal strain and applied strain

研究テーマ：中性子回折による構造材料の応力測定および健全性評価
表　題：中性子イメージプレートによる薄鋼板の応力測定
1-1-38

Stress Measurement in Thin Steel Plate by Means of Neutron Image Plate

T.Sasaki, N.Niimura[1], Y.Morii[1], N.Minakawa[1] and Y.Hirose

Kanazawa University, Kanazawa, Ishikawa 920-1192
[1]Japan Atomic Energy Research Institute, Tokai, Ibaraki 319-1195

Stress Measurement using neutron diffraction technique is a useful tool for the purpose of the investigation on the behavior of practical materials, especially that of inside material. A lot of researches have been made so far on both fundamental matters and application problems. In the conventional neutron stress measurement method, a zero dimensional neutron detector is generally used. A use of two dimensional detector such as, for example, a neutron image plate enables us to obtain huge amount of diffraction data at a stretch. The feature of a lot of data expects us more precise and detailed stress analysis. The present study was made to find the possibility of the neutron image plate for the stress measurement, and as the first step a tensile stress measurement for thin steel plates was performed.

The material used was steel, JIS S50C. The specimen was processed to have a geometry of 150mm length, 15 mm width and 2 mm thickness. It was then heat-treated for stress release under the condition of 650 deg C for 30 mins. For an application of stress measurement, a steel plate jointed on a stainless steel using self-heated sintering method (SHS method) with mixed powder of nickel and aluminum. the thickness of the steel was 2 mm as same as the above tensile test. The residual stress in the steel emerged after the joint process was measured by the present neutron image plate method.

Fig.1 shows the relation between the stress obtained by the present method and applied stress. The stress measured was calculated by means of so-called the cosα method. The applied stress was calculated multiplying the strain detected by the strain gauge method and the Young's modulus of the specimen. It can be seen that the slope of the line is about 0.8 and the intersection which means the initial stress of this method is about -450MPa. The initial stress in the figure was caused by the difference of absorption of each diffracted beam from each deepness of the specimen. Since the penetration depth of the neutron beam is generally large than that of x-ray beam, a theoretical understanding on such initial stress is necessary for the stress measurement. As a simple approach, we used Fig.1 as a calibration curve for a steel having thickness of 2 mm in order to the residual stress measurement of SHS sample.

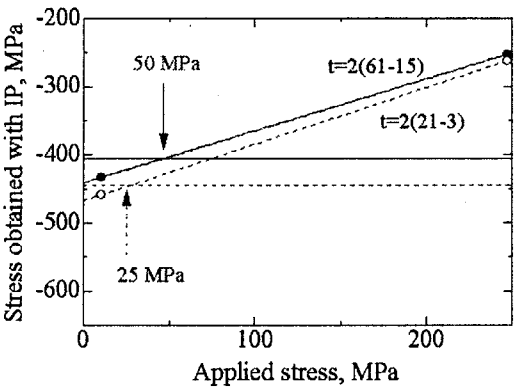


Figure 1: The relation between the stress obtained by the present method and applied stress.

Fig.2 shows the neutron diffraction pattern obtained from the SHS sample (211 diffraction from the steel layer). The stress was calculated from the diffraction image through the same method as the above tensile test), which was also plotted in Fig.1. As the stress obtained in this case also involved the similar initial stress, it should be corrected to obtain

原子炉：JRR-3M　　装置：RESA(T2-1)　　分野：中性子散乱（構造）

the residual stress in the SHS sample. The stress at the transverse axis dropped from the cross point shown in Fig.1 can be estimated as the residual stress in the SHS sample, because the initial stress was removed from the raw data. The stress resulted in about 35 to 50 MPa, which is reasonable from the prediction of thermal expansion coefficient between the materials of each layer of SHS sample.

The present method is useful for the residual stress measurement of thin plate with higher accuracy. This is also applicable for layers put into other materials as the very deep penetration of neutron beams. This method has also possibility to be able to evaluate stress distribution in practical materials through the analysis of diffraction image diffracted from allover the depth of the material using the stress gradient analysis developed in the field of the x-ray stress analysis. The effect of the initial stress discussed above should be considered for this purpose, which is the authors ' next main theme.

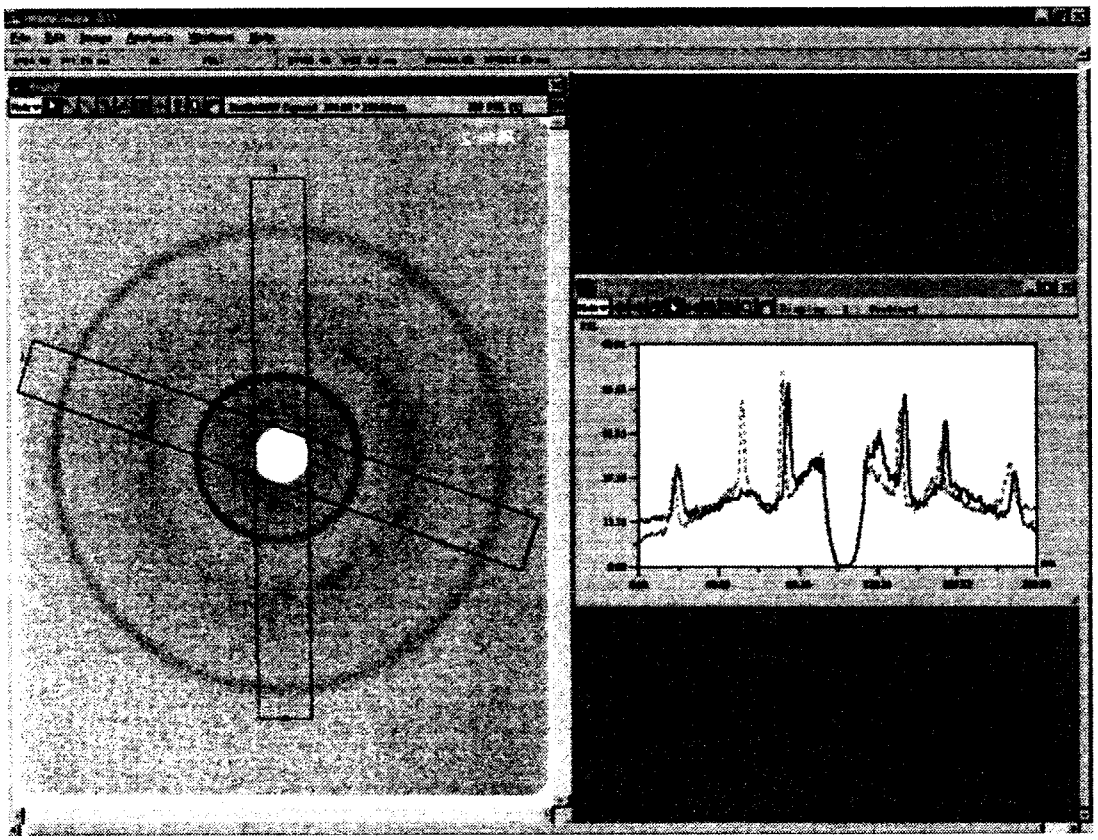


Figure 2: The neutron diffraction pattern obtained from the SHS sample (211 diffraction from the steel layer).

研究テーマ：クリプトメラン型MnO_2の研究
表　題：クリプトメラン型MnO_2の中性子回折

1-1-39

Neutron diffraction study for locating proton in cryptomelane-type MnO_2 crystal

Masamichi Tsuji, Katsunori Kawasaki,[1] Yasuo Tanaka[2] and Yoshinobu Ishii[3]

Research Center for Carbon Recycling and Energy,Tokyo Institute of Technology
[1]Graduate School of Physics, Tokyo Institute of Technology
[2]Central Research Laboratory, Japan Tobacco, Inc.
[3]Advanced Science Research Center, JAERI, Tokai, Ibaraki 319-1195

Manganese dioxides form a family of the typical mixed-valence compounds and are represented by the chemical composition $(A,H)_xMnO_{2-x}$. H^+ is responsible for cation exchange, being variable with the extent of Mn^{3+} substitution. The cation uptake mechanism depends on the crystal structure and the preparation routes, showing different degree of cation exchange and redox process. A cryptomelane-type manganic acid (CMA) having the 2 x 2 type tunnel structure with the diameter of 0.28 nm has been studied by chemical and thermal analyses, ESCA, ESR, MASNMR, XRD and chemical thermodynamics of cation exchange.[1, 2, 3] Very high selectivity for K^+, Rb^+, and Ba^{2+} ions can be interpreted on a basis of cation exchange with the H^+ in the tunnel. The objective of the present work was to locate H^+ ions responsible for the cation exchange.

Samples were prepared by mixing $MnCO_3$ and BtOK at 8 and 20 mol % as the K^+ content and heating at 700 ℃. Then, K^+ in the product was leached for H^+ by conc HNO_3. These H^+ form CMAs were immersed in LiOH to prepare the Li^+ form, and then Li^+ was removed by contact with DNO_3 solution in D_2O. DNO_3 was prepared by percolating DCl solution in the NO^{3-} form Dowex 1-X8 column. D^+ form samples were dehydrated by heating at 60 ℃ overnight. Measurements were conducted by mean of High Resolution Powder Diffractometer (HRPD) installed at JRR-3M in JAERI. Figure 1 shows a diffraction pattern of deutrated cryptomelane-type MnO_2 measured at 10 K. We continue Rietveld refinement for this diffraction pattern by using a software package of RIETAN-2000 in current studies.

References

1) Y. Tanaka, M. Tsuji and Y. Tamaura: Phys. Chem. Chem. Phys., 2, 1473-1479 (2000).
2) M. Tsuji and Y. Tanaka: J. Mater. Res., 16, 108-114 (2001).
3) M. Tsuji, H. Kanoh and K. Ooi: Mat. Res. Soc. Symp. Proc., Vol.658, GG6.25.1-GG6.25.6 (2001).

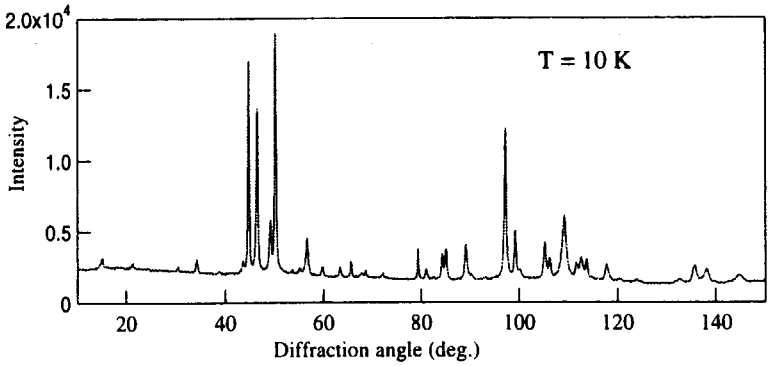


Figure 1: Diffraction pattern of deutrated cryptomelane-type MnO_2 measured at 10 K.

原子炉：JRR-3M　　装置：HRPD(1G)　　分野：中性子散乱（構造）

研究テーマ：多重極限環境下における中性子散乱実験法の研究
表　題：高温におけるフッ化バリウムの中性子粉末回折

1-1-40

Neutron Powder Diffraction Study on BaF_2 at High Temperature

T.K. Datta and Y.Ishii[1]

Experimental Nuclear and Reactor Physics Division, Institute of Nuclear Science and Technology, Atomic Energy Research Establishment, Savar, Dhaka, Bangladesh
[1]Advanced Science Research Center, JAERI, Tokai, Ibaraki 319-1195

Barium fluoride is a CaF_2-type crystal structure. Since CaF_2-type crystals have a order-disorder transition at high temperature of 80% of its melting temperature, this crystal became a super ionic conductor above the transition temperature. This transition temperature is closely related to the thermal vibration amplitude of fluoride atoms. To clarify the thermal vibration of BaF_2 at high temperature, we measured temperature dependence of intensities of diffraction lines of BaF_2 powder.

Neutron diffraction experiments were carried out by using High-Resolution Powder Diffractometer (HRPD) installed at JRR-3M in JAERI. BaF_2 powder sample was contained in a vanadium sample holder that its dimension was 50 mm height and 8 mm diameter. This sample holder was mounted in a ILL high temperature furnace. Measurement temperatures were 295 K, 650 K, 600 K, 850 K, 1000K, 1150 K and 1350 K. Wavelength of used neutrons was 1.16 Å.

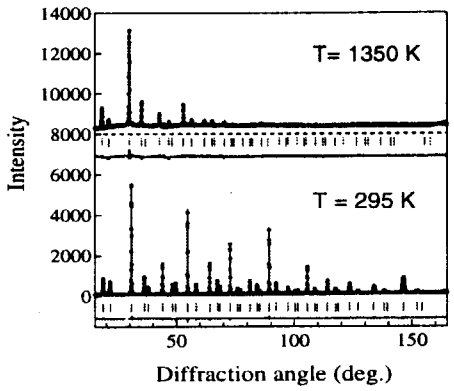


Figure 1: Diffraction patterns of BaF_2 measured at 295 K and 1350 K.

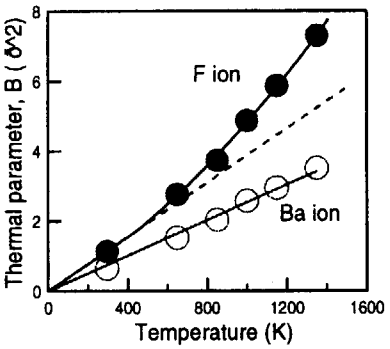


Figure 2: Temperature dependence of thermal parameter of Ba-ion and F-ion.

Diffraction patterns of BaF_2 measured at 295 K and 1350 K are shown in Fig.1. From this figure one can see that the intensities of diffraction lines above 120 deg. for are weakened . These diffraction patterns were refined by Rietveld method using a software package of RIETAN-2000. Results of refinements based on CaF_2 model were very good for all measured temperature except 1350 K. Temperature dependence of thermal parameter related to thermal vibration amplitude is shown in Fig. 2. Open and solid circles indicate the thermal parameter of Ba ion and F ion, respectively. Temperature dependence of thermal parameter for Ba ion has a linear relationship with temperature. While the thermal parameter of F ion increases with increasing temperature above 500 K. Since Ba-ion occupants a $m\bar{3}m$ symmetry site that has an inverse symmetry, it is well understood that thermal vibration of Ba-atom is harmonic. While anharmonic thermal vibration of F-atom became strong above 500 K.

原子炉：JRR-3M　　装置：HRPD(1G)　　分野：中性子散乱（構造）

研究テーマ：多重極限環境下における中性子散乱実験法の研究
表　題：メタンーエタン水化物の構造研究
1-1-41

Neutron Diffraction Study on Metane-Ethane Hydrate

Y. Ishii, C.J. Rawn,[1] A.J. Rondinone,[1] L.A. Stern,[2]
S. Circone,[2] S.H. Kirby,[2] and B.C. Chakomakos,[1]

Advanced Science Research Center, JAERI, Tokai, Ibaraki, 319-1195 Japan
[1]Oak Ridge National Laboratory, Oak Ridge, Tennessee 37831 USA
[2]U.S. Geological Survey, Menlo Park, California 94550 USA

Clathrate hydrates areinclusion compounds where a variety of guest molecules can be occluded in a host lattice formed from an ice-like hydrogen bonded network. The host lattice forms in such a way that polyhedral cavities are created. Two common atomic arrangements that result are cubic and designated as structure I and structure II. Structure I consists of two types of polyhedra, the smaller polyhedra are formed from twelve pentagonal faces and the larger polyhedra are formed from twelve pentagonal faces and two hexagonal faces. Structure II also consists of two types of polyhedra, similar to structure I the smaller polyhedra are formed from twelve pentagonal faces, however, the larger polyhedra are formed from twelve pentagonal and four, instead of two, hexagonal faces. To crarify the structure of metane-ethane hydrate, we conducted neutron diffraction studies.

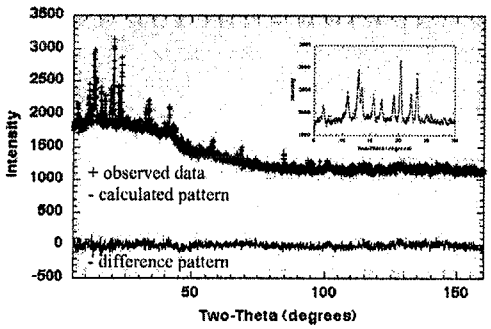


Figure 1: Comparison of the observed neutron powder diffraction data (+) with the calculated pattern (solid line) and corresponding difference pattern based on the 30 variable refinement.

Neutron powder diffraction data were collected on the High Resolution Powder Diffractometer (HRPD) at the JRR-3M research reactor at JAERI. Wavelength of neutrons was 1.1635 Å. For temperature control a closed-cycle He refrigerator equipped with two temperature sensors was used. Samples in sealed vanadium cans were removed from storage in N_2(l) and immediately attached to the precooled cold-tip of the refrigerator under a glovebag filled with He gas. During this process the sample did not warm above 100K. Diffraction patterns were collected at 12, 40, 100, 130, 160, 190, 220, and 250 K.

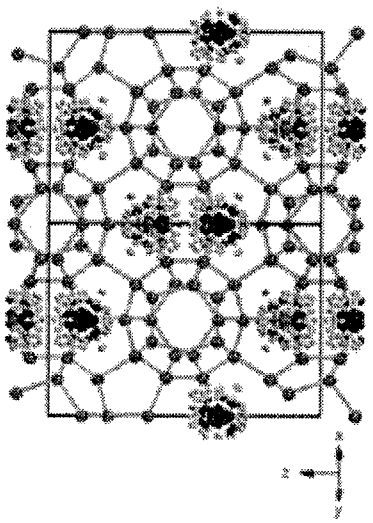


Figure 2: Structure of C_3H_8 hydrate based on the refined atomic coordinates.

The software package, GSAS, was used for the Rietveld refinements with a rigid body constraints. Structural refinements on the neutron powder diffraction data confirmed that hydrate samples synthesized with propane gas crystallize as structure type II hy-

原子炉：JRR-3M　　装置：HRPD(1G)　　分野：中性子散乱（構造）

drate. Figure 1 shows the comparison of the observed neutron powder diffraction pattern with the calculated structural model. There were no extra diffraction peaks indicating the presence of ice. The high back is due to incoherent scattering from the H atoms associated with the guest molecule. The structure type II hydrate at 12 K shown in Figure 2.

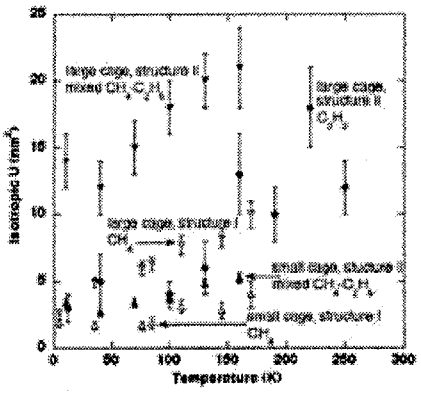


Figure 3: The atomic displacement parameters for the C_3H_8 guest molecules in the eight large cages of structure II compared to the small cage guest molecules (CH_4 only) and large cage guest molecules (CH_4 and C_2H_6) in mixed methane-ethane hydrate that crystallizes as structure II and the CH_4 molecules in both the small and large cages of structure I methane hydrate.

The atomic and molecular displacement parameters, U, for the D and O atoms in the host lattice and the guest C_3H_8 molecule are also determaind. The atomic and molecular displacements help to describe the positional disorder found in gas hydrates. The propane molecule has similar positional disorder as the D and O atoms in the host lattice as evidenced by the similar U(T=0) intercepts. Figure 3 compares the molecular displacement parameters for the C_3H_8 molecules in the large cages of the structure II propane hydrate with the CH_4 molecules in both the large and small cages of the structure I methane hydrate and the CH_4 molecules in the small cages of the structure II mixed methane-ethane hydrate. Figure 3 suggests that this mixed cage has more positional disorder, most likely due to the sharing of different guest molecules, than small or larger cages occupied by a single guest molecule. Figure 3 also indicates that the guest molecules in the large cages have more positional disorder than the guest molecules in the small cages. The large error for the C_3H_8 molecular displacement parameters are most likely due to the shape of the molecule and the resulting rigid body. Figure 4 shows the methane, ethane, and propane molecules and the corresponding rigid bodies for comparison.

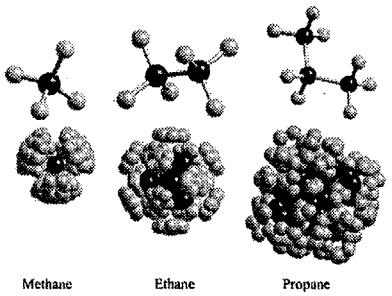


Figure 4: Methane, ethane, and propane molecules and the corresponding rigid bodies.

Atomic coordinates and atomic and molecular displacement parameters of the structure II propane hydrate have been determined from Rietveld refinements of neutron powder diffraction data collected at 12 K. The C_3H_8 molecules, located in the eight larger polyhedral cavities of a deuterated host lattice, were described using rigid-body constraints. From temperature dependence of lattice parameters, the instantaneous CTE was calculated and compared to that of a structure I hydrate, prepared with only CH_4 as the guest molecule, and a structure II hydrate, prepared with a mixture of CH_4 and C_2H_6 as the guest molecules, and D_2O ice from the literature. The thermal expansion behaviour of the three hydrates is similar and does not show the negative thermal expansion behaviour displayed by D_2O ice. The temperature dependence of the atomic and molecular displacement parameters suggests that the C_3H_8 guest molecule has similar positional disorder to the D and O atoms of the host lattice and to other gas hydrates formed from only one type of guest molecule.

研究テーマ：多重極限環境下における中性子散乱実験法の研究
表　題：トリメチレン水化物の構造研究

1-1-42

Neutron Diffraction Study on Trimethlene Oxide Deuterate

Y. Ishii, A.J. Rondinone,[1] C.J. Rawn[1] and B.C. Chakomakos[1]

Advanced Science Research Center, JAERI, Tokai, Ibaraki, 319-1195 Japan
[1]Oak Ridge National Laboratory, Oak Ridge, Tennessee 37831 USA

Trinethlene oxide (TMO) hydrate is of great interest because it forms structure I and II hydrate depending on stoichiometry. To clarify the crystal structure of two different types,

TMO deuterates were studied with a neutron diffraction technique that well suited for studying materials composed of light element. TMO deutrates were prepared by mixing TMO and deuterium oxide, and these solutions were added drop wise to vanadium cans suspended in liquid nitrogen, respectively. Each can was then capped and placed in to a freezer at 240 K for two weeks for annealing.

Neutron diffraction experiments of TMO deutrates were conducted by High-Resolution Powder Diffractmeter (HRPD) installed at JRR-3M in JAERI. Diffraction data were collected at 10, 40, 70, 100, 130, 160, 190, 220 and 250 K. Wavelength of used neutrons was 1.1635 A.

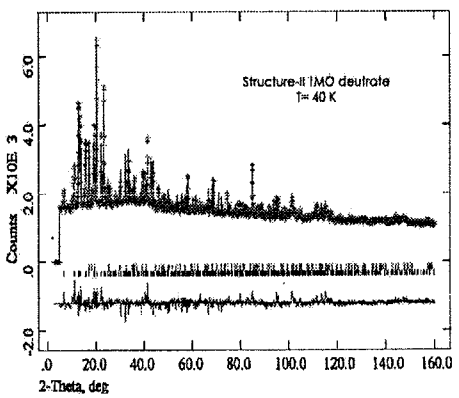


Figure 1: Diffraction patterns of structure-II TMO deutrates measured at 40 K.

Diffraction patterns were analyzed using the General Structure Analysis System (GSUS) software program. Figure 1 shows a diffraction pattern of the structure-II of TMO deutrates measured at 40 K. In this figure, solid line indicates the result of Rietveld refinement.

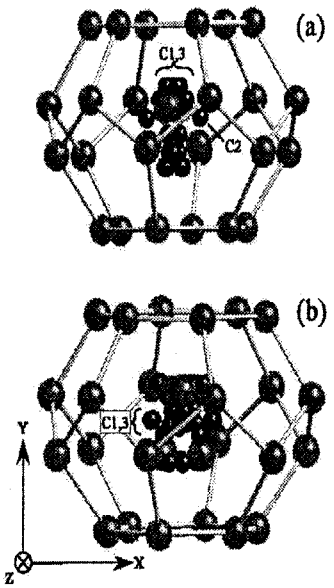


Figure 2: Crystal structure of structure-I TMO deutrate at 40 K(a) and high temperature(b). Carbons 1 and 3 closest to hexagonal face at 40 K. At higher temperature these carbons turn inward.

An illustration of crystal structure of the structure-I TMO deutrate is shown in Fig. 2. From these measurements and analysis, it is found that structure-I TMO deutrate exhibits a structural transition above 146.5 K attributed to a change in motion of the guest molecules. The motion could be an additional degree of freedom representing rapid rotation and/or reorientation.

原子炉：JRR-3M　　装置：HRPD(1G)　　分野：中性子散乱（構造）

研究テーマ：多重極限環境下における中性子散乱実験法の研究
表　題：剛体束縛条件下での包接水化物回折パターンの最適化
1-1-43

The Use of Rigid Body Constraints in Rietveld Refinements of Neutron Diffraction Data of Clathrate Hydrate

B.C. Chakoumakos, C.J. Rawn, A.J. Rondinone, S.L. Marshall,[1] L.A. Stern,[2]
S. Circone,[2] S.H. Kirby,[2], C.Y. Jones,[3] B.H. Toby,[3] and Y. Ishii[4]

Oak Ridge National Laboratory, Oak Ridge, Tennessee 37831 USA
[1]Electrochemical Systems, Inc., Knoxville, Tenneessee 37922 USA
[2]U.S. Geological Survey, Menlo Park, California 94550 USA
[3]National Institute of Standerds and Technology, Gaithersburg, MD 20899 USA
[4]Advanced Science Research Center, JAERI, Tokai, Ibaraki, 319-1195 Japan

A charaqcteristic feature of the clathrates is the rotational disorder of the guest molecules. The rotational disorder is dynamics and presists even to low temperature. Complete freezing out of the rotations of guest molecules has not been observed in any case.

Rietveld refinement of neutron powder diffraction data is a well established approach to determine crystal structure of many materials. In practice, extraction of as much of this information as possible requires high quality diffraction data and paticular attension to details of the refinement model to accommodate the intrinsic disorder of the clathrate and rotational disorder of the guest molecules. The rigid body formalism is a well establish that can be used to model the lotational disorder of the guest molecules in the Rietveld refinement method.

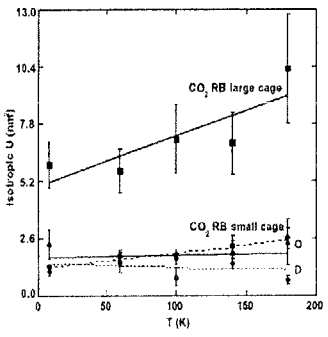


Figure 1: Temperature dependence of the stomic and rigid body displacement parameters for CO_2 hydrate.

Neutron powder diffraction data were collected as a function of temperature for hydrates of methane, carbon dioxide, tetrahydrofuran and trimethlene oxide by High Resolution Powder Diffractometer(HRPD) installed at JRR-3M. Wavelength of neutrons was 1.1635 Å. These diffraction data were refined by Rietveld method using the General Structure Analysis System(GSAS) software. Figure 1 shows the resulting root-means square displacement probability of the large cage guests in the carbon dioxide hydrate, and Fig. 2 shows the root-means square displacement of CO_2 rigid body in the small and large cages as compared to the atoms making up the host lattice.

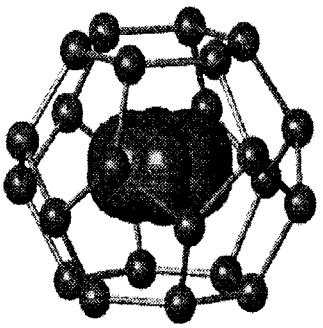


Figure 2: Root mean-square displacement amplitude of the disorderd CO_2 rigid body occupying the large case of CO_2 hydrate at 100 K.

The temperature dependence of the root-means square displacement can provide a measure of the positional disorder of the guest molecules in its cage, and can be further correlated with dynamical pictures given by quasi-elastic neutron scattering method.

原子炉：JRR-3M　　装置：HRPD(1G)　　分野：中性子散乱（構造）

研究テーマ：多重極限環境下における中性子散乱実験法の研究
表　題：テトラヘドロファン水化物の構造研究

1-1-44

Structure Study on Tetrahydrofuran Deuterate by Neutron Powder Diffraction

Y. Ishii, C. Y. Jones,[1] S.L. Marshall,[2] C.J. Rawn[2] and B.C. Chakomakos[2]

Advanced Science Research Center, JAERI, Tokai, Ibaraki 319-1195
[1]National Institute of Standerds and Technology, Gaithersburg, MD 20899 USA
[2]Oak Ridge National Laboratory, Oak Ridge, Tennessee 37831 USA

Studies of natural gas hydrate have been motivated by their potential as an energy source and have dominated research interests in the class of water-based inclusion compounds known as clathrate hydrates. However, numerious experimental and theoretical studies of tetrahydrofuran (THF) hydrate and other easily-synthesized clathrate hydrates have made a significant contributionto the state of knowledge of the crystal structures and gyest-host/guest-guest interactions.

Crystal structure of the THF-deutrate and its temperature dependence were studied with neutron diffraction measurements at 7, 75, 140, 205 and 265 K using High-Resolution Powder Diffractometer (HRPD) installed at the JRR-3M reactor hall. The diffraction data were refined by Rietveld method using the GSAS software program.

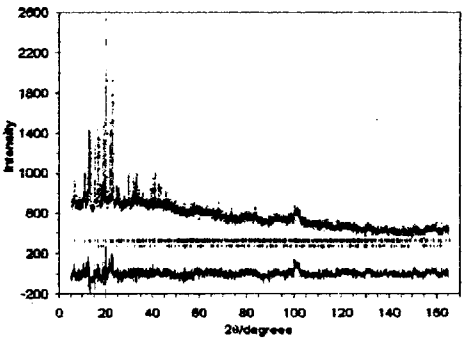


Figure 1: Diffraction pattern of THF deutrate measured at 265 K. Refinement result indicates by a solid line.

Figure 1 shows the result of refinement for THF deutrare measured at 265 K. Temperature dependence of the lattice parameter of THF deutrate shown in Fig. 2. For

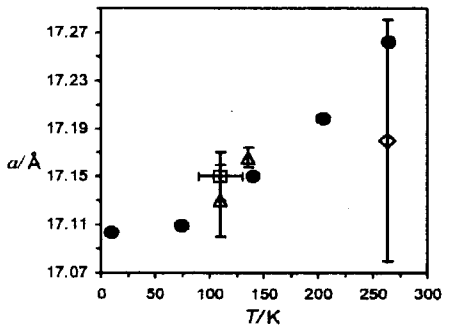


Figure 2: Temperature dependence of the lattice parameter for THF deutrate frpm this study. The error bars are smaller than the symbols themselves. For comparison, lattice parameters on THF hydrate obtained from the kiterature are plotted. Diamond-von Stsckelberg and Meuthen; square-Bertie and Jacobs; triangle–Sargent and Calvert.

comparison, lattice parameters on THF hydrate obtained from the kiterature are plotted. Diamond–von Stsckelberg and Meuthen[1)]; square–Bertie and Jacobs[2)]; triangle–Sargent and Calvert.[3)] From the temperature dependence of the lattice parameter, it is found that the thermal expansivity of THF deutrate was shown to be grater than that of ice Ih in the same temperature range, as observed in previous studies of other clathrates. From 7 to 140 K, the volume of the small cage decreases slightly and that of the large cage increases, and between 140 and 205 K the trend is reversed.

References

1) von Stackelberg, M.Y.: Meuthen, B. Z. Electrochem, **62**, 130 (1958).
2) Sargent. D.F. and Calvert. L. D.: J. Phys. Chem. **70**, 2689 (1966).
3) Bertie. J. E., Jacobs. S. M.: J. Chem. Phys., **69**, 4105 (1998).

原子炉：JRR-3M　　装置：HRPD(1G)　　分野：中性子散乱（構造）

1. 中性子散乱 2)磁　性

1. Neutron Scattering　2) Magnetism

This is a blank page.

研究テーマ：CMR効果を示す $Sm_{0.55}Sr_{0.45}MnO_3$ の磁気揺らぎ

表題：CMRマンガン酸化物 $Sm_{0.55}Sr_{0.45}MnO_3$ の金属強磁性状態におけるスピン波励起

1-2-1

Spin-Wave Excitations in the Metallic Ferromagnetic State of the CMR Manganite $Sm_{0.55}Sr_{0.45}MnO_3$

H. Hiraka[1], K. Hirota[2], Y. Endoh[1], Y. Tomioka[3] and Y. Tokura[4]

[1]*Institute for Materials Research, Tohoku University*

[2]*Department of Physics, Tohoku University*

[3]*Joint Research Center for Atom Technology*

[4]*Department of Applied Physics, University of Tokyo*

In the colossal magneto-resistive (CMR) phenomena of manganites, several degrees of feedom, i.e. lattice, charge/orbital and spin interplay and as the result many interesting properties appear. $Sm_{0.55}Sr_{0.45}MnO_3$ is a typical CMR compound showing a drastic metal-insulator transition at the Curie temperature $T_C \simeq 130$ K. [1] In order to reveal the important role of magnetism, we performed an inelastic neutron-scattering (INS) study, particularly, on the spin-wave excitations in the metallic and ferromagnetic state. A cylindric single crystal (0.4 cc) was mounted on the triple-axis spectrometers TOPAN and HET at JRR-3M. We succeeded in establishing the ferromagnetic dispersion along $[\zeta, 0, 0]$ throughout the cubic Brillouin zone ($\Gamma \rightarrow X$). In the small-q region, the spin-wave excitation is isotropic and follows the ferromagentic q^2-proportionality (the left inset of Fig. 1). However, the dispersive relation is remarkably suppressed beyond the half point toward X. The data points over the entire zone are well explained by applying a $3D$ Heisenberg model with exchange interactions up to fourth neighbour ($J_1 = 0.82$ meV, $J_4 = 0.49$ meV and $J_2 = J_3 = 0$, the curve in Fig. 1). The dominant spin interaction is, therefore, parallel to the linear Mn-O-Mn bonding axes with the spin-spin distances of a_{cub} and $2a_{cub}$. The result strongly suggests the anisotropic Mn orbitals extending along the cubic ridge direction. Upon raising temperature, the collective excitations at X point suddenly dissappear at T_C (the right inset of Fig. 1). It is newely found that the spectral weight transfers to the quasielastic scattering and connencts to the diffuse component with the antiferromganetic propagation vector $\mathbf{Q} = (1/2, 0, 0)$. [2] Combined with other experiments from the X-ray [3] and Raman scattering [4], the spin dynamics in $Sm_{0.55}Sr_{0.45}MnO_3$ should connenct intimately to the directional orbitals of e_g-electrons.

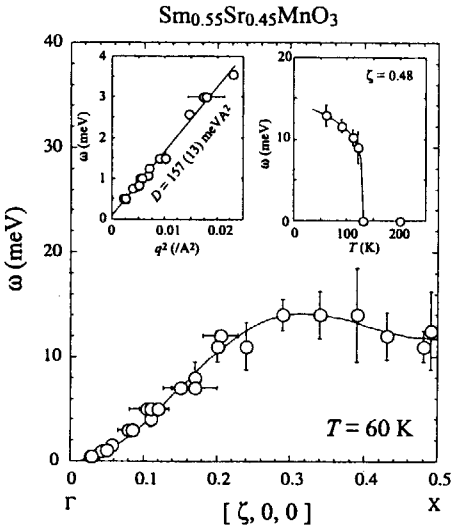


Fig. 1. The ferromagnetic spin-wave dispersion of $Sm_{0.55}Sr_{0.45}MnO_3$ along the cubic $[\zeta, 0, 0]$ direction. The left inset shows the q^2-dependence in the small-q range taken at along the symmetric axes $[\zeta, 0, 0]$, $[0, \zeta, \zeta]$ and $[\zeta, \zeta, \zeta]$, where the stiffness constant is 157(13) meVÅ^2. The right inset represents the sudden dissapearance of the zone-boudary peak at T_C.

References

[1] Y. Tomioka *et al.*, Appl. Phys. Lett. **70**, 3609 (1997).

[2] H. Hiraka *et al.*, J. Phys. Soc. Jpn. **70**, Suppl. A 88 (2001).

[3] S. Shimomura *et al.*, Phys. Rev. Lett. **83**, 4389 (1999).

[4] E. Saitoh *et al.*, J. Phys. Soc. Jpn. **69**, 2403 (2000).

使用施設：JRR-3M，装置：TOPAN(6G)，分野：2

研究テーマ：高圧下における NaV_2O_5 の磁気励起
表題：高圧下における NaV_2O_5 の中性子非弾性散乱

1-2-2 Inelastic neutron scattering of NaV_2O_5 under high pressure

M. Nishi[1], T. Yosihama[1], K. Kakurai[3], K. Nakajima[1], Y. Fujii[1], M. Isobe[2], Y. Ueda[2], M. Yethiraj[4], J. A. Fernandez-Baca[4], W. Montfrooij[4] and S. Nagler[4]
[1]*Neutron Scattering Lab., ISSP, Univ. of Tokyo, 106 Shirakata, Tokai, Ibaraki, 319-1106, Japan*
[2]*M. D. C. Lab., ISSP, Univ. of Tokyo, 5-1-5 Kashiwanoha, Kashiwa, 277-8581, Japan*
[3]*Advanced Science Research Center, JAERI, Tokai, Ibaraki, 319-1195, Japan*
[4]*Solid State Division, Oak Ridge National Lab., Oak Ridge, TN 37831-6033, USA*

In 1996 Isobe and Ueda reported the existence of the spin-Peierls (SP) transition at Tsp = 35 K in inorganic NaV_2O_5 [1]. In contrast to the first inorganic SP system $CuGeO_3$ the temperature dependence of the magnetic susceptibility for T > Tsp can be well described by the theoretical Bonner-Fisher curve with J = 560 K for a uniform S = 1/2 chain. The presence of superlattice reflections were confirmed at (h+1/2, k+1/2, l+1/4) for NaV_2O_5 by X-ray diffraction [2]. Yosihama *et al.* confirmed the existence of the magnetic excitation gap of 9.8 meV at T = 7 K by inelastic neutron scattering [2,3]. More recently the crystal structure of NaV_2O_5 at room temperature was found not to correspond to the space group P21mn with two kinds of V sites with V^{4+} and V^{5+}, as originally thought, but a Pmmn structure with only one site of $V^{4.5+}$ [4]. It is now believed that the transition of NaV_2O_5 at 35 K is related the onset of a charge-ordered phase and not a spin-Peierls transition. This low-temperature phase has a singlet ground state below 35 K.

The inelastic neutron scattering measurements were performed using the ISSP-PONTA triple axis spectrometer installed at JRR-3M of JAERI in Tokai. The measurements were performed using the fixed final energy mode with E_f = 14.7 meV using a horizontal and vertical focusing analyzer. Aligned small single crystals (0.34 g) of NaV_2O_5 were mounted ((h, k, 0) zone) in a micro cell filled with Fluorinert 75 as pressure transmitting fluid. The high pressure was obtained using a clamped-type pressure cell designed by Onodera *et al.* [5]. The high-pressure cell was set on the cold tip of a gas-helium circulation type cryostat and cooled down to 4 K. The quoted pressure of 0.90 GPa was determined from the measured lattice constant of NaCl single crystal at 4 K.

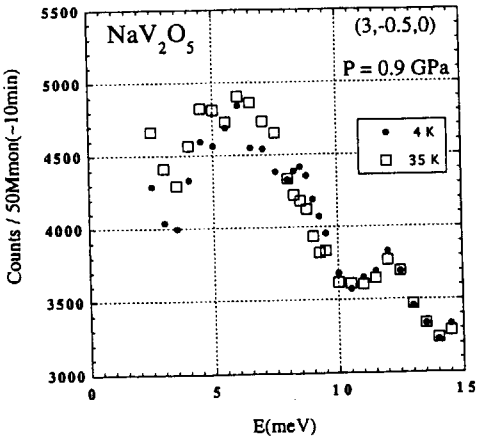


Fig. 1. Neutron scattering intensity profiles at Q = (3, -0.5, 0) at 0.9 GPa for T = 4 and 35 K.

As shown in Fig. 1 the data at 35 K shows an increased intensity at the lower energies due to magnetic diffuse scattering from the sample. The peaks at 5, 6.5 and 12 meV are perhaps phonon scattering from the pressure cell structural materials. The magnetic scattering signal was obtained by subtracting the neutron scattering intensity at 35 K from that at 4 K and then making a correction for the diffuse magnetic scattering using the Lorentzian fit around elastic position (E=0meV) as shown in Fig. 2. The transition temperature T_C = 26.2 K was determined from the temperature dependence of the neutron scattering intensity at (6, 0, 0) Bragg peak. The data obtained at Q = (h, -0.5, 0) with h=3, 2.75 and 2.5 were fitted to Lorentzian and Gaussian functions and the full width at half maximum of Gaussian fitted peaks at 9 meV are 1.4, 0.9 and 2.9 meV, respectively. We cannot distinguish whether these peaks have a real intrinsic broadening or if they consist of

使用施設：JRR-3M, 装置：PONTA(5G), 分野：2

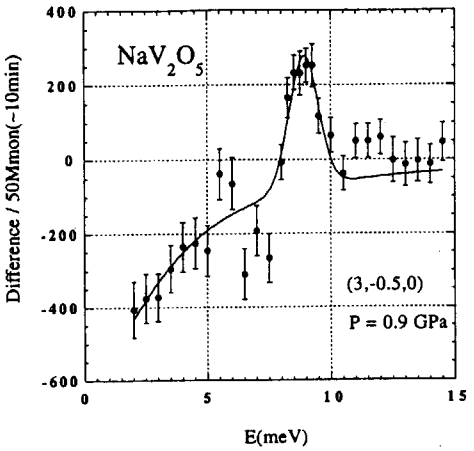


Fig. 2. Subtracted neutron scattering intensity at 35 K from that at 4 K at Q = (3, -0.5, 0) at 0.9 GPa. The solid lines is Lorentzian and Gaussian-fit results.

hand, the central energy of these peaks are about 9 meV and the spin excitation gap E_g at 0.9 GPa lie within a bandwidth of 0.1 meV along inter-chain direction parallel to a^*-axis. This can be compared to the ambient pressure bandwidth of 3 meV and E_g of 10 meV [3]. This experimental result should be related to the crystal structure change from (2xa, 2xb, 4xc) to (2xa, 2xb, c) above 0.9 GPa observed by X-ray scattering [6]. The pressure dependence of E_g and T_C in NaV_2O_5 is opposite to that for $CuGeO_3$ [7]. When the ratio of E_g to T_C is normalized, the pressure dependence of E_g is smaller than that of T_C as shown in Fig. 3 and this result may be related to the fact that in NaV_2O_5 we have a charge order transition and not spin-Peierls transition as originally thought.

References

[1] M.Isobe and Y. Ueda, J. Phys. Soc. Jpn. **65** (1996) 1178.
[2] Y. Fujii *et al.*, J. Phys. Soc. Jpn. **66** (1997) 326.
[3] T. Yosihama *et al.*, J. Phys. Soc. Jpn. **67** (1998) 744.
[4] A. Meetsma *et al.*, Acta Crystallogr., Sec **C54** (1998) 1558.
[5] A. Onodera *et al.*, Jpn. J. Appl. Phys. **26** (1994) 152.
[6] K. Ohwada, *et al.*, J. Phys. Soc. Jpn. **69** (2000) 639.
[7] M. Nishi *et al.*, Physica **B241-243** (1998) 537.

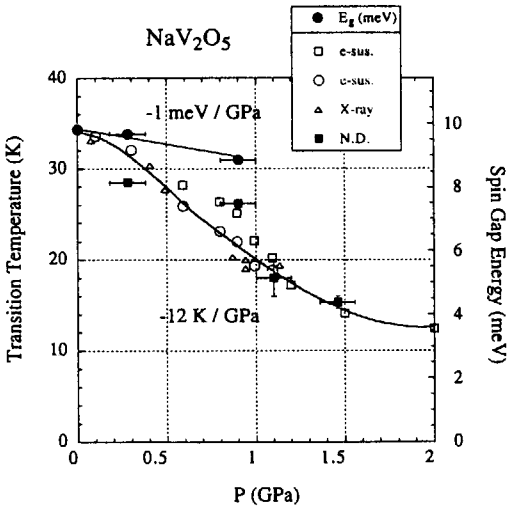


Fig. 3 P-T phase diagram of the phase transition temperature and the plot of spin gap energy normalized at ambient pressure. Solid line is the guide to eyes

研究テーマ：$Ba_3LnM_2O_9$ (Ln = La–Lu, Y; M = Ru, Ir)の磁気構造
表題：$Ba_3TbRu_2O_9$の結晶構造と磁気構造

1-2-3 Crystal and Magnetic Structures of $Ba_3TbRu_2O_9$

Yoshihiro Doi[1], Makoto Wakeshima[1], Yukio Hinatsu[1], Aya Tobo[2], Kenji Ohoyama[2], and Yasuo Yamaguchi[2]

[1]*Division of Chemistry, Graduate School of Science, Hokkaido University, Sapporo 060-0810*

[2]*Institute for Materials Research, Tohoku University, Sendai 980-8577*

A quaternary oxide $Ba_3TbRu_2O_9$ has a 6H-perovskite structure with space group $P6_3/mmc$. Its magnetic susceptibility and specific heat measurements showed that the magnetic transition occurred at 9.5 K [1].

In order to determine the magnetic structure, powder neutron diffraction measurements were performed at 2 and 15 K, and at room temperature using the Kinken powder diffractometer for high efficiency and high resolution measurements, HERMES, installed at JRR-3M reactor with a neutron incident wave length (λ = 1.8196 Å). Crystal and magnetic structures were determined by the Rietveld analysis.

Figure 1 shows the observed and calculated diffraction patterns. The Rietveld analyses of data collected at 15 K and room temperature indicate that $Ba_3TbRu_2O_9$ adopts the 6H-perovskite structure (Fig. 2(a)). In this structure, the cation sites within the face-sharing octahedra are occupied by Ru^{4+} ions, and those within the corner-sharing octahedra are occupied by the Tb^{4+} ions.

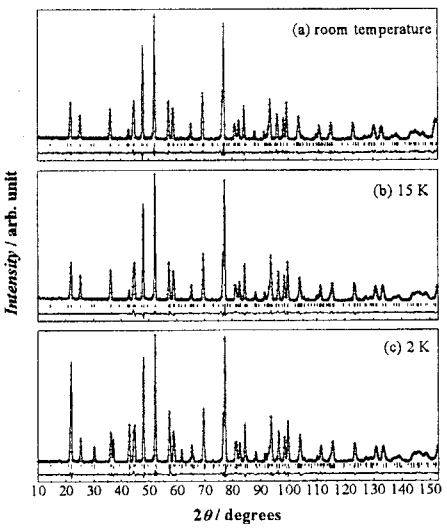


Fig. 1 Powder neutron diffraction profiles for $Ba_3TbRu_2O_9$ at room temperature, 15 K, and 2 K.

The data collected at 2 K show a number of low angle peaks, which are not observed above 15 K. They are the magnetic peaks due to an antiferromagnetic ordering of Tb^{4+} ions. These peaks are indexed in the crystallographic unit cell with odd values of l; however, the (00l) peaks are negligibly weak. These facts indicate that two Tb^{4+} ions occupying the 2a Wyckoff positions have antiparallel magnetic moments with each other, and that the direction of ordered moments is parallel to the c axis. The magnetic structure of $Ba_3TbRu_2O_9$ is illustrated in Fig. 2(b). In this magnetic structure, the magnetic moments of the Tb^{4+} ions order ferromagnetically in the c plane, and these ferromagnetic sheets are stacked antiferromagnetically along the c axis. The ordered magnetic moment of Tb^{4+} ions is determined to be 6.84(4) μ_B. This value is reasonable for Tb^{4+} ($4f^7$).

On the other hand, the ordered moments of Ru ions were not determined. This may be due to an absence of long range magnetic ordering of the Ru ions.

References

[1] Y. Doi *et al.*: *J. Mater. Chem.* **11** (2001) 3135.

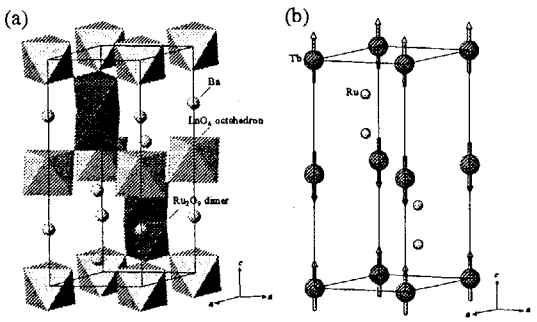


Fig. 2 The crystal structure at room temperature (a) and magnetic structure at 2 K (b) of $Ba_3TbRu_2O_9$.

使用施設：JRR-3M, 装置：HERMES, 分野：2. Magnetism

研究テーマ：三角格子バナジウム硫化物 $BaVS_3$ 単結晶の中性子散乱
表題：$BaVS_3$ 配向結晶の中性子散乱

1-2-4 Neutron Scattering of $BaVS_3$ Oriented Crystals

Masayuki Shiga[1], Hiroyki Nakamura[1], Tomoaki Yamasaki[2], Masakazu Nishi[3] and Kazuhisa Kakurai[4]

[1] *Department of Materials Science and Engineering, Kyoto University*
[2] *Graduate School of Human and Environmental Studies, Kyoto University*
[3] *Neutron Scattering Laboratory, Institute for Solid State Physics, The University of Tokyo*
[4] *Advanced Science Research Center, Japan Atomic Energy Research Institute*

Origin of the metal-insulator transition (T_{MI} = 70 K) of $BaVS_3$ (hexagonal $P6_3/mmc$) is still mysterious in spite of a long history of investigations. Pure Peierls instability expected from the one-dimensional arrangement of V atoms is now doubtful because in fact the conduction exists between the chains and the conductivity is nearly isotropic [1]. On the other hand, pure Mott instability due to the strong electron correlation was also refused because a symmetry breaking, i.e., superlattice formation, was found at T_{MI} by resent X-ray diffraction measurements of single crystalline $BaVS_3$. According to the results the chemical V site separates into 2 sites as a manner of $-V_A-V_A-V_B-V_B-$ along the *c* direction. To resolve this complex situation we performed neutron scattering experiments of single crystals. The main purpose of this study is to get information on the spin and charge states in the ground state below T_X = 30 K by probing the detailed magnetic structure.

Single crystals of $BaVS_3$ were synthesized by a Te flux methods. The shape of the crystal is like a fine needle with the hexagonal *c* direction along the long axis. The crystals is typically in several mm length and 0.1 ~ 0.4 mm diameter. The mass is less than 1 mg. For neutron scattering experiments about 1000 pieces of crystals are collected and oriented along the *c* axis on thin Al plates. Hence hexagonal *a* axes of the crystals are expected to orient at random. To fix the crystals we used conventional adhesive paste diluted in acetone. Neutron scattering experiments were performed with a triple-axis spectrometer ISSP-PONTA-5G installed at JRR-3M in JAERI. Measurements were carried out at a incident energy k_i = 2.67 Å^{-1} with a collimation sequence open-80'-80'-80'.

All results obtained so far are consistent with the magnetic modulation vector **q** = (0.226, 0.226, 0) determined from powder diffraction experiments [3]. One of preliminary results is shown in Fig. 1, which are difference profiles between data measured at 10 K and 50 K. The value of the horizontal axis was normalized by hexagonal a^*, although the lattice is slightly distorted to orthorhombic below T_S = 240 K. Top and bottom figures corresponds to elastic diffraction profiles measured at L = 1/2 and 0, respectively. Although the experimental accuracy is not enough to determine the precise magnetic structure due to high back ground originating in scattering from protons included in the adhesive paste, no appreciable magnetic peak at L = 1/2 indicates that the V site separation revealed by the X-ray measurements does not correspond to explicit separation of the spin (or charge) state, for example, to 0 μ_B and 1 μ_B. This suggests a nearly uniform spin and charge state even below T_X.

Efforts to reduce the back ground and low-energy and high-resolution experiments are now in progress.

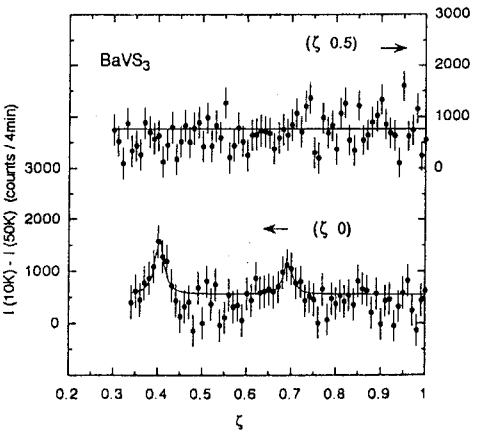


Fig. 1 Difference profiles between 10 K and 50 K

References

[1] G. Mihaly *et al.*: Phys. Rev. B 61 (2000) R7831,

[2] H. Nakamura *et al.*: J. Phys. Soc. Japan 69 (2000) 2763.

[3] T. Inami *et al.*: to appear in Phys. Rev. B.

使用施設：JRR-3M、装置：PONTA(5G)、分野：2. Magnetism

研究テーマ：$RbCo_{1-x}Mg_xF_3$ の原子秩序、磁気秩序、磁気励起
表題：$RbCo_{1-x}Mg_xF_3$ の原子秩序と磁気秩序

1-2-5

Atomic and Magnetic Order in $RbCo_{1-x}Mg_xF_3$ System

K. Motoya, R. Masaoka, J. Kikuchi and S. Itoh[1]

Department of Physics, Faculty of Science and Technology, Tokyo University of Science, Noda 278-8510
[1]Institute of Materials Structure Science, KEK, Tsukuba 305-0801

$RbCoF_3$ crystallizes in the cubic perovskite structure (space group Pm-3m) and antiferromagnetically orders below T_N~100K. For the $RbCo_{1-x}Mg_xF_3$ system T_N decreases with increasing x and ferrimagnetic order with the hexagonal structure appears for $0.3<x<0.68$.[1)] In order to clarify the crystal and magnetic structure of the $RbCo_{1-x}Mg_xF_3$ system, especially to inspect the possible presence of atomic order, we made specific heat, magnetic sus-ceptibility, magnetization and neutron diffraction measurements. In this report we present the result of powder neutron diffraction measurements for x=0.33, 0.40, and 0.50 samples.

Figure 1 shows the powder neutron diffraction pattern taken at room temperature and the result of Rietvelt analysis for x=0.33. The hexagonal $BaTiO_3$-type structure (space group $P6_3/mmc$) gives the best fit to the data. In this structure Co and Mg atoms occupy 2a and 4f sites. For x=0.33, 13% of 2a site and 42% of 4f site are occupied by Co atoms, therefore, Co atoms prefer 4f site.

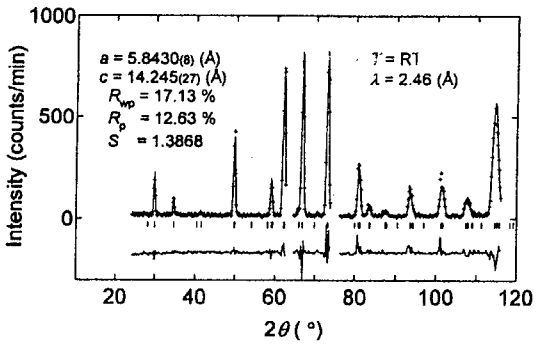


Fig.1 Neutron diffraction pattern and the result of Rietvelt analysis of $RbCo_{0.33}Mg_{0.67}F_3$.

Figure 2 shows the occupation factor of Co atoms (g) as a function of Co concentration x. For all samples, partial atomic order among Co and Mg atoms was observed. Note that the relation x=1/3g(2a)+2/3g(4f) is fulfilled. Deviation from the dashed line, which is the expected value for random occupation, increases with decreasing x.

Relation between the atomic order and the saturation moment in the ferrimagnetic phase will be discussed based on the super-exchange interaction path among 2a and 4f sites in the forthcoming paper.

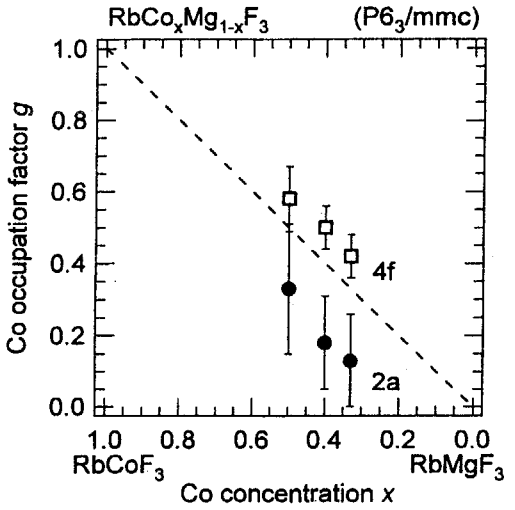


Fig.2 Occupation factor of Co atoms as a function of Co concentration x.

Reference

1) M.W.Shafer and T.R.McGuire: Phys Letters 27A (1968) 676.
J.Phys.Chem. Solids 30 (1969) 1989.

使用施設：JRR-3M, 装置：4G, T1-1 分野：磁性

研究テーマ：高濃度スピングラスにおける磁気相関と磁気励起
表題：高濃度合金 $Fe_{65}(Ni_{1-x}Mn_x)_{35}$ における強磁性・反強磁性相関の共存

1-2-6 Ferromagnetic and Antiferromagnetic Correlations in Concentrated Alloy System $Fe_{65}(Ni_{1-x}Mn_x)_{35}$

K. Motoya and K. Hioki

Department of Physics, Faculty of Science and Technology, Tokyo University of Science, Noda 278-8510

A study of a pseudo-binary alloy system $Fe_{65}(Ni_{1-x}Mn_x)_{35}$ was initiated by Shiga to investigate the magnetic state of an iron atom in fcc lattice long before the discovery of spin-glass.[1] Besides the knowledge of the electronic state of the constituent atoms he reported that the alloy is an antiferromagnet in the composition range $0.3<x\leq1.0$, and a ferromagnet for $0\leq x<0.3$. Many experimental works on the $Fe_{65}(Ni_{1-x}Mn_x)_{35}$ and the related systems followed.

A previous neutron scattering study[2] showed that ferromagnetic clusters exist in ferromagnetic and spin-glass phases. The origin of anomalous temperature variation behavior of spin-wave stiffness and spin-wave intensity observed in this and other spin-glass materials is attributed to the presence of magnetic clusters. Recently, we found that magnetic clusters with antiferromagnetic correlation coexist with ferromagnetic clusters in the alloy of x=0.22. This observation showed that the magnetic phase diagrams based on the macroscopic measurements is insufficient to describe the magnetic state of competing interaction systems.

In order to clarify the microscopic magnetic state of the present system, we made a neutron diffraction study of $Fe_{65}(Ni_{1-x}Mn_x)_{35}$ with x=0.05~0.22. Figure 1 shows the temperature variation of amplitude and line width of the magnetic diffuse pattern measured around (110) which is an antiferromagnetic Bragg point for fcc structure. We remark that the magnetic scattering arising from antiferromagnetic as well as ferromagnetic clusters (not shown here) develop far above the spin-glass transition temperature. The present observation showed that ferromagnetic and antiferromagnetic clusters coexist in wide temperature range. Time evolution of these clusters is currently studied by means of time-resolved SANS technique.

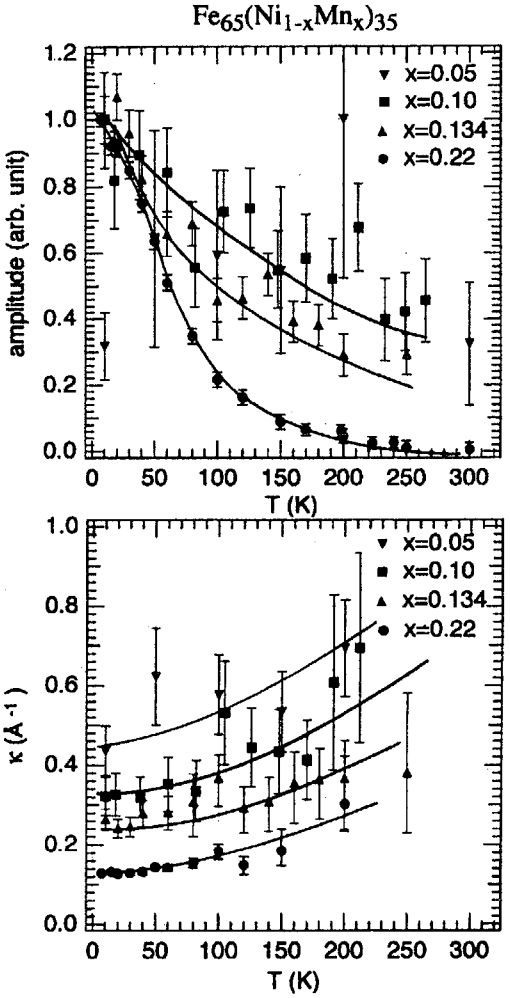


Fig. 1. Temperature variation of the amplitude and the width of the antiferromagnetic peak.

References

1) M.Shiga: J.Phys.Soc.Jpn. 22 (1967) 539.
2) K. Motoya and Y. Muraoka: J.Phys.Soc.Jpn. 62 (1993) 2819.

使用施設：JRR-3M，装置：4G, T1-1 分野：磁性

研究テーマ：偏極中性子を用いた軌道の自由度の研究
表　題：CeB_6 におけるスピン密度分布

1-2-7

Spin density distribution in CeB_6

M. Saitoh, N. Okada[1], E. Nishibori[1], H. Takagiwa, T. Yokoo[2], M. Nishi[3], K. Kakurai[4], S. Kunii[5], M. Takata[1], M. Sakata[1] and J. Akimitsu
Department of Physics, Aoyama-Gakuin University, Tokyo 157-8572
[1]*Dapartment of Applied Physics, Nagoya University, Nagoya 464-8603*
[2]*High Energy Accelerator Research Organization (KEK), Tsukuba 305-0801*
[3]*ISSP, University of Tokyo, Tokai 319-1106*
[4]*Japan Atomic Energy Research Institute (JAERI), Tokai 319-1195*
[5]*Department of Physics, Tohoku University, Sendai 980-8578*

The Kondo compound CeB_6 with a cubic CaB_6-type structure has attracted much attention because of its complicated magnetic phase diagrams [1–5]. It shows the successive phase transitions from the paramagnetic state to the antiferro-quadrupolar (AFQ) ordering at T_Q = 3.3 K, and to the antiferromagnetic ordering at T_N = 2.3 K. The phases are usually denoted as phases I, II and III, respectively.

Our previous polarized neutron diffraction (PND) work on CeB_6 has revealed the spin density distribution of CeB_6, deduced by the maximum entropy method (MEM) using PND data, under an applied magnetic field in parallel to [110]-axis. So we tried to investigate the spin density distribution of CeB_6, under an applied magnetic field in parallel to different axis from the former one.

Single crystals of CeB_6 were grown by the floating zone method. ^{11}B-isotope enriched single crystals of about $5 \times 6 \times 1$ mm^3 in size were used for the PND experiments. The PND experiments were carried out on the triple-axis spectrometer, PONTA, installed at JRR-3M reactor at Tokai JAERI. The PND data were collected at 1.7 K under an applied magnetic field of 5.9 T in parallel to [100]-axes, with the incident neutron energies of 80 meV. The effects of the incomplete polarization (neutron polarization $P_n \sim 95$ %) and the statistical uncertainty estimations were taken into account.

The magnetic form factors, μf, derived from the observed PND data are shown in Fig. 1. The new data set for $H//[100]$ was combined with the old one for $H//[110]$ by scaling to the $(00l)$ reflections, which are common to both data sets.

As shown in Fig.1, the observed form factors are unusually scattered. If the spin densities are

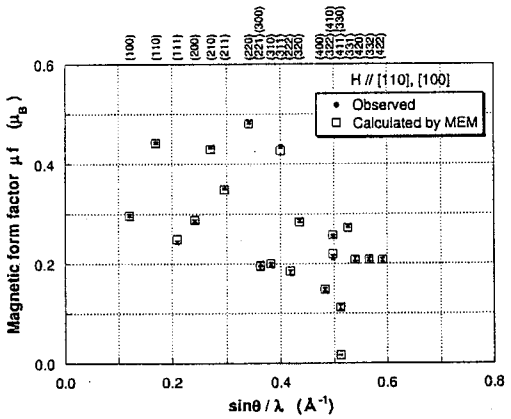


Figure 1: The observed magnetic form factors with solid circles with error bars for each reflection. The calculated values from the obtained MEM spin density are also plotted.

localized on Ce site, the magnetic form factor of Ce in CeB_6 should have to be almost spherical in reciprocal space. As a matter of fact, any theoretical calculation based on the spin localization model at Ce site had never succeeded in reproducing the observed magnetic form factors as shown in Fig. 1. Under these circumstances, a new approach is highly desirable.

The spin density reconstruction by MEM analysis was carried out under the constraint of simple cubic crystal symmetry (space group: $Pm\bar{3}m$) with a computer program ENIGMA [6] using $80 \times 80 \times 80$ pixels. The total magnetic moment of unit cell is fixed on the total +0.8 μ_B; which is the measured magnetic moment at 1.6 K. In MEM analysis, it is assumed that positive density is +1.1 μ_B and negative density is −0.3 μ_B after checking several combinations of positive and negative moments like +0.9 μ_B and −0.1 μ_B, etc. Therefore, it has

原子炉：JRR-3M　　装置：PONTA(5G)　　分野: Magnetism

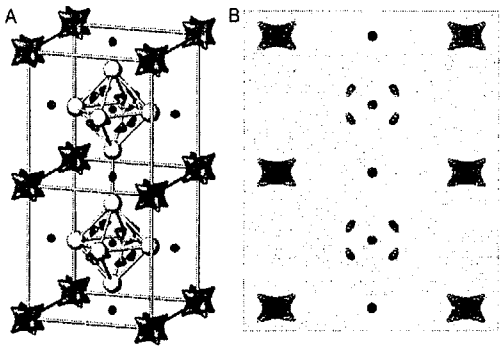


Figure 2: (A) The three-dimensional spin density distribution in CeB_6. (B) The equi-contour ($\pm 0.3\ \mu_B$) surface and the contour map of (110) section (logarithmic scale) in CeB_6.

to be admitted that some ambiguities are remaining in the assumption of the component of antiferro-magnetic moment in the total spin density. Among them, the result with the least reliable factor, 0.98 %, is obtained as the final result of this work. Fig. 2 is the equi-contour surface ($\pm 0.3\ \mu_B$) of total spin density of CeB_6. For the convenience, boron network of CeB_6 is also shown in the figure.

The MEM spin density of CeB_6 is just striking. Although the most of the spin density moment were found to be localized at Ce atomic sites, we found that the magnetic moments exist not only at Ce-site but also at between B_6 octahedral and at the center of triangle bonding in the B_6 octahedral. The significant negative density was also found at the center of B_6 octahedron. The amounts of each magnetic moment are as follows; Ce-site: $+0.444(2)\ \mu_B$; the midpoint between B_6 octahedron: $+0.018(1)\ \mu_B$, the center of triangle surface in the B_6 octahedon: $+0.021(1)\ \mu_B$; the center of B_6 octahedron: $-0.013(1)\ \mu_B$. The spin density at Ce site has the spiny squarish deformation. This characteristic feature can be interpreted as the averaged feature of O_{xy} type AFQ moment, which should show the spiny deformation toward $\langle 111 \rangle$ direction. The calculated magnetic form factors based on the MEM spin density distribution in CeB_6 show very good accordance with the observed values as shown in Fig. 1. The present unexpected peculiar ferromagnetic spin density feature is the first example of spin density localized at non-atomic site. At the present stage, the meaning of the present results are not fully understood but it can be said that both the Boron atom's network as well as Ce atoms contribute to the magnetic properties of CeB_6.

References

[1] T. Fujita, M. Suzuki, T. Komatsubara, S. Kunii, T. Kasuya and T. Ohtsuka: Solid State Commun. **35** (1980) 569.

[2] M. Kawakami, S. Kunii, T. Komatsubara and T. Kasuya: Solid State Commun. **36** (1980) 435.

[3] A. Takase, K. Kojima, T. Komatsubara and T. Kasuya: Solid State Commun. **36** (1980) 461.

[4] S. Nakamura, T. Goto, S. Kunii, K. Iwashita and A. Tamaki: J. Phys. Soc. Jpn. **63** (1994) 623.

[5] M. Hiroi, S. Kobayashi, M. Sera, N. Kobayashi and S. Kunii: J. Phys. Soc. Jpn. **66** (1997) 132.

[6] H. Tanaka, M. Takata, E. Nishibori, K. Kato, T. Iishi and M. Sakata: J. Appl. Crystallogr. (2001) to be published.

研究テーマ：偏極中性子を用いた軌道の自由度の研究
表　題：$La_{0.5}Sr_{1.5}MnO_4$における軌道整列

1-2-8 Orbital Ordering in $La_{0.5}Sr_{1.5}MnO_4$

M. Togasaki, L. Kano, M. Saitoh, M. Takeda[1], M. Nishi[2], K. Hirota[1] and J. Akimitsu
Department of Physics, Aoyama-Gakuin University, 6-16-1 Chitosedai, Setagaya-ku, Tokyo 157-8752, Japan
[1] *Department of Physics, Tohoku University, Aoba-Ku, Sendai, Miyagi 980-8578, Japan*
[2] *Neutron Scattering Laboratory, ISSP, University of Tokyo, Tokai, Ibaraki 319-1106, Japan*

$La_{0.5}Sr_{1.5}MnO_4$ is a layered manganite with average valence of 3.5 at each Mn site. Recent studies have indicated a real space ordering of two distinct Mn sites below T_{CO} = 217 K, with the two sites identified as Mn^{3+} and Mn^{4+} in the *ab* plane and the oxygen atoms in the *ab* plane are 1% breathing modelike movement towards one set of Mn atoms, identified as the higher valent Mn^{4+} sites . The resonant X-ray scattering (RXS) experiment suggested orbital ordering that alternating $3x^2$-r^2 and $3y^2$-r^2 orbitals at each Mn^{3+} site below T_{CO}. However, the contraducted result that the "forbidden" nuclear and magnetic reflections were observed with polarization analysis experiment.

In order to check these points, we investigated the orbital ordering scheme of $La_{0.5}Sr_{1.5}MnO_4$ by means of the polarization analysis.

Single crystal was grown by the floating zone method. The polarization analysis measurments were performed at JRR-3M reactor at Tokai JAERI. The energy of the incident neutrons is 14.7 meV. The data was taken at 8 K under an applied magnetic field of 10 Gauss by Helmholtz coil in parallel with <0 0 1>-axis of single crystal specimen. The procedures for correcting the incomplete polarization (neutron polarization $P_n \simeq 96\%$) will be published elsewhere.

The final experimental results of the nuclear and magnetic intensity are shown in Fig.1 and 2 with diamond. The bars indicate the statistical uncertainties. These ovserved intensity in Fig.1 suggest that distortions of oxygen atoms can not be explained by the suggested model. Magnetic reflections in Fig.2 can be explained by the minority stacking. In order to compere the RXS experiment suggested orbital orderd configuration of the eg electron with the experimental results, we calculated the intensity of magnetic reflection. The best-fitted orbital ordering is suggusted by RXS and two domain state are taken into account in $La_{0.5}Sr_{1.5}MnO_4$.

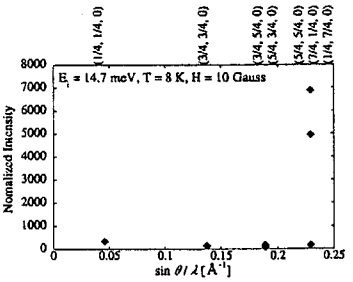


Figure 1: Intensity of the observed nuclear diffractions.

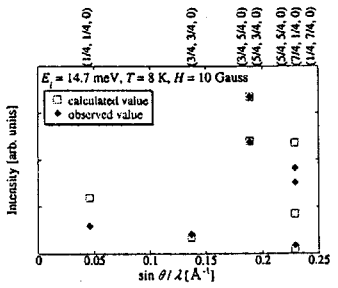


Figure 2: Compartion between the observed (diamond with bars) and calculated (square) diffraction.

原子炉：JRR-3M　　装置：TONTA(6G)　　分野：Magnetism

研究テーマ：A'_3ABO_6型化合物の低温磁気構造
表題：$Ca_3Co_2O_6$の磁気構造に関する中性子回折実験
1-2-9

Neutron Diffraction Study of Magnetic Structure in $Ca_3Co_2O_6$

Seiji Niitaka[1], Kazuyoshi Yoshimura[1], Masakazu Nishi[2] and Kazuhisa Kakurai[3]

[1] *Department of Chemistry, Graduate School of Science, Kyoto University*

[2] *Neutron Scattering Laboratory, Institute for Solid State Physics, University of Tokyo*

[3] *Advanced Science Research Center, Japan Atomic Energy Research Institute*

$Ca_3Co_2O_6$ with the rhombohedral K_4CdCl_6 structure contains linear chains consisting of alternating face-sharing CoO_6 trigonal prisms and CoO_6 octahedra. The chains along the *c*-axis are separated by calcium cations, forming a triangular lattice in the *c*-plane. The magnetic susceptibility of $Ca_3Co_2O_6$ exhibits two anomalies at 25K(=T_1) and 10K(=T_2) [1]. From the experimental results reported previously, the following two models can be given as the possible magnetic structure between T_1 and T_2. One is a ferrimagnetic (FR) structure made up of ferromagnetic Ising spin chains and the other is a partially disordered antiferromagnetic (PDA) structure, where 2/3 of the ferromagnetic Ising spin chains order antiferromagnetically each other and the remaining 1/3 are left incoherent with the other chains as illustrated in ref. [2]. To clarify which magnetic structure is realized, we measured the temperature dependence of the integrated intensity of (110) peak. It is a crucial point in determining the magnetic structure because (110) reflection includes no magnetic component in the case of PDA, while it does a finite magnetic component in the case of FR structure.

The neutron diffraction experiment was performed for an uncrushed sintered pellet of $Ca_3Co_2O_6$ using the HQR diffractometer (T1-1) in the temperature range of 2-32K under applied magnetic fields of 0-2T after ZFC.

Figure 1 shows the temperature dependence of the integrated intensities of the (110) peak. The intensity at 0T shows no increase below T_1, indicating that $Ca_3Co_2O_6$ realizes the PDA state below T_1 similar to Ca_3CoRhO_6 [2]. The intensity at 2T is larger than that at 0T due to a field-induced FR state characterized by a plateau at 1/3 of the saturation magnetization [1]. The decrease in the intensity at 2T below T_2 is probably attributed to the spin freezing suggested by the difference between ZFC and FC below T_2 in the magnetic susceptibility [1].

References

[1] H. Kageyama *et al.*, J. Phys. Soc. Jpn. **67** (1998) 357.

[2] S. Niitaka *et al.*, Phys. Rev. Lett. **87** (2001) 177202.

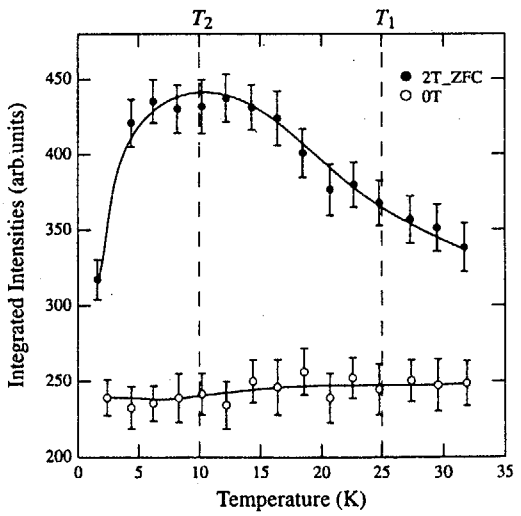


Fig.1 Temperature dependence of the integrated intensity of the (110) peak at 0T(○) and 2T(●). The solid lines are guided to the eye.

使用施設：JRR-3M, 装置：HQR (T1-1), 分野：2.Magnetism

研究テーマ：Pt3Fe の磁気構造
表題：Pt3Fe の磁気構造

1-2-10

The magnetic structure of Pt3Fe

Y.Higashiyama and Y.Tsunoda
School of science and engineering, Waseda University, Okubo 3-4-1, Shinjuku-ku, Tokyo 169-8555, Japan

The PtFe alloys with containing about 25% of iron have the cubic Cu_3Au structure for which corners and centers of the unit cell are occupied by iron and platinum atoms, and have an antiferromagnetic structure. In Fig.1 temperature variations of magnetic peak intensities are shown, the peak intensity at (.5.50) reciprocal lattice point which is observed in high temperature phase (<180K) is reduced when the peak at (.500) observed in low temperature phase (<90K) appears.

In 1960's, Bacon proposed the magnetic structure at the high temperature phase as shown in Fig.2. The (110) ferromagnetic sheets couple antiparallel. In low temperature phase, he proposed that there is a wrong placed iron atom in the cubic face which couple ferromagnetically with the nearest neighbour iron atoms [Fig.3]. In this case, the model of Fig.3, the magnetic scattering at (.500) is expected to be a short range order. The elastic scattering peak of (.500) is apparently a Bragg peak. In Fig.2 the magnetic moments of irons in (001) planes couple unparallel each other, while the coupling along the [001] axis is parallel despite the lattice parameter of [100] is equal to [001]. Thus, this model is considered to be very unstable.

We conducted neutron scattering experiment to check if the Bacon's model is really correct. At 100K, strong inelastic scattering is observed at (.500) both Pt75Fe25 and Pt76Fe24 samples. Based on the Bacon's model, latter sample is thought to have less wrong placed iron atoms in the cubic face because the (.500) magnetic peak intensity is extremely weak. This result indicates that the model of the low temperature phase is not come from the wrong placed iron atoms and spin correlations which appears at the low temperature phase is already developed in the high temperature phase. Now we propose the new magnetic structure model for the low temperature phase which makes magnetic scattering peaks at (.500) and (.5.50) without thinking the wrong placed iron atoms [Fig.4].

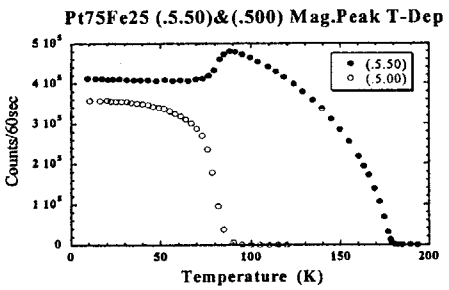


Fig.1 Temperature variations of magnetic peak intensities (.5.50) & (.500)

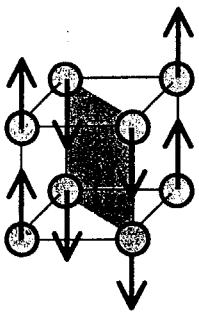


Fig.2 Bacon's magnetic structure of Pt3Fe in high temperature phase

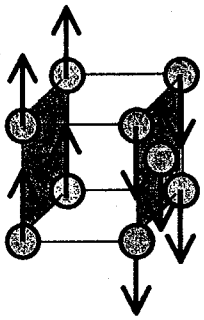


Fig.3 Bacon's magnetic structure of Pt3Fe in low temperature phase

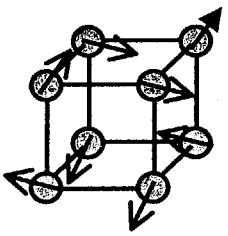


Fig.4 The new magnetic structure of Pt3Fe in low temperature phase

・ Reference

[1] G.Bacon, A.E.R.E., Harwell and J. Crangle, Department of Physics, University of Sheffield

使用施設：ＪＲＲ－３Ｍ、装置：Ｔ１－１、分野：２.Magnetism

研究テーマ：CuMn ASRO と Dynamics
表題：PdMn スピングラスのスピンダイナミクス

1-2-11

Spin-dynamics in PdMn spin-glass alloy

H. Hama and Y.Tsunoda
Department of Applied Physics, School of Science and Engineering,
Waseda University, 3-4-1, Ohkubo, Shinjyuku, Tokyo, 169-8555, Japan

The PdMn alloy with Mn content below 5 at.% shows ferromagnetic behavior at low temperature, but the alloy with higher Mn content displays typical characteristics of a spin-glass; a cusp type anomaly and remanent magnetization in susceptibility measurements, but no obvious peak around the freezing temperature in the specific heat. In neutron scattering measurements, satellite diffuse peaks had been observed at the $(1 \pm \delta, 0, 0)$ positions accompanied with the atomic short range order peak at (100).

For examining dynamics of PdMn spin-glass alloy we measured temperature dependence of the neutron magnetic diffraction intensity with changing the window of the energy resolution.

We used PdMn single crystal with Mn concentration of 18 at.%. The single crystal was grown by the bridgeman method by using a furnace with carbon electrode. Neutron diffraction measurements were carried out at the C1-1 and T1-1 triple axis spectrometers of JRR-3M, Tokai, Japan.

Neutron diffraction patterns obtained at 12 K by scanning along the line connecting the (000) and (200) points in reciprocal space are given in Fig1. The nuclear scattering contribution coming from the broad atomic short range order peak centered at (100) has been subtracted using the data measured at 102 K (>>Tf) for obtaining magnetic diffuse peaks.

The temperature dependence of the 'elastic' intensities for three different energy-resolution experiments is shown in Fig2. The scattering vector Q=(0.78,0,0) corresponds to the center of one of the incommensurate magnetic peaks for this sample. These energy-resolutions determined by the vanadium incoherent scattering in each measurement are given in the Fig2.

Experimental data show that the kink of the intensity variation approaches to Tf obtained by the magnetic susceptibility measurements as increasing the energy-resolution, that is to say decreasing the speed of the incident neutron. This is the same phenomenon observed in the spin-dynamics of CuMn [Ref1,2]. Thus, the origin of the spin-glass like behavior in PdMn alloys can be ascribed to the dynamics of the fluctuating spin-density-wave clusters just as observed in CuMn alloys.

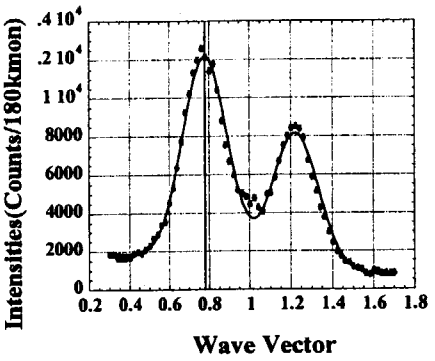


Fig1. Neutron magnetic intensity around (100) obtained at 12K. The atomic short-range order peak at 102 K has been subtracted out.

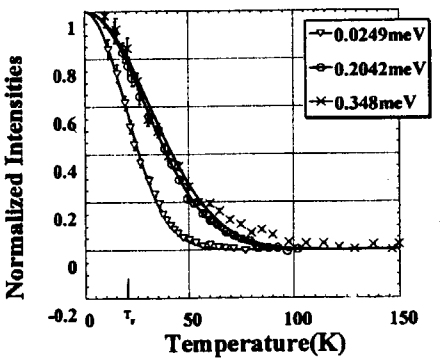


Fig2. Temperature dependence of the 'elastic' component of the satellite peak intensities studied at (0.78,0,0) point in three different energy-resolution.

Reference

1) J.A.Gotaas, J.J.Rhyne and S.A.Werner J.Appl.Phys.57 (1985)

2) S.A.Werner, J.J.Rhyne and J.A.Gotaas, Solid State Commun56, 457 (1985)

3) Y,Tsunoda and N,hiruma ,J.L.Robertson and J.W.Cable Phys.Rev.B.56 (1997)

使用施設：JRR-3M、装置：T1-1、C1-1、分野：2.Magnetism

研究テーマ:Mn_3Pt 合金のスピンゆらぎ
表題:Mn_3Pt 合金についてフラストレーション系における試料依存性

1-2-12
Sample Dependence of Frustration System in Mn_3Pt Alloy

T.Ikeda and Y.Tsunoda
School of science and engineering, Waseda University, Okubo 3-4-1, Shinjuku-ku, Tokyo 169-8555, Japan

The ordered alloy Mn_3Pt has a Cu_3Au-type lattice structure, in which Pt and Mn atoms occupy at the corner and face center of fcc structure, respectively. This alloy is antiferromagnet with the first order AF-AF magnetic transition at T_t=400K below Neel temperature (T_N=475K). High temperature phase and low temperature phase are named as F-phase and D-phase, respectively. The magnetic structures are triangular below T_t and collinear between T_t and T_N. The magnetic structure of F-phase has a special feature that one third of all Mn atoms have no magnetic moments. This may be reasonable if we consider the molecular field of the Mn site surrounded by eight n.n Mn atoms. To investigate the dynamics of these spins, we performed inelastic neutron scattering measurements at T1-1 (HQR) triple axis spectrometer. In the F-phase, inelastic diffuse scattering was observed along Brillouin zone boundary of fcc structure. The distribution of inelastic diffuse scattering indicates that Mn spins are dynamically fluctuating with some spin correlation. Since the dynamical fluctuation comes from the symmetrical configuration of Mn spins, this fluctuation would relate to the atomic long-range order parameter. Thus, two stoichiometric samples, 75 at. % of Mn, with the different atomic long-range order parameter x were prepared by means of different heat treatments. The atomic long-range order parameter x was determined by comparing the observed intensity ratios of (100) to (200) nuclear Bragg peaks in neutron scattering measurements. SampleA and SampleB were estimated to be x=0.99 and x=0.55, respectively. The constant Q scan of each sample studied at 1 0.25 0 in the RLP are given in Fig.1. These data show that inelastic scattering is observed only in the F-phase. In the SampleA, inelastic scattering distributes toward a high-energy region. However, in the SampleB, quasi-elastic scattering is observed around the center of E=0meV. In the SampleB with x=0.55, the Mn spins would be pinned due to the substitution of Mn and Pt atoms. In the case of the SampleA with x=0.99, Mn spins are fluctuating with high frequency due to the high symmetry of the n.n Mn spins.

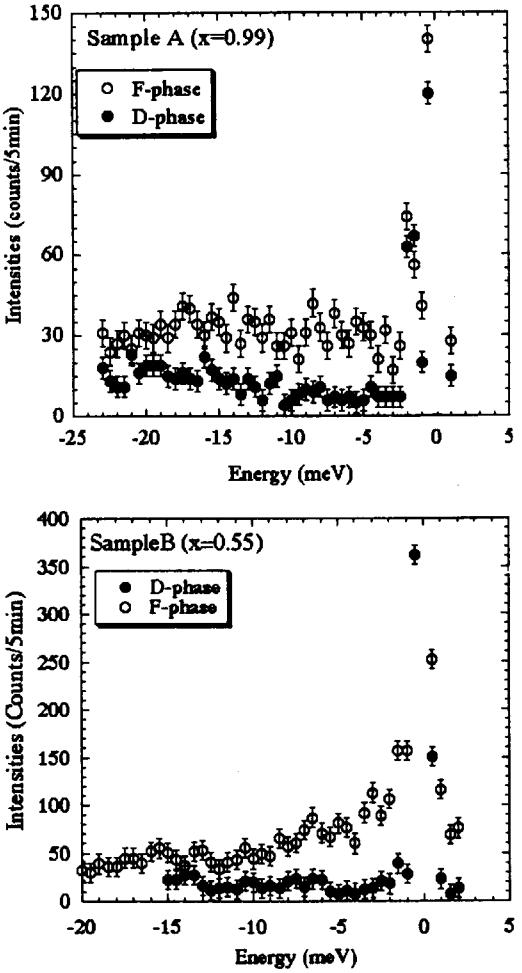


Fig.1. Constant Q=(1 0.25 0) scans in the sampleA and sampleB at the D- and F-phase. Open and filled circles represent the data for the F-phase and the D-phase, respectively.

使用施設:JRR-3M, 装置:T1-1(HQR), 分野:2.Magnetism

研究テーマ：
表題：フラストレーション系 $^{110}CdFe_2O_4$ の粉末中性子回折

1-2-13 Neutron powder diffraction for frustrated $^{110}CdFe_2O_4$

K. Kamazawa, S. Hashiguchi, and Y. Tsunoda
Dept. of Appl. Physics, Waseda Univ., Ohkubo 3-4-1, Shinjuku-ku, Tokyo, 169-8555 Japan

$CdFe_2O_4$ has a normal spinel structure, and the magnetic ions construct the corner sharing tetrahedra. This structure is the same as pyrochlore and C15 inter-metallic Laves Phase compound. Therefore we considered that $CdFe_2O_4$ is one of substance of the frustration system, because magnetic susceptibility data is similar to the data of $ZnFe_2O_4$. Using powder neutron scattering measurement with isotope $^{110}CdFe_2O_4$, we obtained diffuse scattering at around 30° (See Fig. 1) which is different from the angle of $ZnFe_2O_4$. It indicates that the first neighbor Fe^{3+} ions couple antiferromagnetically and frustration occur between these Fe^{3+} ions. The lattice constants and u-parameter are difference between $CdFe_2O_4$ and $ZnFe_2O_4$: ($CdFe_2O_4$; 8.715 Å , $ZnFe_2O_4$; 8.52 Å), ($CdFe_2O_4$; u=0.3925, $ZnFe_2O_4$; u=0.3852). Considering the results of $ZnFe_2O_4$ and $^{110}CdFe_2O_4$, it is worth while to notice that the position of Q where magnetic diffuse scattering goes out changes such largely, just replaced Zn to Cd. $ZnFe_2O_4$ takes 95 ° between the nearest neighbor Fe^{3+} angle and the interaction is week ferromagnetic (almost paramagnetic), on the other hand $CdFe_2O_4$ takes 99° between the nearest neighbor Fe^{3+} angle and the interaction is antiferromagnetic. Therefore, we consider that the nearest neighbor Fe-O-Fe super exchange interaction (antiferromagnetic) become dominant and the interaction changed dramatically. Temperature dependence of the diffuse scattering at the strongest intensity still exists around 60K (See Fig. 2), though that of $ZnFe_2O_4$ extinguishes around 30K.

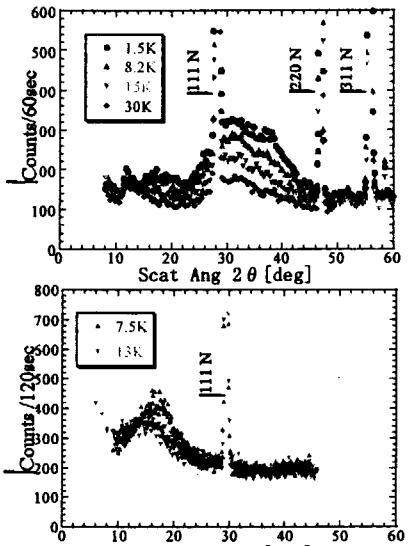


Fig. 1 Comparison of θ-2θ scans for $CdFe_2O_4$ (upper) and $ZnFe_2O_4$ (lower).

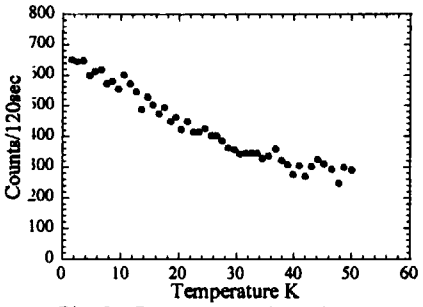


Fig. 2 Temperature dependence for $^{110}CdFe_2O_4$ at 2θ=31°

使用施設：JRR-3M, 装置：HQR(T1-1), 分野：2. Magnetism

1-2-14
研究テーマ：
表題：フラストレーション系 $ZnFe_2O_4$ 単結晶の中性子磁気散乱

Magnetic Neutron Scattering Measurements in Frustrated $ZnFe_2O_4$ Single Crystal

K. Kamazawa[1], Y, Tsunoda[1], H. Kadowaki[2], and K. Kohn[3]
[1]*Dept. of Appl. Physics, Waseda Univ., Ohkubo 3-4-1, Shinjuku-ku, Tokyo, 169-8555 Japan*
[2]*Dept. of Physics, Tokyo Metropolitan Univ., Hachioji-shi, Tokyo, 192-0397 Japan*
[3]*Dept. of Physics, Waseda Univ., Ohkubo 3-4-1, Shinjuku-ku, Tokyo, 169-8555 Japan*

$ZnFe_2O_4$ is one of geometrical frustration substance, and the data of elastic neutron scattering had already reported. This report is summarized about the energy spectra at several reciprocal space. There are two kinds of spin motions in $ZnFe_2O_4$. Even though very high-energy resolution, the energy spectrum of antiferromagnetic diffuse scattering are elastic peaks. In ferromagnetic diffuse scattering positions, there are inelastic peaks. With increasing temperature, the inelastic peaks gradually shift toward E=0 meV and they become quasielastic peaks at high temperature. Fig. 1 shows the |Q| dependences of the inelastic peak center and the line width (FWHM), which were determined using "damped harmonic oscillator (DHO) peak" $S(Q,\omega) =$

$$A\left(\frac{k_f}{k_i}\right)\frac{\omega}{1-exp(-\hbar\omega/kT')}\frac{\omega_0^2\Gamma_2}{(\omega^2-\omega_0^2)^2+\omega^2\Gamma_2^2}$$

where, A is proportionality coefficients, ω_0 is peak center, Γ is FWHM, T' is temperature. kf and ki are incident and scattered neutron wave vectors, respectively. The horizontal axis |Q| is written by the distance from 1 1/2 0. The data show that there is very soft dispersion relation originated from strong diffuse scattering position in low temperature. In addition, there is a energy gap. The inelastic peak center has still finite energy at 15K. We consider that they concerns with frustration.

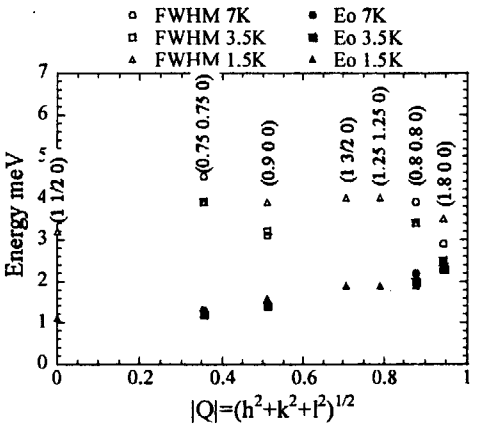


Fig.1 The |Q| dependences of the inelastic peak center and the line width (FWHM), which were determined using "damped harmonic oscillator (DHO) peak". The horizontal axis |Q| is written by the distances from 1 1/2 0. Though fitting curves were calculated by actual temperatures T, the peak center and the FWHM don't almost change.

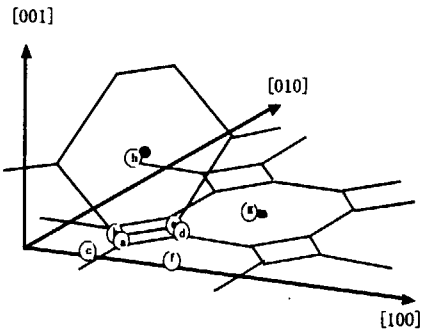


Fig. 2 Diagram of reciprocal space for ZnFe2O4. The ope circles labeled with alphabet indicate positions where we observed energy spectrum. The solid circles indicate nuclear reflections and the solid lines denote Brillouin zon boundaries of the fcc structure.

使用施設：JRR-3M, 装置：HER(C1-1), 分野：2. Magnetism

研究テーマ：正方晶四極子化合物 $Ho^{11}B_2C_2$ および $Tb^{11}B_2C_2$ の特異な長周期構造
表題： HoB_2C_2 の単結晶中性子散乱

1-2-15 Neutron Diffraction Study on Single Crystal HoB_2C_2

A. Tobo[1], T. Ohmori[1], T. Matsumura[2], N. Oumi[2], K. Hirota[2],
K. Ohoyama[1], H. Yamauchi[1], H. Onodera[1] and Y. Yamaguchi[1]

[1] *Institute for Materials Research, Tohoku University, Sendai, 980-8577 Japan*
[2] *Department of Physics, Tohoku University, Sendai, 980-8578 Japan*

HoB_2C_2 shows both of an antiferroquadrupolar (AFQ) ordering and an antiferromagnetic (AFM) ordering. Complicated magnetic behavior of the systems which have both of an AFQ ordering and an AFM ordering have been attracting many interests, but HoB_2C_2 is striking because T_Q is lower than T_N. It is reported that an AFM transition occurs at $T_N = 5.9$ K and an AFQ ordering transition at $T_Q = 4.5$ K in HoB_2C_2 from magnetization and heat capacity measurements [1, 2]. Hence, in the field-temperature phase diagram of HoB_2C_2, we obtained a new intermediate phase, phase IV, between T_Q and T_N.

The neutron diffraction measurements using powdered $Ho^{11}B_2C_2$ sample shows that the magnetic structure below T_Q is described by four propagation vectors of k_1=[1 0 0], k_2=[0 1 1/2], k_3=[0 0 0] and k_4=[0 0 1/2] [3]. On the other hand, phase IV, between T_Q and T_N, is a magnetic state with long periodicity. From our preliminary measurements on the single crystal sample, we saw three type of magnetic components around the (1 0 0) magnetic Bragg point: the (1 0 0) Bragg peak which appears below $\sim T_Q$, the (1+δ δ δ') satellite peaks, and the small uniform scattering intensity observed in the region whose vertices are the satellite peaks. In order to clarify the nature of magnetic structure in phase IV, we further investigated neutron diffraction measurements on the single crystal $Ho^{11}B_2C_2$ using TOPAN (6G) spectrometer installed at JRR-3M, JAERI.

In Fig. 1, we show the magnetic scattering profiles around the reciprocal lattice point (1 0 0) at various temperatures. The temperature region where the (1+δ δ δ') satellite peaks appear corresponds to phase IV in zero field. The uniform scattering intensity is also observed in the phase IV, but it remains at the temperatures higher than T_N. The satellite peaks are broader than resolution, especially along the c^*-axis. The estimated correlation length along the c-axis is about between 11 and 14 Å. This indicates that phase IV is a short-range magnetic ordered state.

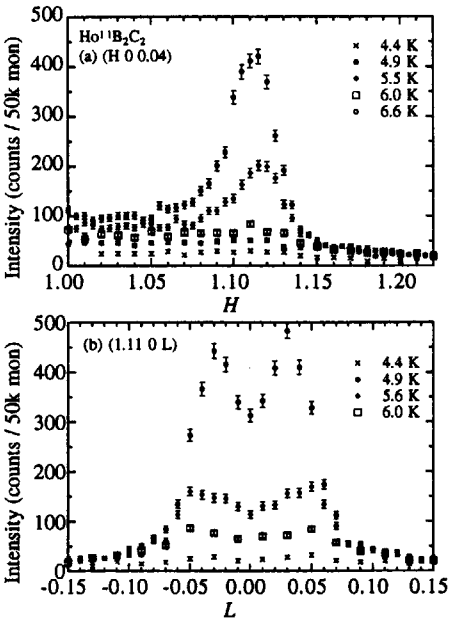


Fig. 1. Magnetic scattering profiles around the reciprocal lattice point (1 0 0) at various temperature of the single crystal $Ho^{11}B_2C_2$. (a) Profile along (H 0 0.04), and (b) along (1.11 0 L). In order to catch the satellite peaks, the vertical a-axis was tilted by 5.7°.

References

[1] H. Onodera *et al.*, J. Phys. Soc. Jpn. 68 (1999) 2426.
[2] H. Shimada *et al.*, J. Phys. Soc. Jpn. 70 (2001) 1705.
[3] K. Ohoyama *et al.*, J. Phys. Soc. Jpn. 69 (2000) 3401.

使用施設：JRR-3M，装置：TOPAN (6G)，分野：2 magnetism

研究テーマ：$U_3Pd_{20}Si_6$ における5f電子の局在性の研究
表題：$U_3Pd_{20}Si_6$ の磁気形状因子

1-2-16 Magnetic Form Factor of $U_3Pd_{20}Si_6$

H. Sagayama[1], K. Kuwahara[1], M. Kohgi[1], M. Nishi[2], K. Nakajima[2], N. Aso[2], Y. Koike[3], N. Metoki[3], N. Tateiwa[4], N. Kimura[5], H. Aoki[5]

[1]Department of Physics, Tokyo Metropolitan University, Hachioji, Tokyo 192-0397, Japan
[2]Insitute for Solid State Physics, University of Tokyo, Tokai, Ibaraki 319-1195, Japan
[3]Advanced Science Research Center, JAERI, Tokai, Ibaraki 319-1195, Japan
[4]Faculty of Engineering Science, Osaka University, Toyonaka, Osaka 860-8531, Japan
[5]Center for Low Temperature Science, Tohoku University, Sendai 980-8545, Japan

$U_3Pd_{20}Si_6$ crystallizes in a cubic crystal structure of space group Fm-3m[1], where U atoms occupy two different sites (4a and 8c). This structure is isomorphous as that of the rare earth compounds $R_3Pd_{20}X_6$ (R = rare earth, X = Si, Ge) which have been studied extensively due to their unique crystal structure where both of U-sites are under rather high cubic symmetry[2-4]. Macroscopic measurements shows that it undergoes successive phase transitions at T_N = 19 K and T_C = 2 K[1]. Neutron diffraction measurements revealed that U ions at 4a site order antiferromagnetically whereas those at 8c site are paramagnetic, and that latter ions order ferromagneitically below T_C[5]. Temperature dependences of magnetic susceptibility, specific heat and elastic constant indicate that the 5*f*-electron state of U atoms in this compound are well localized[1,6]. Actually, inelastic neutron scattering experiments revealed the existence of well-defined crystal field excitations[5,7] as well as spin wave excitations[5,8]. Currently, study of U-based metallic compounds is one of major subjects in the condensed matter physics because more than a few U-based materials show unusual properties such as unconventional super conductivity. However, 5*f*-electron state in these materials is less understood compared to those of 3*d* and 4*f* electrons in materials because of its intermediate nature between those of the 3*d*- and 4*f*-electron cases. Therefore, it is worthwhile to do a detailed study of the 5*f* electron state of $U_3Pd_{20}Si_6$ as an reference material since such typical localized electron behaviors are rather rare in U-based metallic compounds. We have performed a polarized neutron diffraction experiment on $U_3Pd_{20}Si_6$ to study magnetic form factor of the U atoms, which gives direct information on the 5*f*-electron state in this material.

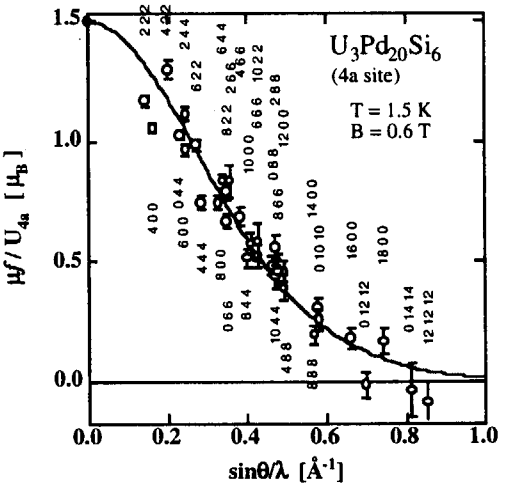


Fig. 1. The magnetic amplitudes μf of $U_3Pd_{20}Si_6$ as function of $\sin\theta/\lambda$. The solid and dashed lines represents the theoretical 5f form factor of free U^{3+} and U^{4+} respectively.

A single crystal sample of $U_3Pd_{20}Si_6$ (~4 x 2 x 0.5 mm^3) was placed in a superconducting split-coil magnet with [0 1 −1] axis vertical to the scattering plane. The experiment has been done with the triple-axis spectrometer

研究テーマ：$U_3Pd_{20}Si_6$ における5f電子の局在性の研究
表題：$U_3Pd_{20}Si_6$ の磁気形状因子

PONTA(5G) installed at JRR-3M reactor, JAERI. A polarized incident neutron beam with the wavelength of 1.015 Å produced by a Cu_2MnAl polarizer was used. The condition of the collimators is open-40'-sample-80'-open. The experiment was performed at 1.5 K where the 8c site U ions order ferromagnetically. A magnetic field of 0.6 T was applied along the [0 1 −1]-axis to make a single domain sample. Polarization of the incident beam was 0.93.

Fig. 1 depicts the magnetic amplitudes μf of U atom at 4a site of $U_3Pd_{20}Si_6$ as a function of $\sin\theta/\lambda$, where μ and f are magnetic moment and form factor, respectively. Here, we neglect the effect of the ferromagnetic component of U atoms at 8c site because they order antiferromagnetically and the induced moment is considered to be small. In Fig. 1, the calculated form factor of a U^{4+} free ion based on the dipole approximation is also shown by a solid line. Its value at $\sin\theta/\lambda = 0$ is normalized to the magnetization value per 4a site U atom. The observed form factor values are rather close to the free ion values as many of U-based metallic compounds including some unusual uranium compounds such as the heavy-electron superconductor UPt_3. However, it can be also seen that the data show some scattering around the calculated form factor. It may indicate an anisotropy of the 5*f*-electron distribution due to the crystal field.

Reference

1) N. Tateiwa *et al.*, J. Phys. Soc. Jpn. **69** (2000) 1517.
2) J. Kitagawa *et al.*, J. Alloy and compounds **247** (1997) 48.
3) A. Dönni *et al.*, J. Phys. Condens. Matter **19** (1998) 7219.
4) L. Keller *et al.*, Physica B **259-261** (1999)336.
5) N. Tateiwa *et al.*, J. Phys. Soc. Jpn. **70** (2001) 2425.
6) N. Tateiwa, Thesis, Tohoku Univ. 1998.
7) K. Kuwahara. *et al.*, **312-313** (2002) 899.
8) N. Aso *et al.*, **312-313** (2002) 897.

研究テーマ：重い電子系UGe_2の5f電子状態
表題：UGe_2における磁気形状因子の異方性

1-2-17 Anisotropy of Magnetic Form Factor in UGe_2

H. Sagayama[1], K. Kuwahara[1], K. Iwasa[1], M. Kohgi[1], M. Nishi[3], K. Nakajima[3], N. Aso[3], K. Kakurai[4], Y. Haga[4], Y. Onuki[2,4]

[1]Faculty of Science Tokyo Metropolitan University, Hachioji, Tokyo 192-0397, Japan
[2]Advanced Science Research Center, JAERI, Tokai, Ibaraki 319-1195, Japan
[3]Insitute for Solid State Physics, University of Tokyo, Tokai, Ibaraki 319-1195, Japan
[4]Faculty of Science Osaka University, Kashiwa, Chiba 277-8581, Japan

UGe_2 is a heavy-fermion ferromagnetic compound with a Curie temperature of 52 K[1,2]. Recently, superconductivity in a single crystal of this material was discovered by Saxena *et al.* under high pressure(~1.3 GPa)[3]. It crystallizes in the base-centered orthorhombic structure (Cmmm)[4,5]. The magnetization along the a-axis, which is the direction of easy axis, shows a spontaneous magnetic moment of $1.43\mu_B$/U, whereas the b- and the c-axis are hard directions for magnetization[1,2]. Thermal expansion and transport properties also show strong anisotropy[2,6]. We have already measured the magnetic form factors in the [0kl] plane at 2K (ferromagnetic phase) at ambient pressure and 1.4GPa by applying a magnetic field of 2 T along the [100] direction, namely the a-axis. They are similar to that of free ion U^{3+} and U^{4+}, and no anisotropy of the form factor was found at ambient pressure in the experimental error[10]. In order to obtain the information on the three dimensional extent of 5*f*-electrons in UGe_2, we have performed polarized neutron scattering experiments to measure the magnetic form factor in the [h0l] plane of the field induced moment of U atoms at 60K (paramagnetic phase) at ambient pressure by applying a magnetic field of 6 T along the [010] direction, namely the b-axis. This is because the b-axis is hard direction for magnetization and it is difficult to measure the magnetic form factor in the [h0l] plane in the ferromagnetic state.

The single crystal sample of UGe_2 used in the experiment is nearly parallelepiped with the shortest axis oriented to the c-axis (10 × ~3.5 × 0.5 mm^3). It was placed in a superconducting split-coil magnet with hard magnetization b-axis vertical to the scattering plane, and magnetic field was applied along the b-axis. The experiment has been done with the triple-axis spectrometer PONTA(5G) installed at JRR-3M reactor, JAERI. An incident neutron beam polarized along b-axis with the wavelength of 1.015 Å was produced by the Cu_2MnAl polarizer. A set of collimators of OPEN-80'-80'-OPEN (2-axis mode) was used.

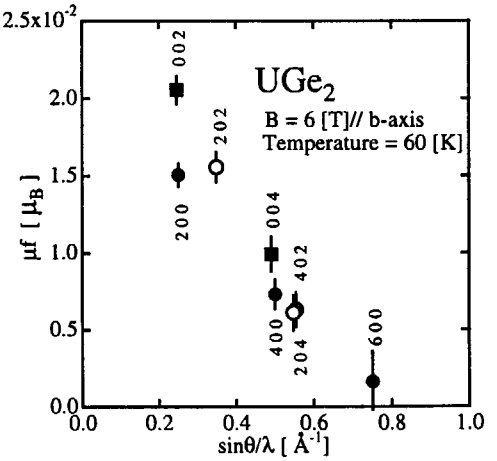


Fig. 1. The magnetic amplitudes μf of UGe_2 as function of $\sin\theta/\lambda$. The closed circles and squares denote the observed μf associated with scattering vector parallel to [100] and [001] direction, respectively. The open circles denote with the μf associated with the other scattering vectors.

JRR-3M, PONTA, 2.Magnetism

研究テーマ：重い電子系UGe_2の5f電子状態
表題：UGe_2における磁気形状因子の異方性

The analysis has done based on the assumption that the magnetization is localized on the uranium site. Figure 1 shows the magnetic amplitude μf of UGe_2 as a function of $\sin\theta/\lambda$, where μ and f are magnetic moment and the magnetic form factor of 5*f*-electrons, respectively. It can be seen that there is a large anisotropy of magnetic form factor in UGe_2. The μf is more expanded along the [100] direction than along [001]. The observed anisotropy of μf may imply that the density of 5f-electrons in UGe_2 is elongated along the a-axis. In order to clarify the state of 5f-electron in UGe_2 more accuracy, further experiments and analysis are necessary.

Reference

1) A. Menovsky *et al.*: in *High magnetic Field in High Field Magnetism*, edited by M. Date (North-Holland Publishing Company, 1983)
2) Y. Onuki *et al.* : J. Phys. Soc. Jpn. **61** (1992) 293.
3) S. S. Saxena *et al.* : Nature **406** (2000) 587.
4) K. Oikawa *et al.*: J. Phys. Soc. Jpn. **65** (1996) 3229.
5) P. Boulet *et al.*: J. Alloy and compounds **247** (1997) 104
6) G. Oomi *et al.* : Physica B 186-188 (1993) 758-760.
7) K. Satou *et al.* : J. Phys. Soc. Jpn. **61** (1992) 1827.
8) Y. Onuki *et al.* : J. Phys. Soc. Jpn. **60** (1991) 2127.
9) A. B. Shick *et al.* : Phys. Rev. Lett. **86** (2001) 300.
10) H. Sagayama *et al.* : J. Phys. Soc. Jpn. **70** Suppl. A (2001) 28.
11) K. Kuwahara *et al.* : Physica B **312-313** (2002) 28 106-108

1-2-18

研究テーマ:希土類マンガン酸化物 RMn_2O_5 の磁気構造解析
表題: 強誘電-反強磁性体 YMn_2O_5 単結晶の中性子散乱

Neutron Scattering of Ferroelectric-antiferromagnetic YMn_2O_5 Single Crystal

I. Kagomiya[1], Y. Fukuda, H. Kimura and Y. Noda and K. Kohn[1]
[1]*Department of Physics, Waseda University, Shinjyuku-ku, Tokyo 169-8555, Japan,*
Institute of Multidisciplinary Research for Advanced Materials, Tohoku University,
Aoba-ku, Sendai 980-8577, Japan

Rare earth manganese oxides RMn_2O_5(R=Sm-Lu, Y or Bi) are ferroelectric below T_{CE}=～40 K, where a spontaneous polarization appears along *b*-direction of orthorhombic structure (*Pbam*). The origin of the ferroelectricity is presumably related to the magnetic long-range order reported in these oxides. In support to this, the ferroelectric Curie temperature T_{CE} (25-39 K) is close to the antiferromagnetic Néel temperature of the Mn^{3+} and Mn^{4+} moments (about 45 K).

We are trying to confirm a conjecture that the ferroelectric spontaneous polarization is induced by the magnetic long-range order. In our previous neutron scattering measurement, the magnetic structure of YMn_2O_5 changes at T_{CE}=39 K from incommensurate (1/2-δ 0 1/4) to commensurate (1/2 0 1/4) with respect to the lattice period.[1] The aim of this study is to know the details of both the crystal and the magnetic structures.

Neutron diffraction measurement of YMn_2O_5 was performed by a 4-circle diffractometer (FONDER) installed in the guide hall of the JRR3M at JAERI. Nuclear Bragg reflections were collected at 25 K and 48 K, and magnetic Bragg reflections at 25 K. The condition of the measurement is tabulated in Table I.

No lattice distortion was observed in the nuclear Bragg reflections at 25 K. Parameters of the crystal structure at 25 K and 48 K can be refined as *Pbam*. The estimated *R*-factors were 4.53 % and 4.81 %, respectively.

Magnetic structure is estimated by refining spin components of 16 manganese ions in the magnetic unit cell. The possible model of the magnetic structure is shown in Fig. 1. This model is obtained on the assumption that there are only the x components of the spins.

Table I: numbers and reciprocal range of the collected reflections.

	25 K magnetic	25 K nuclear	48 K nuclear
numbers	498	298	325
h	0～8.5	0～8	0～8
k	0～10	0～10	0～10
l	0～5	0～4	0～5

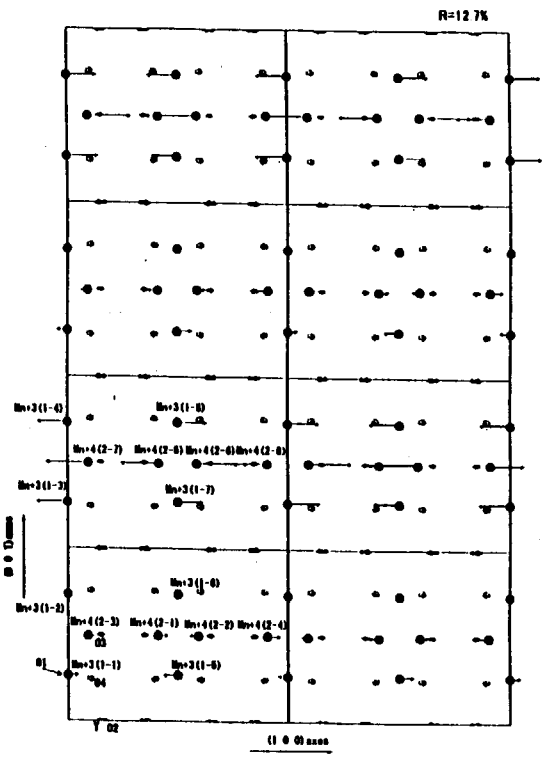


Fig. 1 The possible magnetic structure of YMn_2O_5

Reference

[1] I. Kagomiya, H. Kimura, Y. Noda and K. Kohn: J. Phys. Soc. Jpn. **70** (2001) Suppl. A pp.145-147.

使用施設: JRR3M, 装置: FONDER, 分野: 2. Magnetism

研究テーマ：二次元変調構造をもつ $TbRu_2Ge_2$ のメタ磁性
表題：二次元変調構造をもつ $TbRu_2Ge_2$ のメタ磁性

1-2-19 Metamagnetism of $TbRu_2Ge_2$ with a two-dimensional modulated magnetic structure.

T. Shigeoka, S. Kawano[1], M. Takahashi[2] and M. Nishi[3]

Faculty of Science, Yamaguchi University, Yamaguchi, 753-8512, Japan

[1]Reearch Reactor Institute, Kyoto University, Kumatori, Osaka 590-0494, Japan

Institute of Materials Science, University of Tsukuba, Tsukuba, 305-8573, Japan

[3]Institute for Solid State Science, University of Tokyo, Chiba, 277-8581, Japan

The ternary compound $TbRu_2Ge_2$ with the tetragonal $ThCr_2Si_2$-type structure orders antiferromagnetically below T_N=37 K. The antiferromagnetic structure has been reported to be a one-dimensional long period modulation with the propagation vector Q=(0.233, 0, 0) [1]. Recently, however, pulsed neutron study showed that it becomes a two-dimensional square-wave modulation at low temperatures [2]. The compound shows a multi-step (at least 6-step) metamagnetic process along the c-axis at low temperatures. This process had been explained on the basis of a one-dimensional model [3]. It should be, however, explained by a two-dimensional model. Neutron diffraction study under magnetic fields on a $TbRu_2Ge_2$ single crystal compound has been carried out to determine magnetic structures of field-induced magnetic phases. The experiments have been performed on the triple-axis spectrometer PONTA installed at JRR-3M in JAERI, Tokai. The single crystal was mounted in a cryomagnetic system so that the c-axis was vertically oriented to make scan in the a*-b* reciprocal plane. Magnetic fields were applied up to 2.2 T along the c-axis and temperature was down to 1.6K

Figure 1 shows the neutron diffraction patterns scanned along the low symmetry line, (1-τ, k, 0) (τ=0.7647) under various magnetic fields. Many magnetic satellites are seen under all magnetic fields, which can be indexed by the fundamental period τ, such as (1- τ, n τ, 0) (n=integer). Along the symmetry lines such as the (1, k, 0) line, many magnetic satellites are also observed such as (1, nτ, 0). This fact indicates that field-induced magnetic structures are two-dimensional ones. Detail analysis is now in progress.

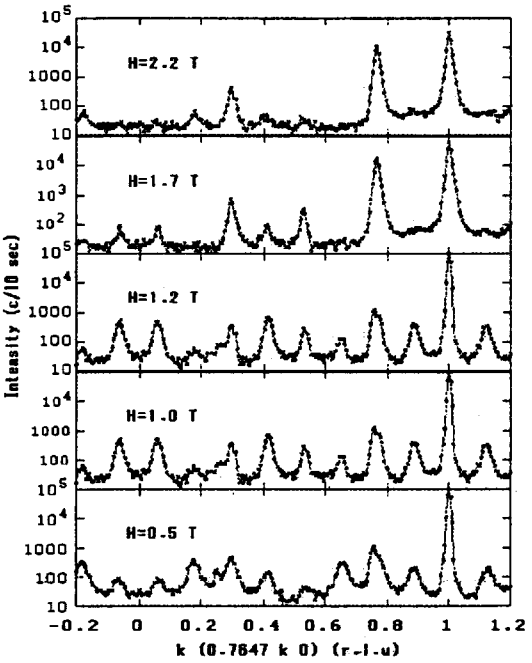


Fig. 1 Neutron diffraction patterns along the low symmetry line of the (1-τ, k, 0) (τ=0.7647) at 1.6 K under various magnetic fields on a $TbRu_2Ge_2$ single crystal.

References

[1] T. Shigeoka et. al., Physica B 237-238 (1997) 572.

[2] S. Kawano et. al., J. Phys. Soc. Jpn., 70 (2001) Suppl. A 0 9 .

[3] A. Garnier et. al., Phys. Rev. B 57(1998) 5235.

JRR-3M, PONTA （5 G）, 2. Magnetism

研究テーマ：強相関5f電子化合物の異常磁性
表題：強相関5f電子系URu_2Si_2の異常磁性

Unusual Magnetism in the Strongly Correlated 5f-Electron System 1-2-20 URu_2Si_2

H. Amitsuka[1], M. Yokoyama[1], J. Nozaki[1], S. Itoh[1], K. Watanabe[2], S. Kawarazaki[2], H. Yoshizawa[3], and J.A. Mydosh[4]

[1]*Graduate School of Science, Hokkaido University, Sapporo 060-0810, Japan*
[2]*Graduate School of Science, Osaka University, Toyonaka 560-0043, Japan*
[3]*Neutron Scattering Laboratory, ISSP, University of Tokyo, Tokai 319-1106, Japan*
[4]*Kamerlingh Onnes Laboratory, Leiden University, 2300 RA Leiden, The Netherlands*

The heavy-electron superconductor URu_2Si_2 has attracted particular interest for its curious, second-order, phase transition at 17.5 K ($\equiv T_o$) [1], where antiferromagnetic (AF) order with an extremely small ordered moment ($\mu_{ord} = 0.03 \pm 0.01$ μ_B/U) is observed [2]. Recent experiments of neutron scattering [3] and ^{29}Si NMR [4] performed under hydrostatic pressure have revealed that inhomogeneous AF order with a normal size of moment ($\mu_{ord} \simeq 0.25$ μ_B/U) is induced by pressure P, at least, in the range 0.3 – 0.83 GPa. Simple extrapolation to ambient pressure strongly suggests that the tiny AF moment is ascribed to 1 % volume fraction of this AF phase. The true nature of the 17.5 K transition is thus attributed to an unidentified, nonmagnetically ordered phase which occupies the rest 99 % of the crystal. In order to clarify the nature of this unusual two-phase competition, we have embark upon the study of uniaxial stress effects [5].

The single crystalline URu_2Si_2 was prepared in a tri-arc furnace using the Czochralski technique, and annealed in an evacuated sealed quartz tube at 1000 °C for one week. The crystal was shaped into a plate (5 × 5 × 1 mm ^{3}) with (110) basal planes. The uniaxial stress σ was applied by means of a top-loading type of piston device installed in a ^{4}He cryostat. The elastic neutron scattering measurements were performed on the triple axis spectrometer GPTAS(4G) at the JRR-3M reactor, by using neutrons with momentum of 2.660 Å^{-1}. Double PG(002) filters and 40'-80'-40'-80' horizontal collimation were adopted.

Figure 1 shows the σ dependence of μ_{ord} obtained from the (111) magnetic Bragg reflections at 1.4 K. For zero-stress cooled process, we found the $\mu_{ord}(\sigma)$ curve showing a clear hysteresis loop. Considering the previous results of NMR [4], μ_{ord} measures not the true moment value but the AF volume fraction. The observed hysteresis thus indicates that the process of the AF volume evolution is irreversible; i.e., the AF phase is metastable and separated from the hidden order by a first order phase transition.

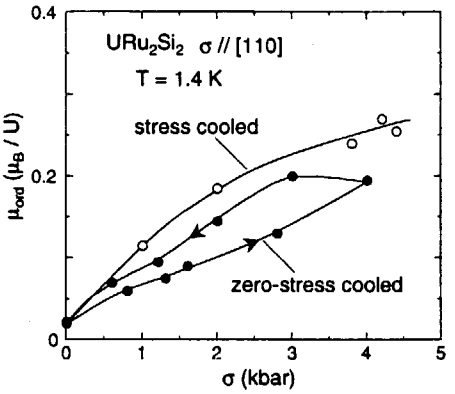


Fig. 1 Uniaxial-stress dependence of the volume-averaged AF staggered moment of URu_2Si_2.

References

[1] T.T.M. Palstra *et al.*, Phys. Rev. Lett. **55** (1985) 2727; W. Schlabitz *et al.*, Z. Phys. B **62** (1986) 171; M.B. Maple *et al.*, Phys. Rev. Lett. **56** (1986) 185..
[2] C. Broholm *et al.*, Phys. Rev. Lett. **58** (1987) 1467.
[3] H. Amitsuka *et al.*, Phys. Rev. Lett. **83** (1999) 5114; J. Phys. Soc. Jpn. **69** (2000) suppl. A. 5.
[4] K. Matsuda *et al.*, Phys. Rev. Lett. **87** (2001) 87203.
[5] M. Yokoyama *et al.*, J. Phys. Soc. Jpn. **71** (2002) suppl. 264.

使用施設：JRR-3M, 装置：GPTAS:(4G), 分野：2. Magnetism

研究テーマ：幾何学的三角格子フラストレーションが部分的に解けた Ising 反強磁性体におけるドメインキネティックス

表題：二等辺三角格子反強磁性体 CoNb2O6 におけるドメイン形成過程の不純物効果

Non-magnetic impurity effect on domain growth kinetics in isosceles triangular antiferromagnet $CoNb_2O_6$

1-2-21

H. Okano, S. Mitsuda, M. Kumagai, S. Kobayashi[1]

Department of Physics, Tokyo University of Science, Kagurazaka, Shinjuku-ku, Tokyo, 162-8601

[1]*Satellite Venture Business Laboratory, Gunma University, Tenjin-cho, Kiryu-shi, Gunma, 376-8515*

As one of model materials of triangular lattice antiferromagnet with a partially released geometrical frustration, recently we have studied an isosceles triangular Ising antiferromagnet $CoNb_2O_6$. The system exhibits slow domain-growth-kinetics that time evolution of the correlation length is well fitted to power law with anomalously low growth exponent $n \cong 0.2$ in the antiferromagnetic (AF) phase [1]. To investigate how domain-growth-kinetics characteristic to the isosceles-triangular geometry of frustrated spins in $CoNb_2O_6$ is modified on substitution of a small amount of Mg^{2+} none-magnetic impurities, we have studied $Co_{1-x}Mg_xNb_2O_6$ sample with $x = 0.01$. It turned out that as a result of strong suppression of domain-growth-kinetics, 1 % substitution of none-magnetic impurities prevents system from AF ordering and serves apparent incommensurate state down to the temperature of $T = 0.2$ K, in which thermodynamically equivalent four types of AF domain arrange quasi-regularly along the b axis with phase shift of $\pi/2$ [2]. These suggest that 1 % substitution of none-magnetic impurities is too much to study impurity effects on domain-growth-kinetics. Therefore, as a next step we performed further neutron scattering experiments at GPTAS(4G) and HER(C1-1), choosing the sample with $x = 0.005$, which seems to be suitable to study none-magnetic impurity effects on domain-growth-kinetics.

In Fig. 1, we show the time evolution of the correlation length along the a axis ($\xi_a(t)$) and the b axis ($\xi_b(t)$), obtained from the (h 1/2 0) and (3 k 0) transverse scans, respectively. As was in the sample with $x = 0.00$, both $\xi_a(t)$ and $\xi_b(t)$ are fitted to the power law with growth exponent $n \cong 0.2$ and ac susceptibility reflecting the number of spins on domain wall also shows power law decay with $n \cong -0.2$. As is clearly seen in Fig. 1, $\xi_a(t)$ is not affected by none-magnetic impurities, whereas $\xi_b(t)$ is strongly suppressed by only 0.5 % substitution of none-magnetic impurities, as applied magnetic field does for the sample with $x = 0.00$. These findings indicate that a small amount of none-magnetic impurities suppress domain-growth-kinetics not in the a direction but in the b direction. Experimentally observed anisotropic suppression of domain-growth-kinetics due to none-magnetic impurities was confirmed by our Monte Carlo simulation with cluster heat bath method, and can be explained by estimating activation energy of domain wall as anisotropic suppression by external magnetic field was explained for the sample with x=0.00.

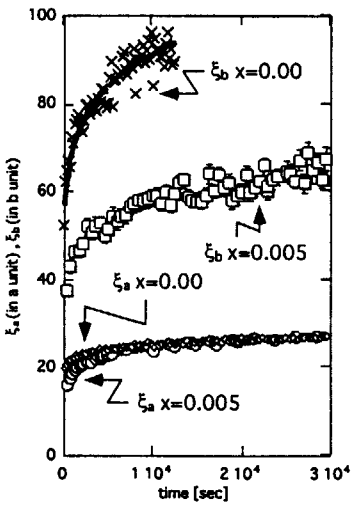


Fig. 1 Time evolution of $\xi_a(t)$ and $\xi_b(t)$ at $T = 1.5$ K under zero magnetic field.

References

[1] S. Kobayasehi, S. Mitsuda, T. Jogetsu, J. Miyamoto, H. Katagiri, and K. Kohn, Phys. Rev. B **60**, R9908 (1999).

[2] H. Okano, S. Mitsuda, K. Prokes, BENSC experimental reports (2001)

使用施設：JRR-3M, 装置：GPTAS(4G),HER(C1-1), 分野：2

研究テーマ：強磁性と反強磁性相互作用の共存する Fe, Mn 合金
表題：$(Mn_{1-x}Ru_x)_3Ga$ 合金の中性子散乱による研究

1-2-22 Neutron Diffraction Study on Mn_2RuGa Alloy

T. Hori[1], K, Ohoyoama[2] and Y. Yamaguchi[2]
[1]*Shibaura Institute of Technology*
[2]*IMR, Tohoku University*

We have found that Mn_2RuGa alloy have an ordered b.c.c. structure; the Curie temperature and saturation magnetization are 450 K and 23 emu/g (= 1.15 μ_B per a chemical fotmula) at 4.2 K, respectively. We have made neutron diffraction experiments for powdered Mn_2RuGa alloy at temperature between 10 K and 500 K by using HERMES. For analysis of neutron data, we have assumed 4 sites in a unit cell and these atomic coordinates are as follows: 4a (0, 0, 0), 4b (1/2, 1/2, 1/2), 4c (1/4,1/4,1/4) and 4d (3/4, 3/4, 3/4). When we assume each site being occupied by different kind of atoms, three kinds of atomic structure factors are easily obtained;

$F = 4[f_a - f_b \pm i(f_c - f_d)]$ for h,k,l all odd,

$F = 4(f_a + f_b - f_c - f_d)$ for $(h+k+l)/2$ odd,

$F = 4(f_a + f_b + f_c + f_d)$ for $(h+k+l)/2$ even,

where f_a, f_b, f_c and f_d are nuclear scattering amplitude of atoms on each site. Unfortunately, nuclear scattering amplitude of Ga and Ru atoms are nearly equal. Therefore we cannot distinguish Ga and Ru. Scattering amplitude $b_{Mn} = -0.373$, $b_{Ga} = 0.729$ and $b_{Ru} = 0.722$ in 10^{-12} cm are used in the Rietveld analysis.

Fig. 1 shows observed neutron diffraction pattern for Mn_2RuGa ($x = 0.33$) alloy at 480 K ($> T_C$). It is remarkable that the 200 line is absent in the observed diffraction pattern. This result suggests that Mn atom occupies mainly the 4a and 4d sites, and Ga and Ru the 4b and 4c sites. We assumed a fictitious atom with the average neutron scattering amplitude of Ga and Ru atom, and analyzed by the Rietveld refinement.The site occupancy obtained by the analysis are shown in Table 1.

We have made neutron diffraction experiments under a magnetic field for the Mn_2RuGa alloy using KSD diffractometer. The field was applied parallel to scattering vector. The 111 and 200 intensities decrease with applied field. It is suggested that the alloy has a collinear ferrimagnetic structure. For detailed analysis of neutron diffraction data, we assumed that magnetic moment μ_a is plus, μ_c and μ_d are minus direction, and $\mu_b = 0$ because the occupancy of Mn atom in the 4b site is little, where μ_a, μ_b, μ_c and μ_d are the average magnetic moments per atom for the 4a, 4b, 4c and 4d sites, respectively. We easily determined values of the magnetic moments of Mn atoms for each site, and obtained that $\mu_a = 4.15\mu_B$ (it means 4.6 μ_B/Mn atom), $\mu_c = 0.63\mu_B$(1.9μ_B/ Mn atom) and $\mu_d = 2.37\mu_B$(3.3μ_B/ Mn atom) at 10 K.

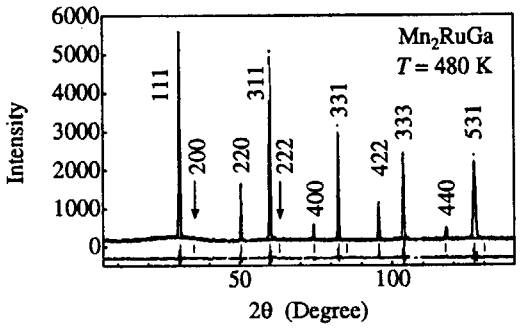


Fig. 1. Observed (+) and calculated (a line) neutron diffraction patterns for Mn_2RuGa alloy at 480 K. The difference between the observed and calculated intensities is shown by the lower curve.

Table 1. The site occupation for the Mn_2RuGa alloy from obtained by Rietveld analysis.

Mn_2RuGa		
site	Mn	Ru/Ga
4a	0.900	0.100
4b	0.049	0.951
4c	0.334	0.666
4d	0.717	0.283

使用施設：JRR-3M，装置：HERMES(T1-3) and KSD(T1-2)，分野：2. Magnetism

研究テーマ：三元系 Ni_2In 型金属間化合物の磁性
表題：$(Mn_{1-x}Pd_x)_2Ga$ の磁性と中性子散乱による研究

1-2-23 Magnetic and Neutron Diffraction Study on $(Mn_{1-x}Pd_x)_2Ga$

H. Shiraishi, T. Hori, K. Ohoyama[a], Y. Yamaguchi[a]
Shibaura Institute of Technology
[a]*IMR, Tohoku University*

New pseudo binary intermetallic compounds $(Mn_{1-x}Pd_x)_2Ga$ of Ni_2In ($B8_2$) type structure are found in the range of $0.3 \leq x \leq 0.6$. Magnetization at $T = 4.2$ K and $H = 9.5$ k0e increases with increasing x up to $x = 0.5$ and it reaches maximum value of 70 emu/g. In the higher x range $x \geq 0.5$, the magnetization decreases with increasing x. The x dependence of Curie temperature changes in the similar mannar with x dependence of magnetization but shows a minimum at $x = 0.35$. The temperature dependence of magnetization σ shows a concave in the all range of x. For example, the $\sigma - T$ curve for $x = 0.4$ is shown in the Fig. 1.

We have carried out the neutron diffraction experiments to determine the magnetic structure of $(Mn_{1-x}Pd_x)_2Ga$ with $x = 0.4$ using HERMES installed in the JRR-3M in JAERI. The atom arrangement corresponding to minimum values of disagreement factor R is as follows: in the Ni_2In type structure,

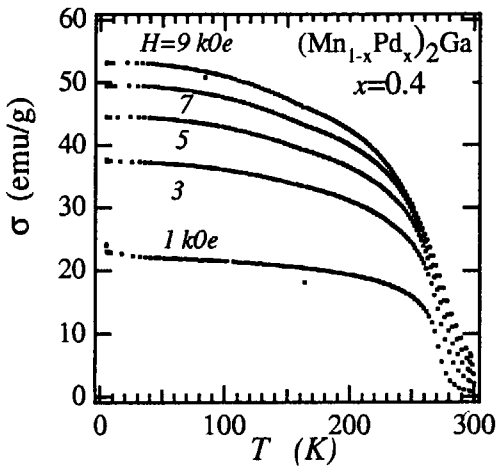


Fig. 1. The $\sigma - T$ curve at several magnetic field for $x = 0.4$.

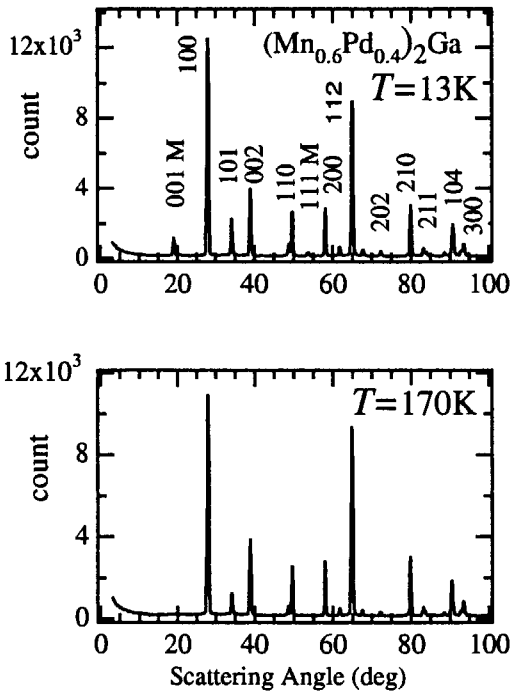


Fig. 2. Neutron diffraction patterns at temperature 13 K and 170 K for $x = 0.4$.

the 2(a) site is entirely occupied by Mn, the 2(d) site by Pd and residual Mn randomly and 2(c) site by Ga. A preferred occupation of Pd on the 2(d) site is observed. We observed the neutron diffraction patterns for $x = 0.4$ at several temperatures. Fig. 2 shows a part of the diffraction patterns for $x = 0.4$ in the low Bragg angle region at $T = 13$ K and 170 K. In the patterns at $T < 170$ K, the (001) and (111) magnetic reflection is observed, indicating the presence of antiferromagnetic component lying in the basal plane. The detailed analysis is now in progress.

使用施設：JRR-3M，装置：HERMES(T1-3) and KSD(T1-2)，分野：2. Magnetism

研究テーマ：GdB_2C_2およびSmB_2C_2の磁気構造の研究
表題：中性子回折によるGdB_2C_2の磁気構造の研究

1-2-24

Neutron diffraction study on the magnetic structure of GdB_2C_2

Y. Yamaguchi, K. Ohoyama, H. Yamauchi, K. Indoh, H. Onodera
Institute for Materials Research, Tohoku University, Sendai 980-8577, Japan

There are two purposes in this study. One is to see performance of our powder neutron diffractometer, HERMES[1], for very heavy neutron absorber, GdB_2C_2. The other is to see the magnetic structure of
GdB_2C_2 as a compound of tetragonal RB_2C_2 family in which antiferroquadrupolar and magnetic interactions compete.

Tetragonal RB_2C_2 compounds are known as in which antiferroquadrupolar(AFQ) interaction is very strong. For example, AFQ ordering temperature of DyB_2C_2 is 24.7K about one order higher than other type of AFQ ordering compounds[2]. The magnetic unit cell below the Neel temperature, 15.3K, is two times large compared with the chemical one along the c-axis, and two rare earth layers are in it perpendicular to the c-axis. The magnetic moments lie in the c-plane, and the direction oscillates as 0-70-0-70 degrees along the c-axis. This structure is considered to come from competing of AFQ and antiferromagnetic(AFM) interactions. In order to study quadrupolar interaction in these compounds, we wanted to know the magnetic structure due to purely magnetic interaction, and chose GdB_2C_2 in the present study, because Gd has no quadrupolar moment and the interaction is purely magnetic.

Magnetic structures of Gd compounds are very hard to study because of heavy absorption of neutrons by Gd atoms. Absorption cross section for 1 A neutrons is tremendous for Gd as it being 44890 barns. The size is about 64 times larger than B and 20 times larger than Cd. So usually we have to use an isotope for neutron scattering experiment though it is very expensive. But it is true that when we use a very high efficient diffractometer and reflection geometry we can obtain diffraction patterns even for very heavy absorber. Therefore in the present study we try to obtain data of GdB_2C_2 using natural Gd for neutron diffraction experiment by the HERMES diffractometer.

In the present experiment a powder sample of GdB_2C_2 was pasted on an aluminum plate using epoxy resin. And

使用施設：JRR-3M、装置：HERMES(T1-3)、分野：磁性

reflection geometry of the sample plate was used with a fixed inclination angle of 20 degrees to the incident beam direction. Diffraction data were taken by step scanning of counter bank with a stepping angle of 0.1 degrees.

Temperature dependence of the magnetic susceptibility measured on a single crystal of GdB_2C_2 shows that it is antiferromagnetic with T_N=46.5K and the magnetic moments are in the c-direction[3].

Neutron diffraction patterns obtained for GdB_2C_2 at 2.2K and 60K as shown in Fig.1. We can see magnetic peaks of 101, 210 and 211. There should be 100 magnetic peak around 19, degrees but it was cut by the sample itself because sample inclination angle is 20 degrees. Intensities of 001 and 002 reflections are emphasized because preferred orientation exists as the c-plane being parallel to the sample plate. We concluded that the simple magnetic structure shown in Fig.2 is realized in GdB_2C_2 which comes from purely magnetic interaction, and this is the fundamental feature of the magnetic interaction in the RB_2C_2 family at least for medium members of rare earth ions except for the end members, CeB_2C_2 and TmB_2C_2[4].

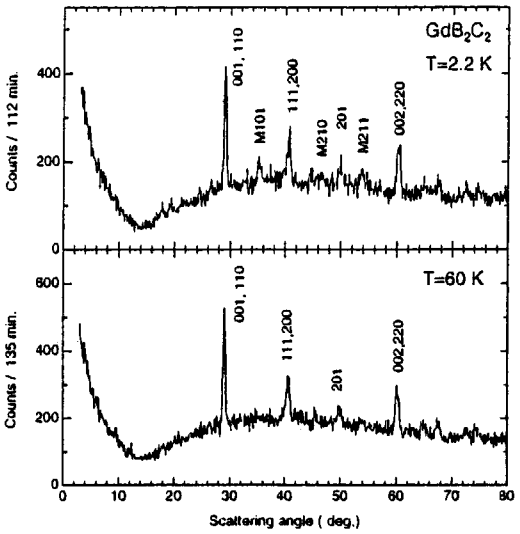


Fig. 1. Neutron diffraction patterns of GdB_2C_2 obtained on HERMES at 2.2K(upper) and 60K(lower).

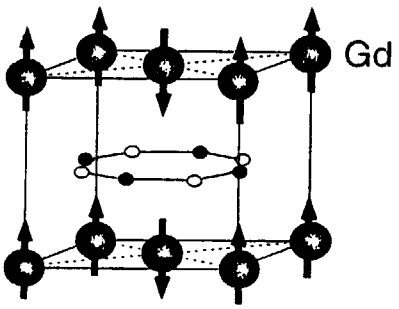


Fig. 2. Magnetic structure of GdB_2C_2 below T_N with k=(100). The octagon with black and white circles is B-C layer.

References

[1] K. Ohoyama et al., Jpn. J. Appl. Phys. 37 (1998) 3319.

[2] H. Yamauchi et al., J. Phys. Soc. Jpn. 68 (1999) 2057.

[3] Y. Yamaguchi et al., J. Appl. Phys. A (in press).

[4] K. Ohoyama et al., J. Phys. Sopc. Jpn. Suppl. A 70 (2001) 121.

研究テーマ：β-$Na_{0.33}V_2O_5$の磁気構造
表題：β-Na0.33V2O5 の低温磁気構造（Ⅰ）

1-2-25

Magnetic Structure of β-$Na_{0.33}V_2O_5$ at Low Temperature(Ⅰ)

S. Nagai[1], M. Nishi[1], K. Nakajima[1], Y. Fujii[1], K. Kakurai[2], T. Yamauchi[3], J. Yamaura[3], M. Isobe[3], Y. Ueda[3]

[1]*Neutron Scattering Lab., ISSP, University of Tokyo, 106 Shirakata, Tokai, Ibaraki, 319-1106*

[2]*Advanced Science Research Center, JAERI, Tokai, Ibaraki 319-1195*

[3]*Materials Design and Characterization Lab., ISSP, University of Tokyo, 5-1-5 Kashiwanoha, Kashiwa, Chiba, 277-8581*

β-$Na_{0.33}V_2O_5$ is a mixed valence systems of V^{4+}(S=1) and V^{5+}(S=0) with the mole ratio V^{4+}: V^{5+}=1:5. It undergoes structural phase transition at 136 K accompanied by charge ordering, and magnetic long range ordering phase transtision at T_N=24 K[1]. In Fig. 1(a), the crystal structure is shown. It belongs to the monoclinic (β=109.6°) system and has the C2/m symmetry at room temperature. The extinction rule of magnetic Bragg reflection requires the position of the magnetic moments to choose C-face centered lattice, as shown in Fig. 1(b), where the lattice unit along b axis is taken to be 6b in accordance with the observed propagation vector of 1/6b* as in the magnetic Bragg peaks at (h, k+-1/6,l) h+k=odd. The purpose of the present study is to get information of the direction of magnetic moments on the linear chain vanadium sites, where the conjecture is examined that there exists an easy axis lying in ac plane.

Experimental

We performed polarization analysis measurement with β- $Na_{0.33}V_2O_5$ single crystal with the size of 8×5×3 mm^3 on the triple axis spectrometer ISSP PONTA, installed at the 5G beam port in the JRR-3M reactor hall. The wavelength was chosen to be 2.67 (Å) using PG(002) monochromator. Collimations of open, 80', 80', open were chosen in order from upper stream, and PG filter were inserted before the monochromator to suppress the contamination of higher order wavelength beam. A He-gas closed type cryostat were used to achieve 7 K at the lowest. The scattering plane was chosen to be (hk0), and a Helmholtz coil was mounted around the sample table to provide horizontal(**P//Q**) or vertical field(**P⊥Q**), **Q** being the scattering vector at the sample position. The degree of polarization of the incident beam was 95 % for horizontal field and 97 % for vertical field, which were estimated from the measurement of nuclear fundamental reflections at (600) and (020), respectively.

Result

In Table.1, the depolarization corrected peak intensities of (0, 5/6, 0) Bragg reflection are summarized. The intensity with **P//Q** configuration is almost purely SF and shows that this reflection is of magnetic origin. The small, but finite, NSF intensity is probably due to the imperfect parallelity of **P** and **Q** in the experiment. And the intensity from SF process decreases when the configuration is changed to **P⊥Q**, and the intensity is found in the NSF process. This is the c-component of magnetic moment modulated with the period of 6b. This c-component amounts to about 20 % of the moment parallel to **a'**, which is seen in the SF intensity in **P⊥Q** configuration. This support the conjecture that the magnetic moments on the linear chain site have an easy axis in ac plane, and the newly obtained information is that this axis is directed at an angle of 20±2° from **a'** axis, the axis in the ac plane and perpendicular to the **c** axis, as shown in Fig.2.

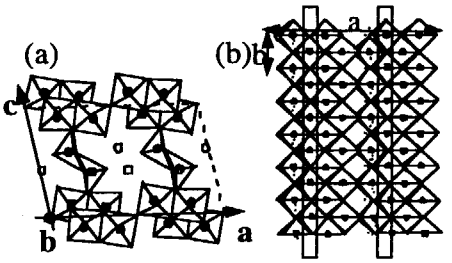


Fig. 1(a); The crystal structure of β - $Na_{0.33}V_2O_5$. (b); The spatial correlation of the positions of magnetic moments having C-face centered symmetry.

	NSF (cnts/sec)	SF (cnts/sec)
P//Q	0.029(0.006)	0.45(0.01)
P⊥Q	0.088(0.007)	0.36(0.01)

Table. 1; Depolarization corrected peak intensities at (0, 5/6, 0) Bragg reflection.

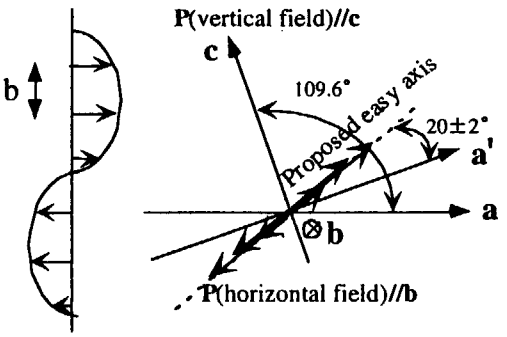


Fig. 2; The direction of the easy axis lying in ac plane.

[1] H. Yamada and Y. Ueda: J. Phys. Soc. Jpn. **68** (1999) 2735.

使用施設：JRR-3M, 装置：5G (ISSP PONTA), 分野：磁性

研究テーマ：β-$Na_{0.33}V_2O_5$の磁気構造
表題：β-$Na_{0.33}V_2O_5$の低温磁気構造（Ⅱ）

1-2-26
Magnetic Structure of β-$Na_{0.33}V_2O_5$ at Low Temperature(Ⅱ)

S. Nagai[1], M. Nishi[1], Y. Fujii[1], K. Kakurai[2], T. Yamauchi[3], J. Yamaura[3], M. Isobe[3], Y. Ueda[3], H. Kimura[4], Y. Noda[4]

[1]*Neutron Scattering Lab., ISSP, University of Tokyo, 106 Shirakata, Tokai, Ibaraki, 319-1106*

[2]*Advanced Science Research Center, JAERI, Tokai, Ibaraki 319-1195*

[3]*Materials Design and Characterization Lab., ISSP, University of Tokyo, 5-1-5 Kashiwanoha, Kashiwa, Chiba, 277-8581*

[4]*Institute of Multidisciplinary Research for Advanced Materials, Tohoku University, Aoba-ku, Sendai 980-8577*

β-$Na_{0.33}V_2O_5$ is a compound belonging to the beta-vanadium oxide familiy, expressed as β-$A_xV_2O_5$ (A=Li, Na, Ag, Ca, Sr, etc.). In these compounds (we often call them "beta-vanadate"), metallic atoms can crystallize as monovalent or divalent cation between the V_2O_5 layers with a wide composition range of x[1]. A systematic study varying the concentration of cations revealed that in the case of A = Li, Na, Ag, phase transition ralated to a magnetic long range ordering commonly takes place at x = 0.33[2]. The purpose of the present study is the determination of the magnetic structure of β-$Na_{0.33}V_2O_5$, which will lead to comprehensive understanding of the transport property of β-vanadates from microscopic view point.

Experimental

Based on the extinction rule of the magnetic Bragg reflections in (hk0) plane previously revealed in the 2000 fiscal year on ISSP PONTA, we performed diffraction experiment with β-$Na_{0.33}V_2O_5$ single crystal on the four axis diffractometer FONDER, installed at the T2-2 beam port on the T2 thermal neutron guide tube. The size of the sample was 8×5×3 mm^3. The wavelength was chosen to be 1.5729 (Å) using Si(422) monochromator. The $\lambda/2$ contamination was about 1.2 %, which was estimated by comparing the observed (010) reflection (absent position) with fundamental (020) reflection. With the aid of a He-gas closed type cryostat, we gathered magnetic Bragg reflections at 8 K, well below the magnetic ordering temperature 24 K.

Result

One of the important results we obtained was an information related to the easy axis of the antiferromagnetic spin ordering. When the collinearity of the magnetic structure is assumed as has been suggested by the polarized neutron diffraction experiment on PONTA, the orientation factor expressed as $\kappa \times (S \times \kappa)$ remains outside the phase part of the structure factor, so we can determine the direction of the easy axis by comparing intensities from equivalent magnetic Bragg reflections with different scattering vector Q. As the polarized neutron analysis measurement performed on ISSP PONTA left a question about the sign of the angle 20(+-2) ° between the easy axis and a' axis, which is the axis in the ac plane directed perpendicular to the c axis, magnetic reflections at such Q with nonzero component of both h and l need to be observed. In Fig. 1(a), the reflections from (3, 1/6, 1) and (3, 1/6, -1) are shown, where the signal from the former reflection is smaller than the statistical error of the back-ground while that from the latter is clearly seen. On the other hand, the angle between a' axis and the projection of the scattering vector (3, 1/6, 1) on the ac plane is 22.3° , and the angle between a' axis and the projection of (3, 1/6, -1) is 30.1° as shown in Fig. 1(b). So if we assume the easy axis is directed at an angle of 15° from a' axis in counterclockwise manner, it leads to the smaller value of $\kappa \times (S \times \kappa)$ with $\kappa // (3, 1/6, 1)$, thus the weaker signal at (3, 1/6, 1) is explained.

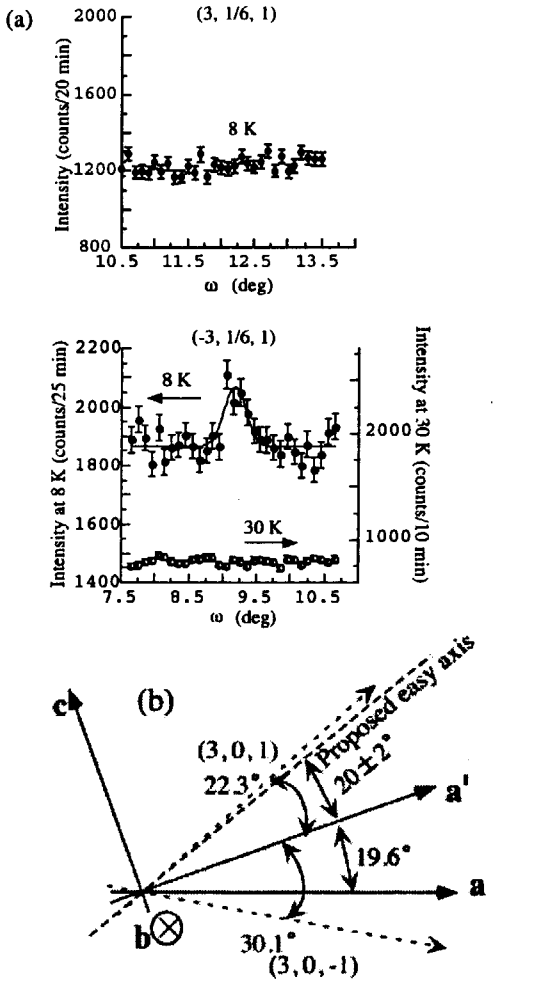


Fig. 1(a): Bragg reflections at (3, 1/6, 1) and (3, 1/6, -1).
(b): Configuration of scattering vector on the crystal structure.

[1] H. Yamada and Y. Ueda: J. Phys. Soc. Jpn. **68** (1999) 2735.
[2] Y. Ueda: J. Phys. Soc. Jpn. **69** (2000) Suppl. B. 149.

使用施設：JRR-3M, 装置：FONDER, 分野：磁性

研究テーマ:RPdSn (R=Tb, Ho, Er)化合物の磁気構造
表題:TbPdSn の粉末中性子回折
1-2-27

Powder Neutron Diffraction Measurements of TbPdSn

Y. Andoh, G. Nakamoto[1], M. Kurisu[1], T. Tsutaoka[2] and S. Kawano[3]
Faculty of Education and Regional Sciences, Tottori University, Tottori 680-8551, Japan
[1]*Japan Advanced Institute of Science and Technology, Ishikawa 923-1292, Japan*
[2] *Graduate School of Education, Hiroshima University, Hiroshima 739-8524, Japan*
[3]*Reearch Reactor Institute, Kyoto University, Osaka 590-0494, Japan*

TbPdSn is one of the equiatomic ternary Tb compounds which crystallize in the orthorhombic (*Pnma*) TiNiSi-type structure. The compound has three magnetic phases (T_N=23 K, T_1=12.2 K, T_2=2.5 K) and exhibits a multi-step metamagnetic transition in the lowest temperature phase, when magnetic field is applied along the easy magnetization direction of the *b*-axis [1]. It has also been revealed from the neutron diffraction measurements at 1.8 K that there are two kind of magnetic reflections with different propagation vectors, $\boldsymbol{Q}_1$ = (1, 0, 0.45) and $\boldsymbol{Q}_2$ = (0, ~0.4, 1) [2]. In this work, powder neutron diffraction measurements have been performed to examine the temperature dependence of the magnetic reflections in detail.

Neutron diffraction measurements were made by using the HQR spectrometer of JRR-3M of JAERI at Tokai in the temperature range from 3.8 K to 22 K.

Figure 1 shows the powder diffractions at Phase II (T_2<T<T_1) and Phase I (T_1<T<T_N). Using a model of two kinds of propagation vectors, we have indexed the magnetic reflections as shown in Fig. 1 and summarized them in Table 1. Obtained propagation vectors are in good agreement with those of single crystal measurements. At 3.8 K and 10 K (Phase II), some reflections could not be indexed by assuming only $\boldsymbol{Q}_1$ and $\boldsymbol{Q}_2$. These peaks seem to origin from higher order magnetic reflections.

Further diffraction measurements are in progress to clarify the magnetic structure in each phase in the compound.

Table I. The propagation vectors of TbPdSn at 3.8 K, 10 K, 16 K and 22 K. (a = 7.1735 Å, b =4.5861 Å, c = 7.9099 Å)

	T (K)	$\boldsymbol{Q}_1$	$\boldsymbol{Q}_2$
II	3.8	(1.005,0.093,0.449)	(0.004,0.425,0.949)
	10	(1.000,0.103,0.441)	(0.004,0.413,0.960)
I	16	(0.980,0.144,0.401)	(0.024,0.365,0.969)
	22	(0.978,0.176,0.404)	(0.017,0.361,0.970)

References

[1] Y. Andoh *et al.*, Meeting Abstract of Phys. Soc. Jpn. **54**, 2 Part 3 (1999) 365.
[2] Y. Andoh *et al.*, Activity report on neutron scattering research, 7 (2000) 104.

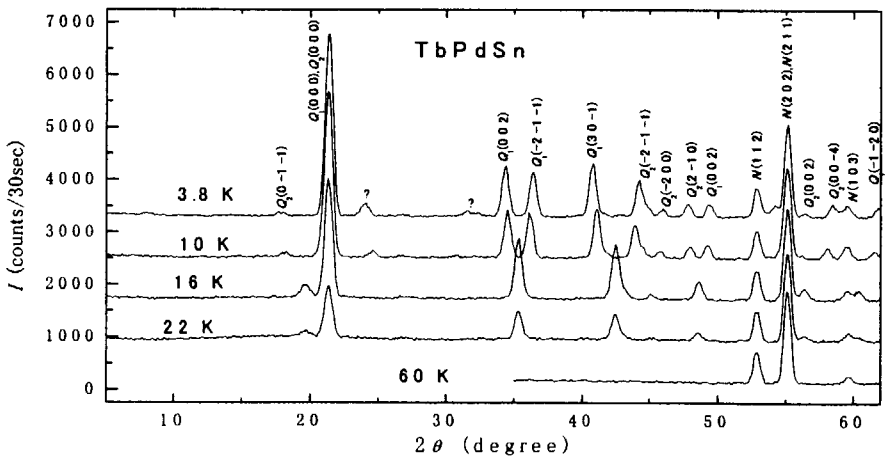


Fig.1. Powder neutron diffraction data for TbPdSn at 3.8 K, 10 K, 16 K and 22 K.

研究テーマ：URu_2Si_2の17.5転移に関する研究
表題：重い電子系化合物URu_2Si_2のフォノン分散

1-2-28 Phonon Dispersion in the heavy-electron compound URu_2Si_2

K. Kuwahara[1], K. Iwasa[1], M. Kohgi[1], M. Yokoyama[2] and H. Amistuka[2]
[1]*Department of Physics, Tokyo Metropolitan University, Tokyo 192-0397, Japan*
[2]*Graduate School of Science, Hokkaido University, Sapporo 090-0810, Japan*

The second-order phase transition at $T_o = 17.5$ K in the tetragonal heavy-electron compound URu_2Si_2 is one of the most interesting issue in this material. Recent NMR measurement under pressure revealed the coexistence of antiferromagnetic and paramagnetic regions below T_o, where the two regions are spatially separeted [1]. However, the nature of the intrinsic order parameter in the paramagnetic region below T_o has not been identified yet. Regarding the intrinsic order parameter below T_o, the importance of the orbital degrees of freedom of the 5f electrons has been argued. Among the various scenarios, one of the candidate for the order parameter below T_o is a quadrupole of the 5f electrons [2, 3].

If the phase transition at T_o is an antiferoquadrupolar (AFQ) ordering with a wave vector $\boldsymbol{Q}$, the transverse acoustic (TA) phonon with a propagation vector $\boldsymbol{q}$ and a polarization vector $\boldsymbol{u}$, coupled to the quadrupole moment with the same symmetry, may show a softening near T_o at $\boldsymbol{q} = \boldsymbol{Q}$. From the previous inelastic neutron experiment in the $(h\ k\ 0)$ scattering plane [4], however, no tendency of the softening was observed in TA phonon branches for $\boldsymbol{q} \parallel [1\ 0\ 0]$ and $\boldsymbol{u} \parallel [0\ 1\ 0]$ and for $\boldsymbol{q} \parallel [1\ 1\ 0]$ and $\boldsymbol{u} \parallel [1\ \bar{1}\ 0]$ in the Brillouin zone. For further check on the possibility of the softening due to the AFQ ordering , we have measured the temperature dependence of the dispersion curves of URu_2Si_2 for other propagating direction of phonons by inelastic neutron scattering.

Single crystal of URu_2Si_2 used in this study was the same crystal as was used in the previous experiment. The inelastic neutron scattering experiment has been done using the triple axis spectrometer TOPAN (6G) at the JRR-3M, Tokai. Pyrolitic graphite (002) crystals were used as monochromator and analyzer. For suppressing higher-order contaminations, a pyrolitic graphite filter was placed between sample and analyzer. The constant-Q scans were performed in the $(h\ 0\ l)$ scattering plane with a fixed final energy of 14.7 meV. The horizontal collimation was set to be (open)-60'-60'-(open). The sample was cooled in a closed-cycle refrigerator.

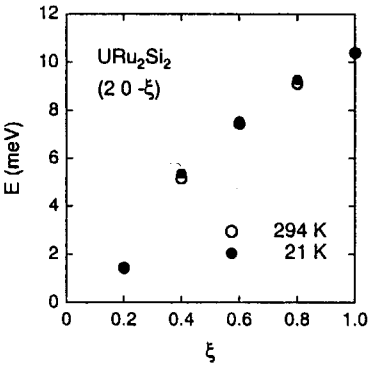


Fig. 1. The TA phonon dispersion of URu_2Si_2 for $\boldsymbol{q} \parallel [0\ 0\ 1]$ direction at 294 K (○) and 21 K (●).

Figure 1 shows the TA phonon dispersion curve of URu_2Si_2 for $\boldsymbol{q} \parallel [0\ 0\ 1]$ and $\boldsymbol{u} \parallel [1\ 0\ 0]$. The observed dispersion curve also depends only little on temperature. Thus the large anomaly related to the phase transition at T_o seems to be absent in the TA phonon branches along the $[\xi\ 0\ 0]$, $[\xi\ \xi\ 0]$ and $[0\ 0\ \xi]$ symmetry directions.

References

[1] K. Matsuda *et al.*, *Phys. Rev. Lett.* **87** (2001) 087203.
[2] H. Amitsuka and T. Sakakibara, *J. Phys. Soc. Jpn.* **63** (1994) 736.
[3] P. Santini and G. Amoretti, *Phys. Rev. Lett.* **73** (1994) 1027.
[4] K.Kuwahara *et al.*, Activity Report on Neutron Scattering Research **8** (2001) 164.

研究テーマ：CoO の格子ひずみと磁気モーメント
表題：CoO の格子ひずみと磁気モーメント

1-2-29 Lattice Distortion and Magnetic Moment in CoO

Keisuke Tomiyasu and Yorihiko Tsunoda
Department of Applied Physics, School of science and engineering, Waseda University
3-4-1 Ohkubo, Shinjuku-ku, Tokyo 169-8555 Japan

The effects of an orbital angular momentum on several physical properties in solid are one of open questions in recent solid-state physics. As one of the effects, we have paid attention influence of the lattice distortion to the direction of magnetic moment through the orbital moment in CoO. The orbital angular momentum of Co^{2+} ion in CoO is not quenched.

Above the Neel temperatures, MnO, CoO and NiO have the rocksalt structure, below their Neel temperatures, they all are distorted and have the type-II fcc magnetic structure, that is, the ferromagnetic sheets of the magnetic moments in the (111) planes, stacked antiferromagnetically along the [111] directions.

However, there are differences between them in the directions of their distortions and magnetic moments. MnO and NiO contract rhombohedrally along [111] direction and the directions of their moments are parallel to $[11\bar{2}]$ direction within the (111) plane. However, only CoO contracts tetragonally along the [001] direction and the moments are parallel to $[1,1,\overline{2.7}]$.

Fortunately, the tetragonal distortion of CoO is second order like, that is, the magnitude of the distortion increases gradually as the temperature decreases from T_N=290[K] to about 100[K] and saturates below about 100[K]. So, we can obtain the relation between the magnitude of the distortion and the directions of the magnetic moments in CoO by measuring the powder pattern at several temperatures from T_N=290[K] to 100[K].

The results are shown in fig.1 and 2. Fig.1 shows the temperature dependence of integrated intensities at the several reciprocal lattice points and fig.2 shows the temperature dependence of the direction of the magnetic moments by estimating from ratio of the intensities with Watson-Freeman's form factor of Co^{2+} ion. The direction of the moments approaches to the one within the (111) plane as the distortion decreases and does to the [001] direction as the distortion increases. This result is consistent with the cases of MnO and NiO. In other words, the tetragonal contraction yields component within the (111) plane of the magnetic moment. We consider this component as the orbital moment and now investigate the experiments to proof the expectation.

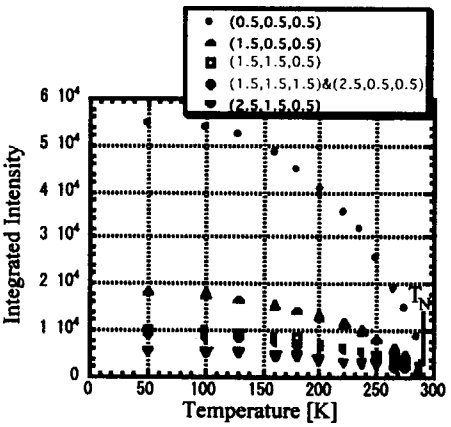


Fig.1 Temperature dependence of integrated intensities at the several magnetic reciprocal lattice points.

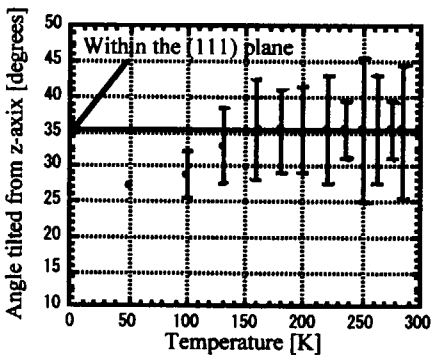


Fig.2 Temerature dependence of the angle of the magnetic moment tilted from z-axis.

1-2-30
磁化プラトーをもつND_4CuCl_3における磁気励起
量子スピン系ND_4CuCl_3における磁気励起

Magnetic Excitations in the quantum spin system NH_4CuCl_3

A. Oosawa, T. Ono, K. Kakurai[1,2] and H. Tanaka

Department of Physics, Tokyo Institute of Technology, Oh-okayama, Meguro-ku, Tokyo 152-8551
[1]Advanced Science Research Center, Japan Atomic Energy Research Institute, Tokai, Ibaraki, 319-1195
[2]Neutron Scattering Laboratory, ISSP, The University of Tokyo, Tokai, Naka-gun, Ibaraki 319-1106

NH_4CuCl_3 has a monoclinic structure (space group $P2_1/c$). The crystal structure is composed of planar dimmers of Cu_2Cl_6, which are stacked on top of one another to form infinite double chains parallel to the crystallographic a-axis. The double chains are located at the corners and center of the unit cell in the bc-plane, and are separated by NH_4^+ ions [1].

The notable feature of magnetic properties in NH_4CuCl_3 is the magnetization plateaus of the one-quarter and three-quarters of the saturation magnetization between H_{c1} = 5.0 T and H_{c2} = 12.8 T, and between H_{c3} = 17.9 T and H_{c4} = 24.7 T for $H \parallel a$, respectively [1]. Because the magnetization plateaus was also observed in the powder sample, the origin of the plateau can be attributed to quantum effect.

In order to investigate the magnetic excitations in NH_4CuCl_3, neutron inelastic scattering experiment was performed on deuterated ND_4CuCl_3 using the C1-1 ISSP-HER spectrometer installed at JRR-3M, Tokai. It was confirmed that NH_4CuCl_3 and ND_4CuCl_3 exhibit the same magnetic properties. The constant-k_f mode was taken with a fixed final neutron energy E_f of 4.4 meV. In order to gain intensity, the horizontal focusing analyzer with the applicable collimations was used. A PG-filter and a Be-filter were used to suppress the higher order contaminations. We stacked four single crystals of ND_4CuCl_3 with a total volume of approximately 1cm^3. The samples were mounted in an ILL-type orange cryostat with it's a^*- and c^*-axes in the scattering plane.

Figure 1 shows the constant-Q energy scan profile in ND_4CuCl_3 for Q = (0, 0, 1.6) at T = 1.6 K. Two excitations are clearly observed near E = 1.8 and 3 meV. The scan profile was fitted with two Gaussians as shown by the solid line in Fig. 1. It was confirmed that the origin of both excitations is magnetic from their temperature dependence.

Figure 2 shows the dispersion relations $\omega(Q)$ in ND_4CuCl_3 for Q = (h, 0, 1) and (0, 0, l). Two excitations were observed in all scans. Both excitation branches are less dispersive. We also measured along Q = (h, 0, 2h+1) and (h, 0, -2h+1), which are most dispersive and less dispersive directions, respectively, in isostructural compounds $KCuCl_3$ and $TlCuCl_3$ [2]. However, the remarkable difference compared with Q = (h, 0, 1) and (0, 0, l) was not observed.

The magnetic excitations at Q = 0 in NH_4CuCl_3 have been already investigated by the ESR measurements [3]. Two singlet-triplet excitations were observed. Their zero field excitation energy excitations were observed at 388 GHz (1.60 meV) and 708 GHz (2.93 meV), which are the same as the excitation energies at Q=(0, 0, 1). Thus, we infer that the two magnetic excitations observed in the present measurements correspond to two singlet-triplet excitations observed by the ESR measurements. Since NH_4CuCl_3 undergoes magnetic ordering at zero field, there exists a gapless excitation. The gapless ESR excitation expressed by $\omega/\gamma=H$ was observed. Thus, we expect that one more excitation exists below 0.5 meV.

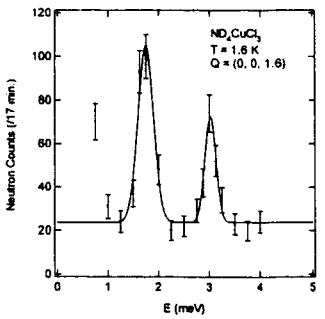


Fig. 1 Constant-Q energy scan profile in ND_4CuCl_3 for Q =(0, 0, 1.6) at T=1.6 K.

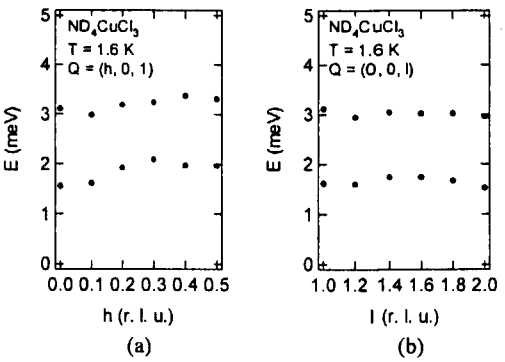


Fig. 2 Dispersion relations $\omega(Q)$ in ND_4CuCl_3 for (a) Q = (h, 0, 1) and (b) Q = (0, 0, l).

Reference

[1] W. Shiramura *et al.*: J. Phys. Soc. Jpn. **67** (1998) 1548. [2] A. Oosawa *et al.*: Phys. Rev. B **65** (2002) 094426. [3] B. Kurniawan *et al.*: Phys. Rev. Lett. **82** (1999) 1281.

使用施設：JRR-3M，装置：HER(C1-1)，分野：2. Magnetism

準1次元S=1/2反強磁性スピン系Cs_2CuBr_4における磁気励起

歪んだ擬2次元3角格子反強磁性体Cs_2CuBr_4の中性子非弾性散乱研究

1-2-31 Inelastic Neutron Scattering Study on Quasi-Two-dimensional Distorted Triangular Antiferromagnet Cs_2CuBr_4

T. ONO[1], H. TANAKA[1], K. NAKAJIMA[2] and K. KAKURAI[2,3]
[1]Department of Physics, Tokyo Institute of Technology, Tokyo 152-8551
[2]NSL, Institute for Solid State Physics, University of Tokyo, Ibaraki 319-1106
[3]ASRC, Japan Atomic Energy Research Institute, Ibaraki 319-1195

Cs_2CuBr_4 has an orthorhombic crystal structure with space group *Pnma*. Magnetic Cu^{2+} ions make a distorted triangular lattice in the *bc*-plane as shown in Fig. 1. The magnetic properties of the present system were investigated by means of the specific heat and the magnetization measurements [1]. Cs_2CuBr_4 undergoes magnetic ordering at T_N = 1.4 K, which is more than twice as large as T_N = 0.62 K in the isostructurel Cs_2CuCl_4 [2]. It was found that Cs_2CuBr_4 exhibits the magnetization plateau at approximately one third of the saturation magnetization in the ordered state for the magnetic field parallel to the *b* and *c*-axes [1]. The magnetization plateau should be stabilized by the quantum fluctuation.

In order to investigate the magnetic excitations of Cs_2CuBr_4 in the paramagnetic phase, we have performed neutron inelastic scattering experiments. The measurements were performed on the triple axis spectrometer HER installed at JRR-3M, Tokai. All measurements were performed in the fixed-k_f mode. The second, the third and the forth collimators were chosen as open-80'-80'. The sample was mounted in an ILL-type orange cryostat with its a^* and b^*-axes in the scattering plane.

Figure 2 shows the dispersion relation of Cs_2CuBr_4 along the b^* direction measured at T=1.5 K. Thick gray curve is the guide for eyes. The dispersion has the maximum and minimum at around Q=(0, 0.8, 0) and (0, 0.5, 0), respectively. This dispersion behavior is similar to that in Cs_2CuCl_4 [3]. The excitation energy at Q=(0, 0.8, 0) is about three times as large as that in Cs_2CuCl_4. This indicates that the exchange interactions in Cs_2CuBr_4 are about three times as large as those in Cs_2CuCl_4. Now precise neutron elastic and inelastic scattering measurements below T_N = 1.4 K are in progress.

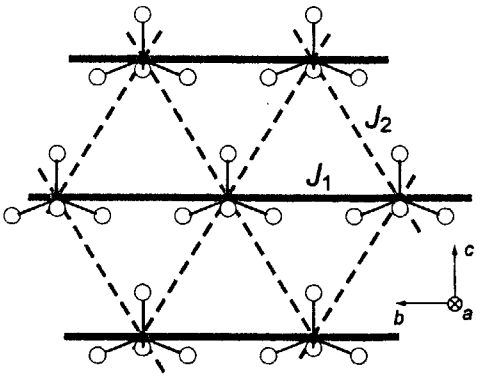


Fig. 1: Arrangement of Cu^{2+} ions in the *bc*-plane and exchange interactions in Cs_2CuCl_4 and Cs_2CuBr_4. Black circles and open circles denote Cu^{2+} ion and Br- ion, respectively.

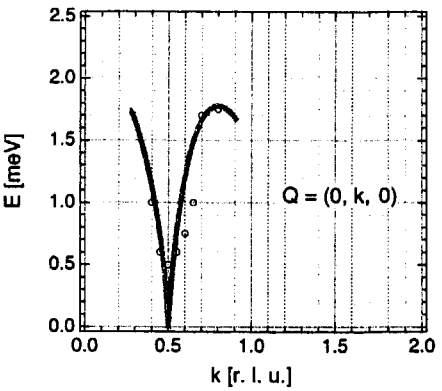


Fig. 2: Dispersion relation along the b^*-axis measured at T= 1.5 K. Thick gray line is the guide.

[1] H. Tanaka *et al.*: Prog. Theor. Phys. Suppl. No.145 (2002) 101. [2] R. Coldea *et al.*: J. Phys.: Condens Matter **8** (1996) 7473. [3] R. Coldea *et al.*: Phys. Rev. Lett. **86** (2001) 1335.

使用施設：JRR-3M，装置：HER(C1-1)，分野：2. Magnetism

1-2-32

研究テーマ：希土類化合物 RRu_2X_2(R: Tb, Dy, X: Si, Ge)における高次磁気変調構造

表題：$TbRu_2Ge_2$における2次元磁気変調構造の中性子回折

Neutron Diffraction Studies of Two-Dimensional Magnetic Modulation in $TbRu_2Ge_2$

S. Kawano, M. Toda, M. Takahashi[1], T. Shigeoka[2] and N. Iwata[2]

Research Reactor Institute, Kyoto University, Kumatori, Sennan, Osaka 590-0494, Japan
[1]Institute of Materials Science, University of Tsukuba, Ibaraki 305-8573, Japan
[2]Faculty of Science, Yamaguchi University, Yamaguchi 753-8512, Japan

Rare-earth compound, $TbRu_2Ge_2$ crystallizes in the tetragonal $ThCr_2Si_2$ type structure, in which only Tb ions are simply arranged in the body centered tetragonal lattice and bear the magnetic moment. The compound exhibits a successive magnetic transition: T_N=37K, T_t=30K and T_t'=4.3K. At the high temperature phase (HTP) of $T_N>T>T_t$, two domains with $Q_1=(q_1\ 0\ 0)$, q_1=0.235 and with $Q_2=(q_2\ 0\ 0)$, q_2=0.247 coexist with equal amount, and at the intermediate temperature phase (ITP) of $T_t>T>T_t$', the Q_2 domain disappears and only Q_1 domain is remained. The magnetic structures in these regions are one-dimensional expressed with $Q=(q\ 0\ 0)$ along the a-axis [1]. On the other hand, at the low temperature phase (LTP) of $T<T_t$', many magnetic satellites are observed on low symmetry lines in the a^*-b^* reciprocal plane as well as on the high symmetry lines in pulsed-neutron diffraction experiments [2]. The existence of those satellites suggests that the spin configuration is not one-dimensional, which has been reported so far [3], but two-dimensional. Since there are some difficulties in the precise estimation of satellite intensities for pulsed-neutron experiments, reactor neutron experiments are necessary.

Figure 1 gives a contour map of distribution of Bragg neutron intensities in the a^*-b^* reciprocal plane obtained from k-scanning data for every $1/17a^*$ step at 1.6K. The diffusive Debye-Scherrer rings in the figure are due to scattering from Al of a cryostat and the sample holder. The other peaks can be indexed with odd harmonics components of main satellites from the (2 0 0) or (1 1 0) nuclear reflection. The satellites on the high symmetry lines are indexed with fundamental $Q=(q\ 0\ 0)$, q=4/17 and its odd harmonics, while those on the low-symmetry lines are indexed with $Q=(mq\ nq\ 0)$, where q=4/17, and m, n=odd. The reflections on the low-symmetry lines disappear around 4.3K, which is in agreement with T_t' indicative of susceptibility anomaly at low temperatures. Those

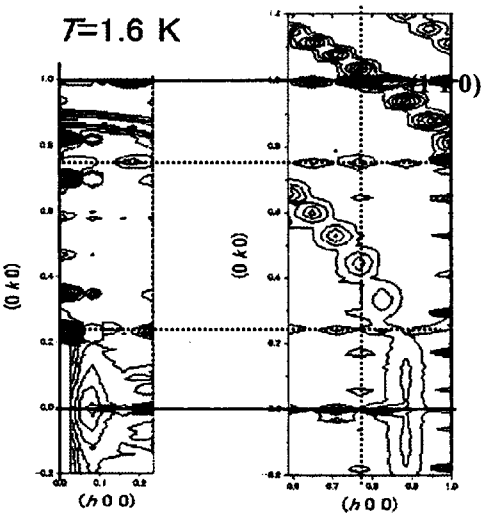


Fig. 1. Distribution of Bragg intensities in the a^*-b^* reciprocal plane for the LTP of $TbRu_2Ge_2$. The k-scan data are lacking from h=5/17 to h=9/17 and around the origin. Thick lines of (0 k 0), (h 0 0), (1 k 0) and (h 1 0) indicate the high symmetry lines, and the dotted lines are q=4/17 equivalent low symmetry lines. Debye-Scherrer rings from the cryostat and the sample holder appear relatively large.

patterns can be described as a model of a $17a \times 17a \times c$ magnetic unit cell containing two paramagnetic sites. The paramagnetic sites correspond to node positions of long-period magnetic waves, and also, the positions are strongly frustrated. Intensity data are still insufficient, because satellites on low-symmetry lines are usually smaller by several hundred times than those on high-symmetry lines.

[1] T. Shigeoka et al., Physica B **237-238** (1997) 572.
[2] S. Kawano et al., J. Phys. Soc. Jpn., **70** (2001) Suppl. A 209.
[3] A. Garnier, et al., Phys. Rev. B **57** (1998) 5235.

使用施設：JRR-3M, 装置：HQR(T_{1-1}), 分野：2. Magnetism

研究テーマ: $Sr_{1-x}La_xRuO_3$ および $Sr_{2-x}La_xRuO_4$ の磁性
表題: $Sr_{1-x}La_xRuO_3$ の電子構造

1-2-33

Electronic structures of $Sr_{1-x}La_xRuO_3$

H.Nakatsugawa[1] and Y.Oohara[2]

[1]*Materials Science, Department of Mechanical Engineering and Materials Science, Faculty of Engineering, Yokohama National University, Tokiwadai, Hodogaya-Ku, Yokohama 240-8501*

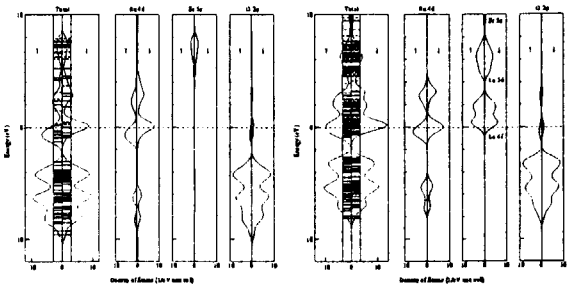
[2]*Neutron Scattering Laboratory, Institute for Solid State Physics, University of Tokyo, Shirakata 106-1, Tokai 319-1106*

Polycrystalline samples of $Sr_{1-x}La_xRuO_3$ (x= 0.0, 0.1, 0.2, 0.3, 0.4, and 0.5) were synthesized by a conventional solid state reaction method. All of the sintered pellets were analyzed at room temperature, using an X-ray diffractometer with step scanning. The powder XRD patterns show a single-phase compound with the *Pnma* type space symmetry (No.62) for every sample. The sample for x=0.5 also was analyzed at room temperature, using a neutron diffraction study. Neutron scattering measurements were carried out on the ISSP triple-axis spectrometer HQR installed at T1-1 experimental port in JRR-3M in JAERI (Tokai).

No impurity peak was detected in the present powder XRD or neutron diffraction measurements, and all samples of $Sr_{1-x}La_xRuO_3$ had the $GdFeO_3$ type orthorhombic perovskite structure. All three lattice constants, *a*, *b* and *c*, increase with increasing x, although Sr^{2+} (0.144 nm) is replaced with La^{3+} (0.136 nm). There is however an anomaly around x=0.3 in the lattice constant. This must be because electronic structures and magnetic properties change at x=0.3.

The average net charges evaluated for $[Sr_{16}Ru_3O_{16}]^{12+}$ and $[Sr_8La_8Ru_3O_{16}]^{18.5+}$ clusters at x=0.0 and 0.5 are +2.28*e* and +1.98*e* for Ru, +1.95*e* and +1.97*e* for Sr, and -1.63*e* and -1.43*e* for O, respectively. There must be a small covalent component in the bonding between a cation and an anion. Total DOS and partial DOS of $SrRuO_3$ (x=0.0) and $Sr_{0.5}La_{0.5}RuO_3$ (x=0.5) are illustrated in Fig.1 together with energy level diagrams. All of the theoretical lines in Fig.1 are the results computed by broadening discrete MO energy eigenvalues, using Gaussian function of 0.5 eV full width at half maximum (FWHM) for easy visualization of the DOS. As shown in Fig.1 (a), the filled band located from -10 eV to 0 eV is mainly composed of Ru *4d* and O *2p* orbital at x=0.0. This indicates that the electronic structure around Fermi level consists of Ru *4d* and O *2p* orbital which are hybridized. Figure 1 (b) demonstrates the energy levels at x=0.5. The electronic structure around Fermi level consists of Ru *4d*, La *4f*, O *2p* orbital which are also hybridized.

There is an energy difference between up and down spin in Ru *4d* partial DOS which forms FM states. The energy difference between up and down spin in Ru *4d* partial DOS in $SrRuO_3$ (x=0.0) is larger than that in $Sr_{0.5}La_{0.5}RuO_3$ (x=0.5). This means that FM states are suppressed with increasing x. The unoccupied DOS located above Fermi level is mainly made up of Ru -O and Sr -O hybridization, even though La -O hybridization is included at x=0.5 as shown in Fig.1 (b). The La - O hybridization above Fermi level affects the magnetic local environment around Ru and the local charge state of Ru. Moreover, the local electron densities throughout the Ru - O network and the charge distribution with increasing *x* are likely to fluctuate by this hybridization. Such a fluctuation weakens somewhat the Ru - O hybridization and also the FM interaction between Ru *4d* spins. As a result, FM states in $Sr_{1-x}La_xRuO_3$ are suppressed.



(a) (b)

Fig1. Energy level diagrams and total and partial density of states of (a) $SrRuO_3$ (x=0.0) by $[Sr_{16}Ru_3O_{16}]^{12+}$ cluster and (b) $Sr_{0.5}La_{0.5}RuO_3$ (x=0.5) by $[Sr_8La_8Ru_3O_{16}]^{18.5+}$ cluster.

使用施設：JRR-3M, 装置：HQR(T1-1), 分野：2.Magnetism

研究テーマ：金属間化合物 R_7Rh_3(R= Tb, Ho, Er)の磁気構造
表題：Ho_7Rh_3単結晶の中性子回折

1-2-34 Neutron Diffraction Studies on Ho_7Rh_3 Single Crystal

T. Tsutaoka, T. Tokunaga, Y. Andoh[1], S. Kawano[2],
G. Nakamoto[4] and M. Kurisu[4]

Graduate School of Education, Hiroshima University, Higashi-Hiroshima 739-8524, Japan
[1]Faculty of Education and Regional Sciences, Tottori University, Tottori 680-8551, Japan
[2]Reearch Reactor Institute, Kyoto University, Kumatori, Osaka 590-0494, Japan
[3]Japan Advanced Institute of Science and Technology, Ishikawa 923-1292, Japan

The rare earth compound Ho_7Rh_3 crystallizes in the hexagonal ($P6_3mc$) Th_7Fe_3 type structure. From magnetic measurements, we found that there are two magnetic phase transitions; a paramagnetic to antiferromagnetic (A.F.) at T_N = 34 K and the A.F. to ferrimagnetic at T_C = 22 K. In the Ferrimagnetic Phase, small spontaneous magnetization in the c-plane and a metamagnetic transition along the c-axis were observed. We have made neutron diffraction studies to determine the magnetic structure of Ho_7Rh_3 and found that Ho_7Rh_3 has and incommensurate helical structure with the propagation vector Q = (0, 0, 0.38) at 1.5 K. In this work, more detailed studies have been made using single crystal samples.

Single crystalline samples were prepared by the Czochralski method using a tri-arc furnace. Neutron diffraction measurements were made in the a^*-c^* reciprocal plane using the HQR spectrometer of JRR-3M of JAERI at Tokai in the temperature range from 1.5 K to 42 K.

Figure 1 shows the magnetic and nuclear reflections in the a^*-c^* reciprocal plane. The magnetic reflections appear at the positions indexed with the propagation vector Q = (0, 0, 0.38). Therefoe, magnetic structure at 1.5 K is helical along the c-axis. Further, a new reflection peaks (1, 0, ±0.16), (1, 1, ± 0.16) and (2, 0, ±0.16) were found. Figure 2 shows the (0 0 0)$^{\pm}$, (0 0 2)$^{+}$ and (1 0 –0.15) reflection peak intensities as a function of temperature. (1 0 –0.15) reflection peak intensity disappears at T_C and the other two peaks disappear at T_N. This indicates that the Q_Z = 0.16 component relates to the ferromagnetic structure below T_C. The Q_Z component of (0 0 0)$^{\pm}$ reflections does not change with temperature up to T_N. Incommensurate structure of Ho_7Rh_3 is considered to be almost the same as commensurate one of Tb_7Rh_3[1]. More precise investigation using single crystals is in progress.

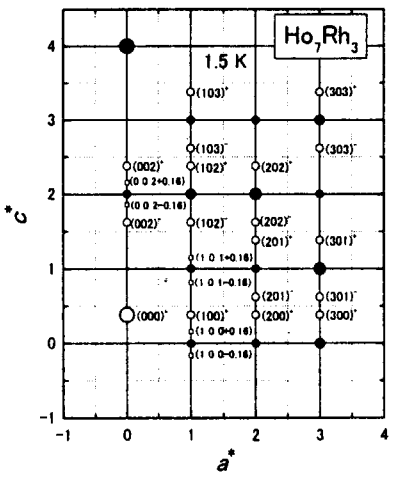


Fig.1 Magnetic and nuclear reflections in the a^*-c^* reciprocal plane.

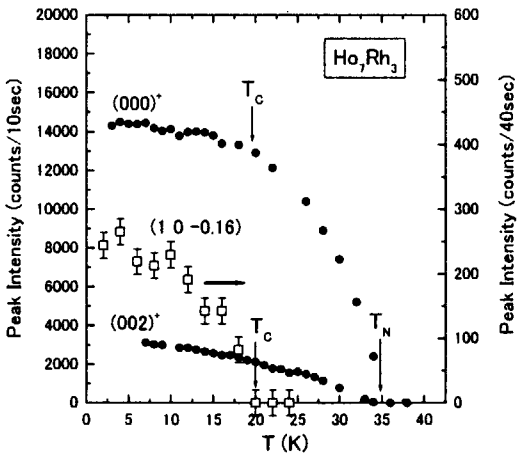


Fig.2 (0 0 0)$^{\pm}$, (0 0 2)$^{+}$ and (1 0 –0.15) intensities of Ho_7Rh_3 as a function of temperature.

[1] T. Tsutaoka *et. al.* : J. Phys. Soc. Jpn., **70** Suppl. A (2001) 212.

JRR-3M, HQR(T1-1), 2. Magnetism

研究テーマ：無秩序非磁性状態をもつ希土類金属間化合物の結晶場励起
表題：Ce_2PdSi_3における磁気相関と結晶場励起

1-2-35 Magnetic Correlations and crystal field excitations in Ce_2PdSi_3

A. Dönni[1], Y. Nemoto[1], H. Mitsunobu[1], T. Goto[1], H. Kitazawa[2], N. Aso[3], S.R. Saha[4]
[1] *Graduate School of Science and Technology, Niigata University, Niigata 950-2181, Japan*
[2] *Nanomaterials Laboratory, National Institute for Materials Science, Ibaraki 305-0047, Japan*
[3] *Neutron Scattering Laboratory, Institute for Solid State Physics, The University of Tokyo, Ibaraki 319-1106, Japan*
[4] *Department of Physics, Tokyo Metropolitan University, Tokyo 192-0397, Japan*

The ternary intermetallic compounds U_2TSi_3 and Ce_2TSi_3 (T = Pd, Rh, Ru) crystallize in a derivative of the hexagonal AlB_2-type structure with the magnetic atoms (U, Ce) fully ordered on the aluminum site 1a (0, 0, 0) and the non-magnetic atoms (T/Si) both on the boron site 2d (1/3, 2/3, 1/2). These systems are of particular interest because of complex magnetic properties, which dependent on the degree of structural disorder of T and Si atoms, can vary between simple spin-glass behavior (U_2PdSi_3), spin-glass behavior with extended short-range ferromagnetic correlations (U_2RhSi_3), absence of spin-glass behavior (U_2RuSi_3), long-range antiferromagnetic order (Ce_2RhSi_3) and coexisting different types of short-range antiferromagnetic correlations (Ce_2PdSi_3) [1].

Ce_2PdSi_3 has a high degree of structural disorder and the competition between ferromagnetic and antiferromagnetic Ce - Ce exchange interactions leads to two successive magnetic phase transitions at $T_{N1} \approx 3.7$ K and $T_{N2} \approx 2.4$ K with two different kinds of coexisting antiferromagnetic short-range correlations. The dominating magnetic Bragg peaks can be indexed [2] with an incommensurate magnetic propagation vector $\mathbf{k_1} \approx [0, 0, 0.21]$. On PONTA spectrometer have performed elastic and inelastic neutron scattering experiments on three different Ce_2PdSi_3 samples to study magnetic correlations and crystal field excitations. Two polycrystalline samples were prepared by arc-melting and annealing for 5 days at 900°C by using high quality Ce-4N material, "PC(4N)", and normal quality Ce-3N material, "PC(3N)". Additional measurements were performed on a Ce_2PdSi_3 single crystal "SC" already used in [3]. The magnetic susceptibility data shown in Fig. 1 reveal a strong sample dependence of magnetism in Ce_2PdSi_3 [4], the magnetic phase transition at $T_{N1} \approx 3.7$ K is most

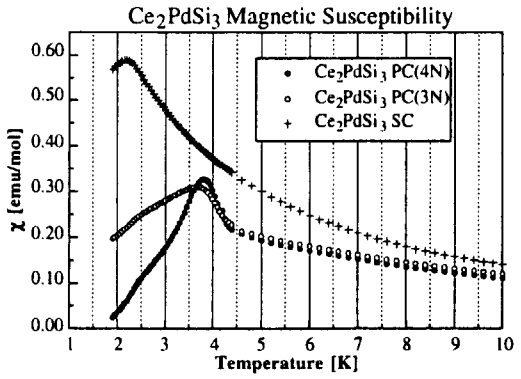


Fig. 1 Temperature dependence of magnetic susceptibility (ZFC, H=0.010T) for different Ce_2PdSi_3 samples.

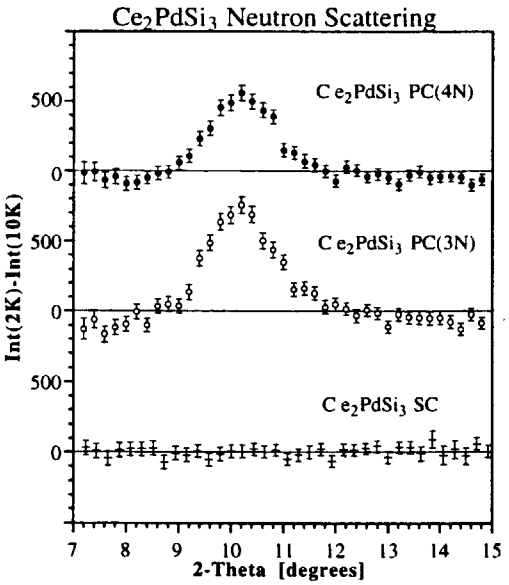


Fig. 2 Ponta neutron diffraction data showing the sample dependence of the strongest magnetic Bragg peak of Ce_2PdSi_3.

使用施設：JRR-3M、装置：PONTA(5G)、分野：2. Magnetism

研究テーマ：無秩序非磁性状態をもつ希土類金属間化合物の結晶場励起
表題：Ce_2PdSi_3における磁気相関と結晶場励起

pronounced in the high-quality sample "PC(4N)", smeared out in the medium quality sample "PC-3N" and completely absent in the single crystal "SC". The elastic neutron diffraction data shown in Fig. 2 confirm these results: The incommensurate magnetic Bragg peak (0, 0, 0.24) is observed with a similar peak shape in both polycrystalline samples but is absent in the single crystal. Typical inelastic neutron scattering pattern measured for Ce_2PdSi_3 "PC(4N)" are shown in Fig. 3. Compared to 2 K, the broad crystal field excitation near 12 meV shifts to slightly smaller energy (10 K) and decreases in intensity (50 K).

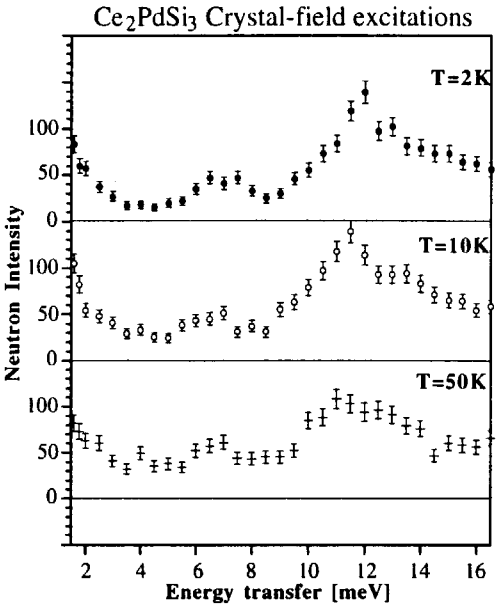


Fig. 3 Sample Ce2PdSi3 "PC(4N)". Constant-Q scans at selected temperatures measured with constant analyzer energy 14.8 meV. Ce2PdSi3.

References

[1] B. Chevalier et al., J. Alloys Compounds **233** (1996) 150.
[2] A. Szytula et al, J. Magn. Magn. Mater. **202** (1999) 365.
[3] S.R. Saha et al., Phys. Rev. B **62** (2000) 425.
[4] A. Dönni et al. unpublished results

使用施設：JRR-3M、装置：PONTA(5G)、分野：2. Magnetism

研究テーマ：三角格子系 $R_{1-x}Ca_xMnO_3$ におけるスピン秩序のドーピング依存性

表題：六方晶 $LuMnO_3$ の磁気的性質とドーピング効果

1-2-36 Magnetic properties of hexagonal $LuMnO_3$ and their doping effect

T. Katsufuji[1,2*], M. Masaki[1], Y. Moritomo[3], K. Ohoyama[4], K. Kitazawa[1,2], and H. Takagi[1]

[1]*Dept. of Advanced Materials Science, Univ. of Tokyo,* [2]*SORST, JST,* [3]*CIRSE, Nagoya University,* [4]*Inst. for Materials Research, Tohoku University*

Hexagonal managnites $RMnO_3$ (R is rare earth) are rare compounds in the sense that ferroelectricity and magnetism coexist in one compound.[1] In these compounds, the Mn ions, each of which is surrounded by three in-plane and two apical oxygen ions (a MnO_5 polyhedron), form triangular-lattice layers. As to their ferroelectricity, it is known that the triangular lattice of the Mn ions has a superstructure (a trimerization of Mn ions), and this distortion leads to the absence of centrosymmetry of the crystal (the space group $P6_3cm$) and the appearance of ferroelectric polarization perpendicular to the layers. Concerning their magnetism, the ordering pattern of the Mn moments is the so-called 120° structure, where the Mn moments lie within a layer and neighboring Mn moments in a layer are aligned by 120° different directions.

The main purpose of the present study is to pursue the doping effect in hexagonal $RMnO_3$. We tried several different types of doping into hexagonal $RMnO_3$, and found that R^{3+} can be replaced with Zr^{4+}, i.e., nominal electron doping into the Mn site (the formation of Mn^{2+} ion). Associated with this doping, it is found that magnetic susceptibility is enhanced and Weiss temperature, $|\theta|$ is suppressed. To investigate the spin structure of Zr-doped samples, neutron powder diffraction measurements were performed using the Kinken powder diffractomater for high efficiency and high resolution measurements (HERMES) installed at the JRR-3M reactor at the Japan Atomic Energy Research Institute, Tokai, with wavelength 1.8196Å. The samples used in the present study are $LuMnO_3$ and $Lu_{0.8}Zr_{0.2}MnO_3$, both of which are made by conventional solid state reaction.

The powder diffraction patterns of $LuMnO_3$ and $Lu_{0.8}Zr_{0.2}MnO_3$ at 300 K and 10 K are shown in Fig.1. As can be seen, the magnetic Bragg peaks observed for $LuMnO_3$ (shown by arrows) at 10 K are substantially suppressed for the Zr-doped sample. Considering the fact that $|\theta|$ is also suppressed with Zr doping, we conclude that the interaction between Mn^{3+} and Mn^{2+} is ferromagnetic, and the system becomes a spin-glass state for the Zr-doped sample, because of the coexistence of antiferromagnetic (between Mn^{3+} and Mn^{3+}) and ferromagnetic interactions.

Another notable feature (though barely seen in Fig. 1) is a broad peak around the (100) peak (~20°, forbidden in $LuMnO_3$), most strongly observed around T_N, which can be assigned to a magnetic diffuse scattering. What is striking is that this magnetic diffuse scattering survives at least up to 220 K (~ 3 T_N) for $LuMnO_3$. For the Zr-doped sample, the magnetic diffuse scattering exists even at the lowest temperature. This indicates that Zr doping changes the long-range ordering of the Mn moments into short-range clusters, consistent with a spin-glass picture above.

Reference

* Present address: Department of Physics, Waseda University, Tokyo 169-8555, Japan.

[1] T. Katsufuji *et al.*, Phys. Rev. B **64**, 104419 (2001), and references therein.

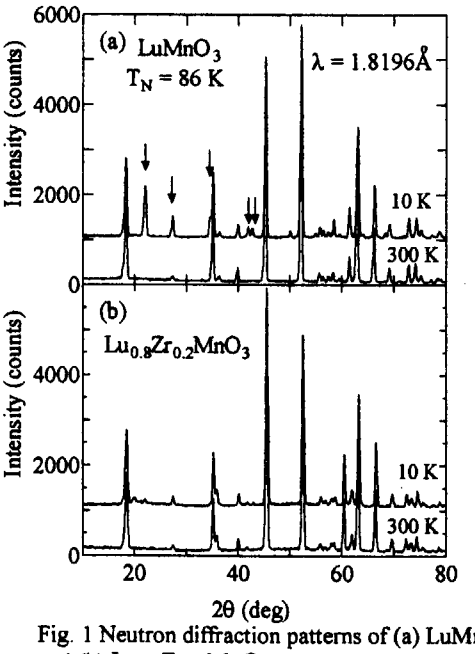


Fig. 1 Neutron diffraction patterns of (a) $LuMnO_3$ and (b) $Lu_{0.8}Zr_{0.2}MnO_3$ at 100 K and 300 K

使用施設：JRR-3M: HERMES(T1-3), 分野：2

1-2-37

研究テーマ：$ZnCr_2O_4$の中性子散乱

表題:$ZnCr_2O_4$単結晶の磁気中性子散乱における電場磁場冷却効果 II

Field Cooling Effect in Magnetic Neutron Scattering of $ZnCr_2O_4$ Crystal II

I. Kagomiya[1], Y. Hata[2],M. Toki[1], E. Kita, K. Kohn[1], K. Siratori[3], K. Nakajima[4] and K. Kakurai[2]

Institute of Applied Physics, Tsukuba University, Tsukuba, Ibaraki 305-8557, Japan,
[1]Department of Physics, Waseda University, Shinjyuku-ku, Tokyo 169-8555, Japan,
[2]Advanced Science Research Center Japan Atomic Energy Institute, Ibaraki, 319-1195 Japan,
[3]Department of Physics, Kyushu University, Fukuoka, 812-8581, Japan,
[4]Institute for Solid State Physics, University of Tokyo,Kashiwa, Chiba 277-8581, Japan

Normal spinel $ZnCr_2O_4$ is a typical example of a geometrically frustrated system. It has a first-order antiferromagnetic transition at T_N=12(±1) K. We wish to make clear how the frustration is relaxed at the transition. For this purpose we will going to know the spin structure below T_N. Magnetic Bragg reflections of the type (h/2, k/2, l) and (h/2, k/2, l/2) have been observed. However, the magnetic structure has not been clear. Because the presence of antiferromagnetic domains makes the problem difficult to be solved, it is effective to investigate the effect of magnetic and magnetoelectric field cooling in controlling the domains. According to our previous study, a magnetic field cooling approximately along the [110] brings a remarkable change in the integrated intensity, while that along the [100] is not effective. The purpose of this study is to obtain the further information of the effect of magnetic field cooling.

We used the PONTA diffractometer installed at JRR-3M in JAERI with the incident wavelength 2.358 Å. A single crystal sample was set so that the [111] direction of the phase was vertical. The integrated intensities of the reflections on the (111) reciprocal plane as depicted in Fig. 1 are compared after cooling from about 100 K to 2.6 K in the following conditions. (1)Cooling in magnetic field of 6 T applied along the [111] (MFC). (2)Cooling in both magnetic (6 T) and electric (about 2 kV/cm) fields applied simultaneously (MEFC). The fields are along the [111], and along the [110] , respectively. We confirm the position of the nuclear Bragg (220) before every measurement run.

The intensities of the reflections E～F and H after MFC or MEFC increase as compared with the intensities on the ZFC . On the other hand, the intensities of the A～D after MFC or MEFC is lower than them in ZFC. Figure 2 shows profiles of the A, E and H with MFC.

The results are expressed by the difference of the integrated intensities after MFC or MEFC and ZFC, $\Delta I=|I_{ZFC}-I_{FC}|/I_{ZFC}\times 100$. The ΔI estimated at the A～D and E～G reflection is about 50 %, while the ΔI of the H is about 30 %. Difference between MFC and MEFC of any reflections is not clear. Remarkable changes of the integrated intensities with the MFC or MEFC along the [111] and no effect of [100] cooling are is an evidence that unique axis of the spin structure is along the [111].

Collecting a lot of magnetic reflections with the field cooling is necessary in order to solve the spin structure. We are now preparing an experiment to record further more magnetic reflections on (111) reciprocal plane and some other reciprocal planes.

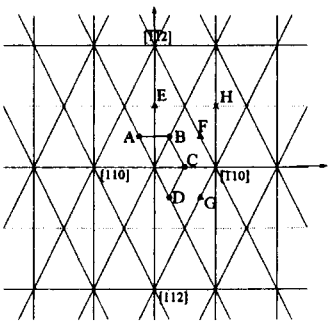


Fig. 1 (111) reciprocal plane of $ZnCr_2O_4$

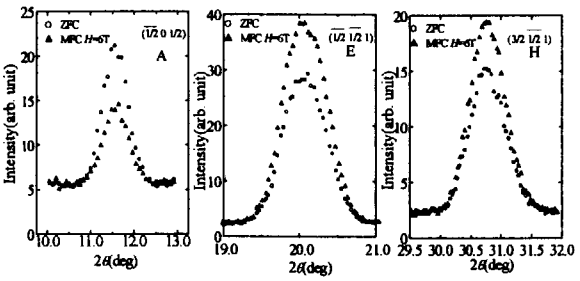


Fig.2 Profiles of magnetic Bragg reflections after ZFC and MFC.

研究テーマ：La1-xCaxMnO3,x=0.08-0.25の磁気揺らぎと電荷整列

表題：$La_{1-x}Ca_xMnO_3$, x=0.05-0.2の冷中性子散乱

1-2-38

Cold neutron scattering study of $La_{1-x}Ca_xMnO_3$ with x=0.05-0.20

S.Begum, Y.Ono, Y.Miyazaki, Y.Tomioka[1], Y.Tokura[2] and T.Kajitani
Department of Applied Physics, Graduate School of Engineering,
Tohoku University, Sendai 980-8579, Japan
[1]Joint Research Center for Atom Technology (JRCAT), Tsukuba, 305,Japan
[2]Department of Applied Physics, University of Tokyo, Tokyo 113-0033,Japan

Cold neutron inelastic scattering measurement for the 113-type La(Ca)-Mn-O perovsikite single crystals grown by one of the present authors (Tomioka) is carried out using AGNES. Low energy and nearly dispersionless magnon mode was discovered in the present system by Hennion et al [1] and Moussa et al.[2] The low energy magnon mode was found in the q-range close to the gamma-point in the charge ordered anti-ferromagnetic phase(CAF) of $La_{1-x}Ca_xMnO_3$ with x=0.05 and 0.08 in the energy range less than 2meV. There are two kinds of separated magnon branches in the system, i.e. , the low energy branch and the ferromagnetic one both of which have gaps of approximately 1meV and 3meV at the gamma point, respectively. The latter one has a close similarity with that in the La-Mn-O system[3]. .Previously, low energy excitation mode was observed in the powder samples of the same system with x=0.08-0.20 in the ferromagnetic insulator phase (FI) by AGNES[4].

Present work shows low energy excitation in the q-range close to 1/2 0 1/2 point, the zone boundary, and 020 point at temperatures from Curie point down to 18K. Care must be taken for the present Pnma crystal setting.(The b-axis of this setting corresponds to the c-axis of Hirota's crystal). It is interesting that the low energy mode was observed in the vicinities either of the zone boundary and the zone center, an indication of relatively weak and local interplaner magnetic coupling. It is pointed out that similar nearly flat low energy mode is observed either in the CAF and FI phases.

Figure1 (a) and (b) show observed inelastic scattering intensities in the samples with x=0.15 and 0.20. The energy values of the peaks are seen at E=1.0meV and 0.9meV in the x=0.15 and 0.20 samples, respectively. The same peak is found at E=1.2meV in the x=0.05 sample, decreasing with increasing hole density.

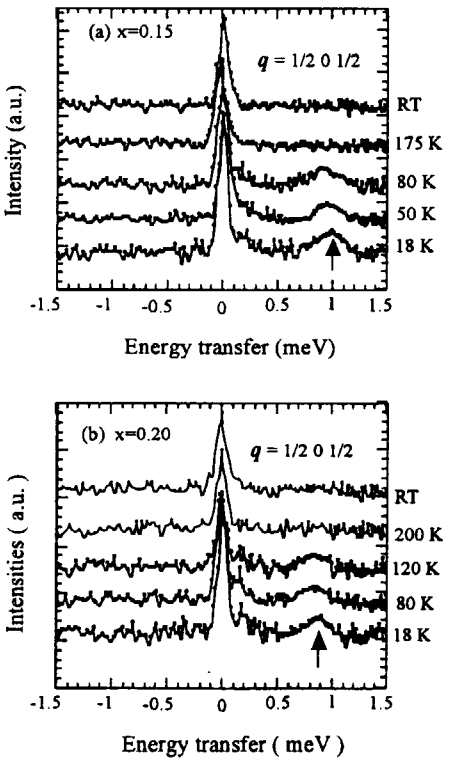


Fig.1 Temperature dependent inelastic scattering intensity of x=0.15(a) and 0.20(b) samples.

References

[1]Hennion et al:Phys.Rev.B56(1997) R497.
12299. [2]F.Moussa et al.:ibid 60(1999) 12299.
[3]K.Hirota et al.:J.Phys.Soc.Jpn 65(1996) 3736.
[4]S.Begum et al.:Activity Rep.7(2000) 73.

使用施設：JRR3M, 装置：AGNES(C3-1-1), 分野：2. Magnetism

研究テーマ：特異な異常Hall効果をもつスピネル化合物の磁気構造
表　題：$SrFe_{1-x}Co_xO_3$の磁気構造と異常ホール効果

1-2-39

Magnetic Structure and the Anomalous Hall Effect of $SrFe_{1-x}Co_xO_3$

Y.Yasui[1], T.Ido[1], S.Iikubo[1], M.Ito[1], M.Sato[1] and K.Kakurai[2]
[1]*Department of Physics, Nagoya University, Furo-cho, Chikusa-ku, Nagoya 464-8602*
[2]*Advanced Science Research Center, JAERI, Tokai, Ibaraki 319-1199*

$SrFe_{1-x}Co_xO_{3-\delta}$ with distorted perovskite structure has the helical spin ordering at x ~0.0 [1] with the modulation vector is along [111] [2]. For x>0.2, the system has the ferromagnetic moment below the temperature T_C [1, 2]. Sintered samples of the compound were prepared and then, annealed at 320 °C under the oxygen pressure of 60 atm. Their resistivities ρ, Hall resistivities ρ_H and magnetizations M have been measured as functions of temperature(T) and magnetic field (H) to search effects of the possible nontrivial spin structure (or effects of the spin chiral ordering, where the chirality χ is locally defined as $\chi \equiv \boldsymbol{S}_1 \cdot (\boldsymbol{S}_2 \times \boldsymbol{S}_3)$ for three spins $\boldsymbol{S}_1$, $\boldsymbol{S}_2$ and $\boldsymbol{S}_3$) on ρ_H, which have been often argued [3, 4], since the observation of the very striking T- and H-dependences of ρ_H of $Nd_2Mo_2O_7$ [5, 6, 7].

The Hall resistivity ρ_H was measured as follows. First, it was measured at the lowest T (~5 K) after zero field cooling with H being kept constant, by rotating the sample with respect to the H direction and then, by increasing H stepwise to take the ρ_H-H curve. Then, H was turned to zero by the oscillating mode, and T was raised above T_C. After lowering T to the next measuring value, ρ_H was measured by the processes stated above. These processes were repeated many times to obtain the whole ρ_H-T curves. The same samples were used in the measurements of ρ_H and M to avoid the ambiguity introduced by the effects of the demagnetizationfield. T and H were changed in the same order in both measurements ρ_H and M not to introduce possible ambiguities due to the hysteretic effects. Neutron data were taken with the T1-1 triple axis spectrometer at JRR-3M.

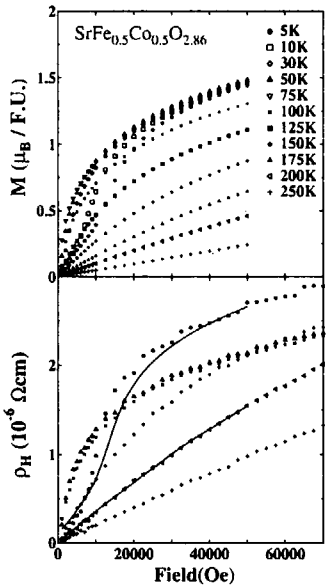


Figure 1: Magnetization M(top) and the Hall resistivity ρ_H(bottom) of $SrFe_{1-x}Co_xO_3$ are plotted against the applied field H at various fixed T values.

The M-H curves taken with increasing H after the zero field cooling are shown in the top of Fig. 1 for the sample with x=0.5, for example. For the sample δ=0.14 and T_C is ~100 K. Because M in the low field region(H<~2 T) decreases with decreasing T below ~50 K and because the significant hysteresis of the M-T curves was also observed below ~70 K(not shown) at H=1 T with varying T up and then, down, we think that the system has the reentrant spin glass phase. This idea is supportedby the neutron data: The profiles of the reflections of the magnetic components become diffuse-like with decreasing T, as shown in the top of Fig. 2 for the 100 reflection at 10 K. (In the bottom panel, the increase of the profile

JRR-3M, HQR(T1-1), 2.Magnetism

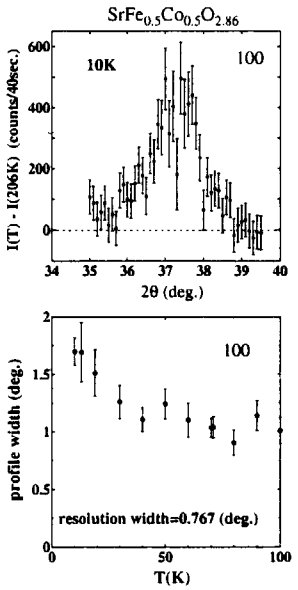


Figure 2: Magnetic scattering profile observed around 100 point(top) and its width plotted against T.

width can be seen with decreasing T.)

Considering that M does not exhibit the saturating behavior up to 5 T even at 5 K and that the hysteretic behavior of M-T curves can be observed even at H>1 T, we think that nontrivial local spin structure is realized even in the reentrant spin glass phase at low T(<∼70 K). The structure can probably be derived by adding ferromagnetic component to the helical structure similar to that observed for x=0. The hysteretic behavior is most significant for x=0.4 ∼ 0.6. In the bottom of Fig. 1, the H-dependence of ρ_H is shown for x=0.5, for example. The data have been fitted by the equation $\rho_H=R_0H+4\pi R_sM$, which is used for ordinary ferromagnets. Satisfactory fits have been obtained in the T-region where the hysteretic behavior of the M-T curves is not seen(See the fitted line at 200 K, for example.) In contrast, in the low T region where the hysteretic behavior is significant, we cannot get satisfactory fits (See the line at 5 K, for example.). It is remarkable in the T-region where the good fits cannot be

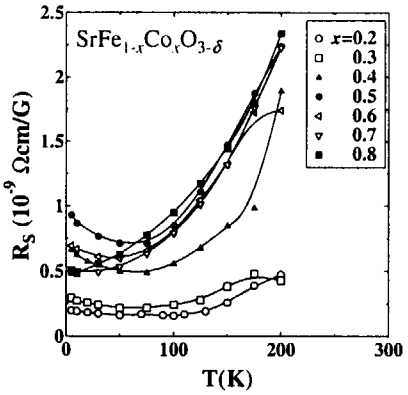


Figure 3: Anomalous Hall coefficient R_s is plotted against T for various x values(see text for details).

found, coincides with the region of the glassy behavior of M.

In Fig. 3, the T-dependences of R_s obtained by the fittings are shown for various x values. In the relatively high T region, R_s decreases, as for ordinary ferromagnets, with decreasing T. However, for x=0.4 ∼ 0.6, where the glassy behavior appears most significantly, R_s increases with lowering T, in the glassy phase.

As one of the candidate mechanisms of the deviation of ρ_H, we note the possible coupling of M and proposed by Tatara and Kawamura [4]: The coupling induces the uniform component of χ, which induces a new component of ρ_H, in addition to those treated by the classicaltheories.

References

[1] S. Kawasaki, M. Takano and Y. Takeda: J. Solid State Chem. **121** (1996) 174.
[2] T. Takeda, Y. Yamaguchi, H. Watanabe: J. Phys. Soc. Jpn. **33** (1972) 967.
[3] K. Ohgushi, S. Murakami and N. Nagaosa: Phys Rev. B **62** (2000) R6065.
[4] G. Tatara and H. Kawamura: cond-mat /0204096.
[5] S. Yoshii, S. Iikubo, T. Kageyama, K. Oda, Y. Kondo, K. Murata and M. Sato: J. Phys. Soc. Jpn. **69** (2000) 3777.
[6] S. Iikubo, S. Yoshii, T. Kageyama, K. Oda, Y. Kondo, K. Murata and M. Sato: J. Phys. Soc. Jpn. **70** (2001) 212.
[7] Y. Taguchi, Y. Oohara, H. Yoshizawa, N. Nagaosa and Y. Tokura: Sience **291** (2001) 2573.

研究テーマ：$Nd_{2-x}Y_xMo_{2-y}Ti_yO_7$ 単結晶の磁気構造
表　題：$Nd_2Mo_2O_7$ の磁気構造と異常ホール効果

1-2-40

Magnetic Structure and the Anomalous Hall Effect of $Nd_2Mo_2O_7$

Y. Yasui[1], S. Iikubo[1], H. Harashina[1], T. Kageyama[1], M. Ito[1], M. Sato[1] and K. Kakurai[2]
[1]*Department of Physics, Nagoya University, Furo-cho, Chikusa-ku, Nagoya 464-8602*
[2]*Advanced Science Research Center, JAERI, Tokai, Ibaraki 319-1199*

$Nd_2Mo_2O_7$ consists of individually formed networks of corner-sharing Mo_4- and Nd_4-tetrahedra and exhibits a ferromagnetic transition at temperature T=T_C=93 K, where the Mo-moments primarily order. The ordering of the Nd-moments becomes significant below ~30 K. The low T magnetic structure is non-collinear for both the Mo- and Nd-moments [1]. Unusual behavior of the Hall resistivity(ρ_H) of $Nd_2Mo_2O_7$ has been reported by the authors' group [2]: Above 30 K, the data of ρ_H is well described by ρ_H=R_0H+$4\pi R_sM$ as for ordinary ferromagnets, where R_0 and R_s are the ordinary and anomalous Hall coefficients, respectively, and M is the total magnetization. However, below ~30 K, the expression no more works and instead, ρ_H=R_0H+$4\pi R_sM_{Mo}$+$4\pi R'_sM_{Nd}$ ($R_s \cdot R'_s$<0) has been found to describe the experimental results rather well, where M_{Mo} and M_{Nd}, and R_s and R'_s are the net magnetizations and the anomalous Hall coefficients corresponding to the Mo- and Nd-moments, respectively. The existence of the two components in ρ_H is supported by the doping effect studies [3]. R_s and R'_s are found not to exhibit significant decrease as T approaches zero in contrast to the case of ordinary ferromagnets. None of classical theories can describe these results. A new proposal has been made that the ordering of the spin chirality χ which is locally defined as $\chi=\boldsymbol{S}_1\cdot\boldsymbol{S}_2\times\boldsymbol{S}_3$ for three spins $\boldsymbol{S}_j$ (j=1~3) contributes to the Hall resistivity [4].

Here, neutron scattering studies in the applied magnetic field $\boldsymbol{H}$(//[0$\bar{1}$1]) up to 5.7T have been carried out to clarify the relationship between the order of χ and the behavior of ρ_H. The neutron measurements were carried out by using the triple axis spectrometer HQR(T1-1) of JRR-3M of JAERI, where double axis condition was adopted. The crystal was oriented with the [0$\bar{1}$1] axis vertical. In the zero and finite magnetic field $\boldsymbol{H}$(//[0$\bar{1}$1]), the neutron elastic scattering intensity has been measured on a single crystal of $Nd_2Mo_2O_7$ at various $\boldsymbol{Q}$-point at 113 K(>T_C) and 1.6 K(<T_C). The magnetic scattering intensity I_{mag} was obtained by taking the differences between the observed integrated intensities at two temperatures, where the absorption and extinction corrections were made, though the results of the analyses do not sensitively depend on the extinction corrections. At 1.6 K, the Mo-moments align along the direction nearly parallel to the [001] or other equivalent axes, but have the slight tilting by the angle α=3(± 3)° towards the local principal axes, while the Nd-moments are along

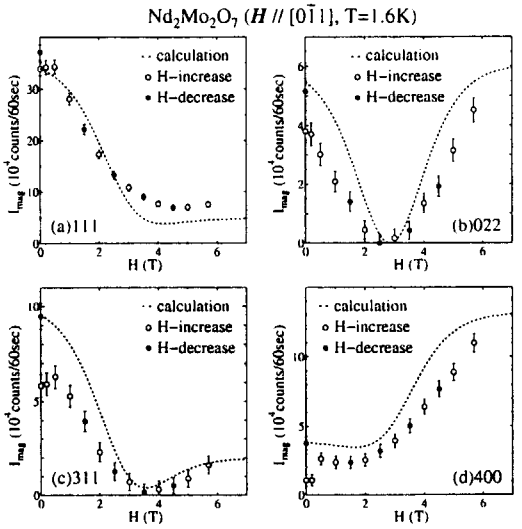


Figure 1: Intensities of several magnetic reflections are plotted against H, applied along [0$\bar{1}$1].

JRR-3M, HQR(T1-1), 2.Magnetism

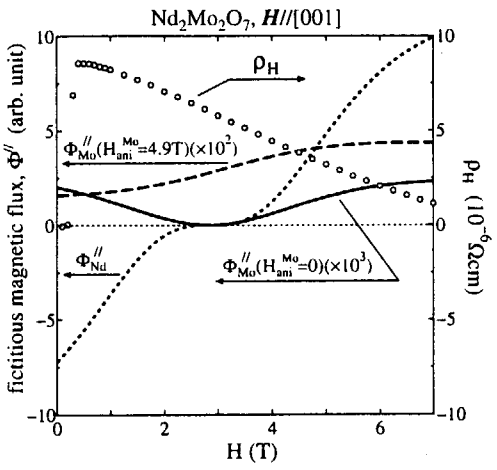


Figure 2: Fictitious magnetic flux of the Mo- and Nd-moments along $\boldsymbol{H}$(//[001]), $\boldsymbol{\Phi}^{\parallel}_{\mathbf{Mo}}$ and $\boldsymbol{\Phi}^{\parallel}_{\mathbf{Nd}}$, respectively, is shown at 1.6 K against H.

their principal axes with their net magnetization being antiparallel to that of the Mo-moments. The results indicate that there exists the relatively strong axial anisotropy at the Nd sites.

We have determined the magnetic structure at 1.6 K as a function of H, where the Mo-Mo and Mo-Nd exchange fields and the single ion anisotropy of the Mo- and Nd-moments are considered as the parameters and so chosen that they can reproduce the H-dependence of the observed magnetic scattering intensities, the examples of which are shown in Figs. 1(a)-1(d). The obtained ordering patterns at 1.6 K in the field H=5.7 T indicates that the Mo-moments align along the direction nearly parallel to $\boldsymbol{H}$(//[0$\bar{1}$1]) but they are tilted from the direction by the single ion anisotropy and the Mo-Nd exchange interaction. For the two Nd sites with the principal axes (parallel to the corresponding lines connecting the center of gravity with the sites) perpendicular to H, the magnitude and directions of the Nd-moments hardly change. with increasing H up to 5.7 T, because the anisotropy is very large. For the other Nd-sites, the population of the moments with the anti-parallel component to H decreases with keeping directional vectors along the principal axes and the average magnitude of the moments also changes. We have also determined the magnetic structures under the conditions $\boldsymbol{H}$//[001] and [111] by using the same parameters as used for $\boldsymbol{H}$(//[0$\bar{1}$1]).

In the chiral order mechanism of ρ_H, the spin chirality χ makes the fictitios magnetic flux of the Mo- and Nd-moments, $\boldsymbol{\Phi}_{\mathbf{Mo}}$ and $\boldsymbol{\Phi}_{\mathbf{Nd}}$, respectively. We calculate them at 1,6 K as a function of H by using the H-dependent magnetic structure determined here. Their components parallel to H, $\boldsymbol{\Phi}^{\parallel}_{\mathbf{Mo}}$ and $\boldsymbol{\Phi}^{\parallel}_{\mathbf{Nd}}$ is proportional to the anomalous Hall conductivity(, which is approximately considered to be proportional to the anomalous Hall resistivity here). They are shown in Fig. 2 for $\boldsymbol{H}$//[001] for two effective magnetic fields, $H_{\rm ani}{}^{\rm Mo}$=4.9 T and 0 introduced to consider the single ion anisotropy of the Mo-moments. The curves of $\boldsymbol{\Phi}^{\parallel}_{\mathbf{Mo}}$ shown in Fig. 2 do not agree with the experimentally observed ρ_H [2] shown by the open circles in Fig. 2. The observed curves of ρ_H cannot be described by the combinations of $\boldsymbol{\Phi}^{\parallel}_{\mathbf{Mo}}$ and $\boldsymbol{\Phi}^{\parallel}_{\mathbf{Nd}}$, either, though the anomalous Hall resistivity can basically be described, as stated above, by the sum of two components from $M_{\rm Mo}$ and $M_{\rm Nd}$ These results indicate that the chiral order mechanism does not describe the behavior of ρ_H of the present system.

References

[1] Y. Yasui, Y. Kodama, M. Kanada, m. Ido, H. Harashina, M. Sato and K. Kakurai : J. Phys. Soc. Jpn. **70** (2001) 284.

[2] S. Yoshii, S. Iikubo, T. Kageyama, K. Oda, Y. Kondo, K. Murata, and M. Sato : J. Phys. Soc. Jpn. **69** (2000) 3777.

[3] T. Kageyama, S. Iikubo, S. Yoshii, Y. Kondo, M. Sato and Y. Iye : J. +hys. Soc. Jpn. **70** (2001) 3006.

[4] K. Ohgushi, S. Murakami and N. Nagaosa : Phys. Rev. B **62** (2000) R606.

研究テーマ：正方晶四極子秩序化合物 $R^{11}B_2C_2$ の結晶場分裂
表題：正方晶 $Nd^{11}B_2C_2$ での結晶場

1-2-41 Crystal Electric Field in Tetragonal $Nd^{11}B_2C_2$

K. Ohoyama[1], A. Tobo[1], K. Hirota[2], H. Onodera[1] and Y. Yamaguchi[1]
[1]*Institute for Materials Research, Tohoku Univ., Sendai 980-8577, Japan*
[2]*Dept. of Physics, Tohoku Univ., Sendai 980-8578, Japan*

The tetragonal LaB_2C_2 type RB_2C_2 (R=rare earth) system shows various and characteristic magnetic and quadrupolar behaviour caused by coexistent competition among antiferroquadrupolar (AFQ) and antiferromagnetic (AFM) interactions and magnetic anisotropy by crystalline electric field (CEF) effects [1, 2]. Of this system, DyB_2C_2 undergoes an AFQ ordering at T_Q=24.7 K and a further transition to an AFM state with a weak ferromagnetic component at T_C =15.3 K. HoB_2C_2 exhibits an AFQ ordering at T_Q=4.5 K under zero magnetic field as well, even though a magnetic ordered state exists between T_Q and T_N=5.9 K(> T_Q) [2] Note that the strict ground state by CEF in the RB_2C_2 system is a doublet which has no degree of freedam of quadrupolar moments.

We think that the AFQ orderings in RB_2C_2 require a quasi-doublet or quasi-triplet ground state with very small energy gap between the strict ground states and the first excited states. Thus, to understand the mechanism of AFQ orderings in RB_2C_2, it is indispensable to make clear the low-lying CEF levels of this system. For this purpose, we performed inelastic scattering experiments on the triple axis spectrometer TOPAN at the JRR3-M reactor of JAERI.

Since level schemes in DyB_2C_2 and HoB_2C_2 are expected to be too complicated to clarify, the sample for the present experiments was a polycrystalline sample of $Nd^{11}B_2C_2$ because Nd has a simple level scheme with only five doublets. The experimental conditions were as follows; collimation was B-60-S-PG-60-B, E_f=14.7 meV, the sample dimension was ϕ12mm×15mm.

Fig.1 shows energy spectra with Q=2Å^{-1} at T=12.5K and room temperature. We observed obvious excitations at ϵ=7.5meV and 17.5meV with a small shoulder around 21 meV at T=12.5K. These three excitations are magnetic ones because of its T and Q dependence. The relatively sharp peak at 22meV at room temperature is a phonon component because of its Q-dependence.

We have already confirmed that the excitation at 17.5meV at T=12.5K consists of two excitation at about 16.5meV and about 18meV by high resolution experiments on the CAT spectrometer at KENS. Thus, we were able to determine the level scheme with five doublets: 0-7.5meV-16.5meV-18meV-21meV. Using this level scheme and results of detailed magnetisation measurements, we can obtain accurate CEF parameters in NdB_2C_2; furthermore, CEF parameters for the other RB_2C_2 compounds can be probably expected through extrapolation from the parameters for NdB_2C_2.

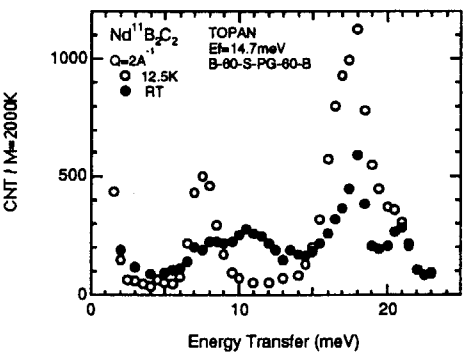


Fig. 1. Energy spectra of a polycrystalline sample of $Nd^{11}B_2C_2$ at Q=2.0Å^{-1} obtained on TOPAN. Open and closed circles show spectra at T=12.5K and room temperature, respectively.

References

[1] H. Yamauchi, H. Onodera, K. Ohoyama, T. Onimaru, M. Kosaka, M. Ohashi and Y. Yamaguchi: J. Phys. Soc. Jpn. **68** (1999) 2057.
[2] H. Onodera, H. Yamauchi and Y. Yamaguchi: J. Phys. Soc. Jpn. **68** (1999) 2526.

使用施設：JRR-3M，装置：TOPAN(6G)，分野：2. Magnetism

研究テーマ：正方晶 TmB_2C_2 の磁気構造に対する La ドープの効果
表題：正方晶 TmB_2C_2 の磁気構造に対する La ドープの効果

1-2-42 La-dope effect on the magnetic structure in tetragonal TmB_2C_2

K. Ohoyama[1], K. Indoh[1], A. Tobo[1], H. Onodera[1] and Y. Yamaguchi[1]
[1]*Institute for Materials Research, Tohoku Univ., Sendai 980-8577, Japan*

DyB_2C_2 undergoes an antiferroquadrupolar (AFQ) ordering at T_Q=24.7 K and a further transition to an antiferromagnetic (AFM) state with a weak ferromagnetic component at T_C =15.3 K [1]. HoB_2C_2 exhibits an AFQ ordering at T_Q=4.5 K as well, even though a magnetic ordered state exists between T_Q and T_N=5.9 K(> T_Q) [2]. Various and anomalous behaviour observed in RB_2C_2 is thought to be caused by coexistent competition between AFQ and AFM interactions [1, 2]. Thus, understanding roles of AFM interactions in RB_2C_2, as well as those of AFQ interactions, must be indispensable.

The fundamental magnetic coupling in RB_2C_2 is thought to be k=(1,0,0) type one: the coupling in the *c*-plane is antiferromagnetic and that along the *c* direction is ferromagnetic. TmB_2C_2 which is the heavier end of this system, however, has a k=(1,0,1/2) type AFM structure below T_N=16.5 K. Since TmB_2C_2 has the largest unit cell, particularly the longest *c*, we expected that the distance between magnetic atoms probably plays important roles to determine its magnetic coupling. Under this expectancy, we tried to determined magnetic structures in La-doped TmB_2C_2 compounds because La-dope reduces the unit cell.

We performed neutron powder diffraction experiments of a powder sample of $Tm_{0.85}La_{0.15}{}^{11}B_2C_2$ on Kinken powder diffractometer HERMES at the JRR-3M reactor in JAERI. Neutrons with a wavelength of 1.8196Å were obtained by the 3 3 1 reflection of the Ge monochromator and 12′-blank-sample-22′ collimation.

Figure 1 shows powder patterns of $Tm_{0.85}La_{0.15}{}^{11}B_2C_2$ at 2.2K and 30.1K. The lattice constant *a* and *c* were determined as *a*=5.3312(5)Å, *c*=3.4856(6)Å at *T*=30.1K, while *a*=5.3234(3)Å, *c*=3.4596(2)Å for TmB_2C_2 at 25K; reduction is 0.15% for *a*, and 0.75% for *c*. As shown in Fig.1, we observed the sharp 101/2 magnetic Bragg peak at 2.2K, indicating that the magnetic structure is basically the same as that in TmB_2C_2. However, broad scattering was also observed around the (1,0,0) position. Magnetic origin of this diffuse scattering is evident because it was not observed at 30.1K. The fact that diffuse scattering was observed around (1,0,0) which is the same position of the fundamental coupling in RB_2C_2 indicates that reduction of the unit cell develops the fundamental (1,0,0) correlation, though the (1,0,0) correlation is a short range one.

From the present experiments, we can conclude that the distance between magnetic atoms is an important factor to determine magnetic couplings in RB_2C_2.

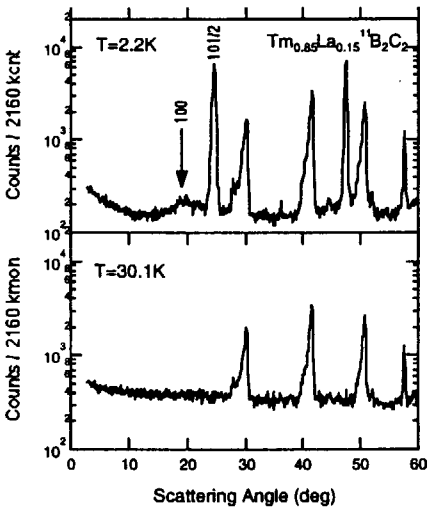


Fig. 1. Powder diffraction patterns of $Tm_{0.85}La_{0.15}{}^{11}B_2C_2$ at 2.2K and 30.1K observed on HERMES.

References

[1] H. Yamauchi *et. al.*: J. Phys. Soc. Jpn. **68** (1999) 2057.
[2] H. Onodera *et. al.*: J. Phys. Soc. Jpn. **68** (1999) 2526.

使用施設：JRR-3M，**装置**：T1-3(KPD)，**分野**：2. Magnetism

研究テーマ：$PrFe_4P_{12}$における低温秩序相の磁気特性と電子状態
表題：$PrFe_4P_{12}$におけるPrイオン4f電子状態の四重極秩序

1-2-43 Antiferro-quadrupolar ordering of Pr-ion 4f-electron state in $PrFe_4P_{12}$

K. Iwasa, L. Hao, M. Nakajima, M. Kohgi, H. Sugawara, Y. Aoki, T. D. Matsuda[1] and H. Sato

Department of Physics, Tokyo Metropolitan University, Hachioji, Tokyo 192-0397, Japan
[1] Advanced Science Research Center, Japan Atomic Energy Research Institute, Tokai, Ibaraki 319-1195, Japan

$PrFe_4P_{12}$ crystallizing in a cubic structure with Im $\bar{3}$ exhibits heavy-electron phenomena and a phase transition at T_A = 6.5 K [1, 2]. This low-temperature phase is suppressed by external magnetic field and disappears above around H = 5 T. No magnetic reflection was seen in neutron powder diffraction below T_A [3], in spite of a cusp of magnetic susceptibility at T_A like an antiferromagnetic (AF) ordering [2]. At outside of the low-temperature phase in the H-T phase diagram, the heavy-electron phenomena which is novel for Pr-based compounds were observed. X-ray diffraction experiments revealed a crystal-lattice modulation characterized by the wave vector $\boldsymbol{q}$ = (1, 0, 0) with a dominant Fe-ion longitudinal displacement in the low-temperature phase [4]. The superlattice formation is caused by the Fermi-surface nesting predicted in the band structure study [5]. In order to investigate a role of Pr-ion 4f electrons in the phase transition, we measured neutron diffraction from a single-crystal sample under magnetic field.

The experiments with neutron wavelength of 2.35 Å were performed by a spectrometer PONTA (5G). Sample temperature was controlled down to T = 1.5 K and magnetic field was applied up to H = 5.8 T in the [0, 1, -1] direction.

Figure 1 depicts profiles thorough the reciprocal-lattice points $\boldsymbol{Q}$ = (1, 0, 0), (1, 1, 1) and (3, 0, 0). As the result of (3, 0, 0), superlattice reflections at $\boldsymbol{Q}$ = (h, k, l) with odd numbers of $h + k + l$ were detected below T_A at H = 0. On the other hand, intensities at (1, 0, 0) and (1, 1, 1) do not show observable temperature dependence thorough T_A. These reflections at H = 0 are ascribed to the crystal-lattice modulation as observed by the X-ray diffraction experiment. Applying external magnetic fields below T_A, in addition to ferromagnetic intensities at $\boldsymbol{Q}$ = (h, k, l) with $h + k + l$ = even, the superlattice-reflection intensities also increase with increasing magnetic field as shown in Fig. 1. At the phase boundary of H = 5 T and T = 1.6 K, these intensities suddenly disappear.

We analyzed the observed superlattice-reflection intensities by taking into account the crystal-lattice modulation and a field-induced AF structure of the Pr ions. The model based on the Fe-ion coordinate represented as (1/4 + δ, 1/4 + δ, 1/4 − 2δ) is adopted for the crystal-lattice modulation as in the previous X-ray study [4, 6]. For the magnetic structure, we assumed two different magnetic moments μ_1 and μ_2 induced at the corner and body-centered Pr-ion sites in the unit cell along the applied-field direction. Calculated superlattice intensities with varied δ and $\mu_1 - \mu_2$ reproduce the magnetic-field-dependent intensity pattern. Evaluated magnetic-field dependences of these parameters are shown in Fig. 2. The value of $\delta \cong 0.2 \times 10^{-3}$ at lower magnetic field is very close to the X-ray diffraction result. The AF amplitude $(\mu_1 - \mu_2)/2$ increases up to $0.06\mu_B$/Pr just below the critical magnetic field of 5 T. Above this magnetic field, the lattice modulation and the AF structure vanish and the uniform ferromagnetic structure appears.

The theoretical work on the phase transition of $PrFe_4P_{12}$ suggested a split of a non-magnetic

研究テーマ：$PrFe_4P_{12}$における低温秩序相の磁気特性と電子状態
表題：$PrFe_4P_{12}$におけるPrイオン4f電子状態の四重極秩序

doublet crystal-field state Γ_{23} due to coupling between the Pr-ion state and the tetragonal Fe-ion lattice distortion [6, 7]. Because the Fe-ion arrangements around the corner and body-center Pr-ion sites are different, the two Pr-ion states align on these sites with the wave vector q = (1, 0, 0), and the different size of magnetic moments are induced on these sites. Therefore, we conclude that $PrFe_4P_{12}$ exhibits antiferro-quadrupolar (AFQ) ordering of Pr-ion 4f-electron states below T_A.

It is novel that the low-temperature phase of $PrFe_4P_{12}$ is produced by a coupling between the AFQ ordering of 4f-electron states and the gap formation by Fermi-surface nesting with the crystal-lattice modulation by the wave vector $2k_F \cong (1, 0, 0)$.

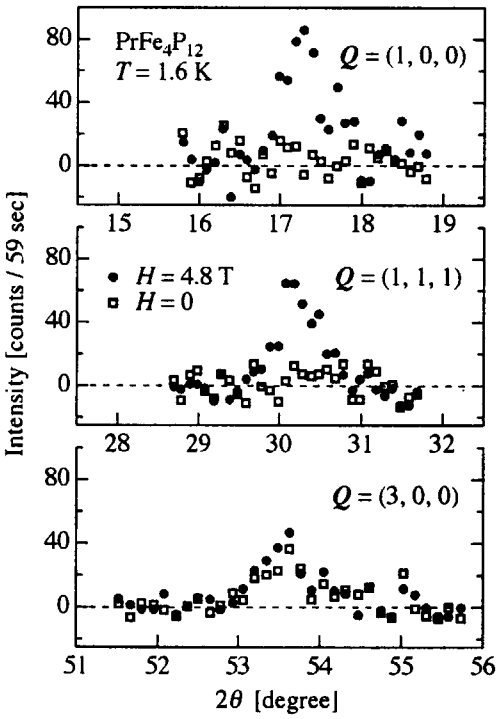


Figure 1. Neutron diffraction profiles at Q = (1, 0, 0), (1, 1, 1) and (3, 0, 0) at 1.6 K and 4.8 T (solid circles) or zero field (open squares). Background intensities measured at 10 K and at zero field was subtracted.

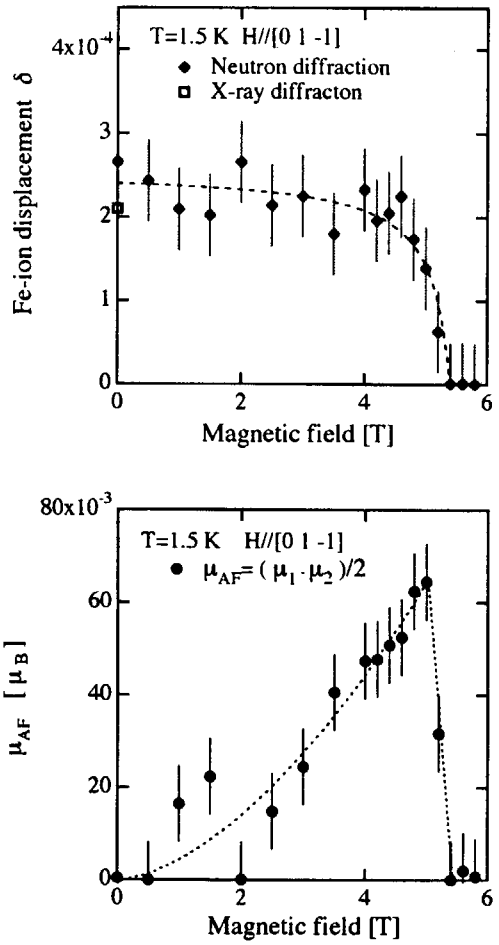


Figure 2. Magnetic-field dependences of the Fe-ion displacement parameter δ and the antiferromagnetic amplitude $(\mu_1 - \mu_2)/2$ at 1.5 K.

References

1) M. S. Torikachvili *et al.*: Phys. Rev. B **36**, 8660 (1987), H. Sato *et al.*: Phys. Rev. B **62**, 15125 (2000).
2) Y. Aoki *et al.*: Phys. Rev. B **65** 064446 (2002).
3) L. Keller *et al.*: J. Alloys and Compounds **323-324**, 516 (2001).
4) K. Iwasa *et al.*: Physica B **312-313**, 834 (2002).
5) H. Sugawara *et al.*: J. Phys. Soc. Jpn. **69**, 2938 (2000), H. Harima, K. Takegahara, Physica B **312-313**, 843 (2002).
6) S. H. Curnoe *et al.*: Physica B **312-313**, 837 (2002).
7) K. Takegahara *et al.*: J. Phys. Soc. Jpn **70**, 1190 (2001).

研究テーマ: TbRhSn,TbPtSn 化合物の磁気構造

表題:TbPtSn 化合物の中性子回折

1-2-44

Neutron Diffraction Study on TbPtSn

M. Kurisu[1], G. Nakamoto[1], T. Himi[1], Y. Andoh[2], T. Tsutaoka[3], Y. Makihara[4] and S. Kawano[5]

[1]*Japan Advanced Institute of Science and Technology, Ishikawa 923-1292, Japan*

[2]*Department of Environmental Sciences, Tottori University, Tottori 680-8551, Japan*

[3]*Graduate School of Education, Hiroshima University, Hiroshima 739-8524, Japan*

[4]*Physics Department, Kyushu Kyoritsu University, Fukuoka 807-8585, Japan*

[5]*Research Reactor Institute, Kyoto University, Osaka 590-0494, Japan*

Magnetic properties have recently been reported of Tb equiatomic ternary compounds with the orthorhombic TiNiSi structure, TbNiSn, TbPdSn and TbRhGe [1-3]. Neutron diffraction and bulk magnetic measurements on single crystals have indicated that their magnetic properties are characterized by successive magnetic phase transitions below 20 K, incommensurate magnetic structures and metamagnetism along the *b*-axis in the ordered states. In the present study, we report the results of bulk magnetic measurements and the powder neutron diffraction experiments on isomorphic compound TbPtSn.

Ingots of TbPtSn compound were prepared by arc-melting the constituent elements. Neutron diffraction measurements were carried out by using the HQR spectrometer of JRR-3M of JAERI at Tokai in the temperature range from 1.5 K to 30 K.

The magnetic susceptibility shows that there are two anomalies at T_N = 14 K and T_1 = 2.4 K (Fig.1). The magnetization curve indicates the metamagnetic transitions at 30 kOe and 50 kOe at 1.8 K.

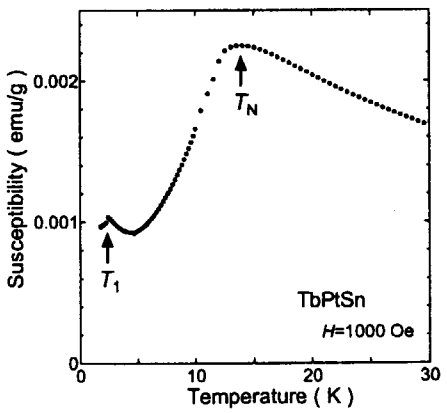


Fig.1. Temperature dependence of magnetic susceptibility of TbPtSn.

The powder diffraction patterns at various temperatures are depicted in Fig.2. It is indicated that a change in magnetic structure occurrs between 10 K and 11 K. With regard to the magnetic transition at T_1 = 2.4 K, there is not strong evidence to conclude that a different magnetic phase exists below T_1 from the neutron diffraction. An analysis is under way to examine the magneric structure at the lowest temperature.

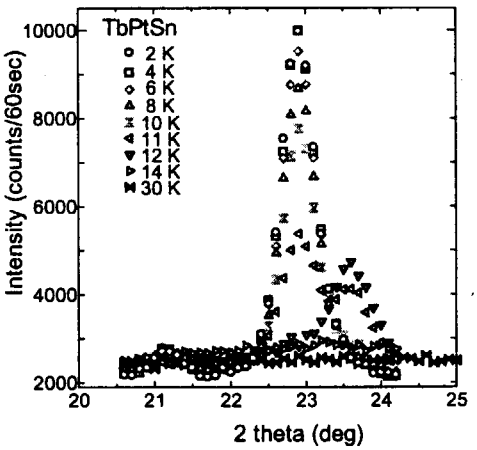


Fig.2. Powder diffraction pattern of TbPtSn.

References

[1] M.Kurisu *et al.*, Physica B **201** (1994) 107.

[2] Y.Andoh *et al.*, Physica B **237-238** (1997) 575.

[3] S.Kawano *et al.*, J. Magn. Magn. Mater. **182** (1998) 393.

[4] Y.Andoh *et al.*, KURRI Prog. Rep. 2000, 5.

JRR-3M, HQR (T1-1), 2. Magnetism

研究テーマ：NiOにおける臨界スピン揺動
表題：NiOの常磁性散乱

1-2-45 Paramagnetic Scattering from NiO

Y. Todate[1], K. Nakajima[2] and K. Kohn[3]
[1]*Physics Department, Ochanomizu University, Otsuka, Bunkyo-ku, Tokyo 112-8610*
[2]*Neutron Scattering Laboratory, ISSP, Shirakata, Tokai, Ibaraki 319-1195*
[3]*School of Science and Engineering, Waseda University, Okubo, Shinjuku-ku, Tokyo 169-8555*

It is essentially important to investigate the paramagnetic spin dynamics in NiO, which is a prototypical antiferromagnetic insulator classified into the strongly correlated electron systems. Although the local electronic structure observed by the photoelectron spectroscopy does not show a significant change near the magnetic ordering temperature, the information is totally absent on the low energy dynamical response of the localized, mutually interacting moments in the paramagnetic state in NiO. In order to reveal the characteristics of the spin dynamics, the paramagnetic scattering experiments have been carried out. The preceding experiments with the time-of-flight inelastic spectrometer have shown rather sharp, intense inelastic scattering. [1] For a further detailed study, experiments have been carried out on the triple-axis spectrometer PONTA (5G) at JRR-3M.

In the present study, the paramagnetic (and critical) scattering from a single crystal NiO were measured in the temperature range from 300 to 614 K ($1.17T_N$). The measurements were mostly made with the conventional constant-k_f mode with E_f=14.7 meV. A preliminary polarized neutron experiment was also carried out and the magnetic inelastic signals were confirmed with sufficient intensity. The inelastic magnetic scattering is centralized around the antiferromagnetic zone centers such as Q=(0.5, 0.5, 0.5) or (0.5, 1.5, 1.5). The observed magnetic response is characterized by the large energy width extending over a energy of 30meV. It is possible to construct an intensity map from a series of constant-E measurements. The map observed around Q=(0.5, 1.5, 1.5) and at T=555 K ($1.06T_N$) is shown in Fig. 1. A peak of the zone-boundary TA-phonon has been observed around 26meV but its intensity can be subtracted without distorting the contour.

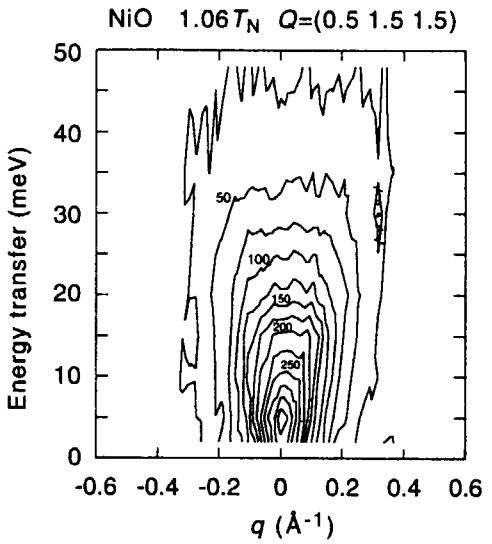


Fig. 1 Observed intensity map around Q=(0.5 1.5 1.5) and at T=555 K ($1.06T_N$). The direction of q is [110]. The scattering from phonons has been subtracted.

The observed scattering function has been analyzed assuming the conventional double-Lorentzian-formed $S(Q,\omega)$. As seen in the figure, the rod-like intensity distribution corresponds to the large spectral width Γ_q. It is important to note that the coefficient Λ is as large as 800 meVÅ^2, when the q^2-dependence of Γ_q, i.e., $\Gamma_q=\Lambda q^2+\Gamma_0$ is assumed. It is interesting to investigate the origin of this large spectral width in the paramagnetic NiO, because the large spectral width is considered to be a characteristic of the metallic systems [2], and also because of the particular situations in NiO such as the type-II AF structure in the FCC lattice.

References

[1] Y. Todate: J. Phys. Soc. Jpn., **70** (2001) Suppl. A 97.
[2] A. Yazaki, et al.: J. Phys. Soc. Jpn., **63** (1994) 748.

使用施設：JRR-3M、装置：PONTA(5G) 、分野：2.Magnetism

Pt-Mn合金の構造ゆらぎと磁性との関連性についての研究
秩序化合金Pt-14.4 at.%Mn の磁気構造

1-2-46 Magnetic structure in ordered Pt-14.4 at.%Mn

M. Takahashi, T. Sembiling, K. Ohshima and Y.Noda[1]
Institute of Materials Science, University of Tsukuba,Tsukuba 305–8573, Japan
[1]Institute for Materials Research, Tohoku University, Sendai 980–8577, Japan

Disordered Pt–rich Pt–Mn alloys have been known to exhibit spin-glass behavior similar to the Cu–Mn alloys. The magnetism of the alloys is explained by the same mechanism as that in Cu–Mn alloys, i.e., dynamically fluctuating SDW clusters with broad distribution of relaxation times [1]. In the disordered alloys, short-ranged SDW causes magnetic diffuse scattering at $(1\pm\delta,0,0)$ and its equivalent positions. Recently, neutron diffraction measurements have revealed two ordered phases in the alloys with Mn concentration around 14.4 at.% [2]. Below the order-disorder transition temperature, a Cu_3Au type ordered structure appears and at low temperature, an ABC_6 type ordered structure with a unit cell $2\times2\times2$ as large as that of the fundamental fcc cell was found to be stable. In this work, we studied magnetic structure in Pt-14.4 at.%Mn with ABC_6 type ordered structure.

Single crystal diffraction measurements were performed using FONDER installed at T2-2, JRR3-M in Tokai, JAERI. Figure 1 shows the contour map around at (0 1 1/2) on [001] plane with $l = 1/2$. Two magnetic peaks are observed at (-1/4 1 1/2) and (0 -3/4 1/2) with broad magnetic diffuse scattering elongated along $[1\bar{1}0]$ at T=7.5 K. As temperature is raised, intensities of the magnetic peaks decrease rapidly and almost disappear at T=20.5 K though the diffuse scattering remains same intensity. It survives even at R.T. with much broader distribution. The observed magnetic peaks and diffuse scattering are explained as follows; peaks at (-1/4 1 1/2) and (0 -3/4 1/2) are due to a long-ranged magnetic order on ABC_6 type ordered structure, whereas diffuse scattering along $[1\bar{1}0]$ is due to the short-ranged SDW newly appeared around (0 1 1/2) for smaller Brillouin zone in the ordered structure. The present results show coexistence of the magnetic long-range order and SDW clusters in the alloy.

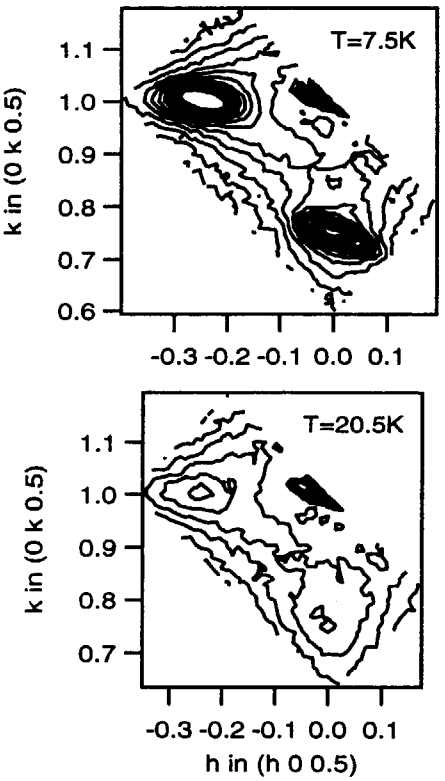


Fig.1 The contour map around at (0 1 1/2) on [001] plane with $l = 1/2$ at 7.5 K and 20.5 K.

References

[1]Y. Tsunoda, J. Magn. Magn. Matter **177-181**, 1337 (1998).
[2] M.Takahashi et al., J. Phys. Soc. Jpn. **71** (2002) 681.

課題名 ：$CeFe_2$の高圧力下での中性子散乱
表題 ：高圧下で発達した$CeFe_2$中の反強磁性スピン揺らぎ

1-2-47 Evidence of the anisotropically developed antiferromagneticspin fluctuation in $CeFe_2$ under high pressures

T. Fujiwara[1], H. Fujii[1], Y. Ishii[2], S. Koiwai[2], M. Kosaka[2], Y. Uwatoko[3], M. Nishi[3] and K. Kakurai[3]
[1]*Faculty of Integrated Arts and Sciences, Hiroshima University, Hiroshima 739-8521, Japan*
[2]*Faculty of Science, Saitama University, Saitama 338-8570, Japan*
[3]*Institute for Solid State Physics, University of Tokyo, Chiba 277-8581, Japan*

Itinerant electronsystem $CeFe_2$ with the lowest T_C=230K and the smallest M_S=2.3μ_B/f.u. at 4.2K among C15 cubic Laves phase RFe_2 family is located near an instability of ferromagnetism. Because the Fe3*d*–Fe3*d* ferromagnetic exchange interaction competes with an antiferromagnetic spin correlation with propagation vector q=(1/2, 1/2, 1/2) and an energy of ~1-3meV due to Ce4*f*–Fe3*d* hybridaizations [1]. Therefore, it is of interest to know how this system does behave under hydrostatic pressure. Magnetization measurements on single crystal $CeFe_2$ under high pressures up to 8kbar indicated that the magnetization along the each principal axis is quite anisotropically suppressed at 5K even in the cubic symmetry by applying the hydrostatic pressure [2]. To clarify the origin of this anomalous behavior, we performed the neutron scattering experiment on single crystal $CeFe_2$ under pressures.

Neutron scattering experiments for single crystal $CeFe_2$ were performed under ambient pressure and 15 kbar below 270 K both in the double-axis and triple axis modes using a Triple-Axis Spectrometer (5G-PONTA) at JRR-3M reactor of JAERI.

Fig.1(a) shows the (111) peak intensity in the triple-axis mode as a function of temperature under P ~ 15 kbar. Here, the triple-axis mode was fixed to zero energy transfer ΔE = 0. In this figure, the upper part than the dotted line indicates the contribution of magnetic scattering to the (111) peak intensity, in which the nuclear scattering contribution is the smallest. As is recognizable in Fig.1(a), the (111) peak intensity under 15 kbar begins to decrease significantly around T^* ~ 110 K with decreasing temperature without any transition and the magnetic contribution to the peak intensity becomes only half of that under P = 1 bar at T = 4.2 K. In addition, any other magnetic elastic peak has not been found in the reciprocal (110) plane. This indicates that the suppression of magnetization is not attributed to the long range antiferromagnetic ordering and the Fe static magnetic moment under P ~ 15 kbar shrinks only half of that under P = 1 bar. Subsequently, we carried out the linear scan around <1/2, 1/2, 1/2> reciprocal lattice point in the double-axis mode without energy analyzer. Therefore, in this mode, the observed scattering intensity contains both the contributions from elastic and inelastic magnetic scattering. As is seen in Fig.2(b), a small clear peak under P ~ 15 kbar in double-axis mode is recognizable around the <1/2, 1/2, 1/2> reciprocal lattice point. We can see an appreciable magnetic contribution in the <1/2, 1/2, 1/2> intensity. It should be noted that we observed no magnetic contribution on the <1/2, 1/2, 1/2> reciprocal point in the double-axis mode under 1 bar, except for the λ/2 contamination of the (111) reflection. Therefore, the above result can be interpreted as one of the evidence that the antiferromagnetic spin fluctuation with a propagation vector q = (1/2, 1/2, 1/2) develops in $CeFe_2$ under 15 kbar.

References

[1] L Paolasini et al., Phys. Rev. B58 (1998) 12117.
[2] H. Fukuda et al., J. Magn. Magn. Mater, 226-230 (2001) 1200

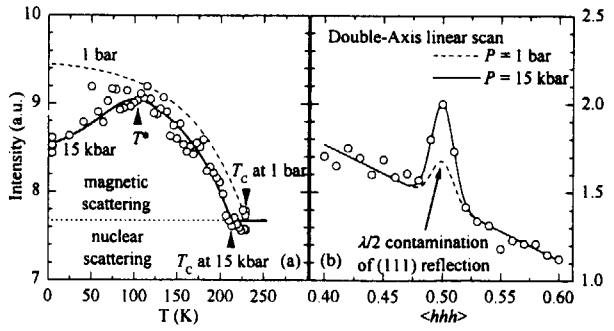


Fig.1(a) The (111) peak intensities in the triple-axis linear scan with ΔE = 0 under P = 1 bar and 15 kbar as a function of temperature for $CeFe_2$, and (b)the scattering intensity in double-axis linear scan without energy resolution under P ~ 15 kbar around the <1/2, 1/2, 1/2> reciprocal lattice point.

研究テーマ：垂直型中性子回折ワイセンベルグカメラの試作研究
表題：中性子回折カメラによる $KMnF_3$ における反強磁性相転移

1-2-48

Antiferromagnetic Phase Transition in $KMnF_3$ by means of Neutron Diffraction Camera

M.Hidaka[1], S.Takahashi[1], S.Watanabe[1,2]and Y.Kawamura[2]
1.Department of Physics, Faculty of Science, Kyushu University, Fukuoka 812-0053, Japan
2.Neutron Scattering Laboratory, ISSP, University of Tokyo, Tokai, Ibaragi 319-1106, Japan

A neutron diffraction camera method is often convenient to easily check quality of a used specimen. We can also get visual images of diffraction spots and diffuse scattering in a reciprocal lattice space around a special crystal axis by using the camera method. Since a sheet-like neutron detector, imaging plate (IP), is developed, the neutron camera method is more powerful for investigations of crystal and magnetic structures. We tried to study magnetic phase transitions in a perovskite-type compound $KMnF_3$, using the Neutron diffraction camera.

We carried out measurements of some diffraction spots of $KMnF_3$ at T2-2 experimental station in JRR-3. A tentative neutron camera was equipped on a magnet, called to be"SAIKORO", which was set on a camera gonio-stage and gives maximum magnetic field of about 8kOe. A single crystal having a size of about 2 x 2 x 4mm^3. The used neutron wavelength at T2-2 was 1.5627 Å. A functional DC-magnet called to be " SAIKORO" was set on a camera gonio-stage. The magnet gives a maximum magnetic field of about 8kOe. A small CTI-type cryostat was inserted in a pole gap of the magnet by hanging from a side-flange of the magnet. Size of focused incident Neutron beam was about 10mm in vertical and 6mm in horizontal.

Figure 1 shows a rotational visual image around a pseudo-cubic axis [001] of $KMnF_3$ taken at 40K with exposure time of 30 minutes and rotational angle of 6 degrees. Thus, in the figure, a (1,1,0) nuclear fundamental reflection is in a 0-layer, while magnetic reflections of (1/2,1/2,1/2) and (1/2,1/2, -1/2) are in a 1/2-layer and −1/2-layer, respectively. $KMnF_3$ shows successive

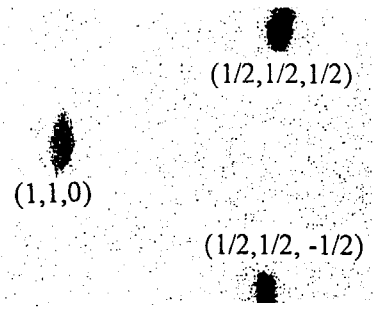


Fig.1.Visual image of rotational diffraction patterns of $KMnF_3$, taken at 40K with exposure time of 30 minutes.

magnetic phase transitions at about 88K and 83K. An uni-axial antiferromagnet occurs in the region from 88K to 83K. On the other hand, an antiferromagnet having weak ferromagnetic component occurs below 83K. Crystal structural phase transitions also occur at about 83K, 93K and 185K..

In order to study a magnetic filed effect to the magnetic structure, we carried out measurements of integrated intensity of the (1/2,1/2,1/2) magnetic reflection as functions of magnetic field and temperature. During the experiments, the magnetic filed was applied to be parallel to pseudo-cubic [100] of $KMnF_3$. The [100] axis is a magnetic easy axis. The exposure time was 15 minutes and the rotational angle 3 degrees at each measurement. Some results are shown in Figure 2. At the respective temperature from 60K to 100K, the data were taken by vertically sifting the IP-sheet cassette, whose front was screened by a Cd-

plate having a window to measure only the (1/2,1/2,1/2) magnetic reflection. The window width was 10mm in vertical and the

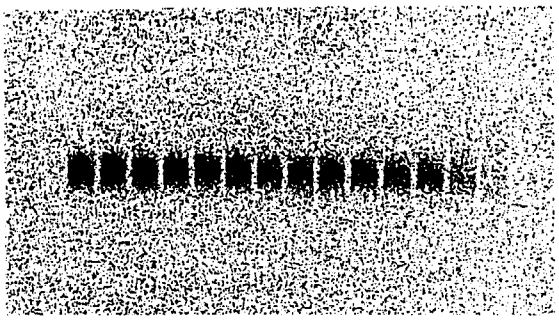


Fig.2.Visual image of the (1/2,1/2,1/2) magnetic reflection in $KMnF_3$, taken at the respective temperature from 60K(left) to 100K(right) with exposure time (15min.) and rotational angle (3 °).

cassette was shifted by12mm. The applied magnetic field was 8kOe. Figure 3 (a) and (b) represent peak profiles of the visual images of (1/2,1/2,1/2) magnetic reflection under the applied magnetic field of 0Oeand 8kOe, as like those in Fig.2, respectively.

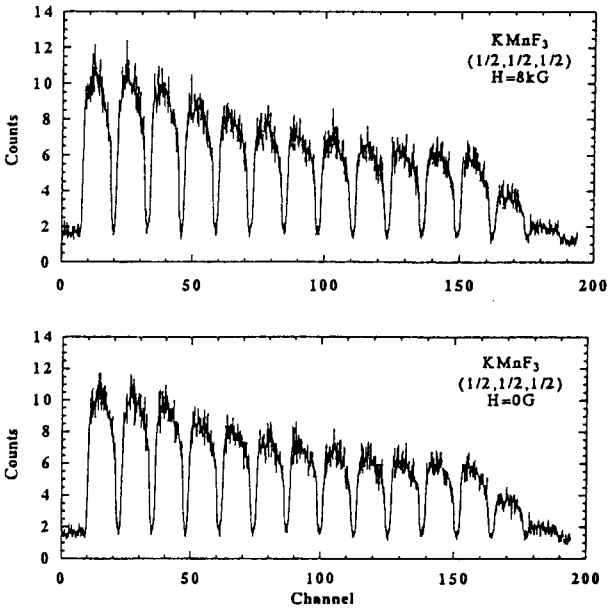


Fig.3.Peak profiles of the (1/2,1/2,1/2) magnetic reflections; (a)H=0Oe and (b)H=8kOe.

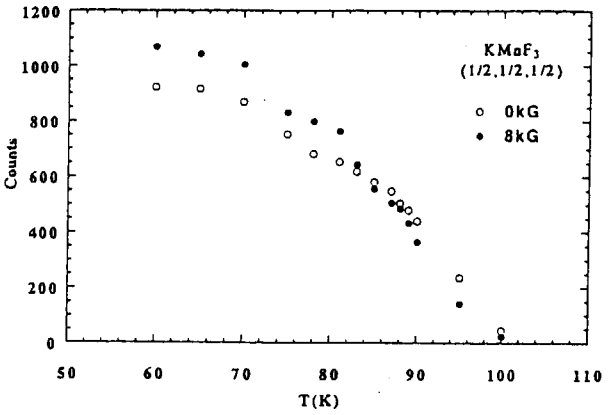


Fig.4.Intensity of the (1/2,1/2,1/2) magnetic reflection in $KMnF_3$ under the applied magnetic field, as shown in Figs.3(a) and (b).

In the figure, an ordinate refers to total counts / total vertical pixel numbers in each horizontal pixel of the imaging plate (IP), while an abscissa to the horizontal channel number in IP.

We measured total counts of the (1/2,1/2,1/2) magnetic reflection at the respective temperature, as shown in Figs.3 (a) and (b). The results are shown in Fig.4. The data denoted by open circles and solid circles are taken under the applied magnetic field of 0Oe and 8kOe, respectively. We found the magnetic field effect to the temperature dependence of the intensity. Although we need to accurately measure the intensity, it was confirmed that there are two magnetic transition at about 83K and 90K. Furthermore, the antiferromagnetic diffuse scattering was also found in region from about 90K to 100K. Thus, the neutron camera gives a possibility to study crystal and magnetic diffuse scattering, though ordinary neutron detectors of counter-type are very useful and functional than the neutron camera method. In Fig.4, we are interested in new modulation of the intensity at about 73K under the applied magnetic field of 8kOe.

研究テーマ：スピネル混晶系 $Zn_{1-x}Cu_xCr_2Se_4$ の磁気構造相転移
表題：$ZnCr_2Se_4$ における構造的、磁気的相転移間の相関

1-2-49

Correlation between the structural and antiferromagnetic phase transitions in $ZnCr_2Se_4$

M.Hidaka[1], N.Tokiwa[1], M.Fujii[2], S.Watanabe[3] and J.Akimitu[4]

1Department of Physics, Faculty of Science, Kyushu University, Fukuoka 812-0053, Japan.
2Department of Physics, Faculty of Education, Oita University, Oita 870-1192, Japan
3Neutron scattering Laboratory, I.S.S.P., University of Tokyo, Tokai, Ibaraki 319-1106,Japan
4Department of Physics, Aoyama Gakuinn University, Chitosedai, Setayaga-ku, Tokyo 157-8572, Japan.

$ZnCr_2Se_4$ has a normal-type spinel structure shown in Fig.1, where arrows will be described later. The structure is mainly characterized by 8 tetrahedra of $ZnSe_4$ (A-site) and 16 octahedra of $CrSe_6$ (B-site) in its cubic structural unit cell having a lattice constant of about 10.50Å. It is well known that Cr^{3+} ions preferably locate in the B-sites in the spinel structure. The $CrSe_4$ chain is made along [110] by owing two Se^{2-} ions between the neighbor octahedra. These chains are also isolated each other by the $ZnSe_4$ tetrahedra. $ZnCr_2Se_4$ is a semiconductive antiferromagnet having the spiral spin order of Cr^{3+} below about 20K. More recently, Hidaka et al.[1] argued from neutron powder diffraction that $Zn_{1-x}Cu_xCr_2Se_4$ with x=0.15 and 0.30 show a new anti-ferromagnetic transition at about 23K and 24.5K, in addition to the ferromagnetic transition at about 410K and 415K, respectively. It was also found that $Zn_{1-x}Cu_xCr_2Se_4$ with x=0.50 and 0.60 show an antiferromagnetic phase transition at about 24 K and 28K, respectively, in addition to a ferromagnetic phase transition at about 420K. However, the antiferromagnetic phase was not observed in $Zn_{1-x}Cu_xCr_2Se_4$ with $x > 0.75$. Temperature dependence of lattice constants taken by X-ray powder diffraction suggested that a structural phase transition in $ZnCr_2Se_4$ occurs at about 20K to be of first order from a cubic to tetragonal symmetry [2]. Thus, we carried out to re-study a correlation between structural and magnetic phase transition in $ZnCr_2Se_4$. The measurements were done at HQR in JRR-3. At the present experiments, a [-110] edge of the octahedral shape of the present crystal was set up to be parallel to a vertical rotation axis of the diffractometer. That is, the cubic axes of [001] and [110] were in a horizontal plane. From neutron powder diffraction [1], it was found that substituted spinels $Zn_{1-x}Cu_xCr_2Se_4$; $0.0 \le x \le 0.3$ show the incommensurate magnetic reflections having an cubic symmetry index of $(h \pm q_0, k, \ell)$ with $q_0 \sim 0.470$ at 2.5K. Thus, we carried out measurements of integrated intensity of $(0,0,q_0)$ magnetic peak as a function of temperature, to determine the antiferromagnetic phase transition temperature. It was found that the magnetic phase

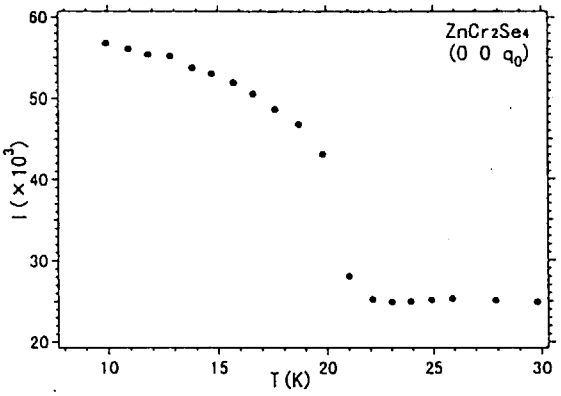


Fig.1. (I-T) of the antiferromagnetic peak of $(0,0,q_0)$.

transition occurs at about 21K (T_N) and a magnetic diffuse scattering appears above T_N, as like neutron powder patterns [1].

In order to study a thermal modulation of an incommensurate periodicity of the spiral spin order along C axis, we simultaneously measured

peak profiles of the (2,2,2) fundamental reflection and the satellite-like (2,2,2 ± q_0) magnetic reflections by a ℓ - scan along a reciprocal lattice axis of C* at respective temperature. Figs. 2(a), (b) and (c) show the peak profiles of the (2,2,2−q_1), (2,2,2) and (2,2,2+q_2) as a function of temperature,

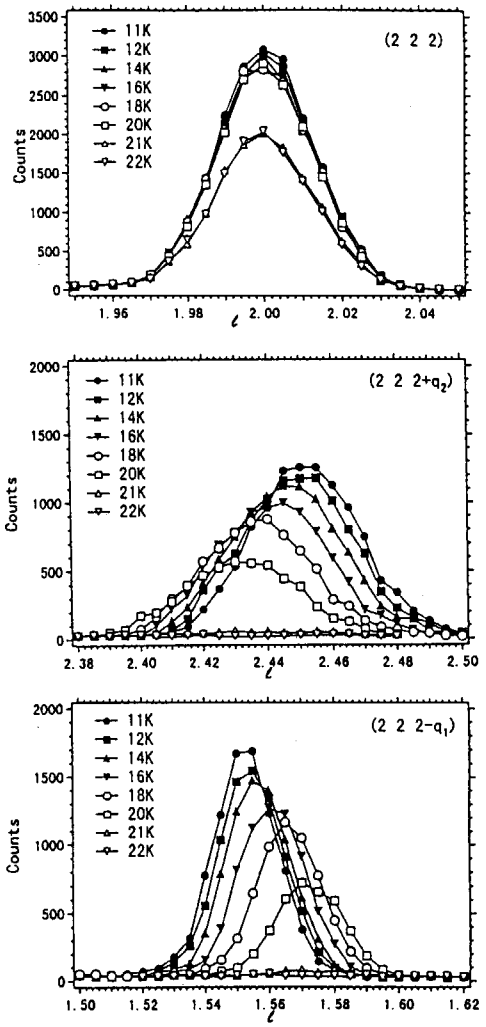


Fig.2. Temperature dependence of the peak profiles of the fundamental reflection of (2,2,2), and magnetic reflections of (2,2,2−q_1) and (2,2,2+q_2).

respectively. It was found that, on heating, the anti-ferromagnetic reflections of (2,2,2−q_1) and (2,2,2+q_2) reduce the intensity and inversely shift the peak position each other to the (2,2,2) reflection, while the peak position of (2,2,2) reflection does not depend on temperature. To accurately obtain the q_1 and q_2 as a function of temperature, we did a Gaussian curve-fitting to the peak profiles of the reflections in Figs. 2(a), (b) and (c). The results are shown in Fig.3, where $q_0 = (q_1 + q_2)/2$. Therefore, it was considered that an incommensurate periodicity of the spiral spin order is slightly modulated along C axis.

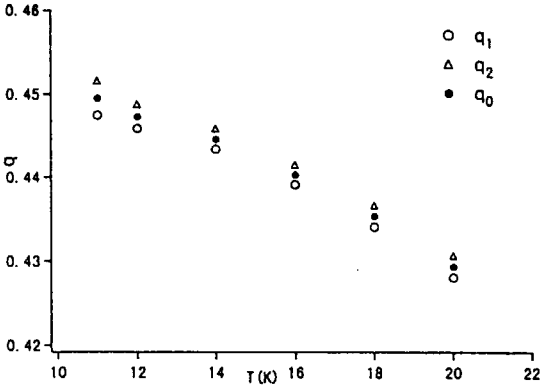


Fig.3. Temperature dependence of q_0, q_1 and q_2, refined by the Gaussian curve fitting to the peaku profiles shown inFig.2(a),(b) and (c).

However, the temperature dependence of q_1, q_2 and q_0 shows a first-order transition at about 21K, as like the first-order property of the structural phase transition. Thus, we argued that the structure phase transition at T_C mainly results from a construction of spiral magnetic long-range order along C axis. We could often observe an unusual rod-like magnetic diffuse scattering, when the crystal was cooled gradually by passing through the structural phase transition. The diffuse scattering was passed through a reciprocal lattice point of (h, h, h+q_0) to be approximately parallel to [111]. The rod-like magnetic diffuse scattering disappeared above T_N. This means that there is two-dimensional anti-ferromagnetic spin order appears in a single [111] plane but its planar spin order perfectly disappears between adjacent [111] planes.

[1]M.Hidaka, N.Tokiwa, T.T.Wai et al.,Phase transitions, in print(2001).

[2]R.Kleinberger and R.de Kouchkovsky, CR Acad.Sci.(France),262,628(1966).

スピングラス合金Pt1-cMncの磁気励起
スピングラス合金Pt-Mnの磁気励起
1-2-50

Magnetic excitation in Pt-Mn spin glass alloy

M. Takahashi, T. Sembiling and K. Ohshima[1]
Institute of Materials Science, University of Tsukuba,Tsukuba 305–8573, Japan

The mechanism of spin-glass behavior in Cu-Mn and Pt-M or Pd-M alloys (M represents 3d metal) has been explained by a dynamical fluctuation of short-ranged SDW [1]. In these alloys, the SDW dose not develop to long-ranged because of the absence of atomic long-range order. Recently, in Pt rich Pt-Mn alloys, ABC_6 type ordered phase is found to exist around 14.4 at.%Mn [2]. By long annealing, long-range order of the structure develops in the alloys. However, magnetic susceptibility shows clear spin-glass behavior in both ordered and disordered alloys. In the susceptibility data for the ordered 14.4 at.%Mn alloy, antiferromagnetic transition is found with $T_N = 20$ K along with the spin-glass behavior. From the diffraction measurements, the static magnetic structure is shown to consist of antiferromagnetic long range order and short-ranged SDW in the alloy. In the data, magnetic peaks for the long range order appear below T_N with diffuse scattering for the short-ranged SDW remaining even at R.T.. The diffuse scattering is elongated along [110] and [1$\bar{1}$0] on (001) plane at around (1/2 1/2 0) and also observed at equivalent positions with the symmetry of ABC_6 type structure.

In order to understand magnetism in the ordered alloy, we have performed inelastic neutron experiment using TOPAN in JRR3-M in Tokai, JAERI. In fig.1, inelastic patterns of the diffuse scattering at around (1/2 1/2 0) are shown. Their intensities increase at temperature higher than T_N and show a maximum at 40 K, whereas the elastic component increases with decreasing temperature (fig.2). The results indicate that in the ordered alloy, a dynamical structure is governed by the short-ranged SDW though static structure forms antiferromagnetic long range order.

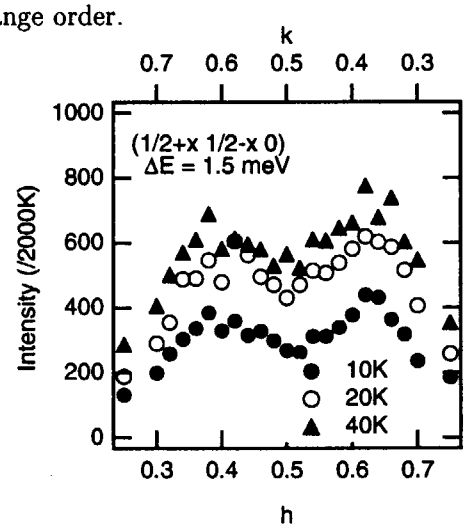


Fig.1 Inelastic patterns at at 1.5 meV.

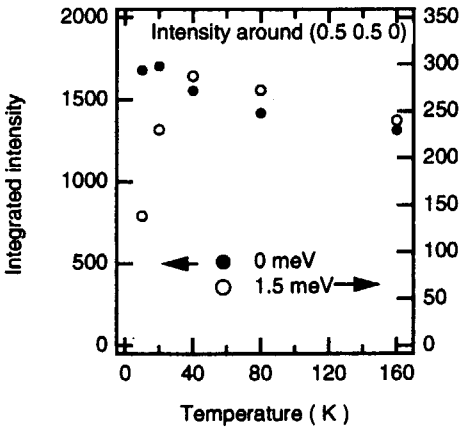


Fig.2 Temperature dependences of elastic and inelastic components.

References

[1] For example, Y. Tsunoda and J. W. Cable, Phys. Rev. B **46**, 930 (1992).
[2] M.Takahashi et al., J. Phys. Soc. Jpn. **71** (2002) 681.

KCuF3の磁気構造と軌道秩序
KCuF3の磁気構造解析
1-2-51

Magnetic structure analysis of $KCuF_3$

M. Takahashi
Institute of Materials Science, University of Tsukuba,
Tsukuba 305–8573, Japan

$KCuF_3$ is one of the typical example of the one-dimensional antiferromagnet with $S = 1/2$. In spite of the pseudo-cubic crystal structure, it forms antiferromagnetic quantum linear chains along the c−axis as a result of the orbital ordering of Cu^{2+} holes. It turns into a long-range ordered state at low temperature owing to the very weak interchain exchange interaction. The magnetic structure below T_N is a type-A ordering with the spins lying in the c-plane due to the very weak XY-like anisotropy. By neutron diffraction measurements, the spin direction in the c-plane was proposed to be parallel to [100] in a unit cell of a perovskite structure [1]. On the other hand, magnetic resonance studies have shown that due to the Dzyaloshinsky and Moriya (DM) interaction, it has an eight-sublattice magnetic structure and substantial easy direction is along [110] and its equivalent axis [2]. In this study, neutron diffraction measurements with a single crystal $KCuF_3$ have been performed by using Four-circle Off-center-type Diffractometer FONDER in JRR-3M at Tokai JAERI, to confirm the spin structure reported by resonance measurements and investigate Cu^{2+} orbital ordering based on the actual magnetic structure.

A single crystal sample grown by a precipitation method with about 13 mm^3 in volume was used in the experiment. There are two different crystal types in $KCuF_3$ which are named (a) and (d) type respectively owing to the difference of the displacement of flourines in the sequence along the c-axis. We examined the nuclear reflections belonging to both types and found that the sample is almost (a) type. The Néel temperatures for (a) and (d) types are 39 and 22 K, respectively. In the sample, T_N is found to be 39 K confirming that the sample is mainly (a) type.

Over 80 magnetic reflections up to 8 $Å^{-1}$ have been measured below and above T_N and differences between them are regarded as magnetic scattering. The obtained magnetic form factors are shown in fig.1 in which absorption and Lorents factor were corrected. For full analysis, accurate ratio of (a) type to (d) type in volume and distances between Cu – F of Cu – F_6 octahedron should be known for the sample. Powder diffraction measurements for the same sample are now in plan for these structural parameters.

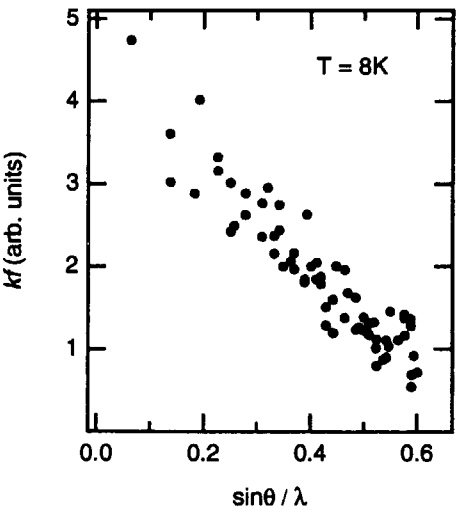


Fig.1 Observed magnetic form factor at 8 K.

References

[1] H. Ikeda and K. Hirakawa, J. Phys. Soc. Jpn. **35** (1973) 722.
[2] I. Yamada and N. Kato, J. Phys. Soc. Jpn. **63** (1994) 289.

研究テーマ：スピネル混晶系 $Zn_{1-x}Cu_xCr_2Se_4$ の磁気構造相転移
表題：置換スピネル化合物 $Zn_{1-x}Cu_xCr_2Se_4$；x＝0.50,0.60 の反強磁性相転移

1-2-52

Antiferromagnetic Phase Transition in Substituted Spinel of $Zn_{1-x}Cu_xCr_2Se_4$; x=0.50 and 0.60

M.Hidaka[1], N.Tokiwa[1], H.Fujii[2]and K.Ohoyama[3]

1.Department of Physics, Faculty of Science, Kyushu University, Fukuoka 812-0053, Japan
2.Faculty of Science, Oita University, Oita 870-1192, Japan
3.Insitite of Materials Research, Tohoku University, Sendai 980-8577, Japan

$ZnCr_2Se_4$ and $CuCr_2Se_4$ have a normal spinel-type structure, which is mainly characterized by a strong preference of Cr ions to locate in the octahedral site. $ZnCr_2Se_4$ spinel is an anti-ferromagnetic insulator or semiconductor below 20K. The magnetic structure is mainly characterized by a spiral spin order of Cr^{3+} ions. $CuCr_2Se_4$ is a ferromagnetic metal below 420K. $Zn_{1-x}Cu_xCr_2Se_4$ show an ideal solid solution and non-modification of the normal spinel structure. The magnetic and electronic properties of $Zn_{1-x}Cu_xCr_2Se_4$ depend on Cu-concentration x. It is known that an antiferromagnetic semiconductor occurs in $x < 0.10$ and their Nèel temperature (T_N) is about 20K, while an ferromagnetic metal occurs in $0.2 \leq x \leq 1.0$ and their Curie temperature (Tc) is about 380 ~ 420K.

More recently, Hidaka et at. [1] argued that the substituted spinels with x=0.15 and 0.30 show a new antiferromagnetic transition at about 23.0K and 24.5K, in addition to a ferromagnetic transition at about 410K and 415K, respectively. We considered that the magnetic phase diagrams should be re-studied to interpret a complex correlation between the magnetic and electronic properties in $Zn_{1-x}Cu_xCr_2Se_4$. Because it has been known that the substituted spinels with x=0.15 and 0.30 are not the anti-ferromagnet but semiconductive spin glass and metallic conical ferromagnet, respectively. Thus, we carried out measurements of some magnetic reflection in $Zn_{1-x}Cu_xCr_2Se_4$ with $0.50 \leq x \leq 1.0$, using a high-resolution neutron diffractometer, HERMES, in JRR- 3. The used wavelength of incident neutron beams was about 1.820 Å. The partial powder diffraction patterns of $Zn_{1-x}Cu_xCr_2Se_4$ with x = 0.50, 0.60 and 0.75 are shown in Figs. 1(a), (b) and (c), respectively. In the figures), the thin and thick solid-lines represent the data taken at about 2K and 40K, respectively.

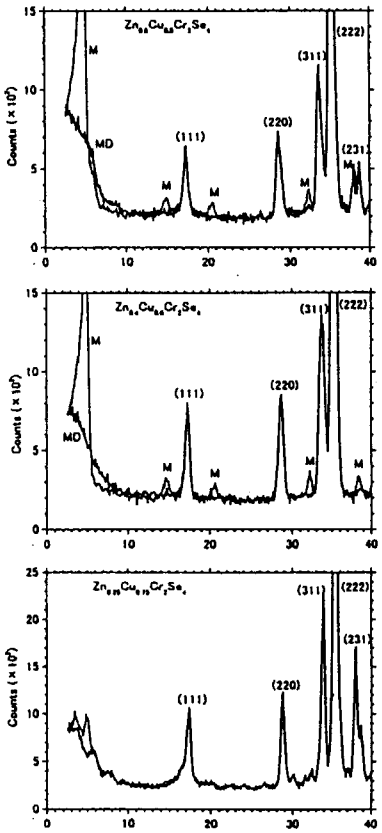


Fig.1. Peak profiles of $Zn_{1-x}Cu_xCr_2Se_4$ with x=0.50, 0.60 and 0.75, taken by neutron powder diffraction.

Notations of (1,1,1), (2,2,0), (3,1,1) and (2,2,2) mean an index for fundamental reflections, while a notation 'M' a magnetic reflection. The magnetic reflections appear only in the anti-ferromagnetic phase below (T_N). The magnetic reflection having a strongest intensity in Zn_{1-x}

$_xCu_xCr_2Se_4$ with x=0.50 and 0.60 was observed at about 2θ = 4.69 and 4.90 degrees at 2K, respectively. However, we could find only weak magnetic reflections at about 2θ = 5.0 degrees in $Zn_{0.25}Cu_{0.75}Cr_2Se_4$, as shown in Fig.1(c). Therefore, we considered that the antiferromanetic phase transition in $Zn_{1-x}Cu_xCr_2Se_4$ occurs in the region of $0.0 \leq x < 0.75$. Furthermore, the magnetic diffuse scattering denoted with MD was also observed at 40 K in Figs. 1(a), (b) and (c). The magnetic diffuse scattering decreased its intensity as increasing the specimen temperature and disappeared above about 70K.

In order to index such the magnetic reflections, we deducted the counts of the powder patterns taken at 2K from those taken at 40K in $Zn_{0.5}Cu_{0.5}Cr_2Se_4$. The resulting difference curve is shown in Fig.2. In the figure, all of the peak-profiles were the magnetic reflections. Furthermore, the magnetic diffuse scattering (MD) can be confirmed by negative counts in the figure. Since the magnetic reflections are related to the spiral spin-configuration, the satellite-like magnetic reflections could be indexed by (h±Q, k, ℓ) with Q = 0.470 as shown in Fig. 2. The calculated peak positions of the magnetic reflections are shown with thick vertical lines in Fig. 2. The value of Q in $Zn_{0.4}Cu_{0.6}Cr_2Se_4$ is 0.493, in contrast with 0.470 for $Zn_{1-x}Cu_xCr_2Se_4$ with $0.0 \leq x \leq 0.50$.

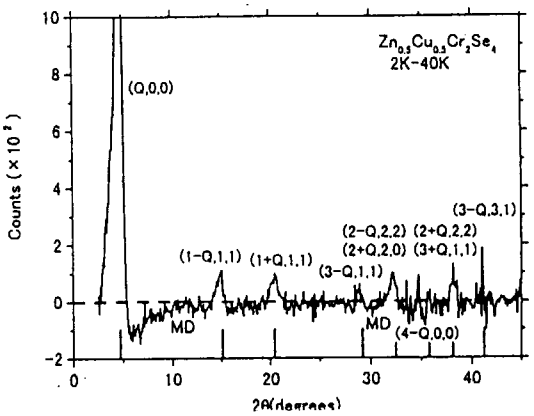


Fig.2.Difference plot between the neutron powder patterns taken at 2K and 40K for $Zn_{0.5}Cu_{0.5}Cr_2Se_4$.

We carried out measurements of an integrated intensity of the magnetic reflection having the index (Q,0,0) in Fig.1(a) and (b), in order to find transition temperature in $Zn_{1-x}Cu_xCr_2Se_4$ with x = 0.50 and 0.60. The results are shown in Figs. 3(a) and (b). Since the magnetic diffuse scattering occurs above the phase transition, it is not easy to separate the intensity between the magnetic reflection and the magnetic diffuse scattering in the vicinity of the transition temperature.

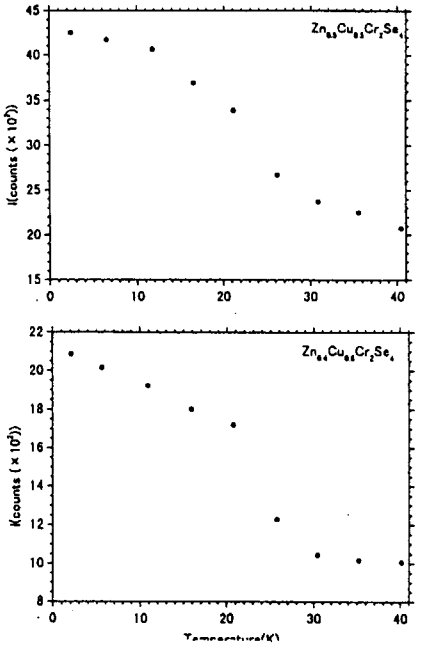


Fig.3.Temperature dependence of the intensity of first-magnetic reflection in for $Zn_{1-x}Cu_xCr_2Se_4$; x=0.50 and 0.60.

Thus, we approximately determined the transition temperature by calculating a derivative point of the intensity curve shown in Figs. 3(a) and (b). The results suggested that the magnetic transition occurs at about 25K in $Zn_{1-x}Cu_xCr_2Se_4$ with x = 0.50 and 0.60. We also measured the magnetization of the present spinels using a SQUID magnetometer. The results showed the antiferromagnetic phase transition occurring at 24K and 28K for $Zn_{1-x}Cu_xCr_2Se_4$ with x = 0.50 and 0.60, respectively.

[1].M.Hidaka,N.Tokiwa,T.T.Wai et al.,Phase transitions, in print (2001),

研究テーマ：多重極限環境下における中性子散乱実験法の研究
表　題：局在5f電子系$U_3Pd_{20}Si_6$の磁気構造及び磁気相図

1-2-53

Magnetic structure and H-T phase diagram in a localized 5f system $U_3Pd_{20}Si_6$

N. Metoki[1], Y. Koike[1,2], Y. Haga[1], K.A. McEwen[3], M. Kohgi[4], N. Aso[5], N. Tateiwa[6], T. Komatsubara[7], N. Kimura[7] and H. Aoki[7]

[1]ASRC-JAERI, Tokai, Naka, Ibaraki 319-1195
[2]Japan Science and Technology Corporation, Kawaguchi, Saitama 332-0012
[3]Dep. of Phys. and Astro., Univ. College London, Gower St., London WC1E 6BT, UK
[4]Department of Physics, Tokyo Metropolitan University, Hachioji, Tokyo 192-0397
[5]NSL-ISSP, University of Tokyo, Ibaraki 319-1106
[6]Res. Cent. for Mat. Sci. at Extreme Conditions, Osaka Univ., Toyonaka, Osaka 560-8531
[7]Center for Very Low Temperature Science, Tohoku University, Sendai 980-8545

Actinide based intermetallic compounds attract strong interests because of the variety of their magnetic and electronic properties.[1)] The 5f electrons in most of uranium intermetallic compounds exhibit itinerant character, which is due to strong hybridization with conduction electrons. Up to now only a few uranium compounds have been reported as localized 5f systems. Recently we have found a new uranium intermetallic compound $U_3Pd_{20}Si_6$.[2)] The localized character was suggested by the Curie-Weiss behavior in magnetic susceptibility. The purpose of this study is to clarify the crystal and magnetic structure and the H-T phase diagram in $U_3Pd_{20}Si_6$.

Powder diffraction data were measured using HRPD at λ = 1.162 Å with the collimation of 6'-12'-6'. Single crystal diffraction and inelastic scattering were measured using triple-axis spectrometers TAS-1, TAS-2, and LTAS. The sample was cooled by using a conventional dilution refrigerator (DR) or a liquid-He-free DR[3)] with a liquid-He-free 10 T magnet.[4)]

Figure 1 shows the crystal structure of $U_3Pd_{20}Si_6$. Uranium atoms occupy two different crystallographical sites, 4a-fcc site and 8c simple cubic site which has a half unit of the crystallographical unit cell. The space group is $Fm\bar{3}m$. The structural parameters obtained by neutron diffraction have been published elsewhere.[5)] Upon cooling down the sample, magnetic peaks were superposed at odd integer nuclear reflections, (111), (311), (331), etc as shown in Fig. 2(a). Therefore the propagation vector is [111]. These magnetic peaks are explained in terms of the antiferromagnetic ordering on 8c site. The propagation vector [111] can be described as [1/2 1/2 1/2], when the indices are denoted by the 8c simple cubic cell. The magnetic ordering on 4a site can be ruled out, because the magnetic scattering only at the odd integer reflections can not be explained by any kind of magnetic ordering on 4a site. Below T_C = 2 K we observed additional magnetic intensities at all nuclear reflections (Fig. 2(b)). This is due to the ferromagnetic ordering on 4a site. The moment size was determined to be 1.83 ± 0.05 μ_B for 8c site. The moment on 4a site 1.1 μ_B for H = 0 is strongly suppressed and recovered in the magnetic field up to 1.6 μ_B for H = 10 T. This suppression would be a result of the strong frustration of 4a site due to the coupling with 8c site.

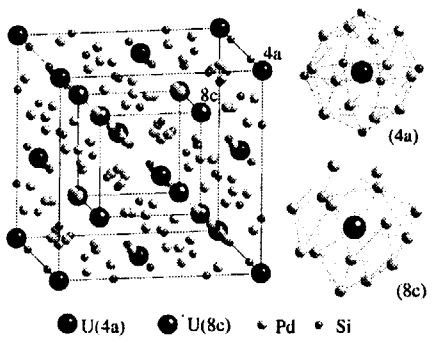


Figure 1: The crystal structure of $U_3Pd_{20}Si_6$.

原子炉：JRR-3M　　装置：TAS-2(T2-4)　　分野：中性子散乱（磁性）

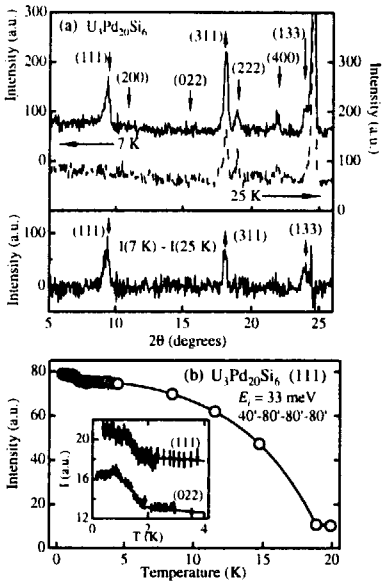


Figure 2: (a) The powder diffraction profile of $U_3Pd_{20}Si_6$. (b) The temperature dependence of the (111) and (022) peak intensities.

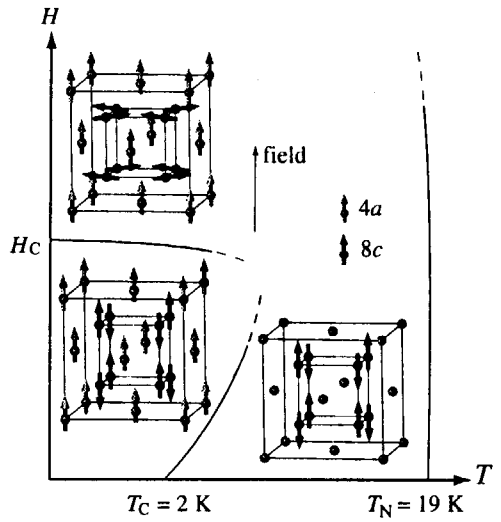


Figure 3: The $H-T$ phase diagram of $U_3Pd_{20}Si_6$.

Figure 3 shows the $H-T$ phase diagram of $U_3Pd_{20}Si_6$ determined by neutron diffraction.[6] For $T_C < T < T_N$ only 8*c* spins exhibit antiferromagnetic ordering. The magnetic easy axis is along ⟨100⟩ for 8*c* spins. Below $T_C = 2$ K, the ferromagnetic ordering on 4*a* site coexists with 8*c* antiferromagnetic ordering. The collinear structure is realized in the ground state. Our neutron diffraction experiments with magnetic field unambiguously revealed the collinear interaction between 4*a* and 8*c* spins. The origin of this collinear interaction is an open question. It can not be explained with Heisenberg interaction which is cancelled out within the inter-site nearest neighbor pairing. The cancellation of the dipole field is also clear. Therefore we conclude that the higher-order exchange and/or quadrupole interaction would be the origin of this unusual collinear interaction.

With applying field, we observed spin flop of 8*c* site at $H_C \sim 5$T against the uniaxial anisotropy induced by this collinear interaction. This is a new type of spin flop related to the higher-order interaction in the coexistence of ferromagnetic and antiferromagnetic sublattice ordering.

The existence of the metamagnetic behavior in $U_3Pd_{20}Si_6$ was reported for the first time in magnetization measurement.[7] The present study revealed the origin of the metamagnetic transition by means of neutron scattering on a single crystal under high-field.

References

1) For example, V. Sechovsky, L. Havela, *Handbook of Magnetic Materials* (Elsevier Science, Amsterdam 1998) vol. 11, p. 1. Chemistry of Rare Earths (Elsevier Science B.V. 1994) vol. 19 chap. 130, p. 1.
2) N. Tateiwa, N. Kimura, H. Aoki and T. Komatsubara, J. Phys. Soc. Jpn. **69**, 1517 (2000).
3) Y. Koike, Y. Morii, T. Igarashi, M. Kubota, Y. Hiresaki and K. Tanida, Cryogenics **39**, 579 (1999).
4) S. Katano *et al*, Proceeding of ICNS2001.
5) N. Tateiwa, N. Metoki, Y. Koike, K. Oikawa, N. Kimura, T. Komatsubara and H. Aoki, J. Phys. Soc. Jpn. **70**, 2425 (2001).
6) Y. Koike *et al*, Phys. Rev. Lett. to be published.
7) N. Tateiwa, T. Sakon, M. Motokawa, N. Kimura, H. Aoki and T. Komatsubara, J. Phys. Soc. Jpn. **70**, 1853 (2001).

研究テーマ：多重極限環境下における中性子散乱実験法の研究
表　題：UCr_2Si_2 の磁気構造

1-2-54

Magnetic structure in an itinerant $5f$ antiferromagnet UCr_2Si_2

T. D. Matsuda[1], N. Metoki[1], Y. Haga[1], S. Ikeda[1,2], and Y. Ōnuki[1,2]

[1]ASRC-JAERI, Tokai, Naka, Ibaraki 319-1195
[2]Graduate School of Science, Osaka University, Toyonaka, Osaka 560-0043

UT_2X_2 is one of the traditional $5f$ electron systems that the unusual magnetic and transport properties have been studied systematically for various compounds with different transition metal T and X=Si, Ge. In UCr_2Si_2 the small number of d-electrons and small distance between U atoms give rise to enhanced itinerant character of the $5f$-electrons. In fact, this compound shows strong anisotropic susceptibility which obeys Curie-Weiss law with effecitive moment 2.54 μ_B/U much smaller than uranium free ion. The electronic specific heat 80 mJ/K^{2}mol is the signature for the heavy fermion with medium mass enhancement. There is an antiferromagnetic ordering below T_N = 27 K. The magnetic entropy was roughly the half of Rln2. The purpose of this study is to clarify the magnetic structucture of UCr_2Si_2 by means of neutron scattering.[1)]

The neutron scattering experiments were carried out using the triple axis spectrometers LTAS and TAS-2. The energy was 4.66 meV and 14.7 meV for LTAS and TAS-2, respectively. We used Be and/or PG filters to remove the higher order contaminations.

The antiferromagnetic peaks were searched with polycrystalline sample with use of LTAS. At 8 K we observed antiferromagnetic peaks at the scattering angle of the (-$\frac{1}{2}$,$\frac{1}{2}$,0) and (-$\frac{1}{2}$,$\frac{1}{2}$,1) peak positions as shown in Fig. 1.

Figure 2 (a) shows the contour plot of the magnetic scattering intensity around the (-$\frac{3}{2}$,$\frac{3}{2}$,0) magnetic reflection in the (h,k,0) scat-

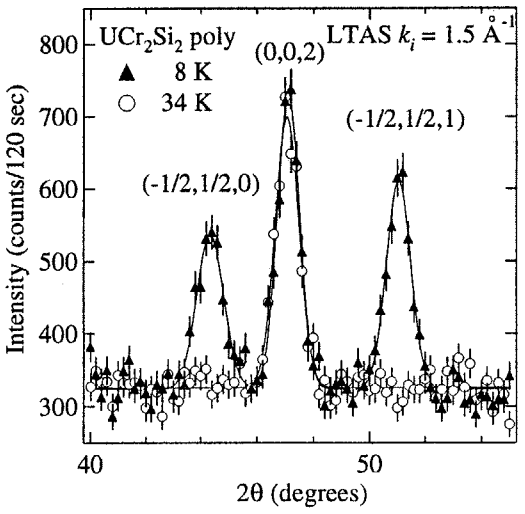


Figure 1: The powder diffraction pattern of UCr_2Si_2 at T= 8 K and 34 K.

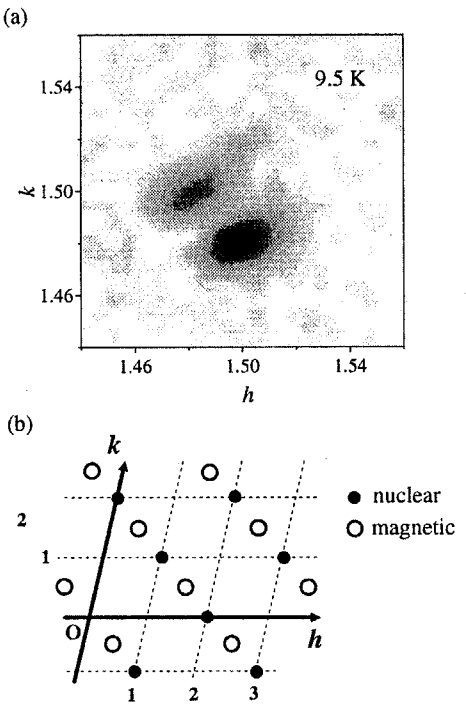


Figure 2: (a) The contour plot of the scattering intensity around (-$\frac{3}{2}$,$\frac{3}{2}$,0) magnetic reflections. (b)The position of the magnetic (close circles) and nuclear (open circles) reflections in the (h,k,0) scattering plane.

原子炉：JRR-3M　　装置：LTAS(C2-1)　　分野：中性子散乱（磁性）

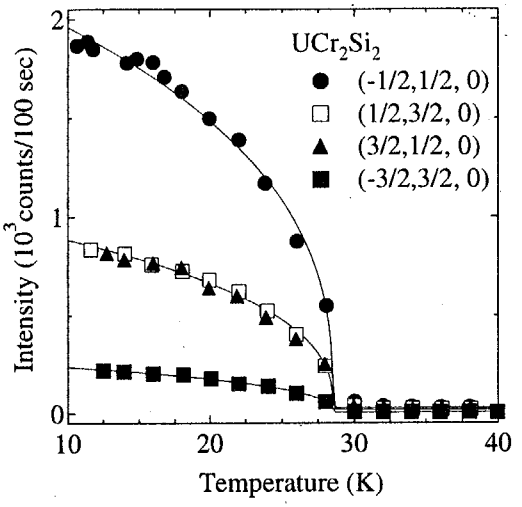


Figure 3: The temperature dependence of the antiferromagnetic Bragg intensities.

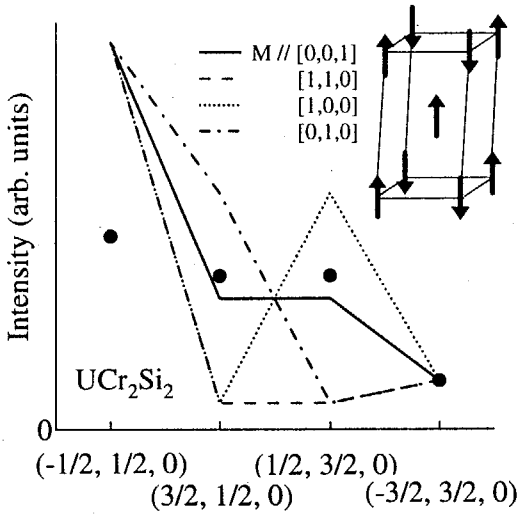


Figure 4: Integrated intensities of the magnetic reflection at 7 K for UCr_2Si_2. The experimental results (close circles) are compared to model calculations with different moment directions described in the figure.

tering plane. We observed splitting of the magnetic peaks. This splitting is due to the domain structure associated with the stractural transition of UCr_2Si_2. UCr_2Si_2 has a tricilinic structure below T_a = 210 K. From the peak position, we conclude that the antiferromagnetic wave vector is Q= [$-\frac{1}{2}$,$\frac{1}{2}$,0] . It should be noted that the wave vector [$-\frac{1}{2}$,$\frac{1}{2}$,0] is not equivalent to the [$\frac{1}{2}$,$\frac{1}{2}$,0] in the low temperature triclinic structure. The a^*-b^* reciprocal plane and the position of the antiferromagnetic reflections are shown in the schematic view graph in Fig. 2 (b).

The magnetic peak intensities were measured as a function of temperature. The peak intensities showed a clear nature of the magnetic order parameter as plotted in Fig. 3.

The observed integrated intensities of the magnetic reflections were compared with model calculations, using the following equation,

$$I_{mag} \quad (\boldsymbol{Q}) \propto | F_{mag}(\boldsymbol{Q}) |^2 f^2(\boldsymbol{Q})(\sin\alpha)^2 L(\theta),$$

where F_{mag} is the magnetic structure, f is the magnetic form factor of uranium U^{3+} free ion, α is the angle between the ordered magnetic moment and the scattering vector Q and L is the Lorentz factor.

The experimental results are well explained by the model calculation with the ordered moment of uranium 0.65 μ_B/U parallel to the [0,0,1] direction. The weaker intensity at the ($-\frac{1}{2}$,$\frac{1}{2}$,0) antiferromagnetic peak than the expected one from the model calculations is most probably due to the extinction, since this reflection is rather strong. The obtained magnetic structure is displayed schematically in the inset of Fig. 4. The obtained moment size is consistent with that of typical itinerant 5f antiferromagnet, UGa_3[2], $UPtGa_5$ and $UNiGa_5$.[3] The direction of the moment is consistent with the uniaxial anisotropy in magnetic susceptibility, where the c-axis is the easy axis.

References

1) T. D. Matsuda, N. Metoki, Y. Haga, S. Ikeda, T. Okubo, K. Sugiyama, N. Nakamura, K. Kaneko and Y. Ōnuki, J. Phys. Soc. Jpn., to be published.
2) A. Murasik, J. Leciejewicz, S. Ligenza, A. Zygmunt, Phys. Stat. Sol. (a) **23** (1974) K147;A. C. Lawson, A. Williams, J. L. Smith, P. A. Seeger, J. A. Goldstone, J. A. O'Rourke, Z. Fisk, J. Magn. & Magn. Mater. **50** (1985) 83.
3) Y. Tokiwa, Y. Haga, N. Metoki, Y. Ishii and Y. Ōnuki, J. Phys. Soc. Jpn., **71** (2002) 725.

研究テーマ：多重極限環境下における中性子散乱実験法の研究
表　題：遍歴5f反強磁性体UPt_2Si_2における磁気励起

1-2-55

Magnetic Excitations in an itinerant 5f antiferromagnet UPt_2Si_2

N. Metoki[1], Y. Koike[1,2], N. Bernhoeft[3], G. H. Lander[1,4], Y. Tokiwa[1,5], Y. Haga[1], Y. Ōnuki[1,5]

[1]ASRC-JAERI, Tokai, Naka, Ibaraki 319-1195
[2] JST, Kawaguchi, Saitama 332-0012
[3] DRFMC, DEA/Grenoble, 38054 Grenoble Cedex 9, France
[4] EC-JRC, Inst. for Transuranium Element, 2340-76125 Karlsruhe, Germany
[5]Graduate School of Science, Osaka University, Toyonaka, Osaka 560-0043

The wide variety of behaviour exhibited by 5f electrons is one of the most intriguing problems in strongly correlated electron systems. The spectrum, encompassing localised, heavy fermion, non-fermi liquid and itinerant aspects, depends on the strength of the hybridization with valence and ligand electron states. Materials in the UT_2Si_2 system play an important role in our understanding as the hybridisation can be controlled by varying the transition metal element T. In this respect the unusual transition at T_0 = 17 K and the superconductivity in URu_2Si_2 are especially interesting with, on the other hand, UPt_2Si_2 (T_N = 37 K, M=1.7μ_B) being considered as an example of an antiferromagnet with localised 5f states. The susceptibility [1] and specific heat [2] of the latter material were understood in terms of the crystalline electric field (CEF) levels suggested by a previous neutron scattering study on a polycrystalline sample [3] whilst the large drop of the resistivity at T_N and the anisotropic behaviour remained unexplained [3]. The purpose of this study is to reveal the magnetic excitations of UPt_2Si_2 in single crystalline samples.

Single crystalline samples were grown by the Czochralski-pulling method in a tetra-arc furnace under argon gas atmosphere. The manetic excitation was measured with three single crystal rods aligned within the accuracy of 0.3 degrees on a triple axis spectrometer LTAS with fixed E_f = 3.5 meV.

Figure 1 shows the crystal structure of UPt_2Si_2. UPt_2Si_2 has the $CaBe_2Ge_2$-type structure with space group P4/nmm. The uranium magnetic moments order antiferomagnetically below T_N = 37 K.

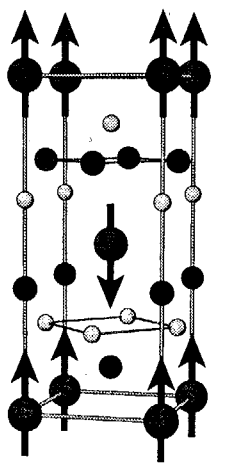


Figure 1: The crystal and magnetic structure of UPt_2Si_2.

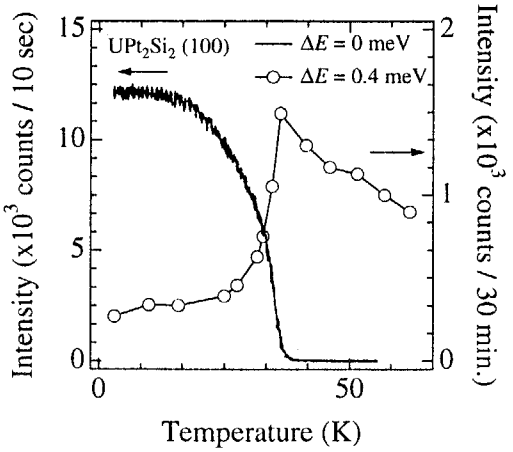


Figure 2: The intensity of the (100) antiferromagnetic Bragg peak and the inelastic component at ΔE = 0.4 meV in UPt_2Si_2, denoted by close and open circles, respectively.

原子炉：JRR-3M　　装置：LTAS(C2-1)　　分野：中性子散乱（磁性）

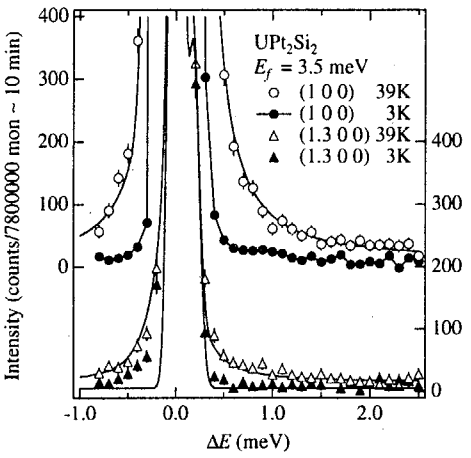


Figure 3: The inelastic scattering profile at $Q = (100)$ and (1.3 0 0), denoted by circles and triangles, respectively. The spectra were measured at 3.1 K (close symbols) and 38 K (open symboles), respectively.

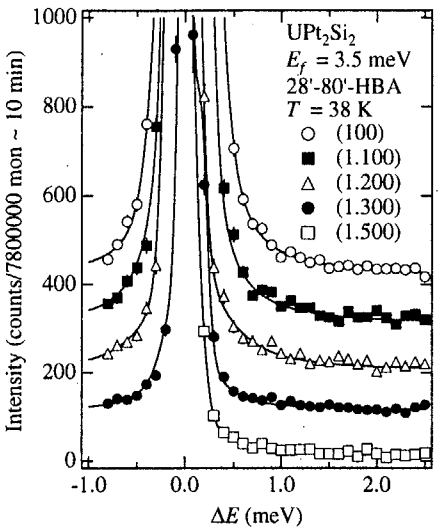


Figure 4: constant-Q profile of UPt_2Si_2 as a function of Q measured at T = 38 K.

The magnetic structure can be described by the antiferromagnetic stacking of the ferromagnetic basal plane along the c-axis as shown in Fig. 1. The uranium moment 1.67 μ_B/U is parallel to the c-axis.

The temperature dependence of the (100) antiferromagnetic Bragg intensity is plotted in Fig. 2. The intensity exhibits a clear nature of the magnetic order parameter. The intensity at the neutron enrgy loss $\Delta E = 0.4$ meV increases with elevating temperature and showed a maximum at T_N. It means that there is a low energy magnetic excitation.

The existence of the low energy component of the magnetic excitation is clearly demonstrated by the inelastic scattering profile shown in Fig. 3. On the (1 0 0) antiferromagnetic zone-center we observed pronounced quasi-elastic peak at T = 38 K, slightly above T_N. This quasi-elastic scattering can be fitted by Lorentzian line shape with the full width of 0.15 meV. This excitation decreases in intensity with decreasing temperature. At $Q = (1.3\ 0\ 0)$ a weaker and broader quasi-elastic scattering with width of 0.4 meV was observed. Figure 4 shows the magnetic excitation spectra of UPt_2Si_2 measured as a function of Q. It is clearly seen that the low energy quasi-elastic scattering has a maximum intensity around the antiferromagnetic zone center (100). We concluded that this low energy quasi-elastic component is spin fluctuations of the heavy quasi-particles due to hybridization between $5f$ and conduction electrons. Very recently similar low energy excitation has been observed in the heavy fermion superconductors UPd_2Al_3 [4], UPt_3 [5], and $5f$ itinerant antiferromagnet UGa_3. [6] It is also found even in the localized $5f$ antiferromagnet, $U_3Pd_{20}Si_6$. [7] Therfore the existence of the low energy quasi-elastic component due to quasi-particles is a general feature in uranium intermetallic compounds, because $5f$ electrons in uranium has rather strong hybridization effect.

References

1) G. J. Nieuwenhuys, Phys. Rev. **B35**, 5260 (1987).
2) H. Amitsuka *et al.*, Physica **B177**, 173 (1992).
3) R. A. Steeman *et al.*, J. Magn. Magn. Mater. **76&77**, 435 (1988), J. phys. Condens. Matter **2**, 4059 (1988).
4) N. Metoki *et al.*, Phys. Rev. Lett. **80**, 5417 (1998); N. R. Bernhoeft *et al.*, *ibid*, **81**, 4244 (1998).
5) N. R. Bernhoeft*et al.*, J. phys. Condens. Matter **7**, 7325 (1995).
6) S. Coad *et al.*, Physica **B281&282**, 200 (2000).
7) N. Metoki*et al.*, to be published.

研究テーマ：多重極限環境下における中性子散乱実験法の研究
表　題：遍歴 $5f$ 反強磁性体 $UNiGa_5$ 及び $UPtGa_5$ の結晶及び磁気構造

1-2-56

Neutron Scattering Study of the Magnetic and Crystal Structures in Itinerant-$5f$ Antiferromagnets $UNiGa_5$ and $UPtGa_5$

Y. Tokiwa[1,2], Y. Haga[1], N. Metoki[1], Y. Ishii[1] and Y. Ōnuki[1,2]

[1]ASRC-JAERI, Tokai, Naka, Ibaraki 319-1195
[2]Graduate School of Science, Osaka University, Toyonaka, Osaka 560-0043

Very recently we succeeded in growing single crystals of uranium intermetallic compounds $UTGa_5$ (T: Fe, Co, Ni, Ru, Rh, Os, Ir, Pt). These are iso-structural compounds of heavy fermion superconductors Ce115 and/or $PuCoGa_5$ with the $HoCoGa_5$-type tetragonal structure with space group (P4/mmm), as shown in Fig 1. [1] This crystal structure can be described by a stacking of uniaxially distorted UGa_3 layer with the $AuCu_3$-type structure and a transition metal layer along the [0,0,1] direction. $UTGa_5$ (T: Ni, Pd, Pt) are typical itinerant $5f$ antiferromagnet, while the other compounds exhibit Pauli-paramagnetic behavior. [2, 3] We revealed the crystal and magnetic structures of $UNiGa_5$ and $UPtGa_5$. [4]

Polycrystalline samples were synthesized by arc-melting and subsequent annealing. Single crystals were grown by the Ga self-flux method. The detail of sample preparation technique has been published elsewhere. [2, 3] Neutron scattering experiments were carried out using HRPD and TAS-1.

Figure 2 shows a powder diffraction pattern of $UNiGa_5$ at 8 K. The profile was satisfactorily analyzed by the $HoCoGa_5$-type structure. The structural parameters have been published eleswhere. [4] The UGa3 layer is more compressed in $UPtGa_5$ than in $UNiGa_5$ due to the larger ionic radius of Pt.

Figure 3(a) shows the result of the (h,h,h) scan for $UNiGa_5$ at 10 and 90 K, below and above T_N(=86 K), respectively. We observed clear antiferromagnetic reflections with half integer reflection indices such as (1/2,1/2,1/2) and (3/2,3/2,3/2). These data indicate that the antiferromagnetic propagation vector in $UNiGa_5$ is [1/2,1/2,1/2]. On the other hand, the antiferromagnetic peak of $UPtGa_5$ was observed at the Bragg points with half integer $l/2$ Therefore we conclude that the propagation vector in $UPtGa_5$ is [0,0,1/2]. No magnetic scattering was observed at (0,0,1/2), indicating the direction of the magnetic moment to be along the [0,0,1] in $UPtGa_5$.

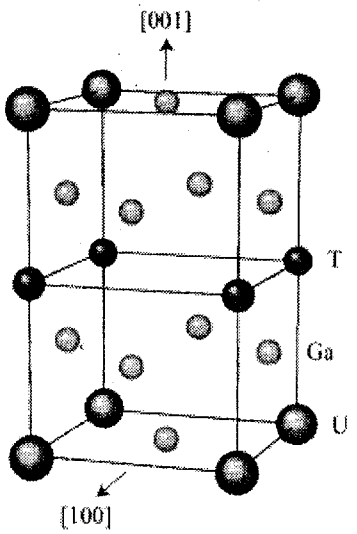


Figure 1: Crystal structure of $UTGa_5$.

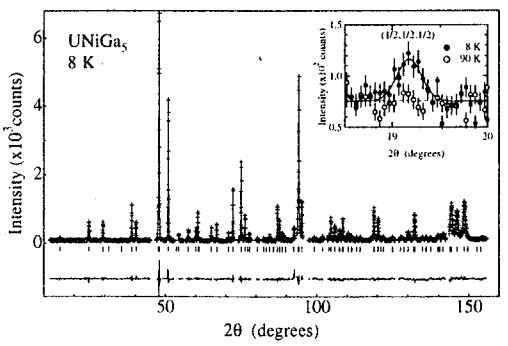


Figure 2: Crystal structure of $UTGa_5$.

原子炉：JRR-3M　　装置：TAS-1(2G)　　分野：中性子散乱（磁性）

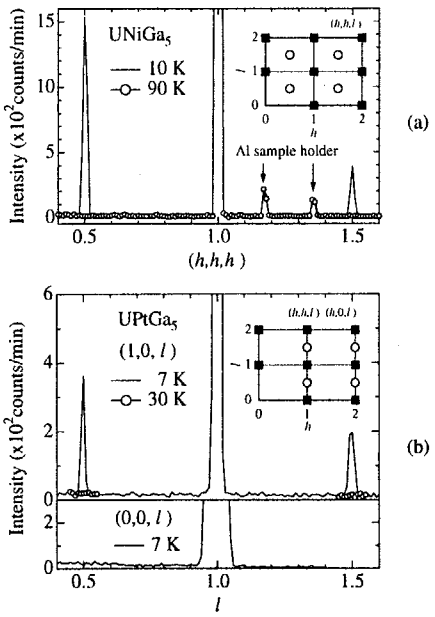


Figure 3: Elastic neutron scattering profile in the (a) (h,h,h) scan in $UNiGa_5$ and (b) $(1,0,l)$ and $(0,0,l)$ scans in $UPtGa_5$. Insets: The positions of the nuclear (solid squares) and magnetic (open circles) peaks.

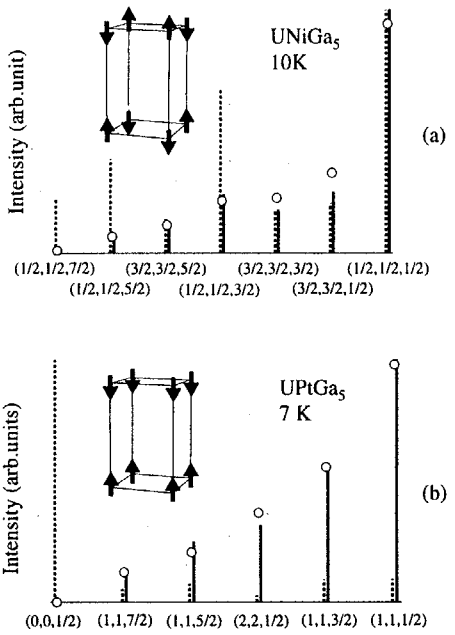


Figure 4: Integrated intensities of the magnetic reflections at 10 K for (a) $UNiGa_5$ and (b) $UPtGa_5$, respectively. Open circles are experimental results, while solid and dotted lines are model calculations with the magnetic moment parallel and perpendicular to the [0,0,1] axis, respectively.

From the propagation vector, the magnetic structures can be proposed as shown in Fig 4. In $UNiGa_5$ the uranium moment has the Néel-type structure. Namely adjacent spins orient along the opposite direction. On the other hand, magnetic moments of uramium atoms in $UPtGa_5$ are aligned ferromagnetically in the (0,0,1) plane and stacked antiferromagnetically along the [0,0,1] direction ($\uparrow\downarrow$). Fig 4 is the integrated intensities of the antiferromagnetic reflections. The experimental results are well explained by the model calculation with the moment parallel to the [0,0,1] direction. The magnetic moments were estimated to be $0.9\pm0.1\,\mu_B$/U and $0.24\pm0.03\,\mu_B$ in $UNiGa_5$ and $UPtGa_5$, respectively. The Ni and Pt moment should be negligibly small.

The magnetic structures in $UNiGa_5$ and $UPtGa_5$ are considerably different. The nearest-neighbor interaction has opposite sign. At present we have no definitive explanation for the unusual difference in magnetic structure. We believe, however, that the U-$5f$ and Ga-$4p$ hybridized band plays a significant role for the antiferromagnetic propagation vector. It is well known that the magnetic ordering is closely related to the electronic and orbital configuration. Therefore it might be possible to find out a configuration which gives rise to the cross over of the interaction in the basal plane between antiferromagnetic and ferromagnetic, when the p-f hybridization changes with stress due to the difference in ionic radius.

References

1) Yu. N. Grin, P. Rogl and K. Hiebl, J. Less Common Met. **121** (1986) 497.
2) Y. Tokiwa, Y. Haga, E. Yamamoto, D. Aoki, N. Watanabe, R. Settai, T. Inoue, K. Kindo, H. Harima and Y. Ōnuki: J. Phys. Soc. Jpn. **70** (2001) 1744.
3) Y. Tokiwa, S. Ikeda, Y. Haga, T. Okubo, T. Iizuka, K. Sugiyama, A. Nakamura and Y. Ōnuki, J. Phys. Soc. Jpn. **71** (2002) 845.
4) Y. Tokiwa, Y. Haga, N. Metoki, Y. Ishii and Y. Ōnuki, J. Phys. Soc. Jpn. **71** (2002) 725.

研究テーマ：先端偏極中性子散乱によるスピン-格子物性の研究
表　題：辺共有 CuO_2 鎖を有する $Ca_2Y_2Cu_5O_{10}$ の磁気構造

1-2-57

Magnetic structure of the coupled edge-sharing CuO_2 chains in $Ca_2Y_2Cu_5O_{10}$

M. Matsuda, K. Kakurai, H. Yamaguchi[1], T. Ito[1], C. H. Lee[1] and K. Oka[1]

ASRC, Japan Atomic Energy Research Institute, Tokai, Ibaraki 319-1195
[1]National Institute of Advanced Industrial Science and Technology, Tsukuba, Ibaraki 305-8568

An interesting feature in the edge-sharing CuO_2 chain, in which copper spins are coupled by the nearly 90° Cu-O-Cu interaction, is that the magnetic moments can be induced at oxygen sites because of a strong Cu d-O p hybridization in the CuO_2 chains. An existence of the magnetic moments in the CuO_2 chains is predicted theoretically in Li_2CuO_2. [1)] and observed experimentally in $La_9Ca_5Cu_{24}O_{41}$. [2)]

From a powder diffraction study, [3)] a possibility of a small amount of the magnetic moments at oxygen sites is suggested. However, the number of the magnetic Bragg peaks used for the magnetic structural analysis is only 5 and errors of the magnetic intensities are rather large because the magnetic intensities are weak except an intense (0,0,1) peak. As the result, the statistics are not enough to analyze the data quantitatively. In this study, we performed neutron diffraction measurements using a single crystal in order to elucidate the magnetic moment at oxygen sites in the ferromagnetic edge-sharing CuO_2 chains $Ca_2Y_2Cu_5O_{10}$.

The single crystal of $Ca_2Y_2Cu_5O_{10}$ was grown using a traveling solvent floating zone method in air. The dimensions of the rod shaped crystal were $\sim 6\Phi \times 25$ mm^3. The neutron scattering experiments were carried out on the 3-axis spectrometer TAS-2.

The magnetic Bragg reflections are expected at (even, even, odd) and (odd, odd, even) from the magnetic structure determined by the powder diffraction studies. [3, 4)] If the magnetic moments are localized at Cu sites and point along the b axis, the magnetic Bragg intensity should decrease monotonically with increasing Q, mainly due to the magnetic form factor and the Lorentz factor.

Figure 1 shows an elastic scan along $[h, h, l]$ measured at 9 K. The integrated intensities of a number of magnetic peaks were obtained from θ-2θ scans as shown in Table I. Along $[0, 0, l]$ and $[2, 2, l]$, the magnetic intensities decrease with increasing Q. On the other hand, along $[1, 1, l]$ the magnetic intensities shows a modulation and has a maximum at (1,1,2). This behavior is similar to that observed along $[h, 0, 1]$ in $La_6Ca_8Cu_{24}O_{41}$.

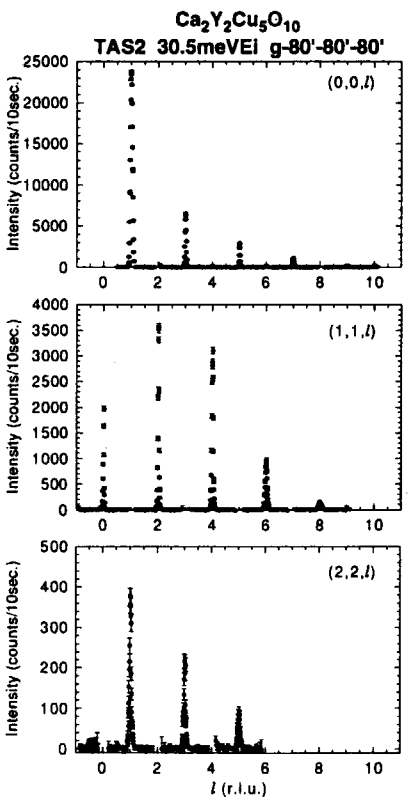


Figure 1: Elastic neutron scans of $Ca_2Y_2Cu_5O_{10}$ along $[0, 0, l]$ (a), $[1, 1, l]$ (b), and $[2, 2, l]$ (c) measured at T=9 K. The data at T=35 K were subtracted as background.

原子炉：JRR-3M　　装置：TAS-2(T2-4)　　分野：中性子散乱（磁性）

Table 1: Observed integrated (I_{obs}) and calculated intensities (I_{calc}) of magnetic Bragg reflections on $Ca_2Y_2Cu_5O_{10}$. The measurements were performed at T=9 K. I_{Cu} represents the intensity calculated by assuming the magnetic moments only at the Cu sites.

(h,k,l)	I_{obs}	I_{calc}	I_{Cu}
(0,0,1)	105(4)	152	90.6
(0,0,3)	18.3(2)	19.8	22.9
(0,0,5)	8.0(2)	5.4	8.5
(0,0,7)	4.3(2)	4.4	3.6
(0,0,9)	1.6(1)	2.7	1.5
(1,1,0)	4.8(1)	6.2	10.2
(1,1,2)	9.0(1)	8.9	8.6
(1,1,4)	10.1(1)	10.0	5.6
(1,1,6)	5.1(1)	4.4	2.9
(1,1,8)	1.4(1)	1.0	1.4
(2,2,1)	2.4(1)	2.6	1.6
(2,2,3)	1.6(1)	1.1	1.3
(2,2,5)	1.0(1)	0.58	0.93
χ^2	–	2.9	9.8

As shown in Table 1, a simple model that assumes magnetic moments only at the Cu sites does not describe the modulation of the intensity along $[1,1,l]$. One possibility to explain the modulation would be that the Cu moments do not point exactly along the b axis but between the a and b axes. However, this structure also requires the similar modulation of magnetic intensities along $[2,2,l]$. Therefore, it is more plausible that moments induced on the oxygen sites present in the magnetically ordered phase as described below.

The result of a least-square fitting shows that the moment at the oxygen site is 14±2% of that at the Cu site. The fitted magnetic intensities agree reasonably well with the observed ones as shown in Table 1. Assuming that the total moment in a CuO_2 unit is $\sim 0.9\mu_B$, which is determined from the powder diffraction measurement, [3, 4] the ordered Cu moment is estimated to be $\sim 0.7\mu_B$ and the O moment is $\sim 0.1\mu_B$. Although there is an ambiguity in the absolute value of the magnetic moment, a ratio between copper and oxygen moments should be quite accurate. Note that the absolute value of the ordered moment in $Ca_2Y_2Cu_5O_{10}$ ($\sim 0.9\mu_B$) is larger than in $La_5Ca_9Cu_{24}O_{41}$ ($\sim 0.2\mu_B$) [2] probably because the interchain coupling along the b axis is larger so that the quantum fluctuation is more suppressed. The fraction of the oxygen moment in the CuO_2 unit is 22±4%, which is similar to that in $La_5Ca_9Cu_{24}O_{41}$ ($\sim$17%). [2] This fact suggests that the covalency between the Cu and O ions in the CuO_2 chain is similar in both compounds.

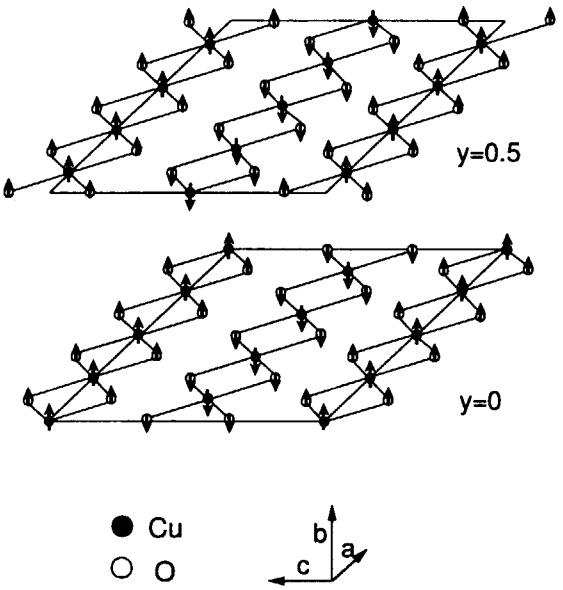


Figure 2: A proposed model for the magnetic structure in the CuO_2 chain. Closed and open circles represent copper and oxygen ions, respectively.

References

1) R. Weht and W. E. Pickett, Phys. Rev. Lett. **81** (1998) 2502.
2) M. Matsuda, K. M. Kojima, Y. J. Uemura, J. L. Zarestky, K. Nakajima, K. Kakurai, T. Yokoo, S. M. Shapiro and G. Shirane, Phys. Rev. B **57** (1998) 11467.
3) M. Matsuda, K. Ohoyama and M. Ohashi, J. Phys. Soc. Jpn. **68** (1999) 269.
4) H. F. Fong, B. Keimer, J. W. Lynn, A. Hayashi and R. J. Cava, Phys. Rev. B **59** (1999) 6873.

研究テーマ：高濃度スピングラスにおけるスローダイナミックスの機構
表　題：中性子小角散乱法による高濃度スピングラススローダイナミックスの研究

1-2-58

SANS Study of Slow Dynamics in Concentrated Spin Glasses

K. MOTOYA, K. HIOKI and J. SUZUKI[1]

Department of Physics, Tokyo University of Science, Noda 278-8510
[1]Advanced Science Research Center, JAERI, Tokai, Ibaraki 319-1195

Although the problem of slow dynamics, or long time relaxation phenomena, has long been a central issue of the spin-glass research, the experimental studies on slow dynamics have been limited to macroscopic measurements. In order to clarify the mechanism of slow dynamics, the application of microscopic experimental method such as time-resolved neutron scattering technique has been needed. In the previous neutron scattering studies on concentrated spin-glass alloys we showed that the magnetic clusters play an important role for the reentrant spin-glass (RSG) transition and that a wide variety of spin dynamics observed in various RSG materials can be attributed to the differences in the size and the number of magnetic clusters. [1)] Based on this finding, we speculate that the mechanism of slow dynamics might be closely related to the time evolution of magnetic clusters which can be detected by small-angle neutron scattering (SANS) experiment.

We have made time-resolved SANS experiments on several kinds of concentrated spin glass materials of which characteristics in the stationary state had been clarified in the previous neutron scattering experiments. [1, 2, 3)] In this report, we present a result of the time-resolved SANS experiment of a typical spin glass alloy $Fe_{0.70}Al_{0.30}$ in magnetic field. Results in zero magnetic field of the present sample and other RSG alloys have already been reported elsewhere. [4, 5)]

$Fe_{0.70}Al_{0.30}$ alloy used in the present experiment transforms to the ferromagnetic phase below 510K then enters the paramagnetic phase below 160K and finally it enters the spin-glass phase at 70K. Microscopic characterizations of the magnetic "phases" of the present alloy system was extensively investigated by elastic and inelastic neutron scattering measurements. [2, 6)]

Time-resolved SANS experiments were made utilizing the SANS-J spectrometer installed at the JRR-3M reactor of JAERI-Tokai. The incident-neutron wavelength and band-width are λ=0.45-0.65nm and $\Delta\lambda/\lambda$=0.10-0.14, respectively. The momentum-transfer range of $0.03<q<2$ nm^{-1} was covered by changing the sample-detector length between 1.35 to 10m. Sample was rapidly cooled to the RSG phase in zero field. After the waiting time t_w magnetic field was applied and a series of time-resolved SANS patterns was taken up to 20hrs with a typical time window of 10-30min. Observed SANS patterns (scattering intensity as a function of momentum transfer q) are well traced by a Lorentzian (LOR) function

$$I(q) = \frac{A}{q^2 + \kappa^2}$$

within the q range of $0.06<q<0.3$ nm^{-1}. Based on a simple model, the LOR form is attributed to the scattering from magnetic clusters with correlation length of $1/\kappa$. [1, 2, 7)]

In Fig.1, we show the time variation of κ measured under (a) H=0 Oe and (b) H=500 Oe at representative temperatures. In zero field the time variation of κ is more pronounced as temperature increases, however the initial value (κ at time=0) does not change so much with temperature. Under H=500Oe, the initial value and the time variation behavior are quite different from those in zero field. At T=10K, the initial value is nearly same as that in H=0. At high temperatures the initial value is remarkably larger than that of at H=0, which means κ suddenly increases by the application of field. Time variation of

原子炉：JRR-3M　　装置：SANS-J(C3-2)　　分野：中性子散乱（磁性）

κ either in H=0 Oe or in H=500 Oe is well traced by a simple function

$$\kappa(t) = \kappa_0 + A \exp\left(-\frac{t}{t^*}\right)$$

with a temperature dependent characteristic time t^*. In Fig. 2 we show $1/t^*$ as a function of temperature. Detailed analysis and discussion including the results of macroscopic measurements will be presented elsewhere. [8]

References

1) K. Motoya, S. Kubota and K. Nakaguchi: J. Phys. Soc. Jpn. **68** (1999) 2351.
2) K. Motoya, S. M. Shapiro and Y. Muraoka: Phys. Rev. B. **28** (1983) 6183.
3) K. Motoya and Y. Muraoka: J. Phys. Soc. Jpn. **62** (1993) 2819.
4) K. Motoya, K. Hioki and J. Suzuki: J. Phys. Soc. Jpn. **70** (2001) suppl. A 139. (2000) 29.
5) K. Motoya, K. Hioki and J. Suzuki: Appl. Phys. (in press)
6) H. A. Child: J. Appl. Phys. **52** (1981) 1732.
7) K. Motoya, S. Kubota and S. M. Shapiro: J. Mag. Mag. Mater. **140-144** (1995) 75.
8) K. Motoya, K. Hioki and J. Suzuki: XII Int. Conf. on Small-Angle Scattering.

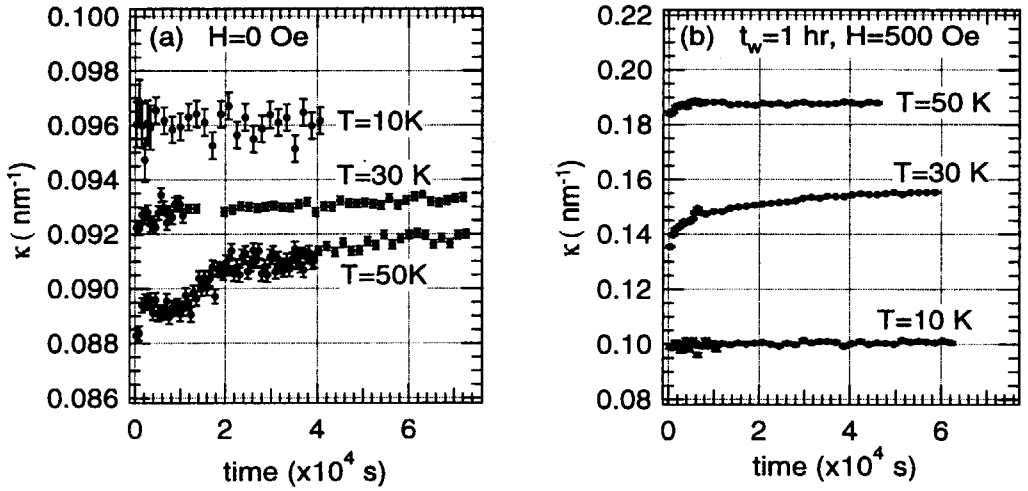


Figure 1:

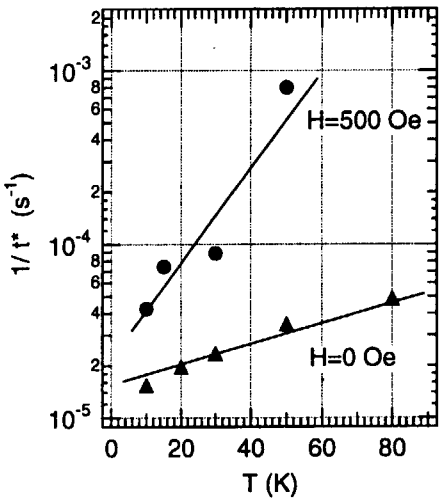


Figure 2:

研究テーマ：$Cr_{1-x}Te_x$ 系の磁気構造
表　題：$Cu_{1-x}Zn_xCr_2Se_4$ の磁気構造と異常ホール効果の関係

1-2-59

Relationship between the Magnetic Structure and the Anomalous Hall Effect of $Cu_{1-x}Zn_xCr_2Se_4$

S. Iikubo, Y. Ohno, Y. Yasui, T. Fukamachi, K. Oda, M. Sato and K. Kakurai[1]

Department of Physics, Nagoya University, Furo-cho, Chikusa-ku, Nagoya 464-8602
[1]Advanced Science Research Center, JAERI, Tokai, Ibaraki 319-1195

In the study of the magnetic and transport properties of $Nd_2Mo_2O_7$, we have reported that its Hall resistivity ρ_H cannot be described by the equation $\rho_H=R_0H+4\pi R_sM$ used for ordinary ferromagnets, where H and M are the applied magnetic field and the uniform magnetization, respectively, and R_0 and R_s are the ordinary and anomalous Hall coefficients, respectively [1]. Instead, an equation $\rho_H=R_0H+4\pi R_sM_{Mo}+4\pi R'_sM_{Nd}$, which has two individual contributions from the Mo- and Nd-moments, M_{Mo} and M_{Nd}, respectively, can describe the T- and H-dependences of ρ_H. Although the equation seems to be a simple extension of the ordinary equation, the T-dependences of the anomalous Hall coefficients R_s and R'_s obtained for the present system cannot be understood by the classical theories. Then, a question arises how this unusual behavior of ρ_H is related with its non-collinear magnetic structure reported by the present authors' group [2]. It is interesting to study effects of the ordering of the spin chirality χ on the behavior of ρ_H, the possibility of which has been pointed out by Ohgushi *et al.* [3].

Here, the spinel type ferromagnet $Cu_{1-x}Zn_xCr_2Se_4$ has been adopted as a candidate, which has the non-trivial spin structure but simpler magnetic behavior than that of $Nd_2Mo_2O_7$ in the sense that it has only one magnetic elements. The transport and magnetic properties as well as the magnetic structures have been studied. At x=0, it is a collinear ferromagnet with Curie temperature $T_C\cong$450 K and at x=1.0, it has the helical structure with the Neel temperature T_N=20 K, and from measurements of the M-H curves, the conical structure is expected for the intermediate x region below the characteristic temperature T_m(~150 K), at which the slope -dM/dT begins to increase gradually with decreasing T. For x=0.5, we have reported the anomalous sign change of ρ_H at around $\sim T_m$ [4].

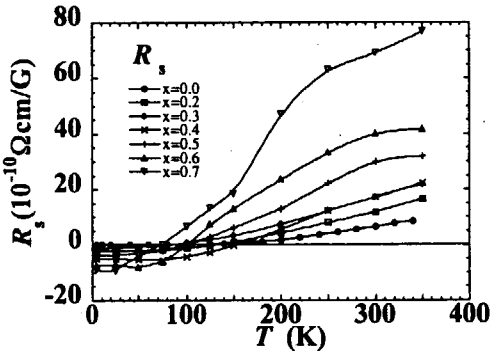


Figure 1: The anomalous Hall coefficients R_s are shown. They are obtained by the fittings H-dependence of ρ_H by using the equation $\rho_H=R_0H+4\pi R_sM$.

Polycrystalline samples which are confirmed to be the single phase by X-ray diffraction are used. The Hall resistivity ρ_H was measured by the four probe method. Neutron diffraction studies have been carried out at JRR-3M of JAERI for three samples with x=0.3, 0.5 and 0.7. Other details of the sample characterizations and physical measurements are described elsewhere [4].

In the analyses of the T- and H-dependences of ρ_H, we have used the equation $\rho_H=R_0H+4\pi R_sM$, and the R_s values obtained here are shown in Fig. 1. R_s of the sample with x=0, which has the collinear magnetic structure, approaches zero, as in the

原子炉：JRR-3M　　装置：TAS-2(T2-4)　　分野：中性子散乱（磁性）

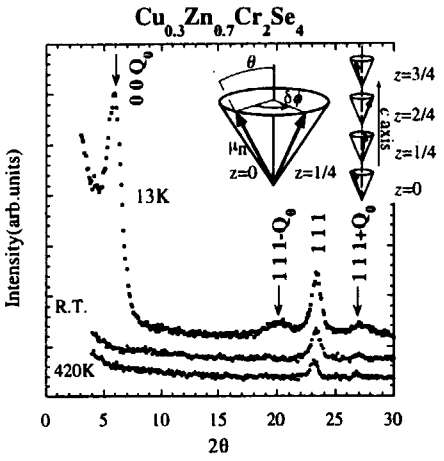


Figure 2: Neutron diffraction patterns of $Cu_{0.3}Zn_{0.7}Cr_2Se_4$ taken at 13 K, room temperature and 420 K. The arrows show the incommensurate magnetic superlattice reflections which indicate the conical magnetic structure.

case of ordinary ferromagnets, while for the other samples, the sign change takes place at around T_m(~ 150 K), suggesting the possible effects of the non-trivial magnetic structure to the behavior of ρ_H.

In Fig. 2, the neutron diffraction patterns taken at 420 K($T>T_C$~390 K), at room temperature and at 13 K are shown for x=0.7, for example. (The wave length =2.4436 Å.). At 13 K, additional reflections can be seen at the angles which correspond to the reciprocal points, (0,0,Q_0), (1,1,1-Q_0) and (1,1,1+Q_0), with the incommensurate vector Q_0~ 0.440 in the unit of reciprocal lattice a^*, indicating that the magnetic structure is non-trivial. The peak intensity of the superlattice reflection at (0,0,Q_0) gradually increases with decreasing T below 150 K. This gradual growth of the superlattice peak or the non-trivial magnetic structure seems to be related to the gradual increase of the magnetization M and the anomalous sign change at around T_m with decreasing T. Considering that the magnetic structure of $Cu_{1-x}Zn_xCr_2Se_4$ changes from the collinear to the helical one with the modulation vector along [001], as x changes from 0 to 1 [5], we adopt a model that the structures of the present samples are conical with the modulation vector along [001] and with the magnetic moments within a z-plane directing the same direction (See inset of Fig. 2 for the details, where θ and $\delta\Phi$ are the tilting angle of the moments from the z axis and the difference of azimuthal angles between the neighboring z-planes, respectively.). Then, by fitting the calculated intensities to the experimentally obtained integrated intensities of the magnetic reflections, values of the fitting parameters, θ, $\delta\Phi$ and the absolute value of the ordered moment μ_n of Cr atom are obtained. The results are as follows. θ=14.5°, $\delta\Phi$=50.3°, μ_n=2.6μ_B, for x=0.3, θ=22°, $\delta\Phi$=42.1°, μ_n=2.49μ_B, for x=0.5, and θ=32°, $\delta\Phi$=39.6°, μ_n=2.57μ_B, for x=0.7.

One of the interesting thing is that the sign change of ρ_H takes place along with the appearance of the conical structure confirmed here by the neutron diffraction. Because the present samples are in the polycrystalline form, we cannot directly argue the effects of the non-trivial structure. However, it is interesting to mention that for the larger value of θ, the larger absolute value of R_s at $T \rightarrow 0$ was observed, which may indicate that the spin chiraility locally defined by $S_1 \cdot S_2 \times S_3$ for three spins S_1, S_2 and S_3, contributes in the present polycrystalline samples. To clarify the relationship between ρ_H and the spin structure, we have to use single crystals and study the detailed behavior of ρ_H in various magnetic field directions.

References

1) S. Yoshii, S. Iikubo, T. Kageyama, K. Oda, Y. Kondo, K. Murata and M. sato : J. Phys. Soc. Jpn. **69** (2000) 3777; *ibid.* **70** (2001) 212.
2) Y. Yasui, Y. Kondo, M. Kanada, M. Ito, H. Hrashina, M. sato and K. Kakurai : J. Phys. Soc. Jpn. **69** (2000) 284.
3) K. Ohgushi et al. : Phys. Rev. B **62** (2000) R6065.
4) K. Oda, S. Yoshii, Y. Yasui, M. Ito, T. Ido, Y. Ono, Y. Kobayashi and M. Sato : J. Phys. Soc. Jpn. **70** (2001) 2999.
5) J. Krok et al. : Phase Transit **4** (1983) 1.

研究テーマ：先端偏極中性子散乱によるスピン-格子物性の研究
表　題：高圧下中性子回折実験によるUGa_3の反強磁性秩序の研究
1-2-60

Neutron diffraction study of antiferromagnetic order in UGa_3 under pressure

M. NAKAMURA[1], Y. KOIKE[1,2], N. METOKI[1], K. KAKURAI[1], Y. HAGA[1], G.H. LANDER[1,3], Y. ŌNUKI[1,4]

[1]Advanced Science Research Center, JAERI, Tokai, Ibaraki 319-1195, Japan
[2]Japan Science and Technology Corporation, Kawaguchi, Saitama 332-0012, Japan
[3]European Commission, JRC, Institute for Transuranium Elements, Postfach 2340, D-76125 Karlsruhe, Germany
[4]Graduate School of Science, Osaka University, Toyonaka, Osaka 560-0043

The nature of $5f$-electrons exhibits various attractive physics. One of the unique characters is the large spin-orbit interaction and the resulting large orbital moment. Many intermetallic actinide compounds exhibit itinerant $5f$-character, due to the strong hybridization with the conduction electrons. The UX_3 systems have $AuCu_3$-type cubic structure and show a great variety of magnetic properties depending on the ligand element. In this study we have tried to discuss the contribution of the orbital magnetic moment in UGa_3 by changing the strength of hybridization with applied pressure[4]. The UGa_3 orders antiferromagnetically at $T_N = 67$ K with a small magnetic moment of $0.6 - 0.8\ \mu_B$. The itinerant character of UGa_3 has been revealed by previous experimental results[1, 2]. The moment direction of UGa_3 is still controversial, although many experiments were performed.

The neutron diffraction measurements were carried out on the triple-axis spectrometers TAS-1 and TAS-2 installed at the research reactor JRR-3M. The scans were performed in the (h, l, l) scattering plane. Quasi-hydrostatic pressure was applied by McWhan-type clamp cell up to $P = 2.2$ GPa. We found that the Néel temperature T_N decreases with the rate of $dT_N/dP = -9.9 \pm 0.4$ K/GPa. This pressure dependence of T_N is in good agreement with the value obtained by magnetic susceptibility measurements, $dT_N/dP = -11 \pm 2$ K/GPa[3]. Furthermore, we observed that the magnetic moment (μ) drastically decreases with increasing pressure, from $\mu \sim 0.6\mu_B$ at 0 GPa to $\mu \sim 0.3\mu_B$ at 2.2 GPa. These features support the itinerant nature of antiferromagnetism.

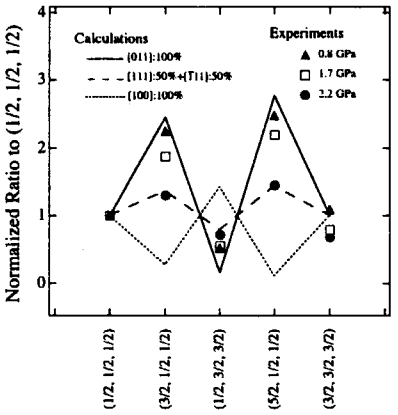


Figure 1: The ratio of intensities at 0.8 GPa (solid triangles), 1.7 GPa (open squares) and 2.2 GPa (solid circles) to those at 0 GPa. The calculated angle factors are also plotted for $\mu \| [011]$ (solid line), $\mu \| [111]$ and $[\bar{1}11]$ (dashed line), and $\mu \| [100]$ (dotted line). All of the data are normalized to the value at (1/2, 1/2, 1/2).

Figure 1 shows the pressure dependence of the integrated intensity divided by the value at ambient pressure. The magnetic peak intensities are measured at 3 K. All the data are plotted by normalizing the intensity at (1/2, 1/2, 1/2) to be unity. The experimental results for the other Bragg points obviously deviates from unity, indicating the changes in relative intensity with pressure. It suggests the modification of the domain population and/or change in moment direction. The intensity of the magnetic peak I_M is described

原子炉：JRR-3M　　装置：TAS-1(2G) TAS-2(T2-4)　分野：中性子散乱（磁性）

as follows,

$$I_M = K\mu^2 L(\theta) \sum_{\tau} \{f(\tau)\}^2 \{1-(\hat{\tau}\cdot\hat{\mu})^2_{av}\} \delta(\boldsymbol{Q}-\tau). \quad (1)$$

The term $\{1-(\hat{\tau}\cdot\hat{\mu})^2_{av}\}$ is referred to as the angle factor, where $\hat{\tau}$ and $\hat{\mu}$ is a unit vector along the reciprocal lattice vector and the moment, respectively. If all the domains are equally populated, the relation of $1-(\hat{\tau}\cdot\hat{\mu})^2_{av} = 2/3$ holds independent of $\boldsymbol{Q}$ and $\boldsymbol{\mu}$. This situation is realized at ambient pressure. In a single-domain sample the angle factors are strongly affected by the direction of $\boldsymbol{Q}$ and $\boldsymbol{\mu}$. The calculated angle factors are also plotted in Fig. 1. We found that the experimental results at 0.8 GPa are well reproduced and that the sample has a single domain with the moment along the [011] direction. A possible explanation for the presence of a single domain is a small residual uniaxial component in our pressure cell. At 2.2 GPa the uranium moment seems to be parallel to the $\langle 111 \rangle$ directions. In the present scattering geometry, both the [111] and [$\bar{1}$11] axes are perpendicular to the uniaxial pressure. The calculated angle factor for [111] is the average for these equivalent directions. The reorientation of the magnetic moment under high pressure is a highly interesting result, however the mechanism of this phenomena remains an open question. It can be easily imagined that the orbital moment and its suppression under pressure play a significant role.

Figure 2 shows the magnetic scattering amplitude $\mu f(\boldsymbol{Q})$ in the ordered antiferromagnetic state at 0 GPa and 2.2 GPa. The values of $\mu f(\boldsymbol{Q})$ at $P = 0$ GPa are obtained based on the constant angle factor $\langle \sin^2\alpha \rangle = 2/3$ for all magnetic peaks, while those at 2.2 GPa are obtained from the averaged angle factor for $\langle 111 \rangle$ directions. Using the dipole approximation[5], we may write

$$\mu f(\boldsymbol{Q}) = \mu \times (\langle j_0 \rangle + C_2 \langle j_2 \rangle), \quad (2)$$

where the functions $\langle j_i \rangle$ are the spherical Bessel function. The coefficient C_2 is given as $C_2 = \mu_L/(\mu_L + \mu_S)$, where μ_L and μ_S are orbital and spin moment, respectively.

The dotted line in the figure is the curve reported by Hiess *et al.*[6] in the form of $\mu f(\boldsymbol{Q}) = 0.63 \times (\langle j_0 \rangle + 2.52\langle j_2 \rangle)$, which suggests $\mu_L/\mu_S = -1.66$. Our experimental data at ambient pressure are in good agreement with the their results[6]. This result indicates that the contribution from orbital moment plays dominant role in the magnetic moment of UGa_3. The dashed line is the *temporary* fitting curve in the form of $\mu f(\boldsymbol{Q}) = 0.3 \times (\langle j_0 \rangle + 3.0\langle j_2 \rangle)$, which suggests $\mu_L/\mu_S = -1.5$. The statistical errors in our preliminary results at $P = 2.2$ GPa are not small enough to distinguish the spin and orbital contribution reliably, although there is an indication that the spin and orbital moments are further compensated under pressure, as predicted in Ref. 6. We need further experiments to obtain a reliable result of the form factor under pressure.

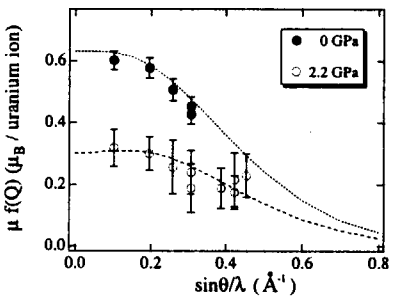


Figure 2: The magnetic scattering amplitude $\mu f(\boldsymbol{Q})$ as a function of $\sin\theta/\lambda$ for UGa_3 both at 0 GPa and 2.2 GPa.

References

1) D. Kaczorowski *et al.*, Phys. Rev. B **48** (1993) 16425.
2) A. Misiuk *et al.*, Bull. Acad. Pol. Sci. Ser. Sci. Chim. **20** (1972) 459.
3) G.E. Grechnev, A.S. Panfilov, I.V. Svechkarev, A. Delin, B. Johansson, J.M. Wills, O. Eriksson, J. Magn. Magn. Mater. **192** (1999) 137.
4) M. Nakamura *et al.*, J. Phys. Chem. Solids **63** (2002) 1193.
5) W. Marshall and S.W. Lovesey, *Theory of Thermal Neutron Scattering* (Oxford University Press, Oxford, 1971).
6) A. Hiess *et al.*, Europhys. Lett. **55** (2001) 267.

研究テーマ：先端偏極中性子散乱によるスピン-格子物性の研究
表　題：磁場中中性子散乱による DyB_2C_2 における反強四極子秩序の研究

1-2-61

Neutron Scattering Study on the Antiferroquadrupolar Order of DyB_2C_2 under Magnetic Fields

H. Yamauchi, K. Ohoyama, S. Katano[1], M. Matsuda[1], H. Onodera and Y. Yamaguchi

Institute for Materials Research, Tohoku University, Sendai, Miyagi 980-8577
[1]Advanced Science Research Center, Japan Atomic Energy Research Institute, Tokai, Ibaraki 319-1195

RB_2C_2 (R＝rare earth) compounds, which exhibit various magnetic properties, have been attracting a great deal of interest, because the interactions between quadrupolar moments representing the asphericity of the $4f$-charge distribution play significant roles in the physical phenomena. In particular, DyB_2C_2 is the first compound with a tetragonal symmetry showing an antiferroquadrupolar (AFQ) ordering. [1, 2, 3] This compound undergoes successive transitions from a paramagnetic phase (I) into an antiferroquadrupolar (AFQ) ordered phase (II) at $T_Q = 24.7$ K, and further into a coexisting phase (III) of the AFQ and antiferromagnetic (AFM) orders at $T_N = 15.3$ K. Below T_N, a strange AFM structure occurs, which is reperesented by four propagation vectors of $\boldsymbol{k}_1 = (1\,0\,0)$, $\boldsymbol{k}_2 = (1\,0\,1/2)$, $\boldsymbol{k}_3 = (0\,0\,0)$, $\boldsymbol{k}_4 = (0\,0\,1/2)$.

Neutrons can disclose the AFQ ordering through the observation of field-induced antiferromagnetic peaks, reflecting the existence of distinct easy axes on the two AFQ sublattices. In order to get new experimental evidence for the AFQ order in DyB_2C_2, we performed neutron scattering experiments under magnetic fields on the triple-axis spectrometer TAS-2 installed at the thermal neutron guide of JRR-3M of Japan Atomic Energy Research Institute (JAERI).

The single crystals of $Dy^{11}B_2C_2$ were grown by the Czochralski method with a tetra-arc furnace. Since natural boron is a strong neutron absorber, B in the sample was replaced with enriched ^{11}B isotope whose absorption cross section is negligible small. The scattering plane was chosen in the a^*-c^* reciprocal lattice plane in order to look for the $(h\ 0\ l)$ type reflections, since the propagation vector of the AFQ ordered structure which is consistent with the magnetic structure below T_N is expected to be $\boldsymbol{k} = (0\,0\,1/2)$ or $(1\,0\,1/2)$. Magnetic fields were applied vertically to the scattering plane, i.e. along [0 1 0] direction, using a He-free type 10 T superconducting magnet developed by JAERI. [4, 5] The details of the reciprocal lattice space investigated are already reported in the previous work. [6]

The application of magnetic fields up to 2.5 T causes the appearance of 1 0 1/2, 1 0 1 and 1 0 3/2 reflections in addition to the nuclear ones, though 0 0 1/2 was not observed. These results are consistent with the previous ones. [6] The rocking curves of 1 0 1/2 and 1 0 1 taken at 19 K for several fields up to 2.5T are shown in Fig. 1. The scan in the paramagnetic phase at 30 K for $H = 2$ T is also shown together (mascles). As can be seen from Fig. 1, the 1 0 1/2 reflection develops rapidly with increasing fields, while no peak is recognized in zero field nor at 30 K for $H = 2$ T within experimental accuracy in the present measurements. The 1 0 1 reflection also exhibits a distinct increase with magnetic fields up to 2.5 T. Because the 1 0 1/2 and 1 0 1 reflections are derived from the components of induced magnetic moments parallel and perpendicular to applied magnetic field, respectively, the intensity of 1 0 1/2 is much larger than that of 1 0 1.

Figure 2 shows integrated intensities of the 1 0 1/2 and 1 0 1 peaks. The background components were subtracted from the data. The arrows with T_N and T_Q indicate the transition temperatures determined from the specific heat measurements. When a magnetic field is applied with $H = 2$ T, 1 0 1/2 and 1 0 1

原子炉：JRR-3M　　装置：TAS-2(T2-4)　　分野：中性子散乱（磁性）

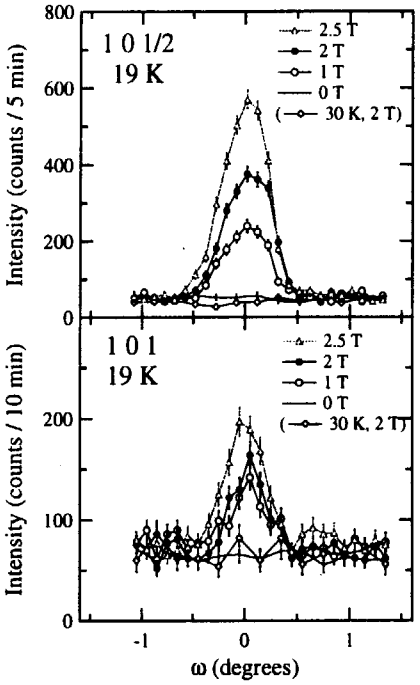


Figure 1: Rocking curves of the induced antiferromagnetic peaks 1 0 1/2 and 1 0 1 at 19 K for several fields up to 2.5T. Mascles indicate the scan at 30 K under 2 T, that is, in the paramagnetic phase. All the data are normalized by the fixed monitor counts.

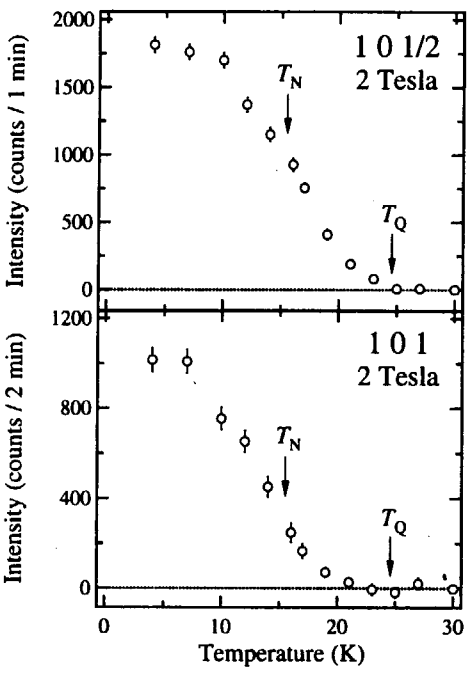


Figure 2: Integrated intensities of the 1 0 1/2 and 1 0 1 peaks. The background components were subtracted from the data. The arrows with T_N and T_Q indicate the transition temperatures determined from the specific heat measurements. [1)]

peaks appear below T_Q. On the other hand, we have already confirmed that magnetic reflections do not exist in the AFQ ordered phase for $H=0$, which indicates that transition occuring in zero field is not associated with magnetic dipole order. [1)] Therefore we can easily conclude that the appearance of the observed peaks is attributed to AFM components of Dy dipole moments induced by applied magnetic fields restricted by the underlying AFQ order.

The next step of our study is to determine the quadrupolar ordered structure and the symmetry type of the quadrupolar order parameter. For this purpose, neutron scattering experiments in the $[1\,1\,0]^*$-c^* scattering plane under magnetic fields along $[\bar{1}\,1\,0]$-axis are now in progress.

References

1) H. Yamauchi, H. Onodera, K. Ohoyama, T. Onimaru, M. Kosaka, M. Ohashi and Y. Yamaguchi: J. Phys. Soc. Jpn. **68** (1999) 2057.
2) Y. Tanaka, T. Inami, T. Nakamura, H. Yamauchi, H. Onodera, K. Ohoyama and Y. Yamaguchi: J. Phys.: Condens. Matter **11** (1999) L505.
3) K. Hirota, T. Matsumura, H. Nakao, Y. Wakabayashi, Y. Murakami and Y. Endoh: Phys. Rev. Lett. **84** (2000) 2706.
4) S. Katano, N. Minakawa, N. Metoki, T. Osakabe, J. Sizuki, K. Oikawa and Y. Matsuoka: *Proceedings of the 4th International Symposium on Advanced Physical Field, Quantum Phenomena in Advanced Materials at High Magnetic Fields* (National Institute for Metals, Tsukuba, 1999) 315.
5) S. Katano, M. Sato, K. Yamada, T. Suzuki and T. Fukase: Phys. Rev. B **62** (2000) R14677.
6) H. Yamauchi, K. Ohoyama, M. Sato, S. Katano, H. Onodera and Y. Yamaguchi: J. Phys. Soc. Jpn. **71** (2002) Suppl. 94.

研究テーマ：先端偏極中性子散乱によるスピン-格子物性の研究
表　題：偏極中性子散乱による Cr/Sn 人工格子の磁気構造の研究
1-2-62

Determination of the Magnetic Structures of Exotic Spin-Density Waves in Cr(001)/Sn Epitaxial films

M. TAKEDA[1,2], K. MIBU[3], J. SUZUKI[1], M. NAKAMURA[1], M. MATSUDA[1], K. KAKURAI[1] and Y. ENDOH[4]

[1]Advanced Science Research Center, JAERI, Tokai, Ibaraki 319-1195
[2]Physics Department, Graduate School of Science, Tohoku University, Sendai 980-8578
[3]Institute for Chemical Research, Kyoto University, Uji 611-0011
[4]Institute for Material Research, Tohoku University, Katahira Sendai 980-8577

Metal Chromium (Cr) is very famous for the incommensurate spin-density-wave (SDW) below the Néel temperature of 311 K [1]. The magnetic properties are drastically modified by circumstances such as impurities, temperature, internal stress and so on. Therefore thin films and multilayers of Cr exhibit a variety of magnetic properties quite different to those of bulk Cr [2].

Recently we have reported exotic SDW states observed in epitaxial Cr(001)/Sn multilayers in which monatomic Sn layers are periodically inserted in the Cr(001) epitaxial films[3, 4, 5]. Unpolarized neutron diffraction measurements revealed that in the multilayers SDWs with complicated waveform were stabilized at low temperatures. The most exotic feature of the SDWs is that their wavelength is not controlled by the nesting vector of the Fermi surface but by the artificial periodicity introduced by the embedded Sn monatomic layers. The constraint of the wavelength of the SDWs is thought to be the pinning of antinode at Cr/Sn interfaces.

We could successfully elucidate the existence of unique SDWs in the Cr/Sn multilayers by unpolarized neutron experiments. However, the determination of the spin orientation in the films is not easy by unpolarized neutrons because it is difficult to normalize intensities at different reciprocal points accurately, especially when one scattering vector is located in in-plane and the other in out-of-plane. Such scattering condition is essential to separate the in-plane and out-of-plane component of spins. We have performed polarized neutron scattering experiments with polarization analysis in order to directly determine the spin orientation of the multilayers.

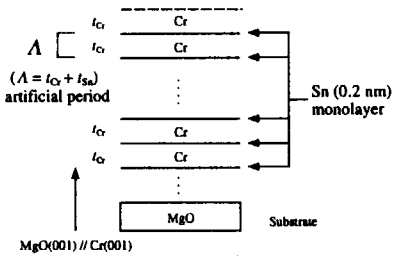


Figure 1: Structure of Cr(001)/Sn epitaxial films with monatomic Sn spacer layer. Several films with different artificial period (Λ) were synthesized. The sample with Λ = 16.0 nm was used in this study.

15 bilayers of [Cr(16.0 nm)/Sn(0.2 nm)] were epitaxially deposited on a MgO(001) substrate with a 5-nm-thick Cr buffer layer by using ultrahigh-vacuum (UHV) deposition. The structure of sample is schematically drawn in Fig. 1. The MgO[001] and the bcc Cr[001] directions are normal to the sample plane, and the MgO[110] and the Cr[010] are parallel each other. We denote the Cr[001] direction as L and the [010] direction as K hereafter.

Polarized neutron diffraction measurements were performed on TAS-1 at JRR-3M in JAERI. The Cu Heusler(111) monochromator and analyzer were employed to produce monochromatic polarized neutron of 14.7 meV and to analyze the diffracted neutrons, respectively. Scans were performed along the L and K directions through the (001) and (010) reciprocal points, where the nuclear peaks of the

原子炉：JRR-3M　　装置：TAS-1(2G)　　分野：中性子散乱（磁性）

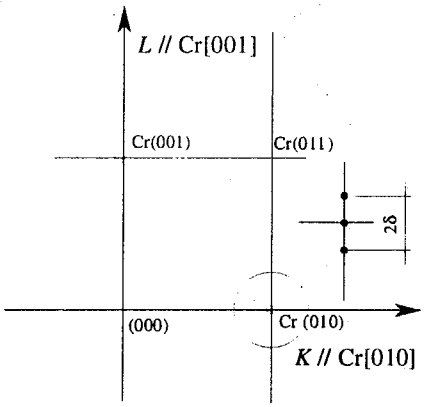


Figure 2: The reciprocal plane of bcc Cr.

bcc structure are forbidden (Fig. 2).

Fig. 3(a) shows the scan along the L direction through (010) point at 290 K. In bulk Cr the satellite peaks from the SDW state appear at $(0, \pm\delta, 1)$, $(0, 0, 1 \pm \delta)$, $(0, 1 \pm \delta, 0)$ and $(0, 1, \pm\delta)$. The incommensurability δ is defined in bulk Cr as $1 - |\vec{Q}|$ where $\vec{Q}$ is the nesting vector of Fermi surface. Since we do not observe such extra satellite peaks, the commensurate antiferromagnetic (CAF) structure is realized in the Cr/Sn multilayer at 290 K.

When neutrons are scattered by magnetic materials, neutron is only sensitive to components of magnetic moment perpendicular to the scattering vector. In addition the direction of neutron spins parallel to the magnetic moments is conserved while that perpendicular to the moments is flipped during the scattering process by magnetic interaction.

In this experiments direction of neutron spins was maintained by a weak vertical magnetic field parallel to the sample plane. Therefore intensities of non-spin-flip (NSF) neutrons in Fig. 3 (a) and (b) are proportional to the square of in-plane component of magnetic moments ($M_{//}$) and that of spin-flip (SF) neutrons to the square of out-of-plane one ($M_{\perp}$).

The intensity ratio between SF and NSF in Fig. 3(a) is approximately 4. This indicates that the ratio of $M_{\perp}$ to $M_{//}$ is 2, which suggests that $\vec{M}$ is not aligned to the principal axis of bcc lattice but is inclined to the sample plane. Another probable explanation of the ratio is coexistence of domains in which

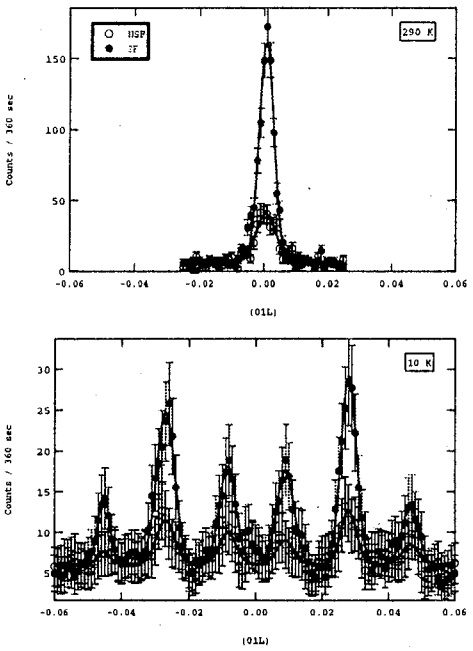


Figure 3: Scans along the L direction by polarized neutrons through (010) reciprocal point at (a) 290K and (b) 20K. Both intensities of spin-flip (SF:●) and non-spin-flip (NSF:○) neutron by scattering process are plotted in the same figure.

directions of $\vec{M}$ are different.

With decreasing temperature the CAF structure gradually transforms to the SDW state accompanied with 6 satellite peaks as shown in Fig. 3(b). The SF/NSF intensity ratio of each satellite peak is almost the same and does not remarkably differ from the CAF structure at 290 K. This suggests that the satellite peaks do not come from independent SDWs of different wavelength but that they can be assigned to the Fourier components of a single SDW with a highly distorted sinusoidal waveform.

References

1) E. Fawcett, Rev. Mod. Phys. **60,** 209 (1988).
2) H. Zabel, J. Phys.: Condensd. Matter. **11,** 9303 (1999).
3) M. Takeda, K. Mibu, K. Takanashi, K. Himi, Y. Endoh, T. Shinjo and H. Fujimori, J. Phys. Soc. Jpn. **69** 1590 (2000).
4) K. Mibu, S. Tanaka and T. Shinjo, J. Phys. Soc. Jpn. **67,** 2633 (1998).
5) K. Mibu and T. Shinjo, J. Phys. D: Appl. Phys. **35,** (2002) in press.

研究テーマ：TbB_{50}の磁気構造の研究
表　題：B_{12}クラスターTbB_{50}-型化合物の磁気構造の研究

1-2-63

Investigation of the Magnetic Structure of a TbB_{50}-type B_{12} Cluster Compound

Takao Mori[1,2], Fujio Izumi[1], Yoshinobu Ishii[3]

[1] National Institute for Materials Science, Advanced Materials Laboratory, Namiki 1-1, Tsukuba, 305-0044, Japan
[2] PRESTO, Japan Science and Technology Agency (JST)
[3] Advanced Science Research Center, JAERI, Tokai, Ibaraki 319-1195, Japan

Magnetic properties of rare earth boride compounds such as the hexaborides have been an extensively researched topic over the years.[1, 2] Recently a striking discovery was found in the magnetically dilute higher boride compounds; the magnetic transition discovered in the REB_{50} and isostructural $REB_{44}Si_2$ compounds.[3, 4] The transition temperature of TbB_{50} for example (T_N = 17 K) is actually comparable to that of the much more magnetically dense TbB_6 in which the magnetic interaction is further mediated by conduction electrons. It has been indicated that the magnetic interaction along the B_{12} chain is critical for the magnetic transition to appear which is a new phenomena in the boron compounds.[3, 4, 5]

In this work, we report on the investigation of the magnetic structure of $Tb^{11}B_{44}Si_2$ in an attempt to further elucidate the nature of this new magnetic transition found in borides.

Because this is such a boron-rich system especial care was taken in preparing the ^{11}B isotope compound. Usually the borothermal reduction of rare earth oxide under vacuum is used for for our boride synthesis.[3] However, in this case since BN crucibles are used, it was found that a small amount of natural isotope ratio boron enters the sample, which is sufficient to hinder the neutron diffraction measurements due to the extremely large cross section of ^{10}B.

We used an arc-melt method to directly synthesize $Tb^{11}B_{44}Si_2$ from the elements. Terbium metal powder (99.9 %), Si powder (99.9 %), and ^{11}B powder (isotope purity of 99.54 %) were used. Arc melt was performed under argon gas. We were successful in obtaining the $Tb^{11}B_{44}Si_2$ phase (with REB_{50}-type structure) as characterized by a high resolution powder x-ray diffractometer (Rigaku Co.; RINT2000) with Cu Kα radiation. Chemical analysis of the samples was done with ICP (inductively coupled plasma atomic emission spectroscopy) after the samples were dissolved in nitric acid for 16 hours at 110 °C. No significant impurity elements were detected, but an impurity phase of B_2O was observed. This impurity phase had never been observed before for our higher boride samples, but was unavoidable with the present synthesis technique, which was especially employed to avoid ^{10}B introduction into the sample.

Magnetic susceptibility was measured by using a Quantum Design SQUID magnetometer from 300 K to 2 K.

Neutron diffraction measurements were done using the high resolution powder neutron diffractometer (HRPD) installed at JRR-3M. The sample was mounted in a closed cycle ^4He gas refrigerator. Neutrons of wavelength of 1.8230 Å were used.

The temperature dependence of the magnetic susceptibility of $Tb^{11}B_{44}Si_2$ is plotted in Fig.1. A drop in the susceptibility is observed at 16 K, indicating the antiferromagnetic transition. The transition temperature is similar to that previously observed for $TbB_{44}Si_2$.[6]

Refinement of the neutron diffraction patterns by RIETAN2000 [7] was attempted. Although the refinement is not optimum yet, the lattice parameters we obtain in the present cycle for $Tb^{11}B_{44}Si_2$ (4 K) were determined as follows: a=16.71 Å, b=17.65 Å, c=9.547Å.

The obtained neutron diffraction difference pattern of $Tb^{11}B_{44}Si_2$ from 300 K to 4 K is

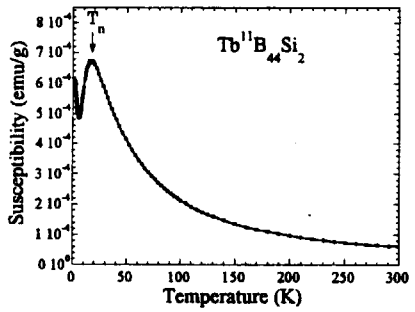


Figure 1: Magnetic susceptibility of $Tb^{11}B_{44}Si_2$.

plotted in Fig.2. The striking feature is that the relatively large peaks originating from B_2O, indicated by the asterixs, disappear at 4 K. There appears to be no trivial explanation for this behavior, since the samples are sealed in cells and in any case an evaporation of B_2O at low temperatures is not reasonable. At present it is not clear whether this is an intrinsic phenomena or is due to some artifact of measurement we have not yet considered, but the behavior is interesting and bears further investigation.

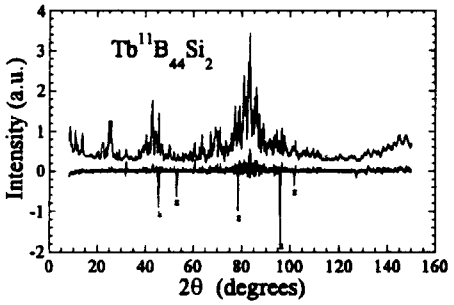


Figure 2: Neutron diffraction difference pattern (300 K subtracted from 4 K) of $Tb^{11}B_{44}Si_2$, plotted together with 4 K pattern.

No significant additional peaks due to magnetic ordering could be observed to appear for the 4 K neutron diffraction pattern. Since the magnetic transition temperature of $Tb^{11}B_{44}Si_2$ is 16 K it is indicated that the transition observed in the REB_{50} systems is not of long range order character, which is valuable new information on these exotic compounds.

To summarize, we have investigated the magnetic structure of $Tb^{11}B_{44}Si_2$ of the REB_{50} system, which display magnetic transitions mediated by a new interaction mechanism in borides. We have found that it is indicated that there is no long range ordering in this new magnetic system. An interesting behavior was observed for impurity B_2O peaks which disappeared at low temperature and bears further investigation.

References

1) B. T. Matthias, T. H. Geballe, K. Andres, E. Corenzwit, G. W. Hull, and J. P. Maita: Science **159** (1968) 530.
2) T. H. Geballe, B. T. Matthias, K. Andres, J. P. Maita, A. S. Cooper, and E. Corenzwit: Science **160** (1968) 1443.
3) T. Mori and T. Tanaka, J. Phys. Soc. Jpn. **68** (1999) 2033.
4) T. Mori and T. Tanaka, J. Phys. Soc. Jpn. **69** (2000) 579.
5) T. Mori and T. Tanaka, IEEE Trans. Mag. **37** (2001) 2144.
6) T. Mori and T. Tanaka, J. Alloys Comp. **288** (1999) 32.
7) F. Izumi, Rigaku-Denki J. **31** No.2 (2000) 17.

研究テーマ：多重極限環境下における中性子散乱実験法の研究
表　題：CeSb と CeBi の圧力-温度磁気相図

1-2-64

Magnetic P-T phase diagrams of CeSb and CeBi

T. Osakabe, A. Hannan[1], D. Kawana[1], K. Kohgi[1] and H. Kitazawa[2]

ASRC, Japan Atomic Energy Research Institute, Ibaraki 319-1195
[1]Department of Physics, Tokyo Metropolital University, Tokyo 192-0397
[2]National Institute for Materials Science, Ibaraki 305-0047

The heavier Ce-monopnictides, CeSb and CeBi exhibit highly unusual and anisotropic magnetic properties as well as Kondo-effect like transport properties in spite of their simple NaCl-type crystal structures and low-carrier-density [1]. The magnetic properties of these compounds were mainly explained by a fundamental microscopic analysis based on the anisotropic p-f mixing effect between the Ce 4f electrons and the neighboring pnictogen 5p valence-holes with Γ_8 symmetry [2]. CeSb is well known with its complicated magnetic phase diagrams below 2 GPa or 10 T revealed by the extensive neutron diffraction studies [3]. Magnetic structures consist of a stacking of ferromagnetic (001) planes with a given sequence. The magnetic moments, which are perpendicular to the ferromagnetic planes, are originated from Γ_8-like state of Ce-ions with the moment of 2 μ_B. Non-magnetic (001) planes with the Γ_7 Ce-ions appear in the so-called AFP phases below 1 GPa. The developments of high pressure techniques on the measurement of transport properties revealed new features of the phase diagram of CeSb up to 8 GPa [4]. A huge enhancement and a sharp drop of the resistivity appear at T_H and T_L above about 2 GPa. This brought forward new problems to be solved, that is, the apparent discrepancy of the phase diagram at around 2 GPa, or whether the magnetic orders exist or not above 2 GPa. On the other hand, in contrast to CeSb case, there have been few reports on the P-T phase diagram of CeBi so far. Nevertheless, the resistivity data show an unusual hump and an inflection point at T_H and T_L, and give the similar phase diagram to that of CeSb above about 2 GPa. Thus, systematic neutron diffraction studies beyond 2 GPa are inevitable to confirm the P-T phase diagrams of these compounds. In this paper, we briefly present our neutron diffraction studies up to 4.6 GPa.

Fig. 1 shows the P-T phase diagram of CeSb obtained in this work together with the data of the previous neutron diffraction [3], the resistivity measurements [4] and X-ray diffraction [5]. Below 1 GPa, the lowest temperature phase AF-IA with the stack ($\uparrow\uparrow\downarrow\downarrow$), all the AFP phases and the highest temperature phase AF-I with the ($\uparrow\downarrow$) are confirmed in our measurements. The transition temperatures are identical with that in ref.[3]. However, above 1 GPa, AF1 and AF2 phases exist in very narrow temperature ranges and disappear at about 2 GPa. Furthermore, T_{AF-IA} and T_{AF-I} shift to considerably higher temperatures of 31 K and 38 K. Above 2 GPa, AF-I and AF-IA phases were clearly observed as higher and lower temperature phases. The new phase boundaries of T_{AF-IA} and T_{AF-I} are smoothly connected through the all P-T area investigated in this work. These results solve the problems mentioned above. Fig. 2 shows the P-T phase diagram of CeBi together with the resistivity data. In marked contrast to CeSb case, the phase diagram consists of only two magnetic phases AF-I and AF-IA. The lower temperature phase AF-IA disappears at around 2 GPa.

As shown in fig. 1 and fig. 2, AF-I phase clearly relates to the unusual enhancement of the resistivity at T_H and the development of AF-IA phase leads to the rapid decrease of the resistivity at T_L. These results indicate that the mechanism of the carrier scattering or the carrier number itself is highly different between the two magnetically ordered phases.

原子炉：JRR-3M　　装置：TAS-1(2G)　　分野：中性子散乱（磁性）

The sudden shrinking of the crystal lattice is observed at T_S, which agrees well with T_H. The origin of this shrinking is clearly evidenced by the direct observation of the modulation of 4f electron orbital on CeSb [6]; the planes with the Γ_8-like state of Ce-ions, which have small effective ionic size due to the p-f mixing effect, appear in the lattice of Ce ions with Γ_7 CEF ground state. It should

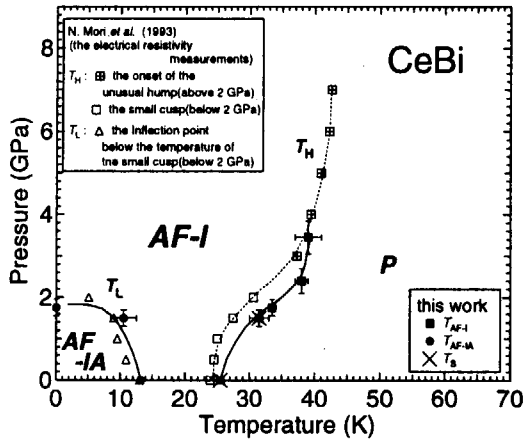


Figure 1: The magnetic P-T phase diagram of CeSb.

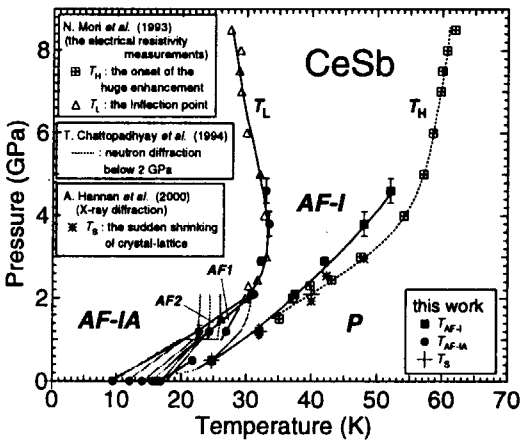


Figure 2: The magnetic P-T phase diagram of CeSBi.

be pointed out that in CeSb non-magnetic Γ_7 planes disappear at about 1 GPa and the phase diagram above 2 GPa bears a close resemblance to the phase diagram of CeBi above ambient pressure, which has no non-magnetic plane. As pointed out for lighter monopnictides CeP and CeAs in ref [7, 8], this behavior is probably understood in terms of the common physical basis for the whole Ce-monopnictides system. In this idea, although the difference of the CEF splittings or pnictgen atoms between the compounds should be considered, the carrier density can be a common physical parameter. That is, the application of pressure increases the carrier density. As a result of this, the p-f mixing effect is highly enhanced. Indeed, the carrier number are estimated to be about 0.04 and 0.06 per Ce for CeSb and CeBi, respectively [9] and the calculated energy gain of the p-f mixing effect in CeBi is much larger than that in CeSb [2]. However, the future development of theoretical works is highly desired to elucidate the problems such as the correspondence between the unusual enhancement of the resistivity and the magnetic orders, or the strong stabilization of the AF-I phase by applied pressure in spite of the small difference of the energy between the AF-I and the AF-IA phases at ambient pressure [2].

References

1) T. Suzuki: JJAP Series **8** (1993) 267.
2) H. Takahashi and T. Kasuya: J. Phys. C, Solid State Phys. **18** (1985) 2697, 2709, 2721, 2731, 2745 and 2755.
3) T. Chattopadhyay, P. Burlet, J. Rossat-Mignod, H. Bartholin, C. Vettier, O. Vogt: Phys. Rev. B **49** (1994) 15096.
4) N. Môri, Y. Okayama, H. Takahashi, Y. Haga, T. Suzuki: JJAP Series **8** (1993) 182.
5) A. Hannan, K. Iwasa, M. Kohgi, T. Suzuki: J. Phys. Soc. Jpn. **69** (2000) 2358.
6) K. Iwasa, Y. Arakaki, M. Kohgi, T. Suzuki: J. Phys. Soc. Jpn. **68** (1999) 2498.
7) T. Osakabe, M. Kohgi, K. Iwasa, K. Kakurai, J.M. Mignot, I.N. Goncharenko, Y. Okayama, H. Takahashi, N. Môri, M. Kubota, H. Yoshizawa, Y. Haga, T. Suzuki: JJAP Series **11** (1998) 123.
8) M. Kohgi, K. Iwasa and T. Osakabe: Physica B **281–282** (2000) 417.
9) R. Settai, T. Goto, S. Sakatsume, Y. S. Kwon, T. Suzuki, Y. Kaneta and O. Sakai: J. Phys. Soc. Jpn. **63** (1994) 3026.

研究テーマ：ランタノイド-白金族元素を含む複合酸化物の磁気構造
表　題：四元系鉄硫化物 $BaPr_2FeS_5$ の磁気構造

1-2-65

Crystal and Magnetic Structure of the Antiferromagnetic Iron Sulfide $BaPr_2FeS_5$

M. Wakeshima, K. Ino, Y. Hinatsu, Y. Ishii[1], Y. Shimojo[1] and Y. Morii[1]

Division of Chemistry, Graduate School of Science, Hokkaido University, Sapporo 060-0810
[1]Japan Atomic Energy Research Institute, Tokai-mura, Ibaraki 319-1195

A quaternary iron sulfide $BaPr_2FeS_5$ has a tetragonal crystal structure with space group, $I4/mcm$, at room temperature. Its magnetic susceptibility and specific heat showed that the antiferromagnetic transition of the Fe^{2+} ions occurred at 40 K and another anomaly occurred at 150 K.

In order to determine the magnetic structure, powder neutron diffraction patterns of $BaPr_2FeS_5$ were measured at 10, 100 and 200 K using a HighResolution Powder Diffractometer (HRPD) in the JRR-3M reactor with a neutron incident wave length (λ = 1.82268 Å). The neutron diffraction data were analyzed with the Rietveld method.

Figure 1 shows the observed and calculated diffraction patterns for $BaPr_2FeS_5$ at 10, 100 and 200 K. The patterns calculated using the crystal structure with the space group of $I4/mcm$ at 100 and 200 K are in good agreement with the observed ones, which indicates that no structural transition occurs between 100 and 200 K. The lattice parameters were refined to be a = 7.8297(5) Å, c = 13.5914(9)Å at 100 K and a = 7.8352(5) Å, c = 13.6028(10)Å at 200 K. Compared with the pattern at 100 and 200 K, additional magnetic Bragg peaks appear in the pattern at 10 K. This result indicates that the Fe^{2+} ions in $BaPr_2FeS_5$ has a long-range magnetic ordering. The magnetic structure of Fe^{2+} at 10 K was determined to have a collinear antiferromagnetic structure which has dimensions $\sqrt{a} \times \sqrt{a} \times c$ in terms of the tetragonal chemical cell. The magnetic moment of Fe^{2+} is estimated to be 2.78(2) μ_B and determined to lie in a parallel direction with the c-axis. The schematic magnetic structure is illustrated in Fig. 2.

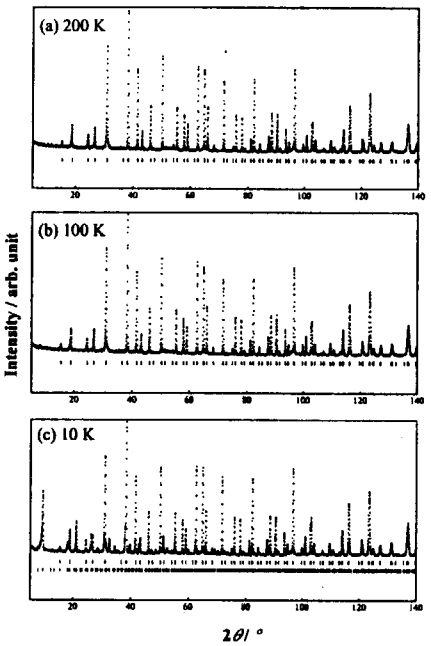


Figure 1: Powder neutron diffraction profiles for $BaPr_2FeS_5$ at 10, 100 and 200 K.

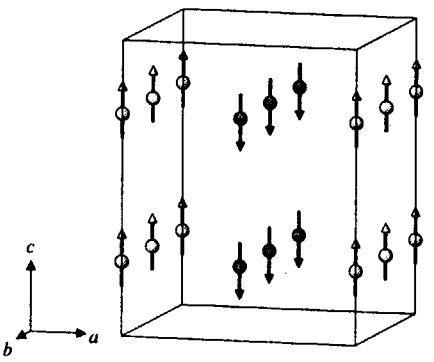


Figure 2: The magnetic structure of $BaPr_2FeS_5$ at 10 K.

原子炉：JRR-3M　　装置：HRPD(1G)　　分野：中性子散乱（磁性）

研究テーマ：ランタノイド-白金族元素を含む複合酸化物の磁気構造
表　題：秩序化ペロブスカイト Ba_2LnRuO_6 (Ln = Tm, Yb)、Sr_2YbRuO_6 の中性子回折

1-2-66

Neutron Diffraction Study on Ordered Perovskites Ba_2LnRuO_6 (Ln = Tm, Yb) and Sr_2YbRuO_6

Y. DOI, Y. HINATSU, Y. SHIMOJO[1] and Y. ISHII[1]

Division of Chemistry, Graduate School of Science, Hokkaido University, Sapporo 060-0810
[1]Advanced Science Research Center, JAERI, Tokai, Ibaraki 319-1195

The ordered perovskite-type compounds Ba_2LnRuO_6 (Ln = Tm, Yb) and Sr_2YbRuO_6 showed magnetic transitions at around 45 K. In order to determine their magnetic structures, powder neutron measurements were performed at 100 and 10 K with a High Resolution Powder Diffractometer (HRPD) in the JRR-3M reactor with a neutron incident wave length (λ = 1.82268Å).

Neutron diffraction profiles measured at 100 K show that the crystal structures of these compounds are monoclinic with space group $P2_1/n$, and the Ln^{3+} and Ru^{5+} ions are structurally ordered at the B sites of the ABO_3 perovskite-type structure.

The data collected at 10 K show a number of low angle peaks, which are not observed at 100 K. (Fig.1) They are magnetic peaks due to an antiferromagnetic ordering of both Ln^{3+} and Ru^{5+} ions. Their magnetic structures were determined by the Rietveld method.

The magnetic structure of Ba_2YbRuO_6 at 10 K is illustrated in Fig.2. In this magnetic structure, the magnetic moments of the Yb^{3+} and Ru^{5+} are ordered antiferromagnetically, respectively. In the *ab* plane, the magnetic moments of Yb^{3+} and Ru^{5+} are coupled ferromagnetically. The direction of the magnetic moments is along the *c* axis. The ordered magnetic moments are listed in Table 1.

The magnetic structure of Sr_2YbRuO_6 is the same as that of Ba_2YbRuO_6, except for the difference in the direction of the magnetic moments (canted from the c axis about 20°). For Ba_2TmRuO_6, it is found that the magnetic moments of Tm^{3+} and Ru^{5+} are coupled ferrimagnetically rather than ferromagnetically in the *ab* plane.

Table 1: Ordered magnetic moments (μ_B) of Ba_2LnRuO_6 (Ln = Tm, Yb) and Sr_2YbRuO_6.

	Ln^{3+}	Ru^{5+}
Ba_2YbRuO_6	0.97(4)	2.57(7)
Ba_2TmRuO_6	1.82(5)	2.36(8)
Sr_2YbRuO_6	0.92(6)	3.0(2)

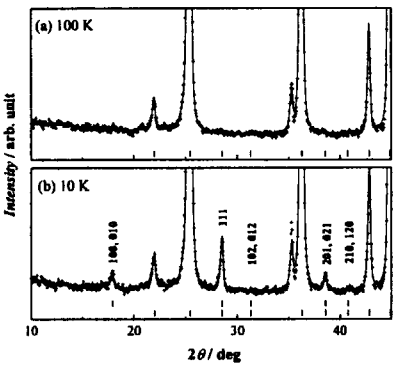


Figure 1: Neutron diffraction profiles for Ba_2YbRuO_6 at (a) 100 K and (b) 10 K.

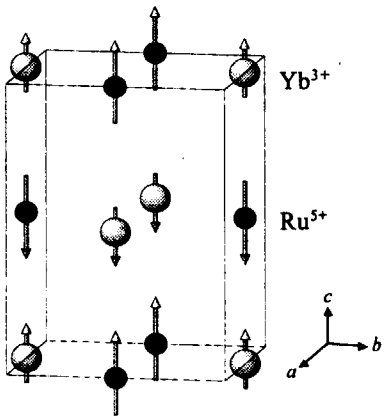


Figure 2: Magnetic structure of Ba_2YbRuO_6 at 10 K.

原子炉：JRR-3M　　装置：HRPD(1G)　　分野：中性子散乱（磁性）

研究テーマ：先端偏極中性子散乱によるスピン-格子物性の研究
表　題：$Pr_{0.5}Ca_{0.5}Mn_{1-y}Cr_yO_3$ ($y = 0$, 0.03) のスピン揺らぎの研究
1-2-67

Spin fluctuations in $Pr_{0.5}Ca_{0.5}Mn_{1-y}Cr_yO_3$ ($y = 0$, 0.03)

J. SUZUKI[1], M. WATAHIKI[1] and T. KATSUFUJI[2]

[1]Advanced Science Research Center, JAERI, Tokai, Ibaraki 319-1195
[2]School of Science and Engineering, Waseda University, Sinjuku-ku, Tokyo 169-8555

$Pr_{0.5}Ca_{0.5}MnO_3$ is an antiferromagnetic insulator showing strong ferromagnetic spin fluctuation in the paramagnetic state [1]. This system changes to a ferromagnetic metal by substituting a small part of the Mn ion by Cr ion. We studied ferromagnetic spin fluctuation of $Pr_{0.5}Ca_{0.5}Mn_{0.97}Cr_{0.03}O_3$ (PCMCO) comparing with that of $Pr_{0.5}Ca_{0.5}MnO_3$ (PCMO) and also studied ferromagnetic ordering of PCMCO with the small-angle neutron scattering instrument (SANS-J) installed in the JRR-3M. The instrument was operated with either $\lambda = 0.35$ or 0.65 nm.

The scattering cross-section of PCMCO consists of coherent and diffuse scattering components. The coherent scattering component is dominant below the ferromagnetic transition temperature $T_C = 140$ K in the q region lower than about 0.2 nm^{-1}. This component has the q^{-4} dependence (Porod law) indicating that the boundary of ferromagnetic domains appearing below T_C is sharp in scattering length density. On the other hand, the diffuse scattering component becomes larger than the coherent scattring component above T_C in the q region larger than about 0.5 nm^{-1}.

Fig.1(a) shows the temperature dependence of the scattering cross-section of PCMCO at $q = 0.071$ nm^{-1}. Below T_C the scattering cross-section normally increases owing to the development of the ferromagnetic long range order. However, as shown in Fig.1(b) the diffuse scattering cross-sections of PCMCO at $q = 1.31$ nm^{-1} shows anomalous behavior. With increasing the temperature, the scattering cross-section starts to increase at about T_C and remains finite even in the temperature region much higher than T_C. This result indicates that the strong ferromagnetic spin fluctuation persists in the paramaganetic state of PCMCO as that of PCMO. In principle, the ferromagnetic spin fluctuations of both systems are expected to be due to the double exchange interaction between Mn spins. The magnitude of the ferromagnetic spin fluctuation of PCMCO is slightly lower than that of PCMO. However, both spin fluctuations have similar Lorentzian q dependence with about 30 nm in correlation length.

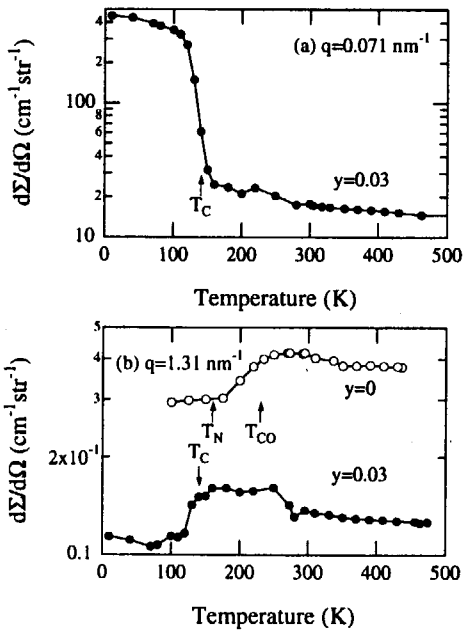


Figure 1: Temperature dependence of the scattering cross-sections of $Pr_{0.5}Ca_{0.5}Mn_{1-y}Cr_yO_3$ ($y = 0$, 0.03) at (a) 0.071 and (b) 1.31 nm^{-1}.

References

1) R. Kajimoto, T. Kakaeshita, Y. Oohara, H. Yoshizawa, Y. Tomioka and Y. Tokura, Phys. Rev. B **58**, R11837 (1998).

原子炉：JRR-3M　　装置：SANS-J(C3-2)　　分野：中性子散乱（磁性）

研究テーマ：多重極限環境下における中性子散乱実験法の研究
表　題：f 電子系化合物 $PrCu_6$ における結晶場励起

1-2-68

Crystalline Electric Field Excitations in f electron compound $PrCu_6$

Y. Morii[1] , Y. Koike[1,2] , N. Metoki[1], Y. Onuki[3]

[1]Advanced Science Research Center, JAERI, Tokai, Ibaraki 319-1195
[2]Japan Science and Technology Corporation, Kawaguchi, Saitama 332-0012
[3]Department of Physics, Graduate School of Science, Osaka University, Toyonaka 560-0043

The dispersion of the crystalline electric field (CEF) excitation in a single crystal $PrCu_6$ has been investigated to understand the enhanced nuclear magnet due to the hyperfine coupling to f electrons associated with the RKKY interaction between f electron spins. The enhancement causes the ordering temparature at 2 mK which is several thousand times higher than that of pure nuclear spin systems.

We have reported the dispersion of CEF along the $h00$, $0k0$, and other axises in the $(hk0)$ plane of the single crystal (40 mm in length, 5 mm in diameter, monoclinic notation; a = 0.509 nm, b = 1.015 nm, c = 0.809 nm β = 91.33 degree).[1)]

Recently we measured the dispersion of CEF at $00l$ ($0.8<l<2.9$) positions in the $(h0l)$ plane. Figure 1 shows the accumulated dispersion relations at low temperatures which clearly show the followings; (1)The CEF excitations are at the energy about 1.7, 2.7, 5.0, 7.4, and 8.9 meV, some of which are different from the previous data from polycrystals.[2)] (2)The first excitation at about 1.7 meV was not observed along the a-axis, Q=(100), which indicates the x-polarization of the f electom moment. This is consistent with the report that the Van-Vleck susceptibility along the a-axis is larger than the other orientations. (3)Similarly the 7.4 and 8.9 meV excitations are considered to have y-polarization, but the 2.7 and 5.0 meV levels have a polarization with x, y, z-components. (4)We found the minimum energy at the forbidden Bragg point (010). The data and the temperature dependence might suggest that Q=(010) would be the antiferromagnetic propagation vector for the nuclear magnetic ordering of $PrCu_6$. (5)The first excited level splits into two modes around the ferromagnetic Bragg points 020 and 002. The splittings could be explained in terms of the mode splitting of the optical and acoustic mode in a non-Bravais lattice.

References

1) Y. Koike et al., Appl. Phys. A, in press.
2) U. Walter et al., J. Phys. Soc. Jpn. **55** (1986) 650.

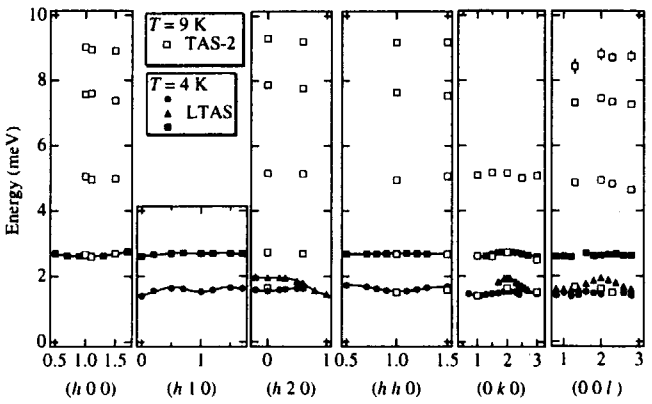


Figure 1: Dispersion of CEF excitation of $PrCu_6$.

原子炉：JRR-3M　　装置：TAS-2(T2-4), LTAS(C2-1)　分野：中性子散乱（磁性）

研究テーマ：先端偏極中性子散乱によるスピン-格子物性の研究
表　題：正方晶 TbB_2C_2 における磁場誘起反強四極子秩序

1-2-69

Field-induced Antiferroquadrupolar Ordering in The Tetragonal TbB_2C_2 Compound

K. KANEKO, S. KATANO[1], M. MATSUDA[1], K. OHOYAMA, H. ONODERA and Y. YAMAGUCHI

Institute for Materials Research, Tohoku University, Sendai 980-8577
[1]Advanced Science Research Center, JAERI, Tokai, Ibaraki 319-1195

In RB_2C_2 system(R=rare earth), coexistence of antiferroquadrupolar (AFQ) and antiferromagnetic (AFM) interactions brings variety and anomalous magnetic properties. In particular, DyB_2C_2 is the first tetragonal AFQ order compound with the high T_Q value of 24.7 K [1, 2]. In addition, HoB_2C_2 also shows an AFQ order transition at T_Q=4.5 K which realized under the magnetic ordered state of T_N=5.9 K [3, 4]. In this report, we show the evidence of another AFQ order compound in RB_2C_2 system, TbB_2C_2.

Because of the large spin-orbit coupling in f electron systems, the effects of the AFQ order in DyB_2C_2 and HoB_2C_2 are revealed in their magnetic structures. In the AFQ+AFM ordered state, the magnetic moments which lie in the c-plane make an twice a period along the [0 0 1] direction with the characteristic coupling angle ϕ of about 70° [4] and 77° [2] in HoB_2C_2 and DyB_2C_2, respectively. These magnetic structures are originate in the four different propagation vectors: the two dominant $\boldsymbol{k}_1 = (1\,0\,0)$, $\boldsymbol{k}_2 = (0\,1\,1/2)$ and the two additive $\boldsymbol{k}_3 = (0\,0\,0)$ and $\boldsymbol{k}_4 = (0\,0\,1/2)$.

TbB_2C_2 is an antiferromagnet with T_N=21.7 K under H=0 [5]. The magnetic structure is described by dominant $\boldsymbol{k}_2 = (0\,1\,1/2)$ with an additive $\boldsymbol{k}_4 = (0\,0\,1/2)$ and a long period component of $\boldsymbol{k}_L = (1\pm\delta\,\pm\delta\,0)$ ($\delta = 0.13$), which differs from the characteristic magnetic structure under the AFQ+AFM ordered states[5]. However, it is notable that the long period component $\boldsymbol{k}_L$ in TbB_2C_2 is common to that between T_N and T_Q in HoB_2C_2 where AFQ interactions supposed to play an important role[4]. In addition, the magnetization processes of TbB_2C_2 reveal resemblant characteristics as those of DyB_2C_2 and HoB_2C_2. It is, therefore, highly probable that an AFQ order is realized in TbB_2C_2 under magnetic fields, though there is no AFQ order under H=0 T [5]. Thus, the aim of this work is to confirm the field-induced AFQ order in TbB_2C_2 by means of neutron diffraction under magnetic fields.

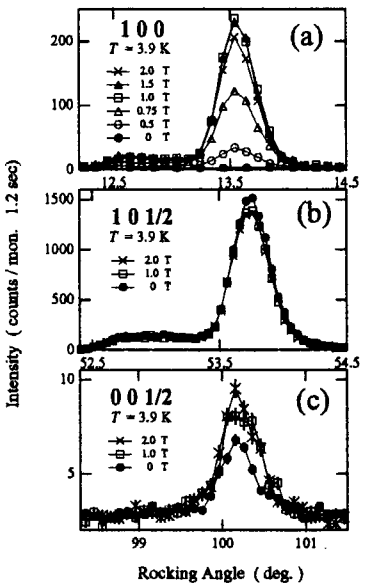


Figure 1: Magnetic field dependence of rocking curves of the (a) 1 0 0, (b)1 0 1/2 and (c) 0 0 1/2 magnetic reflections up to 2.0 T taken at 3.9 K.

A single crystalline sample was grown by the Czochralski method with enriched ^{11}B isotope. The neutron diffraction experiments were carried out on the triple-axis spectrometer TAS-2. The spectrometer was operated in the triple-axis mode with elastic condition. The incident energy was fixed at 13.7 meV and

原子炉：JRR-3M　　装置：TAS-2(T2-4)　　分野：中性子散乱（磁性）

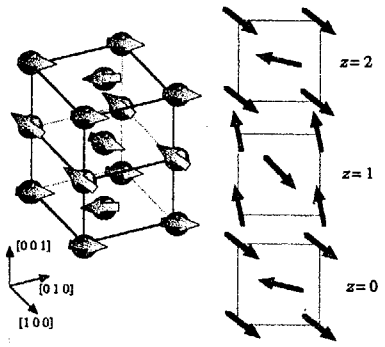


Figure 2: Schematic magnetic structure of TbB_2C_2 under magnetic fields applied along the ⟨100⟩ direction.

two PG filters were used to reduce higher order contamination. Magnetic fields applied along the [0 1 0] direction were generated by a liquid-He-free type 10 T superconducting magnet developed by JAERI[6].

Figure 1 shows magnetic field dependence of the rocking curves of magnetic Bragg reflections, (a) 1 0 0, (b)1 0 1/2 and (c) 0 0 1/2 up to 2.0 T taken at 3.9 K. The small humps observed on the low angle side of main peaks are attributed to the existence of other grains. Under zero field, the intense 1 0 1/2 and the weak 0 0 1/2 magnetic reflections were observed, while no peak was found at (1 0 0). These results were consistent with the previous ones[5]. The application of magnetic fields causes the appearance of a new antiferromagnetic reflection of 1 0 0 even at 0.5 T where the broad transition was observed in the magnetization process along the [0 1 0] direction[5]. This result indicates that the (1 0 0)-type antiferromagnetic component is also needed for the field-induced ordered state in TbB_2C_2. The intensity of the weak magnetic reflection of 0 0 1/2 also exhibits an increase against magnetic fields up to 2.0 T. In contrast, the most intense 1 0 1/2 reflection decreases by just about 8 % from zero to 2.0 T.

Including a field-induced ferromagnetic component which overlaps nuclear peak, the reflections above 0.5 T are associated with the following four propagation vectors; the two dominant $\boldsymbol{k}_1 = (100)$, $\boldsymbol{k}_2 = (011/2)$ and the two additive $\boldsymbol{k}_3 = (000)$, $\boldsymbol{k}_4 = (001/2)$. This indicates that the field-induced magnetic structure of TbB_2C_2 is basically the same as the characteristic structures of DyB_2C_2 and HoB_2C_2 in the AFQ+AFM ordered state.

The magnetic moments of dominant components $\boldsymbol{k}_1$ and $\boldsymbol{k}_2$ are reported to be 5.5 μ_B and 4.4 μ_B in DyB_2C_2, 5.15 μ_B and 3.56 μ_B in HoB_2C_2 [2, 4]. In contrast, the ratio at 1.5 T in TbB_2C_2 is roughly estimated from the integrated intensity to be $\mu_{\boldsymbol{k}_1}$:$\mu_{\boldsymbol{k}_2}$=2.3 μ_B: 5.6 μ_B. The magnetic moment for $\boldsymbol{k}_2$ in TbB_2C_2 is far larger than that for $\boldsymbol{k}_1$, which is different in the case for DyB_2C_2 and HoB_2C_2. The discrepancy among these compounds originates from an angle ϕ. The characteristic angle ϕ is deduced to be 130° in TbB_2C_2, while those angles are reported to be 77° and 69.6° in DyB_2C_2 and HoB_2C_2, respectively[2, 4]. The schematic magnetic structure of TbB_2C_2 under magnetic fields are shown in Fig. 2.

Although the coupling angles ϕ are different, the fundamental structure of the field-induced phase in TbB_2C_2 is common to those of the ground states in DyB_2C_2 and HoB_2C_2, where the AFQ and AFM order coexist. The characteristic magnetic structure in TbB_2C_2 under magnetic fields is hardly explained by only magnetic interactions as well as those in DyB_2C_2 and HoB_2C_2. We believe, therefore, that TbB_2C_2 is the first material which shows a field-induced AFQ ordering.

References

1) H. Yamauchi, H. Onodera, K. Ohoyama, T. Onimaru, M. Kosaka, M. Ohashi and Y. Yamaguchi: J. Phys. Soc. Jpn. **68**, (1999) 2057.
2) H. Yamauchi, Doctor Thesis, Tohoku Univ. (Sendai, 2000).
3) H. Onodera, H. Yamauchi and Y. Yamaguchi: J. Phys. Soc. Jpn. **68**, (1999) 2526.
4) K. Ohoyama, H. Yamauchi, A. Tobo, H. Onodera, H. Kadowaki and Y. Yamaguchi: J. Phys. Soc. Jpn. **69**, (2000) 3401.
5) K. Kaneko, H. Onodera, H. Yamauchi, K. Ohoyama, A. Tobo and Y.Yamaguchi: J. Phys. Soc. Jpn. **70**, (2001) 3112.
6) S. Katano, N. Minakawa, N. Metoki, T. Osakabe, J. Suzuki, Y. Koike, and Y. Ishii: *Proceedings of ICNS 2001* in press.

研究テーマ：中性子散乱による強相関電子系の研究
表　題：ホールをドープしたHaldane系 $Nd_{2-x}Ca_xBaNiO_5$ のスピン揺動

1-2-70

Spin dynamics of hole doped Haldane system $Nd_{2-x}Ca_xBaNiO_5$

T. SASAKI, T. YOKOO[1], S. KATANO[2], K. KAKURAI[2] and J. AKIMITSU

Department of Physics, Aoyama-Gakuin University, Setagaya-ku, Tokyo 157-8572
[1]Institue of Materials Structure Science, KEK, Tukuba, Ibaraki 305-0801
[2]Advanced Science Research Center, JAERI, Tokai, Ibaraki 319-1195

The one-demensional (1D) Heisenberg $S = 1$ chains and $S = 1/2$ ladders have been extensively studied as disordered nonclassical systems after Haldane's prediction in 1983 [1, 2]. It has been well established that the spin gap state still survives in the hole doped ladder compound, and that the spin-gapped phase is favorable for superconductivity [2, 3]. Studies of hole doped Haldane system have only recently been realized experimentally in the compound $Y_{2-x}Ca_xBaNiO_5$ [4, 5], but the resistivity of this system behaves like an insulator and the carriers do not induce metallic behavior. The key picture in the hole doped Haldane system is that induced holes create excitations below the Haldane gap with an incommensurate structure factor. Surprisingly, increased hole doping does not yield a proportional increase in the shift of the peaks from antiferromagnetic zone center (AFMZC).

In this study, we prepared the single crystals of $Nd_{2-x}Ca_xBaNiO_5$ ($x = 0, 0.05, 0.10, 0.20$) by the floating zone method to elucidate the spin dynamics of hole doped Haldane chains. Nd_2BaNiO_5 has shown the same behavior as the Haldane gap obtained in the pure Haldane system Y_2BaNiO_5 above the Néel temperature (T_N), and its behavior is different from that of $CsNiCl_3$ in which the Haldane gap is lost below T_N. In other words, the Haldane state coexists with antiferromagnetic state below T_N, which was recently recognized as a unique model of Haldane-gap quantum spin chain in a strong *staggered* applied field [6, 7]. An effective staggered exchange field acting on 1D chains is generated by 3D magnetic long-range ordering in the auxiliary sublattice of magnetic rare earth ions, which occurs at T_N of several tens of kelvin.

Elastic and inelastic neutron measurements were done on the TAS-1 triple axis spectrometer at JEARI. Neutron beams of fixed final energy $E_f = 14.7$meV were used with pyrolitic graphite filter to eliminate the higher order contaminations. The sample was mounted with the (H, 0, L) reciprocal space parallel to the scattering plane of the triple axis spectrometer. The data from each samples were normalized with the integrated intensity of the (200) Bragg reflection.

Magnetic phase diagram was determined by measuring the temperature dependence of susceptibility and magnetic Bragg peak. A spin-glass like phase in $Nd_{2-x}Ca_xBaNiO_5$ has been observed at the temperature between 3 and 25K as the hole concentration is changed. This is much higher than that($\sim$ 3K) in

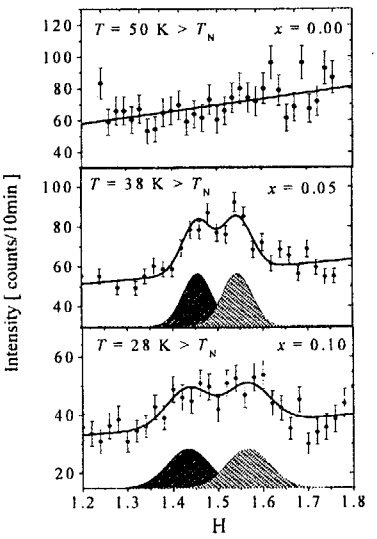


Figure 1: Constant E scans at $E = 5.5$ meV and T=(2+T_N) for three different hole concentrations.

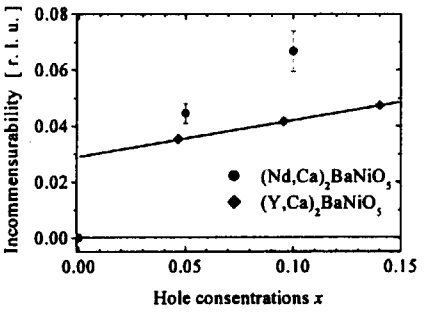


Figure 2: Hole concentration dependence of incommensurability. Full diamonds is the data reported by Xu in $Y_{2-x}Ca_xBaNiO_5$[5].

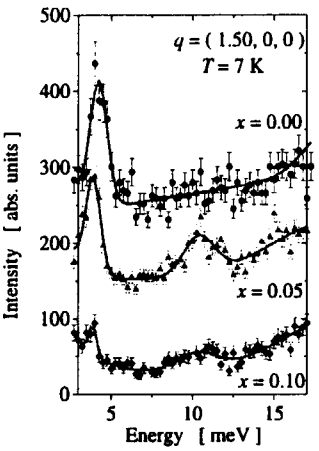


Figure 3: Constant q scans at AFZC. The Haldane gap increses at low temperature.

$Y_{2-x}Ca_xBaNiO_5$[8]. T_g equals to T_N above $x = 0.10$. This suggests that a spin-glass like state and an antiferromagnetic (AFM) state coexist, and holes create ferromagnetic cloud around the holes in the AFM state caused by Nd ions.

The spectrum weights of peaks which can be explained by the incommensurate spin modulation were observed by inelastic neutron scattering at AFMZC [$q = (1.5, 0, 0)$] for E = 3 - 7 meV above T_N in $Nd_{2-x}Ca_xBaNiO_5$ (Fig.1). These peaks have so broad structure. Because observed temperature is relatively high temperatures for the incommensurate spin modulation, we must observe them over T_N. The incommensurability ε which was calculated by two Gaussians centered at $1.5 \pm \varepsilon$, was larger than that of $Y_{2-x}Ca_xBaNiO_5$[5] (Fig.2). How do we account for the inelastic incommensurate spin modulation? The key picture is that induced holes in Haldane chains create the weak ferromagnetic (FM) interaction coupling around holes. The nature of the inelastic incommensurate spin modulation might be caused from the structure factor of the spin part of the hole wavefunctions.

The result is a new excitation spectrum around 11 meV below T_N (Fig.3). This excitation have the dispersion different from the Haldane mode parallel to the chains (the Haldane gap increases at low temperatures). We have not determined what this excitation is caused by. The first possibility is partially due to a weak, previously unobserved Nd crystal-field (CF) excitation. The second possibility is due to the induced holes in the Haldane chains.

References

1) F. D. Haldane, Phys. Rev. Lett. **93**, 464 (1983)
2) E. Dagotto and T. M. Rice, Science **271**, 618 (1996)
3) M. Uehara, T. Nagata, J. Akimitsu, H. Takahashi, N. Môri and K. Kinoshita , J. Phys. Soc. Jpn. **65**, 2764 (1996)
4) J. F. DiTusa, S-W. Cheong, J.-H. Park, G. Aeppli, C. Broholm and C. T. Chen, Phys. Rev. Lett. **73**, 1857 (1994)
5) Guangyong Xu , G. Aeppli, M. E. Bisher, C. Broholm, J. F. DiTusa, C. D. Frost, T. Ito, K. Oka, R. L. Paul, H. Takagi and M. M. J. Treacy, Science **289**, 419 (2000)
6) A. Zheludev , E. Ressouche, S. Maslov, T. Yokoo, S. Raymond and J. Akimitsu, Phys. Rev. Lett **80**, 3630 (1998)
7) T. Yokoo, A. Zheludev, M. Nakamura and J. Akimitsu, Phys. Rev. B **55**, 11 516 (1997)
8) K. Kojima, A. Keren, L. P. Le, G. M. Luke, B. Nachumi, W. D. Wu, Y. J. Uemura, K. Kiyono, S. Miyasaka, H. Takagi and S. Uchida , Phys. Rev. Lett. **75**, 3471 (1995)

1. 中性子散乱 3)超伝導現象

1. Neutron Scattering 3) Superconductivity

This is a blank page.

研究テーマ：二重ハニカム格子超伝導体の構造とフォノン
表題：β-ZrNBrのフォノン状態密度
1-3-1

Phonon Density of States of β-ZrNBr

Shin-ichi Shamoto, Satoru Takeda, Tsuyoshi Kajitani

Department of Applied Physics, Faculty of Engineering, Tohoku University, Sendai 980-8579

Fermi chopper at TOF-type spectrometer AGNES at C3-1-1 of JAERI-JRR3M in Tokai reduces neutron flux to about 1/100 of incident flux. This low flux density is compensated by 199 counters installed at AGNES, which is enough for quasielastic scattering studies of compounds with hydrogen atoms. On the other hand, it is still challenging to study inorganic compounds at AGNES, because of the neutron flux. Among many compounds with light atoms, nitrides are suitable candidates for the study at AGNES, since a nitrogen atom with light mass has relatively large total bound scattering cross section, *i.e.*, 11.5 barn. From this point of view, we have tried to study layered nitride superconductors at AGNES in a wide range of temperature [1]. At low temperature, we found multiple elastic scattering at Al cell and sample dominated scattering intensity. Here, we report high temperature measurement of β-ZrNBr.

Novel layered superconductors, Li_xZrNCl (T_c~15 K), Li_xZrNBr (T_c~13 K), and $Li_x(THF)_yHfNCl$ (T_c~25.5 K), have been discovered by Yamanaka et al. [2]. The conducting layer consists of double honeycomb lattice of $[(Hf, Zr)N]_2$. The conduction band is partially filled by electrons, which are supplied from alkali metals. It is noteworthy that recently discovered high-T_c MgB_2 [3] has similar band structure to the present double honeycomb lattice superconductors but contrasts with that in the sign of doped carriers.

Figure 1 shows powder diffraction patterns of pristine β-ZrNBr at T~ 270 and 600 K by AGNES. On heating, anisotropic intensity decrease can be seen for 00 ℓ scattering in addition to c axis elongation, corresponding to weak van der Waals force in bromine layers. Generalized phonon density of states, GPDOS, of β-ZrNBr is shown in Fig. 2. Sample weight, measuring time and counter number are 3.8 (8.5) g, 40 (55.2) h and 199 (119) for the measurement at 600 (270) K, respectively. Nitrogen atoms contribute 85 % in the total

使用施設: JRR-3M, 装置: AGNES(C3-1-1),
分野: 3.

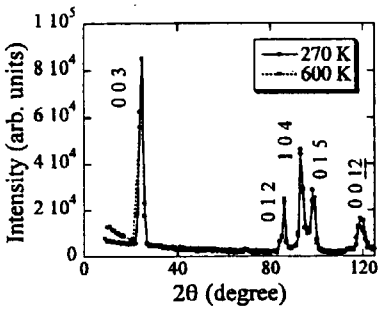


Figure 1. Powder diffraction patterns of β-ZrNBr at T~ 270 and 600 K obtained by AGNES.

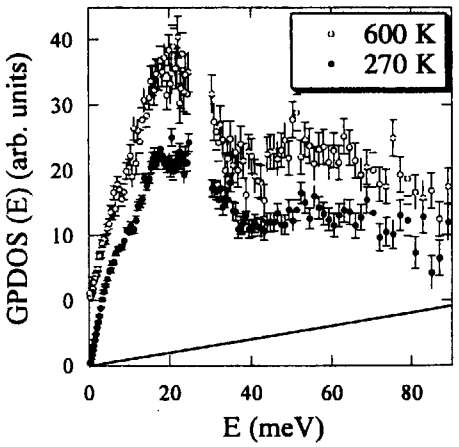


Figure 2. Observed phonon density of states of β-ZrNBr by AGNES. Solid line shows roughly estimated multiple scattering contribution.

GPDOS intensity for β-ZrNBr. Even at 50 meV, hardening of optical phonon upon cooling can be seen in Fig. 2, showing the potential of AGNES for nitride studies.

References

[1] See, for example, S. Shamoto, *et al.*, J. Phys. Soc. Jpn. **70** Suppl. A, 286 (2001).
[2] S. Yamanaka, K. Hotehama and H. Kawaji, Nature **392**, 580 (1998), and a reference therein.
[3] J. Nagamatsu, N. Nakagawa, T. Muranaka, Y. Zenitani and J. Akimitsu, Nature **410**, 63 (2001).

1-3-2

研究テーマ: Relation among crystal structure, stripe order and superconductivity in $(La,Ba,Sr)_2CuO_4$

表題: $(La,Ba,Sr)_2CuO_4$における結晶構造、電荷・スピン秩序、および超伝導の相関

Relation among crystal structure, stripe order and superconductivity in $(La,Ba,Sr)_2CuO_4$

Masaki Fujita[1], Hideto Goka[1], Masaaki Matsuda[2] and Kazuyoshi Yamada[1]

Institute for Chemical Research, Kyoto University, Gokasyo, Uji 611-0011

Advanced Science Research Center, Japan Atomic Energy Research Institute (JAERI), Tokai, 319-1195

Since the discovery of charge and spin-stripe order in lamellar copper oxides [1] the interplay between stripe correlation and superconductivity has attracted considerable attention. However, no evidence of CDW order was so far obtained by diffraction measurements except for the low-temperature-tetragonal (LTT) phase of $La_{1.6-x}Nd_{0.4}Sr_xCuO_4$ system, while SDW order is stabilized at the hole concentration of ~1/8 irrespective of crystal structure. It is therefore important to clarify whether the static and/or the dynamical stripe correlations commonly exist in the high-T_c superconductors.

In order to elucidate the relationship between the crystal structure and the stripe order, we have performed neutron-scattering measurements on $La_{1.875}Ba_{0.125-x}Sr_xCuO_4$ (LBSCO) single crystals, in which the crystal structure can be controlled by varying the Ba and Sr concentration. Most of measurements are done using triple-axis spectrometers TOPAN and HER at JRR-3M, JAERI (Tokai).

We found the clear evidence of stripe order in the samples with x=0.05, 0.065 and 0.075. Superlattice peaks from the charge stripe order observed in the LTT and low-temperature-less-orthorhombic (LTLO) phases dramatically degrade towards the LTO, while the well-defined SDW order remains even in the LTO phase. (Fig. 1)

Furthermore, both the CDW and SDW peak intensities were found to begin appearing at the structural transition temperature (T_{d2}) with similar temperature dependence to that of the order parameter of the (0 1 0). (Fig.2) The coincident appearance of the CDW and SDW orders below T_{d2} is also observed for the x=0.05(T_{d2}=37K) and 0.085 (T_{d2}=30K) samples. These results clearly demonstrate a structural effect on the charge and spin orders in the copper oxides.

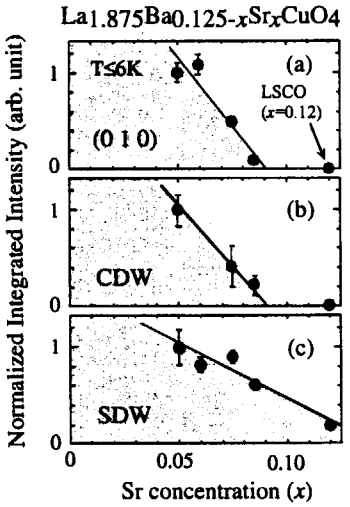


Fig.1 Peak intensity integrated within the plane for (a) (0 1 0), which is allowed in the LTT/LTLO phase, (b) CDW and (c) SDW peaks as a function of Sr concentration. Result for $La_{1.88}Sr_{0.12}CuO_4$ is plotted as a reference. [2] Solid lines are guides to the eye.

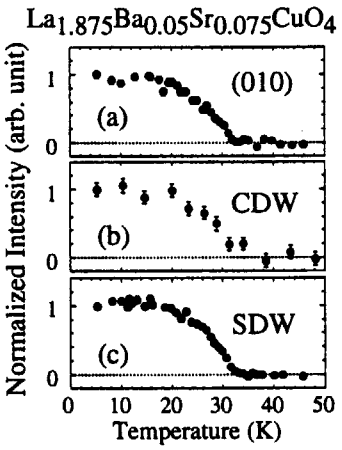


Fig.2 Temperature dependencies of (a) (0 1 0), (b) CDW and (c) SDW superlattice peak intensities in $La_{1.875}Ba_{0.05}Sr_{0.075}CuO_4$.

References

[1] M. Tranquada et al., Nature **375**, 561 (1995).
[2] H. Kimura *et al.*, Phys. Rev. B **59**, 6517 (1999).

使用施設: JRR-3M, 装置: TOPAN,HER, 分野: 超伝導

研究テーマ：$YBa_2Cu_3O_y$ の磁気励起スペクトルの具体的構造
表　題：$La_{1.48}Nd_{0.4}Sr_{0.12}CuO_4$ の磁気励起スペクトル

1-3-3

Magnetic Excitation Spectra of $La_{1.48}Nd_{0.4}Sr_{0.12}CuO_4$

M. Ito[1], Y. Yasui[1], S. Iikubo[1], M. Soda[1], M. Sato[1], K. Kakurai[2] and M. Nishi[3]
[1]*Department of Physics, Nagoya University, Furo-cho, Chikusa-ku, Nagoya 464-8602*
[2]*Advanced Science Research Center, JAERI, Tokai, Ibaraki 319-1199*
[3]*Neutron Scattering Laboratory, ISSP, The University of Tokyo, Tokai 319-1106*

In the study of the superconductivity of Cu oxides, the detailed wave vector($\boldsymbol{q}$)- and energy(ω)-dependences of the magnetic excitation spectra χ'' present important information The spectra may also present information on the role of the fluctuating or dynamical "stripes" in the occurrence of the superconductivity. If they have significant effects on the electron system, we may have to consider $\chi''(\boldsymbol{q}, \omega)$ essentially in the charge ordered background.

We have been studying the detailed structure of $\chi''(\boldsymbol{q}, \omega)$ of $YBa_2Cu_3O_y$ ($YBCO_y$ or YBCO) and reported that the magnetic excitation spectra of $YBCO_y$ ($y \geq 6.5$) can be well understood without effects of dynamical "stripes" [1, 2]. In the study, an expression $\chi(\boldsymbol{q}, \omega)=\chi^0(\boldsymbol{q}, \omega)/\{1+J(\boldsymbol{q})\ \chi^0(\boldsymbol{q}, \omega)\}$ is used for the dynamical susceptibility with the exchange coupling $J(\boldsymbol{q})=J(\cos q_x a+\cos q_y a)$ and the Lindhard function $\chi^0(\boldsymbol{q}, \omega)$ of the electron system. The effective band parameters t_0, t_1 and t_2, which can reproduce the Fermi surface shape are used. Other details can be found in refs. 1 and 2. What we just want to emphasize here is that consideration of the quasi particle broadening is important to suppress the antiferromagnetic ordering and to reproduce the ($\boldsymbol{q}$, ω)- and temperature(T)-dependence of the spectra.

The above results suggest that effects of the dynamical "stripes" is not important for the occurrence of the high-T_c superconductivity and that the effects can be seen only in La214 systems such as $La_{2-x}Ba_xCuO_4$, $La_{1.6-x}Nd_{0.4}Sr_xCuO_4$, and other related systems with $x \sim 1/8$. To study this point in detail, we have deliberately adopted $La_{1.48}Nd_{0.4}Sr_{0.12}CuO_4$ which has the static

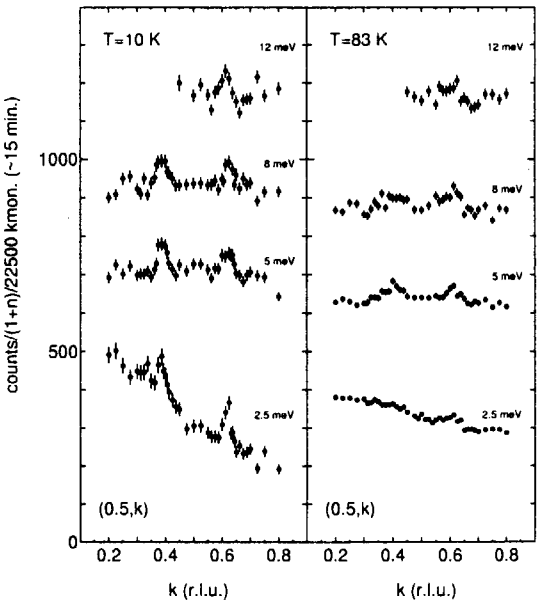


Figure 1: Magnetic excitation spectra $\chi''(\boldsymbol{q}, \omega)$ of $La_{1.48}Nd_{0.4}Sr_{0.12}CuO_4$ measured along (0.5,k,0).

"stripe" order. In the present crystal, the first order transition to the low temperature tetragonal(LTT) phase takes place at ~70 K and the superlattice reflections related to the magnetic and charge order appears at ~60 K with decreasing T ("stripe" order). We have measured the spectra $\chi''(\boldsymbol{q}, \omega)$ to find how effects of the "stripes" appears in $\chi''(\boldsymbol{q}, \omega)$. The data present useful information to study the existence or non-existence of effects of dynamical "stripes" in Cu oxides which exhibit high-T_c superconductivity.

In Fig. 1, the magnetic excitation spectra of $La_{1.48}Nd_{0.4}Sr_{0.12}CuO_4$ taken along (0.5,k,0) at several energies E are shown at 10 K and 83 K. At 10 K, the "stripe" order exists and the sharp spin wave-like excita-

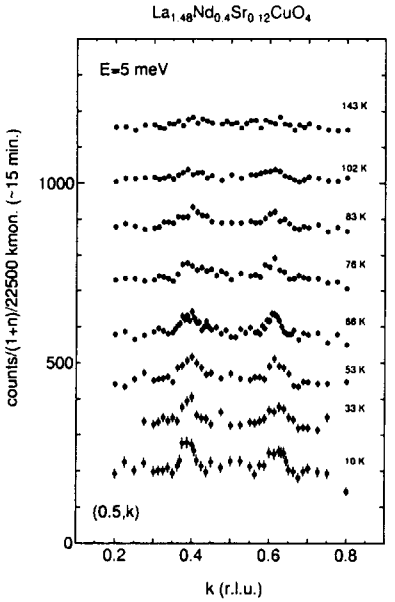


Figure 2: Magnetic excitation spectra $\chi''(q, \omega)$ of $La_{1.48}Nd_{0.4}Sr_{0.12}CuO_4$ measured along (0.5,k,0).

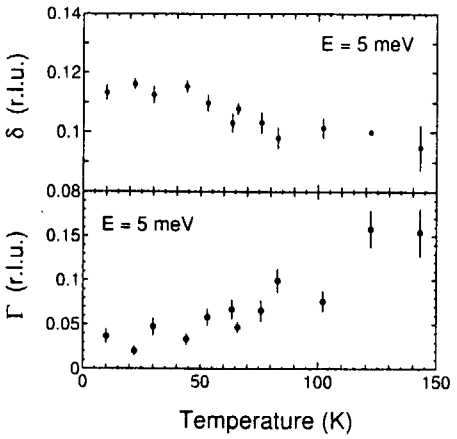


Figure 3: top: Incommensurability δ of the peak of $\chi''(q, \omega)$ of $La_{1.6-x}Nd_{0.4}Sr_xCuO_4$ is plottedagainst T. bottom: The width of the magnetic excitation peak of $\chi''(q, \omega)$ observed by the scan along (0.5,k,0) at E=5 meV are plotted against T. The resolution corrections are made.

tions can be observed at the incommensurate(IC) points, (0.5,0.5±δ,0). The peak intensity is larger for the smaller E. At 83 K, because the magnetic order does not exist, the peak width becomes broader than at 10 K and the low energy peak diminishes.

Figure 2 shows the profiles taken at E=5 meV at several temperatures. We can see that the IC nature survives up to the T region much higher than the temperature T_{CO} of the "stripe" order.

Figure 3 shows the T-dependence of the incommensurability δ(top) and the intrinsic width of the IC peaks(bottom). One of the interesting points is that δ changes from ~0.10 to 0.12 at around T_{CO}. If the periodicity of the one dimensional charge order determines δ, it is equal to 0.12 even at T>70 K. However, δ=0.12 has been observed only in the region of the static order, indicating that δ is rather determined by the Fermi surface effect above 70 K, than the periodicity of the "stripes". The LTT phase may stabilize the "stripe" order and the change of δ takes place just below the transition to the LTT phase.

The robust nature of the IC structure against the T increase (and equivalently in some sense, the rather small width of the IC peaks) indicate(s) that the energy broadening of the electrons should be much smaller than that of $YBCO_y$. This feature is seen in the published data of $La_{1.9}Sr_{0.1}CuO_4$ and $La_{1.85}Sr_{0.15}CuO_4$, too [3, 4]. The large broadening of the quasi particles, which is one of the characteristics of high-T_c systems, is less significant in $La_{2-x}Sr_xCuO_4$(LSCO) system. It is possibly attributed to the existence of the dynamical "stripes" in LSCO.

References

[1] M. Sato, M. Ito, H. Harashina, M. Kanada, Y. Yasui, A. Kobayashi and K. Kakurai: J. Phys. Soc. Jpn. **70** (2001) 1342.

[2] M. Ito, H. Harashina, Y. Yasui, M. Kanada, S. Iikubo, M. Sato, A. Kobayashi and K. Ka-kurai: J. Phys. Soc. Jpn. **71** (2002) 265.

[3] H. Kimura, K. Hirota, H. Matsushita, K. Yamada, Y. Endoh, S-H. Lee, C. F. majkrzak, R. Erwin, G. Shirane M. greven, Y. S. Lee, M. A. Kastner and R. J. Birgeneau: Phys. Rev. B **59** (1999) 6517.

[4] C. Lee, K. Yamada, Y. Endoh, G. Shirane, R. J. Biegeneau, M. A. Kastner, M. Greven and Y. J. Kim: J. Phys. Soc. Jpn. **69** (2000) 1170.

研究テーマ：$YBa_2Cu_3O_y$の磁気励起スペクトルの具体的構造
表　題：$YBCO_{6+x}$の面内フォノンの研究

1-3-4

Neutron Scattering Study on in-plane phonon modes of $YBCO_{6+x}$

M. Ito[1], Y. Yasui[1], M. Kanada[1], S. Iikubo[1], H. Harashina[1], M. Sato[1], K. Kakurai[2] and M. Nishi[3]

[1]*Department of Physics, Nagoya University, Furo-cho, Chikusa-ku, Nagoya 464-8602*
[2]*Advanced Science Research Center, JAERI, Tokai, Ibaraki 319-1199*
[3]*Neutron Scattering Laboratory, ISSP, The University of Tokyo, Tokai 319-1106*

The T_c-suppression found in $La_{2-x}Ba_xCuO_4$ and $La_{2-x-y}Nd_ySr_xCuO_4$ at around the hole carrier concentration $p(=x)\sim 1/8$ is called the "1/8 anomaly", and considered to originate from the formation of the one dimensional charge order or "stripes" in the CuO_2 planes. To study whether the fluctuations of the "stripes" or the dynamical "stripes" have important roles in realizing (or in suppressing) the superconductivity, we have searched effects of dynamical "stripes" on the physical quantities of $YBa_2Cu_3O_y$ (YBCO, $YBCO_y$) and reported that magnetic excitation spectra of YBCO can be understood without effects of dynamical "stripes" in the region of $y\geq 0.5$ [1, 2]. The present paper reports results of phonon measurements.

Mook *et al.* [3, 4] measured the in-plane longitudinal modes of $YBa_2Cu_3O_y$ ($YBCO_y$) system, which have the energies of ~(43~52) meV and are assigned as the B_{2u}/B_{3u} modes at Γ point. They reported the anomalous wave vector ($\boldsymbol{q}$) dependence of the broadening of one of the modes(B_{3u} one), which vibrates perpendicular to the *b*-axis, as the experimental evidence for the existence of the dynamical "stripes" along $\boldsymbol{b}$. Anomalous $\boldsymbol{q}$ dependence of the integrated intensity of the phonon peak has also been reported by their group.

We have measured other in-plane longitudinal phonons, which are also assigned as the B_{2u}/B_{3u} modes at Γ point [5]. (Hereafter, we just call these branches B_{2u}/B_{3u} modes.) As shown in Figs. 1(a) and 1(b), the atomic motions of the $B_{3u}(B_{2u})$ mode in the CuO_2 plane are mainly perpendicular(parallel) to the chain direction(*b*-direction), and the amplitude of the chain oxygen motion is larger for the B_{3u} mode than for the B_{2u} one.

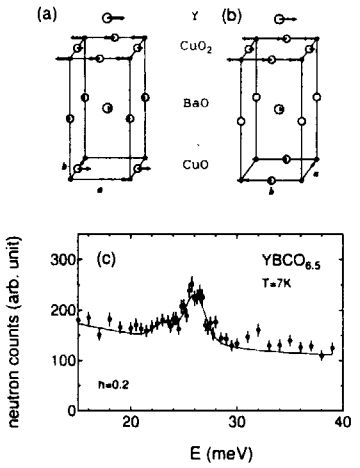


Figure 1: Patterns of the atomic motions of B_{3u}(a) and B_{2u}(b) modes. In (c), the phonon profiles observed for $YBCO_{6.5}$ at 7 K are shown.

Neutron measurements were carried out with spectrometer ISSP-PONTA at JRR-3M of JAERI on single crystals of $YBCO_{6.5}$ ($T_c\sim 50$ K), $YBCO_{6.7}$ ($T_c\sim 62$ K), and $YBCO_{\sim 7.0}$ ($T_c\sim 91$ K). Oxygen numbers y of the crystals were controlled by the annealing temperature. The horizontal collimations were 40′-40′-40′-80′, and to eliminate the higher order contamination the Pyrolytic Graphite (PG) filter was put after the samples. Calculated profiles obtained by convoluting the Lorentzian type phonon profiles with the resolution function, were fitted to the energy-scan profiles at constant reciprocal points $\boldsymbol{Q}=(3+h,0,0)$.

Figure 1(c) shows the energy scan profile of the B_{2u}/B_{3u} phonons taken for $YBCO_{6.5}$ at h=0.2 and at ~7 K. The h value is

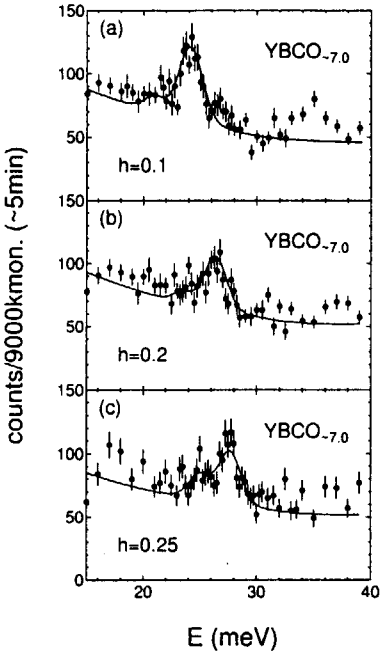


Figure 2: Energy scan profiles of the B_{2u}/B_{3u} phonons taken at ~7 K for $YBCO_{\sim 7}$ at $\boldsymbol{Q}$=(3+h,0,0), h being 0.1, 0.2 and 0.25.

close to the twice of the incommensurability, 2δ, of the magnetic scattering peak. Similar data taken for $YBCO_{\sim 7}$ at ~7 K are shown in Fig. 2 for several h values. Two peaks can be observed in each profile: The higher energy mode has the smaller widths and larger intensities than the lower energy one. The large broadening or large smearing observed for the lower energy mode might be attributed to an effect of the dynamical "stripes". However, the smearing is found in the wide region of h, suggesting that it is not related to the value of 2δ. It is insensitive to the carrier number p or y. Moreover, it seems to be insensitive to the temperature T, too. These facts cannot be explained by considering effects of the dynamical "stripes", which should be stronger in the region of $p\sim 1/8$ and at lower T. Instead, we simply attribute the smearing to the oxygen deficiency at the chain sites, assigning that the lower energy mode is the B_{3u} one, which has the larger amplitude of the chain oxygen

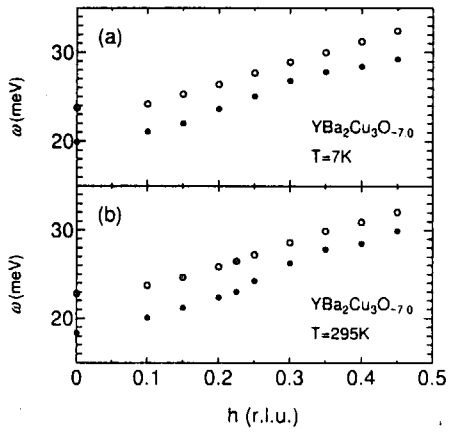


Figure 3: Dispersion curves obtained for $YBCO_{\sim 7}$ at 7 K and 295 K are shown.

vibration than the B_{2u} one. (We think that there exist, even in the sample with y=7, enough amount of oxygen deficiency to bring about the observed smearing of the mode.)

In Fig. 3, dispersion curves obtained for $YBCO_{\sim 7}$ at 7 K and 295 K are shown, where just the smooth $\boldsymbol{q}$-dependence can be observed for all the samples at all temperatures. This result is contrasted to that reported by Mook *et al.* [3, 4], where an anomaly was observed at $\boldsymbol{q}$=2δ.

In summary, although the smearing of B_{3u} phonon mode has been found, its h-, y- and T- dependences indicate that the dynamical "stripes" cannot be considered to be the origin of the smearing. Instead, it is attributed to the chain oxygen deficiency. No anomalous feature has been found in the dispersion curves.

References

[1] M. Sato, M. Ito, H. Harashina, M. Kanada, Y. Yasui, A. Kobayashi and K. Kakurai: J. Phys. Soc. Jpn. **70** (2001) 1342.

[2] M. Ito, H. Harashina, Y. Yasui, M. Kanada, S. Iikubo, M. Sato, A. Kobayashi and K. Ka-kurai: J. Phys. Soc. Jpn. **71** (2002) 265.

[3] H. A. Mook and F. Dogan: Nature **401** (1999) 145.

[4] H. A. Mook, P. Dai, F. Dogan and R. D. Hunt: Nature **404** (2000) 729.

[5] T. Yasuda and S. Mase: J. Phys. Soc. Jpn. **58** (1989) 195.

研究テーマ：$La_{2-x}Sr_xCuO_4$のオーバードープ超伝導相における磁気励起スペクトル
表題：オーバードープ$La_{2-x}Sr_xCuO_4$におけるギャップ型励起の観測

1-3-5

Observation of a gapped excitation in the overdoped $La_{2-x}Sr_xCuO_4$

H. Hiraka, C. R. V. Rao, C. H. Lee[1], Y. Endoh and K. Yamada[2]
Institute for Materials Research, Tohoku University, Sendai 980-8857
[1] *National Institute of Advanced Industrial Science and Technology, Tsukuba 305-8568*
[2] *Institute for Chemical Research, Kyoto University, Uji 611-0011*

The superconducting phase of high-T_c cuprates are generally classified in the underdoped, optimally doped and overdoped regions, according to the carrier-doping level and T_c. Various concepts (e.g., pseudo-gap, quantum critical point, Fermi-liquid,...) are proposed to explain the curious phase diagram. $La_{2-x}Sr_xCuO_4$ (LSCO) is a suitable and unique system for the experimental study over the entire superconducting phase, due to the large capacity for Sr doping. Although low-energy spin fluctuations from the underdoped to optimally doped phases ($0.07 \leq x \leq 0.18$) have been well studied with inelastic neutron scattering (INS), [1, 2, 3] no detailed investigation has been performed in the overdoped phases except for the heavily overdoped sample with $x = 0.25$ (gapless). [2] Therefore, we explored magnetic excitations of the lightly overdoped superconducting phase in $0.18 < x < 0.25$.

Single crystals of $La_{1.80}Sr_{0.20}CuO_4$ were grown by the TSFZ method. We confirmed the Sr concentration with respect to T_c(= 30 K) and the structural phase-transition temperature. The five cylindric crystals ($\sim 5\phi \times$ 20 mm each) were assembled, finally giving the total volume of 2 cc. INS experiments were performed on the triple-axis spectrometer TOPAN installed at the JRR-3M.

Our new finding is a gapped behavior in the low-energy excitation spctra as shown in Fig. 1. In the superconducting state, no magnetic response was observed at $\omega = 3$ meV (Fig. 1(b)), in contrast with the finite incommensurate scattering at $\omega = 4$ meV (Fig. 1(c)). Further, the incommensurate response of $\omega = 3$ meV appears in the normal conducting state (Fig. 1(a)). This gap-type excitation is similar to those observed in optimally doped $x = 0.15$ and 0.18, [1, 2] but different with the gapless energy spectra in

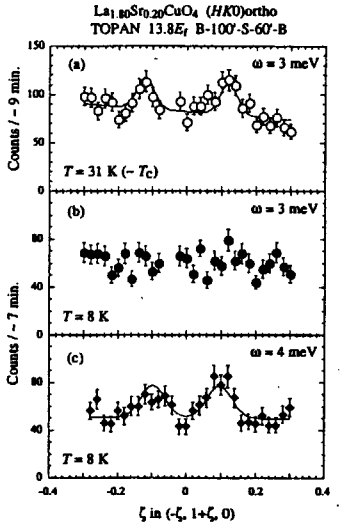


Fig. 1. Low-energy incommensurate scattering of $La_{1.80}Sr_{0.20}CuO_4$ measured around (π, π) at (a) $\omega =$ 3 meV and $T = 31$ K (immediately above T_c), (b) $\omega = 3$ meV and $T = 8$ K, and (c) $\omega = 4$ meV and $T = 8$ K. The curves are guide lines.

the underdoped ($x = 0.10$ [2] and 0.07, [3]) and heavily overdoped pahses ($x = 0.25$ [2]). Through the comparison between the gapped superconductors, the peak-width was found to broaden gradually with keeping a saturated incommensurability (≈ 0.12) as the doping level deepens. The analysis for the resolution-deconvoluted intensity, or $\chi''(\omega)$ is now in progress, which will clarify the relation between the superconductivity and spin fluctuations in terms of the spectral weight.

References

[1] K. Yamada *et al.*, Phys. Rev. Lett. **75**, 1626 (1995); K. Yamada *et al.*, Phys. Rev. B **57**, 6165 (1998).
[2] C. H. Lee *et al.*, J. Phys. Soc. Jpn. **69**, 1170 (2000).
[3] H. Hiraka *et al.*, J. Phys. Soc. Jpn. **70**, 853 (2001).

使用施設：JRR-3M, 装置：TOPAN(6G), 分野：3

研究テーマ：先端偏極中性子散乱によるスピン-格子物性の研究
表　題：$La_{2-x}Sr_xCuO_4$ 低ドープ領域における磁場効果

1-3-6

Magnetic field effect in lightly doped $La_{2-x}Sr_xCuO_4$

M. Matsuda, M. Fujita[1], K. Yamada[1], R. J. Birgeneau[2], Y. Endoh[3] and G. Shirane[4]

ASRC, Japan Atomic Energy Research Institute, Tokai, Ibaraki 319-1195
[1]Institute for Chemical Research, Kyoto University, Gokasho, Uji 610-0011
[2]Department of Physics, University of Toronto, Toronto, Ontario, Canada M5S 1A1
[3]Institute for Materials Research, Tohoku University, Katahira, Sendai 980-8577
[4]Department of Physics, Brookhaven National Laboratory, Upton, New York 11973, USA

Extensive neutron elastic scattering studies have been performed on lightly doped $La_{2-x}Sr_xCuO_4$ ($0< x <0.055$) in order to clarify the static magnetic properties in the spin-glass regime. It is revealed that the static spin correlations in the spin-glass phase show a one-dimensional diagonal spin modulation, in which the direction of the modulation is rotated away by 45° from that in the superconducting phase. [1, 2)]

In this study we examined magnetic field effect of the static magnetic correlations in lightly doped $La_{2-x}Sr_xCuO_4$. One important point is to clarify whether the diagonal incommensurate (DIC) structure is dominated by the charge disproportion or a magnetic origin. Another point is to understand the magnetic anisotropy in doped La_2CuO_4 from a microscopic point of view. The neutron-scattering experiments were carried out on the cold neutron three-axis spectrometers LTAS and the thermal neutron three-axis spectrometer TAS2, using single crystals of $La_{2-x}Sr_xCuO_4$ (x=0.014 and 0.024) grown by the traveling

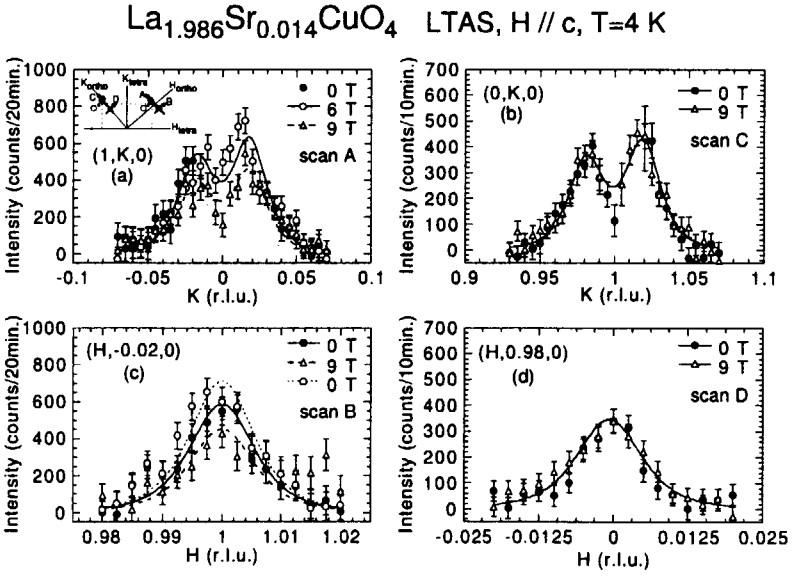


Figure 1: Magnetic elastic intensity around the diagonal incommensurate positions $(1,\pm\epsilon,0)$ and $(0,1\pm\epsilon,0)$ at 4 K in $La_{1.986}Sr_{0.014}CuO_4$ as a function of magnetic field. The scan trajectories are shown in the inset of (a). Open circles in (c) are the data measured at 0 T after a magnetization cycle. Magnetic field is applied perpendicular to the CuO_2 plane. Background intensities measured at a high temperature have been subtracted. The lines are guides to the eyes.

原子炉：JRR-3M　　装置：TAS-2(T2-4), LTAS(C2-1) 分野：中性子散乱（超伝導）

solvent floating-zone method.

Figure 1 shows the magnetic field dependence of the magnetic elastic intensity around DIC positions (1,±ϵ,0) and (0,1±ϵ,0) in $La_{1.986}Sr_{0.014}CuO_4$, which exhibits a coexistence of a Néel ordered phase and a spin-glass phase at low temperatures. The magnetic signal, which develops below ~30 K, originates from the spin-glass phase. The incommensurate peaks are antisymmetric because of the twin structure as shown in the inset of Fig. 1(a). As shown in Figs. 1(a) and 1(c), the magnetic intensity at (1,±ϵ,0) are almost constant between 0 and 6 T and gradually decreases above 6 T.

It is known in pure La_2CuO_4 that applying the magnetic field perpendicular to the CuO_2 plane, the magnetic structure factor of the (100) reflection becomes zero because a spin reorientation transition from La_2CuO_4-type to La_2NiO_4-type occurs. [3, 4] The decrease in intensity in $La_{1.986}Sr_{0.014}CuO_4$ probably originates from this spin reorientation transition. This transition is ascribed to the Dzyaloshinskii-Moriya (DM) antisymmetric exchange terms generated by the small rotation of the CuO_6 octahedra. Because of the DM terms, the magnetic anisotropy is weakly Ising-like and has an easy-axis along the *b* axis. Therefore, it is suggested that the DIC spin structure in the spin-glass phase also has an Ising-like anisotropy.

The magnetic intensity at (0,1±ϵ,0) is almost magnetic field independent as shown in Figs. 1(b) and 1(d). The magnetic signal at (0,1±ϵ,0) is considered to be a tail of (0,1±ϵ,1), which is broad along the *c* axis. [2] The instrumental resolution elongated vertically integrates the tail effectively. The (011) magnetic Bragg peak should decrease under magnetic field. Whereas the (010) magnetic intensity increases. Since the both contributions compensate with each other, the intensity at (0,1±ϵ,0) may be almost unchanged.

Figure 2 shows the magnetic field effect in $La_{1.976}Sr_{0.024}CuO_4$, which shows no long-range AF order but a spin-glass behavior below ~25 K, with field perpendicular to the CuO_2 plane. The magnetic intensity at (1,±ϵ,0) decreases monotonically with increasing magnetic field. The tendency is similar to that in $La_{1.986}Sr_{0.014}CuO_4$ although there is a decrease in intensity between 0 and 5 T and the intensity at 10 T becomes almost half of that at 0 T. This means that the averaged critical field becomes smaller with hole doping. The transition is very broad in the spin-glass phase probably because the cluster size is finite and distributed so that the critical field is also distributed. In this experiment, it is found that the transition temperature, the peak width, and peak positions are almost unchanged under magnetic field although the magnetic intensity decreases. This result indicates that the DIC structure is probably dominated by the charge disproportion.

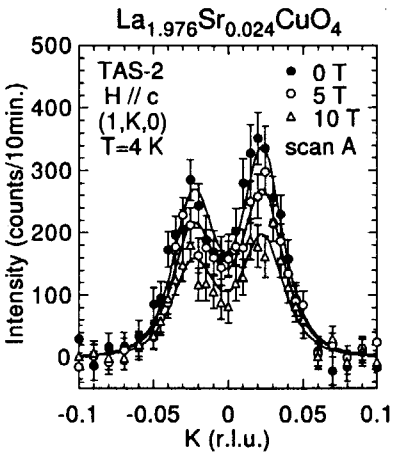


Figure 2: Magnetic elastic intensity around the diagonal incommensurate positions (1,±ϵ,0) at 4 K in $La_{1.976}Sr_{0.024}CuO_4$ as a function of magnetic field. Magnetic field is applied perpendicular to the CuO_2 plane. Background intensities measured at a high temperature have been subtracted.

References

1) S. Wakimoto *et al.*, Phys. Rev. B **60** (1999) R769; S. Wakimoto *et al.*, *ibid.* **61** (2000) 3699.
2) M. Matsuda *et al.*, Phys. Rev. B **62** (2000) 9148.
3) T. Thio *et al.*, Phys. Rev. B **38** (1988) 905.
4) M. A. Kastner *et al.*, Phys. Rev. B **38** (1988) 6636.

研究テーマ：先端偏極中性子散乱によるスピン-格子物性の研究
表　題：電子ドープ型超伝導体 $Nd_{1.86}Ce_{0.14}CuO_4$ における磁場効果

1-3-7

Magnetic field effect on the static magnetic order in the electron-doped superconductor $Nd_{1.86}Ce_{0.14}CuO_4$

M. Matsuda, S. Katano, T. Uefuji[1], M. Fujita[1] and K. Yamada[1]

ASRC, Japan Atomic Energy Research Institute, Tokai, Ibaraki 319-1195
[1]Institute for Chemical Research, Kyoto University, Gokasho, Uji 610-0011

Extensive neutron-scattering studies have been performed on the high-T_c superconductors in order to clarify the interplay between the superconductivity and magnetism. Especially in the hole-doped cuprate superconductor $La_{2-x}Sr_xCuO_4$ and related systems, static and dynamic properties of spin correlations are studied in considerable detail.

In the electron-doped cuprate superconductor, however, the number of neutron-scattering studies is limited. In this study we examined magnetic field effect of the static magnetic correlations in $Nd_{1.86}Ce_{0.14}CuO_4$ (T_c ~25 K). Since the coherence length is ~100 Å in the electron-doped system, which is several times larger than that in $La_{2-x}Sr_xCuO_4$, large magnetic field effect can be expected. Furthermore, the upper critical field H_{c2} is less than 10 T in the electron-doped system so that normal state properties can be easily studied.

The neutron-scattering experiments were carried out on the three-axis spectrometer TAS2, using a large single crystal grown by the traveling solvent floating-zone method. The $(\frac{1}{2}\frac{3}{2}0)$ magnetic Bragg intensity, which mainly originates from the order of both the Cu and Nd moments at low temperatures, shows no magnetic field dependence when the field is applied perpendicular to the CuO_2 plane up to 10 T above H_{c2}, as shown in Fig. 1. This result is much different from that reported in the hole-doped superconductors, in which the quasi-static magnetic order is enhanced under magnetic field. This suggests that the interplay between magnetic order and superconductivity in this system is much different from that in the hole-doped system.

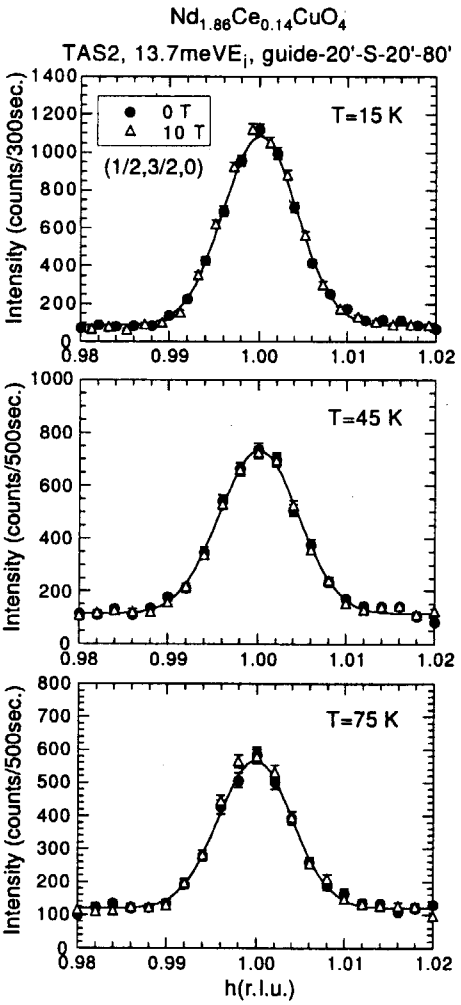


Figure 1: Neutron elastic intensity around the commensurate position $(\frac{1}{2}, \frac{3}{2}, 0)$ in $Nd_{1.86}Ce_{0.14}CuO_4$ under magnetic fields H=0 and 10 T and at T=15, 45, and 75 K. Magnetic field is applied perpendicular to the CuO_2 plane. The solid lines are the results of fits to a Gaussian function for the zero field data.

原子炉：JRR-3M　　装置：TAS-2(T2-4)　　分野：中性子散乱（超伝導）

研究テーマ：T^*系高温超伝導体の磁気励起スペクトル
表　題：$La_{1.48}Nd_{0.4}Sr_{0.12}CuO_4$の面内縦波格子振動の測定

1-3-8

Measurements of the In Plane Longitudinal Phonons of $La_{1.48}Nd_{0.4}Sr_{0.12}CuO_4$

M. Ito, Y. Yasui, S. Iikubo, M. Sato, K. Kakurai[1] and M. Nishi[2]

Department of Physics, Nagoya University, Furo-cho, Chikusa-ku, Nagoya 464-8602
[1]Advanced Science Research Center, JAERI, Tokai, Ibaraki 319-1195
[2]Neutron Scattering Laboratory, ISSP, The University of Tokyo, Tokai 319-1106

The suppression of the superconducting critical temperature T_c observed in $La_{2-x}Ba_xCuO_4$ and $La_{2-x-y}Nd_ySr_xCuO_4$ systems at around the hole carrier concentration $p(=x)\sim 1/8$ is considered to originate from the formation of the one dimensional-like charge ordering or "stripes" in the CuO_2 planes.

To clarify whether the fluctuations of the "stripes" or the dynamical "stripes" have important roles in realizing(or in suppressing) the superconductivity commonly to every high-T_c system, we have studied effects of dynamical "stripes" on the physical quantities of $YBa_2Cu_3O_y$ (YBCO, $YBCO_y$) and reported that magnetic excitation spectra of YBCO can be understood without effects of dynamical "stripes" [1, 2].

The present paper reports results of phonon measurements on single crystals of $La_{1.48}Nd_{0.4}Sr_{0.12}CuO_4$, which has the "stripe" ordered state in the low temperature tetragonal(LTT) phase. Mook *et al.* [3, 4] measured the in-plane longitudinal modes of $YBa_2Cu_3O_y$ ($YBCO_y$) system. These phonons have the energies of ~(43~52) meV and can be assigned as the B_{2u}/B_{3u} modes at Γ point. They reported the anomalous wave vector (q) dependence of the broadening of one of the modes(B_{3u} one), which vibrates perpendicular to the b-axis, as the experimental evidence for the existence of the dynamical "stripes" along b. Anomalous q dependence of the integrated intensity of the phonon peak has also been reported by their group.

Similar studies have also been carried out by the present authors' group for similar longitudinal modes(B_{2u}/B_{3u} modes at Γ point) of $YBCO_y$ with the energy dispersions between ~20 and ~35 meV, where, in contrast with the results of Mook *et al.* [3, 4], significant effects of the dynamical "stripes" have not been found [5]. Considering these results, we have deliberately adopted $La_{1.48}Nd_{0.4}Sr_{0.12}CuO_4$, which has the "stripe" order at low T, to study how significantly we can see effects of the "stripes" on the phonon modes. Neutron data were taken with the TAS-1 spectrometer at JRR-3M.

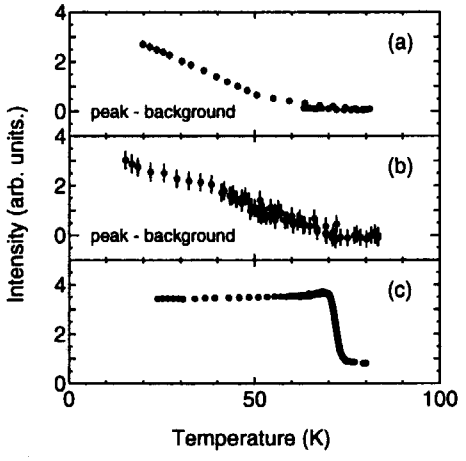


Figure 1: T dependences of the peak intensities of the superlattice reflections observed at (0.5±δ,0.5,0)(a), (2+2δ,0,0)(b) and (1,0,0)(c) in the reciprocal space of $La_{1.6-x}Nd_{0.4}Sr_xCuO_4$.

Figures 1(a)-1(c) show the temperature(T) dependences of the peak intensities the superlattice reflections observed at (0.5±δ,0.5,0), (2+2δ,0,0) and (1,0,0) points, respectively, in the reciprocal space of $La_{1.48}Nd_{0.4}Sr_{0.12}CuO_4$. The data at the point $\boldsymbol{Q}$=(1,0,0) shows that the LTT phase appears suddenly (by the first order transition) at about 70 K with decreasing T. The data at (0.5±δ,0.5,0) and (2+2δ,0,0) show that the ordering of the mag-

原子炉：JRR-3M　　装置：TAS-1(2G)　　分野：中性子散乱（超伝導）

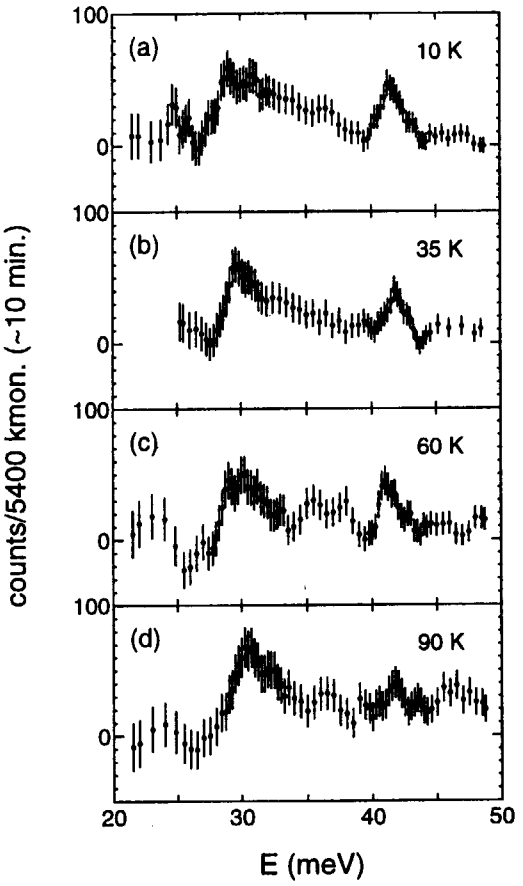


Figure 2: Transfer energy dependence of the neutron scattering intensity measured at several temperatures at $\boldsymbol{Q}$=(4.25,0,0).

netic moments and charges, respectively, appear at around 60 K with decreasing T.

Figures 2(a)-2(d) show the transfer energy(E) dependence of the neutron scattering intensity measured at several temperatures at $\boldsymbol{Q}$=(4.25,0,0), where in-plane longitudinal modes are mainly detected. A broad peak can be seen at around 30 meV and a clear peak can also be observed at around 41 meV. The former peak can be assigned to be the modes which correspond to the B_{2u}/B_{3u} modes observed in our study on $YBCO_y$ system. It also corresponds to the the in-plane longitudinal mode of $La_{2-x}Sr_xCuO_4$, as can be found by comparing the energy dispersions of the present system

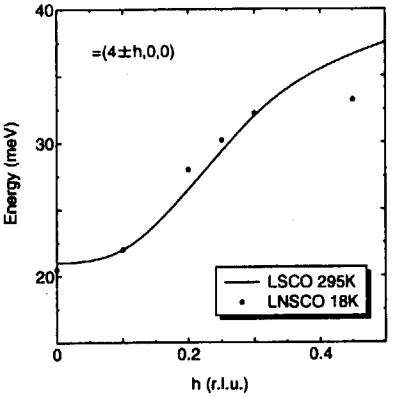


Figure 3: Energy dispersions of $La_{1.48}Nd_{0.4}Sr_{0.12}CuO_4$ and $La_{1.9}Sr_{0.1}CuO_4$.

and $La_{1.9}Sr_{0.1}CuO_4$(See Fig. 3). An effect of the "stripe" formation can be seen as the increase of the width of the peak at around 30 meV: At 90 K(above the temperature of the charge ordering T_{CO}), the peak is relatively sharp and we can therefore see the dip-structure at E~35 meV. It can also be seen at 60 K($\sim T_{CO}$), but cannot be observed at 35 K and 10 K. This result indicates that the broadening increases with the charge order rather than the sudden increase at the transition to the LTT phase.

A rather significant change of the observed spectra is also found in the T-dependence of the peak intensity at E~41 meV. Although the peak intensity seems to be T-dependent even below 35 K, we cannot distinguish, at this moment, if the observed change is induced by the structural transition at 70 K or by the charge ordering.

References

1) M. Sato, M. Ito, H. Harashina, M. Kanada, Y. Yasui, A. Kobayashi and K. Kakurai : J. Phys. Soc. Jpn. **70** (2001) 1342.
2) M. Ito, H. Harashina, Y. Yasui, M. Kanada, S. Iikubo, M. Sato, A. Kobayashi and K. Ka-kurai : J. Phys. Soc. Jpn. **71** (2002) 265.
3) H. A. Mook and F. Dogan : Nature **401** (1999) 145.
4) H. A. Mook, P. Dai, F. Dogan and R. D. Hunt : Nature **404** (2000) 729.
5) M. Ito *et al.* LT23.

研究テーマ：$La_2Cu_{1-x}Li_xO_4$のスピン相関
表　題：$La_2Cu_{1-x}Li_xO_4$における低温磁気散乱
1-3-9

Low Temperature Scattering in $La_2Cu_{1-x}Li_xO_4$

P. K. Mang, N. Kaneko, M. Greven
K. Kakurai[1] and M. Matsuda[1]

Laboratory for Advanced Materials, Stanford University, Stanford CA 94305, USA
[1]Advanced Science Research Center, JAERI, Tokai, Ibaraki 319-1195

The magnetic phase diagram of $La_2Cu_{1-x}Li_xO_4$ (LCLO) bears strong similarity to the more familiar superconducting compound $La_{2-x}Sr_xCuO_4$ (LSCO). At low doping both compounds are antiferromagnets. The boundary of the antiferomagnetic (AF) phase is slightly renormalized in LCLO to $x = 0.03$[1)], compared to $x = 0.02$ for LSCO. Beyond the AF phase boundary, both compounds have spin-glass phases which are quantitatively similar to each other[2)]. Reentrant spin-glass behavior within the AF phase is also present in both compounds. A key difference is that for concentrations $x > 0.055$, LSCO becomes a superconductor while LCLO remains an insulator for all dopings.

Recent results by Matsuda *et al.* for LSCO ($x < 0.02$) have demonstrated first-order phase separation into AF and incommensurately spin-ordered regions at low temperature[3)]. Although previous reports at higher doping ($x = 0.10$) for LCLO reported the absence of an incommensurate spin structure[4)], the strong similarities between the magnetic phase diagrams leaves the behaviour inside the AF phase as an open question.

We conducted high-resolution elastic neutron scattering studies at the cold neutron beamline LTAS. The sample was a single crystal of $La_2Cu_{0.98}Li_{0.02}O_4$ grown by the Travelling Solvent Floating Zone method at Stanford University. As expected, the sample exhibits antiferromagnetic order below a mean transition temperature of $T_N = 125$ K. Our experiment reveals several indications of exciting low-temperature magnetic behaviour.

Figure 1 presents a scan at the AF (100) peak position. The instrumental resolution as measured by $\lambda/2$ is indicated by the dashed line. As is apparent, the width of the peak is broader than resolution at all temperatures below the ordering temperature. This may either indicate that the increased disorder experienced in this system limits the magnetic order to being quasi-long-range, or as suggested by some, the presence of a second component to the scattering function, indicating the presence of topological "skyrmionic" spin structures surrounding the doped Li sites[5)].

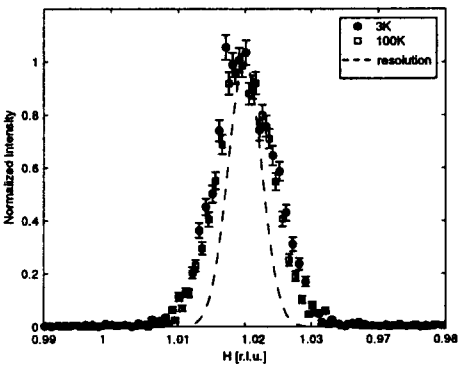


Figure 1: Antiferromagnetic (100) Bragg peak showing a temperature independent width which is broader than the instrumental resolution.

In Fig. 2 we present a measurement of the antiferromagnetic order parameter. The onset of AF order is easily visible at high temperature, marked by the sudden increase in intensity. At low temperature, as highlighted in the inset, a fraction of the intensity is lost. In the low-doped LSCO samples studied by Matsuda *et al.*[3)], a similar loss of intensity is observed at T$\sim$ 30 K and correlates with the appearance of incommensurate peaks in a diagonal stripe geometry.

原子炉：JRR-3M　　装置：LTAS(C2-1)　　分野：中性子散乱（超伝導）

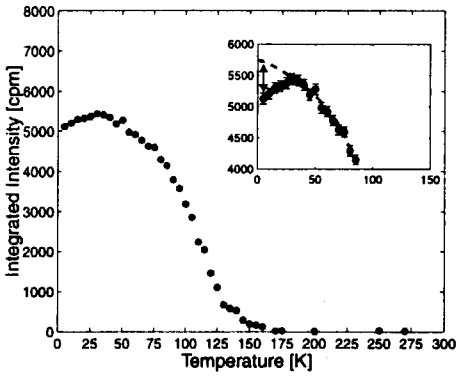


Figure 2: Magnetic order parameter measured at the (100) antiferromagnetic Bragg position.

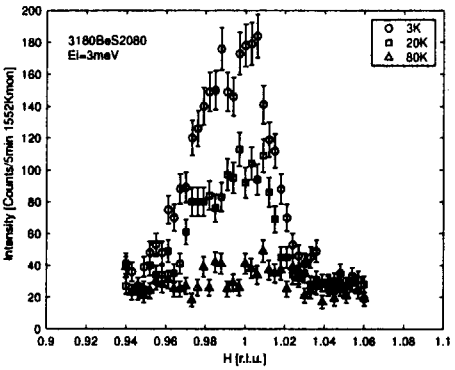


Figure 3: Temperature dependence of the magnetic scattering near (0,1,0.2).

Intrigued by the possibility of similar incommensurate correlations in LCLO, we undertook a detailed survey around the commensurate position in a sample of $La_2Cu_{0.98}Li_{0.02}O_4$. In Fig. 3, we present a series of scans at the (0,1,0.2) position in reciprocal space. The (0,1,0) peak is forbidden by the magnetic structure factor in the La_2CuO_4 spin configuration. Yet, it is very clear from the scans that a broad magnetic scattering rod forms at low temperature. The intrinsic width of the peak is difficult to determine because of the multiple twin domains in our sample. At present our data do not enable us to distinguish between broad scattering at the commensurate position, and incommensurate scattering with a reduced incommensurability. What we have been able to establish is that, if the low-temperature magnetic scattering is incommensurate, then the incommensurability is at most half that observed in samples of LSCO at the same doping level.

The physics of $La_2Cu_{1-x}Li_xO_4$ in the low-doping regime has revealed strong similarities but also intriguing differences with $La_{2-x}Sr_xCuO_4$. Contrasting the two systems is an exciting means of exploring the different ways in which their common parent responds to perturbations of the Mott insulator. Many of the ambiguities in our current analysis are directly attributable to the multi-twin domain nature of our sample. A second round of experiments are planned both within the Néel phase and in the spin-glass regime that lies at higher doping once single-domain samples can be produced.

References

1) J.L. Sarrao *et al.*, Phys. Rev. B **54** 12014 (1996).
2) T. Sasagawa *et al.*, manuscript in preparation.
3) M. Matsuda *et al.*, Phys. Rev. B **65** 134515 (2002).
4) W. Bao *et al.*, Phys. Rev. Lett. **84** 3978 (2000).
5) S. Haas *et al.*, Phys. Rev. Lett. **77**, 3021 (1996).

研究テーマ：単層 BISCO のスピン相関
表　題：単層ビスマス系銅酸化物における磁気揺動の探索
1-3-10

Search for Antiferromagnetic Fluctuations in Bismuth-Based Superconductors

N. Kaneko, P. K. Mang, K. Kakurai[1], M. Matsuda[1], H. Hiraka[2], Y. Endoh[2], K. Nakajima[3] and M. Greven

Laboratory for Advanced Materials, Stanford University, Stanford CA 94305, USA
[1]Advanced Science Research Center, JAERI, Tokai, Ibaraki 319-1195
[2] Institute of Materials Research, Tohoku University, Sendai 980-8577
[3] Institute for Solid State Physics, University of Tokyo, Tokai, Ibaraki 319-1106

It is widely believed that antiferromagnetic fluctuations play an important role in the physics of high-temperature superconductivity. The undoped parent compounds, such as La_2CuO_4, are antiferromagnetic insulators. Upon doping the CuO_2 sheets with a few percent of holes, these materials become metallic and superconducting, with "strange" metallic behavior in the normal state. Neutron scattering studies have demonstrated that dynamic antiferromagnetic correlations are a robust feature of both superconducting and normal states[1, 2, 3, 4, 5, 6].

$La_{2-x}Sr_xCuO_4$ (LSCO) has been the only single-layer hole-doped high-temperature superconductor that has been studied systematically via neutron scattering, since it is relatively straightforward to grow the required large single crystals. Detailed studies have revealed many interesting properties, such as an incommensurate magnetic response[1, 2, 7, 8]. The only other high-Tc family of materials for which sizeable crystals over a wide range of hole-doping have been available for neutron scattering studies is the structurally more complicated bi-layer system $YBa_2Cu_3O_{6+\delta}$ (YBCO)[3, 4, 5, 6, 9]. The magnetic response of YBCO appears to be rather different from that of LSCO. In particular, it was found that the magnetic response is gapped and incommensurate only at high energies, and that there exists a magnetic resonance (at 41meV for optimally doped YBCO) in the superconducting state.

To better understand the connection between antiferromagnetic correlations and high-temperature superconductivity, it will be necessary to study additional materials. Neutron scattering experiments require sizeable samples, a fact that has presented a significant obstacle toward this end. We have succeeded with the growth of sizeable crystals of the single-layer and double-layer Bi-based superconductor $Bi_{2-y}Pb_ySr_{2-x}La_xCuO_{6+\delta}$ (Bi2201). The sample shown in Fig. 1 consists of 6 co-aligned single crystals with total volume of 1.1 cm^3. Initial crystal checks demonstrated the single-grain nature of the individual crystals. Small pieces from these crystals show excellent superconducting properties, with an onset of $T_c \sim 36K$, which compares well with the highest values achieved in LSCO.

In light of the differences observed for LSCO and YBCO, a study of the magnetic response of Bi2201 should yield valuable new information about the connection between superconductivity and antiferromagnetic order and fluctuations. We have begun to pursue neutron scattering measurements to search for antiferromagnetic fluctuations in Bi2201. Specifically, we carried out inelastic neutron scattering measurements on the TAS-1, TAS-2, PONTA, and TOPAN triple-axis instruments at the JAERI JRR-3M research reactor. To our surprise, unlike for LSCO, these measurements reveal no obvious features in the 3-12 meV range, both below and above the superconducting transition temperature. The incommensurate low-energy magnetic scattering may be broader than in LSCO, and therefore harder to detect. Alternatively, the magnetic fluctuations may be gapped, perhaps with a gap much larger than that of optimally-

原子炉：JRR-3M　　装置：TAS-1(2G)　　分野：中性子散乱（超伝導）

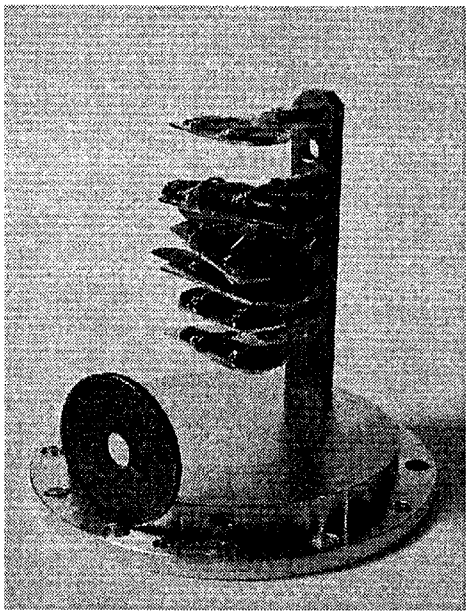


Figure 1: A set of $Bi_{1.7}Pd_{0.3}Sr_{1.6}La_{0.4}CuO_{6+\delta}$ crystals mounted on a sample holder.

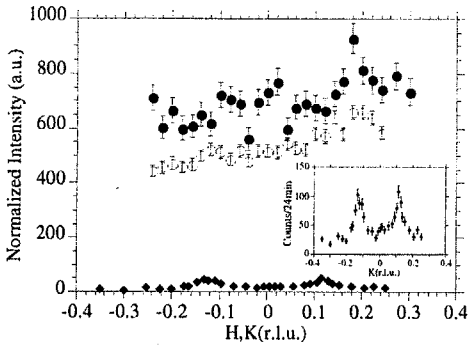


Figure 2: Data around (0,1) for Bi-2201 and corresponding data for $La_{1.85}Sr_{0.15}CuO_4$[10] with energy transfer of 3meV. Closed and open circles are the data for our Bi2201 crystal at T=152K and 40K, respectively. The diamonds are the data for LSCO at 40K. The data was normalized by the counting duration and the volume of the crystals. The inset is a magnified view of the LSCO data.

doped LSCO (about 6 meV). We note, that the experiment is made difficult by the fact that the scattering in Bi2201 results in a very high "background," in large part due to significant low-energy phonon scattering, a result of the complex crystal structure of Bi2201. Figure 2 shows a comparison of our data with data for LSCO to demonstrate the strong difference. We note that we counted as long as 1 hour per point in our inelastic scans. We recently learned that a similar search for antiferromagnetic fluctuations in optimally-doped Bi2201 by Prof. Keimer's group (MPI, Stuttgart, Germany) has failed to discern an antiferromagnetic signal as well[11].

While inelastic neutron scattering experiments reveal a (π, π) resonance in YBCO[3, 4, 5, 9], this feature has not been seen in LSCO. We conducted a search in optimally doped Bi2201, but did not find any evidence for a magnetic resonance peak.

In optimizing the crystal growth, it was very helpful to aim for a sample composition that resulted in the highest possible superconducting transition temperature and in very sharp transition widths. On the other hand, underdoped Bi2201 should exhibit more prominent antiferromagnetic fluctuations. While it has not been possible so far to obtain single crystals at half-filling (i.e., undoped CuO_2 sheets), we have managed to grow samples that are very underdoped and non-superconducting. We have also succeeded in growing antiferromagnetically ordered samples of Y-substituted Bi2212, $Bi_{2.06}Sr_{2.15}Y_{0.71}Cu_2O_8$. Our measurement indicates that T_N=450 K, to our knowledge the first such measurement on this system. Our goal for the near future then is to continue our search for antiferromagnetic correlations in lightly doped Bi2201 and expand the work to Bi2212 near half-filling.

References

1) M.A. Kastner, R.J. Birgeneau, G. Shirane and Y. Endoh, Rev. Mod. Phys. **70**, 897 (1998).
2) G. Aeppli *et al.*, Physica C **318**, 9 (1999).
3) H.F. Fong *et al.*, Phys. Rev. Lett. **78**,713 (1997).
4) H.F. Fong *et al.*, Phys. Rev. B **61**, 14773 (2000).
5) M. Arai *et al.*, Phys. Rev. B **83**, 608 (1999).
6) Y. Sidis *et al.*, Science **288**, 1234 (2000).
7) H. Kimura *et al.*, Phys. Rev. Lett. **59**, 6517 (1999).
8) M. Matsuda *et al.*, preprint (cond-mat/0111228).
9) P.C. Dai *et al.*, Phys. Rev. B **63**, 054525 (2001).
10) K. Yamada *et al.*, Phys. Rev. Lett. **75**, 1696 (1995).
11) private communication.

研究テーマ：電子ドープ型高温超伝導体 $Pr_{1-x}LaCe_xCuO_{4+y}$ のスピン揺動と超伝導の相関
表　題：電子ドープ型高温超伝導体 $Pr_{1-x}LaCe_xCuO_{4+y}$ のスピン揺動と超伝導の相関
1-3-11

Relationship between spin fluctuations and superconductivity in the electron-doped superconductor $Pr_{1-x}LaCe_xCuO_{4+y}$

M.FUJITA, S.KUROSHIMA, T.UEFUJI, M.MATSUDA[1], K.KAKURAI[1] and K.YAMADA

Institute for Chemical Research, Kyoto university, Uji 611-0011
[1]Advanced Science Research Center, JAERI, Tokai, Ibaraki 319-1195

Mechanism of high-T_c superconductivity mediated by spin fluctuations is one of the central topics in highly correlated electron systems. Studies of spin correlations in the hole-doped high-T_c cuprates such as $La_{2-x}Sr_xCuO_4$ (LSCO) and YBa_2CuO_{6+y} have intensively been carried out by neutron scattering experiments, and show an intimate relation between low-energy spin fluctuation and superconducting transition temperature.[1)] However, due to the difficulties in growing large single crystal, no systematic study has been done on the electron-doped system.

Quite recently, we have succeeded in growing large single crystals of $Pr_{1-x}LaCe_xCuO_4$ (PLCCO) and inducing the superconductivity after an oxygen-reducing procedure by heat treatment. Therefore, we have carried out neutron-scattering measurement using TAS-1 and TAS-2 triple-axis spectrometers in order to investigate the relation between spin correlations and the superconductivity.

Reduced x=0.11 sample shows bulk superconductivity with the onset temperature of 26K.[2)] No evidence of antiferromagnetic order was found in the superconducting sample. On the other hand, a clear magnetic Bragg peak appears below ~200K in the as-grown sample which does not show superconductivity down to 2K. These results imply that superconductivity concomitantly appears with the degradation of a magnetic ordering.

Furthermore, we observed clear commensurate spin fluctuations at the antiferromagnetic zone center of (1 0 0) (orthorhombic notation) in both as-grown and reduced x=0.12 samples (Fig. 1), analogous to the result for $Nd_{1.85}Ce_{0.15}CuO_4$.[1)] Therefore, the commensurate spin fluctuations seem to be robust with respect to electron-doping, while the incommensurability of spin fluctuations in the LSCO system dramatically change by hole-doping.[3)] Existence of spin fluctuations in both superconducting phases supports a common role of the magnetism for the high-T_c superconductivity irrespective of the carrier type, although there are different doping-symmetry in the character of spin fluctuations.

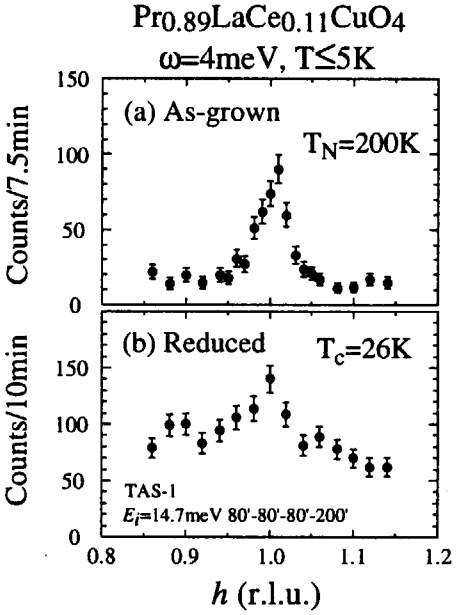


Figure 1: Constant-ω spectra at ω=4meV for (a) as-grwon and (b) oxygen-reduced $Pr_{0.89}LaCe_{0.11}CuO_4$.

References

1) K. Yamada *et al*: in preparation.
2) M. Fujita *et al*: Cond-mat/0203320.
3) K. Yamada *et al*: Phys. Rev. B. **57** (1998) 6165.

原子炉：JRR-3M　　装置：TAS-2(T2-4)　　分野：中性子散乱（超伝導）

研究テーマ :高温超伝導体におけるスピン－格子相関の研究
表題 :高温超伝導銅酸化物における電荷とスピンの自発形成
1-3-12

Charge-Spin Self-Organization in Superconducting Cuprate

T. Egami, J.-H. Chung, Y. Endoh[1], S. Tajima[2] and K. Kakurai[3]

Department of Materials Science and Engineering, University of Pennsylvania, Philadelphia, PA 19104 USA
[1]Institute for Materials Research, Tohoku University, Sendai 980-8577, Japan
[2]Superconductivity Research Laboratory, International Superconductivity Technology Center, Tokyo 135-0062, Japan
[3]Advanced Science Research Center, JAERI, Tokai, Ibaraki 319-1195, Japan

For a long time high-temperature super-conductivity (HTSC) has been thought to occur in a homogeneous crystal via a purely electronic mechanism involving spin excitations [1]. However, lately this view is being challenged by the observation of the spin-charge stripes [2] and observation of various lattice effects [3], including the possible role of phonons [4-6]. Since HTSC occurs in an antiferromagnetic Mott insulator doped with holes, from the beginning it has been a major puzzle how to reconcile the localization tendency due to spin correlation with high supercurrent mobility. A possible solution is to have electronic phase segregation [3] such as the stripe phase formation. However, the stripe phase was observed only for an insulating compounds [2] and its presence in the superconducting phase is highly controversial. In addition our recent study of phonon dispersion [4,5] suggests there are two kinds of stripe phases, one that involves the Néel antiferromagnetic state and the domain boundary dressed with holes (classical stripes) [7] and the other that has the spin-ladder spin-singlet resonant state (quantum stripes) [8,9]. Our phonon results support the latter picture.

Inelastic neutron scattering measurements were carried out with a triple-axis-spectrometer TAS-1 at JAERI-3 reactor at JAERI, Tokai. The sample was a collection of single crystals of $YBa_2Cu_3O_{6.95}$ prepared by the melt-extraction method. If dynamic doubling of the unit cell exists as suggested by the phonon measurement, we expect quasielastic scattering that peaks around $h = n + 0.5$, in the unit of the reciprocal lattice, $a^* = 2\pi/a$. Since the stripes in the adjacent CuO_2 layers are likely to be out-of-phase due to Coulomb repulsion they are likely to be seen around $l \sim 1.5$ (~ 1.9 Å^{-1}). Indeed as shown in Fig. 1 some intensity was seen at the expected $\boldsymbol{Q}$ space $\boldsymbol{Q}$ = (3.5, 0, 1.5) above T_C (= 93 K), for T = 100 and 110K. The data were taken with the energy transfer of 4 meV, and were processed to temperature averaged background and smoothed. The data summed over l = 1.2 – 2.2 are shown in Fig. 2. While the statistical fluctuation is too severe to derive definite conclusions, clearly the data at T_C are anomalous, and it appears that dynamic doubling of the unit cell in the CuO_2 plane is taking place above T_C. The results are consistent with the presence of the cell doubling phase transition at low temperatures that are terminated by the appearance of super-conductivity, a quantum-critical point

原子炉 :JRR-3M　　装置 :TAS-1 (2G)　　分野 :中性子散乱 超伝導)

(QCP) scenario pictured for the charge density waves [10].

Further research on this subject is warranted to improve statistics and confirm the temperature dependence.

References:

[1] P. W. Anderson, *Theory of Superconductivity in the High-TC Cuprates*, (Princeton University Press, Princeton, 1997).

[2] J. M. Tranquada *et al.*, *Nature* **375**, 561 (1995).

[3] T. Egami and S. J. L. Billinge, in *Physical Properties of High Temperature Superconductors V*, ed. D. Ginsberg (Singapore, World Scientific, 1996) p. 265.

[4] R. J. McQueeney, Y. Petrov, T. Egami, M. Yethiraj, G. Shirane and Y. Endoh, *Phys. Rev. Lett.* **82**, 628 (1999).

[5] T. Egami, R. J. McQueeney, Y. Petrov, M. Yethiraj, G. Shirane, and Y. Endoh, *AIP Conf. Proc.* **483**, 231 (1999).

[6] A. Lanzara *et al.*, *Nature* (*London*), **412**, 510 (2001).

[7] J. Zaanen and O. Gunnarsson, *Phys. Rev. B* **40**, 7391 (1989).

[8] D. Rokhsar and S. Kivelson, *Phys. Rev. Lett.* **61**, 2376 (1988).

[9] S. Sachdev, *Science* **288**, 475 (2000); S. Sachdev and N. Read, *Int. J. Mod. Phys. B*

[10] e.g., A. Perali *et al.*, Phys. Rev. B **54**, 16216 (1996).

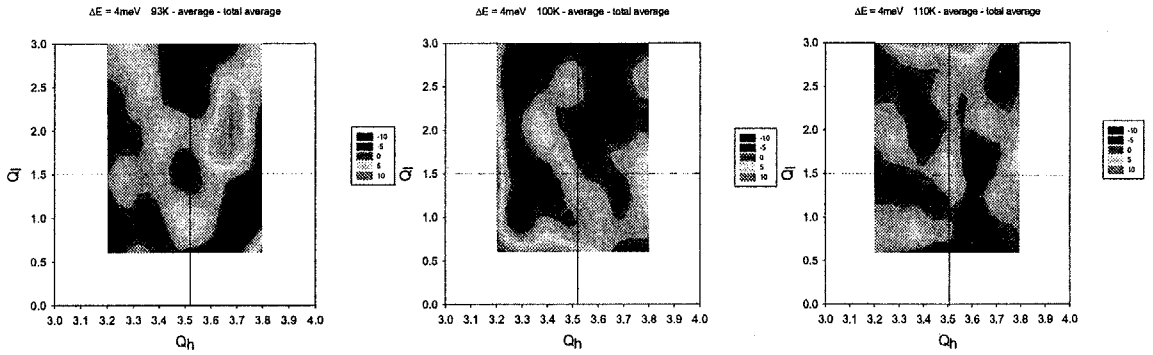


Fig. 1: Differences r.w.t. total average.

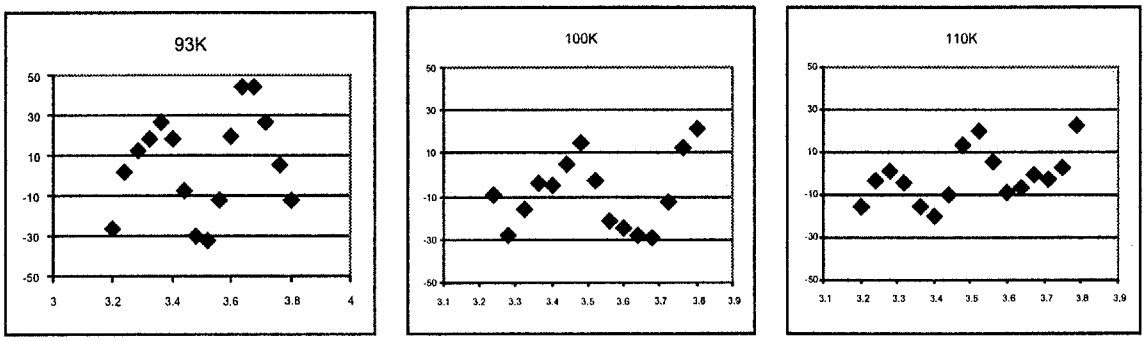


Fig.2: *h*-dependence of difference intensities integrated over *l*=1.2-2.2.

研究テーマ：高温超伝導銅酸化物における反強磁性状態スピン揺動の研究
表　題：Niドープ$La_{2-x}Sr_xCuO_4$における低エネルギー磁気揺らぎ

1-3-13

Low-Energy Spin Fluctuations in the Ni-substituted $La_{2-x}Sr_xCuO_4$

H. Hiraka, T. Chuurei[1], M. Matsuda[2], Y. Endoh, M. Fujita[1] and K. Yamada[1]

Institute for Materials Research, Tohoku University, Sendai 980-8857
[1]Institute for Chemical Research, Kyoto University, Uji 611-0011
[2]Advanced Science Research Center, JAERI, Tokai, Ibaraki 319-1195

It is widely believed that the large magnetic interaction between Cu^{2+} spins ($S = 1/2$) plays an important role for the high-T_c superconductivity in cuprates. A Ni-substitution for Cu could produce a magnetic impurity of $S = 1$ on the Cu-O_2 plane, giving rise to a moderate suppression of T_c compared to the doping of non-magnetic Zn ($S = 0$). In the recent inelastic-neutron-scattering (INS) study for a Ni-substituted optimally doped $YBa_2Cu_3O_7$, a reduction of energy scale of the resonance peak is reported. [1] Therefore, it is interesting to clarify the antiferromagnetic spin fluctuations of Ni-doped $La_{2-x}Sr_xCuO_4$ (LSCO) with respect to the energy spectrum in the wide energy range.

Single crystals of Ni-2% substituted LSCO ($x = 0.15$ and 0.17) were grown by the TSFZ method. The sample volume was about 1.5 cc each. INS experiments were performed at the triple-axis spectrometer TAS-2 installed along the thermal beam port of the guide hall. As a first step, we searched how the Ni impurities modify the low-energy spin excitation in the optimally doped LSCO with an energy gap of 6 meV. [2] Figure 1 shows the low-energy spin fluctuations of $La_{1.85}Sr_{0.15}Cu_{0.98}Ni_{0.02}O_4$ at well below T_c. No clear energy-gap behavior is seen down to 1.2 meV, though the intensity of Fig. 1(a) is not sufficient yet. Similar Q-spectra were obtained in $La_{1.83}Sr_{0.17}Cu_{0.98}Ni_{0.02}O_4$ as well. These results are in contrast with the impurity-free optimally doped LSCO (x=0.15) in which the spin excitations below 3 meV completely disappear in the superconducting state. [2] As for the gap-less behavior, it is similar to the Zn-2% substituted $La_{1.85}Sr_{0.15}CuO_4$, [3] while the ω-dependence of $\chi(\omega)''$ is intermediate between pure LSCO and Zn-doped case (not shown). The qualitative and/or quantitative difference between Ni- and Zn-impurity compounds will be clarified with progressing analyses. We are planning further high-energy experiments.

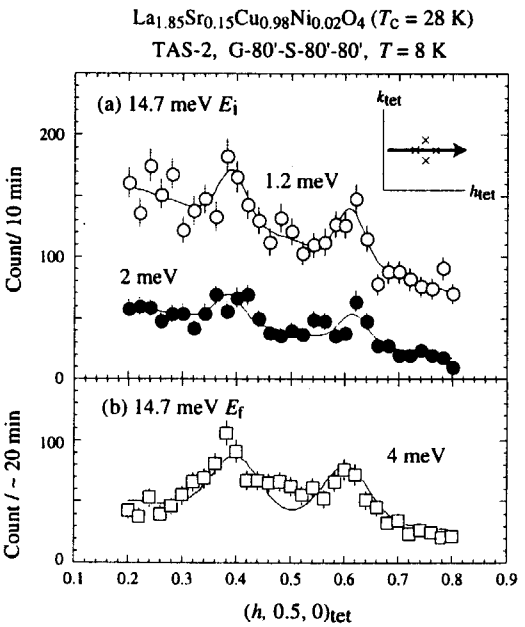


Figure 1: Low-energy incommensurate scattering of Ni-2% doped $La_{1.85}Sr_{0.15}CuO_4$ ($T_c^{onset} = 28$ K) in the superconducting state. (a) $\omega = 1.2$ and 2 meV with the E_i-fixed mode. (b) $\omega = 4$ meV with the E_f-fixed mode. The curves are drawn as a guide to the eyes. The inset shows the scan direction in reciprocal lattice space based on the high-temperature tetragonal notation.

References

1) Y. Sidis *et al.*, Phys. Rev. Lett. **84**, 5900 (2000).
2) K. Yamada *et al.*, Phys. Rev. Lett. **75**, 1626 (1995).
3) M. Kofu, Master Thesis, Tohoku University (2002).

原子炉：JRR-3M　　装置：TAS-2(T2-4)　　分野：中性子散乱（超伝導）

1. 中性子散乱 4)非晶質・液体

1. Neutron Scattering 4) Amorphous・Liquid

This is a blank page.

研究テーマ：中性子スピンエコーを用いた両親媒子膜の温度、圧力効果
表題：中性子スピンエコー法・小角散乱法を用いた両親媒子膜の曲率弾性の温度・圧力依存性の研究

1-4-1

NSE and SANS Studies on the Temperature and Pressure Dependencies of the Curvature Elasticity of Amphiphilic Membranes

Y. Kawabata[1], M. Nagao[2], H. Seto[3], T. Takeda[3] and S. Komura[4]

Graduate School of Bio-Sphere Science, Hiroshima University, [2]Faculty of Integrated Arts and Sciences, Hiroshima University, 1-7-1 Kagamiyama, Higashi-Hiroshima 739-8521, [3]Institute for Solid State Physics, The University of Tokyo, 106-1, Shirakata, Tokai, 319-1106, Department of Chemistry, Faculty of Science, Tokyo Metropolitan University, Tokyo 192-0397, Japan

In a mixture of water, *n*-decane and AOT (dioctyl sulfosuccinate sodium salt), a water-in-oil droplet microemulsion is formed at ambient temperature and pressure at oil rich region. In this system, it has been reported that a phase decomposition is induced by applying either temperature or pressure from a one-phase droplet to a two-phase coexistence of a dilute and a dense droplet phases. In order to understand this phase transition, temperature and pressure dependencies of curvature elasticity of amphiphilic membranes like the bending modulus κ should be clarified.

In this study, we investigated the static and dynamic properties of amphiphilic membranes by means of small-angle neutron scattering (SANS) and Neutron Spin Echo (NSE) in a dilute droplet system. We modified a NSE data analysis procedure proposed by Farago *et al.* [1.2], and could obtain the temperature and pressure dependencies of κ. The temperature and pressure dependencies of κ showed that the mechanisms of the temperature- induced phase transition were different from those of the pressure- induced one. This result is consistent with the previous result at dense droplet region [3].

A mixture of 5.4% vol. of AOT (99 % purity, purchased from Sigma Inc.), 4.6% vol. of D_2O (99.9 at.%-D purchased from Isotec Inc.) and 90% vol. of $C_{10}D_{22}$ (99.9 at.%-D, purchased from Isotec Inc.) was prepared. This composition leads the volume fraction of droplets being 10%.

SANS experiments were carried out at the SANS-U. Temperature was varied from 283 to 353 K with a step of about 3 K. Pressure was varied from 0.1 to 66.5 MPa with a step of about 5 MPa using a high-pressure cell. The mean radius $R_0 = \langle R \rangle$ and the polydispersity index of droplets p ($p^2 = \langle R^2 \rangle / \langle R \rangle^2 - 1$) can be deduced from the obtained SANS spectra using a model proposed by Gradzielski *et al.* [9, 10]. p = 0.16 and R_0 = 32 Å were obtained independent of pressure. With increasing temperature, R_0 decreased from 32 to 28 Å and p increased from 0.16 to 0.18.

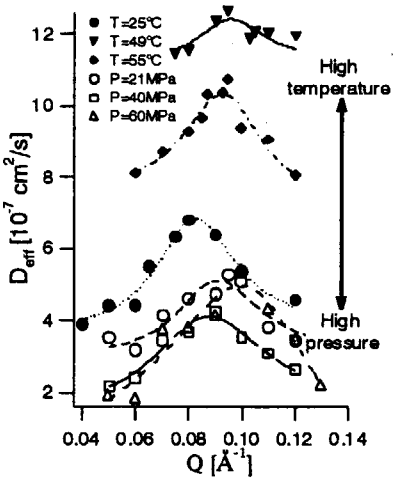


Figure 1: D_{eff} derived from NSE data at various conditions. Lines are fitting results according to the model proposed by Milner and Safran. With increasing temperature, D_{eff} became larger, while it became smaller with increasing pressure.

NSE experiments were performed at the ISSP-NSE. Temperature was varied from 283 to 308 K with a step of 5 K. Pressure was varied from 0.1 to 60 MPa with a step of about 20 MPa. A new high-pressure cell was developed using non-magnetic stainless steel and inconel.

Obtained $I(Q,t)/I(Q,0)$ was analyzed by a model proposed by Milner and Safran [4], which is taken the membrane fluctuation into account. From the fitting to $I(Q,t)/I(Q,0)$ using a single exponential decay function, we could

使用施設：JRR-3M, 装置：NSE(C2-2), SANS-U(C1-2) 分野：Amorphous & Liquid

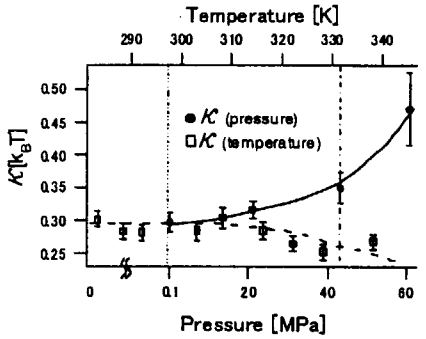


Figure 2: The temperature and pressure dependencies of κ obtained from the Eq. (1). Vertical dotted lines indicate the room temperature and pressure (dotted line) and the phase boundary (dashed line). AOT monolayers become flexible with increasing pressure, while they become rigid with increasing pressure.

obtain diffusion coefficient D_{eff}. The D_{eff} includes two decay components, λ_2 and $\cdot_{tr}$ corresponding to the membrane fluctuation and the translational diffusion of droplets, respectively. In Figure 1, Q dependencies of D_{eff} at various conditions are shown. Lines are the fitting results according to Milner and Safran's model, and λ_2 could be obtained. In order to explain the obtained parameters, we developed the expression of κ, which Farago *et al.* have proposed by using Helfrich's bending free energy [2]. In the Free energy expression, there are three key parameters, spontaneous curvature C_0, bending modulus κ and saddle-splay modulus $\bar{\kappa}$. In the Farago's procedure, some assumptions are necessary to estimate each parameter, because there are only two equations related to these three parameters. In this study, we found the expression to estimate κ without any assumptions.

$$\kappa = \frac{1}{6}\left(\frac{k_B T}{8\pi p^2} + \frac{\lambda_2 R_0^3 (23\eta' + 32\eta)}{24}\right). \qquad (1)$$

Here, η and η' are the viscosities of inside and outside of a droplet. In Figure 2, the temperature and pressure dependencies of κ are shown. It is clear that AOT monolayers become flexible with increasing temperature, while they become rigid with increasing pressure. This tendency is consistent with the result obtained by Nagao *et al.* [3] for the same system at dense droplet region.

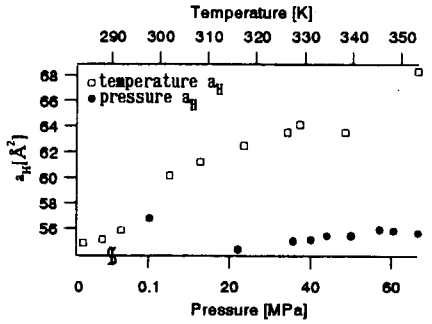


Figure 3: The temperature and pressure dependencies of head-area a_H per AOT molecule.

The temperature and pressure dependencies of the rigidity of monolayers may be interpreted by the behavior of head-area a_H of AOT molecules. We can roughly calculate the head-area a_H by dividing the surface area per drop by the number of surfactant per drop. In Figure 3, the temperature and pressure dependencies of a_H are shown. a_H increased from 52 to 64 Å^2 with increasing temperature while it kept almost constant at about 52 Å^2. This fact can be interpreted as the density of AOT molecules in monolayers decreases with increasing temperature while it increases with increasing pressure. Therefore, we can imagine the following microscopic pictures; the density of AOT molecule in membrane decreases with increasing temperature because of the head-head repulsion due to the dissociation of counterion; on the other hand, it increased with increasing pressure because of the decrease of the steric volume of tail of AOT molecules. These pictures are consistent with those obtained from another NSE experiment at dense droplet region by Nagao *et al.* [3]

References

[1].J. S. Huang, S. T. Milner, B. Farago, D. Richter, *Phys. Rev. Lett.* **59**, 2600, (1987).

[2].B. Farago, D. Richter, J. S. Huang, S. A. Safran and S. T. Milner, *Phys. Rev. Lett.* **65**, 3348, (1990).

[3].M. Nagao, H. Seto, T. Takeda, and Y. Kawabata, J. Chem. Phys. **115**, 10036, (2001).

[4].S. T. Milner and S. A. Safran, *Phys. Rev. A* **36** 4371, (1987).

1-4-2

研究テーマ：液体カルコゲン系の半導体－金属転移に伴うダイナミクス異常

表題：液体カルコゲン系の半導体－金属転移に伴うダイナミクス異常

Dynamic Anomalies Accompanied by the Semiconductor-Metal Transition in Liquid Chalcogen

M.Yao, Y.Ohmasa, H.Kohno and Y.Kawabata

Department of Physics, Graduate School of Science, Kyoto University

[1]*Department of Chemistry, Faculty of Science, Tokyo Metropolitan University*

Recently, sound attenuation measurements for fluid mercury [1] and liquid Te-Se mixtures [2] revealed that the sound attenuation coefficient α shows anomalous increase in their metal-nonmetal (M-NM) transition region. From the frequency dependence of α, their relaxation time is estimated to be of the order of nano-seconds. These anomalies may be related to the fluctuations between the metallic and non-metallic region in the liquid, and it is interesting to study the space- and time-structure of the fluctuations. Neutron spin-echo (NSE) is a powerful technique which gives information on the intermediate scattering function $I(Q,t)$. However, to our knowledge, there is no NSE measurement under such high temperature conditions.

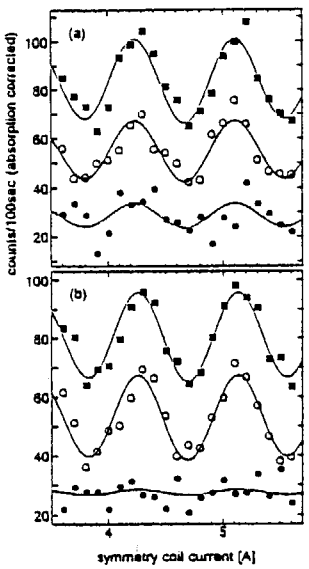


Figure 1: The absorption-corrected NSE signals from liquid Te_3Se mixture at 500C°. The momentum transfer is $Q = 0.03A^{-1}$. The solid squares, the open circles and the closed circles indicate the $I_{BG+cell+sample}$, $I_{BG+cell}$ and I_{sample}, respectively. The precession coil currents are (a) 1A and (b) 10A, which correspond to the Fourier times $t = 0.147$ and 1.47 ns, respectively.

In the present work, we developed a new electric furnace which can be used for NSE measurements up to $\sim$ 600C°. In order not to disturb the magnetic field around the sample, we used non-inductive resistance heaters. By using this furnace, we measured NSE signals for liquid Te_3Se mixture at 500C° as shown in Fig.1. Unfortunately, the scattered intensity from the sample I_{sample} is relatively small compared with the back ground intensity $I_{BG+cell}$, and the statistical error in I_{sample} is very large. However, the echo signal in I_{sample} can be recognized as shown in the Fig. 1(a). It should be noted that the echo signal I_{sample} in Fig. 1(b) (Fourier time t=1.47 ns) is strongly damped compared to I_{sample} in the Fig. 1(a) (t=0.147 ns). Fig.2 shows the intermediate scattering function $I(Q = 0.03A^{-1}, t)$ for liquid Te_3Se mixture at 500C°. From these data, the relaxation time τ is roughly estimated to be $\sim$ 0.2ns.

References

[1] H. Kohno and M. Yao, J. Phys.: Condens. Matter **11** (1999) 5399

[2] M. Yao, N. Itokawa, H. Kohno, Y. Kajihara and Y. Hiejima, J. Phys.: Condens. Matter **12** (2000) 7323

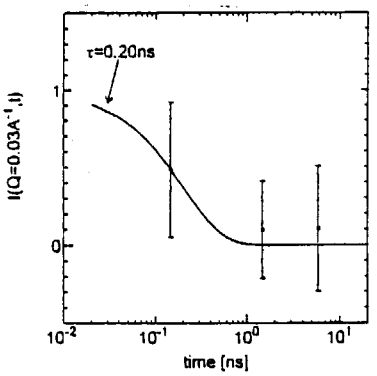


Figure 2: Intermediate scattering function $I(Q = 0.03A^{-1}, t)$ for liquid Te_3Se mixture at 500C°. The solid line indicate $\exp(-t/\tau)$ with $\tau = 0.20$ns.

使用施設：JRR-3M，装置：NSE(C2-2)，分野：4.Amorphous & Liquid

研究課題：両親媒子系複雑液体のスローダイナミックス
表題：中性子スピンエコー法によるDPPC/D_2O/$CaCl_2$系における脂質二重層膜のダイナミクスの研究

1-4-3 Neutron Spin Echo Investigations on Dynamics of Lipid Bilayers in the DPPC/D_2O/$CaCl_2$ System

T. Takeda*, Norifumi Yamada†, Y. Kawabata†, H. Seto* and M. Nagao§

*Faculty of Integrated Arts and Sciences, Hiroshima University, Higashi-Hiroshima 739-8521, Japan

†Graduate School of Bio-Sphere Science, Hiroshima University, Higashi-Hiroshima 739-8521, Japan

§Institute for Solid State Physics, University of Tokyo, Tokai, Naka Ibaraki 319-1106, Japan

In the dipalmitoylphosphatidylcholine (= DPPC)/water system, the liquid crystalline phase L_α appears above the main-transition temperature T_m (about 41°C). The result obtained from neutron spin echo (NSE) experiments on the sample with a lamellar repeat distance d_l = 54 Å could be explained by a mode with a relaxation rate determined mainly by the friction between the two layers constituting the bilayer[1]. d_l varies greatly with an addition of salt in the DPPC/water system. In order to study the dynamics further in undulation of lipid bilayers, NSE experiments were carried out on the dilute lamellar phase of the DPPC/D_2O /$CaCl_2$ system with d_l longer than 300 Å in order to avoid the effect on the single membrane dynamics from neighbouring sheets of membranes.

In small angle neutron scattering (SANS) experiments using SANS-U, we observed the peaks corresponding to d_l for lipid samples in which DPPC dispersed in D_2O solutions with 7mM $CaCl_2$ as shown in Fig. 1 though we had not observed such peaks for the samles with d_l larger than 280Å in small angle X-ray scattering (SAXS) experiments using BL15A at PF in KEK and BL40B2 at SPring8. The disappearance of diffraction peaks in SAXS reflects the X-ray form factor of an bilayer for the lamellar peak which approaches to zero because the undulation of the bilayer increases with d_l. The SANS profiles $I(Q)$ were fitted to the following equation given by Nallet et al[2] as shown in Fig. 1,

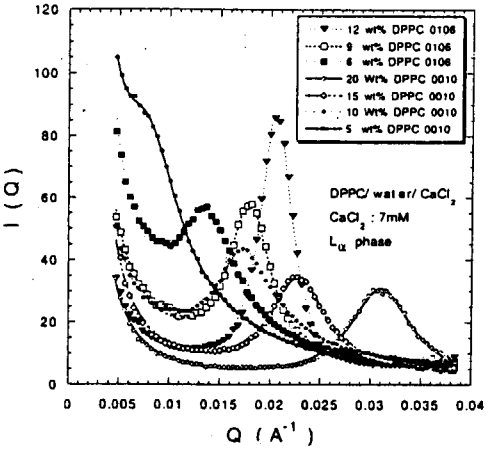


Fig. 1. SANS profiles $I(Q)$ obtained using SANS-U for DPPC/D_2O samples with 7 mM $CaCl_2$ at 52°C. The lines are fitting curves to Eq. (1).

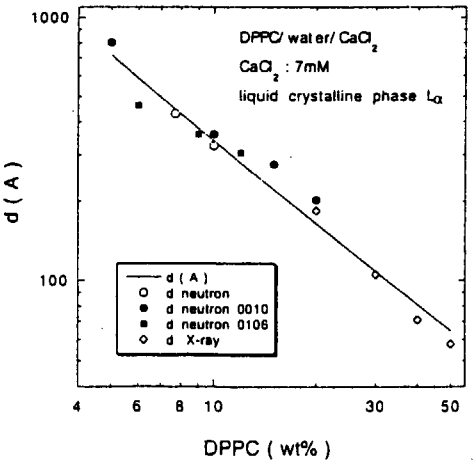


Fig. 2. DPPC cencentration dependence of the lamellar repeat distance d_l obtained from the fitting to Eq. (1). The solid line is a fitting curve to inverse proportion to DPPC concentration.

Facilities and Instruments	Research field
JRR-3M N S E (C2-2)	4. Amorphous & Liquid

$$I(Q) = I_\sigma/(Q^2\xi_\sigma^2 + 1) + I_l/(((Q - 2\pi/d_l)\xi_l)^2 + 1) + I_b \quad , \quad (1)$$

where ξ_σ and ξ_l are the correlation length of the concentration fluctuation of DPPC and the membrane, respectively. The lamellar repeat distance d_l obtained by the fitting are shown in Fig. 2. d_l is roughly in inverse proportion to DPPC concentration as shown in Fig.2.

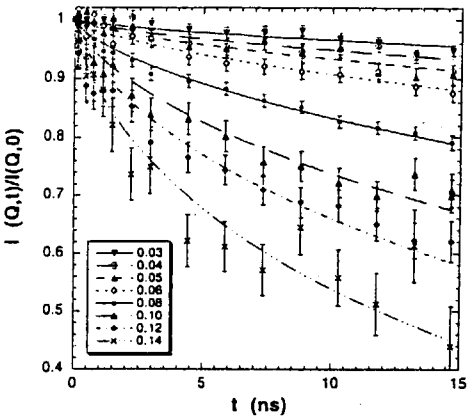


Fig. 3. Intermediate correlation functions $I(Q, t)$ obtained from the NSE experiment for a lipid sample in which 7.7 wt% DPPC dispersed in D_2O solutions with 6.8mM $CaCl_2$ at 52°C.

The scattering vector Q and time t dependent intermediate functions $I(Q,t)$ obtained from the NSE experiments using ISSP-NSE were well fitted to the following equation,

$$I(Q,t) = I(Q,0)\exp[-(\Gamma t)^{2/3}] \quad , \quad (2)$$

as shown in Fig. 3. The relaxation rates Γ obtained from the fitting to Eq.(2) increased as Q^3 over the range of Q from 0.05 Å^{-1} to 0.13 Å^{-1}[3]. So with the case of the non-ionic surfactant n-dodecyl pentaoxylethylene glycol ether ($C_{12}E_5$) /n-octane / D_2O system[4], these NSE results supported the theory presented by Zilman and Granek[5]. They considered an ensemble of membrane plaquettes at random orientations and used the Helfrich bending free energy to describe membrane undulations in sponge and lamellar phases and predicted a stretched exponential relaxation of $I(Q,t)$ as follows Eq.(2) where Γ is given by

$$\Gamma = 0.025\gamma(k_BT/\kappa)^{1/2}(k_BT/\eta)Q^3. \quad (3)$$

Here, κ is the bending modulus of the membrane and η the viscosity of the surrounding medium. Figure 4 shows an example of the temperature dependence of κ estimated in the lipid system using their theory. The values of κ seem to depend strongly on d_l though d_l is longer than 300Å.

1. W. Pfeiffer et al: Europhy. Lett. **23** (1993) 457.
2. F. Nallet et al: J. de Phys. **51** (1990) 2333.
3. T. Takeda et al: J. Phys. Soc. Jpn. **70** (2001) Suppl. A 323.
4. T.Takeda et al: J. Phys. Chem. Solids **60** (1999) 1375.
5. A. G. Zilman and R. Granek: Phys. Rev. Letters **77** (1996) 4788.

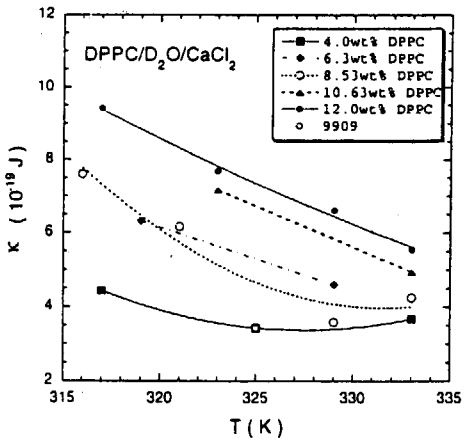


Fig. 4. The dependence of the reduced bending modulus κ of the membrane on the temperature T obtained from NSE experiments for the lipid sample in which DPPC was dispersed in D_2O solutions with 7 mM $CaCl_2$.

研究テーマ：電解質水溶液ガラスのボゾンピークと速いβ緩和
表題：ガラス形成電解質水溶液の速い緩和

1-4-4 Fast Relaxation in Glass-forming Electrolyte Aqueous Solutions

O. Yamamuro, Y. Madokoro, H. Yamasaki, and T. Matsuo

Department of Chemistry, Graduate School of Science, Osaka University, 1-1 Machikaneyama-cho, Toyonaka, Osaka 560-0043, Japan

Introduction

Some of electrolyte aqueous solutions are vitrified easily by cooling. According to previous neutron diffraction studies [1,2], the cations are strongly coordinated by water molecules and the hydrogen-bond network is partly broken by the added ions. We have studied structural and dynamical properties of these solutions by using neutron scattering technique. The purpose of the present work was to search for the evidence for the fast relaxation (sometimes called β relaxation) in aqueous solution glasses. The origin of the fast relaxation is still unknown and one of the most important problems in physics of glasses.

Experimental

The neutron scattering experiments were performed using a direct geometry chopper-type TOF spectrometer AGNES [3]. The elastic energy resolution of this spectrometer was 0.12 meV. Two solutions $LiCl{\cdot}6H_2O$ and $CaCl_2{\cdot}13H_2O$ were prepared by mixing the salts and purified water. The glassy samples were prepared by rapid cooling (2 K min^{-1}) and the crystalline sample (only for $CaCl_2{\cdot}13H_2O$) by annealing the glassy sample at ca. 200 K. The data were collected at every 20 K in the temperature range 20—300 K. The duration of each measurement was 2—4 h.

Results and Discussion

Figure 1 shows the temperature dependence of the elastic scattering intensities of $LiCl{\cdot}6H_2O$ and $CaCl_2{\cdot}13H_2O$. The elastic intensity was calculated by integrating the data with scattering angles of 89—120° (Q_{av} = 2.36 $Å^{-1}$) over energy region between –0.2 and 0.2 meV. The data of the crystalline and glassy solids lie on a straight line as expected from the Debye-Waller factor $\exp(-\langle u^2\rangle Q^2)$ of a harmonic oscillator ($\langle u^2\rangle \sim T$). In the supercooled liquids, however, excess decrease of elastic intensity was found for both samples. This is a strong evidence that the electrolyte aqueous solution glasses exhibit fast relaxation as most fragile glasses such as polymer and molecular glasses do.

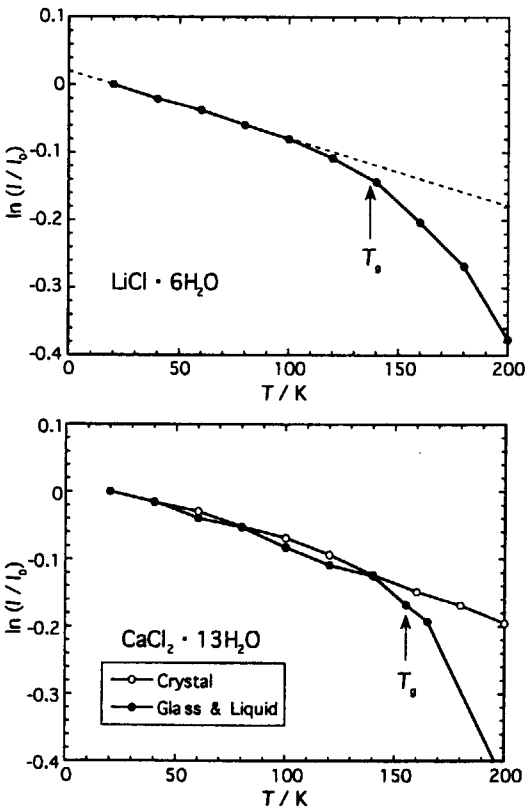


Fig. 1 The temperature dependence of the elastic scattering intensities of $LiCl{\cdot}6H_2O$ (upper) and $CaCl_2{\cdot}13H_2O$ (lower).

References

[1] S. Ansell et al., J. Phys.: Cond. Matter **9**, 8835 (1997). [2] R. H. Tromp et al., J. Chem. Phys. **96**, 8460 (1992). [3] T. Kajitani et al., Physica B **213&214**, 872 (1995).

使用施設：JRR-3M，装置：AGNES (C3-1-1)，分野：4. Amorphous & Liquid

研究テーマ：濃厚電解質水溶液ガラスのボゾンピークと中距離構造
表題：電解質水溶液ガラスの中距離秩序

1-4-5 Medium-Range Order in Electrolyte Aqueous Solution Glasses

O. Yamamuro, Y. Madokoro, H. Yamasaki, and T. Matsuo

Department of Chemistry, Graduate School of Science, Osaka University, 1-1 Machikaneyama-cho, Toyonaka, Osaka 560-0043, Japan

Introduction

The glasses of electrolyte aqueous solutions are typical hydrogen-bond network glasses. According to previous neutron diffraction studies on LiCl solutions [1,2], the cations are strongly coordinated by water molecules and the hydrogen-bond network is partly broken by the added ions. The coordination is known to be stronger as the ionic radius of cation becomes smaller. We have been studying the boson peak of solution glasses with neutron scattering and low-temperature heat capacity measurements [3,4]. We found boson peaks in LiCl, $BeCl_2$, $MgCl_2$, and $CaCl_2$ solution glasses and revealed that the boson peak intensity strongly depends on cations.

The purpose of this work is to find the relation between the boson peak intensity and the medium-range order of amorphous structure. We have measured the neutron diffraction of several electrolyte aqueous solution glasses. The use of neutron is essential since we can investigate the structure of hydrogen-bond network not overshadowed by the scattering from cations and Cl^- ions.

Experimental

The neutron diffraction experiments were performed by using HERMES diffractometer [5] belonging to Institute for Materials Research, Tohoku University. HERMES is installed at the thermal neutron guide (T1) of JRR-3M research reactor of Japan Atomic Energy Research Institute (JAERI). Incident neutrons with wave length of 1.8196 Å was selected by Ge(331) monochromater. The diffraction data were collected at scattering angles of 3—152.5°, corresponding to 0.18—6.70 $Å^{-1}$ of momentum transfer Q, with a step of 0.5°.

The sample solutions, $LiCl{\cdot}4D_2O$, $LiCl{\cdot}6D_2O$, $BeCl_2{\cdot}9D_2O$, $BeCl_2{\cdot}13D_2O$, $MgCl_2{\cdot}13D_2O$, and $CaCl_2{\cdot}13D_2O$, were prepared by mixing the corresponding salts and heavy water in appropriate mass ratios. For $MgCl_2{\cdot}13D_2O$ solution, 30 % of $BeCl_2{\cdot}13D_2O$ was added to suppress crystallization; this solution is called $MgCl_2{\cdot}13D_2O$ hereafter in this report. The liquid samples were confined in cylindrical aluminum or gold-plated copper cans (1.0 mmϕ x 60 mmH). The gold-plated can was used only for $BeCl_2$ solutions to avoid the corrosion of the can. These cans were set in a CTI cryostat. The background scattering from the cell and the cryostat was corrected by the established method.

The measurement was carried out at 275 K (liquid state) and 130 K (glassy state). The glassy samples were prepared by cooling the sample liquid with a cooling rate of ca. 3 K min^{-1}. The duration of the measurement was 6—9 h for each.

Results and Discussion

Figure 1 shows the neutron diffraction pattern of the three solution glasses at 130 K.

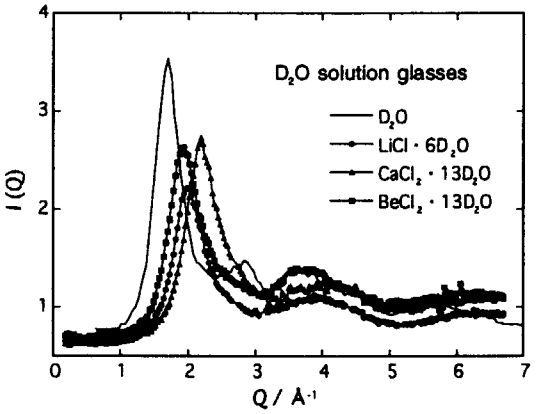


Fig. 1 Neutron diffraction pattern of the three solution glasses and amorphous ice [6].

使用施設：JRR-3M，装置：HERMES (T1-3)，分野：4. Amorphous & Liquid

The data of other solution glasses are not plotted in Fig. 1 to avoid the confusion due to data overlap. The data of vapor-deposited amorphous ice [6] was plotted together for comparison. As shown in Fig. 1, the structure of the solution glasses is much different from that of amorphous ice and also from each other.

To estimate the correlation length of disordered structure, the low-Q side data of the first sharp diffraction peak (FSDP) was fitted to the Lorentzian form

$$I(Q) = a\Delta Q / [(Q-Q_0)^2 + \Delta Q^2] + b$$

The half width ΔQ is approximately related to the correlation length R_c by

$$R_c = 2\pi / \Delta Q$$

This method is the same as that used in oxide glasses by Sokolov et al [7]. Figure 2 shows typical results of the fitting.

Figure 3 shows the relation between the correlation length thus obtained and the intensity of the boson peak determined by the heat capacity measurements [3]; the boson peak appears as a hump of C_p/T^3. T_{bp} in Fig. 3 is the peak temperature of the hump. Though the plotted data are scattered, there is a clear tendency that the solution glass with larger R_c gives larger boson peak intensity. This relation was pointed out also in oxide glasses [7]. The oxide glasses have covalent-bond networks while the solution glasses have hydrogen-bond networks. We may conclude that the boson peak intensity of the network glasses is dominated by the correlation length of disordered structures.

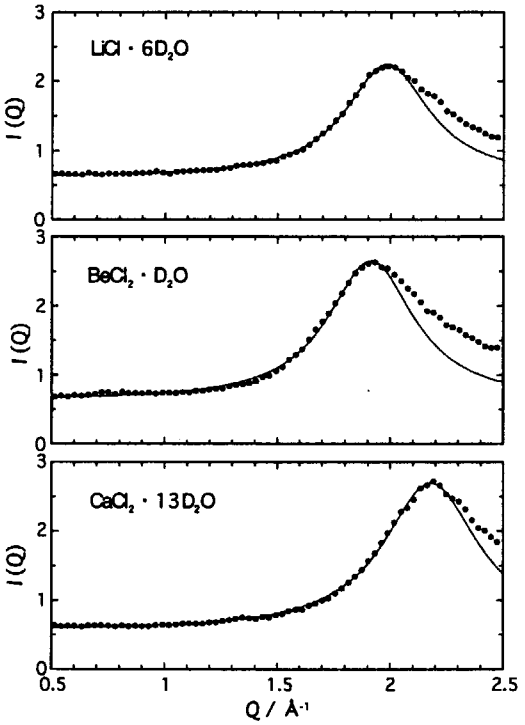


Fig. 2 Fitting of the first peak to the Lorentz function.

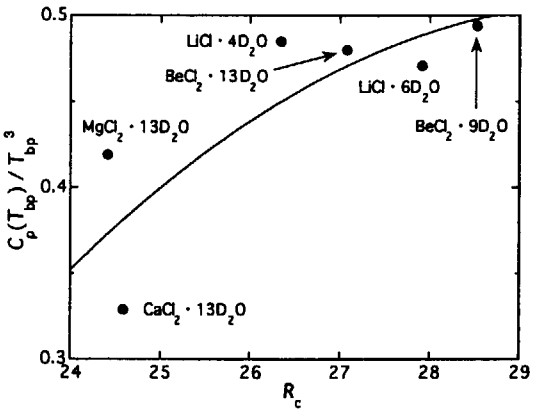


Fig. 3 Relation between the boson peak intensity and the correlation length of disordered structure in solution glasses.

References

[1] S. Ansell et al., J. Phys.: Cond. Matter **9**, 8835 (1997). [2] R. H. Tromp et al., J. Chem. Phys. **96**, 8460 (1992). [3] Y. Madokoro et al., J. Chem. Phys. **116**, 5673 (2002). [4] O. Yamamuro et al., Phisica B, **311**, 84 (2002). [5] K. Ohoyama et al., Jpn. J. Appl. Phys. **37**, 3319 (1998). [6] M. R. Chowdhury et al., J. Non-Cryst. Solids **53**, 247 (1982). [7] A. P. Sokolov et al, Phys. Rev. Lett. **69**, 1540 (1992).

研究テーマ：制限空間内における極性分子のダイナミクス
表題：中性子散乱による MCM-41 メソ孔内のメタノール分子のダイナミクスに関する研究

1-4-6
Neutron Scattering Study on Dynamics of Methanol Molecules in MCM-41

Shigeharu Kittaka,[a] Shuichi Takahara,[a] Yasushige Kuroda,[b] Toshinori Mori,[b] and Toshio Yamaguchi[c]

[a] *Department of Chemistry, Faculty of Science, Okayama University of Science, 1-1 Ridaicho, Okayama 700-0005, Japan*
[b] *Department of Chemistry, Faculty of Science, Okayama University, Tsushima, Okayama 700-8530, Japan*
[c] *Department of Chemistry, Faculty of Science, Fukuoka University, Nanakuma, Jyonan-ku, Fukuoka 814-0180, Japan*

We have investigated dynamics of partially deuterated methanol (CD_3OH) molecules confined in mesopores of MCM-41 by using quasi-elastic neutron scattering (QENS). In the present system, QENS spectra mainly consist of the contribution by hydrogen atom of hydroxyl group. It is expected that dynamics of hydroxyl and methyl groups in the methanol are revealed separately by combining present experiments with previous ones conducted for methanol (CH_3OH) confined in MCM-41.[1] MCM-41 is one of the most suitable sample to study confined liquids, since it has highly controlled cylindrical channels with very narrow pore size distribution.

Three kinds of MCM-41 (C10, C14 and C18) were prepared, whose pore diameters were 2.14, 2.84 and 3.74 nm, respectively. For the neutron scattering measurements, we prepared three kinds of samples having different amounts of adsorbate for each MCM-41. (1) Pore-filled sample: the mesopores are filled with methanol; (2) monolayer sample: the pore wall are covered with monolayer methanol molecules; (3) dry sample: there are no methanol in the pore. QENS measurements were carried out by using time-of-flight type spectrometer AGNES installed at the JRR-3M reactor of Japan Atomic Energy Research Institute. The wavelength of neutron beam was 4.22 Å, the momentum transfer (Q) range 0.68-1.87 $Å^{-1}$, and the temperature range 100-297 K.

The line widths of QENS spectra obtained decreased in the order; bulk > pore-filled > monolayer samples. This means that the motion of methanol molecules becomes slower in the above order. In the dry sample, quasi-elastic broadening was not observed. In order to discuss the effect of pore sizes on the dynamics of methanol molecules, QENS spectra were analyzed by fitting with a linear combination of delta and Lorentzian functions. The delta function component is due to immobile molecules near the pore wall. Figure 1 shows Q-dependence of the half width at half-maximum Γ of the Lorentzian functions for the pore-filled samples at 295 K. As shown in figure 1, Γ values for CD_3OH decrease rapidly at high-Q region by confinement, while those for CH_3OH decrease slowly. This signifies that the motion of hydroxyl groups in methanol molecules is strongly limited by confinement. Detailed analysis is now in progress.

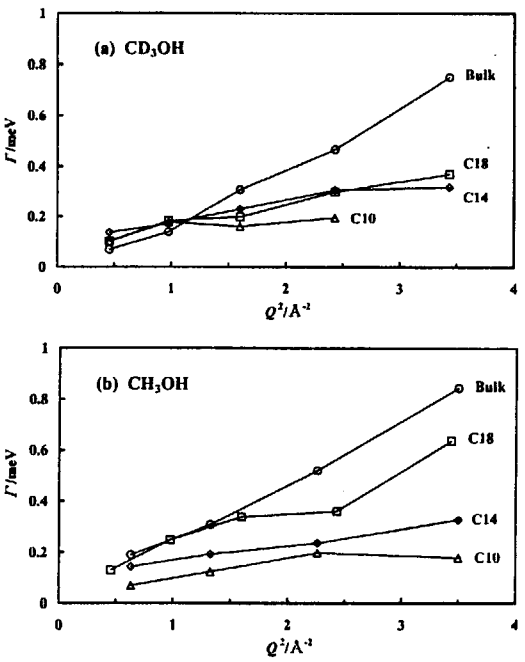


Figure 1. Q-dependence of Γ for the pore-filled samples at 295 K. (a) CD_3OH (this work), (b) CH_3OH (previous work[1]).

References

1 Kittaka, S.; Serizawa, A.; Iwashita, T.; Takahara, S.; Takenaka, T.; Kuroda, Y.; Mori, T. *Studies in Surface Science and Catalysis* **2001,** *132*, 653.

JRR-3M, AGNES(C3-1-1), 4. Amorphous & Liquid

研究テーマ：磁性流体マグネタイト微粒子ブラッグ反射によるドップラーシフト中性子スピンエコー
表題：磁性流体マグネタイト微粒子ブラッグ反射によるドップラーシフト中性子スピンエコー
1-4-7

Doppler Shift Neutron Spin Echo at Bragg Reflection of Magnetite Particle in Ferrofluid

N. ACHIWA, H.NISHIOKA, T.. EBISAWA[A], K. KAKURAI[B], and T. YAGI[B]
Department of Physics, Kyushu University, Fukuoka, 812-8581, Japan
[A]Reseach Reactor Institute, Kyoto University, Kumatori, Osaka 590-0494, Japan
[B]Neutron Scattering Laboratory, ISSP, The University of Tokyo, Tokai, Ibaraki 319-1106, Japan

§1. Introduction

Dynamics of ferrofluid have been studied by the neutron spin echo (NSE) method by Lebedev et. al.[1),2)]

We have firstly applied NSE method for the Bragg reflection of moving magnetite particle crystal in ferrofluid. Bragg reflection of moving particle brings Doppler shift of neutron velocity at scattering. The Doppler shift is caused not only by translational motion but also librational and rotational motions of the partcle crystal. NSE signal by Doppler shift at Bragg reflection directly gives the information of the velocity of moving fine crystals.

In order to study the size of clustering particles in ferrofluid, neutron small angle scattering on the same sample for NSE experiment was measured at three temperatures. There is a tendency for magnetite particles to make clusters with each other with increasing temperature above the room temperature.

§2. NSE for Doppler Shift Velocity

Doppler shift at Bragg reflection from a moving crystal with the velocity vector v is governed in the Laboratory frame by the following two equations.[3)]

$$v_1 - v_0 = \frac{\hbar\tau}{m} \tag{2.1}$$

$$\frac{mv_1^2}{2} - \frac{mv_0^2}{2} = \hbar\tau \cdot v \tag{2.2}$$

which represent the momentum and the energy conservation law. Here, v_0 and v_1 are incident and scattered neutron in the laboratory frame, τ the reciprocal vector of the Bragg reflection. The conventional single Bragg law for a crystal at rest splits into the following two laws for a moving crystal.[3)] For the incident neutron, $2d\sin\theta_0 = \lambda_0(1-f)$, $2d\sin\theta_1 = \lambda_1(1+f)$, where θ_0 and θ_1 are the angle of incidence and of reflection, λ_0 and λ_1 are the wavelengths of the incidence and the reflected neutron in the Laboratory frame, and d the interlayer spacing of the moving crystal. The factor f is defined as

$$f = \frac{2mv\cos\beta}{\hbar\tau}. \tag{2.3}$$

Here β is the angle between τ and v.

For the case of $v \ll v_0$, (also for $f \ll 1$), we estimate the Doppler shift, $\delta v = v_1 - v_0$ as follows from equation (2.2),

$$\frac{\delta v}{v_0} \sim \frac{\hbar\tau \cdot v}{mv_0^2} = (\frac{\hbar\tau}{mv_0})^2 f. \tag{2.4}$$

The shift of Bragg angle, $\delta\theta = \theta_1 - \theta_0$, is also estimated to be,

$$\frac{\delta\theta}{\theta_0} \sim 2f - \frac{\delta v}{v_0}. \tag{2.5}$$

Let us consider NSE method at Bragg reflection of a moving particle crystal. The difference of Larmor precession angle before and after scattering is given by,

$$\delta N = N_0 - N_1 = \frac{\gamma_L}{2\pi}\left[\frac{H_0 l_0}{v_0} - \frac{H_1 l_1}{v_1}\right], \tag{2.6}$$

where γ_L=2.916 kHz/Oe, N is the number of Larmor precessions, l_0 and l_1 the length of the magnetic field H, before and after the scattering, respectively. The the scattered Doppler velocity shift, δv at Bragg reflection of a moving particle crystal gives additional shift of Larmor precession.

$$\delta N = N_0 \frac{\delta v}{v_0}. \tag{2.7}$$

Then, NSE signal is given by the normalised summation of cosine functions of each δN, which is the Fourier transformation of the velocity distribution of Doppler shift.

$$P_{NSE} = P_0 cos(\delta N) =< cos(N_0 \frac{\delta v}{v_0}) > . \tag{2.8}$$

Usually NSE signal is plotted against spin echo Fourier time for inelastic scattering.[4)] For Doppler shift scattering, number of Larmor precession, N_0 is the Fourier parameter. For a fixed velocity of v, δv distributes following eq.(2.4) by all the space angles β. If the velocity of the particle crystal distributes such as Maxwellian function one should again product the Maxwellian distribution function on the cosine distribution function of β. Then, it is not so easy to get the distribution function of particle velocity directly from P_{NSE} but the velocity distribution can be estimated by simulation if we suppose some distribution function of Doppler shift velocity.

§3. Experimental

More than 90 % of water in the magnetite ferro-fluid of FW-40 Matsumoto oil Co. Ltd. Japan is replaced by heavy water by a distillation method. Neutron spin echo at Bragg reflection as well as small angle scattering

JRR-3M, PONTA(5 G) 4, Amorphous and liquid

studies were carried out on magnetite particles in the ferrofluid stabilized by ionized oleic acid in in heavy water which are dispersed in heavy water of which magnetite concentration is about 40 wt% . The particle diffraction patterns of the magnetite in ferrofluid were taken for sample thicknesses of 2 mm, 2.5 mm and 3 mm in thin aluminum containers with rectangular parallelepiped using the ISSP 5G PONTA NSE spectrometer at JRR-3M reactor of JAERI with monochromatic polarized neutron of 0.2353 nm and the velocity of 1681 m. Rather high back ground is due to the high incoherent corss-section of hydrogen in the ionized oleic acid. NSE measurements were carry out for the ferrofluid sample with the thickness of 2 mm at the Bragg peaks of (111) ($2\theta = 60.4°$) reflection of aluminum container, (311)($2\theta = 55.4°$) reflection of magnetite up to the number of Larmor precession a order of 10^3 s. In these NSE spectra, the the back ground intensity for each Bragg intensity were subtracted. The effects of depolarization in NSE polarization of (311) magnetite Bragg reflection through ferrofluid were corrected by normalizing it by the NSE polarization of the (111)aluminum reflection of the sample container.

Small angle scattering experiment on the same ferrofluid was carried out in order to check the clustering state of magnetite particles in the weak applied field of 0.001 T. using reflectometer post of MINE with a wavelength of 1.20 nm at JRR-3M reactor of JAERI.

§4. Experimental Results

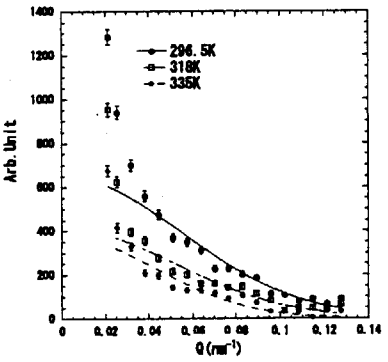


Fig. 1. Small angle scattering of the heavy water based magnetite ferrofluid at 296.5 K, 318 K, and 335 K where fitted curves are spherical radius of 28.7 nm, 30.3 nm and 36.6 nm, respectively.

In Fig. 1 small angle scattering of the heavy water based magnetite ferrofluid At 296.5 K, 318 K and 335 K were fitted with a spherical radius of small angle scattering on the same sample used for the NSE experiment. Obtained particle radius are 29 ± 5 nm, 30 ± 5 nm and 37 ± 4 nm at 296.5 K, 318 K and 335K, respectively. At smaller q region less than 0.04 nm^{-1}, deviations from the theretical curves indicate the existence of some clustered particles in the weak magnetic field of 0.001 T. Though the particle size in the ferrofluid at 296.5 K and 318 K has the similar value of 30 nm, the scattered intensity at 318 K decreases to 64 % of that at 296.5 K in the fitting, which also suggests a proceeding of clustering at 318 K.

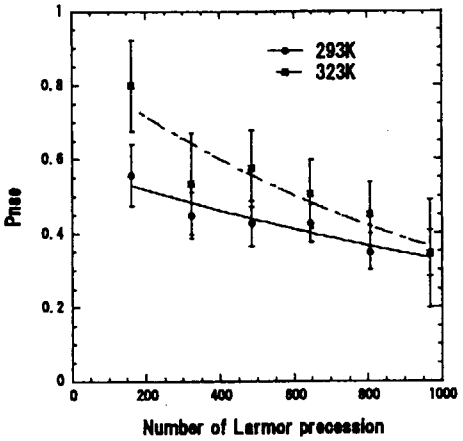


Fig. 2. NSE signals for magnetite Bragg reflection (311) in the ferrofluid at temperatures 293 K and 323 K, which are normalised by NSE signal of Al(111) Bragg reflection. Theoretical curves are fitted with a simple exponential decay function.

In Fig. 2 normalized NSE visibilities are plotted against the number of Larmor precession at three temperatures of 293 K and 323 K. The observed NSE signals at 293 K and 323 K show rather simple decay with increasing of the number of Larmor precession up to 967 turns. If we apply the Lorentzian distribution function of the Doppler shift velocity, we can estimate order of velocity from the exponential decay constant of NSE signal as a function of the precession number as shown in the theoretical curves in fig. (2). The estimated velocity distribution is 1.0 ± 0.2 m/s, 1.7 ± 0.3 m/s at 293 K and 323 K, respectively.

We estimate velocity of the surface part of a free rotating sphere of magnetite by the following equation, supposing rotational kinetic energy of the sphere is equal to $3k_BT/2$.

$$v = \sqrt{\frac{15k_BT}{2M}} \tag{4.1}$$

where k_B is the Bolzman constant, M the mass of particle. Here rotational kinetic energy of the sphere is equal to $3k_BT/2$ is used. Then the estimated velocity for the magnetite particle radius 29 nm and at 293 K is 8.4 m/sec. The observed velocity of 1 m/s which is less than that of the free Brownian motion is due to viscosity including particle particle interaction. For further interpretation of the spin echo signal, precise distribution function of particle velocity must be supposed.

1) V.T. Lebedev, Gy. Torok, Gy. Kali, L. Cser, D.N. Orlova, A.I. Sibilev, J. Magn.Magn. Mater. **201**, 133 (1999).
2) V.T. Lebedev, Gy. Torok, Gy. Kali, L. Cser, D.N. Orlova, A.I. Sibilev, J. Magn.Magn. Mater. **201**, 133 (1999).
3) B. Buras, T. Giebultowicz, Acta Cryst. **A28** 151 (1972).
4) F.Mezei, *Neutron Spin Echo* (Springer-Verlag, 1979)

研究テーマ：PMMA粒子分散系の流動構造と非線形レオロジーに及ぼす粒子間ポテンシャルの効果

表題：PMMA-co-PS粒子/水分散系の流動中性子散乱挙動とレオロジー

1-4-8 Rheo-SANS Behavior of an Aqueous Suspension of Poly(Methyl Methacrylate-co-Styrene) Particles

H. Watanabe,[1] Y. Matsumiya,[1] T. Kanaya,[1] and Y. Takahashi[2]

[1]*Institute for Chemical Research, Kyoto University, Uji, Kyoto 611-0011, JAPAN*
[2]*Department of Molecular and Material Sciences, Interdisciplinary Graduate School of Engineering Sciences, Kyushu University, Hakozaki, Fukuoka 812-8581, JAPAN*

Introduction

Recently, we examined rheology of aqueous suspensions of poly(methyl methacrylate-co-styrene) (MS) particles having partially screened surface charges [1]. The electrostatic shell due to those charges enhanced the zero-shear viscosity η_0, indicating that the shell behaved as a part of the hard-core radius in long time scales where η_0 was measured.

However, under fast shear, the MS particles exhibited no thickening characteristic to hard-core particles [1]. Thus, the electrostatic shell was argued to behave as a soft object under fast flow thereby suppressing the dynamic clustering/thickening of the particles.

In this study, a rheo-SANS experiment was conducted to confirm this argument and identify the structural origin of the thinning behavior.

Experimental

For a suspension of monodisperse MS particles in deuterated water, the rheo-SANS measurement utilizing the Couette cell was made at the SANS-U beam line at the Neutron Scattering Laboratory, Institute for Solid State Physics, University of Tokyo. The incident neutron wavelength was 0.7 nm, and the sample-to-detector distance was 4.0 m. The particles had a radius of 45 nm and the volume fraction of 0.5. The non-Newtonian viscosity η was measured at 25°C together with the SANS intensity I(q) in the velocity-vorticity plane.

Results and Discussion

As shown in Fig.1, η of the MS suspension strongly decreased with the shear rate ($\dot{\gamma}$). Correspondingly, the dependence of I(q) on the wave vector q changed with $\dot{\gamma}$. However, this change was just moderate, as demonstrated in Fig.2 where the I(q) data under the fastest shear ($\dot{\gamma}$=100 s^{-1}) are compared with the azimuthally isotropic data in the quiescent state (dotted curve): The I(q) peak under the shear just moderately shifts to a low-q side but the

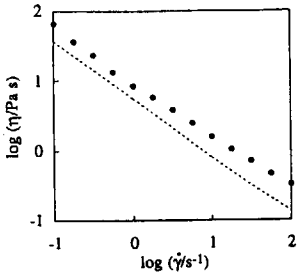


Fig.1 Steady flow behavior of the MS suspension.

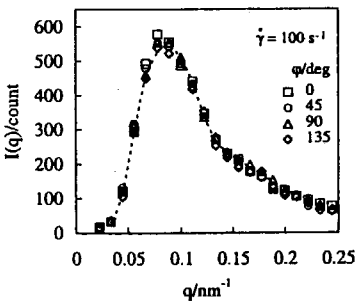


Fig.2 Rheo-SANS data at various azimuthal angles φ defined in a clock-wise direction with respect to the velocity axis. The dotted curve indicates the data in the quiescent state.

data at larger q are insensitive to $\dot{\gamma}$. This result suggests that the particles form no huge clusters under the shear (possibly due to their electrostatic repulsion) to exhibit no thickening.

The moderate peak shift reflects a weak distortion of the spatial distribution of the particles under the shear that could result in the thinning. Thus, we estimated a magnitude of distortion γ from the peak shift value and evaluated a thermodynamic viscosity η_T from this γ [2]. This η_T (dotted curve in Fig.1) was close to the η data, suggesting that the thinning reflects the weak $\dot{\gamma}$ dependence of the particle distribution.

References

[1] M. Horigome, et al., *Rheol. Acta*, in press.
[2] H. Watanabe, et al., *J. Soc. Rheol. Japan*, submitted.

使用施設：JRR-3M, 装置：SANS-U, カテゴリー：4. Amorphous & Liquid

1-4-9

研究テーマ:液体金属における電子―イオン相関
表題：高温における液体 Ge の構造因子と電子―イオン相関

Structure Factors of Liquid Ge at High Temperatures and Electron-Ion Correlation

S. Takeda, Y. Kawakita, T.Enosaki, K.Oshima, H. Aoki* and T. Masaki*

Department of Physics, Faculty of Sciences, Kyushu University 4-2-1 Ropponmatsu, Fukuoka 810-8560 Japan

** Tsukuba Space Center, National Space Development Agency of Japan 2-1-1 Sengen, Tsukuba, Ibaraki 305-8505 Japan*

There are several single-element liquids with anomalous static structures that have a shoulder near the first peak of the structure factors. Liquid Ge is one of such liquids and has attracted attention because of the semiconductor-metal transition on melting[1]. The tetrahedral unit in crystalline and amorphous phases[2] and the relatively low coordination number[3] in the liquid phase around the melting point are in contrast with simple liquid metals.

Many researchers have attempted to interpret the structure of liquid Ge as a mixture between tetrahedral units and the metallic phase, and tend to emphasize the persistence of covalent bonding even in the liquid state. On the other hand, theoretical studies have pointed out a metallic character in the bonding[4]. The ion-ion potential, which has a hard-sphere core with a positive step, reproduced the shoulder in the structure factor.[5] This suggests the existence of two characteristic lengths in liquid metals. From the viewpoint of the homogeneous metallic phase, it is suggested that the shoulder appears at $Q = 2k_F$ corresponding to the diameter of the free-electron Fermi surface, and the atomic configuration is modulated by the Friedel oscillations. There were some differences between earlier X-ray data and neutron data in the low-Q region, with regard to the height of the first peak, and the height and position of the second peak. The aim of this study is to report the exact structural data of liquid Ge by neutron diffraction to high temperature region and provide the electron-ion correlation around Ge^{4+} ion from the diffraction data.

Neutron diffraction was carried out at several temperatures (1000, 1100, 1250, 1500 and 1550°C) under atmospheric pressure of He by HERMES spectrometer system[11]. The spectra were accumulated with two initial angles of 3.0° and 3.5°. The series of solar slits at the front of the counters is suitable for reducing the scattering intensity from the background. The wavelength of neutron beam was 1.8196 Å.

The purity of Ge sample was 99.9999 wt% and the sample was inserted into the cylindrical cell made of glassy carbon. The diameter of the cell was 9.8 mm and its wall thickness was 0.2 mm. The furnace was a 1800C-Furnace constructed by A S Science Products, Ltd, and was provided by NSDA. The heater consists of two concentric cylinders made of 0.05mm thick niobium foils. The temperature of the sample was measured by a W-Re thermocouple.

The helium gas was introduced to keep the liquid sample stable in the carbon cell. Glassy carbon is known to absorb hydrogen, which considerably increases the inelasticity of the neutron scattering. The scattering intensity from the carbon cell at room temperature is compared with that at 1000°C after being normalized by the monitor counts. The observed spectrum at 1000°C does not appear to include the large inelastic contribution which tends to incline the centroid of the interference function.

The observed structure factors of liquid Ge are shown in Fig. 1. The accumulated monitor counts are 16.6×10^6, 2.0×10^6, 8.8×10^6, 16.6×10^6 and 2×10^6 at 1000, 1100, 1250, 1500 and 1550°C. Several researchers have previously measured $S(Q)$ of liquid Ge within 100°C above the melting point (~937 °C) and their structure factors also exhibit the characteristic shoulder in the high-Q region of the first peak [3,8-10]. In our data at 1000°C, the first peak is located at 2.53 $Å^{-1}$ and its peak height is about 1.42, which is consistent with the data of Bellissent-Funel and Bellissent.[8] and Alteholz and Hoyer[10], but slightly small

使用施設：JRR-3M： (HERMES) ,分野：4.Amorphous & Liquids

研究テーマ:液体金属における電子—イオン相関
表題：高温における液体 Ge の構造因子と電子—イオン相関

when compared with the data of Waseda and Suzuki[3] and Salmon[9]. The shoulder appears at around 3.3 $Å^{-1}$ in accordance with data in the literature[3, 8-10]. The second peak is located around 5.1 $Å^{-1}$, similar to the data in refs. 3, 8 and 9, but the peak height is rather low compared with the results of these studies. The temperature dependence of the structure factor is not large, but a clear tendency is evident as shown in Fig. 2. The height of the first peak decreases slightly with increasing temperature and the position moves to the high-Q side. At the highest temperature, the peak position becomes 2.60 $Å^{-1}$. The shoulder becomes inconspicuous and almost disappears at 1550°C. This temperature dependence seems to follow the prediction of the MD simulation at 2000 K [7] where the structure factor resembles that of a simple liquid metal and the first peak is located around 2.7 $Å^{-1}$.

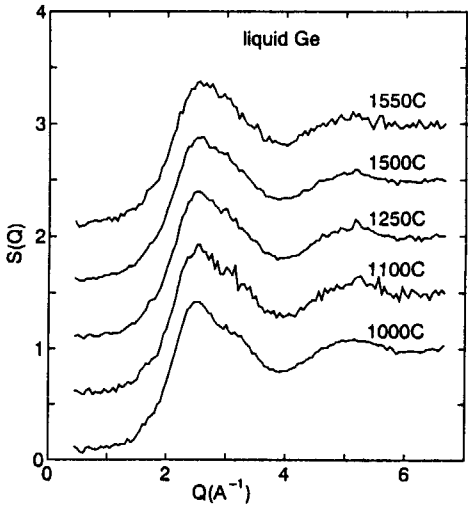


Fig. 1 Structure factors of liquid Ge at several temperatures.

The neutron diffraction data presented in this work are expected to include both the density and temperature dependences of $S(Q)$. Both the position of the principal peak and that of k_F, the Fermi momentum, are roughly proportional to $n^{1/3}$, where n denotes the density of the liquid. Given that the density decreases as the temperature increases, and taking into account the results shown in Fig. 2, we can postulate that our results are dominated by the temperature dependence of $S(Q)$.

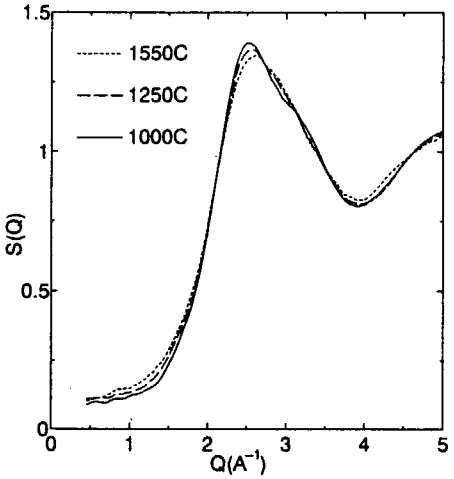


Fig. 2 Temperature dependence of the structure factors around first peak region.

References

1) V.M. Grazov , S.N. Chizhevskaya and N.N. Glagsleva: in *Liquid Semiconductors* (Plenum, New York, 1969) Chap. 3
2) G. Etherington, A. C. Wright, J. T. Wenzel, J. C. Dore, J.H. Clarke and R.N. Sinclair: J. Non-Cryst. Solids **48** (1982) 265.
3) Y. Waseda and K. Suzuki: Z. Phys. B **20** (1975) 339.
4) G. Kresse and J. Hafner: Phys. Rev. B **49** (1994) 14251.
5) M. Silbert and W. H. Young: Phys. Lett. A **58** (1976) 469.
7) R.V. Kulkarni, W.G. Aulbur and D. Stroud: Phys. Rev. B **55** (1997) 6896.
8) M.C. Bellissent-Funel and R. Bellissent: J. Non-Cryst. Solid. **65** (1984) 38.
9) P.S. Salmon: J. Phys. F: Met. Phys. **18** (1988) 2345.
10) Th. Alteholz and W. Hoyer: J. Non-Cryst. Solid. **250-252** (1999) 48.
11) K. Ohyama, T. Kanouchi, K. Nemoto, M. Ohashi, T.Kajitani and Y. Yamaguchi: Jpn. J. Appl. Phys. **37** (1998) 3319.

使用施設：JRR-3M：（HERMES）,分野：4.Amorphous & Liquids

研究テーマ：水－ブトキシエタノール混合溶液中のゆらぎ構造とダイナミクス
表題：スピンエコー法によるブトキシエタノール－水混合系のスローダイナミクス
1-4-10

Slow Dynamics of *n*-Butoxyethanol-Water Mixture by Neutron Spin Echo Technique

Koji Yoshida, Toshio Yamaguchi[1], Michihiro Nagao, and Hideki Seto
[1] Department of Chemistry, Faculty of Science, Fukuoka University, Fukuoka 814-0180, Japan
[2]Institute for Solid State Physics, University of Tokyo, Tokai 319-1106, Japan
[3]Faculty of Integrated Arts and Sciences, Hiroshima University, Higashi-hiroshima 739-8521, Japan

Introduction

It is well known that anomalies in various physicochemical properties of alcohol-water mixtures appear in a water-rich region. These anomalies become enhanced with increasing the size of hydrophobic group of alcohols and have been explained by the formation of molecular aggregates or microinhomogeneities in the mixtures. *n*-butoxyethanol-water mixtures undergo phase separation at a lower critical solution temperature (LCST) of 49 °C[1]. A small-angle neutron scattering (SANS) experiment of the mixture has revealed concentration fluctuations in the mixture at temperatures even below the LCST[2], suggesting that microinhomogeneities on a mesoscopic scale precede the macroscopic separation. The neutron spin echo (NSE) technique is a powerful tool to investigate the dynamics of systems in timescale of 0.1-100 ns in mesoscopic spatial structure of 1-100 nm, and has been widely used in the field of soft materials, such as micelles, microemulsion, and polymers. In this study, NSE measurements have been carried out to reveal the dynamics of the molecular aggregation in a *n*-butoxyethanol-water mixture, in particular, whether such an aggregation is stable like micelles or transit structure in the NSE timescale.

Experiment

An NSE spectrometer is equipped at the $C_{2\text{-}2}$ cold neutron guide port of JRR-3M, JAERI. The scattering vector Q covered was 0.01 - 0.10 $Å^{-1}$. The Fourier time was varied from 0.15 to 15 ns. The measuring time was about 8 h for each Q range at fixed temperatures. A plate of Grafoil was measured for resolution correction.

Deuterated *n*-butoxyethanol (over 98 atom%D, Aldrich), $C_6H_{13}O_2D$, whose hydroxyl part is deuterated since the hydroxyl hydrogen of the alcohol exchanges with water hydrogen, and D_2O (99.95 atom%D, CEA) were used without further purification. The sample solutions were 4 and 9 mol% *n*-butoxyethanol in D_2O and sealed in a quartz cell of 2 mm thickness. The temperature was controlled to within ±0.1 °C with a thermostat to circulate water.

Results and Discussion

The NSE method measures the energy transfer of neutrons at an extremely high energy resolution as a phase shift in the Larmor precession of each neutron spin in a magnetic field. The intermediate correlation function $I(Q,t)$ is defined by the following equation as a function of the wave vector Q and Fourier time t.

$$I(Q,t) = N^{-1}\sum_{k,l}\left\langle \exp\left(iQ\cdot r_k(t)\right)\exp\left(iQ\cdot r_l(0)\right)\right\rangle \qquad (1)$$

Here, N is the number density. The bracket means an ensemble average. In the case of neutron quasielastic scattering, $I(Q,t)$ can be obtained directly from the amplitude of the NSE signal at the spin echo condition. The $I(Q,t)$ obtained from NSE experiments was fitted to the following equation on basis of the Brownian motion,

$$I(Q,t)/I(Q,0) = \exp\left(-\Gamma t\right) \qquad (2)$$

where Γ is the relaxation rate. Figure 1 shows the Q-dependence of the relaxation rate. The diffusion

coefficient D was obtained from the following equation,

$$\Gamma = DQ^2 \quad (3)$$

The values of D have been summarized in Table 1. These values seem to reflect the motion of molecular aggregates because they are ~10^2 times smaller than those of pure water and alcohol. The apparent activation energy, E_a, of the diffusion process is obtained from temperature dependence of the diffusion constant by using the following equation.

$$D = D_0 \exp\left(-\frac{E_a}{k_B T}\right), \quad (4)$$

where D_0 is constant.

The values of E_a at x_{BE} = 0.04 and 0.09 were obtained as about 25 and 23 kJ mol^{-1},respectively, which is larger than the hydrogen bonding energy deduced from the translation of water molecule (19 kJ mol^{-1}) in pure water [3]. This implies that the hydrogen bonding is strengthened due to hydrophobic hydration in the mixtures.

At a temperature near LCST, the correlation length of concentration fluctuations obtained from the SANS increases with temperature. It has been proposed that this increase in correlation length is related to an increase in the alcohol content in a micelle-like model or to an increase in contents of both water and alcohol in a mixed aggregate model[2]. The values of D obtained from the present NSE measurements increase with increasing temperature in spite of an increase in the correlation length obtained from SANS [2]. This discrepancy cannot be explained by the Stokes-Einstein model where a stable aggregation moves independently as a micelle of surfactants. A model proposed from these results is that the molecule aggregation is preserved only for short time (about nanoseconds) characterized by the wavelength of the neutron used.

The present conclusion on the dynamics of the molecular aggregation in the *n*-butoxyethanol-water mixture should be confirmed by further NSE experiments under different pressures and compositions, which are now in progress.

1. N. Ito, T. Fujiyama, and Y. Udagawa, Bull. Chem. Soc. Jpn. **56**, 379 (1983).

2. G. D'Arrigo and J. Teixeira, J. Chem. Soc. Faraday Trans. **86**, 1503 (1990).

3. L. A. Woolf, J. Chem. Soc. Faraday I . **72**, 1267 (1976)

Table 1. Diffusion constants ($D \cdot 10^{11}$ / m^{2}s^{-1}) of BE/water mixtures

	x_{BE} = 0.04	x_{BE} = 0.09
8°C		3.3±0.8
25°C	8.3±0.4	6.6±0.3
37°C	12.2±0.5	8.5±0.3

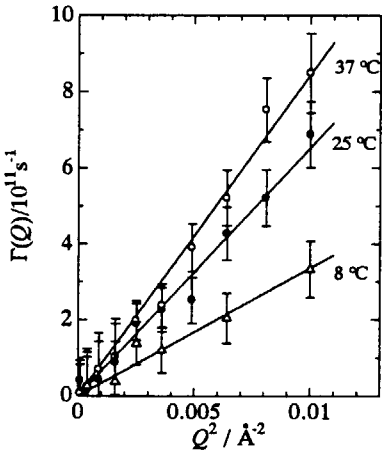


Fig. 1. Q-dependence of the relaxation rates $\Gamma(Q)$ in the *n*-butoxyethanol-water of 0.09 mole fraction at various temperatures.

1-4-11

研究テーマ：光学活性の異なるアミノ酸水溶液中における分子間水素結合構造
表題：D,L- および L-アラニン濃厚水溶液中における水素結合構造

Hydrogen-Bonded Structure in Concentrated Aqueous DL- and L-Alanine Solutions

Y. Kameda, M. Yaegashi, M. Imano, H. Naganuma, K. Mochiduki, T. Usuki and O. Uemura
Department of Material and Biological Chemistry, Faculty of Science, Yamagata University, Yamagata 990-8560, Japan

Optical activity of amino acid molecule plays an important role in various biological systems. Chemical properties of the L-amino acid and the D,L-racemic mixture (equimolar mixture of D- and L-amino acid molecules) are identical, however, the solubility for water is known to be slightly different between L- and D,L- compounds. This solubility difference becomes much enhanced when the solvent is substituted by heavy water. In fact, solubility of L-Alanine to D_2O is ca. 17% lower than that for D,L-Alanine (3 mol% D,L-Alanine in the saturated solution). This difference in the solubility may be related to the different intermolecular hydrogen bonds in the crystalline state.[1] On the other hand, no direct information has been reported on the effect of different optical activities of solute molecules to the intermolecular hydrogen-bonded structure in the aqueous solution.

In this paper, we describe results of neutron diffraction measurements on concentrated aqueous D,L- and L-Alanine solutions with different H/D isotopic ratio in order to obtain direct structural information on the intermolecular hydrogen bonds in solutions involving solute molecules with different optical activities.

D,L- and L-Alanine (natural abundance) were dissolved into D_2O and H_2O/D_2O mixtures to prepare six kinds of aqueous 2.5 mol% D,L- and L-Alanine solutions.

1) (D,L-$ND_2CH_3CHCOOD)_{0.025}(D_2O)_{0.975}$ (96.1%D)
2) (D,L-$N^0H_2CH_3CHCOO^0H)_{0.025}(^0H_2O)_{0.975}$ (35.9%D)
3) (D,L-$N^{0\text{-}2}H_2CH_3CHCOO^{0\text{-}2}H)_{0.025}(^{0\text{-}2}H_2O)_{0.975}$ (66.0%D)
4) (L-$ND_2CH_3CHCOOD)_{0.025}(D_2O)_{0.975}$ (96.1%D)
5) (L-$N^0H_2CH_3CHCOO^0H)_{0.025}(^0H_2O)_{0.975}$ (35.9%D)
6) (L-$N^{0\text{-}2}H_2CH_3CHCOO^{0\text{-}2}H)_{0.025}(^{0\text{-}2}H_2O)_{0.975}$ (66.0%D)

The sample solutions was sealed into a cylindrical quartz cell with 11.8 mm in inner diameter and 1.1 mm in thickness. Neutron diffraction measurements were carried out on the ISSP 4G diffractometer installed at the JRR-3M research reactor, JAERI. The incident neutron wavelength of λ = 1.096 ± 0.003 Å was employed. Scattered neutrons were collected over the angular range of $3 \leq 2\theta \leq 115°$, corresponding to $0.30 \leq Q \leq 9.67$ Å^{-1}. Measurements of scattering intensities were made in advance for a vanadium rod, an empty cell and a background. After corrections for background and absorption, observed neutron count rates were converted to the normalized scattering cross section.

Observed scattering cross sections for the six aqueous 2.5 mol% Alanine solutions are shown in Fig. 1. Although cross sections for the D,L- and L-Alanine solutions with the same H/D isotopic ratio seem very similar, a systematic difference in the lower-Q region can be observed between the D,L- and L-Alanine solutions with the highest D content.

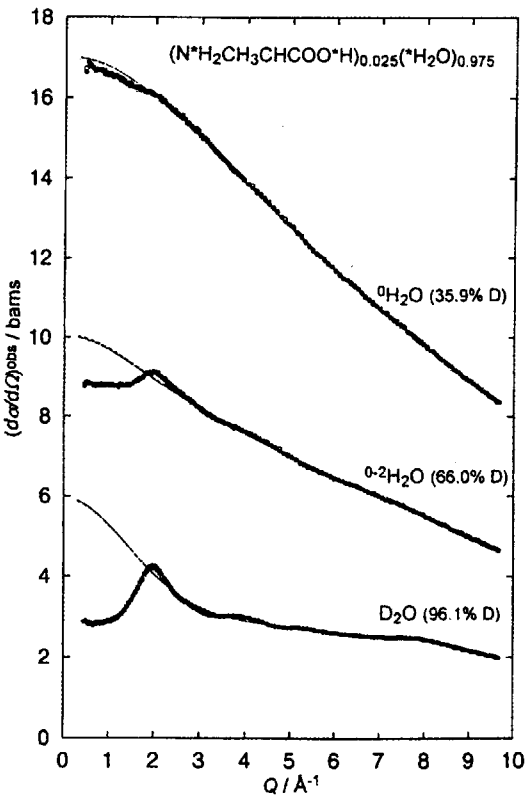


Fig. 1 Scattering cross sections observed for aqueous 2.5 mol% D,L- (●) and L-Alanine (○) solutions. The sum of contributions from the self scattering and in-

The difference in cross sections, $\delta(Q)$ (= [D,L-Alanine solution] - [L-Alanine solution]) are indicated in Fig. 2. Experimental data points are somewhat scattered due to the statistical uncertainties, however, no significant difference in the scattering cross sections for D,L- and L-Alanine solutions can be observed for the $^{0}H_2O$ (35.9 % D) and $^{0\text{-}2}H_2O$ (66.0 % D) solutions within experimental errors. On the other hand, the residual structure is evident in the D_2O (96.1 % D) solutions in which larger difference in the solution structure is expected from the solubility data as mentioned above.

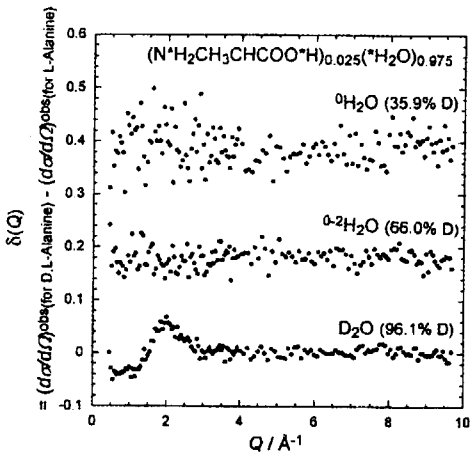


Fig. 2 Observed difference function between scattering cross sections for aqueous 2.5 mol% D,L- and L-Alanine solutions with different D content.

Observed scattering cross sections in Fig. 1 were carefully re-normalized[2] by applying the least squares fitting analysis of the intramolecular interference terms of Alanine and water molecules in the range of $3.0 \leq Q \leq 9.6$ Å^{-1}. The re-normalized difference function, $\Delta i(Q)$, for the D_2O solutions (Fig. 3a) was then Fourier transformed to obtain the difference distribution function $\Delta g(r)$ (Fig. 3b). The structural feature appearing around $r = 2$ Å is identified, which implies that the difference in the intermolecular structure between D,L- and L-Alanine solutions is present at this radial distance.

Figure 4 represents partial distribution functions, $g_{HH}(r)$, $g_{XH}(r)$ and $g_{XX}(r)$ (X: N, O, C) observed for the aqueous 2.5 mol% L-Alanine solution. These distribution functions were obtained by the Fourier transform of partial structure factors, which were derived from a combined analysis of observed intermolecular interference terms. A well defined

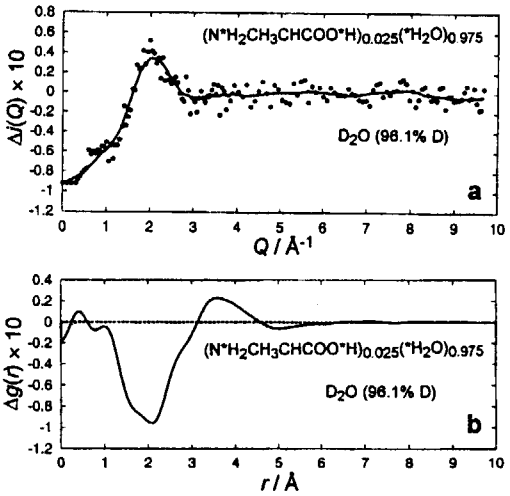


Fig. 3 a) Fully corrected difference function, $\Delta i(Q)$, observed for 2.5 mol% Alanine-D_2O solutions. b) Difference distribution function, $\Delta g(r)$.

first peak at $r = 2$ Å in the present $g_{XH}(r)$ function is attributable to the hydrogen-bonded O···H(D) interaction among solvent water molecules. The position of this intermolecular O···H(D) peak corresponds well to the negative peak observed in the $\Delta g(r)$ function shown in Fig. 3b. The negative intensity of the peak in $\Delta g(r)$ implies that the hydrogen-bonded structure is more pronounced in the L-Alanine solution, which may be consistent with the lower solubility of the L-Alanine molecule.

Further data analysis involving the least squares refinement of the observed partial structure factor is now in progress.

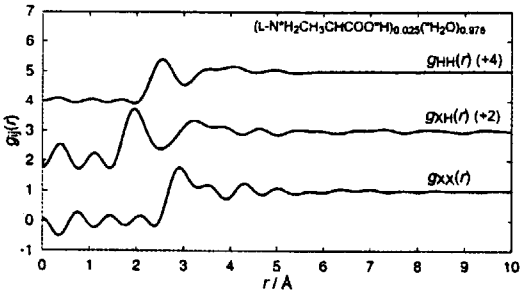


Fig. 4 Partial distribution functions, $g_{HH}(r)$, $g_{XH}(r)$ and $g_{XX}(r)$ (X: O, N, C), observed for the aqueous 2.5 mol% L-Alanine solution.

References

1) H. J. Simpson, JR and R. E. Marsh, *Acta Cryst.*, **20**, 550 (1966).
2) Y. Kameda, T. Usuki and O. Uemura, *Bull. Chem. Soc. Jpn.*, **71**, 1305 (1998).

研究テーマ：超臨界・亜臨界条件における水と水溶液の拡散ダイナミクス
表題：水熱条件下における水と水溶液の拡散ダイナミクス

1-4-12 Diffusion Dynamics of Water and Aqueous Solutions at Hydrothermal Conditions

Nobuyuki Matubayasi[1], Yasuharu Nagai[1], Hideyuki Munemura[2], Masakatsu Misawa[2], and Masaru Nakahara[1]

[1] *Institute for Chemical Research, Kyoto University*

[2] *Faculty of Science, Niigata University*

Super- and subcritical water receives much attention recently as an environmentally benign solvent to often induce a chemical reaction at noncatalytic conditions. In order to understand and control the chemical reaction in this unique solvent, it is essential to elucidate the molecular motion of water and aqueous solutions at super- and subcritical conditions. In general, a chemical reaction proceeds first through the encounters of the reacting molecules. Therefore, since water acts not only as a medium but also as a reactant in the hydrothermal regime, it is of primary interest to characterize the diffusion dynamics of water. In this study, we determine the diffusion constant of high-temperature and high-pressure water at its neat and solution states by means of the quasielastic neutron scattering. Since super- and subcritical water is a good solvent for organic compounds, we employ the aqueous solution of benzene to assess the motional behavior of water at the solution state.

The samples prepared were H_2O, C_6H_6, and their mixture with the benzene mole fraction of 0.05. Pure benzene was also examined to compare the diffusion behaviors of water and organic solvents at high-temperature conditions. All the samples were sealed in quartz capillaries at packing fractions of 60%. The experimental temperature was 290 °C. At this temperature, the pressure is around 10 MPa. The quasielastic neutron scattering measurements were performed using the AGNES facility. The spectra were fit to the Lorentzian form at each momentum transfer Q.

The quasielastic linewidth Γ is shown in Fig. 1 as a function of Q^2. From the jump diffusion model, the diffusion constant was found to be 9.6, 5.3, and 6.5×10^{-4} cm^2/s for neat H_2O, neat C_6H_6, and H_2O in the mixture, respectively. These values are one order of magnitude larger than the typical value of the diffusion constant at ambient conditions. When neat H_2O and C_6H_6 are compared, the ratio of the diffusion constant is similar to the ratio of the viscosity. Since H_2O is smaller in molecular size, this means the breakdown of the hydrodynamic law and shows the apparent expansion of the water molecule due to the hydrogen bonding. When neat H_2O is compared to the mixture, the diffusion constant is observed to become smaller when 5% of benzene is added. This is related to the weakening of the hydrogen bonding of water upon addition of the nonpolar compound. Actually, the proton chemical shift of H_2O was found, as a consistent and complementary observation, to shift upfield upon addition of benzene.

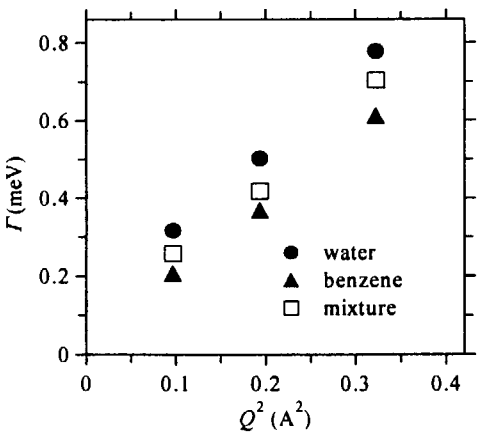


Fig. 1. The quasielastic linewidth Γ as a function of the momentum transfer Q.

使用施設：JRR-3M, 装置：AGNES(C3-1-1), 分野：4. Amorphous & Liquid

1-4-13

研究テーマ：液体ヒ素－テルル混合系における中性子小角散乱
表題：液体ヒ素－テルル混合系の半導体-金属転移領域における小角散乱
Small Angle Scattering of Liquid As-Te Mixtures around Semiconductor-Metal Transition

K. Maruyama, and T. Miyanaga[1]

Faculty of Science, Niigata University, Niigata 950-2181, Japan
[1]*Faculty of Science and Technology, Hirosaki University, Hirosaki 036-8660, Japan*

Liquid As-Te mixtures show the semiconductor to metal transition with increasing temperature. Recent EXAFS[1] and neutron diffraction[2] studies reveals that the network structure of threefold coordinated As and twofold coordinated Te atoms is transformed into the twofold chain structure in the high temperature (metallic) region. In this region, the occurrence of the fluctuation of the interchain correlation is expected. Hence the structural investigation over the scale of over ten ångstroms is important. In order to study this structural change, we have performed the neutron small angle scattering measurements for liquid $As_{20}Te_{80}$ and $As_{30}Te_{70}$ by using SANS-U spectrometer equipped at JRR-3M in JAERI Tokai.

The samples were sealed in the standard silica cell of 5mm thick. The camera distance was set to be 4m. The scattering intensity was accumulated for about six hours for each sample and each temperature. The scattering intensity from the mixtures was very weak and the intensity from silica cell dominates the data in low Q region ($Q < 0.01\text{Å}^{-1}$). Hence we can use the data only over the Q range, $0.01 < Q < 0.1\text{Å}^{-1}$. Figure 1 shows the $I(Q)$ for liquid $As_{20}Te_{80}$ at 400, 450, 500 and 550 °C. The $I(Q)$ increases slightly with decreasing the Q value and becomes nearly constant at $Q \sim 0.03\text{Å}^{-1}$, which suggests that the density or concentration fluctuation of the 100Å scale. The $I(Q)$ increases with increasing temperature. Hence the structure has certain temperature dependence. Figure 2 shows the $I(Q)$ for liquid $As_{30}Te_{70}$ at 400 and 500 °C. The weak scattering intensity seems to arise from the silica cell. So scattering from this sample could not be observed.

By other measurements, some structure in $I(Q)$ was observed in larger Q region ($Q \sim 0.5\text{Å}^{-1}$). Hence we will continue the study on the large scale structure by using other diffractometer.

[1]H. Endo., *et al.*, J. Phys.: Condens. Matter, **12** (2000) 6077.
[2]K. Maruyama, *et al.*, J. Non-Cryst. Solids in print.

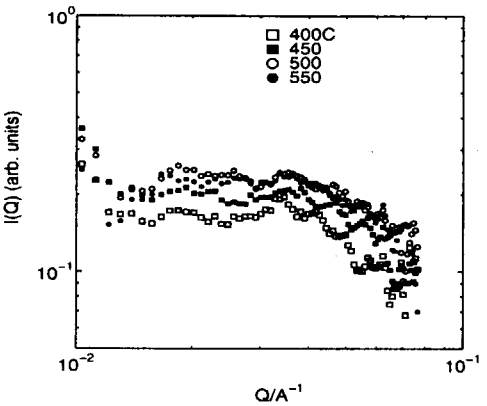


Fig. 1. The $I(Q)$ for liquid $As_{20}Te_{80}$ at 400, 450, 500 and 550 °C.

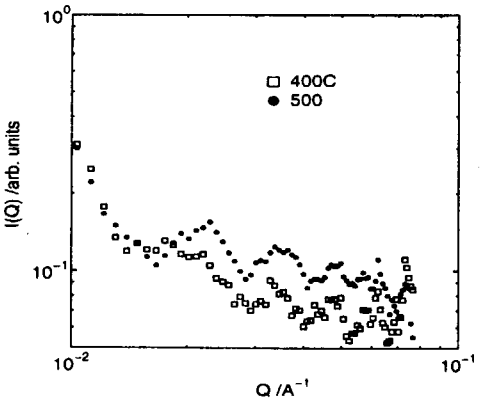


Fig. 2. The $I(Q)$ for liquid $As_{30}Te_{70}$ at 400 and 500 °C.

使用施設：JRR3M、装置：SANS-U(C1-2)、分野：4. Amorphous & Liquid

1-4-14

研究テーマ：液体ヒ素－テルル混合系のネットワーク構造変化

表題：液体ヒ素－テルル混合系の半導体–金属転移領域における構造変化

Structural Changes in Liquid As-Te Mixtures around Semiconductor-Metal Transition

K. Maruyama, T. Shibuya, Y. Kawakita[1]

Faculty of Science, Niigata University, Niigata 950-2181, Japan

[1]Faculty of Science, Kyushu University, Ropponmatsu, Fukuoka 810-8560, Japan

Liquid As-Te mixtures show the semiconductor to metal transition with increasing temperature. Recent EXAFS[1] and neutron diffraction[2] studies reveals that the network structure of threefold coordinated As and twofold coordinated Te atoms is transformed into the twofold chain structure in the high temperature (metallic) region. In this region, the occurrence of the fluctuation of the interchain correlation is expected. Hence the structural investigation over the scale of about ten ångstroms is important. In order to study this structural change, we have performed the neutron scattering measurements for liquid $As_{10}Te_{90}$, $As_{20}Te_{80}$ and $As_{30}Te_{70}$ by using HERMES spectrometer equipped at JRR-3M in JAERI Tokai.

The measurements have been performed with the usual procedure. The scattering intensity was accumulated for about ten hours for each sample and each temperature. After the correction of absorption, scattering from the silica cell and multiple scattering and after the normalization of the efficient of detectors, the structure factor $S(Q)$ for liquid As–Te mixtures was derived as shown in Fig. 1. The obtained $S(Q)$ has enough accuracy for investigation especially in low Q region ($Q < 4\text{Å}^{-1}$).

The obtained $S(Q)$ is nearly the same to that from HIT-II over the middle and high Q region. It is notable that a small but clear prepeak at about Q =1.5Å^{-1} appears in the $S(Q)$. The prepeak is clearer for $As_{20}Te_{80}$ than that for $As_{10}Te_{90}$. For $As_{30}Te_{70}$, the position of the prepeak shifts toward low Q area. And the decrease of peak strength was observed both for $As_{20}Te_{80}$ and $As_{30}Te_{70}$ with increasing temperature. The appearance of the prepeak and its behavior is consistent with the model of structure change[1]. It is notable that at higher temperature another prepeak appears in very low Q region ($Q \sim 0.5\text{Å}^{-1}$), which suggests the creation of the large scale fluctuation caused by the structural transition. As the result, the HERMES spectrometer is very useful for the structural study of the liquid having intermediate range correlation.

In order to investigate the relation between the metal-non metal transition and the structural change, the neutron scattering measurements for the sample of eutectic composition and over the wide temperature range is planned.

[1]H. Endo., *et al.*, J. Phys.: Condens. Matter, **12** (2000) 6077.

[2]K. Maruyama, *et al.*, J. Non-Cryst. Solids in print.

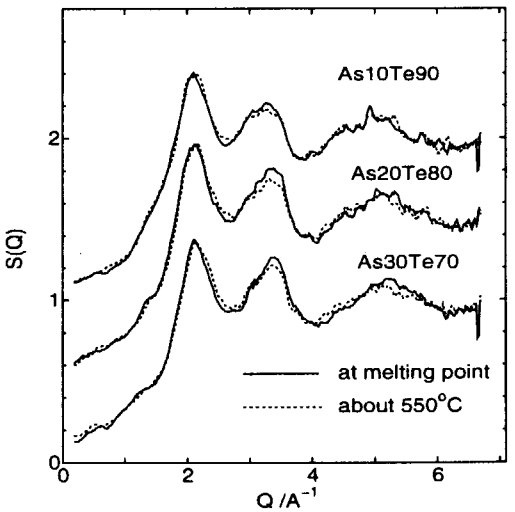


Fig. 1. The structure factor $S(Q)$ for liquid $As_{10}Te_{90}$, $As_{20}Te_{80}$ and $As_{30}Te_{70}$ at just above the melting point (solid lines) and at about 550 °C (dotted lines).

使用施設：JRR3M、装置：HERMES(T1-3)、分野：4. Amorphous & Liquid

研究テーマ：超イオン導電体における構造不規則性と動的性質
表　題：AgI-Ag_2O-V_2O_5 ガラスにおける FSDP の起源

1-4-15

The Origin of FSDP in AgI-Ag_2O-V_2O_5 Glasses

H. TAKAHASHI, N. RIKITAKE, T. SAKUMA[1] and Y. ISHII[2]

Faculty of Engineering, Ibaraki University, Hitachi 316-8511
[1]Faculty of Science, Ibaraki University, Mito, 310-8512
[2]Advanced Science Research Center, JAERI, Tokai, Ibaraki 319-1195

The superionic conducting glasses have high ionic conductivity at ambient temperature. The investigation on the structural features is very important for understanding of the conduction mechanism of the superionic conducting glasses. It is worth noting that the most of the superionic conducting glasses show prepeak in low Q region, that is called FSDP. The origin of the FSDP of superionic conducting glasses is considered to be due to the density fluctuation of glass network. In the previous study, new FSDP was observed in 10AgI-3Ag_2O-2V_2O_5 glass from the elastic neutron scattering experiment[1)] in contrast to the total neutron scattering experiment. In the present study, the elastic neutron scattering experiments were performed for the glasses having different AgI concentration in order to confirm the origin of FSDP in the superionic conducting glasses.

The measurements were performed on the triple-axis spectrometer TAS-2 at JRR-3. The incident neutron wavelength of 0.245 nm is employed. The elastic neutron scattering intensity $I(Q, \omega = 0)$ was recorded in the range $1 \leq Q \leq 45$ nm^{-1} at room temperature. Powdered glass sample filled into a cylindrical vanadium container of 10 mm diameter was used for neutron diffraction.

The elastic scattering intensities for several AgI concentration at room temperature are shown in Fig.1. Only 10AgI-3Ag_2O-2V_2O_5 glass has FSDP at around 4 nm^{-1}. The FSDP is formed by the addition of high concentration of AgI into 3Ag_2O-2V_2O_5 host glass. It is considered that the origin of FSDP is due to the medium range Ag-Ag, Ag-I and/or I-I correlation. The existence of medium range interionic correlation suggests the formation of ordered microdomain, such as AgI cluster. However, AgI microdomain does not increase linearly with AgI concentration based on the composition change of FSDP. The threshold of microdomain formation seems to lie on the 30 to 50 mol% of AgI from the limited data. The investigations on the detailed composition change of FSDP and the contribution of low energy inelastic scattering to FSDP are necessary for the elucidation of the dynamical structure of AgI microdomain.

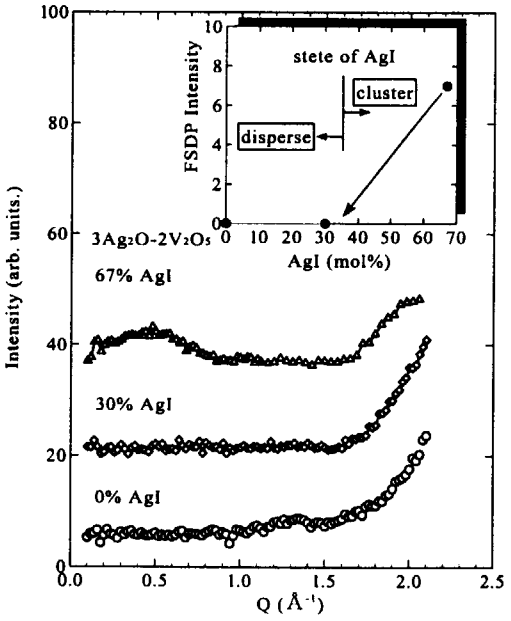


Figure 1: Elastic neutron scattering in low Q range for several AgI concentration of silver vanadate glasses.

References

1) H. Takahashi, N. Rikitake, T. Sakuma and Y. Ishii : JAERI-Review (2002) 82.

原子炉：JRR-3M　　装置：TAS-2(T2-4)　　分野：中性子散乱（液体・不規則物質）

1. 中性子散乱 5)高分子

1. Neutron Scattering 5) Polymer

This is a blank page.

研究テーマ：液晶-高分子混合系における Depletion 効果による秩序形成
表題：多糖分子が誘起する TMV 粒子の結晶化

1-5-1 Polysaccharides Induced Crystallization of TMV Particles

M.Imai[1], N. Uralami[2] and K. Nakaya[1]

1 *Department of Physics, Ochanomizu University, Bunkyo, Tokyo 112-0012, Japan*
2 *Department of Physics, Biology and Informatics, Yamaguchi University, Yoshida, Yamaguchi 753-8512, Japan*

Addition of polymers into colloidal rod system induces an aggregation of rod particles. The effective attractive interaction between the rod particles are explained by simple entropic interaction, so-called depletion.

Recently it is found that chondroitin sulfate (Chs) a kind of polysaccharides induces the aggregation of tobacco mosaic virus (TMV) at very low concentration. The TMV concentration where TMV starts to aggregate for Chs addition is about 1/1000 compared with that for PEO addition, or theoretical prediction based on the depletion interaction. The purpose of this study is to elucidate this enhancement of the depletion interaction induced by the polysaccharides. Especially, we focus our attention on the effect of electrostatic interaction on the inter-TMV distance.

The SANS profiles for the TMV and Chs mixture as a function of Chs concentration ρ_{Chs} is shown in Fig. 1. In the low Chs concentration region (<1.0 mg/ml), the scattering profiles shows monotonic curves, indicating that no regular ordered structure is appeared in the suspension. At ρ_{Chs} = 1.0 mg/ml, a Bragg peak suddenly appears at q=0.014 Å^{-1}, indicating formation of the raft-like aggregates. The repeat distance of the raft-like aggregates is 45 nm which is about 2.5 times larger than the bare diameter of the TMV particle. The peak position is shifted to the higher q side as increasing ρ_{Chs} and obeys a power law of $\rho_{Chs}^{1/4}$ as shown in Fig. 2. In order to explain this behavior, we assume that the total inter-TMV interaction is expressed by sum of the electrostatic interaction (DLVO theory) and the depletion interaction. The obtained peak position as a function of ρ_{Chs} is shown in Fig. 2 with solid line. The theoretical calculation well describes the ρ_{Chs} dependence of the peak position, although the theoretical values are somewhat shifted to the higher q side. Thus the observed experimental results are well explained by the depletion and electrostatic interactions.

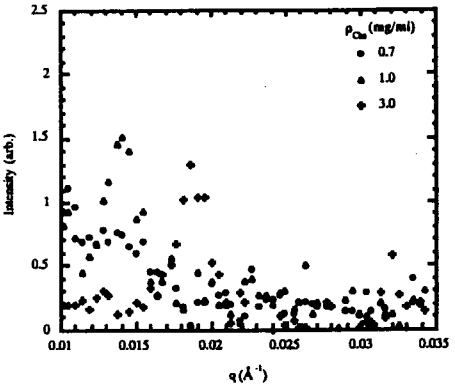


Fig. 1 SANS profiles for the TMV and Chs mixture as a function of ρ_{Chs}.

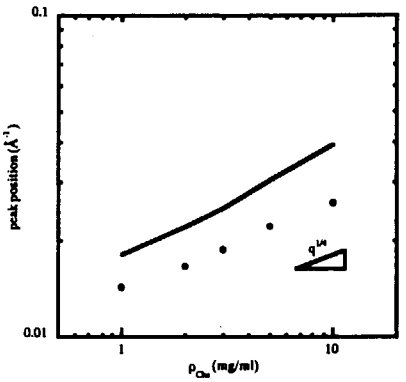


Fig. 2 Relationship between Bragg peak position and ρ_{Chs} observed in TMV and Chs Mixture. Solid line indicates theoretical prediction.

使用施設：JRR-3M, 装置：SANS-U, 分野： Polymer

研究テーマ：トリグリセリドの準安定相におけるグリセロール骨格の構造解析
表題：トリグリセリドの準安定相の構造解析

1-5-2 Structural Analysis of Metastable Phases of Triacylglycerols

Fumitoshi Kaneko and Tatsuya Kawaguchi
Osaka University, Graduate School of Science

Triacylglycerols (TAGs) are main components of natural fats and oils and widely used as raw materials for industrial products. One of the important characteristics of TAGs is polymorphism. In addition to the stable phase, many metastable phases appear by changing crystallization conditions.

Although the metastable states are more significant than the stable state from scientific and industrial point of views, our knowledge of their structures is still deficient, because these phases contain various kinds of disorders and X-ray diffraction method is not so effective for such highly disordered states. In this study, we tried to deduce structural information about the α and sub-α phases using selectively deuterated specimens (d^5-tristearin $[C_3D_5(O_2C(CH)_{16}CH_3)]$).

Fig. 1 shows the powder diagrams of tristearin in β, α, and sub-α phases measured with HERMES. In the ordered phase β, the second-order reflections due to subcell structure around 3.0 $Å^{-1}$ are observed as sharp and intense peaks as well as the first-order reflections around 1.5 $Å^{-1}$. The relative intensity of the second-order reflections is markedly strong compared with that in X-ray diffraction, which makes it possible to deduce the information about the nature of disorder in lateral direction and the dynamical properties for hydrocarbon segments.

The second order reflections in the metastable states α(at 283K) are almost smeared. Since the acyl chains in α are packed in a loose hexagonal subcell, the significant intensity decrease can be ascribed to the effect of activated molecular motions on the Debye-Waller factor.

The sub-α phase transformed from α by cooling exhibits the (200) and (110) reflections of the pseudohexagonal subcell around 1.5 $Å^{-1}$ (Fig. 2) and shows a significantly broadened profile in the second-order reflection region. It is suggested that hydrocarbon chains make the $O_\perp$ like lateral packing with neighboring chains but the structural correlation decreases rapidly with distance.

In the region of $q < 0.5$ $Å^{-1}$ shown in Fig. 2, three intense reflections due to long spacings, (002), (003) and (004) reflections, are observed in the α phase. The deuteration of glycerol backbone results in the significant intesity increase in the (002) and (004) reflections. On the transition from α to sub-α, the intensity of the (004) reflection decreases, which suggests that the subcell structural change induces a small shift of glycerol backbones towards the lamellar interfaces.

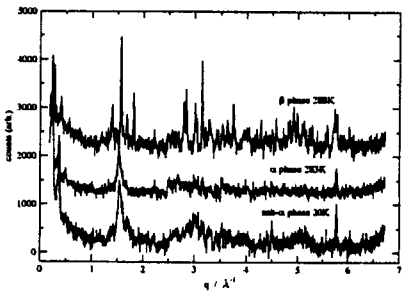


Fig. 1. The diffraction diagram of tristearin

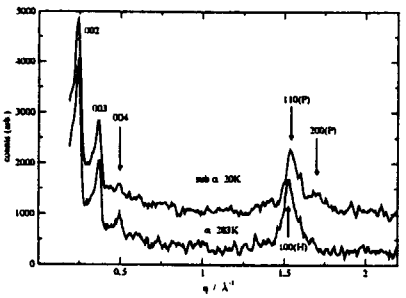


Fig. 2. The diffraction diagram in low q range.

使用施設：JRR-3M, 装置：(Hermes), 分野：

テーマ：天然アルミニウム珪酸塩ゲルとそのポリマーハイブリッドゲルの凝集構造解析
表題：天然アルミニウム珪酸塩ゲルとそのポリマーハイブリッドゲルの凝集構造解析

1-5-3 Analysis of Aggregation Structure of Natural Aluminum Silicate Nanofiber Gel and Its Polymer Hybrids

A. Takahara, K. Yamamoto[*1], K. Hara[*1], M. Sugiyama[*2], M Annaka[*3], M. Nagao[*4], and M. Shibayama[*4]

*Institute for Fundamental Research of Organic Chemistry, [*1]Graduate School of Engineering, Kyushu University,Fukuoka 812-8581, Japan*

*[*2]Graduate School of Science, Kyushu University, Fukuoka 812-8581, Japan*

*[*3]Faculty of Engineering, Chiba University, Chiba 263-8522, Japan*

*[*4]ISSP, The University of Tokyo, Tokai, Ibaraki 319-1195, Japan*

Imogolite is one of aluminosilicate nanotube with a chemical formula of $Al_2O_3SiO_2(H_2O)_n$, consisting of hollow nanotubes with an external diameter of about 2.5 nm and a length from several hundred nanometers to a micrometer [1]. Since imogolite has a high aspect ratio, the dispersion of imogolite in polymer matrix can improve the physicomechanical properties of matrix polymers. Poly(vinyl alcohol) (PVA) was chosen as a matrix polymer since both PVA and imogolite dissolve in water [2]. Small angle neutron scattering (SANS) experiment was performed in order to reveal the structure of imogolite gel and (PVA/imogolite) hybrid gel.

Raw material of imogolite gel was collected from the pumice bed in Kitakami area, Iwate, Japan. Imogolite gel purified of contaminants was dispersed in a weak acidic solution (pH=5.0-6.0) by applying a 42 kHz ultrasonic wave for a week. PVA with degree of polymerization of 1730 was used for the preparation of hybrid gel. (PVA/imogolite) hybrid was prepared by mixing the solutions of imogolite and PVA. Weight fractions of imogolite in hybrid gel were 0, 0.5 and 1.0%. (PVA/imogolite) hybrid gel in the (D_2O/DMSO-d6) (20:80) solvent were prepared. These gels were rapidly cooled from 353K to 253K and were maintained at 253K for 24hr. The neutron scattering experiment was performed with the SANS-U (ISSP) installed at JRR3-M reactor of JAERI (Tokai).

Figure 1(a)(b) shows SANS profiles of imogolite and (PVA/imogolite) hybrid gel. Even though the change of scattering length density of the solvent, no distinct feature was not observed for the scattering from imogolite gel. Since the hydrogen is present at the surface of imogolite, the scattering length density of imogolite increase and that of D_2O decreased due to the hydrogen-deuterium exchange reaction. Thus, the imogolite in D_2O gave very weak scattering. (PVA/imogolite) gel in D_2O showed broad scattering at q=ca.0.3 nm^{-1}. A large increase in scattering at higher q region was observed for the hybrid gel.

1. K. Yamamoto, H. Otsuka, S.-I. Wada, A. Takahara, Chem. Lett., No.11, 1162-1163 (2001)
2. K. Yamamoto, S.-I. Wada, H. Otsuka, A. Takahara, J. Adhesion in pres

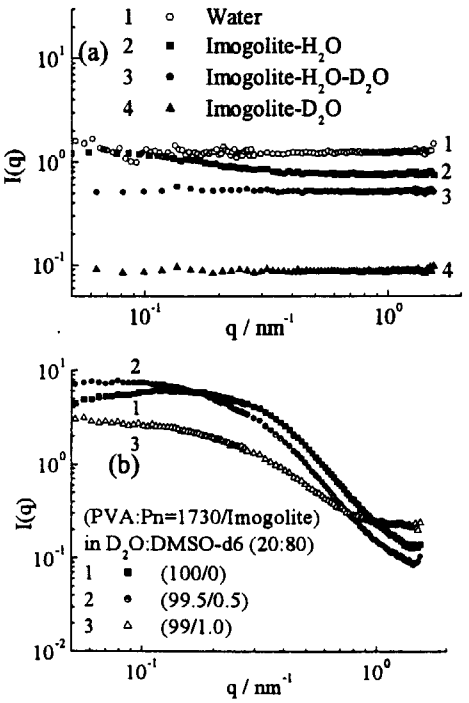


Figure 1 SANS profiles of imogolite gel in various solvents (a) and (PVA/imogolite) hybrid gel in (D_2O/DMSO-d6) (20:80) mixed solvent (b).

JRR-3M, SANS-U(C-1)), Polymer

研究テーマ：高分子ガラス化過程におけるモーショナルスローイングダウン
タイトルの和訳：熱中性子スピンエコー法によるガラス形成高分子の Tg 近傍のダイナミクス

1-5-4

Dynamics of a Glass-forming Polymer near T_g As Revealed by Thermal Neutron Spin Echo Technique

T. Kanaya[1], I. Tsukushi[2], K. Kakurai[3,4], M. Nishi[3], and K. Nakajima[3]

[1]*Institute for Chemical Research, Kyoto University, Uji, Kyoto-fu 611-0011, Japan*
[2]*Chiba Institute of Technology, Narashino, Chiba-ken, 275-0023, Japan*
[3]*NSL, ISSP, University of Tokyo, Tokai, Ibaraki 319-1106, Japan*
[4]*Advanced Science Research Center, JAERI, Tokai, Ibaraki 319-1195, Japan*

Dynamics of a glass-forming polymer has been studied near the glass transition temperature using a spin echo option of thermal neutron triple axis spectrometer (PONTA) at JRR-3M reactor. In this study we carried out measurements of intermediate scattering function $I(Q,t)$ in a wide Q range up to 3.5 Å^{-1} and in a time window of 0.012 to 0.143 ns. The sample used in the experiment is deuterated polybutadiene (PB-d_6) with glass transition temperature T_g = 170 K.

The elastic scattering intensities of PB-d_6 show inter-chain and intra-chain correlation peaks at 1.5 and 2.9 Å^{-1}, respectively, as shown in Fig. 1. The measurements of $I(Q,t)$ were done at Q = 1.5, 2.2, 2.9 and 3.5 Å^{-1}, covering both of the correlation peaks. The observed normalized intermediate scattering functions $I(Q,t)/I(Q,0)$ at 200 K are shown in Fig. 2 after correcting for the resolution function, which was evaluated from a measurement of PB-d_6 at 10 K. By fitting a decay function to $I(Q,t)/I(Q,0)$ we have evaluated the decay rate $\Gamma(Q)$ as a function of Q. The decay rate $\Gamma(Q)$ normalized to $\Gamma(Q$ = 1.5 Å^{-1}) is plotted in Fig. 1, where $\Gamma(Q)/\Gamma(Q$ = 1.5 Å^{-1}) observed by Richter et al. [1] in a low Q range below 2 Å^{-1} is also included. It is interesting to point out that $\Gamma(Q)/\Gamma(Q$ = 1.5 Å^{-1}) shows a minimum at around Q = 1.3 Å^{-1} corresponding to the inter-chain correlations while no minima are observed at around the intra-chain correlation peak (Q = 2.9 Å^{-1}). This suggests that the dynamics of PB-d_6 in a spatial scale of 2.9 Å^{-1} is not affected by the intra-chain potential, and intra-chain atoms move as a rigid body although they have some degrees of freedom.

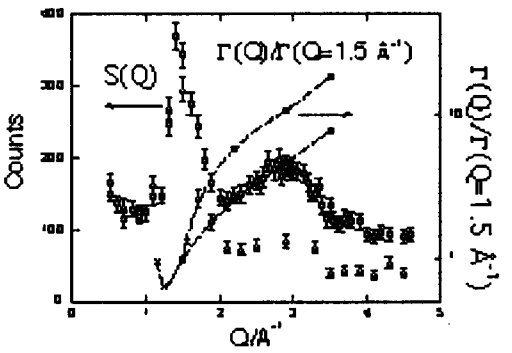


Fig. 1. Elastic intensity of PB-d_6 at 170 and 298 K and normalized decay rate $\Gamma(Q)/\Gamma(Q$=1.5Å^{-1}).

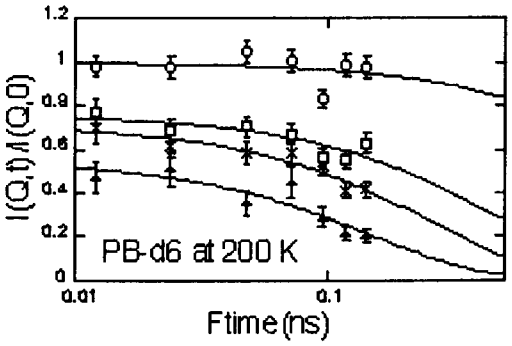


Fig. 2. Normalized intermediate scattering function $I(Q,t)/I(Q,0)$ of PB-d_6 at 200 K.

[1] D. Richter, B. Frick, B. Farago, *Phys. Rev. Lett.*, **61**, 2465 (1088)

使用施設： JRR-3M, 装置：PONTA、分野： , Polymer

研究テーマ：置換ポリアセチレンの高気体透過性機構の解明
タイトルの和訳：ガラス状置換ポリアセチレンのガス透過性における局所運動の役割、

1-5-5 Role of Local Dynamics in the Gas Permeability of Glassy Substituted Polyacetylenes. A Quasielastic Neutron Scattering Study

Toshiji Kanaya, Itaru Tsukushi[1], Keisuke Kaji, Toshikazu Sakaguchi[2], Giseop Kwak[2], and Toshio Masuda[2]

[1]*Institute for Chemical Research, Kyoto University, Uji, Kyoto-fu 611-0011*
[1]*Chiba Institute of Technology, Narashino, Chiba-ken, 275-0023, Japan*
[2]*Department of Polymer Chemistry, Kyoto University, Kyoto 606-8501, Japan*

The local dynamics of 10 substituted polyacetylenes in the glassy state have been investigated in a time range of picoseconds to several tens of picoseconds using a quasielastic neutron scattering spectrometer AGNES installed at the cold neutron guide C3-2-1. We focused our attention on a relationship between the local mobility and the gas permeability of these polymers.

Even in the glassy state, these polymers show quasielastic scattering components, suggesting that certain stochastic motions occur in the glassy state. The dynamic scattering laws $S(Q,\omega)$ of the quasielastic components were well fitted to the sum of two Lorentzians, i.e., the narrow (slow) and broad (fast) components as shown in Fig. 1. It was found that both the relaxation rate Γ_n and the fraction A_n of the narrow (slow) component show positive correlations with oxygen permeability coefficient (PO_2), suggesting that the local mobility of the matrix polymers plays an important role in gas permeability. We then defined local flux F, which is the product of Γ_n and A_n, as a measure of the local mobility to find that F is proportional to the diffusion coefficient of O_2 gas (DO_2), i.e., $F \propto DO_2$ (see Fig. 2). To explain and discuss this relation, we have proposed a random gate model, where mobile side groups in the matrix polymer act as a gate for gas diffusion.

This study has been published in Ref. [1]

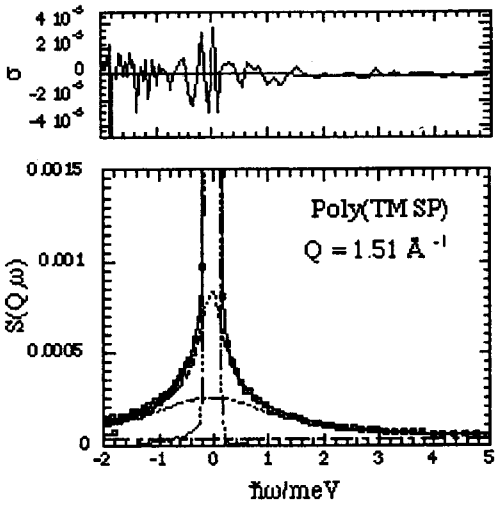


Fig. 1. An example of fits to $S(Q,w)$ of poly[1-(trimethylsilyl)-1-propyne] [poly(TMSP)]. The quasielastic components were well fitted to the sum of two Lorentzians, i.e., the narrow (slow) and broad (fast) components.

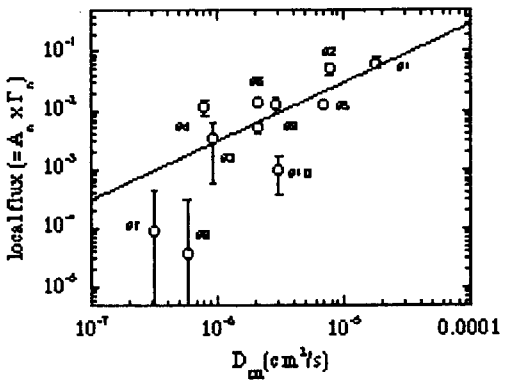


Fig. 2. Relation between local flux F and diffusion coefficient of O_2 gas in 10 substituted polyacetylenes.

[1] T. Kanaya, I. Tsukushi, K. Kaji, T. Sakaguchi, G. Kwak, and T. Masuda, *Macromolecules*, **35**, 5559-5564 (2002)

使用施設： JRR-3M, 装置：PONTA、分野： Polymer

研究テーマ：中性子非干渉性非弾性散乱による配向有限鎖ポリメチレンダイナミックスの固相一液相変化
表題：中性子非干渉性準弾性散乱およびラマン散乱によるオレイン酸α相でのダイナミックス

1-5-6

Neutron Incoherent Quasi-elastic Scattering and Raman Scattering of Oriented Oleic Acid in alpha- phase

N. ACHIWA, T.YOKOYAMA, K.KUMAGAI, M. SUZUKI[A], M. KASAHARA[B], and T. Yagi[B]
Department of Physics, Kyushu University, Fukuoka, 812-8581, Japan
[A]Nippon Oil and Fat Co.ltd.,Amagasaki, Hyougo, 580, Japan
[B]Research Institute for Electronic Science, Hokkaido Univ., Sapporo 060-0812Japan

§1. Dynamical Features in the γ and α phases

We have reported lattice and molecular vibrational modes of oleic acid ($CH_3(CH_2)_7CH=CH(CH_2)_7COOH$) in oriented crystal phases of γ(T<271.0) and α(271.0<T <286.5K) as well as in the liquid phases(T>286.5K) by neutron incoherent inelastic scattering method using TOF spectrometer, AGNES in JRR3M.[1,2] Since oleic acid molecule consists of a couple of finite polymethylene chains connected by ethylene double bond carbon and makes a dimer along the chain axis connected by hydrogen bonds between carboxyl groups in liquid and crystal phases, hierarchical exitations of local modes of finite polymethylene unit have been observed.

Recently we have observed clear difference in the Raman scattering spectra in the γ and α phases as shown in Fig. 1. In the Raman spectra in Fig. 1, lattice phnon

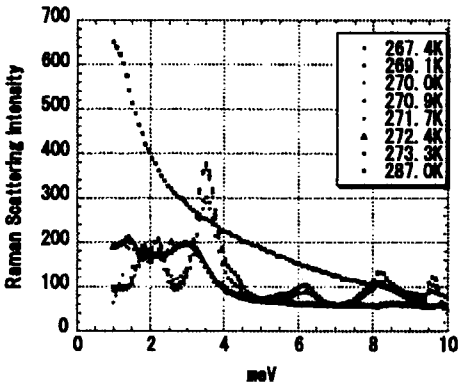


Fig. 1. Raman scattering spectra at several temperatures in three phases of the γ, α and liquid. Here, the γ-α transition temperature and melting point of oleic acid are 271 K and 286.5K, respectively.

bands at 3.5meV and around 2meV in the γ phase overdamp to bands at 3meV and 1.3meV, respectively in the α phase. The enthalpy and entropy changes of the γ to α phase were reported as ΔH=8.76 kJ/mol and ΔS=32.2 kJ K^{-1}/mol, respectively indicating that the α is a kind of disordered phase.[3]

Kobayashi[3] suggested that the terminal methyl groups which are the lameller interface of the bimoleculaer layer of phase γ induce interface melting in the α phase. In order to study the interface melting in the α phase, we have observed quasielastic as well as low energy excitation spectrra of oriented oleic acid in the γ, α and liquid phases using neutron incoherent scattering of hydrogen.

§2. Quasielastic Scattering

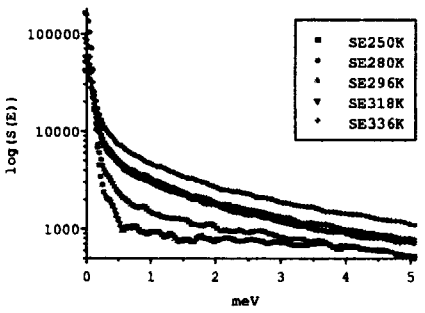


Fig. 2. Quasielastic scattering functions at several temperatures in γ, α, and liquid phase of oleic acid. Here, the γ－α transition temperature and the melting point of oleic acid are 271K and 286.5K, respectively.

Figure 2 shows S(E) of oleic acid in the γ α and liquid phases. Usually for a quasielastic scattering a Lorentzian function of the energy transfer is supposed. But in the α phase, the motion of hydrogen is rather complexed by mixing of translational and rotational coupled motion of finite zigzag chain. Here, in figure 2 in the γ phase, very small amount of quasielastic scattering below 300 μeV is observed. On the cotrary, the tail of quasielastic scattering in the α phase spread out up to 3meV. Of course in the liquid phase, the wider quasi elastic scattering than that in the α phase is observed by free translational motion of zigzag chain. Thus, the smearing out and overdamp of phonon bands observed in the Raman scattering of oleic acid in the α phase in the figure 1 can be explained by a random motion of hydrogen atoms of which most violent motion comes from terminal CH_3-molecule of zigzag chain.

1) T. Yokoyama, N. Achiwa and M.Suzuki : J. Phys. Chem. Solids **60** (1999) 1519.
2) . T. Yokoyama, N. Achiwa and M.Suzuki : J. Phys. Soc. Japan **70** (2001) Soppl. A p329.
3) M. Kobayashi, F. Kaneko, K. Sato, and M. Suzuki : J. Phys. Chem. **90**(1986) 6371.

研究テーマ：圧力ジャンプを用いた多成分高分子混合系の
濃度揺らぎのダイナミックスの研究

1-5-7 Viscoelastic effects on the dynamics of concentration fluctuations in dynamically asymmetric polymer blend

M.Takenaka, H.Hasegawa, S.Saito, H.Takeno, T.Hashimoto, and M.Nagao[1]

Department of Polymer Chemistry, Graduate School of Engineering, Kyoto University, Sakyo-ku, Kyoto 606-8501, Japan

[1]Neutron Scattering Laboratory, The Institute of Solid State Physics, The Universty of Tokyo, Tokai, Naka, Obaraki, 319-1106, Japan

Recently, it has been found that the dynamical assymetry between constituent components in a mixture causes the coupling between stress and diffusion during pahse separation processes of the mixture due to the asymmetric stress division. This coupling is called "viscoelastic effects" and has been found to causes shear-induced phase separation in polymer solutions and non exponential decay in dynamic scattering near equilibrium. Doi and Onuki (DO) have formulated the Time-Dependent-Ginzburg-Landau-type dynamic equation including the dynamical coupling between stress and diffusion. We aim to confirm the DO theory can well-describe the viscoelastic effects on the dynamics of SD in dynamically asymmetric polymer blends as well as to explore how the viscoelasticity affects the growth of the concentration fluctuations in the early stage SD in dynamically asymmetric polymer blends .

The blend sampleused inthis experiment is deutrated polybutadiene (DPB, Mw = 3.74×10^4, Mw/Mn = 1.28) / polyisoprene (PI, Mw=8.5×10^4, Mw/Mn = 1.1) = 50/50 (wt.wt.), where Mw and Mn are, respectively, weight-averaged and number-averaged molecular weight. The DPB/PI has lower critical solution emperature type and upper critical solution pressure type phase diagram. The spinodal temperature of the DPB/PI at 0.1MPa is 314.2K, We measured the time changes in SANS intensity of the mixture after the onset of the pressure drop from 100MPa to 0.1MPa at 38.5K with the SANS-U spectrometer of the Institute for Solid State Physics of the University of Tokyo in JRR-3M at Tokai.

The scattered intensity increases with time at all-observed q-region. The time changes in the scatteredintensity can be well described with Cahn-Hilliard-Cook theory and we obtained the q-dependencies of the growth rate and Onsager linetic coefficient $\Lambda(q)$.Fig.1 show the q-dependence of $\Lambda(q)$. The q^{-2}-dependence can be observed at large q-region. Doi-Oniki predictied the following q-dependence of $\Lambda(q)$:

$$\Lambda(q)=\Lambda(0)/(1+q^2\xi_{ve}^2) \qquad (1)$$

where $\Lambda(0)$ and ξ_{ve} are, respectively, $\Lambda(q)$ at q=0 and the viscoelastic length within which the growth of the concentration fluctuations is supressed by viscoelastic effects. we can well fit the data with eq.(1) and obtained ξ_{ve}=79.9nm . This indicates that the viscoelastic effects has important role in the dynamics of pahse separation processes in dynamically asymmetric polymer blends.

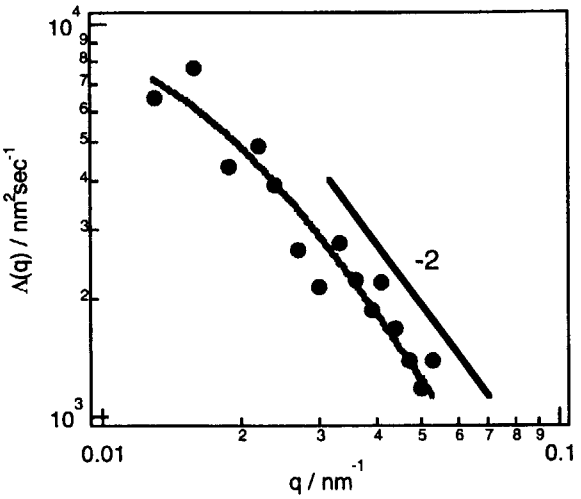


Fig.1 q-dependence of $\Lambda(q)$

JRR-3M, SANS-U, Polymer

1-5-8
高分子の結晶構造
Crystal Structure of Polymers

NEUTRON AND X-RAY STRUCTURE ANALYSES OF POLY(PYRIDOBISIMIDAZOLE) PIPD

Yasuhiro Takahashi
Department of Macromolecular Science, Graduate School of Science, Osaka University
Toyonaka, Osaka 560-0043, Japan

Poly(pyridobisimidazole) PIPD is a fully conjugated polymer with the highest tensile strength, whose chemical structure is shown in Fig. 1.[1] Neutron and X-ray structure analyses of this polymer were carried out. Neutron diffraction has several advantages in comparison with X-ray diffraction: the position of the hydrogen atom can be easily determined, the carbon and nitrogen atoms can be easily distinguished, and furthermore, it is easy to measure the diffraction at low temperature.

Neutron diffraction on the equator were measured by a powder diffractometer HERMES at JRR-3M installed in JAERI at 10, 100, 200, and 295K. X-ray diffraction was measured by an imaging plate at room temperature and the integrated intensities were estimated digitally.

All the reflections could be indexed by the unit cell reported by Klop & Lammers.[2] In Fig. 2, the temperature dependence of the cell parameters asinβ and b measured by neutron diffraction are shown. Two molecular chains pass through the unit cell. From the neutron structure analysis, it was clarified that the crystal assumes the statistical structure between two molecules of the pyridine rings with different orientations. By the constrained least-squares refinements, R-factors reduced to 15.6, 13.0, 16.5, and 10.5% for 12 intensity data at 10, 100, 200, and 295K, respectively. Three dimensional structure was clarified by X-ray data (R = 16.5 % for 17 reflections). The crystal structure of PIPD is shown in Fig. 3. The space group is the $P2_1/a$-C_{2h}^5. The OH bonds extend to outside of the molecule and form the intermolecular hydrogen bonds. The molecule is virtually planar differing from poly(p-phenylenebenzobisoxazole)[3] and poly(p-phenylenebenzobisthiazole),[4] which may be attributed to the intramolecular hydrogen bond NH..O(H).

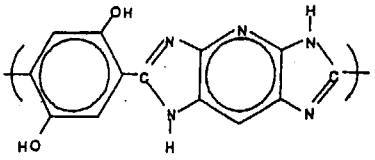


Fig. 1.

1.Sikkema, D. J., *Polymer*, **39**, 5981 (1998).
2. Klops, E. A. and Lammers, M., *Polymer*, **39**, 5987 (1998).
3.Takahashi, Y., *Macromolecules*, **32**, 4010 (1999).
4.Takahashi, Y., *Macromolecules*, **34**, 2012 (2001).

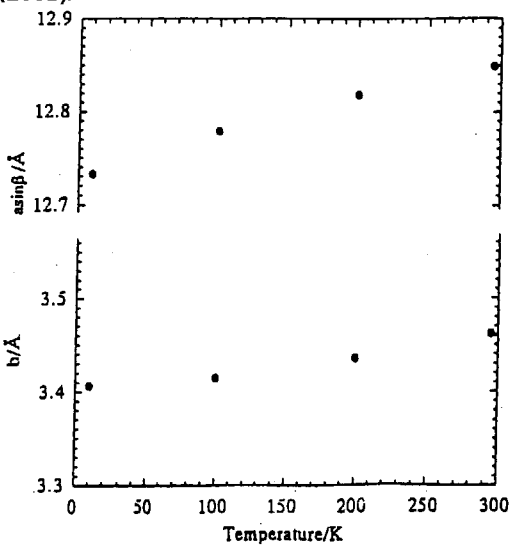


Fig. 2.

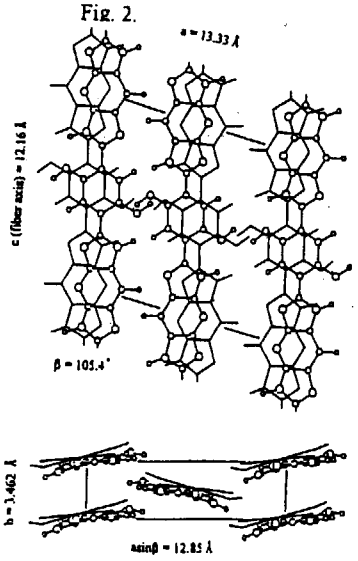


Fig. 3.

使用施設：JRR－3M, 装置：HERMES, 分野： Polymer

研究テーマ：PVA化学架橋ゲルのシネレシスにおける微視的構造変化
表題：ポリビニルアルコールゲルの融解過程における小角中性子散乱測定

1-5-9 SANS Study on Melting Process of Poly(vinyl alchol) Gels

Nobuaki Takahashi, Toshiji Kanaya, Koji Nishida, and Keisuke Kaji
Institute for Chemical Research, Kyoto University, Uji, Kyoto 611-0011, Japan

Small Angle Neutron Scattering (SANS) measurements have been performed on poly(vinyl alcohol) (PVA) gels in a mixture of deuterated dimetyl sulfoxide (DMSO-d_6) and D_2O with volume ratio 60/40 at various temperatures during the melting process. It was previously revealed [1] that the crosslinking points of PVA gel at 25℃ are crystallites and the size has been estimated to be about 70 Å in radius under an assumption of sphere shape of a crystallite. In this study, we have evaluated the structure changes around the crosslinking points during the melting process of the gel.

SANS measurements were carried out on SANS-U spectrometer at a beam port (C1-2) of JRR-3M reactor, Tokai. The gel samples were prepared as follows. A homogenized PVA solution at 100 ℃ was quenched to 27 ℃ to stand for 24 hour to gel. The measurements were carried out at 27 ℃, 45 ℃, 60 ℃, 70 ℃ 80 ℃, 90 ℃, and 100 ℃.

Figure 1 shows SANS intensity $I(Q)$ of the PVA gel at 27 ℃ as a function of Q in double logarithmic form. The scattering intensity $I(Q)$ can be well described by the Ornstein-Zernike (OZ) formula [eq. (1)] in the Q range below about 4×10^{-2} Å^{-1}.

$$I(Q) = \frac{I(0)}{1+\xi^2 Q^2} \qquad (1)$$

where ξ is a correlation length and $I(0)$ is the scattering intensity at $Q = 0$. The solid line in the figure is the best fit of the OZ formula to the observed $I(Q)$. In the high Q range above 6×10^{-2} Å^{-1}, the scattering intensity $I(Q)$ decreases with increasing Q according to a power law with an exponent n.

The correlation length ξ and exponent n are

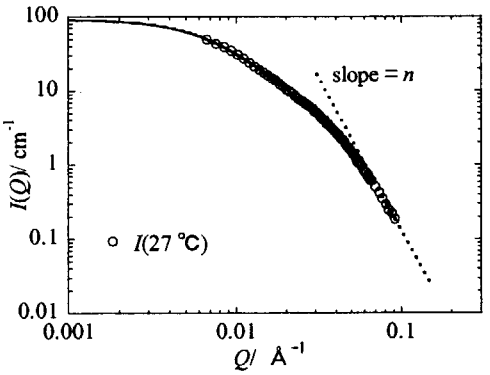


Figure 1. SANS intensity of PVA gel at 27 ℃. The solid and dot lines are the best fit of the OZ formula and power law, respectively.

plotted against temperature in Figure 2. It is noted that the exponent n is close to -4 at 27 to 70 ℃, which is the so-called Porod's law, suggesting the smooth surface of crystallites (crosslinking points) [1].

The melting temperature of the gel has been estimated to be about 75 ℃. Above the melting temperature of the gel, the exponent n gradually increases to -3. It reveals that the surface of

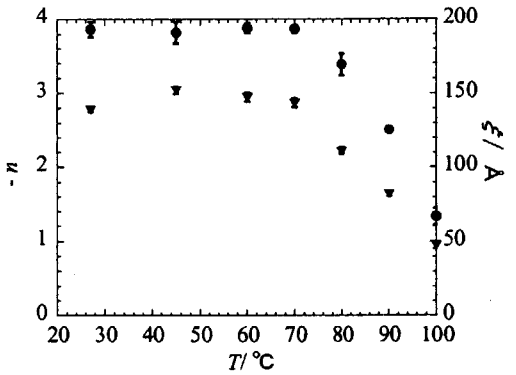


Figure 2. Temperature dependences of negative power law exponent n (●) and correlation length ξ (▼).

使用施設：JRR-3M, 装置：SANS-U（C1-2），分野： Polymer

研究テーマ：PVA 化学架橋ゲルのシネレシスにおける微視的構造変化
表題：ポリビニルアルコールゲルの融解過程における小角中性子散乱測定

crystallites becomes rougher. The correlation length ξ corresponds to an average distance between the nearest neighboring crosslinking points, at least below T_m. The value is 139 Å at 27 ℃ and after showing a miximum (152 Å) at 45 ℃, it decreases with increasing temperature. It is not physically acceptable that the average distance between the nearest neighboring crosslinking points decreases because the number of crystallites must decrease during the melting process.

In order to solve this problem, we calculated distance distribution function $P(r)$, which is defined by inverse Fourier transformation of scattering intensity $I(Q)$ [2],

$$P(r)\sim\left(\frac{2}{\pi}\right)\int rQI(Q)\sin(rQ)dQ \qquad (2)$$

$$\sim 4\pi r^2\gamma(r)$$

where $\gamma(r)$ is a pair correlation function. For calculation of eq.(2), it is necessary to extrapolate the observed scattering curves both to the lower and higher Q ranges. This was made by employing the functions of OZ formula and power law for the lower and higher Q ranges, respectively. The calculated $P(r)$ at 27 and 90 ℃ are shown in Figure 3 (a) and (b), respectively. The broad peak and/or shoulder are observed in $P(r)$ at 27 ℃. Following the previous analysis [1], the broad peaks at 70 Å and 180 Å can be assigned to the intra- and inter-crystallite correlations, respectively. In order to separate two contributions, we fitted the observed $P(r)$ in the small r range with a model function for the intra-crystallite correlation. This model function was calculated under the assumption that shapes of the crystallites are sphere and the distribution of sizes of crystallites (radius) can be represented by a Gaussian. The inter-crystallite correlation $P_{inter}(r)$ was obtained by subtracting $P_{intra}(r)$ from the total $P(r)$. The results are shown in Figure 3 (a) by dotted and dashed lines, which correspond to the intra-crystallite correlation

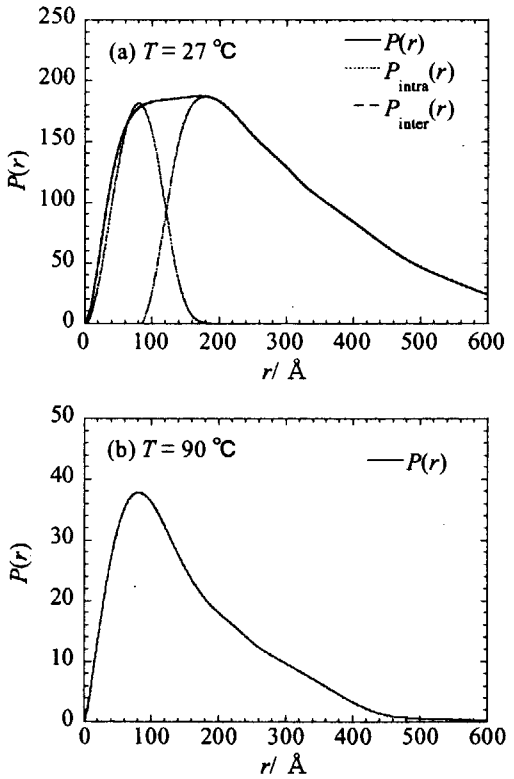


Figure 3. Distance distribution function $P(r)$ of PVA gels at (a) T=27 ℃ and (b) T=90 ℃, respectively.

$P_{intra}(r)$ and inter-crystallite correlation $P_{inter}(r)$, respectively. In Figure 3 (b), we can find the $P_{intra}(r)$ clearly, and the value is about 80 Å. It is close to the correlation length ξ. It indicates that ξ corresponds to the average size of crystallites (intra-correlation of crystallites) when the temperature is above T_m. The power law exponent n is -2.5, suggesting that the crosslinking points don't have even rough surface at this temperature. The detailed analysis is now in progress.

1) T. Kanaya, M. Okura, K. Kaji, M. Furusaka and M. Misawa, *Macromolecules*, 1994, **24**, 5609.
2) K. Kaji, H. Urakawa, T. Kanaya and R. Kitamaru, *Macromolecules*, 1984, **17**, 1835.

使用施設：JRR-3M, 装置：SANS-U（C1-2），分野： Polymer

研究テーマ：1596 1.026 カルボン酸間の水素結合によって不均一性ドメインを形成する弱荷電性高分子ゲルの研究
表題：混合溶媒中で局所的な疎水性ミクロ凝集を有する弱荷電高分子ゲルの構造解析

1-5-10

Structural Analysis of Weakly-Charged Polymer Gels including Local Hydrophobic Micro-Aggregations in Mixed Solvents.

F. IKKAI[1], N. MASUI[2], T. KARINO[3], S. NAITO[1], K. KURITA[4], M. FURUSAKA[5], and M. SHIBAYAMA[6]

[1] *The Inst. of Adv. Sci. Res., L'ORÉAL Tsukuba Center, 5-5 Tokodai, Tsukuba, Ibaraki 300-2635, Japan*
[2] *Dept. of Polym. Sci. & Eng., Kyoto Inst. of Tech., Matsugasaki, Sakyo-ku, Kyoto 606-8585, Japan*
[3] *Dept. of Mat. Struc. Sci., Grad. Univ. for Adv. Studies, 1-1 Oho, Tsukuba, Ibaraki 305-0801, Japan*
[4] *College of Sci. & Tech., Nihon Univ., Kandasurugadai, Chiyoda-ku, Tokyo 101-8308, Japan*
[5] *Neutron Scattering Laboratory, KEK, 1-1 Oho, Tsukuba, Ibaraki 305-0801, Japan*
[6] *Neutron Scattering Laboratory, ISSP, The Univ. of Tokyo, Tokai, Naka-gun, Ibaraki 319-1106, Japan*

Introduction

We have studied the copolymer gels consisting of 12-acryloyloxydodecanoic acid (ADA) and acrylic acid (AA) as a crosslinked protein model, which includes groups capable of hydrophobic and ionizable interactions and hydrogen bonding. The ADA (Fig. 1) has a long-alkyl-side chain and an ionizable carboxyl group, which probably contribute to hydrophobic chain assembly and hydrogen bonding between the ADA side chains, respectively.

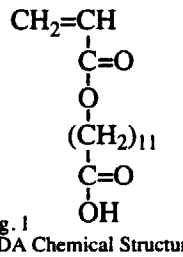


Fig. 1
ADA Chemical Structure

First, the effect of the hydrophobic interaction and the hydrogen bonding has been identified by equilibrium swelling measurement in 1-propanol/water (PrOH/W) and propionic acid/water (PAc/W) mixed solvents. The PrOH and PAc have the almost same "*log P*"[1], the logarithmic partition equilibrium coefficient, which shows the hydrophobicity of the solvent. So, we can ignore the difference of hydrophobic interaction effect, when discussing the solvent effect of PrOH and PAc. Fig. 2 shows the swelling ratio, S_v, of ADA/AA gels in PrOH/W and PAc/W systems as a function of solvent composition, x (= PrOH or PAc mol% in organic solvent/water mixtures). The remarkable shrinking ($S_v \approx 2$) at $x = 0$ mol% proved the hydrophobic association of the long-alkyl-side chains, in which the hydrogen bonding of the carboxyl groups also occurred. The interesting feature was the fact that the S_v of the PAc/W system was larger than that of the PrOH/W system at $x <$ 15 mol% and then the order was inverted at $x >$ 15 mol%. This seems to be due to the difference of hydrogen bonding capability of the carboxyl group in PrOH/W and PAc/W solvents. The aim of this study is to clarify the origin of the difference from a microscopic viewpoint by means of small-angle neutron scattering (SANS).

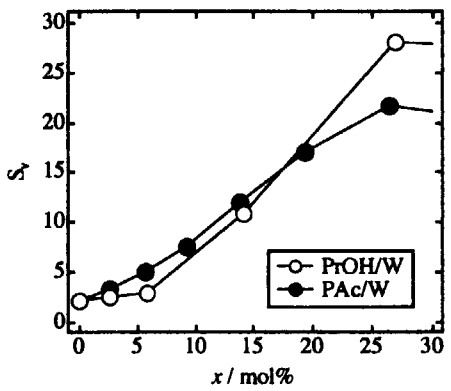


Fig. 2 Swelling behavior of ADA/AA gels.

Experimental

The ADA[2]/AA gels were heat-polymerized in ethanol for 24 h at 60 °C. The monomer composition of ADA in ADA/AA gel was 32.7 mol% and the net monomer concentration was 5 M. SANS measurements (with SANS-U spectrometer at ISSP, Univ. of Tokyo, at λ = 7 Å, at room temperature) were carried out for 1.0 and 1.5 h for 1 and 4 m sample-to-detector distance conditions,

JRR-3M, SANS-U, Polymer

研究テーマ：1596 1.026 カルボン酸間の水素結合によって不均一性ドメインを形成する弱荷電性高分子ゲルの研究
表題：混合溶媒中で局所的な疎水性ミクロ凝集を有する弱荷電高分子ゲルの構造解析

respectively. The solvents of the samples were replaced by deuterated ones, *i.e.*, combinations of D_2O, deuterated 1-propanol (d-PrOH), and deuterated propionic acid (d-PAc).

Results and Discussion

Fig. 3 shows I(q) of ADA/AA gels in d-PrOH/W (a) and d-PAc/W (b) as a function of x in double logarithmic plots. I (q)'s for both systems had a

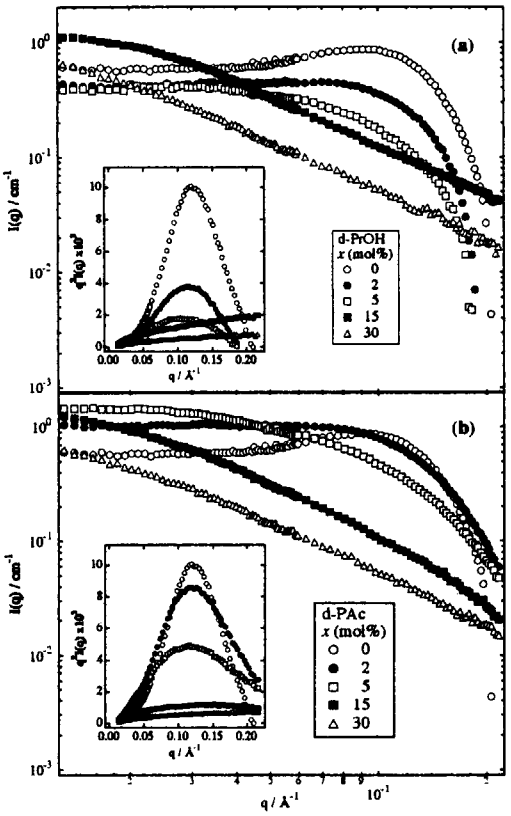


Fig. 3 SANS intensity profiles of ADA/AA gels.

broad scattering peak at x = 0, 2, and 5 mol%, indicating the existence of local periodic hydrophobic micro-aggregations. However, the x dependence of the peak position was different. That is, as shown more clearly in the Kratky plot in the inset, the peak maximum for the d-PrOH/W system (Fig. 3a) shifted to lower q region (54.4 to 59.0 Å in the real space) with increasing x, while that for the d-PAc/W system hardly changed (ca. 55.0 Å). Also, the peak height for the d-PrOH/W system decreased remarkably with increasing x. These differences were explained as follows. The PAc, a kind of acid, attacks the hydrogen bondings between hydroxyl groups at the end of the long alkyl groups and destroys them, following quick disorganization of the hydrophobic aggregation of long-alkyl-side chains. This is reflected to the quick reduction of the peak height in Fig. 3a. On the other hand, the PrOH gradually destroys the hydrophobic aggregation, corresponding to the peak change in Fig. 3b. So, as shown in Fig. 2, the gel at the PAc/W system swelled more quickly with increasing x than that at the PrOH/W system. However, the increase of PAc also reduces the pH in the system, leading to suppression of dissociation of the carboxyl groups on the AA. Therefore, at higher x, S_v of the PAc/W systems becomes lower than that of the PrOH/W systems, as shown at $x >$ 15 mol% in Fig. 2.

Summary

As described above, the ADA/AA gels have the local hydrophobic micro-aggregations in the water-rich solvents. The increase of the organic composition (PrOH or PAc) in the solvent tends to destroy the aggregations. Here, because the effect of disorganization by PAc is stronger than that by PrOH, the S_v for the PAc/W system is larger than that for the PrOH/W system at the low x region. However, since PAc is an acid, it reduces the degree of ionization of acrylic acid, leading to a lowering of S_v, which becomes effective for $x > x_c$ ($15 < x_c <$ 25 mol%) and an inversion of S_v takes place. This result proved that a slight difference in the nature of solvent can lead to a significant difference in forming higher order structure of proteins. The more detailed results and discussion have already published in the full paper[3].

References

1) R. F. Rekker, The Hydrophobic Fragmental Constant. In *Pharmacochemistry Library*, W. T. Nauta, R. F. Rekker, Eds., Elsevier Scentific, Amsterdam (1977)

2) H. Finkelman and M. A. Scafheutle, *Colloid Polym. Sci.*, 264, 786 (1986)

3) N. Masui, F. Ikkai, T. Karino, S. Naito, S. Kunugi, K. Kurita, and M. Shibayama, *Langmuir*, in press.

JRR-3M, SANS-U, Polymer

1-5-11
課題テーマ：1591 1.052 放射線架橋ゲルの不均一構造解析とその構造制御
課題名：小角中性子散乱による感熱応答性高分子ゲルの構造不均一性に関する研究 -放射線架橋ゲルと化学架橋ゲルについて-

Small Angle Neutron Scattering Studies on Structural Inhomogeneities in Temperature Sensitive Polymer Gels: Irradiation Cross-linked Gels vs Chemically Cross-linked Gels

N. Masui,* S. Takata,* T. Norisuye* and M. Shibayama**

**Department of Polymer Science and Engineering, Kyoto Institute of Technology, Matsugasaki, Sakyo-ku, Kyoto 606-8585, JAPAN*
***Neutron Scattering Laboratory, The Institute for Solid State Physics, The University of Tokyo Tokai, Naka-gun, Ibaraki 319-1106, Japan*

Introduction

Polymer gels are gigantic molecules consisting of long branched polymer chains immersed in a solvent. Due to restriction of the chain motion by cross-links, gels possess a very complicated structure and dynamics compared to the corresponding polymer solutions. Poly(*N*-isopropylacrylamide) (PNIPA) gel is a typical example of polymer gels and is usually synthesized by conventional radical polymerization starting from the constituent monomer and cross-linking agents (chemical gels). Another approach to make gels is γ-ray irradiation(γ-ray gels). The resultant gels are more or less homogeneous comparing to that prepared by the conventional method since cross-links are expected to be introduced randomly in space. In our previous report [1], we demonstrated that the neutron scattering functions varied from Lorenz to a power-law behavior with increasing cross-linking density for both types of polymer gels. The scattering functions were successfully reproduced by theoretical structure factor proposed by Panyukov and Rabin(PR theory), which allowed us to evaluate molecular parameters, such as degree of cross-links, interaction parameters and degree of inhomogeneities. In this report, we address the physical significance of the concept of the cross-linking saturation threshold (CST), which defines the maximal achievable density of cross-links in a gel.

Experimental

Poly(*N*-isopropylacrylamide)(NIPA) gels having different cross-link densities were prepared by polymerizing NIPAm monomer with cross-linker, methylene-bisacrylamide (BIS) in water at 20°C. The concentrations of BIS, C_{BIS} were varied from 0 to 35 mM, while that of NIPAm (C_{NIPA}) was kept to 690mM. The cross-linking density for the γ-ray gels was controlled by varying the radiation time (0 ~ 16 Mrad).

Small angle neutron scattering (SANS) measurements were carried out with SANS-U spectrometer of the Institute for Solid Sate Physics, University of Tokyo in Tokai. The wavelength of neutron beam was 7.0Å.

Results and Discussion

Due to non-cancel-out fluctuations of polymer gels, the scattering functions for both the chemical and γ-ray gels exhibited a positive deviation at lower wave vector with increasing the cross-linking degree. As demonstrated in our previous works[1, 3], the scattering functions for PNIPA gels were successfully reproduced by the PR theory. As a consequence, we obtained the degree of

JRR-3M, SANS-U, Polymer

課題テーマ：1591 1.052 放射線架橋ゲルの不均一構造解析とその構造制御
課題名：小角中性子散乱による感熱応答性高分子ゲルの構造不均一性に関する研究 -放射線架橋ゲルと化学架橋ゲルについて-

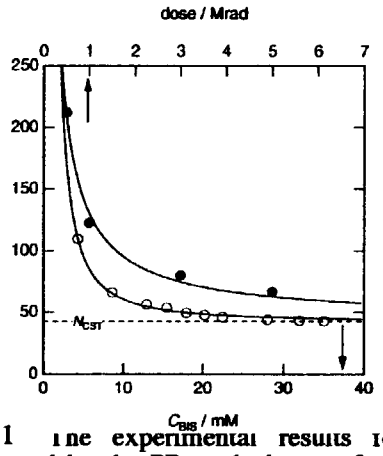


Fig. 1 The experimental results for N evaluated by the PR analysis as a function of cross-linking density for the chemical gels (open circles) and the γ-ray gels (filled circles).

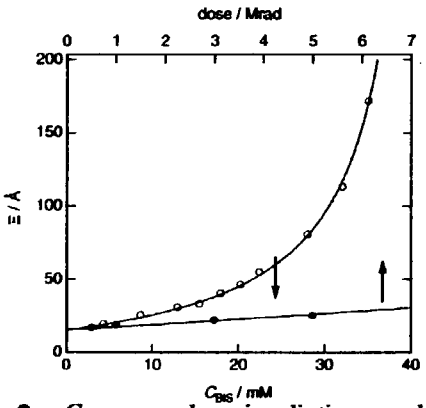


Fig. 2 C_{BIS} and irradiation dose dependence of the inhomogeneity-correlation length at sample preparation, Ξ, for the chemical gels (open circles) and the γ-ray gels (filled circles)

polymerization between cross-links, N, and the Flory's interaction parameter, χ. Figure 1 shows the values of N evaluated by the PR analysis as a function of cross-linking density for the chemical gels (open circles) and the γ-ray gels (filled circles). As expected, N decreased with the degree of cross-linking and approached an asymptotic value for both the chemical and γ-ray gels. The limit, N_{CST}, is called the cross-linking saturation threshold(CST), which can be considered as a point where the number of cross-links introduced to the gel becomes equal to the number of binary contact of monomers.[2, 3] Because of this physical limitation, any additional cross-linking is no longer formed above the CST. Although the results for higher doses were not shown here for the γ-ray gels, a volume shrinking of gels was observed for 16 Mrad, which is located far below the CST. Thus, it can be concluded that the efficiency of the cross-linking formation for the γ-ray gels is much higher than that for the chemical gels and a less number of cross-links is required to form a gel.

Figure 2 shows the C_{BIS} and irradiation dose dependence of the inhomogeneity-correlation length at sample preparation, Ξ, which corresponds to the screening length of the static correlator, for both types of gels. Ξ for the chemical gels is a strong function of C_{BIS}, while that for γ-ray gels is rather constant irrespective of the irradiation dose. The locations of the CST were found to 42.6(mM) and 263 Mrad for the chemical gels and the γ-ray gels, respectively, by extrapolating to the largest cross-linking density limits. The weak irradiation-dose dependence of the γ-ray gels is deduced to be due to random cross-linking and absence of the micro-gel cluster formation during gelation process. Further analyses with dynamic light scattering and dilatometry are now in progress and will be presented in the forthcoming paper.

Reference

[1] T. Norisuye et al., *Activity report on neutron scattering research*, **7**, 232 (2000)
[2] S. Panyukov et al., *Macromolecules*, **29**, 7960 (1996)
[3] T. Norisuye et al., *Polymer, in press*

JRR-3M, SANS-U, Polymer

研究テーマ：両親媒性高分子の会合挙動の解析

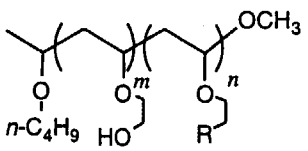
表題：含フッ素両親媒性ブロックコポリマーの水溶液中での会合挙動

1-5-12 Association Behavior of Fluorine-Containing Amphiphilic Block Copolymer in Aqueous Media

Kozo Matsumoto, Hiroaki Mazaki and Hideki Matsuoka

Department of Polymer Chemistry, Kyoto University, Kyoto 606-8501, JAPAN

Fluorinated polymers have attracted much attention because of their unique characteristics such as high hydrophobicity, lipophobicity, chemical stability and biocompatibility. The combination of fluorinated polymers with hydrophilic polymers may lead to a new class of polymeric amphiphiles.[1,2] We have already found that vinyl ether based fluorine-containing amphiphilic block copolymer possesses peculiar properties such as high surface activity and "*fluorophilicity*" in the solubilization of fluorinated dyes in aqueous media. To understand more about this series of block copolymers, here we examined their micelle structures in aqueous media in detail. We utilized small-angle neutron scattering (SANS), small-angle X-ray scattering (SAXS), and dynamic light scattering (DLS) techniques.



F3: R = OCH_2CF_3 $m = 78, n = 23$
F5: R = $OCH_2CF_2CF_3$ $m = 74, n = 22$
F7: R = $OCH_2CF_2CF_2CF_3$ $m = 79, n = 19$
F0: R = CH_2CH_3 $m = 70, n = 22$

Figure 1. Chemical structure of amphiphilic block copolymers

Figure 1 shows the chemical structure of the block copolymers (F3, F5, F7) used in this study. In comparison with the fluorine-containing block copolymers, non-fluorine-containing block copolymer (F0) was also prepared. All samples had approximately the same chain lengths both in hydrophilic segments and in hydrophobic segments.

Figure 2 shows the SANS profiles for 3.2 x 10^{-4} mol/L block copolymer solutions in D_2O. A strong scattering in small angle region suggested a formation of micelles in all cases. The profiles of F0, F5, and F7 showed clear q^{-1} dependence in the lower angle region, indicating the formation of rod-like micelles, while the profile of F3 showed much gentler slope, indicating a possibility of coexistence of rod-like and spherical micelles.

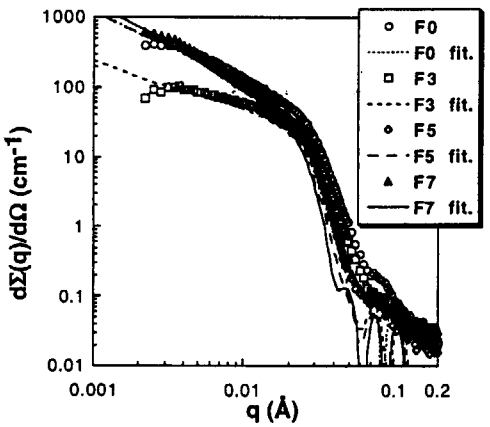


Figure 2. SANS profiles for the block copolymer in D_2O

Figure 3 represents the SAXS profiles of the copolymer solutions measured under the

JRR-3M, SANS-U, . Polymer

same conditions as SANS experiments. The micelle formations were also comfirmed by a strong x-ray scattering in the small angle region. In these cases, a clear second maximum of the scattering due to an intra-particle structure such as core-shell structure was observed around q = 0.04 ~ 0.08 Å^{-1}.

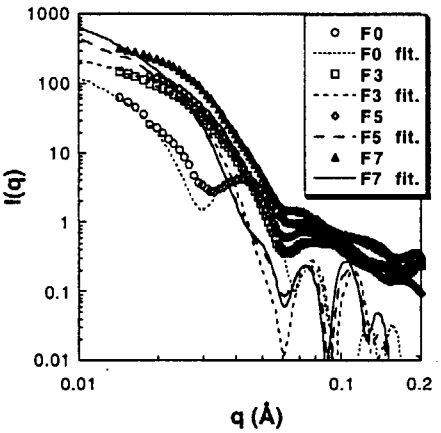


Figure 3. SAXS profiles for the block copolymer aqueous solutions

To analyze these scattering data, we assumed both core-shell rod-like micelle and core-shell spherical micelle models, and calculated the theoretical profiles for SANS and SAXS. Radii of the core (R_c) and the radii of the whole micelle (R_s) in the cross section of spherical micelles and rod-like micelles were assumed to be the same in our models. The solid lines shown in figures 2 and 3 were the fitting curves. They reproduced both experimental data quite well with the same fitting parameters in all cases, which strongly supported the accuracy of the proposed model. The fitting parameters are listed in table 1.

DLS results of the copolymer micelle solutions are consistent with the above considerations. Hydrodynamic size distributions of the block copolymer micelles were bimodal in all cases. Hydrodynamic radii (R_h) of the micelles obtained by double exponential fitting for the time correlation functions were also listed in table 1. Particles of hydrodynamic radius (R_h) = ca.110 Å can be considered as spherical micelles and those of 500 Å or larger R_h as rod-like micelles.

Table 1. Structural Parameters of the Block Copolymer Micelles

polymer	Φ	R_c [Å]	R_s [Å]	$R_{h\text{-}rod}$ [Å]	$R_{h\text{-}sphere}$ [Å]
F3	0.1	53	110	500	100
F5	0.7	53	110	600	100
F7	0.8	55	110	1100	150
F0	0.4	55	120	650	150

Φ: volume fraction of the rod-like micelle

R_c: cross-sectional radius of the micelle core

R_s: cross-sectional radius of the overall micelle

$R_{h\text{-}rod}$: hydrodynamic radius of the rod-like micelle

$R_{h\text{-}sphere}$: hydrodynamic radius of the spherical micelle

It was revealed that F3 mainly formed spherical micelles, F5 and F7 mainly formed rod-like micelles, while F0 formed both spherical and rod-like micelles. Based on these results, we supposed that rod-like micelles are more likely to be formed in the highly fluorinated block copolymers, while the size of spherical micelle and radius of rod-like micelles are almost unchanged regardless of the number of fluorine atoms per monomer unit.

References

[1] Matsumoto, K.; Mazaki, H.; Nishimura, R.; Matsuoka, H.; Yamaoka, H. *Macromolecules* **2000**, *33*, 8295.

[2] Matsumoto, K.; Kubota, M.; Matsuoka, H.; Yamaoka, H. *Macromolecules* **1999**, *32*, 7122.

1-5-13
研究テーマ：中性子スピンエコー法によるイオン性両親媒性高分子の溶液中における会合挙動とダイナミクスの解析
表題：中性子スピンエコー法による片末端が固定されたイオン性高分子鎖のダイナミクス

Neutron Spin Echo Study of the Dynamics of Tethered Polyelectrolyte Chains on Solid Substrate in Aqueous Media

Hideki Matsuoka, Ploysai Kaewsaiha, Takashi Ikeda and Kozo Matsumoto
Department of Polymer Chemistry, Kyoto University, Kyoto 606-01, Japan

In 1999, we performed a systematic Neutron Spin-Echo (NSE) experiment on polymer micelles in aqueous solution. Amphiphilic diblock copolymers were synthesized and their aqueous solutions were measured by NSE to elucidate the dynamic character of polymer micelles, especially the dynamics of "corona" part of the polymer micelle. We found that there were two dynamic modes existed in the system and the time-correlation functions obtained by NSE were well reproduced by a double exponential function. The decay rate Γ both for the fast and slow modes showed an excellent linearity as a function of the square of q (the scattering vector). By independent experiments by SANS and SAXS, the size and shape of the micelle were evaluated. Also, by a dynamic light scattering technique, we evaluated the translational diffusion coefficient of the micelle in water solution. From systematical analyses of these data, it was concluded that the slow mode by NSE corresponded to the translational diffusion of the whole micelle and the fast mode was considered to be a dynamic mode of corona, i.e. hydrophilic polymer chains on the micelle surface. However, the unknown factor was a contribution from "unimer" which is a single polymer chain in the solution. In this study, we have synthesized a novel corona system without unimers, and the dynamics of the corona, i.e. the tethered polyelectrolyte chains has been further investigated.

By following the scheme shown in Figure 1, we have synthesized polyelectrolyte grafted colloidal silica particle. This graft-polymerization reaction was confirmed by IR, ESCA, and ζ-potential experiments. The graft polymer chains have sulfonic acid groups, hence this is a polyelectrolyte grafted colloidal particles. The 1.64 vol.% dispersion was measured by NSE. The q range was from 0.03

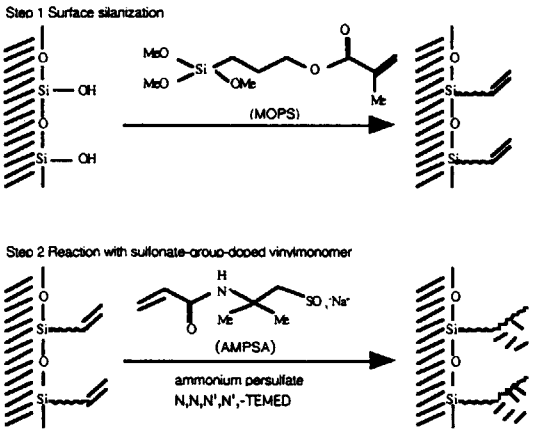


Figure1 Scheme of surface modification

to 0.065 Å^{-1}. Due to the unexpectedly weak scattering intensity, the time correlation function obtained had not enough statistics but it was fitted by exponential function. Γ vs. q^2 plot showed an excellent linearity up to Q=0.05 and smaller Γ value was found at Q=0.065. There is a possibility that the dynamics of corona chains contributed to NSE data at this higher Q regions.

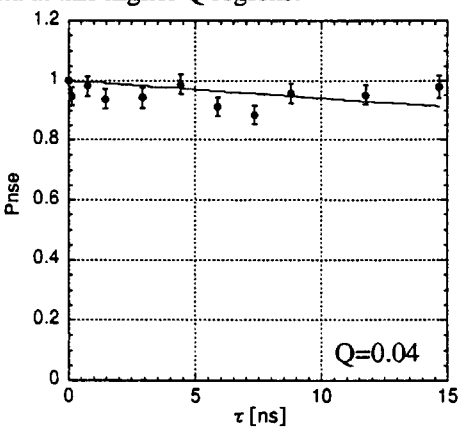


Figure 2 An example of NSE data for polyelectrolyte grafted colloidal silica particles in aqueous dispersion.

References

1) H.Matsuoka, Y.Yamamoto, N.Nakano, H.Endo, H.Yamaoka, R.Zorn, M.Monkenbusch, D.Richter, H.Seto, Y.Kawabata, M.Nagao, ***Langmuir*, 16(24)** 9177-9185 (2000).

JRR-3M, NSE, Polymer

テーマ：中性子反射率測定による高分子界面での分子拡散挙動評価
表題：中性子反射率測定による（ポリスチレン/重水素化ポリスチレン）二層膜界面厚の分子量依存性

1-5-14

Molecular Weight Dependence of Interfacial Broadening at (Polystyrene/Deuterated Polystyrene) Bilayers below Bulk Glass Transition Temperature by Neutron Reflectivity

T. Kajiyama, D. Kawaguchi, K. Tanaka, S. Tasaki*[1], and A. Takahara*[2]

Graduate School of Engineering, Kyushu University, Fukuoka 812-8581, Japan
*[1]*Research Reactor Institute, Kyoto University, Osaka 590-0494, Japan*
*[2]*Institute for Fundamental Research of Organic Chemistry, Kyushu University, Fukuoka 812-8581, Japan*

Molecular motion at polymer surfaces is quite different from that in the interior bulk region due to the free energy difference between surface and bulk. The purpose of this study is to elucidate the depth region, in which segmental mobility is enhanced, based on interdiffusion experiments using (polystyrene/deuterated polystyrene) (h-PS /d-PS) bilayers at a temperature above surface glass transition temperature, T_g^s, and below bulk glass transition temperature, T_g^b.

h-PS and d-PS with various molecular weights were anionically synthesized. Thin films of h-PS and d-PS were prepared by the spin-coating method on silicon wafers. (hPS/dPS) bilayers were prepared by a floating technique as follows. The perimeter of the h-PS film was scored with a blade, and then, floated off onto the surface of distilled water. The h-PS film was picked up onto the d-PS film by attaching the d-PS film from the air side. For interdiffusion experiments, the bilayers were annealed at 365 K, which was above T_g^s and below T_g^b for 152 hrs. The interfacial broadening of the bilayer by annealing was monitored using dynamic secondary ion mass spectroscopy (DSIMS) and neutron reflectivity (NR). The incident beam of oxygen ions with 4k eV and ca. 30 nA was focused onto a 200 μm x 200 μm area of the specimen surface. The incident angle was 45 deg. NR measurements were made using the multilayer interferometer for neutrons (C3-2-2, MINE) at the Institute for Solid State Physics, University of Tokyo. The incident neutrons possess the long wavelength of 1.26 nm and the resolution of 5.1 %. The reflectivity was calculated based on the scattering length density profile along the depth direction by using Spreadsheet Environmental Reflectivity Fitting.

Figure 1 shows the molecular weight dependence of interfacial thickness for (h-PS/d-PS) bilayer films annealed at 365 K for 152 hrs. While the interfacial thickness was smaller than 1 nm before the annealing, it was discernibly evolved after the annealing below T_g^b. Hence, it is clear that segmental mobility at the interfacial region, which used to be surface layer, is much enhanced in comparison with the bulk. Also, the interfacial thickness was almost constant below M_n of 75k and then slightly decreased with increasing molecular weight. This M_n dependence might be explained in terms of the temperature difference between T_g^s and 365 K.

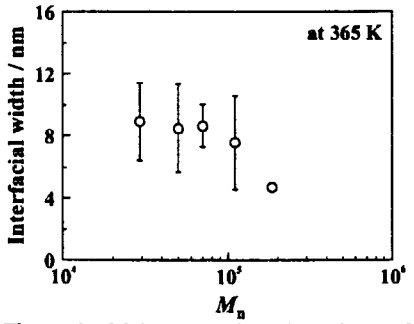


Figure 1 Molecular weight dependence of interfacial thickness for (h-PS/d-PS) bilayers after annealing at 365 K for 152 hrs.

JRR-3M, MINE (C3-2-2), Polymer

テーマ：中性子反射率測定に基づく分子鎖の主鎖・末端構造を制御した高分子薄膜中での末端基の空間分布評価
表題：中性子反射率測定に基づく高分子膜表面近傍での分子鎖末端分布

1-5-15

Chain End Distribution near the Surface in Polymer Films by Neutron Reflectivity

A. Takahara, D. Kawaguchi*[1], K. Tanaka*[1], S. Tasaki*[2], and T. Kajiyama*[1]

Institute for Fundamental Research of Organic Chemistry, Kyushu University, Fukuoka 812-8581, Japan
[1]Graduate School of Engineering, Kyushu University, Fukuoka 812-8581, Japan
[2]Research Reactor Institute, Kyoto University, Osaka 590-0494, Japan

Manifestation of surface functions for polymeric materials is closely related to its surface aggregation structure and thermal molecular motion. One of our goals is to rationalize the distribution of chain end groups in the vicinity of the surface and its role for various surface functionalities. In this report, chain end distribution near the surface under hydrophobic and hydrophilic atmosphere is studied by neutron reflectivity.

The polymer used in this study was symmetric (tridecafluoro-1,1,2,2-tetrahydro-octyl) dimethylsilyl-terminated poly(styrene-d_8-*block*-styrene-*block*-styrene-d_8) triblock copolymer [R_f-P(dSt-St-dSt)-R_f] synthesized via living anionic polymerization. Figure 1 shows the chemical structure of R_f-P(dSt-St-dSt)-R_f. The number average molecular weight (M_n), the molecular weight dispersity (M_w/M_n), PS weight fraction, and functionality was 25.7k, 1.09, 0.744, and 2.02, respectively. Two R_f-P(dSt-St-dSt)-R_f films were coated from toluene solution onto a silicon wafer with native oxide layer by a spin-coated method, and then annealed at 423 K for 24 hrs under vacuum in order to remove any sample preparation history. One of the films was further annealed under water vapor atmosphere at 373 K. At that time, the relative humidity was 100%. NR measurements were made with the multilayer interferometer for neutrons (C-3-2-2, MINE). The incident neutrons possess the long wavelength of 1.26 nm with the resolution of 5.1 %. The reflectivity was calculated based on the model scattering length density profile along the depth direction by using spreadsheet environment reflectivity fitting (SERF).

Figure 2 shows the scattering vector, q, dependence of neutron reflectivity for the R_f-P(dSt-St-dSt)-R_f films annealed under vacuum and water vapor. The solid curves denote the best-fitted reflectivity calculated on the basis of model scattering length density, (b/V), profile along the direction normal to the surface shown in the inset. Since both (b/V) values at the surface were higher than that of its interior region, it seems reasonable to consider that fluoroalkylsilyl end groups are preferentially partitioned to the surface. Also, the surface concentration of chain ends is strongly dependent on the environment such as vacuum and water vapor.

$$R_f\text{—(d-PS)}_{28.6}\text{—(PS)}_{178.8}\text{—(d-PS)}_{28.6}\text{—}R_f$$

$$R_f = -\overset{\overset{CH_3}{|}}{\underset{\underset{CH_3}{|}}{Si}}-(CH_2)_2(CF_2)_5CF_3$$

Figure 1 Chemical structure of R_f-P(dSt-St-dSt)-R_f.

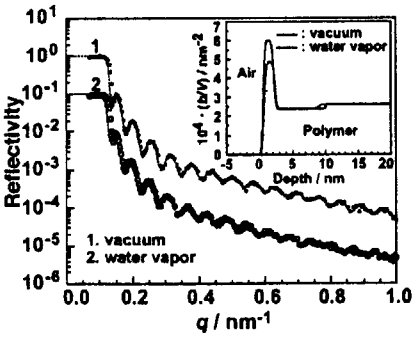


Figure 2 The scattering vector, q, dependence of reflectivity for the R_f-P(dSt-St-dSt)-R_f films. The inset shows the model scattering length density, (b/V), profile along the direction perpendicular to the film surface. See detail in the text.

JRR-3M, MINE (C3-2-2), Polymer

研究テーマ：ABCトリブロックコポリマーの複雑相転移と自己組織化過程に関する研究
表題：ABCトリブロック共重合体の複雑相転移

1-5-16 Complex Microphase Transitions in an ABC Triblock Terpolymer

K. Yamauchi[1], H. Hasegawa[1], T. Hashimoto[1] and M. Nagao[2]
[1]*Department of Polymer Chemistry, Graduate School of Engineering, Kyoto University, Sakyo-ku, Kyoto, 606-8501 Japan*
[2]*Neutron Scattering Laboratory, The Institute for Solid State Physics, The University of Tokyo, Shirakata, Tokai, Naka, Ibaraki, 319-1106 Japan*

Introduction Polyisoprene-*b*-poly(D6-styrene)-*b*-poly(vinyl methyl ether) triblock terpolymer (abbreviated to PI-*b*-DPS-*b*-PVME) is an extremely interesting system, because DPS and PVME have a lower critical solution temperature (LCST)-type phase diagram, while PI and DPS (or PVME) have an upper critical solution temperature (UCST)-type phase diagram. Namely, with increasing temperature the segregation power between PI and DPS decreases and DPS tends to mix with PI. However, PVME is still immiscible with PI while miscibility between DPS and PVME decreases with temperature. Therefore, it is quite interesting to investigate the phase behavior of this terpolymer. Order-disorder transitions with temperature based on the competition of three components of PI-*b*-DPS-*b*-PVME makes the phase behavior extremely rich but complex. However, it can be investigated by using a combined small-angle X-ray scattering (SAXS) and small-angle neutron scattering (SANS) analysis, because they give different contrast for the three components and, therefore, the complementary information.

Experiment PI-*b*-DPS-*b*-PVME (M_n=4.1x10^3, 2.1x10^4 and 3.4x10^3 for each block, respectively) triblock terpolymer sample cast from toluene solution. SANS-U (λ=7.0Å, SDD=4.0m) equipped with a heating stage controlled by TEMCON was used. The SANS data were obtained for a heating and a cooling cycle by 5K step for each between room temperature and 487 K. The SAXS measurement was performed for the cooling cycle from 493 to 300 K.

Results Figure.1 shows the temperature dependence of Bragg spacing D (D is related to q_m by $D=2\pi/q_m$) calculated from SANS(●) and SAXS(○) mesurement. At below 410K, both D shows the same behavior and it means the distance between PI phase and PI phase. This results suggest that spherical microdomains of PI phase are not packing in the matrix of DPS/PVME mixed phase. At temperature above 410 K, D(SANS) decreases sharply, on the other hand, D(SAXS) increases because of the difference of scattering contrast between SANS and SAXS. This results means mixed phase of DPS,PVME is separated each other, and PVME forms spherical morphology. Figure.2 shows the phase behavior model of PI-*b*-DPS-*b*-PVME.

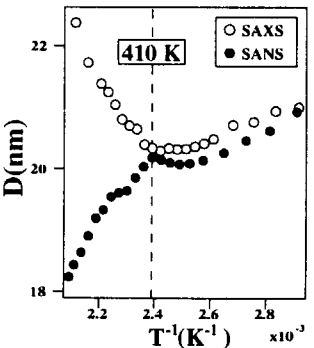


Fig.1 Temperature dependence of D

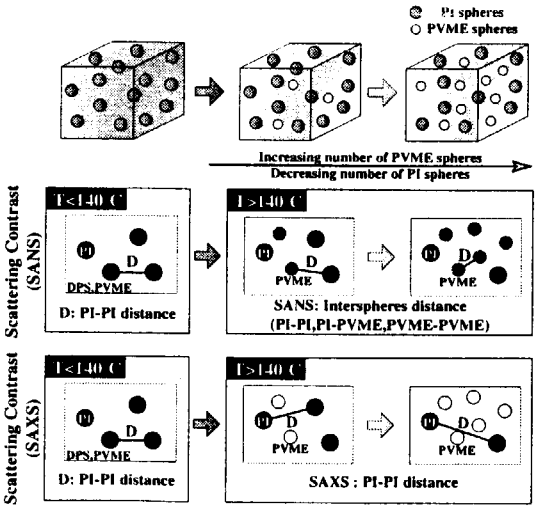


Figure 2. Phase structure model

1-5-17
研究テーマ：界面膜ダイナミクスの droplet 濃度依存性
表題：中性子小角散乱による三元系マイクロエマルションの静的構造の droplet 密度依存性

Small-Angle Neutron Scattering Study on Droplet Density Dependence of Static Structure in a Ternary Microemulsion System

M. Nagao, H. Seto*, and N. Yamada*

*Institute for Solid State Physics, The University of Tokyo, 106-1 Shirakata, Tokai 319-1106, Japan; *Faculty of Integrated Arts and Sciences, Hiroshima University, 1-7-1 Kagamiyama, Higashihiroshima 739-8521, Japan*

A mixture of AOT (Aerosol-OT; dioctyl sulfosuccinate sodium salt), D_2O, and oil forms stable water-in-oil droplet microemulsion in the vicinity of room temperature as shown in Figure 1. The arrow indicates the same water to AOT molar ratio line and it has been believed that the size of droplet is almost constant and only droplet concentration ϕ (the volume fraction of D_2O plus AOT) is different. [1] Seto et al. [2] investigated the static structure of the system by means of small-angle x-ray scattering (SAXS) technique in the droplet concentration region of $0.4 \leq \phi \leq 0.65$ with the water to AOT molar ratio of 40.8. They concluded that the mean droplet radius r and the polydispersity index became small with increasing ϕ. However, their analysis depended on the model of the structure factor $S(Q)$. Thus, their result on the droplet structure had an ambiguity.

Small-angle neutron scattering (SANS) technique has an advantage in determining structures comparing with SAXS; the contrast variation method can be used. In general, an observed scattering intensity can be expressed by the product of $P(Q)$ and $S(Q)$;

$$I(Q) = nP(Q)S(Q). \quad (1)$$

In the case of water-in-oil droplet structure, only the form factor is changed when deuterated oil (film contrast) is used instead of protonated oil (bulk contrast) while the structure factor is the same. In case of polydisperse droplets, $P(Q)$ can be written as,

$$P(Q) = \int F(Q,r)h(r)dr, \quad (2)$$

here, $h(r)$ is a distribution function and $F(Q,r)$ is

$$F(Q,r_c) = \left\{ \frac{4\pi}{3} r_c^3 \Delta\rho f(Qr_c) \right\}^2 \quad (3)$$

for bulk contrast and,

$$F(Q,r_c) = \left\{ \frac{4\pi}{3} \Delta\rho \left[r_c^3 f(Qr_c) - (r_c+\delta)^3 f\{Q(r_c+\delta)\} \right] \right\}^2, \quad (4)$$

for film contrast. Q is momentum transfer, r_c and δ radius of droplet core and thickness of droplet shell, $\Delta\rho$ the neutron scattering amplitude density difference, respectively. The function $f(x)$ is

$$f(x) = 3\frac{\sin x - x\cos x}{x^3}. \quad (5)$$

Hereafter, a *Relative Form Factor*, $R(Q)$, is introduced as a ratio of the scattering

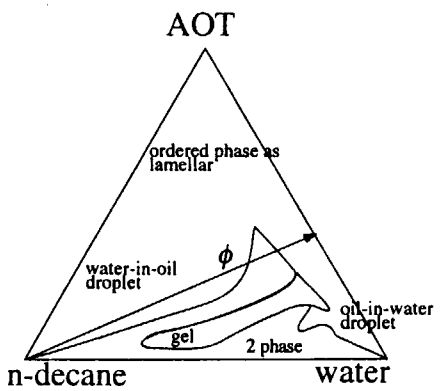


Figure 1: A triangle phase diagram of AOT, D_2O, and *n*-decane system at ambient temperature and pressure.

使用施設：JRR-3M，装置：SANS-U(C1-2)，分野 Softmatter

function of bulk and of film contrast as follows;

$$R(Q)=\frac{I^{\text{bulk}}(Q)}{I^{\text{film}}(Q)}=\frac{P^{\text{bulk}}(Q)}{P^{\text{film}}(Q)}. \qquad (6)$$

With this relation, we can determine the shape of droplets independent of $S(Q)$. Fit parameters are core radii r_c, thickness of droplet shell δ, and the root mean square deviation from the mean of droplet Δr ($\Delta r^2 = \langle r^2\rangle - \langle r\rangle^2$). The polydispersity index p is determined as $p=\Delta r/r_c$.

A SANS experiment at ambient temperature and pressure was done using SANS- U with 7Å of incident neutron beam. The covered Q range was $0.005\leq Q\leq 0.15$Å^{-1}. Mixtures of AOT/D_2O/decane, whose composition was $0.05\leq\phi\leq 0.75$ at water to AOT molar ratio being 32.5, was measured for both the bulk and film contrast.

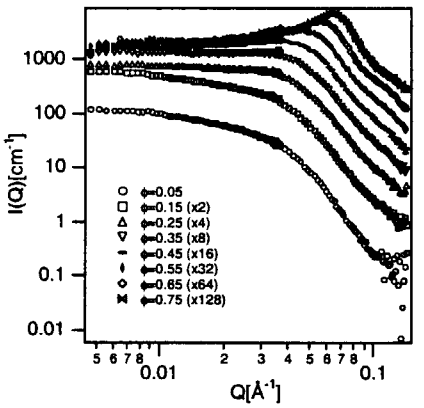


Figure 2: Observed SANS profile from bulk contrast. SANS profiles are shifted as shown in the legend.

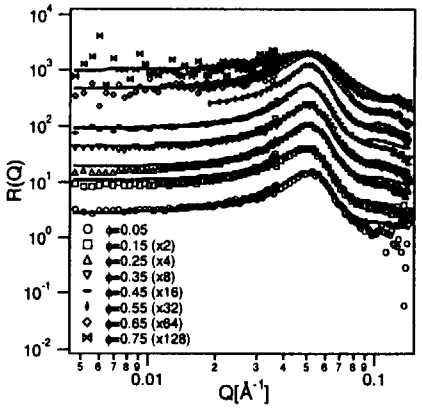


Figure 3: ϕ dependence of $R(Q)$, with shifts following to show in the legend for better visualization. Solid lines indicate fit result according to Eq. (6).

In Fig. 2, observed SANS profiles from bulk contrast samples are shown. With increasing ϕ, a pronounced peak due to the structure factor grew. Dividing SANS profiles of bulk contrast by those of film contrast, $R(Q)$ below ϕ=0.6 were almost the same as shown in Fig. 3. From this plot, it is clear that the droplet shape is unchanged below ϕ=0.6 and it deforms at ϕ>0.6. Solid lines indicated in Fig. 3 are fit result according to Eq. (6). Here, Gaussian form was used for the radius distribution function, $h(r)$. In Fig. 4 obtained fit parameters are shown. r_c and r_s (shell radius of droplet) were constant below ϕ=0.56, where the close-packed structure of spheres occupies, and it decreased above this value. On the other hand, p decreased below ϕ=0.56 monotonically and then it increased. Evaluated structure factor showed that at low ϕ region, the concentration fluctuation was dominant for $S(Q)$ and droplets were well aligned at high ϕ region.

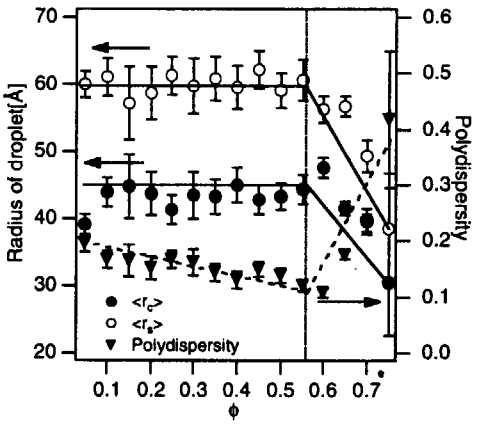


Figure 4: ϕ dependence of obtained fit parameters of droplet form factor. The droplet radius (both core and shell) did not change the size below ϕ=0.56. Above that the parameter dramatically changed. The polydispersity index decreased below the close-packed concentration and then deformation of droplet occurred above that concentration.

References

[1] E. Y. Sheu et al., Phys. Rev. A **39** (1989) 5867.
[2] H. Seto et al., J. Chem. Phys. **115** (2001) 9496.

1-5-18
研究テーマ：アルカン変化によるマイクロエマルジョンの構造変化及び圧力効果
表題：Aerosol-OT/水/ヘキサン系マイクロエマルションにおける温度圧力誘起相転移

Temperature and Pressure-Induced Phase Transition in Aerosol-OT, Water, n-Hexane Microemulsion System

M. Nagao, H. Seto*, Y. Kawabata*§, N. Yamada*, and T. Takeda*

*Institute for Solid State Physics, The University of Tokyo, 106-1 Shirakata, Tokai 319-1106, Japan; *Faculty of Integrated Arts and Sciences, Hiroshima University, 1-7-1 Kagamiyama, Higashihiroshima 739-8521, Japan*

An anionic surfactant AOT (Aerosol-OT; dioctyl sulfosuccinate sodium salt) is typical amphiphile forming a stable microemulsion mixing with water and oil. Because AOT has positive spontaneous curvature at room temperature, it forms water-in-oil type structure. With increasing temperature, the head-head repulsion increases due to the dissociation of counterion from head groups of AOT, and spontaneous curvature changes to negative. Thus, the structure of the system shows a sequence of a phase transition from w/o droplet (positive spontaneous curvature), to lamellar (zero curvature) and finally, to o/w droplet (negative) with elevating temperature. In the case of applying pressure, a pressure-induced phase transition from a dense w/o droplet to a lamellar structure has been observed in AOT, water, and *n*-decane system by means of small-angle neutron scattering (SANS). [1,2]

A measurement of dynamics by means of neutron spin echo (NSE) showed that temperature and pressure dependencies of bending elasticity of membranes were quite different, although static structure appeared were almost the same. [2,3] From these results we have concluded that pressure effects mainly affected to the packing property of tail of amphiphile molecules. Therefore, interactions among tail of amphiphile and oil molecules are quite important to understand nature of self-assembling in microemulsion system.

Eastoe et al. indicated that phase behavior obtained with changing the carbon number, C, of *n*-alkane showed different temperature and pressure dependence below and above C=5. [4] However, the origin of the different phase behavior is not clear.

In this report we demonstrated SANS results obtained in AOT/water/*n*-hexane (C=6) with almost the same composition of sample as previous results in AOT/water/*n*-decane. [1, 2]

A SANS experiment was conducted on SANS-U spectrometer of JRR-3M, JAERI, Tokai. Sample used is a mixture of 20 vol.% of AOT, 40 vol.% of water, and 40 vol.% of *n*-hexane. The incident neutron wavelength was 7.0Å with the wavelength distribution of about 10%, and the sample to detector distance was set to be 2m. The source aperture was 20mm$^{\phi}$ 4m apart from the sample position and the sample slit was 3mm$^{\phi}$. The covered momentum transfer, Q, was ranged over 0.014 to 0.14Å^{-1}. Temperature and pressure were controlled using a high-pressure cell for SANS. [5] Temperature and pressure range were from 298K to 333K and from 0.1MPa to 100MPa, respectively.

In Figure 1, obtained phase diagram in temperature and pressure plane is shown. The phase boundary between droplet phase and lamellar shows negative straight line and the slope indicates -2.6MPa/K. This value is quite different from the previous value (-1.7MPa/K) obtained in AOT / water / *n*-decane by means of SAXS. [6]

§present address: Department of Chemistry, Tokyo Metropolitan University, 1-1 Minamiosawa, Hachioji 192-0397, Japan

使用施設：JRR-3M，装置：SANS-U(C1-2)，分野 Softmatter

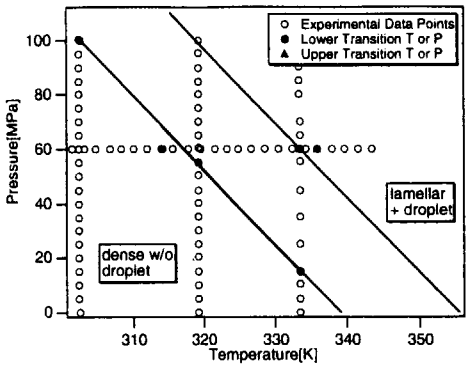


Figure 1: Obtained phase diagram in temperature-pressure plane in AOT/D_2O/*n*-hexane. Open circles were points experimentally accessed, and full circles and triangles obtained phase transition point, respectively. The slope is -2.6MPa/K.

In Fig. 2, pressure variation SANS profile is shown. With increasing pressure a phase transition from the dense w/o droplet to the lamellar structure can be clearly found as the case of decane as oil. In order to analyze such the profiles, we utilized Teubner and Strey model for a broad peak profile at lower Q originated from the dense w/o droplet, and a model proposed by Nallet et al. for a sharp peak profile at higher Q originated from the lamellar

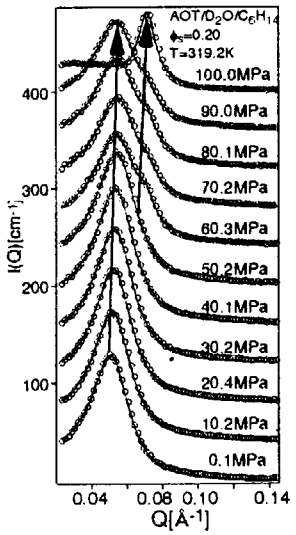


Figure 2: Obtained pressure variation SANS profile in AOT/D_2O/*n*-hexane. The same volume of water and oil was mixed with 20 vol.% of AOT. Temperature was set to be 319.2K. The broad peak appeared at Q~0.05Å^{-1} broaden with increasing pressure and finally at P=100MPa it was disappeared. A lamellar peak at Q~0.06Å^{-1} was appeared above P=50.2MPa.

structure. Fitting results to those equations are shown in Fig. 2 as solid lines.

From the fitting to those theoretical models, we can obtain the mean repeat distance d and the correlation length ξ for both dense droplet phase and lamellar phase. A pressure dependence of d is shown in Fig. 3(a) for 3 temperature conditions, and temperature dependence is shown Fig. 3(b). This showed that the phase behavior with varying temperature and pressure in the system is almost the same as the case of *n*-decane as oil.

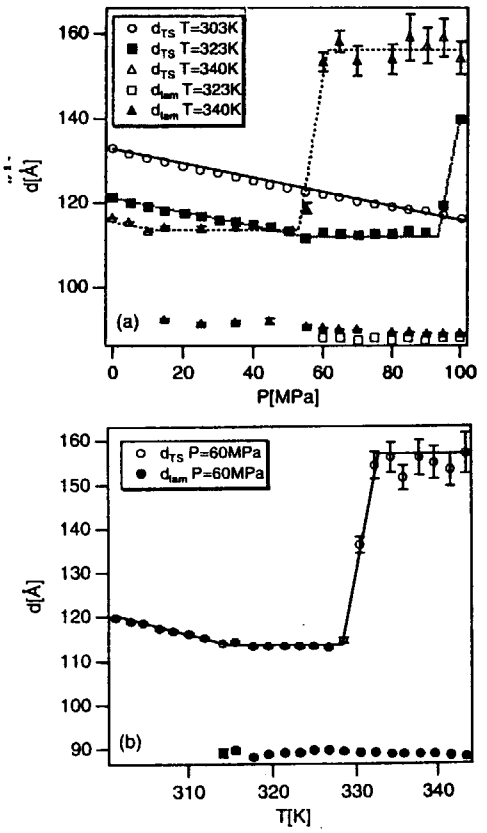


Figure 3: (a) Pressure and (b) temperature dependence of d.

References

[1] M. Nagao and H. Seto, Phys. Rev. E **59**, 3169 (1999).
[2] M. Nagao et al., J. Chem. Phys. **115**, 10036 (2001).
[3] Y. Kawabata, et al., Appl. Phys. A in press.
[4] J. Eastoe et al., J. Chem. Soc. Faraday Trans. **86**, 511 (1990).
[5] H. Takeno et al. Polymer J. **29**, 931 (1997).
[6] H. Seto et al., J. Chem. Phys. **112**, 10608 (2000).

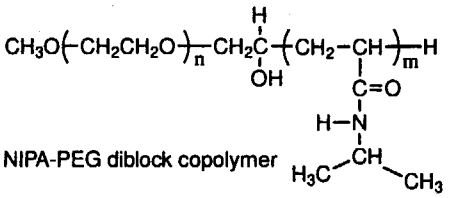
研究テーマ：水溶性ジブロック共重合体の相挙動と自己秩序化
表　題：中性子小角散乱による NIPA-PEG ジブロック共重合体の熱的相挙動に関する研究
1-5-19

Small-angle Neutron Scattering Study on Thermal Phase Behavior of NIPA-PEG Diblock Copolymer

Ryuuhei Motokawa, Masahiko Annaka, and Satoshi Koizumi[1]

Department of Materials Technology, Chiba University, Inage-ku, Chiba 263-8522, Japan
[1]Advanced Science Research Center, Japan Atomic Energy Research Institute, Tokai-mura, Ibaraki 319-1195, Japan

The self-aggregation of block copolymers has attracted much attention both for its intrinsic scientific interest and for its technological importance. We prepared the block copolymer consisting of poly(N-isopropylacrylamide) and poly(ethylene glycol) (NIPA-*b*-PEG) by using ceric ammonium nitrate (IV) as a redox initiator. NIPA polymer is one of the most studied thermo-reversibility responsible polymer which shrinks dramatically in water around 33°C, which is attributed to the microscopic Coil-Globule transition. Therefore NIPA-*b*-PEG aqueous solution shows unique phase behavior with varying temperature.



An aqueous solution of the block copolymer above a critical concentration experience three distinct phases upon heating. One of the phases is a Gel phase that shows reversibility in Sol-Gel transition without noticeable synerisis. The phase behavior is determined by various factors, i.e. the block ratio, the concentration and temperature. Thus PEG rich block copolymer solution can form transparent Gel comprehensively, though NIPA rich form only an opaque Gel. The Gel causes phase separation for strong aggregation of NIPA rich domain further increasing temperature.

We employed pinhole small angle neutron scattering (PSANS) in order to investigate the microscopic structure for NIPA-*b*-PEG in D_2O with spectrometer SANS-J at JAPAN Atomic Energy Research Institute in Tokai. The details for PSANS measurement samples are shown in Table 1. For PSANS measurements, we used a wavelength of 0.65 nm with $\Delta\lambda/\lambda = 14\%$ and two detector positions of 1.5 and 10 m, and q-profiles are obtained gradually increasing temperature from 10°C to 34°C.

Table 1: Sample characteristics.

No.	Block ratio (m:n)	Conc. % (w/v)	M_n	M_w / M_n
1	2 : 1	7	30000	1.23
2	1 : 3	5	9200	1.20

At lower temperature below 20°C, Ornstein-Zernike (OZ) type scattering, which is typical for the semi-dilute polymer solution, was observed. It is interesting to note that excess scattering was observed in addition to OZ-type scattering component in a q-region of $q \leq 0.3$ nm^{-1} above 17°C in spite of Sol state. This excess scattering cannot observe for NIPA homopolymer and NIPA Gel in swelling state. We consider that NIPA and PEG chains segregate with themselves for increasing hydrophobicity of NIPA segment, and the microscopic structure will affect gelation mechanism and structure around high temperature region.

The OZ-type scattering is characterized by two parameters of the forward scattering in-

原子炉：JRR-3M　　装置：SANS-J(C3-2)　　分野：中性子散乱（高分子）

tensity I(q=0) and a correlation length ξ. Figure 1 shows a plot of I(q=0)$^{-1}$ and ξ^{-2} vs inverse absolute temperature 1/T. The Excess scattering (shadow region) was observed above the vicinity of 17°C. We can guess the OZ-type scattering component parameters I(q=0)$_{OZ}^{-1}$ and ξ_{OZ}^{-2} by estimating their along the dashed line level from 17°C to 22°C in Figure 1, because of I(q=0)$_{OZ}^{-1}$ and ξ_{OZ}^{-2} are proportional to inverse absolute temperature in mean field theory. Therefore we can decompose PSANS profiles into OZ-type scattering component and excess scattering component by subtracting the guessed OZ-type scattering component from measurement PSANS profile.

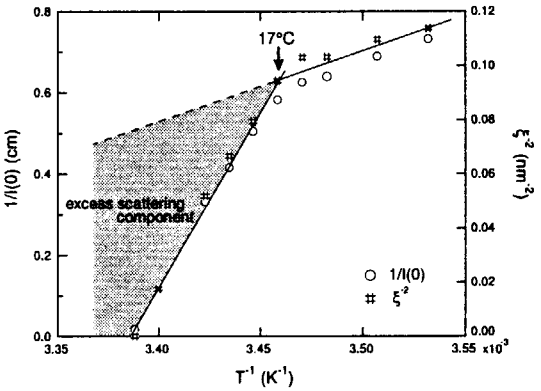


Figure 1: Temperature dependence of inverse forward scattering intensity and squared inverse correlation length, which were estimated by using a so-called OZ-plot for sample No. 1.

Figure 2 shows the decomposition results for PSANS profiles with sample No.1. The excess scattering component was analyzed by adapting the Debye-Bueche (DB) theory of scattering for a heterogeneous system to the case of polymer solution, which is contribution from long-range concentration fluctuations appear in inhomogeneous solutions. The spatial scale of the density fluctuations due to inhomogeneous is estimated by the correlation length ζ_{DB} in DB theory. The two different correlation lengths for fitting parameters (ξ_{OZ} and ζ_{DB}) listed in Table 2. We think that variation trend of the parameter ζ_{DB} is not consistent with Sample No.1. and No.2., because of the NIPA-PEG segregation morphology is different with two samples.

On the other hand, in gel and demixing state we discussed the observed power-low q-behaviors based on the mass and surface fractals and Porod low. Above 30°C, Porod (q^{-4}) region was shown that is the scattering for reflecting on the microstructure of aggregated NIPA rich domain. The two phases surface structure was characterized by Porod plot and we estimated the characteristic interface thickness and the specific surface area. Details will be discussed in future.

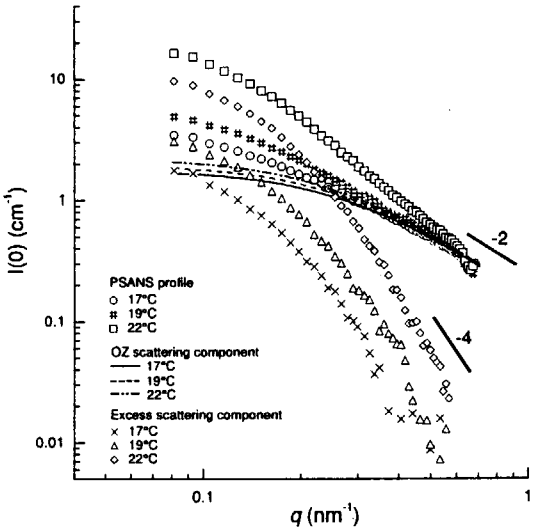


Figure 2: Decomposition of PSANS profiles into OZ-type scattering component and excess scattering component for sample No. 1.

Table 2: Summary of two correlation lengths.

	Sample No. 1		Sample No. 2	
Temperature (°C)	ξ_{OZ} (nm)	ζ_{DB} (nm)	ξ_{OZ} (nm)	ζ_{DB} (nm)
17	3.3	7.0		
18	3.4	6.4	2.9	5.7
19	3.4	6.4		
20	3.6	6.3	3.0	5.7
22	3.6	6.3	3.1	6.4

研究テーマ：先端偏極中性子散乱によるスピン-格子物性の研究
表　題：ポリスチレン／ポリビニルメチルエーテル混合系の相図および動的対称-非対称境界
1-5-20

Phase Diagram for Polystyrene/Poly (vinyl methylether) Blend and Dynamical Symmetry-Asymmetry Crossover Line

Satoshi Koizumi and Hiroyuki Takeno[1]

Advanced Science Research Center, JAERI, Tokai, Ibaraki 319-1195, Japan
[1]Faculty of Engineering, Gunma Univeristy, Kiryu, Gunma, 376-8515, Japan

The polymer blend of polystyrene (PS)/poly (vinyl methylether) (PVME) is characteristic to have a large contrast of glass transition temperature T_g , i.e., T_g for PS or PVME is $T_{g,PS} = 100°C$ or $T_{g,PVME} = -22°C$, respectively. Simultaneously, this blend has a phase diagram of the lower critical solution temperature (LCST) for its mixing behavior, where a critical point is about $145°C$, for the blend with symmetric molecular weights of $M_n = 50K$. Therefore, two T_g's for PS and PVME appear in a single phase. A calorimetric measurement by DSC determines a single glass transition temperature for the blend $T_{g,mix}$, which appears somewhere in a single phase.

The concenpt of dynamical asymmetry, on the other hand, is recently introduced in order to explain the vicoelastic effect observed in the two components system. [2] Originally the dynamical asymmetry is attributed to the difference in size between two components. For example, the blend of polymer/solvent or colloid/solvent belongs to this group. Even for a blend with identical molecular sizes between two components, if there is one-sided interactions among identical molecules, again we can find the dynamical asymmetry in the blend. The polymer blends with a large contrast of T_g belongs to this second group of dynamical asymmetry, changing a degree of asymmetry as temperature changes (thermoreversible dynamical asymmetry).

In the case of PS/PVME blend, in a temperature region higher than $T_{g,PS}$, PS and PVME chains are free from vitrification, showing the dynmical symmetry between two components. However, the thermo-reversible dynamical asymmetry appears as temperature decreases into an intermediate temperature region between $T_{g,PS}$ and $T_{g,mix}$. The thermal cocentration fluctuations, inducing PS-rich or PVME-rich regions, accelarate the dynamical asymmetric picture; PS-rich regions relax more slowly and PVME-rich regions relax faster. The characteristic length scale for the dynamical asymmetry might be in a same order of the correlation length ξ of the thermal concentration fluctuations.

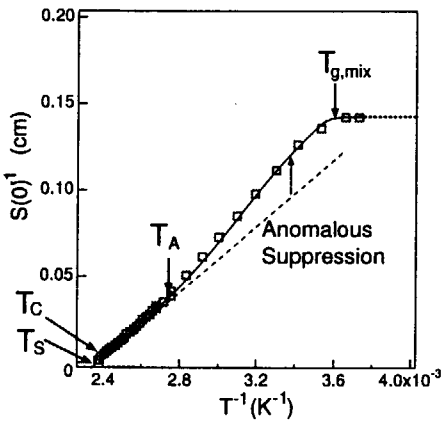


Figure 1: Forward Scattering $S(q = 0)$ for d-PS/PVME (50/50) blend determined according to a Ornstein-Zernike formalism.

According to this motivation, by small-angle neutron scattering (SANS), we tried to determine a dynamical symmetry-asymmetry crossover, which should appear somewhere in a single phase. Deuterated polystyrene (d-PS) was employed in order to have a strong scattering contrast for neutron scattering. The molecular weights of d-PS and PVME are about 50K. We performed SANS measurements over a wide temperature-range in a sin-

原子炉：JRR-3M　　装置：SANS-J(C3-2)　　分野：中性子散乱（高分子）

gle phase from above $T_{g,PS}$ to $T_{g,mix}$. Forward scattering intensity $S(q=0)$ was determined from a small q-region according to a Ornstein-Zernike formalism.

Figure 1 shows the results for the blend of a volume fraction of PS, $\phi_{PS} = 0.5$. In a temperature region higher that T_g for pure PS, inverse of forward scattering intensity $S(q=0)^{-1}$ is well reproduced by using a random phase approximation model (RPA) with a same interaction parameter χ ($\sim A+B/T$). However for the blend of $\phi_{PS} = 0.5$ below about $80°C$, $S(q=0)$ is suppressed anomalously more than expected from the higher temperature region, which was already reported in ref.2. The anomalous suppression becomes more obvious as temperature decreses more, or as PS becomes richer in the blend. Finally at T=$T_{g,mix}$, $S(q=0)$ freezes and dose not show temperature-change anymore.

We attribute this anomalous suppression to appearance of thermo-reversible dynamical asymmetry. In order to explain our idea, we introduce a viscoelastic network-like region richer-in PS, asisted by thermal concenrations fluctuations with a correlation length ξ. In this network-like region, polymer chains moves cooperatively and more slowly as compared with a PVME-richer region. In the temperature region below $80°C$ but still above $T_{g,mix}$, the relaxational modulus $G(t)$ originated from this network-like domains becomes non-decaying and have a life time longer than the characteristic relaxational time of the thermal concentraion fluctuations without a vitrification effect. In such a case, the non-decaying modulus G shifts a critical point to higher temperature (Cahn's Discussion). [3] Therefore, $S(q=0)$ apparently suppressed more than expected in case without non-decaying G. On a basis of this discussion, we define the crossover temperature of dynamical symmetry-asymmetry T_A as the temperature from which $S(q=0)^{-1}$ deviates from a linear decrease according to T^{-1} observed in a higher temperature region.

Figure 2 shows the phase diagram of the PS/PVME blend, indicating a spinodal point

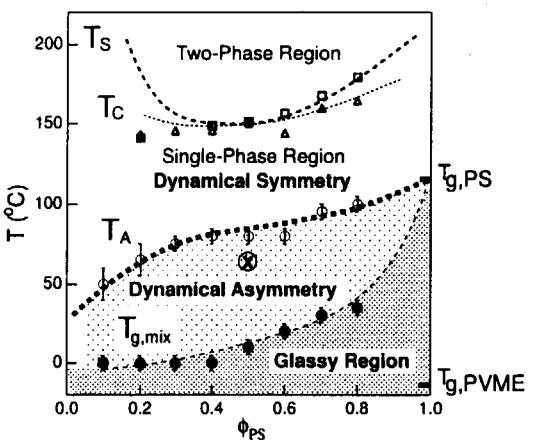


Figure 2: Phase Diagram for the d-PS/PVME blend, showing a spinodal point T_s, a cloud point T_C and a calorimetric glass transition temperature T_g, mix. Dynamical crossover line from symmetry to asymmetry is also included.

T_s, a cloud point T_c and the calorimetric glass transition temperature for the blend $T_{g,mix}$. In Figure 2, we further add the crossover line from dynamical symmetry to asymmetry T_A in this phase diagram. The temperature T_A slightly decreases as a volume fraction of PS decrease. If we induce a shear-field to the blend just below T_A, as marked by a crossed circle for $\phi_{PS} = 0.5$, we could observe an abnormal butterfly pattern as a shear-induced phase separation. [4]

References

1) S. Urakawa et al. Koubunnsi-Kakou, **vol.51**, 202 (2002).
2) D. Schwahn et al. J. Chem. Phys. **87**, 6078 (1987); H. Tekeno, S. Koizumi et al. Macromolecules **29**, 2440 (1996).
3) private discussion with prof. Kawakatsu.
4) S. Koizumi et al in preparation.

研究テーマ：相溶性高分子混合系における動的不均一と濃度揺らぎの関係
表題：ポリスチレン/ポリビニルメチルエーテル混合系の非干渉性弾性散乱
1-5-21

Elastic incoherent structure factors for poly(styrene) and poly(vinyl methyl ether) mixtures

H. Takeno and S. Koizumi[1]

Department of Biological and Chemical Engineering, Faculty of Engineering, Gunma University, Gunma 376-8515
[1]Japan Atomic Energy Research Institute, Tokai, Ibaraki 319-1195

We investigated elastic structure factors for poly (styrene) (PS) and poly(vinyl methyl ether) (PVME) mixtures by use of low energy triple axis spectrometer (LTAS). Because of large incoherent scattering cross-section of hydrogen atom, we mainly observed the elastic incoherent structure factor (EISF) due to the hydrogen atom. In this study, we try to pursue the local motion of the system through EISF due to the hydrogen atoms. We used four samples such as neat PVME, deuterated PS (dPS) and PVME mixture, protonated PS (hPS) and PVME mixture, and neat hPS. If the motion of the system is vibrational, the $\vec{q}$ dependence of EISF is described by the Debye-Waller factor, i.e., $S(\vec{q},\omega=0) \sim \exp(-<u^2>q^2)$, where the quantity $<u^2>$ is the mean square displacement and $q\left(=\frac{4\pi}{\lambda}\sin(\frac{\theta}{2})\right)$ is the magnitude of the scattering vector $\vec{q}$. However, even at low temperature of ca. 10 K, the observed scattering did not obey the Debye-Waller representation and had a peak corresponding to the coherent scattering for all the samples. This result suggests that the effect of the coherent scattering is not negligible. Therefore, in order to reduce the effect of the coherent scattering from the observed scattering, we evaluated $<u^2>$ by using the same procedure as that carried out by Kanaya et al.[1] Namely, we divided it by the scattering at the lowest temperature (ca.10 K). And from plot of the logarithm of the divided intensity $\ln\left[S(\vec{q},\omega=0)_T/S(\vec{q},\omega=0)_{T=ca.10K}\right]$ against q^2, we obtained $<u^2>$ at each temperature. Figure 1 shows the temperature dependence of $<u^2>$ for each sample. $<u^2>$'s of neat PVME and dPS/PVME linearly increase with increase of temperature below 90 K. Above 90 K, they deviate upwards from linear relationship. The quantity $<u^2>$ for hPS shows linear relation against temperature below 200 K and deviates from the linearity above it. On the other hand, the $<u^2>$ for hPS/PVME appears to deviate from linear relationship at both temperatures of 90 K and 200 K. Thus, for dPS/PVME we see the motion of PVME, while for hPS/PVME we see both the motions of hPS and PVME. In comparison of the $<u^2>$ of PVME with that of dPS/PVME, the $<u^2>$ for the latter is larger than that for the former, indicating PVME in the mixture moves in larger space or with larger free volume. This result supports our "interstices model" in the miscibility and glass transition temperature behaviors for this mixture.[2]

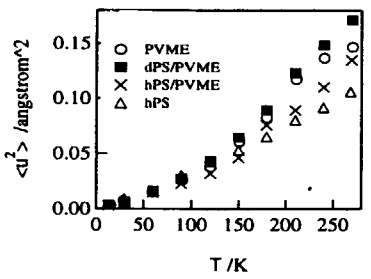


Figure 1: Temperature dependence of mean square displacement for various samples.

References

1) T. Kanaya , T. Kawaguchi, and K. Kaji, J. Chem. Phys., **104**, 3841 (1996)

2) M.Naoki and H. Takeno, to be submitted.

原子炉：JRR-3M　　装置：LTAS(C2-1)　　分野：中性子散乱（高分子）

研究テーマ：相溶性高分子混合系における動的不均一と濃度揺らぎの関係
表題：ポリスチレン/ポリビニルメチルエーテル混合系の小角中性子散乱と誘電研究
1-5-22

Small-angle neutron scattering and dielectric studies on poly(styrene) and poly(vinyl methyl ether) mixtures

H. Takeno, M. Kobayashi, M. Naoki and S. Koizumi[1]

Department of Biological and Chemical Engineering, Faculty of Engineering, Gunma University, Gunma 376-8515
[1]Japan Atomic Energy Research Institute, Tokai, Ibaraki 319-1195

By using small-angle neutron scattering (SANS) and dielectric spectroscopy techniques, we investigated the static mixing behaviors and local molecular motions for poly(styrene) (PS) and poly(vinyl methyl ether) (PVME) mixtures. From SANS measurements, we can obtain the interaction parameter between different components χ, which is a key parameter to understand miscibility of polymer mixtures. However, the χ parameter obtained by SANS is believed to include all factors which influence the miscibility of polymer mixtures, and the physical content is ambiguous. On the other hand, dielectric spectroscopy measurements can give information on the local molecular motion such as side group motion. In this study, by combining SANS and dielectric spectroscopy techniques, we try to understand the physical content of the χ parameter in terms of local molecular motions.

We used two kinds of PVME samples, one of which was purchased from Aldrich (coded as PVME-no6) and the other is from Scientific Polymer Products (coded as PVME-sp2). We evaluated the χ/v_0 for deuterated PS (dPS) and PVME mixtures by a best fit to SANS data in the single phase state with theoretical curve obtained by de Gennes[1)], where v_0 is the reference volume. Figure 1 shows plot of the χ/v_0 against reciprocal temperature for dPS/PVME-no6 and dPS/PVME-sp2. The χ/v_0 increases with decrease of reciprocal temperature, i.e., increase of temperature, indicating the system has a lower critical solution temperature (LCST) type of phase diagram. The χ/v_0 value for dPS/PVME-no6 mixture is larger than that of dPS/PVME-sp2 mixture. If we compare composition dependence of the χ/v_0 for dPS/PVME-no6 mixture at a constant temperature, then the χ/v_0 has a minimum at (70/30) or (80/20) mixture. For dPS/PVME-sp2 the χ/v_0 monotonically decreases with increase of content of PS. The latter result is consistent with the SANS results by Han et al.[2)]

On the other hand, in the dielectric measurements, a local molecular motion of PVME (β_s process), which may be related to side group motion, was found to be largely affected by blending PS, i.e., the dielectric loss peak shifts toward high temperature. Thus, side groups of PVME is predicted to strongly correlate with PS. Moreover, the magnitude of the shift significantly depends on the composition. We compare the composition dependence of the χ/v_0 obtained by SANS with that of relaxation time τ for the β_s process in the dielectric spectroscopy measurements. We estimated the difference between the temperature position at a given τ value (log τ = -4 and -4.5) in the β_s process of PVME and that of the mixture, $\Delta T_{\beta s}$. Figure 2 shows comparison between the composition dependence of the χ/v_0 and that of β_s. Interestingly, there is a strong correlation between the χ/v_0 and $\Delta T_{\beta s}$. If we see dPS/PVME-no6 mixture, $\Delta T_{\beta s}$ is found to increase, when the χ/v_0 decreases. Moreover, $\Delta T_{\beta s}$ has a maximum around stoichiometric mixture in the repeating units, while the χ/v_0 has a minimum at almost the same composition. Both results indicate that correlation between PVME and PS is the strongest at the same composition. Thus, side groups

原子炉：JRR-3M　　装置：SANS-J(C3-2)　　分野：中性子散乱（高分子）

of PVME are considered to play an important role in miscibility of this mixture. Dielectric measurements for PS/PVME-sp2 mixture are in progress now.

References

1) P. G. de Gennes, *Scaling Concepts in Polymer Physics* (Cornell University: Ithaca, NY, 1979).

2) C. C. Han, B. J. Bauer, J. C. Clark, Y. Muroga, Y. Matsushita, M. Okada, Q. Tran-Cong, T. Chang and I.C. Sanchez, Polymer, **29**, 2002 (1988).

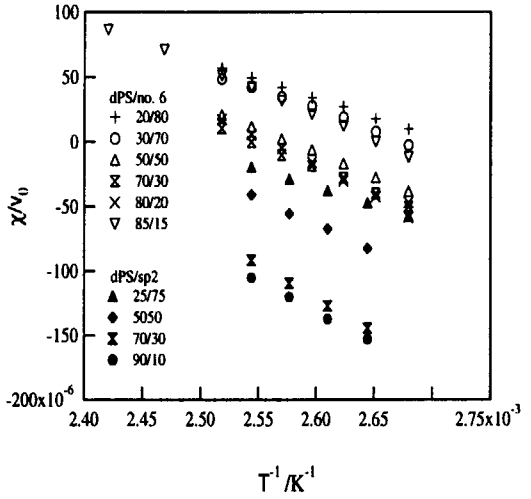


Figure 1: Temperature dependence of the χ/v_0 parameter for dPS/PVME-no6 and dPS/PVME-sp2.

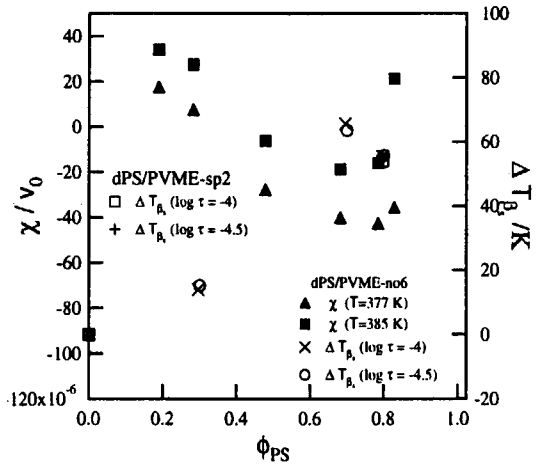


Figure 2: Comparison between composition dependence of the χ/v_0 estimated by SANS and that of the difference between the temperature at a given relaxation time (log τ = -4 and -4.5) for neat PVME and that of mixtures.

研究テーマ：中性子小角散乱法による高分子構造変形のその場観察
表　題：中性子小角散乱による長鎖分岐を持つポリエチレンの研究
1-5-23

Small-Angle Neutron Scattering Study of Long-Chain Branched Polyethylenes

Tatsuya KASAHARA, Takashi SAKURAI, Takeshi FUJII and Satoshi KOIZUMI[1]

Sumitomo Chemical Co., Ltd. Petrochemicals Research Laboratory, 2-1 Kitasode Sodegaura, Chiba 299-0295, Japan
[1]ASRC, Japan Atomic Energy Research Institute, Tokai, Ibaraki 319-1195, Japan

In order to investigate a blending effect of a little number of long branchings of polyethylene in a molten state, we employed small-angle neutron scattering (SANS) with a spectrometer SANS-J at JRR-3M reactor of JAERI. A heating cell, filled with nitrogen gas to avoid thermal degradation, was installed on SANS-J to heat sample specimens. To get a strong scattering contrast for SANS, we specially prepared mixtures of hydrogenous polyethylenes (H-PEs) and a deuterated high-density polyethylene (D-HDPE). Measuring temperatures were 125 and 160°C or 125 and 150°C for the mixture with a H-PE-fraction of 0.2 or 0.5, respectively. The melt structure of the long chain branched linear low-density polyethylene (LCB-LL) in the D-HDPE was compared with that of other H-PEs in the D-HDPE.

Table 1: Characteristics of materials

	Mw	Mn	Br*/1000C
LLDPE	88000	44000	17.8
LCB-LL	74800	34800	20.6
LDPE	60700	18900	20.7**
D-HDPE	100400	24300	-

*: The number of short-chain blanching
**: The number of CH_3

The LCB-LL has a little number of long-chain branchings. The number of long-chain branchings of the LCB-LL is 1.32 a molecule on the average. A linear low-density polyethylene (LLDPE) and a low-density polyethylene (LDPE) that has a large number of long-chain branchings were selected as miscible H-PEs with the D-HDPE. Those were reported in references [1] and [2].

H-PEs and the D-HDPE were mixed by using xylene. D/H composition of blend samples were 80/20 and 50/50. Characteristics of H-PEs and the D-HDPE that were used in this study are shown in Table 1. The LLDPE (EXACT 3030) was purchased from ExxonMobil Chemical Company. The LCB-LL (AFFINITY PF1140) was purchased from The Dow Chemical Company. The LDPE (SUMIKATHENE F200-0) was supplied by Sumitomo Chemical Co., Ltd.

The SANS profiles of the mixtures of D-HDPE/LLDPE and D-HDPE/LDPE in a melt state show an asymptotic decrease according to q^{-2}, over a whole q-region detected by SANS (Figure 1, 2). These asymptotic q-behavior of q^{-2} originate from a local segmental distribution in a Gaussian chain. This results indicate that the LLDPE and the LDPE mixes with the D-HDPE on a molecular length scale.

On the other hand, the profile of the D-HDPE/LCB-LL exhibits two q-regions; in a lower q-region, close to q^{-4} and in a higher q region close to q^{-2}, respectively (Figure 3). The q-behavior of q^{-4} originates from an interfacial structure of phase-separated macrodomains between LCB-LL and D-HDPE (Porod law).

The LCB-LL has about the same number of short-chain branching and is about the same of molecular weight with the LLDPE. Therefore the LCB-LL was estimated to have similar misciblity with the D-HDPE to the

原子炉：JRR-3M　　装置：SANS-J(C3-2)　　分野：中性子散乱（高分子）

LLDPE. However the LCB-LL showes the worse miscible than the LLDPE. Furthermore the LCB-LL had worse miscible than the LDPE that had a lot of long-chain branching.

These results indicate that just a little number of long-chain branching has remarkable effect on the miscibility of polymers.

References

1) K. Tashiro, K. Imanishi, M. Izuchi, M. Kobayashi, Y. Itoh, M. Imai Y. Yamaguchi, M.Ohashi, and R. S. Stein. : Macromolecules **28** (1995) 8484.
2) R. G. Alamo, W. W. Graessley, R. Krishnamoorti, D. J. Lohse, J. D. Londono, L. Mandelkern, F. C. Shehling, and G. D. Wignall. : Macromolecules **30** (1997) 561.

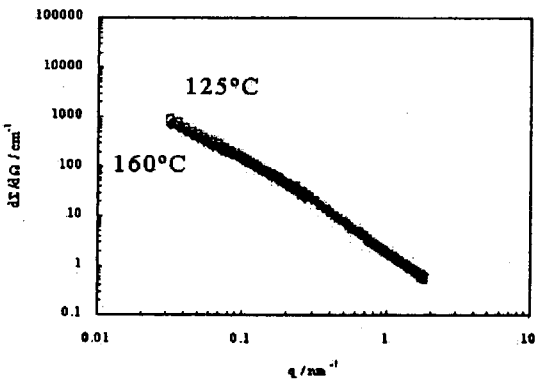


Figure 1: Logarithmic plot of SANS profiles obtained for D-HDPE/LLDPE (80/20) (diamonds at 160°C and squares at 125°C, respectively).

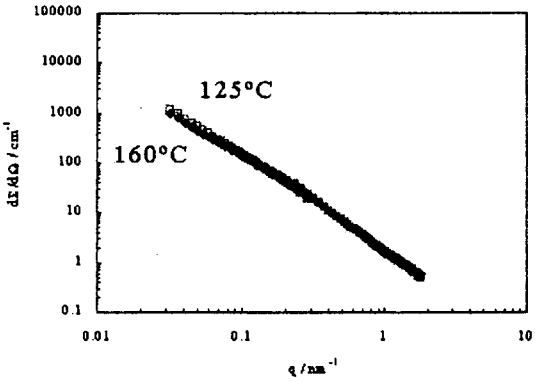


Figure 2: Logarithmic plot of SANS profiles obtained for D-HDPE/LDPE (80/20) (diamonds at 160°C and squares at 125°C, respectively).

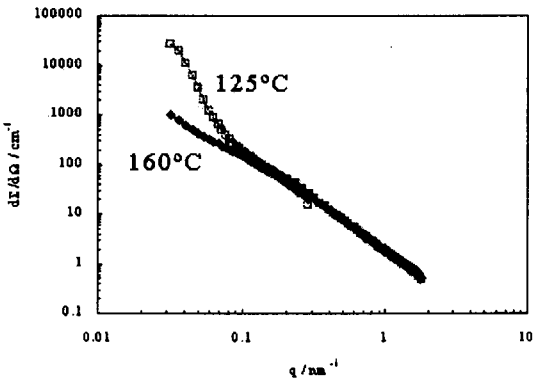


Figure 3: Logarithmic plot of SANS profiles obtained for D-HDPE/LCB-LL (80/20) (diamonds at 160°C and squares at 125°C, respectively).

1-5-24

研究テーマ：リン脂質膜のラメラ構造の圧力依存性

表題：リン脂質 DPPC 水溶液/エタノール系の圧力誘起相転移

Pressure-induced interdigitation of DPPC aqueous solution with small amount of ethanol.

H. Seto[1], H. Nobutou[2], N. Yamada[2], M. Nagao[3], D. Ihara[2] and T. Takeda[1]

[1]*Faculty of Integrated Arts and Sciences, Hiroshima University, Higashihiroshima 739-8521, Japan*

[2]*Graduate School of Biosphere Science, Hiroshima University, Higashihiroshima 739-8521, Japan*

[3]*Institute for Solid State Physics, The University of Tokyo, Tokai 319-1106, Japan*

An aqueous dispersion of dipalmitoyl-sn-glycero-3-phosphatidylcholine (DPPC) exhibit a rich structural polymorphism depending on their environmental conditions such as temperature and pressure. A fluid lamellar phase (L_α) is a basic structural element of biological membranes characterized by lipid bilayers. Two thermotropic lamellar phase transition have been observed below the fluid lamellar phase; a gel-to-gel (L_β'/ P_β') pretransition and a gel-to-liquid crystalline (P_β'/L_α) main transition. In the gel phases, the lipophilic chains of phospholipid molecules are extended and ordered, whereas the chains are conformationally disordered in the fluid lamellar phase. By applying pressure up to about 150 MPa, it transforms to an interdigitated gel phase ($L_{\beta I}$). This structure is the same as the one induced by adding ethanol, [1] however, the microscopic origins of these transitions must not be the same. [2]

The purpose of the present small-angle neutron scattering (SANS) experiment at SANS-U is to clarify the effect of pressure on phospholipids. Because the maximum pressure of our high-pressure cell was about 100 MPa, we prepared aqueous solutions of DPPC with adding small amount of ethanol (between 0.7 M and 1.2 M) in order to decrease the phase transition pressure. [3]

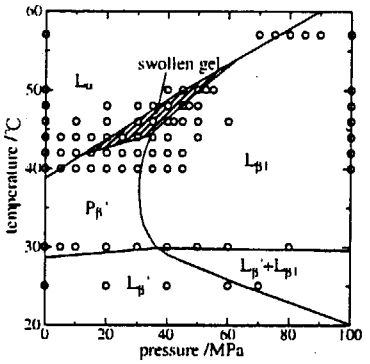


Fig. 1 T-P phase diagram of DPPC / D_2O / C_2H_5OH. Open circles indicate mesured points.

Comprehensive set of SANS profiles of these solutions were collected in the range of $25 \leq T \leq 60$ °C and $0.1 \leq P \leq 100$ MPa. Figure 1 is a phase diagram determined by the present experiment. Observed SANS profiles were analyzed using the model proposed by Lemmich *et al.* [4] It was confirmed that the pressure-induced phase is the interdigitated phase ($L_{\beta I}$) from the thickness of phospholipid layers. (See Table I.)

A new phase, in which a large single peak appeared at around $Q = 0.07$ Å^{-1} was found at $45 \leq T \leq 55$ °C and $15 \leq P \leq 60$ MPa, being among P_β', L_α and $L_{\beta I}$ phases. The observed

使用施設：JRR-3M, 装置：SANS-U(C1-2), 分野：Softmatter

Table I. Thickness of phospholipid layers at each phase.

phase(condition)	thickness / Å
L_α (42°C, 0.1MPa)	43.5
P_β' (30°C, 0.1MPa)	47.3
L_β' (25°C, 0.1MPa)	47.1
$L_{\beta I}$ (42°C, 100MPa)	32.7
swollen gel (48°C, 40MPa)	47.5

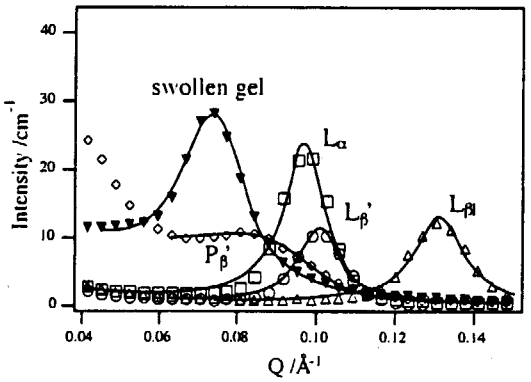


Fig. 2 Typical SANS profiles of L_α (squares), L_β' (circles), P_β' (diamonds), $L_{\beta I}$ (triangles), and the swollen gel phase (full triangles).

SANS profiles of this phase is shown in Fig. 2 comparing with profiles of other phases. The characteristic repeat distance of this phase was about 90 Å, which was 1.3 times larger than that of P_β' phase. The thickness of phospholipid layers of this phase was estimated to be 47.5 Å, which was almost the same as those of L_β' and P_β'. Thus, here we characterize this new phase as a swollen gel phase; only the amont of interlamellar water increases, and the structure of the phospholipid bilayer is the same as that of the P_β' phase.

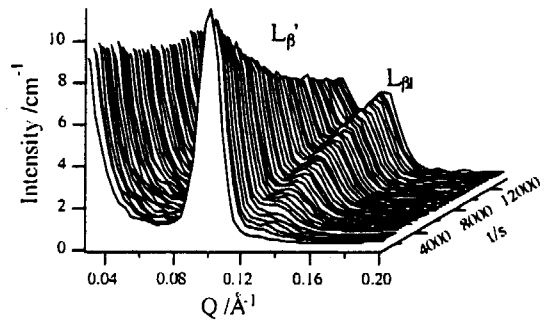


Fig. 3 Time evolution of SANS profile when the pressure was jumped from 60 MPa (L_β' phase) to 70 MPa ($L_{\beta I}$ phase) at T = 28 °C.

The kinetics of the phase transition to the $L_{\beta I}$ phase was investigated by using the time-resolved SANS on pressure-jump. The measurements were done at T = 27 °C (from L_β' to $L_{\beta I}$), 40, 42 °C (from P_β' to $L_{\beta I}$) and 48, 50 °C (from the swollen gel phase to $L_{\beta I}$). In Fig. 3, a typical time-evolution of the SANS profile is shown. The growing process of the interdigitated phase was characterized by a two-state mechanism; the Bragg reflection of a low-pressure phase shrinked, while the peak from the $L_{\beta I}$ phase increased. From the time dependences of the peak intensities, a relaxation time of the phase transition was estimated. At all the conditions, it was larger than 500 sec. This result indicates that the transition process to the $L_{\beta I}$ phase is much slower than the transitions to the other structures. [5]

References

[1] T. Adachi, H. Takahashi, K. Ohki and I. Hatta, Biophys. J., **68** (1995) 1850.

[2] R. Winter and W. –C Pilgrim, Ber. Bunsenges. Phys. Chem., **93** (1989) 708.

[3] S. Kaneshina, K. Tamura, H. Kawakami and H. Matsuki, Chem. Lett. (1992) 1963.

[4] J. Lemmich, K. Mortensen, J. H. Ipsen, T. Hønger, R. Bauer, O. G. Mouritsen, Phys. Rev. E. **53** (1996) 5169.

[5] J. Erbes, A. Gabke, G. Rapp, and R. Winter, Phys. Chem. Chem. Phys., **2** (2000) 151.

This is a blank page.

1. 中性子散乱 6) 生物学

1. Neutron Scattering 6) Biology

This is a blank page.

研究テーマ：光合成色素膜タンパク質複合体の構造解析
表題：光捕集複合体のオリゴマー構造

1-6-1

Oligomeric forms of the light-harvesting complexes from photosynthetic bacteria

Z.-Y. Wang, Y. Muraoka, M. Shimonaga, and T. Nozawa
Department of Biomolecular Engineering, Faculty of Engineering, Tohoku University, Sendai 980-8579 Japan

Light-harvesting (LH) complex serves as a highly efficient molecular machinery for the collection and transfer of solar energy to photochemical reaction centers in photo-synthetic organisms. In purple photosynthetic bacteria, the LH complexes are classified into either of two major types, namely, the core (LH1) and peripheral (LH2) complexes, both comprising two small polypeptides α and β along with bacteriochlorophyll (BChl) and carotenoid molecules. Several resolved LH2 complexes reveal an annular structure of 9 or 8 αβ heterodimers, while electron projection structures from 2D crystals show that the LH1 complexes are composed of larger rings than LH2 containing 16 αβ subunits. The LH1 complex is characterized by a near-infrared absorption at approximately 880 nm (referred to as B880) in detergent *n*-octyl β-D-glucopyranoside(OG). In this study, we report the preliminary results of characterization of the B880 complexes dissolved in deuterated OG using SANS and compare with the calculated scattering profiles and radius of gyrations of the LH2 complexes.

SANS measurements were conducted at room temperature (~22°C) with SANS-U(C1-2) at JRR-3M. Neutron wavelength was 7Å. Both native and carotenoidless B880 complexes from *Rhodospirillum rubrum* were dissolved in 1% deuterated OG solution (D_2O). The SANS data were analyzed by using standard Guinier procedure. Calculations of the scattering profiles and radius of gyration for the LH2 complexes were carried out using the CRYSON program.[1]

Figure 1 shows the scattering profiles of native B880 and carotenoidless(B873) LH1 complexes. From small q range measurement, the radius of gyration was determined to be 65Å. A shoulder was observed at approximately q=0.07Å^{-1} for both the complexes. Similar result was reported for a deuterated LH1 complex solubilized in 0.8% OG, 17% D_2O.[2] This feature was considered to arise from the internal structure, or packing of subunits within the large LH1 particles. To examine this

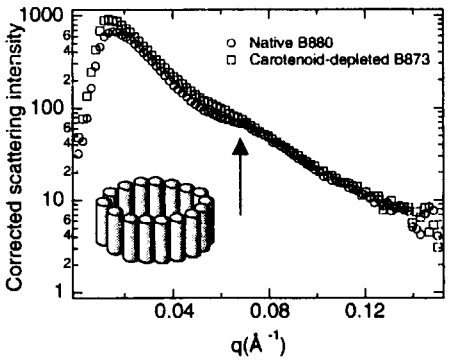


Fig. 1 Semi-logarithmic plots of SANS profiles for the native and carotenoidless LH1 complexes.

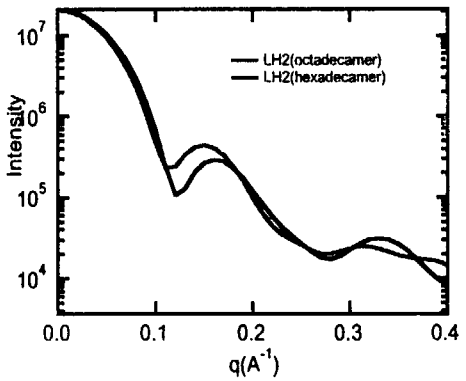


Fig. 2 Calculated scattering profiles for the LH2 complexes of octadecamer and hexadecamer, corresponding to 9 and 8 αβ heterodimers, respectively.

possibility, we compare with the calculated scattering profiles of the smaller LH2 complexes based on their crystal structures. Figure 2 shows the scattering curves over a large q range for two LH2 complexes containing 9 and 8 αβ heterodimers. Radii of gyration for the 9 and 8 αβ heterodimers are 30.3Å and 28.9Å, respectively. Clear difference can be found in the position of the first scattering maximum, which corresponds to number of the subunit and may be used as a useful measure of the size for the ring-like oligomeric structure of light-harvesting complexes. Further detailed data analysis is in progress.

[1] Svergun D.I., et al. *Proc. Natl. Acad. Sci. USA*, **95**, 2262-2272(1998).
[2] Tiede D.M. and Thiyagarajan P. in *Biophysical Techniques in Photosynthesis*. pp. 375-390, (1996), Kluwer Academic Publisher, Netherlands.

JRR-3M, SANS-U(C1-2), . Biology

研究テーマ：中性子小角散乱法による昆虫リポホリンの構造解析
表題：中性子小角散乱法による昆虫リポホリンの構造解析

1-6-2 Small-Angle Neutron Scattering of Lipophorin

C. KATAGIRI[1], M. NAGAO[2], M. SATO[3] and Y. ITO[4]

[1]*Institute of Low Temperature Science, Hokkaido University, Sapporo 060-0819*
[2]*Institute for Solid State Physics, University of Tokyo, Tokai, Naka, Ibaraki 319-1106*
[3]*Graduate School of Integrated Science, Yokohama City University, Yokohama, Kanagawa 236-0027*
[4]*Faculty of Education and Human Sciences, Yamanashi University, Kofu 400-8510*

Lipophorin in the insect blood is a sphere-like particle with a particle weight of about 6.0×10^5 and contains two apoproteins and 40-50% (w/w) lipid. Lipophorin is a unique lipoprotein that serves as a reusable shuttle to transport a variety of lipid classes, including diacylglycerol, cholesterol, and hydrocarbons between tissues. The apoproteins and phospholipids work as a vehicle to load and unload the above lipids. We have already proposed a model of three layered lipophorin (diameter = 168Å) based on small-angle X-ray scattering results, which was supported by the small-angle neutron scattering work with H_2O/D_2O contrast variation. The model consists of an inner core of hydrocarbons surrounded by a layer of diacylglycerol and apolipophorin-II ($M_r=8 \times 10^4$), and a spherical micellar arrangement of the outer hydrophilic surface formed by apolipophorin-I ($M_r=2.5 \times 10^5$) and polar phospholipid headgroups[1,2,3] In the present study, we reared American cockroach on deuterated amino acid mixtures for partially deuterating apolipophorins. The prepared lipophorin was subjected to small-angle neutron scattering analyses with H_2O/D_2O contrast variation (Fig.1). They gave several parameters different from those obtained by the non-treated lipophorin. The model refinement is now in progress.

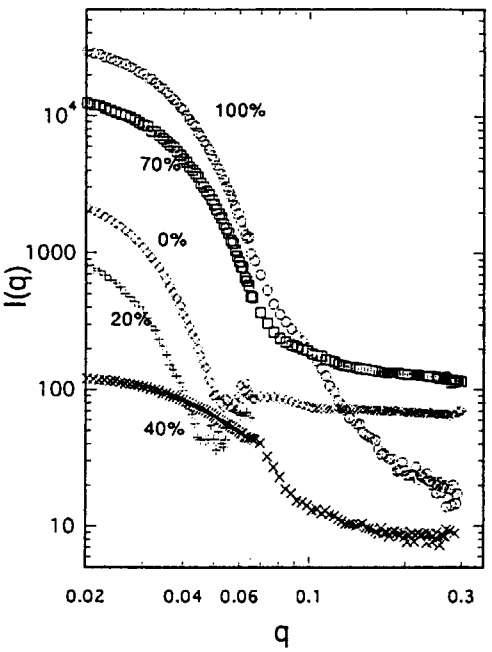


Fig.1 Small-angle neutron scattering curves of the cockroach lipophorin reared on deuterated amino acids.

References

1) C. Katagiri *et al.*, *Biochem.***30** (1991) 9675.
2) C. Katagiri, *J. Crystallographic Soc. Jpn.***36** (1994) 162 [in Japanese].
3) C. Katagiri *et al.*, *Activity Report on Neutron Scattering Research* **3** (1996) 208.

JRR-3M、SANS-U、 Biology

研究テーマ：糖脂質／リン脂質混合ベシクルのミクロドメイン形成とダイナミックス
表題：逆コントラスト変化法によるガングリオシド／ジパルミトイルホスファチジルコリンベシクルの構造解析

1-6-3 Structure analysis of ganglioside/dipalmitoyl phosphatidylcholine vesicle using inverse contrast variation

M. Hirai,[1] T. Hayakawa,[1] K. Koisumi,[1] R. Kan, and H. Iwase.[2]

[1] *Department of Physics, Gunma University, Maebashi 371-8510, Japan.*

[2] *Institute of Materials Structure Science, KEK, 1-1 Oho, Tsukuba 305-0801, Japan*

1. Introduction Gangliosides, glycosphingolipids containing sialic acid residues, locate mainly on the outer surfaces of cell membranes, and are abundant in the tissues of the central nervous system. Recent studies suggest that these molecules not only locate on outer-leaflet of cell membrane but also form lipid microdomains with other particular lipids and proteins in neuronal cells. The microdomains are assumed to have a significant role as a molecular device to localize specific proteins which are evolved in cell-surface signal transduction such as src-family kinases and G proteins. Although the physiological functions of the microdomains is one of the current hot topics in cell biology, the biophysical studies of the formation and functionality of the microdomain are rather poor. Thus, we have carried out small-angle neutron scattering (SANS) measurements to elucidate characteristics of monosialoganglioside (GM1) /dipalmitoyl phosphatidylcholine (DPPC) mixed vesicle as a model of the microdomains.

2. Experimental Here we employed the inverse contrast variation method in the solution neutron scattering methods. As is well known, inverse contrast variation method can avoid a lowering of data statistics that occasionally occurs in the use of the solvent contrast variation method. For this purpose, we dissolved the mixed vesicles in 99.9+ atom % D_2O solvent with 50 mM Hepes adjusted to pH 7. The contrast of the vesicle was varied by changing the molar ratio of DPPC/deuterated-DPPC (d-DPPC). The molar contents of GM1 to DPPC are 0.1 [M/M]. The molar ratios of [DPPC]/[d-DPPC] were 1/0, 0.3/0.7, 0.7/0.3 and 0/1. To prepare small unilamellar vesicles (SUV), we used a high-power ultrasonicator with a probe. SANS experiments were carried out by using a SANS spectrometer installed at C1-2 beam port at JRR-3M, Tokai, Ibaraki, Japan.

3. Results and Discussion Fig. 1 shows the scattering curves from the SUV samples with different inverse contrasts. The insert in Fig. 1 shows the scattering curves of the above samples. In spite of the samples with different contrasts for neutron, all scattering curves for X-ray agree well, indicating that the SUV samples with different molar ratios of DPPC/d-DPPC have a same structure. Thus, the variation of the scattering curves depending on the DPPC/d-DPPC ratio in Fig. 1 is attributed to the change of the contrast. As we successfully measured the GM1/DPPC=0.1/1 SUV vesicle at 5 different contrasts, in other words, at 5 different phases (four from neutron, one from X-ray), we can determine the internal structure of the vesicle. The detailed analyses using the shell-model fitting procedure considering a polydispersity will be seen in elsewhere.

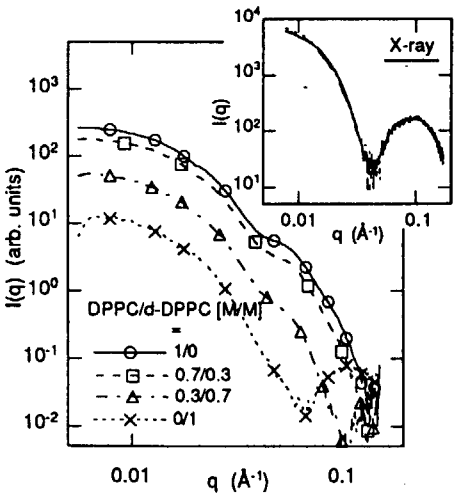


Fig. 1. SANS curves of GM1/DPPC SUV samples with diffrent inverse contrasts at 25 °C. The insert shows X-ray scattering curves of those SUV samples.

JRR-3M, SANS-U(C1-2), 。 Biology

1-6-4

研究テーマ：蛋白質動力学における動的不均一性の評価

表題：中性子非干渉性弾性散乱のq依存性における非ガウス性の起源

The origin of non-gaussianity in q dependence of incoherent elastic neutron scattering

Hiroshi Nakagawa[1], Hironari Kamikubo[1], Itaru Tukushi[2], Toshiji Kanaya[3] and Mikio Kataoka[1],

[1]Department of Material Science, Nara Institute of Science and Technology

[2]Chiba Institute of Technology

[3]Institute for Chemical Reaserch, Kyoto University

A protein takes its unique structure, and structural flexibility is considered to be essential for its function and activity. Thus, the understanding of the protein dynamics is important to reveal the molecular mechanisms of vital phenomena. Neutron scattering is a good tool for studying protein dynamics, because neutron scattering can give us information on both energy and the geometry of the atomic motions.

We measured the incoherent elastic neutron scattering for Staphylococcal nuclease(SNase) under the various temperatures with the use of the triple axis spectrometer, GPTAS. The purpose of the measurement was to reveal the dynamical transitions(so-called glass transition) of SNase and to analyze the q-dependence of EISF. The energy resolution was 1meV, corresponding to the picosecond time scale motions. The measured q-range was from 3.1 to 6.4 $Å^{-1}$.

The q-dependence of EISF can be approximated a Gaussian in low q region, while the deviation from the Gaussian becomes remarkable in rather wide q region. We considered that dynamical heterogeneity of SNase is an origin of the non-Gauusianity appeared in high q region. We assumed that the mean square displacements of hydrogen atoms in SNase can be described with a Gauusian distribution. Under the assumption, the non-gaussianity is reasonably explained in terms of the width of the Gaussian. The distrubution becomes broader as temperature increases.

In the case of myoglobin, the origin of non-gaussian behavior was explained as two site model[1]. In the model, each hydrogen atom in a protein jumps between two sites of different free energy. In the case of bacteriorhodopsin, the non-gaussianity was interpreted as two distinct motions, that is a higher amplitude motion and a lower amplitude motion[2]. In the case of SNase we could not separate into two distinct motions. In the two site model the mean square displacement of each atom is the same, that is not reasonable. It is suggested that the heterogeneity of protein dynamics is one of the origin of non-gaussian in q dependence of incoherent elastic neutron scattering. MD simulation of SNase also gives Gaussian-like distrution in mean square displacement.(J.Smith and J Hayward, personal communication).

References

[1] Doster W.,Cusack S. and Petry W. Nature 337, 754-756(1989)

[2] Lehnert et al. Biophys.J. 75:1945-1952 (1998)

使用施設：JRR-3M、装置：GPTAS(4G)：分野： Biology

研究テーマ：生体分子表面における水分子および共存溶質分子の分布状態

表題：トレハロール水溶液中の短鎖・長鎖ホスファイジルコリン混合系の構造

1-6-5 Structure of Short and Long Chain Phosphatidylcholine mixtures in Trehalose Solutions

Hiroshi Takahashi

Department of Physics, Gunma University, Aramaki4-2, Maebashi, 371-8510 Japan

Trehalose is a natural cryoprotectant. Thus, in order to reveal the mechanism, many studies of the effect of trehalose on model biomembranes have been performed. Based upon the results of such studies, a following hypothesis has been proposed [1]: The presence of trehalose reduces the interfacial area between the lipids and the aqueous phases. To examine above hypothesis, we have investigated the interaction between trehalose and phosphatidylcholines (PCs), which are one of the major phospholipid components of biomembranes. In this study [2], we studied the structure of a binary mixture of short PC (dihexanoyl-PC (diC_6PC)) and long chain PC (dihexadecyl-PC (DHPC)) in trehalose solutions.

DHPC and diC_6PC were dissolved in chloroform and mixed to achieve the molar fraction of DHPC : diC_6PC = 4:1. The solvent was evaporated under a stream of oxygen free dry nitrogen. The dried lipid samples were hydrated in 100 % D_2O containing various concentrations of trehalose by shaking on a Vortex mixer. The total lipid concentration was 25 mM. Small angle neutron scattering (SANS) measurements were performed with the SANS-U spectrometer at JRR-3M reactor at the Japan Atomic Energy Research Institute. The wavelength of the neutron beam was 7 Å. The samples were contained in a rectangular quartz cell with 1 mm optical path length. The data corrections were carried out at about 25 ℃.

Figure 1 shows the SANS curves form the PCs mixtures in trehalose solution. For the mixtures in pure D_2O and 0.4 M trehalose solution, Bragg diffraction peak is observed (d = 52 Å), indicating that a phase separation between multilamellar vesicles of DHPC interdigitated gel bilayers and micellar structures occurs in the mixtures. On the other hand, in high trehalose concentrations, no Bragg diffraction peak is observed. For the cases of 1.6 M trehalose concentration solution, we estimated that the membrane thickness is about 42 Å from the analysis using Kratky-Porod plot of the scattering curve. The value is interpreted as suggesting that, in the DHPC/diC_6PC mixture, DHPC does not form the interdigitated structure but a normal bilayer structure. This result supports the hypothesis proposed by Koynova *et al.* [1]. We assume that the structure of the DHPC/diC6PC mixtures in high concentration trehalose solutions is a bilayer structure with edge of the disk and that the diC_6PC molecules cover the edge of the DHPC bilayer disk.

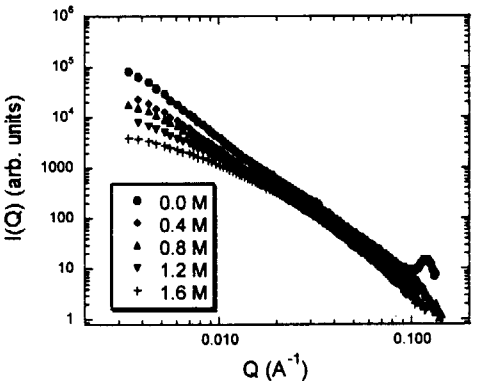


Figure 1 SANS curves of the mixtures of DHPC and diC_6PC in trehalose solution with various concentrations.

References

[1] Koynova *et al.*, *Biochim. Biophys. Acta* **980** (1989) 377-380.

[2] H. Takahashi, *J. Phys. Soc. Jpn.* 70 (2001) Suppl. A 411-413.

JRR-3M, SANS-U, Biology

研究テーマ：細胞における蛋白質の高次構造化不全と細胞の異常死に関する研究
表題：遺伝子から合成されたケラチンタンパク質の自己集合に関する中性子散乱研究

1-6-6

Neutron scattering study on self-assembly of keratin molecules in water

Sachio Naito, Fumiyoshi Ikkai , Takeshi Karino[1], Michihiro Furusaka[1],
Satoru Fujiwara[2], and Nobuo Niimura[2]

The Institute of Advanced Science Research, L'ORÉAL Tsukuba Center, Tsukuba, Ibaraki 300-2635, Japan
[1]High Energy Accelerator Research Organization, Tsukuba, Ibaraki 305-0801, Japan
[2] Japan Atomic Energy Research Institute, Ibaraki 319-1195, Japan

The aim of this study is to clarify structural changes of proteins in apoptosis. Once apoptotic trigger is pulled in a hair cell, the cell begins to produce enormous amount of keratin proteins. Then, SS cross-linking is induced between the molecules and keratin proteins are finally gelated[1]. This type of apoptosis is unusual in normal body but often occurs in cancer, AIDS and Alzheimer disease. Keratin fibril consists of 2 types of keratin, i.e., Type I (~45kDa, acidic) and Type II (~56kDa, basic). It is known that keratin assembles spontaneously as dimer, tetramer, octamer, and multimer, and finally forms 10 nm filaments. However, the organization process and structure of keratin in aqueous solution have not been well understood. We also confirmed the presence of keratin multimers in water by SANS measurement [2]. In this study, we synthesized gene-expressed Type I and Type II keratins and chemically modified the cysteine resides to the s-carboxymethyl alanyl disulfide (R-S-SCH_2COO^-, CMAD), and investigated the structure of keratin proteins in aqueous solution by small-angle neutron scattering (SANS).

SANS was undertaken at SANS-J situated at the end of a cold-neutron guide tube from the JRR-3 reactor. For the present experiment, neutron wavelength λ = 7 Å was used. The distance (L) from the sample to the two-dimensional position-sensitive detector (PSD) was set at 10 m.

We previously measured the keratin solutions (10 mM Tris-HCl buffer solution, pH7) by SNAS. The profiles of Type I and Type II showed a straight line which had a slope of *ca.* −1 (Fig.1-a inserted in Figure 1). This means that Type I and Type II exist as rod-like molecules. However, we could not observe the self-assembled profile between Type I and Type II. In this study, we added 50 mM NaCl to the buffer to control the electro-static repulsion between CMAD residues and to promote the hydrophobic interaction between them. Figure 1 shows the scattering profiles of Type I and Type II, equal molar mixture of Type I and Type II and the theoretical profile when there are no interactions among them. The scattering intensity profile of Type I and

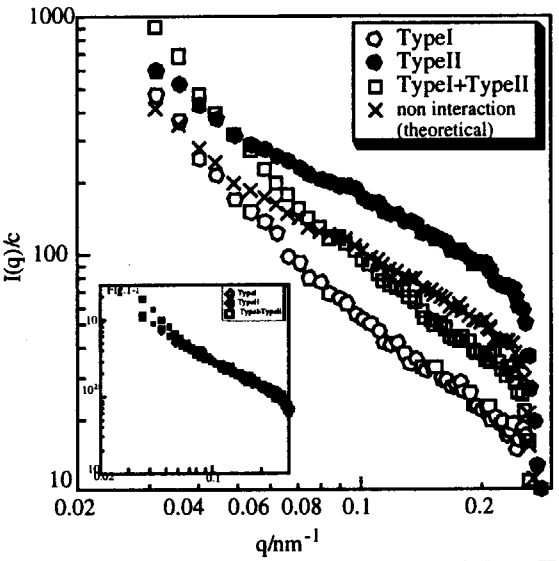


Figure 1. Scattering profiles of Type I and Type II keratins in 10 mM Tris-HCl buffer solution (pH7) containing 50 mM NaCl.

Type II mixture showed the increase of the intensity in the smaller q region and the decrease in the wider q region. This profile was different from that of Type I and Type II respectively, and was also different from the theoretical profile assumed there were not any interactions between them. This result suggested that two types of keratin molecules might self-assemble in the existence of a higher salt concentration without SS cross-linking formation. We are now discussing the structure of keratin protein in various conditions.

Reference

1) F. Ikkai and S. Naito, *Biomacromolecules* 2001,3(3), 482-487.
2) S.Naito et al., JAERI-Review 2001-005, 14.

原子炉：JRR-3M　　装置：SANS-J(C3-2)　　分野：中性子散乱 (生物)

研究テーマ：機能性生体物質の水和構造研究
表　題：細いフィラメント上のトロポニンCの中性子小角散乱測定

1-6-7

Small-Angle Neutron Scattering Measurements of TroponinC on the Thin Filament

Fumiko Matsumoto[1,2], Kouji Makino[2], Kayo Maeda[2], Heiko Patzelt[3], Yuichiro Maeda[2], and Satoru Fujiwara[1]

[1]Advanced Science Research Center, JAERI, Tokai, Ibaraki 319-1195
[2]Laboratory for Structural Biochemistry, RIKEN Harima Inst.,Mikazuki, Hyogo 679-5148
[3]Department of Chemistry, Sultan Qaboos University, Al-Khod 123, Sultanate of Oman

Muscle contraction occurs via sliding of two types of the filaments past each other. These filaments are actin-based "thin" filaments and myosin-based "thick" filaments. The molecular mechanism of the muscle contraction and its regulation is one of the most important problems in biophysics, as it is a typical example of energy transduction mechanisms of living organisms. In vertebrate skeletal and cardiac muscles, muscle contraction is regulated via the interactions between the thin filament proteins, troponin (Tn) C, TnI, TnT, tropomyosin, and actin. These interactions are triggered by binding of Ca^{2+} to TnC. As a first step toward understanding these interactions, we investigated the structure of TnC on the thin filament with and without Ca^{2+}.

Neutron scattering was employed to do this. Structural information of a selected component within a protein complex can be obtained with this method, when it is combined with the strategies of selective deuteration and contrast matching. We prepared the deuterated (d-) TnC by expressing the protein in *E. coli* in D_2O medium containing deuterated algal peptone. The purified d-TnC was exchanged into the native thin filaments by CDTA treatment. The native thin filaments containing d-TnC were then exposed to neutrons under the condition where the contrast of the other components of the thin filaments were matched out with 40% D_2O.

Small-angle neutron scattering measurements of these samples with and without 1.1 mM $CaCl_2$ were done with the Small-Angle Neutron Scattering Instrument (SANS-J) at the guide hall of the reactor JRR-3M in Japan Atomic Energy Research Institute. Neutrons with the wavelength of 6.5 Å($\Delta\lambda/\lambda$ = 12.98%) were employed. Figure 1 shows the extracted scattering curves of d-TnC on the thin filaments with and without Ca^{2+}. These curves showed distinct changes with and without Ca^{2+}, indicating that there are conformational changes of TnC on the thin filaments.

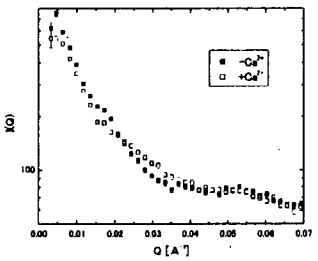


Figure 1: The extracted neutron scattering curves of d-TnC on the thin filaments with and without Ca^{2+}.

Since these curves were obtained from the samples of the very high concentration (the concentration of the thin filament was about 160 mg/ml), a simple analysis, such as the analysis by the Guinier plots, to derive the radius of gyration of d-TnC cannot be applied. Analysis of these scattering curves by model calculation is now underway. Supported by Special Coordination Funds for Promoting Science and Technology from the Ministry of Education, Culture, Sports, Science and Technology, the Japanese Government.

原子炉：JRR-3M　　装置：SANS-J(C3-2)　　分野：中性子散乱（生物）

研究テーマ：機能性生体物質の水和構造研究
表　題：コントラスト変調法を用いた中性子繊維回折による筋肉構造の解析

1-6-8

Analysis of the Muscle Structure from Neutron Fiber Diffraction Measurements Using the Contrast Variation Method

Satoru Fujiwara, Yasunori Takezawa[1], Yasunobu Sugimoto[1], and Katsuzo Wakabayashi[1]

Advanced Science Research Center, JAERI, Tokai, Ibaraki 319-1195
[1]Grad. School of Engineering Science, Osaka University, Toyonaka, Osaka 560-8531

One of the important features of neutron scattering is that it is relatively easy to do the contrast variation measurements by changing D_2O content in the solvent. The contrast variation method is applicable not only to neutron solution scattering[1)], but also to low-resolution neutron crystallography and neutron fiber diffraction as well. We have explored the possibilities of neutron fiber diffraction combined with the contrast variation measurements. We measured the neutron fiber diffraction patterns of frog sartorius muscles under the relaxed state where no tension of the muscle is produced, in various D_2O concentrations. It was shown that under both states, there were reflections having different matching points, indicating that there is a variation of the scattering length density in the unit cell of the muscle structure[2)]. Calculation of the projected density map of the unit cell to the plane perpendicular to the axis of the muscle, using the equatorial reflections showed that it was possible to select the correct neutron phase of these equatorial reflections[3)]. The maps using this correct phase combination showed that the (projected) density of the thick filament region and that of the thin filament region are different.

We also performed similar measurements of the muscles under the rigor state where the myosin heads bind tightly to actin, and found that the contrast dependence of the scattering amplitudes of the observed reflections was similar to that under the relaxed state[4)].

Here we performed again the contrast variation measurements of muscle under relaxed state to measure particularly the intensities of meridional reflections. These reflections arise from the muscle structure projected to the axis of the muscle. The measurements were done with the Small-Angle Neutron Scattering Instrument (SANS-J) at the guide hall of the reactor JRR-3M in Japan Atomic Energy Research Institute. Figure 1 shows the diffraction patterns of muscle under the relaxed state in H_2O and D_2O. The meridional reflections up to 5th order can be observed. The analysis of these patterns is now in progress. Supported in part by Special Coordination Funds for Promoting Science and Technology from the Ministry of Education, Culture, Sports, Science and Technology, the Japanese Government.

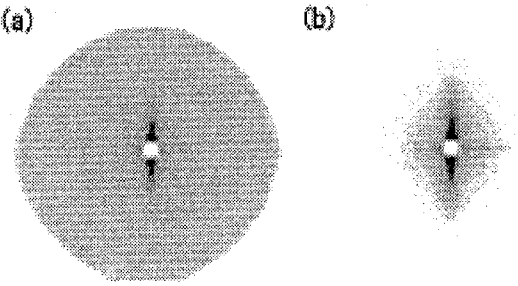


Figure 1: Neutron fiber diffraction patterns of frog sartorius muscle in (a) H_2O and in (b) D_2O. The axis of the muscle is horizontal.

References

1) L. A. Feigin and D. I. Svergun:*Structure Analysis by Small-Angle X-Ray and Neutron Scattering*, (Plenum Press, New York, 1986)
2) S. Fujiwara et al.: J. Phys. Soc. Jpn. **70** (2001) Suppl. A 408.
3) S. Fujiwara et al.: Annual meeting of the Biophys. Soc. Jpn., Osaka, Japan, Oct, 2001.
4) S. Fujiwara et al.: JAERI Review **2002-006** (2002) 18.

原子炉：JRR-3M　　装置：SANS-J(C3-2)　　分野：中性子散乱（生物）

研究テーマ：機能性生体物質の水和構造研究
表　題：ニワトリ卵白リゾチーム - 基質アナログ複合体単結晶の中性子回折

1-6-9

Neutron Diffraction of a Single Crystal of a Complex of Hen Egg-White Lysozyme and Substrate-Analogue

Satoru Fujiwara

Advanced Science Research Center, JAERI, Tokai, Ibaraki 319-1195

Enzymes have their specific activities to produce "products" from "substrates." To study molecular mechanisms of functions of the enzymes, it is important to study the structures of the complexes formed by the enzymes and the substrates. Particularly, since hydrogen atoms may play essential roles in enzyme activities, it is important to know the structure of the enzyme-substrate complex including the hydrogen atoms. Neutron crystallography, which can locate the hydrogens, is one of the important methods to investigate these problems.

Lysozyme has a $\beta(1-4)$ glucosaminidase activity with the ability to hydrolyze a mucopolysaccharide component of some bacterial cell walls releasing N-acetyl amino sugars derived from glucosamine and muramic acid[1]. As a model of the enzyme-substrate complex, we prepared a complex of hen egg-white lysozyme (HEWL) and tri-N-acetylglucosamine (NAG_3). NAG_3 is one of the competitive inhibitors of HEWL, and can be regarded as a substrate analogue. Crystals of HEWL- NAG_3 complex were prepared by co-crystallization[3]. A solution containing 30 mg/ml HEWL in 50 mM sodium acetate (pH 4.3) in D_2O was mixed with a solution containing NAG_3 and NaCl to make 1:1 complex of HEWL and NAG_3. Crystals were formed in about two weeks, and the crystals grew only to the size of about 3 mm^3. The sizes of the crystals were significantly smaller than those of the crystals of HEWL without NAG_3[4, 5].

One of the crystals was set to measure the diffraction patterns with BIX-2 [6]. The space group of the crystals was $P4_32_12$, and the cell parameters were $a = b = 7.91$ nm, $c = 3.66$ nm. The oscillation method of 0.4 degrees has been employed. Figure 1 shows an example of the collected diffraction patterns of the crystal of HEWL- NAG_3 complex. Diffraction spots of at least 0.25 nm resolution have been observed. Exposure time per one frame has been 24 hours. Since the size of the crystal was small, the more exposure time was needed per a frame than the cases of HEWL. The resolution of the diffraction was also worse, presumably because the presence of NAG_3 made each molecule in a crystal more disordered. So far, the data of 20 degrees of rotation range were collected, and the data collection is currently underway.

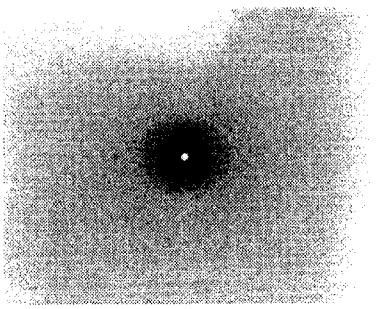


Figure 1: An example of Neutron diffraction patterns of the crystal pf HEWL- NAG_3 complex. Exposure time per one frame has been 24 hours.

References

1) L. N. Johnson and D. C. Phillips: Nature **4986** (1965) 761.
2) N.C.J. Strynadka and M.N.G. James: J. Mol. Biol. **220** (1991) 401.
3) S. Fujiwara et al.: J. Phys. Soc. Jpn. **70** (2001) Suppl. A 408.
4) S. Fujiwara et al.: JAERI Review **99-003** (1999) 13.
5) S. Fujiwara et al.: JAERI Review **2000-005** (2000) 7.
6) S. Fujiwara et al.: Physica B **241-243** (1998) 207.

原子炉：JRR-3M　　装置：BIX-2(T2-3)　　分野：中性子散乱（生物）

研究テーマ ： 機能性生体物質の水和構造研究
表 題 ： 完全重水素化 B-DNA 結晶の中性子回折実験
1-6-10

Neutron diffraction experiments of fully deuterated B-DNA crystal

Toshiyuki Chatake, Shigeki Arai, Takashi Ohara, Kazuo Kurihara, Ichiro Tanaka and Nobuo Niimura

Advanced Science Research Center, Japan Atomic Energy Research Institute, Tokai-mura, Ibaraki-ken, 319-1195, Japan

The neutron diffraction is a very powerful method to determine the detailed structure of biological materials including hydration and hydrogen positions. We are trying to solve the structure of B-DNA duplex by using the neutron diffractmeter BIX-3 with a large single crystal of fully deuterated B-DNA decamar d(CCATTAATGG). In a neutron diffraction experiment, in order to avoid the high background coming from the incoherent neutron scattering of hydrogen atoms, DNA sample was synthesized by fully deuterated nucleotides and crystallized in D_2O solution. A large single crystal was obtained by using the phase diagram information for $MgCl_2$-DNA systems[1] at 6°C for 2 months, in which the size of obtained crystal was 2.0 x 2.0 x 0.3 mm. To measure this crystal by BIX-3, we developed the crystal cooling device.

Fig.1 shows a preliminary neutron diffraction pattern of DNA crystal by use of the crystal cooling device. The exposure time was 4 hours. The wavelength of the incident neutron beam was 2.33Å. The insert shows a used crystal.

Fig.2 shows a scheme of the crystal cooling device which consists of two component parts. Cold dry air, which was obtained from a low temperature circulator (-20°C), cooled the whole of the sample capillary. To prevent the condensation on the surface of sample capillary, the cold gas stream is coaxially surrounded by a little warm and dry stream of air (~10°C). By using this device, the temperature of sample position was kept at 6±1°C for a long time measurement (more than 2 weeks).

The collection of a complete data set of Bragg reflections is presently scheduled.

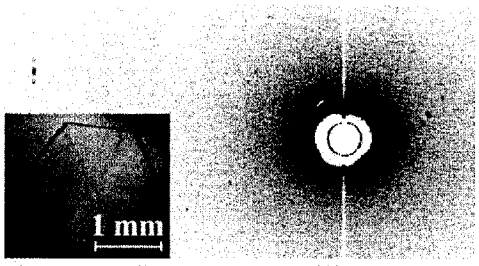


Fig.1 A preliminary neutron diffraction pattern from the grown single crystal. The exposure time is 4 hours. The insert shows a used crystal.

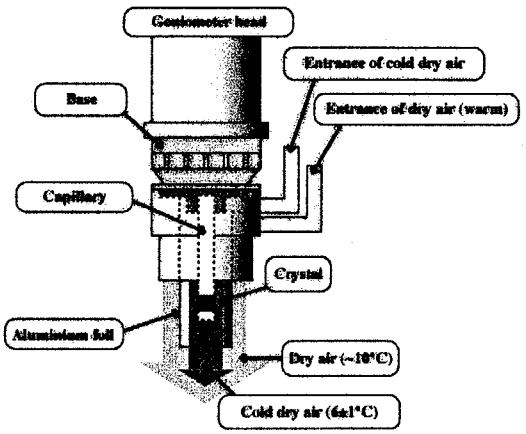


Fig.2 The developed crystal cooling device for the neutron diffractmeter BIX-3.

References

1) S. Arai et al., Acta. Cryst. D. 58 (2002) 151-153.

原子炉：JRR-3M 装置：BIX-3 (1G-A) 分野：生物

研究テーマ：機能性生体物質の水和構造研究
表　　題：ヒトリゾチームの中性子結晶構造解析

1-6-11

Neutron Crystallography of Human Lysozyme

K. Chiba-Kamoshida, T. Matsui[1], A. Ostermann, T. Chatake,
T. Ohhara[2], I. Tanaka, K. Yutani [3]and N. Niimura

ASRC, Japan Atomic Energy Research Institute, Tokai, Ibaraki 319-1195, Japan
[1]Department of Physics, Tohoku University, Sendai 980-8578, Japan
[2]Institute of Material Structure Science, KEK, Tsukuba 305-0801, Japan
[3]Institute for Protein Research, Osaka University, Suita 565-0871, Japan

The most important information from neutron crystallography is that of hydrogen atoms and hydration waters at physiological temperatures. Wild-type human lysozyme (MW 14,700) was selected for our neutron structure determination because it has been studied by many other biophysical methods as one of the most typical examples of stable globular proteins. The activity of human lysozyme is hydrolysis of polysaccharides.

Human lysozyme was obtained using high-yield yeast strain, *Pichia pastoris*. Crystals for neutron experiment were grown in D_2O-based buffer solution at 20 ℃. The size of the single crystal used for the neutron structure determination was 3.0 mm x 1.0 mm x 0.7 mm. Diffraction data were collected with the monochromatic neutron diffractiometer BIX-3 equipped with a neutron imaging plate at room temperature. The total measuring time was 55 days. Crystal shows no degradation even after the relatively long measuring time.

The neutron diffraction data have been analyzed up to 1.8 Å resolution. R-factor was 19.7% (R_{free} = 23.57%). Number of H atoms determined was 955. Number of hydration waters determined was 55. H/D exchange ratio for each amide proton was obtained. In the obtained lysozyme structure, we observed many hydrogen bonds and hydrogen atoms even on the terminal methyl groups of the buried hydrophobic residues. Human lysozyme has many basic amino acids, 14 arginines and 5 lysine residues in the relatively small number of amino acid residues, 130. Those bulky residues are positively charged at the pH condition of 4.3 for the diffraction experiment. Deuterium atoms were well-observed when the deuterium atoms of ND_3 groups form hydrogen bonds with negative charges like carboxyl groups both on main and side chains.

Regarding to intra-molecular interactions, deuterium atoms in one arginine and 3 lysine residues form hydrogen bonds with negatively charged residues existing on some secondary structures far along the primary structure. These hydrogen bonds make two helixes interact or a loop region clip on a stable secondary structure. Hydrogen and deuterium atoms in such residues are well-observed in the nuclear density map.

On the other hand, 5 of the 14 arginine residues and 2 of 5 lysine residues form direct hydrogen bonds with neighboring lysozyme molecules in the crystal. Also in these cases, many hydrogen and deuterium atoms in those residues were clearly observed in the nuclear density map.

After deionization, protein was freezed dried and used for the following crystallization.

原子炉：JRR-3M　　装置：BIX-3 (1G-A)　　分野：中性子散乱（生物）

High population of these large and flexible residues may contribute to the high solublity of the protein and also to the relatively easy crystallization of lysozme molecule.

The authors tried to re-adjust an EBP-Si monochromator for BIX-3, which was 2 plates of 5 mm thickness, by the incident beam width of 20 mm with θ of 22 deg, but the gain factor compared to single plate was only 1.1. After checking many points, the authors found the possibility that the bender iron holders might shield incident and reflected beam. From an experiment as Fig. 1, the maximum loss of intensity was about 20 %.

Reference

[1] I. Tanaka, F. U. Ahmed and N. Niimura, Physica B **283** (2000) 295-298.

1. 中性子散乱 7) 基礎物理学・中性子光学

1. Neutron Scattering 7) Fundamental Physics Neutron Optics

This is a blank page.

研究テーマ：中性子時間エコー干渉計による多重ブラッグ反射、屈折率等による時間遅れ
表題：時間ビート中性子スピン干渉におけるエコー条件

1-7-1

Echo Condition in Time Beat Neutron Spin Interferometry

Norio ACHIWA, Gou SHIROZU, Toru EBISAWA[1], Dai YAMAZAKI[1], Masahiro HINO[1], Seiji TASAKI[1], and Takeshi KAWAI[1]

Department of Physics, Graduate School of Science, Kyushu University, Fukuoka, 8128581, Japan
[1] Research Reactor Institute, Kyoto university, Kumatori-cho, Sennan-gun, Osaka 590-0494, Japan

§1. Introduction

Neutron resonance spin echo method (NRSE) has been developed by Gähler and Golub et al.,[1,2] where spin echo phases are created by radio frequency (RF) flippers. As a modified version of NRSE, they apply the echo of time beat for a TOF neutron spectrometer, MIEZE instrument.[3,4] In the MIEZE spectrometer the sample is downstream of the analyser leaving the signal indifferent to magnetic field and spin flips in the sample. Following their principle, we have developed neutron spin interferometry using these radio frequency flippers.[5-7] In this paper we have firstly demonstrated the difference of time beat depending on the positions of neutron spin depolarizer.

The time beat of neutron intensity at detector position is created by the coherent superposition of the same spin eigenstates of neutrons with different energy states, which are produced with two radio-frequency flippers and polarization analyser.

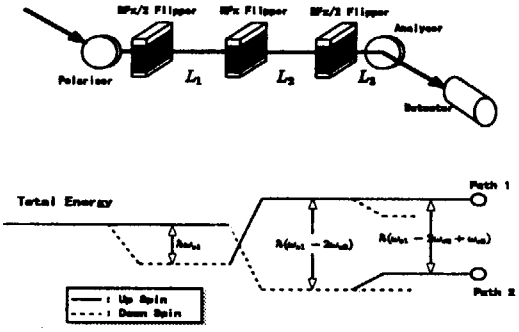


Fig. 1. Arrangement of a time beat neutron spin interferometer with RF spin flippers. The splittings in total energy are given by the exchange of quanta with energies $\omega_{z1}, \omega z2, \omega z3$ by RF flippers.

§2. Quantum beat

A simple cold neutron spin interferometry using radio frequency flippers (RF flipper) is shown in Fig.1, which is similar to the MIEZE spectrometer.

A time beat neutron spin interferometer with RF spin flippers which is installed in C3-1-2 cold guide, JRR-3M, JAERI. These RF flippers consists of two coils, that is, one creates a magnetic field B_z parallel to the quantized axis and another one creates an oscillating field $B_x(t)$ perpendicular to the quantized axis. Assuming the resonance condition for the RF flipper and expressing the oscillating field as $B_x(\sin\omega_z t + \Delta)$, the frequency of the oscillating field, ω is given by,

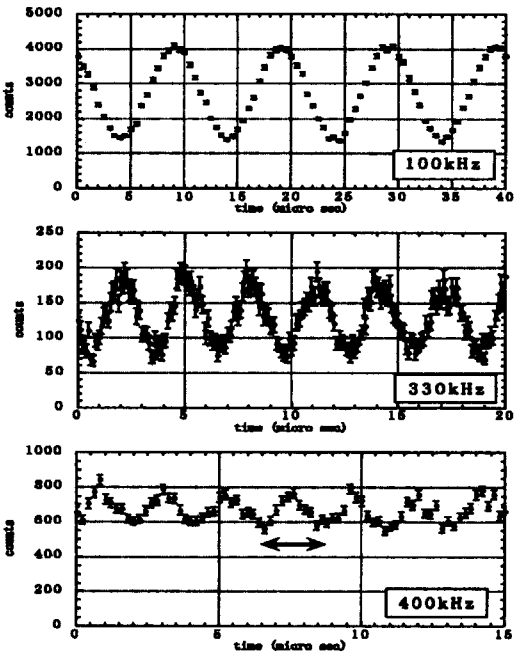


Fig. 2. Typical time beat examples of 100, 330 and 400 KHz.

$$\hbar\omega_z = 2\mu B_z \tag{2.1}$$

where μ is the neutron magnetic moment. The RF flippers function as $\pi/2$ and π when the amplitude B_x satisfies Eqs.(2.2) and (2.3), respectively,

$$\frac{l}{v}(\mu B_x) = \frac{\pi\hbar}{2} \tag{2.2}$$

$$= \pi\hbar \tag{2.3}$$

where l is the length of the RF-flipper and v the neutron velosity.

We consider the case of the following conditions as regards the magnetic fields of the system,

$$B_{z,1} = B_{z,2} = B \gg B_{z,3} = B_g \tag{2.4}$$

where $B_{z,i}$ are the magnetic field in z axis of the i th RF flipper and B_g the guide field, respectively. The three RF flippers function as $\pi/2, \pi$ and $\pi/2$ in turn. The

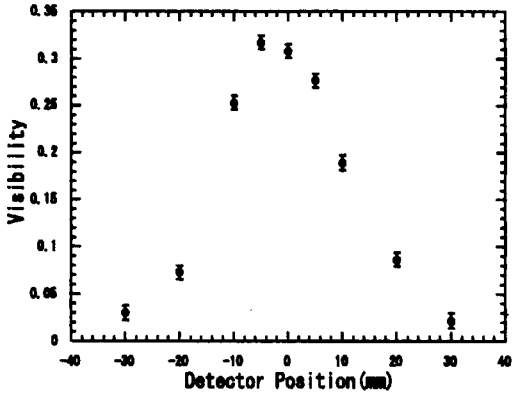


Fig.3. Visibility of the time beat spectrum as a function of the detector position at 330 KHz.

polarized neutron is split into the two spin eigenstates with energy difference with $\hbar\omega_x$ by the first RF $\pi/2$-flippers. The spin state and energy difference of these partial waves are reversed by the second RF π-flippers. The third $\pi/2$-flipper supersplits into two $\uparrow$ and two $\downarrow$ spin neutron states which can be selected by analyser to give two $\uparrow$ spin states with different energy. giving rise to quantum beat of neutron intensity.

The time beat of neutron intensity at the detector positon at $t_d = t_0+t_1+t_2+t_3$ is given by Eqs. (2.5).[8] Here, t_0 is the time when the neutron is incident on RF $\pi/2$-spin flipper, and t_i is given by L_i/v.

$$|\psi_i^{out}(+)|^2 = \frac{1}{2} + \frac{\cos[(2\omega_{x2}-\omega_{x1})t_d + \Delta_0 + \Theta]}{2} \quad (2.5)$$

where the effect of of B_g is neglected and the wavelength dependent phase is given by

$$\Theta = \frac{\omega_{x1}L_1 - (2\omega_{x2}-\omega_{x1})(L_2+L_3)}{v}, \quad (2.6)$$

where L_1 the length between the first and second RF flippers, L_2 the length between the second RF flipper and the sample, L_3 the length between the sample and the detector. The phase difference by the momentum difference, which is in quite analogous situation to the Larmor precession. Accordingly, the this term induces a phase dispersion depending on the velocity resolution of the incident neutrons. Condition $\Theta = 0$ is required in order to observe the interference pattern with high visibility.[6,8,9] This condition is equivalent to the time focussing in the MIEZE spectrometer by Gähler et al..[2,10]

Figure 2 shows a typical time dependent interference pattern with frequencies of 100, 330 and 400 KHz using a fast time analyser.

These figures show that the time beat appears as a function of the neutron detection time $t_d = t_0+t_1+t_2+t_3$ with frequency $2\omega_{x1} - \omega_{x2}$.

Consequently we would observe a time interference in the time spectra. We should note that the time beat only appears at the position of the time echo where detector should be located. The positional dependence of the visibility of oscillating time spectra is shown in Fig. 3.[11,12] Here we have recognized for the high frequency time beat, half width of the beat visibility at detector positon is only ±1cm. So detector should be very thin such as a Li6 solid scintillator of which thickness is below than 0.5mm.

Acknowledgements

This work is supported by a Grant-in-aid for Scientific Reseach from the Japanese Ministry of Education, Science and Culture (No 11694090, 10440122).

1) R.Gähler, R.Golub, Z. Phys. B**65** (1987) 269.
2) R.Gähler, R.Golub, T.Keller, Physica B **180 &** 181 (1992) 899.
3) M.Köppe, M.Bleuel, R.Gähler, R.Golub, P.Hank, T.Keller, Physica B **266** (1999) 75.
4) P.Hank, W.Besenböck, R.Gähler, M.Köppe, Physica B **234-236** (1997) 1130.
5) D.Yamazaki, T.Ebisawa, T.Kawai, S.Tasaki, M.Hino, T.Akiyoshi, N.Achiwa, Physica B 241-243(1998)186.
6) T.Ebisawa, D.Yamazaki, S.Tasaki, T.Kawai, M.Hino, T.Akiyoshi, N.Achiwa, Y. Otake, J. Phys. Soc. Jpn. **67**(1998)1569.
7) T.Ebisawa, S.Tasaki, M.Hino, T.Kawai, Y.Iwata, D.Yamazaki, N.Achiwa, Y.Otake, T.Kanaya, K.Soyama, Journal of Physics and Chemistry of Solids 60,(1999) 1569-1572.
8) D.Yamazaki, private communications.
9) T.Ebisawa, S.Tasaki, D.Yamazaki, G.Shirozu, M.Hino, T.Kawai, T.Kanaya, K.Soyama, N.Achiwa. Physica B,276-278(2000),144.
10) W.Besenböck, P.Hank, M.Köppe, R.Gähler, T.Keller, R.Golub, J. Phys. Soc. Jpn. **65** Suppl.A (1996) 215.
11) N. Achiwa, G. Shirozu, T.Ebisawa, D.Yamazaki, M.Hino, S. Tasaki, T.Kawai, J. Phys. Soc. Jpn. 70(2001) uppl. A 436.
12) T.Ebisawa, S.Tasaki, D.Yamazaki, N.Achiwa, G.Shirozu, T.Kanaya, N.Torikai, M.Hino, T.Kawai, K.Soyama, J. Phys. Soc. Jpn. 70(2001) Suppl. A 442.

研究課題: 冷中性子スピン干渉計の開発とその応用
1-7-2 表題: RF flipperによる冷中性子スピン干渉を用いた分光法の開発

Mieze Spin Echo Method Using RF Flippers

T.Ebisawa, S.Tasaki, R.Maruyama[1], N. Achiwa[2], D.Yamazaki[3], T.Kanaya[4], N.Torikai[5], M.Hino, T.Kawai, K.Soyama[3]

Research Reactor Institute Kyoto University
Department of Nuclear Engineering Kyoto University[1]
Department of Physics, Kyushu University[2]
Japan Atomic Energy Research Institute[3]
Institute for Chemical Research, Kyoto University[4]
Neutron Science Laboratory, High Energy Accelerator Research Organization[5]

We have made three improvements for our Mieze spin echo method using RF flipper[1] with regards to neutron intensity, a new RF flipper applicable to pulsed neutron source and precise polarization control of a neutron beam.

The bender system at C312 port supplies neutrons to beam ports of three channels called CH1, CH2 and CH3 [2]. Neutron intensities increase by about 3 times by replacing the supermirror of the bender with new 3Q supermirrors, which is supported by NOP. Typical parameters and neutron intensities for the three channel beam ports are summarized in Table 1 [3]. The new resonance spin echo system of Mieze type is installed at CH2, which supplies neutrons with wavelength longer than 8.2 Å.

Table 1: Three channel beams at C312 port and typical parameters of the three channels.

Beam port	CH1	CH2	CH3
Bent angle	14.5	24.1	35.1
Intensity	3.0×10^6	1.0×10^6	3000
Beam size	42× 8	42× 7	42× 3
Wavelength	> 7.2 Å	> 8.2 Å	8.8 Å

Neutron intensity reduction in the Mieze spectrometer caused by the long traveling would be prevented by a short neutron guide tube, which is set between the first and second RF flippers.

Radio frequency(RF) flippers applicable to wide band neutrons from pulsed source have been developed [4]. Resonance spin echo methods including the Mieze type will be suitable for a pulsed neutron source, replacing the conventional RF flippers with the new RF flippers.

A precise method of neutron polarization control has been developed from the viewpoint of magnetic mirrors and a spin flipper. We obtain a high neutron polarizability of 0.98. Using this polarization technique we can develop an interesting TOF method with spin flip chopper[5]. A TOF data in CH2 beam port at C312 port is shown in Fig. 1. The flight path length and pulse width are

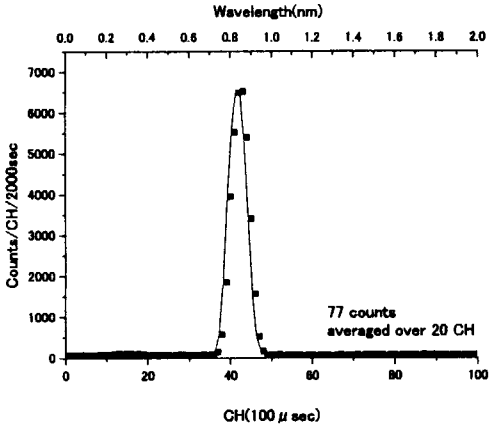


Figure 1: TOF data in CH2 port for neutron beam monochromatized. The peak corresponds to "open" of spin flip chopper.

2.0 m and 500 μ sec, respectively. Neutron counts in the background region are about 77 /CH averaged over 20 channels. Unique performance of spin flip chopper is that the pulse characteristics is controlled by electric circuit.

We are going to make two preliminary applications using this spin echo method to two scattering phenomena. They include neutron inelastic reflection from a polymer with lamellar structure and incoherent inelastic scattering by hydrogen atoms.

References

[1] T.Ebisawa, S.Tasaki, D.Yamazaki, N.Achiwa, G.Shirozu, T.Kanaya, N. Torikai, M.Hino, T.Kawai, K.Soyama, J. Phys. Soc.Jpn 70(2001)Suppl.A 442.

[2] J.Suzuki, K.Soyama, S.Tasaki, T.Ebisawa, Proceedings of ICANS-XV(2000) 547.

[3] J.Suzuki et al, private comunications.

[4] R.Maruyama et al., private comunications.

[5] S.Kawakami et al., private comunications.

JRR-3M, MINE, Fundamental Physics

1-7-3
研究テーマ：多層膜冷中性子干渉計の改良 — 経路間隔の拡大 —
表題：エタロン基板を用いた Jamin 型冷中性子干渉計

Jamin-type interferometer for cold neutrons using etalon plates

M. Kitaguchi [1,3], H. Funahashi [1], M. Hino [2], T. Nakura [1], and H. M. Shimizu [3]
[1] *Department of Physics, Kyoto Univ., Kyoto 606-8502, Japan*
[2] *Research Reactor Institute, Kyoto Univ., Kumatori, Osaka 590-0494, Japan*
[3] *RIKEN, Wako, Saitama 351-0198, Japan*

The authors have established a new type of cold-neutron interferometer based on a pair of etalons coated with multilayer mirrors.

Neutron interferometry is a powerful technique for studying fundamental physics. A large dimensional interferometer for long wavelength neutrons has the advantage to increase the sensitivity to small interactions. Though such a kind of interferometer was realized by using multilayer mirrors[1], the range of experimental application was limited due to the small spatial separation between the two coherent beams.

We used *etalons* in order to enlarge the spatial separation between two parallel waves in *neutron spin interferometer*[2]. The present interferometer consists of several neutron optical components; a neutron polarizer, $\pi/2$ spin flipper coil, π spin flipper coil, phase-shifter coil, $\pi/2$ spin flipper coil, a spin-analyzer mirror, and a pair of etalons (Figure 1). By depositing neutron multilayer mirrors on the parallel planes of an etalon we can produce an optical component which divides the incident neutrons into two parallel paths. And then the two paths are recombined after the reflection off the second etalon. Using etalons with an air gap of 9.75μm in spacing we have observed interference fringes with the contrast of 60%. The experiment was performed using the cold neutron beam line 'MINE' at the JRR-3M reactor in JAERI. The beam had a wavelength of 8.8Å and a bandwidth of 2.4% in FWHM. In the viewpoint of geometrical optics the pair of etalons is equivalent to a *Jamin interferometer* , which is the oldest type of interferometer of visible light.

The present results have demonstrated the feasibility of developing a cold neutron interferometer with a large path separation to carry out high precision measurements and new types of experiment.

References

[1] H. Funahashi et al., Phys. Rev. **A54** (1996) 649.
[2] T. Ebisawa et al., Phys. Rev. **A57** (1998) 4720.

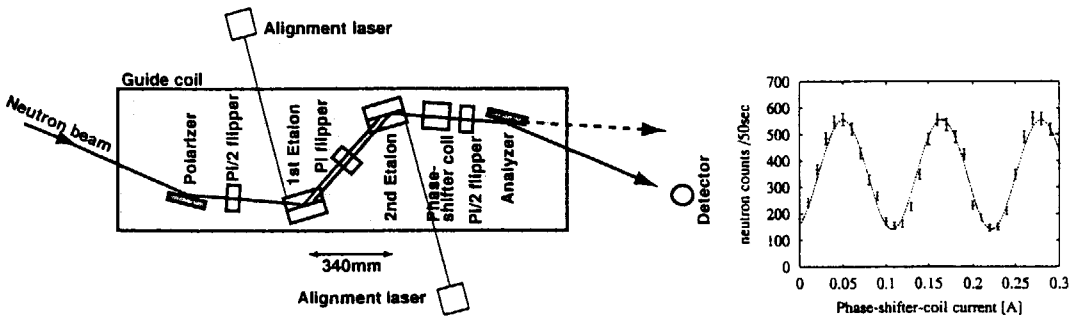


Figure 1: Experimental setup of the interferometer and an interferogram.

使用施設：JRR-3M, 装置：MINE（C3-1-2），分野： Fundamental Physics & Neutron Optics

研究テーマ：ITER真空容器の研究
表　題：ITER真空容器における部分溶け込み溶接の残留ひずみ測定

1-7-4

Neutron Diffraction Measurement of Residual Strain of Partial Penetration Welds for ITER Vacuum Vessel

M. NAKAHIRA, A. MORIAI[1] and N. MINAKAWA[1]

Department of ITER Project, JAERI, Naka, Ibaraki 311-0193
[1]Advanced Science Research Center, JAERI, Tokai, Ibaraki 319-1195

The vacuum vessel (VV) of ITER is a double-walled "doughnut" structure made of stainless steel SS316L with D-shaped cross section. The development of the partial penetration welding by through-wall electron beam welding (EBW) is carried out for the T joint of the outer shell (40-60mm plates) and the rib, because it has advantage from distortion and cost points of view. In this study, neutron diffraction measurement of residual strain of this new welding had been carried out in order to investigate an applicability of the welding to the VV. The configuration of weld and the measurement positions of residual strain are shown in Fig. 1. RESA (Neutron Diffractometer for REsidual Stress Analysis) in the JRR-3 is used for the measurement. Major issue of this measurement is to obtain sufficient neutron intensity within practical exposure time, because the test piece is thick. The neutron intensity was obtained during measurement of strain in two directions. The test condition and results are shown in Table 1 and Fig. 2, respectively. The exposure time of each step is 10 min. These results show that the neutron intensity of measurement in toroidal direction is enough high. But in poloidal direction, the intensity was less than 1/10 of that in toroidal direction. This is because the path-length-difference. The path length of measurement in toroidal direction was about $\sqrt{2} \times 5$ mm but it will be the same as poloidal measurement when the measurement depth is 40 mm (full-depth). It can be concluded that the slit of 3 × 3 mm was too small to obtain sufficient intensity or an exposure time of 10 min was too short. Further survey to find practical test parameter is required.

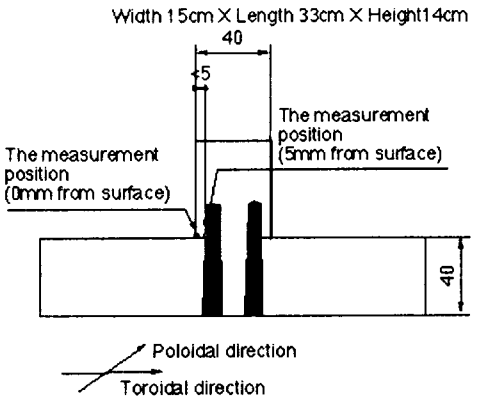


Figure 1: The configuration of weld specimens and the measurement positions

Table 1: Test conditions

Structure	Wave length (Å)	Slit(mm)
FCC (220)	2.09989	3W × 3H

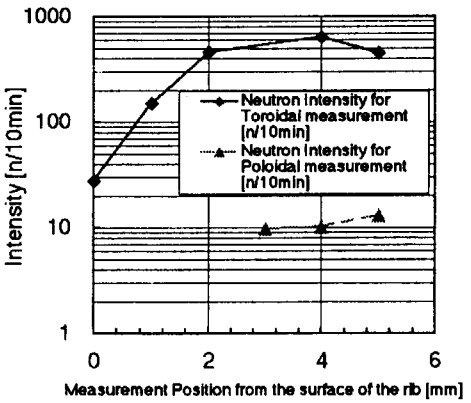


Figure 2: Obtained neutron intensity

原子炉：JRR-3M　　装置：RESA(T2-1)　　分野：中性子散乱（基礎物理）

研究テーマ：中性子回折による構造材料の応力測定および健全性評価
表　題　：レーザピーニング処理されたステンレス鋼のひずみ測定
1-7-5

Strain Measurment in Laser Peened Stainless Steel

Yoshiaki AKINIWA, Keisuke TANAKA, Hidehiko KIMURA,
Nobuaki MINAKAWA[1], Yukio MORII[1]

Nagoya University, Nagoya 464-8603, Japan
[1]Japan Atomic Energy Research Institute, Tokai, Ibaraki 319-1195, Japan

Shot peening treatment has been widely addopted to improve the surface properties such as hardness and strength. Recently, a new technique for the surface treatment was developed by using pulse laser. The laser peening is a promising new technique for the surface treatment of the reactor internals in light water reactors.

In the present study, strain distribution in a stainless steel SUS316NG treated by the laser peening was measured by neutron diffraction method.

The 0.2% proof strength and the tensile strength of the material are 279 MPa and 572 MPa, respectively. The specimen was peened by pulsed laser after annealing at 900 ℃for 30 min. The energy, beam diameter and number of pulse were 200 mJ, 0.8 mm and 3600 pulse/cm^2.

The neutron diffraction from Fe 111 was used for strain measurement. The wave length used was 0.20955 nm. The slit used was 0.35 mm in width and 10 mm in hight. The direction of the lattice strain measured was x, y and z direction as shown in Fig. 1. The arrows indicate laser path.

Figure 2 shows the change of strain with depth from specimen surface. The strains of x and y direction near the surface is compressive. The compressive strain in both direction increases with depth. When the depth is larger than about 1mm, the strain becomes nearly constant.

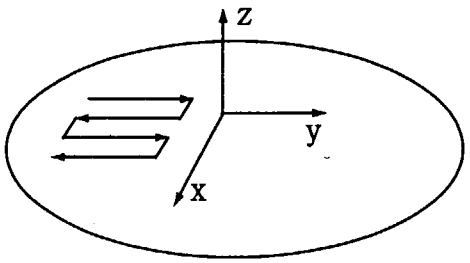


Fig.1. Coordinate.

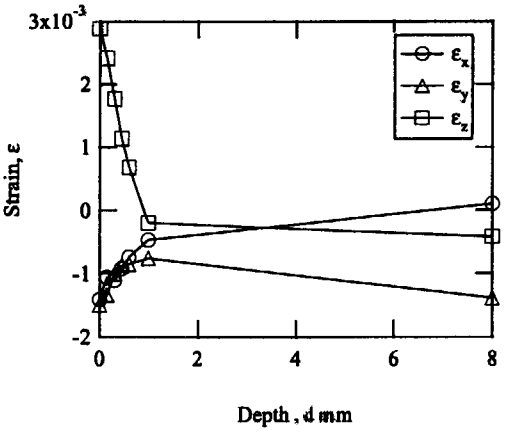


Fig.2. Change of strain with depth.

原子炉：JRR-3M　　装置：RESA(T2-1)　　分野：中性子散乱（基礎物理）

研究テーマ：中性子回折による構造材料の応力測定および健全性評価
表　題：中性子回折法と数値解析に基づく焼入れ鋼の残留応力の測定と検証

1-7-6

Residual Stress Measurement and Verification of Quenched Steel Based on Neutron Diffraction Method and Numerical Analysis

D.Y. Ju[1], R. Mukai[1], N. Minakawa[2]

1 Department of Material Science and Engineering, Saitama Institute of Technology, Fusaiji 1690, Okabe, 369-0293
2 Advanced Science Research Center, JAERI, Tokai, Ibaraki 319-1195

Introduction

Many measurement methods of residual stress have been developed in industry technology such as X-ray diffraction, rapid drilling, ultrasonic method and so on. These techniques have only capability to measure residual stresses near the surface of machine parts. Recently, neutron diffraction method has been developed to measure the residual stress of materials [1]. One of main peculiarities of neutron diffraction is the capability of measuring residual stresses in inside of materials. Using the neutron diffraction technique, many researches for measuring of residual stress in inside space have been carried out and its effectiveness has been verified. From results of some research [1], we can know measurement of the standard lattice spacing of strain-free materials d_0 is very important to increase measuring preciseness and reliability. However, in manufacturing process incorporating temperature history and microstructure variation, complex thermal mechanical behavior results in macro and micro residual stresses and phase transformation as well as texture in materials. When each material point or different area after manufacturing has different microstructure, the measurement and analysis of residual stresses will be difficult, so that it is an open problem and important object how to determine the standard lattice spacing d_0 of strain-free materials to different structure, in which the micro-residual stresses due to variation of phase transformation are main source of internal stress in materials.

This paper presents the measurement with neutron diffraction method for evaluating the residual stresses of quenched steel with large phase transformation. The influence of microstructure due to phase transformation during quenching process on standard lattice spacing d_0 was given. The measurement accuracy is verified by comparison between simulated values of the residual stresses with measured results by XRD and neutron diffraction.

Measurement Method of Residual Stress

Measurement method based on neutron diffraction.
Figure 1(a) presents the schematic of neutron diffraction equipment, which was installed in the thermal neutron guide tub T2-1 port of JRR-3M reactor in JAERI. For precise stress analysis, standard lattice spacing of strain-free materials d_0 must be accurately measured and estimated. Powder diffraction method is a general way of determining the parameter d_0. However, for engineering materials especially those involving large plastic deformations or phase transformations often have preferred crystallographic orientation or non-homogenous distribution of phase or composition, the measured d_0 by powder diffraction method could not coincide with the true original lattice spacing of the material with variable phase and texture. In this measurement, we performed a technique proposed by Minakawa [1] to estimate the d_0 from the measured average lattice space by rotating specimen method shown by Fig.1(b). Rotation target is used to increase the gains contributing to the diffraction peak in different directions. In this way, an average result of lattice strain could be obtained to eliminate the influence of textures and crystal direction formed in materials processing. The residual strains were measured in three mutually perpendicular directions in which were the expected principal axes. Follow equations give the principles for stress measurement with neutron diffraction method by measuring Young's modulus from tensile test and initial lattice spacing d_0.

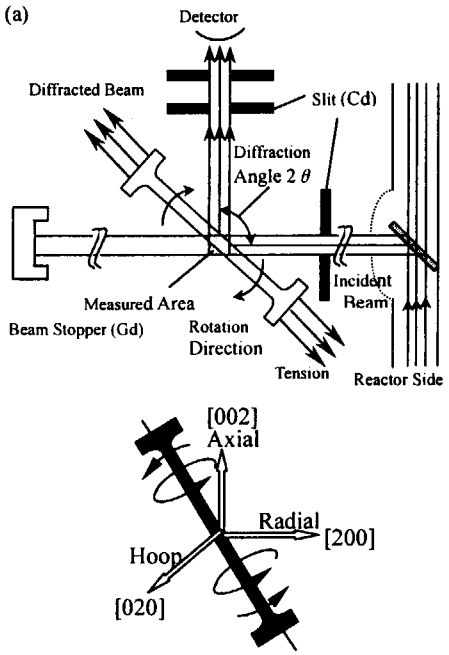


Fig.1 Measuring method of neutron diffraction

$$\sigma_{\cdot} = \frac{E}{(1+\nu)(1-2\nu)}\left\{\varepsilon_{\cdot}(1-\nu)+\nu(\varepsilon_{\cdot}+\varepsilon_{\cdot})\right\} \quad (1)$$

$$\lambda = 2d_{hkl}\cdot Sin\,\theta_{hkl} \quad (2)$$

$$\varepsilon_{hkl} = \frac{d-d_0}{d_0} = -\cot\theta_{hkl}\Delta\theta_{hkl} \quad (3)$$

Here, E, ν, and σ indicate young's modular, Possion's ratio and principle stress, respectively. λ, θ, and ε indicate the

原子炉：JRR-3M　　装置：RESA (T2-1)　　分野：中性子散乱（基礎物理）

wavelength, neutron beam angle and the strain on crystallographic plane, respectively. d and d_0 are the interplanar spacing and standard lattice spacing of strain-free materials, respectively. For the measured specimen of S45C carbon steel material, strains on (110) and (200) crystallographic plane were measured in neutron diffraction. Residual stresses are calculated from measured strains using diffraction elastic constants measured experimentally.

Specimens for tension test A round disk with 30 mm diameter and 10 mm thickness were used in residual stresses measurement. The specimens of S45C carbon steel were measured before and after heat treatment by quenching in water. The quenching process is heating at 850℃ for one hour and then cooling in 20℃ water.

Measurement method based on X-ray method The stress filed in the quenched parts under examination is usually assumed to be two dimensional with σ_z and σ_θ as the principal stresses in the surface. In the direction Φ, σ_z on the plane of the sample can be calculated directly from the slope by the $\sin^2\theta$ method. According to the Bragg's law, the X-ray measured strain can be represented by a relative change in the interplanar spacing of specified crystal planes to define wave-length λ, the initial lattice spacing d_0 and lattice constant a_0 in the unstressed or stress-free condition, respectively, whilst d_ψ and a_ψ are those for the stressed condition in the planes perpendicular to the direction ψ, and 2θ corresponding diffraction angles of the plane. It is already known that the stress-free lattice spacing can be roughly estimated at a definite Ψ^* position where the measured strain is always zero.

Measured and Simulated Results

The measured d_0 in (110) and (200) plane of the tensile specimen before and after water quenching are given in Table. 1. It is obvious that the lattice spacing of strain free material in different positions is different. Due to the non-homogenous distribution of martensite from surface to center for a quenched disk, the initial lattice space decreases a little from surface to center. This result confirmed that the initial lattice space varies as the material phase changes.

From the measured d_0, the strain of lattice could be determined. From the measured stress train curve in tensile test, elastic constants including Young's modulus and Poisson's ratio were obtained and also listed in Table 1. The residual stresses were calculated from the above parameters.

Based on metallo-thermo-mechanical theory, finite element simulation on quenching process of disk are carried out with the same size of the disk model. Under three types of heat transfer coefficient boundaries, the simulated results were given [2]. Comparison of residual stresses on the surface of specimens based on neutron diffraction measurement and thermo-mechanical simulation as well as X-ray method is presented in Fig. 2.

Table 1 Neutron diffraction measured results

Before quenching		Wavelength λ	2.098918 Å
Young's modulus	214.887 GPa	D_0(110)	2.029114
Poisson's ratio	0.301385	D_0(200)	1.434214
After quenching with water		Wavelength λ	2.098918 Å
Young's modulus	198.626 GPa	D_n(110)	2.036831
Poisson's ratio	0.353486	D_n(200)	1.432092

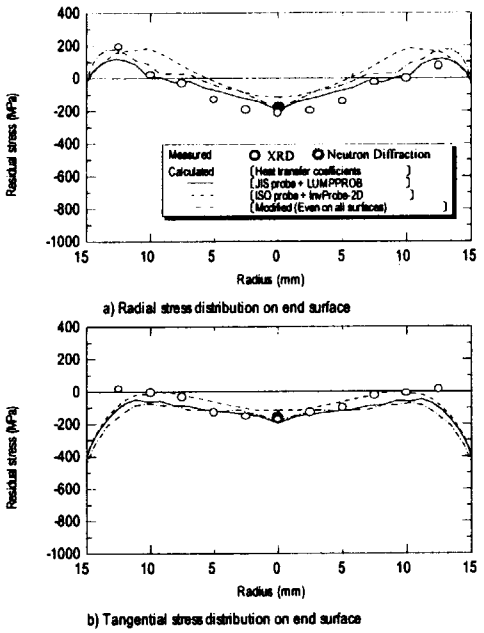


Fig. 2 Comparison of the measured residual stresses with computed values

Summary

Neutron diffraction studies has been conduced to ascertain the level of residual stresses in heat treated disk. Results of these experiments indicates that changes in lattice parameters associated with heat treatment may be attributed to phase transformation and microstructure change in the materials. The results of the simulation were compared with measured residual stresses based neutron diffraction and X-ray methods. From these results, we obtained some useful conclusions:

(1) From the results in research, we can know that effect of the standard lattice spacing d_0 of strain-free materials on residual stresses measurement was very large, so it is important to determine micro-residual stress due to distribution of microstructure after quenching process.

(2) The distribution of residual stresses near surface agrees well with calculated value, when d_0, Young's modulus and Poisson's ratio can be measured by using quenched tensile specimen with enough small size and almost same distribution of micro-structure, such as martensite.

(3) The measured residual stresses confirmed the micro-residual stresses generated due to variation of phase transformation are main source of internal stress in materials of heat-treated parts.

References

[1] N. Minakawa, Y. Morii and Y. Shimojo: Proc. of 6th Int. Conf. on Residual Stresses, Vol.2 (2001) p.1107

[2] T.Inoue, D.Y. Ju and K, Arimoto: Proc. of Inter. Conf. on Quenching and Control of Distortion, ASM International, Vol.1 (1992) p.205

研究テーマ：中性子回折による構造材料の応力測定および健全性評価
表　題　：中性子回折による SiC 粒子強化アルミニウム合金の疲労損傷評価

1-7-7

Evaluation of Fatigue Damage in SiC Particulate Reinforced Aluminum Alloy by Neutron Diffraction

Yoshiaki AKINIWA, Keisuke TANAKA, Hidehiko KIMURA,
Nobuaki MINAKAWA[1], Yukio MORII[1]

Nagoya University, Nagoya 464-8603, Japan
[1]Japan Atomic Energy Research Institute, Tokai, Ibaraki 319-1195, Japan

Structural materials fracture when they are subjected to cyclic loading, even if the load is less than the static strength. This phenomenon is known as fatigue failure. For engineering components, clarification of fatigue properties and development in inspection procedures to detect fatigue damage are very important to obtain a good reliability.

In this study, the neutron diffraction method was used to measure the change of the phase strains of the composite during the fatigue process.

The materials used were aluminum alloy reinforced by silicon carbide particles (SiCp/Al 2024). The volume fraction of SiC particles of the composite is 20% and their average size is 3μm. The 0.2% proof strength is 465 MPa and the tensile strength is 625 MPa. The neutron diffractions from Al 200 and SiC 116 were used for stress measurement.

Figure 1 shows the change of the slope of the relation between applied stress and measured strain obtained from Al200 diffraction. The slope increases with stress cycles. On the other hand, the slope obtained from SiC116 diffraction decreases with stress cycles as shown in Fig. 2. Debonding of the interface between the matrix and the particle was initiated during fatigue process. The strain in the SiC particles was reduced by the debonding. The specimen was broken at N=7500 cycles.

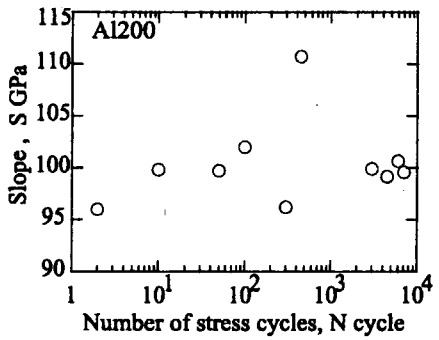


Fig.1. Change of slope in Al phase.

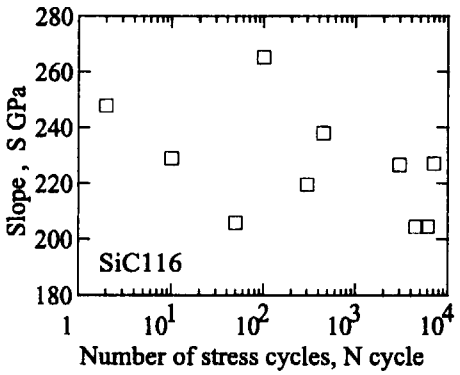


Fig.2. Change of slope in SiC phase.

原子炉：JRR-3M　　装置：RESA(T2-1)　　分野：中性子散乱（基礎物理）

1-7-8
研究ﾃｰﾏ：中性子回折による軸受部品の非破壊残留応力測定
表　題　：中性子回折方法による浸炭ベアリングリングの内部残留応力非破壊測定の予備測定

Feasibility study on nondestructive measurement of residual stress profile in carburized bearing rings using neutron diffraction method

Y. Matsumoto, A. Moriai [1] and N. Minakawa [1]

Corporate Research & Development Center, NSK Ltd., Kanagawa, 251-8501
[1]Advanced Science Research Center, Japan Atomic Energy Research Institute, Ibaraki 319-1195

Feasibility study on nondestructive measurement of residual stress profile in carburized and quenched bearing rings was carried out using neutron diffraction apparatus, RESA at JRR-3M.

The measurement condition is as follows, λ=0.2098885nm, diffraction plane=(110), diffraction angle range (2θ)= 60.5 - 64 degree, slit for incident beam=2mm×2mm, measurement depth=0, 2, 4, 6, 8, 12mm from outer surface. The test sample was SAE9315 carburized and quenched ring, size of which was φ160, φ136 and 50mm in O.D., I.D. and width. No strain d_0 was measured with random rotation method using each depth cubic sample cut from above measured ring.

Figure 1 shows the apparatus and actual measurement. Figure 2 shows result of axial residual stress measurement. The strain values are all positive and no significant difference is found between the surface and core. This means that the residual stress of surface layer in carburized steel ring is tensile although it has normally compressive residual stress. Figure 3 shows that the residual stress of surface layer in axial direction is actually compressive with X-ray measurement method. The result different from the forecast was obtained in this measurement. To develop the measurement analysis technique of quenched steel in the future is important. Neutron diffraction method is attractive for residual stress measurement because of non-destructive measurement.

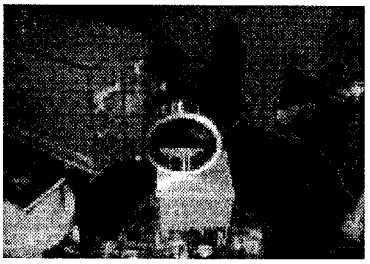


Figure 1 Neutron diffraction apparatus and actual measurement.

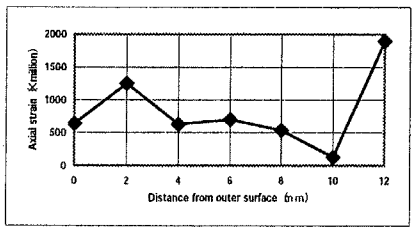


Figure 2 Profile of axial residual stress in bearing ring Measured by neutron diffraction method.

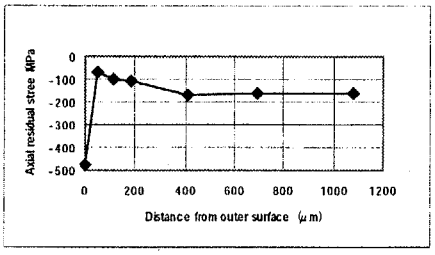


Figure 3　Residual stress of surface layer in axial direction measured by X-ray diffraction method.

原子炉：JRR-3M　　装置：RESA（T2-1）　　分野：中性子散乱（基礎物理）

研究ﾃｰﾏ：Ta,W固体ターゲットの接合材残留応力測定
表　題　：パルス中性子におけるタングステンタンタル接合材料の残留応力測定

1-7-9

Residual strain of W/Ta Joint Material for Spallation Neutron Source

Kenji Kikuchi, Nobuaki Minakawa, Atsushi Moriai, Yukio Morii,
Masayoshi Kawai[1], Michihiro Furusaka[1], Jing-Feng Li[2] and Hiroaki Kurishita[3]

Advanced Science Research Center, JAERI, Tokai, Ibaraki 319-1195
[1]KEK, High Energy Accelerator Research Organization, Tsukuba-shi, Ibaraki 305-0801
[2]Tohoku Univ ,Graduate school of Eng.,Tohoku Univ.mSendai-shi, Miyagi 980-8579
[3]Institute for Materials Research, Tohoku Univ., Oarai-machi, Ibaraku 311-1313

Residual strain near the boundary of Tungsten and Tantalum was measured. Both materials are candidate for a target of spallation neutron source. Tungsten has a good neutron yield as a solid target; however, a disadvantage for usage is brittleness due to irradiation by protons and neutrons, and a corrosive property in water under radiation. So Tungsten is recommended to be cover with cladding material. Tantalum has also a high atomic number so that good material for target except for a high atomic density decaying heat. The property of Tantalum had shown remarkable a loss of ductility after proton bombardment but recently a different data was disclosed from Julich Laboratory. They examined a spent target of ISIS and concluded that Tantalum, which received a damage of 13-dpa, had enough ductility to use as target. The reason is hinted to high purity in chemical composition. So the idea is to make Tantalum –cladded Tungsten target. We chose a HIP, Hot Isostatic Pressing, process to joint them together.

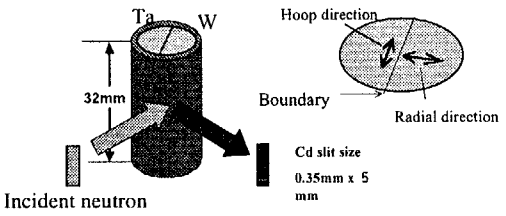


Fig.1 Sample geometry and incident neutron.

The size of solid target is 55x28x76mm. The thickness of cladding tantalum is less than 1mm. This is a real size suitable for KENS target at KEK. The preferable condition for HIP was to avoid re-crystallization of Tantalum in the deeper diffusion length of Tantalum into Tungsten and was found to be 200MPa in press at 1500°C during 3 hrs. Target blocks were manufactured, examined by non-destructive inspection. We found no gap between HIPped boundary by means of ultra-sonic microscope.

This study aims at examining the residual stress near the boundary jointed by HIP. The

原子炉：JRR-3M　　装置：RESA（T2-1）　　分野：中性子散乱（基礎物理）

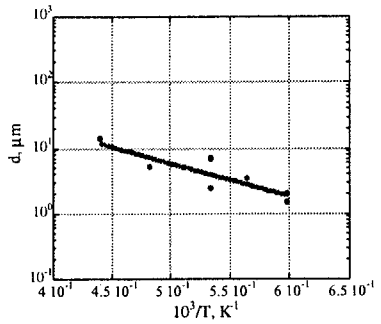


Fig.2 Diffusion depth of Ta into W.

sample is shown in Fig.1. Tantalum and tungsten were stored in the cylinder of Tantalum. Both ends were welded to be capped by Tantalum disks. The sample was treated at the preferable condition. The diffusion depth of Tantalum into tungsten is expected to be 4 μm as shown in Fig.2

The residual strains were measured by RESA. Preparation was done by Measurement of the wavelength of incident beam, Determination of center of distributed incident-beam intensity, and Measurement of powder diffraction of both materials. The strain-free lattice length at (110) was decided to be 2.239602x 10^{-10} m for Tungsten and 2.336669 x 10^{-10} m for Tantalum, respectively.

Figs. 3 and 4 show strains to the component of radial direction and hoop direction, respectively. It is found that near the jointed boundary all of measured strain components showed tension varied in 1000 to 5000 x10^{-6}.

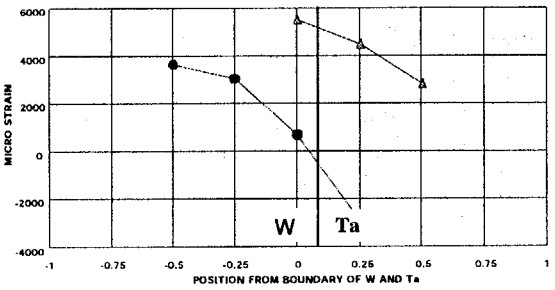


Fig. 3 Strain component to the radial direction.

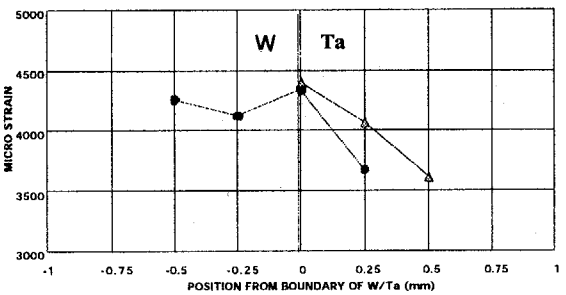


Fig.4 Strain component to the hoop direction.

研究テーマ：中性子回折による構造材料の応力測定および健全性評価
表　題　：タングステン繊維/銅複合材の内部応力回折

1-7-10

INTERNAL STRESS ANALYSIS OF TUNGSTEN FIBER REINFOECED COPPER COMPOSITE

TAKAO HANABUSA[1] and MASAYUKI NISHIDA[2]

[1]Department of Mechanical Engineering, Tokushima University, Tokushima 770-8506
[2]Kobe City College of Technology, Kobe 651-2194

1. Introduction

Fiber reinforced materials have found considerable applications in the improvement of the performance characteristic on engineering materials. However, there is commonly a large difference in the thermal expansion coefficient between the matrix and the fiber. The main cause of thermal stress in such composites is the thermal expansion mismatch between the matrix and the fiber. In this study, the thermal residual stress in the continuous tungsten fiber embedded in the copper matrix was measured by the neutron diffraction method.

2. Conditions of the Neutron Stress Measurement

The specimen used in this investigation is tungsten-fiber (100μm in diameter) reinforced copper composite. This composite was produced by a unidirectional solidifying method. The volume fraction of the tungsten fiber is about 10%. This specimen was annealed at 973K for 2 hours before stress measurement. The thermal residual stresses due to the difference of the coefficient of thermal expansion between the matrix and the fiber were generated in the composite.

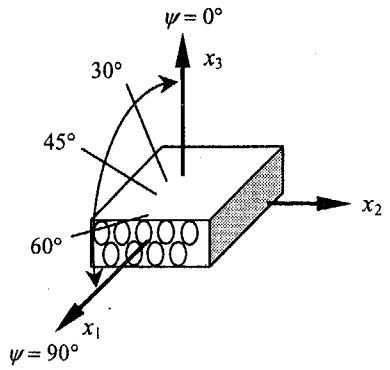


Fig. 1. Coordinate system and definition of the angle ψ.

Figure 1 shows the coordinate system of this composite. The axes x_1 and x_2 are parallel to and x_3 axis is normal to the specimen surface, with x_1 axis being defined as parallel to the fiber direction. The angles ψ between the x_1 axis and the x_2 axis are defined as shown in Fig. 1.

Table 1 shows the conditions of neutron stress measurement. The stress–free lattice spacing of each {hkl} was measured from the bundled tungsten-fiber specimen annealed at 973K, by using the rotating sample attachment.

Table 1: Conditions of neutron stress measurement.

Measurement apparatus	RESA in JAERI
Neutron wave length λ, nm	0.209783 nm
h k l plane and initial lattice spacing d_0, nm	W(110) d_0= 0.223807 W(200) d_0= 0.158214 W(211) d_0= 0.129151
Diffraction angle, deg.	W (110) 2θ = 55.9 W (200) 2θ = 83.0 W (211) 2θ = 108.6
Young's modulus E, GPa	402.7
Poisson's ratio ν	0.28

In this study, two types of neutron stress measurement method were used to investigate the thermal residual stress in the fiber phase of the Cu/W composite. The one is the usual triaxial measurement method by using Hooke's equation, and the other is the $\sin^2\psi$ [1)] method which is commonly used in X-ray stress measurement with the assumption of the plane stress condition. The fundamental equation of $\sin^2\psi$ method is given by the following equation:

原子炉：JRR-3M　　装置：RESA (T2-1)　　分野：中性子散乱（基礎物理）

$$\varepsilon_{\psi} = -\frac{1+\nu}{E}(\sigma_{11}-\sigma_{33})\sin^2\psi + \frac{1+\nu}{E}\sigma_{33} - \frac{\nu}{E}(\sigma_{11}+\sigma_{22}+\sigma_{33}). \quad (1)$$

If the plane stress condition is held in the sample, we can regard as the stress $\sigma_{33} = 0$. Thus, this equation means that ε_{ψ} linearly relates against $\sin^2\psi$, and the longitudinal stress σ_{11} is determined from the slope of the $\sin^2\psi$ diagram. However, when the stress component of σ_{33} cannot be ignored, the $\sin^2\psi$ method leads to the result in the stress value of $\sigma_{11}-\sigma_{33}$.

3. Results of Neutron Stress Measurement

Figure 2 shows the relationship of the neutron diffraction intensity of three types of hkl plane against ψ tilt angle. From this result, it is obvious that the tungsten fiber has a heavy 110 texture along its longitudinal direction. Therefore, the specimen must be adequately tilted for the measurement of $\sin^2\psi$ method.

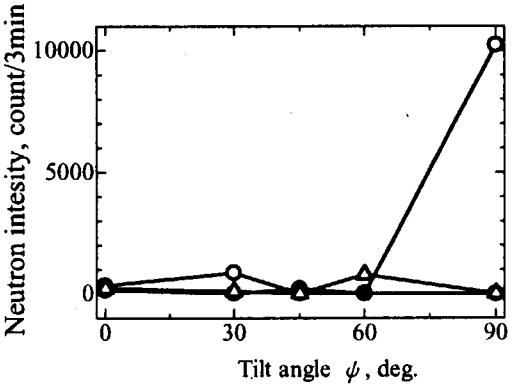


Fig. 2: Diffraction intensity of three {hkl} planes against ψ angle by neutron diffraction.

Table 2 : Combinations of the ψ tilt angle between the measurable plane and the 110 oriented plane.

Measurable plane	ψ tilt angle
110	0, 60, 90
200	45, 90
211	30, 54.7, 73.2, 90

Table 2 shows the combinations of the ψ tilt angle between the measurable 110, 200 and 211 plane in the 110 textured tungsten fiber. All of these ψ tilt angles were employed in neutron stress measurement by using $\sin^2\psi$ method.

Figure 3 show the typical $\sin^2\psi$ diagram described the lattice spacing vs. $\sin^2\psi$ in 200 plane. Owing to the heavy 110 texture, the measurement result in the point of $\sin^2\psi=1.0$ ($\psi=90°$) could not be obtain due to the very weak 200 diffraction. However, the points of the others lie on a line of least square approximate, and this line shows a good linearity in this case. Therefore, the stress in 200 plane might be calculate from the slope of this line by using $\sin^2\psi$ method.

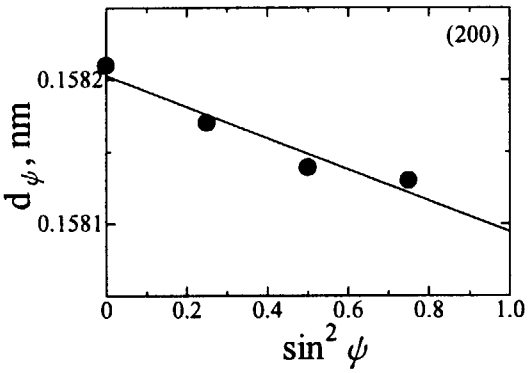


Fig.3: $\sin^2\psi$ diagram for 200 plane.

The results of neutron stress measurement by using the triaxial measurement method as well as the $\sin^2\psi$ method are shown in Table 3. From these results, it can be confirm that all of the stress values are compressive, and the longitudinal stress σ_{11} along the fiber takes the maximum value. The stresses for 200 and 211 planes could not be calculated by the triaxial measurement method, because the diffraction peak in $\psi=0$ (deg.) did not appear from the tungsten fiber which has a strong 110 texture. On the other hand, the $\sin^2\psi$ method gave the stress value from the slope of the $\sin^2\psi$ diagram for each plane of 110, 200 and 211. However, we must note that the results from the $\sin^2\psi$ diagram lead to the stress value $\sigma_{11}-\sigma_{33}$ in the triaxial stress state.

Table 3 Results of neutron stress measurement.

Triaxial measurement method (MPa)				$\sin^2\psi$ method (MPa)
hkl	σ_{11}	σ_{22}	σ_{33}	$\sigma_{11}-(\sigma_{33})$
110	-467	-219	-150	-268
200	-	-	-	-215
211	-	-	-	-209

References

1) T. Hanabusa : Proc. The Sixth Int. Conf. Residual Stresses, UK, 2000. pp. 181-188.

1. 中性子散乱 8)装　置

1. Neutron Scattering 8) Instrument

This is a blank page.

研究テーマ：重水素化ダイアモンドライクカーボンの開発
表題：重水素化ダイアモンドライクカーボンの中性子鏡としての特性

1-8-1

Characteristics of Deuterated Diamond-like Carbon as Neutron Mirror

Y. Kawabata[1], T.Horie[2], M.Hino[1], S. Tasaki[1], K.Yoshida[3], I.Kanno[3] and M.Nakayama[4]

[1] Research Reactor Institute, Kyoto University, Kumatori, Osaka 590-0494, Japan
[2] Faculty of Engineering, Kyoto University, Sakyo-ku, Kyoto 606-8501, Japan
[3] Quantum Science and Engineering Center, Faculty of Engineering, Kyoto University, 611-0011, Japan
[4] R&D Center, TDK Co., Ichikawa, Chiba 272-8558, 375-8501, Japan

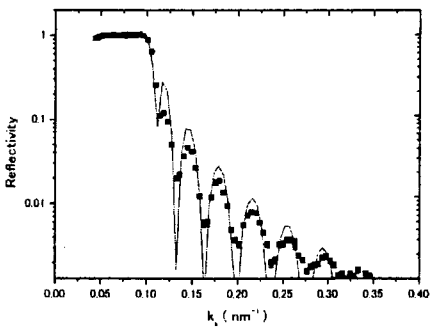
Deuterated diamond-like carbon (D-DLC) was fabricated on silicon wafer and the characteristics as a neutron mirror was measured. The UCN confinement experiments need free surface neutron mirrors to confine UCN in an experimental equipment, though neutron mirrors are usually flat. D-DLC was developed to use as a mirror material of UCN bottle for neutron electric dipole moment (EDM) experiment.

Usually, diamond-like carbon is deposited by the radio frequency plasma chemical vapor deposition (RF-CVD). As usual DLC thin layers made by this method contain a lot of hydrogen, D-DLC has been developed with deuterated hydro-carbon as source gas to eliminate hydrogen in the layer. D-DLC has the advantage as neutron mirror because deuterium has the positive potential and the small absorption cross-section for neutrons.

The surface roughness of D-DLC was measured by the scanning white light interferometry. They have the roughness of Ra = 0.3 - 0.6 nm, and are good enough for monolayer mirrors. The neutron reflectivity measurement shows that the critical wavelength of the total reflection is 59.9 - 62.2 nm. It is almost same with that of natural nickel, 58.0nm, which is usually used as a good material of neutron mirrors. The neutron reflectivity is about 1.0 in the total reflection range. These results show that performance of D-DLC as neutron mirror is completely satisfactory.

The measurements of ERDA & RBS show the number densities of elements in D-DLC layers. The number density of carbon is 6.3 - 6.5 x 10^{22} C/cm^3 and that of deuterium is 4.2 - 4.7 x 10^{22} D/cm^3. The density calculated from these numbers is 1.4 g/cm^3 and it is a little smaller than that of usual DLC layer. The number density of hydrogen in unit area is 1.4 - 3.2 x 10^{16} H/cm^2. This is same with the typical numbers of usual neutron mirrors. So D-DLC is not the solution of the surface hydrogen problem of the UCN bottle experiments.

Though D-DLC is not ideal for UCN bottle, it is a promising neutron mirror. It has a good neutron reflectivity with high quality mirror surface and high potential. It also has a possibility of making a free shape mirror, because DLC is already used on complicated surfaces like molds and tools in manufacturing engineering. It will be useful for neutron guide tubes, neutron benders and focusing devices, because they require many kinds of mirror surfaces, for instance, spherical or parabolic surfaces on both sides of very thin substrates.



Neutron Reflectivity of D-DLC

使用施設：JRR-3M, 装置：MINE(C3-1-2), 分野： Instrumentation

研究課題: 多層膜スピンスプリッターを用いた中性子スピンエコー分光器の開発 II
表題: 多層膜スピンスプリッターを用いた中性子スピンエコー分光器の開発 II

1-8-2 Development of a new spin echo spectrometer using multilayer spin splitters II.

S.Tasaki, T.Ebisawa, M.Hino, R.Maruyama, N.Achiwa, D.Yamazaki[1], T.Kawai
Research Reactor Institute Kyoto University
[1] *Japan Atomic Energy Research Agency*

Modified neutron spin echo (MNSE) methods, in which neutron spin 'precession' is realized other than Larmor precessions, allow us to construct compact NSE spectrometers and hence to combine NSE with other spectrometers. Especially, one of the MNSE methods, Mieze[1], is applicable to measure quasi-elastic scattering accompanying neutron spin-flip process, since in Mieze spectrometer neutron spin echo is realized after spin analyzer. One of the MNSE methods is realized by using the multilayer spin splitters (MSS's), which are composit multilayer consisting of a magnetic mirror, gap layer, and a non-magnetic mirror[2]. When a neutron in a superposing state of magnetic field parallel and anti-parallel states is incident to the MSS, then a phase proportional to the gap layer thickness is introduced since parallel and anti-parallel components are reflected by the different multilayers. The phase shift is equivalent to the Larmor precession angle. The most important feature of the spectrometer is its compactness. In the spectrometer, since Larmor precession magnets are replaced by pairs of multilayer spin splitters, then total size, required electric power are much reduced.

MSS is fabricated with vaccum evaporation system in Res. React. Inst. Kyoto Univ. The magnetic and non-magnetic mirrors consist of permalloy/Ge and Ni/ Ti. The d-spacing for both multilayer is 110Å. The gap layer is made of Ge with thickness of 3500Å. The experiments are carried out at C3-1-2 beam port (MINE) of JRR-3M reactor in Japan Atomic Energy Agency. The wavelength of neutron is 12.5Å. The arrangement of the MSS-NSE spectrometer is shown in Fig.1. The incident neutron is set into the superposing state by the polarizer (P) and the first $\pi/2$-spin flipper ($\pi/2$-1). Then it is incident to the pair of MSS in (+ +) configuration (DMSS1). This configuration is important to deal with the neutrons scattered by the sample, since the phase difference due to the beam divergence is cancel out after the second reflection. The phase introduced by the first pair of MSS's is canceled by the second pair of MSS's (DMSS2) after the π-spin (π) flipper. The neutron is detected after the phase analysis with $\pi/2$-2 and spin analyser (A). To measure the spin echo signal, a phase shifter coil is inserted and the neutrons are counted via the flipper coil current.

The NSE signal for the set-up shown in Fig.1 is presented in Fig.2, and expresses the clear oscillation. In the next step, we are planning to measure the quasi-elastic scattering from some typical samples.

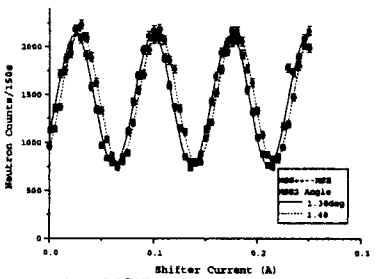


Figure 2: NSE signals for the arrangement shown in Fig.1.

References

[1] P.Hank, W.Bensenböck, R.Gähler, M.Köppe, Physica B **234–236** (1997) 1130–1132

[2] T.Ebisawa, S.Tasaki, T.Kawai, M.Hino, N.Achiwa, Y.Otake, H.Funahashi, D.Yamazaki, T.Akiyoshi, Phys. Rev. A, At. Mol. Opt. Phys. (USA) **57**, 4720 (1998).

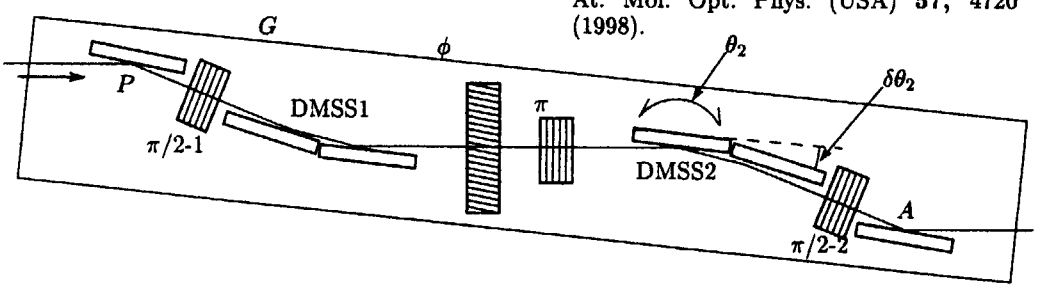


Figure 1: The arrangement for MSS-NSE method.

研究テーマ：パルス中性子イメージング検出法の研究
表　題：中性子イメージング用輝尽性蛍光体 $SrBPO_5:Eu^{2+}$ の特性

1-8-3

Characteristics of Photostimulable Phosphor $SrBPO_5:Eu^{2+}$ for Neutron Imaging

K.SAKASAI, M.KATAGIRI, K.TOH, H.TAKAHASHI[1], M.NAKAZAWA[1] and Y.KONDO[2]

Advanced Science Research Center, JAERI, Tokai, Ibaraki 319-1195
[1]Dept. of Quantum Engineering and System Science, University of Tokyo, Tokyo, 113-8656
[2]Dept. of Applied Physics, Tohoku University, Sendai 980-8579

The neutron imaging plate (NIP) has made a great success in the field of neutron scattering study but the NIP is sensitive to not only neutron but also gamma ray. Therefore, it is difficult to discriminate neutron signal from gamma ray one when the NIP is read out. To overcome the problem, the authors have been studying a $SrBPO_5:Eu^{2+}$ material as a new neutron storage phosphor consisting of light materials.

The $SrBPO_5:Eu^{2+}$ powder sample was prepared by firing raw materials ($SrCO_3$, H_3BO_3, $(NH_4)_2HPO_3$, and $EuCl_3 \cdot 6H_2O$) in a muffle furnace in a nitrogen atmosphereat 600°C for 2 hours and at 800°C for 2 hours. The authors found that this phosphor shows photostimulated luminescence (PSL) at 390 nm by illumination of 635 nm laser light after neutron irradiation without adding any neutron sensitive materials such as Gd.

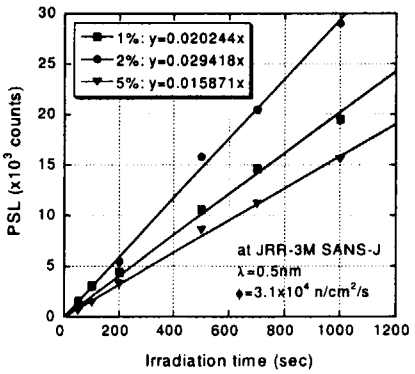


Figure 1: The total PSL output as a function of the neutron irradiation time, where the concentration of Eu in measured samples was changed.

Figure 1 shows the total PSL output as a function of the neutron irradiation time when the concentration of Eu in the samples was changed. It can be seen that the total PSL output was proportional to the irradiation time. Results of linear fitting of the data are also shown in the figure. The slope is proportional to the neutron sensitivity. The optimal concentration of Eu in the samples was 2%.

Table 1: The neutron and gamma-ray sensitivities (S_n and S_γ) of $SrBPO_5:Eu^{2+}$ and BAS-ND

items	$SrBPO_5:Eu^{2+}$	BAS-ND
S_n	1.66×10^{-2}	1.24
S_γ	3.47×10^{-5}	2.19×10^{-2}
S_γ/S_n	2.09×10^{-3}	1.77×10^{-2}

unit:S_n (PSL/mm^2/neutrons), S_γ (PSL/mm^2/gamma)

The authors have also investigated the neutron and gamma sensitivities of the $SrBPO_5:Eu^{2+}$ (2%) sample. Table 1 lists measured neutron and gamma-ray sensitivities of samples compared with those of a BAS-ND neutron imaging plate (Fuji film Co. Ltd.), where the neutron wavelength and gamma-ray energy are 0.5 nm and 662 keV (^{137}Cs gamma-ray source), respectively. One can see that the neutron sensitivity of the $SrBPO_5:Eu^{2+}$ sample is two orders of magnitude lower than that of BAS-ND, while the gamma-ray sensitivity is three orders lower. These results may come from the fact that the BAS-ND sheet contains Gd atoms which has a very large neutron cross section and consists of relatively heavy materials ($BaFBr:Eu^{2+}$). However, the S_γ/S_n ratio of the $SrBPO_5:Eu^{2+}$ sample is ten times better than that of BAS-ND. The low S_γ/S_n ratio is favorable for reducing the gamma-ray influence on the signal.

原子炉：JRR-3M　　装置：SANS-J(C3-2)　　分野：中性子散乱（装置）

研究テーマ：機能性生体物質の水和構造研究
表　題：湾曲完全結晶シリコンモノクロメータにおける対称および完全非対称反射配置(FADG)の比較

1-8-4

Comparison Between Symmetric Diffraction Geometry And Fully Asymmetric Diffraction Geometry (FADG) Of Bent Perfect Silicon Monochromator

M. REFAI MUSLIH[1,2], ICHIRO TANAKA[2], PAVEL MIKULA[3] and NOBUO NIIMURA[2]

[1]National Nuclear Energy Agency, BATAN Indonesia
[2]Advanced Science Research Center, Japan Atomic Energy Research Institute, Tokai, Ibaraki 319-1195, Japan
[3]Nuclear Physics Institute, 25068 Rez, Czech Republic

Reflectivity properties of the fully asymmetric diffraction geometry (FADG) of the bent perfect Si(111)-crystal were experimentally studied. The obtained results are compared with those corresponding to the symmetric diffraction geometry. Both these parameters were measured on the dependence of curvature of the cylindrically bent Si(111)-crystal slab, using the crystal slabs of the same dimensions (200x40x4 mm^3) and the width of the incident beam of 13 mm, 0.209nm wavelength and 1.5 m monochromator to Neutron Imaging Plate distance. It has been found (fig. 1) that the peak intensity of symmetric geometry was about 1.5 times higher with respect to the FADG case, but in case of FADG the irradiated crystal volume was smaller by a factor of 1.9 than symmetric one. FWHM for FADG was relatively independent to the curvature. The FWHM for FADG affected only by thickness of monochromator crystal. It shows the condensation of incoming beam had been occurred.

Concerning the focusing properties, each system has its own advantage. Using the FADG system, it is very easy to make a narrow (comparable to the crystal thickness) parallel-diffracted beam without any Soller collimator. Due to a larger incident angle for white beam with respect to the surface of the crystal slab the irradiated monochromator volume in the FADG case is correspondingly smaller than in symmetric case. However, thanks to the spatial condensation (Fankuchen effect) a high monochromatic beam density may be obtained with the FADG[1]. In case of wide beam, FADG may become better -high intensity and parallel beam- than symmetric geometry.

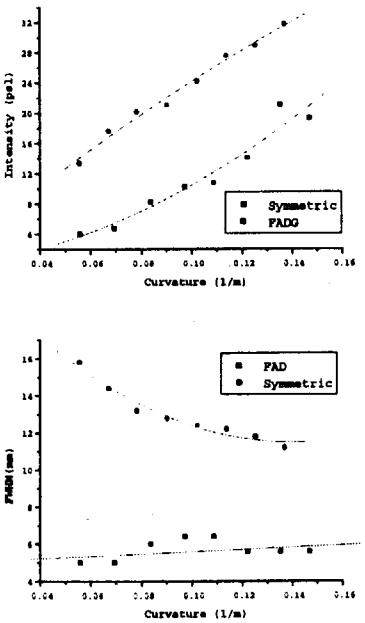


Figure 1: Intensity (upper) and FWHM (lower) as a function of curvature for Symmetric and Fully Asymmetric diffraction geometry.

References

1) P. Mikula, J. Kulda, P. Lukas, M. Vrana, V. Wagner: Nucl. Instrum. and Methods **A338**(1994) 18-26.

原子炉：JRR-3M　　装置：TAS-2(T2-4)　　分野：中性子散乱（装置）

研究テーマ：先端偏極中性子散乱によるスピン-格子物性の研究
表　題：集光型ホイスラーモノクロメータによる偏極中性子ビーム強度の増大化
1-8-5

Improvement of the polarized neutron beam flux in TAS-1 spectrometer by doubly focusing Heusler monochromator

M. NAKAMURA[1], M. TAKEDA[1,2], K. KAKURAI[1]

[1]Advanced Science Research Center, JAERI, Tokai, Ibaraki 319-1195, Japan
[2]Department of Physics, Graduate School of Science, Tohoku University, Sendai 980-8578, Japan

Our research group is currently making efforts to install the CRYOgenic Polarization Analysis Device (CRYOPAD) on TAS-1 spectrometer at JRR-3M reactor in collaboration with French neutron scattering scientists†. We will be able to carry out the zero-field spherical neutron polarimetry (SNP) by using the CRYOPAD[1)]. The zero-field SNP experiments enable us to measure both the longitudinal and transverse components of the final polarization vector, which is impossible by conventional uniaxial polarization analysis[2)]. In the elastic mode CRYOPAD offers a sensitive method for the determination of complicated AF order and the measurement of form factors in special class of AF compounds, in which the magnetic and nuclear scattering occur in the same reflections[3)]. In the inelastic mode CRYOPAD can elucidate that the transverse components may contain direct information on the spin-lattice correlations, e.g. involving the Dzialoshinskii-Moriya interaction[4)].

However, the great improvement of the incident polarized neutron flux is indispensable for utilizing the advantage of CRYOPAD. Therefore, we had to design a new Heusler monochromator. The exact geometry of the primary spectrometer has been optimized using the Monte-Carlo ray-tracing simulation

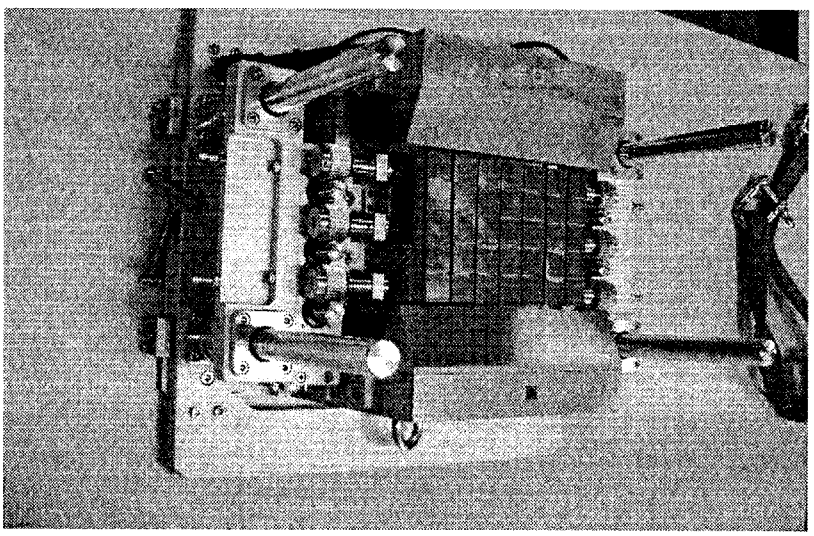


Figure 1: The new TAS-1 Heusler monochromator.

原子炉：JRR-3M　　装置：TAS-1(2G)　　分野：中性子散乱（装置）

software McStas[5]. The magnetic circuit of the monochromator has been optimized by 3D finite-element calculations (PHOTO Series-MAG). A new doubly focusing Heusler monochromator has 140 mm wide and 100 mm height. The Heusler crystals are saturated by a vertical magnetic field closed by a C-shaped iron yoke on the rear side of the monochromator. Old Heusler monochromator was 75 × 70 mm^2 (width × height) area and had no focusing mechanism. As displayed in Fig.1, the new monochromator consists of 35 crystal plates mounted in 7 columns, pivoting around vertical axes to provide variable horizontal focusing. Moreover, the five plates in each of the columns are glued on BN supports inclined by angles corresponding to the vertical focusing, optimized and fixed at E_i=30.5 meV.

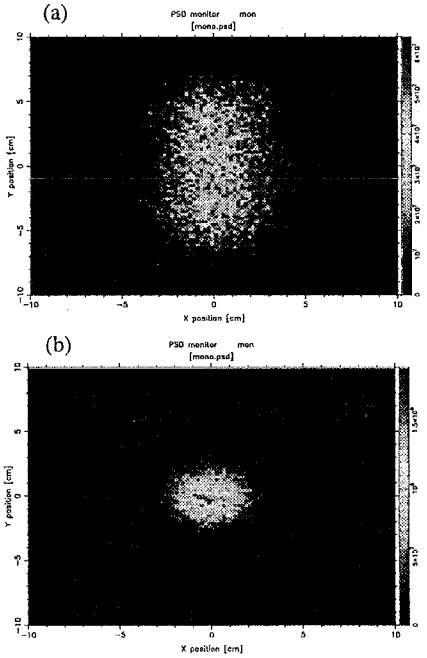


Figure 2: Calculated results of neutron beam distribution at sample position; (a) for old monochromator set-up and (b) for new monochromator set-up.

Figure 2(a) shows the calculated result of neutron beam distribution at sample position for old set-up, and Fig. 2(b) gives one for new set-up. Monte-Carlo simulation results also indicate that, by enlarging the monochromator size and equipment with doubly focusing mechanism, the neutron flux at sample position is about six times larger than old monochromator set-up as shown in Fig.3.

Next step is to build a new Heusler analyzer which gather the scattered neutron beam as much as possible. We have already started the design of a new Heusler analyzer.

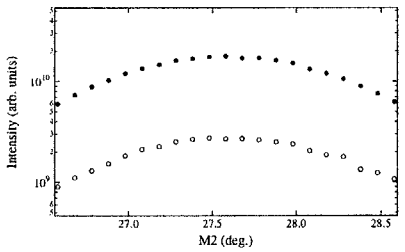


Figure 3: The calculated scattering angle dependence of the neutron beam flux at sample position; (open circle) for old monochromator set-up and (closed circle) for new monochromator set-up.

References

1) F. Tasset *et al.*, Physica B **267-268** (1999) 69.

2) R.M. Moon *et al.*, Phys. Rev. **181** (1969) 920.

3) P.J. Brown *et al.*, Physica B **267-268** (1999) 215.

4) L.P. Regnault *et al.*, Physica B **267-268** (1999) 227.

5) The McStas World-Wide-Web page: `http://neutron.risoe.dk/mcstas/`

† Dr. F. Tasset (ILL) and Dr. L.P. Regnault (CEA-Grenoble)

研究テーマ：多重極限環境下における中性子散乱実験法の研究
表　　題：精密中性子光学における前置結晶によるビーム増強

1-8-6

Beam Enhancement by a Pre-Crystal in the Precise Neutron Optics

H. TOMIMITSU, Y. HASEGAWA[1] and K. AIZAWA[2]

Advanced Science Research Center, JAERI, Tokai, Ibaraki 319-1195
[1]Atominstitut, Austria University, Wien, Austria A-1020
[2]Center for Proton Accelerator Facilities, JAERI, Tokai, Ibaraki 319-1195

We are working on the development and application of the neutron interferometry, where we sometimes feel the lack of the neutron intensities. **Therefore, we tried to realize a convenient method to enhance the neutron flux on the experimental table.** Here, on the premise that the concave crystal that is conventionally used in usual diffraction-work is not suitable for our present purpose of precise neutron optics, because the neutron beams forcibly gathered will not contribute the intensity of the Si-reflected beam.

We tried a pre-crystal of asymmetric reflection, where, as the incident beam of the width W is reflected as the beam width of w, we can expect the reflected beam enhanced by W/w, Fig.1(a).

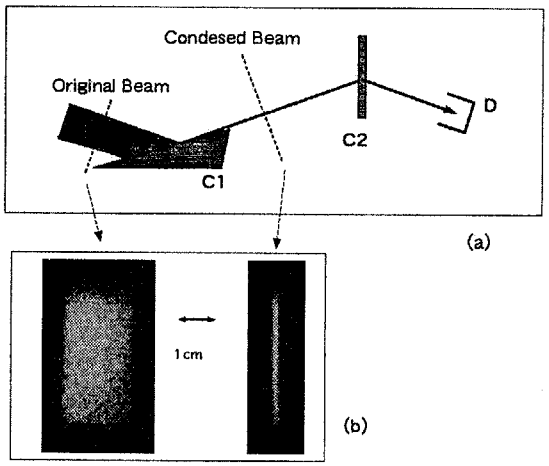


Figure 1: Si Asymmetric Pre-Crystal (C1); Beam Path with Si analyzing crystal C2 (a) and Beam Condensation (b).

We measured the intensity I_p of Si-plate of 2mm thickness put in the neutron beam reflected by the pre-crystal and the intensity I_o of Si-plate put in the incident beam, "original beam" inFig.1(a), without the pre-crystal. We compared, then, if the ratio of I_p/I_o is larger than unity or not. The FWHM and the ratio of the background noises to the peak intensity of the rocking-curve were also compared. Wavelengths, λ in the following tables, of 1.5, 1.56, 1.74, 2.0 and 2.3A were used.

At first, **we tested the asymmetric reflection of a silicon perfect crystal**, because it is rather easy to make up into an expected shape. Although all of those pre-crystal with silicon single crystal with asymmetric reflection gave the condensed neutron beam as expected, Fig.1(b), they showed very large beam-divergence and did not supply any enhanced beam intensity for the following reflection by a silicon crystal, Table 1.

Table 1: Results of Asymmetric Si Crystal

C1	λ	I_p/I_o
Si Plate-111-Bragg	1.5	0.74
〃 -Laue	2.3	0.68
Si Block-220-Bragg	1.52	0.14
〃	1.56	0.27
〃	1.74	1.0

The reason for the above results were supposed that, as predicted in the textbook of the dynamical diffraction, quite the same factor, W/w, affects on the beam-divergence of the diffracted beam from the asymmetric crystal just as the beam condensation.

Next, **we tried the asymmetric reflection of imperfect single crystals**, such as Cu-based alloys, Ni-based super alloy, in addi-

tion to the highly oriented pyrolytic graphite (HOPG), in order to avoid the dynamical effect against the beam divergence mentioned above. On the HOPGs, in addition to the flat HOPG plates as the reference, we tried the asymmetric angle of $11deg.$ and $15deg.$, which were made of HOPG platelets of 10mm width set in the aluminium frames, ground by emery paper and polished with special cloth as smooth as possible, Fig.2.

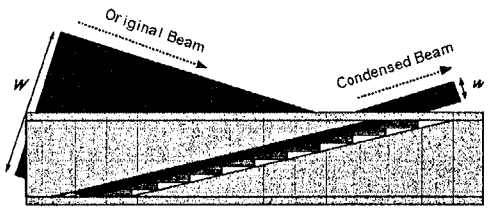


Figure 2: Asymmetric Pre-Crystal made of HOPG-Platelets Set in an Aluminum Frame.

Although we have not systematically tested, the distance between the pre-crystal and the Si plate was found very important parameter, *i.e.*, the shorter the better.

We succeeded in the enhancement of the Si-reflected beam in several cases, Table 2. The best case was the flat *HOPG* with $2.0A$ wavelength and 40mm distance, giving the enhancement of around 3 times.

With shorter wavelengths and longer distance, they gave weaker reflections. With this pre-crystal method, we could not only get stronger intensity but also reduce the ratio of the background noise and the FWHM. Here, it seems rather strange to gain intensity with a flat HOPG. It may be explained with the idea of some kind of integration of coherent part within the original beam by the pre-crystal.

On the other hand, both of asymmetric HOPGs of $11deg.$ and $16deg.$ gave only 2 times or less even with 2.0A wavelength and 40mm distance, while they really concentrated the width of the incident beam as expected.

We tested some conditions of 1'st and 2'nd slits, *i.e.* before- and after the pre-crystal.
(1) With the same cross-section of the 2'nd slit to the 1'st, the reflected intensity is larger more than 115%.
(2) With the fixed height of 7mm of the 1'st slit, the same intensity is obtained with the reduced width of 2mm of the 2'nd slit.
(3) With the same height, the reflected intensity increases with the increasing width up to 4.5mm, and then saturated.
(4) When we chained the *HOPG*s reflections successively, we could not get more intensity than 80-90% of the one-piece reflection, as usually said.
(5) The thicker *HOPG*s of two or three *HOPG* platelets, in addition, gave the same intensity as the one-piece case, just as reported that 2mm is the optimum thickness for thermal neutron reflection as a monochromator by the maker's reports.

Table 2: Results of Asymmetric Imperfect Crystals

λ	C1	I_p/I_o
2.00	PG-flat-2	2.06
	PG-flat-3	3.03
	16PG-Front	1.34
	16PG-Back	1.42
	11PG-Front	1.93
	11PG-Back	2.08
	Ni-111-Bragg	0.63
	Cu-111-Laue	0.58
1.65	PG-flat-2	1.87
	16PG-F-C	0.63
	11PG-Front	0.66
	11PG-Back	0.56
	Ni-111-Bragg	0.24
	Cu-111-Laue	0.38

Further investigation is in progress.

References

1) H.Tomimitsu, Y.Hasegawa and K.Aizawa: *Proc. Int. Conf. Present Status and Future Aspects of Neutron Interferometry*, NSL News Letter 2002-1, ISSP, Univ. Tokyo, 2002, pp.3-6.

研究テーマ：拡散現象のモデル化および高精度拡散係数測定
表　題：中性子構造解析用静電浮遊炉の開発
1-8-7

Development of Electrostatic Levitation Furnace for Neutron Diffraction

H. AOKI, P.-F. PARADIS, T. AOYAMA, T. ISHIKAWA,
T. MASAKI[1], Y. ISHII[2] and T. ITAMI[1,3]

[1]National Space Development Agency of Japan, 2-1-1 Sengen, Tsukuba, Ibaraki 305-8505
[2]Advanced Science Research Center, JAERI, Tokaimura, Ibaraki 319-1195
[3]Graduate School of Science, Hokkaido Univ., N10W8, Sapporo, Hokkaido 060-0810

Liquid structure obtained from scattering experiments is necessary for the prediction of the physico-chemical properties. However, there are only limited studies for high temperature liquids because of the lack of suitable container material for diffraction experiments. In addition, the diffraction intensity of the liquid is much weaker than that of the solid. Moreover, the subtraction of the sharp background peaks of the container material from the sample intensity affects the precision of structural data. Recently, contact-less techniques were applied to materials research[1, 2]. Also, the structure of liquids at high temperatures is frequently studied by levitation methods in combination with synchrotron radiation. However, x-ray is diffracted at the surface and the angle dependence of diffraction intensity is sensitive to the sample position. Therefore, the stability of the sample position is important for precise measurements. Additional difficulties arise when the shape of the sample departs from that of a sphere. This complicates the corrections of diffraction intensity in order to obtain accurate structure factor, $S(k)$. It is not always easy to obtain a complete spherical liquid sample in many levitation techniques. However, electrostatic levitation (ESL) offers a spherical shape which has the advantage to ease data corrections such as the absorption correction. Neutron is of great advantage in obtaining bulk structural data because of its high permeability that minimizes the diffraction intensity at the surface of oxidized sample at high temperatures. If ESL is adopted for neutron diffraction experiments, it is possible to obtain more precise diffraction data for high temperature liquids. In this report, we present the result of the first neutron diffraction experiment carried out with ESL with poly-crystalline alumina.

Neutron diffraction experiment was performed with the HRPD(High Resolution Powder Diffractometer) of JRR-3M in JAERI. The neutron wavelength was 1.823 Å. The neutron collimation setup was open-(M)-20'-(S)-6' in order to make the incident neutron intensity stronger.

The design of the ESL for neutron diffraction experiments was reported earlier[3]. Fig. 1 shows the ESL at HRPD. The furnace had a 0.25 m diameter and a 0.35 m height. The sample position was controlled independently in X,Y,Z directions. A levitated charged sample (Fig. 2) was held at a constant position by a 720 Hz feedback control loop. Stability of the sample position was estimated to be better than ±0.1 mm along the three axes. The sample was a 3 mm diameter alumina sphere coated by platinum with a thickness of a few ten angstroms. During levitation, ultraviolet light was irradiated to the sample to maintain charges through photoelectric emission. The sample could be kept levitated for more than 12 hours. The pressure inside the furnace was about 5×10^{-4} Pa. A cadmium slit was located at 50 mm from the sample position to adjust the incident neutron beam size to eliminate sharp background intensity from the copper electrodes. The slit width was set to be 3 mm, corresponding to sample size.

As shown in Fig. 3, there are no sharp Bragg peaks in the background data. As for the intensity from the sample, peaks of platinum were not observed because the diffrac-

原子炉：JRR-3M　　装置：HRPD(1G)　　分野：中性子散乱（装置）

tion intensity of the platinum coating was far weaker in comparison with that of alumina. Another neutron diffraction experiment of levitated alumina was performed by an aerodynamic levitation technique[4]. The background intensity of our data was weaker than that of the other study because of the absence of sharp peaks. In addition, the baseline of the alumina intensity was flatter than that observed elsewhere[4]. As for the peak width, narrower sharp peaks were observed. Observed peaks in the present study are in reasonable agreement with the literature[5]. This preliminary work illustrated that neutron diffraction and the ESL is a good combination for structural study of liquid state at very high temperatures without any containers.



Figure 2: Horizontal view of the levitated alumina specimen during the experiment. The white sphere is 3 mm diameter alumina which is levitated between the copper electrodes(above and below the sphere).

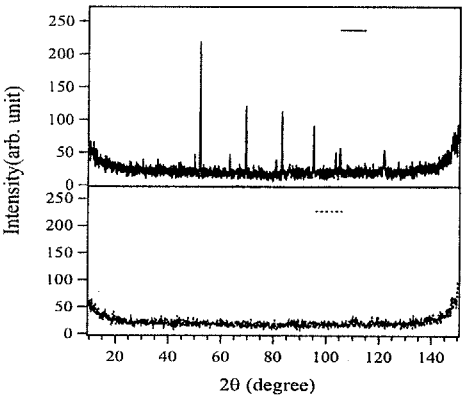


Figure 3: The intensities of levitated alumina specimen and background.

References

1) P.-F. Paradis, T. Ishikawa and S. Yoda, Int. J. Thermophys. **23**(2002)825
2) P.-F. Paradis, T. Ishikawa and S. Yoda, Int. J. Thermophys. **23**(2002)555
3) P.-F. Paradis et. al, J. Non-Cryst. Solids, **in press.**
4) C. Landron et al., Rev. Sci. Instrum., **71**(2000)1745
5) N. Maslen et al., Acta Cryst., **B49**(1993)973

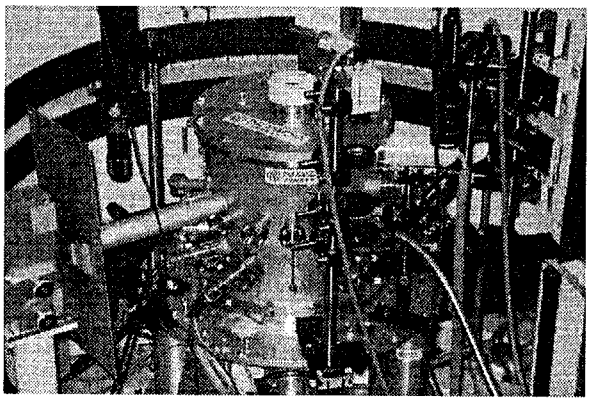


Figure 1: The developed electrostaric levitation furnace at HRPD.

研究テーマ：イメージングプレートを用いた気液界面測定用水平型中性子反射率計の開発
表題：イメージングプレートを用いた気液界面測定用水平型中性子反射率計の開発

1-8-8 Development of Neutron Reflectometer for Air/Water Interface with Imaging Plate

Hideki Matsuoka, Mihoko Matsutani, Emiko Mouri, Atsushi Moriai[1], Kazuhiko Soyama[1]

Department of Polymer Chemistry, Kyoto University, Kyoto 606-8501, Japan
[1]Japan Atomic Energy Researeh Institute, Tokai, Naka, Ibaraki 319-1195

For the water surface system, such as a lipid monolayer on water, polymer monolayers, and monolayer-polymer complex, the reflectivity measurement is the unique technique to evaluate their nanostrucutre on water directly, not in dried state[1,2]. We have been continuing the project for construction of NR for water surface. In 1999, we had succeeded to detect a neutron reflection from water (D_2O) by LTAS (C2-1) in JRR-3M. By using an imaging plate (IP), the off-specular reflection was also detected. Last year, we developed a novel NR optical system as shown in Fig.1. We used 3Q-supermirrors to change the incident neutron beam in combination with monochromator tilt. By this system, NR profile from free surfaces can be obtained without changing sample surface position in vertical direction.

By using this system, we carried out a reflectivity measurement for silicon wafer. A typical example is shown in Fig.2. The wavelength of neutron was chosen to be 3.4Å. The slit width was 0.5mm and 0.3mm for the slits at before monochrometer and before sample position, respectively. The distance between these two slits was 1.5m. The size of Si wafer was 20mmx20mm, and the accumulation time was 30sec for 2theta from 0 to 0.5 degree, 300sec for 0.5 to 3.0 degree, and 5000sec for over 3 degree. This NR profile for Si wafer showed a typical decay for flat and smooth surface and the statistics is also enough under these experimental conditions. The reflectivity down to the order of 10^{-5} was detected and the measurable Q range was found to be more than 0.15 $Å^{-1}$. For the measurements on monolayers and self-assemblies on water surface, the reflectivty down to 10^{-6} should be detected and the Q range should cover up to 0.3$Å^{-1}$, which might be possible with minor modification of this system such as a reduction of background intensity.

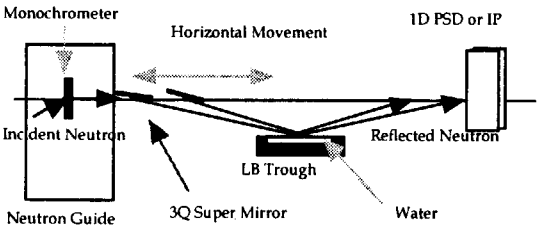


Figure 1 New optical setup of LTAS as a reflectometer for water surface.

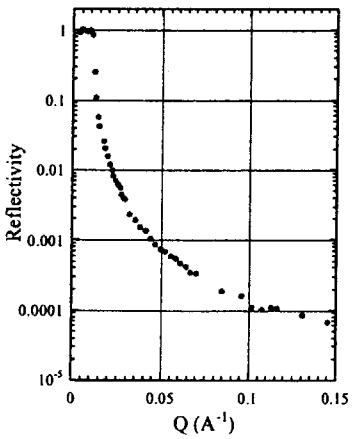


Figure 2 NR profile for Silicon wafer by LTAS.

Reference
(1) H.Matsuoka, E.Mouri, K.Matsumoto, The Rigaku Journal, 18(2), 54-67 (2001).
(2) E.Mouri, K.Matsumoto, H.Matsuoka, H.Yamaoka, Langmuir, 18(10), 3865-3874 (2002).

原子炉：JRR-3M　　装置：LTAS(C2-1)　　分野：中性子散乱（装置）

研究テーマ：多層膜ミラーの非鏡面反射に関する研究
表題：Off-specular reflection from Ni/Ti multilayers

1-8-9

Off-specular reflection from Ni/Ti multilayers

Kazuhiko Soyama[1] and Cao Bin[1,2]

[1]Japan Atomic Energy Researeh Institute, Tokai, Naka, Ibaraki 319-1195
[2] Kyushu University, Hakozaki, Higashi, Fukuoka 812-8581

Multilayer mirrors of Ni/Ti with periodical d-spacing in nanometer range, may be utilized for neutron focussing and imaging devices. However, due to the interface roughness of Ni/Ti multilayers, vertical correlation give rise to off-specular (diffuse) scattering which leads to decreasing the resolution of these optical devices. For evaluating and reducing the intensity of diffuse scattering in a rough interface, theoretical and experimental study has been conducted.

Rocking curves of Ni/Ti multilayer with d=100 Å and 20bi-layers were measured at small 2θ angles. The measurements were carried on a reflectometer of the LTAS (C2-1) using cold neutron with a characteristic wavelength of 3.8 Å.

The measurement performed at the second (qz=0.0303Å-1) and third (qz=0.0641Å-1) Bragg peaks of sample are shown in Fig.1 together with the calculations obtained with DWBA model. The calculation method is based on the extension of DWBA for layered system which has been performed by Holy et al.. In Fig.1, we have found a good quantitative agreement between the calculation and measured curve. The diffuse scattering is strongly structured, the striking feature being the large constructive interference occurring at the maximum of the second Bragg peak. The best fit gives 50 Å and 0.2 for the correlation length ξ and the h exponent, respectively. The vertical correlation length ξz is estimated as 500 Å, corresponding to one forth of the total thickness of the multilayer. In addition, due to the effect of measurement background, the diffuse neutron scattering is covered under the background at the wing curve, therefore the calculation gives lower intensities than the measurement.

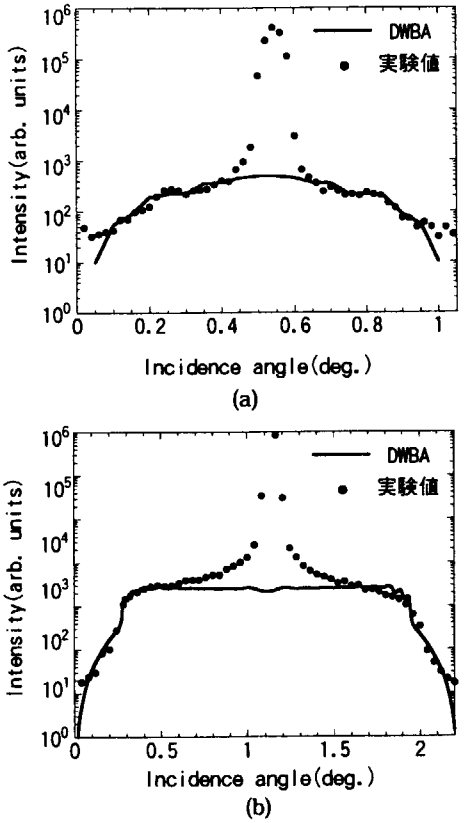


Fig.1 Rocking curves for Ni/Ti multilayer going through the second (a) and third (b) Bragg peaks. Solid lines represent fits using DWBA model.

References

1) C. Bin, K. Soyama, ICANS-XV 2000, JAERI-Conf 2001-002, 592-599

原子炉：JRR-3M　　装置：LTAS(C2-1)　　分野：中性子散乱（装置）

研究テーマ：多重極限環境下における中性子散乱実験法の研究
表　題：薄肉型ch-cut Siを用いた中性子極小角散乱装置の特性

1-8-10

The characteristic of the very small-angle neutron scattering instrument using thin type ch-cut Si

K. AIZAWA and H. TOMIMITSU[1]

Center for Proton Accelerator Facilities, JAERI, Tokai, Ibaraki 319-1195
[1]Advanced Science Research Center, JAERI, Tokai, Ibaraki 319-1195

We are attempting the development of very small-angle neutron scattering instrument which used ch-cut Si of 111 symmetrical reflection. The contents of the development are increase of incidence neutron intensity, the improvement of the profile of the rocking curve of the 2nd crystal which is the basic characteristic, etc. We have used symmetrical 5 bounce - 5 bounce reflective arrangement using the elements of the slab thickness of 10 *mm* - 10 *mm* (medium thick type) or 10 *mm* - 30 *mm* (thick type) on neutron wavelength of 0.25 *nm*. Among these, thick type has been used in order to remove the reflective neutron from back surface simply. The S/N ratio was about 4.3×10^4 in medium thick type, and was about 9.8×10^3 in thick type. From these facts, the influence of thermal diffuse scattering (TDS) from slab can be considered as a factor of the background which determines a S/N ratio. Then, in order to reduce TDS, the ch-cut Si optical elements for 3 bounce - 3 bounce symmetrical reflection for wavelength 0.2 *nm* of the 2 *mm* slab thickness were made as test pieces, and the basic characteristic of very small-angle neutron scattering instrument using it was measured. A schematic layout of new ch-cut Si optical element is shown in Fig. 1.

The experiment was carried out using the PNO instrument installed in JRR-3M in Japan Atomic Energy Research Institute. An example of an obtained rocking curve of the 2nd crystal is shown in unit of q in Fig. 2. The peak intensity of rocking curve is about 1300 *cps*, $FWHM$ is about 1.38 *sec*, and a S/N ratio is about 1×10^5. Compared with the former, Fig. 2 shows that the improvement of S/N ratio is more than twice. Based on this result, the experiment using ch-cut Si of thinner slab is under plan. On the other hand, the deviation from the measured data and theoretical curves is observed in the region of $q >$ $\sim 2\times10^{-4}$ nm^{-1}. The reason is considered to be the influence of back surface reflection. Then, wrapping processing of back surface or vacuum evaporation of Cd to the back surface is considered to remove back surface reflection.

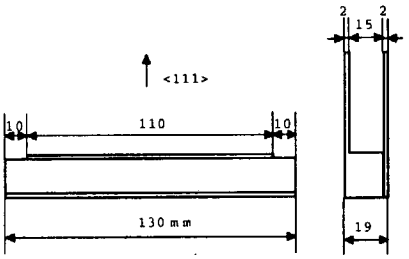


Figure 1: Schematic layout of thin type ch-cut Si.

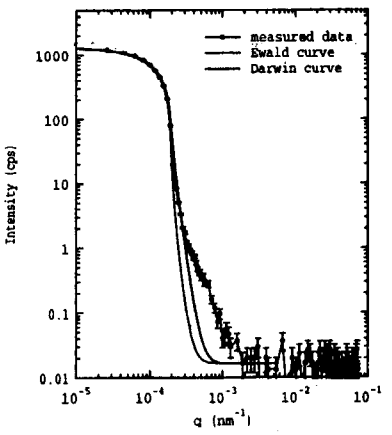


Figure 2: A example of 2nd Si rocking curve in unit of q with theoretical curves

原子炉：JRR-3M　　装置：PNO(3G)　　分野：中性子散乱（装置）

研究テーマ：機能性生体物質の水和構造研究
表　題：生体高分子用中性子回折装置（BIX-3M）

1-8-11

A new single crystal diffractometer for biological macromolecules (BIX-3M)

K. Kurihara, I. Tanaka, T. Chatake, A. Ostermann and N. Niimura

Advanced Science Research Center, JAERI, Tokai, Ibaraki 319-1195, Japan

Hydrogen atoms occupy about half of the atoms in a protein molecule, and water molecules of hydration always surround a protein. There is no doubt that they play an important role in physiological functions. They are indispensable substances in many naturally-occuring processes. In addition, H atoms are intimately involved in the folding and stabilization of protein structure through hydrogen bonds. Therefore, the determination of accurate positions of hydrogen atoms of a protein and its hydration water molecules is an important information for understanding the mechanism, function, and stability of many important proteins.

A neutron diffractometer (BIX-3) at JRR-3M of the JAERI has been applied to the structure determination of rubredoxin from *Pyrococcus furiosus* (1.5Å resolution)[1], its 3-point mutant (1.6Å)[2] and sperm whale myoglobin (1.5Å)[3]. Those results led to increase of activity of the neutron protein crystallography. Therefore a much higher performance is now required to shorten the measurement time and/or get more accurate diffraction data.

We have constructed a new single-crystal diffractometer for neutron protein crystallography (BIX-3M) at 1G-A site of JRR-3M of the JAERI. Since BIX-3 has been already installed at 1G-A site, the layout of the monochromator house is also changed so that the two diffractmeters are located at the opposite sides of the monochromater house. The main architecture of BIX-3M is based on that of BIX-3 (Figure 1). The details of the architecture and the performance of BIX-3 is discussed elsewhere[4,5]. BIX-3M uses an elastically-bent perfect-Si (EBP) crystal monochromator and a neutron imaging plate (NIP) as BIX-3. To shield the neutron- and γ-background from the environment in the reactor hall the diffractometer is covered by a cylinder which consists of two layers, 50mm thick B_4C + resin against neutron (outside) and 50mm thick lead against γ-ray (inside). In addition, several optimizations of the monochromator and modifications from BIX-3 are carried out as follows,

(1) 2.6Å is used instead of 2.35Å as the wavelength for the incident neutron which gives a larger intensity on the detector and larger separation between Bragg reflections.

(2) A super mirror guide composed of Ni/Ti multi-layers (3.6Q) is installed inside of a flight tube to increase the intensity by reflecting thermal neutrons on the walls of the guide.

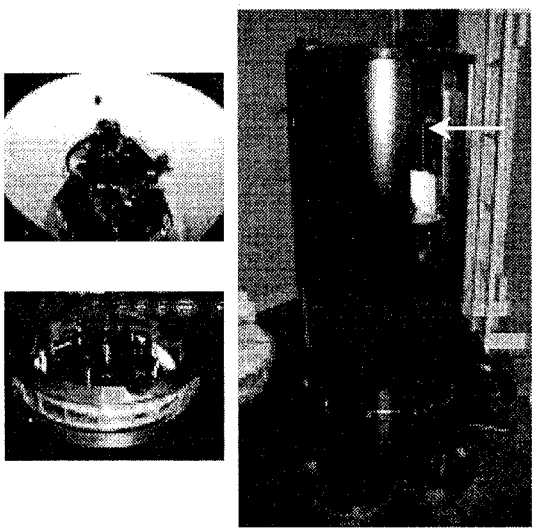


Figure 1. BIX-3M without cylinder shield (right), the NIP and laser modules (left top), and the reading rod and erasing lamp (left bottom). The neutron beam comes from the right side. During data collection the NIP is located at the top position (white arrow). In the reading procedure the NIP cylinder moves down and is scanned by the laser with a reading rod rotating. After the reading the NIP is initialized by an erasing lamp and moves up to the top position.

原子炉：JRR-3M　　装置：BIX-3M(1G-B)・BIX-3(1G-A)　　分野：中性子散乱（装置）

Table 1. Comparison of the specification of BIX-3M and previous BIX-3.

	BIX-3M	Previous BIX-3
Monochromator	EBP-Si (111) / (311)	EBP-Si (111) / (311)
Wavelength	2.60Å / 1.36Å	2.35Å / 1.23Å
Beam size at monochromator	80 mm × 44 mm	40 mm × 44 mm
Flight tube	with 3.6Q super mirror	without super mirror
NIP size	450 mm × 980 mm	450 mm × 980 mm
Camera constant (radius)	200 mm	200 mm
d-min (along the horizontal line)	1.4Å /0.7Å	1.2Å /0.6Å
Total gain	1.69	1

(3) The neutron beam size from the reactor is 80mm × 44mm. However, only the bottom half of it has been used for the previous BIX-3 at the monochromator position. After the modification of the monochromator house, a new monochromator composed of three elastically-bent perfect-Si plates is used to cover the full size of the beam.

The comparison between BIX-3M and previous BIX-3 is summarized at Table. 1. The peak intensity of BIX-3M at the sample position is measured to be about 1.25 times larger than previous BIX-3. As the reflectivity of the sample is proportional to the 3rd power of the wavelength, the final gain for the integrated intensity of the Bragg spots are estimated to be 1.69 times larger. Supposing that 800 fames are measured for one data set with 60 min/frame under those conditions, only 22.5 days is necessary for BIX-3M whereas 36 days are required in the case of previous BIX-3.

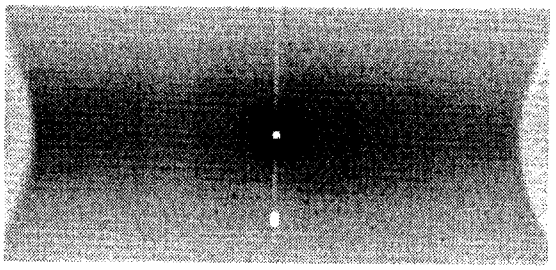


Figure 2. An example of a diffraction pattern taken by BIX-3M. The sample was a sperm whale myoglobin crystal. Space group is $P2_1$ with unit-cell parameters a=64.5Å, b=30.8Å, c=34.8Å, α=90°, β=105.7°, γ=90° Exposure time was 60 minutes.

On the other hand, the background also increases to be at most 1.56 times in the low-resolution range. Thus in that region intensity (S) / background (B) ratio is almost same as in previous BIX-3. However, in the high-resolution range the increment of the background is less than 1.56 times so that it is concluded that data quality (S/B) in BIX-3M is better than in previous BIX-3. The BIX-3M is scheduled to be shifted closer to the monochromator by about 25cm. This yields an additional gain factor of 1.5.

Figure 2 shows an example of the diffraction images from a protein crystal taken by BIX-3M.

In conclusion, as mentioned above, BIX-3M shorten the collection time of diffraction data sets. In addition, since it is still difficult to get large crystals of proteins and other biological macromolecules, a higher performance of BIX-3M increases the possibility to apply neutron crystallography to such biomacromolecules.

References

1) K. Kurihara et al., Supplement A to J. Phys. Soc. Jpn. 70, (2001), 400-402.
2) T. Chatake et al., submitted paper.
3) A. Ostermann et al., Biophysical Chemistry 95, (2002), 183–193.
4) I. Tanaka et al., J. Phys. Chem. Solids 60, (1999), 1623-1626.
5) I. Tanaka et al., J. Appl. Cryst. 35, (2002), 34-40.

This is a blank page.

1. 中性子散乱 9)その他

1. Neutron Scattering 9) Others

This is a blank page.

研究テーマ：パイロクロアの軌道秩序に供なう酸素シフトの解析

表題：パイロクロア化合物 $Cd_2Re_2O_7$ における構造相転移

1-9-1 Structural Phase Transition in Pyrochlore Compound $Cd_2Re_2O_7$

M. Toda[1], Y. Wakabayashi[1], R. Tazaki[1], H. Sawa[1], H. Kimura[2], Y. Noda[2] and Z. Hiroi[3]

[1]*Photon Factory, Institute of Materials Structure Science, Tsukuba, Ibaraki 305-0801, Japan.*
[2]*Institute for Multidisplinary Research for Advanced Materials, Tohoku University, Sendai 980-8577, Japan.*
[3]*The Institute for Solid State Physics, The University of Tokyo, 5-1-5 Kashiwanoha, Kashiwa, Chiba 277-8581 Japan.*

$Cd_2Re_2O_7$ is the first superconductor (Tc ~ 1 K) which have been found among cubic pyrochlore oxides [1]. Peculiar interplay between geometrically frustrated anti-ferromagnet and superconductivity is expected to realize in this system. The electrical resistivity measurements, and 4C-XRD experiments have revealed the existence of the second order phase transition around 200 K [2]. The results of Re-NQR experiments have suggested the breaking of symmetry of three-fold axis in the temperature range of 5~100 K [3]. Now, we are interested in the relationship between the structural changes and electrical resistivity at low temperatures, especially in the shift of oxygen and its effect to the band structure.

We have performed 4-circle neutron diffraction experiments on spectrometer FONDER, which is installed at T2-2 beam port of the thermal guide at the JRR-3M research reactor of JAERI. The wavelength of neutron was 1.5648 Å. ^{114}Cd was used to avoid the absorption of neutron. The size of the single crystal was 3.0mm × 3.5mm × 2.0mm; which was enough small compared to the beam diameter (10mm).

Figure 1 shows the peak-profile of the Bragg reflection (040) measured by ω-scan (scan speed ~ 0.2 deg./min). A single peak was measured at ω = 17.77° and at T=250 K (peak width; Δ = 0.166(7)°). With lowering temperatures at 50 K, an additional peak appeared at around ω=17.98°. This peak might come from the contribution of a new domain, which was produced owing to the structural phase transition at around 200K. The superlattice peak of (020) reflection was also measured at below 150 K. The intensity of the reflection was rather weak (the counts of the peak was about 30cts); although, it seemed for us that the peak was also split for this reflection. The crystal structure analysis comparing with the synchrotron X-ray data is now in progress.

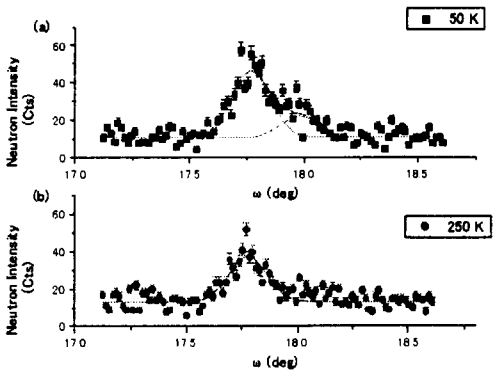


Fig. 1 The peak profile of (040) Bragg reflection at 50 K (a) and 250 K (b).

[1]M. Hanawa *et al.*, Phys. Rev. Lett., **87**, 187001, (2001).
[2] Z. Hiroi *et al.*, cond-mat/0203178
[3] O. Vyaselev *et al.*, cond-mat/0201215

使用施設：JRR-3M, 装置：FONDER (T2-2), 分野：9. Others

研究テーマ：リチウム２次電池正極活物質の構造解析
表題：$LiCoPO_4$ と Li_2CoPO_4F の構造と電池特性

1-9-2 Structure and Battery Properties of $LiCoPO_4$ and Li_2CoPO_4F

Shigeto OKADA, Mizuki UENO, Yasushi UEBO and Jun-ichi YAMAKI

Institute of Advanced Material Study, Kyushu University,

Kasuga Koen 6-1, Kasuga 816-8580 Japan

Introduction

Normal spinel $LiMnMO_4$ (M:Co [1], Cr [2]) and inverse spinel $LiNiVO_4$ [3] with 4.5 – 5 V plateau have been investigated as post 4 V cathodes. We introduced that phospho-olivine $LiMPO_4$ with a theoretical capacity of 170 mAh/g should be a strong candidate for a new high-voltage cathode with superior capacity in the previous report.

In this report, the structure of ordered-phospho-olivine $LiCoPO_4$ and fluoride phosphate Li_2CoPO_4F (the latter previously unreported) were identify by Neutron diffraction and the cathode properties were compared using coin cells.

Experimental

Conventional solid-state reactions were employed to synthesize the phospho-olivines. $LiCoPO_4$ were prepared from stoichiometric amounts of reactants Li_2CO_3, P_2O_5 and CoO. The mixtures were presintered at 500 °C for several hours. After firing at 780 – 820 °C for 2 days with an intermittent grinding, the mixtures were quenched using liquid nitrogen. Moreover, obtained $LiCoPO_4$ was mixed with LiF and heated at 780°C for 78 hours in vacuumed quartz tube. Both obtained powders, $LiCoPO_4$ and Li_2CoPO_4F were indexed as orthorhombic in the space group Pnma by XRD (Rigaku RINT2100HLR/PC), using monochromatized CuKα radiation. Neutron diffraction data were taken at powder diffractometer, HERMES [4], at JRR-3M reactor in Japan Atomic Energy Research Institute. The structural parameters were refined by Rietveld analysis using RIETAN 97β [5].

We fabricated the cathodes for electrochemical characterization by blending powders of the active material $LiMPO_4$ with acetylene black (Denki Kagaku Co., Ltd.) and F-210L PTFE Teflon binder (Daikin Industry Ltd.) in a weight ratio of 70 : 25: 5. We measured the cathode properties in a coin-type cell (type 2032 made from SUS316) with a nonaqueous electrolyte (1M $LiPF_6$/Ethyl Methyl Sulfone, Tomiyama Pure Chemical Industries, Ltd.) and polypropylene separator (Celgard 3501) against a Li metal anode.

Results and discussion

Interatomic distances for $LiCoPO_4$ obtained from Rietveld refinements of neutron diffraction are shown in Table 1. According to Shannon's ion radii in MO_6, M-O interatomic distances in Table 2 suggest every transition metals have 2+ high spin state in initial $LiMPO_4$ olivine matrix.

研究テーマ：リチウム２次電池正極活物質の構造解析
表題：$LiCoPO_4$ と Li_2CoPO_4F の構造と電池特性

Table 1. Interatomic distances for $LiMPO_4$

M-O bond length[Å]	Co	Mn [6]	Fe [6]	Ni [6]
M - O (1)	2.150	2.23	2.25	2.150
M - O (2)	2.084	2.14	2.00	2.070
M - O (3) ×2	2.187	2.13	2.03	2.072
M - O (3) ×2	2.060	2.30	2.30	2.150
Average	2.151	2.205	2.151	2.110

Table 2. Shannon's Ion radii in MO_6

6-fold coordinated ion radii [7]	Co^{2+}	Mn^{2+}	Fe^{2+}	Ni^{2+}
High Spin	2.145	2.23	2.18	2.09
Low Spin	2.05	2.07	1.98	—

Table 3. Interatomic distances for Li_2MPO_4F

M-O bond length[Å]	Li_2CoPO_4F	Li_2NiPO_4F [8]
M (1) - O (2) ×2	1.9960	2.011
M (1) - O (5) ×2	2.0872	2.070
M (1) - F (2) ×2	2.1637	2.081
M (2) - O (6) ×2	2.0092	2.013
M (2) - O (4) ×2	2.0606	2.036
M (2) - F (1) ×2	2.1552	2.082
Average	2.0382	2.032

On the other hand, the interatomic distance for Li_2MPO_4F indicates that Co has 2+ low spin state in initial Li_2CoPO_4F matrix as shown in Table 3. The quesi- open circuit voltage charge-discharge profiles of identified $LiCoPO_4$ and Li_2CoPO_4F are shown in Fig.1. It found that the fluoride phosphate Li_2CoPO_4F is a new 5-volt class cathode as $LiCoPO_4$ and the open circuit voltage is higher than that of $LiCoPO_4$.

JRR-3M, HERMES(T1-3), 9. Others

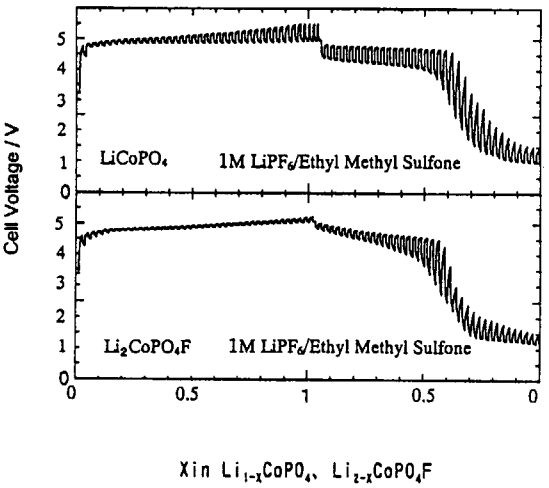


Fig.1 QOCV of $LiCoPO_4$and Li_2CoPO_4F.

References

1. H.Kawai, M.Nagata, H.Tsukamoto and A.R.West, *Electrochem. and Solid-State Letters*, 1, No.5, 212(1998).
2. C.Sigala, A.Verbaere, J.L.Mansot, D. Guyomard, Y. Piffard, M.Tournoux, *J. Solid State Chem.*, 132, 372(1997).
3. G.Fey, W.Li and J.R.Dahn, *J. Electrochem. Soc.*, 141, (1994) 2279.
4. K.Ohoyama, T.Kanouchi, K.Nemoto, M.Ohashi, T. Kajitani and Y.Yamaguchi, *Jpn.J.Appl.Phys.*, 37, 3319(1998).
5. F.Izumi, in "The Rietveld Method" (R.A.Young, Ed.), Chap.13, Oxford Univ. Press, Oxford, (1993).
6. O.Garcia-Moreno et.al., *Chem. Mater.*, 13, 1570-1576 (2001).
7. R.D.Shannon, *Acta Crystallogr.*, A32, 751 (1976).
8. M.Dutreilh, C.Chevalier, M.El-Ghozzi and D.Avignant, *J. Solid State Chem.*, 142, 1-5 (1999).

研究テーマ：リチウム２次電池正極活物質の構造解析
表題：カルサイト型 MBO_3 の構造と電池特性

1-9-3 Structure and Battery Properties of Calcite-type MBO_3 (M:V, Fe)

Shigeto OKADA, Yasushi UEBO and Jun-ichi YAMAKI

Institute of Advanced Material Study, Kyushu University,

Kasuga Koen 6-1, Kasuga 816-8580 Japan

Polyanionic compounds such as NASICON-type $Fe_2(SO_4)_3$ and $Li_3Fe_2(PO_4)_3$ [1] have engendered much interest as rare metal free cathodes for next generation lithium secondary batteries. However, there have been few studies as anode. The skeleton structures built up from both MO_6 octahedra and XO_n polyhedral anion, allow both the redox potential energy and electrochemical properties to be tuned by the combination of M and X. The corner sharing 3D matrix should be suitable anode for not only lithium-ion batteries but also sodium-ion batteries.

In this paper, we tried to design the polyanionic anode with much lighter BO_3 group and synthesize it with suitable low redox potential as anode by chemical substitution in $FeBO_3$.

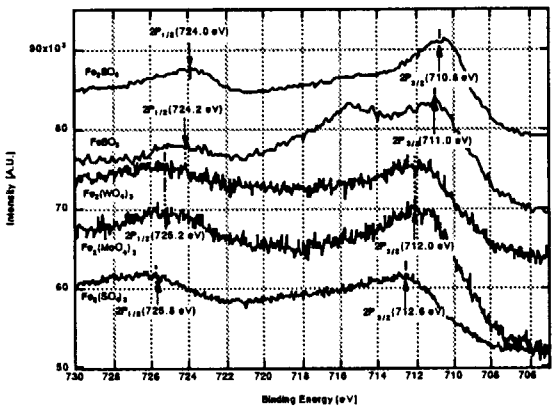


Fig.1 XPS spectra of Fe 2p for the typical iron anode and cathodes with various polyanions.

Figure 1 shows XPS spectra of Fe 2p for the typical iron anode and cathodes with ferric ion and various polyanions. The stronger the X-O bonding (S-O > Mo-O = W-O > B-O), the weaker is the Fe-O bonding and hence, the larger the open circuit voltage (OCV). The 1.8 eV deference in the Fe 2p binding energy of ferric sulfate and ferric borates, reflects a 2 V difference in the OCV. The theoretical capacities estimated by Fe^{3+}/Fe^{2+} redox reaction are 234 mAh/g (856 mAh/cc) for calcite $FeBO_3$ and 293 mAh/g (1272 mAh/cc) for norbergite Fe_3BO_6, respectively. However, the 1.6 V mean voltage on lithium intercalation into ferric borates is unfortunately still too high as anode for lithium-ion batteries [2].

The OCV for rhombohedral $Fe_2(SO_4)_3$ is about 1 V higher than that of $V_2(SO_4)_3$ [3]. On the analogy of this, we tried to replace the redox couple from Fe^{3+}/Fe^{2+} to V^{3+}/V^{2+} in $FeBO_3$. Mixed V_2O_3 and H_3BO_3 were preheat at 670 °C for 24 h and calcined at 1200 °C for 24h in Ar-H_2 (5%) to avoid oxidation of V^{3+}. The XRD profile of obtained VBO_3 powder is well refined by Rietveld analysis (REITAN97-β [4]) based on the crystal parameters of $FeBO_3$ with R-3c space group as shown in Fig.2.

The charge/discharge profile in Fig.3 shows the reversible capacity of VBO_3 is 420 mAh/g

and the mean voltage of VBO_3 is 1 V lower than that of $FeBO_3$ as our expect. Looking at the redox potentials, VBO_3 should have the best performance as an anode material, when compared to the iron borate.

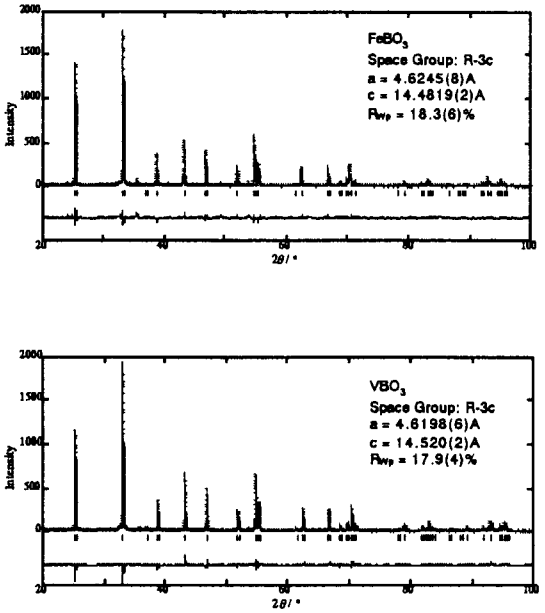


Fig.2 Observed, calculated and difference plots for X-ray diffraction pattern of $FeBO_3$ and VBO_3.

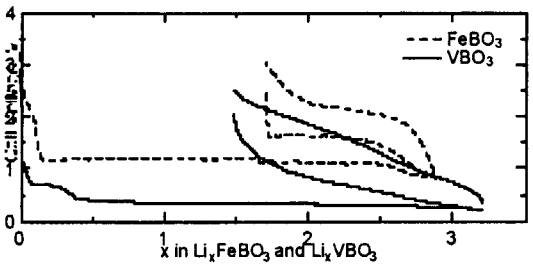


Fig.3 Charge and discharge curves of $FeBO_3$ and VBO_3.

References:

1. S. Okada, K. S. Nanjundaswamy, A. Manthiram, J. B. Goodenough, H. Ohtsuka, H. Arai and J. Yamaki, *36th Power Sources Conf.*, June 6-9, (1994)110-116.
2. J. L. C. Rowsell, J. Gaubicher and L. F. Nazar, *J. Power Sources*, 97-98 (2001)254-257.
3. K. S. Nanjundaswamy, A. K. Padhi, J. B. Goodenough, S. Okada, H. Ohtsuka, H. Arai and J. Yamaki, *Solid State Ionics*, 92 (1996)1-10.
4. F. Izumi, "*The Rietveld Method*", (R. A. Young, Ed), Chap.13, Oxford Univ. Press, Oxford (1993).

研究テーマ：中性子回折による構造材料の応力測定および健全性評価
表　題：3層構造材 [WC-10mass%Ni]-[SUS304]-[WC-10mass%Ni] の残留応力測定
1-9-4

Residual Strain Measurement of the Three Layers Material, [WC-10mass%Ni]-[SUS304]-[WC-10mass%Ni]

K. INOUE, T. TSUJIKAMI, M. OHYANAGI, M. SUGIMOTO,
N. MINAKAWA[1] and A. MORIAI[1]

Faculty of Science and Technology, Ryukoku University, Seta, Otsu 520-2194
[1]Advanced Science Research Center, JAERI, Tokai, Ibaraki 319-1195

The thermal residual stress in the three layers material, [WC-10mass%Ni]-[SUS304]-[WC-10mass%Ni] has been investigated by RESA. The sample was 40mm in diameter and the thickness of each layer was about 4 mm. A photograph of the sample is shown in Fig. 1.

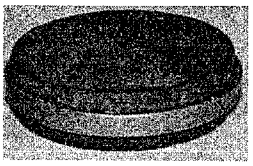


Figure 1: Photograph of the three layers sample.

The raw materials of the composite [WC-10mass%Ni] are powders of W, C and Ni with an average size of 5-8μm, and the middle layer is made of a plate of SUS304. The sample was made by Self-propagating High-temperature Synthesis / Static Pseudo Isostatic Compaction (SHS/SPIC) equipment, which is shown in Fig. 2.

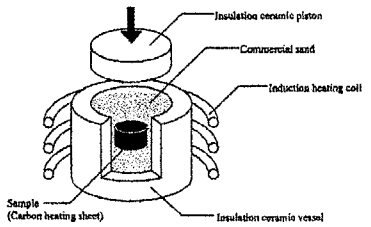


Figure 2: Scheme of a SHS/SPIC equipment.

The green compact, which was formed beforehand to three layers by cold isotropic press, was wrapped by carbon sheet and was pressed isostatically by commercial sand. The pressure was 25 MPa. The carbon sheet was ignited by an induction heating. Then, the combustion wave of about 1800 K propagated toward the center of the sample with a speed of 1-100 mm/s. The sample cooled down rapidly after the combustion wave passed. The SEM image of the composite material, [WC-10mass%Ni], is shown in Fig. 3, where the white region is WC and the black region is Ni. As shown in Fig. 1, the middle [SUS304] layer is forced out from the edge. The situation is quite different from the case of the three layers material, [WC-10mass%Ni]-[Ni]-[WC-10mass%Ni], of which the middle layer was made from Ni in powder state. In this case the middle [Ni] layer shrinks inside the edge.[1,2)]

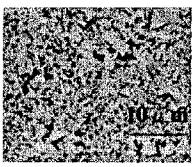


Figure 3: SEM image of [WC-10mass%Ni].

The wavelength of neutron beam was 2.0995 Å. As the size of slits for incident and reflected beams were 2 mm × 2 mm respectively, we were able to observe the small area of the sample. On the mid plane of the [SUS304] layer, we observed 200 reflection, for axial, radial and hoop directions, from the small area of SUS304 at 0, 10, 15, 16, 17 and 18 mm positions apart from the center. On the interface between [WC-10mass%Ni] and [SUS304],

原子炉：JRR-3M　　装置：RESA(T2-1)　　分野：中性子散乱（その他）

we observed 200 reflection, for axial, radial and hoop directions, from the small area of SUS304 at 0, 15 and 18 mm positions apart from the center. For the estimation of the strain, we obtained the standard lattice spacing, d_0, using the 200 reflection of the single layer material, [SUS304(plate)], made by the same synthesis method. During the observation of the reflection, the sample was rotated around the χ, ϕ directions using two small motors on the goniometer, to obtain the average lattice spacing for all directions.

The 200 reflection peak for axial direction from the center of mid plane of the [SUS304] layer and that from the center of the boundary between [SUS304] layer and [WC-10mass%Ni] layer, are shown in Fig.4 (a) and (b), as the examples of the peaks of 200 reflection of SUS304. In Fig.4 (b), we also see the Ni 200 reflection peak on the right hand side, which comes from the Ni region of composite [WC-10mass%Ni] layer. To estimate the stress, we used Young's modulus of 113.6 GPa and the Poisson ratio of 0.262, which were obtained from the 200 reflection of SUS304 under tensile test.[3)]

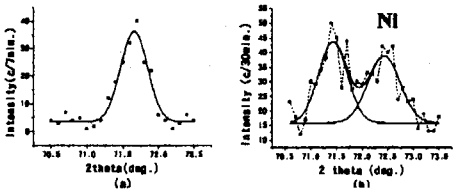


Figure 4: Data plot and the Gauss fitting of the 200 reflection of SUS304 for axial direction. (a) from the center the mid plane of the [SUS304] layer and (b) from the center of the boundary of two layers.

The residual stress deduced from the strain at each position of the middle [SUS304] layer is shown in Fig. 5. We see that the middle [SUS304] layer shows a very complex stress depending on each position and direction. At the interface between two layers, SUS304 feels a large tensile stress in the three directions, whereas at the mid plane of the layer,

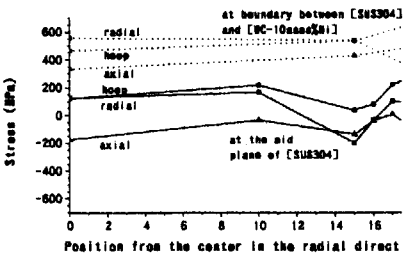


Figure 5: Stress for three directions at each position of the middle layer [SUS304], estimated from the data by RESA.

SUS304 feels a weak tensile stress in the radial and hoop directions and a weak compressive stress in the axial directions. We see that the stresses of [SUS304] change drastically at the radial position of 14-18mm from the center, especially on the mid plane. They have a tendency to become more compressive.

As a result of the previous measurements by RESA,[1,2)] we found that the middle [Ni] layer of the three layers [WC-10mass%Ni]-[Ni]-[WC-10mass%Ni], experiences almost no strain. The reason of the difference of the strain between the [SUS304] middle layer and the [Ni] middle layer is presumably due to the difference of the state of the original material. When the original materials are all powders, there is no macro strain in any place of the sample. We conclude that the original materials in the powder state has a great advantage to synthesize a plural layers material by SHS/SPIC equipment. We are able to avoid the occurrence of the clack or the fracture of the materials.

References

1) T. Tsujikami, K. Inoue, M. Kawagai, M. Ohyanagi, N. Minakawa, Y. Morii and T. Saito : J. Phys. Soc. Jpn. 70 (2001) Suppl. A 523.
2) K. Inoue, H. Nakamura, T. Horikawa, H. Kawashima, T. Tsujikami and N. Minakawa : Materials Science Research International. Special Technical Publication-1, (2001) 439.
3) N. Minakawa, S. Ohkido and Y. Tsuchiya: private communication. (1995).

研究テーマ：中性子回折による構造材料の応力測定および健全性評価
表　題：中性子回折によるフェライト-セメンタイト鋼における変形機構の検討
1-9-5

Deformation Behavior of Ferrite-Cementite Steels Examined by Neutron Diffraction

A. KANIE , Y.TOMOTA[1] , T. SUZUKI[1] , A. MORIAI[2]
N. MINAKAWA[2] and Y. MORII[2]

Graduate student of Ibaraki University, Hitachi, Ibaraki 316-8511
[1]Faculty of Engineering , Ibaraki University, Hitachi, Ibaraki 316-8511
[2]Japan Atomic Energy Research Insititute, Tokai, Ibaraki 319-1195

1. Introduction

We have reported changes in ferrite {110} lattice spacing along the tensile direction by in-situ neutron diffraction during tensile deformation to investigate deformation mechanism in pearlitic steels[1)]. In this study, in-situ neutron diffraction during tensile deformation was performed for two pearlitic steels with different cementite volume fractions. Lattice plane strains in ferrite and cementite along the tensile and its perpendicular directions were determined to examine stress partitioning between the two constituent phases.

2. Experimental procedures

Chemical compositions of tested steels are shown in Table 1. Samples with fully pearlitic structure were prepared by the following heat-treatments : B03 and B04 austenitization at 1273K for 0.6ks and isothermal transformation at 823K for 1.2ks followed by air cooling for B03 and B04, and austenitization at 1173K for 3.6ks and hot rolling at 1143K followed by air cooling for SK5. Tensile specimens with a gauge length of 120mm, width of 3mm and thickness of 2mm were prepared. In-situ neutron diffraction profiles were obtained during tensile deformation by using RESA , JRR-3M at Japan Atomic Energy Research Institute. Tensile load was applied in a step by step manner and in-situ neutron diffraction spectra were recorded during a temporary stops of the loading (creep mode). Changes in lattice plane strains for ferrite {110} and cementite {212} were measured.

Table 1: Chemical compositions of steels used(mass%)

steel	C	Si	Mn	P	S	N
B03	0.58	0.04	1.5	0.005	—	0.004
B04	0.77	0.04	1.5	0.005	—	0.004
SK5	0.85	0.25	0.4	0.009	0.004	—

3. Results and Discussion

Figure 1 shows nominal stress-strain curves for the pearlitic steels. It is known that yield stress(YS) of pearlitic steel is dependent on lamellar spacing(S_0), while work-hardening and tensile strength(TS) is dependent on cementite volume fraction(f_θ). As seen, YS and TS are found larger in B04 than in B03 because o f smaller S_0 and larger f_θ for B04.

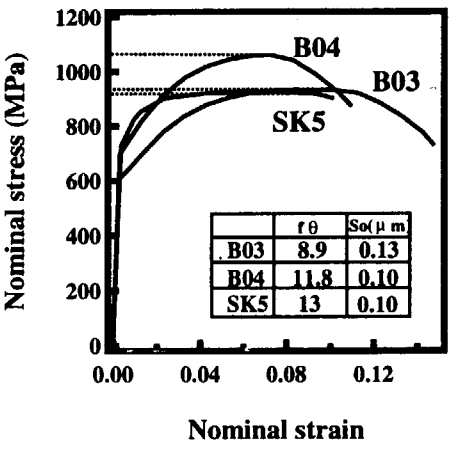


Figure 1: Nominal stress-strain curves for B03 B04 and SK5.

原子炉：JRR-3M　　装置：RESA(T2-1)　　分野：中性子散乱（その他）

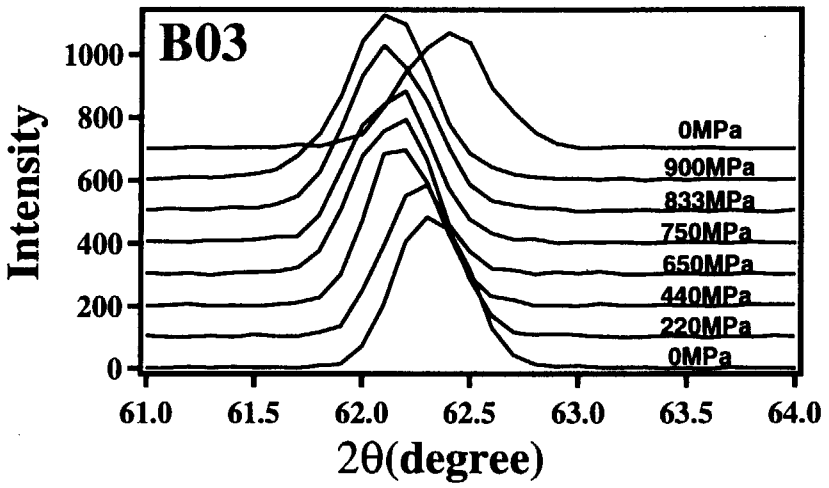


Figure 2: Ferrite(110) diffraction profiles at various applied stresses for B03.

Figure 2 shows ferrite(110) peak at various stresses for B03. A peak shifts to lower angle with increasing of the applied stress. Figure 3 shows stress estimated from lattice plane strains in ferrite and cementite as a function of the applied stress(σ_a) for B04. After the onset of plastic flow, i.e., yield strength of 500MPa, stresses in ferrite(σ_α) and in cementite(σ_θ) differs from each other. The following stress equilibrium condition holds among σ_a, σ_α,σ_θ and f_θ.

$\sigma_a=\sigma_\alpha(1\text{-}f_\theta)+\sigma_\theta f_\theta$ ————(1)

Such stress partitioning leads to large work-hardening in a pearlitic steel[2]. Under σ_a of 800MPa, σ_α andσ_θ are estimated to be 613 and 2500MPa respectively. In SK5 steel, the maximum stress of cementite was determined to be 2700MPa.

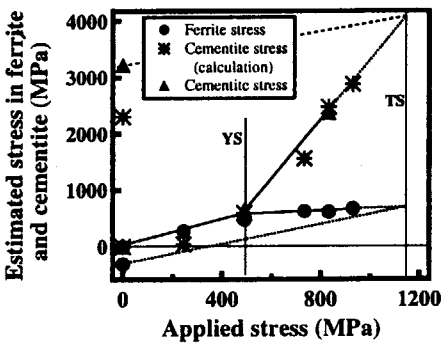


Figure 3: Stress partitioning between ferrite and cementite during tensile deformation for B04.

References

1) Y. Tomota, S. Harjo, A. Kanie, P. Lukas, D. Neov, Y. Abe., CAMP-ISIJ, **13**(2000), 1198.
2) A. Kanie, J. H. Park and Y. Tomota : Fifth Workshop on the Ultra-Steel, Tsukuba, 2001 p. 196.

研究テーマ：中性子回折による構造材料の応力測定および健全性評価
表　題：TRIP 型複合組織鋼を用いた引張変形その場中性子回折実験

1-9-6

In Situ Neutron Diffraction Experiment during Tensile Deformation for a TRIP Type Multi-Phase Steel

Y. TOMOTA, H. TOKUDA, N. MINAKAWA[1], A. MORIAI[1], Y. MORII[1], Y. ADACHI[2] and M. WAKITA[2]

Department of Materials Science, Ibaraki University, Hitachi, Ibaraki 316-8511
[1]Advanced Science Research Center, JAERI, Tokai, Ibaraki 319-1195
[2]Sumitomo Metal Industries Ltd., Amagasaki, Hyogo 660-0819

[Introduction]

Trip type multi-phase steels are characterized by an excellent combination of strength, ductility and response to high-speed deformation. The stress-induced martensitic transformation of retained austenite is known to contribute to such favorable properties, but the transformation behavior during deformation has not been made clear. Recent development of neutron diffraction experiment enables us to find deformation and transformation behavior in situ during deformation.

[Experimental Procedures]

A steel Used was prepared by a laboratory process at Sumitomo metal industries Ltd.. Chemical analysis for the steels showed 0.10C, 1.2Si, 1.3Mn, 0.01P and < 0.01S in mass%. Hot rolled (TMCP) sheets with 2 mm in thickness were made. Their microstructure consisted of ferrite, bainite and retained austenite. The angler dispersion neutron diffraction with wavelength of 0.2096724 nm was performed during step-wise tensile testing by using RESA at JAERI. The gauge volume of neutron diffraction was $15 \times 3 \times 2$ mm^3 so that the average lattice strains in bulk specimen were evaluated. Plate specimens were extended step by step and neutron diffraction profiles for austenite (111) and ferrite (110) planes were obtained at each step.

[Results and Discussion]

The change in diffraction intensity related to austenite volume fraction revealed that the onset of stress-induced martensitic transformation took place at approximately 400 MPa. The change in (111) austenite lattice plane spacings were measured along longitudinal and vertical directions with respect to the applied stress. The spacings measured were transformed to strains using the spacing before loading as a reference distance. The results are depicted in Fig.1. The change is apparently divided into three regimes; (i) elastic deformation below 400 MPa, (ii) stress partitioning between austenite and ferrite caused by the preferential plastic flow in the ferrite matrix and (iii) stress-induced transformation contributes to the change in stress partitioning. The data from ferrite (110) peak verify these conclusions. The higher flow stress of retained austenite and formation of strong martensite are speculated to yield larger uniform elongation.

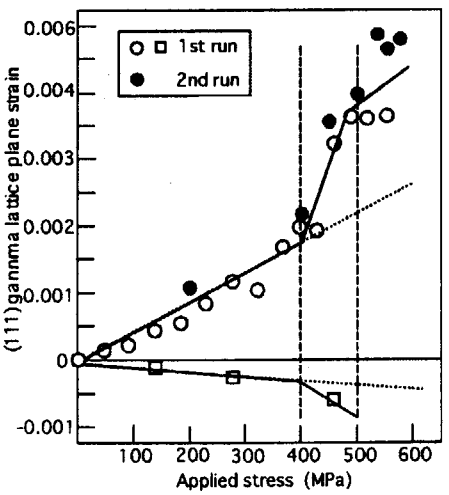


Figure 1: Lattice plane strain of (111) austenite as a function of applied stress.

原子炉：JRR-3M　　装置：RESA(T2-1)　　分野：中性子散乱（その他）

研究テーマ：中性子回折による構造材料の応力測定および健全性評価
表　題：Fe-Mn-Si 形状記憶合金における変形および回復の中性子その場観察
1-9-7

In situ observation of deformation and recovery behavior by neutron diffraction in an Fe-Mn-Si shape memory alloy

A. ONIZAWA, Y. TOMOTA[1], S. TORII[1], T. SUZUKI[1],
A. MORIAI[2], N. MINAKAWA[2] and Y. MORII[2]

Graduate student, Ibaraki University, Hitachi, Ibaraki 316-8511
[1] Faculty of Engineering, Ibaraki University, Hitachi, Ibaraki 316-8511
[2] Advanced Science Research Center, JAERI, Tokai, Ibaraki 319-1195

[Introduction]

The shape memory effect in Fe-Mn-Si based alloys generates by the stress induced transformation from austenite (γ:fcc) to epsilon martensite (ε:hcp) and its reverse transformation on heating. The transformations are caused by the forward and backward movement of Shockley partial dislocations. The variant selection of stress induced ε-martensite was restricted to a few orientations with respect to the tensile direction. The details of the transformations and then the improvement of shape memory have not been made clear. In this study, changes in lattice plane strains and volume fractions of the constituents were measured in situ by neutron diffraction during tensile straining.

[Experimental Procedures]

An Fe-28Mn-6Si-5Cr shape memory alloy was used (numerals refer to mass chemical composition). Round bars with 35mm in diameter were made through an industrial process and austenitized at 1273K for 3.6ks in a muffle type furnace followed by quenching into water with ice. Tensile specimens were prepared from the bars using a spark-cutting machine. The neutron diffraction experiments were performed with RESA at modified JRR-3M. The (111) and (200) diffraction peaks of γ and the $(10\bar{1}1)$ of ε were measured by the angle dispersion method at several steps of loading. A gauge volume for neutron diffraction was $10\times3\times6$ mm^3. Tensile load was kept constant during θ-2θ scan with a point counter. Diffraction angles were determined by a curve fitting with a Gauss function for the measured profiles.

[Results and Discussion]

Fig.1 shows the changes in lattice plane strain for $\gamma(111)$ and (200) along vertical (axial) and horizontal (transversal) directions. Both of them increase linearly up to approximately 250MPa. After that, $\gamma(111)$ deviates from the linear increase but γ (200) maintains the linearity. This suggests the stress-induced transformation, i.e., movement of partial dislocation occurs preferentially in (111) family grains. At the same time, integral intensities of $\varepsilon(10\bar{1}1)$ in the both directions were increased gradually with straining, but their increasing rates were different from each other.

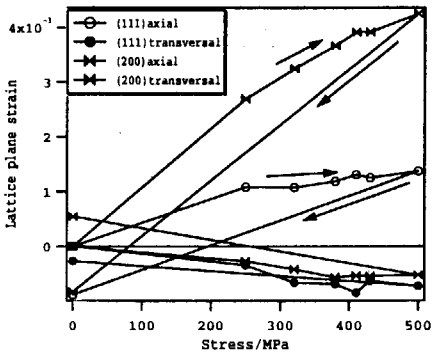


Figure 1: Changes in lattice plane strain for each planes.

原子炉：JRR-3M　　装置：RESA(T2-1)　　分野：中性子散乱（その他）

研究テーマ：中性子回折による構造材料の応力測定および健全性評価
表　題：伸線パーライト鋼の集合組織測定
1-9-8

Texture measurement by neutron diffraction for pearlite steel wires

T. SUZUKI, Y.TOMOTA[1], A.KANIE[2]
Y.MORIAI[3], N.MINAKAWA[3] and Y.MORII[3]

The Research Center for Superplasticity, Faculty of Engineering,
Ibaraki University, Hitachi, Ibaraki 316-8511
[1]Department of Materials Science, Faculty of Engineering, Ibaraki University
[2]Graduate student of Ibaraki University
[3]Japan Atomic Energy Research Institute, Tokai, Ibaraki 319-1195

1.Introduction

Heavily drawn pearlite steel wires are known to show the highest strength in commercially available materials. The reason of the ultra-high strength is however unclear. We have found that the yield strength anisotropy in a drawn pearlitic steel wire by compression tests along five different directions[1)]. This anisotropy is much influenced by heat treatment. Here, the reason of the anisotropy is speculated either residual phase stress in cementite and the ferrite matrix, ferrite texture or the both. First, we measured the residual phase stress by neuron diffraction and found a good correspondence with the yield strength anisotropy[2)]. Then, we secondly examined the ferrite texture in this study. Here two samples, P2 and P4 explained in chapter 2, were used because the strong anisotropy were observed in P2 but scarcely in P4.

2.Experimental procedure

A hypereutectoid steel with chemical compositions of 0.85C, 0.24Si, 0.82Mn, 0.011P, 0.01S, 0.02Al and 0.05Cr in mass percent was used in this study. Hot-rolled rods with 11mm in diameter were patented through an industrial process to produce fully pearlitic structure. They were then drawn to wires with 5.5mm in diameter, where reduction in area was 75 percent (P2). After that, some of the drawn wires were aged at 698K for 0.6ks (P4: Zn-plating simulated heat). Specimens size of ϕ 5.5 × 5mm were prepared for texture measurement by using RESA at JRR-3, JAERI. Figure 1 shows geometrical arrangements for measurement, ferrite (110) radiation was employed. The angles ϕ and χ are defined as depicted in Fig.1. The scanning with respect to ϕ and χ was performed at 5° intervals, and the measured ranges of ϕ and χ were from 0 ° to 180 ° and from 0 ° to 90 ° , respectively. Texture was evaluated by 110 pole figure.

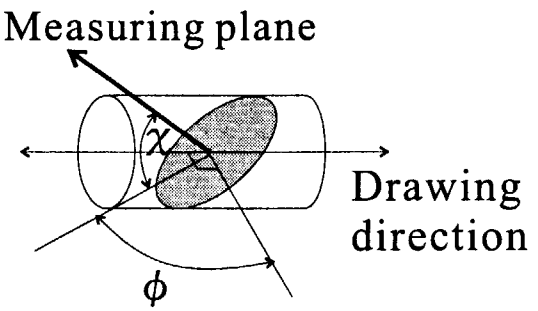


Figure 1: Geometrical arrangements for texture measurement.

3.Result and Discussion

Figure 2 shows a part of the 110 pole figure of a P2 specimen. Pole densities were projected onto a plane perpendicular to the extrusion direction using the mean pole densities as units. The concentric distribution around the center is observed, where the maximum intensity is 6.8. Another concentric-circular distribution is found at approximately 60° declined from center. This apparently shows the formation of 110 fiber texture of ferrite phase.

原子炉：JRR-3M　　装置：RESA(T2-1)　　分野：中性子散乱（その他）

Figure 3 shows a part of the 110 pole figure of a P4 specimen. The pole figure of the P4 specimen is similar to that of P2 specimen, where, the maximum intensity is 6.2. Consequently, the texture evolved by the drawing was hardly changed by the annealing at 698K.

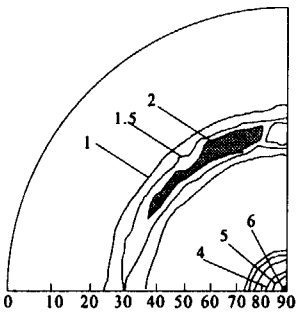


Figure 2: 110 pole figure of a P2 specimen.

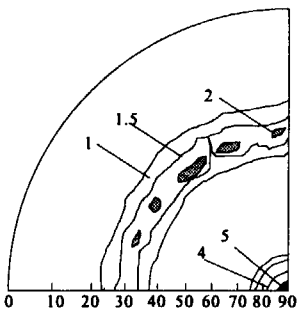


Figure 3: 110 pole figure of a P4 specimen.

According to the results by the neutron stress measurement, the phase residual stress are generated by the drawing and relaxed by the subsequent annealing. They are balanced among pearlite colonies as well as between cementite and ferrite. Because the ferrite matrix was totally compressed along the drawing direction for P2, the residual phase stresses were concluded to bring the yield strength anisotropy. The strong fiber texture is thus found to give minor influence.

Texture measurement is usually conducted by X ray diffraction, however, the quantity of information is not satisfactory in the case of small specimen. In this study, detail texture measurements were performed by using neutron diffraction.

References

1) T.Suzuki, M.Isaka, T.Terashima, A.Kanie, Y.Tomota, M.Umemoto and K.Tsuchiya: CAMP-ISIJ, **14**(2001), 1065.
2) T.Suzuki, Y.Tomota, Y.Moriai, N.Minakawa and Y.Morii: JAERI-Review 2002-006, 101.

研究テーマ：冷中性子磁気光学系の基礎研究
表　題：冷中性子光学素子の開発

1-9-9

Development of optical devices for cold neutrons

H.M Shimizu, T. Adachi, T. Oku, K. Ikeda, H. Sato, Y. Takizawa, K. Morimoto, S. Morita, H. Ohmori, K. Sakai[1] F. Tokanai[2], K. Sasaki[3], Y. Kiyanagi[3] and J. Suzuki[4]

RIKEN, Wako, Saitama 351-0198
[1]Department of Physics, Tokyo Institute of Technology, Ohokayama, Meguro 152-8551
[2]Department of Physics, Yamagata University, Yamagata 990-8560
[3]Atomic Science and Nuclear Engineering, Hokkaido University, Sapporo, Hokkaido 060-8628
[4]Advanced Science Research Center, JAERI, Tokai, Ibaraki 319-1195

Recently, we have developed optical devices for cold neutrons and have demonstrated the capability of focusing and polarizing a neutron beam by magnetic lenses that do not attenuate the neutron beam [1, 2, 3]. We have designed and fabricated compound Fresnel-type refractive lenses for cold neutrons. Fresnel lens made of single-crystal MgF_2 are better than vitreous silica [4] due to its higher purity and much reduced microstructure. For the convenience of fabrication, an array of parallel prisms of triangular cross section was assembled to form a compound refractive prism [5]. This development lays an important groundwork for the eventual design of two-dimensional compound refractive lenses. Additionally, such a one-dimensional neutron prism may have potential applications such as energy analyzers for time-of-flight neutron spectroscopy.

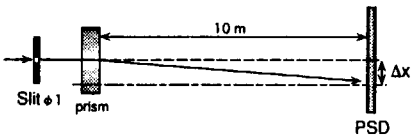


Figure 1: Setup of the experiment.

Setup of the experiment is shown in Fig.1. The intensity profiles for wavelength of 4, 8, 12, and 15 Å are shown in Fig. 2 as a part of the results. The wavelength resolution ($\Delta\lambda/\lambda$) of neutron beam is 13%. Neutron beam was refracted by the prism. Refracted angle depended on wavelength of neutrons, therefore the prism works as a spectroscope. There is a little of reflected component on the parallel surfaces to the beam at around $\Delta x = 0$. No component of the high-energy time-independent (delayed) neutrons [5] is observed. In order to understand these results quantitatively, we performed numerical simulations of the refractive prism, taken into account the effects of prism geometry, beam collimation, small-angle scattering and neutron transmission from the MgF_2 single crystals. Obviously, the detailed experimental results cannot be explained solely by the effects included in the simulation. Other factor due to stray scattering have to be investigated further.

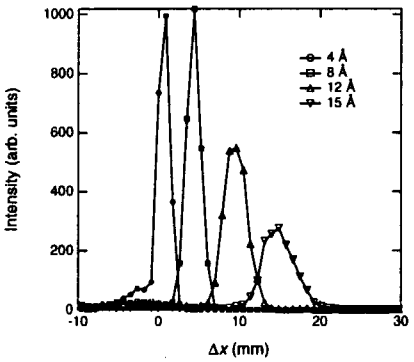


Figure 2: The intensity profiles for wavelength of 4, 8, 12, and 15 Å.

We also designed and fabricated compound Fresnel-type refractive lenses for cold neutrons. One device consisted of 49 pieces of Fresnel lens made of MgF_2. Focusing function and performance was evaluated. As a

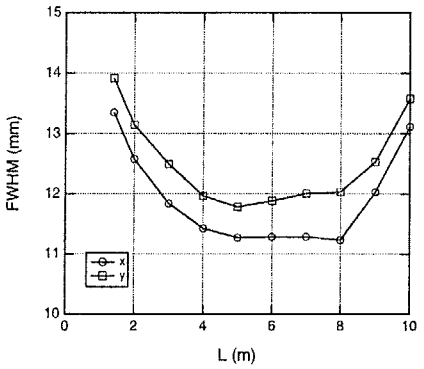


Figure 3: The size of focused beam depending on lens-detector distance at wavelength 14.4 Å.

typical result, Fig. 3 shows the size of focused beam depending on lens-detector distance, L, at wavelength 14.4 Å. Designed focusing point at wavelength 14.4 Å in this setup should be 5 m of lens-detector distance. The result showed somewhat longer focal length. The reason of this difference would be effect of surface roughness. To make clear this difference, simulation program including the effect of surface roughness has been developed.

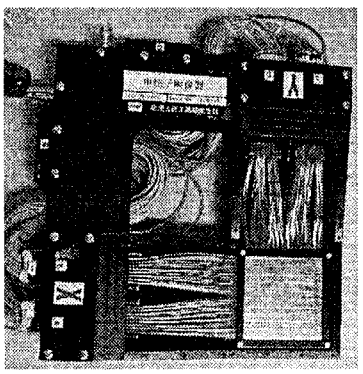


Figure 4: The picture of the detector. One of the covers is opened.

In order to make sure the function of these optical devices, 2-dimentional survey must be required after a exit of these devices. To make experiment progress efficiently, 2-dimensional neutron detector has been highly required to develop the neutron optical devices. We are developing the 2-dimentional detector based on neutron scintillator reading out with wavelength shifting fiber crossing each other [6]. The picture of the detector is shown in Fig. 4. The typical result is shown in Fig. 5, which is image of cadmium slit slanting. Width of opened lines of cadmium slit is 0.5 mm. Distance between slits is 5 mm. Now, spatial resolution was about 0.5 mm in FWHM and detecting efficiency was about 10 % for cold neutrons. The detecting efficiency should be increased for practical application.

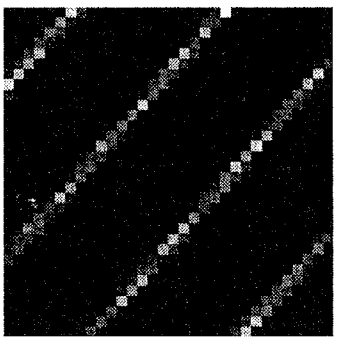


Figure 5: Image of cadmium slit slanting. Width of opened lines is 0.5 mm. Pixel size in the image is 0.5 mm × 0.5 mm.

References

1) H. M. Shimizu, H. Kato, T. Oku, Y. Suda, Y. Ogawa, H. Iwasa, T. Kamiyama, Y. Kiyanagi, and T. Wakabayashi, Physica B, **241-243,** 172-174 (1998).
2) H. M. Shimizu, Y. Suda, T. Oku, H. Nakagawa, H. Kato, T. Kamiyama, C. Otani, H. Sato, T. Wakabayashi, and Y. Kiyanagi,Nucl. Instrum. Methods A **430,** 423-434 (1999).
3) H. M. Shimizu, T. Oku, H. Sato, C. Otani, H. Kato, Y. Suda, H. Nakagawa, T. Kamiyama, Y. Kiyanagi, and T. Wakabayashi, Physica B, **276-278,** 63-64 (2000).
4) T. Oku, S. Morita, S. Moriyasu, Y. Yamagata, H. Ohmori, Y. Takizawa, H. M. Shimizu, T. Hirota, Y. Kiyanagi, and J. Suzuki, Nucl. Instrum. Methods A, **462,** 435-441 (2001).
5) T. Adachi, T. Oku, S. Morita, H. Ohmori, Y. Takizawa, H. M. Shimizu, J. Suzuki, C.-K. Loong, K. C. Littrell, and R. Goyette, Appl. Phys. A, in press.
6) K. Sakai, T. Adachi, A. Gorin, T. Ino, K. Kuroda, A. Manuilov, K. Morimoto, T. Oku, R. Ryazantsev, H. M. Shimizu, J. Suzuki, and F. Tokanai, Appl. Phys. A, in press.

研究テーマ：中性子回折による構造材料の応力測定および健全性評価
表　題：高周波焼入れしたS45C丸棒の残留応力測定

1-9-10

Residual Strain Measurement of S45C Round Bar Hardened by Induction

K. INOUE, T. HORIKAWA, T. TSUJIKAMI, M. SUGIMOTO,
N. MINAKAWA[1], A. MORIAI[1] and F. IKUTA[2]

Faculty of Science and Technology, Ryukoku University, Seta, Otsu 520-2194
[1]Advanced Science Research Center, JAERI, Tokai, Ibaraki 319-1195
[2]Heating Machine Division, Neturen Co., Tanuma, Hiratsuka 254-0013

The residual strain of the S45C round bar hardened by induction heating was measured by neutron diffraction apparatus, RESA. The diameter of the bar was 20 mm and the length was 60 mm. The surface of the bar was hardened by induction heating of 50kHz. The temperature of the surface was increased up to 950 °C. After heating for 8.5 s, it was cooled down to 26.9 °C with the water. The depth of the hardened layer was 1 ～ 3 mm. It is expected that the martensitic phase occurs in this layer, whereas the inner region is not hardened in the ferritic phase.

The sample installed on the goniometer of RESA is shown in Fig. 1. We determined the wave length of neutron beam precisely for each machine time, using Si poly-crystal. It was about 2.10 Å. We used a peak of 110 reflection of the S45C sample. On the circular cross section at the center of the bar, the strain for the axial, radial and hoop directions at each position of 0, 2, 4, 6 and 10 mm from the surface was measured.



Figure 1: Sample installed on the goniometer of RESA.

The 110 reflections of the two round bars of the same size were measured for the estimation of standard lattice spacing, d_0. One is heat treated to obtain the martensitic phase for the whole of the sample, and the other is not heat treated and in ferritic phase. During the observation of the reflection, the sample was rotated around the χ, ϕ directions using two small motors on the goniometer, to obtain the average lattice spacing for all directions. The value of d_0 for (110) plane of martensitic phase was 2.0311 Å and that of ferritic phase was 2.0289 Å. We could not observe the separation of the peaks which is expected for the tetragonal structure of martensitic phase.

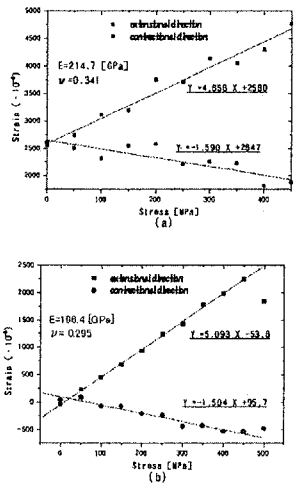


Figure 2: Strain versus applied stress obtained from the 110 reflection, (a) for a heat treated specimen and (b) for a non heat treated specimen.

The Young's modulus and the Poisson ratio of a heat treated specimen and of a non heat treated specimen were measured by RESA, using the tensile test equipment. The heat treated specimen was cooled down with water-

原子炉：JRR-3M　　装置：RESA(T2-1)　　分野：中性子散乱（その他）

solution of polymer. The 110 reflection was used. The results are shown in Figs. 2 (a) and (b). We see the linearity of the data in Fig. 2 (b) is good, whereas the data in Fig. 2 (a) are dispersed. The dispersion is presumably due to the existence of the defects, the grain boundary of the texture and so on, caused by rapid quenching. The Young's modulus, E, for martensitic phase is 214.7 GPa and that for ferritic phase is 196.4 GPa. The Poisson ratio, ν, for martensitic phase was 0.341 and that for ferritic phase was 0.295. For the values of E and ν at the region where the martensitic phase and the ferritic phase coexist, we use the average value weighted by the volume fraction of each phase. The volume fractions was estimated by finite element method (FEM). [1)]

The typical observed reflection peaks for three directions from the position at 2mm from the surface on the central circular cross section of the bar are shown in Figs. 3 (a) to (c). We see that for axial direction shown in Fig. 3 (a) the data points are scattered remarkably in spite that we expend 40 minutes for one datum point. This is because the path length of the neutron beam inside the sample is long for the measurement of axial direction.

The calculated residual stress for three directions at each position of the circular cross section at the center of the bar is shown in Fig. 4. Near the surface where the material is hardened, the residual stress for radial direction is tensile and large, whereas the stresses for axial and hoop directions are compressive. We see that at the inner position the stress is small.

The residual stress at each position on the central axis of the bar, which was also measured by RESA, will be published elsewhere.

References

1) F. Ikuta: Internal Report of Neturen Co. (2000) (in Japanese).

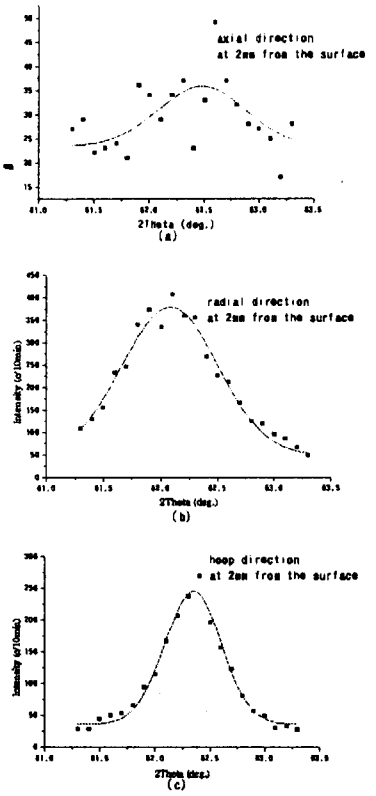


Figure 3: Reflection peaks from the position at 2mm from the surface on the central circular cross section (a) for axial direction, (b) for radial direction and (c) for hoop direction.

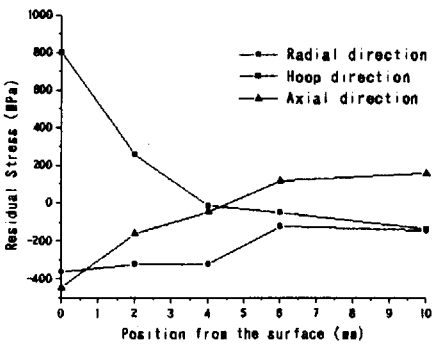


Figure 4: Residual stress at each position on the central circular cross section of the heat treated round bar.

研究テーマ：研究炉利用高度化の技術開発
表　題：中性子減速材容器の残留応力測定
1-9-11

Measurement of Residual Stress in the Neutron Cold Moderator Cell for High Intensity Proton Accelerators II

A. Moriai[3,1], H. Kogawa[2], M. Kaminaga[2],
N. Minakawa[1,3], Y. Horiguchi[1]

[1]Department of Research Reactor, JAERI, Tokai, Naka, Ibaraki, 319-1195, Japan
[2]Center for Neutron Science, JAERI, Tokai, Naka, Ibaraki, 319-1195, Japan
[3]Advanced Science Research Center, JAERI, Tokai, Ibaraki 319-1195

Residual stresses in the side wall of an aluminum alloy neutron cold moderator cell for Japanese spallation neutron source(JSNS)[1] was investigate by neutron diffraction method as the sequel to the previous study[2] on the front wall. Diffraction strains measurement was performed in the same conditions as that of the previous study, but the size of Cd masks aperture restricting gauge volume were chosen 4mm^{ϕ} to suit the wall thickness of the side wall. Figure-1 shows horizontal and vertical cross sectional views of the cell, and measurement region in the side wall is a hatched area. Each strain component in x, y and z directions for 10 gauge volumes were measured as change in the Al(111) lattice plane spacing.

Figure-2 shows the estimated residual stress distribution in the side wall of the moderator cell. The stresses in all three coordinates exhibit compressive stress state throughout the measured range, but show a slight increase response toward tension in between z=6mm and z=12mm, and then take a maximum compression peak at z=10mm. Contrary to this, the stress response of the front wall in the previous study in the same range assumed a minimum compression value around z=10mm.

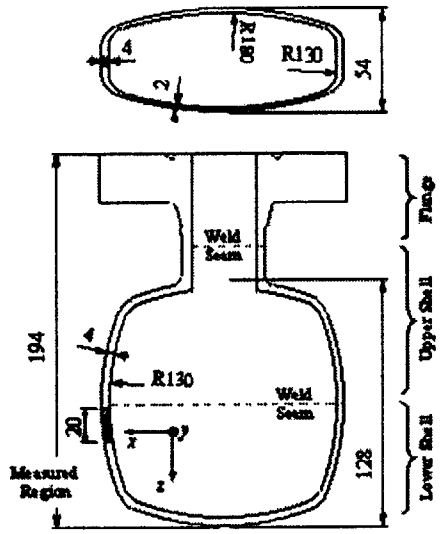


Figure 1: Fig.1 Cross-sections of the neutron cold moderator cell for high-intensity proton accelerators. A view in the top shows a horizontal-section along the weld seam.

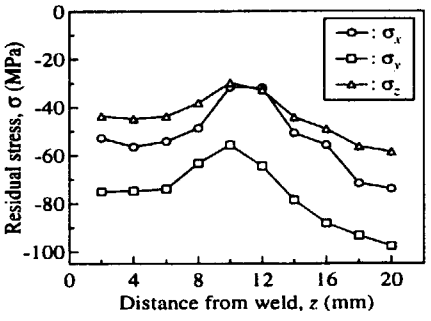


Figure 2: Fig.2 Residual stress distributions in the base metal near weld of the A7N01-T6 moderator cell.

References

1) The Joint Project for High-Intensity Proton Accelerators, ed. the Joint Project Team of JAERI and KEK, JAERI-Tech 2000-003.
2) Progress Report on Neutron Scattering Research, JAERI-Review 2000-006, p.93.

原子炉：JRR-3M　　装置：RESA(T2-1)　　分野：中性子散乱（その他）

研究テーマ：中性子回折による構造物の残留応力測定
表　題：中性子回折によるピーニングされたSUS304鋼のき裂周りの残留応力測定

1-9-12

Measurement of residual stress distribution vicinity of the crack on peened surface of type 304 stainless steel by neutron diffraction method

S.Okido, K.Enomoto, T.Machida, M.Hayashi, Y.Morii[1] and N.Minakawa[1]

Mechanical Engineering Research Laboratory, Hitachi Ltd. Hitachi, Ibaraki 317-8511
[1]Advanced Science Research Center, JAERI, Tokai, Ibaraki 319-1195

Shot peening (SP) deforms and hardens a metal surface plastically with particles of metal or glass. As a result, compressive residual stress appears and the surface properties are improved. Cracks, not only those caused by SCC, in compressive residual stress fields are difficult to propagate unless an external load is applied. The cracks on the peened material, consequently, will not propagate without the external load. So residual stress measurement by neutron diffraction was discussed to the peened materials.

The materials used in this research were stainless steel Type-304. The specimens were 10 mm wide, 50 mm long, and 3 mm thick. These were extended under a strain range of 0.4 % and soaked in an autoclave for 500 hours, at a temperature of 562 K, in which the concentration of dissolved oxygen was 8 ppm.

RESA was used in the measurement of lattice strain. The 111 diffraction of γ-Fe in type-304 steel was used in the measurement of strain. The wavelength, λ was 0.20731. Measurements were performed in steps of 0.1 mm to a depth of 0.5 mm and in steps of 0.2 mm to a depth of 1.0 mm-depth. Cadmium masks were inserted in both the incoming beam and the diffracted beam to define a sampling volume of 0.2x0.2x10 mm^3. The stresses were obtained from Hooke ' s law using lattice strains in three directions. For 111 diffraction the Young ' s modulus, E_{111}, was 249 GPa and the Poisson ' s ratio, ν_{111} was 0.28.

The results of surface residual stress vicinity of crack on the surface obtained from before and after peened specimen are shown in Fig. 1. In the case of before peened specimen, residual stresses were almost 0 MPa since they were released by crack progress. In the case of after peened specimen, residual stress were compressive and at about 500 MPa and 400 MPa. These compressive stresses decreased rapidly and changed to tensile at a depth of 0.5 mm. The surface residual stresses were nearly same in spite of flat or notched.

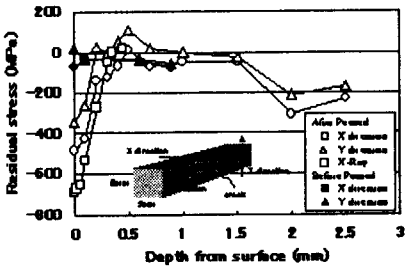


Figure 1: Residual stresses distribution of stainless steel before and after peened.

The values of residual stress obtained by x-ray diffraction are also shown in Fig. 1. It was found that the result for residual stress as obtained by neutron diffraction almost agreed with those from x-ray diffraction.

According to the principle of superposition, the load on the crack surface controls the stress intensity factor K at the crack tip. The sum of load on the crack surface and K decreases if a compressive residual stress exists at the surface. As the result, the crack growth rate in the depth direction will decrease. The prevention effect of crack propagation on the surface is greater than that in depth direction since the compressive residual stress will prevent the crack from opening. As the result, crack propagation on the surface was arrested. These results means if compressive stress slightly exist at the surface, crack progress is prevented.

原子炉：JRR-3M　　装置：RESA(T2-1)　　分野：中性子散乱（その他）

研究テーマ：多重極限環境下における中性子散乱実験法の研究
表　題：大型試料の内部応力測定の可能性について

1-9-13

The possibility of internal stress measurement of the King-size sample

Nobuaki Minakawa, Atsushi Moriai, Yukio Morii

Advanced Science Research Center, JAERI, Tokai, Naka, Ibaraki 319-1195

We performed evaluation about the possibility of an internal residual stress measurement using king-size aluminum alloy material. As for the engine of the airplane, the ship, and the automobile, many aluminum alloy material is used for the purpose of the lightening, the cooling performance and the lifetime improvement. In order that to improve the radiation effect of engine temperature, it is performed that expand surface area or a cooling water passage is puffed up etc. Therefore, big space is located in the inside of engine, and there are few neutron pass lengths than an actual size pass length. This measurement used the RESA equipment. This engine is the water-cooled type, which is made by the aluminum alloy, the specific gravity is about 2.88. The void ratio in the engine, which was found from the weight, is about 50%. The neutron absorption coefficient μ is about 0.125(cm^{-1}) as for 0.21 nm neutron wavelength. The incidence neutron intensity of RESA is about 3×10^5 ($n/cm^2/sec$), and the slit of incidence and reflection used 3 mm × 3 mm. The measurement position and size of engine is shown in Fig. 1.

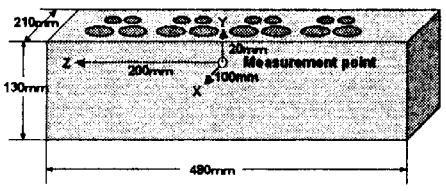


Figure 1: The size and a measurement position of engine.

In an internal residual stress measurement, we have to do a neutron diffraction measurement about 3 axial directions of X, Y, and Z. The neutron total pass length in the engine to get the diffraction of the measurement position is 191 mm at the X-axis, 55 mm at the Y-axis, and 309 mm at the Z-axis. I/I_0 with consideration to the void ratio is 0.3 in measurement of the X-axis, at the Y-axis is 0.71 and at the Z-axis is 0.15. The measurement neutron wavelength of RESA used for 0.2098 nm. The measurement index and the diffraction angle thought the gauge volume as important, selected Al (220) near right-angled, and diffraction angle was used at the 94.28 degrees. Al (220) diffraction pattern of the measuring points in A and B are shown in Fig. 2.

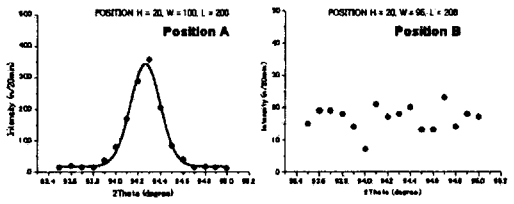


Figure 2: Al (220) diffraction pattern of the measuring points A and B.

The neutron diffraction pattern by gauge volume of doing about 27 mm^3 is good gauss distribution position A. But in a certain measurement part, a diffraction pattern position B might not be obtained at all. It is interpreted that this is in order that having measured for the space part to the gauge volume. In the case of a huge aluminum sample, at RESA, it proves that an internal strain can be measured with a 3 mm × 3 mm incidence neutron beam size. Moreover, in order that to measure the position, which cannot be viewed with a sufficient precision, when considering the method of doing incidence neutron beam to a measurement position in the precision of less than ± 1mm with the working drawing or the 3-dimensional drawing by the ultrasonic scanner etc., it proves that it is also practical use.

原子炉：JRR-3M　　装置：RESA(T2-1)　　分野：中性子散乱（その他）

2. 中性子ラジオグラフィ

2. Neutron Radiography

This is a blank page.

研究テーマ：中性子ビーム利用技術に関する開発研究
表　　題：パルス中性子ラジオグラフィ用電子撮像システムの開発

2-1

パルス中性子ラジオグラフィ用電子撮像システムの開発

松林政仁、持木幸一[1]、村田裕[1]、桑子雅史[1]、中川哲郎[1]、池野豊[1]、増子大輔[1]、伊藤覚[1]
日本原子力研究所　東海研究所　大強度陽子加速器施設開発センター
[1]武蔵工業大学　工学部　電子情報工学科

パルス中性子ラジオグラフィの中性子飛行時間撮影法では中性子散乱実験装置で要求される程度の時間分解能は必要としないが、高計数特性（高時間分解能）と高空間分解特性を兼ね備えた中性子シンチレーション検出器の開発が必要とされている。本研究では、中性子用蛍光体の前面及び後面に X-Y の直交した２方向に配置された波長変換光ファイバ群から出力される微弱光をマルチチャンネル光電子増倍管で受光し、検出点のX-Yアドレスを30ns以下で出力する電子回路の試作を行った。

システムの試作において、波長変換ファイバの断面形状が角型と丸型との場合で比較し、蛍光体との接触面積が大きくなる角型の方が効率の点において優れていることを確認した。また、回路の入力信号となる光電子増倍管からのパルス出力を中性子蛍光体として広く使用されている^{6}LiF:ZnS(Ag)を用いて確認した。これらの結果から、今後検出器の大面積化に伴い大規模化が予想されるエンコーダ部分の設計に必要な基礎データを取得した。

今後は熱中性子ラジオグラフィ装置を用いて、空間分解能と計数特性の観点から最適な読み出しレイアウトの検討を進める。回路は高速のプログラマブル論理素子を使用し,将来の大型システムの基幹要素となるものである。

フェーズコントラストイメージング

ピンホールを用いた中性子フェーズコントラスト(PC)イメージングの予備実験を冷中性子ラジオグラフィ装置場で中性子イメージングプレートを用いて実施した。ペン先部を撮影した結果では、図１に示すとおりオリジナル画像では曲導管及びピンホールのバリ等によるアーティファクトが観察されたが、背景補正後の画像にはボール部及びインク部をはっきりと観察できた。

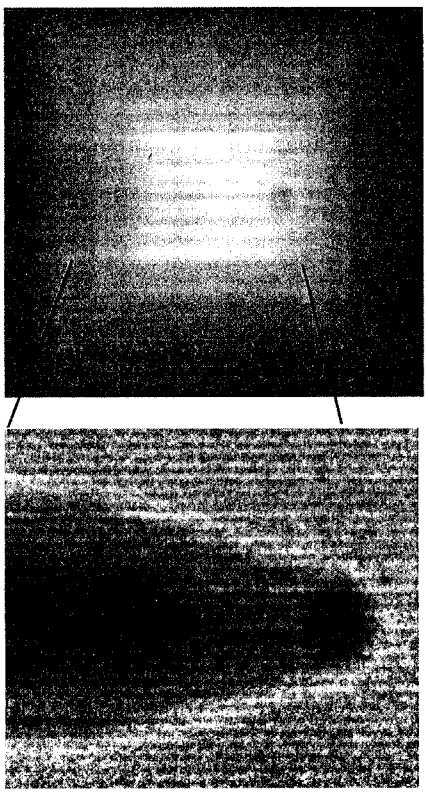


図１ PCイメージング
上：オリジナル画像、下：背景補正

原子炉：JRR-3M　　装　置：TNRF, CNRF　　分　野：中性子ラジオグラフィ（その他）

研究テーマ：中性子ビーム利用技術に関する開発研究
表　　題：中性子ラジオグラフィを用いたストロボ撮影技術に関する研究

2-2

中性子ラジオグラフィを用いたストロボ撮影技術に関する研究

松林政仁、日引　俊[1]、三島嘉一郎[1]、宇根崎博信[1]
日本原子力研究所　東海研究所救助　中性子科学研究センター
[1]京都大学　原子炉実験所　核エネルギー基礎研究部門

大強度陽子加速器の中性子散乱施設のうちパルス中性子ラジオグラフィ装置(PNR)のストロボ撮影で必要とされる検出器の開発を行った。現在 JRR-3M 中性子ラジオグラフィ装置に設置されている高速度撮像システムは高速度カメラと蛍光コンバータを光学レンズにより接続したものであるが、大強度陽子加速器の核破砕中性子源から発生されるパルス中性子ビームには高エネルギー中性子及びγ線が含まれることから蛍光コンバータとカメラを光ファイバーを用いて接続する等カメラの遮蔽を十分に行う必要がある。

本年度は光ファイバー接続を導入した撮像システムを熱中性子ラジオグラフィ装置場に仮構築し、模擬撮影により問題点の摘出を行った。蛍光コンバータ（シンチレータ部分）とカメラ部分を光ファイバー接続するための 20cm 長のファイバーバンドルはプラスチック光ファイバ(三菱レイヨン製エスカ 1mmϕ) を用いて試作した。シンチレータは高輝度の LiF-ZnS(Ag)をファイバーバンドル中性子入射端面側にシリコングリースで取付け、冷却型 CCD カメラでファイバーバンドル出射端を撮影した。その結果、シンチレータの発光を直接カメラで撮影した場合の輝度：15330 に対して、ファイバーバンドル出射端での輝度が 8930 となり、ファイバーバンドル使用による輝度の低下は 60%程度であることが分かった。また、二次元のイメージを確認するために、フィルム法で使用されるマーカーの撮影を行った。撮影結果を図１に示す。マーカーのレイアウトは c)に示すとおりであり、形状はプラスチックに鉛でできた文字が埋められている。従って、中性子による透過画像では文字部分の輝度が高い状態となる。マーカーのあり、なしを示す a)及び b)を比較しても良く分からないが、両画像を用いた背景補正により得られた画像 d)ではマーカーの位置がはっきりと確認できる。但し、文字の位置は凡そ確認できるが形状“A”をとらえるところまでは至っていない。また、バンドル製作に伴う画像歪みの影響が確認された。

今後は、イメージ領域を広げるために入射側をテーパー状に拡大する方策を開発する。

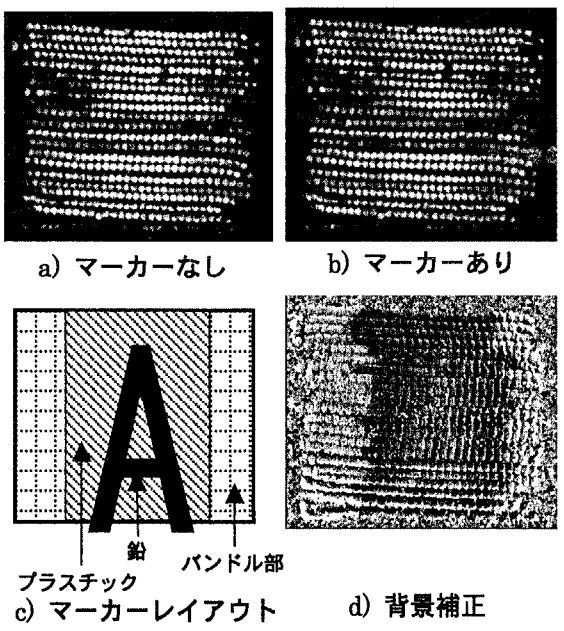


図１　ファイバーバンドル使用撮影画像

原子炉：JRR-3M　　装　置：TNRF, CNRF　　分　野：中性子ラジオグラフィ（その他）

研究テーマ：中性子ビーム利用技術に関する開発研究
表　　題：再帰型２液相分離系水溶液における濃度ゆらぎの空間発展の可視化

2-3

再帰型２液相分離系水溶液における濃度ゆらぎの空間発展の可視化

松林政仁、三沢正勝[1]
日本原子力研究所　東海研究所　大強度陽子加速器施設開発センター
[1]新潟大学　理学部　化学科

1-プロパノール水溶液は組成・温度によらず一様に混合しているが、これに少量の塩(KCl)を添加すると、ある温度範囲（例えば 40℃～60℃の間）で２液相に分離する。本研究ではこの特異な相分離過程における濃度ゆらぎの空間・時間発展を中性子ラジオグラフィにより可視化した。

可視化は冷中性子ラジオグラフィ装置において蛍光コンバータと SIT 管カメラを組合わせた実時間撮像システムを用いて行い、画像をリアルタイムでレーザーディスクに記録した。レーザーディスクに記録された画像はフレームグラバーボードによって 8bit(256 階調)の 640x480pixels 画像に変換された後、IP-Lab Spectrum により画像解析された。

光学用石英ガラスセル内に封入した KCl 添加のプロパノール水溶液を室温から 80℃まで変化させながら濃度ゆらぎから相分離にいたる過程でのゆらぎ構造の空間発展を可視化した。図 1 に水溶液の透過画像を示す。石英ガラスセルは殆ど中性子に対して透明であり、溶液部のみが可視化された。その結果、相分離温度（50℃）で相分離に伴う２相間の透過率の違いが可視化画像上で階段状に確認できた。（図２参照）

水溶液の温度をパラメータとした可視化実験により、昇温過程においても降温過程においても同じ 50℃で相分離が起こることを確認した。その際、温度変化過程の違いによる相の界面位置に変化は見られなかった。さらに、塩の添加量を１ミリ mol 程度減じて添加して行った実験では相分離は観察されなかった。

本研究により、当該水溶液の冷中性子透過率データを得ることができたが、相分離過程は時間的にゆるやかであることから、高階調分解能を有する冷却型 CCD カメラを用いたシステムにより空間的にも高精度で測定可能である見通しが得られた。

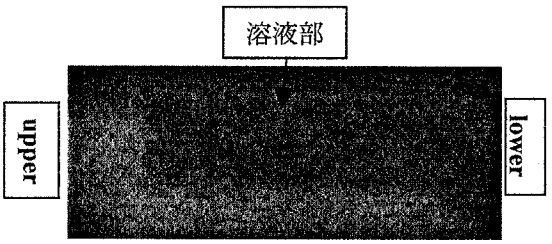


図１　水溶液透過画像

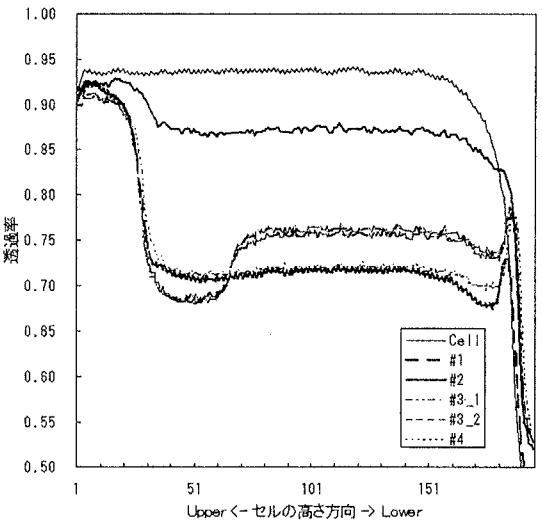


図２　中性子透過率

原子炉：JRR-3M　　装　置：CNRF　　分　野：中性子ラジオグラフィ（その他）

研究テーマ：中性子ラジオグラフィによる沸騰流のボイド率計測
表　題　　：中性子ラジオグラフィによる沸騰開始点の計測

2-4

中性子ラジオグラフィによる沸騰開始点の計測

呉田 昌俊、 秋本 肇
日本原子力研究所
エネルギーシステム研究部
熱流体研究グループ

当研究グループでは、中性子ラジオグラフィ（NRG）を用いて狭い流路内を流れる熱的に非平衡な沸騰流（サブクール沸騰流）を高時間分解能で可視化し、瞬間ボイド率分布および時間平均ボイド率分布を計測してきた[1]。平成13年度は、NRGを熱流体計測に応用して計測されるボイド率分布から沸騰開始点を計測した。

実験は、JRR-3M熱中性子ラジオグラフィ実験施設（TNRF-2）を利用した。ボイド率分布計測実験には、沸騰流NRG実験用矩形流路（流路間隙が3mmおよび5mm、加熱長100mm、流路幅30mm、加熱幅20mm）を用いた。図1にこの試験体と水循環ループの概略図を示す。このループ内を水が流れ、試験体の中で沸騰が始まる。

図2に瞬時ボイド率を計測した一例を示す。図2は、約1000フレーム毎秒で記録したNRG画像を画像処理して得られたボイド率の分布を示しており、これは動画観察用画面の1コマを示している。沸騰開始点は、実際の時間と逆方向に画像処理を行って統計的に評価を行った。図2条件での沸騰開始点を測定した結果を図3に示す。図3から、沸騰開始点の統計的分布と変動幅が分かり、これらのデータから沸騰開始点計算式を導出できた。

本成果により、狭隘短加熱長矩形流路体系でのボイド率を解析的に計算可能となり、除熱限界を高精度で計算できるようになった[2]。

次ステップとして、将来型原子炉の炉心を模擬した稠密バンドル流路内二相流のボイド率計測や、ボイド率の3次元分布を計測するための技術開発を進めている。

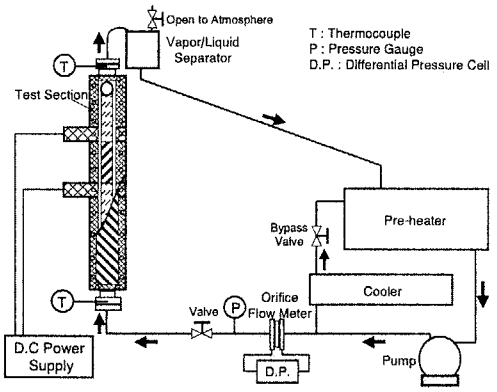


図1　ボイド率の計測実験用水循環ループ

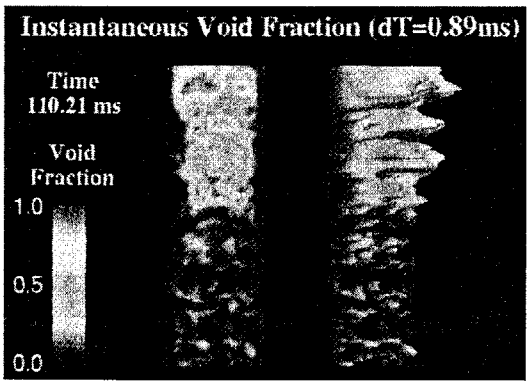


図2　瞬時ボイド率の計測

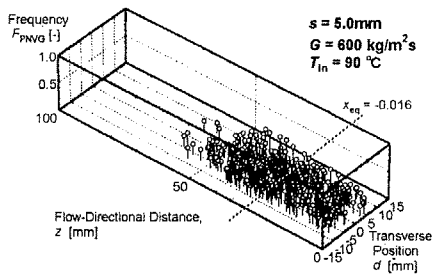


図3　沸騰開始点の計測

参考文献
1) Nuclear Technology, Vol.136, (2001), pp.241-254
2) Int. J. Heat and Mass Transfer, Vol.46-7, (2003), pp. 1171-1181.

原子炉：JRR-3　装置：熱中性子ラジオグラフィ施設　分野：中性子ラジオグラフィフィ（熱水力）

2-5 JRR-3M冷・熱中性子を用いたラジオグラフィ技術の高度化－III

Development of Advanced Neutron Radiography Techniques Using Thermal and Cold Neutrons from JRR-3M, Part III

京都大学原子炉実験所　三島嘉一郎、齊藤泰司
電力中央研究所　神戸　満

K. Mishima, Y. Saito, *Research Reactor Institute, Kyoto University*
M. Kambe, *Central Research Institute of the Electric Power Industry*

1．研究の目的

本研究は、これまでに開発した中性子ラジオグラフィ高速度撮像技術と熱中性子ラジオグラフィ画像の定量化法（Σ－スケーリング法）とを応用して、①超安全・超小型原子炉 RAPID-L の自己作動型反応度制御装置の基礎的特性を調べるとともに、更なる中性子ラジオグラフィ技術の革新を目指して、②熱中性子ラジオグラフィ高速度撮像法を用いた気液二相流計測における技術的課題を明らかにし、また、③画像処理による流体計測の新しい可能性を追求するものである。以下にそれぞれの研究の概要を述べる。

(1) 超安全・超小型原子炉 RAPID-L の自己作動型反応度制御装置の特性

超安全・超小型原子炉 RAPID-L は、図１に示すようなウラン窒化物燃料リチウム冷却高速炉であり、電気出力２００ｋＷの月面及び火星基地用原子炉として開発されている。この原子炉では、無人の完全自動運転を実現するために、自己作動型反応度制御系（LEM 及び LIM）を有する。LEM(Lithium Expansion Module)は、図２に示すように、Li-6 を満たしたリザーバーと封入管よりなり、Li-6 の液面は封入管の途中にくるようにし、封入管の下部は不活性ガスが封入される。この Li-6 の液面は、水銀温度計のようにリザーバーの温度上昇により下降する。そのため、炉心出力の上昇に伴う冷却材出口温度の上昇によりリザーバー内の Li-6 が膨張して液面が炉心内に下降し、

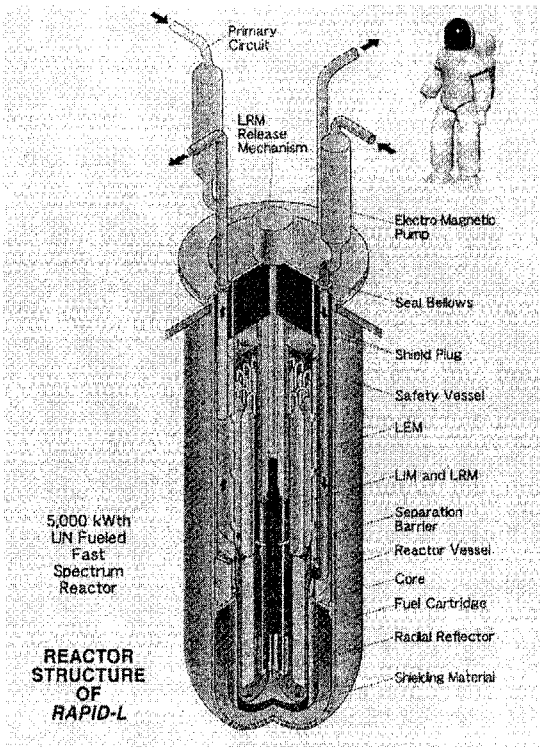


図１　RAPID-L 概念図

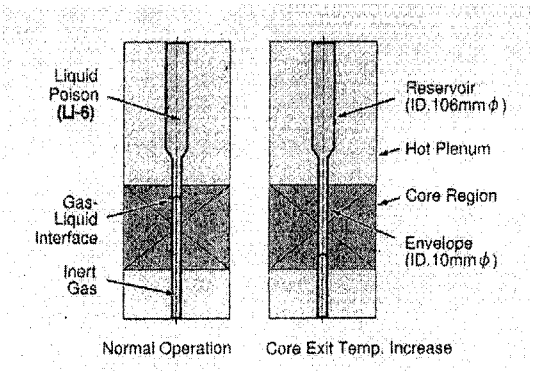


図２　LEM 概念図

JRR-3M　7R(TNRF2)、　中性子ラジオグラフィ装置、　熱流体工学

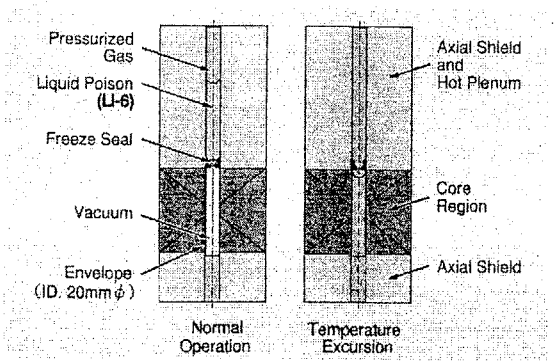


図３　LIM 概念図

中性子吸収材としての Li-6 が炉心に入ることにより負の反応度を印加する。LIM(Lithium Injection Module)は、図３に示すように、封入管はフリーズシールにより区切られ、上部には Li-6 とカバーガスが、下部（炉心）部は真空に保たれる。カバーガスは適当に加圧される。炉心温度が上昇しフリーズシールが溶融すれば、Li-6 が炉心部に注入され、負の反応度を急速に印加し、炉を停止する仕組みである。本研究では、本研究では、この LEM および LIM の作動特性を中性子ラジオグラフィにより可視化し確認することを目的とする。

(2) 高速度撮像法による気液二相流計測の検討

高速度撮像法の流体計測への応用における技術的課題に関しては、すでに平成１０年度までの共同利用研究により、ボイド率や気泡の速度などの物理量の計測に有効であることを示し、また、撮像速度と気液二相流のボイド率の計測誤差との関係などについて調べた。しかしながら、これらの物理量は時間平均量に限られており、瞬時の物理量の計測においては、高速で動く流体粒子の画像のブレのため新たな誤差が生じる可能性がある。中性子ラジオグラフィに関しては、画質の劣化、とくに画像のエッジのボケは、コンバータの平行度、物質内散乱、幾何学的不明確さ、運動の不明確さ、撮像系のノイズによると考えられ、これまで検討されているが、運動する流体粒子の速度の影響については明らかにされていない。そこで、本研究では、気泡を模擬した穴を明けた回転円盤を用いて、瞬時ボイド率計測に対する気泡速度の影響を調べることを目的とする。

(3) 画像処理による流体計測法の開発

本研究では、中性子ラジオグラフィにより得られた画像を処理することにより、溶融金属二相流の液相内の速度場を PIV 法を用いて計測することを目的とする。

溶融金属二相流は、液体金属冷却高速炉の炉心溶融事故時の溶融炉心内のスチールの沸騰現象を模擬したものである。この現象を解析するための SIMMER-III コードでは気泡挙動に関する構成式がいくつか使われているが、これらの構成式の検証用のデータを取得することが本来の目的である。

２．研究の方法および成果

２．１　超安全・超小型原子炉 RAPID-L の自己作動型反応度制御装置の特性

(1) LEM の作動特性

図４に実験装置の概略を、図５に Ta 製および SUS 製の２種類の LEM 試験体および実験条件を示す。先に述べたように LEM 試験体上部には Li(本実験の場合は、通常の Li を用いた)を封入し、下部は Ar＋He のカバーガスを封入した。この試験体を加熱することにより Li の液面は下降するので、この液面の動きを可視化し、液面の位置と温度との関係を求めることが本実験の目的である。この実験では、LEM 試験体内の Li の液面を精度良く測定する必要があり、また、液面は温度上昇によりゆっくりと動くため、撮像系に CCD カメラを用い、コンバータとしては ^{6}LiF/ZnS:Ag（化成オプトニクス NR コンバータ）を用いた。

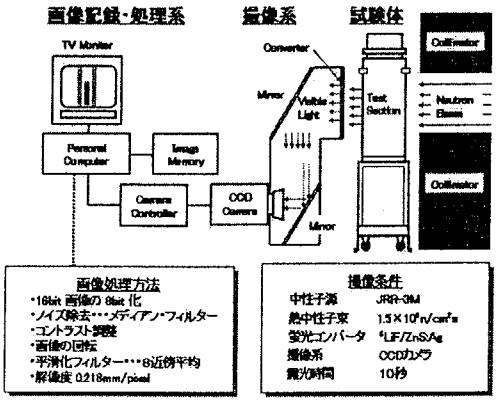


図４　LEM 可視化実験装置および撮像条件

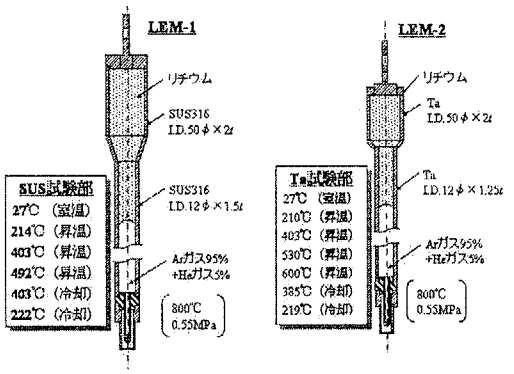


図５　LEM 試験体および実験条件

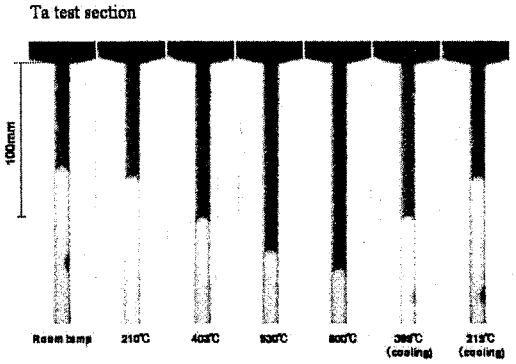


図６　Ta 試験体の画像

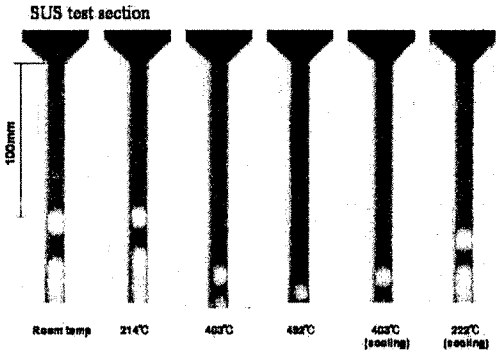


図７　SUS 試験体の画像

撮像条件などは図４に示してある。

実験では、試験体を可搬型加熱装置内に収納し、徐々に昇温しながら図５に示す温度において試験体の中性子透過像を記録した。

得られた画像を図６、７に示す。この画像は、原画像に 16 ビット画像（512 階調）の８ビット化（256 階調）→ノイズ除去（メディアン・フィルター）→コントラスト調整→画像の回転→平滑化

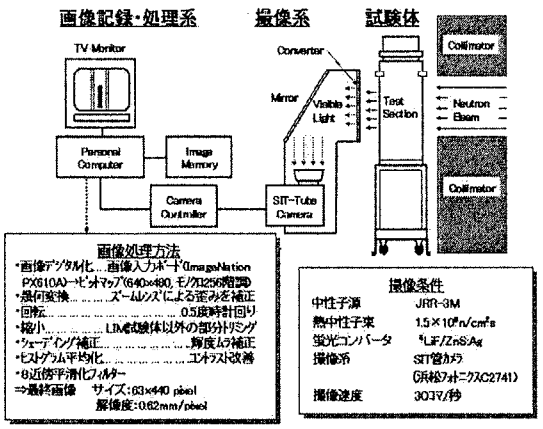


図８　LIM 可視化実験装置および撮像条件

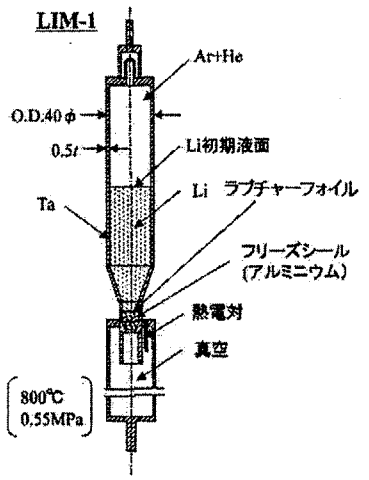


図９　LIM 試験体

フィルター（８近傍平均）→処理後の画像（解像度 0218mm/画素）の画像処理を施したものである。これらの画像より、いずれの LEM 試験体も所期の作動特性を満たしていることが確認された。

(3) LIM の作動特性

LIM の場合、フリーズシールの溶融に伴って液体 Li が急速に移動するため、可視化実験では動画の撮影が必要である。このため、図８に示すような実験装置を用いた。撮像系には SIT 管カメラを用い、コンバータとしては ^{6}LiF/ZnS:Ag （化成オプトニクス NR コンバータ）を用いた。LIM 試験体を図９に示す。この試験体のフリーズシールは材質がアルミニウムであり、６６０℃で作動する設計である。

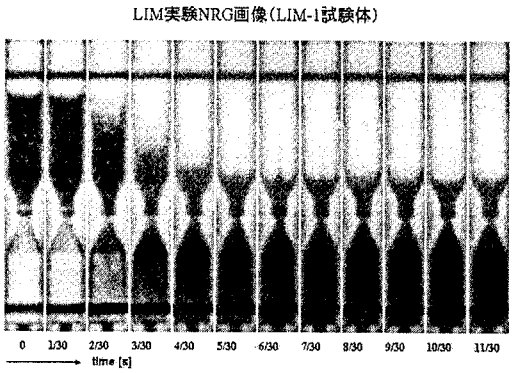


図１０　LIM 実験により得られた画像

実験では、試験体を可搬型加熱装置内に収納し、約６００℃まで昇温した後、一旦温度上昇をやめ、撮像系を作動させた後、再び温度上昇を開始し、フリーズシールが作動して Li が下部のシリンダー内に移動を終わるまで続けた。このようにして得られた画像を図１０に示す。この場合、１コマ１／３０秒の時間で進行する。従って、Li の移動は、約６コマ、すなわち約０．２秒で完了していることが示され、所期の作動特性を満たしていることが確認できた。

２．２　高速度撮像法による気液二相流計測の検討

この研究では、図１１に示すような、気泡を模擬した適当な大きさと深さの穴をいくつか明けたステンレス鋼製円盤を回転させて、この動きを可視化して画像を処理することにより、瞬時のボイド率を求め、これと円盤の回転から求められる瞬時のボイド率とを比較することにより、瞬時ボイド率の計測誤差の評価を行った。この実験では、円盤の回転速度は０から３５０ｒｐｍ（接線速度０から１．５ｍ／ｓに相当）とした。また、この計測誤差に及ぼすイメージ・インテンシファイアのゲート時間の効果も調べた。

撮像系としては、イメージ・インテンシファイアー（Photoron C6276-01MOD）付きの高速度ビデオ（Photoron FastCam-Ultima）を用い、コンバータには ^{6}LiF/ZnS:Ag（化成オプトニクス NR コンバータ）を用いた。

得られた画像の例を図１２に示す。この図で、

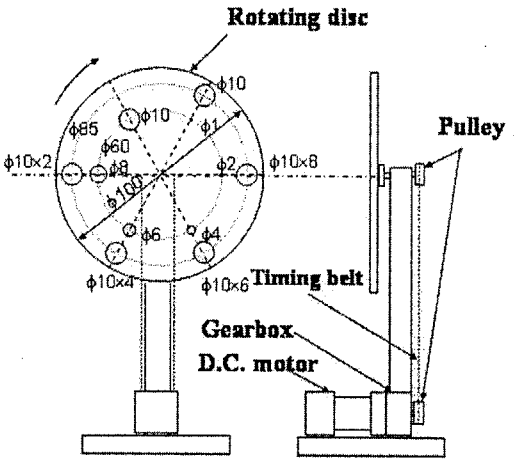


図１１　気泡の運動を模擬する回転円盤

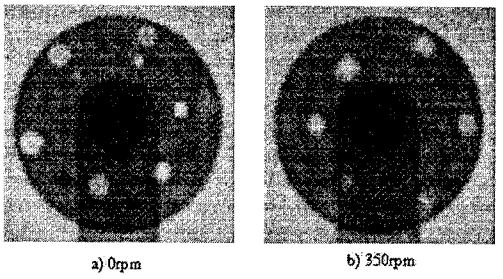


図１２　回転円盤の瞬時画像
（撮像速度 500fps、ゲート開放時間 1.8ms）

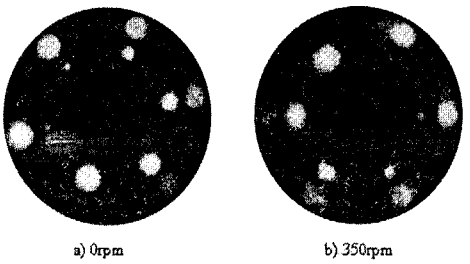


図１３　回転円盤の瞬時画像より求めた瞬時ボイド率

回転速度が３５０ｒｐｍの場合は、明らかに残像がみられる。従って、この画像をもとに得られた瞬時ボイド率分布は、図１３に示すように、静止した円盤のボイド率分布とは異なる。ここで、ボイド率は、Mishima らによるΣースケーリング法を用いて計算した。

次に、静止した円盤の画像を時間平均してボイド率分布もとめた結果を図１４に示す。この図か

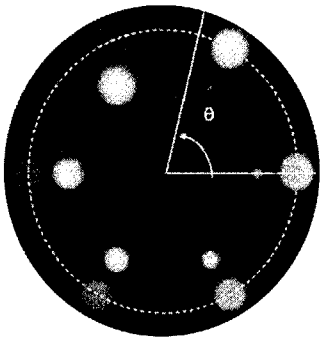


図１４　静止しした円盤の時間平均ボイド率

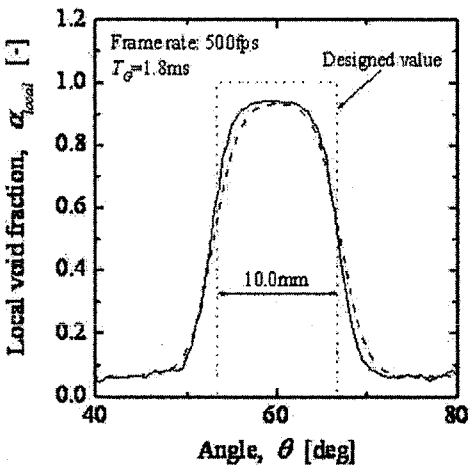


図１５　静止した穴の周りのボイド率分布

ら、特定の穴（直径 10mm）の位置のまわりのボイド率分布を求めた結果を図１５に示す。図中、理論線は点線で示している。これよりボイド率分布にはエッジの効果が現れていることが分かる。回転する円盤の時間平均ボイド率は、原画像をそのまま時間平均した場合は、図１４と比較できない。そこで、Lagrange 的に時間平均したボイド率分布を静止した円盤の時間平均ボイド率分布と比較した。Lagrange 的時間平均した回転円盤のボイド率分布を図１６に示す。これより、円盤の回転速度が上がるに連れて画像のブレの影響が時間平均ボイド率にも現れていることが分かる。同じデータから、特定の穴の周りのボイド率分布をグラフに表せば図１７のようになる。これより、時間平均ボイド率分布は、静止円盤にもみられたエッジの効果の他に、ブレによる分布のゆがみも

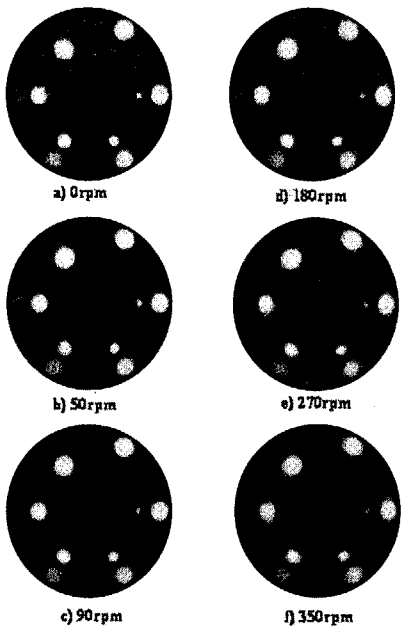


図１６　回転円盤の時間平均ボイド率

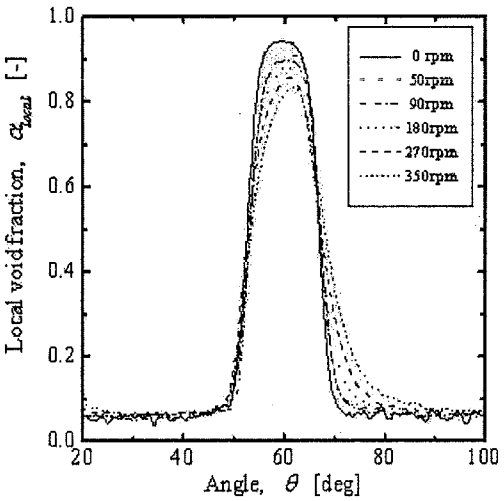


図１７　動く穴の周りの時間平均ボイド率分布

みられる。このような画像のブレの影響は、回転速度のみではなく、イメージ・インテンシファイアのゲート開放時間が長くなっても現れることが本研究により確認できた。

これらの結果を検討した結果、瞬時局所のボイド率の計測誤差は主にコンバータの光減衰特性に依存し、線速度が 1.5m/s のときのピークのボイド率の値に対して 20%程度の誤差を含む。従って、現在の撮像系では、瞬時局所のボイド率分布の計測誤差評価においてはコンバータの光減衰特性

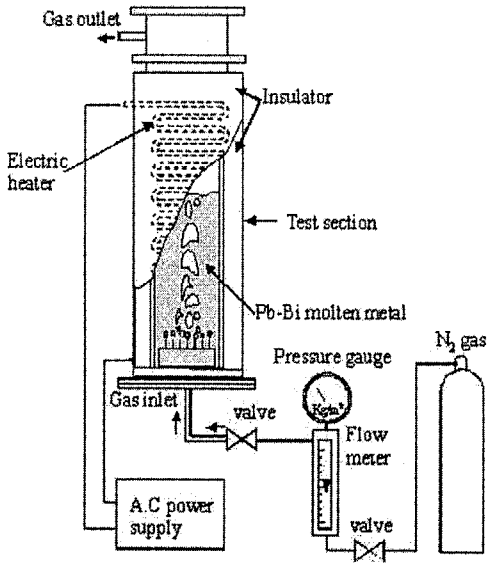


図１８　溶融金属―窒素ガス二相流試験部

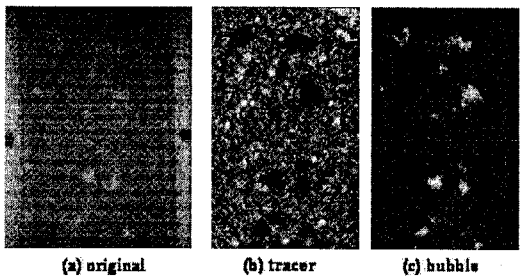


図１９　原画像、トレーサ粒子画像及び気泡画像

を考慮する必要があることが明らかになった。

２．３　画像処理による流体計測法の開発

本研究では、中性子ラジオグラフィにより得られた画像を処理することにより、溶融金属二相流の液相内の速度場をPIV法を用いて計測することを目的とする。用いた試験部の概略を図１８に示す。これを中性子ラジオグラフィ設備に設置し、試験部内の溶融金属内の気泡挙動を可視化した。溶融金属にはPb/Bi合金を、気相として窒素ガスを用い、試験部容器下部のノズルより注入した。溶融金属にはトレーサとして直径約1～1.5mmの$AuCd_3$粒子を混入させた。実験中Pb/Biの温度は150℃とした。

撮像系には、SIT管カメラ（Hamamatsu C2741：30fps）と高速度ビデオ（Photoron FastCam-ultima）

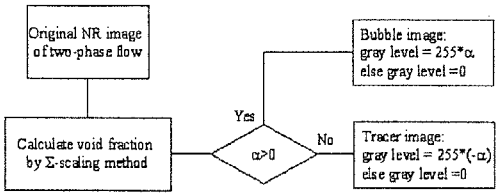


図２０　画像処理のロジック

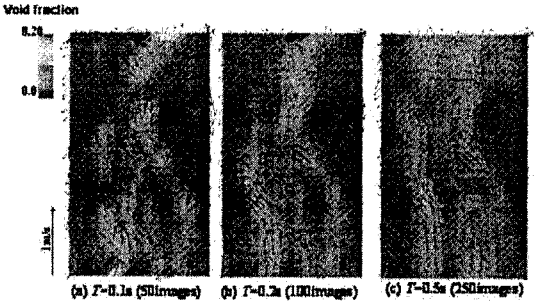


図２１　速度ベクトル計測に対する画像積分時間の影響

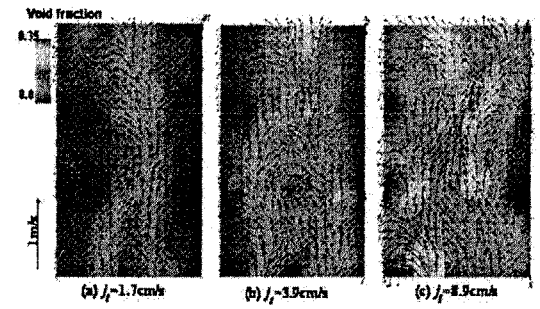


図２２　溶融金属二相流中のボイド率分布と速度ベクトル場

を用い、コンバータには^{6}LiF/ZnS:Ag（化成オプトニクス NR コンバータ）を用いた。

得られた画像の原画像、原画像を処理して得られたトレーサ粒子の画像及び気泡の画像を図１９に示す。これらの画像を求める際には、原画像から気泡とトレーサ粒子とを弁別する必要があるが、これには、図２０のようなロジックを用いた。すなわち、原画像からΣ―スケーリング法によりボイド率を求め、ボイド率が正の領域は気泡とし、その他の部分は液相としてトレーサ粒子像を得た。このトレーサ粒子の画像に濃度相関によるPIV法を用いて速度場を求めた。

図２１は、PIV法により得られた速度ベクトル場の結果に対する画像積分時間の影響を示す。こ

のように、画像積分時間が短い場合、速度ベクトルの変動が大きくて、流れのシステマティックな挙動が隠されてしまうことが分かる。また逆に積分時間が非常に長い場合、二次流れのような変動成分は平均化されてしまう。従って、流れの変動の時間スケールに応じて適切な画像積分時間を設定する必要がある。

以上の結果より、中性子ラジオグラフィにより得られた画像を処理し、PIV 法を用いることにより液相速度場の計測が可能であることが示された。

3．得られた結果の評価

本研究により、中性子ラジオグラフィの流体計測への新しい応用例が示されたほか、高速度撮影によるボイド率計測において、計測誤差に対する気泡の画像のブレの影響が明らかになり、また、コンバータの光減衰特性の重要性が明らかになった。さらに、流体計測への応用の可能性を広げる技術開発としては、PIV による液相速度ベクトル場の計測法が提案され、その有効性が示された。これらの成果は、いずれも、熱中性子による中性子ラジオグラフィ技術の高度化およびその流体計測への応用に対して有益は知見を提供するものと考えられる。今後は、さらに、中性子ラジオグラフィと画像処理法とを組み合わせた流体計測技術の高度化と、新しい要素として、パルス中性子の利用技術の開発のための基礎的な研究を行う予定である。

4．成果の公表

本研究により得られた成果の一部あるいは全部を、国際会議あるいは雑誌に公表したものは以下のとおりである。

(1) T. Hibiki, K. Mishima, Y. Saito, Y. Tobita, K. Konishi, and M. Matsubayashi, "Study on Flow Characteristics in Gas-Molten Metal Mixture Pool Simulating Core Disruptive Accident of FBR," Proceedings of the 5th Joint ASME/JSME Thermal Engineering Conference, San Diego, USA (1999).

(2) Y. Saito, T. Hibiki, K.Mishima, K. Moriyama, and J. Sugimoto, "Visualization Study on Hot Particle-Water Interaction by Using Neutron Radiography," Proceedings of 2nd International Symposium on Two-Phase Flow Modeling and Experimentation, May 23-25, 1999, Pisa, Italy.

(3) K. Mishima, T. Hibiki, Y. Saito, J. Sugimoto, and K. Moriyama, "Visualization Study of Molten Metal-Water Interaction by Using Neutron Radiography," Nucl. Eng. Des., **189** (1999) 391-403.

(4) K. Mishima, T. Hibiki, Y. Saito, H. Nishihara, Y. Tobita, K. Konishi, and M. Matsubayashi, "Visualization and Measurement of Gas-Liquid Metal Two-Phase Flow with Large Density Difference Using Thermal Neutrons as Microscopic Probes," Nucl. Instrum. Methods Phys. Res., **A424** (1999) 229-234.

(5) H. Nakamura, Y. Sibamoto, Y. Anoda, Y. Kukita, K. Mishima, and T. Hibiki, "Visualization of Molten-Metal/Water Interaction Using High-Frame-Rate Neutron Radiography," Nucl. Technol., **125** (1999) 213-224.

(6) T. Hibiki, Y. Saito, K. Mishima, Y. Tobita, K. Konishi, and M. Matsubayashi, "Study on Flow Characteristics in Gas-Molten Metal Mixture Pool," Nucl. Eng. Des., **196** (2000) 233-245.

(7) Y. Saito, T. Hibiki, K. Mishima, Y. Tobita, T. Suzuki, and M. Matsubayashi, "Visualization and Measurements of Liquid Phase Velocity and Void Fraction of Gas-Liquid Metal Two-Phase Flow by Using Neutron Radiography," Proceedings of 9th International Symposium on Flow Visualization (2000).

(8) Y. Saito, K. Mishima, Y. Tobita, K. Suzuki and M. Matsubayashi, "Velocity Field Measurement in Gas-Liquid Metal Two-Phase Flow with Use of PIV and Neutron Radiography Techniques," Proceedings of 9th International Conference on Nuclear Engineering ICONE-9, Nice, France (2001).

2-6

厚い水性試料の中性子ラジオグラフィー
Neutron radiography of thick hydrogenous materials with use of an imaging plate neutron detector.

加藤 一夫　藤田保健衛生大学衛生学部
Kazuo KATO, Fujita Health University School of Health Sciences
松本 元一　名古屋大学工学部
Gen' ichi MATSUMOTO, Faculty of Engineering Nagoya University,
新村 信夫、芳賀 裕子　日本原子力研究所 先端基礎研究センター
Nobuo NIIMURA, Yuuko HAGA, Advanced Science Research Center,
Japan Atomic Energy Research Institute
松林 政仁　日本原子力研究所 研究炉技術開発室
Masahito MATSUNAYASHI, Research Reactor Technology Develop Division,
Japan Atomic Energy Research Institute
池田 泰　　日本ファインセラミックセンター
Yasushi IKEDA, Japan Fine Ceramic Research Center Institute

1. はじめに

核磁気共鳴等の研究から生体内の水構造は病態に応じて変化することがわかってきた。生体においてその重要な構成成分である水が中性子に対するクロスセクションが非常に大きいため中性子ラジオグラフィーの応用が困難であった。
中性子ラジオグラフィーを用いて病変のイメージングができれば診断および治療に非常に有用である。また悪性腫瘍の治療に中性子照射が用いられるが中性子ラジオグラフィーを利用しての照射部位での線量の正確な測定は治療におおいに役立つであろう。散乱断面積の大きな水性試料の、中性子ラジオグラフィでは、散乱線の影響が無視できない。またバックグランドの低減には、中性子遮蔽材料の散乱の研究が必要である。種々な遮蔽材の後方散乱、厚い水性試料に関する中性子ラジオグラフィーの空間分解能の向上に関する研究を行った。

2. 実験

1)中性子入射側からイメージングプレート(ＩＰ)、試料の順に密接して配置し、ビーカーの中央から一方に試料を設置し、試料からの後方散乱を撮像した(図１)。試料として、面積は種々であるが、ＳｉＣ(５ｍｍｔ)、Si_3N_4(５ｍｍｔ)、Ｓｉ単結晶(１０ｍｍｔ)、ボロンゴム(１０ｍｍｔ)、濃縮B_4C(５ｍｍｔ)、リチウムタイル(１０ｍｍｔ)、アルミ(１ｍｍｔ)、すず(０．５ｍｍｔ Ｘ２)、鉛(０．５ｍｍｔ)、パラフィン(４．３ｍｍｔ)、水晶セル中の水道水(１、２、４，１０ｍｍｔ)を使用した(表１)。
ＩＰは、γ線用(γＩＰ)、およびＧｄをコンバーターとして５０％、発光物質を５０％含有する１４５μｍ厚の中性子用(ＩＰ－ＮＤ)を使用した。

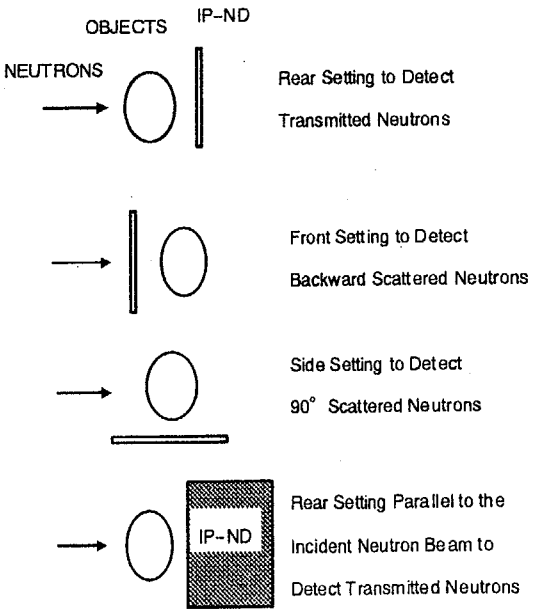


図１．試料とＩＰとの設置位置

研究施設・装置　JRR-3M, 中性子ラジオグラフィー装置　　研究分野　構造解析

中性子はＪＲＲ－３Ｍ熱中性子ラジオグラフィー装置Ｎｏ．２を使用し３秒照射した。

表１；試料のサイズ

	W(mm)	L(mm)	T(mm)
SiC	40	40	5
Si_3N_4	58	58	5
Si crystal	40	120,150	10
B rubber	104	100	10
B_4C	100	100	5
Li tile	100	100	10
Al	250	300	1
Sn	100	100	0.5X2
Pb	42	250	0.5
Paraffin	60,63	40	4.3
Water	10	40	1
Water	10	40	2
Water	10	40	4
Water	10	40	10

２）２００　ｍｌビーカー内の水 および５　ｃｍ厚パラフィンブロックの９０度散乱像を撮像した。試料を中性子照射野の外側縁に設置し、ＩＰ－ＮＤを試料の側方に約５　ｃｍ離して中性子照射野外に設置した。

３）試料とＩＰ－ＮＤとの間隔を大きくしたときに、距離による透過像の変化を研究するために、イメージングプレート感受性面を中性子ビームと平行方向（試料とは垂直方向）に設置して２００　ｍｌビーカー内の水および４　ｍｍ厚クオーツセル中の水の透過ラジオグラフィを撮影した。

４）試料とＩＰ－ＮＤとの間隔を１５　ｍｍとして透過ラジオグラフィを撮影した。

３．結果および考察

１）試料からの後方散乱部位の photostimulating luminescence(PSL)値の、試料から離れたところの中性子照射部位での PSL 値に対する比（測定散乱強度比）を表２に示した。測定散乱強度比は、パラフィンと水を除いて、γ線用ＩＰでの測定値の方が、中性子用ＩＰでの測定値より高かった。(中性子用ＩＰでの測定散乱強度比）／（γ線用ＩＰでの測定散乱強度比）は、特にＰｂ，０．８９、B_4C，０．７９、Ｓｎ，０．９８で顕著であり、中性子との反応による電離線の放射が顕著に認められた。パラフィン、１．１８、水、１．０２，１．０６（図２，図３、４ｍｍｔ)、１．０９，１．０７（１～１０ｍｍｔ）では、中性子用ＩＰでの測定値のほうが高く、中性子の散乱の寄与が高いという予測の通りであった。

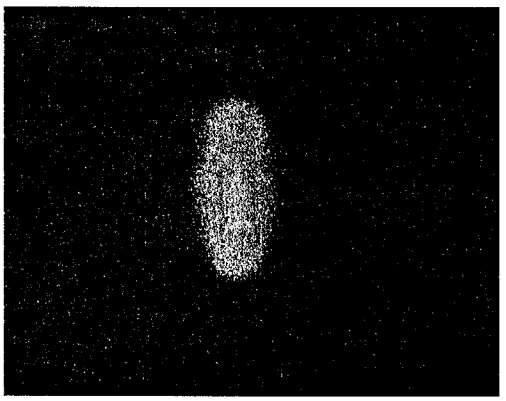


図２．4mm 厚クオーツセル中の水の後方散乱像(IP-ND)。

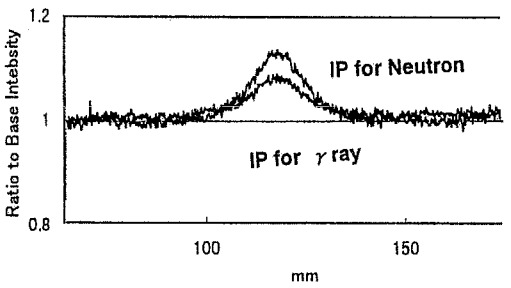


図３．4mm 厚クオーツセル中の水の後方散乱プロファイル。

ＪＲＲ３Ｍ中性子ラジオグラフィ装置でのｎｅｕｔｒｏｎｓ／γは、６．２５Ｘ10^6（ｎｅｕｔｒｏｎｓ／cm^2・ｍＲ）であるが、γ線用ＩＰでの測定散乱強度がどの程度中性子用ＩＰでの測定散乱強度に反映しているかは不明である。中性子用ＩＰでの測定散乱強度比のプロファイルとγ線用ＩＰでの測定散乱強度比のプロファイルが類似しているのは興味深い結果であった。

この結果より中性子用イメージングプレートを使用する際には中性子だけでなくガンマ線に対しても散乱および放射の少ない遮蔽が必要と考えられる。ガンマ線用の遮蔽材料では中性子照射によるその材料からのガンマ線の放射が高く単純には、中性子用イメージングプレート使用時のガンマ線の遮蔽には困難が伴う。ガンマ線および中性子の散乱および

表２．試料からの後方散乱部位のPSL値の、試料から離れたところの中性子照射部位でのPSL値に対する比（測定散乱強度比）

	中性子用IP	ガンマ線用IP	IP-ND/γ IP
水 １ mm	1.102	1.079	1.02
水 2mm	1.135	1.071	1.06
水 ４ mm	1.167	1.072	1.09
水 １０ mm	1.158	1.084	1.07
濃縮 B_4C ５ mm	1.141	1.450	0.79
ボロンラバー １０ mm	1.149	1.226	0.94
リチウムタイル	1.137	1.188	0.96
すず １ mm	1.249	1.280	0.98
鉛 ０．５ mm	1.419	1.599	0.89
Si_3N_4	1.186	1.158	1.02
SiC	1.154	1.170	0.99
Si crystal	1.178	1.194	0.99
Al	1.120	1.124	0.99
パラフィン４．３ mm厚	1.233	1.049	1.18

放射量の測定とともに遮蔽としてどのような物質を組合せ、または単独で使用すればよいかは今後の課題である。

２）９０度散乱；水道水を満たした200ml ビーカー内の水による散乱像は、ビーカーを中心にした散乱強度の高い部分があり、彗星の尾のように入射反対側へ低い散乱強度の部分がみられた(図４)。

パラフィンブロックでは、中性子入射側前縁から強度の高い散乱像が広く入射側に拡がっており、入射反対側へは入射側よりやや低い散乱強度の部分が狭い面積で認められた（図５)。

３）２００ml ビーカー中の水では試料直後の画像上での水の幅は６９mm、２００mm 離れた部での水の幅は６８mm で２００mm 離してもほとんど画像上では像の広がりの変化はみられなかった（図６)。４mm厚のクオーツ中の水でも画像上の幅は試料直後で１３mm、２００mm 離れた所で１２mm であった。

後方散乱に関しても IP を試料の中性子入射側に水平に設置して同様の実験を行ったが、IP の残像の影響で正確なデータを得るに至っていない。

４）４ mm厚の水と中性子用ＩＰの間隔を変えての透過ラジオグラフィでの試料透過部位の PSL 値の、試料から離れたところの中性子照射部位でのPSL 値に対する比（測定透過強度比）は、０ mm；

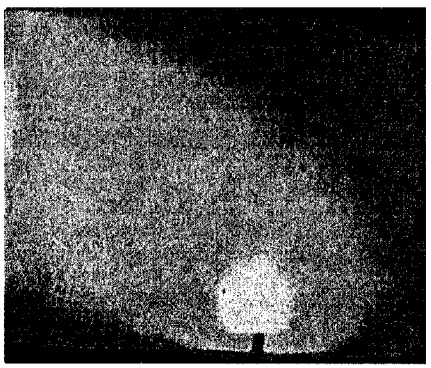


図４．２００ ｍｌビーカー内の水による９０度散乱像（ＩＰ－ＮＤ)。照射３秒。図の右側が中性子入射側。黒マークピンはビーカー中心位置。

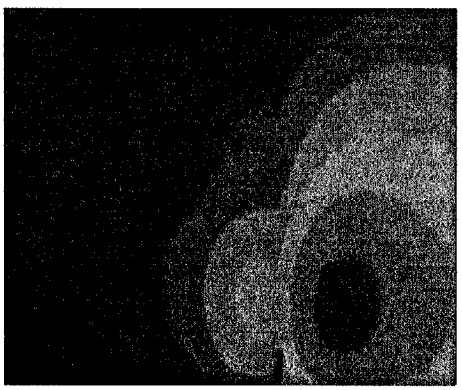


図５．５ ｃｍ厚パラフィンブロックの９０度散乱像（ＩＰ－ＮＤ)。照射３秒。図の右側が中性子入射側。黒マークピンはパラフィン前縁。

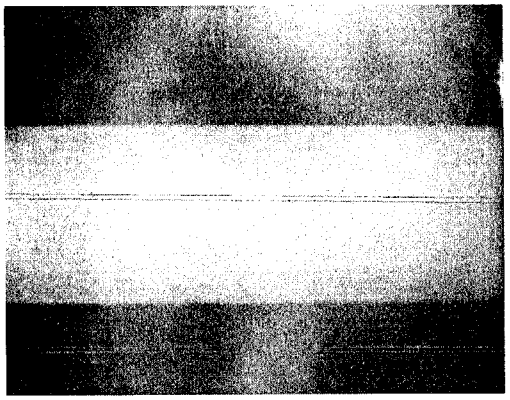


図６．２００ml ビーカー中の水の試料からの距離の変化による中性子透過像（ＩＰ－ＮＤ)。図の左側が中性子入射側。

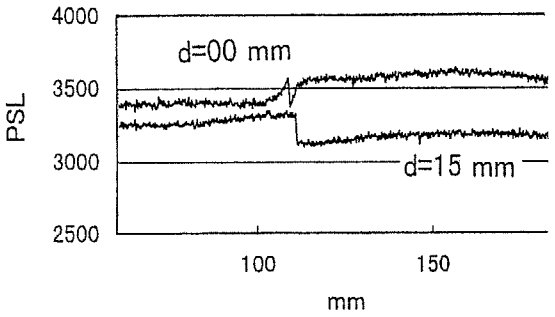


図７．試料からの間隔 0mm、と 15mm の Sn1mmt の中性子透過像の PSL プロファイル。図の右側部分が試料部分のプロファイル

０．５９，１０ ｍｍ；０．５１，２０ ｍｍ；０．５０．３０ ｍｍ；０．４７，４０ ｍｍ；０．４９であった。試料と中性子用ＩＰの間隔を１５ｍｍとした透過ラジオグラフィでは、試料とＩＰを密接して撮影したものより試料部分の強度が低下した（測定透過強度比、Ｐｂ，０ ｍｍ；１．０８、１５ｍｍ；０．９３、Ｓｎ，０ ｍｍ、１．０６、１５ ｍｍ、０．９８（図７)、パラフィン ０ ｍｍ；０．７９、１５ ｍｍ；０．５０)。

中性子用ＩＰでの透過ラジオグラフィにおいて、試料とＩＰの間隔を長くするとＬ／Ｄの関係で像が不明瞭となる。間隔を長くした方が散乱線やガンマ線の影響を低減できるが、１０～２０ ｍｍ程度で十分量低減されると考えられた。

Sn１ｍｍ厚の中性子ＩＰによる透過像では、試料と１５ｍｍ離して撮影した像の方が、Sn板の保持に使用したプラスチックテープの像が明瞭に認められた（図８）のに対して、IPを密接して撮影した像（図９）ではそれが認められなかった。

１２０ｇのラットの中性子 IP の透過像では、試料との間隔を０ｍｍ、１０ｍｍ、30mm と変えて撮影したが、画像上では変化が認められなかった。

４．まとめ

ＩＰ－ＮＤ使用により試料による中性子後方散乱像、および９０度散乱像が撮像できた。使用したＩＰ－ＮＤは中性子だけでなくγ線にも高い感度があるため、ＩＰ－ＮＤを使用してより鮮明な透過中性子ラ

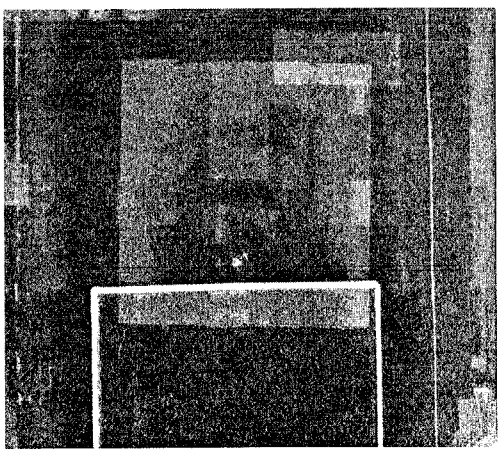


図８．試料からの間隔 15mm の Sn1mmt の中性子透過像（ＩＰ－ＮＤ)、白線はスペーサーの透過像

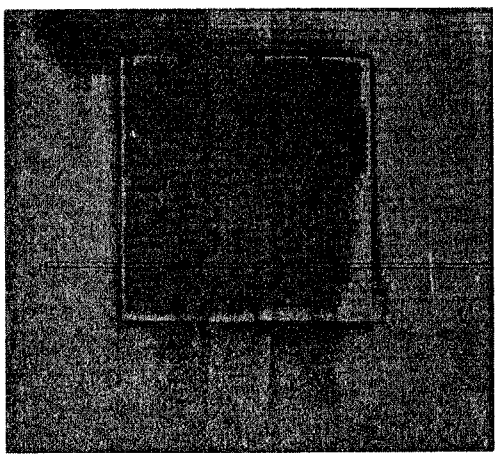


図９．試料からの間隔 0mm の Sn1mmt の中性子透過像（ＩＰ－ＮＤ）

ジオグラフィー像を得るためには、試料からのγ線を含めた中性子の散乱の状況を知ることが役に立つであろう。

参考文献

[1] Matsumoto, G., Kato, K., et al. in Neutron Radiography(4) p333-337, (1992)
[2] Ikeda, Y., Yamamoto, K. and Matsumoto, G. Nondestr. Test. Eval., 11, 129-138 (1994)
[3] Zanarini, M., Chirco, P., Rossi, M., et al., IEE Transaction on Nuclear Science, 42, 580-584 (1995)
[4] Matsumoto, G. & Kato, K. Med. Imag. Tech. 13, p885-891 (1995)
[5] Matsumoto, G. & Kato, K. Fifth World Conference on Neutron Radiography ed., J. P. Barton, Gordon and Breach Science Publ. (Langhorne, U. S. A.) p702-708(1997)
[6] Kato, K., Matsumoto, G. et al. Nucl. Instr. Methods in Phys. Res. Section A. 377, p123-125 (1996)
[7] Kato, K., Matsumoto, G. et al. Fifth World Conference on Neutron Radiography. ed C. O. Fischer, J. Stade, W, Bock, Deutsche Gesellschaft fuer Zerstroerungsfreie Pruefung e.V. Berlin, Germany, p758-764 (1997)

成果の公表

学会発表

(1) Kato, K., Matsumoto, G., Haga, Y., Niimura, N., and Matsubayashi, M. Neutron radiography of back scattering using an imaging plate neutron detector. 6th World Conf. Neutron Radiography, Osaka, Japan, 1999. 17-21, May.
(2) 加藤一夫、松本元一、新村信夫、松林政仁。ＩＰを用いた中性子ラジオグラフィでの散乱線測定。第２回パルス中性子ラジオグラフィ研究会、２００１年、筑波、３月
(3) 加藤一夫、松本元一、新村信夫、松林政仁。イメージングプレートを用いた中性子ラジオグラフィの散乱線およびガンマ線の影響。中性子ラジオグラフィ高度技術の開発と応用専門研究会、２００１年、熊取、１０月

学会誌等

(1) K. Kato, G. Matsumoto. Y. Haga, N. Niimura and M. Matsubayashi. Experience of backward scattered neutron measurements using a neutron sensitive imaging plate. Nondestr. Test. Eval., 16, 413-422, 2001, April.

2-7 JRR-3M TNRF・CNRFにおけるIP・NR技術の開発と応用研究
Development of Advanced Neutron Radiography Using Imaging Plates at JRR-3M TNRF and CNRF

名古屋大学 工学研究科 玉置昌義、増永優作、田口晋平、飯田一寛、岡田 誠

Nagoya Univ., Engineering Masayoshi Tamaki, Yuusaku Masunaga, Sinnpei Taguchi, Kazuhiro Iida, Makoto Okada

はじめに

本研究では、イメージングプレートの開発、散乱中性子及びガンマ線の影響を除去することで中性子ラジオグラフィ技術による定量解析精度を高めること、定量解析する上での冷中性子ラジオグラフィ固有の問題を解決することを目的とし、さらに、イメージングプレートに取り入れた新しい概念を冷却型 CCD 撮像系に用いてシステムの定量性向上に関する手法の開発を目指した.

具体的には、ＪＲＲ－３Ｍ　ＴＮＲＦ・ＣＮＲＦの中性子ビームを利用するラジオグラフィの高度化技術の開発を目指して、イメージングプレート技術のＮＲ技術への展開、ＣＣＤ冷却型固体撮像素子の利用による広ダイナミックデジタルラジオグラフィの開発などの基礎実験を実施した。以下に概要をまとめる。

（1） イメージングプレート関係

（1－1）中性子ラジオグラフィ用イメージングプレートの開発と特性評価

まずカドミウムのステップウェッジを撮像し、中性子透過率を求めて比較した。さらに、中性子透過率を指数関数的減衰からずれる原因がコンバータの性質、特にコンバータの放出する二次放射線にあると考え、これを確認するための実験および解析を行った。

実験：中性子ラジオグラフィ実験は、日本原子力研究所 JRR－3M の TNFR において、熱中性子を用いて行った。撮像試料としては中性子の散乱による影響が現れないように、厚さが約 0.1mm で変化する Cd 製のステップウェッジ及び厚さ約 0.9 mm の Cd 製シャープエッジを用いた。照射時間は Gd 直接法では 1sec、Dy 直接法では 5sec、Dy 間接法では 3sec とした。

この実験では、被写体と検出媒体を密着させ撮影することで入射中性子ビームの非平行による影響を考えないこととした。またこの検出系を Li タイルで囲み、照射孔内での中性子の散乱による影響を最小限にした。

まず上記の IP 撮影法により、Cd のステップ像を撮像し中性子の透過率を求め、諸手法における直線性の比較を行った。次に Cd のシャープエッジ像を撮像し、フィッティング関数を用いて解析した。IP の読み取りはＢＡＳ2000 を用い、画素サイズを 100μm ×100μm とした。

結果：fig. 1 に、前述した３手法によって Cd のステップウェッジの NR 像から計算した中性子透過率を示す。Gd をコンバータとして用いた場合に比べ、Dy

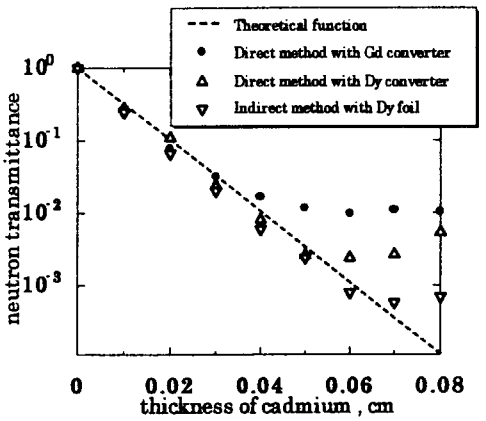


fig.1 Neutron transmission curves of Cadmium obtained with various NR methods

を用いた場合の方が直線性に優れ、透過率が 10^{-3} 程度までは指数関数的減衰に従うことが分かった。

考察及び今後の課題：IP を用いた中性子ラジオグラフィの手法では、コンバータとして Dy を利用した手法は Gd を利用したものより定量性に優れていることが確認された。しかし、放射化によってＤｙから放出されるβ線、γ線のエネルギーは大きく、空間分解能を劣化させ、定量性を損なう原因となっている。そこで、中性子の透過率が 10^{-3} 以下のように低いときには、画像の広がりのため、測定結果に誤差を生じてしまうので、定量的な解析を行うためには、コンバータの性質を考慮して、適切な補正を行う必要がある。

（1－2）新 Dy 入りイメージングプレートの開発

中性子コンバータとしてジスプロシウム(Dy)を用いた手法は、照射場においてγ線の影響を受けないため、中性子用 IP(BAS-ND)に比べて定量解析に向いており IP のダイナミックレンジ(5 桁)を考慮すれば、より低い透過率までの定量解析が期待できる。

さらに中性子ラジオグラフィにより定量解析を行うためには、中性子の散乱成分を除去することが重要であることは、従来の研究で明らかにされている。IP は薄い PSL 体保護膜、(中性子コンバータ＋PSL 体)、PET 製支持体、の順に 3 層の構造をしており、保護膜の方向から中性子を入射させる。PSL 体中のコンバータに捕獲されなかった中性子は、支持体層を通り抜けるか、またはここで散乱される。この散乱成分が再び PSL 体に入射し、コンバータに捕獲されるという現象が生ずる。また、コンバータ後方からの中性子がコンバータに入射することがある。これらの IP 支持体側からの後方散乱中性子の影響を除くため、(コンバータ＋PSL 体) と支持体との間に強中性子吸収体層を挿入した IP (図２) を新たに考案・試作し従来の手法と実験的に比較した。

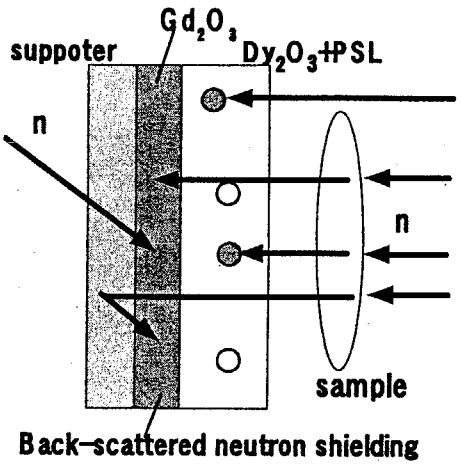


図1　新IP構造モデル

実験及びデータ処理：中性子ラジオグラフィ実験は日本原子力研究所 JRR-3M にある CNRF , TNRF2 ビーム孔を用いて行った。従来の IP と比較・評価するために従来の３つの IP－NR 法及び中性子遮蔽体層 (Gd_2O_3) の上に Dy_2O_3＋PSL 体を均一に塗布した新しい IP の４手法を用いて行った。Dy_2O_3 をコンバータとして練りこんだ IP では照射直後 IP 画像をいったん消去して 2 時間 30 分間自己露光させた。それぞれの手法において被写体として評価用ステップウェッジ状の Dy, Cd を用いた。IP リーダー (BAS-1800, BAS-2000) で読み取ったデジタル画像データから NR 画像の特性、中性子透過率などを評価した。

結果及び考察： 図３に例として新 IP で求めた冷中性子透過率の Dy 厚さ依存性を示す。

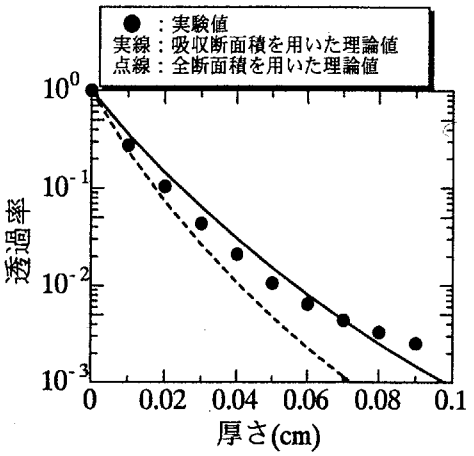


図２ Dyｽﾃｯﾌﾟｳｪｯｼﾞの実験値と理論値 (冷中性子)

被写体である Dy の断面積は全断面積に占める散乱断面積の値が一割程度と無視できないために全断面積による透過率の理論値と吸収断面積のみによる透過率の理論値を求めて示した。実際の被写体内で散乱された中性子のうちのいくらかしか IP に吸収されないことを考えれば、実験値はそのことをよく表わしている。シミュレーション等を用いて正確に評価することが今後の課題である。また表１にそれぞれの手法におけるシャープウェッジの空間分解能を示す。Dy をコンバータとして用いると分解能が悪くなっているが、これはβ線のエネルギーが高いためである。他方、Dy を用いた新 IP はγ線の影響を消去できるので図２で示したごとく中性子透過率を定量的に評価できる利点を持つことが確認できた。

表１　それぞれの IP における空間分解能

		IP－NR 手法		
		BAS	転写法	新 IP
半値幅 (μm)	cold	135	350	215
	thermal	170	350	350

(１－３) 成果の公表

1) M. Tamaki (Invited Talk)
"Imagoing plates, Converters and Neutron energies for developing quantitative neutron

radiography,"
Presented at 6th World Conference on Neutron Radiography, (Osaka, 1999.5.17-21).
2) Y.Masunaga, M.Tamaki, O.Nishiguchi, K.Yoneda, Y.Kukita,
"Characterization of imaging plates for quantitative neutron radiography,"
Presented at 6th World Conference on Neutron Radiography, (Osaka, 1999.5.17-21).
3) O.Nishiguchi, M.Tamaki, M.Oda, M.Matsubayashi, Y.Kukita,
"Application of imaging plates for quantitative thermal and cold neutron radiography,"
Presented at 6th World Conference on Neutron Radiography, (Osaka, 1999.5.17-21).
4) M.Tamaki, Y.Masunaga, K.Tuchida, S.Taguchi, K.Yoshii, S.Fujine, H.Kobayashi,
"Applications of imaging plate for fast and epi-thermal neutron radiography,"
Presented at 6th World Conference on Neutron Radiography, (Osaka, 1999.5.17-21).
5) M.Tamaki, O.Nishiguchi, Y.Masunaga, S.Tazaki, S.Iwai, Y.Kukita,
"Diminishing procedure of gamma-ray fogging using new type imaging plate for advanced quantirative neutron radiography,"
Presented at 6th World Conference on Neutron Radiography, (Osaka, 1999.5.17-21).
6) 玉置昌義、岩井定彦、錬石恵子、田崎誠二、
"中性子画像変換方法"、
特願平９－１９０５３０.

（2） 冷却型 CCD 撮像系関係

（２－１）C-CCD 式ラジオグラフィ用コンバータの開発

冷却型 CCD(C-CCD)撮像装置はダイナミックレンジ、直線性、及び無歪位置検出に優れている。この C-CCD カメラを用いる中性子ラジオグラフィの定量性向上を目指した。CCD カメラによる中性子ラジオグラフィの定量性を妨げる成分として、散乱中性子成分、γ線成分と CCD 素子の長時間撮影による暗電流があげられる。本研究ではそれらの成分除去する方法を個々に行った。またその他の定量性を妨げる成分としてコンバータから CCD カメラまでの間に入ってくるまわりこみ成分の評価を行った。そしてこれらの手法を組み合わせた統合実験を行い総合的にシステム評価を行った。

実験及び解析： 実験は日本原子力研究所 JRR-3M 熱中性子ラジオグラフィ装置で行った。

1) 乱中性子成分除去実験ではハニカムコリメータを用いて散乱中性子成分を除去した。X-Y 駆動装置を用いて、ハニカムコリメータを 16 通り移動させて、ハニカムコリメータの位置をずらした画像を 16 枚撮影した。得られた 16 通りの画像を重ねあわせることによって、ハニカムコリメータの影を消去した。

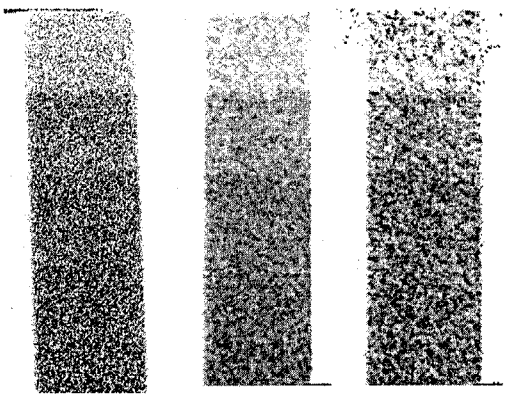
2) γ線成分除去実験では、Gd_2O_3-ZnS(Ag)を原料とした中性子コンバータと ZnS(Ag)を原料としたγ線コンバータを製作した。2 種類のコンバータで得られた画像データをγ線に対する感度比をかけて引き算することにより、γ線成分を除去した。

3) まわりこみ成分除去実験では、コンバータから出てくる光を遮蔽するカバーを製作した。カバー有りとカバー無しのデータの引き算をすることにより、まわりこみ成分を除去した。この方法は、暗電流も同時に消去できる。

4) 1)、2)、3)の実験を組み合わせて統合実験をおこない評価した。

結果および考察：

1) 統合実験で得られた Fe ステップの画像を図に示す。

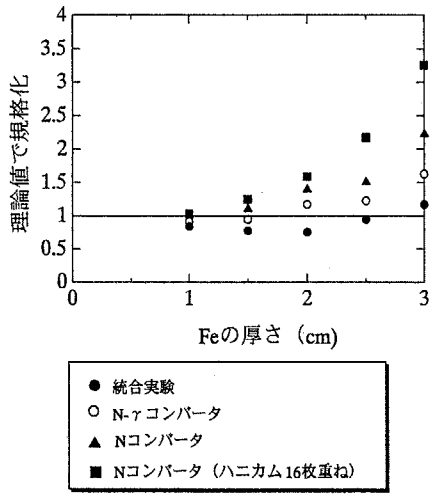


中性子コンバータ　ハニカム１６枚重ね　統合実験

解析処理による画像比較

2) 画像から評価した Fe ステップの透過率を理論値で規格化して次図に示す。最も統合実験の透過率曲線が理論値に近づいた。γ線コンバータを用いた結果が理論値より下がり気味になるのは、γ感度比が高く評価されてたことによると考えられる

3) 今回予定していた全ての手法を取り入れた統合実験で、これらの手法の有効性を示し、本研究の目的はほぼ達成できた。



透過率の手法間比較

（２－２）Dy入り中性コンバータの開発

中性子ラジオグラフィの原理とは、中性子源からコリメータで引き出された平行の中性子ビームを被写体にあて、透過してきた中性子をコンバータと撮像機とを組み合わせて中性子画像を得るという仕組みである。この中性子ラジオグラフィにおける、定量的解析を向上させる方法は幾つか存在するが、本実験ではコンバータに着目した。γ線の影響を受けない間接法を採用し、半減期と放射化断面積の観点から Dy_2O_3+ZnS(Ag)コンバータを用いた。この Dy には、三つの同位体が存在しそれぞれの異なる特性をもっている。^{165}Dy と ^{165m}Dy の崩壊特性について表にまとめた。また ^{165}Dy と ^{165m}Dy は、^{164}Dy の(n，γ)

165Dy と 165mDy の崩壊特性

	半減期	崩壊形式	Ar(a,b)	反応断面積(barn)	γ線とβ線のenergy(MeV)
^{165}Dy	1.26m	β- 100%	^{164}Dy(n,γ)	1700(250)	0.29(β1.7%)
					1.19(β15%)
					1.29(β83%)
					0.094(γ)
^{165m}Dy	2.33hr	IT 97.76%	^{164}Dy(n,γ)	1000(150)	0.88(β1.9%)
		β- 2.24%			1.03(β0.16%)
					0.094(γ)

反応によって、生成されるという特性を利用し、中性子ラジオグラフィの新システムの構築をめざした。

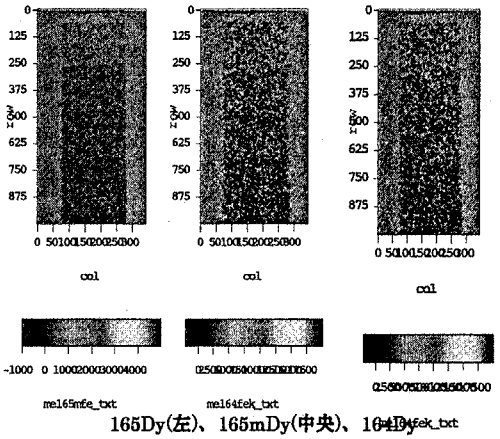
実験及び解析： 実験は日本原子力研究所 JRR-3M 熱中性子ラジオグラフィ装置(TNRF-2)で行った。

原子炉から中性子線を照射開始から CCD カメラを用いて、二分間撮影し、一分おき、再度二分間撮影した。この方法でまず五枚撮影した。照射開始 105 分後から、再度二分ずつ五枚撮影した。計十枚の撮影が終わってから照射を終わらせた。照射終了直後から五分間撮影し、一分間空け、再度五分間撮影という方法で二十枚の画像を撮影した。

また、コンバータからの蛍光を遮蔽する事により、コンバータ以外から入ってくる放射線と光のみを撮影し、CCD カメラの暗電流成分の除去とノイズ成分の除去をした。

得られた画像から、中央値フィルタ法を用いて、画像処理を行い ^{165}Dy と ^{165m}Dy、^{164}Dy それぞれの画像を分離した。

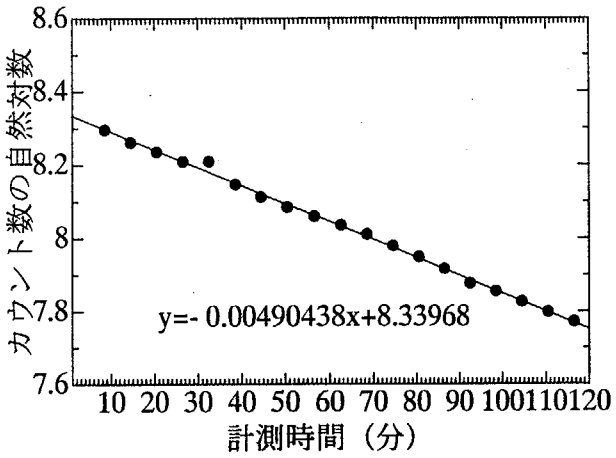
結果：^{165}Dy と ^{165m}Dy、^{164}Dy それぞれの画像を図に示した。



165Dy(左)、165mDy(中央)、164Dy の画像

また ^{165}Dy のみの画像から崩壊関数を導き出し、その図の示す曲線半減期を求めた。

導き出された半減期が、2.30 時間となり、文献値の 2.33 時間と合致したと言える。これらの実験結果から Dy 入り中性子コンバータの新システムが構築できたと言える。



165Dy の崩壊特性

（2－3）成果の公表

1）田口晋平、他　：日本原子力学会「2000 年秋の大会」（青森学会）
「冷却型 CCD カメラを用いた中性子ラジオグラフィの開発」
2）田口晋平、他　：日本中性子科学会「第一回年会」（仙台学会）
「冷却型 CCD カメラを用いた定量的中性子ラジオグラフィ手法の開発」
3）Shinpei Taguchi et al. :7th World Conference on Neutron Radiography（イタリヤ，2002.9.発表予定）[Development of Quantitative Techniques of Digital Neutron Radiography using Cooled CCD-camera].

（3）今後の計画

以上のようにこの３年間で得られた成果を生かして、次年度以降に計画しているパルス中性子ラジオグラフィ技術の開発に生かしていく．

2-8 多色発光蛍光体を用いた中性子・γ線ラジオグラフィの研究

Neutron - γ -ray Radiography Using Multi-color Scintillator

持木幸一、村田裕、桑子雅史、木本亨尚、佐藤貴樹、中川哲郎、池野豊、増子大輔

K. Mochiki, Y. Murata, M. Kuwako, Y. Kimoto, T. Sato, T. Nakagawa, Y. Ikeno and D. Masuko

武蔵工業大学 Musashi Institute of Technology

1. はじめに

中性子ラジオグラフィとγ線ラジオグラフィは互いに相補的な情報を得ることができる。原子炉からはこれらの放射線が同時に放出されているので、同時に透過像を得ることが期待できる。一方、（株）東芝の日塔等が、Gd系の赤色蛍光コンバータを開発し、従来のGd系緑色蛍光コンバータと組み合わせて，中性子とX線（γ線）の透過像を、カラーフィルムを用いて取得し、その有効性を実証した[1]。カラーフィルムでは実時間性にかけるため、我々は、従来から行なってきた電子撮像法による同時取得を試みた。大別して静止画と動画の撮像のためのシステムを開発した。静止画は、さらに冷却型モノクロ CCD と光学カラーフィルタを用いる方法と、冷却型カラーCCD を使用する方法を開発した。動画では、高速に切換可能な液晶カラーフィルタと高感度TV用CCDを使用する方法と、3板式高感度カラーCCDを使用する方法を開発した。以下、順を追って報告する。

2. 2色発光コンバータ

2.1 2色発光コンバータ

Fig.1 に 2 色発光コンバータ[1]の概略図を示す。このコンバータは、Gd_2O_2S(Tb)と Gd_2O_2S(Eu)の2層構造になっており、第 1 層では熱中性子に対する捕獲断面積が大きいGdで熱中性子が吸収され同時に電子が放出される。この電子によりEuが励起され、赤色に発光する。γ線の吸収でもEuが励起され、赤色に発光する。同様なことが第 2 層でも起こる。しかし、第2層は蛍光体がTbであるため緑色に発光する。 Fig.2 に発光スペクトルを示す。

ここで、第1層の厚みをほとんどの熱中性子を吸収する厚みに設計し、したがって第2層ではγ線の発光成分が多くなるようにする。こうすることで、γ線は各層で検出されるのに対し、熱中性子は第1層で多く検出される。したがって、熱中性子成分の抽出では赤色画像中のγ線成分を緑色画像によって除去し、γ線成分の抽出では緑色画像中の熱中性子成分を赤色画像によって除去すれば良い。

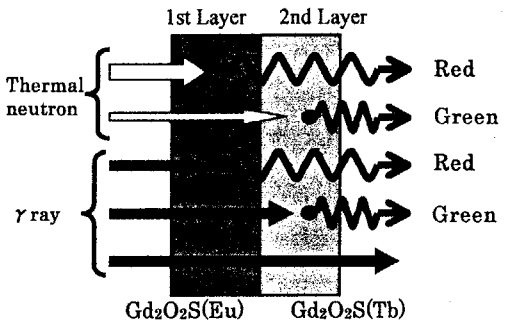


Fig1. Schematic view of 2-color fluorescence Converter

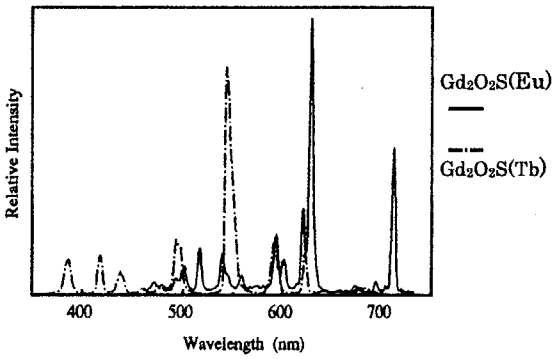


Fig.2 Spectra of red and green scintillator

2.2 中性子画像、γ線画像の抽出法[2],[3]

熱中性子成分とγ線成分を抽出する原理は、静止画と動画について区別なく適用されている。すなわち、赤と緑の画像は、光学フィルタを使用して分離して撮像されたり、カラーCCDでは、取得画像の色信号を分離して求めている。こうして得られた赤画像と緑画像から熱中性子線画像とγ線画像を抽出するための計算法を次に示す。

2色発光コンバータの第1層からの出力には、熱中性子成分とγ成分がある。赤画像[Robj(i,j)]は、CCD の暗電流画像 [D(i,j)]を用いて式(1)の様になる。

ＪＲＲ－３Ｍ ７Ｒ 中性子ラジオグラフィ装置、非破壊検査、イメージング

$$Robj(i,j) = In(i,j)\cdot An(i,j)\cdot Bn_1(i,j)\cdot Z_R(i,j) + I\gamma(i,j)\cdot A\gamma(i,j)\cdot B\gamma_1(i,j)\cdot Z_R(i,j) + D(i,j) \cdots\cdots (1)$$

ここで、
In(i,j) ：熱中性子強度
Iγ(i,j)：γ線強度
An(i,j) ：熱中性子に対する被検体透過率
Aγ(i,j)：γ線に対する被検体透過率
$Bn_1(i,j)$：熱中性子が第1層で吸収される割合
$B\gamma_1(i,j)$：γ線が第1層で吸収される割合
$Z_R(i,j)$ ：赤に対する光学フィルタの透過率とCCDの効率を考慮した係数
である。また、被検体を設置していない赤画像（赤のシェーディング画像）[Rshd(i,j)]は式(2)のように示される。

$$Rshd(i,j) = In(i,j)\cdot Bn_1(i,j)\cdot Z_R(i,j) + I\gamma(i,j)\cdot B\gamma_1(i,j)\cdot Z_R(i,j) + D(i,j) \cdots\cdots (2)$$

第2層からの出力でも第1層と同じようなことが起こり，緑フィルタを設置した時のCCDからの出力（緑画像）[Gobj(i,j)]、及び被検体を設置していない緑画像（緑のシェーディング画像）[Gshd(i,j)]はそれぞれ式(3)と(4)で示される。

$$Gobj(i,j) = In(i,j)\cdot An(i,j)\cdot Bn_2(i,j)\cdot Z_G(i,j) + I\gamma(i,j)\cdot A\gamma(i,j)\cdot B\gamma_2(i,j)\cdot Z_G(i,j) + D(i,j) \cdots (3)$$

$$Gshd(i,j) = In(i,j)\cdot Bn_2(i,j)\cdot Z_G(i,j) + I\gamma(i,j)\cdot B\gamma_2(i,j)\cdot Z_G(i,j) + D(i,j) \cdots\cdots (4)$$

ここで、
$Bn_2(i,j)$：熱中性子が第2層で吸収される割合
$B\gamma_2(i,j)$：γ線が第2層で吸収される割合
$Z_G(i,j)$ ：緑に対する光学フィルタの透過率とCCDの効率を考慮した係数
である。これら5種類の画像データを用いて次の計算を行い中性子画像 N(i,j)とγ線画像γ(i,j)を求めることができる。

$$N(i,j)=\frac{\{Robj(i,j)-D(i,j)\}-k1\{Gobj(i,j)-D(i,j)\}}{\{Rshd(i,j)-D(i,j)\}-k1\{Gshd(i,j)-D(i,j)\}} = An(i,j) \quad (5)$$

$$\gamma(i,j)=\frac{\{Gobj(i,j)-D(i,j)\}-k2\{Robj(i,j)-D(i,j)\}}{\{Gshd(i,j)-D(i,j)\}-k2\{Rshd(i,j)-D(i,j)\}} = A\gamma(i,j) \quad (6)$$

ここで、k1とk2は係数であり、

$$k1 = \{B\gamma_1(i,j)\cdot Z_R(i,j)\} / \{B\gamma_2(i,j)\cdot Z_G(i,j)\}$$
$$k2 = \{Bn_2(i,j)\cdot Z_G(i,j)\} / \{Bn_1(i,j)\cdot Z_R(i,j)\}$$

であるが、実際の処理では目視により各値を決定している。これについては、3.1.2節にて詳しく述べる。以下の記述では、(5)、(6)をそれぞれ、つぎの(7)、(8)で表記する。

$$n = Red - k1\cdot Green \cdots\cdots (7)$$
$$\gamma = Green - k2\cdot Red \cdots\cdots (8)$$

ここで、
n ：中性子線画像
γ ：γ線画像
Red ：赤画像
Green ：緑画像
である。

3. 静止画撮像システム

ＣＣＤにモノクロとカラーの冷却型2種類を使用した。それぞれ、フルフレーム型で解像度と感度が高いこと、一度の測定で2色の画像が取得できることの長所がある。カラーカメラは自作した。

3.1 モノクロＣＣＤ撮像[6, 8, 11]

3.1.1 撮像システム

Fig.3に撮像システムの概略図を示す。Table 1に実験を行なったJRR-3MのTNTF2のフィールド特性を示す。赤と緑の画像は回転交換式光学フィルタと冷却型モノクロCCDカメラによって撮像される。まず、アクリル板（厚さ5, 10, 15mm）でn－γ線量比を変化させて、熱中性子とγ線の発光成分の強度比の依存性を調べた。

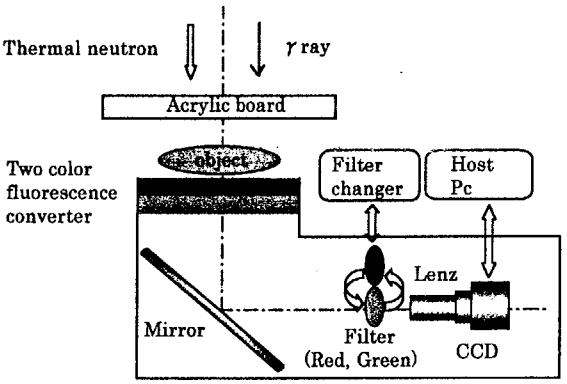


Fig.3 Schematic view of the imaging system

Table 1 Characteristic of the TNRF2

Thermal neutron	n/γ	Cd比	L/D	Radiation field [mm]
1.5×10^8 [n/cm2/s]	62.5 [$n\cdot cm^{-2}\cdot \mu Sv^{-1}$]	130	H:176 V:153	255×305

CCDからのデータは14Bitのデジタルデータとして取得され、オフラインでパソコンで処理された。

3.1.2 透過画像

Fig.4 に、この実験で使用した被検体を示す。

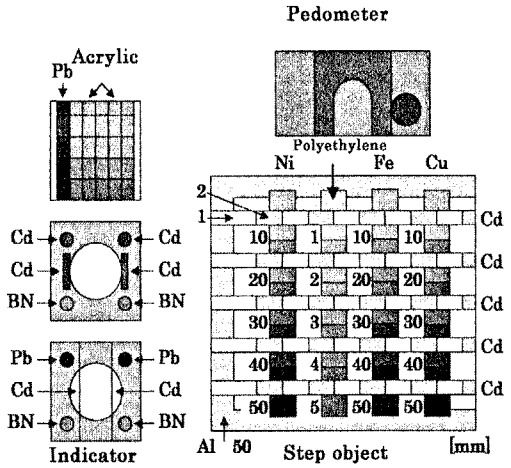
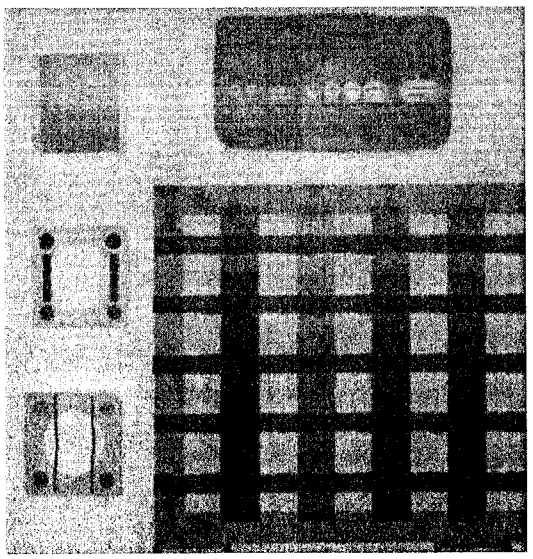


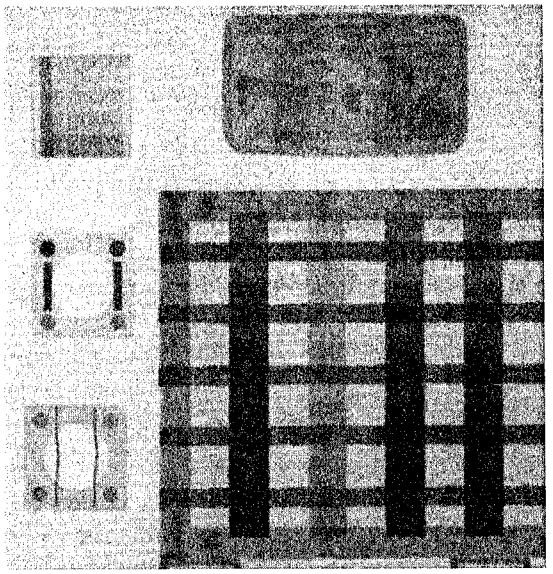
Fig.4 Schematic view of object

Fig.5 に、10 mmのアクリル板を使用して取得された赤画像及び緑画像を示す。赤、緑両方の画像とも熱中性子成分及びγ線成分のどちらも含まれているが、赤では熱中性子成分、緑ではγ線成分が多く含まれているのがわかる。

これらの画像から、つぎに中性子とγ線の成分を分離抽出するが、ここでk1とk2の決め方について述べる。これらは現在目視によって最適値を決めており、その例としてγ線を抽出する場合をFig.6に示す。

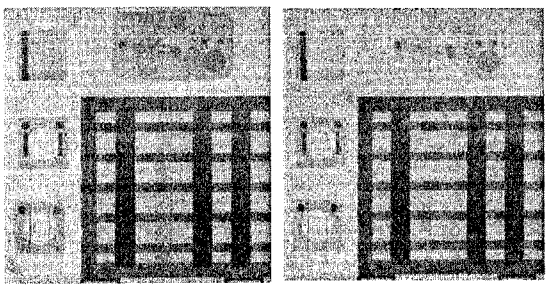


(a) Red Image

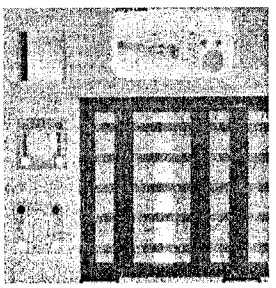


(b) Green Image

Fig.5 Raw red and green images



(a) k2＝0.45　(b) k2＝0.52 (best)



(c) k2＝0.60

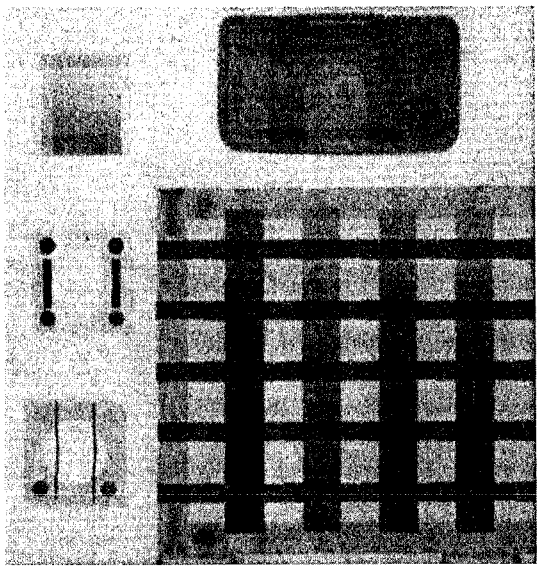
Fig.6 Dependency of γ ray image on the coefficient k2 value.

目視評価の際、ASTMインジケータのPb部分、アクリルステップやステップ被検体のポリエチレン部分を評価の対象とした。k2＝0.45の場合、アクリル部分に影が残っているため、熱中性子が残っていることが確認できる。そのため係数が小さい事がわかる。また、k2＝0.60の場合、アクリル

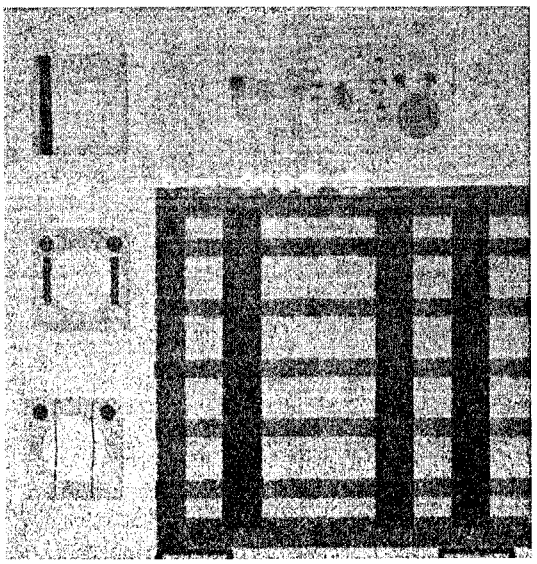
部分やBN部分が白く反転していることから、係数が大きい事がわかる。このようにして、係数を判定し(7)、(8)の式をそれぞれ、

$$n = \text{Red} - 0.74 \cdot \text{Green} \cdots\cdots (9)$$
$$\gamma = \text{Green} - 0.52 \cdot \text{Red} \cdots\cdots (10)$$

とし、それぞれ熱中性子線画像、γ線画像を抽出した。その結果をFig.7に示す。



(a) Neutron component



(b) γ-ray component

Fig.7 Extracted thermal neutron and γ ray images.

Fig.7より、γ線成分をあらわした画像では、BNやアクリル、ポリエチレンが透過しやすいのがわかる。また万歩計は電池の部分で減衰しているのがわかる。逆に熱中性子画像では、Pbは透過し、アクリルのステップウェッジや万歩計の内部が見て取れるような透過画像になっている。

以上より、画像間演算により静止画での熱中性子線成分とγ線成分が、抽出されていることが確認できた。

3.1.3 アクリルの厚さの検討

熱中性子、γ線ラジオグラフィの同時撮像を行う場合、2つの画像を最大限に有効に活用するためには、2つの画像のN/Sの和が最低となるのが望ましい。そこで、撮像時間が一定で、N/Sの和が最低となる熱中性子成分とγ線成分の輝度比(n/γ)を求めるため、被検体の前にアクリル板を設置し、設置なし、5mm、10mm、15mmと変化させた。Fig.8に相対標準偏差とn/γとの関係を示す。

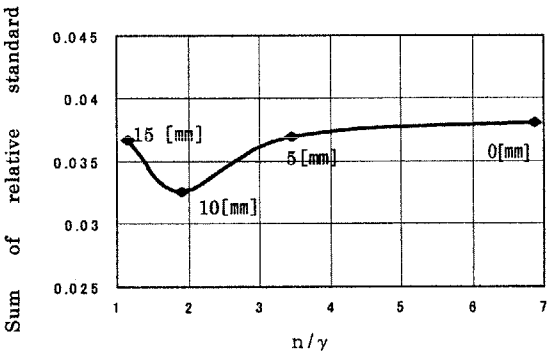


Fig.8 Relation of the sum of relative standard deviation and n/γ.

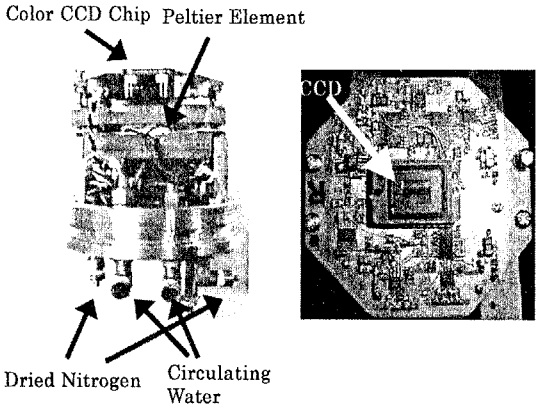
Fig.8よりアクリルの厚みが10mmの時に最良な画像が得られることがわかる。

3.2 カラーCCD撮像[4, 5, 8, 10]

3.2.1 撮像システム

中性子とγ線の強度が時間的に変化するような場では、赤色画像と緑色画像を同時に取得できると良い。また、将来の中性子線源であるパルス中性子源でも、パルス毎に強度が異なる時には，同時取得は有効である。そこで、カラーCCDチップを搭載した冷却型カメラを製作し、中性子－γ線ラジオグラフィを試みた。撮像素子はProgressive Scan CCD Image Sensor ICX085AK (SONY製)であり、有効画素数1300(H) x 1030(V)、画素サイズ6.7[μm] x 6.7[μm]、受光面サイズ2/3インチである。カラーCCDの色フィルタは

原色フィルタであり、高い色再現性を示し、画像処理に適している。このカラーＣＣＤを組み込んだカメラの側面をFig.9(a)に、正面をFig.9(b) に示す。カメラ部の底面にはペルチェ素子用冷却水のためのコネクタと、ＣＣＤ表面の露結防止用乾燥窒素のためのコネクタがある。



(a) Side view. (b) Top view.

Fig. 9 Cooled color CCD camera.

3.2.2 透過画像

実験は、同様に被検体の前方に厚さ 10[mm]のアクリル板を設置して撮像を行った。Fig.10 に被検体を示す。被検体を露光時間 87.8 [sec] で８フレーム撮像した。この８フレームに対して暗電流補正を施しフレーム間フィルタリングを行った原画像（カラー画像）を Fig.11 に示す。カラー画像の赤色成分と緑色成分を分離した画像を Fig.12 に示す。これらの画像から、熱中性子成分とγ線成分を抽出した画像を Fig.13 に示す。

同じ係数を用いて、他の被検体のデータについ

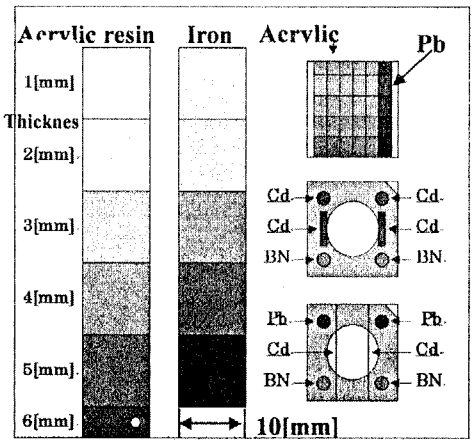


Fig.10 Inspecting objects; Step-wedges of acrylic resin and ion and ASTM indicators.

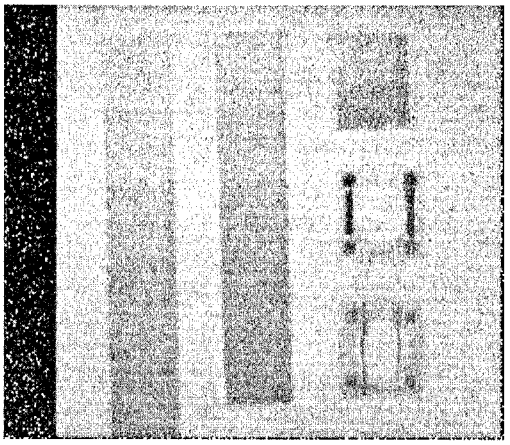
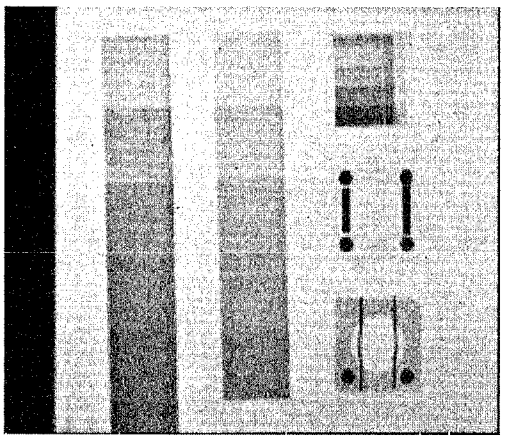
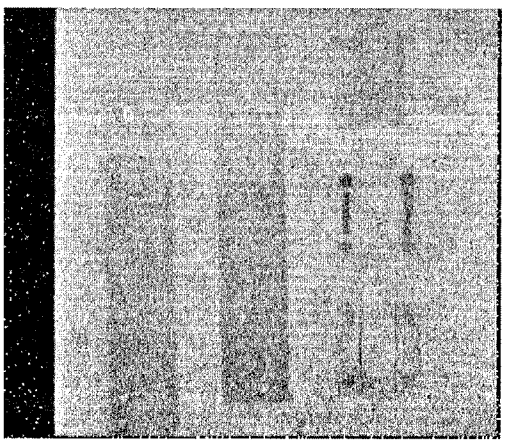


Fig.11 Pre-processed raw color image with acrylic resin plate of 10 mm thick.



(a) Red component.

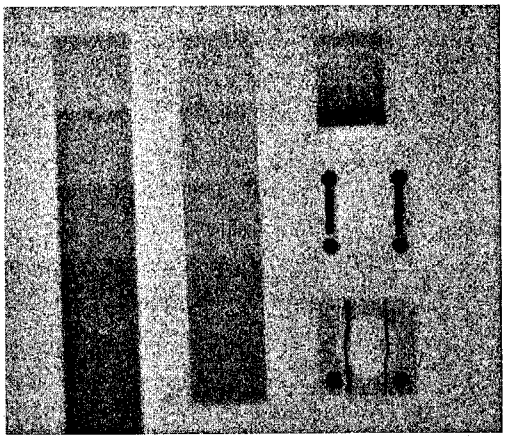


(b) Green component

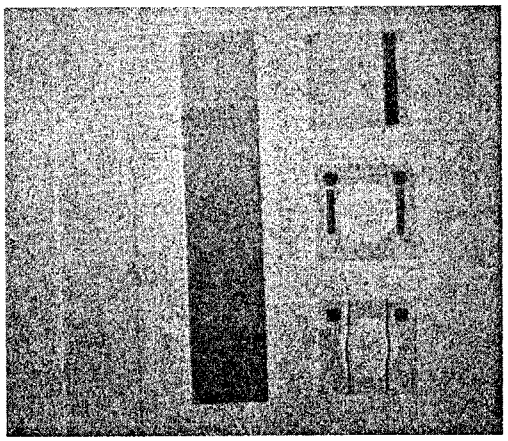
Fig.12 Separated images.

ても処理した。被検体は、プラスチック製のおもちゃ（ピカチュウ）、9[v]の電池、PIC(マイコン)である。撮像条件は同じである。ただし、４フレ

ーム撮像し、４フレームに対して暗電流補正を施しフレーム間フィルタリングを行なって，γ線によるインパルス性ノイズを除去した。熱中性子とγ線成分の画像に分離するために前回使用した係数を用いて画像間演算した結果を図１１に示す。図より熱中性子成分とγ線成分の画像に分離できているのがわかる。また、γ線成分の画像から９[v]の電池が６つの層になっていることや電池の内部の配線を可視化できている。このことから、同じ撮像条件であれば、同じ係数を用いて熱中性子とγ線成分の画像に分離することができることがわかった。

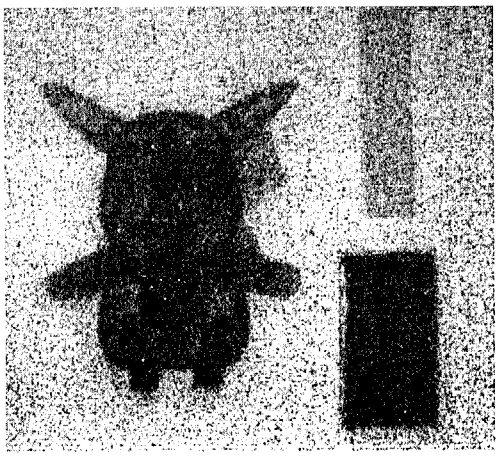


(a) Neutron image.

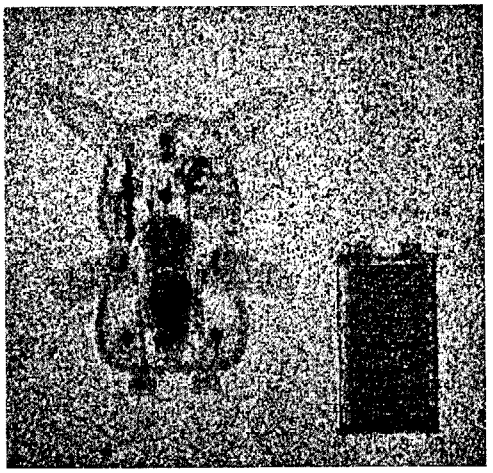


(b) γ-ray component

Fig.13 Derived images.



(a) Thermal neutron image



(a) Gamma ray image

Fig.14 Derived images with the same coefficients.

4. 動画像撮像システム

静止画実験によって開発された画像間演算法を動画像に応用するために、実時間演算処理が可能な動画像信号処理装置を開発した。また、動画用カメラとしては、高速に透過光のスペクトルを選択できる電圧制御の液晶フィルタを用いたものと、ＲＧＢに対応した３つのＣＣＤ素子を有する３板式カラーカメラで、(株) 東芝により特別に高感度化がなされたものを使用した。

4.1 液晶フィルタ方式撮像[2,3]

4.1.1 撮像システム

高感度なカラーCCD カメラを実現すべく、Fig.15 に示す動画像用撮像カメラを構築して使用した。２色発光コンバータからの光を、液晶フィルタとモノクロ CCD カメラにより時分割に色分離して取得する。液晶フィルタは、透過スペクトルを電気信号により瞬時に選択ができる光学フィルタである。Fig.16 にこの撮像系を使った信号処理システムの概略図を示す。CCD で取得された画像は、10(12)bit デジタルデータとして実時間処理装置に取り込まれ、暗電流・シェーディング補正、ディジタルフィルタ、フレーム間演算、リカーシブフィルタ、及び擬似カラー化処理をリアルタイムで施され、モニタと VTR に出力される。な

お 30 フレーム/秒のフレームレートで撮像し、赤フレーム、緑フレーム、ダミーフレームの周期で取り込み、熱中性子及びγ線の画像は 10 フレーム/秒で出力される。

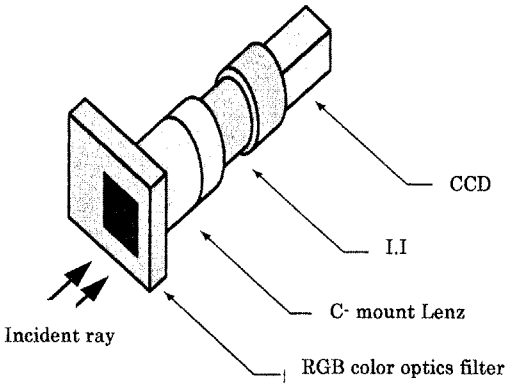


Fig.15 Camera for dynamic imaging.

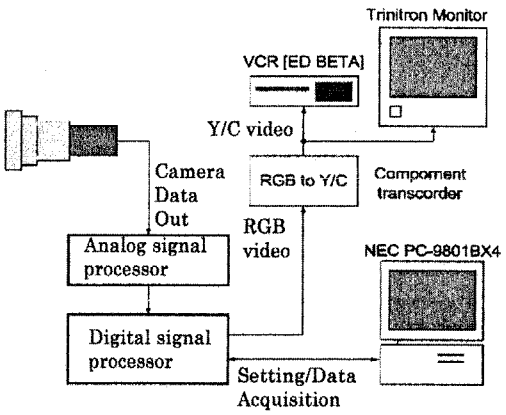


Fig.16 Block diagram of the real time image processing system

4.1.2 透過画像

この実験で使用した被検体を Fig. 17 に示す。

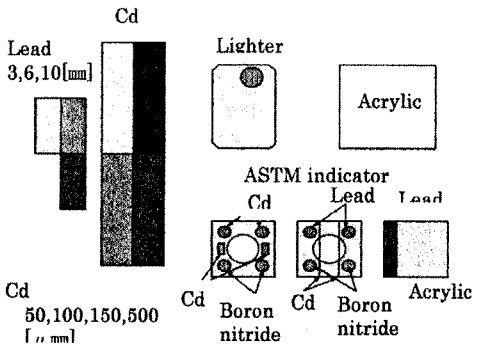
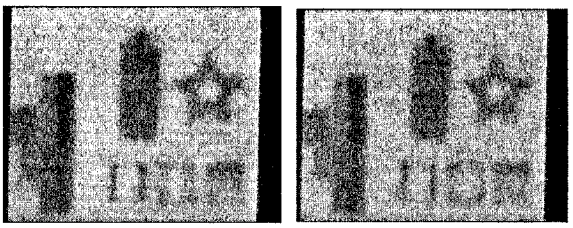


Fig.17 Schematic view of the objects

被検体は、厚さ(3 ㎜,6 ㎜,10 ㎜)の異なる鉛板、厚さ(50μm, 100μm,150μm,200μm)の異なるカドミウム板、ATSM インジケータ 3 種、100 円ライタ、厚さ 4 ㎜の星型アクリル板であり、これらを Al 板に貼り付け水平に移動させて撮像した。Fig.18 に赤フレームと緑フレームの画像を示す。



(a) Red Frame Image (b)Green Frame Image

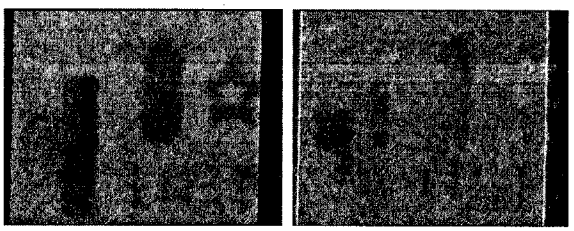
Fig.18 Raw red and green frame images.

イメージ・インテンシファイア (II) を使用しているため、解像度の低い画像となっている。また、赤色画像と緑色画像との相違点を認識しずらいが、ASTM インジケータの鉛とアクリルを組み合わせたものにおいて、緑色画像のほうがアクリル部分の影が薄く、鉛部分の影が濃い事がわかる。また１００円ライタの本体部分はプラスチックであるため赤色画像のほうが、影が濃い事がわかる。ここで、静止画と同様に、式(7)、(8)を用いて、係数を目視により k 1＝0.75、k 2＝0.80 と決定し、以下の式(11)、(12)を用いて実時間で画像間演算を行った。

$$n = \text{Red} - 0.75 \cdot \text{Green} \quad \cdots\cdots (11)$$

$$\gamma = \text{Green} - 0.80 \cdot \text{Red} \quad \cdots\cdots (12)$$

その結果を Fig.19 に示す。



(a) Neutron frame image (b) γ ray frame image

Fig.19 Derived thermal n and γ ray frame images.

ASTM インジケータがどちらの画像も見難くなっている。しかし、その他の被検体は確認することができる。星型のアクリル板は中性子線成分の画像に見られ、γ線成分では透過していることが確認できる。１００円ライターやカドミウム板についても同じことが言える。逆に、鉛は、熱中性子線成分の画像では透過して見ることができない

が、γ線成分の画像では吸収されて見ることができる。以上のことより、リアルタイムで熱中性子とγ線透過像が表示できたと言える。

4.2 3板式高感度カラーＣＣＤ撮像[9, 12]

4.2.1 撮像システム

（株）東芝が調整した3板式高感度カラーＣＣＤカメラを使用し、赤と緑のビデオ信号を 12bit のデジタル信号に変換して、実時間信号処理装置で画像処理した。

4.2.2 透過画像

実験で使用した被検体を Fig. 20 に示す。

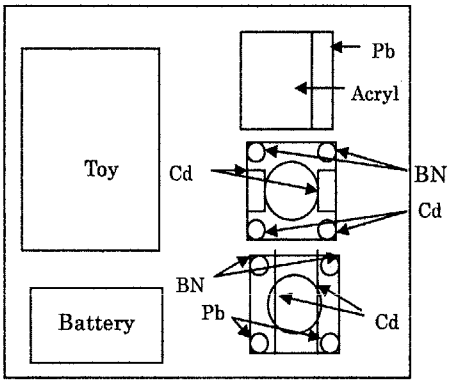
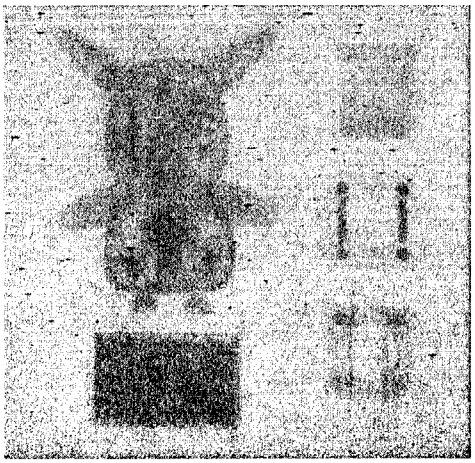


Fig.20 Layout of the objects

アクリル 10mm を使用して取得した赤色および緑色画像を Fig.21 に示す。次に、実時間処理を行った中性子画像・γ線画像のフレーム画像を Fig.22 に示す。このときの係数 k1、k2 はそれぞれ 0.4 と 0.6 であった。

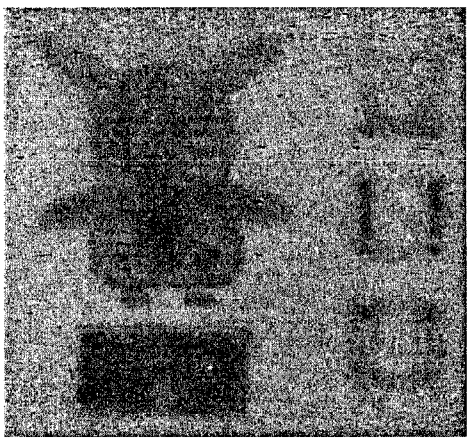


(a) Red frame image

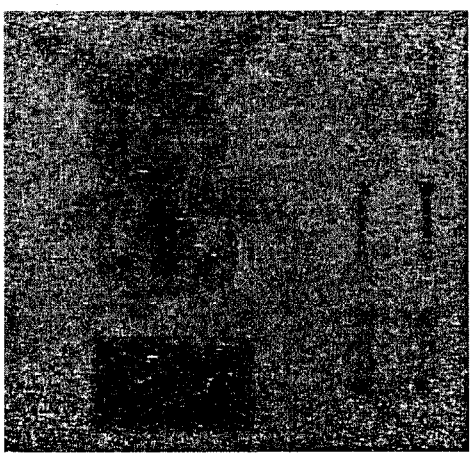


(b) Green frame image

Fig.21 Raw red and green frame images



(a) Neutron frame image



(b) γ-ray frame image

Fig.22 Derived neutron and γ-ray frame images

Fig.22 のおもちゃ部分を注目して見ると、中性子画像ではプラスチックの輪郭がはっきり現れているのに対し、γ線画像では内部の電池のほうがよく見えている。また、インジケータを比較すると、上と下のインジケータの鉛部分が中性子画像ではほとんど見えないのに対し、γ線画像では検出できていることがわかる。以上より、中性子画像とγ線画像に分離可能であることが分かった。液晶フィルタを用いた画像と比較してみると、カラーCCD カメラ使用時のほうが被検体の輪郭が鮮明であり、分解能が向上していることが分かる。つぎに階調分解能を比較した。これは被検体が無い部分での出力の揺らぎである標準偏差で比較した。256 階調で表示した場合、モノクロ CCD の標準偏差は約 12 であったが、カラーCCD では約 4.9 に改善されていた。

5. まとめ

(株)東芝が開発した２色発光コンバータを利用した中性子・γ線の同時ラジオグラフィのために静止画用と動画用のシステムを開発し、JRR-3M の TNRF-2 において実験し、各システムの特性を評価した。静止画用には、モノクロとカラーの冷却型ＣＣＤカメラを使用し、γ線によるホワイト・ノイズの除去法や、赤色と緑色の画像から中性子とγ線の画像を抽出する手法を開発した。画質は前者が優れていた。

この手法を実時間で実行する動画用システムも開発し、液晶フィルタと３板式カラーＣＣＤを使用する２種のシステムを開発し、実時間表示が出来ることを実証した。また、画質は後者の方が勝っていた。

この中性子・γ線同時ラジオグラフィの画質は、根本的にγ線線量に依存しており、高い線量が望ませる。しかし、TNRF-2 の照射場は熱中性子用に低く設計されているため、やむおえずアクリル板で n/γを低下させて同時撮像した。

動画においては、まだ十分な性能が得られていない。しかしながら、静止画においては、１台のＣＣＤカメラだけて撮像し、これまでにない、画素ずれのない中性子とγ線のラジオグラフィ像を表示することに成功した。

今後は、ｎ－γＣＴへの応用を進めるとともに、動画の改良を継続して行く予定である。

最後になりましたが、この研究においてキーポイントとなる２色発光蛍光コンバータや３板式カラーＣＣＤカメラを提供していただいた、(株) 東芝の日塔光一氏と小長井主税氏に感謝する次第です。

参考文献

1) Nittoh, K.: Discriminated neutron and X-ray radiography using multi-color scintillation detector, Nucl.instrument & Methods, A428 (1999).
2) 中川哲郎、佐藤貴樹、持木幸一、他５名；多色蛍光コンバータを用いた中性子ラジオグラフィ，第 28 回可視化情報シンポジウム，予稿論文集，pp321-324(2000).
3) 池野豊、中川哲郎、持木幸一；２色発光コンバータを用いた中性子・γ線ラジオグラフィ，応用物理学会放射線分科会主催放射線夏の学校 (2000).
4) 木本享尚、川上慎輔、池野豊、持木幸一、村田裕；二色発光コンバータと冷却型カラーＣＣＤを用いたＮ－γラジオグラフィ，日本原子力学会 2001 年 春の年会, C48 (2001).
5) K. Mochiki, Y. Murata, K. Nittoh; Neutron Gamma Ray Radiography Using a Two-Color Luminescent Scintillator, 4th International Topical Meeting on Neutron Radiography , (2001).
6) 持木幸一, 日塔光一；マルチカラーシンチレーター，応用物理学会放射線分科会／日本医学物理学会合同シンポジウム「医学応用物理と生体情報イメージング計測」(2002).
7) K. Mochiki; Research of Two Phase/Dynamic Phenomenon using Neutron Radiography, Radiography Workshop 2002 at Pohang, Korea, 20 March 2002.
8) 増子大輔, 持木幸一, 村田裕, 日塔光一, 小長井主税；マルチカラーシンチレータを用いた中性子・ガンマ線同時ＣＴ，電気学会 計測研究会 (2002).
9) 池野豊, 持木幸一, 村田裕, 日塔光一, 小長井主税；カラー・ラジオグラフィのための動画像実時間信号処理装置の開発，電気学会研究会 計測研究会 (2002).
10) 増子大輔, 池野豊, 伊東覚, 持木幸一, 村田裕, 日塔光一, 小長井主税；冷却型カラーＣＣＤカメラを用いた熱中性子－γ線透過像の同時取得，非破壊検査協会 (2002).
11) 持木幸一；中性子イメージング，日本ラジオアイソトープ協会、サマースクール、岩手県滝沢村 (2002).
12) K. Mochiki, Y. Ikeno, Y. Murata, K.Nittoh; Color Radiography, WCNR in Roma (2002) (to be presented).

成果の公表

上記参考文献の(2) から(12)は、この研究で得られた成果を公表したものです。

This is a blank page.

3. 放射化分析

3. Neutron Activition Analysis

This is a blank page.

研究テーマ：広域環境モニタリング試料の微量元素分析
表　　題：フィッショントラック法を用いた微量核分裂性物質の分析

3-1

フィッショントラック法による天然ウラン含有粒子の検知

髙井　木の実、江坂　文孝[1]、小野寺　貴史、桜井　聡、臼田　重和、渡部　和男[1]

日本原子力研究所　環境科学研究部　環境技術開発グループ
[1]日本原子力研究所　環境科学研究部　分析科学研究グループ

IAEAは保障措置強化・効率化策の一環として保障措置環境試料分析法を導入した。これは、原子力関連施設の内外で採取した環境試料（スワイプ、植物、水、土壌試料等）中に含まれる極微量の核物質の同位体組成を調べることにより、未申告の原子力活動及び核物質を検知するものである。現在、原研ではスワイプ材上に捕集された極微量のウラン及びプルトニウムの同位体組成分析法の技術開発を行っている。本研究はスワイプ試料中の極微量ウラン検出のためのパーティクル分析法開発の一端である。

パーティクル分析では、試料中の核物質を含有する数μm の粒子一個一個について、二次イオン質量分析法（SIMS）により同位体分析を行っている。しかしながら、現法ではサブミクロンサイズの粒子を検知・分析することが難しいため、フィッショントラック法の応用を検討している。本報告では、天然ウランを含む粒子を用いた予備実験について述べる。

原研施設内で採取したスワイプ試料から吸引法により粒子を回収した。これらの粒子の中には天然ウランを含む粒子が存在することが、他の実験から既知である。捕集された粒子はポリカーボネート溶液と混合し、これをフィルム状に乾燥させ、粒子をポリカーボネートに閉じ込めた形の照射試料とした。このポリカーボネートは固体飛跡検出器の役割を果たす。試料はポリエチレン袋に封入し、熱中性子フルエンス 9×10^{14}/cm^{2}で照射した。この際、試料中の235Uの誘導核分裂により、ポリカーボネート中に核分裂片による飛跡（フィッショントラック）が形成される。このフィッショントラックを明瞭にするため、照射した試料を放射能減衰させた後、55℃の 6N-NaOH 中で10分間エッチング処理した。試料は純水で十分に濯ぎ、乾燥させた後、顕微鏡観察した。

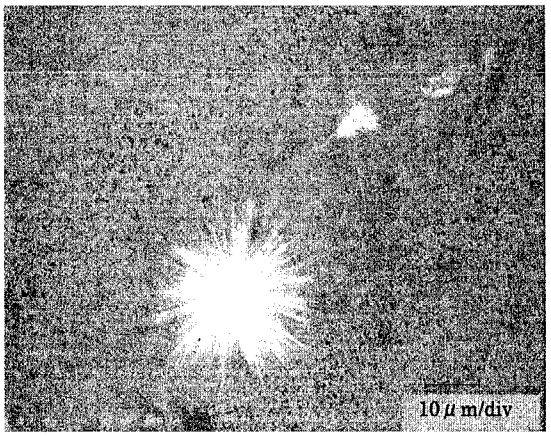


図1 天然ウランによるフィッショントラック

図1は、デジタルマイクロスコープ（3,000倍）でフィッショントラックを観察した写真である。このように、ウランを含む微小粒子を顕微鏡下で検知することができた。今後は本法の有効性について、粒子径とウラン濃縮度の面から検討を進める。また、環境試料にフィッショントラック法を適用し、検知された粒子をピックアップし、表面電離型質量分析法（TIMS）により粒子毎の同位体分析を行う予定である。

原子炉：JRR-4　　装　置：気送管　　分　野：放射化分析（環境科学）

研究テーマ：中性子放射化分析法の環境影響元素・物質研究に対する新利用法と高度化技法の開発
表題：臭素同位体比(Br-81/Br-79比)測定法の開発による土壌浸透水の野外・長期間追跡への利用

3-2 土壌水を追跡するための臭素同位体比測定法の開発

木方展治、藤原英司
農業環境技術研究所

１．はじめに

農耕林地での浸透水の動きを正確かつ精密に把握することを目的に、安定同位体でラベルしたBr-79あるいはBr-81を利用するトレーサ手法について、土壌のサンプリング法、土壌水および土壌の分析法（放射化分析等）などの基礎的事項の検討を行った。

２．実験方法

90atom%Br-79および90atom%Br-81の臭化アンモニウム試薬を水溶化した後、自然存在比レベルの臭化アンモニウム液と混合して臭素同位体存在比の異なる溶液を作成した。試料液0.1mLをろ紙に吸収させ、検量線作成用試料とした。また前作で小麦を栽培していた圃場から、ハンマーによる打ち込み式採土器を用いて、直径5cmの塩化ビニル製容器に表層腐植質クロボク土壌を充填し、長さ29.5cmの土壌カラムを作成した。土壌カラムに90atom%Br-79、90atom%Br-81および通常同位体比の100mgL^{-1}臭化アンモニウム溶液10mLを１カラムに１種添加した。採取した雨水を原則として毎日10～20mLカラムに注水して得た浸透水100μLをろ紙に吸収させ、照射試料とした。

試料を原研研究炉のJRR3気送管およびJRR4水力照射筒（熱中性子束；$5\times10^{17}m^{-2}s^{-1}$）で２～10分間照射した。30分以上冷却後、Ge(Li)半導体検出器により実効測定時間(live time)200秒以上をかけ、非破壊法で測定した。全臭素は、イオンクロマトグラフ法により分析した。

３．結果および考察

1)臭素の同位体量に対し、生成放射能をプロットすると0～8μgの範囲において、Br-79でBr-80mの37keV、Br-81でBr-82の554keVおよび776keVの光電ピークについて相関係数0.99以上の１次回帰直線（検量線）を書くことができた。カプセル内位置が異なる試料から作成した２本の検量線の差はほとんどなかった。測定時間500秒でBr-82の測定を行うことにより、0.01ngのBr-81含量の差を定量できると考えられた。

2)カラムからの浸透水を照射した場合に、Br-80m、Br-82とも大きな妨害ピークは無く、両核種の光電ピークが顕著に現れた。経時的試料採取の結果、浸透水中の臭素同位体の差が明らかに認められた（図１）。両同位体の合計は、臭素全量にほぼ一致した（図２）。

3) 土壌についてもBr-79とBr-80の分析を非破壊放射化分析法で行えることが確認できた。

以上の結果は、臭素の同位体をトレーサ試験に適用できる可能性が高いことを示した。

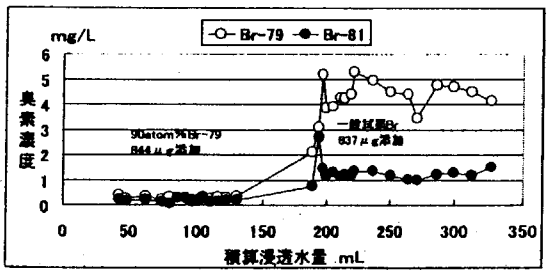


図１　カラム浸出水のBr-79とBr-81

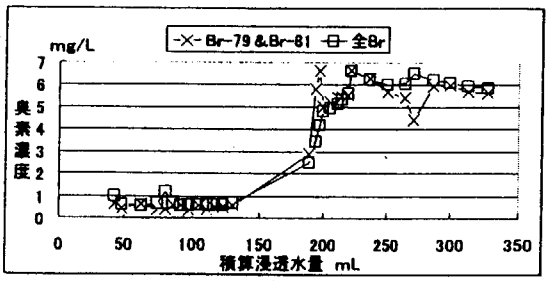


図２　カラム浸出水の臭素同位体合量と全臭素の比較

参考文献
第39回理工学における同位元素・放射線研究発表会要旨集(2002), p.115

原子炉：JRR-3M、JRR-4　　装置：気送管　　分野：放射化分析（環境、農・水産物）

研究テーマ：ヨウ素同位体核種の陸水・土壌・地層・植物系における広域的・地球化学的分布と挙動
表題：放射性ヨウ素の土壌蓄積性と浸透性の把握

3-3 ヨウ素の野外環境中の土壌・水系における分布と移行

木方展治、結田康一
農業環境技術研究所

目的：再処理工場から大気中に放出される長寿命^{129}Iの地表へ降下後の土壌・水系における挙動解明の一環として、現在環境中での存在量がきわめて小さい^{129}Iに替えて、非放射性ヨウ素^{127}Iを指標とするヨウ素の土壌水・水における動態解明、特に土壌への蓄積や土壌からの溶出・流動について、野外で実証的に解明する。

方法：つくば市農業環境技術研究所内の水田、畑地および林地の実験圃場（図1）において、第1帯水層下の常総粘土層まで（0～6m）の深度別土壌のほか、降水、かんがい水、田面水、深度別土壌水（0.2mから2.5m）、第1帯水層地下水を4年間にわたって継続的に採取した。

水田圃場の採水システムと土壌断面を写真1に示した。

水試料中ヨウ素はICP-MS法を主体とし、一部試料は放射化分析法で分析し、クロスチェックを行った。土壌中ヨウ素は放射化分析法（化学分離法）により定量した。

結果：1）表層土壌中ヨウ素含量は、畑地や林地が水田より1桁以上高かった。しかし、両圃場とも下層ほど漸減、さらに還元的環境となる地下水面以深では急減して、水田との差異はほとんどなくなった（図2）。

水田の場合、夏季かんがい期には還元化が著しい作土層より下にあり、非かんがい期には地下水面より上となる比較的酸化的な50～89cm層（2Bw層）のヨウ素濃度は作土層の4～5倍と高く、上層から浸透してきたヨウ素が吸着・集積したことを示唆していた。

2）土壌水中ヨウ素濃度は、土壌中ヨウ素含量とは逆に水田が畑地や林地より桁違いに高くなっていた（かんがい期）。これは土壌のたん水化で還元的環境となり、ヨウ素が溶出したためと推定された。また、還元化が進んだ層ほど高く、20cm＞50cm＞田面水＞100cm以深であった（図3）。

水田では、かんがい期、特に土壌の還元化が進むかんがい後期になると、非かんがい期に蓄積していた分も含めて、排水路や地下水層へヨウ素が流出していくことが示唆された。その結果、表層土壌中のヨウ素含量が畑地や林地よりも桁違いに低くなっていると考えられた。

3）畑地・林地の土壌水中ヨウ素濃度は、水田のような季節変動は見られず、畑地表層（20cm）が平均2.2μgL^{-1}と高かった以外、畑地0.4μgL^{-1}、林地0.2μgL^{-1}前後と、降水の平均1.6μgL^{-1}より1桁近く低かった（図3）。降水に伴って供給されたヨウ素のほとんどを表層土壌が吸着・蓄積した結果、畑地・林地の表層土壌のヨウ素濃度が高レベルであったと推定された。畑地が林地より表層土壌中ヨウ素含量が低いのは、畑地は機械耕うん等の影響で透水性が林地より悪く、大雨時には冠水して還元的になり、土壌からのヨウ素溶出率が増加するためと推定された（図2）。

参考文献

1）「天然バリアKd」専門研究会報告書（2000），p5～20
2）第39回理工学における同位元素・放射線研究発表会要旨集（2002），p22

原子炉：JRR-3M、JRR-4　　装置：気送管　　分野：放射化分析（環境、農・水産物）

研究テーマ:ラジオアイソトープ技術者の養成
表　　題 :実習　放射化分析

3-4 貝殻中の銅・ﾅﾄﾘｳﾑの放射化分析

上沖　寛
国際原子力総合技術センター（東京研修センター）

本研究は、ＲＩ技術者の養成を目的とする研修コースの中で実習教科として行うものである。本報告では、平成13年度の研究炉をもちいた成果として、国内原子力技術および放射線利用に関係する人材養成を行った基礎課程およびアジア・太平洋地域開発途上国の原子力分野人材養成への国際援助としてＪＩＣＡと協力して行った原子力基礎技術コースにおいての実習教科としての放射化分析について報告する。

原子力の基礎として中性子核反応の理論や応用を理解させることは重要である。放射化分析の実際を経験させることはこれらの知識の理解を深めるのに大変重要であり、結果としてガンマ線スペクトル解析による放射能測定法および非密封ＲＩの安全取扱法を習得させることになる。

平成13年度は基礎課程とＪＩＣＡ原子力基礎技術コースの中で3回の放射化分析実習を行った。分析試料は海水産の大アサリであり、炭酸カルシウムをマトリックスにして微量元素を含有する。分析目的核種は、放射化生成核種のガンマ線スペクトルで主成分となるﾅﾄﾘｳﾑ24、放射化生成物が陽電子壊変を伴い陽電子消滅ピークを主要放射線ピークとする銅64である。照射条件は研究炉の気送管で2～5分間照射とし、ナトリウムと銅の標準試料と共に大アサリ貝殻の照射を3回行った。

銅の分析：

銅64の陽電子消滅放射線は、他の放射化生成核種からの高エネルギーガンマ線や宇宙線が物質にもたらす電子対生成による放射線と同一放射線であるから、銅64の分析には化学分離を必要とした。簡単な銅の化学分離法として金属亜鉛により銅イオンを還元させて銅の沈殿分離を行った。この化学分離の操作は、30分間の所用時間で0.1ppm Cu 濃度に対して5%の精度で分析された。本実習は、生成核種を同定および定量することにより核反応の理解を深め、ＲＩ実験における放射線被ばくに対する工夫、除染、サーベイ等、一連の安全取扱いの基礎を習得させるものとして有効であった。

本実験による研修生の被ばく線量は、線源が10^6Bq位に対し最大1μSv程度であった。

原子炉：JRR－3M、JRR－4　　装置：気送管　　分野：放射化分析（環境）

研究テーマ：中性子放射化分析法の環境影響元素・物質研究に対する新利用法と高度化技法の開発
表　　題：金属元素類（重金属元素等）の同位対比測定法の開発による土壌中の挙動解明

3-5

安定同位体による土壌有機物中重金属の標識化

櫻井泰弘、木方展治、牧野知之、菅原和夫
農業環境技術研究所

環境中の無機元素（Cd, Se, Zn, Cu等）の動態解明や影響評価に資するために、野外での使用が可能である安定同位体(SI)による環境物質の標識化法と中性子放射化分析によるこれら安定同位体の高精度測定法を開発する。本年度はモリブデン、セレンの安定同位体の中性子放射化分析法による高精度検出条件とセレン、カドミウムのSIによる土壌有機物（フルボ酸）中の無機元素の標識化を行う。

堆肥を連用した淡色黒ボク土壌から抽出精製したフルボ酸をカチオン交換樹脂、アニオン交換樹脂でイオン交換後、Se-74またはCd-114で標識化した(表１)。放射化は日本原子力研究所研究炉JRR-3Mで、5.2×10^{17}($m^{-2}s^{-1}$)の熱中性子束を600秒間照射し、１日間冷却後、Ge検出器と波高分析器により、生成した放射性核種のγ線スペクトルを計測(300～1500 秒)した。

1)Mo-98とSe-74の両元素とも12000～50000 ngでγ線ピーク面積と相関係数0.98以上での検量線が得られ、SIトレーサとして利用できることが示された。5.2×10^{17}($m^{-2}s^{-1}$)の中性子束を600秒間照射、1日冷却、300秒のγ線計測時間でMo-99(半減期66 h, 181 keV, 739 kev)は約100 ng, Se-75(半減期120d, 136 keV, 264 keV)は約10 ngまでの定量が可能であった。

2)Cd-114はH型の樹脂で陽イオン交換したフルボ酸がOH型の樹脂で陰イオン交換したフルボ酸に比べて約3.4倍量のCd-114が結合した。Se-74は陰イオン交換したフルボ酸が陽イオン交換フルボ酸よりも約2倍量のSe-74と結合した(図1)。

このことはフルボ酸の無機元素をSIで高濃度に標識化する条件として、SIイオンのイオン形態(カチオン、アニオン）に応じたイオン交換樹脂による前処理が有効であることを示している。

表1 安定同位体によるフルボ酸の標識化

フルボ酸5000 μ g/mLの水溶液調製
↓
イオン交換(Amberlite CG120 or CG400)
↓
イオン交換フルボ酸(＋Cd-114, Se-74
↓　　各1000 μ g/mL)
カラム吸着(Amberlite XAD-7)
↓　洗浄(＋H_2O)
溶離(10% NH_3 soln.)
↓　濃縮・回収(凍結乾燥)
安定同位体標識化フルボ酸

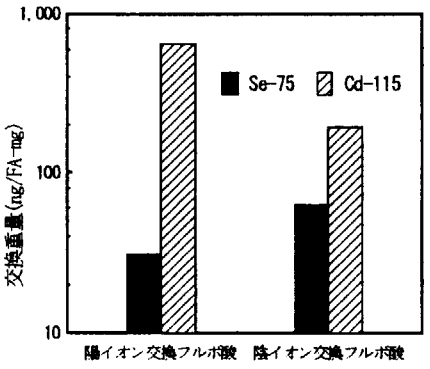


図1　イオン交換したフルボ酸(FA)への同位体元素交換量

原子炉：JRR-3　　装置：気送管　　分野：放射化分析（農・水産物）

研究テーマ：広域環境モニタリング試料の微量元素分析
表　　題：広域環境モニタリング試料の微量元素分析

3-6 広域環境モニタリング試料の微量元素分析（2）

宮本ユタカ[1]，齋藤陽子[2]，桜井　聡[2]，臼田重和[2]
[1]原研，環境科学研究部，放射性核種データ解析研究グループ
[2]原研，環境科学研究部，環境技術開発グループ

はじめに

大気に放出された極微量の放射性核種や大気汚染物質の挙動，分布などを評価するために，これらの直接的な輸送媒体である大気浮遊塵の量や組成についてモニタリングすることは重要である。本研究では大気浮遊塵を捕集し，放射化分析法で元素分析を行った。捕集はエアーダストサンプラーによる方法に加え，松葉表面に付着したものを洗い落として採取した。大気浮遊塵は植物の葉の表面に付着されやすいことが知られている。特に松葉は常緑樹であるため，数年前の松葉を採取することで容易に長期間にわたって蓄積された大気浮遊塵の入手が可能となる。

これら２つの方法で捕集した大気浮遊塵の元素分析の結果から，大気浮遊塵の発生起源や環境中における挙動，分布について調べることを試みた。

実験方法

大気浮遊塵の捕集に使用したエアーダストサンプラーは，ハイボリュームエアーダストサンプラーおよび粒径の分級が可能な８段型のアンダーセンサンプラーである。また，降雨開始時から雨水を採取してメンブランフィルターでろ過し，雨水にけん濁している大気浮遊塵（以下，「けん濁浮遊塵」とする）を集めた。ハイボリュームサンプラーによる捕集は2001年の５月～８月にかけて行い，天候の変化に応じて２～６日間毎にフィルターを交換した。アンダーセンサンプラーは2001年１月～２月の１ヶ月間行った。また，松葉は2001年１月に採取した。これら全てを原研東海研内で行った。

エアーサンプラーで大気浮遊塵を捕集したフィルターの一部を切り取り，それを照射試料とした。松葉表面に付着した大気浮遊塵は，水またはアセトンで松葉を超音波洗浄して洗い落とした。その洗浄液を蒸発させて，蒸発残さを集め，照射試料とした。それをJRR-3MのPN-3で10秒間，あるいはPN-2で10分間照射した。比較標準試料として日本地質調査所製のJB-1a, JA-1, JA-3, JG-1aを用いた。

結果と考察

図１は，ハイボリュームサンプラーで捕集した浮遊塵について定量した元素の内，いくつかについて示したものである。晴天時に捕集したもの（白色）と雨天時に捕集したもの（灰色）に分類して示した。また，けん濁浮遊塵中の元素濃度を同時期にエアーサンプラーで捕集した試料のヒストグラムの横に黒色で示した。採取時期の違いによって各元素濃度の変動幅は４倍以上あり，極端に濃度が高くなる時期もあった。単純にけん濁浮遊塵が降雨によって大気から洗い流されたものであると仮定するならば，大気浮遊塵の元素濃度に対する降雨の影響はけん濁浮遊塵と同時期にエアーサンプラーで捕集した大気浮遊塵の元素濃度を比較することで調べることができると考えられる。この考えをもとに元素濃度の比較から定量元素を３つに分類した。

グループ１：雨水に可溶な成分に含まれるもの[Na, Cl, V, As, V]。けん濁浮遊塵の方がエアーサンプラーのものよりも２倍以上濃度が低い。特にClについては全てのけん濁浮遊塵から検出することができなかった。

グループ2:雨水に難溶な成分に含まれるもの[Al, Fe, Sc, Th等]。けん濁浮遊塵の方がエアーサンプラーのものよりも濃度が高い。

グループ3:決まった傾向を示さないもの[Zn, Br]。

得られた結果から，晴天時と雨天時における大気浮遊塵の元素濃度組成の違いについては，Na,Cl,Vでは平均して雨天時の方が晴天時よりも低いことが分かった。

アンダーセンサンプラーで捕集した浮遊塵は，４－５μmと１μm以下の部分に２つのピークを持つ粒径分布を持っていた。粒径が大きい粒子に多く含まれるScと，粒径が小さい粒子に多く含まれるVの元素濃度比をアンダーセンサンプラーの各段について求め，松葉から採取した浮遊塵の大きさをV/Sc比から見積もった。図２に粒径に対するV/Sc比を示す。松葉を水またはアセトンで超音波洗浄して得た試料のV/Sc比も図中に並べて示した。V/Sc比から判断すると，水洗浄，アセトン洗浄ともに洗い落とされた浮遊塵は粒径が２μm以上の大きな粒子で，洗浄方法の違いによって付着している成分の粒径に違いはなかった。

原子炉：JRR-3M　装置：照射設備（PN-2, PN-3）　利用分野：放射化分析（環境）

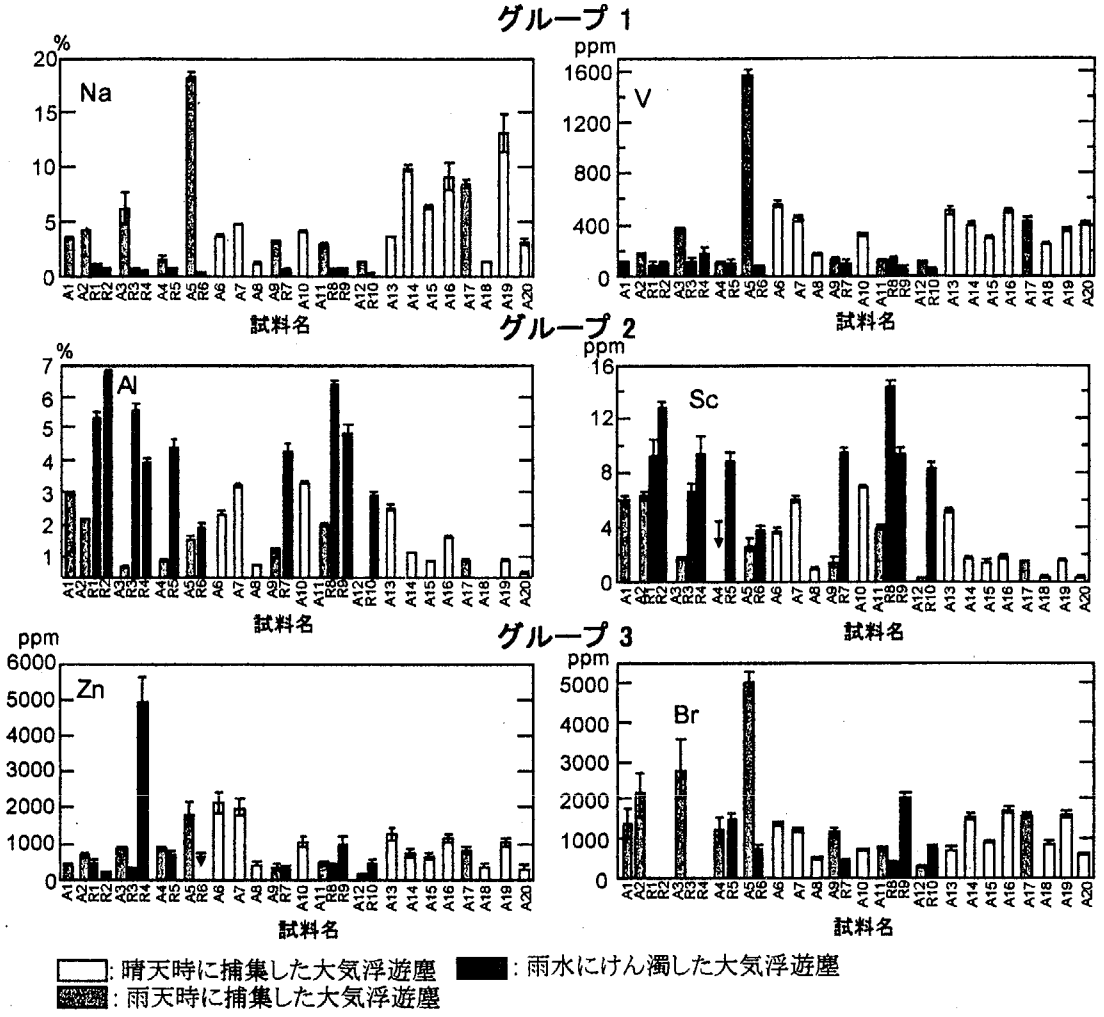


図１ ハイボリュームサンプラーで捕集した大気浮遊塵および雨水にけん濁した大気浮遊塵の元素濃度

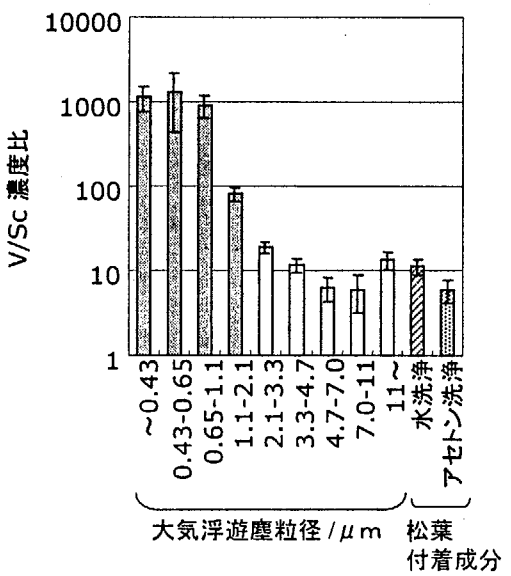


図２ 分級した大気浮遊塵および松葉付着成分のV/Sc 濃度比

研究テーマ：多重ガンマ線分析の分析化学への応用
標　　題：多重ガンマ線分析による高感度多元素同時定量

3-7 多重ガンマ線分析法による高感度多元素同時定量の応用 -古代中国青銅器の分析-

Application of high sensitive determination by using multiparameter coincidence method -Analysis for an ancient Chinese bronze vessel-

初川雄一、篠原伸夫、藤暢輔、大島真澄

物質科学研究部原子核科学研究グループ

ガンマ線の同時測定を用いた多重ガンマ線分析法を中性子放射化分析法と組み合わせることにより高感度の元素定量法を開発してきた(1)-(3)。今回多重ガンマ線分析法を利用し、古代中国製の青銅器の微量元素分析を行ったので報告する。分析した試料は殷代(紀元前 1500 年頃から紀元前 1050 年頃)の青銅器で有蓋の酒器（図-１）であり、この底部を削ることにより 41.208m g の粉末を採集した。照射は原研・研究炉において短（５秒）・中（１５分）・長時間（８時間）の３種類の照射を同一の試料に対して行いそれぞれ異なる半減期を有する核種の分析を試みた。特に主要成分である Cu からの生成する ^{64}Cu（半減期 12.7 時間）からの妨害が少なくなるように測定を行った。試料と一緒に純 Cu 箔（2.396m g）、標準岩石試料 JB-1a, 及び Ag, Au, Ir の標準溶液試料をろ紙上で風乾させたものを標準として原子炉にて照射した。 原子炉における中性子照射後に試料は詰替えられ多重ガンマ線分析装置 GEMINI において多重ガンマ線の同時測定を行った。定量は同時に照射した照準試料のガンマ線強度との比から得た。また測定時に Ge 検出器やデーター収集系において発生するデッドタイムの補正は測定試料と同時に^{133}Ba の標準線源を測定しそのピークの数え落としから見積もった。 得られた結果を表１に示した。

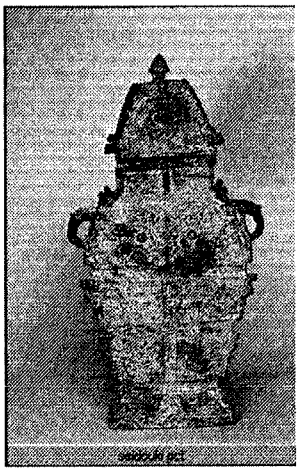


図-1 分析に用いた古代中国の青銅器

元素	核種	ppm	誤差	元素	核種	ppm	誤差
Ca	Ca-47	0.69%	0.08	La	La-140	57.7	0.6
Sc	Sc-46	4.34	0.01	Ce	Ce-143	82	10
Ti	Sc-48	0.60%	0.2	Eu	Eu-152	0.31	0.01
Mn	Mn-56	200	10	Gd	Gd-153	0.72	0.06
Fe	Fe-59	0.88%	0.01	Tb	Tb-160	0.2	0.01
Co	Co-60	30.7	0.2	Yb	Yb-169	1	0.1
As	As-76	53	6	Yb	Yb-175	2.2	0.3
Se	Se-75	6.6	1.1	Lu	Lu-177	0.13	0.01
Br	Br-82	35	1	Hf	Hf-181	2.3	0.03
Mo	Mo-99	5	1	Ta	Ta-182	0.26	0.01
Ag	Ag-110	310	10	Ir	Ir-194	17ppb	3
Sn	Sn-125	0.71%	0.02	Au	Au-198	66	8
Sb	Sb-124	22	1	Th	Pa-233	3.8	0.2
Cs	Cs-134	1.12	0.02	U	Np-239	3.4	0.2
Ba	Ba-131	118	4				

表１青銅器試料の微量元素分析結果

文献
(1)Y. Hatsukawa, et al.,J. Radioanalyt. Nucl. Chem. 248, (2001) 121-124,
(2) Y. Hatsukawa et al. Nucl. Instr. Meth. A482 (2002) 328-333,
(3)Y. Toh et al.,HealthPhys.,83 (2002), 110-113

原子炉：JRR-3、JRR-4　　装置：気送管

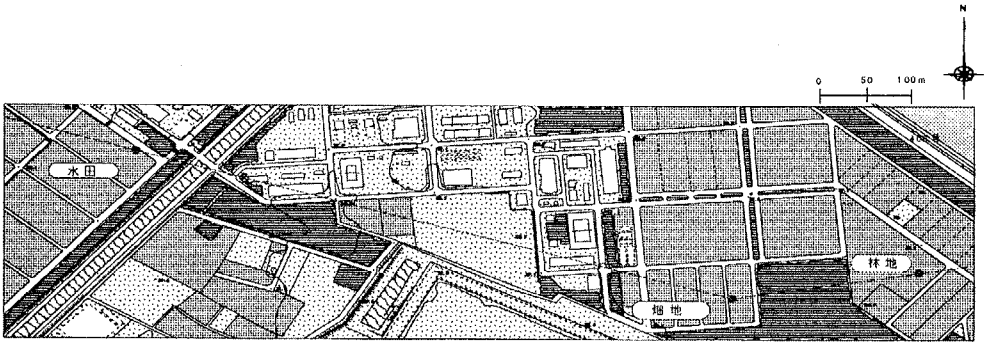
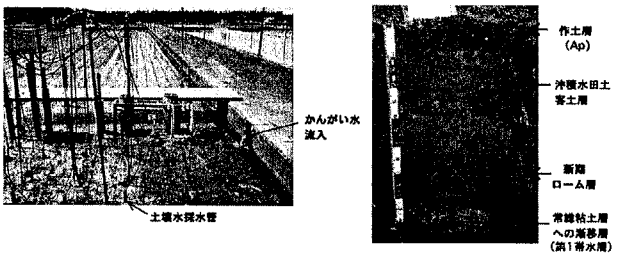


図１　実験圃場（つくば市農環研構内）の位置）



土壌水・地下水採水システム の配置　　土壌断面：台地造成田（細粒質灰色低地土）

写真１　水田圃場

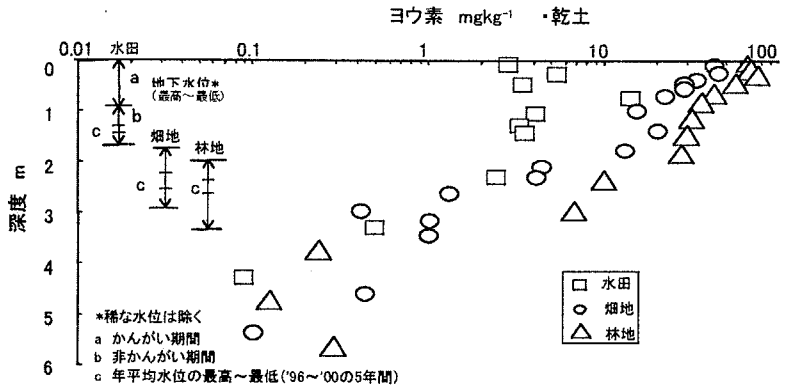
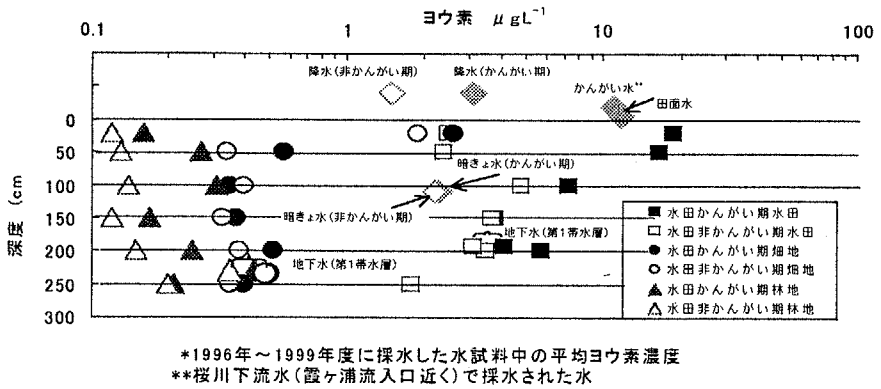


図２　土壌中ヨウ素の深度分布



*1996年～1999年度に採水した水試料中の平均ヨウ素濃度
**桜川下流水（霞ヶ浦流入口近く）で採水された水

図３　土壌水等試料中の平均ヨウ素濃度

3-8

宇宙物質の中性子放射化分析（3）

Neutron activation analysis of the extraterrestrial materials

海老原充、中原弘道、大浦泰嗣、G. W. Kallemeyn、S. K. Latif、箕輪はるか、平山圭輔
永峰隆行、瀬戸口美奈、柴剣宇、仲本朝嗣、西野朋恵、山口亮、李暁林
M. Ebihara, H. Nakahara, Y. Oura, G. W. Kallemeyn, S. K. Latif, H. Minowa, K. Hirayama,
T. Nagamine, M. Setoguchi, J. Chai, T. Nakamoto, T. Nishino, R. Yamaguchi, X. Li
東京都立大学大学院理学研究科
Graduate School of Science, Tokyo Metropolitan University
米田成一
S. Yoneda
国立科学博物館理工学研究部
Department of Science and Engineering, National Science Museum

1　はじめに

平成11年度から13年度にかけて、標記課題で原研施設を利用した共同研究を行った。この間に行った研究は2つに分類できる。1つは宇宙物質の非破壊中性子放射化分析（機器中性子放射化分析）（INAA）であり、もう一つは目的元素を絞って高感度な分析を行う放射化学的中性子放射化分析（RNAA）である。どちらにおいても、いくつかの異なる種類の隕石について、その元素含有量を正確に求め、その元素存在に基づいて、それらの隕石が形成された太陽系初期の物質の進化について考察することを目的とした。中性子放射化分析法は宇宙物質の元素分析法としてはもっとも有効な分析法であり、今後も宇宙物質の元素分析を行う上で、中性子放射化分析法を積極的に利用していく予定である。

本報告では、隕石中に微量に存在する希土類元素をRNAAで定量する新しい方法についてのべ、ついでその方法を用いてパラサイト隕石中のかんらん石に存在する超極微量の希土類元素をした結果について述べる。またINAAの例として、このパラサイト隕石中の金属部分の組成を求めた例についてのべる。これらの記述によって、中性子放射化分析が隕石試料の分析にどのように利用され、どのような成果が得られるかが明らかになるものと期待される。

地球や火星など太陽系の岩石型惑星は、原始太陽系星雲からの凝縮、集積、熱変成作用による分別を経て今日に至っている。上に述べたパラサイト隕石とは分化した隕石の1つであり、惑星の成因や内部構造の進化を推定する上で重要な隕石である。このパラサイトを構成するかんらん石中の微量元素存在度の存在度をもとに、これらの物質が太陽系初期にどのような変遷を経たかを議論することができる。特に希土類元素の相対存在度は、結晶化・溶融による分別過程を考察するのに適している。

2　微量希土類元素のRNAAによる定量法の確立

岩石中の微量な希土類元素(REE)の分析には、一般に中性子放射化分析法（NAA)および同位体

研究施設名と装置
JRR-3M, JRR-4

研究分野
宇宙化学

希釈質量分析法(MS-ID)が用いられている。MS-ID は感度の点で優れた分析法であるが、前処理にともなう誤差や試薬等からの汚染の可能性がある。NAA は、正確さの点で優れており、特に中性子照射後に化学分離操作を行なう RNAA を用いると、感度良く分析できる。岩石中の微量希土類元素を RNAA を用いて定量する場合、放射化学的妨害元素となるスカンジウム等を分離・除去する必要がある。本研究ではイオン交換分離法を用いた分離法を検討し、標準岩石試料に用いた。

〈実験操作〉

標準岩石試料 JP-1（かんらん岩）約 80mg を石英管に封入し、日本原子力研究所の原子炉 JRR-3 (1×10^{14} n/cm^{2}sec)で 100 時間、中性子照射した。約 1 週間冷却後、担体とともにるつぼ中でアルカリ熔融し、水酸化物およびフッ化物沈殿を生成して上澄みを分離した。沈殿を塩酸に溶かし、陰イオン交換樹脂を充填したカラムに通した。Fe, Cr などクロロ錯体を形成する元素は陰イオン交換樹脂に吸着し、希土類元素と分離される。溶出液から水酸化物沈殿として希土類元素を捕集し、臭化水素酸に溶解して、陽イオン交換カラムに通した。このカラムでは Sc が樹脂に吸着し、希土類元素は溶出する。この陽イオン交換樹脂による分離を 2 回繰り返した。溶出液 から水酸化物沈殿として希土類元素を回収し、少量の硝酸に溶かして一部を化学収率測定用に保存し、残りをろ紙上で滴下、乾燥させて密封し、ガンマ線測定用試料とした。(Fig.1)

〈ガンマ線スペクトル測定〉

ガンマ線の測定には、都立大学 RI 研究施設のゲルマニウム半導体検出器、および、日本原子力研究所の多重ガンマ線検出装置(GEMINI)を使用した。これは１２台のゲルマニウム検出器を球形に配置した装置で、複数のガンマ線を同時に測定し 2 次元マトリクスに展開するため、高いエネルギー分解能を持つ。各ゲルマニウム半導体検出器はゲルマニウム酸ビスマス(BGO)シンチレータ検出器で囲まれ、反同時計数することにより、コンプトン散乱によるバックグラウンドを低減している。この装置を使用して、都立大学の装置では ^{46}Sc のコンプトン散乱によるバックグラウンドのために検出できなかった ^{169}Yb、^{154}Eu を測定することができた。

〈化学収率測定〉

RNAA においては、目的元素の担体を添加してから放射化学分離操作を行ない、化学収率を求めて放射能測定値を補正する。化学収率の測定法としては従来、再放射化法を用いてきたが、この方法は場所や時間の制約が大きい。誘導結合プラズマ発光分析法(ICP-AES)は操作の簡便性、安全性、経済性などの点で優れた分析法である。感度や汚染の可能性の点では NAA に劣るものの、RNAA の化学収率測定に利用する場合は、担体として加える元素の量を ICP-AES の最適分析条件にあわせることができるので、正確な測定が可能である。したがって本研究では、ICP-AES を用いて RNAA の化学収率を測定する方法の検討を行なった。

分析感度および相互干渉を考慮し、La, Nd, Eu, Ho, Yb の 5 元素を定量元素として選んだ。内標準元素として Cd を加え、これら 5 元素と共に測定した。各元素間の相互干渉の程度を見積もるため、各元素ごとの標準溶液について、複数の波長で発光強度を測定した。その結果から最も干渉の少ない波長を測定波長として選定した。各元素における干渉は 1ppm あたり 0.007ppm 以下であり、測定濃度領域(0.5～2ppm)では約 1％の補正を行なった。また、定量精度を求めるため、試薬を調製した同一の溶液を繰り返して測定した。20～50 試料の一連の分析における分光強度の変動は<10％であり、内標準元素による補正を行なうと<6％になった。RNAA の化学収率測定の際には、1 時間ごとに標準試料を測定して分光強度の補正を行なった。収率測定の結果はそれぞれの試料で 20～60％であった。放射化学分離操作における希土類元素間での分別は見られなかった。

〈結果〉

標準岩石試料 JP-1 の希土類元素存在度を CI コンドライト隕石の存在度で規格化したパターンを Fig.2 に示す。定量値は RNAA による文献値[1]と良い一致を示している。しかし地質調査所(GSJ)から公表されている参考値と比較すると、軽希土類元素で系統的に低い値が得られた。おそ

らく地質調査所の値は汚染のため高い値を示す測定値も含まれているのではないかと思われる。

3 パラサイト隕石かんらん石中の超微量希土類元素のRNAAによる定量

パラサイトは石鉄隕石の一種で、鉄-ニッケル合金（metal）とかんらん石（olivine）が主成分である。鉄-ニッケル合金は分化した小惑星のコア（核）の主成分であり、かんらん石はマントル物質であると考えられるため、パラサイトは小惑星のコア-マントル境界で形成されたという考えが広く受け入れられているが、その形成過程は明らかではない。

パラサイトのかんらん石中の希土類元素存在度は、マントル物質であるかんらん石が隕石母天体内部で分離・結晶化した時の元素の分配状態を反映していると思われる。しかし、希土類元素はかんらん石の結晶に入りにくいため、存在度が低く、正確な分析は困難である。また、パラサイトは落下後かなりの年月が経過してから発見されることが多く、その間の風化の影響が著しい。地球表層の岩石や土壌は隕石に比べ希土類含有量が高く、わずかの汚染でも高い定量値が得られる。また、地表物質の希土類元素存在度はコンドライト隕石に比べて相対的に軽希土類に富むため、規格化したパターンに影響を及ぼす。

これまでに、RNAAとMS-IDによる測定結果の報告例がある。初期のRNAAによる測定ではコンドライトレベルの希土類元素が含まれていると報告された[2]。MS-IDによる測定は、試料を酸処理して分析したものであり、RNAAによる値より1から2桁低い値が得られた[3)4)]。そのためRNAAによる定量値は地球物質の汚染が完全に除去できていなかったとされた。MS-IDによる定量値をCIコンドライト隕石の値で規格化した希土類元素存在度パターンは、軽希土類元素と重希土類元素に富み中希土類付近に極小をもつ「V字型」パターンを示している。このような微量の希土類元素を分析した例は他にないため、パラサイトのかんらん石中の希土類元素はこのようなパターンを示すものとされ、分別過程の説明が試みられている。しかし、これをかんらん石の結晶構造から説明することは無理があるように思われる。

本研究では、あらかじめ確立した極微量希土類元素の定量法をパラサイト隕石に応用し、かんらん石本来の希土類元素存在度を求め、その規格化パターンから母天体でのかんらん石の晶出過程を考察した。

（実験）

パラサイトの塊を金槌で砕き、かんらん石の多結晶の塊を取り出した。顕微鏡下でグラインダーを使用し、金属部分と暗色に変色した結晶を削り取った。直径約0.5mmの粒を集め、約80mgを石英管に封入し、中性子照射した。照射後、化学分離操作前に、洗浄のため塩酸で10～20分表面を溶かした。実験操作、ガンマ線スペクトル測定、化学収率測定は前述の方法と同様である。

（結果と考察）

希土類元素存在度をCIコンドライト隕石の値で規格化したパターンをFig.3に示す。定量結果から次の2種類のパターンが得られた。(1)軽希土類に乏しく重希土類に富む右上がりの直線的なパターン。(2)軽希土類から中希土類にかけてほぼ平坦で重希土類に富むパターン。(1)のLaの値は上限値が得られたのみだが、もし重希土から中希土の直線上に位置するとするとコンドライト含有量の10^{-6}～10^{-7}になり、本分析法でもほとんど定量不可能である。地球表層の物質は相対的に軽希土類元素に富むので、もし地球起源物質の汚染を受けると相対的に軽希土類の存在度が高くなるはずである。よって(1)のパターンがかんらん石本来のパターンで、(2)のようなパターンを示す試料は地球起源物質による汚染を完全に除去できていないと思われる。これまでの文献値もおそらく汚染を受けた見かけのパターンであろう。このパターンは、かんらん石が平衡状態で晶出した場合の、分配係数から予想されるパターン[5]と整合的である。これは、このパラサイトの母天体からかんらん石が平衡状態で晶出したことを示唆している。

4 パラサイト隕石金属中のINAA

鉄-ニッケル合金からなる鉄隕石は、ppmレベルの親鉄元素を含み、その微量元素組成の違いをもとにグループ別に分類され、隕石母天体のマグ

マの進化史が議論されている[6]。パラサイト隕石も同様に金属部分の微量元素存在度をもとに、メイングループとそれ以外に分類されている[7]。メイングループ・パラサイトは、鉄隕石のIIIABグループと同じ（組成の）母天体から分化したものと考えられている。

〈実験〉

パラサイト隕石の金属部分をダイヤモンドカッターで切断し、2～3mm角の塊を切り出した。顕微鏡下でグラインダーを使用し、付着している錆などを削って除去し、金属部分だけを取り出した。20～100mgの塊をポリエチレン袋に封入し、照射用試料とした。立教大学原子炉TRIGAII原子炉(1.5×10^{12}n/cm2sec)で100秒中性子照射し、照射後約60秒後に100秒間ガンマ線スペクトル測定を行ない、Cu, Ge, Rhを定量した。その後、同一試料を30分照射して約1日後に約1000秒測定し、Ga, As, Auを定量した。数ヵ月冷却後、さらに6時間照射し、数日後に約5000秒測定し、Fe, Co, Ni, Irを定量した。

〈結果〉

Fe, Ni, Co, Cu, Ge, Ga, Au, As, Irおよび、パラサイト隕石ではいままでに報告例のなかったRhの定量値が得られた。Fig.4, 5はそれぞれ、AuとNi、GaとGeの相関図である。ほとんどの分析値は、報告されているパラサイトの値の範囲内にある。Fig.6には、パラサイトおよび鉄隕石中の親鉄元素存在度をニッケルの定量値で規格化した値を、鉄隕石(IIIAB)の値[8]と共に示した。パラサイトの値と鉄隕石の値を比較すると、Co, Cuの値には差がなく、Au, Asでは明らかにパラサイトの方が高い値を示している。Irでは鉄隕石間でのばらつきが大きく、パラサイトはその最も低い値に近い。これらの傾向はパラサイト隕石の金属部分はIIIAB鉄隕石と同じ起源を持ち、より分化が進んだ母天体のコアであるという推定7)を支持する。

References

1) M.Ebihara, S. Kimura, H Akaiwa (1994) Anal.Chem.351, 514-520.
2) R.A.Schmitt, R.H.Smith, D.A.Olehy (1964) Geochim.Cosmochim.Acta28, 67-86.
3) A. Masuda (1968) Earth Planet.Sci.Lett. 5, 59-62.
4) T.Saito, HShimizu, A.Masuda (1988) Geochim. Cosmochim. Acta 32, 159-182.
5) G.A.McKay (1986) Geochim. Cosmochim. Acta 50, 69-79.
6) W.R.Kelly, J.W.Larimer (1976) Geochim. Cosmochim. Acta 41, 93-111.
7) E.R.D.Scott (1977) Geochim. Cosmochim. Acta 41, 349-360.
8) J.T.Wasson, X.Ouyang, J.Wang, E.Jerde (1989) Geochim. Cosmochim. Acta 53, 735-744.

研究成果（発表論文）

（共同研究の期間にJRR-3M、JRR-4を用いて得られた成果を報告したもの）

1. 海老原充（1999）放射化分析は地球外物質の分析にどのくらい有効か？鉱物学雑誌 28, 131-138.
2. P. Kong, M. Ebihara and H. Palme (1999) Siderophile elements in Martian meteorites and implications for core formation in Mars. Geochim. Cosmochim. Acta 63, 1865-1875.
3. P. Kong, M. Ebihara and H. Palme (1999) Distribution of siderophile elements in CR chondrites: Evidence for evaporation and recondensationduring chondrule formation. Geochim. Cosmochim. Acta 63, 2637-2652.
4. M. Ebihara, K. Shinotsuka, H. Ozaki and Y. Oura (2000) Critical evaluation of CI chondrites as the solar system standard of elemental abundances. In *Origin of the elements in the solar system* (ed. O. K. Manuel), pp. 289-300, Kluwer Academic/PlenumPublishers, New York.
5. P. Kumar, M. Ebihara, and S. K. Bhattacharya(2001) ^{196}Hg/^{202}Hg ratio and Hg content in meteorites and terrestrial standard rocks: A RNAA study. Geochem.J. 35, 101-116.
6. M. K. Weisberg, M. Prinz, R. N. Clayton, T. K. Mayeda, N. Sugiura, S. Zashu and M. Ebihara (2001) A new metal-rich chondrite grouplet. Meteorit. Planet. Sci. 36, 401-418.

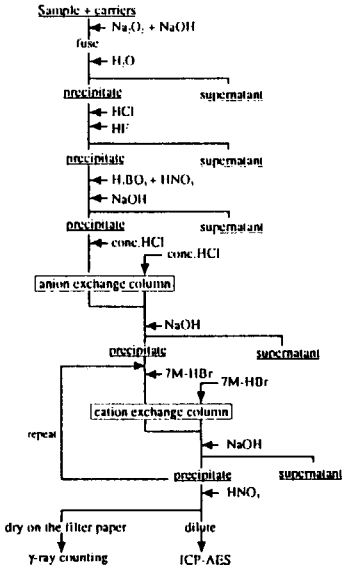


Fig.1 Procedure of radiochemical separation for REE

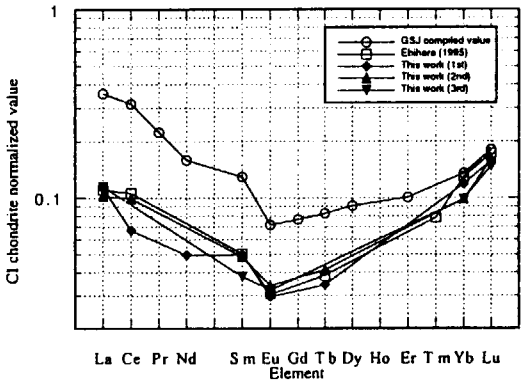


Fig.2 CI chondrite normalized REE abundances in geological standard rock, JP-1 (peridotite)

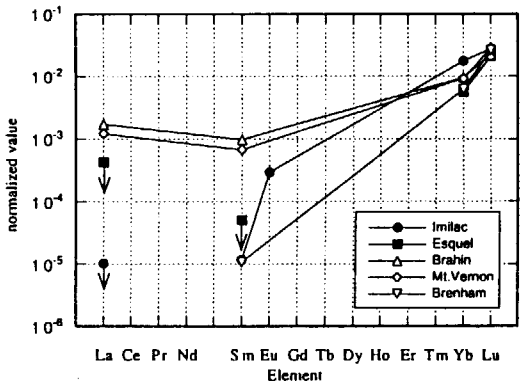


Fig.3 CI chondrite normalized REE abundances in pallasite olivine

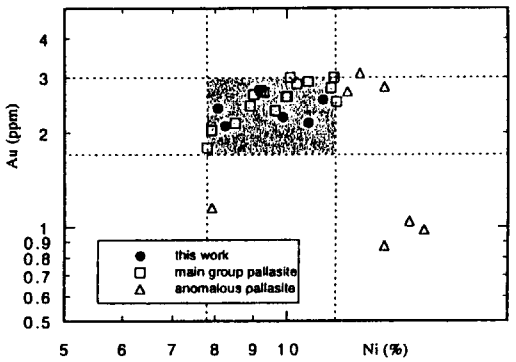


Fig.4 Logarithmic Au-Ni diagram for pallasite metal
Elemental abundances in main group pallasites are 7.8-11.7% for Ni and 1.7-3.0ppm for Au. Data from Scott (1977)

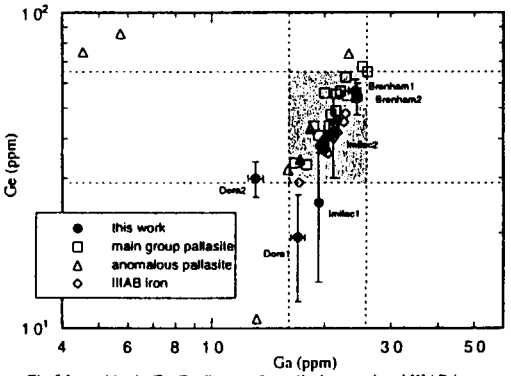


Fig.5 Logarithmic Ge-Ga diagram for pallasite metal and IIIAB iron meteorite
Elemental abundances in main group pallasites are 16-26ppm for Ga and 29-65ppm for Ge. Data from Scott (1977)

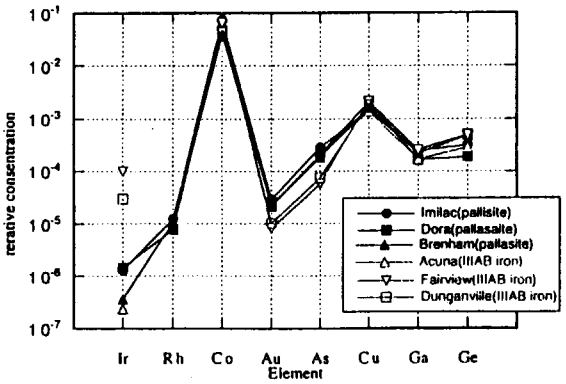


Fig.6 Ni-normalized elemental abundances in pallasite metal and iron meteorite
Data of iron meteorite from Wasson et al. (1989)

3-9

南九州の四万十帯に関するＩＮＡＡとＦＴ年代測定

INAA and FTD for sedimentary rocks from the Shimanto Terrane of South Kyushu, Japan

鹿児島大学教育学部
鈴木達郎

Tatsuo Suzuki
Faculty of Education, Kagoshima University

1. 緒言

南九州は地質学的には西南日本外帯に属し、鹿児島県はそのなかでもほとんどが四万十帯に含まれる。四万十帯は白亜系とみられる四万十帯北帯と古第三系とみられる四万十帯南帯に分けられている（例えば、宇都ほか, 1997)。薩摩半島や北薩地方の基盤をなすものはほぼ四万十帯北帯に属する堆積岩類であり、それを新第三紀以降の火山岩類が覆っている。とくに第四紀のいわゆるシラスなど大規模火砕流に厚く覆われている。薩摩半島地域などの四万十帯については、近接地域に橋本（1962a・1962b）や米田・岩松（1987）はあるが、この地域には通産省資源エネルギー庁（1981）による調査・研究があるだけで従来その地質構造のみならず堆積岩類の詳細についての研究は不充分であった。その地質構造についても宮崎県・大分県で近年詳しく調べられている（寺岡・奥村, 1992；など）ようなものなのか、また鹿児島湾形成にともなう鹿児島地溝などがあるために、それとは異なったものなのか、ということについても良好な露頭が不足するために地層の追跡が不充分で、未だ明らかになっているとはいい難い。この地域においては堆積岩類の詳細な性質を検討することがそのような問題解決にも有効であると考えられる。

一方機器中性子放射化分析（INAA）によれば、多数の試料について多元素同時分析が可能であるので、堆積岩類のキャラクタリゼーションが容易にできると期待できる。またフィッション・トラック年代測定によれば、砕屑性のジルコン・アパタイトを含めてその起源を議論するデータが容易に得られるだけでなく、その地域の熱史についてのデータも得られると期待できる。これらの観点から南九州地域の基盤をなす古期岩類、とくに四万十帯における堆積岩類の検討を行ってきている。現在まだ進行中の部分も多いが、今までに得られた結果をここに報告する。

2. 分析試料

南九州に広く分布する四万十帯から，鹿児島県下の阿久根市、日置郡吹上町、日置郡金峰町、川辺郡川辺町、鹿児島市、川辺郡知覧町、揖宿郡喜入町、川辺郡笠沙町から頁岩・砂岩を採取した。砂岩試料はとくに厚層の砂岩層を選んでいる。今回 INAA による分析値を報告するのは、砂岩 8 点、頁岩 4 点の合計 12 点である（Table 1)。また日置郡東市来町江口浜、川辺郡笠沙町高崎から花崗岩質岩礫を見出してフィッション・トラック年代測定用の試料とした。

Table 1. 分析試料

Sp No.	岩石名	採取地
S85	細粒砂岩	阿久根市大川表川内
H71	頁岩	日置郡吹上町北平
S87	中粒砂岩	日置郡吹上町北平
H68	頁岩	日置郡金峰町和田
H63	頁岩	日置郡金峰町和田
S88	細粒砂岩	日置郡金峰町厚佐野
S82	中粒砂岩	日置郡金峰町池辺門前
H77	頁岩	日置郡金峰町金峰山
S83	中粒砂岩	日置郡金峰町白川
S89	中粒砂岩	日置郡金峰町新山
S90	中粒砂岩	揖宿郡喜入町樋高
S86	細粒砂岩	川辺郡笠沙町高崎
Eg-Zr	花崗岩礫	日置郡東市来町江口浜
Kz-Zr	花崗岩礫	川辺郡笠沙町高崎

3. 中性子放射化分析

中性子放射化分析法による元素定量のための試料作成は以下のようにおこなった。採取したそれぞれ数 kg 以上の原岩試料をまず数 cm 大にして，さらにジョークラッシャーで粉砕し数 mm 大にする。これを縮分器で縮分して数

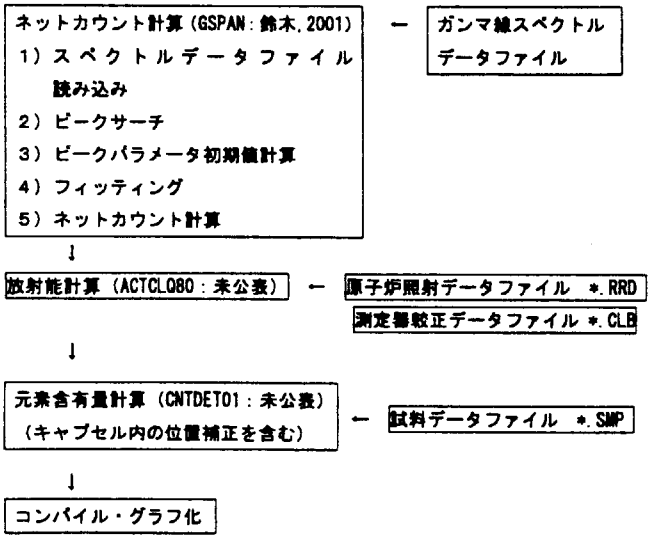


Fig.1. ＩNAAにおけるデータ解析のながれ

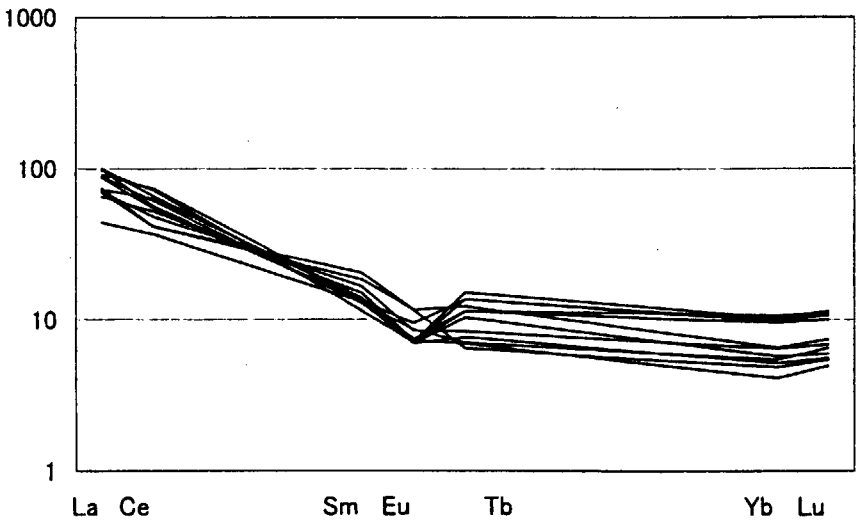


Fig.2 四万十帯砂岩・頁岩のＩＮＡＡによるランタノイド組成パターン

Table 2. 四万十帯砂岩・頁岩のＩＮＡＡによる元素組成

Element or Constituent	Nuclide	S85	H71	S87	H68	H63	S88	S82
Na_2O (%)	Na-24	4.94 ±0.017	4.22 ±0.027	4.29 ±0.018	3.34 ±0.021	1.54 ±0.012	2.59 ±0.013	4.64 ±0.015
Sc (ppm)	Sc-46	7.96 ±0.031	14.99 ±0.051	5.78 ±0.025	12.86 ±0.044	14.17 ±0.047	14.75 ±0.048	6.87 ±0.027
Cr (ppm)	Cr-51	43.66 ±4.07	66.21 ±6.19	35.66 ±3.34	64.93 ±6.01	61.19 ±5.68	77.43 ±7.14	40.46 ±3.77
Fe_2O_3(%)	Fe-59	3.29 ±0.027	5.21 ±0.039	2.37 ±0.022	5.14 ±0.036	5.34 ±0.037	5.9 ±0.040	3.07 ±0.025
Co (ppm)	Co-60	7.31 ±0.145	14.31 ±0.247	5.56 ±0.126	12.36 ±0.202	13.44 ±0.214	15.16 ±0.231	6.47 ±0.132
Rb (ppm)	Rb-86	71.62 ±21.25	171.47 ±47.72	73.80 ±21.40	113.81 ±31.90	187.62 ±52.04	137.23 ±38.37	35.07 ±8.89
Sr (ppm)	Sr-85	552.30 ±45.56	302.43 ±55.47	327.17 ±32.84	245.45 ±38.95	- -	225.67 ±36.33	343.91 ±34.84
Zr (ppm)	Zr-95	95.11 ±20.83	129.46 ±27.29	84.20 ±14.83	142.88 ±25.00	- -	153.85 ±27.12	116.46 ±18.23
Cs (ppm)	Cs-134	1.36 ±0.203	27.15 ±3.21	1.10 ±0.162	14.78 ±1.75	14.01 ±1.66	9.21 ±1.10	1.28 ±0.183
Ba (ppm)	Ba-131	599.16 ±50.48	455.52 ±69.94	507.84 ±46.26	311.51 ±41.40	326.06 ±62.20	354.80 ±63.51	210.41 ±25.77
La (ppm)	La-140	25.84 ±0.302	36.93 ±0.448	27.14 ±0.324	36.27 ±0.420	33.45 ±0.382	32.61 ±0.364	26.54 ±0.299
Ce (ppm)	Ce-141	45.89 ±0.681	62.97 ±0.978	39.47 ±0.570	53.94 ±0.737	70.96 ±0.949	58.39 ±0.827	60.88 ±0.830
Sm (ppm)	Sm-153	4.12 ±0.025	6.55 ±0.028	3.68 ±0.024	6.24 ±0.036	5.30 ±0.032	6.28 ±0.035	3.88 ±0.023
Eu (ppm)	Eu-152	0.978 ±0.021	1.27 ±0.032	0.881 ±0.020	1.11 ±0.023	0.890 ±0.022	1.30 ±0.028	0.942 ±0.021
Tb (ppm)	Tb-160	0.463 ±0.091	0.656 ±0.133	0.355 ±0.077	0.748 ±0.135	0.640 ±0.129	0.824 ±0.146	0.414 ±0.087
Yb (ppm)	Yb-175	1.58 ±0.130	2.67 ±0.209	1.19 ±0.103	2.48 ±0.191	2.35 ±0.181	2.56 ±0.196	1.27 ±0.109
Lu (ppm)	Lu-177	0.259 ±0.027	0.420 ±0.042	0.205 ±0.022	0.405 ±0.040	0.381 ±0.038	0.435 ±0.043	0.211 ±0.023
Hf (ppm)	Hf-181	3.66 ±0.11	4.40 ±0.153	3.13 ±0.096	4.89 ±0.142	3.96 ±0.128	4.50 ±0.137	3.76 ±0.108
Ta (ppm)	Ta-182	0.483 ±0.067	0.962 ±0.119	0.636 ±0.074	0.913 ±0.106	1.07 ±0.119	0.911 ±0.106	0.568 ±0.073
Th (ppm)	Pa-233	7.50 ±0.38	13.97 ±0.678	8.43 ±0.421	12.87 ±0.622	14.06 ±0.677	12.45 ±0.605	8.14 ±0.411
U (ppm)	Np-239	1.75 ±0.311	2.62 ±0.463	1.70 ±0.303	2.64 ±0.454	2.84 ±0.476	2.69 ±0.458	1.51 ±0.278

Standard = AGV1

Table 2. 四万十帯砂岩・頁岩のＩＮＡＡによる元素組成（続き）

Element or Constituent	Nuclide	H77	S83	S89	S90	S86	MAG	SGR
Na2O (%)	Na-24	2.33 ±0.022	3.89 ±0.014	4.06 ±0.018	4.86 ±0.024	4.39 ±0.018	3.84 ±0.012	3.43 ±0.013
Sc (ppm)	Sc-46	14.22 ±0.049	6.35 ±0.026	6.2 ±0.025	10.12 ±0.039	9.34 ±0.037	17.00 ±0.048	4.81 ±0.019
Cr (ppm)	Cr-51	64.32 ±5.98	37.36 ±3.49	34.73 ±3.25	28.95 ±2.86	45.45 ±4.30	107.59 ±9.83	31.47 ±2.92
Fe2O3 (%)	Fe-59	5.35 ±0.039	2.7 ±0.023	2.48 ±0.022	3.15 ±0.029	3.79 ±0.032	6.79 ±0.038	2.68 ±0.020
Co (ppm)	Co-60	12.69 ±0.222	5.95 ±0.126	6.22 ±0.125	3.44 ±0.120	9.47 ±0.187	21.11 ±0.265	11.33 ±0.161
Rb (ppm)	Rb-86	132.68 ±37.03	69.12 ±0.68	78.06 ±22.33	55.03 ±16.48	60.13 ±18.42	143.85 ±41.27	90.57 ±26.95
Sr (ppm)	Sr-85	269.67 ±27.00	358.3 ±33.88	354.76 ±32.79	204.22 ±36.84	367.01 ±44.18	- -	340.36 ±28.26
Zr (ppm)	Zr-95	- -	114.09 ±20.21	83.77 ±21.82	- -	114.57 ±21.95	117.75 ±29.70	108.97 ±16.26
Cs (ppm)	Cs-134	8.71 ±1.04	1.25 ±0.181	1.62 ±0.217	1.40 ±0.219	2.19 ±0.303	9.13 ±1.08	5.34 ±0.636
Ba (ppm)	Ba-131	- -	779.99 ±54.75	489.89 ±44.70	534.21 ±70.57	472.57 ±62.12	450.81 ±49.48	256.72 ±30.94
La (ppm)	La-140	35.69 ±0.441	31.94 ±0.348	23.90 ±0.29	16.14 ±0.253	25.40 ±0.316	40.79 ±0.418	20.65 ±0.266
Ce (ppm)	Ce-141	68.81 ±0.994	52.26 ±0.752	49.81 ±0.710	35.21 ±0.739	39.73 ±0.666	84.91 ±0.961	43.14 ±0.587
Sm (ppm)	Sm-153	6.14 ±0.038	4.51 ±0.026	1.91 ±0.103	3.00 ±0.023	4.25 ±0.027	7.24 ±0.038	1.77 ±0.085
Eu (ppm)	Eu-152	1.17 ±0.027	1.05 ±0.020	0.850 ±0.017	0.745 ±0.021	1.01 ±0.025	1.42 ±0.024	0.496 ±0.013
Tb (ppm)	Tb-160	0.746 ±0.140	0.542 ±0.102	0.366 ±0.077	0.389 ±0.099	0.639 ±0.092	1.04 ±0.154	0.317 ±0.063
Yb (ppm)	Yb-175	2.40 ±0.189	1.41 ±0.118	1.01 ±0.089	1.34 ±0.115	1.61 ±0.135	2.51 ±0.208	0.968 ±0.1
Lu (ppm)	Lu-177	0.410 ±0.042	0.226 ±0.025	0.187 ±0.02	0.246 ±0.027	0.281 ±0.03	0.381 ±0.041	0.295 ±0.029
Hf (ppm)	Hf-181	3.97 ±0.133	3.54 ±0.103	3.18 ±0.095	2.78 ±0.114	4.28 ±0.136	3.51 ±0.101	1.23 ±0.053
Ta (ppm)	Ta-182	1.03 ±0.117	0.538 ±0.068	0.514 ±0.065	0.433 ±0.055	0.477 ±0.082	1.19 ±0.114	0.412 ±0.051
Th (ppm)	Pa-233	13.25 ±0.644	7.73 ±0.392	7.56 ±0.375	5.61 ±0.296	7.72 ±0.393	11.83 ±0.602	5.35 ±0.306
U (ppm)	Np-239	2.87 ±0.498	1.46 ±0.27	1.4 ±0.258	1.26 ±0.257	1.87 ±0.24	2.65 ±0.485	5.3 ±0.853

Standard = AGV1

100 g程度にする。さらに縮分して数g程度にしたものをメノウ製ポットミルで微粉末とする。この粉末試料を110℃1晩乾燥し、ポリエチレン製の薄手の袋に100mgから200mg程度を秤量して照射試料とする。目的試料20個から30個にUSGS（アメリカ合衆国地質調査所）の標準岩石試料G-2・AGV-1およびGSJ（通産省工業技術院地質調査所，現 産業技術総合研究所）の標準岩石試料JR-1・JB1aを加えて順序をチェックして照射用キャプセルに詰める。これを日本原子力研究所東海研究所の研究用原子炉JRR-3M・JRR-4の中性子フルエンスに合わせて時間を調節して目的に適した照射施設で中性子照射をおこなう。今回はJRR-4のTパイプ350kW出力時で90分、100kW出力時で5時間、またJRR-3M PN2では15分間の照射をおこなった。JRR-4のTパイプでは水中で照射するため防水に注意が必要であるが、3号炉気送管でインナーとして使用されるバイアルに試料を詰めその口を接着して封じることで目的を達しえた。照射後3日ないし1週間程度冷却後，中寿命核種定量のため，また2週間ないし1ヶ月後に長寿命核種の定量のための測定をおこなった。ガンマ線スペクトル測定では中寿命核種に関しては、大学開放研の実験室で、他の核種に関しては鹿児島大学共同利用RI実験室において実施した。

ガンマ線スペクトロメトリーは，フロッピーディスクに保存したスペクトルデータを用いて，まずネットカウント計算（GSPAN：鈴木，2001b），ついで放射能計算（ACTCLQ80：鈴木，未公表），元素定量計算（CONTDET7：鈴木，未公表）の計算プログラムを使用しておこなった。その解析に必要な計算プログラムとデータファイルをフローチャートとしてFig.1に示した。

定量計算ではSiO_2成分として試料の岩質の比較的近いUSGS（アメリカ合衆国地質調査所）のAGV1のデータ（Potts et al., 1992）を標準値としGSJ（旧 工業技術院地質調査所，現 産業技術総合研究所）のJR1・JB1aを位置補正のためのワーキングスタンダードとして使用している。

得られた分析結果をTable 2に示す。USGS（アメリカ合衆国地質調査所）の標準岩石試料の堆積岩試料であるMAG・SGRについての分析結果も併せて示したが、現在知られるデータ（Potts ほか，1992）と良く一致している。Table 2の試料の配列順序はTable1に従って、ほぼ北から南の順である。ランタノイドのMasuda-Corryellプロットを Fig.2に示した。

これらのデータからは、砂岩・頁岩の相違はあるが、大略似たような元素組成であり、まだ特徴づけるためには充分とはいえない。しかし詳細に見るとき砂岩のなかでも区分できる可能性はあると見られる。また四万十帯中の鹿児島湾から29,000年前に噴出した本邦有数の大規模火砕流堆積物である入戸火砕流堆積物のINAAによる元素組成（鈴木，2002）とほぼ似たものであることは極めて示唆にとみ、今後の重要な研究課題である。さらに広域に試料を収集し、この地域の地質の帯状構造と微量元素組成に関連があるのかどうかなどを詳細に検討する必要があると思われる。

4. フィッション・トラック年代測定

鹿児島県日置郡東市来町江口浜、川辺郡笠沙町高崎に分布する四万十帯相当層から見出した花崗岩質岩礫からジルコン・スフェイン・アパタイトを抽出してフィッション・トラック年代の測定を試みた。中性子照射はJRR-3M PN1で20秒間おこなった。また外部ディテクターとして使用した白雲母は46%HF 23℃ 12分間、ジルコンはNaOH・KOH・($LiOH \cdot H_2O$)の共融液（Zaun and Wagner, 1985）200℃ 6～8時間でエッチングして、適正なトラックを検出しえた。なお年代測定値の算出にあたっては、モニターガラスとしてCN1を、年代標準試料としてフィッシュ・キャニオン・タフのジルコン（FC3）を使用したゼータ法によった。

今回の測定では、江口浜の試料では、7.3Maが、笠沙町高崎の試料からは70.1Maの年代値が得られた。その詳細はB0値による較正法（Suzuki, 2000）との相互検討のうえ別に報告する。笠沙町高崎のジルコン試料では測定困難なグレインもあるが計測できないトラック密度ではない。江口浜の試料では良好なトラックが検出でき、両者ともほぼ信頼できる結果であるといえる。従ってその地質学的解釈が必要である。これらの試料はともに白亜紀の堆積岩に含まれる礫であるから、その初生的年代値は白亜紀以前の数値が期待される。従って笠沙町高崎の試料はその堆積時に削剥レベルに達していたほぼ同年代の花崗岩質岩がもたらされたと説明できるが、江口浜の試料では熱的イベントにより若返ったと考えざるをえない。実際、江口浜周辺の四万十相当層には14Maの花崗岩質岩の貫入が見られるほか、一部にはそれ以降の活動と見られる石英脈などもある。薩摩半島における金鉱床生成に関わる鉱化作用の時期のひとつが7Maにあることを併せて考える

ときこの測定結果は極めて興味深い。その解釈の是非はこの地域を含む広域での砂岩中の砕屑性ジルコンの年代測定によって明らかになると思われるので、現在その測定を準備中である。

5. まとめと今後の課題

南九州とくに鹿児島県薩摩半島地域の四万十帯の堆積岩類から砂岩・頁岩を採取してその放射化分析による元素組成分析を試み、12 点の分析値を検討し、この地域の堆積岩類の特徴を明らかにした。またこれらの堆積岩類の供給源に関わる問題解決に有効な花崗岩質岩礫試料のフィッション・トラック年代値の一部を報告した。

これらの調査・研究をさらに広域に広げて南九州四万十帯の地質学的特徴、とくに中生代白亜紀以降の堆積史・熱史を明らかにしていきたい。

6. 謝辞

一部の試料採取については、鹿児島大学教育学部地学教室（当時）の冨田　裕・山口幸作・税所篤司の諸氏の助力があった。また試料の中性子照射とそのガンマ線測定については、東京大学原子力研究総合センター東海分室大学開放研究室・鹿児島大学共同利用 RI 実験室にお世話になった。これら関係各位に深甚の謝意を表する。

7. 引用文献

橋本　勇（1962a）：鹿児島県北薩地方の時代未詳層群の層序と構造．九大教養部地学研報．8，p.47-62.

橋本　勇（1962b）：鹿児島県野間池付近の中生界の層序と構造．九大教養部地学研報．8，p.63-70.

松本達郎・大塚裕之・大木公彦（1973）：鹿児島県下の四万十帯から産出した白亜紀化石．地質雑，79，p.703-704.

Potts, P.J., Tindle, A.G. and Webb, P.C. (1992): *Geochemical reference material compositions*. Whittles Publishing. 313pp.

Suzuki, T. (2000): B_0 value of uranium doped glasses: a proposal for the standardization of fission track ages. *On Track*, Vol.10, No.2, p.9-10.

鈴木達郎（2001）：GSPAN：ガンマ線スペクトル解析プログラム．鹿児島大学教育学部研究紀要（自然科学編），Vol.52，p.33-44.

鈴木達郎（2002）：中性子放射化分析による入戸火砕流堆積物の微量元素組成．鹿児島大学教育学部研究紀要（自然科学編），Vol.53，p.29-44

寺岡易司・奥村公男（1992）：四万十帯北帯の構造区分と白亜紀砂岩組成．地質学論集，38，p.261-270.

通産省資源エネルギー庁（1981）：昭和 53 年度広域調査報告書「北薩・串木野地域」．92 p．

宇都浩三・阪口圭一・寺岡易司・奥村公男（1997）：20 万分の 1 地質図「鹿児島」．通産省地質調査所.

Zaun, P.E. and Wagner, G. (1985): Fission-track stability in zircons under geological conditions. *Nucl. Tracks*, 10(3), p.303-307.

米田茂夫・岩松　暉（1987）：鹿児島県北薩地方の四万十累層群の層序と地質構造．地質雑，93，p.881-895.

8. 成果の発表

Suzuki, T. (2002): Neutron absorption in NIST RSM 963 glass estimated by fission-track analysis and gamma-ray spectrometry. Abst. 21th Internat. Conf. Nucl. Tracks in Solids, New Delhi, India. (in press).

Suzuki, T. (2002): Detection efficiency of fission-track in glasses estimated by spike irradiation technique. Abst. 21th Internat. Conf. Nucl. Tracks in Solids, New Delhi, India. (in press)

Suzuki, T. (2002): Fission track dating of a Moldavite using B0 age calibration. Abst. 21th Internat. Conf. Nucl. Tracks in Solids, New Delhi, India. (in press)

鈴木達郎（2002）：等温プラトー法および B0 法を用いたガラスのフィッション・トラック年代測定．地球化学会 2002 年会講演要旨集（印刷中）

鈴木達郎（2002）：中性子放射化分析．RI センターニュース（鹿児島大学アイソトープ総合センター），No.2, p.2-3

鈴木達郎（2002）：中性子照射場の特性からみた放射化分析．k0 標準化放射化分析研究会（平成 14 年 3 月 29 日、日本原子力研究所東海研究所）

鈴木達郎（2002）：中性子放射化分析による入戸火砕流堆積物の微量元素組成．鹿児島大学教育学部研究紀要（自然科学編），Vol.53，p.29-44

鈴木達郎（2002）：フィッション・トラック年代測定における中性子モニター用標準ガラスの再検討．立教大学原子炉利用共同研究成

果報告書 UTRCN-29, p.187-191
鈴木達郎 (2001)： B_0 較正法によるフィッション・トラック年代測定値の標準化. 日本火山学会講演予稿集, 2001, No.2, p.49
鈴木達郎 (2001)：中性子放射化分析によるシラスの微量元素組成. 平成 13 年度鹿児島県新技術開発推進協議会研究成果報告会 (平成 13 年 7 月 16 日, 鹿児島大学稲盛会館).
鈴木達郎 (2001)：中性子放射化分析によるシラスの微量元素組成. 鹿児島県新技術開発推進協議会調査研究報告 No.38, p.17-26.
鈴木達郎 (2001)： GSPAN：ガンマ線スペクトル解析プログラム. 鹿児島大学教育学部研究紀要 (自然科学編), Vol.52, p.33-44.
Suzuki, T. (2000): B_0 value of uranium doped glasses: a proposal for the standardization of fission track ages. *On Track*, Vol.10, No.2, p.9-10.
Suzuki, T. (2000): B_0 value of dosimeter glasses for fission-track dating. Absts. 20th Internat. Conf. Nucl. Tracks in Solids, Portoroz, Slovenia, p.66.
Suzuki, T. (2000): Obsidian fission-track dating using lutetium, zirconium and gold neutron monitors. Geol. Soc. Australia Absts. Ser. No.58, Absts. 9 th Internat. Conf. Fission Track Dating and Thermochronology, Lorne, Australia, p.311-312.
鈴木達郎 (2000)：黒曜石のフィッション・トラック年代測定値の標準化--とくに Au・Zr モニターによる放射化反応率測定の試み. JAERI Review 2000-004, p.354-357.

3-10 中性子放射化分析による環境汚染指標生物ダンゴムシの検討

川西幸子[1]、野川憲夫[2]、澤幡浩之[3]、森 実[4]

Biological Monitoring of Pollution on Armadillidium vulgare (Latreille) by instrumental Neutron Activation Analysis

Sachiko Kawanishi, Norio Nogawa, Hiroyuki Sawahata, Minoru Mori

1.武蔵野短期大学 Musashino Junior College; 2.東京大学アイソトープ総合センター RadioisotopeCenterforNuclear Science and Technology; The University of Tokyo; 3.東京大学原子力研究総合センター 東海分室 大学開放研究室 Research Center for Nuclear Science and Technology, The University of Tokyo; 4.東京大学生産技術研究所 Institute of Industrial Science, The University of Tokyo

1．研究の目的と意義

大気環境汚染、特に粒子状物質汚染調査の一環として、環境指標になり得るものを検討することは、人を含めた生態系への環境汚染の影響を把握する意味で必要である。陸生等脚類の Armadillidium vulgare(Latreille) は乾燥にもかなり耐え、食性が広く、主として、落ち葉や朽ち木、あるいは生葉、野菜、節足動物の死骸なども食べる。行動範囲も狭く、寿命は普通 2～3年である。地域の環境状況を反映している可能性がある。このテーマに関係する文献は、山本ら[1)]（福岡県衛生公害センター）が、重金属 Cd,Cu,Pb,Zn を原子吸光で測定し、Cd,Cu,Zn について生物濃縮を認めている。また、D.Drobune ら[2)]は陸生等脚類の他種 Porcelio scaber, Qniscus asellus において、生態毒物学室内実験を行い、Co をカエデ葉に添加し、500μg／g以上で毒性よりも摂食抑制が出ると報告している。本研究はまず汚染元素を摂取するかどうか、また摂取した場合の汚染元素の保持能力をトレーサー実験により検討した。次に、都区部を中心として近郊各地から、試料を集め、中性子放射化分析により、保有元素の分析を行い汚染マップを作成した。

2．実験方法

2．1 代謝挙動の検討

汚染元素の例として、Sb のアイソトープによるトレーサー実験を行った。^{124}Sb（半減期 60 日、中性子放射化した金属Ｓｂ粒子を王水に溶解し NaOH で中和した溶液）を 馬鈴薯（一辺約 1.5ｃｍ 立方体）に添加した飼料で3日間飼育し、無添加飼料に切り替えて、死亡まで経過を３５日間調べた。放射能の体内残量は各段階で個体を水洗し，コブラ（クワンタム）5003 自動ガンマーカウンター（PACKARD）て測定した。

2．2 摂取後体内保持元素量の検討

馬鈴薯飼料〈一辺約 1.5ｃｍ立方体〉に Co,Ce,Sb,Zn,Ba 各 10ppm, Sc,Fe 各5ppm,pH6.4 調整試薬を添加して飼育３日後の個体を、無添加試料で飼育した対照個体と共に、中性子放射化分析により、この７元素を定量し比較した。

2．3 吸収部位（甲殻部と他部位）の検討

フィールドの廃棄物焼却炉近傍 2 個所、A(都区)および B(川崎市)地点より採集した 3 個体の平均値を中性子放射化分析＊により算出した。

2．4 東京都 23 区および近隣市部のフィールド調査

〔2000 年5 月 23 日～2000 年6 月 30 日〕 1 区および市において 1～3 個所で、原則として成虫、雄、３個体を目安に採集したが、見つからない所は死体、幼生を集めた。また、その近傍の食餌落葉を同時に採集した。採集した試料は水洗し、ろ紙、キムワイプで拭き取り、デシケーターで恒量化するまで乾燥後、二重のポリエチレン袋封入し、更にろ紙（No. 51A）を挟んで閉じ、中性子放射化分析により、前記の７元素を定量した。

研究施設と装置名：日本原子力研究所東海研究所 JRR-3 Autosamplechanger Ge-SSD、東京大学アイソトープ総合センター AutosamplechangerSC-100L

研究分野：環境科学

3．分析結果と考察

3．1 汚染元素の保持能力

^{124}Sb による室内アイソトープ実験の結果は、多量に摂取した場合、排出しながらも、40～80%保持したまま死に至っている。一方、低量摂取の場合は、長生き出来て 5%保持して死亡した。いずれも例数が少なく、数値的に結論を出すことは出来ないが、傾向が読み取れる。少なくとも、高い保持量が出た場合、汚染の検知に役立つと思われる。

3．2 吸収部位の検討

フィールドで採集していると、死骸があり、特に甲殻の残骸が見つかることがある。この部位で汚染調査が出来ればよく、厳密な検討ではないが、甲殻部に汚染元素が浸透しているかどうかを調べた。この 7 種の元素で、他の部位と共に浸透している元素は Ce 以外すべてに認められ、Ba 濃度は他部位より高く、付近の土壌の濃度よりも高い。このことは死骸の甲殻が残る場合、生体でなくても環境調査が出来る可能性がある。

3．3 東京都 23 区および近隣市部のフィー ルド調査

東京都 23 区および近隣 25 市部、合計 48 地域の 59 個所で Armadillidium vulgare を採集した。この 7 元素の一部、Co と Sb につき、地図上に濃度分布として表わしたのが図 1 である。ただし、あくまでもそのスポットの反映であり、地域を代表する数値ではないことを前提としている。 また、個体と同所の葉成分の関係を調べた。 これらの結果から、次のような事が考えられる。

（1）高濃度地点と環境汚染負荷

幾つかの高濃度地点は環境汚染負荷が大きいと推定される地点であった。特に、ほぼすべての元素で突出した値を示した［港区―1］は生体が見つからず、死骸のみであった。都心の中でも最も中心部であるが、公園でも発見出来なかった。一方、線路を横切る地下道でつながった飛び地である［港区―2］は生体が存在し、逆に 7 元素とも低めである。他のピーク、［世田谷区―1］は環状 8 号に面し、死骸も多くみられた場所である。［杉並区－1］は焼却炉近傍であり、［川崎市］も廃棄物処理場近傍であった。すべての元素ではないが、高い傾向が見られた。また、近隣市部では、所沢市、小平市、海老名市に高い値がでている。また、揮発性人為発生源汚染元素[3) 4)]として注目されている Sb についても、［港区―1］に続き、［世田谷区―1］、［新宿区－2］、［台東区］、［小平市］に、高い傾向がみられる。

（2）生物濃縮

食餌葉と個体の汚染濃度を比較した結果は、ばらつきは大きいが、幾何平均で、Zn, Ba, Co が個体に濃縮されている。特に、［港区－1］は 7 元素全てで葉を上まわり、最高 30 倍にもなっている。このことは分析試料として、葉植物に対して二次資料ではあるが、生物濃縮を示し、1 ヶ月～2 年の過去を含めた現在を反映している試料として意味があると考えられる。

（3）分析方法としての意義

文献 1）における Cd,Cu,Zn の分析法は原子吸光法であった。Zn 以外は別元素の条件になったが、今回の中性子放射化分析は次の点で有用であると思われる。① 試料の前処理がなくて済むため、試料の量が少なくて済む。1 回の分析に必要最小量は前者数 g に対して後者 20～30m g （1 個体）即ち 1／100 で出来る。このことは生態系に影響を与えないで済む。（死骸の甲殻も試料になる）②また、そのため一度に多くの試料数（100 単位）を分析できる。 ③条件が合致する多種の微量元素を同時に分析できる。特に、今日、注目されつつあるレアメタル汚染を解明するために、役立つと思われる。

4．まとめ

室内実験およびフィールド調査から、陸生等脚類の Armadillidium vulgare は環境汚染指標生物となり得ると考えられる。中性子放射化分析法を用いて分析することにより、容易に多数の検体を扱えて、広域の調査が出来ることが確かめられた。この方法による環境汚染濃度の東京 23 区近隣市部調査は、限られた地点ではあるが、予想以上に、汚染の実態が示された結果になった。 この 7 元素 Co,Ce,Sb,Sc,Fe,Zn,Ba の分析は照射 20 分、クーリング期間 7 日後および 37 日後に測定する条件で適当であることが分かった。

［参考文献］

1） 山本英穂、他：「大気汚染に由来する環境汚物質の陸生節足動物に及ぼす影響」全国公害研究会誌 4 （2）111－117（1979）

2） D.Drobne,S.P.Hopkin : “ Ecotoxicological Laboratory Test for Assessing the Effects ofChemicals on Terrestrial Isopods “ Bull. Environ. Contam. Toxicol. 53 : 390－397.（1994）

3） 久保田正亜：「忍び寄る日本のレアメタル汚染」化学と生物、35,12（1997）4）川西幸子、他：「一般廃棄物焼却炉近傍表土の中性子放射化分析」武蔵野短期大学研究紀要 第 13 輯 11（1999）

[成果の公表]
川西幸子、野川憲夫、澤幡浩之、森 実：「環境汚染指標生物の調査研究―陸生等脚類の検討」武蔵野短期大学研究紀要 第15輯、11～18（2001）

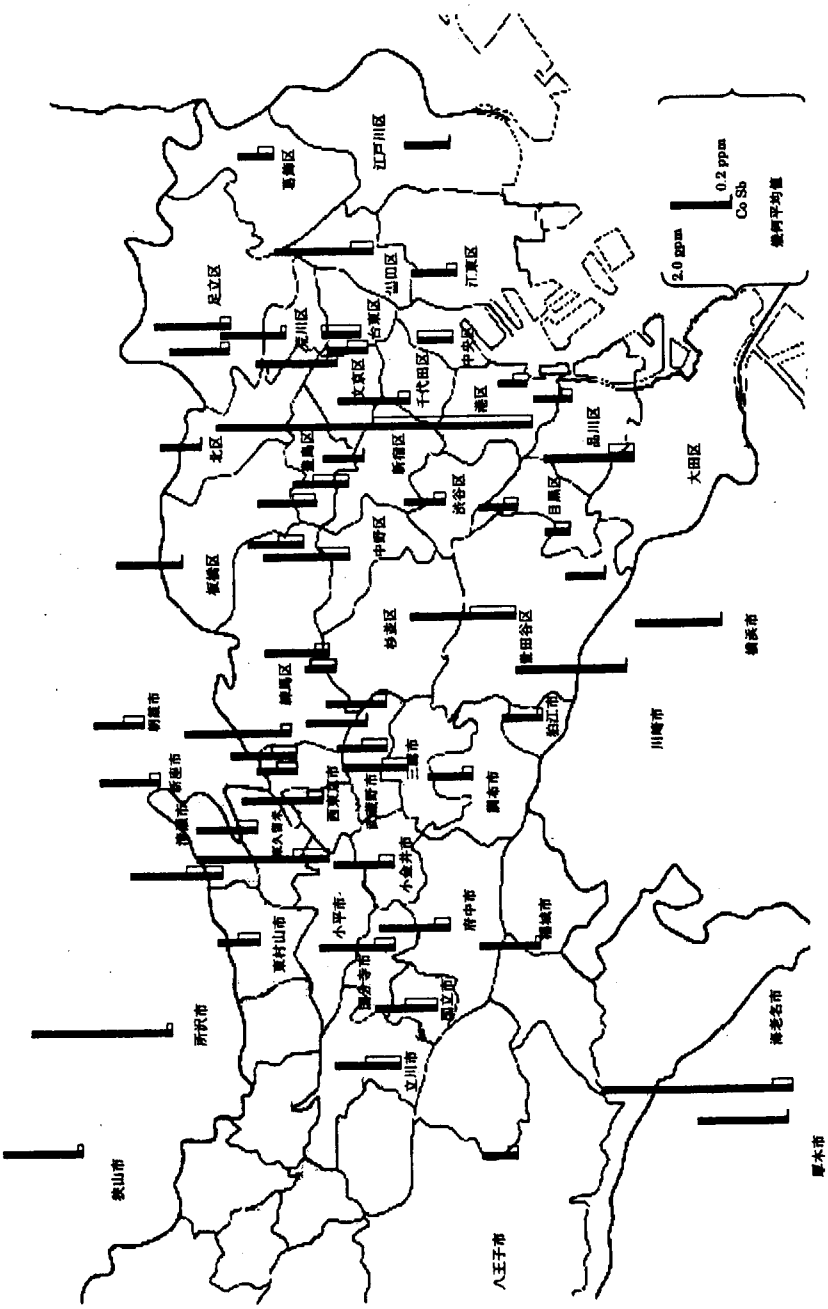


図１　東京都区部・近隣市部 採集地と Co，Sb の分析結果

3-11 地衣類を環境指標として用いるための基礎研究

Basic study for using lichen as an environmental index

筑波大学化学系　関　李紀　斎藤陽子

Riki SEKI, Yoko Saito*, Department of Chemistry, University of Tsukuba

*present address: R&D Group for Environmental Technology, JAERI

1．はじめに

地衣類は藻類と菌類の共生体でとして知られる複合生物であることはよく知られている。日本ではお正月の生け花にウメノキゴケのついた梅の枝が使われたり、山登りの途中にはサルオガセがよく見られたりと人々の目によく触れたものであった。また一方、ロンドンの亜硫酸ガス濃度と地衣類の生育状況の調査などから、知られているように、大気汚染には非常に弱い生物であることも知られている。しかし、火山の噴気が噴出している地帯のようにほかの植物が生育していない場所にも生育し、極地から熱帯まで世界中に分布しているので、環境指標として適しているのではないかと考えて本研究に着手した。地衣類の共生は藻類が光合成によって生成する養分を菌類にあたえ、菌類はすみかを藻類に提供することで成立し、環境から太陽の光と水さえあれば生育可能のはずで、以前は日本各地に普通に見られた生物であった。ところが近年非常に減少しており、当初は環境と地衣類の組成について調査し、環境指標として地衣類を用いる可能性を研究する目的で開始したのであったが、少しでも試料のあるうちに組成の傾向を明らかにすることが急務であると考えるようになった。そのため、なるべく多くの元素について熱中性子放射化分析により、地衣類の元素組成を明らかにし、元素組成の種による差異，種類によるちがい、場所による違いを調べることを本研究の目的とした。

地衣類は大きく分けて樹枝状地衣、葉状地衣、固着地衣の 3 種類あり、固着地衣は木の幹や岩石、建造物などの基物に深く進入して存在し、葉状地衣も基物と分離は簡単ではない。そこで、樹枝状地衣を中心として葉状の地衣のうちでも広く分布しているウメノキゴケなどを試料として放射化分析により元素組成の傾向を明らかにした。

2．実験について

試料

樹枝状地衣は空気の清浄な地域でしか生育していなかったので、山梨県、長野県、北海道などで採取したものが多い。採取した地衣類の数はおよそ 90、種は 10 種あまりであった。

そのうち樹枝状地衣ではハナゴケ *Cladonia rangiferina*、ミヤマハナゴケ *Cladina stellaris*、ワラハナゴケ *Cladina arbuscula*、トゲシバリ *Cladia aggregata*、ショクダイゴケ *Cladonia crispate* ホグロハナゴケ *Cladonia amaurocraea*、ワラハナゴケモドキ *Cladina mitis*、葉状地衣ではウメノキゴケ *Parmotrema tinctorum*、キウメノキゴケ *Flavoparmelia caperata*、マツゲゴケ *Rimelia clavulifera* などを分析した。

採取した地衣類を超純水（Mill-Q:＞15MΩ）で洗浄し、乾燥して標本を作製し、一部をとり、種の同定を行った。一部を精秤して放射化分析用の試料とした。

研究施設と装置名：立教大学原子炉、JRR-3M、PN-1
研究分野：中性子放射化分析、環境科学

原子炉照射と測定

半減期の短い核種を用いる元素（Na, K, Mg, Al, Cl, Ca, V, Mn, As, Br, Iなど）については立教大学の原子炉の回転試料棚で5分間照射し、直ちに測定した。比較的長い半減期のもの(Cr, Fe, Co)はF孔で1時間照射し、筑波大学に持ち帰りアイソトープセンターでガンマ線の測定をした。

また、Fe, Co, Csについては日本原子力研究所のJRR-3Mの気送管PN-1で20分照射して約20日後、筑波大学アイソトープセンターでガンマ線測定を行った。

3．結果と考察

立教大学の原子炉の回転試料棚で5分間照射した試料のγ線スペクトルの1例を図1に示す。試料は恐山周辺で採取した樹枝状地衣のヤマトハナゴケ *Cladonia carassensis* subsp.*japonica* で、多くの元素とともに他の地域で採取した地衣には見られないヒ素が390±40 ppm検出された。

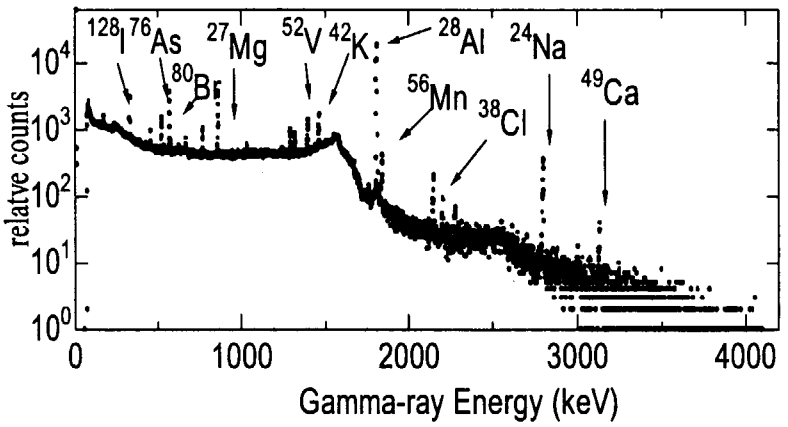


図1. 立教大学原研のTRIGA-II回転試料棚で5分間熱中性子照射した恐山付近に生育するヤマトハナゴケ *Cladonia carassensis subsp.japonica* のγ線スペクトル

一般に地衣類中の元素はその地衣の種、採取場所などによって、変動があるが、同じ場所で採取した別の種類の地衣類中の元素濃度を比較した。

次に示す図2は北海道、美瑛で採取した樹枝状の地衣、ショクダイゴケ、ホグロハナゴケ、ハナゴケ、ワラハナゴケモドキの4種を分析した結果である。図3には石鎚山周辺で採取した葉状地衣のウメノキゴケ、マツゲゴケ、キウメノキゴケの結果を示した。元素濃度は樹枝状、葉状を比較すると、一般に葉状地衣の元素濃度が高く、特にカルシウムとマンガンで顕著である。カルシウムはウメノキゴケとキウメノキゴケでは2.5%、4.5%含まれることになり、マツゲゴケとは異なる機能を持つことが予想される。これは他の地域で採取したものについても同様の傾向であった。

また、火山地帯におけるヒ素や、筑波山神社の銅屋根からの下に生育するマツゲゴケに45.2ppmの銅が検出されたことなど多くの興味ある結果が得られた。

指標として地衣類は生育環境を反映する元素組成をすることがわかった。

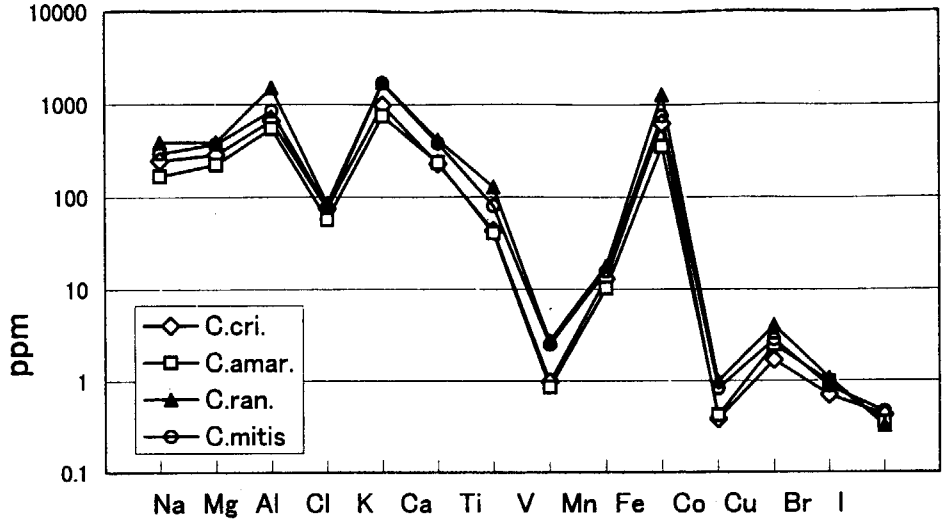


図2 北海道美瑛で採取した樹枝状地衣類ショクダイゴケ、ホグロハナゴケ、ハナゴケ、ワラハナゴケモドキの元素濃度(ppm)

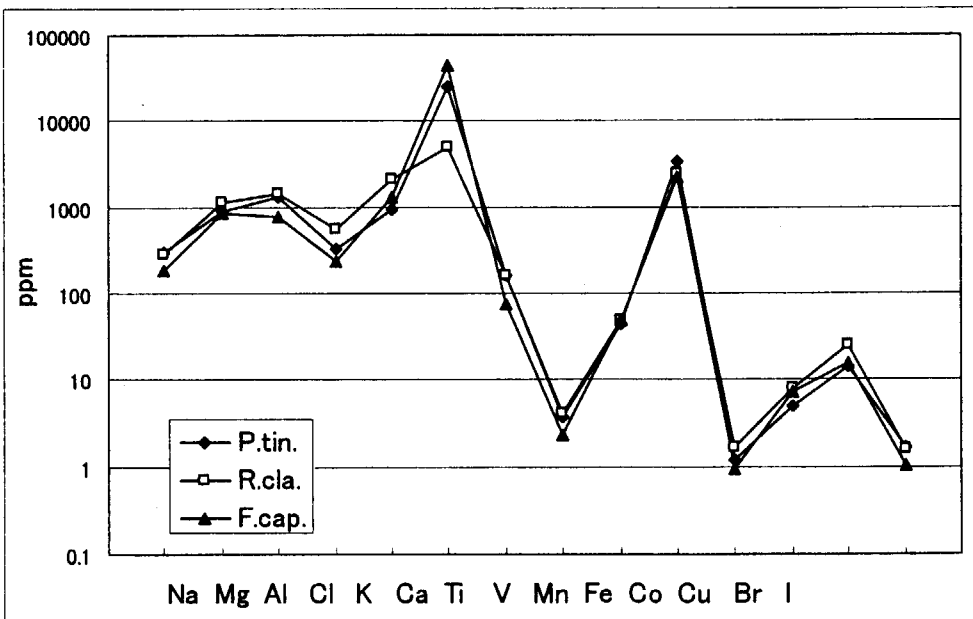


図3 石鎚山周辺で採取した葉状地衣類ウメノキゴケ、マツゲゴケ、キウメノキゴケの元素濃度(ppm)

成果の公表

1.齋藤陽子、関　李紀、池田龍一「日本産地衣類中の微量元素の定量」第 35 回理工学における同位元素研究発表会（1998 年 6 月）

2.齋藤陽子、関　李紀、池田龍一「地衣類中の金属元素について」地衣類研究会第 27 回（1998 年 8 月）

3.齋藤陽子、関　李紀、池田龍一「日本産地衣類の元素の定量」環境科学会 1998 年会（1998 年 10 月）

4.齋藤陽子、柏谷博之、池田龍一、関　李紀「環境指標としての地衣類」第 43 回放射化学討論会（1999 年 10 月）

5. R. Seki, Y. Saito, H. Kashiwadani, Lichens as an Indicator of Chemical Elements in Japan. The Fourth international Association of Lichenology.(September, 2000 Barcelona)

6. Y. Saito, R. Seki, H. Kashiwadani, Lichens as an Indicator of Radiocesium in Japan. The Fourth international Association of Lichenology.(September, 2000 Barcelona)

3-12

アーバスキュラー菌根の形成が宿主植物の各種元素の吸収に及ぼす影響

鈴木弘行*・熊谷 宏*・野川憲夫**・澤幡浩之***・川手 稔***・大橋國雄*,****

*千葉大学アイソトープ総合センター・**東京大学アイソトープ総合センター・

東京大学原子力研究総合センター・*千葉大学薬学部

Influence of arbuscular mycorrhizal colonization on uptake of various elements by host plant.

H. Suzuki*, H. Kumagai*, N. Nogawa**, H. Sawahata***, M. Kawate*** and K. Oohashi*, ****

*Radioisotope Research Center, Chiba University; **Radioisotope Center, University of Tokyo;

***Research Center for Nuclear Science and Technology, University of Tokyo; and

****Faculty of Pharmaceutical Sciences, Chiba University

1. 緒言

高等植物の根の組織内あるいは表面において植物と糸状菌が共生関係を営んでいるものを菌根と呼ぶ。菌根は陸上植物の約 80％に認められ，特にアブラナ科やアカザ科を除く農作物や草本植物はアーバスキュラー菌根(AM)を形成する。

AM の形成によって根の周りには AM 菌の外生菌糸が伸長する。この外生菌糸には N, P, Zn, Cu などの植物養分を植物に輸送する能力がある (Ames et al. 1983; Kothari et al. 1991; Li et al. 1991)。さらに近年では，AM 菌の外生菌糸が Na, Sr, Se などの植物非必須元素を植物に輸送することも明らかにされた(Suzuki et al., 2001)。このため，AM 菌の外生菌糸による元素輸送は宿主植物の様々な元素の吸収に重要な役割を果たしていると考えられる。

AM の形成が植物養分の吸収に及ぼす影響については，Marschner and Dell (1994)などの総説にまとめられており，AM の形成は植物の養分吸収を改善することが報告されている。しかし，植物多量要素である Mg についての知見など，いくつかの植物養分の吸収に対する AM の形成による影響はまだ明らかにされていない。一方，非必須元素の吸収に対して AM の形成が及ぼす影響はほとんどの元素について明らかにされていない。また，Zn や Mn などいくつかの元素については，AM の形成によって元素吸収が増加する場合と増加しない場合のあることが報告されている (Jackson et al. 1973; Kothari et al. 1990; Lambert et al. 1991; 依藤・鈴木 1995; 鈴木ら 2000)。 このような現象は，AM の形成が宿主植物の養分や非必須元素の吸収に影響を及ぼす機構を外生菌糸の元素輸送能のみで説明できないことを示唆している。このため，AM の形成が宿主植物の元素吸収に及ぼす影響を解析するためには，外生菌糸の元素輸送能よりも AM の活性（たとえば AM の発達状態）の点から検討を加えることが重要である。

しかし AM の形成と宿主植物の元素吸収に関連のある現在までに報告された知見には，宿主植物と AM 菌の組み合わせ，植物の生育史，AM の発達状態などがそれぞれの実験において異なることや，同時測定の対象となった元素数が少ないなどの問題点があるため，既報の知見を利用して AM の形成が宿主植物の養分や非必須元素の吸収に及ぼす影響を AM の発達状態のような AM の活性の点から解析することは容易ではない。

そこで本研究では，植物の生育史を栄養生長期，生殖生長期の前半（開花期），生殖生長期の後半（開花期と登熟期）の 3 つの生育時期に分け，それぞれの時期において採取した AM の発達状態が異なる植物体を放射化分析することによって，AM の形成が宿主植物の様々な元素の吸収に及ぼす影響について AM の存在，AM の発達状態，植物の生育史の点を踏まえた解析を行った。

研究施設・装置：JRR-3M(PN-1, 2); JRR-4(気送管)，研究分野：中性子利用分析・放射化分析

2. 試料および方法

宿主植物としてマリーゴールド (*Tagetes patula* L., 品種名：ボナンザスプレー), 接種 AM 菌として *Glomus etunicatum* (Becker and Gerdemann)を使用した。試験区は前年度に採取した AM 菌を接種源として用いた AM 区，共生能力が低下した前々年度に採取したAM菌を接種源として用いたLAM区，無接種の対照区の 3 試験区を設けた。培土にはオートクレーブ滅菌（121℃，1 時間）した川砂（利根川砂）を使用した。川砂は 400g を内径 9cm のポットに充填した。各ポットにはマリーゴールドの種子を 4 粒播種し，播種後 AM 区と LAM 区にはそれぞれの AM 菌の胞子を約 200 胞子接種した。また，対照区には AM 区で用いた胞子をオートクレーブ滅菌（121℃，15 分）したものを約 200 胞子添加した。

栽培は気温 25℃，湿度 65%，照度 15,000Lx（明期 16 時間，暗期 8 時間）に調節したバイオトロン内で行った。栽培期間中は 1 日 2 回ポットの重量を測定し培土の水分量を最大容水量の約 55%に維持するために蒸留水を与えた。また，播種後 7 日目に 1 ポットあたり 1 個体に間引きを行い，播種後 8 日目からは毎日液肥を与えた。液肥の組成は別報 (Suzuki et al. 2001)に示した。植物体は各試験区とも 21 ポットずつ栽培し，播種後 29 日，50 日，68 日目にそれぞれ 7 ポットずつ採取した。各採取日は植物の生育史において，播種後 29 日目は栄養生長期，播種後 50 日目と 68 日目は生殖生長期の前半（開花期）と後半（開花期と登熟期）にそれぞれ相当した。採取した植物体は根部と地上部に分け，地上部は直ちに新鮮重を測定した。根部は蒸留水で洗浄し，ペーパータオルを用いて付着する水分を取り除いた後新鮮重を測定した。採取した植物体は 4 個体を放射化分析に用い，残る 3 個体を AM 形成率の測定に用いた。

放射化分析に用いる植物体の根部は，付着する培土を入念に取り除くために，さらに超音波洗浄を行った。地上部については蒸留水ですすぎ洗浄した。ただし，播種後 50 日目と 68 日目の場合は地上部をさらに茎葉部と花弁部に分けて蒸留水ですすぎ洗浄した。洗浄した根部，茎葉部，花弁部は 80℃で 48 時間かけて乾燥した。また，AM 形成率の測定は別報（Suzuki et al. 2000）に示した方法によって行った。

乾燥した植物体は粉砕器を用いて粉砕した。粉砕した植物体，培土，種子，標準試料から約 20～50mg を秤量し，ポリエチレン袋に封入した。また，液肥については 1mL をポリエチレン袋に分取し，デシケーター中で乾燥したものをそのまま密封した。各試料を封入したポリエチレン袋はさらに別のポリエチレン袋に封入し，これを照射試料とした。

放射化分析は測定対象の核種を半減期別に短寿命核種，中寿命核種，長寿命核種に分け，それぞれの測定を次のような手順で行った。短寿命核種の場合，試料は日本原子力研究所東海研究所の原子炉 JRR-4 の気送管で 10～30 秒照射し，1 分間冷却後，ゲルマニウム半導体検出器を用いて 3 分間測定した。中寿命核種と長寿命核種場合では，試料を日本原子力研究所東海研究所の原子炉 JRR-3M の PN-1 あるいは PN-2 で 10 分間照射した。そして 1 週間冷却後に中寿命核種の測定をゲルマニウム半導体検出器を用いて 3000 秒間行った。また長寿命核種の測定は 4 週間以上冷却後にゲルマニウム半導体検出器を用いて 65000 秒間行った。

各測定結果はボンフェローニ法による多重検定を行い試験区間の有意差を解析した。

3. 結果および考察

3.1 植物生育と AM 形成

各生育時期における対照区，LAM 区，AM 区の植物体新鮮重と AM 形成率を表 1 に示した。播種後 29 日目では地上部と根部の新鮮重に差は認められなかった。また，LAM 区と AM 区では AM の形成が認められたが，両試験区の AM 形成率は 10%未満でありほとんど同じであった。このため，栄養生長期における AM の形成は未発達であり，AM の

影響も新鮮重に現れなかったと考えられる。

播種後 50 日目では，地上部の新鮮重が AM 区で最も高くなった。しかし，根部の新鮮重は 3 つの試験区間でほとんど同じであった。AM 形成率は対照区＜LAM 区＜AM 区の順に高くなった。播種後 68 日目では，地上部の新鮮重と AM 形成率は播種後 50 日目の場合と同様の傾向を示した。しかし，根部の新鮮重については LAM 区が 3 つの試験区の中で最も小さくなった。播種後 50 日目と 68 日目における植物体地上部の新鮮重が AM 形成率の高かった AM 区において対照区や LAM 区よりも有意に増加したことは，生殖生長期の前半と後半における AM の発達が植物体地上部の新鮮重の増加に寄与したためと考えられる。一方，播種後 50 日目と 68 日目における根部新鮮重には対照区と AM 区との間で試験区間差が認められなかったことから，生殖生長期の前半と後半における AM の発達は根部新鮮重にほとんど影響を及ぼしていないと考えられる。しかし播種後 68 日目における LAM 区の根部新鮮重が対照区よりも有意に低下した点については，播種後 50 日目における LAM 区の根部新鮮重が対照区とほぼ同じであったことから，AM が未発達であることが根部新鮮重の低下に直接的に影響を及ぼしてはいないと考えられる。むしろ，AM が未発達であることと植物の生育史が生殖生長期の後半であることとの関係が根部新鮮重の低下に強い影響を及ぼしていると考えられる。

3.2 放射化分析

放射化分析の結果，実験に用いた培土からは Na, Mg, Al, Cl, K, Ca, Sc, Cr, Mn, Fe, Co, Zn, Rb, Sr, Cs, Ba, La, Ce, Sm, Eu, Yb, Lu, Hf, Th の 24 元素が検出された。また，液肥からは Na, Mg, Cl, K, Ca, Mn, Fe, Zn, Br の 9 元素が検出された。表 2 に培土の元素含有率と各採取日までに与えた施肥に伴う元素投与量を示した。植物体からは，培土から検出された元素から Ba と Hf を除いた 22 元素に Br を加えた 23 元素が検出された。また，種子からは Na と K が検出された。図 1 に種子と植物体の各元素の結果をまとめ植物体 1 個体あたりの含有量として示した。植物体中の Mg, Ca, Br を除く 20 元素の含有量は施肥に由来する元素投与量を上回っていたため，これらの元素の植物体中含有量の大半は培土に由来すると考えられる。Mg と Ca については，植物体中含有量が施肥に由来する元素投与量の範囲内であったことから，培土に由来する量は少ないと考えられる。Br については，培土を測定する場合の検出感度の低下のために培土の Br 含有率を求められなかったため，培土の Br 量を土壌や岩石の Br と Cl の濃度比が 1:20～1:52 であることに基づいて推定し(結田 1990)，施肥由来の Br 量を差し引いた植物体中の Br 含有量が培土中の Br に由来すると判断した。

各元素の含有量は 3 つの試験区間で比較しその結果を試験区間差の有無に基づいて 7 つの型に分類した。表 3 に各元素の分類結果と多重検定の結果から導いた考察を示した。また，各分類型の番号は数字の増加と共に元素吸収に対する AM の影響が小さくなるように配列した。

播種後 29 日目の場合では Cr の含有量が LAM 区において最も少なくなり，対照区と LAM 区の間では有意差が認められた。Cr 含有量の試験区間での違いはVI型に属したことから， Cr 吸収は AM が未発達であるために低下した可能性があるが，播種後 29 日目における AM 形成率には LAM 区と AM 区の間で違いが認められていない。このため，LAM 区と AM 区における AM の発達状態には AM 形成率のような指標では評価できない活性の違いがあるのかもしれない。また，Cr 以外の元素の含有量には試験区間での違いがほとんど認めらなかった（含有量の試験区間での違いはVII型に属する)。このため AM の形成は栄養生長期における Cr 以外の元素の吸収に対してほとんど影響を及ぼさないと考えられる。

播種後 50 日目と 68 日目では各元素の含有量に試験区間の違いが認められ始めた。播種後 50 日目

の場合，各元素の含有量の試験区間での違いは 5 種類の型に分類することができた。Ⅰ型には Co と Lu が該当した。Co の含有量は LAM 区と AM 区よりも対照区において高くなり，Lu の含有量は対照区よりも LAM 区と AM 区において高くなった。しかし LAM 区と AM 区との間では Co と Lu の含有量に違いは認められなかった。このため，生殖生長期の前半においては AM の発達状態よりも AM の存在が Co 吸収を低下させ，一方で Lu 吸収を増加させていると考えられる。Ⅲ型に属する Cl，Mn，Zn，Cs，Ce とⅣ型に属した Na，Mg，Eu については，AM区における含有量が最も高くなり，対照区とAM区との間で有意差が認められた。このため生殖生長期の前半において，これらの元素の吸収に対する AM の影響は AM が発達した場合にのみ現れると考えられる。Ⅴ型に属した Sc については AM 区における含有量が最も高くなった。しかし，有意差はAM区と対照区との間で認められず，むしろ LAM 区と AM 区の間で有意差が認められた。このため生殖生長期の前半における Sc 吸収はAMの存在よりもAMの発達状態による影響を強く受けていると考えられる。Al，K，Ca，Cr，Fe，Br，Rb，Sr，La，Sm，Yb，Th の 12 元素はⅦ型に属していたので，生殖生長期の前半におけるこれらの元素の吸収には AM の存在と AM の発達状態はほとんど影響を及ぼさないと考えられる。

播種後 68 日目の場合，各元素の含有量の試験区間差の違いは 5 種類の型に分類できた。分類型の数は播種後 50 日目と同じであったが播種 68 日目ではⅠ型とⅣ型に属する元素がなく，代わってⅡ型とⅥ型に属する元素が現れた。Cl はⅡ型に属した唯一の元素であり，その含有量はLAM区＜対照区＜AM区の順に増加した。このため，生殖生長期の後半における Cl 吸収は AM の存在と AM の発達状態の両方から影響を受けていると考えられる。また 3 つの試験区の Cl 含有量の順序は AM が未発達である場合には Cl 吸収の低下，発達した場合には Cl 吸収の増加を引き起している可能性も示している。しかし Cl は播種 50 日目ではⅢ型に属していることから，Cl 吸収の低下には AM が未発達であることに植物の生育史が生殖生長期の後半に属したこととが関係していると考えられる。Ⅲ型に属した元素は Na，Sc，Zn，Br，Sr，La，Ce，Sm，Eu，Yb，Lu の 11 元素であり，播種後 50 日目よりもその元素数は増加した。これらの 11 元素がⅢ型に属したことは，生殖生長期の後半における AM の発達が元素の吸収を高めていると考えられる。特に Br，Sr，La，Sm，Yb は播種後 50 日目では AM 形成の影響を受けにくいと考えられるⅦ型に属していたので，AM 区においてこれらの元素の含有量が増加する要因を AM の発達だけで説明することはできない。このため，AM 区におけるこれらの元素の吸収の増加には AM の発達と植物の生育史との関係が重要な影響を及ぼしていると考えられる。Ⅴ型に属した元素は Al，Ca，Mn，Fe，Cs であり，この 5 元素の含有量はいずれも AM 区で最も高くなった。これらの元素の生殖生長期の後半における吸収は AM の存在よりも AM の発達状態による影響を強く受けていると考えられる。特に Al，Ca，Fe は播種後 50 日目ではⅦ型に属していたので，播種後 68 日目の AM 区におけるこれらの 3 元素の吸収の増加には AM の発達と植物の生育史との関係が重要であると考えられる。一方，Mn と Cs は播種 50 日後ではⅢ型に属していたので播種後 68 日目においてⅤ型に属したことは，Mn と Cs の吸収が AM の発達状態と植物の生育史との関係によって変化しやすいことを示している。このため LAM 区と AM 区との間でしか含有量に顕著な違いを示さないⅤ型の元素の吸収について AM の影響を解析するためには，植物の生活史の一部だけでなく植物の生育史の全体を通した解析が重要であると考えられる。Ⅵ型には Cr と Rb が属し，両元素の含有量はLAM区において最も少なくなった。このため生殖生長期の後半において AM が未発達であることは Cr と Rb の吸収 の低下と関係があると思われる。またⅦ型に属した元素は Mg，K，Co，Th の 4 元素であり，その数は播種後 50 日目よりも

少なくなった。Ⅶ型に属した Co や Mg は播種 50 日後ではそれぞれⅠ型とⅣ型に属したので，Co や Mg の吸収は生殖生長期の後半においては AM の存在や AM の発達状態による影響を受けにくくなると考えられる。K と Th については植物の生育史の各時期のいずれにおいてもⅦ型に属したことから，これらの元素の吸収は植物の生育史の全体を通して AM の存在や AM の発達状態の影響を受けにくいと考えられる。しかし，本実験よりも施肥養分量が少ない条件において栽培したマリーゴールドでは，AM 菌を接種したマリーゴールドの K と Th の含有量が無接種の場合よりも高くなることが報告されている (鈴木. 2000)。このため K と Th の吸収については AM の形成と植物の生育史との関係にさらに施肥養分量との関係を加えた解析が必要である。

以上の結果から，植物体から検出された 23 元素の吸収に対する AM の形成の影響を次のように総括した。

1) K と Th 以外の 21 元素の吸収は植物の生育史を通したいずれかの時期において AM の形成による影響を受けると考えられた。
2) AMが十分に発達していない栄養生長期では，Cr を除くほとんどの元素の吸収に AM の形成は影響を及ぼさないと考えられた。
3) 生殖生長期の前半では，AM の発達は Na, Mg, Cl, Mn, Zn, Cs, Ce, Eu の吸収の増加と関係があると考えられた。また，生殖生長期の後半では AM の発達は Na, Sc, Zn, Br, Sr, La, Ce, Sm, Eu, Yb, Lu の吸収増加と関係があると考えられた。
4) 生殖生長期の前半においては，AM の発達よりも，AM の存在が Co 吸収の低下と Lu 吸収の増加に寄与していると考えられた。
5) 生殖生長期の後半における Cl 吸収は AM の存在と AM の発達状態の両方から影響を受けていると考えられた。特に，AM の発達状態の違いは Cl 吸収の増加と低下といった異なった結果をもたらすと考えられた。
6) 生殖生長期の前半における Sc 吸収および後半における Al, Ca, Mn, Fe, Cs の吸収は AM の存在よりも AM の発達状態による影響を強く受けると考えられた。さらに，これらの元素の吸収傾向を生殖生長期の前半と後半で比較することによって，これらの元素の吸収は AM の発達状態と植物の生育史との関係によって変化しやすいと考えられた。

4. 要約

アーバスキュラー菌根(AM)の形成が植物による様々な元素の吸収に及ぼす影響を明らかにするために放射化分析法を用いた解析を行った。実験には宿主植物としてマリーゴールド（*Tagetes patula* L.），接種 AM 菌として *Glomus etunicatum* を用いた。様々な元素の吸収に対する AM の形成による影響は，AM の発達状態が異なるマリーゴールド（無接種の対照区，AM の発達していない LAM 区，AM が発達した AM 区）の元素含有量を比較して解析した。また上述のマリーゴールドは栄養生長期，生殖生長期の前半（開花期），生殖生長期の後半（開花期と登熟期）の 3 つの時期に分けて採取し，様々な元素の吸収に対する植物の生育史による影響も考慮して解析を行った。放射化分析は日本原子力研究所の JRR-3M と JRR-4 の原子炉を利用して行った。

植物体からは Na, Mg, Al, Cl, K, Ca, Sc, Cr, Mn, Fe, Co, Zn, Br, Rb, Sr, Cs, La, Ce, Sm, Eu, Yb, Lu, Th の 23 元素が検出された。K と Th 以外の 21 元素の吸収については植物の生育史を通したいずれかの時期において AM の形成による影響を受けると考えられた。そして，AM の形成による影響は AM が十分に発達していない栄養生長期よりも AM が発達した生殖生長期において顕著に認められると考えられた。特に，生殖生長期の前半における Na, Mg, Cl, Mn, Zn, Cs, Ce, Eu の吸収と生殖生長期の後半における Na, Sc, Zn, Br, Sr, La, Ce, Sm, Eu, Yb, Lu の吸収は，AM の発達によって増加すると考えられた。また，生殖生長

期の前半においては，AM の発達よりも AM の存在が Co 吸収の低下と Lu 吸収の増加に影響を及ぼしていると考えられた。

5. 引用文献

Ames, R.N., Reid, C.P.P., Porter L.K., and Cambaradella, C.: Hyphal uptake and transport of nitrogen from two ^{15}N labelled sources by *Glomus mosseae*, a vesicular-arbuscular mycorrhizal fungus., New Phytol., 95, 381-396, 1983

Jackson, N.E., Miller, R.H. and Franklin, R.E.: The influence of vesicular-arbuscular mycorrhizae on uptake of ^{90}Sr from soil by soybeans., Soil Biol. Biochem., 5, 205-212, 1973

Kothari, S.K., Marschner, H. and Römheld, V.: Direct and indirect effects of VA mycorrhiza and rhizosphere microorganisms on mineral nutrient acquisition by maize (*Zea mays* L.) in a calcareous soil. New Phytol., 116, 637-645, 1990

Kothari, S.K., Marschner, H. and Römheld, V.: Contribution of VA mycorrhizal hyphae in acquisition of phosphorus and zinc by maize grown in a calcareous soil., Plant Soil, 131, 177-185, 1991

Lambert D.H. and Weidensaul, T.C.: Element uptake by mycorrhizal soybean from sewage-sludge-treated soil. Soil Sci. Am. J., **55**, 393-398, 1991

Li, X-L., Marschner H. and George E.: Acquisition of phosphorus and copper by VA-mycorrhizal hyphae and root-to-shoot transport in white clover., Plant Soil, 136, 49-57, 1991

Marschner, H. and Dell, B.: Nutrient uptake in mycorrhizal symbiosis. *In* Management of mycorrhizas in agriculture, horticulture and forestry, Ed. A.D. Robson, L.K. Abbott, and N. Malajczuk, p.89-102, Kluwer Academic Publishers, Dordrecht, 1994

鈴木弘行・熊谷 宏・野川憲夫・松岡弘充・大橋國雄：放射化分析法による菌根形成マリーゴールドの金属元素分析，土肥誌，71，90-93，2000

Suzuki, H., Kumagai, H., Oohashi, K., Sakamoto, K., Inubushi, K., Enomoto, S. and Ambe, F.: Uptake of 15 trace elements in arbuscular mycorrhiozal marigold measured by the multitracer technique., Soil Sci. Plant Nutr., 46, 283-289, 2000

Suzuki, H., Kumagai, H., Oohashi, K., Sakamoto, K., Inubushi, K. and Enomoto, S.: Transport of trace elements through the hyphae of an arbuscular mycorrhiozal fungus into marigold determined by the multitracer technique., Soil Sci. Plant Nutr., 47, 131-137, 2001

依藤敏昭・鈴木源士：根と共生して作物を強くする菌根菌の活かし方, p.24～25, 農文協，東京, 1995

結田康一：農業生態系におけるヨウ素および臭素の動態，微量元素・化学物質と農業生態系，p.112～135，農林水産省農業環境技術研究所編，養賢堂，東京 (1990)

6. 成果の公表

[学術論文]

鈴木弘行：アーバスキュラー菌根を形成した植物の有害微量元素吸収，そのメカニズムと phytoremediation への応用，土と微生物，投稿中

Suzuki, H., Kumagai, H., Nogawa, N., Sawahata, H., Kawate, M., and Oohashi, K.: Influence of arbuscular mycorrhiza on uptake of essential and non-essential elements by host plant., Soil Sci. Plant Nutr., 投稿準備中

表1　播種29日，50日，68日後に採取した各試験区の植物体地上部と根部の新鮮重およびAM形成率[1)]

試験区	29日			50日			68日		
	地上部(g)	根部(g)	AM形成率(%)	地上部(g)	根部(g)	AM形成率(%)	地上部(g)	根部(g)	AM形成率(%)
対照区	1.40 a[2)]	1.16 a	0	6.11 a	2.84 a	0	7.68 a	3.85 b	0
LAM区	1.27 a	1.01 a	7	6.24 a	2.87 a	18	8.03 a	3.02 a	26
AM区	1.54 a	1.18 a	9	6.95 b	2.96 a	51	9.56 b	3.43 ab	46

1）植物体地上部と根部の新鮮重は植物体7個体の平均値，AM形成率は植物体3個体の平均値．

2）表中の同一英文字はボンフェローニ法による多重検定において危険率5％水準では試験区間に有意差がないことを示す．

表2 培土の放射化分析結果、各元素の1ポットあたりの含有量および施肥に由来する元素量

元素	元素含有率 (mg kg^{-1})	ポット中の元素量 (mg)	施肥由来の元素量 (μg ポット$^{-1}$) 播種29日後	播種50日後	播種68日後
Na	10.5×10^3	4.20×10^3	588	1.18×10^3	1.68×10^3
Mg	10.8×10^3	4.32×10^3	2.52×10^3	5.04×10^3	7.20×10^3
Al	59.2×10^3	23.7×10^3	0	0	0
Cl	300	120	405	811	1.16×10^3
K	21.0×10^3	8.40×10^3	8.40×10^3	16.8×10^3	24.0×10^3
Ca	17.8×10^3	7.12×10^3	8.40×10^3	16.8×10^3	24.0×10^3
Sc	14.2	5.7	0	0	0
Cr	21.8	8.7	0	0	0
Mn	766	306	42.0	84.0	120
Fe	31.4×10^3	12.6×10^3	81.9	164	234
Co	10.4	4.2	0	0	0
Zn	185.6	74.2	8.4	16.8	24.0
Br	N.D.*)	(2.3～6) **)	0.4	0.8	1.2
Rb	96.1	38.4	0	0	0
Sr	125	50	0	0	0
Cs	5.4	2.2	0	0	0
Ba	365	146	0	0	0
La	14.3	5.7	0	0	0
Ce	38.4	15.4	0	0	0
Sm	2.9	1.2	0	0	0
Eu	1.4	0.6	0	0	0
Yb	6.4	2.6	0	0	0
Lu	0.3	0.1	0	0	0
Hf	5.4	2.2	0	0	0
Th	3.3	1.3	0	0	0

*): 検出限界以下，**): 文献による推定値（結田 1990）.

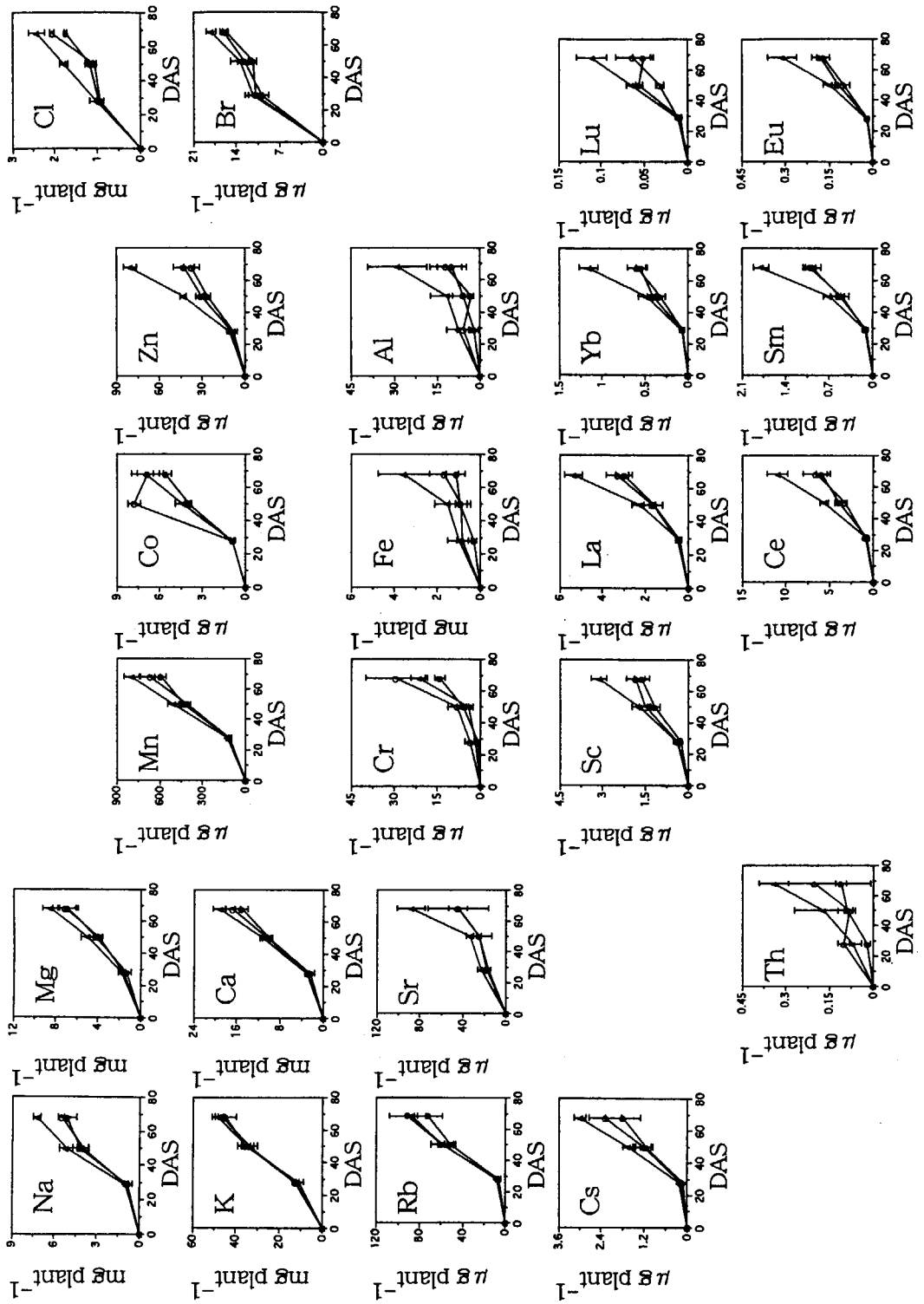


図1 各試験区の植物体中の元素含有量の変化
（○：対照区，●：LAM区，▲：AM区，図中の値と誤差線は植物体4個体の平均値と標準偏差を示す．）．

表3　多重検定の結果の概要

分類型	多重検定の結果[1)]			多重検定の結果からの考察	各分類型に対応する元素		
	対照区 vs LAM区	対照区 vs AM区	LAM vs AM区		播種29日後	播種50日後	播種68日後
Ⅰ型	*	*	NS	AMの存在は含有量の試験区間差に影響を及ぼしているが，AMの発達状態は影響を及ぼしていない。		Co, Lu	
Ⅱ型	*	*	*	AMの存在とAMの発達状態が含有量の試験区間差に影響を及ぼしている。			Cl
Ⅲ型	NS	*	*	AMの存在とAMの発達状態が含有量の試験区間差に影響を及ぼしているが，その影響はAMが発達した場合に限られる。		Cl, Mn, Zn, Cs, Ce	Na, Sc, Zn, Br, Sr, La, Ce, Sm, Eu, Yb, Lu
Ⅳ型	NS	*	NS	Ⅲ型と同様であるがAMによる影響はⅢ型よりも弱い。		Na, Mg, Eu	
Ⅴ型	NS	NS	*	AMの存在よりもAMの発達状態の違いが含有量の試験区間差に影響を及ぼしている。		Sc	Al, Ca, Mn, Fe, Cs
Ⅵ型	*	NS	NS	AMの存在は含有量の試験区間差に影響を及ぼしている。しかし，その影響はAMが発達していない場合に限られる。	Cr		Cr, Rb
Ⅶ型	NS	NS	NS	AMの存在とAMの発達状態は含有量の試験区間差にほとんどど影響を及ぼしていない。	Na, Mg, Al, Cl, K, Ca, Sc, Mn, Fe, Co, Zn, Br, Rb, Sr, La, Ce, Sm, Eu, Yb, Lu, Cs, Th	Al, K, Ca, Cr, Fe, Br, Rb, Sr, La, Sm, Yb, Th	Mg, K, Co, Th

1) ボンフェローニ法による多重検定の結果；*：危険率5％水準で試験区間に有意差があることを示す，NS:有意差なし。

3-13
中国で採取された風成塵堆積物の放射化分析

Neutron Activation Analysis of aeolian sediment samples in China

豊田和弘・篠塚良嗣・渡辺厚志・長谷部清
（北海道大学・大学院地球環境科学研究科）
Kazuhiro Toyoda, Yoshitsugu Shinozuka, Atsushi Watanabe, Kiyoshi Hasebe
(Graduate school of Environmental Earth Science, Hokkaido Univ.)

I 中国東北部と中国中央部の黄土高原で採取された風成塵堆積物

【緒言】　近年、風成塵堆積物は季節風変動や乾湿変動など過去の環境変動の指標となるものとして注目されている。特に、中国内陸部の黄土高原を中心として広い範囲に堆積している風成塵堆積物は、タクラマカン砂漠やゴビ砂漠などの内陸部の乾燥地域から舞い上がった風成塵が、偏西風などにより運搬され、過去に連続的に降下して、堆積したものとされている。しかし、その正確な起源地や運搬経路については現在でも不明な点が多い。

本研究では図１に示した、黄土高原に位置する「蘭州」で採取された風成塵堆積物に加え、文献値の少ない中国北東部の大連近郊の「七頂山」及び内モンゴル地域に近い「天山」についても無機化学分析を行い、その化学組成から、その地域的な特徴と約１２万年前から現在までの時代変化について検討をおこなった。

【実験】　Ti、Al、Fe、Mg、Caなどの試料中の主成分元素はICP発光分析で測定し、Hf、Rb、Cs、Coや希土類元素などの微量元素の定量は日本原子力研究所の原子炉にて中性子放射した後、γ線測定をおこなった。分析した試料の数はバルク分析では３地点から主に採取された計２００試料、堆積後の風化作用によるCaなどの溶出の影響を除くために、塩酸により炭酸塩相などを除去した残渣成分については３地点計９０試料である。さらに風成塵の運搬過程で粒度による分別をうけるという観点から、３地点それぞれ８試料ずつをふるいにより粒度別に分離をおこない、同様に無機化学分析をおこなった。

【結果と考察】　バルク分析の結果に文献値を合せて比較すると、中国北東部と内陸部の黄土高原とでは風成塵堆積物の無機化学組成は明らかに異なることがわかった。黄土高原の「蘭州」ではMgやFeに比較的富んだ玄武岩質の鉱物を多く含むのに対して、中国北東部の「天山」及び「七頂山」ではHf、Ybなどに相対的に富み、花崗岩質の鉱物を多く含む、というように地域的な特徴をもつ。

次に粒度別に分離した試料を比較すると、遠方より運搬されたと考えられる２０μmよりも細粒な成分の化学組成は３地点でやや重なる範囲の値を示すのに対して、６３μmよりも粗粒の成分の化学組成は地域的な化学組成の違いが顕著にみられた。このことより、地域的な特徴は試料採取地点に起源する物質の寄与が大きいためと考えられ、

JRR-3 PN、JRR-4 Tパイプ、γ線スペクトロメトリー、堆積物の放射化分析

一方、細かい粒度の成分については各地域で起源地が同じであることが推測できた。この共通の起源地については、タクラマカン砂漠などの化学組成の文献値が今後報告される事で、本研究のデータはその同定に貢献すると考えている。

さらに酸抽出残渣のいくつかの化学組成の時代変化は浮遊性有孔虫の酸素同位体比時代区分と同期しているように見える（図２）。粒度別試料の結果とこの化学組成の変遷とを考え合わせると、過去約１２万年間で、風成塵試料中には氷期はより遠方を起源とする成分が多く含まれ、間氷期には試料採取地点の近隣地域を起源とする成分の寄与が相対的に増加したと考えられる。

つまり、寒冷な時期には偏西風にのって大陸内部の乾燥地域より、細粒物質が大量に運搬されるのに対し、温暖な時期には夏季季節風が活発化し大陸内部は比較的湿潤で、風成塵の運搬量が減少し、遠方からの寄与が減少したことが記録されていると推測できる。

ただし、現時点では３つのコアの測定試料の数が少なく、より確かな考察をするにはもう少し垂直化学分布データの時間分解能を高める必要がある。その後に、本研究内容について学術雑誌に投稿したいと考えている。

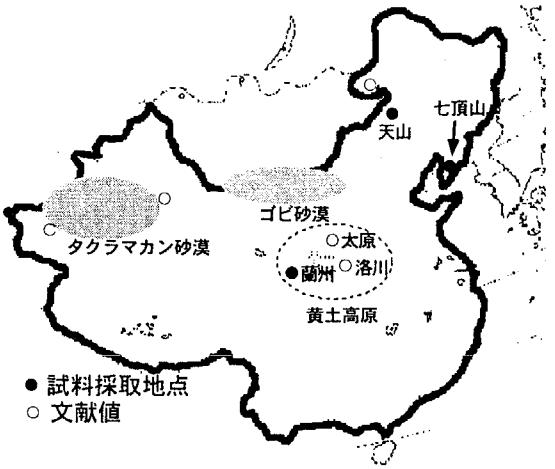


図1. 試料採取地点

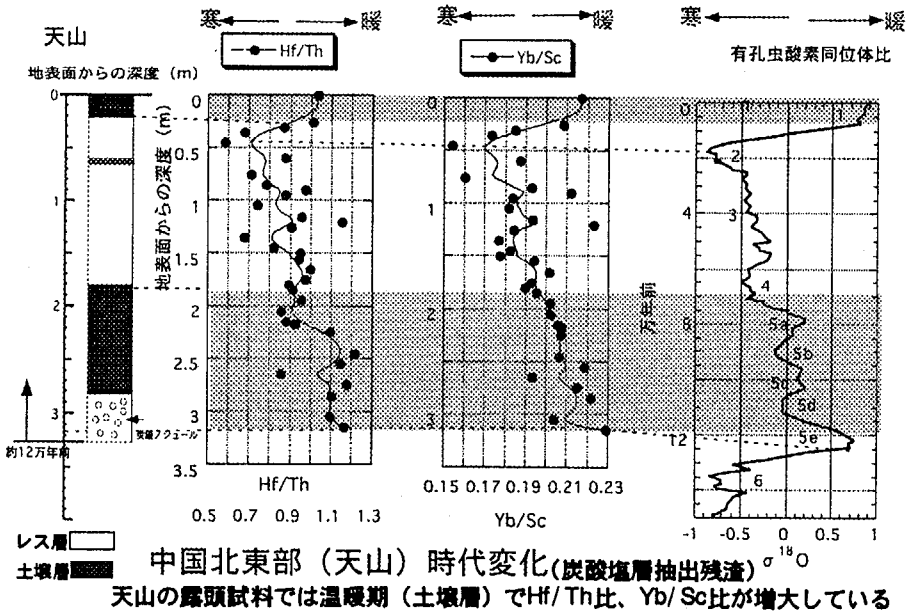


図２.

Ⅱ　古カトマンズ湖のラビバーワンコア中の無機化学成分の垂直分布

【予報】　ヒマラヤ山脈の南斜面に位置するカトマンズ盆地で採取された218m長のラビバーワンコアはインドモンスーンの変動とヒマラヤ山脈の上昇の双方の過去300万年の歴史を記録していると考えられる。これらは日本の気候変動に大きく連動しているので興味深い。

前述と同様に機器中性子放射化分析を用いて、ラビバーワンコアの深度7m～41mの部分から約0.2mおきに採取された164個の試料中の長寿命核種の測定を行い、微量成分10元素と鉄含有量の定量を行った。河成層である深度12m以浅の試料は深度12m以深に比べてハフニウム含有量、セリウム含有量、及びトリウム／スカンジウム比が高く、花崗岩質屑屑物の寄与が大きいと推定された。

一方、深度12m～41mの試料についてはトリウム／スカンジウム比の値が0.9～1.2の間を緩やかに変動している。これが気候変動に伴う風成塵の寄与の大きさの変化を意味しているかどうか興味のあるところである。また、深度22m～31mの鉄含有量の変動がやや激しく、酸化還元状態の大きな変動を示していると考えられる。

またセシウム含有量のみが時代を経るにつれて著しく減少している。これについてはICP発光分析などで他のアルカリ元素含有量が測定された後に考察したい。今後は、短寿命核種の測定に加えて、既に採取されている深度41m以深の試料についても機器中性子放射化分析を行っていきたい。

成果の報告

○学会発表

Chemical composition of core sediments from Lake Suigetsu and reconstruction of environmental changes during the Last Glacial period.　篠塚良嗣& 豊田和弘
ALDP/ELDP国際シンポジウム
2001 11月8日
福井県水月花ホテル

Oxidation Kinetics of Manganese (II) by Spore Coats of Marine Bacillus sp. SG-1.　.豊田和弘
ターナーレクチヤーアワー、
2002年1月、
ミシガン大学地球科学教室

Evaluation of some inorganic elemental cycles in Lake Biwa anterior to the urban-industrial activity.　豊田和弘
ソウル大学との環境科学合同シンポジウム
2002年8月6日、北海道大学

○学術雑誌

2001「マイクロ波加熱分解法と熱外中性子放射化分析法による土壌試料中ヒ素の迅速定量法の検討」篠塚良嗣・豊田和弘、
ぶんせき、2001. No.4, 401-403.

2002 Complex tsunami waves suggested by the Cretaceous-Tertiary boundary deposit at the Moncada section, western Cuba.
R. Tada, Y. Nakano, M.A. Iturralde-Vinent, S. Yamamoto, T. Kamata, E. Tajika, K. Toyoda, S. Kiyokawa, D. Garcia Delgado, T. Oji, K. Goto, H. Takayama, R.Rojas-Consuegra, and T. Matsui
The Geological Society of America Special Paper
356.109-125.

2002 Chemical composition of a drilled core of Lake Biwa in Japan and implications for source changes during the past 430,000 years, K. Toyoda
Quaternary International
(in press)

カツオドリ(*Sula leucogaster*)の有機態ハロゲン (Cl, Br, I)

3-14 Extractable Organohalogens (EOX) in Brown Booby (*Sula leucogaster*)

河野公栄、松田宗明、脇本忠明
M. Kawano, M. Matsuda and T. Wakimoto
愛媛大学農学部
Faculty of Agriculture, Ehime University

1. はじめに

人工有機塩素化合物(DDTs, PCBs, CHLs等)は、生態系の高次生物に高濃度に濃縮されることが知られ、特に海洋生態系の高次生物である海生哺乳類や海鳥に比較的高い濃度で蓄積していることが明らかにされている。しかしながら、近年上記の所謂既知化合物以外に未知の有機塩素化合物を含む有機ハロゲン化合物がむしろ既知有機塩素化合物より高濃度で生物や土壌・底質中に存在していることが次第に明らかにされ、未検討の有機ハロゲン化合物による環境汚染が懸念されている。それら未知有機ハロゲン化合物の環境中における蓄積レベルと蓄積特性に関する検討結果は、未知化合物の検索・同定や環境汚染物質としての評価を行う上で有力な情報となることが期待される。そこで本課題では、海洋生態系の高次捕食者である海鳥 カツオドリ(*Sula leucogaster*)を対象に、未知有機ハロゲン化合物の存在レベルと蓄積性について、上記の代表的な人工有機塩素化合物と比較検討した。有機態ハロゲン(Extractable organohalogens: EOX)は機器中性子放射化分析法で測定した。なお未知有機ハロゲン化合物総濃度は、機器中性子放射化分析で得られた有機態ハロゲン濃度とGC-MS, GC-ECDで得られた個別有機ハロゲン化合物濃度を比較検討する事によって求めた。

2. 試料と方法

試料は、1993年夏季に沖縄県仲ノ神島において許可のもとに採集された雛5検体、幼鳥2検体、成鳥2検体、合計9検体を個別化合物の分析に、さらに上記の試料のうち5検体(雛2検体、幼鳥1検体、成鳥2検体)をEOX分析に供した。分析には皮下脂肪を用い、有機溶媒による抽出の後、カラムクロマトグラフィーによる妨害物除去後、GC-MS, GC-ECDにより個別化合物を定量した。一方、有機溶媒による抽出の後、無機ハロゲンを除去し、放射化分析法により有機態ハロゲンを計測した。なおEOXとして有機態塩素(EOCl), 有機態臭素(EOBr)及び有機態ヨウ素(EOI)を測定した。EOX分析は、調製した有機溶媒抽出液を試料容器に入れ、日本原子力研究所の原子炉JRR-4を用いた。なお、放射化には中性子束3.7x10^{13}n/cm^2・秒で、2分間照射し生成した放射性核種^{38}Cl (1642 keV, 2167keV), ^{80}Br (617keV, 666keV), ^{128}I (443keV)をγ-スペクトロメトリーにより計測した。

3. 結果と考察

分析対象の人工有機塩素化合物(DDTs, PCBs, CHLs、総化合物として30種程度) が、全ての試料から検出され、濃度順位はPCBs>DDTs>CHLs>HCHs>HCBであった。これらは今日知られている代表的な環境残留性の強い人工合成有機塩素化合物である。一方、これら既知有機塩素化合物に由来する総塩素量とEOCl濃度を比較すると前者は10%以下であった。このことはカツオドリ体内に蓄積している有機塩素化合物の実に90%以上が、未知の有機塩素化合物であることを意味している。即ち、未同定の有機塩素化合物が比較的高濃度で存在していることが明らかとなった。Fig.1に各試料のEOX組成、Fig.2に既知と未知有機塩素化合物に由来する既知

研究施設と装置名
JRR-3, 4 気送管

研究分野
放射化分析

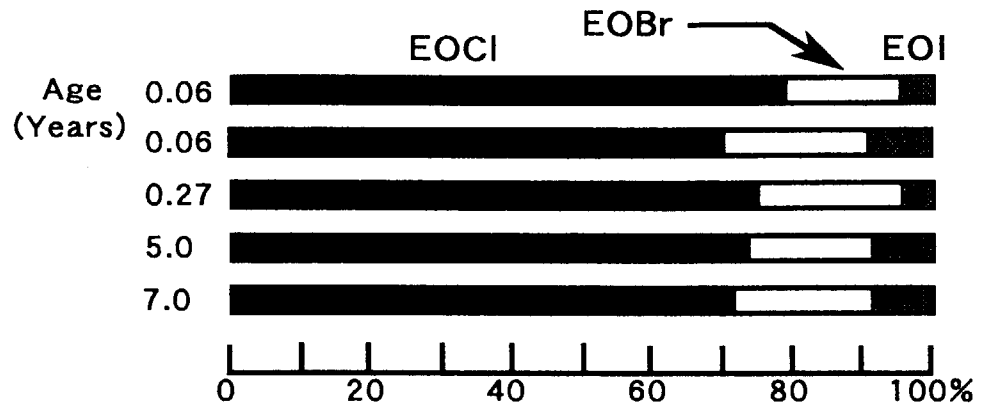


Fig. 1. EOX compositions in adipose tissue of the brown booby samples from Nakanokami Island.

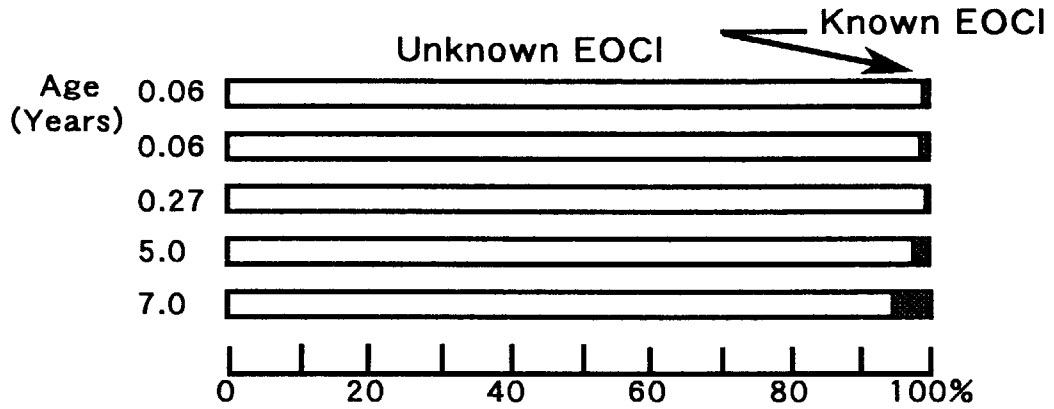


Fig. 2. Known EOCl and unknown EOCl compositions in adipose tissue of the brown booby samples from Nakanokami Island.

EOCl及び未知EOClの組成割合を示す。本研究で得られたカツオドリ中の未知EOCl組成は、先に検討したキアシシギの場合が平均73%に比べ大きい割合を示し、カツオドリには比較的高い濃度の未検討の有機塩素化合物が蓄積していることが明らかとなった。

鳥類の齢査定法が確立されていないため、野生鳥類の成長に伴うPCBs, DDTsなどPOPsの体内蓄積変動に関する情報は少ない。そこで本研究では、特に、標識によって齢が明らにされている試料を用い既知・未知有機塩素化合物を含むEOXの蓄積性について明らかにした。その結果、EOXの濃度順位はEOCl>EOBr>EOIであり、成長段階におけるハロゲン間の存在割合に大きな相違は見られずEOClが最も高濃度であった。成長に伴うEOXの蓄積に関して、PCBs等に由来する既知EOX濃度(脂肪重当たり)は雛から幼鳥期にかけて濃度低下が見られたが、その後次第に体内濃度は上昇した(Fig.3)。

この濃度の一時的低下は、急速な成長による希釈効果によるものと考えられる。既知EOClと同様な蓄積傾向をEOIも示した(Fig.3の上段図)。一方、未知EOClとEOBrについては、雛から幼鳥期にかけて一時的な濃度低下は見られたものの、既知EOClほど顕著な成長に伴う濃度上昇は見られなかった(Fig.3の下段図)。既知・未知EOCl、EOBr及びEOIは上述のようにそれぞれ特徴的な蓄積パターンを示した。

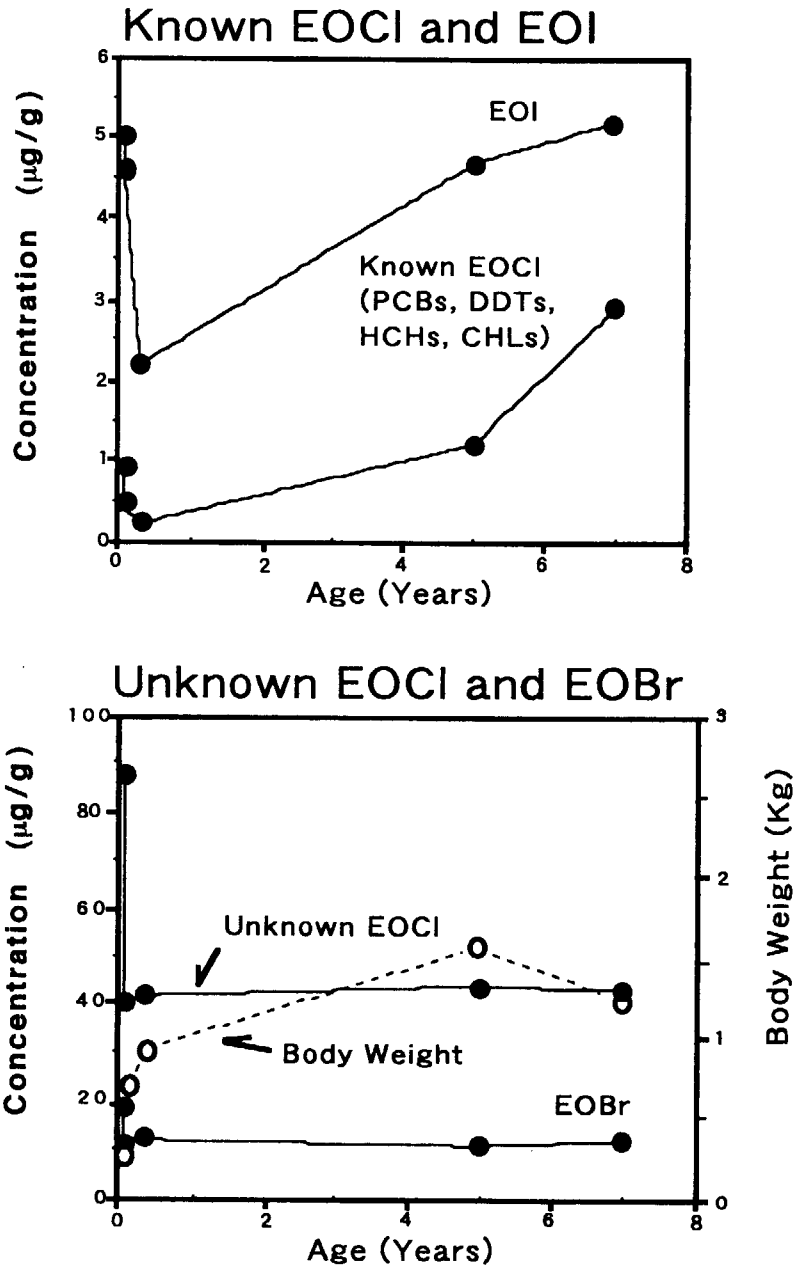


Fig. 3. Relationships between age and concentrations of known EOCl, unknown EOCl, EOBr and EOI in adipose tissue of brown booby collected at Nakanokami Island, South Ryukyus.

以上の結果、EOIは必須性の化合物より構成されることが考えられる。それに対して未知EOClとEOBrは蓄積性が低いことから非必須性であることが推定される。これらEOX濃度は比較的高いことから毒性など生体影響についてもさらに検討する必要がある。

成果の公表

学術誌等

(1)Loganathan, B.G., Kawano, M., Sajwan, K.S. and Owen, D.A.: Extractable organohalogens (EOX) in sediment and mussel tissues from the Kentucky Lake and Kentucky Dam Tailwater, USA. Toxicological and Environmental Chemistry, 79: 233-242(2000).

(2)M. Kawano, H. Kohno, J. Falandysz and T. Wakimoto, Extractable organohalogens (EOX) in brown booby (*Sula leucogaster*) from Nakanokamishima Island, South Ryukyus, Japan, Organohalogen Compounds, 52, 104-107 (2001).

学会講演等

(3)松井三明、鹿島勇治、河野公栄、松田宗明、脇本忠明: 廃棄物焼却灰のダイオキシン類・多環芳香族化合物とバイオアッセイ. 日本環境化学会, 第9回環境化学討論会講演要旨集、p36-37, 札幌、6月20～22日(2000).

(4)河野公栄、山本恭資、河野裕美、脇本忠明、仲ノ神島産カツオドリ(*Sula leucogaster*)における残留性人工有機塩素化合物と有機態塩素(EOCl)の蓄積特性、第9回環境化学討論会講演要旨集、p436-437、札幌、6月20～22日(2000年).

(5)松井三明、鹿島勇治、河野公栄、松田宗明、土井陸雄、脇本忠明: 焼却灰中ダイオキシン類の毒性評価　化学分析とバイオアッセイの比較検討. 日本衛生学雑誌、第５５巻、１号、ｐ.４１５、大阪市、3月28～30日((2000).

(6)河野公栄、K.カンナン、鹿島勇治、松井三明、J.P.ギーシー、脇本忠明、塩素製造工場付近に棲息する生物中の有機態ハロゲン(EOX)、第37回理工学における同位元素研究発表会、要旨集 p174、東京、7月3日～5日 (2000).

(7)河野公栄、河野裕美、脇本忠明、仲ノ神島産カツオドリ(*Sula leucogaster*)に蓄積する有機態ハロゲン(EOX)の機器中性子放射化分析、第44回放射化学討論会、日本放射化学会誌、1、別冊2、p120、神戸　9月12～14日(2000).

(8)M.Kawano, J. Falandysz, T. Wakimoto, Instrumental neutron activation analysis of extractable organohalogens (EOX) in Antarctic marine organisms. Journal of Radiochemical Sciences, Vol.2, Supplement, p.76 (2001).

(9)河野公栄、河野裕美、脇本忠明、仲ノ神島産カツオドリ(*Sula leucogaster*)に蓄積する有機態ハロゲン(EOX). 第10回環境化学討論会講演要旨集、 p366-367、松山, 5月(2001).

(10)Kawano, M., Falandysz, J. and Wakimoto, T., Instrumental neutron activation analysis of extractable organohalogens (EOX) in Antarctic marine organisms. 2001 Asia-Pacific Symposium on Radiochemistry and 2001 Annual Meeting of the Japan Society of Nuclear and Radiochemical Science/ The 45th Symposium on Radiochemistry. Proceeding. Fukuoka, October 30th - November 1st, (2001).

招待講演等

(11)河野公栄、脇本忠明、茂田良光、環境における未知有機ハロゲン化合物の存在とその挙動、「放射化分析の新展開」放射化分析研究会・日本放射化学会・放射化分析分科会、高エネルギー加速器研究機構・田無分室、田無市、3月21-22日 (2000).

(12)Masahide Kawano, Measurement of extractable organohalogens (EOX: chlorine, bromine and iodine) in environmental samples by neutron activation analysis. Key lecture at The Sixth International Symposium on Advanced Analytical Techniques and Applications,Kyungnam University, Korea, November 6-7 (2000).

3-15 岩石の酸性変質と二次鉱物の生成に伴うランタノイドの移動

Mobility of lanthanides accompanying rock alteration and formation of secondary minerals in acidic environment.

[1]大井隆夫, [1]木川田喜一, [1]大平力也, [2]本多照幸
([1]上智大学理工学部化学科, [2]武蔵工業大学原子力研究所)
[1]Takao OI, [1]Yoshikazu KIKAWADA, [1]Rikiya OHIRA, [2]Teruyuki HONDA
[1]Faculty of Science and Technology, Sophia University,
[2]Atomic Energy Research Laboratory, Musashi Institute of Technology

1. はじめに

火山地域においては，酸性の火山ガスや湧水などの火山性流体により岩石が酸性変質を受け，広範囲にわたる火山変質地帯が形成される場合がある．このような変質地帯においては，岩石成分の分解，溶脱，運搬が継続的に行われ，火山地域における物質循環における重要な役割を担っている．しかしながら岩石の変質とは，単純な岩石成分の溶脱現象だけではなく，その地質や環境に応じた二次鉱物の生成過程とが密接に関わったきわめて複雑な現象であることから，未だその体系的理解には至っていない．したがって岩石の変質現象の理解を深めるために，複雑に重なり合った様々な物理・化学現象を紐解き，個々の現象の詳細を明らかにしていくことが求められている．その中で本研究は，火山地域において広く見られる硫気変質地帯中に一般的に認められる変質二次鉱物"アルナイト"に着目し，そこに微量に含まれるランタノイドをトレーサーとして用いることにより，通常の主成分元素の挙動のみでは知り得ない変質過程の詳細を，アルナイトの生成過程を通して捉えようとするものである．

アルナイト(alunite：明礬石)は $KAl_3(SO_4)_2(OH)_6$ で示される二次鉱物であり，火山性の酸性変質地帯には広く見られる変質鉱物である．アルナイトの K を Na あるいは Ca で置換したものはそれぞれ，ナトロアルナイト(natroalunite)，フアンジャイト(huangite)と呼ばれ，これらはアルナイトグループ鉱物と総称される．また，カリウムの一部をナトリウムおよびカルシウムで置換した(Na, Ca, K)$Al_3(SO_4)_2(OH)_6$ の組成式で示される鉱物は南石(minamiite)と名付けられ，群馬県草津白根火山地域の奥万座が模式地となっている [1]．このように天然において産出するアルナイトは，実際には K, Na, Ca 端成分の固溶体として幅広い組成を持って産出する．

これまでの研究 [2-3]により，アルナイトに微量に含まれるランタノイドの，周辺岩石(母岩)に対する存在度パターンは，相対的に軽ランタノイドに富み，アルナイトに特有のパターンを示すことが示唆されており，アルナイトの生成過程にランタノイドの相互分別過程が内在する可能性が示されている．このような相互分別機構を解明することは，アルナイトの生成過程を理解する上で大きな役割を果たすものである．

そこで本研究では，アルナイトグループ鉱物中に含まれるランタノイド並びに，ランタノイドとその存在量の相関性が期待 [4]される Sr および Ba に着目し，アルナイトの生成過程に介在する，これら元素が関与する化学的現象を明らかにすることを第一の目的とした．

2. 実験

本研究を進めるにあたり，大きく分けて二つの実験を行った．ひとつは天然に産するアルナイトの分析であり，もうひとつは，実験室内で人工的にランタノイドを添加したアルナイトを合成する実験である．

2. 1. 天然産出アルナイトの分析

試料

研究施設と装置名：JRR-4 S-パイプ，T-パイプ，気送管
研究分野：地球化学的試料の放射化分析

本研究で用いたアルナイト試料は，群馬県草津白根火山地域で採取した17試料であり，その内訳は草津白根山の山頂火口湖である水釜から2試料，万座空噴源泉周辺から4試料，奥万座源泉周辺から11試料である．採取試料のいくつかは，色調の違いにより組成あるいは組織が明らかに異なると判断される複数の部分から成っており，このような場合には色調により試料を分け，それぞれ異なる試料として取り扱った．また，草津白根火山の基盤岩を成す高井溶岩[5]を比較のために用意した．試料採取地点はFig. 1に示してある．

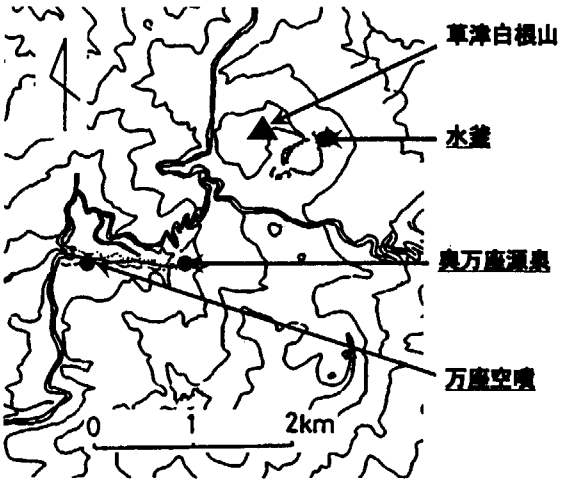


Fig. 1 試料採取場所

草津白根火山地域

本研究では群馬県草津白根火山地域を研究対象地域として取り上げている．草津白根山は群馬県北西部，長野県との県境近くに位置する，現在も活発に火山活動を続ける活火山である．山頂には北東から南西にかけてそれぞれ"水釜"，"湯釜"，"涸釜"と呼ばれる三つの山頂火口湖が並んでいる．最も大きな湯釜は，湖底からの火山ガスと酸性熱水の供給が知られ，強酸性の湖水を湛えている．この地域で最も活発な火山ガス噴気孔群は山頂の北側，水釜の外壁下に位置するが，東麓側中腹の殺生河原と，西麓側の万座地域にも噴気孔群があり，これらは広範囲な火山変質地帯を形成している．また，東麓の草津温泉と西麓の万座温泉は古くからこの地域の代表的温泉として知られ，共に酸性の温泉水を湧出しているが，その地表下においてはやはり岩石・土壌の酸性変質が広範囲に認められる．

天然試料の分析操作

採取されたアルナイト試料は，風乾後，粉砕し，粉末X線回折法(XRD)による鉱物種の同定を行い，湿式分析法並びにフッ化水素酸分解法を併用したICP発光分析法および炎光光度法により主成分元素の定量を行った．

ランタノイド並びにストロンチウム，バリウムの定量には非破壊中性子放射化分析法を用いた．日本原子力研究所東海研究所のJRR-4を中性子源として用い，高純度ゲルマニウム半導体検出器並びに4096ch波高分析器を用いてγ線の計測を行った．なお，いくつかの試料のランタノイドの定量のみ立教炉(TRIGA-II)を中性子源として用いた．中性子照射からγ線測定までの流れは，既報[6-7]に準じた．

2. 2. 実験室におけるアルナイトの合成

まず，希硫酸に過剰量のランタノイド酸化物を溶解させ，室温におけるランタノイドの混合飽和溶液を調製した．次に，この飽和溶液を用いて以下の二通りの実験を行った．

カリウムーランタノイドー硫酸複塩の生成実験

ランタノイドはカリウム，ナトリウムなどのアルカリ金属と硫酸複塩を形成することが知られている．そこでアルナイトの合成実験に先立ち，混合ランタノイド飽和溶液と硫酸カリウム溶液を所定の温度，時間で反応させることでカリウムーランタノイドー硫酸複塩の合成を試みた．実験手順は以下の通りである．

先に用意した飽和ランタノイド硫酸水溶液と，室温における飽和硫酸カリウム水溶液とを同体積ずつ取り，テフロン製の密閉容器内で，25℃，40℃，80℃，120℃で各々7日間，および室温において49日間反応させた．所定の反応日数終了後，反応溶液は0.1μmのメンブランフィルターを用いて濾過した．濾液中のランタノイドを定量し，出発溶液に含まれるランタノイド濃度との濃度差から元素ごとに固相への分配比を求めた．

水熱合成法によるアルナイトの合成

アルナイト生成に伴いアルナイト中に取り込まれるランタノイドの相互分別現象を実験的に確かめるため，以下の手順によりランタノイド添加系でのアルナイト合成実験を行った．

ほぼ飽和の硫酸カリウムアルミニウムと硫酸アルミニウムの混合水溶液に，ランタノイド混合飽和溶液を添加した後，200℃，80 kg cm^{-3} の条件下でアルナイトを水熱合成した．反応開始から72時間後に反応容器ごと急冷し，生成物を 0.1μm のメンブランフィルターで濾別した後，蒸留水で十分洗浄した．出発原料中ならびに合成

Table 1 アルナイト試料の主成分およびSr，Ba濃度分析値

Sample name	MIZ1	MIZ2	KAR1	KAR2a	KAR2b	KAR3	OKU1	OKU2	OKU3a
Color				white	gray				white
Location	Mizugama	Mizugama	Manza-Karabuki	Manza-Karabuki	Manza-Karabuki	Manza-Karabuki	Okumanza	Okumanza	Okumanza
(wt.%)									
SiO_2	2.67	0.08	12.44	60.45	35.39	47.34	1.92	3.89	18.17
Na_2O	2.45	2.19	0.70	0.29	0.50	0.58	2.06	2.82	1.02
K_2O	6.51	4.59	8.56	3.27	4.98	4.18	2.36	5.18	6.52
CaO	0.09	1.71	0.11	0.06	0.06	0.06	3.34	0.24	0.11
MgO	0.01	0.00	0.01	0.03	0.03	0.03	0.00	0.01	0.01
Al_2O_3	33.85	37.01	29.88	11.96	18.20	18.81	34.88	33.51	26.76
T-Fe_2O_3	0.71	0.02	0.19	0.69	4.80	0.50	0.01	3.96	2.85
MnO	0.00	0.00	0.00	0.00	0.03	0.00	0.00	0.00	0.00
TiO_2	0.09	0.00	0.09	0.52	0.71	0.61	0.02	0.38	0.48
P_2O_5	0.45	0.24	1.65	0.20	0.22	0.08	0.19	0.29	0.17
SO_4	40.15	36.26	37.75	15.38	34.92	22.26	35.36	50.71	39.00
H_2O	-	-	-	1.87	2.91	0.69	-	0.20	0.40
(ppm)									
Sr	1.1E+03	1.5E+03	3.7E+03	3.4E+02	4.8E+02	3.5E+02	4.1E+02	2.2E+03	1.2E+03
ERR(%)	3.4	3.7	2.5	8.7	6.8	23.6	5.5	7.8	4.8
Ba	3.5E+02	4.2E+02	6.9E+02	8.0E+02	4.9E+02	1.5E+02	1.1E+02	1.2E+02	3.3E+02
ERR(%)	10.9	11.6	10.4	4.6	6.5	19.5	13.8	40.1	10.3

Sample name	OKU3b	OKU4a	OKU4b	OKU5	OKU6a	OKU6b	OKU6c	OKU7	Takai lava
Color	gray	white	gray		white	gray	black		
Location	Okumanza	Okumanza	Okumanza	Okumanza	Okumanza	Okumanza	Okumanza	Okumanza	
(wt.%)									
SiO_2	26.92	23.83	42.28	7.80	5.35	66.90	55.80	2.81	62.16
Na_2O	1.26	0.96	0.86	2.16	2.06	0.81	0.56	2.12	2.86
K_2O	4.47	6.35	3.46	7.55	7.49	2.35	1.65	7.22	2.23
CaO	0.12	0.09	0.13	0.21	0.23	0.31	0.23	0.21	5.73
MgO	0.01	0.02	0.02	0.00	0.00	0.04	0.05	0.00	2.92
Al_2O_3	21.23	26.44	16.16	31.90	31.00	13.10	10.04	31.96	15.86
T-Fe_2O_3	8.77	0.60	7.31	0.11	0.27	1.66	16.60	0.07	7.01
MnO	0.00	0.00	0.00	-	-	-	-	-	0.11
TiO_2	0.58	0.52	0.73	0.01	0.01	0.90	2.29	0.01	0.68
P_2O_5	0.07	0.10	0.11	0.41	0.41	0.32	0.27	0.37	0.13
SO_4	46.78	33.10	37.08	38.70	40.50	16.10	17.30	40.80	-
H_2O	0.36	0.30	0.42	-	-	-	-	-	-
(ppm)									
Sr	6.6E+02	1.2E+03	7.4E+02	4.0E+03	4.7E+03	1.2E+03	7.0E+02	4.0E+03	-
ERR(%)	5.7	4.0	4.4	3.8	3.4	5.3	5.7	4.3	
Ba	3.3E+02	4.4E+02	1.6E+02	4.1E+02	4.9E+02	2.6E+02	1.5E+02	3.0E+02	-
ERR(%)	6.8	7.4	13.1	7.8	4.1	11.8	12.1	7.0	

ERR(%): Erros in gamma ray counting.

したアルナイト中のランタノイドを定量し，アルナイトの生成に伴うランタノイドの相互分配を求めた．

合成実験試料の分析操作

複塩生成実験ならびに水熱合成実験における生成物(固相)は，乾燥，粉砕して XRD によりその化学種の同定を行った．また，各出発原料(出発溶液)中，および複塩生成実験後の液相中のランタノイド組成は，ICP 発光分析法により行った．

水熱合成実験により得られた合成物中のランタノイド組成は天然試料の場合と同様に，JRR-4 を中性子源とした非破壊中性子放射化分析法により求めた．

3. 結果と考察

3. 1. 草津白根地域産出の天然アルナイト

主成分並びにストロンチウム，バリウムの定量結果を Table 1 に示した．また，ランタノイドの定量結果を Table 2 に示した．分析試料中の重ランタノイドの含有濃度が全体的に低かったため，中性子放射化分析法による定量がそれほど困難ではない Yb, Lu が検出限界以下となるものが多かったことが分かる．

XRD 測定の結果，全ての試料にアルナイトの存在を確認し，ナトリウムの含有量の多い試料にはナトロアルナイトが，カルシウム含有量の多い試料にはミナミアイトがそれぞれ含まれていた．また，ケイ酸の含有量が多い試料には，石英あるいは蛋白石の回折ピークが認められた．したがって，XRD による鉱物の同定結果は主成分分析結果と良く一致している．

天然アルナイトのランタノイドパターン

Table 2 アルナイト試料のランタノイド定量値

Sample name		La	Ce	Nd	Sm	Eu	Gd	Tb	Dy	Ho	Tm	Yb	Lu
MIZ1*	(ppm)	2.7E+01	5.3E+01	1.6E+01	5.9E-01	1.5E-01	ND	ND	3.1E-01	7.0E-02	8.0E-02	2.9E-01	4.0E-02
	ERR(%)	3.2	1.7	7.0	2.5	4.2			6.4	51.4	56.8	27.6	12.6
MIZ2*	(ppm)	7.2E+00	1.5E+01	6.1E+00	1.4E+00	3.6E-01	ND	ND	2.2E-01	ND	ND	2.3E-01	9.0E-02
	ERR(%)	5.6	2.6	22.3	4.3	3.1			4.0			14.3	11.9
KAR1*	(ppm)	4.7E+01	1.2E+02	3.4E+01	3.0E+00	6.1E-01	1.6E+00	ND	4.9E-01	ND	ND	4.7E-01	ND
	ERR(%)	2.0	4.8	13.1	2.4	8.5	22.1		8.9			26.2	
KAR2a	(ppm)	1.3E+01	1.9E+01	ND	9.2E-01	1.9E-01	ND	ND	4.6E-01	ND	ND	7.3E-01	ND
	ERR(%)	6.6	5.6		5.5	6.9			14.0			27.6	
KAR2b	(ppm)	1.3E+01	2.3E+01	ND	9.8E-01	1.6E-01	ND	ND	ND	ND	ND	1.2E+00	ND
	ERR(%)	9.8	4.4		3.4	25.2						40.7	
KAR3	(ppm)	2.1E+01	3.4E+01	ND	1.7E+00	5.4E-01	ND	5.3E-01	8.0E-01	ND	ND	8.1E-01	1.3E-01
	ERR(%)	3.0	3.6		3.5	7.0		7.3	10.9			11.3	7.9
OKU1*	(ppm)	3.3E+00	6.6E+00	2.9E+00	5.9E-01	2.8E-01	ND	6.6E-02	2.3E-01	ND	ND	ND	2.1E-02
	ERR(%)	9.1	18.9	14.5	1.8	3.1		24.8	7.7				21.5
OKU2	(ppm)	1.9E+01	3.3E+01	ND	3.3E+00	1.3E+00	ND	4.0E-01	6.9E-01	ND	ND	4.5E-01	6.0E-02
	ERR(%)	6.4	4.4		6.9	6.2			5.7			14.4	11.7
OKU3a	(ppm)	1.4E+01	3.1E+01	1.3E+01	3.6E+00	8.5E-01	ND	7.1E-01	6.7E-01	ND	ND	1.2E+00	1.5E-01
	ERR(%)	4.2	6.2	35.9	6.4	7.2		61.8	8.8			23.9	6.7
OKU3b	(ppm)	1.0E+01	2.0E+01	1.1E+01	1.7E+00	4.6E-01	ND	ND	5.9E-01	ND	ND	ND	1.9E-01
	ERR(%)	8.8	5.0	37.2	6.4	7.5			15.4				11.9
OKU4a	(ppm)	1.3E+01	1.8E+01	ND	1.8E+00	5.5E-01	ND	ND	1.0E+00	ND	ND	1.9E+00	1.2E-01
	ERR(%)	6.3	6.3		6.2	8.2			16.2			24.3	15.0
OKU4b	(ppm)	1.5E+01	2.9E+01	ND	2.2E+00	7.1E-01	ND	ND	1.1E+00	ND	ND	ND	9.4E-02
	ERR(%)	7.7	3.3		6.4	10.9			9.9				26.6
OKU5	(ppm)	4.0E+01	7.3E+01	3.2E+01	1.2E+01	2.4E+00	ND	6.0E-01	1.0E+00	ND	1.8E+00	4.6E-01	ND
	ERR(%)	1.2	1.5	15.6	0.7	2.3		13.8	23.7		4.9	26.7	
OKU6a	(ppm)	3.2E+01	6.2E+01	4.6E+01	8.9E+00	2.0E+00	ND	7.2E-01	ND	ND	7.6E-01	8.9E-01	ND
	ERR(%)	1.4	1.7	9.9	0.9	2.1		14.9			19.7	151.6	
OKU6b	(ppm)	1.9E+01	4.0E+01	2.5E+01	6.4E+00	1.3E+00	ND	3.5E-01	1.4E+00	ND	1.3E+00	8.5E-01	1.5E-01
	ERR(%)	1.3	2.5	12.5	3.8	3.5		12.0	9.1		3.7	12.9	11.1
OKU6c	(ppm)	1.3E+01	2.7E+01	1.8E+01	4.2E+00	8.7E-01	ND	2.4E-01	9.2E-01	ND	1.4E+00	1.1E+00	2.2E-01
	ERR(%)	2.4	4.0	20.7	5.3	2.4		25.6	11.2		4.9	15.4	11.6
OKU7	(ppm)	3.3E+01	6.6E+01	4.1E+01	1.0E+01	2.1E+00	ND	4.4E-01	1.2E+00	ND	1.3E+00	ND	ND
	ERR(%)	1.1	1.7	10.2	0.9	1.7		12.6	16.2		9.9		
TAKAI	(ppm)	1.1E+01	2.2E+01	1.2E+01	3.4E+00	1.1E+00	ND	5.2E-01	3.5E+00	ND	ND	2.6E+00	4.1E-01
LAVA	ERR(%)	3.8	5.0	27.9	5.9	5.1		12.1	16.0			7.0	5.1

ERR(%): Erros in gamma ray counting.
*: 立教炉を利用しての分析値

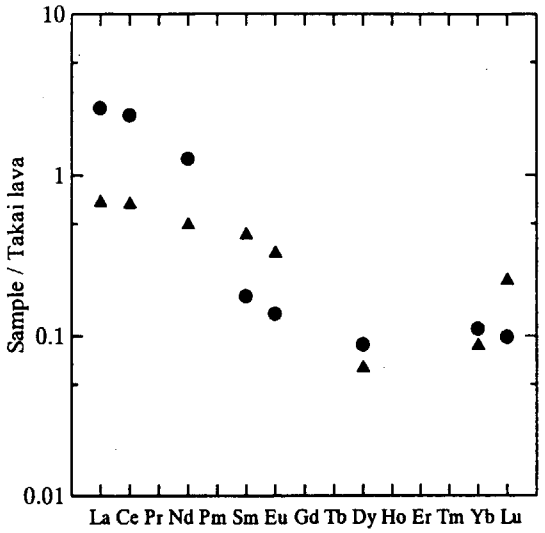


Fig. 2 水釜産出アルナイト試料のREEパターン
●;MIZ1, ▲;MIZ2.

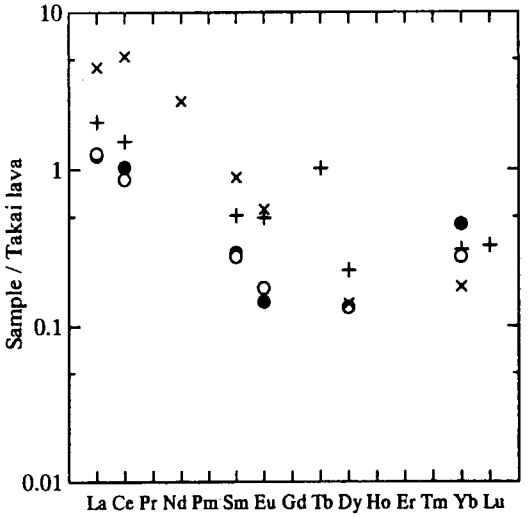


Fig. 3 万座空噴産出アルナイトのREEパターン
×;KAR1, ○;KAR2a, ●;KAR2b, ＋;KAR3.

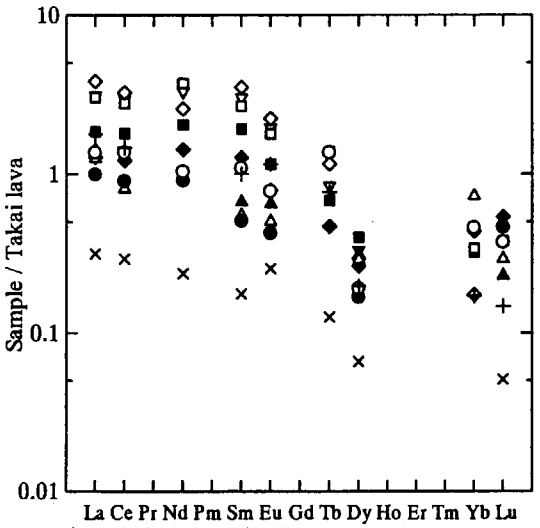


Fig. 4 奥万座産出アルナイトのREEパターン
×;OKU1, ＋;OKU2, ○;OKU3a, ●;OKU3b,
△;OKU4a, ▲;OKU4b, ◇;OKU5, □;OKU6a,
■;OKU6b, ◆;OKU6c, ▽;OKU7.

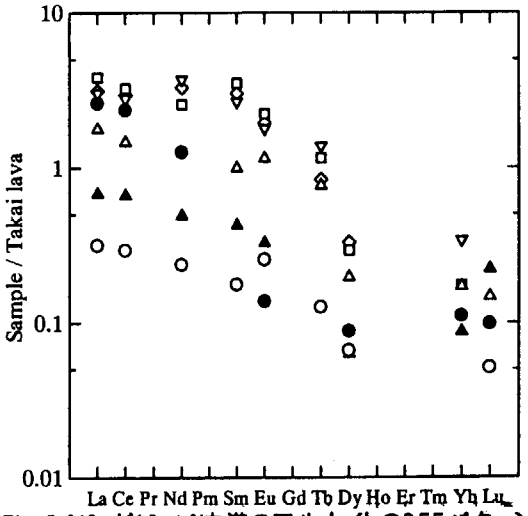


Fig. 5 SiO_2が10wt.%未満のアルナイトのREEパターン
○;OKU1, △;OKU2, □;OKU5, ▽;OKU6a,
◇;OKU7, ●;MIZ1, ▲;MIZ2.

Table 2 に示した各アルナイト試料のランタノイド定量値を，この地域の基盤岩として知られる高井溶岩中のランタノイド定量値で規格化することで得られたランタノイド存在度パターン(Masuda-Coryell plot)を Figs. 2, 3, 4 に示した．これを見ると，試料ごとにランタノイドの含有濃度に違いはあるものの，何れの試料も重ランタノイドに比較して軽ランタノイドに相対的に富んだ類似のパターンを示すことが分かる．また，その傾向は試料の採取位置に依らずに共通のものである．したがって，これはアルナイトに共通のランタノイド存在パターンであると考えられる．

Table 1 を見て分かるとおり，今回分析した試料の中には数 10 wt.%から大きいものでは 60 wt.%を越える SiO_2 濃度を示すものがある．このような SiO_2 濃度の高い試料は XRD の結果から，アルナイトと共に蛋白石，あるいは非晶質シリカのような，理想的には SiO_2 のみから成る変質鉱物が共存している試料であることが分かっている．そのため，純粋なアルナイトにおけるランタノイドの挙動を見極めるために，Fig. 5 に SiO_2 の濃度が 10 wt.%未満であった7試料のみのランタノイドパターンを示した．これを見ると，やはり試料ごとにランタノイド濃度に違い

があるが，試料間のランタノイド濃度差は，重ランタノイドよりも軽ランタノイドで大きいように見ることが出来る．すなわちアルナイトの生成に伴うランタノイドの相互分別現象は，軽ランタノイドにおいてより大きいと見なせる．また，パターンの形状はTb－Dy付近でプロットの繋がりに連続性を欠き，この前後でランタノイドの挙動に差異があることが示唆される．すなわち，Tbより軽いランタノイドでは，やや弓形になりながら，軽いものほど相対的濃縮傾向が強くなるような連続的な変化を示すのに対し，Dyより重いランタノイドでは，元素間での明瞭な分別が認められない．

以上の点を整理すると，アルナイトにおけるランタノイドの分別現象は，Tb－Dyを境界としてその前後で異なっており，その差異の生じる原因としての何らかの物理・化学的現象がアルナイトの生成過程に関与していること考えられる．また，軽ランタノイドにおいて，軽い元素ほど相対的に濃縮する傾向を示し，その濃縮傾向の強さが原子番号と共にほぼ連続的に変化することから，そこには，おそらくはイオン半径に依存するような何らかの分別現象が介在しているものと考えられる．

ストロンチウム，バリウムおよびランタノイド含有濃度間の相関性

Table 1を見ると，ストロンチウムの含有量は300 ppm程度から多いものでは4,000 ppmを越えるものまで非常に幅広い範囲にわたっている．数千ppmに達するストロンチウム濃度は一般的な火山岩中の存在量に比較して極めて高い．一方，バリウムは100～800 ppmの範囲にあり，ストロンチウムに対して試料間での濃度のばらつきは若干小さく，また一般的な火山岩と比較して特異的に高い値ではない．以上より少なくともストロンチウムは明らかにアルナイト中に濃縮していると見ることができる．

Fig. 6にストロンチウム濃度とバリウム濃度の相関図を示す．ここからは一見，両元素の濃度間には有意な相関性は無いように見えるが，一方で図中の直線A，Bで示したような複数の独立した相関性が存在している可能性も否定できない．ここで奥万座産出のアルナイト試料の中でケイ酸の濃度が10 wt.%未満のものに対する回帰直線（相関係数0.90）が直線Aであり，ケイ酸濃度が10 wt.%以上のものに対する回帰直線（相関係数0.54）が直線Bである．万座空噴並びに水釜産出のアルナイト試料は分析数が少なく，かつ，万座空噴産出ではケイ酸濃度の低い試料がひとつしか得られなかったことから，ここでその相関性について議論することはできないものの，少なくとも奥万座産出の分析試料を見る限り，ケイ酸濃度の低い，すなわち，不純物の少ないアルナイト試料においては，ストロンチウム濃度とバリウム濃度との間には有意な相関性があると見ることが可能である．

ストロンチウムとバリウムのようなアルカリ土類は，単

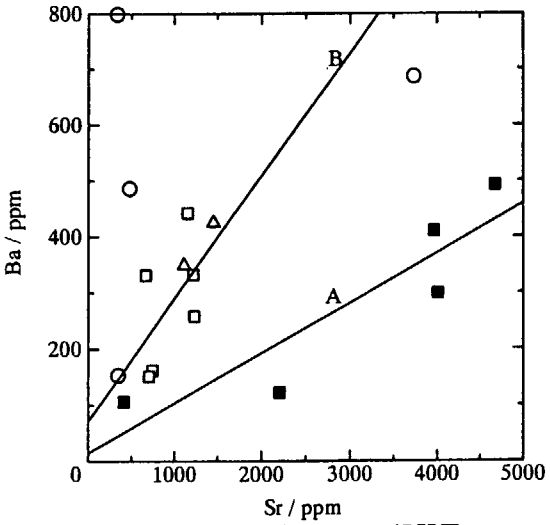


Fig. 6. 天然アルナイト試料のSr-Ba相関図
○；万座空噴，△；水釜，□；奥万座(SiO_2 ≧ 10 wt.%)，■；奥万座 (SiO_2 ＜ 10 wt.%).

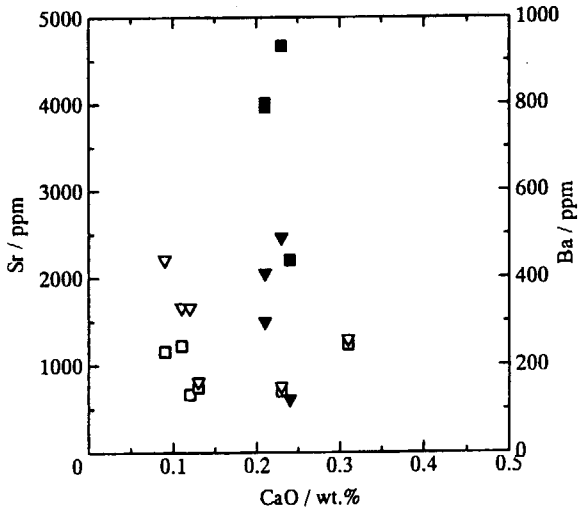


Fig. 7 奥万座産出アルナイト試料のCa-SrおよびCa-Ba相関図
□；Sr (SiO_2 ≧ 10 wt.%)，■；Sr (SiO_2 ＜ 10 wt.%)，△；Ba (SiO_2 ≧ 10 wt.%)，▲ Ba (SiO_2 ＜ 10 wt.%).

純にはアルナイトグループ鉱物中で同じアルカリ土類であるカルシウムを置換していると想像される．もし両元素がアルナイトグループ鉱物中のカルシウムの一部を置換しているのであれば，アルカリ金属濃度に対してカルシウム濃度が高い試料，すなわち，ミナミアイトを多く含む試料ほどそれらの含有量は高くなるはずである．しかしながら，実際には最もカルシウム濃度が高いOKU1のストロンチウム，バリウム濃度は全試料中でかなり低濃度の部類に属し，OKU1を除外してもカルシウム濃度との間には相関性は認められない(Fig. 7)．したがって両元素はカルシウムとの単純な置換により取り込まれているものではない．

ストロンチウムとバリウムを含むアルナイト類似鉱物としては，walthierite ($Ba_{0.5}Al_3(SO_4)_2(OH)_6$)，gorceixite ($BaAl_3(PO_4)(PO_3OH)(OH)_6$)，goyazite ($SrAl_3(PO_4)_2(OH)_5\cdot(H_2O)$)などが知られているが，一般にイオン半径の大きいストロンチウム，バリウムは対となる陰イオンとして硫酸イオンよりもリン酸イオンあるいはヒ酸を好む．一方，奥万座産出のアルナイト中には，微小なcrandallite ($CaAl_3(PO_4)_2(OH)_5\cdot(H_2O)$)の結晶が存在することが報告されており[4]，また，今回の草津白根火山地域産出の天然アルナイト試料の分析値においても，軽ランタノイド濃度とリン濃度との間に良好な正の相関性が認められる(Fig. 8)ことから，crandalliteのカルシウムサイトをランタノイドに置き換えた組成を有するflorencite ($(La,Ce,Nd)Al_3(PO_4)_2(OH)_6$)のようなリン酸塩鉱物中にランタノイドが取り込まれている可能性が高い．したがってストロンチウムやバリウムもリン酸を伴った鉱物を形成し，アルナイト中に共存している可能性は高いと思われる．そこでFig. 9に奥万座産のアルナイト試料におけるリン濃度とストロンチウム，バリウム濃度との相関図を示した．これを見ると，ケイ酸濃度が低く，純度の高いアルナイト試料においては，両元素濃度共にリン酸濃度との間に比較的良い相関性(相関係数 $r > 0.9$)を有し，やはりストロンチウムとバリウムがリン酸と対になってアルナイト中に取り込まれていることを示す結果となった．さらに同じく奥万座産のアルナイト試料について，ストロンチウム濃度とランタン濃度との相関性(Fig. 10)を求めたところ，ケイ酸濃度の大小にかかわらず，全ての試料を通して良好な相関性(相関係数 0.93)が認められ，ストロンチウムと軽ランタノイドがアルナイトの生成過程において挙動を共にしていることが示された．

以上の結果より，火山地域における岩石の酸性変質に伴って生成するアルナイト中に微量に含まれるストロンチウム，バリウムは，アルナイト類似の含リン酸鉱物として存在している可能性が高いと言える．またその際，軽ランタノイドもストロンチウムに付随して含リン酸鉱物中に取り込まれているものと考えられる．

3. 2. アルナイト合成実験

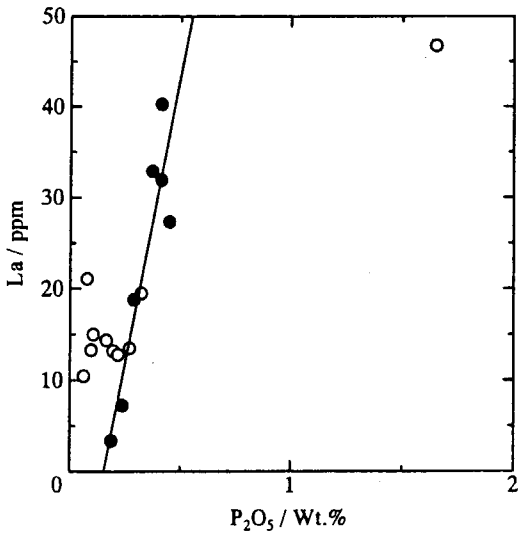


Fig. 8 天然アルナイト試料のP－La相関図
○; $SiO_2 \geqq 10$ wt.%, ●; $SiO_2 < 10$ wt.%

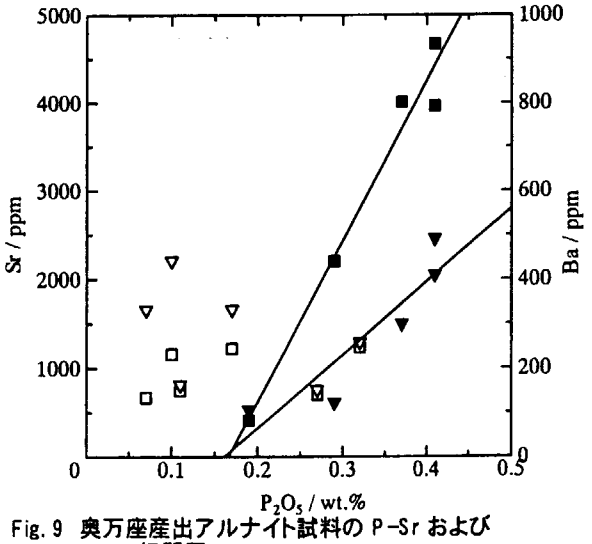


Fig. 9 奥万座産出アルナイト試料のP－SrおよびP－Ba相関図
□; Sr ($SiO_2 \geqq 10$ wt.%), ■; Sr ($SiO_2 < 10$ wt.%),
▽; Ba ($SiO_2 \geqq 10$ wt.%), ▼; Ba ($SiO_2 < 10$ wt.%).

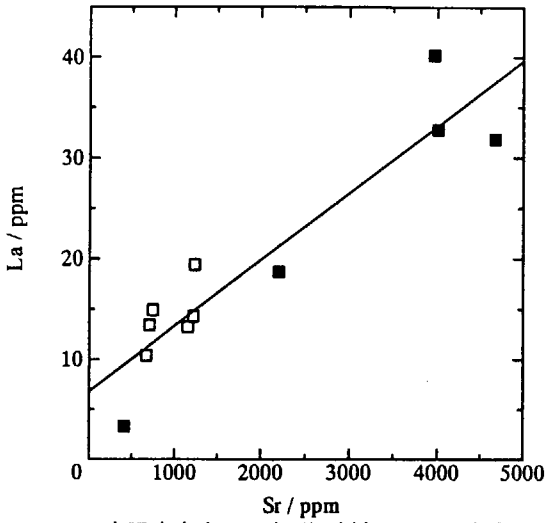


Fig. 10 奥万座産出アルナイト試料の Sr-La 相関図
□; $SiO_2 \geqq 10$ wt.%, ■; $SiO_2 < 10$ wt.%

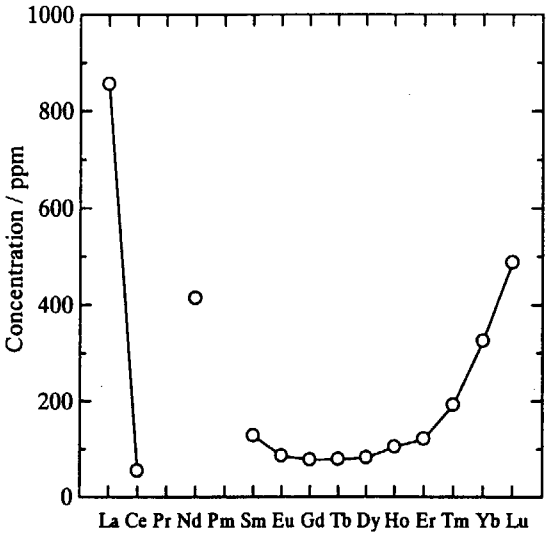


Fig. 11 飽和ランタノイド硫酸水溶液の組成

飽和ランタノイド硫酸水溶液の組成

室温にて 13 元素の酸化ランタノイドを希硫酸に溶解することで得られた飽和ランタノイド硫酸水溶液の組成を Table 3 および Fig. 11 に示した. Fig. 11 から分かるように, 約 5 mol dm^{-3} の硫酸濃度の元で, ランタノイドの溶存濃度は軽ランタノイド, 重ランタノイドの両極で高く, その中間で低いものとなった. ここで Ce の溶解度が La, Nd に比較して極度に小さいが, これは, 今回用いた Ce 以外の酸化ランタノイド試薬が+3 価の Ln_2O_3 であったのに対して, Ce のみ+4 価の酸化物($Ce^{IV}O_2$)であったためである.

カリウム-ランタノイド-硫酸複塩の生成に伴うランタノイドの相互分別

反応実験終了後の反応溶液の濾液中に含まれるランタノイド濃度と出発原料中のランタノイド濃度との差から固相中に取り込まれたランタノイドの物質量を求め, それを出発原料中に存在していたランタノイドの物質量で規格化することで得られた各元素の分配比を Fig. 12 に示した. これを見ると, 何れの反応条件においても固－液間でランタノイドの相互分別が生じていることが分かる. しかしながら, その分別状況は反応温度により異なっている. 室温と 25℃における分配パターンは一致し,

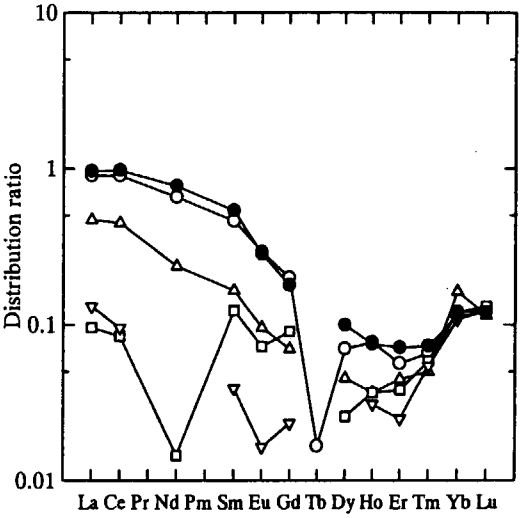


Fig. 12 カリウム-ランタノイド-硫酸複塩の生成に伴うランタノイド分配比
○; 25℃ × 7日間, △; 40℃ × 7日間,
□; 80℃ × 7日間, ▽; 120℃ × 7日間,
●; 室温 × 49日間.

40℃におけるパターンも軽ランタノイドにおける分配比が小さくなるものの, やはり同様のパターンと見なすことが出来る. また, そのパターン形状は天然のアルナイトに見られるランタノイドパターンと良く一致する. 一方, 80℃, 120℃における分配パターンは, 非常にばらつきが大きく, 明らかに 40℃以下で見られた分配パターンとは異なっている. しかしながら, 再後端の Tm から Lu に

Table 3 飽和ランタノイド硫酸水溶液の組成

成分	SO_4	La	Ce	Pr	Nd	Pm	Sm	Eu	Gd	Tb	Dy	Ho	Er	Tm	Yb	Lu
	(mol/dm^3)	(ppm)														
濃度	5.3	856	54.4	-	414	-	128	85.6	77.4	78.3	81.7	104	121	192	325	488

かけての部分では，全ての条件においてそのプロットがほぼ一致し，反応温度における違いが認められない．室温における反応後の残渣の XRD パターンが $Ln_2K_{10}(SO_4)_8$ の回折パターンと一致することから，ここで生じたランタノイドの相互分別現象は，カリウムーランタノイドー硫酸複塩の生成によるものであると考えられるが，その複塩の生成は軽いランタノイドほど強い温度依存性を有することが分かる．

合成アルナイトにおけるランタノイドの相互分別と天然産出アルナイトの比較

水熱合成により得られた合成アルナイト中に含まれるランタノイドの物質量を，出発原料中に含まれるランタノイドの物質量で規格化することにより得られたランタノイドの分配パターンを Fig. 13 に示す．このパターンを見ると La から Tb 付近まで原子番号が増加するにつれて連続的に分配比が小さくなるが，Tb より後ろ，Yb までは分配比に変化が認められず，Lu において再び大きく分配比を下げている．このようなパターンは，軽ランタノイドで左上がりを示し，Tb 付近を境界にその前後で傾向が異なるという点で，カリウムーランタノイドー硫酸複塩に認められた分配比パターンや，天然産出アルナイトに認められる存在度パターンと共通である．したがってこの結果は，天然におけるアルナイトの生成過程において，硫酸複塩が関与することで，アルナイトに独特のランタノイド相互分別現象が生じていることを強く示唆するものである．

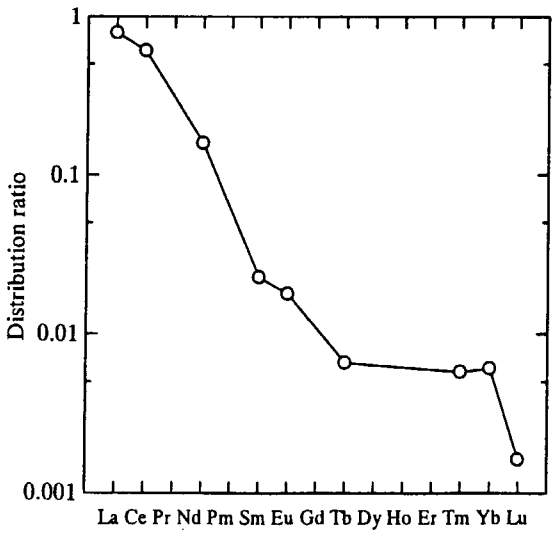


Fig. 13 合成アルナイトのランタノイド分配比

4. まとめ

本研究により，岩石の酸性変質に伴うアルナイトの生成過程に関して，以下の点が明らかになった．

(1)天然産出のアルナイトに共通のランタノイド存在度パターンが見出された．この存在度パターンはアルナイトに特徴的なものであり，軽ランタノイドほどアルナイト中に取り込まれやすい．

(2)天然産出のアルナイトにおいては，軽ランタノイド，ストロンチウム，バリウムおよびリンの含有量の間には，相互に正の相関性が認められ，軽ランタノイドの一部はストロンチウム，バリウムと共にアルナイト類似のリン酸塩鉱物中に取り込まれている可能性が高い．

(3)実験室で合成したカリウムーランタノイドー硫酸複塩ならびに，ランタノイドを添加した合成アルナイトに認められるランタノイドの分配比のパターンは，天然産出のアルナイトの存在度パターンと類似しており，天然産出アルナイトに特有のランタノイド相互分別現象は，上記複塩が生成することにより生じる可能性が強く示唆された．

(4)火山地域における岩石の酸性変質に伴うアルナイトの生成は，カリウムーランタノイドー硫酸複塩が生成しうる環境の元に生じているものと考えられる．

引用文献

1) Ossaka, J., Hirabayashi, J., Okada, K., Kobayashi, R., Hayashi, T., 1982. Crystal structure of minamiite, a new mineral of the alunite group. Amer. Mineral., 67, 114-119.

2) Terakado, Y. and Fujitani, T., 1998. Behavior of the rare earth elements and other trace elements during interactions between acidic hydrothermal solutions and silicic volcanic rocks, southwestern Japan. Geochim. Cosmochim. Acta, 62, 1903-1917.

3) 木川田喜一，宇留賀恵，大井隆夫，本多照幸，1998. アルナイトグループ鉱物のランタノイド元素．1998 年度日本地球化学会年会講演予稿集．

4) Matsubara, S., Matsuyama, F., Kiyota, K., Kato, A., 1998. Huangite from Okumanza, Gunma Prefecture,

Japan. Mineral. J., 20, 1-8.

5) 早川由紀夫, 1983. 草津白根火山の地質. 地質学雑誌, 89, 511-525.

6) Honda, T., Oi, T., Ossaka, T., Nozaki, T., Kakihana, H., 1989. Determination of rare earth elements in hot spring water and crater lake water samples by neutron activation analysis incorporating coprecipitation process using aluminium as a collector. J. Radioanal. Nucl. Chem., 130, 81-97.

7) Honda, T., Oi, T., Ossaka, T., Nozaki, T., Kakihana, H., 1989. Determination of rare earth elements in hot spring and crater lake waters by epithermal neutron activation analysis. J. Radioanal. Nucl. Chem., 133, 301-315.

成果の公表

紀要等

1. 木川田喜一, 大井隆夫, 本多照幸, 群馬県万座地域産出アルナイト中のストロンチウム並びにバリウム含有量. 平成 13 年度 武蔵工業大学原子力研究所研究所報.

学位論文等

1. 大平力也, 2000 年度 上智大学理工学部化学科卒業論文. 群馬県奥万座地域における岩石の変質とランタノイドパターン.
2. 三國智史, 2001 年度 上智大学理工学部化学科卒業論文. アルナイトの生成に伴うランタノイド元素の分別現象.
3. 村田有美, 2001 年度 上智大学理工学部化学科卒業論文. 硫酸酸性環境下でのランタノイドの挙動.

学会発表等

1. Kikawada, Y., Uruga, M., Oi, T., Honda, T., Mobility of lanthanides accompanying formation of alunite group minerals. Third International Symposium on Nuclear Analytical Chemistry, 2001.

研究テーマ： 環境関連物質の分析高度化研究
表　　題： 中性子放射化分析の研究

3-16

中性子放射化分析の研究

米沢仲四郎，松江秀明，Sri Wardani
環境科学研究部 分析科学研究グループ

1．はじめに

平成12年度と13年度は，JRR-3M，JRR-4の気送管及び水力照射設備を使用し，1) 熱外中性子放射化とコンプトンサプレッションγ線スペクトル測定による生体試料中の微量ヨウ素の定量，2) k_0 法による多元素標準物質，及び3) 底質標準物質の分析を実施した。

2．Non-destructive determination of trace amounts of iodine in biological samples by epithermal neutron activation and Compton suppression gamma-ray spectrometry[1]

The importance of iodine in radiation protection, medicinal, nutritional and epidemiological research studies demands an accurate determination of traces of iodine in biological materials. Radioactive nuclides such as ^{38}Cl and ^{24}Na produced from matrices interfere in the trace determination of iodine in biological materials when ^{128}I (hail-life 24.99 min) is applied for NAA of iodine. The interference, however, can be reduced by employing epithermal activation and Compton suppression γ-ray spectrometry because the resonance integral of iodine is larger than those of Cl and Na, and the emitting γ-ray energy of ^{128}I is lower than those of ^{38}Cl and ^{24}Na. In the present study, epithermal neutron activation analysis in conjunction with Compton suppression spectrometry has been examined for the determination of iodine in various biological samples.

A sample was irradiated at JRR-4 pneumatic tube using Cd filter for 10 s to 5 min together with an iodine standard. The γ-ray spectra were measured by a Compton suppression spectrometer using a Ge-BGO detector system.

When compared with the case of thermal neutron activation, radioactivity of ^{38}Cl and ^{24}Na induced by the epithermal neutron activation using Cd filter at JRR-4 PN irradiation facility decreased by factors 8.5 and 7.0, respectively, however, the induced radioactivity of ^{128}I decreased by only factor 1.8. The Compton background counts at ^{128}I 443 keV region suppressed by factors 4.3, and 11 for ^{38}Cl and ^{24}Na, respectively, by the Compton suppression γ-ray spectrometry compared to the single mode γ-ray measurement. The detection limits of iodine in biological samples by 1) conventional thermal neutron activation and normal γ-ray measurement, 2) epithermal activation and normal γ-ray measurement, and 3) epithermal activation and the Compton suppression γ-ray measurement were 2600 ppb, 450 ppb and 14 ppb, respectively. More than 35 ppb of iodine in various materials such as human diets, bovine muscle, non-fat milk powder, oyster tissue and human thyroid were determined. The analytical results agreed well with other reported values.

3．Multi-element determination for the characterization of SMELS samples by k_0-INAA[2]

Three types of Synthetic Multi-Element Standard (SMELS), which were spiked with a total of 33 elements into a phenol-formaldehyde resin, have been prepared at IRMM, Geel and INW, Gent for QC/QA of k_0-NAA. Co-operative analysis of the SMELSs has been carried out by several laboratories to characterize the elemental concentration of the spiked elements. We were determining the elemental concentrations in the SMELSs by k_0-INAA using the NAA facilities of the JRR-3M reactor at JAERI.

Samples (50 to 100 mg) were sealed in high-purity polyethylene film and irradiated for 10 s to 20 min in the pneumatic tube irradiation

原子炉: JRR-3M, -4　　装置：気送管，水力照射設備　　分野：中性子放射化分析（分析化学一般）

facility of the JRR-3M with a neutron flux higher than 10^{13} n cm^{-2} s^{-1}. After cooling during periods corresponding to the half-lives of the measured radionuclides, gamma-ray spectra were measured using calibrated high-purity Ge detectors and the spectra obtained were analyzed by the HYPERMET-PC program. Elemental concentrations in the samples were calculated by the KAYZERO program using the parameters obtained for the calibration of the detector and the neutron spectrum. In the detector calibration, detection efficiency and P/T curves for the Ge detectors were measured using calibrated gamma-ray sources. The solid angle and coincidence summing correction parameters for the samples were calculated by the SOLCOI program. The neutron spectrum parameters of the irradiation channel such as alpha, f and Fc were measured by irradiating Au-Al wires (IRMM 530) and Zr foils.

Elemental determination of the spiked elements were also carried out by comparative standardization irradiating standard samples for the corresponding elements together with samples. Analytical results of the SMELSs by the k_0 and comparative standardization will be reported.

4．k_0法による底質標準物質の分析[3,4]

中性子放射化分析法（NAA）は，多元素を高感度で，且つ正確に定量することができることから標準物質の認証値を決めるための必要不可欠な分析法となっている．De Corte らによって開発された k_0-NAA 法は，比較標準試料を使用しないで多元素を 3.5%以下の正確さで定量することができる．独立行政法人産業技術総合研究所計量標準総合センター（NMIJ/AIST）では，有害金属分析用の標準物質として港湾と湖の二種類の底質試料を調製し，現在その共同分析が行われている．筆者らはこの共同分析に参加し，k_0-NAA により，これらの標準物質の多元素定量を行った．

定められた方法によって乾燥させた二種類の底質試料約 0.1 g を高純度のポリエチレン袋中にはかりとり，三重に封入した．中性子モニターとして Al-Au 合金（IRMM-530, Au: 0.1%）0.015 g, Zr 板（純度 99.7%, 厚さ 0.1 mm）0.1 g をポリエチレン袋に封入し，中及び長寿命核種の測定の場合は試料と同時に，また半減期が分オーダーの短寿命核種測定の場合は，試料とは別に中性子照射をした．分析は，測定する核種の半減期に応じ，短寿命，中寿命及び長寿命核種に分けて行った．中性子照射には JRR-4 を使用し，短寿命核種測定の場合は気送管で 10 sec, 中及び長寿命核種測定では TB-パイプで 2～20 min 照射した．γ線スペクトル測定は，あらかじめ検出効率とピーク対全計数（P/T）比測定によって校正した高純度 Ge 検出器を使用して行った．得られたγ線スペクトルを HYPERMET-PC プログラムによって解析し，k_0 法の解析プログラム KAYZERO/SOLCOI によって元素濃度を定量した．

本分析により，短寿命核種測定では Mg, Al, Cl, Ca, Ti, V, Mn が，中寿命核種測定では Na, K, As, Br, La が，そして長寿命核種測定では Sc, Cr, Fe, Co, Zn, Rb, Ba, Cs, Ta, Th 等の合計 22 種類以上の元素が定量された．また，既に多くの定量値が報告されている池底質（NIES No.1）と River Sediment (NIST SRM1645)標準物質も分析し，定量値の正確さを評価した．

5．成果の公表

1 C. Yonezawa, H. Matsue, M. Yukawa: "Non-destructive determination of trace amounts of iodine in biological samples by epithermal neutron activation and Compton suppression gamma-ray spectrometry", J. Radioanal. Nucl. Chem., **255**, 105 (2003).

2 C. Yonezawa, H Matsue: "Multi-element determination for the characterization of SMELS samples by k_0-INAA at JAERI", The 3rd International k_0-Users Workshop, Bruges, Belgium, 23-28 September 2001.

3 米沢仲四郎，松江秀明，Sri Wardani: "k_0-機器中性子放射化分析法による底質標準物質の多元素定量"，第 63 回分析化学討論会，2002 年 5 月，姫路市で発表。

4 松江秀明，米沢仲四郎: "k_0 法に基づく即発γ線分析及び中性子放射化分析による底質標準物質の多元素定量"，第 46 回放射化学討論会，2002 年 9 月，札幌市で発表。

This is a blank page.

4. ＲＩの製造

4. Production of Radio Isotopes

This is a blank page.

4-1

イットリア微小球の原子炉照射実験

Reactor Irradiation Experiment for Yttria Microspheres

日本原子力研究所[*1]
(株)シミズテック[*2]
(財)放射線利用振興協会[*3]
(株)東京ニュークリア・サービス[*4]

小林勝利[*1]、○反田孝美[*1]、小畑 敬[*1]、清水泰博[*2]、澤田良樹[*2]、斎藤 誠[*2]、麻田能嗣[*2]、佐伯秀也[*3]、根本正弘[*4]、岩本清吉[*1]
(KOBAYASHI, Katsutoshi; SORITA, Takami; OBATA, Takashi; SHIMIZU, Yasuhiro; SAWADA, Yoshiki; SAITO, Makoto; ASADA, Yoshitugu; SAEKI, Hideya; NEMOTO, Masahiro; IWAMOTO, Seikichi)

1. はじめに

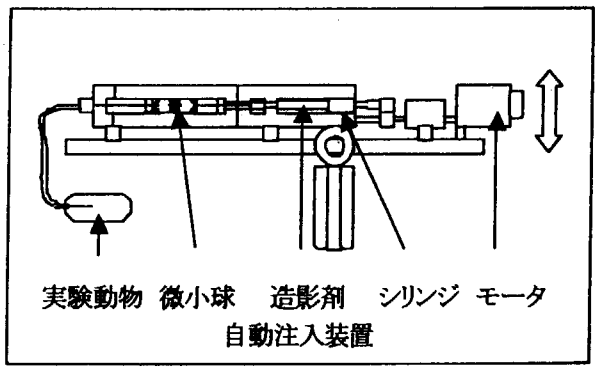
諸外国では、放射性微小球を血管造影剤とともにカテーテルをとおして直接肝腫瘍近傍に送り込み、β線照射により患部を切除することなく腫瘍部のみ治療する内用療法が行われている。^{90}Y(半減期:64.10h)は、最大エネルギーが約 2.3MeV の純β線放出核種であり、ガラス微小球($^{90}Y_2O_3$-Al_2O_3-SiO_2など)は化学的耐久性が高いことなどから、治療用線源として注目されている。

ここでは、京都大学工学研究科及び㈱高周波熱錬が共同開発したイットリウムの存在率が高いガラス微小球(Y_2O_3:直径 20～30 μm)を用い、術者の被曝と汚染防止を兼ね、注入量を一定に制御する注入システムを独自に開発するため、注入カプセル設計・製作、原子炉照射、放射性核種分析、^{90}Y の生成量測定、微小球の詰替え及び注入試験などを実施したので報告する。

2. 実験方法

最初に、微小球と原研カタログ製品である ^{90}Y 製造用ターゲット(Y_2O_3 粉末)をそれぞれ約 50mg づつ高純度石英アンプルに封入し、原子炉(JRR－3M)の水力照射孔(熱中性子束:9×10^{13} n・cm^{-2}・s^{-1})で1～1.5 時間照射した。アンプル中の照射済み試料の外観および移動具合を比較し、それぞれ、6M 塩酸溶液と 30%過酸化水素水で加温溶解後、一部を高純度ゲルマニウム検出器で測定した。また、同時に照射したフラックスモニターから熱中性子照射量を求め、^{90}Y の生成量を計算した。原研で開発した東京理工社製の双子型微少カロリーメータを用い、石英アンプルに封入したままで非破壊により ^{90}Y の放射能を測定し、この値を基準として定常測定用のキャピンテック社製電離箱の感度を校正した。

高純度アルミニウム製カプセル内の微小球を注入カプセルに移し替えるための専用装置を用い、遠隔操作により詰替えた後、図のような「自動注入装置」により注入試験を行った。



自動注入装置

3. 結果および考察

照射した微小球は、Y_2O_3 粉末と比べ難溶性であり、動物実験に適用可能と考えられる。^{90}Y の比放射能は、1および 1.5 時間照射直後でそれぞれ、6.1 および 11 MBq/mg であり、^{90}Y の放射性核種純度は、99.9%以上であった。

アルミニウム製カプセルを十分に乾燥させると微小球が移動しやすくなり、注入カプセルへの充填率は80～97%であった。今後、動物注入実験に向けシステムの最適化を図る予定である。

[*1] Japan Atomic Energy Research Institute; [*2] Shimizutech Co., LTD.;
[*3] Radiation Application development Association; [*4] Tokyo Nuclear Services Co., LTD.

This is a blank page.

5. 原子炉材料照射試験

5. Irradiation Test of Reactor Materials

This is a blank page.

研究テーマ：核融合炉ブランケット照射試験に関する技術開発
表　　題：耐放射線小型モータの開発

5-1

JRR-4を用いた小型モータの照射試験

石塚悦男[1]、中道　勝[1]、菅　智史[2]
[1]日本原子力研究所大洗研究所、茨城県東茨城郡大洗町成田町字新堀3607
[2]（株）ユニマック、三重県員弁郡北勢町麻生田1326-1

国際熱核融合実験炉（ITER）では、原型炉用ブランケットを開発するために、試験用ブランケットを取付け、核融合反応で発生した中性子を実際に利用して、発電と燃料生産の実証試験が行われる。試験用ブランケット開発の一環として、試験用ブランケットの設計データを取得するため、JMTRを用いた炉内機能試験が計画されている。炉内機能試験では、ITERの運転を模擬するために、小型モータで窓付の中性子吸収体を回転させることにより、熱中性子束をパルス状に可変できる照射試験体の開発が必要となる。このため、耐放射線性小型モータを開発し、照射試験を行った。

モータの開発に際しては、γ線照射環境で使用されていた小型ACサーボモータ（従来品）の基本設計を用い、コイル用巻線及びコイル用成形・固定材には、耐放射線性に優れたポリイミド銅線（導体線径 0.18mm）及び MgO、Al_2O_3 等の絶縁材を含有したシリコン樹脂を用いた。また、マグネット及びベアリング潤滑剤には、各々Nd-Fe 及び耐放射線性のポリフェニルエーテルを用いた。試作モータの基本性能は、出力6W、定格トルク 13 g-cmであり、照射試験に必要なトルク（10 g-cm以上）を満足している。

従来品と開発品の AC サーボモータの耐放射線性を比較するため、JRR-4 の炉プールを利用して照射試験を実施した。試料容器には、従来品と開発品のACサーボモータを各1台装荷し、炉停止後にモータを運転し、回転数を測定して正常に動作していることを確認した。開発品のACサーボモータは、JMTRでの照射試験と比較することで減速ギヤの寿命を明らかにするため、減速ギヤを取外して照射試験を行った。

照射試験の結果を図1に示す。JMTRで照射した開発品（ギアあり）[1]は、JRR-4で照射した従来品（ギアあり）より、耐放射線性が1桁以上向上したことが明らかになった。また、JMTRの照射試験と比較すると、同じ開発品であっても、「ギアなし」の方の耐放射線性が向上していた。この原因は、減速ギアの有機系の潤滑剤が固化したためと考えられる。このため、潤滑剤を無機系に変更する、或はオイルレスの減速ギアやベアリングを使用すれば、更に耐放射線性が向上すると考えられる。

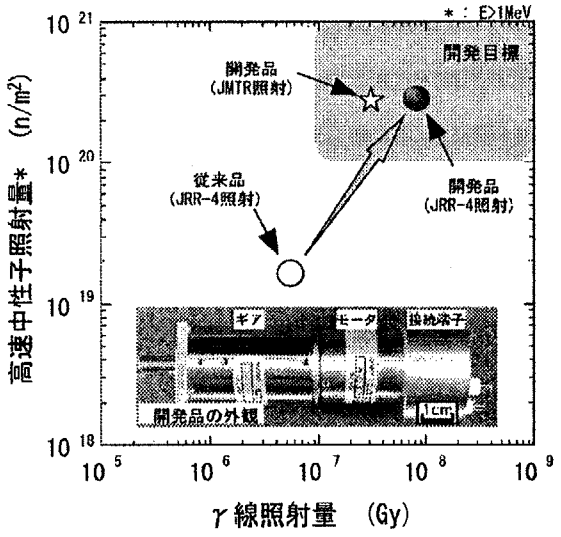


図1　小型モータの照射試験結果

参考文献
1) E.Ishitsuka et.al, Fusion Engrg. Des.51-52 (2000) 829-835.

原子炉：JRR-4　　装　置：炉プール　　分　野：原子炉燃料・材料（核融合炉）

研究テーマ: 原子力材料の照射効果
課題: 固体増殖材からのトリチウム放出挙動

5-2
Tritium Release from Neutron-Irradiated Li_2O Sintered Pellets: Fluence Dependence

Takaaki Tanifuji Daiju Yamaki and Shiro Jitsukawa

1. Introduction

Li_2O is one of the principal candidates for tritium breeding materials in the fusion reactor system. In the solid breeding materials, various kinds of irradiation defects are produced by exposing to high energy radiations during the fusion reactor operations. These irradiation defects are considered to affect the tritium release behavior from and the tritium inventory in the solid breeding materials. Many researchers have investigated the production and reduction behavior of the point defects in Li_2O such as F^+ center and Li colloid, and effects of the defects on tritium release behavior from Li_2O by using methods of ESR, optical absorption and so on.

In the present study, the neutron fluence dependence on the tritium release behavior from sintered Li_2O with various bulk density (71-89%T.D.) was investigated. Various fluence of thermal neutron irradiation ($4x10^{20}$-$2x10^{23}$ n/m2) was performed to investigate the effects of irradiation defects on the tritium release behavior.

2. Results and Discussion

A: Lower density region (71-86%T.D.)

Figure 1 shows the tritium release rate from sintered Li_2O with 71%, 81% and 86%T.D. in the constant heating rate (2K/min.) tests. It is shown that the temperature of the tritium release peak shift to higher temperature with increase of neutron fluence(Li burn up), that is, 570K for $4x10^{20}$ n/m^2, 590K for $2x10^{21}$ n/m^2, 610K for $2x10^{22}$ n/m^2 and 620K for $2x10^{23}$ n/m^2. In lower density region(71%-86%T.D.). It means the tritium release behavior depends on the neutron fluence significantly. It suggests that tritium trapping in irradiation defects plays an important role in the tritium release behavior.

B: Intermediate density region (87-89%T.D.)

Figure 2 shows the tritium release rate from sintered Li_2O with 87% , 88% and 89%T.D. in the constant heating rate (2K/min.) tests. It is shown that the temperature of the tritium release peak shift to higher temperature with increase of neutron fluence, that is, 620K for $4x10^{20}$ n/m^2, 640K for $2x10^{21}$ n/m^2, 660K for $2x10^{22}$ n/m^2 and 680K for $2x10^{23}$ n/m^2. From the comparison between fig.1 and 2, it is found that the temperature of the peaks in the intermediate density region (87-89%T.D.) is higher 50K than that in the lower (71-86%T.D.) for the same neutron fluence by apploxmately specimens. This results suggest that the rate determining step in the intermediate region is different from that in the lower.

As shown in figure 3, in the lower density region(71%-86%T.D.), the open and closed porosity show 25% and 3.5% for 71%T.D., and 11% and 3% for 86%T.D., respectively, that is, the ratio of the closed to the open porosity between 0.14-0.27. This

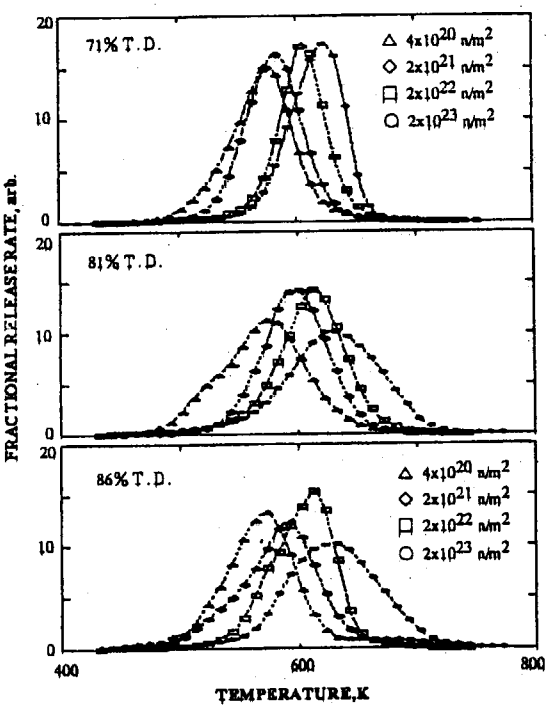


Fig. 1. Fluence dependence for tritium release rate from sintered Li_2O pellets of 71–86% TD during a temperature ramp of 2 K/min.

原子炉: JRR-4　　装置: S-パイプ　　分野: 核融合炉材料

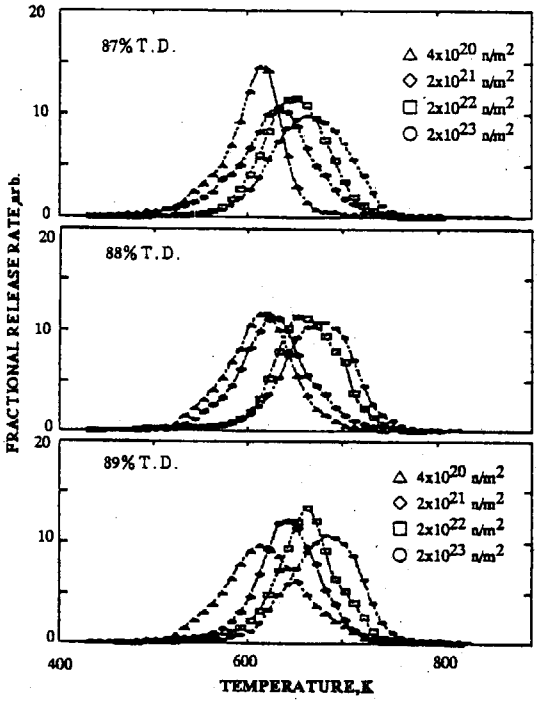


Fig. 2. Fluence dependence for tritium release rate from sintered Li_2O pellets of 87–89% TD during a temperature ramp of 2 K/min.

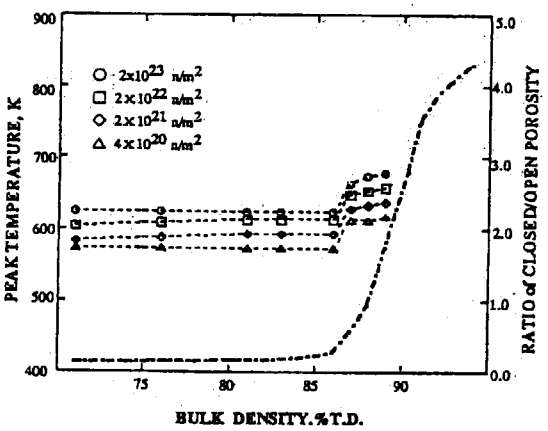


Fig. 3. Fluence and porosity dependence for tritium release peak temperature from sintered Li_2O pellets of 71–89% TD during a temperature ramp of 2 K/min.

large open porosity ratio to the closed is considered to the small contribution of interconnected pores to the tritium release, and to become make the cause of the constant temperature of the peak in this density region for same neutron fluence . In the intermediate density region (87-89%T.D), the ratio of closed to open porosity between 0.57-1.8. The difference of the temperature of the peaks between the lower and intermediate density region is considered to be caused by the change of the ratio of closed to open porosity

It suggests that the rate determining step of the tritium release in the intermediate density region is considered as the advection through the open pores via adsorption and desorption on the inner wall of the pores, or the diffusion in the gas phase in the interconnected pores[1].

3. Conclusion

The tritium release behavior from Li_2O sintered pellets with various densities (71-89%T.D.) is investigated by the constant heating rate tests. It is clarified that there is a porosity dependence of the tritium release rate in the density range over 87%T.D., while no dependence is observed in the density range under 86%T.D., and there is a neutron fluence dependence of the tritium release rate in the density range under 89%T.D. From these results, it is considered that the rate determining step of the tritium release changes with the density change, described as follows: (1) lower density region (71-86%T.D.): the detrapping of tritium trapped in the point defects due to the recovery of the defects; (2) intermediate density region (87-89%T.D.): the migration through the interconnected pores via adsorption and desorption on the inner wall of the interconnected pores, and the diffusion in the gas phase in the interconnected pores.

It is clarified that the tritium release process from sintered pellet consists of many elemental mechanisms and is significantly affected by porosity and neutron fluence. The production and reduction of irradiation defects under high energy radiation such as neutron are considered to play an important role in the assessment of stability and tritium release characteristics of solid breeding materials.

Reference

[1]T.Tanifuji,D.Yamaki.T.Takahashi,A.Iwamoto, J.Nucl.Mater.283-287(2000)1419

This is a blank page.

6. 即発ガンマ線分析

6. Prompt Gamma-ray Analysis

This is a blank page.

研究テーマ：環境関連物質の分析高度化研究

表　　題：中性子即発γ線分析の研究

6-1

中性子即発γ線分析の研究

松江秀明，米沢仲四郎

環境科学研究部 分析科学研究グループ

1. はじめに

報告者らは，これまでに JRR-3M の冷及び熱中性子ビームを使用する中性子即発γ線分析法(PGA)を開発し，各種分野の試料分析に応用してきた。本年度は，冷中性子ビーム(第1～3，7サイクル)と熱中性子ビーム(第4～6サイクル)を使用し，1) k_0 法による多元素定量法の検討，2) 底質標準物質の分析と，3) 大学との協力研究を実施した。

2. k_0法による多元素定量法の検討

k_0 法による元素定量法のための k_0 係数を冷及び熱中性子ビームで測定し，その評価を行った。表1に k_0 係数の測定値を示す。PGA が有効な27元素について，ほぼ3%以下の精度で k_0 係数を測定し，1) 他の研究施設(ハンガリーIKI，米国NIST)との比較，2) 核データによる計算値，3) 標準物質の分析によって評価した結果，非 1/v 元素(Sm, Cd, Gd など)を除きほぼ 10%の正確さであることを確認した。

更に、k_0 係数の汎用性を高めるため，中性子スペクトルによる k_0 係数への影響の補正法の検討を行った。中性子エネルギーに対する中性子捕獲反応断面積のデータベースである JENDEL-3.2 と研究炉部の鈴木正年氏より提供を受けた冷及び熱中性子ビームの中性子飛行時間法(TOF)により測定された中性子エネルギー分布スペクトルに基づき g 係数を数値計算し，この係数を用いた補正法の討を行った。これまでに、Cd については，その補正に成功したが，Sm と Gd については，満足な補正結果が得られていない。

3. 底質標準物質の分析

PGA は，正確さが優れていることや，他の方法では困難な元素の分析が可能であること等から標準物質の調製には不可欠な分析法となっている。本研究では，k_0- PGA により新たに有害金属分析用として独立行政法人産業技術総合研究所計量標準総合センター(NMIJ/AIST)で調製された2種類の底質試料(港湾と湖)の多元素定量を行った。k_0-PGA では元素の絶対濃度を求めることができないため，標準添加法により Ti の絶対濃度を定量し，それらの値から各元素の絶対濃度を求めた。本分析により軽元素を中心とした H, B, Si, K, Ti, Cr, Mn, Fe, Cd 等の 15 元素の定量を行うことができた。

4. 協力及び共同研究

JRR-3M の即発γ線分析装置を使用し，大学との協力研究(3 件)として，中性子ビームガイドを用いた高速荷電粒子の化学的挙動の研究(大同工業大学工学部)，廃棄物埋立によるホウ素汚染の機構解明(東京大学大学院　新領域創成科学研究科)，即発γ線分析法による地衣類の研究(筑波大学化学系)を実施した。

5. 成果の公表

1) C. Yonezawa: "Prompt gamma-neutron activation analysis with reactor neutrons", Zeev B. Alfassi ed. "Non-destructive elemental analysis", Blackwell Science, Oxford, U.K., (2001).

原子炉: JRR-3M　　装置：即発γ線分析装置　　分野：即発γ線分析(分析化学一般)

2) 米沢仲四郎: "原子炉中性子による即発ガンマ線分析", 分析化学, **51** (2002) 61.

3) C. Yonezawa, H. Matsue, K. McKay, P. Povinec: "Analysis of marine samples by neutron-induced prompt gamma-ray technique and ICP-MS", J. Radioanal. Nucl. Chem., **248** (2001) 719.

4) H. Matsue, C. Yonezawa: "Multielement determination of typical diet reference materials by neutron-induced prompt gamma-ray analysis using k_0 standardization", J. Radioanal. Nucl. Chem., **249** (2001) 11.

5) H. Matsue, C. Yonezawa: "Neutron spectrum correction of k_0-factor for k_0-based neutron-induced prompt gamma-ray analysis", J. Radioanal. Nucl. Chem., **255** (2003) 125.

6) H. Matsue, C. Yonezawa: "Measurement and evaluation of k_0 factors for PGA at JAERI", J. Radioanal. Nucl. Chem., in press.

表1 塩素の1951 keV γ線に対する $k_{0,Cl}$ 測定値

Element	Energy keV	Cold $k_{0,Cl}$	Cold Error	Thermal $k_{0,Cl}$	Thermal Error
H	2223	1.86	0.0058	1.80	0.0045
B	478	359	3.5	371	31
C	4944	0.000643	0.0000077	0.000762	0.000023
N	4505	0.00698	0.0000140	0.00573	0.000056
Na	472	0.116	0.00060	0.116	0.0014
Si	3540	0.0214	0.000087	0.0218	0.00010
P	637	0.00481	0.000080	0.00470	0.000077
S	841	0.0576	0.0012	0.0554	0.0012
Cl	786+788	1.36	0.0039	1.32	0.0080
K	770	0.129	0.00061	0.127	0.00057
Ca	1942	0.0464	0.00061	0.0469	0.0010
Ti	1381	0.592	0.0062	0.5827	0.0059
Cr	834	0.143	0.0016	0.140	0.0012
Mn	314	0.151	0.0062	0.150	0.00078
Fe	352	0.0272	0.00069	0.0270	0.00055
Co	277	0.624	0.0052	0.610	0.0027
Ni	465	0.0821	0.00093	0.0804	0.00061
Sr	898	0.0427	0.00041	0.0417	0.0021
Cu	278	0.0772	0.00028	0.0755	0.00053
Cs	117	0.169	0.0017	0.169	0.0012
Cd	558	62.1	1.5	79.9	0.84
Ba	627	0.0109	0.00012	0.0110	0.00014
Hg	368	7.10	0.083	7.03	0.15
Sm	334	118	1.0	146	4.3
Gd	182	216	1.3	255	3.1
Pb	7367	0.00328	0.000018	0.00338	0.000056

研究テーマ：環境関連物質の分析高度化研究

表　　題：中性子ビームガイドを用いた高速荷電粒子の化学的挙動の研究

6-2

中性子ビームガイドを用いた高速荷電粒子の化学的挙動の研究

酒井陽一[*1]、久保謙哉[*2]、小林義男[*3]、山田康洋[*4]、荘司準[*5]、齋藤崇[*4]、米沢仲四郎，松江秀明

環境科学研究部 分析科学研究グループ

**1：大同工業大学；*2：国際基督教大学；*3：理化学研究所；*4：東京理科大学；*5：東京都立大学*

1. はじめに

JRR-3M の中性子ビームガイドを用いた中性捕獲反応によって生成する高エネルギー状態にある粒子の化学的挙動を追跡することを行ってきた。今年度は以下の2つの中性子捕獲反応について実験を行った。

(1) $^{10}B(n,\alpha)^{7*}Li$ 反応

(2) $^{56}Fe(n,\gamma)^{57*}Fe$ 反応

2. $^{10}B(n,\alpha)^{7*}Li$ 反応

$^{10}B(n,\alpha)^{7*}Li$ 反応で生成する高エネルギー$^{7*}Li$ から放出される478keV即発γ線のドップラー広がりを測定・解析することによりホウ素の化学的・物理学的状態についての情報が得られることを、これまで示してきた。14年度は地球科学、環境科学的な試料にこのドップラー広がり法を適用することを行った。平成14年3月に名古屋でサンプリングした黄砂に対して、JRR-3M の PGA 装置で 478keV-即発γ線を測定した。この黄砂試料のドップラー広がり即発γ線形に対する解析は、我々が開発した方法を用いた(M.K.Kubo and Y.Sakai: J. Nucl. Radiochem. Sci., Vol.1, 83 (2000))。解析は$^{7*}Li$の物質中での減速定数 D を実験値として与える。D は物質の元素組成、密度によって決まる値である。理論的にはLSS モデルを適用することにより計算される。この計算値との比較により、黄砂中のホウ素は、アルミノシリケートマトリクス中に存在するものであろうと結論した。

3. $^{56}Fe(n,\gamma)^{57*}Fe$ 反応

$^{56}Fe(n,\gamma)^{57*}Fe$ 反応で生成する $^{57*}Fe$ から放出される 14keV-即発メスバウアーγ線をプローブとする短寿命化学種の追跡についても研究した。これはJRR-3M の PGA 装置とメスバウアー分光器の組み合わせではじめて可能になる実験である。金属（α-Fe）、合金（ステンレススチール）では、メスバウアーシグナルが観測されたが、化合物ではシグナルが弱く、さらなる実験条件の改善が必要であることがわかった。

4. 成果の公表

$^{7*}Li$ に関しては以下の、1)として学会発表を行った。$^{57*}Fe$ のメスバウアー実験については、2)のメスバウアー分光研究会シンポジウムで招待（依頼）講演として発表された。題目からわかるように、この研究は将来の大強度陽子加速器の建設を視野に入れた萌芽的な研究である。今後の発展が期待されよう。

1） 酒井陽一、大下一政、久保謙哉、松江秀明、米沢仲四郎：「黄砂の鉄とホウ素のメスバウアー分光法と即発γ線ドップラー広がり法によるキャラクタリゼーション」 2002 日本放射化学会年会（9.2002 札幌）で講演

2） 久保謙哉：「大強度陽子加速器とメスバウアー研究」 メスバウアー分光研究会会誌、No.3、22、(2002.3)

原子炉：JRR-3M　　装置：即発γ線分析装置線　　分野：即発γ線分析（分析化学一般）

This is a blank page.

7. その他

7. Others

This is a blank page.

研究テーマ：研究炉利用高度化の技術開発
表　　題：患者頭部ファントムとJCDS計算値との比較　—臨床的線量評価研究—
7-1

Comparison of Dosimetry by the Realistic Patient Head Phantom and by the Patient's Brain, and the JCDS Calculation - A Clinical Dosimetry Study

K. Endo[1], A. Matsumura[1], T. Yamamoto[1], T. Nose[1], K. Yamamoto[2], H. Kumada[2]
T. Kishi[2], Y. Torii[2], T. Kashimura[2], and S. Ohtake[2]

Department of Neurosurgery, Institute of Clinical Medicine, University of Tsukuba[1]
Department of Research Reactor, Tokai Research Establishment, JAERI[2]

Introduction

Since the 1990s, University of Tsukuba and JAERI have been studying BNCT mainly as a curative therapy for malignant glioma. Using conventional BNCT in a 1990s clinical trial, we irradiated patients without a computational planning system, depending on gold wires as the neutron detector and semiconductor detector. We treated 9 cases with mixed thermal-epithermal neutron flux in BNCT 1). Subsequently, the JCDS was developed to calculate the BNCT dosimetry for more correctly with the epithermal neutron beam by JAERI 2). A realistic phantom model of a patient head was developed for use in applying the system to complex three-dimensional objects too. This realistic phantom has advantages for biomedical study; it provides a similar CT model for use in computational simulation and a model for the real radiation field condition in an in-vitro phantom experiment.

In this study, the realistic phantom was used to optimize the JCDS by correlating the data from the phantom measurement to that by the calculation, using the JCDS and the direct measurement in the patient's brain obtained from actual BNCT operations.

Materials and Methods

A set of CT data (40 slices at a 5mm pitch) from a BNCT patient was used to produce the solid formative model phantom using the Rapid Prototyping Technique. With SURFACER (Imageware Company), the three-dimensional solid surface model was built from the point data extracted from the CT data on the computer. We then converted the original surface data into STL-type data for use in the stereolithography format, and input the transformed data to Magics RP (rapid prototyping software). At this stage the phantom surface was 3mm thick and the structure was empty; it could hold water. The SOLIFORM-500B (Teijin Seiki Company, Japan) utilizes ultraviolet rays to harden resin, and was used to make a more solid structure. The resin selected for the RPT was the TSR-810, an epoxy acrylate resin that provided a thin, hard layer.

A mixed thermal-epithermal neutron beam (thermal neutron beam mode 1: TNB-1) was applied to the neutron source in vivo in the clinical cases of BNCT irradiation. In an experiment, the realistic phantom was irradiated with the neutron beam in the same mode by a reactor power of 3.5MW. The measurement condition with the JCDS was corresponded to the experimental condition.

In the procedure of the intraoperative BNCT with TNB-1 mode, the thermal neutron flux distributions are calculated using gold wires which are directly placed on the brain surface. The thermal neutron flux was simulated using a simultaneous β-γ coincidence-counting device.

In the experiment using the realistic phantom, the thermal neutron flux distributions on the brain surface of the phantom were also measured by means of 31 gold foils (5mm in square 0.01mm in thickness), which were located at the sites on the brain surface where the clinical dosimetry was measured . And the realistic phantom was settled the irradiation place with Patient Setting System 3, 4). Further, in order to verify the performance of JCDS by comparing with the data of the phantom experiments, the thermal neutron flux using the JCDS were calculated by simulating the realistic phantom experiment.

In this study, we try to compare with dosimetry by the realistic phantom, by the

clinical measurement, and by the JCDS calculation.

Results

The profiles of thermal neutron flux on the brain surface calculated using the realistic phantom showed close agreement with the measurements obtained by clinical dosimetry; a relatively high dose area at the parietal lobe was shown by both methods. Using JCDS, it may be possible that the pin-point peak is not calculated because the calculation is based on the average dose of each 1cm^3 voxel size.

Discussion

Factors that may have led to the discrepancy between findings of the realistic phantom, JCDS and those determined by clinical dosimetry in BNCT are as follows: 1) Blood clot and cerebrospinal fluid overlying the brain surface during the irradiation; 2) Lack of data of the Lithium helmet (it's quality of the material or geometry size and so on); 3) The accuracy of reappearance produced differences in the thermal neutron flux between JCDS and the realistic phantom. If these factors are more closely considered, the dosimetry data can be evaluated more exactly.

To reproduce more accurate irradiation in BNCT, we must evaluate the gold wires, which are settled in the realistic phantom to calculate the thermal neutron flux. And then these data are used to evaluate the actual dosimetry to the organ and so on.

Further optimization of the simulation technique will be needed in order for BNCT, and particularly intraoperative BNCT, to be applied as a more reliable and effective therapeutic modality.

Conclusions

In conclusion, use of an individual patient's realistic phantom is one of the more effective methods by which to verify the JCDS data and the clinical dosimetry. This phantom can be used as an in vitro tool, arranging the cells in the phantom so that it approximately reproduces the real conditions of exposure to clinical radiation.

In the future, using these simulation techniques, we will be able to simulate the dosimetry for each patient at the experimental stage and obtain much more reliable and effective therapeutic irradiation by BNCT.

REFERENCES:

1. A Matsumura, T Yamamoto et al. : Intraoperative Boron Neutron Capture Therapy for Malignant Gliomas : Fast Clinical Results of Tsukuba Phase I/II Trial using JAERI Mixed Thermal Epithermal Neutron Beam, Ninth International Symposium on Neutron Capture Therapy for Cancer, pp. 29 –30, (2000)
2. T. Kumada, Y. Torii, K. Yokoo, K. Yamaguchi, K. Saito, A. Matsumura, Y. Nakagawa, H. Sakurai : A Development of Computational Dosimetry System for BNCT at JRR-4, Eighth International Symposium on Neutron Capture Therapy for Cancer (1998)
3. H Kumada, K Yamamoto, Y Torii, A Matsumura, T yamamoto, Y Nakagawa : Development of the Patient Setting System for BNCT at JRR-4, Ninth International Symposium on Neutron Capture Therapy for Cancer, pp. 281-282, (2000).
4. H Kumada, A Matsumura, Y Nakagawa : Development of the Patient Setting System for Medical Irradiation with Research Reactor, Trans. At. Energy Soc. Japan Vol.1, No.1 (in Japanese), pp. 59-68, (2002)

原子炉：JRR-4　　装置：中性子ビーム設備　　分野：

研究テーマ：研究炉利用高度化の技術開発
表　　題：JRR-4 中性子ビームの放射線生物学的特性

7-2

Radiobiological Characterization of JRR-4 Neutron Beams

T. Yamamoto[1], A. Matsumura[1], K. Yamamoto[1], H. Kumada[1], N. Hori[2], Y. Torii[2], K. Endo[1], A. Matsushita[1], F. Yoshida[1], Y. Shibata[1] and T. Nose[1]

Department of Neurosurgery, Institute of Clinical Medicine, University of Tsukuba[1]
Department of Research Reactor, Tokai Research Establishment, JAERI[2]

Introduction

For evaluating the biological response of the tumor and healthy tissue to neutron beams, and for comparing the clinical results of BNCT at different institutions with accuracy, all of the physical dose components and their RBE values of each beam must be determined separately. In this study, physical dosimetry and *in vitro* cell survival assays were performed to determine the RBE of each dose component for the beams, which have not been previously characterized at JRR-4.

Materials and Methods

An epithermal beam (epithermal neutron beam mode: ENB), a mixed thermal-epithermal beam (thermal neutron beam mode 1: TNB-1) and a thermal beam (thermal neutron beam mode 2: TNB-2) were used as the neutron source for in vitro and physical measurements. For determining the neutron flux, the activation of nickel and of gold foils with or without cadmium covers was measured. The neutron energy spectrum was also calculated using the Monte Carlo Code, MCNP 4B. The γ ray dose was measured with a thermoluminescent dosimeter (TLD) that had a beryllium oxide as a thermoluminescent material and was covered with quartz glass (Panasonic 170LS).

V79 Chinese hamster cells in the stage of exponential cell growth were preincubated for 6h with 10B-enriched boric acid at 10B concentrations up to 15μg10B/ml medium. The cells in suspension in polyethylene cryotubes were irradiated with each neutron beam for the colony formation assay. The RBE values were calculated by comparing the D0 value of subtracted each dose component to the D0 of 150 cGy for 250 kVp X rays.

Results

The slopes with the survival curve of V79 cells for all dose components were steeper for ENB compared to TNB-1 and TNB-2 (Fig.1). Comparing the D_0 values for the separated response to boron neutron capture reaction in ENB, TNB-1 and TNB-2 to the D_0 value of 150 cGy for γ rays, corresponding RBE (${}^{BA}RBE_{boron}$) values of 4.07 ± 0.22, 2.98 ± 0.16, and 1.42 ± 0.07 were obtained. The beam RBE (RBE_{beam}) values based on the D_0 values for R_{beam} were 1.22 ± 0.16, 1.23 ± 0.16, and 1.21 ± 0.16 for ENB, TNB-1 and TNB-2, respectively. The RBE ($RBE_{neutron}$) values based on the D_0 values for the high-LET dose components were 2.50 ± 0.32, 2.34 ± 0.30, and 2.17 ± 0.28 for ENB, TNB-1 and TNB-2, respectively.

Discussion

The surviving fraction of the neutron beam with or without the presence of ^{10}B depended highly on the neutron beam used, according to the epithermal and fast neutron content in the beam. The most significant difference was seen in the survival fractions of the boronated cells, and the ${}^{BA}RBE_{boron}$ for ENB (3.99) was 2.8-fold higher than that for TNB-2. The energy range 1 keV to 0.5 MeV is important for the biological response to the dose components in BNCT (4). The neutron fluences determined by the gold activation method are used to estimate the absorbed dose from boron neutron capture and nitrogen capture reactions, for each of the three spectra. Since the foil activation technique only measures neutron energies in a restricted range, leading to a systematic error in the calculation of the RBE values for the different dose components. The RBE value for boron neutron capture reactions was, particularly in the beam with

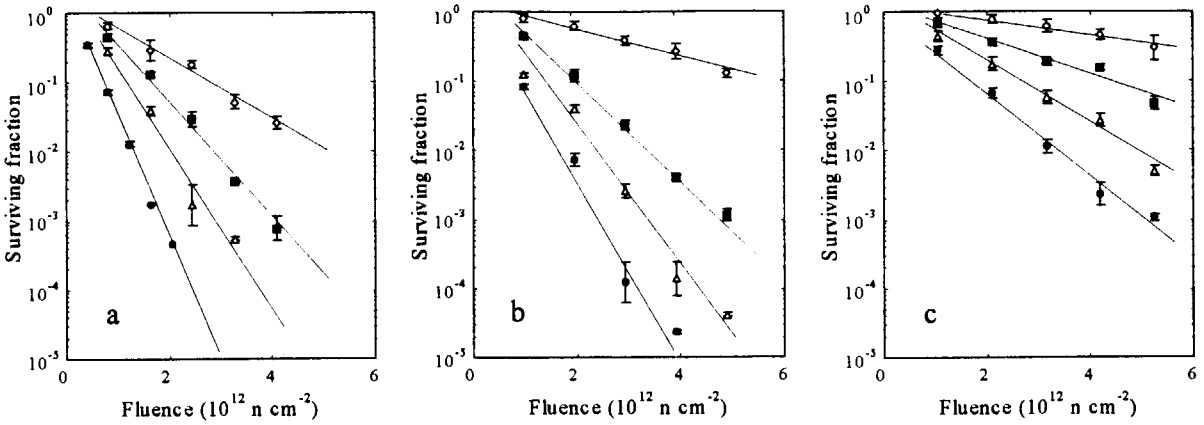


Fig.1 Survival curve of V79 cells incubated with 0 (◇), 5 (■), 10 (△), and 15 (●) μg^{10}B/ml medium of ^{10}B obtained after irradiation with ENB (a), TNB-1 (b) and TNB-2 (c) at JRR-4.

high epithermal content, considerably influenced by the determination of neutron fluences which depend on the capture cross section of boron in the epithermal energy range (~ 10^3 barns). The previously reported RBE values for the boron capture reaction and the high-LET dose components using *in vitro* endpoints ranged 2.3 – 3.7 and 1.9 – 3.7, respectively (1,1,2,3). The variation of reported RBE values for the dose components in BNCT seems to be partially caused by the nonuniformity of dose distribution, the inhomogeneity in subcellular boron distribution (1), and the different experimental conditions. However, the data in this paper, by comparing different neutron beams with uniform dose distributions and the same experimental conditions, indicate that the neuron energy of a beam is the primary factor for the variation of RBE values. Further investigation is needed to evaluate the *in vivo* and *in vitro* in-phantom radiobiological effect with variable neutron beams to assess the clinical results from individual BNCT trials as well as the other particle and ionizing radiation therapies.

REFERENCES:

1. Coderre JA, *et al.*: Derivations of relative biological effectiveness for the high-LET radiations produced during boron neutron capture irradiations of the 9L gliosarcoma *in vitro* and *in vivo*. *Int J Radat Oncol Biol Phys* **27**: 1121-1129, 1993
2. Davis MA, *et al.*: Relative biological effectiveness of the ^{10}B(n, α)^{7}Li reaction in HeLa cells. *Radiat Res* **43**: 534-553, 1970
3. Fukuda H, *et al.*: RBE of a thermal neutron beam and the ^{10}B(n, α)^{7}Li reaction cultured B-16 melanoma cells. *Int J Radiat Biol* **51**: 167-175, 1987
4. Gabel D, *et al.*: The Relative Biological Effectiveness in V79 Chinese Hamster Cells of the Neuron Capture Reactions in Boron and Nitrogen. *Radiat Res* **98**: 307-316, 1984
5. Watkins P, *et al.*: Dosimetry for BNCT in theory and practice, In *Advances in Neutron capture Therapy. Medicine and physics. Vol. 1.*, Amsterdam, pp. 141-146, Elsevier, 1997

原子炉：JRR-4　　装置：中性子ビーム設備　　分野：

研究テーマ：研究炉利用高度化の技術開発
表　　題：JCDS 計算値と患者頭部内線量測定値との比較研究

7-3

Comparative Study of the JCDS Calculation and Patient Brain Dose Measurements

T. Yamamoto[1], A. Matsumura[1], K. Yamamoto[2], H. Kumada[2], Y. Torii[2], K. Endo[1], A. Matsushita[1], Y. Shibata[1] and T. Nose[1]

Department of Neurosurgery, Institute of Clinical Medicine, University of Tsukuba[1]
Department of Research Reactor, Tokai Research Establishment, JAERI[2]

Introduction

Intraoperative irradiation has been utilized with a thermal beam as part of the BNCT procedure to facilitate neutron penetration (1). In an intraoperative BNCT (IOBNCT) trial with a mixed thermal-epithermal beam at JRR-4, dose simulation has been found to play a minor role in IOBNCT because of difficulties in achieving the complicated simulation of 3-dimensional dose distribution in the postsurgical brain (4). The vascular boron dose (0.33 x blood boron dose) is determined based on activation of the gold wires that are arranged directly in the surgical field. Some of these are withdrawn and utilized for the calculation of irradiation time (2).

JAERI computational dosimetry system (JCDS), the dose planning system for BNCT, has been tested in the ongoing IOBNCT and will be put to practical use in the dose planning of IOBNCT with an epithermal beam. In the present study, the JCDS calculations of the clinically treated cases were compared to direct measurements in the patient's brain.

Materials and Methods

Nine patients with malignant glioma underwent the IOBNCT with the mixed thermal-epithermal beam at JRR-4 using BSH as the boron compound. Irradiations were performed as the maximum vascular boron dose as 10.8 Gy, which is 80% of the previously reported tolerance dose to avoid radiation necrosis (3). Following the craniotomy, two sets of gold wire were placed on or inserted into the postsurgical brain for the direct measurement of thermal neutron flux. The irradiation time was calculated by extrapolating the clearance curve of the blood boron levels and thermal neutron flux measured by the set of gold wire that was withdrawn 15 minutes after the beginning of each irradiation (intra-irrad measurement). The rest of the gold wires were measured after the irradiation and were used for the retrospective evaluation of 2-dimensional thermal neutron distribution on the brain surface as well as around the postsurgical cavity (post-irrad measurement). The 3-dimensional dose distributions for the same cases were calculated by JCDS for the retrospective evaluation based on the actual head position of the individual treatment. The maximum thermal neutron flux in the irradiated volume and the mean target vascular dose by JCDS were compared to those obtained from the intra-irrad measurements and the post-irrad measurements. Case 1 was omitted from the comparison in the maximum vascular boron dose because the dose of this case had been planned as 13 Gy. The regional doses of the volume with radiation injury were also calculated.

Results

The slopes with the survival curve of TNB-2, respectively.

The maximum thermal neutron flux on the brain surface from the intra-irrad measurements and the post-irrad measurements averaged 2.20±0.32 and 2.33±0.37 (109 cm-2sec-1), respectively (Table 1). The vascular boron dose on the brain surface derived from the post-irrad measurements averaged 11.4±1.2 (9.6-12.7) Gy. From the JCDS calculation, the maximum thermal neutron flux in the irradiated volume averaged 2.21±0.33 (109 cm-2sec-1). The mean vascular dose of the brain in the target volume varied from 3.5 to 7.8 Gy and averaged 5.7 Gy.

Radiation necrosis was found in 4 of 9

cases (Case 1,2,5,6). The vascular dose of the volume with radiation necrosis averaged 5.9 Gy (3.0-9.3). No significant difference was seen in the target vascular dose between the cases with and without radiation necrosis. Oculomotor palsy was found in 3 of 9 cases (Case 1,2,5). The boron dose of the cavernous sinus in the case with and without oculomotor palsy was 4.28 Gy (3.5-5.0) and 2.08 Gy (1.1-5.1), respectively.

Discussion

The maximum boron vascular dose of 10.8 Gy derived from the intra-irrad measurement was equivalent to the target boron vascular dose of 5.7 Gy obtained by the dose calculation with JCDS, which should be considered as the reference dose in future BNCT dose-planning. The mean vascular dose in radiation necrosis (5.9 Gy) was similar to the mean target vascular dose, implying the presence of a high risk of radiation necrosis with dose escalation.

The difference between the intra-irrad and post-irrad measurements was caused primarily by the sampling error in the intra-irrad measurements, in which both the number and arrangement of the withdrawn gold wires were restricted by the intraoperative irradiation procedure. Moreover, the JCDS calculation showed considerable variation in the vascular boron dose in the target volume according to the individual case (3.5 to 7.8 Gy). This dose variation suggests the technical limitations of dose control with direct measurement; therefore, volume-dose control with a practical simulation system is needed for intraoperative irradiation.

Thermal neutron flux calculated by JCDS was found to be equal to or less than that of the measurement except for Case 8, in which the scheduled head position was modified by a technical problem. This difference between calculation and measurement may be related to the voxel size used in JCDS, and to the influence of surgical drapes and clots overlying the gold wires on the thermal neutron distribution. Further evaluation is recommended for the practical use of JCDS in IOBNCT, which requires the simulation of complex conditions such as the geometry of the postsurgical brain and the influence of surgical equipment.

REFERENCES:

1. Sweet WH, *et al*: Boron-slow neutron capture therapy of gliomas. **Acta Radiol** 1: 114-121, 1963.
2. Nakagawa Y, Hatanaka H: Boron neutron capture therapy: Clinical brain tumor studies. **J Neurooncol** 33: 105-115, 1997.
3. Nakagawa Y, *et al.*: Boron neutron capture therapy in Japan-combination of surgical procedure and epithermal neutron, In: **Proceedings of Ninth International Symposium on Neutron capture therapy for Cancer**, pp33-34, 2000.
4. Yamamoto T, *et al.*: In-phantom two-dimensional thermal neutron distribution for intraoperative boron neutron capture therapy of brain tumours. **Phys. Med. Biol. 47**: 2387-2396, 2002

Case No.	1	2	3	4	5	6	7	8	9
Thermal neutron flux (intra-irrad)	2.40	2.24	1.99	2.50	2.60	2.26	2.31	1.59	1.92
Thermal neutron flux (post-irrad)	2.77	2.50	1.99	2.63	2.61	2.31	2.50	1.63	2.05
Thermal neutron flux (JCDS)	2.2	2.5	1.7	2.4	2.6	2.2	1.8	2.53	2.0
Vascular boron dose (post-irrad)	14.4*	12.7	10.3	10.6	9.6	10.9	12.5	12.0	12.7
Target vascular boron dose (JCDS)	7.5*	5.6	4.8	6.2	3.5	6.1	4.4	7.8	7.5

Table 1
Thermal neutron flux (10^9 n $cm^{-2}sec^{-1}$) and vascular boron dose (Gy) in nine cases. Data were calculated by gold wire measurements (intra-irrad, post-irrad) or JCDS. *The maximum vascular boron dose on the brain surface was planned as 13 Gy in Case 1.

原子炉：JRR-4　　装置：中性子ビーム設備　　分野：

研究テーマ：超流動反応場の原子・分子研究

表　　題：液体ヘリウム中でのトリチウムの化学反応

7-4

1.6 K ^{3}He-^{4}He量子媒体中における再結合反応, H+T→HT 及びT+T→T_2, への超流動の影響

荒殿　保幸

日本原子力研究所　先端基礎研究センター

〒319-1195　茨城県那珂郡東海村白方白根 2-4

ヘリウムは反応性が無いことから、化学反応においては気相反応のモデレータとしての役割しか与えられてこなかった。しかしながら、凝縮相（液体、固体）は、非常な低温であること、最も大きい量子パラメータを持つことに加えて特に超流動現象がマクロに現れる唯一の物質として、多くの低温物理学者を魅了し続けてきている。一方、化学の観点から見ると、物質との相互作用が非常に小さいことや低温であることから、凝縮相中の原子、電子、イオン等はバブル原子、スノーボールといった特異な化学形態やトンネル反応のような低温特有の化学現象が期待され、レーザ分光を中心とした研究が近年盛んになってきた。しかしながら、そのような特異な媒体中での化学反応に関する研究は全くなされていない。本研究は、^{3}He(n, p)T反応によって生成する水素原子とトリチウム原子との結合反応、H+T→HT 及び T+T→T_2を^{3}He-^{4}He混合媒体中で観察したものである。図1に示すように^{3}He-^{4}He混合溶液は温度、混合割合によって超流動(s)・常流動(n)相へと変化する。本報告は1.6 Kの実験結果である。したがって、s・n間の転移点は^{3}Heの割合が0.35にある。^{3}Heの割合を0.1から0.95まで変化させた溶液をJRR-3M ガイドホール熱中性子ビーム（中性子束：3-4x10^{10} m^{-2} s^{-1}）で約40時間照射した。生成したHT, T_2をラジオガスクロマトグラフで分離しそれぞれの相対収率を求めた。図2にT_2の相対収率[T_2/(HT+T_2)= $(Y_{T_2})_{exp}$]を示す。図から明らかなように^{3}Heの割合が0.95～0.35（n領域）においては収率は一定であるのに対し、0.35付近から収率の急激な増加が観察されこの変極点は相図のs・n転移点に相当する。二流体理論によれば、s領域は、実際にはs・n成分の混合体であり^{3}Heの割合によってその比は変化する。実験的に求められた0.35以下でのs・n成分の割合と0.35～0.95でのn領域での収率を利用し、反応がs成分及びn成分中で起こると仮定すると、n成分中での同位体効果（Y_{HT}/Y_{T_2}）は110±17, s成分中では56±14となる。同じ温度領域での気相反応ではこのような大きな同位体効果は無く、本実験結果は、バブル状のH, T原子のトンネル反応によるためと考えられる。又s・n成分間での違いは、反応系のコヒーレンス性との関わりを示唆している。

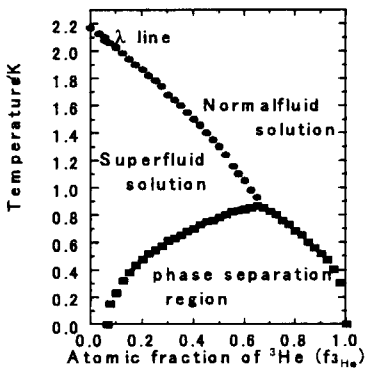


図1　^{3}He-^{4}He 混合溶液の相図

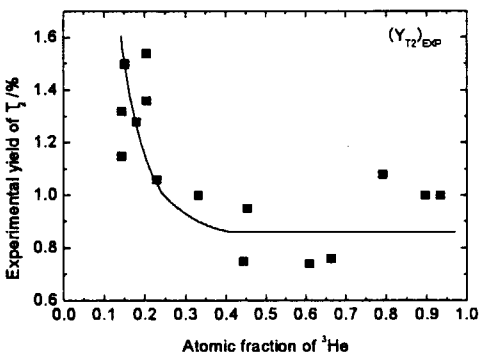


図2　T_2の相対収率の^{3}He 濃度依存性

原子炉 ：JRR-3M 装置 ：低温化学実験装置　　分類 ：その他（放射化学）

研究テーマ：フィッション・トラック年代測定
表　　題：FT年代測定のためのディテクターの開発

7-5

ＤＡＰプラスティックディテクターの特性とフィッション・トラック年代測定への応用

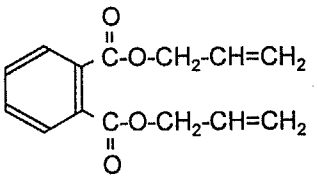
岩野英樹[1]・吉岡　哲[1]・檀原　徹[1]・鶴田隆雄[2]
[1]:(株)京都フィッション・トラック
[2]:近畿大学原子力研究所

フィッション・トラック（FT）年代測定法は、鉱物(おもにジルコンやアパタイト）中の ^{238}U が一定の速さで自発的に核分裂し、その際できた傷跡の密度が、試料の年代とU濃度に比例するという原理の上に成り立っている。U濃度は熱中性子照射によって誘導核分裂させた ^{235}U の誘導FT密度から求められ、一般的に誘導FTは、鉱物に密着させた外部ディテクター上で測定される。このことから、照射後に分析するディテクターの取扱いには十分な配慮が必要である。

従来FT年代測定法では、外部ディテクターとして天然の鉱物の白雲母が使われてきた。最近、白雲母の放射化分析から Sc-46(半減期 84 日)と Ta-182(半減期 115 日)が突出して放射化されることが明らかになった。また通常の照射条件(JRR-4、3.5MW 90 秒)おいて、放射能濃度は照射後 6 ヶ月経過しても 1000Bq/g を超え、放射線障害防止の観点からも白雲母は安全な材料とは言い難い。

今回、固体飛跡検出器の新材料として注目されているジアリルフタレート（diallyl phthalate：DAP）樹脂[1,2,3,4,5,6]をFTディテクターとしてテストした。DAP樹脂は、97%のDAPモノマーと3%のIPPモノマーの混合物を重合させて作られるポリカーボネイトで(図１)、核分裂片のように重荷電粒子のみに感度を示し、α粒子に感度を示さない特徴がある。 DAP のエッチングには60℃の PEW-65 溶液（15% KOH, 65%エタノール, 20%水）が用いられ、FT のエッチピットは楕円になる(図２)。

まず、改良点として最も重要な DAP の放射化の程度を調べた。JRR-4 炉(3.5MW)において熱中性子照射を 18 秒間行い、放射化分析を行った。照射から 24 時間後 Na-24 と Br-82 のピークがわずかに検出されたが、ほぼバックグランドといってよい程度であった。照射から 2 週間後再測定した際には検出ピークは全くなく、放射能濃度も検出限界以下であった。この結果から DAP 樹脂が放射化しないFTディテクターとして極めて優れた特性をもつことが確かめられた。最近、DAP ディテクター上の FT 密度が画像処理により自動測定出来ることが報告され[6]、DAP は白雲母ディテクターの代替として、今後広く利用されることが期待される。



DAP: Diallyl phtalate ($C_{14}H_{14}O_4$)

図 1. DAP モノマーの分子構造 (Tsuruta, 2000)

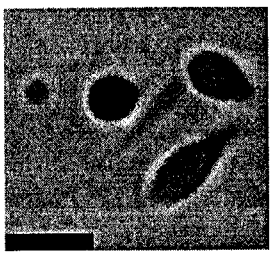


図 2. DAP 上のフィッション・トラック

参考文献

1) Tsuruta, T. (1999) Radiat. Meas., 31, 99-102.
2) Tsuruta, T. (2000) Radiat. Meas., 32, 289-297.
3) Tsuruta, T. (2001a) Radiat. Meas., 34, 167-170.
4) Tsuruta, T. (2001b) American Society for Testing and Materials, 100, 789-796.
5) 小口・鶴田 (2001) 第 1 回先進放射線応用シンポジウム(大阪大学), 103-106.
6) 吉岡哲・鶴田隆雄・岩野英樹・檀原徹 (2002) FT　ニュースレター, 第 15 号, 1-8.

原子炉:JRR-4　　装　置:気送管　　分　野:その他(放射年代学)

研究テーマ： Re-186m への中性子捕獲断面積測定
表題：天然レニウムにおける中性子捕獲断面積の測定

7-6

Measurements of neutron capture cross section on $^{nat.}$Re

T. Shizuma and T. Hayakawa

Advanced Photon Research Center, JAERI, Tokai, Ibaraki 309-1195, Japan

In an odd-odd nucleus ^{186}Re, a long-lived isomer (hereafter expressed as ^{186m}Re) with spin and parity of 8^+ is previously known. A half-life of ^{186m}Re was measured as 2×10^5 y [1]. While a main path of neutron capture on ^{185}Re is that to the ground state ^{186g}Re, which has a cross section of $\sigma = 112$ mb, a small fraction for a ^{185}Re $\rightarrow$ ^{186m}Re path has been reported with a neutron capture cross section of 0.3 % with respect to that for the ^{185}Re $\rightarrow$ ^{186g}Re path. Recently, we have identified that a chain reaction of ^{185}Re(n,γ)^{186m}Re(n,γ)^{187}Re via ^{186m}Re plays an important role in production for both of ^{187}Re and ^{187}Os, which would perturbs the abundance ratios of those nuclei. A pair of ^{187}Re/^{187}Os is famous for a nuclear chronometer to deduce an age of the Galaxy [2]. In order to obtain an absolute value, we have made a new neutron capture cross section measurement.

Natural rhenium foils with a thickness of 52 mg/cm^2 were irradiated by thermal neutrons derived from JRR-4 at JAERI. After 6-h irradiation, the samples were kept in the reactor pool for 4 months to reduce activities of ^{186g}Re and ^{188g}Re. A neutron flux was estimated as 5×10^13 /s/cm^2 by a Co-Al flux monitor. Two HP-Ge detectors were used to measure emitted γ rays. Figure 1 shows a γ-ray energy spectrum obtained 4 months after the neutron irradiation. Most of the peaks are assigned as γ rays emitted after β decays of ^{184}Re. For these γ rays, two components of half-lives of 38 d and 169 d are confirmed, which correspond to the ground state and the isomeric state at 188 keV, respectively. The ^{184}Re was produced by a fast neutron induced reaction of ^{185}Re(n,2n). Since the ^{184}Re activities have the half-lives comparable as the present experimental conditions, relevant γ-ray peaks are enhanced. For the neutron capture to ^{186m}Re, in spite of its very long half-life and the strong contaminant from ^{184}Re decays, we have succeeded to observed a 137 keV γ ray in ^{186}Os emitted after β decay of ^{186m}Re. Detailed analysis is now in progress.

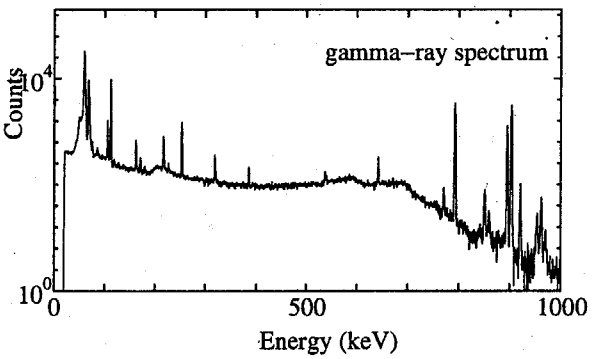


Fig. 1. A γ-ray spectrum measured 4 months after neutron irradiation

References

[1] D.W. Seegmiller *et al.*, Nucl. Phys. A185 (1972) 94

[2] K. Yokoi *et al.*, Astron. Astrophys. 117 (1983) 65

原子炉：JRR-4　　装置：気送管　　分野：核物理

7-7
悪性脳腫瘍に対する熱外中性子による中性子捕捉療法のための基礎的・臨床的研究

筑波大学臨床医学系脳神経外科
能勢忠男、松村　明、山本哲哉、吉田文代、張　天、高野晋吾
筑波大学臨床医学系麻酔科
豊岡秀訓、水谷太郎、高橋　宏

Basic and clinical research of epithermal neutron capture therapy for malignant brain tumors

Department of Neurosurgery and Anesthesiology Institute of Clinical Medicine, University of Tsukuba, Ibaraki, Japan

【目的と意義】中性子捕捉療法（以下、BNCT）で利用されるα線は予め投与された硼(ほう)素素化合物(^{10}BSH)を取り込んだ組織内でのみで発生し、飛程が短いため(-10μm)限局性に作用する．また、X・γ線と比べ細胞周期や組織内酸素濃度による影響が少なく、生物効果の大きい高エネルギー粒子線であるという放射線生物学的特長を有しており、従来の方法で難治の悪性神経膠腫に対しその治療効果が期待されている。腫瘍に選択的に治療を行い、正常脳は障害が少ないことが特徴である。

筑波大学では 1998 年 10 月以降、日本原子力研究所の医療用原子炉施設(JRR-4)において、従来開頭照射 BNCT で用いられてきた熱中性子に進達度の高い熱外中性子を加えた熱・熱外混合中性子ビームを用いた BNCT の Phase I/II 臨床試験を行い、本治療法の有効性について検証を行っている。

【対象と方法】

1．対象患者の適応決定

本研究は筑波大学医の倫理委員会にて承認された。プロトコールについては日本原子力研究所の施設利用協議会ならびに医療照射専門部会で承認を受けた。患者適格性は組織学的に証明された anaplastic astrocytoma または glioblastoma で、年令 18-70 才、Karnofsky Performance Scale (KPS) 50%以上、過去に放射線治療・化学治療が行われていない、増強 MR 上の腫瘍辺縁が脳表から 6 cm 以内といった条件を満たすものである［1］。対象となる患者は 1 例ごとに筑波大学内の放射線治療検討会で適応について検討し、治療計画を医療照射専門部会委員に提示し、承認を得た。

2．治療の手順

患者はまず通常の初回手術において病巣の可及的全摘出を行った．中性子捕捉療法の際には照射に用いる硼素化合物 BSH は BNCT 照射開始予定時刻の 12 時間前から点滴静注した。当日は全身麻酔下に照射のための開頭手術を行い、開頭術野での照射中測定による熱中性子フラックス値と全血中 ^{10}B 濃度をもとに算出した血管硼素線量に対し，正常脳の耐容血管硼素線量 10.8 Gy を基準として照射時間を決定した．開頭術野を除く部分はフッ化リチウムサーモプラスチックを用いて熱中性子を遮蔽した．照射終了後は閉頭手術を行い，病院に搬入して術後管理を行った。

【治療結果の中間分析】

1999年10月より2002年7月までにJRR-4混合ビームを用いて開頭 BNCT を行ったのは

日本原子力研究所東海研究所、JRR－4 号炉、生物に対する放射線効果

anaplastic astrocytoma (AA) 4 , glioblastoma(GBM) 5 の初発例計 9 例で，年令は平均 51.6 才(20-66)，男性 3 名、女性 6 名であった。K.P.S.は 80-100 の症例が多く、Case 4 は治療直前に DIC を併発していたため 40 であった。用いた硼素物理線量(α線量)は一回照射で 10.8 Gy であり、各症例の照射条件によって多少の違いはあるがγ線量(7.4 Gy)と陽子線等の線量も含まれる。診断確定後の平均観察期間は 17.7 ヶ月(3.3-33.8)で、9 例中 4 例が生存し観察中である．治療後 6 ヶ月の MR 上の最大反応では Case 8 が播種性に再発し進行したのに対し、4 例で縮小が認められ、画像上腫瘍の残存がなかった 4 例で不変のまま経過した。再発を認めたのは 5 例(Case 3,4,5,6,8)で、うち Case 4 は生存、Case 3 を除く 3 例が再発で死亡した．再発形式は局所再発が 1 例、遠隔または播種性再発が 4 例であった．解析時点で 9 例中 3 例(Case 1,2,5)に放射線壊死および動眼神経麻痺(Case 5 では一過性)が認められた．生存期間中央値は GM で 15.4 M、AA で 16.0 M である。

【考察】

生存期間および生存率の算定については観察期間が短く，症例も少ないため現時点での評価は困難であるが、治療に対する早期反応については治療直後に播種性再発をきたした Case 8 を除き不変または縮小が見られている．glioblastoma の放射線治療では治療線量の増加により生存期間の延長が認められているが，70 - 80 Gy の高線量が照射された場合でも，照射野中心部から再発することが示されている [2]．X 線に陽子線を併用した 90 Gy までの dose escalation では，局所制御率および生存期間中央値が改善される一方で，辺縁部分での再発や放射線壊死を高率に認めた [3]．術中 BNCT で得られる腫瘍線量はこれを上回るものと考えられており、治療早期の局所反応はその結果と考えられる．

熱外中性子を取り入れた現在の熱・熱外混合中性子ビームによる BNCT では深部の線量分布が増加する一方、従来の熱中性子ビームでは一般的でない N. III や N. VI の障害が見られた．通常 BNCT では硼素薬剤濃度の低い正常組織は障害されにくいとされているが、高硼素薬剤濃度の血液を含む海綿静脈洞部での中性子分布が増加することでこれらの障害が発生する可能性が考えられる．進達度の低い従来の熱中性子ビームでは、脳表の線量を実測することで照射条件が決定されたが、この方法は現在行っている熱・熱外混合中性子ビームの BNCT でも用いられている．熱外中性子を含むビームでは、BNCT で発生する複数の放射線(硼素線量、γ線量、窒素線量、速中性子線量)と開頭術野の複雑な形状による複雑な線量分布[4]を高い精度でシミュレーションすることが重要であり、現在線量計画・位置決めシステムの検証を行っている[5]．

今後の方針としてはまず線量計画・位置決めシステムを用いて純粋な熱外中性子用いた臨床治験を開始してその安全性・効果を検証する。

さらに将来的には BNCT を boost 照射として位置付けて他の放射線治療と併用する方法や、硼素薬剤の改良によって治療効果が改善することが望まれる。ガドリニウム化合物との併用などは動物実験レベルである程度実用化できるのではないかと考えている[6]。

1. Matsumura A, Shibata Y, Yamamoto T,

日本原子力研究所東海研究所、JRR－4 号炉、生物に対する放射線効果

Yamada T, Fujimori H, Nakai K, Nakagawa Y, Hayakawa Y, Issiki M, Nose T: The University of Tsukuba BNCT research group: first clinical experiences at JAERI. In: **Advances in Neutron Capture Therapy-Vol.1 Medicine and physics**, Larsson, Crawford and Weinreich ed., Elsevire, pp46-50, 1997.

2. Lee SW, Fraass BA, Marsh LH, Herbort K, Gebarski SS, Martel MK, Radany EH, Lichter AS, Sandler HM: Patterns of failure following high-dose 3-D conformal radiotherapy for high-grade astrocytomas: a quantitative dosimetric study. **J Radiat Oncol Biol Phys** 43: 79-88 1999.
3. Fitzek MM, Thornton AF, Rabinov JD, Lev MH, Pardo FS, Munzenrider JE, Okunieff P, Bussière M, Braun I, Hochberg FH, Hedley-Whyte ET, Liebsch NJ, Harsh IV GR: Accelerated fractionated proton/photon irradiation to 90 cobalt gray equivalent for glioblastoma multiforme: results of phase II prospective trial. **J Neurosurg** 91: 251-260, 1999.
4. Yamamoto T, Matsumura A, Yamamoto K, Kumada H, Shibata Y, Nose T: In-phantom two-dimensional thermal neutron distribution for intraoperative boron neutron capture therapy of brain tumours. **Phys. Med. Biol.** 47 (21 July 2002) 2387-2396
5. Kumada H, .Torii Y, Saito K, Yamaguchi Y, Matsumura A, Nakagawa Y, Sakurai F: The development of a computational dosimetry system for BNCT at JAERI. In Hawtrhrone et al. eds, **Frontiers in Neutron Captuer Therapy Vol.1**, Kluwer Academic/Plenum Publishers, New York, pp611-614, 2001.
6. Zhang T, Matsumura A, Yamamoto T, Yoshida F, Nose T, Shimojo N: Comparison of two Brain Tumor-Localizing MRI Agents : GD-BOPTA and GD-DTPA .-The study of Magnetic Resonance Imaging and Inductively Coupled Plasma Atomic Emission Spectroscopy with Rat Brain tumors-. **AJNR Am J Neuroradiol** 23: 15-18, 2002.

7-8

低温核偏極による局在モーメントと交換相互作用の研究
A Study of Exchange Interactions Between Localized Moments by Low Temperature Nuclear Orientation

西村　克彦（富山大工），大矢　進（新潟大理），大坪　隆（新潟大理）、泉川　卓司（新潟大RI），武藤　豪（高エネ研），川村　淑恵（新潟大自然），佐々木　恵（新潟大自然）
K. Nishimura (Toyama Univ.), S. Ohya (Niigata Univ.), T. Ohtsubo(Niigata Univ.), T. Izumikawa (Niigata Univ.), S. Muto (KEK), Y. Kawamura (Niigata Univ.), M. Sasaki (Niigata Univ.).

1．研究の目的と意義

磁気異方性（magnetic anisotropy）は磁性研究における重要なテーマであり，特に磁性材料の開発研究における主テーマといえる。$Nd_2Fe_{14}B$（ネオマックス）は広く利用されている強磁性材料である。$Pr_2Fe_{14}B$ は $Nd_2Fe_{14}B$ を上回る磁気異方性を持っており、擬三元系 $(Pr_xNd_{1-x})_2Fe_{14}B$ の多くの研究がある。しかしPrとNdの交換相互作用やそれらの磁気異方性の解明は一般的な磁性研究手段では難しい[1]。

この研究の目的(1)は，放射性同位元素をプローブとする低温核偏極法(LTNO)により，多重磁性イオンを含む（反）強磁性化合物における異種磁性イオン間の交換相互作用や個別の磁気構造を調べることである。研究の意義は，新しい磁性研究手段を確立すること。また，新しい機能を持った磁性材料を開発するのに重要な情報を提供することである。

強磁場と低温により偏極した核の核磁気共鳴法(BF-NMRON)は，放射線検出の検出感度とNMRの測定精度を兼備し，超微細相互作用の大変有効な研究手段である[2]。この実験手段を用いると，例えばNbとCuのようにほとんど固溶しない希薄合金における核緩和過程を研究できる。しかし，実験手法が難しく，過去に3例の報告があるのみである。近年ナノ構造材料が開発されてきており，BF-NMRONのようなppmオーダーの元素濃度と合金元素の幅広い組合せに適した微視的磁性研究手段を本邦において確立することが目的(2)である。その意義は，新しい極希薄合金における超微細相互作用の情報を提供できること。

2．研究の方法と結果

2.1　LTNOによる $RENiAl_4$ の磁気異方性研究

「擬三元系希土類化合物 $(Pr_xNd_{1-x})NiAl_4$ におけるPr－Nd交換相互作用とそれらの磁気異方性」を研究テーマとして，多重磁性イオンを含む反強磁性化合物のLTNO実験をした。$RENiAl_4$（RE：希土類元素）は，$YNiAl_4$ 型の斜方晶の結晶構造を持つ[3]。$PrNiAl_4$ や $NdNiAl_4$ の単結晶試料を用いた磁性研究から，結晶異方性を反映した大きな磁気異方性が報告されている[3-5]。

この研究に使用した単結晶は，高周波炉を用いた回転引上げ法（Cz法）により作成した。原材料は純度3Nの希土類元素と4Nのニッケルである。タングステン坩堝を使用し，約0.5気圧のアルゴンガス雰囲気中で育成した。結晶方位はX線ラウエ法により決定した。試料の整形は放電カッターで行った。

$PrNiAl_4$ は，ネール温度が8.4Kで，a軸が磁化容易軸である。温度2K，外部磁場約3Tで，a軸の磁化で磁気転移が観測される。7Tで磁化は $M_s^a(Pr) = 2.68\,\mu_B$ であり，Pr^{3+} イオンの飽和磁気モーメント $3.20\,\mu_B$ の約85%である。b軸，c軸とも磁化困難軸であり，$M_s^b(Pr) = 0.21\,\mu_B$ である。SQUIDによる磁化の測定結果をFig. 1a示した。中性子回折実験により磁気構造が調べられており，伝播ベクトルは(010)と報告されている[3]。

Fig. 1bは，$NdNiAl_4$ の磁化測定結果で，ネール温度が9.5K，b軸が磁化容易軸であり，約4.2Tで磁気転移する。外部磁場7Tでb軸の磁化は $M_s^b(Nd) = 1.8\,\mu_B$ であり，Nd^{3+} の飽和磁気モーメント $3.27\,\mu_B$ の約半分である。7Tでa軸の磁化は $M_s^a(Nd) = 1.15\,\mu_B$ である。

研究施設・装置：JRR-3M 水力照射孔　　研究分野：核物性，固体物理、核物理

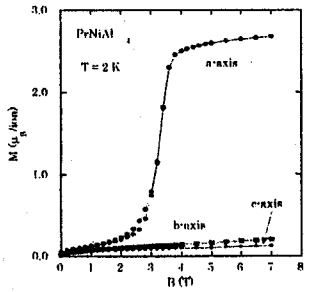


Fig.1a Magnetzation of $PrNiAl_4$ at 2 K.

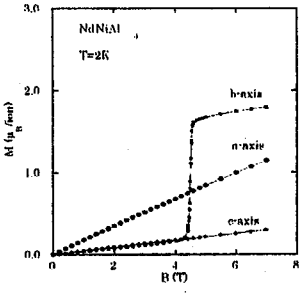


Fig.1b Magnetzation of $NdNiAl_4$ at 2K

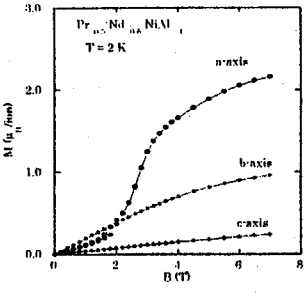


Fig.1a Magnetzation of $Pr_{0.5}Nd_{0.5}NiAl_4$ at 2K

Pr と Nd を混合した $Pr_{0.5}Nd_{0.5}NiAl_4$ では，ネール温度は，5.7K に下降する。Fig. 1c に示すように，磁化は a 軸だけで磁気転移を示す。外部磁場 7T での磁化は，$M_s^a=2.16\mu_B$，$M_s^b=0.97\mu_B$ である。これらの値は，a 軸で $[M_s^a(Pr)+M_s^a(Nd)]/2=1.9\mu_B$ より少し大きい。b 軸では $[M_s^b(Pr)+M_s^b(Nd)]/2=1.0\mu_B$ とほぼ等しい。磁化測定でわかるのはここまでである。Pr や Nd イオンの個別の磁気構造に関する情報は得られない。また，a 軸や b 軸の磁化に，Pr と Nd のモーメントがどのように寄与するのかわらない。

$Pr_{0.5}Nd_{0.5}NiAl_4$ 中における Pr と Nd の個別の磁気構造を調べるために LTNO の実験をした。実験試料は，磁化測定に使った試料を，a, b, c 軸に沿って，サイズ 3x2x0.1mm 程度に整形したものである。それを原子炉からの熱中性子で 10 分間程度照射し，^{142}Pr と ^{147}Nd を生成した。

偏極した放射性原子核から放出されるγ線の放射角度分布は，

$$W(\theta)=1+f\sum_{\lambda=2,4}U_\lambda A_\lambda B_\lambda Q_\lambda P_\lambda(\cos\theta)$$

で記述する[6]。$W(\theta)$をγ線異方性と呼ぶ。この実験では，偏極していないγ線計数率で規格化した偏極状態のγ線計数率を表す。$W(\theta)$は0より大きな実数値であり，核偏極度が無い場合は1になる。$0<W(\theta)<1$ の場合を負のγ線異方性，$1<W(\theta)$を正のγ線異方性と呼ぶことにする。$U_\lambda A_\lambda$は放射の多重極度に依存したパラメータである。Q_λは使用した検出器の立体角補正のパラメータ。整列パラメータ B_λは，温度や超微細相互作用定数の関数であり，核偏極度を表す。パラメータ P_λはルジャンドル関数であり，角度θは核偏極方向とγ線の放射方向の成す角度である。γ崩壊はパリティを保存する過程であるので，λが奇数の項は現れない。つまり $W(\theta)$は，強磁性状態と反強磁性状態の核偏極を区別しない。よって，磁気転移がメタ磁性転移である場合外部磁場を変化させると磁化では大きな変化が観測されるが，$W(\theta)$は連続である。

Fig. 2a に ^{142}Pr の簡略化した核崩壊図を示した[7]。^{142}Pr は半減期が 19.2h でβ崩壊し，^{142}Nd の励起状態から 1576keV のγ線を放射する。核偏極させるのは ^{142}Pr の基底状態で，その核偏極状態をγ線の $W(\theta)$ で観測する。1576keVγ線の $W(\theta)$を，温度をパラメータとして描くと Fig. 2b のようになる。計算では，Pr^{3+}自由イオンに対する超微細磁場の計算値 $B_{HF}=337T$[8]が ^{142}Pr の核磁気モーメント$\mu=0.234\mu_N$ [7]

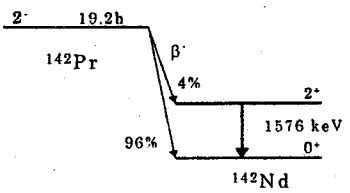


Fig.2a Simplified decay scheme of ^{142}Pr.

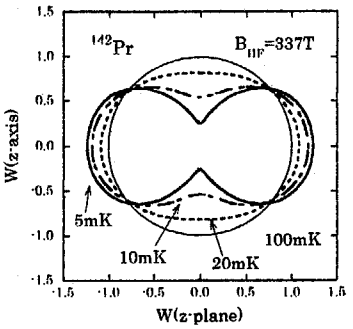


Fig.2b Calculated γ-ray anisotropy of ^{142}Pr..

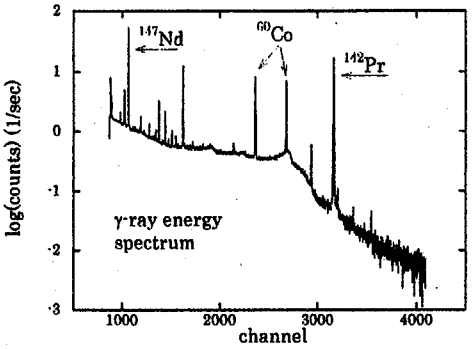


Fig.2c γ-ray energy spectrum of ^{142}Pr, ^{147}Nd, ^{54}Mn, ^{60}Co.

に作用するとした。偏極度が増すと核スピン方向の計数率が減少し，垂直方向の計数が増加する。

Fig. 2c はγ線のエネルギースペクトルである。^{147}Nd の 531keV ピーク，^{142}Pr の 1576keV ピーク，他に ^{60}Co (hcpCo) や ^{54}Mn (Ni) 核温度計から放出されたピークもある。

LTNO 実験は新潟大学理学部とニュー・サウス・ウェールズ大学（キャンベラ）の ^{3}He/^{4}He 希釈冷凍機を用いて行った。

Fig. 3a は，$Pr_{0.5}Nd_{0.5}NiAl_4$ 中における ^{142}Pr と ^{147}Nd の $W(\theta)$の温度依存性である。外部磁場を a 軸方向に 1 T 印加した。温度が下がるに従い核偏が進行し，^{142}Pr の $W(\theta)$は，a 軸方向（Pr//a）で負のγ線異方性（$W(\theta)<1$）を示し，b 軸方向（Pr//b）で正のγ線異方性（$W(\theta)>1$）を示している。この結果は，Pr のモーメントが，a 軸方向に整列していることを示している。^{147}Nd の $W(\theta)$も ^{142}Pr と同様に変化しており，Nd のモーメントも a 軸方向に整列していることがわかる。

Fig. 3 b は，$Pr_{0.5}Nd_{0.5}NiAl_4$ 中における ^{142}Pr と ^{147}Nd の $W(\theta)$の磁場依存性である。外部磁場を a 軸方向に印加した。^{142}Pr の $W(\theta)$は，磁気転移が起こる磁場 3T 前後であまり変化していない。a 軸方向の Pr//a は負のγ線異方性（$W(\theta)<1$）を示し，b 軸方向の Pr//b は正のγ線異方性（$W(\theta)>1$）を示している。この結果は，Pr のモーメントが，a 軸方向に整列していることを示している。つまり，Pr のモーメントはメタ磁性転移をしていると考えられる。

一方，^{147}Nd の $W(\theta)$は，外部磁場の掃引にともない大変大きな変化を示す。a 軸の $W(\theta)$は，低磁場側と

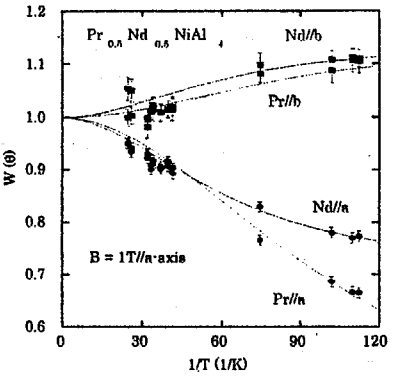


Fig.3a Temperature dependence of γ-ray anisotropies, $W(\theta)$, of oriented ^{142}Pr and ^{147}Nd in $Pr_{0.5}Nd_{0.5}NiAl_4$ single crystal.

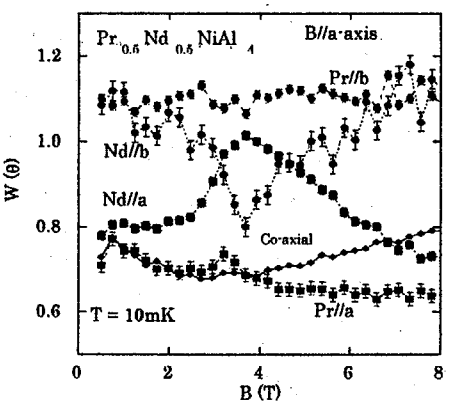


Fig.3b Field dependence of γ-ray anisotropies, $W(\theta)$, of oriented ^{142}Pr and ^{147}Nd in $Pr_{0.5}Nd_{0.5}NiAl_4$ single crystal at 10 mK.

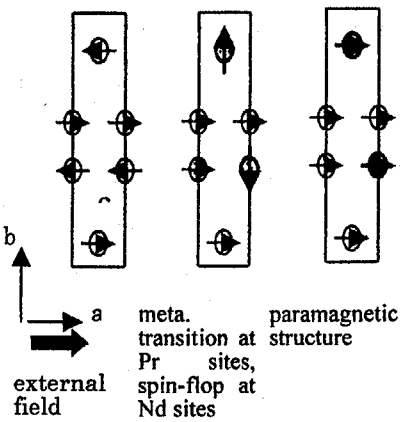


Fig.3c Magnetic structure at fields, before, during and after the magnetic phase transition.

高磁場側で $W(\theta)<1$ であり，磁気転移付近で $W(\theta)>1$ になる。b 軸の $W(\theta)$は，これと反対の振る舞い

をしてる。この変化は，スピンフロップ磁気転移により説明できる。

初めNdのモーメントは，Prのモーメントとの交換相互作用で，a軸に整列している。Prの磁気構造は，b面に平行な面内で強磁性的配列で，最近接面間で反強磁性的である。(Fig. 3c参照)Prのモーメントがメタ磁性転移をすると，Ndのモーメントに作用していた面間の反強磁性的な交換相互作用の方向が反転し，面内の強磁性的な交換相互作用と競合することになる。結果的に，Pr－Ndの交換相互作用は弱められ，Ndのモーメントは自身の磁化容易軸であるb軸方向へ整列するものと思われる。さらに外部磁場を増すとNdのモーメントは外部磁場との相互作用で回転する。

2.2 BF-NMRONによる^{110m}Agの核緩和

BF-NMRONによる核緩和時間の測定は，過去にAg中の^{110m}Agの1例報告されているのみである[9]。新潟大学理学部では，希釈冷凍機に新たに12Tの超伝導磁石を設備し，BF-NMRONの測定システムを構築している。

この測定手段で観測される放射性原子核の核磁気共鳴周波数は，主に外部磁場に支配される。よって，外部磁場強度を正確に校正することが重要である。そこではじめに磁場強度の校正のため，BF-NMRONの共鳴周波数と核緩和時間が報告されている^{110m}Ag(Ag)の実験を計画した。実験試料は厚さ3μm程度のAg箔を原子炉からの熱中性子で1週間照射して^{110m}Ag生成した。

Fig. 4aはBF-NMRONの共鳴スペクトルである。縦軸は^{110m}Agのβ崩壊後に放射される658，764，885，937keVγ線の計数の和，横軸はRF磁場周波数である。共鳴中心周波数は54.64MHzであり，外部磁場が11.922(2)Tであることがわかった。

RF磁場を共鳴周波数に合わせていったん^{110m}Ag核を共鳴状態にしてから，RF磁場を切ると，核緩和過程が観測される。Fig. 4bはその緩和過程の曲線である。指数関数で解析した結果緩和時間を98(57)sと得た。これは過去の報告結果と一致する。試料温度は10(1)mKである。^{109}Agの NMR測定の結果と比較するため核g因子で規格化した$(T_1Tg^2)^{-1}$を計算した。^{110m}Agで$(T_1Tg^2)^{-1}=2.8(1.9)$[1/Ks]，^{109}Agで$(T_1Tg^2)^{-1}=1.6(0.2)$[1/Ks]であり，誤差内で一致する。

3．結果の評価と今後の方針

LTNOによるRENiAl4の研究を通じ，「多重磁性イオンを含む反強磁性化合物において希土類イオンは，固有の磁気構造と磁気異方性を持つ」場合があることがわかった。このような情報はユニークであり，LTNOが磁性研究における新しい実験手段になることがわかる。今後は$(Pr_xNd_{1-x})_2Fe_{14}B$のような実用材料の基礎的研究に応用していきたい。

BF-NMRONによる核緩和やナイトシフトの研究は，^{90}Nb(Cu)，^{90}Nb(Nb)，^{96Tc}(Nb)，^{101m}Rh(Cu)などでも行われた。NbのCuに対する固溶濃度は0.1%以下であり，一般のNMRデータがなく，貴重なデータと考える。合金材料に微量に添加されている元素の微視的

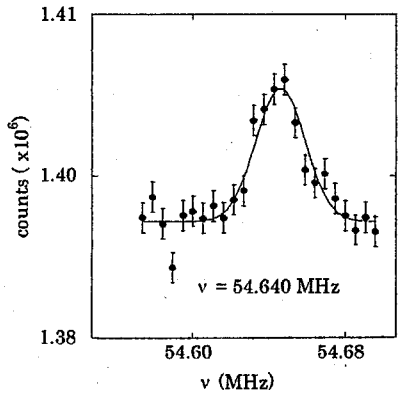


Fig. 4a BF-NMRON resonance spectrum of ^{110m}Ag in Ag at 10 mK

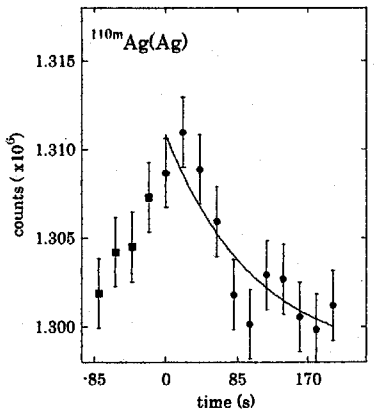


Fig. 4b BF-NMRON relaxtion curve of ^{110m}Ag in Ag with a field of 11.922T at 10 mK.

研究手段として応用していきたい。

以上，この研究の目的は達成されたが，今後も同様の研究を継続し磁性に関するユニークな研究成果を公表するとこが重要であると考える。

［参考文献］

[1] Y. Yu et al., J. Magn. Magn. Mater. 221 (2000) 382.
[2] W. Brewer and M. Kopp, Hyperfine Interact,, 2 (1976) 299.
[3] T. Mizushima et al., J. Phys. Soc. Japan 66 (1997) 3970.
[4] T. Mizushima et al., J. Phys. Soc. Japan 68 (1999) 637.
[5] T. Mizushima et al., J. Magn. Magn. Mater. 140-144 (1995) 925.
[6] K.S. Krane, in *Low-Temperature Nuclear Orientation*, eds. N.J. Stone and H. Postma, (North-Holland, Amsterdam, 1986) Ch.2.
[7] R. B. Firestone and V. S. Shirley, "Table of Isotopes", eighth edition, (Wiley Interscience, New York, 1996) Appendix.
[8] B. Bleaney, in *Magnetic Properties of Rare Earth Metals*, ed. R.J. Elliott, Ch.8(Plenum: New Ypork, 1972)
[9] W.D. Hutchison et al., Hyperfine Inter. 75 (1992) 253.

成果の公表

学会発表

・西村克彦，森克徳，大矢進，W. D. Hutchison, D. H. Chaplin, “低温核偏極による RNi 中の Pr, Nd, Pm の磁気構造”，1999 年 3 月，広島，日本物理学会第 54 回年会

・大矢進，大坪隆，出淵善智，後藤淳，西村克彦，武藤豪，“外部強磁場 NMR-ON による ^{90}Nb 及び ^{101m}Rh の磁気モーメント”，1999 年 9 月，島根，日本物理学会秋の分科会

・西村克彦，森克徳，石川義和，大矢進，W.D. Hutchison, S.J. Harker, D.H. Chaplin, “低温核偏極法による多重希土類磁性イオンの磁気構造”，2000 年 3 月，大阪，日本物理学会春の分科会

・西村克彦，森克徳，石川義和，大矢進，W.D. Hutchison, D.H. Chaplin, “低温核偏極による $RENiAl_4$ のメタ磁性”，2000 年 9 月，新潟，日本物理学会第 55 回年会

・大矢進，佐藤洋恵，川村淑恵，山口由高，加藤智美，佐藤光彦，泉川卓司，後藤淳，武藤豪，西村克彦，“BF-NMRON を用いた ^{95,96}Tc, ^{106m,110m}Ag の Bohr-Weisskopf 効果の研究”，2000 年 9 月，新潟，日本物理学会第 55 回年会

・後藤淳，川瀬洋一，大久保嘉高，谷口秋洋，谷垣実，大矢進，佐藤洋恵，川村淑恵，“^{147}Nd の核整列実験”，2001 年 3 月，東京，日本物理学会第 56 回年会

・西村克彦，大矢進，川村淑恵，佐藤洋恵，“低温偏極核の核磁気共鳴法による 4d 金属の K シフトと緩和”，2001 年 9 月，徳島，日本物理学会秋季大会

・大坪隆，川村淑恵，佐々木恵，渡辺茂夫，鈴木守，佐藤憲司，佐藤功，大矢進，泉川卓司，武藤豪，西村克彦，“^{48}Sc の磁気モーメントおよび ScFe 系の NMR-ON”，2002 年 3 月，滋賀，日本物理学会第 57 回年会

・後藤淳，大矢進，大坪隆，川村淑恵，佐々木恵，武藤豪，西村克彦，谷垣実，谷口秋洋，大久保嘉高，川瀬洋一，“強磁性体中の希土類原子核の NO 及び NMR-ON”，2002 年 3 月，滋賀，日本物理学会第 57 回年会

学術雑誌

・S. Ohya, H. Sato, T. Izumikawa, J. Goto, S. Muto, K. Nishimura, 'Hyperfine anomalies of ^{95}Tc-^{96}Tc and ^{106}Ag^{m}-^{110}Ag^{m} using brute-force nuclear magnetic resonance on oriented nuclei', Phys. Rev. C63 (2001) 044314.

・K. Nishimura, W.D. Hutchison, D.H. Chaplin, T. Yasukawa, K. Mori, Y. Isikawa, S. Ohya, S. Muto, 'Low-temperature nuclear orientation studies of metamagnetic of (RE)$NiAl_4$ single crystals', J. Magn. Magn. Mater. 226-230 (2001) 1126.

・S. Ohya, Y. Izubuchi, J. Goto, T. Ohtsubo, S. Muto, K. Nishimura, 'Brute-force NMR-ON on ^{90}NbCu, ^{101m}RhCu and ^{110m}AgAg', Hyperfine Interactions 133 (2001) 105.

・K. Nishimura, W.D. Hutchison, D.H. Chaplin, S.J. Harker, K. Mori, S. Ohya, 'Nuclear orientation studies of magnetism in single crystal $Pr_{0.5}Nd_{0.5}Ni$', Hyperfine Interactions 133 (2001) 121.

・K. Nishimura, S. Ohya, Y. Kawamura, T. Ohtsubo, T. Izumikawa, S. Muto, K. Mori, 'Nuclear spin relaxation of extremely dilute impurities using brute-force NMRON', J. Phys. Soc. Japan, 71(2002)1589.

・K. Nishimura, S. Ohya, Y. Kawamura, T. Ohtsubo, T. Izumikawa, S. Muto, 'Knight shifts of ^{90}Nb, ^{93m}Mo, ^{96}Tc, and ^{101m}Rh in Nb using Brute-Force NMRON', Hyperfine Interactions (in press).

7-9

内部起源粒子線による石英中の常磁性格子欠陥の生成効率の研究

Paramagnetic lattice defects in quartz created by internal alpha and alpha recoil particles

豊田　新　岡山理科大学理学部

Shin Toyoda

Faculty of Science, Okayama University of Science

(1) はじめに

電子スピン共鳴年代測定は、第四紀と呼ばれる、人類が発生し、発展してきた、最近約200万年間の時代の年代測定法として注目され、サンゴ、鍾乳石、テフラ、断層粘土、化石の歯、骨、石膏などの試料に適用されてきた (Ikeya, 1993)。この方法は、自然放射線によって鉱物中に生成する熱的に安定な常磁性格子欠陥やラジカルが年代と共に蓄積することを利用している。すなわち、年代測定を行う試料のＥＳＲ信号強度を測定した後に、自然放射線による被曝を模擬した人為ガンマ線照射を行い、信号の生成効率を求めることにより、自然放射線による総被曝線量を求める。この値を別に求めた自然放射線による年間線量率で割って年代を算出する。

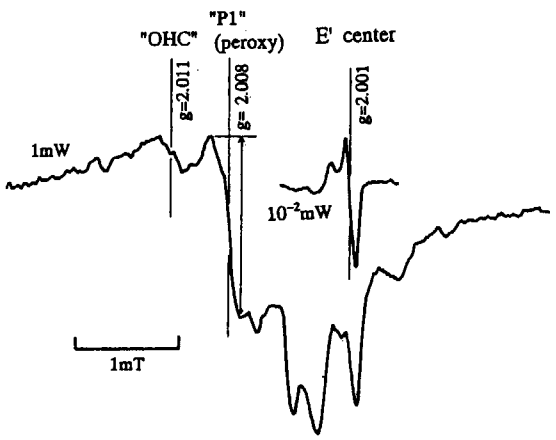


図１　花崗岩中の石英に見られる典型的なＥＳＲ信号。室温の測定で E_1 中心が観測される。

この年代測定法は信号の熱安定性から、その適用範囲が第四紀に限られるとされてきたが、花崗岩に含まれる石英中の酸素空孔に関連したＥＳＲ（電子スピン共鳴）信号（E_1 中心）の強度と、花崗岩の年代の間に相関があることが見出され (Odom and Rink, 1989)、ＥＳＲ年代測定が、第四紀だけでなく、10億年までの範囲で適用可能である可能性が示された。

筆者は、この E_1 中心とその前駆体である酸素空孔との関連を調べ、花崗岩中の石英についても珪素－珪素の結合が、ホール中心から供給されるホールを捉えることによってこの E_1 中心が生成することを示した。また、ガンマ線照射後300℃で15分間加熱することによって、酸素空孔の相対的な量を E_1 中心の信号強度として測定できることを提案した (Toyoda and Ikeya, 1991)。この方法を用いて、花崗岩の石英中の酸素空孔量と年代とによい相関があることを報告した (Toyoda et al., 1992; Toyoda et al., 1996)。

しかし、自然の花崗岩中の石英に生成する酸素空孔の生成過程については、微量に含まれるウラン、

コバルト60ガンマ線照射施設（高崎）
JRR-3　気送管
放射線とイオンビームによる物質構造の研究と改質

トリウム及びその娘核種からのアルファ反跳粒子のためか（Rink and Odom, 1991）、それとも外部からのベータ線、ガンマ線によって生成するのか（Toyoda et al., 1996）明らかではない。

(2)目的

アルファ反跳粒子によって石英中に酸素空孔が生成するとの立場では、酸素空孔の生成量を理論計算によって行っている（Rink and Odom, 1991）。しかし、この生成量が、実際にＥＳＲで、E_1 中心として測定される酸素空孔量と一致するのかどうか、明らかではない。本研究では、人為的にアルファ及びアルファ反跳核種を石英中に生成させ、これによってつくられる酸素空孔の量をＥＳＲによって実験的に測定しようとした。

(3)方法

石英内部からアルファ線及びアルファ反跳核種を放出させるため、ホウ素をドープした石英を、日本電波工業（株）に依頼して製作した。そして、自然の熱水作用で生成した石英とあわせ、15 種類の試料を準備した。これらの試料に熱中性子を照射すると、熱中性子が ^{10}B と下記の反応をすることで、アルファ粒子及びアルファ反跳粒子が内部で石英を照射することになる。

$$^{10}B + n \rightarrow {}^{4}He + {}^{7}Li$$

また、リチウムについても同様の次の反応があるのでこれについても考慮した。

$$^{6}Li + n \rightarrow {}^{4}He + {}^{3}H$$

照射後石英試料をＥＳＲ測定することにより、生成した酸素空孔量を知り、理論計算と比較する。

(4)試料

準備した試料中のホウ素の含有量を、熱中性子即発ガンマ線分析により定量した。また、各試料をフッ化水素酸で溶解後、ＩＣＰ質量分析計によりリチウムの含有量を測定した。結果を表１に示す。

表１　本研究で分析した石英試料中のホウ素及びリチウムの含有量（ppm）。

試料番号	リチウム濃度	ホウ素濃度
2	3.4	2.45
3	25.0	0.71
4	17.0	0.70
5	3.5	0.53
6	0.04	1.52
2037	14.1	2.33
11+x	14.1	1.25
11-x	16.4	0.71
11z	3.7	0.81
12+x	22.6	4.09
12-x	15.5	3.33
12z	2.3	0.46
13+x	40.5	7.81
13-x	32.8	6.58
13z	12.8	1.68

(5)熱中性子照射と ESR 測定

それぞれ粉末にした石英試料を、石英ガラス管あるいはアルミニウム管に封入し、原子炉 JRR-3 の気送管、PN-1 を使用して熱中性子照射を行った。熱中性子のフルーエンス率は、5.2×10^{13} n/cm^2 s で、10 分、30 分、60 分の照射を行った。

照射後十分時間をおいてから、試料を開封し、電気炉で 300℃で 15 分加熱を行った後に、各試料の ESR 測定を行った。日本電子製 RE-3X を用い、測定条件は、室温で、マイクロ波出力 0.01mW、磁場変調幅 0.1mT、g=2.001 付近の 5mT の幅の掃引とした。測定の時定数は、信号強度の大きさによって設定した拡大率に対応させ、0.1 から 1 秒、掃引時間は 4 分から 16 分とした。

観測された E_1 中心の信号のピーク値を測定し、測定時の信号の拡大率、試料の質量によって規格化した。試料の測定と同時にマンガンマーカーを測定したが、マーカーの信号強度は 3%程度しか変化しなかったので、各々の試料の測定に際して、感度に変

化はなかったものと判断した。

(6)酸素空孔生成量の理論計算

計算コード、TRIM（Ziegler, 1989）を用いて今回の実験条件で、アルファ及びアルファ反跳粒子の照射によって生成する酸素空孔の量を計算した。

核反応のエネルギーから、それぞれの粒子の運動エネルギーを計算した。TRIM の計算においては、それぞれ 500 個の粒子を入射させ、生成する酸素空孔の数を計算した。その結果、それぞれ 1 個あたり、0.841MeV の ^{7}Li で 102 個、1.473MeV の ^{4}He で 47 個、2.731MeV の ^{3}H で 23 個、2.049MeV の ^{4}He で 48 個生成することがわかった。

(7)結果と議論

実験の結果を図 2 に示す。横軸が TRIM によって計算された、10 分の熱中性子照射によって生成する酸素空孔量、縦軸がそれぞれの ESR 測定によって得られた E_1 中心の信号として測定されているはずの酸素空孔の量である。

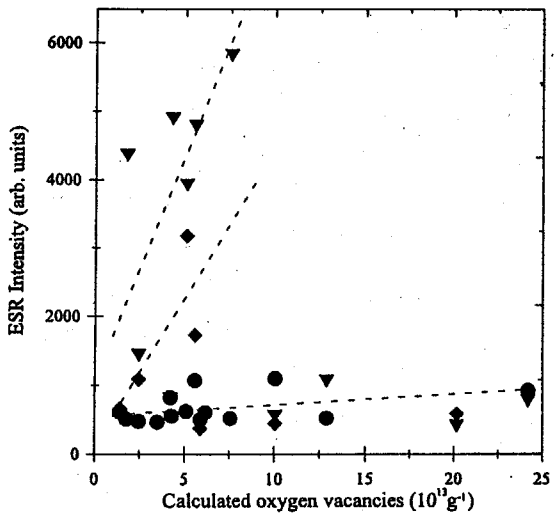


図 2　酸素空孔の生成量の計算値に対する、測定された E_1 中心の信号強度。●：10 分　◆：30 分　▼：60 分。破線はそれぞれ、最小二乗法によって得られた直線、ただし、30 分と 60 分のデータについては増加の傾向の見られる左の部分のデータのみにあてはめたものである。

理想的には、10 分、30 分、60 分のそれぞれの照射について、それぞれデータが直線上にのるはずであるが、残念ながらばらついた結果となってしまった。10 分のデータについては、多少右上がりの傾向が見て取れるが、30 分及び 60 分についてはむしろ酸素空孔が多く生成しているはずの試料で ESR 信号強度が小さくなっている。ただ、左の部分については増加の傾向が見て取れる。

予想に大きく反する結果が得られたのであるが、検討を重ねた結果、原因として次のようなことが考えられる。図 2 の右の酸素空孔が多く生成しているはずの試料は、ホウ素をより多く含んだ、人工水晶である。液体窒素温度での ESR 測定によって、石英中のアルミニウムがホールを捉えたアルミニウム中心の信号を測定してみると、これらの人工水晶では信号強度が小さく、図では左の方に示される自然の石英のほうでアルミニウム中心の信号強度は大きかった。石英中の E_1 中心は、酸素空孔にホールが捉えられて生成する。従って、人工水晶では純度が高く、不純物としてのアルミニウムの量が少なく、アルミニウム中心が生成しにくいため、加熱によって供給されるホールが十分でなく、酸素空孔が十分に生成していてもそれが全部 E_1 中心として ESR 測定で検出できなかった可能性がある。

筆者によって主張されてきた、酸素空孔の量を E_1 中心の信号強度として測定する方法（Toyoda and Ikeya, 1991）は自然の石英の、不純物であるアルミニウムを「十分に」含んだ石英を用いて提案されたものである。このような不純物の少ない人工水晶について、同様の現象が成立するのかどうか、検討が必要である。

自然の石英中の酸素空孔を用いることによって、花崗岩の年代測定のほか、石器の加熱温度の測定（Toyoda et al., 1993）、風成塵の起源の推定（Ono et al., 1998）など地球科学的に興味深い研究課題が多い。そうした意味で、自然の石英中の酸素空孔の生成過程の研究は重要であるが、この課題に取り組むためには、上に述べた基礎的な、酸素空孔と E_1 中心の信

号の生成との関係に戻って、再度検討を重ねなければならないと考えられる。

引用文献

Ikeya, M. (1993) New applications of Electron Spin Resonance, World Scientific, Singapore, 500p.

Odom, A. L. and Rink, W. J. (1989) Natural accumulation of Shottky-Frenkel defects: Implications for a quartz geochronometer, *Geology*, 17, 55-58.

Ono, Y., Naruse, T, Ikeya, M., Kohno, H., and Toyoda, S. (1998) Origin and derived courses of eolian dust quartz deposited during marine itope stage 2 in East Asia, suggested by ESR signal intensity, *Global Planet. Change*, 18, 129-135.

Rink, W. J. and Odom, A. L. (1991) Natural alpha recoil particle radiation and ionizing radiation sensitivities in quartz detected with EPR: implications for geochronometry, *Nucl. Tracks Radiat. Meas.*, 18, 163-173.

Toyoda, S. and Ikeya, M. (1991) Thermal stabilities of paramagnetic defect and impurity centers in quartz: Basis for ESR dating of thermal history, *Geochem. J.* 25, 437-445.

Toyoda, S., Ikeya, M., Morikawa, J. and Nagatomo, T. (1992) Enchancement of oxygen vacancies in quartz by natural external beta and gamma ray dose: a possible ESR Geochronometer of Ma-Ga range, *Geochem. J.* 26, 111-115.

Toyoda, S. and Ikeya, M. (1993) The use of electron spin resonance (ESR) for the determination of prehistoric lithic heat treatment, *Appl. Radiat. Isot.* 44, 227-231.

Toyoda, S. Rink, W. J., Schwarcz, H. P., and Ikeya, M. (1996) Formation of E_1' precursors in quartz: applications to dating and dosimetry, *Appl. Radiat. Isot.*, 47, 1393-1398.

成果の公表

学術雑誌

豊田新 (2001) 石英による電子スピン共鳴年代測定とその応用, ぶんせき, 315, 136-141.

S. Toyoda, W. J. Rink, C. Yonezawa, T. Kagami (2001) In-situ production of alpha particles and alpha recoil particles in quartz applied to ESR studies of oxygen vacancies, Quatern. Sci. Rev., 20, 1057-1061.

S. Toyoda and W. Hattori (2000) Formation and decay of the E_1' center and of its precursor, Appl. Radiat. Isot., 52, 1351-1356.

学会発表

S. Toyoda, ESR dating of quartz: Applications and issues, Third Asia-Pacific EPR/ESR Symposium (APES'01), Oct. 29-Nov. 1, 2001, Kobe University, Kobe, Japan.

S. Toyoda, T. Asai, and K. Komuro, The E_1' center and oxygen vacancies in quartz of uranium ore and their formation processes, International Symposium on New Prospects of ESR Dosimetry and Dating (ESRDD), Oct. 25-27, 2001, Osaka University, Osaka, Japan.

浅井貴之，豊田新，小室光世，堀川循正　粒子線によって石英中に生成する常磁性格子欠陥とカソードルミネッセンス　第16回ESR応用計測研究発表会　2000年12月2日　大阪大学

S. Toyoda, K. Komuro, and H. Isobe, A new tool to investigate the migration of radioactive elements in uranium ores: the ESR signal associated with oxygen vacancies in quartz. 2000 Western Pacific Geophysics Meeting, June, 27-30, 2000, Tokyo.

豊田新・浅井貴之　内部照射α線及びα反跳核種によって石英中に生成する酸素空格子　第15回ＥＳＲ応用計測研究会　1999年12月3-4日　岡山理科大学

豊田新　内部照射α線によって石英中に生成する格子欠陥　第8回原子力研究総合センターシンポジウム　1999年12月1日-2日　東京大学

豊田新・米澤仲四郎・加賀見俊彦・浅井貴之　内部照射α線によって石英中に生成するESR信号と年代測定　1999年度日本地球化学会年会　1999年9月29日－10月1日　工業技術院筑波共用講堂

S. Toyoda, W. J. Rink, T. Kagami, and C. Yonezawa, Paramagnetic defects in quartz created by internal alpha particles. 9th International Conference on Luminescence and Electron Spin Resonance Dating, Sep. 6-10, 1999, Complesso Monumentale del San Michele a Ripa in Trastevere, Rome, Italy.

研究テーマ：研究炉の高度化の技術開発
表　　題：JRR-4 を使ったホウ素中性子捕捉療法のためのマルチリーフコリメータの特性測定

7-10

Characteristic Measurements of the Multi-Leaf Collimator for Boron Neutron Capture Therapy at JRR-4

H.Kumada, T.Kishi, N.Hori, K.Yamamoto and Y.Torii
Japan Atomic Energy Research Institute, Tokai, Ibaraki, Japan

Summary

The Multi-leaf Collimator, which can form various beam outlet shapes for Neutron Capture Therapy, was developed in Japan Atomic Energy Research Institute. This collimator consists of stacked movable leaves, which are made of polyethylene mixed with LiF, in a set of 60. By sliding the individual leaves, a proper beam outlet shape can be formed for a particular patient. By applying the new collimator to NCT, an adequate dose can be delivered to the target region with minimized dose delivery in the healthy tissue outside the target field

Introduction

In the Neutron Capture Therapy (NCT), one of the primary concerns in irradiation is to deliver the highest possible dose to the target region while protecting the surrounding healthy tissues. Especially in epithermal neutron beam NCT, it is necessary to control the dose distribution in the radiation field because the high-energy neutron(epithermal to fast neutron) and secondarily-generated gamma-ray spread widely to the radiation field and surrounding tissues. In thermal neutron beam BNCT that has been performed in Japan, patient's head outside of the target region was covered with a thermo-plastic plate mixed with enriched Lithium (Li-helmet) in order to focus the radiation field, and to shield the surrounding healthy tissues. However, to perform the epithermal neutron beam NCT, alternative techniques and equipment were required to control the irradiation dose distribution inside/outside of the target region due to the Li-helmet's inability to shield the high-energy neutron. Thus the Multi-Leaf Collimator (MLC) for NCT, which can form various beam outlet shapes, was developed in JAERI. The MLC consists of a series of 60 movable leaves(the size of one leaf is 110×6×60mm), which are made of polyethylene mixed with LiF, stacked in layers, so that any proper shape of the beam outlet can be formed for a particular patient by sliding the individual leaves.Fig.1 shows the front view of the MLC.

In order to confirm the characteristic performance of the MLC, several experiments and calculations were carried out. This report describes the MLC performance and its applicability to actual NCT.

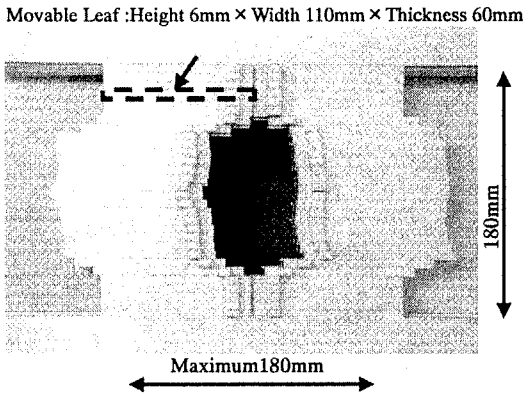


Fig.1 The front view of the Multi-Leaf Collimator.

Materials and Methods

To verify the MLC's characteristic performance, the results of experiments with the MLC were compared with the existing performance data of the conventional circular collimators, which have already been applied to the thermal neutron beam BNCT. Therefore, in the verification test, the MLC beam outlet was arranged to circular shapes, though the MLC is capable of forming a variety of beam outlet shapes. The beam spectrum in the experiments was set to ENB mode[1], which is scheduled to be applied in epithermal neutron beam BNCT in JRR-4. Thermal neutron flux and gamma-ray dose were measured around the beam outlet in free beam condition. Thermal neutron flux was measured by foil activation

method. For measurement of the beam performance, the gold foils or gold wires were positioned in the center of the aperture. And to confirm the shielding effect and the leakage level of the stacked leaves, the detectors were positioned on the surface of the leaves, including the boundary lines of individual leaves.

To verify its applicability to NCT, water phantom experiments were performed to measure thermal neutron flux distribution around the irradiation field. The gold wires were placed radially in the phantom to measure two-dimensional distribution of thermal neutron flux around the radiation field. In addition, several calculations using MCNP-4C were carried out in order to evaluate various beam outlet shapes and the high-energy neutron behavior.

Results and Discussion

In free beam condition, the maximum thermal neutron flux in the aperture of the MLC's outlet was 2.7×10^9 ($cm^{-2}sec^{-1}$). It is approximately 90% compared with the performance of the conventional collimator whose shape has been optimized for the neutron beam collimation. Thermal neutron flux, high-energy neutron flux and gamma-ray dose on the surface of the stacking leaves were less than 1/10 compared with the value in the aperture of the outlet. In the phantom experiments, the two-dimensional distribution of thermal neutron flux was comparable to the distribution of the conventional collimator beam, though the rate of the thermal neutron flux was reduced approximately by 15%.

Fig.2 shows a phantom experiment simulation calculated with MCNP-4C, in which the MLC beam outlet was arranged to "L" shape. The distribution of high-energy neutron flux on the surface of the MLC is shown in Fig.3. This result indicates that the high-energy neutron beam can be controlled correspondingly to the beam outlet shape of the MLC, and that the outlet shape influences distribution of thermal neutron flux in phantom.

These verification results prove that the MLC is able to shield the high-energy neutron outside the aperture, and it is able to make an essential dose distribution to the radiation region. And the MLC has a potential to deliver a proper dose distribution to a complex target field while suppressing the irradiation dose to surrounding critical organs and tissues by changing the outlet shape.

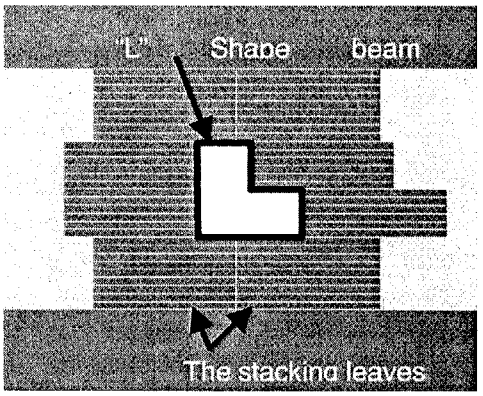


Fig.2 A simulation with MCNP-4C, in which the MLC beam outlet was arranged to "L" shape.

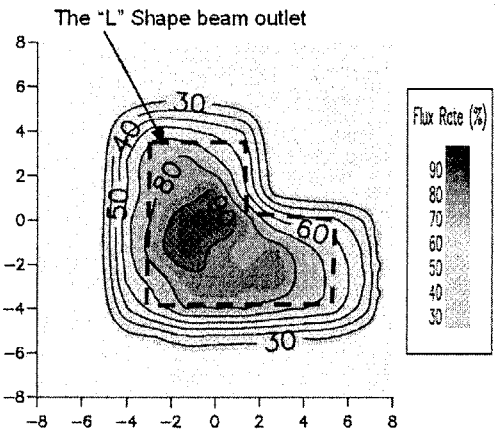


Fig.3 The high-energy neutron flux distribution on the surface of the MLC.

Conclusions

By applying the Multi-Leaf Collimator to NCT, proper dose delivery can be executed to the target region while minimizing the dose to surrounding healthy tissues.

Reference

1) K. Yamamoto et al., "Characteristics of Neutron Beam at JRR-4 for BNCT", Abstracts Ninth International Symposium on Neutron Capture Therapy for Cancer, Osaka, Japan, 2000, p243-244

研究テーマ：核破砕中性子源材料の開発

表題：　W/Ta固体ターゲットの開発

7-11

核破砕中性子源用 W/Ta 接合材の残留歪み

菊地賢司,皆川宣明,盛合敦,川合将義[1],古坂道弘[1],李敬鋒[2],栗下裕明[3]

原研　東海村

[1]高エネ研　つくば市大穂

[2]東北大　仙台市青葉区荒巻字青葉

[3]東北大　大洗町成田町

核破砕中性子源として開発したW/Ｔａ固体ターゲット接合部の残留歪みを測定した。Wは中性子源として優れているが、陽子・中性子による照射脆化、高温水や放射線下では腐食に弱く、被覆材Taで被って使う。WとＴａの間に隙間があると、核発熱するWの除熱が進まないので、熱抵抗となる隙間が無いように接合させて使用する。接合材をHIP製作するに当たり、温度、圧力をパラメータにしてＲ＆Ｄを実施した結果、再結晶化を防ぎ、拡散深さを大きくする点から、１５００℃、２０００気圧で３時間がベストとわかった。この条件で製作した接合強度を評価する目的で、接合境界部に残留している歪みを、中性子回折で測定した。接合モデル材は粉末から焼結したW、Ｔａであり、直径約１０mm、高さ４５mm、厚さ１mmのＴａ筒に、はめあいの精度に加工したＴａとWの円筒を半割にし、もとのＴａ筒に入れ、別のＴａの蓋をし、HIP処理してある。ＨＩＰ接合したW/Taの残留歪みを中性子回折で測定した（図１）。その結果、半径方向歪みはW側でやや引張り、Ｔａ側で引張り、円周方向歪みはW側、Ｔａ側とも同程度の引張りの残留歪みが残っていることが明らかになり、ターゲット伝熱接合界面の機械的状況がわかった。ターゲットはＫＥＮＳで中性子源としてすでに使用中である。

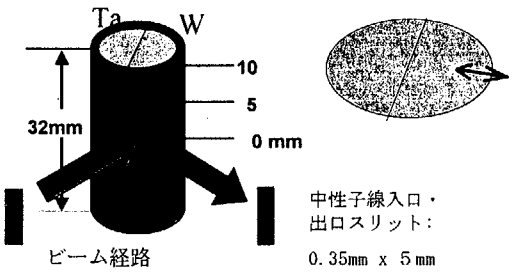


図1　W/Ta 接合材とビーム経路

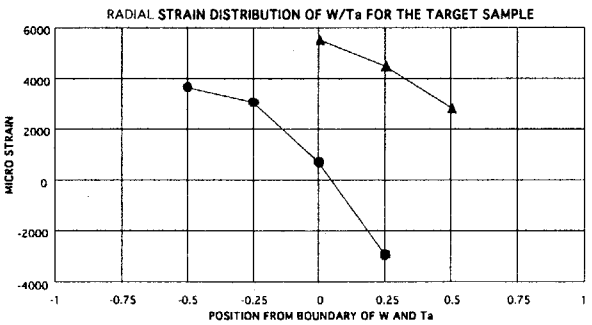


図2　半径方向歪みの測定例

3号炉、RESA、1-(1)

7-12

Research Theme: Basic and Clinical Study for Boron Neutron Capture Therapy
Title: Intraoperative Boron Neutron Capture Therapy using Thermal/Epithermal Mixed Beam

A Matsumura[1], T.Yamamoto[1], Y.Shibata[1], K.Nakai[1], Z.Tiang[1], A.Matsushita[1], S.Takano[1], K.Endo[1], K.Yamamoto[2], H.Kumada[2], Y.Torii[2], T.Mizutani[3], H.Takahashi[3], H.Toyooka[3], T.Nose[1]
Department of Neurosurgery[1] and Anesthesiology[3], University of Tsukuba, Ibaraki, Japan
Department of Research Reactor, Japan Atomic Energy Institute[2], Tokai, Ibaraki, Japan

INTRODUCTION

A new clinical phase I/II trial has been conducted for intraoperative boron neutron capture therapy (IOBNCT) using mixed thermal/epithermal neutron beam at Japan Atomic Energy Institute (JAERI). At JAERI, medical equipment such as operation room and remote anesthesia monitoring system has been implemented. The interim results of the clinical trial will be presented.

MATERIALS AND METHODS

From October 1999 to July 2001, 7 patients (4 glioblastoma; GBM, 3 anaplastic astrocytoma; AA) have been treated at JAERI with the new mixed neutron beam and IOBNCT. BSH (100mg/kg) were given 12hours prior to irradiation at JRR-4. In selected cases, the clearance of the blood boron concentration and tumor boron concentration were measured by administrating 1g BSH at the first debulking surgery.

RESULTS AND DISCUSSION

The initial response (including two complete response (CR), two partial response (PR)) was 100% in patients having macroscopic residual tumor. Including patients with no residual tumor on MRI, the effective rate was also 100%. Because the patient's number is small, it is too early to discuss about the final results. However, all the patients treated by IOBNCT showed better clinical survival if compared to RTOG classification by Curran (1993).

The median survival time (MST) in GBM was 19.8 months and 16.8 months in AA. There was one directly tumor related death among 7 cases. Other two patients died of pneumonia and pancytopenia 15.4 and 16.7 months after initial operation followed by BNCT, respectively. IOBNCT with mixed thermal/epithermal neutron beam provide better primary radiation effect than conventional therapy in selected cases.

There have been recurrent tumors outside the irradiation field in three cases, which may suggest the necessity of using more powerful beam such as pure epithermal beam to cover wider area of the clinical target volume with more irradiation dose.

1. Matsumura A, et al. Intraoperative boron neutron capture therapy using thermal/epithermal mixed beam. Research and Development in Neutron Capture Therapy, Sauerwein W, Moss R, Wittig A eds., Monduzzi Editore, Bologna, pp1073-1078, 2002
2. 松村　明、山本哲哉、柴田　靖ら：混合熱・熱外中性子を用いた悪性神経膠腫に対する中性子捕捉療法。田渕和雄、白石哲也編。ポストシークエンス時代における脳腫瘍の研究と治療。九州大学出版会、pp427-435, 2002.
3. Yamamoto T, Matsumura A, Yamamoto K, et al. : Comparison of patient brain dose measurements and the JCDS calculation. Research and Development in Neutron Capture Therapy, Sauerwein W, Moss R, Wittig A eds., Monduzzi Editore, Bologna, pp415-418, 2002
4. Nakai K, Matsumura A, Yamamoto T, et al.:Failure pattern in the patients who underwent intraoperative boron neutron capture therapy (IOBNCT). Research and Development in Neutron Capture Therapy, Sauerwein W, Moss R, Wittig A eds., Monduzzi Editore, Bologna, pp1135-1138, 2002

謝　辞

本報告書の発刊にあたり、多くの皆様から多大なご協力を頂きました。編集に際し、ご協力頂いた、東京大学物性研究所柴山充弘氏、東京大学原子力研究総合センター高野正美氏、研究炉部長小林晋昇氏、（現安全管理室長）、研究炉部次長中島照夫氏（現材料試験炉部長）に深く感謝致します。

付　録

Appendix

This is a blank page.

付 録

原研研究炉の利用設備一覧

１．ＪＲＲ－３Ｍ

１）実験設備

実 験 孔	実 験 装 置
１Ｇ	高分解能粉末中性子回折装置（ＨＲＰＤ）
１Ｇ－Ａ	生体高分子結晶構造解析用中性子回折計（ＢＩＸ－Ｉ）
２Ｇ	三軸型中性子分光器（ＴＡＳ－１）
３Ｇ	中性子トポグラフィ及び精密光学実験装置（ＰＮＯ）
４Ｇ	汎用三軸型中性子分光器（ＧＰＴＡＳ）
５Ｇ	偏極中性子散乱装置（ＰＯＮＴＡ）
６Ｇ	東北大学中性子散乱分光器（ＴＯＰＡＮ）
７Ｒ	中性子ラジオグラフィ装置（ＴＮＲＦ）
Ｔ１－１	中性子偏極回折装置（ＨＱＲ）
Ｔ１－２	単結晶中性子回折装置（ＫＳＤ）
Ｔ１－３	粉末中性子回折装置（ＨＥＲＭＥＳ） （ＫＰＤ）
Ｔ１－４－１	即発ガンマ線分析装置（ＰＧＡ）
Ｔ１－４－１Ａ	化学反応実験装置（ＬＣＥ）
Ｔ１－４－３	ＴＯＦ型中性子反射率計（ＴＯＦ）
Ｔ１－４－４	中性子ラウエ回折装置（ＬＡＵＥ）
Ｔ２－１	残留応力測定中性子回折装置（ＲＥＳＡ）
Ｔ２－２	中性子４軸回折装置（ＦＯＮＤＥＲ）
Ｔ２－３	中性子ＩＰ付生体物質中性子回折計（ＢＩＸ－Ⅱ）
Ｔ２－４	高分解能三軸型中性子分光器（ＴＡＳ－２）
Ｃ１－１	高エネルギー分解能三軸型中性子分光器（ＨＥＲ）
Ｃ１－２	二次元位置測定小角散乱装置（ＳＡＮＳ－Ｕ）
Ｃ１－３	超高分解能後方散乱装置（ＵＬＳ）
Ｃ２－１	冷中性子散乱実験デバイス開発装置（ＬＴＡＳ）
Ｃ２－２	中性子スピンエコー分光器（ＮＳＥ）
Ｃ２－３－１	冷中性子ラジオグラフィ装置（ＣＮＲＦ）
Ｃ２－３－２	即発ガンマ線分析装置（ＰＧＡ）
Ｃ２－３－２Ａ	化学反応実験装置（ＬＣＥ）
Ｃ２－３－４	ＴＯＦ型中性子反射率計（ＴＯＦ）
Ｃ２－３－５	中性子ラウエ回折装置(ＬＡＵＥ)
Ｃ２－３－６	中性子寿命測定装置（ＮＬＴ）
Ｃ２－３－７	パルス中性子機器開発装置（ＣＨＯＰ）
Ｃ３－１－１	高分解能パルス冷中性子分光器（ＡＧＮＥＳ）
Ｃ３－１－２	多層膜中性子干渉計／反射率計（ＭＩＮＥ）
Ｃ３－２	中性子小角散乱装置（ＳＡＮＳ－Ｊ）

2）照射設備

水力照射設備	HR－1，2
気送照射設備	PN－1，2
放射化分析用照射設備	PN－3
均一照射設備	SI－1
回転照射設備	DR－1
垂直照射設備	VT－1，RG－1～4 BR－1～4，SH－1

2．JRR－4

1）実験設備

プール
中性子ビーム設備
散乱実験設備
冷却水循環ループ
医療照射設備（BNCT）
即発ガンマ線分析装置

2）照射設備

簡易照射筒	Tパイプ（水力）
	Sパイプ
	Dパイプ
	Nパイプ
気送管照射設備	PN

国際単位系 (SI) と換算表

表 1　SI 基本単位および補助単位

量	名称	記号
長さ	メートル	m
質量	キログラム	kg
時間	秒	s
電流	アンペア	A
熱力学温度	ケルビン	K
物質量	モル	mol
光度	カンデラ	cd
平面角	ラジアン	rad
立体角	ステラジアン	sr

表 2　SI と併用される単位

名称	記号
分，時，日	min，h，d
度，分，秒	°，′，″
リットル	l，L
トン	t
電子ボルト	eV
原子質量単位	u

1 eV = 1.60218 × 10^{-19} J

1 u = 1.66054 × 10^{-27} kg

表 5　SI 接頭語

倍数	接頭語	記号
10^{18}	エクサ	E
10^{15}	ペタ	P
10^{12}	テラ	T
10^{9}	ギガ	G
10^{6}	メガ	M
10^{3}	キロ	k
10^{2}	ヘクト	h
10^{1}	デカ	da
10^{-1}	デシ	d
10^{-2}	センチ	c
10^{-3}	ミリ	m
10^{-6}	マイクロ	μ
10^{-9}	ナノ	n
10^{-12}	ピコ	p
10^{-15}	フェムト	f
10^{-18}	アト	a

表 3　固有の名称をもつ SI 組立単位

量	名称	記号	他の SI 単位による表現
周波数	ヘルツ	Hz	s^{-1}
力	ニュートン	N	$m \cdot kg/s^2$
圧力，応力	パスカル	Pa	N/m^2
エネルギー，仕事，熱量	ジュール	J	N·m
工率，放射束	ワット	W	J/s
電気量，電荷	クーロン	C	A·s
電位，電圧，起電力	ボルト	V	W/A
静電容量	ファラド	F	C/V
電気抵抗	オーム	Ω	V/A
コンダクタンス	ジーメンス	S	A/V
磁束	ウェーバ	Wb	V·s
磁束密度	テスラ	T	Wb/m^2
インダクタンス	ヘンリー	H	Wb/A
セルシウス温度	セルシウス度	℃	
光束	ルーメン	lm	cd·sr
照度	ルクス	lx	lm/m^2
放射能	ベクレル	Bq	s^{-1}
吸収線量	グレイ	Gy	J/kg
線量当量	シーベルト	Sv	J/kg

表 4　SI と共に暫定的に維持される単位

名称	記号
オングストローム	Å
バーン	b
バール	bar
ガル	Gal
キュリー	Ci
レントゲン	R
ラド	rad
レム	rem

1 Å = 0.1 nm = 10^{-10} m

1 b = 100 fm^2 = 10^{-28} m^2

1 bar = 0.1 MPa = 10^5 Pa

1 Gal = 1 cm/s^2 = 10^{-2} m/s^2

1 Ci = 3.7 × 10^{10} Bq

1 R = 2.58 × 10^{-4} C/kg

1 rad = 1 cGy = 10^{-2} Gy

1 rem = 1 cSv = 10^{-2} Sv

（注）

1. 表 1 − 5 は「国際単位系」第 5 版，国際度量衡局 1985 年刊行による。ただし，1 eV および 1 u の値は CODATA の 1986 年推奨値によった。
2. 表 4 には海里，ノット，アール，ヘクタールも含まれているが日常の単位なのでここでは省略した。
3. bar は，JIS では流体の圧力を表わす場合に限り表 2 のカテゴリーに分類されている。
4. EC 閣僚理事会指令では bar，barn および「血圧の単位」mmHg を表 2 のカテゴリーに入れている。

換　算　表

力	N(=10^5 dyn)	kgf	lbf
	1	0.101972	0.224809
	9.80665	1	2.20462
	4.44822	0.453592	1

粘　度　1 Pa·s(N·s/m^2) = 10 P(ポアズ)(g/(cm·s))

動粘度　1 m^2/s = 10^4 St(ストークス)(cm^2/s)

圧力	MPa(=10 bar)	kgf/cm^2	atm	mmHg(Torr)	lbf/in^2(psi)
	1	10.1972	9.86923	7.50062 × 10^3	145.038
	0.0980665	1	0.967841	735.559	14.2233
	0.101325	1.03323	1	760	14.6959
	1.33322 × 10^{-4}	1.35951 × 10^{-3}	1.31579 × 10^{-3}	1	1.93368 × 10^{-2}
	6.89476 × 10^{-3}	7.03070 × 10^{-2}	6.80460 × 10^{-2}	51.7149	1

エネルギー・仕事・熱量	J(=10^7 erg)	kgf·m	kW·h	cal(計量法)	Btu	ft·lbf	eV
	1	0.101972	2.77778 × 10^{-7}	0.238889	9.47813 × 10^{-4}	0.737562	6.24150 × 10^{18}
	9.80665	1	2.72407 × 10^{-6}	2.34270	9.29487 × 10^{-3}	7.23301	6.12082 × 10^{19}
	3.6 × 10^6	3.67098 × 10^5	1	8.59999 × 10^5	3412.13	2.65522 × 10^6	2.24694 × 10^{25}
	4.18605	0.426858	1.16279 × 10^{-6}	1	3.96759 × 10^{-3}	3.08747	2.61272 × 10^{19}
	1055.06	107.586	2.93072 × 10^{-4}	252.042	1	778.172	6.58515 × 10^{21}
	1.35582	0.138255	3.76616 × 10^{-7}	0.323890	1.28506 × 10^{-3}	1	8.46233 × 10^{18}
	1.60218 × 10^{-19}	1.63377 × 10^{-20}	4.45050 × 10^{-26}	3.82743 × 10^{-20}	1.51857 × 10^{-22}	1.18171 × 10^{-19}	1

1 cal = 4.18605 J（計量法）

= 4.184 J　（熱化学）

= 4.1855 J　（15 °C）

= 4.1868 J（国際蒸気表）

仕事率　1 PS（仏馬力）

= 75 kgf·m/s

= 735.499 W

放射能	Bq	Ci
	1	2.70270 × 10^{-11}
	3.7 × 10^{10}	1

吸収線量	Gy	rad
	1	100
	0.01	1

照射線量	C/kg	R
	1	3876
	2.58 × 10^{-4}	1

線量当量	Sv	rem
	1	100
	0.01	1

（86 年 12 月 26 日現在）

研究炉利用における研究成果集（平成13年度）

R100
古紙配合率100%
白色度70%再生紙を使用しています